Black Sea Journal of Engineering and Science

Volume 8 | Issue 5

ISSN: 2619 - 8991

BS Journals

BLACK SEA JOURNAL OF ENGINEERING AND SCIENCE

(BSJ ENGIN SCI)

Black Sea Journal of Engineering and Science (BSJ Eng Sci) is a double-blind peer-reviewed, open-access international journal published electronically 6 times (January, March, May, July, September, and November) in a year by since January 2018. It publishes, in English and Turkish, full-length original research articles, innovative papers, conference papers, reviews, mini-reviews, rapid communications or technical note on advances in a wide range of scientific disciplines from all fields of engineering and science and from any source.

ISSN 2619 - 8991

Phone: +90 362 408 25 15

Fax: +90 362 408 25 15

Email: bsjsci@blackseapublishers.com

Web site: http://dergipark.gov.tr/bsengineering

Sort of publication: Periodically 6 times (January, March, May, July, September, and November) in a year

Publication date and place: September 15, 2025 - Samsun, TÜRKİYE

Publishing kind: Electronically

PUBLISHER

Karyay Karadeniz Yayımcılık Ve Organizasyon Trade Limited Company

DIRECTOR IN CHARGE

Prof. Dr. Uğur ŞEN

REVIEWERS OF THE ISSUE*

Prof. Dr. Abdullah Tuğrul SEYHAN, Eskişehir Technical University, Department of Materials Science and Engineering, Materials Science, TÜRKİYE

Prof. Dr. Anıl AKDOĞAN, Yıldız Technical University, Department of Mechanical Engineering, Mechanical Engineering, TÜRKİYE

Prof. Dr. Başar ÖZTAYŞİ, İstanbul Technical University, Department of Industrial Engineering, Fuzzy Computation, TÜRKİYE

Prof. Dr. Cafer GENÇOĞLAN, Kahramanmaraş Sütçü İmam University, Department of Biosystems Engineering, Animal Barns, TÜRKİYE

Prof. Dr. Devrim AKCA, Işık University, Department of Computer Engineering, Photogrammetry and Remote Sensing, TÜRKİYE

Prof. Dr. İlker Murat KOÇ, İstanbul Technical University, Department of Mechanical Engineering, Mechanical Engineering, TÜRKİYE

Prof. Dr. Mustafa BOĞA, Nigde Ömer Halisdemir University, Bor Vacobolary School, Animal Nutrition, TÜRKİYE

Prof. Dr. Rahime CEYLAN, Konya Technical University, Department of Electrical-Electronics Engineering, Artificial Intelligence, TÜRKİYE

Prof. Dr. Ruhsar YANMAZ, Ankara University, Department of Horticulture, Vegetable Growing and Treatment, TÜRKİYE

Prof. Dr. Serdar AKBAYRAK, Necmettin Erbakan University, Department of Basic Sciences, Inorganic Green Chemistry, TÜRKİYE

Prof. Dr. Sinan APAK, Fenerbahçe University, Department of Industrial Engineering, Multiple Criteria Decision Making, TÜRKİYE

Prof. Dr. Şener AKINCI, Marmara University, Department of Biology, Plant Physiology, TÜRKİYE

Assoc. Prof. Dr. Ahmet Onur PEHLİVAN, Türk-Alman University, Department of Civil Engineering, Civil Engineering, TÜRKİYE

Assoc. Prof. Dr. Anıl NİŞ, İstanbul Gelişim University, Department of Civil Engineering, Civil Engineering, TÜRKİYE

Assoc. Prof. Dr. Aycan Mutlu YAĞANOĞLU, Atatürk University, Department of Animal Sciences, Biometry, TÜRKİYE

Assoc. Prof. Dr. Ayhan ATIZ, Çukurova University, Department of Physics, General Physics, TÜRKİYE

---

* The ranking is arranged alphabetically within the academic title

Volume 8, Issue 5 (2025)

Table of Contents

Research Articles

1. INVESTIGATION OF CHANGES IN SALT AND MICROALGAL POPULATION STATUS IN ÇEVLİK (SAMANDAĞ, HATAY), POMPEI (MEZİTLİ, MERSİN) COASTAL REGION MARINE WATER RESOURCES
Melda MERAL ÖCAL, İlkcan YALÇIN, Dilek TEKDAL.....1268-1272

2. EFFECT OF SOIL-STRUCTURE INTERACTION ON THE TORSIONAL BEHAVIOR OF L-SHAPED RC BUILDINGS UNDER BI-DIRECTIONAL GROUND MOTIONS
Ibrahim OZ.....1273-1278

3. ANALİTİK HİYERARŞİ PROSESİ (AHP) VE BULANIK MANTIK YAKLAŞIMLARININ İHALEYİ KAZANACAK KURULUŞUN SEÇİMİNDE KULLANILMASI
Serhat ALTINTAŞ, Latif Onur UĞUR.....1279-1296

4. DETECTION OF PINE PROCESSIONARY MOTH (THAUMETOPOEA WILKINSONI) NESTS USING DEEP LEARNING
Fatih GENÇTÜRK, Cemal IŞILAK, İsmail Serkan ÜNCÜ.....1297-1306

5. KUZU RASYONLARINDA KULLANILAN DUT YAPRAKLARININ ANTİ-METANOJENİK VE ANTİ-PROTEOLİTİK ETKİLERİNİN BELİRLENMESİ
Mesut ERER, Adem KAMALAK.....1307-1312

6. YÜKLEME HIZININ DÖRT NOKTALI EĞİLME ETKİSİ ALTINDAKİ AAC LENTOLARIN EĞİLME PERFORMANSINA ETKİSİ
Yaşar ERBAŞ.....1313-1319

7. DIFFERENTIABLE RAY TRACING-BASED ANALYSIS OF TRANSMITTER DEPLOYMENT STRATEGIES IN SITE-SPECIFIC SCENARIOS
Onem YILDIZ.....1320-1327

8. CONTACTLESS DETECTION OF ELECTRICAL MACHINE BEARING FAULTS: A RADAR-BASED SOLUTION
Yunus Emre ACAR, Salih Bilal CETINKAL.....1328-1338

9. EVALUATION OF SALT STRESS TOLERANCE IN LETTUCE (*Lactuca sativa* L.) CULTIVARS UNDER HYDROPONIC CONDITIONS
Alim AYDIN.....1339-1348

10. BİNA ZARFININ RENK KOYULUĞUNUN BİNANIN TS 825'E GÖRE HESAPLANAN YILLIK ENERJİ İHTİYACI ÜZERİNDEKİ ETKİSİ
Abdullah Huzeyfe AKCA.....1349-1357

11. A BIBLIOMETRIC ANALYSIS ON UNIVERSITY CAMPUS DESIGN
Fazıl AKDAĞ, Fatma Betül KÜNYELİ, Murat Çağlar BAYDOĞAN.....1358-1372

12. A CONTEMPORARY APPROACH TO SOLVING SELECTION PROBLEMS: THE ENTROPY-BASED PERFORMANCE MEASUREMENT (EBPM) METHOD
Furkan Fahri ALTINTAŞ.....1373-1400

13. HELMINTH EGGS CONTAMINATION OF COMMONLY CONSUMED LEAFY GREEN VEGETABLES IN KIRŞEHİR PROVINCE, TÜRKİYE
Nuri ERCAN……1401-1405
14. CHAOTIC SPEED CONTROL OF A DC MOTOR USING THE SPROTT-A SYSTEM FOR ROBOTIC END-EFFECTOR APPLICATIONS
Yusuf HAMİDA EL NASER, Berk DEMİRSOY, Kenan ERİN, Mert Süleyman DEMİRSOY……1406-1414
15. KAMU BİNALARINDA ENERJİ YÖNETİMİ İÇİN MAKİNE ÖĞRENMESİ YAKLAŞIMLARI
Vildan ARSLANTÜRK, Betül TURANOĞLU ŞİRİN……1415-1428
16. ANALYSING THE CHANGE OF ABOVEGROUND BIOMASS DENSITY (AGBD) USING EARTH OBSERVATION AND MACHINE LEARNING TECHNOLOGY: ALANYA CASE
Ercüment AKSOY……1429-1439
17. UNVEILING ANTIBODY-MEDIATED ALLOSTERY IN INTERLEUKIN-1ß VIA CONFORMATIONAL SAMPLING AND MACHINE LEARNING
Arzu UYAR……1440-1449
18. PRECLINICAL EVALUATION OF BRIGIMADLIN (BI 907828) AS A NOVEL MDM2 INHIBITOR IN ACUTE LYMPHOBLASTIC LEUKEMIA
Erhan APTULLAHOĞLU……1450-1459
19. CUSTOMER LIFETIME VALUE PREDICTION IN MOBILE GAMING INDUSTRY: FUZZY LOGIC APPROACH
Ahmet Tezcan TEKİN……1460-1467
20. APPLICATION OF GIS IN FLOOD RISK ANALYSIS AND MITIGATION STRATEGIES: THE CASE OF ULUOVA AND IKITEPE STREAMS
Muhammed UYMAZ, Meral KORKMAZ……1468-1477
21. TÜRKİYE'NİN BİLGİSAYAR, ELEKTRONİK VE OPTİK ÜRÜNLERİ DIŞ TİCARETİNİN MAKİNE ÖĞRENMESİ İLE TAHMİNLENMESİ
Tolga HASTAOĞLU, Tolga AYDIN……1478-1492
22. OPTIMIZING ACCURACY OF ABRASIVE WATERJET CUTTING SYSTEM: A COMPREHENSIVE STUDY ON MECHANICAL AND SOFTWARE COMPENSATION STRATEGIES ON 5-AXIS CNC WATERJET CUTTING MACHINE AND ANALYSIS USING DESIGN FMEA
Uğur ŞİMŞİR……1493-1503
23. THE EFFECT OF COMMON-MODE NOISE IN QUADRATURE RADAR SYSTEMS: ROTATING DISC IMBALANCE ESTIMATION
Yunus Emre ACAR……1504-1513
24. HAVALİMANLARINDA YOLCU TAŞIMACILIĞININ KARBON EMİSYONLARINA ETKİSİ: SCHİPHOL HAVALİMANI ÖRNEĞİ
Firdevs Didem GÖÇMEN……1514-1524
25. OPPORTUNITIES FOR THE USE OF AGRIVOLTAIC SYSTEMS IN ANIMAL BARNS: A CASE STUDY OF WATER BUFFALO BARNS
Elif TÜRKBOYLARI, Ahmet Nedim YÜKSEL……1525-1530
26. PRODUCTION AND CHARACTERIZATION OF SPOROPOLLENIN REINFORCED ALGINATE-BASED COMPOSITE FILMS
Bahar AKYUZ YILMAZ……1531-1536

27. THE EFFECTS OF DEVELOPMENTS IN DIGITAL TECHNOLOGIES ON THE ACTIVITIES OF MARITIME BUSINESSES AND SHIPS
Murat SAKA, Tayfun ACARER.....*1537-1547*
28. EXPLORING THE ADSORPTION PERFORMANCE OF EGGSHELL POWDER FOR METHYLENE BLUE REMOVAL FROM WASTEWATER
Emine KAYHAN.....*1548-1555*
29. A CHAIN RULE FOR REDUCED FUNCTIONAL DIFFERENTIAL INCLUSIONS AND STABILITY THEOREMS
Nurgul GÖKGÖZ.....*1556-1560*
30. EFFECT OF WORMHOLE DEFECTS ON ELECTRIC FIELD DISTRIBUTION UNDER COMPOSITE VOLTAGE
Murat FİDAN, Emre TUNÇ.....*1561-1576*
31. ENHANCED PHOTOCATALYTIC DEGRADATION OF METHYL RED DYE VIA HYDROTHERMALLY SYNTHESIZED MANGANESE TUNGSTATE
Mehmet KAYHAN.....*1577-1584*
32. NUMERICAL INVESTIGATION OF HYDROFOIL CAVITATION USING OPENFOAM: EFFECT OF THICKNESS AND CAMBER
Mehmet Numan KAYA.....*1585-1594*
33. OPTIMIZATION OF COAGULATION PROCESS PARAMETERS FOR REACTIVE RED 120 DYE USING FERRIC CHLORIDE VIA RESPONSE SURFACE METHODOLOGY
Sevtap TIRINK.....*1595-1604*
34. DESIGN AND DEVELOPMENT OF TOPOLOGICALLY OPTIMIZED EARLY FIRE DETECTION MOBILE ROBOT
Hilmi Saygin SUCUOGLU.....*1605-1616*
35. FARKLI ARAZİ KULLANIMLARINDA TOPRAK ORGANİK KARBON MİKTARININ BELİRLENMESİ: ALAÇAM İLÇESİ ÖRNEĞİ
Ali İMAMOĞLU.....*1617-1627*
36. ALÜMİNYUM KLORÜR ($ALCL_3$) BAZLI KLOR-ALKALİ ELEKTROLİZİ İLE HİDROJEN ÜRETİMİNİN EKSERJİ TEMELLİ İNCELENMESİ
Serdal DAMARSEÇKIN.....*1628-1633*
37. MOLECULAR IDENTIFICATION, ENZYMATIC ACTIVITY AND ANTIBIOTIC RESISTANCE PROFILES OF BACTERIA ISOLATED FROM MERLANGIUS MERLANGUS
Hayrettin SAYGIN, Huseyin Sezgin CAĞLAR, Semra SAYGIN.....*1634-1644*
38. UTILIZATION OF CONCRETE WASTE AS A CEMENT REPLACEMENT: INFLUENCE OF CALCINATION ON REACTIVITY AND PERFORMANCE
Hüseyin ULUGÖL.....*1645-1651*
39. IN SILICO ASSESSMENT OF AMINO ACID–PROTEIN INTERACTIONS IN CORONARY ARTERY DISEASE: MOLECULAR INSIGHTS FOR FUNCTIONAL BIOLOGY
Reşat DİKME, Adem NECİP.....*1652-1658*

Reviews

MICROPLASTICS: AN OVERVIEW OF SOURCES, DISTRIBUTION, AND REMOVAL METHODS
Arife ŞİMŞEK, Şule SANCAK, Gülfem BAKAN.....*1659-1673*

Black Sea Journal of Engineering and Science
doi: 10.34248/bsengineering.1681666

Open Access Journal
e-ISSN: 2619 – 8991

Research Article
Volume 8 - Issue 5: 1268-1272 / September 2025

INVESTIGATION OF CHANGES IN SALT AND MICROALGAL POPULATION STATUS IN ÇEVLİK (SAMANDAĞ, HATAY), POMPEI (MEZİTLİ, MERSİN) COASTAL REGION MARINE WATER RESOURCES

Melda MERAL ÖCAL[1]*, İlkcan YALÇIN[1], Dilek TEKDAL[1]

[1]*Mersin University, Faculty of Science, Department of Biotechnology, 33343, Mersin, Türkiye*

Abstract: Earthquakes remain among the most devastating natural disasters, and despite technological advancements, accurate prediction regarding their timing, location, and magnitude is still unattainable. Recent research highlights the significance of remote sensing indicators, such as chlorophyll-a (Chl-a) concentrations, sea surface temperature (SST), and salinity, as potential earthquake precursors. This study aimed to investigate variations in these marine parameters in the aftermath of the 2023 Kahramanmaraş earthquake and its aftershocks, particularly focusing on coastal areas in Samandağ (Hatay) and Mezitli (Mersin), Türkiye. Marine water samples were collected from Pompei and Çevlik beaches. Key physicochemical parameters, including pH, temperature, and electrical conductivity(EC), were measured immediately upon collection. Samples were also processed for Chl-a analysis through acetone extraction and spectrophotometric measurements, and a portion was transferred to nutrient media for algal isolation. Microscopic analyses revealed significant differences in algal compositions between the two sites. While samples from Mezitli primarily showed the presence of *Cylindrotheca closterium* and other pennate diatoms, those from Samandağ exhibited higher species diversity, including *Thalassionema, Syracosphaera, Grammatophora,* and various flagellates and amoebae. Notably, despite lower pH and EC values in Samandağ, the site showed more diverse algal presence, suggesting a complex response of microalgal communities to post-seismic marine conditions. The findings emphasize the dynamic interplay between environmental parameters and biological diversity in marine ecosystems affected by seismic activity. The measured ecological parameters are vital indicators of ecosystem health and may influence physiological functions such as osmoregulation in marine algae. This study contributes to understanding the relationship between seismic events and coastal marine ecosystems. It underscores the importance of long-term monitoring to track ecosystem changes and the potential use of Chl-a concentration, as well as algal diversity, as early indicators of environmental stress. Such insights are vital for marine conservation strategies in earthquake-prone regions.

Keywords: Chlorophyll-a (Chl-a), Algal diversity, Environmental stress, Marine water quality, Seismic activity

***Corresponding author:** Mersin University, Faculty of Science, Department of Biotechnology, 33343, Mersin, Türkiye
E mail: meldameralocal@mersin.edu.tr (M. MERAL ÖCAL)
Melda MERAL ÖCAL https://orcid.org/0000-0002-5628-6154
İlkcan YALÇIN https://orcid.org/0009-0003-0017-9987
Dilek TEKDAL https://orcid.org/0000-0002-4545-9005

Received: April 22, 2025
Accepted: May 25, 2025
Published: September 15, 2025

Cite as: Meral Ocal M, Yalcın İ, Tekdal D. 2025. Investigation of changes in salt and microalgal population status in Çevlik (Samandağ, Hatay), Pompei (Mezitli, Mersin) coastal region marine water resources. BSJ Eng Sci, 8(5): 1268-1272.

1. Introduction

Earthquake occurrences originating within the Earth's crust are commonly known as earthquakes and are categorizable into three main types: collapse, volcanic, and tectonic (Sür, 1993). Türkiye experiences earthquakes predominantly of tectonic origin in regions prone to significant seismic activity, except for volcanic events detected in the Erciyes, Nemrut, and Mount Ararat regions (Lahn, 1949). Noteworthy geological features such as the vertical slip fault line between Antakya and Maraş, along with analogous fault lines in the various areas, including the Gediz, Büyük, and Küçükmenderes valleys, Edremit, Gökova, Gemlik, İzmit Bays, Sapanca, İznik lakes, and the Muş plain, contribute to the formation of grabens - collapsed areas between two elevated masses - in Anatolia (Sür, 1993). Although the Hatay region is the most susceptible area within the Southern Anatolia earthquake zone, neighboring regions, including Mersin, Tarsus, Adana, Ceyhan, Kozan, and their environs, also face considerable seismic risks. Notable seismic events in the Southern Anatolia earthquake zone encompass the Ceyhan (Adana) earthquake of 1945, the İskenderun earthquake of 1951, the Ceyhan earthquakes of 1952 and 1998, and the Kahramanmaraş earthquake of 2023 (Sür, 1993).

In our country, a significant earthquake measuring 7.7 Mw (Moment Tensor) (±0.1) struck at a depth of 8.6 km, with its epicenter located in the Pazarcık district of Kahramanmaraş, on February 6, 2023, at 04:17 local time, followed by a subsequent major earthquake registering 7.6 Mw at a depth of 7 km, originating in the Elbistan district of Kahramanmaraş (AFAD, 2023). These seismic events were not limited to Türkiye; their effects were felt across neighboring countries, including Syria,

Lebanon, Iran, Egypt, and Iraq. After the primary earthquakes, nearly 1300 aftershocks with magnitudes reaching up to 6.7 MW occurred, with aftershock activity persisting notably in the southern regions of Türkiye, particularly in Hatay province and its vicinity, causing disruptions and distress among local communities. Provinces most severely impacted by these earthquakes within Türkiye include Adana, Adıyaman, Diyarbakır, Gaziantep, Hatay, Kilis, Malatya, Kahramanmaraş, Osmaniye, and Şanlıurfa.

Despite advancements in modern technology, predicting the timing, location, and magnitude of earthquakes remains elusive, making earthquakes one of the most destructive natural disasters. Therefore, remote sensing data, encompassing lithospheric and atmospheric activities, is crucial for detecting precursors to impending earthquakes. Recent studies indicate anomalies on land, in the oceans, atmosphere, and ionosphere before earthquakes (Singh et al., 2006). Hence, identifying abnormalities in these data is essential for early warning purposes. Particularly, increases in chlorophyll-a (Chl-a) concentration and salt concentration on the sea surface, as well as rises in sea surface temperatures (SST), are regarded as the most valuable data in remote sensing (Singh et al., 2006; Alvan et al., 2012). The presence of many seismic fault lines along continental coastal belts is interpreted to cause a significant rise in SST levels. It has been reported that elastic deformation in rocks prior to earthquakes, the formation of microcracks, gas emissions, and other chemical or physical activities in the Earth's crust lead to changes in oceanic parameters (Nadri and Hanzaei, 2020). Changes in chlorophyll concentrations, indicative of fluctuations in plankton populations on the ocean surface and the primary productivity of phytoplankton biomass in the oceans, are also indicators of earthquakes. The increase in Chl-a concentration is attributed to changes in the thermal structure of water and fluctuations in SST associated with alterations in stress regimes in the epicentral region (Singh et al., 2006).

Studies have shown that 28, 46, 48, and 51 days before the Gujarat (India) earthquake of magnitude 7.7 Mw in 2001, chlorophyll-a levels exceeded permissible limits by 35%, 15%, 45%, and 85%, respectively (Singh et al., 2006; Nadri and Hanzaei, 2020). Similarly, investigations conducted 20 days before and 18 days after the Sumatra (Indonesia) earthquake of magnitude 6.9 Mw in 2004 revealed chlorophyll-a levels of 110% and 190%, respectively (Tang et al., 2009; Nadri and Hanzaei, 2020). In the case of the Java (Indonesia) earthquake of magnitude 6.2 Mw in 2006, chlorophyll-a analysis conducted 42 days before and 15-16 days after the earthquake indicated sudden increases to 136.84%, 52.63%, and 107.89%, respectively Nadri and Hanzaei, 2020). Before earthquakes, an increased rate of energy exchange between the surface and the atmosphere can lead to an increase in surface latent heat flux (SLHF) (Alvan et al., 2012). It has been found that SLHF migrates from high-stress regions to low-stress regions before earthquakes and emerges in the low-stress areas on the surface (Singh et al., 2006). The Gulf regions south and west of the epicenter of the Gujarat earthquake are low-stress areas where maximum SLHF anomalies are observed. The thermal energy released before the earthquake modifies the thermal structure of water, leading to increases in SST and SLHF, bringing nutrient-rich water closer to the ocean surface and causing an increase in Chl-a concentration. It is noted that these increases continue during the aftershock period and return to normal afterward (Alvan et al., 2012).

Changes in surface temperature can be monitored using thermal infrared sensors such as NOAA-AVHRR and microwave radiometers like AMSR-E/Aqua (Alvan et al., 2012). Medium Resolution Imaging Spectroradiometer (MODIS) is commonly used for Chl-a concentration and SST monitoring; however, in cases of cloudy or overcast conditions, this monitoring may not occur, and potential risk situations may go undetected (Singh et al., 2006). Therefore, it is crucial to develop sensors that can determine Chl-a and SST ratios more economically and independently of weather conditions in the future.

The Wenchuan earthquake in China in 2008 and subsequent secondary geological hazards are reported to have caused widespread damage to the vegetation-soil system in northwest China (Lin et al., 2017). However, during major earthquakes, nutrient-rich and well-structured original soil can easily be disrupted by earthquake-induced geohazards, undermining the surface soil structure. This leads to increased soil aeration and infiltration capacity and decreases in hydrological adjustment functions, drainage, bulk density, and temperature, posing a severe erosion risk (Lin et al., 2017). More research is needed to assess soil disturbance and recovery potential, soil management practices, and the feasibility of geotechnical and biological measures in disturbed areas.

Monitoring chlorophyll concentrations with higher spatial and temporal resolutions could provide early information about impending coastal earthquakes (Singh et al., 2006). Chemical activities before, during, and after coastal and near-coastal earthquakes can cause changes in chlorophyll levels on the water surface, and this parameter could be used as an earthquake precursor in future research.

The research materials will be obtained from the areas affected by the earthquake that occurred on February 6, 2023, in Hatay province, specifically from Çevlik Beach in the Samandağ district and also from Pompei Beach in the Mezitli district of Mersin province. The reasons for selecting these regions include the availability of previous studies conducted in these areas, allowing for comparisons with the data to be obtained within the project's scope. Additionally, both regions have historical significance as ancient cities dating back to antiquity, and are earthquake-prone areas.

Samandağ is situated west of Hatay province and is a

coastal district built on the delta of the Asi River. Çevlik, located northwest of Samandağ district, is historically known as the ancient city of Seleucia Pieria (Kayıkçı, 2019). The Çevlik region covers a 5 km portion of the 14 km long Samandağ beach (Görün, 2006). A Master's thesis completed by Görün (2006) focused on the seasonal variation of harmful algae species Goniodoma and Ceratium in the Çevlik beach area. The study collected marine water samples from four stations between 2003 and 2004, determining pH values ranging from 6.54 to 8.42 and salinity levels varying between 21.5% and 36.9%. Additionally, Görün (2006) reported high nitrate levels during autumn. It is known that the sea temperature in the Eastern Mediterranean is between 11-14°C in February and fluctuates between 25-28°C in August (Polat et al., 2000; Işık, 2002; Kayıkçı, 2019). Pompei Beach is located in Soli, an ancient port city founded by the Rhodolians, also known as Soli Pompeiopolis. It is also called the area where the Great Cilicia Earthquake of 1269 occurred (Anonymous, 2018; Kök and Kahya Sayar, 2022).

2. Materials and Methods

2.1. Field Visit and Material Acquisition

Fieldwork planned for obtaining marine water samples was conducted in the areas affected by the 2023 Kahramanmaraş earthquake and the ongoing aftershocks in the Samandağ district of Hatay province, as well as in the Mezitli and Yenişehir districts of Mersin province, where the earthquake was felt. The coordinates of the sampling locations were recorded using the Global Positioning System (GPS 12XL, Garmin; Google Maps application) (Table 1), and the samples were carefully labeled accordingly. The samples were filtered through GF/F filters in volumes ranging from 100 to 500 mL based on density. The filtered samples were then placed into 15 mL Falcon tubes, to which 90% acetone was added and extracted using a homogenizer. Subsequently, the samples were kept in the dark in a refrigerator overnight. Upon removal from the refrigerator, the samples were centrifuged at 3000 rpm for 10 minutes, and the absorbances at 750 nm, 664 nm, 647 nm, and 630 nm were measured using a 1 cm cuvette. 90% acetone was used as a blank. The measurement at 750 nm was corrected for turbidity by subtracting it from the measurements at the other three wavelengths (Holm-Hansen and Riemann, 1978; New et al., 2017).

Table 1. Information on the sampling locations from earthquake-affected areas

Sample Code and Name	Latitude (N)	Longitude (E)	Region	Date of Collection
1. Çevlik Beach	36° 07′	35° 54′	Samandağ, Hatay	22.02.2023
2. Pompei Beach	36° 73′	34° 53′	Mezitli, Mersin	22.02.2023

2.2. Salt Measurement

The electrical conductivity (EC) of each water sample was determined using an electrical conductivity meter (WTW series-inoLab-Cond-720), according to Richards (1954).

2.3. pH Measurement

The pH of each sample was determined using a pH meter with a glass electrode (Hanna Instruments-HI 2211).

2.4. Microscopic Analyses of Algal Species

Approximately 100 mL of each water sample was also filtered for chlorophyll analysis. Without delay, the water samples' conductivity, temperature, and pH levels were measured, and a portion of each sample was transferred to a nutrient medium for algal isolation.

3. Results

Water samples were collected from Çevlik Beach in the Samandağ district of Hatay province and Pompei Beach in the Mezitli district of Mersin province on February 22, 2023. They were analyzed for algal composition (Figures 1 and 2). The water samples' conductivity, temperature, and pH levels were measured and given in Table 2. The results of the algal isolation and analyses are shown in Figure 3. While samples from Mezitli primarily showed the presence of *Cylindrotheca closterium* and other pennate diatoms, those from Samandağ exhibited higher species diversity, including *Thalassionema, Syracosphaera, Grammatophora,* and various flagellates and amoebae. Despite lower pH and EC values in Samandağ, the site showed more diverse algal presence, suggesting a complex response of microalgal communities to post-seismic marine conditions.

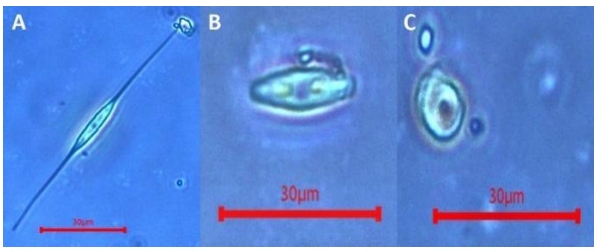

Figure 1. Microscopic examination of algal composition in a water sample collected from Pompei beach in Mezitli, Mersin, on the day of collection; Possible species based on microscope observation; A. *Cylindrotheca closterium*, B. Pennat, C. Oval; scale bar 30 µm.

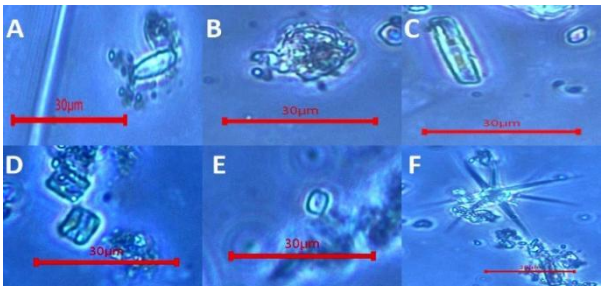

Figure 2. Microscopic examination of algal composition in a water sample collected from Çevlik beach in Samandağ, Hatay, on the day of collection; Possible species based on microscope observation; A. Thalassionema, B. Syracosphaera, C. Pennat, D. Grammatophora, E. Flagellate, F. Amoeba; scale bar 30 µm.

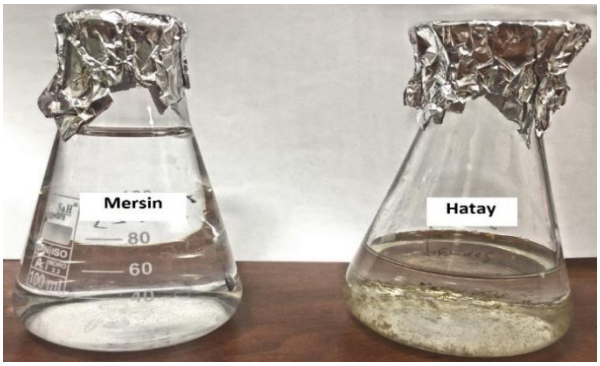

Figure 3. Appearance of samples cultured for algal isolation from marine water samples obtained from Pompei beach in Mezitli, Mersin, and Çevlik beach in Samandağ, Hatay, on February 22, 2023, during the first week of culture.

Table 2. pH, temperature, and electrical conductivity (EC) values of marine water samples obtained from Pompei beach in Mezitli, Mersin, and Çevlik beach in Samandağ, Hatay, on February 22, 2023.

Sample	Location	pH	EC (µs/m)	Temperature (°C)
1	Mersin	7.45	38.8	20.2
2	Hatay	6.63	32.4	18.6

4. Discussion

This study's examination of coastal marine water resources in Çevlik and Pompei has yielded critical insights into the dynamics of salt, chlorophyll, and mineral element content, alongside the status of microalgal populations. Detecting varied algal species such as *Cylindrotheca closterium* and *Thalassionema* in these areas underscores the biological diversity and complexity of marine ecosystems under study. Such diversity is pivotal for ecological resilience and productivity, reflecting the findings of Jones et al. (2018), who emphasized the importance of microalgal diversity in sustaining marine food webs and biogeochemical cycles.

The measured pH, electrical conductivity, and temperature across the sites provided vital environmental parameters for evaluating these ecosystems' health and stability. The slight alkalinity and varied salinity levels observed align with Smith et al. (2020) research, which found that these factors critically influence microalgal growth rates and composition. These environmental conditions, particularly salinity, have been shown to affect the osmoregulatory processes of marine algae, as Lee and Anderson (2019) discussed, impacting their distribution and abundance.

Furthermore, transferring water samples to nutrient media for algal isolation is a significant step toward isolating and identifying algal species' specific roles within these ecosystems. This methodology aligns with the approach of Green et al. (2021), who utilized similar techniques to catalog algal species in coastal regions, highlighting the necessity of understanding species-specific responses to environmental changes.

The findings from this investigation are particularly relevant in the context of recent environmental disturbances, such as the earthquake that affected the regions of Hatay and Mersin. Studies by Patel and Singh (2017) have shown that seismic activities can significantly alter marine water quality, potentially impacting microalgal populations. This underscores the importance of continuous monitoring and research to assess the long-term effects of environmental changes on aquatic biodiversity and ecosystem services.

The comprehensive analysis of algal diversity and environmental parameters conducted in this study contributes valuable knowledge to the field of marine ecology, particularly in understanding how external stressors such as earthquakes affect coastal marine ecosystems. This research lays the groundwork for future studies to explore the resilience and adaptability of aquatic ecosystems to environmental changes. Continued efforts in this direction are essential for developing strategies to conserve and manage marine biodiversity effectively, ensuring the sustainability of these vital resources.

5. Conclusion

This study highlights the interplay between algal populations and environmental parameters in coastal marine ecosystems. By documenting changes in salt, chlorophyll, and mineral content and examining microalgal population status, this research provides insight into the potential impacts of environmental disturbances on marine biodiversity. Future research should focus on longitudinal studies to track these ecosystems' responses over time, offering crucial data for conservation efforts and managing aquatic resources in the face of global environmental changes.

Author Contributions

The percentages of the authors' contributions are presented below. All authors reviewed and approved the final version of the manuscript.

	M.M.O.	I.Y.	D.T.
C	40	30	30
D	40	30	30
S	40	30	30
DCP	30	40	30
DAI	50	30	20
L	40	30	30
W	40	20	40
CR	50	30	20
SR	40	30	30
PM	35	30	35
FA	20	30	50

C=Concept, D= design, S= supervision, DCP= data collection and/or processing, DAI= data analysis and/or interpretation, L= literature search, W= writing, CR= critical review, SR= submission and revision, PM= project management, FA= funding acquisition.

Conflict of Interest

The authors declared that there is no conflict of interest.

Ethical Consideration

Ethics committee approval was not required for this study because there was no study on animals or humans.

Acknowledgements

The authors thank Prof. Dr. Elif Eker Develi for the microscopic analyses and characterization of the algal species.

References

AFAD. T.C. İçişleri Bakanlığı afet ve acil durum yönetimi başkanlığı, 2023. 06 şubat 2023 Pazarcık (Kahramanmaraş) Mw 7.7 Elbistan (Kahramanmaraş) Mw 7.6 depremlerine ilişkin ön değerlendirme raporu, Kahramanmaraş, Türkiye, pp: 83.

Alvan HV, Azad FH, Omar HB, 2012. Chlorophyll concentration and surface temperature changes associated with earthquakes. Nat Hazards, 64: 691–706.

Anonymous 2018. Soli Pompeipolis antik kenti. URL: https://www.essizmersin.com/tr/2/antik-kentler-ve-kaleler/soli-pompeipolis-antik-kenti/86 (accessed date: March 5, 2022).

Görün A, 2006. Ecology and seasonal change of harmful algae Goniodoma (Goniodomataceae) and Ceratium (Ceratiaceae) in Çevlik Region (Hatay), Eastern Mediterranean. MSc thesis, Hatay Mustafa Kemal University, Institute of Science, Hatay, Türkiye, pp: 20-32.

Green DA, Thompson EI, Willis SP, 2021. Advances in algal isolation techniques and their significance for marine biodiversity studies. J Exp Mar Biol Ecol, 489: 58-66.

Holm-Hansen O, Riemann B, 1978. Chlorophyll a determination: Improvements in methodology. Oikos, 30: 438-447.

Isık O, 2002. Phytoplankton distribution, diversity, and nutrients at the north-eastern Mediterranean coast of Türkey (Karataş-Adana). Turk J Bot, 26: 77-86.

Jones AR, Smith BL, Nguyen CD, 2018. The importance of microalgal diversity in marine ecosystems: Implications for food webs and biogeochemical cycles. J Mar Biol Ecol, 450(2): 123-137.

Kayıkçı S, 2019. Seleucia Pieria antik kenti (Çevlik-Samandağ-Hatay) ve yakın çevresinin florası. MSc thesis, Hatay Mustafa Kemal Üniversitesi, Hatay, Türkiye, pp: 82.

Kök DS, Kahya Sayar Y, 2022. Savranda Kalesi mimari değerlendirmesi. Online J Art Des, 10(3): 114-134.

Lahn E, 1949. Türkiye yer depremleri ile tektonik arasındaki münasebetler hakkında. Türk Coğrafya Derg, 11(12): 95-101.

Lee HO, Anderson TJ, 2019. Osmoregulation in marine algae: Understanding salt stress responses in a changing environment. Aquat Bot, 158: 23-32.

Lin Y, Deng H, Du K, Li J, Lin H, Chen C, Zhang G, 2017. Soil quality assessment in different climate zones of China's Wenchuan earthquake-affected region. Soil Tillage Res, 165: 315–324.

Nadri M, Hanzaei AM, 2020. Anomaly detection in time series of chlorophyll around the time and location of large coastal earthquakes using random forest method. J Geomatics Sci Technol, 10(2): 165-174.

New OOYY, Su MC, Kyaw KT, 2017. Extraction and determination of chlorophyll content from microalgae. Int J Adv Res Publ, 1(5): 298-301.

Patel S, Singh AK, 2017. Seismic activities and their impact on marine water quality: A review. Environ Monit Assess, 189(4): 176.

Polat S, Sarihan E, Koray T, 2000. Seasonal changes in the phytoplankton of the northeastern Mediterranean (Bay of Iskenderun). Turk J Bot, 24(1): 1-12.

Richards LA. 1954. Diagnosis and Improvement of Saline and Alkali Soils. USDA Agriculture Handbook No. 60, Washington, D.C., USA, pp: 124-135.

Singh RP, Dey S, Bhoi S, Sun D, Cervone G, Kafatos M, 2006. Anomalous increase of chlorophyll concentrations associated with earthquakes. Adv Space Res, 37: 671–680.

Smith JK, Zhang L, Patel RM, 2020. Impact of salinity and pH on marine microalgae growth rates and community composition. Mar Environ Res, 145: 103-114.

Sür Ö, 1993. Türkiye'nin deprem bölgeleri. Türkiye Coğrafyası Derg, 2: 53–68.

Tang D, Zhao H, Satyanarayana B, Zheng G, Singh RP, Lv J, Yan Z, 2009. Variations of chlorophyll-a in the northeastern Indian Ocean after the 2004 South Asian tsunami. International journal of remote sensing, 30(17): 4553-4565.

Black Sea Journal of Engineering and Science
doi: 10.34248/bsengineering.1663812

Open Access Journal
e-ISSN: 2619 – 8991

Research Article
Volume 8 - Issue 5: 1273-1278 / September 2025

EFFECT OF SOIL-STRUCTURE INTERACTION ON THE TORSIONAL BEHAVIOR OF L-SHAPED RC BUILDINGS UNDER BI-DIRECTIONAL GROUND MOTIONS

Ibrahim OZ[1]*

[1]*Kirsehir Ahi Evran University, Faculty of Engineering and Architecture, Department of Civil Engineering, 40100, Kirsehir, Türkiye*

Abstract: This study investigates the seismic torsional response of a nine-story L-shaped reinforced concrete (RC) building, with particular emphasis on the effects of soil-structure interaction (SSI). Using three-dimensional nonlinear dynamic analyses in SAP2000, the building's performance was evaluated under 30 pairs of scaled bidirectional ground motion records. SSI effects were modeled using the substructure method, with soil properties corresponding to ZC soil class as defined by the Turkish Seismic Code (TBEC-2018). Torsional behavior coefficients (ηbi) were computed from the displacement differentials obtained, and fragility curves were developed using ηbi as the engineering demand parameter. The results showed that SSI increased the fundamental periods by approximately 8% and torsional irregularity by up to 30% compared to fixed-base conditions. Fragility analysis indicated that the probability of exceeding the critical ηbi value of 1.2 was approximately 10% under fixed-base conditions and about 40% when SSI was considered. These findings highlight the significant impact of SSI on the torsional response of irregular structures and emphasize the importance of accounting for SSI effects in the seismic design and performance assessment of RC buildings.

Keywords: Torsional irregularity, Soil-structure interaction, Nonlinear dynamic analysis, Fragility curve, L-shaped building

***Corresponding author:** Kirsehir Ahi Evran University, Faculty of Engineering and Architecture, Department of Civil Engineering 40100, Kirsehir, Türkiye.
E mail: ibrahim.oz@ahievran.edu.tr (I. OZ)
Ibrahim OZ https://orcid.org/0000-0003-3152-3675

Received: March 23, 2025
Accepted: June 11, 2025
Published: September 15, 2025

Cite as: Oz İ. 2025. Effect of soil-structure interaction on the torsional behavior of l-shaped RC buildings under bi-directional ground motions. BSJ Eng Sci, 8(5): 1273-1278.

1. Introduction

Recent severe earthquakes, particularly those occurring in our country, have underscored the necessity for reinforced concrete (RC) buildings to exhibit sufficient resistance under seismic loads. To achieve desirable seismic performance during earthquakes, RC structures must possess essential attributes such as adequate lateral strength, stiffness, and ductility (Abdel Raheem et al., 2018). Consequently, the plan layout of an RC building plays a critical role in its design under seismic loading. Regulatory provisions specifying the requirements for RC structures constitute the most crucial criteria for ensuring seismic resilience (Abdel Raheem et al., 2010). Although RC frames with regular structural configurations are comparatively easier to design and predict in terms of seismic response, architectural considerations and site-specific constraints often preclude the feasibility of uniformly regular structural layouts (Abdel Raheem et al., 2018).

In practical scenarios, almost all structures exhibit some form of irregularity, rendering torsional coupling effects unavoidable under seismic excitation (Sucuoglu and Kaatsiz, 2021). For engineers designing irregular buildings in regions with high seismicity, ensuring structural safety is the paramount objective (Solomon and Hemalatha, 2013; Ozer and Inel, 2025). Particularly for L-shaped buildings, asymmetrical distributions of mass, stiffness, and strength arising from plan irregularities frequently exceed the rotational and translational limits defined by seismic codes, potentially resulting in significant damage. Additionally, re-entrant corners and lateral-torsional coupling can substantially amplify seismic demands on the structure. Therefore, the design of structural elements within irregular regions requires meticulous attention (Abdel Raheem et al., 2018). Field investigations conducted following major earthquakes have highlighted increased damage rates in irregular structures (De Stefano and Pintucchi 2008) and (Das et al., 2021). Consequently, the design and seismic performance assessment of RC buildings exhibiting torsional effects become considerably more complex compared to symmetric buildings (Abdel Raheem et al., 2018; Sucuoglu and Kaatsiz, 2021).

In recent years, advancements in computational software and engineering knowledge have accelerated research on soil-structure interaction (SSI). Numerous studies in the literature have demonstrated that incorporating SSI significantly alters the dynamic response of structures, particularly affecting their fundamental vibration periods Najar et al., (2025), Bharti et al., (2025) and increasing story drifts (Shirzadi, 2020). Although the necessity of utilizing torsionally irregular buildings underscores the

importance of studying the combined influence of SSI and torsional behavior, there remains a notable gap in the literature regarding such investigations. This study addresses this gap by analyzing the torsional irregularity of a nine-story L-shaped RC building, comparing its response under both fixed-base conditions and considering SSI effects. The findings indicate that incorporating SSI can increase torsional irregularity by up to 30%, emphasizing the importance of considering SSI effects in both the design and evaluation of RC buildings.

2. Materials and Methods

2.1. Structure and SSI model

In this study, a reinforced concrete building with a simple L-type frame structure was used, having a total height of 29.9 m, with the first-floor height at 3.5 m and each of the remaining 8 floors at 3.3 m. Reinforced concrete columns were selected with dimensions of 60x60 cm, while beam dimensions were considered as 25x50 cm. According to the Turkish Earthquake Code, the structure's importance factor was taken as 1, and the seismic load reduction factor was selected as 8. During the modeling phase, walls and slabs were not individually modeled but were incorporated only as loads. Dead and live loads were chosen as 5 kN/m, while wall loads were set as 3.25 kN/m. Cross-section stiffness values were defined as 0.7EI for columns and 0.35EI for beams in accordance with TBEC-2018. In the study, concrete compressive strength was considered as 30 MPa, reinforcement yield strength as 420 MPa, and transverse reinforcement spacing in confinement regions was set at 10 cm. The foundation of the building was modeled using frame elements with a depth of 80 cm.

Three-dimensional structural models were developed using SAP2000, a widely recognized structural analysis software for dynamic assessments. To accurately capture the nonlinear behavior of frame structural members, lumped fiber-hinge elements were employed, with hinges directly defined based on material nonlinearity. Each hinge was modeled using fiber elements, with stiffness derived directly from the nonlinear characteristics of the material. According to (Carvalho et al 2013)., a single hinge at each member end is sufficient to simulate biaxial bending, and the hinge length was set at 0.5 times the section height. The structural axis spans were selected as 5 meters, resulting in a total span of 50 meters in both directions, and the ratio of the non-irregular part to the L-shaped arms was considered as 4. A visual representation of the three-dimensional computer model of the structure is presented in Figure 1.

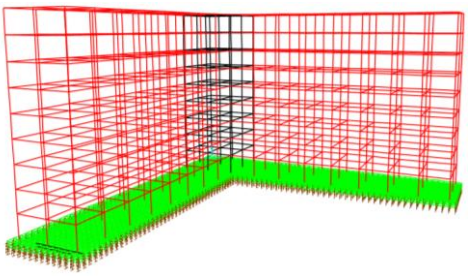

Figure 1. Three-dimensional view of the modeled L-type building.

In the study, the substructure method was used to avoid the computational load imposed by the direct method. A comparison of substructure method with the direct method was conducted in the study by (Oz, 2025). In the method under consideration, the surface stiffness values are to be multiplied by the embedment effects, and the radiation damping for embedded footings is given by the formulas presented in Table 1. The arrangement of the springs at the foundation level is illustrated in Figure 2 and Figure 3.

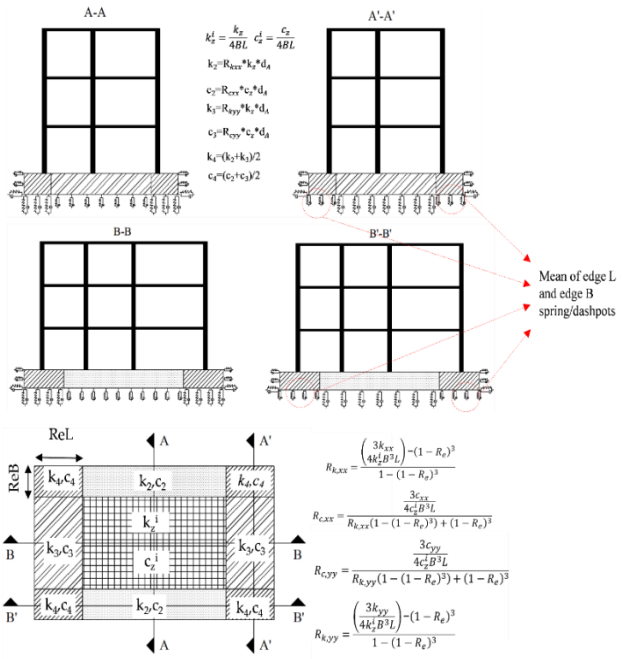

Figure 2. SSI Modeling: stiffness and damping expressions for raft foundation systems.

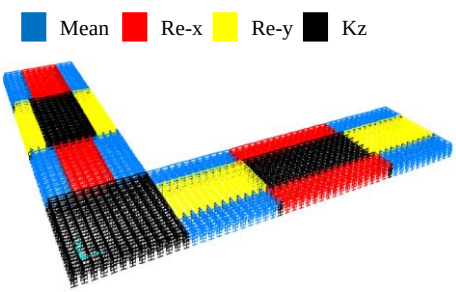

Figure 3. Spring groups and their layout used in the L-shaped building.

Table 1. The formulas used for calculating soil springs

Radiation Damping Ratios for Embedded Footings	Elastic Solutions for Static Stiffness of Rigid Footings at the Ground Surface
$\beta_z = \left[\frac{4[\psi(L/B) + (D/B)(1 + L/B)]}{(K_{z,emb}/GB)}\right]\left[\frac{a_0}{2\alpha_z}\right]$	$K_{z,\text{sur}} = \frac{GB}{1-v}\left[3.1\left(\frac{L}{B}\right)^{0.75} + 1.6\right]$
$\beta_y = \left[\frac{4[L/B + (D/B)(1 + \psi L/B)]}{(K_{y,emb}/GB)}\right]\left[\frac{a_0}{2\alpha_y}\right]$	$K_{y,\text{sur}} = \frac{GB}{2-v}\left[6.8\left(\frac{L}{B}\right)^{0.65} + 0.8\left(\frac{L}{B}\right) + 1.6\right]$
$\beta_x = \left[\frac{4[L/B + (D/B)(\psi + L/B)]}{(K_{x,emb}/GB)}\right]\left[\frac{a_0}{2\alpha_x}\right]$	$K_{x,\text{sur}} = \frac{GB}{2-v}\left[6.8\left(\frac{L}{B}\right)^{0.65} + 2.4\right]$
$\beta_{zz} = \left[\frac{(4/3)[3(L/B)(D/B) + \psi(L/B)^3(D/B) + 3(L/B)^2(D/B) + \psi(D/B) + (L/B)^3 + (L/B)]a_0^2}{\left(\frac{K_{zz,emb}}{GB^3}\right)\left[\left(\frac{1.4}{1 + 3(L/B-1)^{0.7}}\right) + a_0^2\right]}\right]\left[\frac{a_0}{2\alpha_{zz}}\right]$	$K_{zz,sur} = GB^3\left[4.25\left(\frac{L}{B}\right)^{2.45} + 4.06\right]$
$\beta_{yy} = \left[\frac{(4/3)\left[\left(\frac{L}{B}\right)^3\left(\frac{D}{B}\right) + \psi\left(\frac{D}{B}\right)^3\left(\frac{L}{B}\right) + \left(\frac{D}{B}\right)^3 + 3\left(\frac{D}{B}\right)\left(\frac{L}{B}\right)^2 + \psi\left(\frac{L}{B}\right)^3\right]a_0^2}{\left(\frac{K_{yy,emb}}{GB^3}\right)\left[\left(\frac{1.8}{1 + 1.75(L/B-1)}\right) + a_0^2\right]} + \frac{\left(\frac{4}{3}\right)\left(\frac{L}{B} + \psi\right)\left(\frac{D}{B}\right)^3}{\left(\frac{K_{yy,emb}}{GB^3}\right)}\right]\left[\frac{a_0}{2\alpha_{yy}}\right]$	$K_{yy,sur} = \frac{GB^3}{1-v}\left[3.73\left(\frac{L}{B}\right)^{2.4} + 0.27\right]$
$\beta_{xx} = \left[\frac{(4/3)\left[\left(\frac{D}{B}\right) + \left(\frac{D}{B}\right)^3 + \psi\left(\frac{L}{B}\right)\left(\frac{D}{B}\right)^3 + 3\left(\frac{D}{B}\right)\left(\frac{L}{B}\right) + \psi\left(\frac{L}{B}\right)\right]a_0^2}{\left(\frac{K_{xx,emb}}{GB^3}\right)\left[\left(\frac{1.8}{1 + 1.75(L/B-1)}\right) + a_0^2\right]} + \frac{\left(\frac{4}{3}\right)\left(\psi\frac{L}{B} + 1\right)\left(\frac{D}{B}\right)^3}{\left(\frac{K_{xx,emb}}{GB^3}\right)}\right]\left[\frac{a_0}{2\alpha_{xx}}\right]$	$K_{\text{xx, sur}} = \frac{GB^3}{1-v}\left[3.2\left(\frac{L}{B}\right) + 0.8\right]$

While calculating the springs representing the soil medium used in the study, the guidelines from the National Institute of Standards 2012– Soil-Structure Interaction for Building Structures – were utilized (NIST, 2012). The unit weight of the considered soil was taken as 20 kN/m^3, the shear wave velocity as 400 m/s, and the Poisson's ratio as 0.3. The modeled soil corresponds to ZC soil class according to TBEC-2018 (TBEC-2018). The first three modes of the analyzed L-type building for both fixed-base (FB) and ZC (SSI) conditions are presented in Table 2. The flexural behavior of the foundation was considered in the analysis to more accurately reflect its realistic response (OZ, 2025).

2.2. Selection of ground motions

In the study, it was assumed that the L-type building is located in Hatay, and the coordinates were selected as latitude 36.20^0 and longitude 36.15^0 using the Türkiye Earthquake Hazard Maps Interactive Web Application. The seismic ground motion level was selected as Design Basis Earthquake, and the local soil class was chosen as ZC, which corresponds to the soil type considered in the study, to determine the design spectrum.

A total of 30 acceleration records were selected from the PEER (PEER, 2021) Strong Ground Motion Database in accordance with the considered V_{s30} value. The SRSS spectra of the selected records, their average spectrum, and the determined target spectrum are presented in Figure 4. The parameters of the selected records are shown in Table 3.

Table.2 Period elongations by SSI effects

Model	Mode 1 (sec)	Mode 2 (sec)	Mode 1 (sec)
FB	1.671	1.592	1.515
SSI	1.827	1.711	1.629
Elongation Ratio (%)	8.54	6.95	7.00

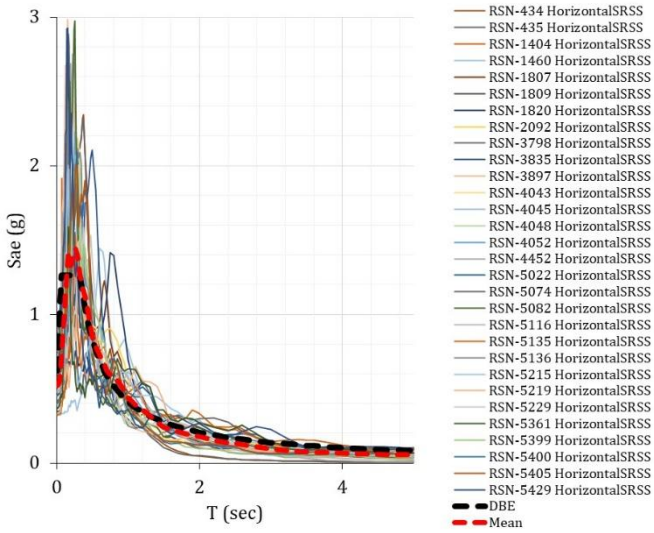

Figure 4. Elastic acceleration spectrum of the scaled records for 5 % damping.

Table.3 Ground motion properties used in the study

Record Sequence Number	Magnitude	Rjb (km)	Vs30 (m/sec)	Sae (g)
434	6.88	100.220	445.660	2.344
435	6.88	100.220	445.660	2.317
1404	7.62	110.300	465.860	2.148
1460	7.62	114.280	429.490	1.444
1807	7.13	146.510	442.020	1.487
1809	7.13	112.260	414.030	1.424
1820	7.13	171.890	430.690	1.417
2092	6.70	119.840	424.900	1.527
3798	7.13	177.390	418.830	1.433
3835	7.90	139.110	428.080	2.106
3897	6.61	101.340	481.500	2.983
4043	6.60	190.890	477.350	2.190
4045	6.60	104.820	441.840	1.670
4048	6.60	133.300	412.230	2.184
4052	6.60	155.460	477.350	2.227
4452	7.10	118.210	485.040	2.749
5022	6.80	147.650	431.940	1.432
5074	6.80	134.370	467.350	2.889
5082	6.80	131.500	406.760	2.973
5116	6.80	106.860	487.670	1.477
5135	6.80	182.610	440.000	1.554
5136	6.80	158.140	427.040	2.314
5215	6.80	195.890	478.540	2.004
5219	6.80	131.020	432.690	1.488
5229	6.80	146.600	473.500	1.586
5361	6.80	141.960	423.000	1.592
5399	6.80	125.850	471.230	2.065
5400	6.80	159.010	461.740	2.090
5405	6.80	158.820	425.880	2.006
5429	6.80	142.100	471.420	2.928

3. Results and Discussion

In this study, the Newmark-beta method (Newmark, 1959) was employed for time-history analysis. To ensure unconditional stability, the gamma (γ) and beta (β) coefficients were set to 0.5 and 0.25, respectively. Rayleigh damping was used to formulate the damping, and the damping ratio was assumed to be 5%. The mass and stiffness proportional coefficients were determined based on different period values, and were considered for viscous proportional damping. When determining the number of modes considered in this study, it was ensured that the mass participation rate of the modes exceeded 95%, which corresponds to the first 12 modes for this study.

The torsional behavior coefficients (η_{bi}) obtained from Nonlinear Dynamic Time History Analyses performed in both the x and y directions for 30 acceleration records will be discussed in this section. Within the scope of the study, only the torsional behavior of a 9-story reinforced concrete building was considered. While calculating the torsional behavior coefficients, the ends of the L-shaped arms and the corner of the building were taken into account. The points where the torsional behavior was considered are shown in Figure 5.

After determining the minimum (Δ_{imin}) and maximum (Δ_{imax}) displacements per story as specified in the code from the displacements obtained from the nonlinear dynamic time history analyses, the averages ($\Delta_{iaverage}$) of these displacements were calculated, and the torsional behavior coefficient was computed separately for each story. These expressions are given by $\Delta_{iaverage}$ in equation 1, and the story torsional behavior coefficient η_{bi} is calculated using equation 2.

$$\Delta_{iaverage} = \frac{\Delta_{imax} - \Delta_{imin}}{2} \quad (1)$$

$$\eta_{bi} = \frac{\Delta_{imax}}{\Delta_{iaverage}} \quad (2)$$

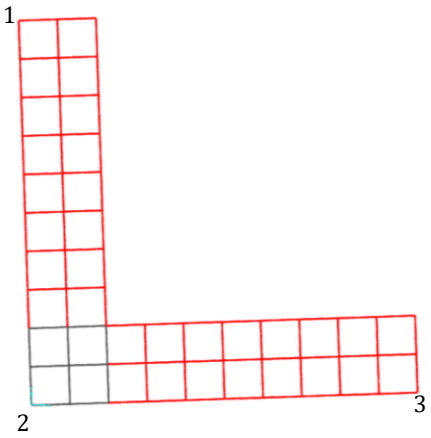

Figure 5. Considered corner points of L shape structure.

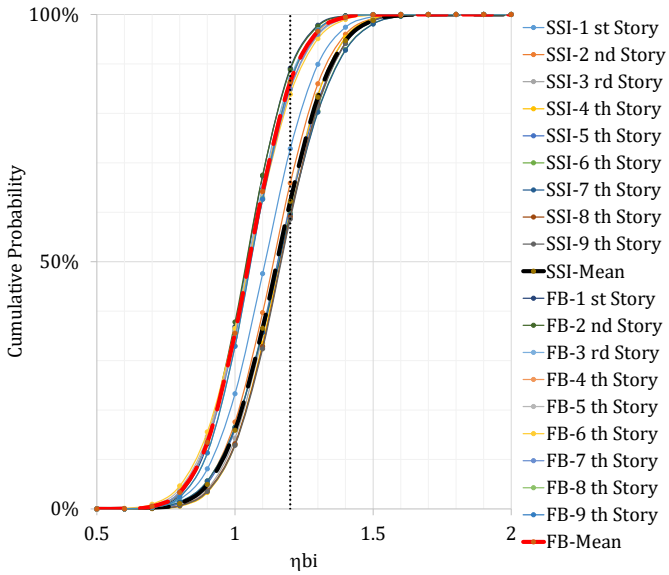

Figure 6. Fragility curves for torsional irregularity.

The fragility curves presented in Figure 6 are developed using a lognormal cumulative distribution function (CDF) to estimate the probability of exceeding specific damage states, with the torsional behavior coefficient (η_{bi}) used as the engineering demand parameter (EDP) (Forcellini, 2021). The fragility function is formulated based on equation 3, and the probabilities of exceedance for isolator displacements are also illustrated in Figure 4.

$$P(D > s \mid IM) = \Phi \frac{\ln(IM) - \ln(\mu)}{\sigma} \quad (3)$$

In this context:

P represents the probability of structural damage (D) exceeding a given damage state;

Φ denotes the standard normal cumulative distribution function;

IM is the selected intensity measure value;

σ is the standard deviation of the natural logarithm of the

seismic intensity measure;
μ is the mean of the natural logarithm of the seismic intensity measure.

4. Conclusions

In this study, nonlinear time history analyses were performed using 30 different bi-directional ground motion pairs by applying two horizontal components simultaneously, to evaluate the torsional behavior of a nine-story L-shaped reinforced concrete building under seismic loading. The analyses were conducted for both fixed-base and soil-structure interaction (SSI) conditions. Torsional behavior coefficients (ηbi) were calculated for each story based on the displacements obtained from these analyses. Fragility curves developed using ηbi as the engineering demand parameter showed that the probability of exceeding the critical ηbi value of 1.2 was approximately 10% for the fixed-base condition and about 40% under SSI. These observations clearly demonstrate the significant influence of SSI on torsional response and highlight the importance of accounting for SSI effects in the seismic design and performance assessment of torsionally irregular structures.

Author Contributions

The percentages of the author' contributions are presented below. The author reviewed and approved the final version of the manuscript.

	I.O.
C	100
D	100
S	100
DCP	100
DAI	100
L	100
W	100
CR	100
SR	100
PM	100
FA	100

C=Concept, D= design, S= supervision, DCP= data collection and/or processing, DAI= data analysis and/or interpretation, L= literature search, W= writing, CR= critical review, SR= submission and revision, PM= project management, FA= funding acquisition.

Conflict of Interest

The author declared that there is no conflict of interest.

Ethical Consideration

Ethics committee approval was not required for this study because of there was no study on animals or humans.

References

Abdel Raheem KA, Abdel Raheem SE, Soghair HM, Ahmed MH, 2010. Evaluation of seismic performance of multistory buildings designed according to Egyptian code. J Eng Sci Assiut Univ, 38(2): 381-402.

Abdel Raheem SE, Ahmed MM, Ahmed MM, Abdel-shafy AG. 2018. Evaluation of plan configuration irregularity effects on seismic response demands of L-shaped MRF buildings. Bull Earthq Eng, 16: 3845-3869.

Bharti AK, Garg V, Chandrawanshi S. 2025. A critical review of seismic soil-structure interaction analysis. J Istruc, 72: 108221.

Carvalho G, Bento R, Bhatt C. 2013. Nonlinear static and dynamic analyses of reinforced concrete buildings-Comparison of different modelling approaches. Earthq Struct, 4(5): 451-470.

Das PK, Dutta SC, Datta TK. 2021. Seismic behavior of plan and vertically irregular structures: state of art and future challenges. Nat Hazards Rev, 22(2): 04020062.

De Stefano M, Pintucchi B. 2008. A review of research on seismic behaviour of irregular building structures since 2002. Bull Earthq Eng, 6: 285-308.

Forcellini D. 2021. Analytical fragility curves of shallow-founded structures subjected to soil-structure interaction (SSI) effects. Soil Dyn Earthq Eng, 141: 106487.

Najar IA, Ahmadi R, Amuda AG, Mourad R, Bendary NE, Ismail I, Tang S. 2025. Advancing soil-structure interaction (SSI): a comprehensive review of current practices, challenges, and future directions. J Infrastruct Preserv Resil, 6(1): 5.

Newmark NM. 1959. A method of computation for structural dynamics. J Eng Mech Div, 85(3): 67-94.

NIST G. 2012. Soil-structure interaction for building structures. National Earthquake Hazards Reduction Program (NEHRP), California, USA, pp: 1-20.

Oz I. 2025. Seismic pounding effects of typical midrise reinforced concrete structures subjected to soil–structure interaction effects. J Steng, 151(2): 05024005.

Ozer E, Inel M. 2025. The effect of single and combined use of base isolator and fluid viscous damper on seismic performance in a conventional RC building with torsional irregularity. J Build Eng, 101: 111898.

PEER. Pacific Earthquake engineering research center. Strong ground motion database. https://ngawest2.berkeley.edu/ (accessed date: November 15, 2024).

Shirzadi M, Behnamfar F, Asadi P. 2020. Effects of soil–structure interaction on inelastic response of torsionally-coupled structures. Bull Earthq Eng, 18: 1213-1243.

Solomon AA, Hemalatha G. 2013. Limitation of irregular structure for seismic response. Int J Civil Struct Eng, 3(3): 579-590.

Sucuoğlu H, Kaatsız K. 2021. Torsional ductility spectrum for predicting ductility distribution in simple asymmetric-plan structures. Earthq Eng Struct Dyn, 50(2): 538-559.

TBEC. 2018. Turkish seismic earthquake code. TBEC, Ankara, Türkiye, pp: 1-416.

Black Sea Journal of Engineering and Science
doi: 0009.0003.1905.6346/1638291

Open Access Journal
e-ISSN: 0000 – 0000

Araştırma Makalesi
Cilt 8 - Sayı 5: 1279-1296 / Eylül 2025
Volume 8 - Issue 5: 1279-1296 / September 2025

ANALİTİK HİYERARŞİ PROSESİ VE BULANIK MANTIK YAKLAŞIMLARININ İHALEYİ KAZANACAK KURULUŞUN SEÇİMİNDE KULLANILMASI

Serhat ALTINTAŞ[1]*, Latif Onur UĞUR[1]

[1]*Düzce University, Graduate Education Institute, Department of Civil Engineering, Düzce, Türkiye*

Özet: Bu çalışmanın amacı, yüklenici seçim süreçlerinde kazanan kuruluşun, özellikle Analitik Hiyerarşi Prosesi ve Bulanık Mantık yaklaşımlarının entegrasyonunu incelemekte ve bu yöntemlerin etkinliğini değerlendirmektedir. Çalışma inşaat sektörüne yüklenici seçim kriterleri anlayışana ve en iyi yüklenici seçim süreçlerinin analiz edilmesi, seçilmesi için bir yöntem olan Analitik Hiyerarşi Prosesi ve Bulanık Mantık yaklaşımları ile katkıda bulunacaktır. Bu bağlamda kullanılan yöntemler, firmaların performansını objektif bir şekilde ölçülerek karşılaştırılmıştır. Sağlanan Python betiğinin Analitik Hiyerarşi Prosesi ve Bulanık Mantık yöntemlerini kullanarak yüklenici firmaların değerlendirilmesinin nasıl gerçekleştirdiğini detaylı bir şekilde açıklamaktadır. Çalışmada, ihalede başarılı bir yüklenici seçimi karar verme süreci için kritik faktörleri belirlemek, bu faktörleri değerlendirmek ve sonuçları analiz etmek amacıyla Analitik Hiyerarşi Prosesi ve Bulanık Mantık yöntemlerinin nasıl uygulanabileceğini detaylı bir şekilde açıklamaktadır. Ayrıca, her iki yaklaşımın avantajları, dezavantajları ve uygulama bağlamında karşılaştırılması yapılarak, ihale süreçlerinde karar verme süreçlerinin iyileştirilmesine yönelik öneriler sunulmaktadır. Bu çalışmanın Analitik Hiyerarşi Prosesi sonuçlarına göre; Firma-1 %78 ile en iyi performansa sahip firma olarak öne çıktığı tespit edilmiştir. Kalite, teknik yeterlilik ve maliyet gibi kriterlerde yüksek puanlar almış olduğu sonucuna varılmıştır. Bulanık Mantık sonuçlarına göre; Firma-1 yine %68.20 ile en yüksek puanı almış, ancak Bulanık Mantıkta bazı farklılıklar olduğu tespit edilmiştir. Bulanık mantıkta Firma-15, Firma-8 gibi firmalar öne çıkarken, Analitik Hiyerarşi Prosesi sonuçlarında daha geride kalan firmalar olduğuda tespit edilmiştir. Bu da Bulanık Mantık değerlendirme kriterlerinin esnekliğini ve bu iki yöntemin farklı neticeler verebileceği sonucuna varılmıştır. Bu çalışma, iş dünyasındaki profesyoneller, akademisyenler ve karar alıcılar için ihale süreçlerinde etkili karar verme stratejileri geliştirmek amacıyla bir temel oluşturmayı hedeflemektedir.

Anahtar Kelimeler: Python, Analitik hiyerarşi prosesi, Çok kriterli karar verme, Bulanık mantık

Use of Analytical Hierarchy Process and Fuzzy Logic Approaches in Selection of the Organization That Will Win the Tender

Abstract: The purpose of this study is to examine the integration of the winning organization, especially Analytical Hierarchy Process and Fuzzy Logic approaches, in contractor selection processes and evaluate the effectiveness of these methods. The study will contribute to the understanding of contractor selection criteria in the construction industry and Analytical Hierarchy Process and Fuzzy Logic approaches, which are a method for analyzing and selecting the best contractor selection processes. The methods used in this context were compared by objectively measuring the performance of the companies. It explains in detail how the provided Python script performs the evaluation of contractor companies using Analytical Hierarchy Process and Fuzzy Logic methods. The study explains in detail how Analytical Hierarchy Process and Fuzzy Logic methods can be applied to identify critical factors for the decision-making process of successful contractor selection in the tender, evaluate these factors and analyze the results. Additionally, by comparing the advantages, disadvantages and application context of both approaches, suggestions are offered to improve decision-making processes in tender processes. According to the Analytical Hierarchy Process results of this study; It was determined that Company-1 stood out as the company with the best performance with 78%. It was concluded that it received high scores in criteria such as quality, technical competence and cost. According to Fuzzy Logic results; Company-1 again received the highest score with 68.20%, but it was determined that there were some differences in Fuzzy Logic. While companies such as Company-15 and Company-8 stand out in fuzzy logic, it has also been determined that there are companies that lag behind in the Analytical Hierarchy Process results. This shows the flexibility of Fuzzy Logic evaluation criteria and the conclusion that these two methods can give different results. This study aims to provide a basis for professionals, academics and decision makers in the business world to develop effective decision-making strategies in tender processes.

Keywords: Python, Analytic hierarchy process, Multi-criteria decision making, Fuzzy logic

***Sorumlu yazar (Corresponding author):** Düzce University, Graduate Education Institute, Department of Civil Engineering, Düzce, Türkiye
E mail: serhat_altintas@msn.com (S. ALTINTAŞ)
Serhat ALTINTAŞ https://orcid.org/0009-0003-1905-6346
Latif Onur UĞUR https://orcid.org/0000-0001-6428-9788

Gönderi: 12 Şubat 2025 **Received:** February 12, 2025
Kabul: 11 Haziran 2025 **Accepted:** June 11, 2025
Yayınlanma: 15 Eylül 2025 **Published:** September 15, 2025

Cite as: Altıntaş S, Uğur LO. 2025. Using analytical hierarchy process and fuzzy logic approaches in selecting the organization that will win the tender. BSJ Eng Sci, 8(5): 1279-1296.

1. Giriş

İnşaat sektörü, ülkelerin ekonomik büyümesi ve kalkınması açısından kritik bir öneme sahiptir. Ekonomik faaliyetlerin temel itici güçlerinden biri olan bu sektör, ulusların sürdürülebilir kalkınması için vazgeçilmez bir unsur olarak değerlendirilmektedir. Diğer yapıların yanı sıra binaların, yolların, köprülerin sağlanması, istihdam yaratılması, gayrisafi yurtiçi hasılaya, milli gelire, ekonomik büyümeye ve dünya ekonomisinin gelişmesine yapılan katkılarında göstergesi olduğu belirtilmektedir. Ekonomik katkıya ve ekonomik kalkınmayı yönlendiren bir etken olmasına rağmen, sektörde yürütülen inşaat projelerinin, geç teslim süreçleri, maliyet, kalite ve güvenlik performansı projelerin temel hedeflerini karşılamama özelliği taşıdığı da bilinmektedir. Bu durumların oluşmasındaki temel süreç özellikle dünyanın gelişmekte olan inşaat pazarlarında inşaat projelerinin ihale sürecinde bölüm kriterlerinin verimsiz uygulanmasından kaynaklanan zayıf yüklenici seçimi ve kaynaklarla ilgili sorunlarla da ilişkilendirilmektedir (Okereke vd., 2022).

Yüklenici değerlendirmesi ve seçimi, inşaat projelerinde (ister kamu ister özel sektör olsun) hayati bir süreç olduğu ifade edilmektedir. Müşterinin gereksinimleri ve proje hedefleri doğrultusunda projeyi teslim edebilecek deneyimli ve uygun bir yüklenicinin seçilmesi amaçlanmaktadır. Yüklenici seçimi, inşaat projelerinin başarısını ve ilerlemesini etkileyen önemli bir karar süreci olup bu, yüklenicinin yanlış seçilmesi durumunda sonuçların düşük kalite, programın aşılması ve projenin maliyet performansında istenmeyen zarar ve artışlara sebep olacağı anlamına gelmektedir. En iyi teklif sahibinin başarısı çoğu zaman ihale gereksinimlerinin uygunluğuna, müşterinin ve proje yöneticilerinin bilgi ve deneyimlerine dayanan zor bir iştir. Müşterinin bir proje için yetenekli bir yüklenicinin seçimine yönelik kararını etkileyen temel göstergeler dizisi yüklenici seçim kriterleri olarak bilinmektedir (Eze vd., 2020).

Yüklenici seçim kriterleri, zaman, maliyet ve kalite performansıyla ilgili ön yeterlilik ve ihale değerlendirme kriterlerinin bir karışımıdır. Proje müşterilerinin ve danışmanların kararları, diğerlerinin yanı sıra yüklenicilerin geçmiş performansı, benzer bir işteki önceki deneyimler, müşterilerin yüklenicilerle ilgili bilgi ve deneyimleri, mali kapasite ve yüklenicilerin itibarı gibi faktörler tarafından şekillendirilmektedir. Bu faktörler, eldeki iş için yüklenici seçimini ve gelecekteki patronajı da etkilemektedir (Onyeagam vd., 2019).

Yüklenici değerlendirme kriterleri, proje teslimiyle ilgili risklerin en aza indirilmesine, müşteri için değerin en üst düzeye çıkarılmasına ve proje üyeleri arasında uzun vadeli bir ilişki kurulmasına yardımcı olmaktadır. Seçim kriterlerinin etkili bir şekilde takip edildiği şantiyelerde kazalar da azalmaktadır. En düşük teklif kriterini kullanma geleneği, proje performansında her zaman en iyi sonuçlar vermemektedir. Etkili yüklenici bölümü için birçok kriter savunulmaktadır. Yüklenici veya müteahhit seçiminde yalnızca teklif fiyatına odaklanmak, projelerin teslimine yaşanan sorunların temel nedeni olmaktadır. Ülkemizde olduğu gibi diğer birçok ülkede de hala en düşük teklifi veren kesim geleneğinin uygulamada olduğunu görülmektedir. Araştırmalar, en düşük teklifi verenin projeyi planlanan sürenin ve maliyetin aşıldığı ve kalitenin tehlikeye girebileceği bir duruma sokma olasılığının yüksek olduğunu göstermektedir (Maqsoom vd., 2020).

Bunun nedeni, proje temellerini ve yüklenicilerin kar ve gelirlerini etkileyen sorunlara neden olduğu tespit edilen en düşük maliyet anlayışı olduğu ve yüklenicilerin ön yeterliliği ve bölümlerine ilişkin çalışmalar, özellikle uluslararası sahnelerde çok büyük rol oynamaktadır. Ayrıca yüklenicilerin seçim kriterlerinin proje müşterileri ve inşaat performansı üzerindeki faydaları araştırmacılar tarafından ayrıntılı olarak ele alınmadığı ve yüklenicilerin seçimi ve ön yeterliliğine ilişkin mevcut az sayıda çalışma yüklenici seçim kriterlerine odaklanmaktadır (Eke vd., 2019; Khoso vd., 2021).

Bu bağlamda, bu çalışmada küresel pazarlarda rekabetin arttığı günümüzde, ihale süreçlerinin etkili bir şekilde yönetilmesi ve kazanan kuruluşun belirlenmesi, bir organizasyonun sürdürülebilirliği ve başarısı için kritik bir öneme sahip olmaktadır. Çok kriterli karar verme yöntemleri, özellikle Analitik Hiyerarşi Prosesi ve Bulanık Mantık, karmaşık kararlar almak ve belirsizlikle başa çıkmak için kullanılan önemli araçlardır. Bu çalışma, ihale süreçlerinde kazanan kuruluşun belirlenmesinde çok kriterli karar verme yöntemlerinin uygulanmasını ele almaktadır. İhale süreçlerinde karar verme, çeşitli faktörlerin bir araya geldiği karmaşık bir süreçtir. Maliyetler, kalite, süre, teknik yetenekler gibi çeşitli kriterler göz önüne alınmalı ve bu kriterlerin ağırlıkları belirlenmektedir. Bu noktada, Analitik Hiyerarşi Süreci ve Bulanık Mantık gibi yöntemler, karar verme sürecini yapılandırmak ve belirsizlikle başa çıkmak adına değerli araçlar sunmaktadır. Yüklenicilerin seçimi, bir teklifin değerlendirilmesi ve yüklenicinin uygunluğunun değerlendirilmesi için temel olarak kullanılan belirli kriterlere bağlı olup inşaat projelerinde uygun yüklenicinin değerlendirilmesi ve seçimi için bir dizi faktör ve kriteri tanımlayan çok sayıda çalışma bulunmaktadır. Herhangi bir müşterinin temel faaliyetlerinden biri yüklenici seçimi olup en iyi yükleniciyi seçmek için uygun ve kesin bir yöntem olmadan, bir projenin tamamlanması muhtemelen etkilenmektedir. Bu çalışmada Analitik Hiyerarşi Prosesi ve Bulanık Mantık yaklaşımlarının ihaleyi kazanacak kuruluşun seçiminde kullanılması incelenmektedir. Bu model, proje yönetim ekiplerinin, yalnızca en düşük teklife dayanmayan bir seçim sürecinde tatmin edici sonuçlar sunma olasılığı en yüksek olan yüklenicileri belirlemesine yardımcı olabileceği planlanmaktadır. Bu çalışma inşaat sektörüne iki şekilde katkıda bulunmaktadır; birincisi, seçim kriterleri anlayışını önem derecelerini de kapsayacak şekilde genişletmekte, ikincisi ise en iyi yüklenicinin analiz edilmesi ve seçilmesi için yeni bir yöntem olan Analitik Hiyerarşi Prosesi ve

Bulanık Mantık yaklaşımlarını uygulamaktadır. Çalışmamız kapsamında tespit edilen literatür taraması geniş ölçekli, mevcut araştırmaları kapsaması ve çalışmanın yeniliği ve özgünlüğü konusunda zayıflıklara yol açmaması adına, en yakın sonuçları veren ulusal alanda ve uluslararası alanda yapılan makaleden oluşmaktadır. Bu kapsamda yapılan literatür çalışmaları aşağıdaki gibidir;

1.1. Bulanık Mantık (Fuzzy Logic) Alan Yazın Literatür Taraması

Betonarme binaların deprem performansının bulanık mantık yöntemiyle değerlendirilmesi ile ilgili çalışmada, binaların performansı beton basınç dayanımı, kat sayısı, zemin kat alanı, kolon ve perde alanı ve mimari parametreler dikkate alınarak değerlendirilmiştir. Çalışmada Afyon, Bingöl ve Van illerinde sırasıyla 2002, 2003 ve 2011 yıllarında meydana gelen depremlerden etkilenen 18, 28 ve 146 binanın verileri kullanılmış, 192 bina verisinden 94 bina veri olarak işlenerek MATLAB (matrix laboratory) bulunan bulanık mantık kuralları uygulanarak test edilmiştir. Değerlendirilen binalar hafif, orta ve ciddi hasar görmüş veya yıkılmış binalar olup, önerilen yöntem, hızlı ikinci aşama (veya ikinci düzey) değerlendirme olarak sınıflandırılmıştır. Sonuçlara göre %88 başarı oranına ulaşılmış olup, bu durum betonarme binaların sismik performansının belirlenmesinde kullanılabilecek bulanık mantık yönteminin önemini olduğu sonucuna varmışlardır (Yıldız vd., 2024).

Yığma duvarların mekanik davranışının belirlenmesinde bulanık mantık yöntemleri ile yapılan çalışmada, malzeme özelliklerinin yanı sıra duvarın mekanik davranışı, yerinde duvar testleri ve sayısal analizlerin de gerekli olduğu, akıllı öğrenme tekniklerinin desteğiyle duvarların durumunun tahminlene çalışması yapılmıştır. Bu, deneyi ve modellemeyi destekleyecek bulanık mantık gibi matematiksel araçların kullanımının, çalışılan olgunun tekrarlanmasına gerek kalmadan karmaşık mühendislik sorunlarının çözümünde faydalı olduğunu tespit etmişlerdir. Duvarın davranışının daha doğru ve hızlı bir şekilde analiz edilebilmesi için akıllı öğrenme tekniklerinden biri olan bulanık yöntem kullanılarak analizler yapılmış ve deneysel analizin uygulandığı çalışmalardaki verilerle karşılaştırılmış, duvarın davranışı, esnekliği ve enerji kapasitesi tahmin edilmeye çalışılmıştır. Bulanıklaştırmada, duvarın özelliklerini etkileyecek malzeme parametreleri ve duvar yük kapasiteleri girdi olarak kullanılmış, farklı çalışmalardan otuz beş veri seti, deney ve modelleme verisi alınarak, tahmin sonuçları ampirik sonuçlarla karşılaştırıldığında faydalı ve uygulanabileceği sonucuna varmışlardır. (Zengin vd., 2023).

'SMRGT' olarak bilinen yeni bir bulanık mantık modelinin akış katsayısı oranını tahminlemesi ile ilgili çalışmada, bulanık mantık sistemi üzerine kurulu bir akıllı model kullanılmıştır. Bulanık modelde yağış, sıcaklık, nem, eğim ve arazi kullanım verileri girdi değişkenleri olarak dikkate alınmış, veriler basit fonksiyonu ve bulanık kural oluşturma tekniğine (SMRGT) ilişkin orijinal açıklaması, bulanık Mamdani metodolojisine dayandırılmış ve çıktı olarak akış katsayısını kullanılmıştır. Modelin sonuçları mevcut verilerle karşılaştırıldığında maksimum, minimum, ortalama, standart sapma, çarpıklık, varyasyon ve korelasyon katsayıları yedi istatistiksel parametre olduğu, dört tür hata kriteri, Ortalama Mutlak Göreli Hata (MARE), Ortalama Karesel Hata (MSE), Ortalama Mutlak Hata (MAE) ve Ortalama Karekök Hata (RMSE) olduğu ve dağılım diyagramından oluştuğu sonucuna varmışlardır (Güzel vd., 2024).

1.2. Analitik Hiyerarşi Proses (AHP) Alan Yazın Literatür Taraması

Endonezya'da petrol ve gaz sektöründe hizmet sunan yerel bir firmada dünya petrol fiyatlarının düştüğü 2015 yılında kurulmuştur. 2024'ün başlarında SOE'den ve özel sektörden Jambi Projesi, Lampung Projesi, Jambi Projesi ve Cepu Projesi olmak üzere 4 ihale teklifi almış ancak birim sınırlamaları nedeniyle bu firmanın bir karar alma süreci olmadığı için yapılan bu çalışmada 3 projeye yönelik önerilerde bulunmak amacıyla Analitik Hiyerarşi Süreci (AHP) kullanılmıştır. Bu Analitik Hiyerarşi Süreci değerlendirmesinde kullanılan kriterler pazarlama ve satış, müşteriler, finansal fizibilite, yönetim ve proje spesifikasyonlarıdır, bu kriterlerin her birinin çeşitli alt kriterleri ve toplam 13 alt kriterde toplanmıştır. Değerlendirmeye göre en yüksek ağırlığa sahip kriter finansal fizibilite (%51,4), en yüksek ağırlığa sahip alt kriter ise ödeme gücü (%22,9) olduğu tespit edilmiştir. Yapılan değerlendirme sonrasında sıralamaya göre alınması önerilen 3 proje Jambi projesi (%33,4), Cepu Projesi (%30,7) ve Lampung Projesi (%19) olduğu sonucuna varılmıştır. Bu analiz, KİT girişimlerinin özel sektör girişimlerinden daha güçlü ödeme kabiliyetine, güvenilirliğe ve algılanan kârlılığa sahip olduğunu da göstermektedir (Wibisono vd., 2024).

Yükleniciler inşaat projelerinde tamamlayıcı bir rol oynamaktadır ve onların nitelikleri projenin başarısının çeşitli yönlerini doğrudan etkilemektedir. Yüklenicilerin tarafsız seçimi dünya çapında inşaat sektöründe, özellikle de nihai seçimde tarafsızlığın önemli olduğu kamu projelerinde bir zorluk olduğu ifade edilmektedir. Yüklenicileri değerlendirirken, seçim sürecini insan beyni için zorlu hale getiren çok sayıda faktörün dikkate alınması gerekmektedir. Bu çalışmada, bulanık teoriyi uygulayarak yüklenicinin ön yeterliliğini değerlendirmek için iki yöntemi tanıtmakta ve karşılaştırmaktadır. Buradaki fikir, yüklenicilerin seçimiyle ilgili karar vermede insan yargılarının matematiksel bir sistemde kullanılmasını kolaylaştırmaktır. Çalışmada Buckley yöntemini kullanarak seçim kriterleri için bulanık ağırlığın belirlenmesine dayanmaktadır. Daha sonra yüklenicilerin yeterlilik sıralamasında Bulanık TOPSIS ve Bulanık SAW yöntemleri kullanılmıştır. Uygulanan yöntemin, yüklenicilerin nitelik bazlı seçiminin kalitesini artırdığı ve uygun olmayan yüklenicilerin işe alınmasından kaynaklanabilecek olası kayıpları önleyebileceği sonucuna varılmıştır (Tafazzoli vd., 2024).

Tedarikçi seçme süreci, endüstriyel inşaat projelerinin

yönetiminde zorlu bir süreçtir. Yapılan bu çalışmada inşaat şirketleri, birden fazla veri tabanına yayılmış büyük miktarda veri üretmekte olup bu veriler, gelecekteki projelere ilişkin kararları desteklemek amacıyla kullanılmadığını tespit etmişlerdir. Bu soruna çözüm bulmak amacıyla endüstriyel projelerde uzmanlaşmış inşaat firmalarına özel bir veri ambarı geliştirilmiştir. Metodoloji olarak, inşaat yönetimi kararlarını desteklemek ve tedarikçileri farklı iş türleri için değerlendirmek için doğrudan sorgulamalara olanak tanıyan ve ilgili raporları üreten Çevrimiçi Analitik İşleme (OLAP) kullanmışlardır. Bu yaklaşımı benimseyen inşaat şirketlerinin, projeleri için hangi tedarikçileri seçecekleri konusunda daha bilinçli kararlar alarak ekonomik performanslarının arttığı tespit edilmiştir. Bu şirketlerin, ellerindeki verilerden yararlanarak karar verme süreçlerinin kalitesini artırabileceği ve endüstriyel inşaat projelerinin süreçlerinin iyileştirebileceği sonucuna varmışlardır (Ahmad vd., 2023).

1.3. Python Alan Yazın Literatür Taraması

Python ile difüzyon sınırlı toplama; dendritik yapılar ve algoritmik sanat üzerine yapılan çalışmada, difüzyon sınırlı toplama, basitliği ve nano ve mikropartikül toplamaları gibi fizikteki geniş uygulamaları nedeni ile bu çalışmada Python ile difüzyon sınırlı toplama algoritması yazılmıştır. Python'un Turtle kütüphanesi, toplamı büyüdükçe bilgisayar monitöründe çizmek için kullanılmış ve algoritma Raspberry Pi üzerinde çalıştırılmıştır. Difüzyon sınırlı toplama simülasyonu için ucuz ve taşınabilir bir ortam oluşturularak algoritmada iki farklı seçenek yerleştirilmiştir. Sonuçlar çarpışmadan sonra birincil parçacığın agreganın dışına dönmesine izin vermediği ve ikincisinin, birincil parçacığın agreganın hem içinden hem de dışından süzülmesine izin verdiği tespit edilmiştir. Algoritma ile 500-2000 birincil parçacıktan oluşan küresel dendritik yapılar elde edildiği bu yapıların fraktal boyutu 1,68 civarında olduğu, poroziteleri %50'nin altında ve dönme yarıçapları da hesaplanarak dendritik yapıları kullanan algoritmik sanat örnekleri de verilebileceği sonucuna varmışlardır (Allahverdi vd., 2024).

Elektrikli scooter ve bisikletler için yol ağı kısıtlamalarının python tabanlı değerlendirilmesi ile ilgili yapılan çalışmada, elektrikli scooterlar için optimal yol tercihlerinde dikkate alınan parametrelerden eğim, yol sınıfı, yol uzunluğu ve arazi örtüsü parametreleri üzerinde, bir başlangıç noktası ve bir yolun bulunduğu çeşitli uygulamalar ve incelemeler yapılmıştır. Araştırma için en kısa yol problemini, maliyet hesaplamalarını ve çeşitli veri işleme yöntemlerini kullanmak için Dijkstra Algoritması, QGIS GIS yazılımı, Python programlama dili ve çeşitli modüller kullanılarak uygulamalar çalışma başlıkları altında karşılaştırılmış ve farklı parametrelerin optimal rota tercihlerine etkisi karşılaştırılarak tartışılmıştır. Araştırma sonuçları parametrelerin farklı çalışmalardaki uygulamalarda sonuçları doğrudan etkilediği, çeşitlilik getirdiği ve beklenen sonuçların elde edildiği tespit edilmiştir. Elektrikli scooter gibi araçların kat edebileceği maksimum mesafe veya süre gibi ek parametrelerin eklenmesi, daha hassas ve çeşitli kaynakların kullanılması bu tür araştırmaların önemini daha da geliştireceği sonucuna varmışlardır (Erener vd., 2024).

C# ve Python programlama dillerinin SQL SERVER DML işlemlerinde performans ve kodlama açısından karşılaştırılması üzerine yapılan çalışmada, programlama dilleri arasında en yaygın kullanılan C# ve Python dilleri, işlem performansı ve SQL DML (veri manipülasyonu) gerçekleştirmek için yazılması gereken kod miktarı açısından değerlendirmişlerdir. En yaygın kullanılan veri tabanı yönetim sistemlerinden biri olan MSSQL veri tabanı üzerinden ınsert, select, update, delete gibi işlemleri gerçekleştirilerek ve işlem sonuçlarını ekrana yazdırarak işleme performansı açısından her iki programlama dilinin de diğerine önemli bir üstünlüğü olmadığı gözlendi ancak işlem sürelerine bakıldığında matematiksel olarak Python dili daha iyi performans sergilediği tespit edilmiştir. Ayrıca kod boyutu ve okunabilirlik açısından C# genel olarak kod okunabilirliği açısından daha okunabilir bir dil olarak değerlendirilse de bu çalışma için yazılan programlar bağlamında iki programlama dili arasında kod okunabilirliği açısından bir fark tespit edilmemiştir. Sonuçlar kod boyutu açısından Python açık bir üstünlük sağladığı, her iki dilin birbirine göre üstün özelliklere sahip olduğu ve bu iki dil arasında veri işleme dili (DML) işlemlerinde birbirlerine tercih sebebi olabilecek kesin bir üstünlüğün olmadığı, dil seçimi projenin gereksinimlerine, ekosisteme ve ekibin becerilerine göre yapılması gerektiği sonucuna varmışlardır (Yeşilyurt vd., 2024).

2. Materyal ve Yöntem

Bu çalışmada, ihale süreçlerinde çok kriterli karar verme yöntemlerinin etkinliğini değerlendirmek amacıyla çeşitli ihalelere ait veriler kullanılacaktır. Çalışmada kullanılan materyal ve yöntemler, firmaların performansını objektif bir şekilde ölçülerek karşılaştırılmıştır. Sağlanan Python betiğinin Analitik Hiyerarşi Prosesi ve Bulanık Mantık yöntemlerini kullanarak yüklenici firmaların değerlendirilmesinin nasıl gerçekleştirdiğini detaylı bir şekilde açıklamaktadır.

2.1. Bulanık Mantık

Bulanık mantık, 1965 yılında Kaliforniya Üniversitesi'nde Lotfi Zadeh tarafından bulunmuş ve geliştirilmiş ve "bulanık" adını verilmiştir. Geleneksel bilgisayar mantığının kafa karıştırıcı veya kesin olmayan verileri işleyemeyeceğine inanılmaktadır. İnsanlar gibi, bir bilgisayar da "doğru ve yanlış" içinde geniş bir değer aralığını entegre edebilmektedir. Bunlar "kesinlikle evet", "belki evet", "söyleyemem", "belki hayır" ve "kesinlikle hayır" şeklinde olabilmektedir (Umarusman, 2023; Çetinkaya vd., 2024). Bulanık mantık, bir makine öğrenme çerçevesi veya yapay zeka kullanıldığında karar verme stratejisi olarak kullanılmaktadır. Genel olarak "0 ile 1" arasında değişen gerçek değişken değerlerinin değerlendirilmesi olarak ifade edilmektedir. Bulanık

mantık, "0 ile 1" arasındaki gerçek sayıları temsil etmek için uygulanmakta olup, bulanık mantık oldukça belirsiz olan her şeyi ifade etmektedir. Bir senaryo belirsiz olduğunda, bilgisayar "doğru ve yanlış" bir sonuç üretemeyebilmektedir. Boole Mantığına göre, "1 doğru'yu, 0 ise yanlış'ı" temsil etmektedir. Buna karşılık, bulanık mantık yöntemi, "doğru ve yanlıştan" daha fazla potansiyel değer olabilecek bir sorunun tüm belirsizliklerini dikkate almakta olup bulanık mantık, problem çözümleri olarak kesin değerler elde etmek için kullanılmaktadır (Kannan vd., 2023; Özdem vd., 2024; Öztekin., 2024).

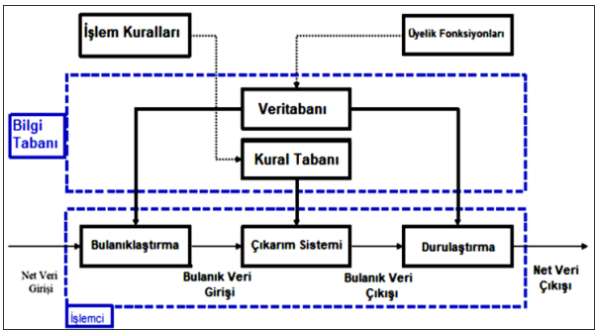

Şekil 1. Bulanık mantık sistemi işleyişi.

2.2. Analitik Hiyerarşi Prosesi

Analitik Hiyerarşi Süreci, 1970'li yıllarda matematikçi Thomas L. Saaty tarafından geliştirilen bir karar verme tekniğidir. Analitik Hiyerarşi, orijinal olarak geliştirilen Çok Kriterli karar verme yöntemlerinden biri olduğu belirtilmektedir. Kısaca ikili karşılaştırmalardan oran ölçekleri elde etme yöntemi olup karar vermeye yardımcı olmak için değerlendirme problemlerinde fayda teorisinin kullanılması zaten iyi bilinen resmi bir yaklaşım olduğu ifade edilmektedir. Ancak fayda teorisine dayalı karar verme modelleri, karar vericinin farklı kriter veya hedeflere yönelik değer ölçeklerini temsil eden fayda fonksiyonlarının oluşturulmasını gerektirmektedir (Prıncıvıshvamalar vd., 2023). Bu yöntem, çok kriterli karmaşık bir problemi bir hiyerarşi yapısına basitleştirmektedir. Hiyerarşi, karmaşık bir problemin çok seviyeli bir yapıda temsili olarak tanımlanır; burada ilk seviye hedef/amaç/amaçtır, ardından alt seviyeler, kriterler ve alt kriterler gelir ve son seviyeye kadar alternatifler gelmektedir. Bu yaklaşımla, karmaşık bir problem bölümlere ayrılabilir ve daha sonra bir hiyerarşi biçimine düzenlenebilir, böylece problem daha yapılandırılmış ve sistematik görünmektedir (Gürler, 2023).

Analitik Hiyerarşi Süreci yöntemi dört ana aşamadan oluşmaktadır. Birincisi, modeli bir hiyerarşiye göre yapılandırmak; ikincisi, kriterlerin alt kriterlerin ve alternatiflerin önemlerine göre ikili karşılaştırmalar yoluyla karşılaştırmalı yargısını yürütmek; Üçüncüsü, ikili karşılaştırmaların sonucunu bir değerlendirme matrisinde özetlemek; son olarak, normalleştirilmiş değerlendirme matrisinden elde edilen alternatiflerin tercihlerinin sırasını sentezlemektir. Otuz beş yıldan fazla bir süredir varlığını sürdüren Analitik Hiyerarşi Süreci, çok çeşitli uygulama alanlarında uygulanmakta olup metodolojisi, özellikle problem modelleme, çiftler arası karşılaştırmalar, yargı ölçekleri, türetme yöntemleri, tutarlılık endeksleri, eksik matris, ağırlıkların sentezi, duyarlılık analizi ve grup kararları alanlarında bazı sınırlamaları aşmak amacıyla daha da geliştirilmiştir [94, 95]. Analitik Ağ Süreci (ANP), bağımlılıklarla ilgilenen Analitik Hiyerarşi Süreci'nin bir genellemesi olup, gerçek hayattaki birçok Çok Kriterli karar verme (MCDM) problemi, farklı kriterler arasındaki etkileşimi ve bağımlılığı, ayrıca iç ve dış bağımlılıklar şeklinde farklı alt kriterler arasındaki etkileşimi ve bağımlılığı veya kriterlere alternatiflerden gelen geri bildirimler içerebilmektedir. Analitik Ağ Süreci yöntemi, ağdaki yukarıda belirtilen unsurlar arasındaki tüm bu etkileşimleri, bağımlılıkları ve geri bildirimleri modellemeye olanak tanımlanmaktadır (Jagoda vd., 2020; Mızrak vd., 2023).

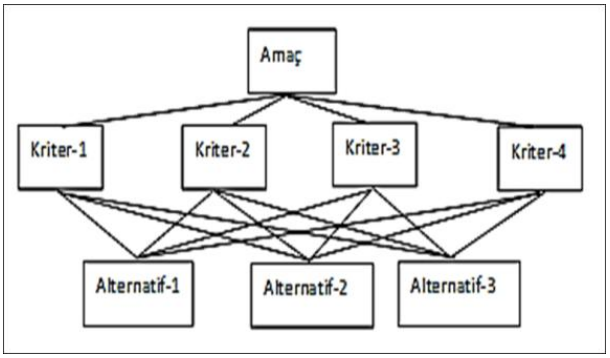

Şekil 2. AHP yönteminin hiyerarşik yapısı.

2.3. Python Programlama Dili

Python, basitliği ve okunabilirliğiyle tanınmış bir programlama dilidir. Guido van Rossum tarafından yaratılmış ve ilk olarak 1991'de yayınlanmıştır. Python, önemli miktarda boşluk kullanımıyla kod okunabilirliğini vurgulamaktadır. Nesne yönelimli, prosedürel ve işlevsel programlama dahil olmak üzere birden fazla programlama paradigmasını desteklemektedir. Python'un kapsamlı standart kütüphanesi, sağlam çerçeveleri ve geniş topluluk desteğiyle, onu web ve yazılım geliştirmeden bilimsel ve matematiksel hesaplamaya kadar çeşitli uygulamalar için oldukça çok yönlü ve uygun hale getirmektedir. Sözdizimi sezgisel olacak şekilde tasarlanmıştır ve kodu daha okunabilirdir, bu da onu programlamaya yeni başlayanlar için mükemmel bir seçim haline getirmektedir. Güçlü ve kullanıcı dostu veri analizi kütüphaneleri sayesinde Python, veri bilimi ve makine öğreniminin yükselişinde de önemli bir rol oynamaktadır. Artan popülaritesi ve geniş kapsamlı uygulamalarıyla Python, dünyada en çok aranan programlama dillerinden biri haline gelmiştir (Lazebna., 2021; Allahverdi vd., 2024; Erener vd., 2024).

Şekil 3. Python programlama dili ekran görüntüsü.

2.4. Veri Setleri

Farklı sektörlerden ve büyüklüklerden gelen ihalelerin detaylı bir analizi için seçilmiştir. Bu ihaleler, maliyet, süre, kalite, teknik kapasite gibi çeşitli kriterlerin değerlendirildiği tipik ihale süreçlerini temsil etmektedir. Çalışmanın temel metodolojisi, çok kriterli karar verme yöntemlerinin uygulanması ve sonuçlarının değerlendirilmesini içermektedir. İlk aşamada, ihale süreçlerinde önemli olan faktörler belirlenecek ve bu faktörlerin ağırlıkları Analitik Hiyerarşi Prosesi kullanılarak tespit edilecektir. Daha sonra, belirsizlikle başa çıkmak ve bulanık bilgiyi işlemek için Bulanık Mantık yöntemleri uygulanacaktır. Analitik Hiyerarşi Prosesi aşamasında, karar vericilerle yapılan görüşmeler ve literatür taraması sonucunda belirlenen kriterler için bir karar matrisi oluşturulmuş, ardından bu matris üzerinden ağırlık vektörleri hesaplanacaktır. Bulanık mantık aşamasında ise, belirlenen kriterlerin bulanıklık dereceleri uzman görüşleri ve geçmiş veri analizleri kullanılarak belirlenmiş, Bulanık Mantık kuralları oluşturulmuş ve çıkarım süreci gerçekleştirilecektir. Sonuçlar, Analitik Hiyerarşi Prosesi ve Bulanık Mantık yöntemlerinin ayrı ayrı ve birlikte uygulanmasının getirdiği avantajlar ve dezavantajlar açısından karşılaştırılacak ve değerlendirilecektir. Bu aşamadan elde edilen bulgular, ihale süreçlerinde karar verme stratejilerini iyileştirmek için öneriler sunmak amacıyla analiz edilecektir.

2.5. İhale Süreçlerindeki Karar Verme Zorlukları ve İhtiyaçları Belirleme

İhale süreci genellikle, potansiyel teklif sahiplerinin uzmanlık, deneyim ve mali istikrarlarına göre değerlendirildiği ön yeterlilik aşamasından başlayarak birkaç aşamadan oluşmaktadır. Bu aşama, müşterinin projeye teklif vermeye davet edebileceği en nitelikli ve yetenekli yüklenicileri belirlemesine yardımcı olduğu için çok önemlidir. Ön yeterliliğin ardından yüklenici ve alt yüklenicilerin teklifleri sunulur ve bunlar daha sonra müşteri veya ihaleyi veren kuruluş tarafından değerlendirilir ve karşılaştırılmaktadır. Bu aşama, yüklenicinin önerdiği proje zaman çizelgesi, bütçe ve kalite standartları da dahil olmak üzere tekliflerin kapsamlı bir incelemesini içermektedir. Teklifler değerlendirildikten sonra müşteri genellikle en yüksek teklifi verenleri ikinci tur müzakerelere katılmaya davet edilmektedir. Bu aşamada müşteri, teklif sahiplerinden ek bilgi veya açıklama talep edebilir ve ayrıca sözleşme şartlarını müzakere etmektedirler. Son olarak, başarılı teklif sahibine bir sözleşme verilmektedir. Sözleşme genellikle proje için ayrıntılı spesifikasyonlar ve gereksinimlerin yanı sıra üzerinde anlaşılan bütçe ve zaman çizelgesini de içermektedir. Başarılı teklif sahibi daha sonra projeyi yönetmekten ve projenin zamanında, bütçe dahilinde ve gerekli kalite standartlarında tamamlanmasını sağlamaktan sorumlu olmaktadır. Bu süreçte inşaat dünyasında bir proje için teklif verme süreci karmaşık ve zorluklarla dolu olabilmektedir. Hem müteahhitler hem de taşeronlar için inşaat ihale süreci, dikkatle yönetilmesi gereken çeşitli zorluklar getirmektedir. Çalışmada ihale süreçlerindeki yüklenici seçimi karar verme zorlukları ve ihtiyaçları beş ana başlık altında aşağıdaki şekilde tespit edilmiştir. Bunlar;

-Yüklenici seçimindeki firmaların yanlış veya eksik ihale belgeleri,

-Yüklenici seçimindeki firmaların ihale hazırlığı için sınırlı süre,

-Yüklenici seçimindeki firmaların paydaşlar arasında etkisiz iletişim,

-Yüklenici seçimindeki firmaların değerlendirme sürecinde şeffaflık eksikliği,

-Yüklenici seçimindeki firmaların uygun olmayan teklif sahiplerinin teklif vermesidir.

İnşaat ihale süreci zorluklarla dolu olabilir ancak bu zorlukların doğru araç ve stratejilerle ele alınması, sorunsuz ve etkili bir ihale sürecinin sağlanmasına yardımcı olabilmektedir. Paydaşlar arasındaki iletişim ve işbirliği kanallarının iyileştirilmesi, net satın alma süreçlerinin, kalite güvence kriterlerinin oluşturulması ve yetkin değerlendirme süreçlerinin sağlanması, en uygun yüklenicinin seçilmesine ve müşteri beklentilerini ve son kullanıcıları karşılayacak başarılı proje tesliminin takip edilmesine yardımcı olmaktadır.

2.6. Araştırmanın Ana Amacını ve Alt Hedeflerini Tanımlama

Bu çalışmanın ana amacı Analitik Hiyerarşi Prosesi ve bulanık mantık yaklaşımlarının ihaleyi kazanacak yüklenici kuruluşun seçiminde kullanılması incelenmektedir. Bu model, proje yönetim ekiplerinin, yalnızca en düşük teklife dayanmayan bir seçim sürecinde tatmin edici sonuçlar sunma olasılığı en yüksek olan yüklenicileri belirlemesine yardımcı olabileceği planlanmaktadır. Bu amaçla çalışmamızın alt hedefleri aşağıdaki gibidir. Bunlar;

-Yüklenici olacak firmanın tespit edilmesi,

-Yüklenici olacak projenin tamamlanması için en iyi maliyetin tespit edilmesi,

-Yüklenici olacak firmanın önceki projelerde sunduğu iş kalitesini tespit edilmesi,

-Yüklenici olacak firmanın projeyi zamanında teslim etme oranının tespit edilmesi,

-Yüklenici olacak firmanın genel itibarı ve güvenilirliğinin tespit edilmesi,

-Yüklenici olacak firmanın teknik donanım ve insan kaynakları açısından projeyi başarıyla tamamlayabilme yeteneğinin tespit edilmesi,
-Yüklenici olacak firmanın finansal sürdürülebilirlik ve ödeme gücünün tespit edilmesi,
-Yüklenici olacak firmanın proje yönetimi alanındaki deneyimi ve başarısının tespit edilmesi,
-Yüklenici olacak firmanın iş güvenliği politikaları ve güvenlik performansının tespit edilmesi,
-Yüklenici olacak firmanın geçmişte katıldığı ihalelerdeki deneyimi ve başarısının tespit edilmesi,
Yukarıda tespit edilen ihale süreçlerindeki yüklenici seçimi karar verme zorluklarına çözüm olacak ihtiyaç gereksinimleri Analitik Hiyerarşi Prosesi ve Bulanık Mantık yöntemlerinin ayrı ayrı ve birlikte uygulanmasının getirdiği avantajlar ve dezavantajlar açısından karşılaştırılacak ve değerlendirilecektir. Bu çalışma inşaat sektörüne iki şekilde katkıda bulunmaktadır; birincisi, seçim kriterleri anlayışını önem derecelerini de kapsayacak şekilde genişletmekte, ikincisi ise en iyi yüklenicinin analiz edilmesi ve seçilmesi için yeni bir yöntem olan Analitik Hiyerarşi Prosesi ve Bulanık Mantık yaklaşımlarını uygulanmaktadır.

2.7. Veri Toplama ve Hazırlığı

Bu bölümde bir inşaat sözleşmesinin verilmesinden önce yüklenicilerin değerlendirilmesi ve seçilmesi, inşaat sürecinin hayati bir parçası olup, potansiyel teklif sahiplerinin ön yeterliliklerinin belirlenmesi ve ön yeterlilik alan yükleniciler tarafından sunulan tekliflerin değerlendirilmesiyle ilgili prosedürler normalde bir müşterinin temsilcisi tarafından gerçekleştirilir ve nihayetinde proje için bir yüklenicinin seçilmesine yol açmaktadır. Niteliklendirme ve teklif değerlendirme süreçleri yeterli ve uygun kriterlerin geliştirilmesini gerektirmektedir. Bu genişleme, alternatif proje teslim sistemleri biçimlerinin daha fazla kullanılmasına yol açmaktadır. Analitik Hiyerarşi Prosesi ve Bulanık Mantık yaklaşımlarını gibi bir kararalma aracının yüklenici seçimi ve yeterliliğine uygulanması, bir projenin başarılı olmasını sağlamak için özellikle yararlı olabilmektedir. Çünkü herhangi bir projeyi tamamlamak için nitelikli ve yetenekli bir yüklenici seçmek, ayrılan bütçe dahilinde ve kabul edilebilir kalitede sonuçların zamanında teslim edilme olasılığını artırmaktadır. Kriterlere göre seçilerek analiz edilen 20 firmaya ait veriler Tablo 1'de gösterilmektedir.

Tablo 1. Kriterlere göre tespit edilen firmalara ait veriler

Firma	Maliyet	Kalite	Zamanında Teslimat	Güvenilirlik	Teknik Yeterlilik	Mali Güç	Proje Yonetimi Deneyimi	İş Güvenligi	İhale Geçmisi
F-1	125691	100	82,06379	100	100	100	100	100	100
F-2	476831,9	81,576292	46,37702	11,5530959	23,2676324	33,899788	28,16163106	1,63556	47,248454
F-3	485248	88,675543	75,54676	41,1484854	13,316957	64,458599	47,74398319	19,0727	55,200686
F-4	427801,6	60,585448	27,80838	96,6084522	23,5487959	11,832721	72,67384559	24,3099	18,497055
F-5	367112,2	71,851496	29,34507	90,3050004	58,6347647	21,08464	44,00924302	64,6558	76,138631
F-6	358366,8	21,49091	57,62001	74,5516294	85,0367883	55,254696	51,45189189	2,34221	3,006312
F-7	365188,8	44,365538	73,3296	6,976147	32,8515461	67,372957	47,26719094	30,8722	74,002802
F-8	437234	27,17402	100	32,8019939	71,0257713	86,551698	3,30663336	65,4243	1,3240223
F-9	497091,8	75,239285	17,08962	41,9495226	47,4295853	6,2581924	82,78015668	43,2158	48,629519
F-10	431496,7	3,9519628	97,16725	32,4954457	11,8209254	40,334345	4,285768393	14,3463	48,466612
F-11	393172,6	54,196154	52,58181	3,10625138	51,0540495	3,630633	40,4419065	82,3861	38,595519
F-12	569707,1	30,833276	60,87462	25,4799581	72,8112176	58,7015	65,26528722	25,0675	92,576313
F-13	419438,3	57,264337	86,33551	32,0123465	16,2229912	22,37205	68,68386092	78,7986	42,221536
F-14	241289,2	13,370506	55,9347	4,26275217	16,0620337	93,083187	71,44169731	31,168	51,194812
F-15	262880,2	85,995815	68,33709	78,063393	49,0516448	8,9751372	84,4535481	72,2139	71,731648
F-16	393536,8	29,470616	19,36219	48,116497	5,88422905	0,3569318	42,97691199	90,6638	69,411284
F-17	420747,3	59,447782	88,91087	31,9232722	95,9016203	34,307616	44,44841694	38,3783	46,344065
F-18	499787,7	33,277981	67,03671	5,41361159	69,6881486	15,303499	18,42409174	60,6696	27,427158
F-19	204388,4	87,966485	55,2917	13,8741765	3,53605537	76,881881	90,26208212	75,6193	11,689797
F-20	600909,7	2,0698024	3,220199	47,0256358	5,06651477	15,766301	2,412032007	10,6415	34,433456

2.8. İhale Verilerini Toplama

Bu bölümde ihale verilerini toplama süreçleri açıklanmakta olup, bunlar; firma (company), maliyet (cost), kalite (quality), zamanında teslimat (timely delivery), güvenilirlik (reliability), teknik yeterlilik (technical capability), mali güç (financial strength), proje yönetimi deneyimi (project management experience), iş güvenliği (work safety) ve ihale geçmişi (tender history)

şeklinde detaylandırılarak tanımları ile aktarılmaktadır.

Firma (Company); İhaleye katılan firmaların isimleri, her satır bir firmayı ve bu firmanın çeşitli kriterlerdeki performansını temsil etmektedir.

• Veri Tipi: Kategorik (string)

Maliyet (Cost); Projenin tamamlanması için firmanın sunduğu tahmini maliyet; Maliyet, firmanın projeyi ne kadar düşük bütçeyle tamamlayabileceğini göstermektedir.

• Veri Tipi: Sayısal (int).
• Değer Aralığı: 200.000 TL - 600.000 TL.
• Örnek Değerler: 300.000 TL, 450.000 TL.

Kalite (Quality); Firmanın önceki projelerde sunduğu iş kalitesini göstermektedir. Bu, firmanın projeyi titizlikle ve yüksek teknik yeterlilikle tamamlayabilme yeteneğini yansıtmaktadır.

• Veri Tipi: Sayısal (float).
• Değer Aralığı: 0% - 100%.
• Örnek Değerler: 85%, 90%, 95%.

Zamanında Teslimat (Timely Delivery); Firmanın projeyi zamanında teslim etme oranını göstermektedir. Projeyi planlanan sürede tamamlayabilme yeteneğini yansıtmaktadır.

• Veri Tipi: Sayısal (int).
• Değer Aralığı: 0% - 100%.
• Örnek Değerler: 90%, 85%, 95%.

Güvenilirlik (Reliability); Firmanın genel itibarı ve güvenilirliğini temsil etmekte olup, müşteri ilişkilerinde ve proje yönetimindeki güvenilirlik derecesini yansıtmaktadır.

• Veri Tipi: Sayısal (float).
• Değer Aralığı: 0% - 100%.
• Örnek Değerler: 87%, 92%, 88%.

Teknik Yeterlilik (Technical Capability); Firmanın teknik donanım ve insan kaynakları açısından projeyi başarıyla tamamlayabilme yeteneğini göstermektedir.

• Veri Tipi: Sayısal (float).
• Değer Aralığı: 0% - 100%.
• Örnek Değerler: 89%, 94%, 91%.

Mali Güç (Financial Strength); Firmanın finansal sürdürülebilirlik ve ödeme gücü, projeyi başarılı bir şekilde yönetme ve tamamlamada firmanın mali yapısını yansıtmaktadır.

• Veri Tipi: Sayısal (float).
• Değer Aralığı: 0% - 100%.
• Örnek Değerler: 85%, 91%, 90%.

Proje Yönetimi Deneyimi (Project Management Experience); Firmanın proje yönetimi alanındaki deneyimi ve başarısı, daha önceki projelerdeki başarılarına dayalı olarak ölçülmektedir.

• Veri Tipi: Sayısal (float).
• Değer Aralığı: 0% - 100%.
• Örnek Değerler: 88%, 93%, 90%.

İş Güvenliği (Work Safety); Firmanın iş güvenliği politikaları ve güvenlik performansı, çalışanlarının güvenliğini ne ölçüde sağlayabildiğini göstermektedir.

• Veri Tipi: Sayısal (float).
• Değer Aralığı: 0% - 100%.
• Örnek Değerler: 92%, 88%, 95%.

İhale Geçmişi (Tender History); Firmanın geçmişte katıldığı ihalelerdeki deneyimi ve başarısı; daha önceki ihalelerdeki performansı temel almaktadır.

• Veri Tipi: Sayısal (float).
• Değer Aralığı: 0% - 100%.
• Örnek Değerler: 82%, 85%, 90%.

Verileri Düzenleme ve Analize Hazır Hale Getirme; Bu bölümde verileri düzenleme ve analize hazır hale getirme aşamaları teknik detayları ve tanımlamaları ile birlikte aktarılmaktadır. Python kodları firmaların çeşitli kriterlere göre değerlendirilmesi, karar verme süreçlerinde önemli bir yer tutmaktadır. Bu süreçte kullanılan yöntemler, firmaların performansını objektif bir şekilde ölçmeyi ve karşılaştırmayı sağlamaktadır. Bu rapor, sağlanan Python betiğinin AHP ve Bulanık Mantık yöntemlerini kullanarak firmaların değerlendirilmesini nasıl gerçekleştirdiğini detaylı bir şekilde açıklamaktadır.

load_data(file_path); load_data(file_path), bu fonksiyon, belirtilen excel dosyasını yüklemektedir. Veri setinin başarılı bir şekilde yüklenip yüklenmediğini kontrol eder ve olası hataları yakalamaktadır.

• Parametreler; file_path: Yüklenecek Excel dosyasının yolu ve adıdır.
• İşlevler; Excel dosyasını pandas DataFrame olarak okumaktadır.
• Dosya bulunamazsa veya başka bir hata oluşursa, uygun hata mesajını görüntüler ve programı sonlandırılmaktadır.

Veri Kontrolleri;

• "Firma" sütunu kontrolü; Veri setinde "Firma" sütununun varlığı kontrol edilmektedir. Bu sütun, firmaların isimlerini içerir ve değerlendirme sürecinde kritik bir rol oynamaktadır.
• Kriter sütunlarının belirlenmesi; "Firma" sütunu dışındaki tüm sütunlar kriter olarak belirlenmektedir. Bu kriterler, firmaların değerlendirilmesinde kullanılacak faktörleri temsil etmektedir.
• Eksik verilerin kontrolü ve doldurulması; Veri setinde eksik değerler (NaN) kontrol edilmektedir. Eksik değerler, ilgili sütunun ortalama değeri ile doldurularak tamamlanmaktadır. Bu, analizlerin doğruluğunu artırmaktadır.

AHP Ağırlıklarının Belirlenmesi; Bu bölümde AHP ağırlıklarının belirlenmesi aşamaları teknik detayları ve tanımlamaları ile birlikte aktarılmaktadır.

Ağırlıkların Tanımlanması; AHP yönteminde, her kriterin toplam ağırlığa katkısı belirlenir. Ağırlıkların toplamının 1 olması gerekmektedir. Betikte, ağırlıklar sabit bir dizi olarak tanımlanmıştır:

weights = np.array([0.2, 0.15, 0.1, 0.1, 0.15, 0.1, 0.1, 0.05, 0.05])

Bu ağırlıklar, kriterlerin önem sırasına göre atanmıştır. Kullanıcı gereksinimlerine göre bu ağırlıklar kullanıcı girişi veya bir yapılandırma dosyasından alınabilmektedir.

validate_weights(weights); validate_weights(weights), bu fonksiyon, verilen ağırlıkların toplamının 1 olup

olmadığını kontrol etmektedir.
• İşlevler, ağırlıkların toplamını hesaplamaktadır.
• Toplam 1'e yakın değilse, hata mesajı verir ve programı sonlandırmaktadır.
• Toplam 1'e yakınsa, doğrulama mesajı görüntülemektedir.
Veri Normalize Etme (AHP); Bu bölümde veri normalize etme (AHP) aşamaları teknik detayları ve tanımlamaları ile birlikte aktarılmaktadır.
normalize_data(df, criteria_columns, method='min-max'); normalize_data(df, criteria_columns, method='min-max'), bu fonksiyon, veri setindeki kriterleri belirli bir yöntemle normalize etmektedir. Normalizasyon, farklı ölçekteki verilerin karşılaştırılabilir hale getirilmesini sağlamaktadır.
Parametreler;
• df: Orijinal veri seti.
• criteria_columns: Normalize edilecek kriter sütunları.
• method: Kullanılacak normalizasyon yöntemi ('min-max' veya 'z-score').
İşlevler;
• Maliyet kriteri; özel olarak 200.000 TL ile 600.000 TL arasında 0-100 aralığına normalize edilmektedir. Değerler 0-100 arasında sınırlandırılmaktadır.
• Diğer kriterler; Seçilen yönteme bağlı olarak min-max veya z-score yöntemiyle 0-100 aralığına normalize edilmektedir. Desteklenmeyen bir yöntem seçilirse, hata mesajı verir ve programı sonlandırmaktadır.
Normalizasyon Yöntemleri; Bu bölümde min-max normalizasyon ve z-score normalizasyonu aşamaları teknik detayları ve tanımlamaları ile birlikte aktarılmaktadır. Birçok makine öğrenme algoritması, veri noktalarının özelliklerini karşılaştırarak verilerdeki eğilimleri bulmaya çalışmaktadır. Ancak, özellikler büyük ölçüde farklı ölçeklerde olduğunda bir sorun ortaya çıkmaktadır. Normalizasyonun amacı her veri noktasının aynı ölçeğe sahip olmasını ve böylece her özelliğin eşit derecede önemli olmasını sağlamaktatır.
Min-max normalizasyonu, verileri normalleştirmenin en yaygın yollarından biri olup, her özellik için, o özelliğin minimum değeri 0'a, maksimum değeri 1'e ve diğer her değer 0 ile 1 arasında bir ondalığa dönüştürülmektedir (eşitlik 1).

$$X_{\text{normalized}} = \left(\frac{X - X_{\min}}{X_{\max} - X_{\min}}\right) \times 100 \quad (1)$$

Z-Score Normalizasyonu; Z-puanı normalizasyonu, bu aykırı değer sorununu önleyen bir veri normalleştirme stratejisidir (eşitlik 2).

$$X_{\text{normalized}} = \left(\frac{X - \mu}{\sigma}\right) \times 100 \quad (2)$$

Burada, μ ortalama ve σ standart sapmadır.
Burada, μ özelliğin ortalama değeri ve σ özelliğin standart sapmasıdır. Bir değer özelliğin tüm değerlerinin ortalamasına tam olarak eşitse, 0'a normalize edilmektedir. Ortalamanın altındaysa, negatif bir sayı olacaktır ve ortalamanın üzerindeyse, pozitif bir sayı olmaktadır. Bu negatif ve pozitif sayıların büyüklüğü, orijinal özelliğin standart sapması tarafından belirlenmektedir. Normalize edilmemiş veriler büyük bir standart sapmaya sahipse, normalize edilmiş değerler 0'a daha yakın olmaktadır.
AHP Skorlarının Hesaplanması; Bu bölümde AHP skorlarının hesaplanması aşamaları teknik detayları ve tanımlamaları ile birlikte aktarılmaktadır.
calculate_ahp_scores (normalized_data, weights); calculate_ahp_scores(normalized_data, weights), bu fonksiyon, normalize edilmiş verilere göre AHP skorlarını hesaplamaktadır.
Parametreler;
• normalized_data; Normalize edilmiş veri seti.
• Weights; Ağırlık dizisi.
İşlevler;
• AHP skorları, normalize veriler ile ağırlıkların noktasal çarpımı (dot product) alınarak hesaplanmaktadır.
• Sonuç, her firma için 0-100 aralığında bir skor oluşturmaktadır.
Bulanık Mantık Skorlarının Hesaplanması; Bu bölümde bulanık mantık skorlarının hesaplanması aşamaları teknik detayları ve tanımlamaları ile birlikte aktarılmaktadır.
setup_fuzzy_logic(df); setup_fuzzy_logic(df), bu fonksiyon, Bulanık Mantık (Fuzzy Logic) sistemini kurar ve her firma için bulanık skorları hesaplanmaktadır.
İşlevler;
• Girdi değişkenlerinin tanımlanması; Kriterler için evren aralıkları (0-100) belirlenmektedir. Her kriter için Bulanık mantık üyelik fonksiyonları otomatik olarak tanımlanmaktadır (low, medium, high).
• Çıktı değişkeni; Sonuç için 0-100 aralığında bir üyelik fonksiyonu tanımlanmaktadır (düşük, orta, yüksek).
• Kuralların tanımlanması; Belirli kriter kombinasyonlarına göre sonuç üyelik fonksiyonları atanmaktadır. Örneğin, maliyet kötü (poor) ve kalite iyi (good) olduğunda sonuç yüksek (yüksek) olmaktadır.
• Kontrol sistemi ve simülasyon; Tanımlanan kurallara göre bir kontrol sistemi oluşturulmaktadır. Her firma için kriter değerleri girilerek simülasyon çalıştırılır ve bulanık skor hesaplanmaktadır.
• Sonuçların eklenmesi; Hesaplanan bulanık skorlar, veri setine yeni bir sütun olarak eklenmektedir (Bulanik_Skor). Eksik skorlar uygun bir değerle (örneğin, 0) doldurulmaktadır.
Sonuçların Görselleştirilmesi; Bu bölümde sonuçların görselleştirilmesi aşamaları teknik detayları ve tanımlamaları ile birlikte aktarılmaktadır.
visualize_top_firms; visualize_top_firms(df, score_column, top_n=5, title='Firma Sıralaması', ylabel='Skor', file_name=None), bu fonksiyon, en yüksek skor alan N firmayı bar grafiği olarak görselleştirmektedir.
Parametreler;
• df: Veri seti.
• score_column: Görselleştirilecek skor sütunu

(AHP_Skoru veya Bulanik_Skor).
• top_n: Görselleştirilecek en üstteki firma sayısı.
• title: Grafik başlığı.
• ylabel: Y ekseni etiketi.
• file_name: Grafiğin kaydedileceği dosya adı (opsiyonel).
İşlevler;
• Firmalar, belirtilen skor sütununa göre azalan sırada sıralanmaktadır.
• En üstteki top_n firma seçilir ve bar grafiği oluşturulmaktadır.
• Skor değerleri barların üzerine yazdırılmaktadır.
• Grafik dosyaya kaydedilir (isteğe bağlı) ve ekranda görüntülenmektedir.
visualize_score_distribution; visualize_score_distribution (df, score_column, title, xlabel, file_name), bu fonksiyon, belirtilen skor sütununun dağılımını histogram ve yoğunluk grafiği ile görselleştirilmektedir.
Parametreler;
• df: Veri seti.
• score_column: Görselleştirilecek skor sütunu.
• title: Grafik başlığı.
• xlabel: X ekseni etiketi.
• file_name: Grafiğin kaydedileceği dosya adı (opsiyonel).
İşlevler;
• Skor dağılımı histogram ve KDE (Kernel Density Estimation) grafiği ile gösterilmektedir.
• Grafik dosyaya kaydedilir (isteğe bağlı) ve ekranda görüntülenmektedir.
visualize_all_firms; visualize_all_firms(df, ahp_score_col, fuzzy_score_col, top_n=10, file_name=None), bu fonksiyon, en yüksek skor alan top_n firmayı hem AHP hem de Bulanık Mantık skorları ile yan yana bar grafiği olarak görselleştirilmektedir.
Parametreler;
• df: Veri seti.
• ahp_score_col: AHP skor sütunu.
• fuzzy_score_col: Bulanık Mantık skor sütunu.
• top_n: Görselleştirilecek en üstteki firma sayısı.
• file_name: Grafiğin kaydedileceği dosya adı (opsiyonel).
İşlevler;
• Firmalar, AHP skoruna göre sıralanır ve en üstteki top_n firma seçilmektedir.
• Her firma için AHP ve Bulanık skorları yan yana barlar olarak gösterilmektedir.
• Skor değerleri barların üzerine yazdırılmaktadır.
• Grafik dosyaya kaydedilir (isteğe bağlı) ve ekranda görüntülenmektedir.
AHP ve Bulanık Mantık Skorlarının Karşılaştırılması; Bu bölümde AHP ve bulanık mantık skorlarının karşılaştırılması aşamaları teknik detayları ve tanımlamaları ile birlikte aktarılmaktadır.
compare_scores; compare_scores(df, score_column1, score_column2), bu fonksiyon, iki farklı skor arasındaki korelasyonu görselleştirmekte ve hesaplamaktadır.
Parametreler;
• df: Veri seti.
• score_column1: İlk skor sütunu (örneğin, AHP_Skoru).
• score_column2: İkinci skor sütunu (örneğin, Bulanik_Skor).
İşlevler;
• Skorlar arasında bir scatter plot (saçılım grafiği) oluşturulmaktadır.
• Her nokta, bir firmayı temsil eder ve iki skor arasındaki ilişkiyi gösterilmektedir.
• Korelasyon katsayısı hesaplanır ve grafik üzerine yazdırılmaktadır.
• Grafik dosyaya kaydedilir (korelasyon_scatter.png) ve ekranda görüntülenmektedir.
Korelasyon Matrisi Görselleştirme; Bu bölümde korelasyon matrisi görselleştirme aşamaları teknik detayları ve tanımlamaları ile birlikte aktarılmaktadır. Korelasyon matrisi, veri setindeki tüm skorlar ve kriterler arasındaki korelasyonları gösterilmektedir. Bu, hangi kriterlerin birbirleriyle güçlü veya zayıf ilişkiler içinde olduğunu anlamak için kullanılmaktadır.
İşlevler:
• AHP_Skoru, Bulanik_Skor ve tüm kriterler arasındaki korelasyonlar hesaplanmaktadır.
• Seaborn'un heatmap fonksiyonu kullanılarak ısı haritası şeklinde görselleştirilmektedir.
• Korelasyon değerleri grafikte annotasyon olarak gösterilmektedir.
• Grafik dosyaya kaydedilir (korelasyon_matrisi.png) ve ekranda görüntülenmektedir.
Sonuçların Kaydedilmesi; Bu bölümde sonuçların kaydedilmesi aşamaları teknik detayları ve tanımlamaları ile birlikte aktarılmaktadır.
save_results; save_results(df, output_file), bu fonksiyon, hesaplanan skorlar ve diğer bilgilerin bulunduğu veri setini belirtilen bir Excel dosyasına kayıt etmektedir.
Parametreler;
• df: Veri seti.
• output_file: Kaydedilecek Excel dosyasının adı ve yolu.
İşlevler:
• Veri seti, belirtilen dosya adına göre Excel formatında kaydedilmektedir.
• Kaydetme işlemi sırasında herhangi bir hata oluşursa, hata mesajı görüntülenmektedir.

3. Bulgular

3.1. Bulanık Mantık Skorları

Geliştirilen Python tabanlı analiz aracı, firmaların çeşitli kriterler doğrultusunda değerlendirilmesi için kapsamlı bir analiz süreci sunmaktadır. Analitik Hiyerarşi Prosesi (AHP) yöntemi ile kriter ağırlıklarının belirlenmesi ve skorların hesaplanması sağlanırken, Bulanık Mantık sistemi sayesinde daha esnek ve insan benzeri değerlendirmeler gerçekleştirilmektedir. Sonuçların görselleştirilmesi ve kaydedilmesi işlemleri, elde edilen verilerin daha kolay yorumlanmasına ve paylaşılmasına katkı sağlamaktadır (Zengin vd., 2023; Aslan vd., 2024; Günal vd., 2024; Yıldız vd., 2024). Söz konusu analiz aracı, firmaların performansını objektif bir şekilde değerlendirmek ve karşılaştırmak amacıyla etkili yöntemler sunmaktadır. Ayrıca kullanıcılar, aracı kendi

veri setlerine ve özel ihtiyaçlarına uyarlayarak daha geniş kapsamlı bir değerlendirme yelpazesi oluşturabilmektedir. (Özdemir 2024; Eltaleb vd., 2024; Lüy vd., 2024; Özarslan-Yatak vd., 2024).

Bulanık mantık skorlarına göre en iyi 5 firma; bulanık mantık skorlama, yaklaşık dize eşleştirme, bulanık ad eşleştirme veya bulanık dize eşleştirme olarak da bilinen, veri tablosu kümelerindeki benzer ancak aynı olmayan öğeleri tanımlayan bir yapay zeka ve makine öğrenme teknolojisidir. Yaklaşık dize eşleştirme, belirli kelimeler yanlış yazılmış, kısaltılmış veya atlanmış olsa bile yaklaşık eşleşmeleri bulmaya yardımcı olur, arama motorlarında yoğun olarak kullanılan bir işlevdir. (Yıldırım vd., 2023; Akarslan-Kodaloğlu vd., 2023; Mızrak 2023; Alsaadoun vd., 2024; Alsmadi vd., 2024).

Sonuç olarak, yaklaşık dize eşleştirme bir eşleşme puanı sağlar ve mükemmel bir bulanık eşleşme olmayan kelimeleri, ifadeleri ve dizeleri tanımlamak için kullanılmaktadır. Bulanık mantık skorlama, tıp alanında, finansal hizmetlerde, sosyal güvenlik dolandırıcılığını belirlemede ve daha birçok alanda belirsiz veri kümelerini birleştirmek için vazgeçilmez bir araç haline gelmiştir. Sonuç olarak Bulanık Mantık skorlama, modern işletmelerin genellikle zahmetli ve zahmetli olan manuel çoğaltma işinde sayısız adam-saat tasarrufu sağlamasına yardımcı olmaktadır (Anlak vd., 2023; Boyacıoğlu vd., 2023; Şimşek vd., 2023; Uysal vd., 2023; Yılmaz vd., 2023).

Çalışmamıza ait Bulanık Mantık skorlarına göre en iyi beş firma Şekil 1'de gösterilmekte olup Bulanık Mantık analiz sonuçlarına göre "Firma-1" %68.20 ve "Firma-15" ise %62.31 ile öne çıktığı tespit edilmiştir.

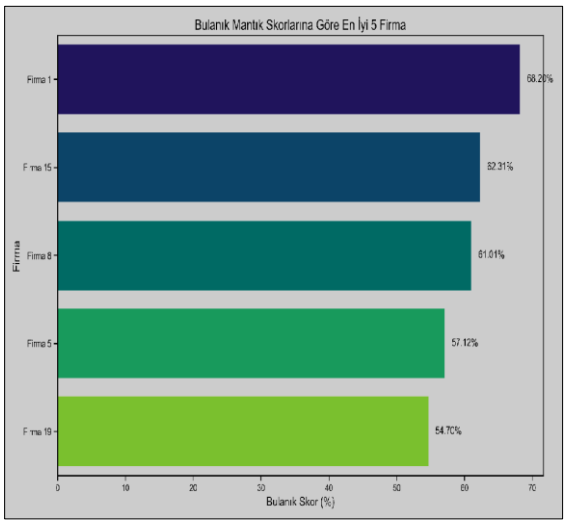

Şekil 1. Bulanık mantık skorlarına göre en iyi 5 firma.

Literatürde bulanık mantık modelleme ile matematiksel başarı üzerine yapılan çalışmada, bulanık mantık yöntemiyle oluşturulan modelden elde edilen yüzeyde aktif katılımın başarı üzerinde olumlu etkisi varken, yokluğun olumsuz etkisi bulunmaktadır. Aktif katılımın yüksek, devamsızlığın az olduğu durumlarda yüksek başarı elde edildiği belirtilmektedir. Aktif katılımın az, devamsızlığın yüksek olduğu durumlarda başarının düşük olduğu tespit edilmiştir. Çalışmada bulanık mantık sisteminden elde edilen değerler gerçek değerlerle karşılaştırılmış ve benzerlik oranı %80 olarak bulunmuştur (Uyhan vd., 2022).

Bulanık mantık skorlarının dağılımı; Bulanık dağılım kümeleri, üyelik değerlerinin toplamı 1'e eşit olan sonlu bir alanda tanımlanan bulanık kümeler olup, bu tür bulanık kümeler, öznel olasılık dağılımlarının ve öznel ağırlık dağılımlarının modelleri olarak hizmet edebilmektedir. Bu dağılımları bulanık kümeler olarak düşünmek, bulanık kümelerin işlemlerini ve daha genel olarak son on yıllarda geliştirilen bulanık kısıtlamaların hesabını bu tür dağılımlara genişletme olanağı vermektedir (Ahmad vd., 2023; Tubpawatin vd., 2023; Tafazzoli vd., 2024; Wibisono-Adhipradana vd., 2024). Bulanık dağılım kümeleri üzerindeki bu temel işlemler, bulanık mantık yöntemlerinin öznel olasılık ve ağırlık dağılımlarına uygulanması için bir temel oluşturabilmektedir. Bu işlemler, öznel olasılık dağılımları ve öznel ağırlıklandırma fonksiyonları ile akıl yürütme modelleri geliştirmek için ve ağırlık dağılımları çok kriterli, çok kişili ve çok nitelikli karar alma modellerinde kullanılabilmektedir (Marović vd., 2021;Rustandi vd., 2021; Putri vd., 2022; Thanh vd., 2022; Warrad vd., 2022).

Çalışmamıza ait bulanık mantık skorlarının dağılımı Şekil 2'de gösterilmekte olup grafik açıklamasına göre firmaların bulanık mantık skorlarının dağılımını Histogramda, en fazla firmanın skoru %45 ile %50 arasında yoğunlaştığı tespit edilmiştir. Analiz sonuçları bu dağılımı, firmaların çoğunlukla orta düzey performans gösterdiğini, sadece birkaç firma daha yüksek (%60 ve üstü) veya daha düşük (%40 altı) performans sergilediği sonucuna varılmıştır.

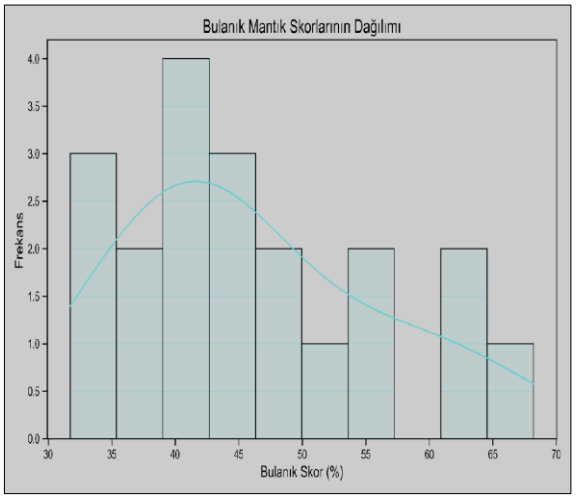

Şekil 2. Bulanık mantık skorlarının dağılımı.

Literatürde elektrikli araçların dağıtım transformatörlerinin yaşlanmasına etkisinin bulanık mantık kullanılarak tahminlemesi ile ilgili çalışmada, bulanık mantık ile tahminde elde edilen sonuçlar verilen yaklaşık değerlerle test edildiğinde %95,321 oranında

gerçekleştiği görülmüş hataların %1.652'si tanımlanan kurallara göre elde edilmiştir. Bulanık mantık sayısal verilerin niteliksel özelliklere göre sınıflandırılması ile yapılan tahminler sonucunda bulanık mantık ile tahminde doğruluk oranı %96,973 olarak bulunmuştur (Akar, 2024).

3.2. Analitik Hiyerarşi Prosesi Skorları

Bu bölümde Analitik Hiyerarşi Prosesi skorlarına göre en iyi 5 firma ve Analitik Hiyerarşi Prosesi skorlarının dağılımı grafik ve analiz sonuçlarına yer verilmektedir.

Analitik Hiyerarşi Prosesi skorlarına göre en iyi 5 firma; Analitik Hiyerarşi Prosesi süreci, basit hesaplamalara dayanan çok kriterli karar verme yöntemi olup, Analitik Hiyerarşi Prosesi tekniği karar verme analizini iyileştirebilir ve karmaşık karar almayla başa çıkmak için güçlü bir araç sağlayabilmektedir (Ahmad vd., 2023; Tubpawatin vd., 2023; Tafazzoli vd., 2024; Wibisono-Adhipradana vd., 2024). Ayrıca, kararların hem nitel hem de nicel yönlerini dikkate alır ve kriterler arasındaki karmaşık ilişkileri bir dizi karşılaştırmaya indirgemektedir. Dahası, bu yöntem ayrıştırma kurallarına, karşılaştırmalı yargılara ve önceliklerin sentezine dayanır ve temel matematiği içermektedir. Analitik hiyerarşi prosesi, alternatifleri ve nitelikleri kullanır ve değerlendirme için alternatifleri bir nitelik hiyerarşisi içinde yapılandırmaktadır. Çiftler halinde karşılaştırma yoluyla Analitik Hiyerarşi Prosesi, 1'den 9'a kadar bir ölçek kullanarak alternatifler için sıralama tercihini ve nitelikler için ağırlıklandırma tercihini ortaya çıkarmakta ve daha yüksek puanlar daha büyük göreceli tercihi göstermektedir (Rustandi vd., 2021; Marović vd., 2021; Putri vd., 2022; Thanh vd., 2022; Warrad vd., 2022).

Çalışmamıza ait analitik hiyerarşi skorlarına göre en iyi beş firma Şekil 3'de gösterilmekte olup analitik hiyerarşi skorları analiz sonuçlarına göre "Firma-1" %78, "Firma-12" %60 ile en iyi performansa sahip firmalar olduğu tespit edilmiştir. Bu sıralama, Analitik Hiyerarşi Prosesi kriterlerine göre hangi firmaların genel anlamda daha iyi performans sergilediğini sonucuna varılmıştır.

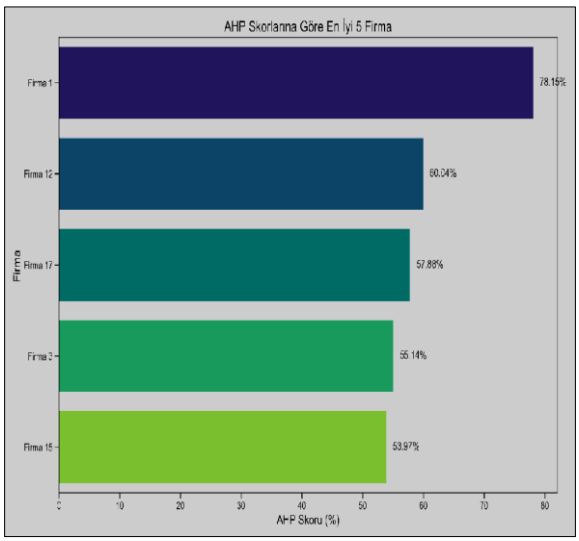

Şekil 3. AHP skorlarına göre en iyi 5 firma.

Şimşek vd. (2022) tarafından gerçekleştirilen çalışmada, analitik hiyerarşi süreci yöntemi kullanılarak havayolu işletmelerinde pilot seçimi değerlendirilmiştir. Literatür taraması ve uzman görüşleri doğrultusunda 3'ü üst, 14'ü alt olmak üzere toplam 17 kriter belirlenmiş ve ikili karşılaştırma matrisi ile kriterlerin yerel ve global ağırlıkları hesaplanmıştır. Bulgulara göre en önemli işe alım kriteri, 0,321 küresel ağırlık endeksi ile uçuş tecrübesi olarak tespit edilmiştir. Bunu sırasıyla toplam uçuş saati (0,243) ile karar verme ve problem çözme yetkinliği (0,096) izlemiştir. Görsel ve işitsel hafıza yetenekleri ise en düşük ağırlıklara (0,007) sahip kriterler olarak belirlenmiştir. Elde edilen sonuçlar, hava taşımacılığı sektöründe kullanılan işe alım kriterlerinin bu çalışmadaki bulgularla büyük ölçüde örtüştüğünü göstermektedir.

3.3. Analitik Hiyerarşi Prosesi Skorlarının Dağılımı

Analitik hiyerarşi süreci, karar almanın yapılandırılmış ve şeffaf bir yolu olup Analitik hiyerarşi süreci ile alacağımız kararları adım adım ilerleyen bir sürece dönüşür, bu da karar almayı basitleştirir, iş birliğini mümkün kılar ve kararların kalitesini artırmaktadır (Hoseinpoor, 2019; Ojokoh vd., 2020; Razi vd., 2020; Afolayan vd., 2021; Naik vd., 2021). Analitik hiyerarşi süreci, stratejik hedeflerinizi, projeleri puanlamak için kullandığınız bir dizi ağırlıklı kriter olarak yakalamanızı sağlamaktadır. Analitik hiyerarşi prosesi skor dağılımı temeli, ikili karşılaştırma sorularını, cevabınızı "eşit derecede önemli" (oran=1) ile "çok önemli" (oran=9) arasında değişen, tercihlerin yoğunluğunu temsil eden dokuz puanlık bir ölçekten seçerek skorlanmaktadır (Irma vd., 2018; Jabbarzadeh 2018; Yarahmadi vd., 2018; Morkunaite vd., 2019; Najiazarpour vd., 2019).

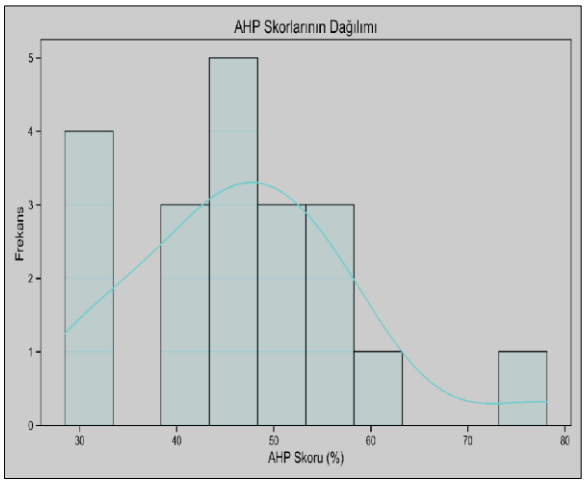

Şekil 4. AHP skorlarının dağılımı.

Çalışmamıza ait analitik hiyerarşi prosesi skor dağılımı gösteren histogram Şekil 4'de gösterilmekte olup analitik hiyerarşi prosesi skor dağılımı analiz sonuçlarına göre genellikle %40-60 aralığında toplanmıştır. Bu durum, firmaların büyük çoğunluğunun ortalama performans sergilediği sonucuna varılmıştır.

Acar vd. (2022) tarafından yapılan çalışmada, mağaza

müdürü seçiminde Analitik Hiyerarşi Prosesi (AHP) yöntemi kullanılmıştır. Literatür taraması ve uzman görüşleri doğrultusunda oluşturulan hiyerarşik model üzerinden yapılan ikili karşılaştırmalar sonucunda, adaylar arasında en uygun seçimin belirlendiği ifade edilmiştir.

3.4. Korelasyon Matrisi

Korelasyon matrisi, değişkenler arasındaki korelasyonun gösterin bir matris olup, tüm olası değer çiftleri arasındaki korelasyonu bir matris biçiminde verilmektedir. Bir korelasyon matrisi, bir veri kümesindeki iki değişken arasındaki ilişkiyi değerlendirmek için kullanılan istatistiksel bir teknik olup, matris, her hücrenin bir korelasyon katsayısı içerdiği bir tablodur; burada 1 değişkenler arasında güçlü bir ilişki, 0 nötr bir ilişki ve -1 güçlü olmayan bir ilişki olarak kabul edilmektedir. En yaygın olarak regresyon modelleri oluşturmada kullanılmaktadır. Çoklu doğrusal regresyonda korelasyon matrisi, bir modelin bağımsız değişkenleri arasındaki korelasyon katsayılarını belirlemektedir (Erdin vd., 2021; Acar vd., 2022; Keringingo vd., 2022; Şimşek vd., 2022; Uyhan vd., 2022; Akar 2024).

Çalışmada ait korelasyon matrisi grafik açıklaması Şekil 5'de gösterilmekte olup, korelasyon matrisi, analitik hiyerarşi prosesi ve bulanık mantık skorları ile kriterler arasındaki ilişkinin derecesini göstermektedir. Kırmızı tonlar pozitif korelasyonu (güçlü bağımlılık), mavi tonlar ise negatif korelasyonu gösterdiği tespit edilmiştir. Korelasyon matrisi analiz sonuçlarına göre; analitik hiyerarşi prosesi skoru ile "kalite" arasında yüksek pozitif korelasyon olduğu (0,63), bu, kalite arttıkça Analitik Hiyerarşi Prosesi skorunun da arttığı tespit edilmiştir. analitik hiyerarşi prosesi skoru ile "teknik yeterlilik" arasında da yüksek bir pozitif korelasyon (0,73) tespit edilmiş olup bu da analitik hiyerarşi prosesi skorunun büyük oranda teknik yeterlilikten etkilendiğini göstermektedir. Bulanık skor ile "iş güvenliği" arasında güçlü bir ilişki bulunmakta olup, (0,72), bu da iş güvenliğine daha fazla önem veren firmaların bulanık mantık sisteminde daha yüksek skor aldığı sonucuna varılmıştır.

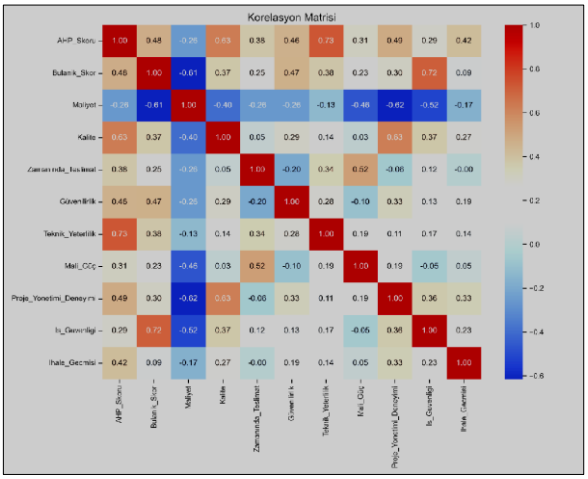

Şekil 5. Korelasyon matrisi.

Keringingo vd. (2022) çalışmalarında, Burundi'de patates üretim sistemi seçiminde Analitik Hiyerarşi Prosesi (AHP) yöntemini kullanmışlardır. Çok kriterli karar verme süreci ile yapılan değerlendirme sonucunda, Victoria çeşidinin en uygun patates türü olarak belirlendiği ifade edilmiştir.

3.5. Analitik Hiyerarşi Prosesi ve Bulanık Skorların Firma Bazında Karşılaştırılması

Bulanık mantık, dilsel yargılar, farklı kişiler için farklı önem düzeyleri tasvir edilebilmektedir. Bulanık mantık önem düzeyindeki bu değişimi yakalamak için sıklıkla kullanılmaktadır. Üyelik derecesi, genellikle iki eksen diyagramında gösterilen üyelik fonksiyonuyla verilmektedir. Yatay eksen bulanık kümelerin etki alanı elemanlarını temsil eder ve dikey eksen üyelik derecesini temsil eder; burada sıfır üyeliksizlik anlamına gelir ve bir tam üyelik anlamına gelmektedir (Erdin vd., 2021; Acar vd., 2022; Şimşek vd., 2022; Keringingo vd., 2022; Uyhan vd., 2022; Akar 2024).

Analitik hiyerarşi prosesi tedarikçi veya yüklenici gibi farklı seçimler kriterleri için sıklıkla kullanılmaktadır. Bulanık mantık yönteminde olduğu gibi Analitik hiyerarşi prosesi de sorunu hiyerarşik bir yapıda formüle etmektedir. Temel fark, bir karşılaştırma matrisi A'da toplanan ikili karşılaştırmalar yoluyla kriterlerin göreceli ağırlıklarının (önemlerinin) ve alternatiflerin performanslarının ortaya çıkarılmasıdır. Analitik hiyerarşi prosesi, Bulanık mantık yönteminden farklı olarak hiyerarşinin derinliğinden bağımsız kriter ağırlıklarına sahip olup bu özellik geçerlidir çünkü her seviyedeki kriter ağırlıklarının toplamı her zaman 1'e eşittir (Erdin vd., 2021; Acar vd., 2022; Keringingo vd., 2022; Uyhan vd., 2022; Şimşek vd., 2022; Akar 2024). Çalışmada Analitik Hiyerarşi Süreci ve Bulanık Mantık skorlarının firma bazında karşılaştırılması grafik açıklaması Şekil 6'da ve Tablo 2'de kriterlere göre tespit edilen firmalara ait verilerin sonuç tablosu gösterilmekte olup, bu grafikte her firmanın hem Analitik hiyerarşi süreci hem de bulanık mantık skorları yan yana verilmektedir.

Analitik hiyerarşi süreci ve bulanık mantık skorlarının firma bazında karşılaştırılması analiz sonuçlarına göre "Firma-1", hem analitik hiyerarşi süreci hem de bulanık mantık skorlarında en yüksek değere sahip olduğu, bu firmanın genel performansının çok iyi olduğu tespit edilmiştir.

"Firma-15" analitik hiyerarşi süreci skoru bulanık mantık skorundan daha düşük olduğu, bu firma performansının Analitik Hiyerarşi Süreci kriterlerine göre düşük olduğunu, ancak bulanık mantık sisteminde daha yüksek puan aldığı tespit edilmiştir. "Firma-12" ve "Firma-9" gibi firmalarda analitik hiyerarşi süreci skorları oldukça yüksek iken, bulanık skorları daha düşük çıkmış olup, bu durum, Analitik Hiyerarşi Süreci ve Bulanık Mantık yöntemlerinin farklı değerlendirme şekillerine sahip olduğunu sonucuna varılmıştır.

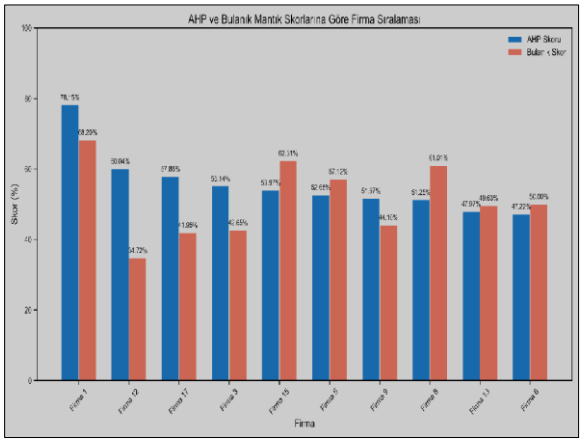

Şekil 6. AHP ve bulanık mantık skorlarına göre firma sıralaması.

Literatüre baktığımızda Coğrafi Bilgi Sistemleri ortamında kırsal yangın riski değerlendirmesi bulanık mantık ve Analitik Hiyerarşi Süreci yaklaşımlarının kullanımı ile ilgili çalışmada, Türkiye'nin yedi coğrafi bölgesinde kırsal alan yangın riskini değerlendirmektedir. Çalışma analiz için analitik hiyerarşi süreci ve bulanık mantık yaklaşımları kullanılarak bu yaklaşımları Coğrafi Bilgi Sistemleri ile entegre edilerek gerçekleştirilmiştir. Çalışmanın sonuçları, yangın riski değerlendirmesi için oluşturulan bazı modeller biraz farklı sonuçlar verse de Ege, Akdeniz ve Marmara bölgelerinin kırsal alan yangın risk düzeylerinin en yüksek olduğu bölgeler olduğunu, Analitik Hiyerarşi Süreci ve Bulanık Mantık yaklaşımlarıyla elde edilen yangın risk değerlendirme sonuçları coğrafi bölgeler bazında örtüşdüğü ve kırsal alan yangın risk değerlendirmesi için Analitik Hiyerarşi Süreci ve Bulanık Mantığın Coğrafi Bilgi Sistemleri ile entegre edilmesi, gerekli planlamanın yapılmasında ve çevrenin sürdürülebilirliğinin sağlanmasında geçerli, güvenilir ve çok önemli sonuçlar sağladığı sonucuna varmışlardır (Erdin vd., 2021).

Table 2. Kriterlere göre tespit edilen firmalara ait verilerin sonuç tablosu

Firma	Maliyet	Kalite	Zamanında Teslimat	Güvenilirlik	Teknik Yeterlilik	Mali Güç	Proje Yönetimi Deneyimi	İş Güvenliği	İhale Geçmişi	AHP Skoru	Bulanık Skor
F-1	125691	100	82,0637864	100	100	100	100	100	100	78,146699	68,19616
F-2	476831,89	81,576292	46,377018	11,553096	23,2676324	33,89979	28,16163106	1,635557	47,24845	42,75084	31,73573
F-3	485248,02	88,675543	75,5467636	41,148485	13,316957	64,4586	47,74398319	19,07274	55,20069	55,142942	42,64843
F-4	427801,55	60,585448	27,8083802	96,608452	23,5487959	11,83272	72,67384559	24,3099	18,49705	46,029768	32,86449
F-5	367112,19	71,851496	29,3450693	90,305	58,6347647	21,08464	44,00924302	64,65583	76,13863	52,647756	57,11534
F-6	358366,82	21,49091	57,6200142	74,551629	85,0367883	55,2547	51,45189189	2,342208	3,006312	47,216689	50
F-7	365188,83	44,365538	73,3296047	6,976147	32,8515461	67,37296	47,26719094	30,8722	74,0028	43,430851	37,00043
F-8	437234,02	27,17402	100	32,801994	71,0257713	86,5517	3,30663336	65,42432	1,324022	51,250741	61,0107
F-9	497091,81	75,239285	17,089624	41,949523	47,4295853	6,258192	82,78015668	43,21583	48,62952	51,667594	44,0968
F-10	431496,7	3,9519628	97,1672465	32,495446	11,8209254	40,33435	4,285768393	14,34633	48,46661	33,130777	38,76424
F-11	393172,61	54,196154	52,5818066	3,1062514	51,0540495	3,630633	40,4419065	82,38606	38,59552	40,350988	43,92845
F-12	569707,12	30,833276	60,8746194	25,479958	72,8112176	58,7015	65,26528722	25,06748	92,57631	60,040572	34,72446
F-13	419438,3	57,264337	86,3355092	32,012346	16,2229912	22,37205	68,68386092	78,79855	42,22154	47,965238	49,62704
F-14	241289,21	13,370506	55,9347043	4,2627522	16,0620337	93,08319	71,44169731	31,16799	51,19481	31,716968	39,03761
F-15	262880,24	85,995815	68,3370877	78,063393	49,0516448	8,975137	84,4535481	72,21393	71,73165	53,968012	62,3094
F-16	393536,83	29,470616	19,3621868	48,116497	5,88422905	0,356932	42,97691199	90,66385	69,41128	32,684422	48,35463
F-17	420747,26	59,447782	88,9108663	31,923272	95,9016203	34,30762	44,44841694	38,37828	46,34407	57,880605	41,95425
F-18	499787,65	33,277981	67,03671	5,4136116	69,6881486	15,3035	18,42409174	60,66963	27,42716	44,352471	43,4869
F-19	204388,44	87,966485	55,291702	13,874176	3,53605537	76,88188	90,26208212	75,61931	11,6898	40,835953	54,70098
F-20	600909,67	2,0698024	3,22019898	47,025636	5,06651477	15,7663	2,412032007	10,64148	34,43346	28,452646	39,87455

4. Tartışma

Bu çalışmada, ihale süreçlerinde yüklenici seçimi ile ilgili çok kriterli karar verme yöntemlerinin etkinliğini değerlendirmek amacıyla çeşitli ihalelere ait veriler kullanılarak veri setleri, farklı sektörlerden ve büyüklüklerden gelen ihalelerin detaylı bir analizi için seçilmiştir. Bu ihaleler, maliyet, süre, kalite, teknik kapasite gibi çeşitli kriterlerin değerlendirildiği tipik ihale süreçlerini temsil etmektedir. Çalışmanın temel metodolojisi, çok kriterli karar verme yöntemlerinin uygulanması ve sonuçlarının değerlendirilmesini içermektedir. İlk aşamada, ihale süreçlerinde önemli olan

faktörler belirlenecek ve bu faktörlerin ağırlıkları Analitik Hiyerarşi Prosesi kullanılarak tespit edilmiştir. Daha sonra, belirsizlikle başa çıkmak ve bulanık bilgiyi işlemek için bulanık mantık yöntemleri uygulanmıştır. Analitik Hiyerarşi Prosesi aşamasında, karar vericilerle yapılan görüşmeler ve literatür taraması sonucunda belirlenen kriterler için bir karar matrisi oluşturulmuş, ardından bu matris üzerinden ağırlık vektörleri hesaplanmıştır.

Bulanık Mantık aşamasında, belirlenen kriterlerin bulanıklık dereceleri uzman görüşleri ve geçmiş veri analizleri kullanılarak belirlenmiş; ardından bulanık mantık kuralları oluşturularak çıkarım süreci tamamlanmıştır. Yapılan analiz sonuçlarına göre, çalışmada elde edilen bulanık mantık skorları incelendiğinde, "Firma-1" %68,20 ve "Firma-15" %62,31 skorları ile öne çıkan firmalar olarak tespit edilmiştir (Uyhan vd., 2022). Bulanık Mantık modelleme ile matematiksel başarı üzerine yapmış olduğu çalışmasında çalışmamız ile örtüşen ve benzerlikler gösteren sonuçlara ulaşmışlardır.

Çalışmada grafik açıklamasına göre firmaların bulanık mantık skorlarının dağılımını Histogramda, en fazla firmanın skoru %45 ile %50 arasında yoğunlaştığı tespit edilmiştir. Analiz sonuçları bu dağılımı, firmaların çoğunlukla orta düzey performans gösterdiğini, sadece birkaç firma daha yüksek (%60 ve üstü) veya daha düşük (%40 altı) performans sergilediği sonucuna varılmıştır. Akar'a göre (2024) elektrikli araçların dağıtım transformatörlerinin yaşlanmasına etkisinin bulanık mantık kullanılarak tahminleme üzerine yapmış olduğu çalışmasında çalışmamız ile örtüşen ve benzerlikler gösteren sonuçlara ulaşmıştır.

Çalışmamıza ait analitik hiyerarşi skorları analiz sonuçlarına göre "Firma-1" %78, "Firma-12" %60 ile en iyi performansa sahip firmalar olduğu tespit edilmiştir. Bu sıralama, Analitik Hiyerarşi Prosesi kriterlerine göre hangi firmaların genel anlamda daha iyi performans sergilediğini sonucuna varılmıştır. Şimşek vd. (2022) Analitik Hiyerarşi Süreci ile havayolu işletmelerinde pilot seçimi üzerine yapmış oldukları çalışmada çalışmamız ile örtüşen ve benzerlikler gösteren sonuçlara ulaşmışlardır.

Çalışmamıza ait Analitik Hiyerarşi Prosesi skor dağılımı gösteren histogram analiz sonuçlarına göre genellikle %40-60 aralığında toplanmıştır. Bu durum, firmaların büyük çoğunluğunun ortalama performans sergilediği sonucuna varılmıştır. Acar vd. (2022) mağaza müdürü seçiminde analitik hiyerarşi sürecinin kullanılması ile ilgili yapmış oldukları çalışmada çalışmamız ile örtüşen ve benzerlikler gösteren sonuçlara ulaşmışlardır.

Çalışmamıza ait korelasyon matrisi, Analitik Hiyerarşi Prosesi ve Bulanık Mantık skorları ile kriterler arasındaki ilişkinin derecesini göstermektedir. Kırmızı tonlar pozitif korelasyonu (güçlü bağımlılık), mavi tonlar ise negatif korelasyonu gösterdiği tespit edilmiştir. Korelasyon matrisi analiz sonuçlarına göre; Analitik Hiyerarşi Prosesi skoru ile "kalite" arasında yüksek pozitif korelasyon olduğu (0.63), bu kalite arttıkça Analitik Hiyerarşi Prosesi skorunun da arttığı tespit edilmiştir. Analitik Hiyerarşi Prosesi skoru ile "teknik yeterlilik" arasında da yüksek bir pozitif korelasyon (0.73) tespit edilmiş olup bu da Analitik Hiyerarşi Prosesi skorunun büyük oranda teknik yeterlilikten etkilendiğini göstermektedir. Bulanık skor ile "iş güvenliği" arasında güçlü bir ilişki bulunmakta olup, (0.72), bu da iş güvenliğine daha fazla önem veren firmaların Bulanık Mantık sisteminde daha yüksek skor aldığı sonucuna varılmıştır. Keringingo vd. (2022) Burundi'de patates yetiştirme kararlarının analitik hiyerarşi proses yöntemi ile analizi ile ilgili çalışmada çalışmamız ile örtüşen ve benzerlikler gösteren sonuçlara ulaşmışlardır.

Çalışmamıza ait Analitik Hiyerarşi Süreci ve Bulanık Mantık skorlarının firma bazında karşılaştırılması grafik açıklaması her firmanın hem Analitik Hiyerarşi Süreci hem de Bulanık Mantık skorları yan yana verilmektedir. Analitik Hiyerarşi Süreci ve Bulanık Mantık skorlarının firma bazında karşılaştırılması analiz sonuçlarına göre "Firma-1", hem Analitik Hiyerarşi Süreci hem de Bulanık Mantık skorlarında en yüksek değere sahip olduğu, bu firmanın genel performansının çok iyi olduğu tespit edilmiştir. "Firma-15" Analitik Hiyerarşi Süreci skoru Bulanık Mantık skorundan daha düşük olduğu, bu firma performansının Analitik Hiyerarşi Süreci kriterlerine göre düşük olduğunu, ancak Bulanık Mantık sisteminde daha yüksek puan aldığı tespit edilmiştir. "Firma-12" ve "Firma-9" gibi firmalarda Analitik Hiyerarşi Süreci skorları oldukça yüksek iken, bulanık skorları daha düşük çıkmış olup, bu durum, Analitik Hiyerarşi Süreci ve Bulanık Mantık yöntemlerinin farklı değerlendirme şekillerine sahip olduğunu sonucuna varılmıştır. Erdin vd. (2021) Bulanık Mantık ve Analitik Hiyerarşi Prosesi yaklaşımlarını kullanarak coğrafi bilgi sistemi ortamında kırsal yangın risk değerlendirmesi ile ilgili yapmış oldukları çalışmada çalışmamız ile örtüşen ve benzerlikler gösteren sonuçlara ulaşmışlardır.

Çalışmamız ile ilgili analiz sonuçları özetle; hem Analitik Hiyerarşi Prosesi hem de Bulanık Mantık yöntemlerini kullanarak firmaların çok kriterli değerlendirmesini yapılmıştır. Analitik Hiyerarşi Prosesi yöntemi daha keskin ve belirli ağırlıklara dayanarak sonuç verirken, Bulanık Mantık daha esnek ve kriterler arası geçişkenlik sunarak firmalar değerlendirilmiştir.

Analitik Hiyerarşi Prosesi sonuçlarına göre; Firma-1 %78 ile en iyi performansa sahip firma olarak öne çıkmaktadır. Kalite, teknik yeterlilik ve maliyet gibi kriterlerde yüksek puanlar almış olduğu sonucuna varılmıştır.

Bulanık Mantık sonuçlarına göre; Firma-1 yine %68.20 ile en yüksek puanı almış, ancak Bulanık Mantıkta bazı farklılıklar bulunmaktadır. Bulanık Mantıkta Firma-15, Firma-8 gibi firmalar öne çıkarken, Analitik Hiyerarşi Prosesi sonuçlarında daha geride kalan firmalar bulunmaktadır. Bu da bulanık mantığın değerlendirme kriterlerinin esnekliğini ve bu iki yöntemin farklı sonuçlar verebileceği sonucuna varılmıştır.

5. Sonuç

Bu çalışmada incelenen yüklenici seçimi için karar modeli, uzmanların bilgisini bir araya getirerek ve belirsiz bilgileri yöneterek aynı anda değerlendirilen birden fazla kriteri içermektedir. Her kriterin göreceli önemini belirlemek için kriterlerin sırasını belirlemek üzere Python betiği, firmaların çeşitli kriterlere göre değerlendirilmesi için kapsamlı bir analiz süreci sunmaktadır. Analitik Hiyerarşi Prosesi yöntemi ile kriter ağırlıklarının belirlenmesi ve skorların hesaplanması sağlanırken, Bulanık Mantık sistemi ile daha esnek ve insan benzeri değerlendirmeler yapılmaktadır. Sonuçların görselleştirilmesi ve kaydedilmesi işlemleri ise, elde edilen verilerin daha kolay yorumlanmasını ve paylaşılmasını sağlamaktadır. Betiğin sunduğu bu süreçler, firmaların performansını objektif bir şekilde değerlendirmek ve karşılaştırmak için etkili araçlar sunmaktadır. Kullanıcı, betiği kendi veri setine ve ihtiyaçlarına göre özelleştirerek daha geniş bir değerlendirme yelpazesi oluşturabilmektedir.

İhale süreçlerinde karar verme stratejilerini iyileştirmeye yönelik proje hedeflerine ulaşmak için "en iyi" yüklenicileri seçmek amacıyla proje yönetiminde çok kriterli seçim yöntemleri uygulanmalıdır. Yüklenici seçimi, bir projenin bütçe ve program dahilinde tamamlanmasını ve sonuçların iyi kalitede olmasını sağlamak için kritik bir görevdir. Çok kriterli yüklenici seçiminin amacı, çoklu seçim hedeflerine dayalı bir değerlendirme kullanarak mevcut seçenekler kümesinden "en iyi" yükleniciyi belirlemektir. Uygun bir yüklenicinin seçimi oldukça faydalıdır ve daha az yetenekli bir yükleniciye proje verilmesi durumunda karşılaşılabilecek birçok riski ortadan kaldırmaktadır.

Analitik Hiyerarşi Prosesi, seçilen kriterlere göre en iyi genel alternatifi seçmek için karar alma süreçlerinin her alanına uygulanabilen güçlü bir araç olarak ortaya çıkmıştır. Ayrıca esnekliği ve etkinliği nedeniyle Analitik Hiyerarşi Prosesi, proje yönetimi alanında, özellikle yüklenici seçiminde karar alma veya problem çözme için güvenilir bir araç olarak seçilebileceği sonucuna varılmıştır. Bu nedenle, niteliksel yargılar söz konusu olduğunda Analitik Hiyerarşi Prosesi tercih edilmeli ayrıca ikili karşılaştırmalar, verilen yargılardaki tutarlılığın analiz edilmesine de olanak sağlamaktadır. Ancak bazen sorunun karmaşıklığı, belirsizliği nedeniyle kesin bir yargıya varmak mümkün olamamaktadır.

Erdin vd. (2021), belirsizliklerin yönetiminde bulanık sayıların uygun bir araç olduğunu ifade etmiştir. Bulanık Analitik Hiyerarşi Prosesi, her iki yöntemin birleştirilmesiyle her iki tekniğin de avantajını elde edecektir. Bazı durumlarda kriterler doğrudan (niceliksel olarak) ölçülebilir. Ortalama ve varyans anlamında net değerler veya bulanık olabilirler. Bu durumda puanları kesin olarak bilindiği için ikili karşılaştırma yapılmasına gerek yoktur. Bu değerler, net veya bulanık doğasıyla küresel puanı hesaplamak için doğrudan kullanılabilir. Niceliksel ve niteliksel kriterlerin bir arada değerlendirildiği durumlarda, Hibrit Bulanık Analitik Hiyerarşi Prosesi yöntemi etkili bir şekilde kullanılabilmektedir. Bu, önceki iki yöntemin tüm güçlü yönlerini miras alacaktır; ancak bu aynı zamanda Analitik Hiyerarşi Prosesi'nin iyi bilinen bazı sorunlarını da beraberinde getirecektir. Bunlar;

- Yargı ölçeği örneğin klasik Analitik Hiyerarşi Prosesi'de 9 ile sınırlıdır.
- Sıralamanın tersine çevrilmesi problemi çok tartışıldı ancak hiçbir zaman tam olarak çözümlenememiştir.
- Tutarlılık kontrolü, matrislerde çelişkili yargılara izin verdiği için eleştirildi veya makul matrisleri red etmektedir.

Dış kaynak kullanımı sürecinden tam olarak yararlanmak için en iyi yükleniciyi seçmek ilk önemli adım olmakla birlikte, dilbilimsel değerlendirmelerin belirsizlik ve kesinlik nedeniyle sayısal ölçeğe çevrilmesinin zor olduğu dikkat çekmektedir. Bu nedenle Bulanık Mantığın kullanılmasını savunulmaktadır. Analitik Hiyerarşi Prosesi'nin ise tutarlılık analizi, puanların birliğe toplanmasına normalizasyona ve duyarlılık analizi yapabilme yeteneğine olanak sağlaması nedeniyle üstün olduğu görüşünü de savunulmaktadır.

Bu çalışmada Analitik Hiyerarşi Prosesi ve Bulanık Mantık yaklaşımlarının ihaleyi kazanacak kuruluşun seçiminde kullanılması incelenmiştir. Bu modelin, proje yönetim ekiplerinin, yalnızca en düşük teklife dayanmayan bir seçim sürecinde tatmin edici sonuçlar sunma olasılığı en yüksek olan yüklenicileri belirlemesine yardımcı olabileceği düşünülmektedir. Bu çalışma inşaat sektörüne iki şekilde katkıda bulunmaktadır; birinci, seçim kriterleri anlayışını önem derecelerini de kapsayacak şekilde genişletmekte, ikincisi ise en iyi yüklenicinin analiz edilmesi ve seçilmesi için yeni bir yöntem olan Analitik Hiyerarşi Prosesi ve Bulanık Mantık yaklaşımlarını uygulayabilecekleri umulmaktadır.

Katkı Oranı Beyanı

Yazarların katkı yüzdeleri aşağıda verilmiştir. Yazarlar makaleyi incelemiş ve onaylamıştır.

	S.A.	L.O.U.
K	50	50
T	50	50
Y	50	50
VTI	50	50
VAY	50	50
KT	50	50
YZ	50	50
KI	50	50
GR	50	50
PY	50	50
FA	50	50

K= kavram, T= tasarım, Y= yönetim, VTI= veri toplama ve/veya işleme, VAY= veri analizi ve/veya yorumlama, KT= kaynak tarama, YZ= Yazım, KI= kritik inceleme, GR= gönderim ve revizyon, PY= proje yönetimi, FA= fon alımı.

Çıkar Çatışması

Yazar herhangi bir çıkar çatışması olmadığını beyan etmektedir.

Etik Değerler

Bu çalışma için hayvanlar ve insanlar üzerinde çalışma yapılmadığından etik kurul onayı gerekmemektedir.

Teşekkür

Yazar, Düzce Üniversitesi İnşaat Mühendisliği Bölümü'ne teşekkür eder.

Referanslar

Acar E, Karpuz-Enücük G. 2022. Using the analytic hierarchy process for store manager selection: a real case study. J Econom Stat, 1(36): 63-76.

Afolayan H, Ojokoh BA, Adetunmbi A. 2021. Feedback integrated web-based multi-criteria group decision support model for contractor selection using fuzzy analytic hierarchy process. Intell Syst Appl, 1251(2): 511-528.

Ahmad AM, Jrad F, Makia S. 2023. A Data-driven approach to supplier selection in industrial construction projects. J Univ Duhok, 26(2): 201-215.

Akar O. 2024. Estimation of the effect of electric vehicles on the aging of distribution transformers using fuzzy logic. Balk J Electr Comput Eng, 12(3): 199-205.

Akarslan-Kodaloğlu F, Kodaloğlu M. 2023. Determining the drying rates of fabrics with different knit structures by fuzzy logic method. Int J Comput Exp Sci Eng, 9(2): 191-196.

Allahverdi Ç, Allahverdi Y. 2024. Diffusion Limited Aggregation Via Python: Dendritic Structures and algorithmic art. JSR A, 58(1): 99-112.

Alsaadoun S, Tchier F. 2024. Proposed intelligent irrigation system for riyadh city using fuzzy logic. EPSTEM, 28(1): 397-407.

Alsmadi O, Abu-Hammour Z, Mahafzah K. 2024. Digital systems model order reduction with substructure preservation and fuzzy logic control. EPSTEM, 28(1): 14-22.

Anlak S, Düven E. 2023. Improving end-point position control in hydraulic testing machines with a fuzzy logic based approach. JARNAS, 9(3): 531-544.

Aslan B, Areta-Hızıroğlu O. 2024. Prediction of lung cancer with fuzzy logic methods: a systematic review. FATHER, 4(2): 155-192.

Boyacıoğlu NM, Kocakulak T, Batar M, Uyumaz A, Solmaz H. 2023. Modeling and control of a PEM fuel cell hybrid energy system used in a vehicle with fuzzy logic method. Int J Comput Exp Sci Eng, 7(4): 295-308.

Çetinkaya A. 2024. Fuzzy logic approach for predicting student achievement in scratch. Konjes, 12(2): 344-357.

Eke G, Elgy J, Wedawatta G. 2019. Establishing a link between contractor selection strategy and project outcomes: simulation study. J Constr Eng Manag, 145(10): 1-36.

Eltaleb M, Çelik H. 2024. PLC controlled fuzzy logic-based egg hatching machine. Turk J Sci Technol, 19(2): 339-350.

Erdin C, Çağlar M. 2021. Rural fire risk assessment in geographic information system environment using fuzzy logic and AHP approaches. Pol J Environ Stud, 30(6): 4971-4984.

Erener ŞA. 2024. Python-based evaluation of road network constraints for electric scooters and bicycles: İzmit example. IJEG, 9(1): 34-48.

Eze EC, Awodele IA, Adegboyega AA, Onyeagam OP, Guto JA. 2020. Assessment of the triggers of inefficient materials management practices by construction SMEs in Nigeria. Int J Real Estate Stud, 14(1): 38-56.

Günal AY, Mehdi R. 2024. Application of a new fuzzy logic model known as 'SMRGT' for estimating flow coefficient rate. FOREIGN, 8(1): 46-55.

Gürler C. 2023. Ranking the factors affecting the choice of crowdfunding web sites with analytic hierarchy process. DEU Sos Bilim Enst Derg, 25(1): 187-203.

Hoseinpoor MA. 2019. The combination of DEA and AHP approach in the selection of contractors participating in tenders. Holos, 35(2): 1-15.

Irma B, Baihaqi I. 2018. The integration of AHP and QFD for contractors selection. J Adv Technol Eng Res, 4(3): 118-129.

Jabbarzadeh A. 2018. Application of the AHP and TOPSIS in Project Management. J Project Manage, 3(5): 125-130.

Jagoda JA, Schuldt SJ, Hoisington AJ. 2020. What to do? Let's Think Using the Analytical Hierarchy Process to Make Decisions. Front Young Minds, 8(78): 1-12.

Kannan J, Jayakumar V. 2023. Sustainable method for tender selection using linear diophantine multi-fuzzy soft set. Commun Fac Sci Univ Ank Ser A1 Math Stat, 72(4): 976-991.

Keringingo T, Karakayacı Z. 2022. Analysis of potatoes growing decisions with the analytic hierarchy process method in Burundi. Eurasian J Agric Econ, 2(1): 15-28.

Khoso AR, Yusof AM, Chen ZS, Wang XJ, Skibniewski MI, Memon NA. 2021. Embedded remote group environment through modification in macbeth – an application of contractor's selection in construction. J Civil Eng Manage, 27(8): 595-616.

Lazebna N. 2021. English-language basis of python programming language. Res Bull Ser Philol Sci Natl Univ Zaporizhzhya Polytech, 1(1): 371-376.

Lüy M, Metin NA, Civelek Z. 2024. Maximum power point tracking with incremental conductance and fuzzy logic controller in solar energy systems. El Cezeri J Sci Eng, 11(1): 120-130.

Maqsoom A, Bajwa S, Zahoor H, Thaheem MJ, Dawood M. 2020. Optimizing contractor's selection and bid evaluation process in construction industry: client's perspective. J Constr, 18(3):

445-458.

Marović MP, Hanak T. 2021. A multi-criteria decision support concept for selecting the optimal contractor. Appl Sci, 11(1660): 1-17.

Mızrak F, Culduz M. 2023. Application of analytic hierarchy process (ahp) in evaluating educational leadership theories for effective school management. Avrasya Sos Ekon Aras Derg, 10(4): 137-164.

Mızrak F. 2023. Analyzing criteria affecting decision-making processes of human resource management in the aviation sector – a fuzzy logic approach. J Aviation, 7(3): 376-387.

Morkunaite Z, Bausys R, Zavadskas EK. 2019. Contractor selection for sgraffito decoration of cultural heritage buildings using the WASPAS-SVNS method. Sustainability, 11(22): 1-24.

Naik MG, Kishore R, Dehmourdi SAM. 2021. Modeling a multi-criteria decision support system for prequalification assessment of construction contractors using CRITIC and EDAS models. Oper Res Eng Sci Theory Appl, 4(2): 79-101.

Najiazarpour S, Pouresfandyani H. 2019. Assessment and selection of contractors in specific contracting projects with supply chain approach using GRAY and AHP methods as decision support. Mod Appl Sci, 13(4): 51-60.

Ojokoh BA, Afolayan AH, Adetunmbi AO. 2020. Performance analysis of fuzzy analytic hierarchy process multi-criteria decision support models for contractor selection. Sci African, 9(471): 1-12.

Okereke RA, Pepple DI, Ihekweme NM. 2022. Assessment of the major contractors' selection criteria and their impacts in civil engineering construction projects. J Eng Technol Ind Appl, 8(36): 4-13.

Onyeagam OP, Eze EC, Adegboyega AA. 2019. Assessment of quantity surveying firms' process and product innovation drive in Nigeria. Seisense J Manage, 2(2): 22-38.

Özarslan Yatak M, Hisar Ç, Şahin F. 2024. Fuzzy logic controller for half vehicle active suspension system: an assessment on ride comfort and road holding. Int J Automot Sci Technol, 8(2): 179-187.

Özdem B, Düğenci M, İpek M. 2024. Determination of electricity production by fuzzy logic method. APJESS, 12(1): 14-20.

Özdemir G. 2024. Bitcoin price prediction with fuzzy logic. A HANDFUL, 28(2): 259-269.

Öztekin E. 2024. 1D Fuzzy Inverse Logic Method and Its Use in the Design of Thick Reinforced Concrete Columns. Sigma, 42(2): 459-474.

Prıncıvıshvamalar J, Rajesh N, Brundha B. 2023. Properties of double fuzzy b-open sets. Konuralp J Math, 11(1): 90-96.

Putri CG, Nusraningrum D. 2022. Subcontractors selection of building construction project using analytical hierarchy process (AHP) and technique for others reference by similarity (TOPSIS) methods. J Theory Appl Manage, 15(2): 261-273.

Razi PZ, Ramli NI, Ali MI, Ramadhansyah PJ. 2020. Selection of contractor by using analytical hierarchy process (AHP). Mater Sci Eng, 712(1): 1-7.

Rustandi D, Imaroh TS. 2021. Analysis fuzzy ahp for optimization contractor selection using multi-criteria in determining the best alternative contractor. Dinasti Int J Manage Sci, 2(6): 899-914.

Şimşek H, Ertürk FN, Şeker R. 2023. A Fuzzy logic approach and path algorithm for time and energy management of smart cleaning robots. Gazi Univ J Sci, 36(3): 1034-1048.

Şimşek H, Özaslan İH, Eryılmaz İ. 2022. Pilot selection in airline organizations with the analytical hierarchy. Process J Aviation, 6(2): 218-227.

Tafazzoli M, Hazrati A, Shrestha K, Kisi K. 2024. Enhancing contractor selection through fuzzy TOPSIS and fuzzy SAW techniques. Buildings, 14(6): 1861-1875.

Thanh NV, Hai NH, Lan NTK. 2022. Fuzzy MCDM model for selection of infectious waste management contractors. Comput Mater Continua, 72(2): 2191-2202.

Tubpawatin N, Srinon R. 2023. Influential criteria for large-scale factory and warehouse main contractor selection used for end-to-end procurement risk management. Proc Int Conf Ind Eng Oper Manage, 14(16): 926-937.

Umarusman N. 2023. Multi-objective de novo programming with type-2 fuzzy objective for optimal system design. Alphanumeric, 11(2): 101-124.

Uyhan R, Gök Z. 2022. Mathematical success with fuzzy logic modeling. Erzincan Univ J Sci Technol, 15(3): 862-872.

Uysal LK, Altın N. 2023. Modelling and fuzzy logic based control scheme for a series hybrid electric vehicle. J Energy Syst, 7(1): 106-120.

Warrad OI, Abdulaal RMS, Bafail O, Alamoudi MH. 2022. Four integrated MCDM models for construction contractors' selection application at Al-Quds University. Int Rev Basic Appl Sci, 9(4): 317-329.

Wibisono Adhipradana ST, Yudo A. 2024. Project selection of Indonesian local oil and gas service company using analytical hierarchy process (AHP). Int J Curr Sci Res Rev, 7(1): 395-400.

Yarahmadi P, Dashti S, Sabzghabaei GR. 2018. Assessment and ranking of contractors from the point of view HSE performance using multi-criteria decision making method (AHP and TOPSIS) in Imam Khomeini port complex. J Occup Hyg Eng, 4(4): 70-80.

Yeşilyurt M, Ayik YZ. 2024. Comparison of C# and Python programming languages in terms of performance and coding on SQL server DML operations. NanoEra, 4(1): 23-33.

Yıldırım E, Avcı E, Akgün Tanbay N. 2023. Prediction of unconfined compressive strength of microfine cement injected sands using fuzzy logic method. Asian J Educ Soc Stud, 11(2): 87-94.

Yıldız MA, Kıpçak F, Erdil B. 2024. Evaluation of earthquake performance of reinforced concrete buildings with fuzzy logic method. Bitlis Eren Univ J Sci, 13(3): 601-617.

Yılmaz H, Altun AA, Bilen M. 2023. Data center control application with fuzzy logic. Adv Artist Intel Res, 3(2): 54-65.

Zengin B, Usta P, Onat Ö. 2023. Fuzzy logic methods for determining the mechanical behavior of masonry walls. Researcher, 3(2): 86-96.

Black Sea Journal of Engineering and Science
doi: 10.34248/bsengineering.1644650

Open Access Journal
e-ISSN: 2619 – 8991

Research Article
Volume 8 - Issue 5: 1297-1306 / September 2025

DETECTION OF PINE PROCESSIONARY MOTH (*Thaumetopoea wilkinsoni*) NESTS USING DEEP LEARNING

Fatih GENÇTÜRK[1]*, Cemal IŞILAK[2], İsmail Serkan ÜNCÜ[3]

[1]*Isparta University of Applied Sciences, Faculty of Technology, Department of Computer Engineering, 32260, Isparta, Türkiye*
[2]*Erzincan Binali Yildirim University, Ali Cavit Çelebioğlu Civil Aviation College, Department of Avionics, 24002, Erzincan, Türkiye*
[3]*Isparta University of Applied Sciences, Faculty of Technology, Department of Electrical-Electronic Engineering, 32260, Isparta, Türkiye*

Abstract: The pine processionary moth, widely found in Southern and Central Europe, North Africa, and the Middle East, causes significant economic and ecological losses in forests. This pest feeds on the needles of pine species, posing a greater threat than forest fires in Türkiye, where a large portion of the timber resource is made up of pine trees. This study aims to detect nests of the pine processionary moth residing on trees. A custom dataset was created using aerial images of infested pine trees. A deep learning model was trained using this dataset to facilitate nest detection. Using the YOLOv7 network, training and testing were performed on two datasets of different sizes. The analysis revealed that the dataset with a larger number of images yielded better performance in detecting pine processionary moth nests. The detection success of the model for nests was measured as 92.5% based on the mAP@0.5 metric. The findings of this study demonstrate the effectiveness of the proposed method for accurate and high-resolution detection of pine processionary moth nests in forestry applications. Moreover, these findings highlight the method's potential to support pest density monitoring and the identification of intervention priority areas. Future research should investigate the applicability of the proposed approach to other pest species and explore its integration into real-time monitoring and pest management systems for large-scale operations.

Keywords: Pine processionary moth, Deep learning, YOLOv7, Artificial intelligence, Forest pests, Classification

***Corresponding author:** Isparta University of Applied Sciences, Faculty of Technology, Department of Computer Engineering, 32260, Isparta, Türkiye
E mail: fatihgencturk@isparta.edu.tr (F. GENÇTÜRK)
Fatih GENÇTÜRK https://orcid.org/0000-0001-8557-5572
Cemal IŞILAK https://orcid.org/0000-0002-2445-0220
İsmail Serkan ÜNCÜ https://orcid.org/0000-0003-4345-761X

Received: February 21, 2025
Accepted: June 12, 2025
Published: September 15, 2025

Cite as: Gençtürk F, Işılak C, Üncü İS. 2025. Detection of pine processionary moth (Thaumetopoea wilkinsoni) nests using deep learning. BSJ Eng Sci, 8(5): 1297-1306.

1. Introduction

Forest pests can significantly hinder forest development. While fires are often considered the greatest threat to forests, insects can cause damage that exceeds the harm inflicted by fires both globally and in Türkiye (Özdal, 2002).

The Pine Processionary Moth (PPM), prevalent in the Middle East, Central and Southern Europe, and North Africa, has emerged as one of the most destructive pests in Türkiye. Its presence persists in Mediterranean, Aegean, Black Sea, and Marmara regions. The PPM damages several pine species, including red pine (Pinus brutia), black pine (Pinus nigra), Scots pine (Pinus sylvestris), Aleppo pine (Pinus halepensis), maritime pine (Pinus pinaster), and stone pine (Pinus pinea) (Özay, 2004).

PPM primarily damages trees during its larval stage, where the larvae feed on the needles of pine species. When their numbers reach sufficient levels, they can defoliate the trees completely. Trees infested with PPM larvae exhibit significantly reduced photosynthesis compared to non-infested counterparts due to their lack of leaves (Babur, 2002).

Larvae of PPM can typically be observed in higher elevations after the first half of August. These caterpillars feed on the nearest needles, forming silken nests. As the larvae develop, they may shift to new shoots, feeding on additional needles and forming sturdier, larger second nests. This cycle continues until the formation of a fourth nest. By this stage, the larvae have consumed all the needles, leaving only the stubs. With 150 to 300 larvae found in these nests, caterpillars rest during the day and emerge at night to feed. The increase in needle consumption occurs as the larvae molt five times throughout the fall and winter, leading to greater damage to the trees. The transition of larvae to the pupal stage begins in higher elevations by the end of March and occurs in lower elevations by May (Çanakçıoğlu, 1993; Yüksel, 2019).

Significant damage from PPM has been reported, reducing tree development by 24% in diameter, 36% in height, and 54% in total growth (Carus, 2004). Similarly, annual growth in slash pine forests has decreased by 34.6% to 39.7%, with subsequent years showing a decline of 43.1% to 58.3% (Avcı and Altunışık, 2016). In another study analyzing the loss in diameter and volume

growth of red pine trees affected by PPM, three different test sites were identified. The analysis showed that the loss in height and diameter growth at breast height was 35%, 50%, and 55% for the three sites, respectively. Similarly, the loss in volume growth was found to be 17%, 37%, and 44% (Erkan, 2011). In a separate study conducted to understand the impact of PPM on biomass growth, 30 maritime pine samples were analyzed. The reduction in biomass growth caused by PPM was reported to range between 37% and 73% on average (Arnaldo et al., 2010). In Türkiye, approximately 56% of forest areas consist of pine trees. Given that PPM negatively impacts the development of these forests, effective combat against the pest is of vital importance (Özay, 2004). Control measures against PPM include mechanical, chemical, biological, and biotechnical methods. Mechanical control involves removing the pest from its environment regardless of its life stage, typically by collecting egg sacs and winter nests and disposing of them far from their host trees. Biotechnical control aims to capture PPM using pheromone traps during the adult's active period from July to September. Chemical control seeks to eliminate PPM when it spreads across large areas, employing stomach and contact insecticides. Various chemicals are used for this purpose. Biological control involves utilizing natural enemies such as fungi, viruses, bacteria, birds, insects, plant oils, parasitoids and predators, and microbial pathogens to curb the pest population (Cebeci et al., 2010; Anonymous, 2016).

Timely detection of harmful species is crucial in the fight against forest pests. Early identification of harmful species helps protect tree health and maintain ecological balance by facilitating the implementation of necessary preventive measures. Further, the surveillance of temporal and spatial effects of pests is required for maximizing the efficiency of control tactics and for priority setting. In this strategy, a number of studies are being carried out that employ a range of techniques and methodologies, with particular focus on aerial photography analysis.

Gooshbor et al. (2016) analyzed the invasion of the green oak leaf roller (Tortrix viridana) in Zagros oak forests. Landsat satellite images were used for this purpose. The NDVI (Normalized Difference Vegetation Index) values from pre- and post-invasion periods were compared. The results showed a significant decrease in NDVI values during the post-invasion period compared to the pre-invasion period. The analysis demonstrated that NDVI values can be effectively used to monitor green oak leaf roller infestations.

Cardil et al. (2017) conducted a study in a pine forest in Spain to assess tree damage caused by PPM. Images captured using a drone equipped with an RGB (Red, Green, Blue) sensor were analyzed. Image processing was performed with the help of the "Agisoft Photoscan Professional" software. Using MLC (Maximum Likelihood Classification), trees were classified based on the extent of leaf damage caused by the infestation. Three different classes were defined for tree-based classification: non-infested, partially infested, and fully infested trees. The classification achieved an accuracy rate of 79%. Ziya et al. (2018) conducted a study involving image analysis to detect the presence and severity of leaf spot disease in a sugar beet field. RGB images of the field were captured using a drone. The study utilized 12 representative classes to determine the severity of the disease. Images were taken from a height of 30–60 cm above the ground, depending on plant height and lighting conditions, and were analyzed using the Matlab image processing library. The image processing was performed in the Lab color space. Disease severity was determined through operations such as K-means clustering, pixel labeling, segmentation, and contrast enhancement. The results were compared with expert assessments and found to be highly consistent.

Cardil et al. (2019) examined and classified the impact of PPM infestation on defoliation in pine and oak trees. The study, conducted in Spain, collected aerial images of trees using a drone equipped with RGB and multispectral sensors. Tree defoliation was analyzed using NDVI and ExG (Excess Green) indices derived from the images. For tree-based classification, three different classes were defined: non-defoliated, partially defoliated, and fully defoliated trees. The classification achieved an accuracy rate of 81.8%. Kerkech et al. (2020) conducted a study on the detection and mapping of mildew disease in vineyards located in France. Images were captured using a drone equipped with RGB and infrared sensors. The proposed method is based on the fusion of RGB and infrared images. Deep learning was used to distinguish between healthy and diseased areas, as well as shadow and ground sections in the images. The study employed the SegNet architecture, which was found to be suitable for detecting and mapping the disease. The method achieved an accuracy rate of 87% at the leaf level and 92% at the vine level. Chen et al. (2021) developed an intelligent pest management system for controlling Tessaratom papillosa. This study, conducted in Taiwan, utilized an exploratory drone to capture RGB images and an agricultural drone for spraying operations. To enable real-time image processing, an NVIDIA Jetson TX2 board was used to run the Tiny-YOLOv3 deep learning algorithm. A spraying map was generated to allow farmers to monitor pest distribution in real time and take preventive actions. Pest locations detected from the images were used to determine the optimal spraying route. The proposed model significantly improved efficiency compared to conventional spraying methods by reducing pesticide consumption, time spent, and total labor requirements. The study reported a reduction of 87.5% in pesticide use, 53% in spraying time, and 50% in required labor.

Akıncı and Göktoğan (2022), in their recent study, carried out a study in Eskişehir aimed at identification and mapping of PPM nests. A quadcopter equipped with four motors and an RGB sensor was used in the study for

image acquisition. According to acquired images, identifications of nests have been conducted and geographical coordinate locations at nest centers have been calculated. In training and testing, feature pyramid network (FPN) and UNet architectures have been used. Conclusions drawn through deep learning-based image segmentation revealed that the generated nest map can become a beneficial contribution in combating PPM.In Kahramanmaraş, the severity of red pine PPM infestations was evaluated using Landsat 8 OLI satellite imagery and remote sensing techniques. The minimum, average, maximum, and sum NDVI values were calculated for the years before (2016) and after (2022) the PPM infestation. These NDVI values were compared using SPSS statistical software and t-tests, and there was a significant difference between the values calculated before and after the infestation (Özcan and Sivrikaya, 2022).

A review of the literature reveals that the detection of pine processionary moths and similar forest pests has traditionally relied on low-resolution satellite imagery and conventional image processing techniques. For instance, studies by Gooshbor et al. (2016) and Özcan and Sivrikaya (2022) employed NDVI analyses to evaluate forest health at the regional scale. Cardil et al. (2017, 2019) conducted tree-based classifications focused on the severity of damage, reporting accuracy rates between 79% and 81.8%. Ziya et al. (2018) applied classical image processing techniques to detect leaf spot disease but did not incorporate object-based deep learning approaches. More recent studies by Kerkech et al. (2020) and Chen et al. (2021) implemented deep learning-based segmentation methods; however, their research focused respectively on mildew detection in vineyards and optimization of pesticide spraying in agriculture. Akıncı and Göktoğan (2022), on the other hand, focused on mapping PPM nests using Unmanned Aerial Vehicle (UAV) imagery by applying different deep learning architectures.

Taken together, these studies suggest that object-based, high-precision nest detection methods remain relatively underrepresented in the current literature. Addressing this gap, the present study proposes a method that utilizes high-resolution UAV imagery and the YOLOv7 architecture to detect individual nests, with clearly reported accuracy metrics. As part of this study, a custom dataset comprising 700 images collected under real-world conditions was constructed. The model trained using this dataset achieved a mAP@0.5 score of 92.5%. These findings highlight the potential of the proposed approach to contribute to early warning systems, the planning of pest management strategies, and the development of future autonomous monitoring frameworks.

2. Materials and Methods

In this study, the YOLOv7 model was employed for object detection. Since training deep learning models like YOLOv7 requires substantial computational resources, including high-performance CPUs and GPUs, a cloud-based platform was preferred. Specifically, Google Colaboratory (Google Colab) (Anonymous, 2017) was selected due to its widespread use in artificial intelligence research, its free access to powerful GPU resources, and its compatibility with Python-based deep learning frameworks. The platform's support for the NVIDIA Tesla P100 GPU with 16GB memory provided sufficient computational capacity for training while eliminating the need for dedicated local hardware.

The necessary YOLOv7 configuration files and dependencies were installed within the Colab environment. After annotating the custom dataset, the image and label files were structured in appropriate directories in Google Drive and linked to the Colab runtime. A total of 700 annotated images were prepared, with 560 used for training.

2.1. Creating the Dataset

Utilization of aerial imagery to monitor forest pests is of numerous advantages, offering a more effective and efficient way of doing this compared to the traditional ground-based methods. Getting clear images between trees in rugged terrain can be quite hard to obtain. Additionally, since PPM nests can be found in the upper parts of trees, images were captured using two different UAVs: the DJI Mini 2 and the custom-built UAV (Figure 1). After identifying the area where the nests were found, the drone was flown over the trees, capturing 32 different videos with an integrated RGB camera.

Figure 1. The custom-built UAV employed for image acquisition.

These videos were recorded onto a memory card. Subsequently, a small code written in Python was employed to extract images from the video data, resulting in a total of 500 images. Of these, 400 images (80%) were used for training, while 100 images (20%) were designated for testing. To improve the dataset, the number of frames was extended from 500 to 700 by incorporating additional real images obtained under

different lighting conditions and angles. This adjustment maintained the split of 80% for training and 20% for testing. In the final dataset, 560 images were allocated for training, and 140 images were used for testing. Video recordings obtained from 50 trees containing nests feature a total of 86 different nests. Each frame may contain a single nest or multiple nests. During the recording process, the position of the drone was continually adjusted to capture images from various angles. Additionally, by altering the drone's horizontal and vertical distances from the nests, images were acquired from different elevations and distances. Sample images obtained from the same tree at varying angles and distances are presented in Figure 2.

Figure 2. Sample images of the tree and its nests, captured from various angles and distances, representing the dataset content.

A dataset was created from a stand located approximately 150 meters inside the Isparta-Antalya highway at the 23rd kilometer, roughly 3.5 kilometers from Güneyce village. The coordinates of the area are 37.6503026° latitude and 30.7258255° longitude. The region, which spans 32 hectares and is situated at an elevation of 700 meters above sea level, was scanned. The area selected for data collection was identified as the starting point of the stand due to the higher density of nests present (Figure 3).

Figure 3. The area from which images were obtained for the dataset.

2.2. YOLO

YOLO, which stands for "You Only Look Once," is a deep learning method. Its first version was developed in 2016 by Joseph Redmon, Ali Farhadi, and Santosh Divvala (Redmon et al., 2016). This architecture enables object classification and detection through the processing of the information in one pass by a convolutional neural network (CNN). YOLO formulates object detection as a regression problem in which one or more bounding boxes and corresponding class probabilities are predicted following a single network pass. Consequently, visual components are processed once to predict the coordinates for every class category (Terven et al., 2023). The YOLO network is more efficient and higher performing than other approaches. By modifying the model size, it can provide a trade-off between performance and accuracy; reducing the model size can increase speed, and enlarging it can produce more precise results (Ali and Zhang, 2024). Figure 4 illustrates the architecture of the original YOLO model, which includes 24 convolutional layers plus 2 fully connected layers (Redmon et al., 2016).

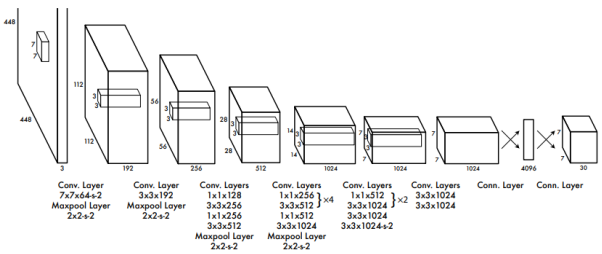

Figure 4. YOLO architecture (Redmon et al., 2016).

Due to its flexible architecture and ability to balance inference speed and detection accuracy, YOLO has become a preferred method in many real-time object detection tasks, especially in resource-constrained environments. In this study, YOLOv7 was selected as the

detection backbone, given its high accuracy and improved computational efficiency compared to earlier YOLO versions and other popular object detectors such as Faster R-CNN, SSD, or EfficientDet (Zhang et al., 2024). While these alternative architectures demonstrate superior detection performance, their increased processing time and hardware requirements limit their applicability to embedded platforms such as the Jetson TX2 or AGX Xavier. Following a detailed comparative analysis of available YOLOv7 variants, the YOLOv7-Tiny model was chosen due to its balanced performance in terms of detection accuracy and real-time suitability for embedded systems. As shown in Table 1, YOLOv7-Tiny is capable of running at 19 FPS on TX2 and 23 FPS on AGX Xavier, making it suitable for real-time deployment in UAV-based scenarios (Işilak et al., 2023).

Table 1. YOLOv7 and YOLOv8 model FPS results (640×640) on TX2, Xavier, and T4 GPUs.

Platform / Model	TX2	AGX Xavier	Tesla T4
V7-Tiny	52.5ms/19FPS	43.0ms/23FPS	11.1ms/90FPS
V7-XL	409.5ms/2FPS	82.3ms/12FPS	28.4ms/35FPS
V8-N		47.8ms/20FPS	10.4ms/96FPS
V8-XL		176ms/6FPS	34.6ms/29FPS

2.3. YOLOv7

YOLOv7, released in July 2022, is the seventh generation of the YOLO family. This neural network has achieved remarkable improvements in detection speed and accuracy compared to its previous ancestors because of some architectural innovations. YOLOv7 methodology attained 56.8% Average Precision (AP) when evaluated on the COCO dataset and exhibited an inference speed of between 5 frames per second (FPS) and 160 FPS and hence a more accurate and faster real-time object detection system compared to its predecessors (Nguyen et al., 2022; Wang et al., 2022).

YOLOv7 is designed using Extended Efficient Layer Aggregation Networks (E-ELAN). E-ELAN, developed based on ELAN architecture, enhances the model's learning capacity by increasing the number of features added through group convolution. Specifically, it ensures efficient parameter utilization through strategies for expanding, shuffling, and merging feature maps (expand, shuffle, merge cardinality). Figure 5 presents the E-ELAN and ELAN architectures (Wang et al., 2022).

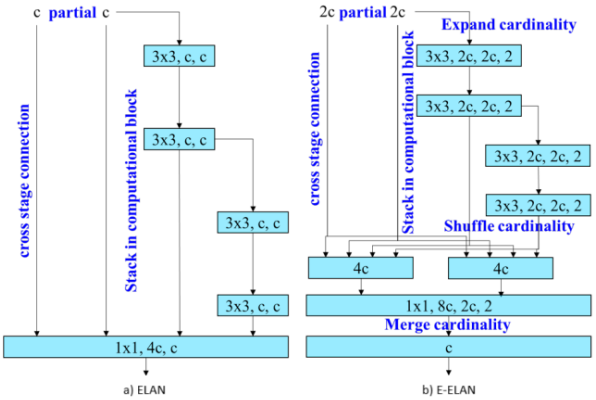

Figure 5. a) ELAN architecture and b) E-ELAN architecture (Wang et al., 2022).

One of the reforms introduced by YOLOv7 is the model scaling method. The primary aim of model scaling is to adjust the core characteristics of the model to meet different application requirements. Through model scaling, the model's width (number of channels), depth (number of stages), and resolution (input image size) can be optimized. Another innovation is the planned reparameterization process. RepConv (Re-parameterized Convolution) is a method that combines multiple kernels within a single convolutional layer with 1x1 and 3x3 convolutions along with an identity connection. Yet, the identity connection part of RepConv has the potential to interfere with the learning mechanisms of other components of architectures such as ResNet and DenseNet. To solve this problem, a variant known as RepConvN was created. RepConvN is a tailored version of RepConv that lacks identity connections, thereby enabling the preservation of parameter efficiency while enhancing model accuracy. Additionally, YOLOv7 has optimized the label assignment process, enhancing prediction consistency across different layers of the model and consequently improving object detection accuracy. The creation of object bounding boxes has also been refined, particularly in accurately detecting overlapping boxes, which is evaluated using the Intersection over Union (IoU) metric (Wang et al., 2022).

For this study, the YOLOv7 framework was implemented. The appropriate hyperparameters for the model were identified, and the training and testing protocols were established. The batch size was set to 16, while the number of epochs was 100. The SiLU (Sigmoid Linear Unit) activation function was integrated with YOLOv7. Data annotation was carried out using the web-based platform "makesense.ai" (Anonymous, 2022).

2.4. Evaluation Metrics

YOLO network employs the Intersection over Union (IoU) metric to calculate how much overlap exists between two bounding boxes. During labeling, bounding boxes are drawn around the targeted object, referred to as the ground truth boxes. As the network begins training, the predicted bounding boxes are generated. The YOLO network compares the ground truth boxes with the

predicted boxes. The greater the overlap between the boxes, the higher the IoU value, which leads to improved detection quality. Conversely, as the IoU value decreases, detection quality declines. The method for calculating IoU is illustrated in Figure 6.

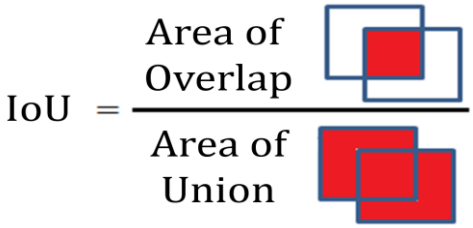

Figure 6. Calculating the IoU Value

For evaluating the training and testing performance of the network, various metrics are available. To calculate these metrics, the values in the confusion matrix must be known. The confusion matrix consists of four values—True Positive (TP), True Negative (TN), False Positive (FP), and False Negative (FN) which quantify the accuracy between actual and predicted classes (Table 2).

Table 2. Confusion Matrix

Confusion Matrix		Actual Values	
		Positive	Negative
Predicted Values	Positive	TP	FP
	Negative	FN	TN

- **TP** refers to instances that are correctly predicted as positive by the model.
- **TN** indicates instances that the model correctly predicts as negative.
- **FP** denotes instances that are incorrectly predicted as positive while being negative.
- **FN** represents instances that are incorrectly predicted as negative while being positive.

Using the values from the confusion matrix, metrics such as Precision, Recall, and F1-score can be calculated (equations 1, 2, 3).

$$Precision = \frac{\text{TP}}{\text{TP} + \text{FP}} \quad (1)$$

$$Recall = \frac{\text{TP}}{\text{TP} + \text{FN}} \quad (2)$$

$$F1_{Score} = 2 \times \frac{\text{Recall} \times \text{Prec}}{\text{Recall} + \text{Prec}} \quad (3)$$

One of the most common evaluation metrics in deep learning-based object detection models is the mean Average Precision (mAP) value. The mAP value is computed by averaging the precision and recall performance across all classes. Initially, the Average Precision (AP) for each class is determined using the Precision-Recall curve. The Area Under Curve (AUC) is calculated to obtain the mean precision. Finally, the average of the AP values calculated for all classes yields the mAP value (Equation 4). The "N" in Equation 4 refers to the number of classes. Different mAP metrics exist based on IoU thresholds. For instance, mAP@0.5 indicates the average precision calculated based on results where the IoU value is 0.5 or higher. When expressed as mAP@0.5:.05:.95, it refers to the average of mAP values calculated for IoU values ranging from 0.5 to 0.95, with increments of 0.05 (Padilla et al., 2020).

$$mAP = \frac{1}{N}\sum_{i=1}^{N} AP_i \quad (4)$$

3. Results and Discussion

This study aimed to detect nests containing PPM larvae using a deep learning-based YOLOv7 architecture. The dataset utilized for this purpose is outlined in Section 2.1. Initially, the YOLOv7 network was trained using a dataset consisting of 500 images. Of these images, 400 were allocated for training and 100 for testing. A total of 123 annotations were made in the 100 images designated for testing. The confusion matrix of the model trained with the dataset of 500 images is presented in Figure 7.

The performance metrics, including Precision, Recall, the Precision-Recall curve, and the F1-score graph, of the models trained with 500 and 700 images are presented in Figures 8 and 9, respectively.

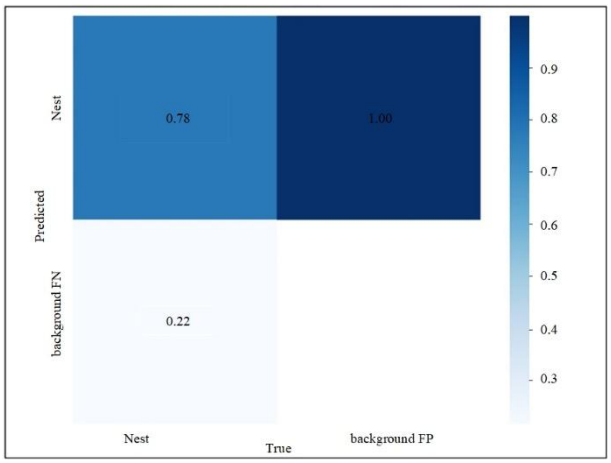

Figure 7. The confusion matrix of the model trained with 500 images.

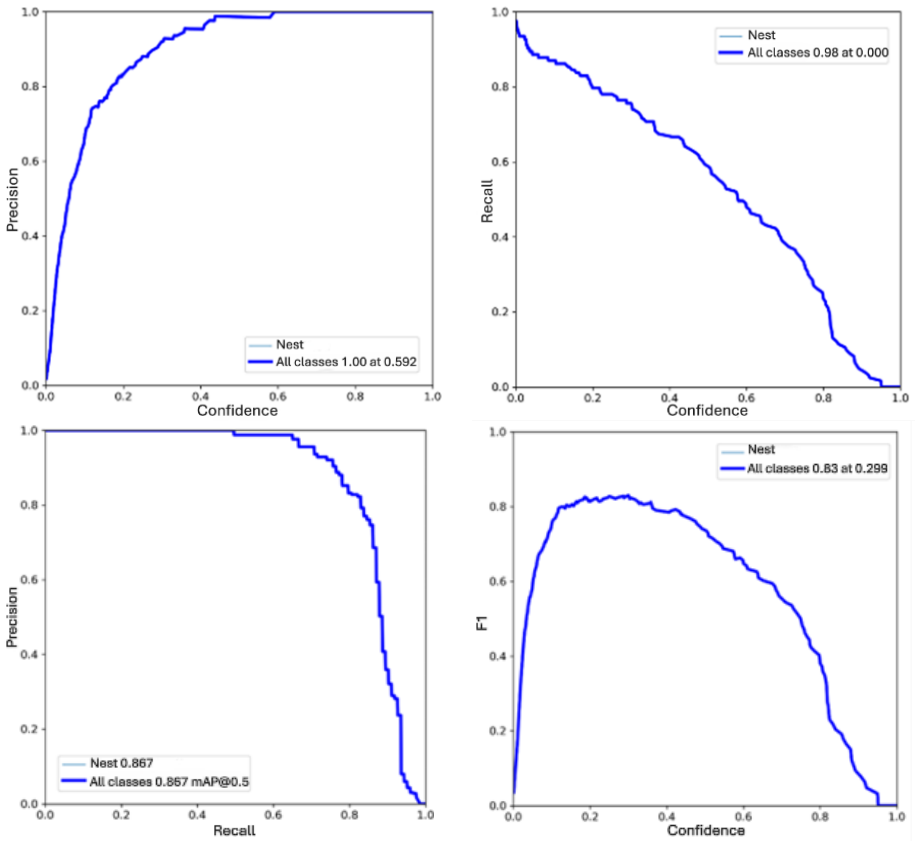

Figure 8. The performance metrics of the model trained with 500 images.

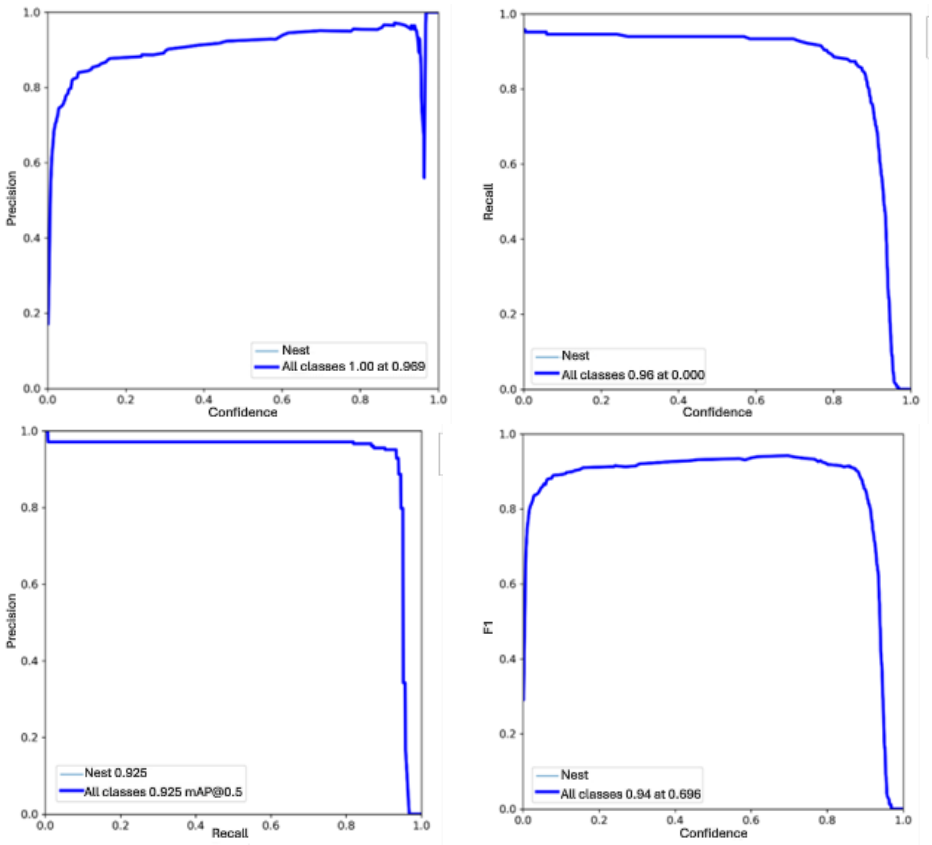

Figure 9. The performance metrics of the model trained with 700 images.

The model trained with a dataset of 500 images exhibited a mean Average Precision at 0.5 (mAP@0.5) value of 0.867. To assess the impact of the number of images in the dataset on success rates, 200 additional images captured at different times of the day were incorporated into the dataset, increasing the total number of images to 700. Of the 700 images captured from the videos, 560 were allocated for training and 140 for testing, following an 80% and 20% split, respectively. The confusion matrix of the model trained with the dataset of 700 images is presented in Figure 10.

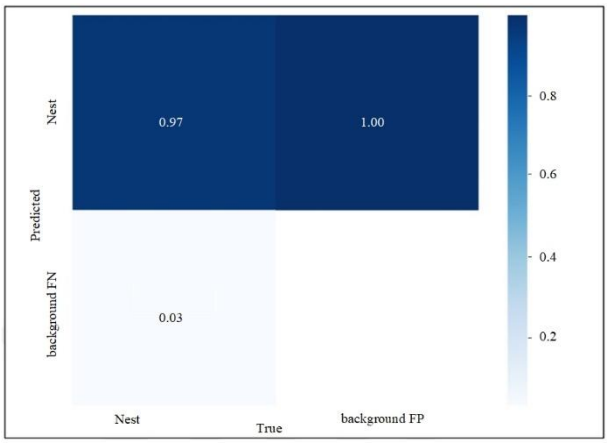

Figure 10. The confusion matrix of the model trained with 700 images.

The training and testing processes conducted with 500 and 700 image datasets revealed that the performance metrics varied despite the constant iteration count. The achieved performance rates are presented in Table 3.

Table 3. Achieved Performance Metrics

Images in Dataset	mAP@0.5	F1-Skor
500	0.867	0.83
700	0.925	0.94

As shown in Table 3, incorporating additional real-world images into the dataset led to a significant improvement in the model's overall performance, particularly in mAP and F1 scores. The inclusion of 200 additional images captured at different times of the day allowed the model to better learn environmental variables such as light angle and intensity. In the initial dataset, intense light reflections occasionally caused the model to misclassify bright surfaces as nests or overlook nests due to low contrast. Including such examples in the training process reduced the model's sensitivity to lighting conditions and improved detection accuracy. However, some limitations remained during field applications. Complex backgrounds, nest-like natural structures, and environmental heterogeneity occasionally led to false positives. Therefore, incorporating background images without any nests into the training process may enable the model to more accurately recognize such patterns, thereby reducing misclassifications particularly related to background elements. These findings suggest that training the model with more diverse and environmentally representative datasets could further enhance detection performance and generalizability. Figure 11 shows sample detections of pine processionary moth nests generated by the model.

From a real-world application perspective, the spatial accuracy of the detected nests is particularly important for operational use, especially in large forested areas. Factors such as flight duration, image resolution, and processing capacity must be taken into account in such contexts. Therefore, it is recommended that the model be integrated with user-friendly interfaces and real-time decision support systems to enhance its practical usability. Furthermore, this study, which focuses on the detection of pine processionary moth nests, could provide greater value to forest management practices if extended to include quantitative analysis of pest density and assessment of damage severity. These enhancements would support the development of more comprehensive and effective intervention strategies in the field.

Figure 11. PPMs detected under different lighting levels and environments.

4. Conclusion

The pine processionary moth is a globally prevalent pest whose population is rapidly increasing due to climate change. In Türkiye, it is commonly found in the Mediterranean, Aegean, Marmara, and Black Sea regions, particularly along the coastal areas. PPM larvae feed on the needles of coniferous trees, causing significant economic and ecological losses in forest ecosystems. Given that a large portion of Türkiye's forests consists of coniferous trees, the risk posed by this pest is considerable. In this regard, a deep learning-based solution was proposed to contribute to the fight against PPM by identifying their nests.

A preliminary custom dataset of 500 images was established to train the YOLOv7 network. The dataset contained nest images captured from different distances and angles and was divided into 80% for training and 20% for testing. The YOLOv7 network was trained and tested using the Google Colaboratory environment. The dataset of 500 images yielded an mAP@0.5 of 0.867 and an F1-score of 0.83. To develop the model further, an additional 200 images captured in different light intensities were included, and the results obtained showed mAP and F1-score improvements. With the increased dataset of 700 images, the mAP@0.5 was 0.925 and the F1-score was 0.94.

The uncontrolled spread of forest pests poses a significant threat to ecosystem health, making their timely and precise detection critically important. This study demonstrates that the developed deep learning-based model can accurately detect PPM nests. Although the current implementation is limited to a single pest species, the model could be extended in future studies to identify multiple pest types by training it on more diverse datasets. Such an enhancement could lay the groundwork for an integrated forest pest monitoring system. In addition, the use of long-term image data may enable the observation of spatial and temporal changes in pest distribution, thus supporting more data-driven intervention planning. Future work should aim to improve the model's generalizability across diverse environmental conditions, reduce false detections through architectural optimizations, and integrate the system with real-time decision support mechanisms. Field testing of the proposed method over larger areas would further contribute to evaluating its operational effectiveness in real-world forestry applications.

Author Contributions

The percentages of the authors' contributions are presented below. All authors reviewed and approved the final version of the manuscript.

	F.G.	C.I.	İ.S.Ü.
C	40	20	40
D	40	20	40
S	30	20	50
DCP	60	20	20
DAI	40	40	20
L	40	30	30
W	40	30	30
CR	40	30	30
SR	40	30	30
PM	30	30	40
FA	40	40	20

C=Concept, D= design, S= supervision, DCP= data collection and/or processing, DAI= data analysis and/or interpretation, L= literature search, W= writing, CR= critical review, SR= submission and revision, PM= project management, FA= funding acquisition.

Conflict of Interest

The authors declared that there is no conflict of interest.

Ethical Consideration

Ethics committee approval was not required for this study because of there was no study on animals or humans.

Acknowledgements

This article was written as a part of master's thesis titled "Development of A Spraying Drone That Can Detect Pine Processionary Moth Nest by Deep Learning" at Isparta University of Applied Sciences Thesis no: 777725. https://tez.yok.gov.tr/UlusalTezMerkezi/tezSorguSonucYeni.jsp

References

Akıncı Ş, Göktoğan AH. 2022. An eco-friendly fight against thaumetopoea pityocampa infestations in pine forests using deep learning on UAV imagery. IEEE, In 2022 Innovations in Intelligent Systems and Applications Conference (ASYU), pp: 1-6.

Ali ML, Zhang Z. 2024. The YOLO framework: A comprehensive review of evolution, applications, and benchmarks in object detection. Computers, 13: 336.

Anonymous. 2016. Orman bitkisi ve bitkisel ürünlerine arız olan zararlı organizmalar ile mücadele yöntemleri. URL: https://www.ogm.gov.tr/tr/e-kutuphane-sitesi/EgitimDokumanlari/Orman%20Zararl%C4%B1lar%C4%B1yla%20M%C3%BCcadele/Orman%20Bitkisi%20ve%20Bitkisel%20%C3%9Cr%C3%BCnlerine%20Ar%C4%B1z%20Olan%20Zararl%C4%B1%20Organizmalar%20ile%20M%C3%BCcadele%20Y%C3%B6ntemleri.pdf. (accessed date: January 14, 2025).

Anonymous. 2017. Google Colab. URL:

https://colab.research.google.com (accessed date: February 09, 2024).

Anonymous. 2022. Get started now. URL: makesense.io (accessed date: January 12, 2025).

Arnaldo PS, Chacim S, Lopes D. 2010. Effects of defoliation by the pine processionary moth Thaumetopoea pityocampa on biomass growth of young stands of Pinus pinaster in northern Portugal. iForest, 3:159.

Avcı M, Altunışık A. 2016. Isparta çam ormanlarında çam kese böceği (Thaumetopoea wilkinsoni Tams, 1926) (Lep.: Notodontidae) zararının artım üzerine etkisi. Türkiye Entomoloji Bülteni, 6:231-244.

Babur H. 2002. Thaumetopoea Pityocampa (Schiff.) çam gençliğinde zarar miktarı. ülkemiz ormanlarında çam keseböceği sorunu ve çözüm önerileri sempozyumu April 24-25, Kahramanmaraş, pp: 37-43.

Çanakçıoğlu H. 1993. Orman entomolojisi, İstanbul Üniversitesi orman fakültesi yayınları. (pp: 29-36).

Cardil A, Otsu K, Pla M, Silva CA, Brotons L. 2019. Quantifying pine processionary moth defoliation in a pine-oak mixed forest using unmanned aerial systems and multispectral imagery. Plos One, 14: e0213027.

Cardil A, Vepakomma U, Brotons L. 2017. Assessing pine processionary moth defoliation using unmanned aerial systems. Forests, 8:, 402.

Carus S. 2004. Impact of defoliation by the pine processionary moth (Thaumetopoea pityocampa) on radial, height and volume growth of calabrian pine (Pinus brutia) trees in Türkiye. Phytoparasitica, 32: 459-469.

Cebeci HH, Oymen RT, Acer S. 2010. Control of pine processionary moth, Thaumetopoea pityocampa with Bacillus thuringiensis in Antalya, Türkiye. J Environ Biol, 31: 357-361.

Chen CJ, Huang YY, Li YS, Chen YC, Chang CY, Huang YM. 2021. Identification of fruit tree pests with deep learning on embedded drone to achieve accurate pesticide spraying. IEEE Access, 9:21986-21997.

Erkan N. 2011. Impact of pine processionary moth (Thaumetopoea wilkinsoni Tams) on growth of Turkish red pine (Pinus brutia Ten.). Afr J Agric Res, 6: 4983-4988.

Gooshbor L, Bavaghar MP, Amanollahi J, Ghobari H. 2016. Monitoring infestations of oak forests by Tortrix viridana (Lepidoptera: Tortricidae) using remote sensing. Plant Prot Sci, 52: 270-276.

Işilak C, Durmaz O, Şalk Y, Çevılkalp H, Dutağaci H, Gırgın T. 2023. Measuring electromagnetic field strength in base stations using unmanned aerial vehicles. In 2023 31st Signal Processing and Communications Applications Conference (SIU) (pp: 1-4). IEEE.

Kerkech M, Hafiane A, Canals R. 2020. Vine disease detection in UAV multispectral images using optimized image registration and deep learning segmentation approach. Comput Electron Agric, 174:105446.

Nguyen HV, Bae JH, Lee YE, Lee HS, Kwon KR. 2022. Comparison of pre-trained yolo models on steel surface defects detector based on transfer learning with gpu-based embedded devices. Sensors, 22:9926.

Özay FŞ. 2004. Çam keseböceği (Thaumetopoea pityocampa Schiff.) (Lepidoptera-Thaumetopoeidae) ve mücadele yöntemleri. Kavak ve Hızlı Gelişen Orman Ağaçları Araşt. Enst. Müd. Kavakçılık Araştırma Dergisi, 30:55-65.

Özcan GE, Sivrikaya F. 2022. Determining Infestation of pine processionary moth using remote sensing. 4th Intercontinental Geoinformation Days, June 20-21, Tabriz, pp: 99-102.

Özdal MH. 2002. Çam Keseböceği ile adacıklarla mücadele yöntemi, Ülkemiz ormanlarında çam keseböceği sorunu ve çözüm önerileri sempozyumu bildiri kitabı, Kahramanmaraş, pp: 226.

Padilla R, Netto SL, Da Silva EA. 2020. A survey on performance metrics for object-detection algorithms. In *2020 international conference on systems, signals and image processing (IWSSIP).* IEEE, pp: 237-242.

Redmon J, Divvala S, Girshick R, Farhadi A. 2016. You only look once: Unified, real-time object detection. In Proceedings of the IEEE conference on computer vision and pattern recognition. pp: 779-788.

Terven J, Córdova-Esparza DM, Romero-González JA. 2023. A comprehensive review of yolo architectures in computer vision: From yolov1 to yolov8 and yolo-nas. Mach Learn Knowl Extr, 5: 1680-1716.

Wang C-Y, Bochkovskiy A, Liao HYM. 2022. YOLOv7: Trainable bag-of-freebies sets new state-of-the-art for real-time object detectors. arXiv. http://arxiv.org/abs/2207.02696.

Yüksel H. 2019. Investigation of the relationship between altitude and biological and ecological characteristics of egg and egg batch in thaumetopoea wilkinsoni tams, 1924 and thaumetopoea pityocampa (den. & schiff., 1775) (lepidoptera: notodontidae) populations. Master's Thesis, Bartın University, Institute of Science, Bartın, pp:59.

Ziya A, Mehmet MO, Yusuf Y. 2018. Determination of sugar beet leaf spot disease level (Cercospora beticola Sacc.) with image processing technique by using drone. Curr Inves Agri Curr Res 5 (3)-2018. Mediterranea, 34(3): 149-156.

Zhang Z, Xie X, Guo Q, Xu J. 2024. Improved YOLOv7-Tiny for object detection based on UAV aerial images. Electronics, 13(15): 2969.

Black Sea Journal of Engineering and Science
doi: 10.34248/bsengineering.1642846

Open Access Journal
e-ISSN: 2619 – 8991

Araştırma Makalesi (Research Article)
Cilt 8 - Sayı 5: 1307-1312 / Eylül 2025
Volume 8 - Issue 5: 1307-1312 / September 2025

KUZU RASYONLARINDA KULLANILAN DUT YAPRAKLARININ ANTİ-METANOJENİK VE ANTİ-PROTEOLİTİK ETKİLERİNİN BELİRLENMESİ

Mesut ERER[1]*, Adem KAMALAK[2]

[1]*Kayseri Provencial Directorate of Agriculture and Forestry, 38090 Kocasinan, Türkiye*
[2]*Kahramanmaraş Sütçü İmam University, Faculty of Agriculture, Department of Animal Science, 46100, Kahramanmaraş, Türkiye*

Özet: Hayvancılık sektöründe metan emisyonlarının azaltılması çevresel sürdürülebilirliği sağlamanın yanında yemden kaynaklı enerji kayıplarını önlemek açısından büyük önem taşımaktadır. Bu çalışma, kuzu rasyonlarında kullanılan dut (Morus alba) yapraklarının anti-metanojenik ve anti-proteolitik etkilerini belirlemeyi amaçlamaktadır. Çalışmada, farklı oranlarda (%0, %5, %10, %15, %20) rasyona dahil edilen dut yapraklarının in vitro sindirim parametreleri üzerindeki etkileri değerlendirilmiştir. Çalışmada, farklı oranlardaki dut yapraklarından oluşturulan rasyonların kimyasal bileşimi, in vitro gaz üretimi, metan emisyonu, sindirim derecesi ve fermantasyon parametreleri incelenmiştir. İn vitro koşullarda yapılan çalışmada elde edilen bulgular dut yaprağının CH4 (ml) üretiminin 14,81-15,22, NH3-N üretiminin ise 47,88 49,30 arasında değiştiğini göstermiş ve istatiksel olarak önemli bulunmamıştır. Bu bulgular farklı oranlarda kullanılan dut yaprağının anti-metanojenik ve anti-proteolitik etkisinin olmadığını göstermiştir. Rasyona dut yaprağının ilave edilmesinin fermantasyon parametreleri üzerinde olumsuz bir etkisinin olmaması ve dut yaprağının besin değerleri özellikle protein içeriğinin yüksek olmasından dolayı, ruminant hayvanların beslenmesinde kullanılan kaba yemlerin yeterince üretilmediği bölge ve mevsimlerde ucuz ve alternatif yem kaynağı olarak dut yapraklarının kullanılmasının kaba yem açığının giderilmesine katkıda bulunacağı düşünülmektedir.
Anahtar kelimeler: Dut yaprağı, Kuzu rasyonu, Metan emisyonu, Anti-metanojenik etki, Anti-proteolitik etki

Determination of Anti-Methanogenic and Anti-Proteolytic Effects of Mulberry Leaves Used in Lamb Rations

Abstract: Reducing methane emissions in the livestock sector is of great importance not only for ensuring environmental sustainability but also for preventing energy losses originating from feed. This study aims to determine the anti-methanogenic and anti-proteolytic effects of mulberry (Morus alba) leaves used in lamb rations. The effects of mulberry leaves included in the ration at different levels (0%, 5%, 10%, 15%, 20%) on in vitro digestion parameters were evaluated. The chemical composition, in vitro gas production, methane emission, digestibility, and fermentation parameters of rations containing different proportions of mulberry leaves were examined. Findings obtained under in vitro conditions showed that CH_4 (ml) production ranged between 14.81 and 15.22, and NH_3-N production ranged between 47.88 and 49.30, with no statistically significant differences. These results indicate that mulberry leaves used at different inclusion levels do not exhibit anti-methanogenic or anti-proteolytic effects. Since the inclusion of mulberry leaves in the ration did not have a negative effect on fermentation parameters and due to their high nutritional value especially protein content it is considered that mulberry leaves could contribute to closing the forage gap as a cheap and alternative feed resource in regions and seasons where sufficient roughage for ruminant feeding is not produced.

Keywords: Mulberry leaf, Lamb ration, Methane emission, Anti-methanogenic effect, Anti-proteolytic effect

***Sorumlu yazar (Corresponding author):** Kayseri Provencial Directorate of Agriculture and Forestry, 38090 Kocasinan, Türkiye
E mail: mesuterer@hotmail.com (M. ERER)
Mesut ERER https://orcid.org/0000-0001-6637-584X
Adem KAMALAK https://orcid.org/0000-0003-0967-4821

Gönderi: 19 Şubat 2025 **Received:** February 19, 2025
Kabul: 13 Haziran 2025 **Accepted:** June 13, 2025
Yayınlanma: 15 Eylül 2025 **Published:** September 15, 2025

Cite as: Erer M, Kamalak A. 2025. Determination of anti-methanogenic and anti-proteolytic effects of mulberry leaves used in lamb rations. BSJ Eng Sci, 8(5): 1307-1312.

1. Giriş

Hayvancılık insan beslenmesi için önemli bir besin kaynağı oluşturmasının yanı sıra diğer endüstri kollarına da hammadde sağlaması nedeniyle ülke ekonomilerinde önemli bir yer tutmaktadır. Her ekonomik faaliyet gibi tarım ve hayvancılıkta stratejik öneme sahip olan bir ekonomik faaliyettir ve diğer faaliyetler gibi büyük oranda doğal kaynakların kullanımına dayanmaktadır. Doğal kaynakların kullanımı ile gerçekleştirilen hayvancılığın çevreye olan etkisi genele yayılan bir etki göstermekte ve çevreyle etkileşiminde etkileyen ve etkilenen durumuna getirmektedir. Hayvansal orjinli besin maddelerinin üretilmesinde kaynak oluşturan ruminant hayvanlar insan beslenmesi için gerekli proteinlerin üretilmesinde öneme sahiptirler. İnsanlar ve diğer çiftlik hayvanlarının sindiremediği selülozu ve protein tabiatında olmayan nitrojenli bileşikleri değerlendirerek besin zincirine katkıda bulunmaktadırlar (Kutlu vd., 2005).

Sindirim sistemleri bakımından monogastrik

hayvanlardan farklılık gösteren ruminant hayvanların beslenmeleri amacıyla tükettikleri karbonhidratlar rumende fermantasyon işlemine maruz kalmakta ve fermantasyon sonucu uçucu yağlar, karbondioksit, metan ve H_2 oluşmaktadır. Oluşan CO_2 ve H_2 rumende bulunan metanojenik mikroorganizmalar tarafından metan gazına dönüştürülmektedir. Enterik metan olarak adlandırılan ve rumende oluşan metan gazı hayvan tarafından kullanılmamakta ve doğaya salınmaktadır. Doğaya salınan ve hayvanın genetik kapasitesi, rasyonun besin maddesi durumu, yemde kullanılan katkı maddesine göre değişiklik göstererek oluşan enterik metan yemlerle birlikte alınan enerjinin %2-12'sinin kaybına neden olmaktadır (Jonhson ve Jonhson 1995). Hayvanlar tarafından kullanılamayarak doğaya salınan enerjinin yine hayvanlar tarafından kullanılması sağlanarak meydana gelen enerji kaybının önlenmesi dolayısıyla bu enerjiyi elde etmek için kullanılan yem materyalinin israf edilmesinin önlenilmeye çalışılması için çalışmaların yapılması oldukça önemlidir. Bu nedenle, hayvancılıkta metan emisyonunu azaltmak hem enerji kayıplarını azaltmak hem de çevresel etkileri minimuma indirmek amacıyla bilimsel çalışmalara konu olmaktadır (Kamalak vd., 2021; de Morais vd., 2023).

Metan, karbondioksitten sonra gelen en önemli sera gazı olarak bilinmektedir (Akın, 2006). Metan moleküllerinin su tutma kapasitesi CO_2 moleküllerinin 20 katıdır ve küresel ısınmaya önemli derecede etki etmektedir. (Van Nevel ve Demeyer, 1996; Aksay vd., 2005). Sera gazı salınımı 1990 ve 2021 yılları arasında %157.1 artmış ve artan bu sera gazlarının %56.5'nin tarım ve hayvancılıktan kaynaklandığı bildirilmiştir (TÜİK 2023). Küresel anlamda iklim değişikliklerinin tarımsal büyümeyi olumsuz etkilediği günümüzde, hayvancılık sektörünün modern bilimsel tekniklerle desteklenmesi gerekmektedir.

Hayvansal üretimin sürdürülebilirliğini sağlamak ve kaynak verimliliğini artırmak için, alternatif yem kaynakları üzerine yapılan çalışmalar giderek daha fazla önem kazanmaktadır. Son yıllarda, bazı bitki türlerinin hayvan beslemesindeki kullanımları, ruminant hayvanlarda hem metan salınımını azaltma hem de protein sindirimini iyileştirme potansiyelleriyle dikkat çekmektedir (Bilal ve Kamalak, 2022; Kılıç ve Boğa, 2021; Selçuk ve Kamalak, 2022). Bu çalışmanın amacı, kuzu rasyonlarına farklı oranlarda katılan dut yapraklarının hem anti-metanojenik ve anti-proteolitik etkilerini hem de rasyona katkı oranını belirlemektir.

2. Materyal ve Yöntem

Dut (Morus alba) yaprakları Nisan ve Mayıs aylarında toplanarak gölgede kurutulmuştur. Kuzu rasyonlarında kullanılacak olan yonca otu, buğday samanı, arpa danesi, buğday danesi, yulaf danesi, buğday kepeği, pamuk tohumu küspesi ve ayçiçeği küspesi gibi kaba ve kesif yemlerin ticari firmalardan temin edilmiştir. Dut yaprakları kullanılarak oluşturulacak rasyonda kullanılan kaba ve kesif yemler 1 mm boyutta olacak şekilde yem öğütme makinasıyla öğütülerek kimyasal analizler ve in vitro gaz, metan, sindirim ölçümleri için uygun hale getirilmiştir. Yemler naylon torbalar içerisinde buzdolabında saklanmıştır. Dut yaprakları ile rasyonları oluşturacak kaba ve kesif yemlerin kimyasal kompozisyonu belirlemek amacıyla analizleri üç tekerrürlü olarak yapılmıştır.

2.1. Rasyonların oluşturulması

Öğütülmüş olan dut yaprağı, 0-200 g/kg oranlarında rasyona eklenerek Tablo 1'de gösterilen rasyonlar hazırlanmıştır. Dut yaprağı, genellikle yonca otunun yerine kullanılmıştır. Enerji ve protein içeriği dengesini sağlamak amacıyla diğer yem ham maddelerinin katkı oranlarında küçük düzenlemeler yapılmıştır. Bu düzenlemeler sonucunda rasyonlar izo-kalorik ve izo-nitrojenik özellikte tasarlanmıştır. Kompozisyonları ve enerji değerleri belirlenen, dut yaprakları yonca kuru otu yerine %0, %5, %10, %15, %20 oranlarında ikame edilerek izo-kalorik ve izo-nitrojenik rasyonlar hazırlanmıştır.

Tablo 1. Dut yaprağının katılmasıyla oluşan rasyonların bileşimi

Yem Ham Maddeleri	Dut Yaprağının Katkı Oranları (g/Kg)				
Arpa	145	145	145	145	145
Dut Yaprağı	0	50	100	150	200
Bitkisel Yağ	17	20	24	28	32
Buğday Kepeği	260,41	255	246	237,3	228,5
Ayçiçeği Tohumu Küspesi	51.59	54	59	63.7	68.5
Yonca Otu	500	450	400	350	300
Tuz	10	10	10	10	10
Kireç Taşı	15	15	15	15	15
Mineral-Vitamin	1	1	1	1	1
ME (kcal/kg)	2651	2648	2648	2649	2649
HP (g/kg)	170	170	170	170	170

HP= ham protein, ME= matabolik enerji.

2.2.Kimyasal analizler

Kuru madde oranı dut yaprağı örneklerinin 105 °C de 2 saat bekletilmesiyle, ham kül oranı ise yem örneklerinin 550 °C'de 8 saat yakılmasıyla belirlenmiştir. Dut yaprakları ve rasyonlarda kullanılan kaba ve kesif yemlerin ham protein içerikleri Kjedahl yöntemiyle tespit edilmiştir. Kjedahl yöntemiyle örneklerin azot içeriği belirlenmiş ve bulunan azotun 6.25 ile çarpımıyla ham protein oranı belirlenmiştir. Ham yağ oranının belirlenmesinde Soxhlet aleti kullanılmıştır (AOAC 1990). Dut yapraklarının kondense tanen içeriklerinin belirlenmesinde Makkar vd., (1995)'nın geliştirdiği n-Butanol yöntemi kullanılmıştır.

2.3.Dut yaprakları ve rasyonların *in vitro* gaz ve metan üretimlerinin, metabolik enerji ve organik madde sindirim derecesinin belirlenmesi

Laboratuvarda yapılmış olan *in vitro* çalışmalar için gerekli izinler Kahramanmaraş Sütçü İmam Üniversitesi, Ziraat Fakültesi Yerel Etik Kurulundan gerekli izin alınmıştır (Protokol No: 2023/1-3). Dut yaprakları ve kuzu rasyonlarının *in vitro* gaz ölçümleri Menke vd. (1979) geliştirtiği *in vitro* gaz ölçüm sistemi kullanılarak yapılmıştır. Fermantasyon sonunda tamponlanmış rumen sıvısının amonyak içeriği de belirlenmiştir. Dut yaprakları katılarak elde edilen rasyonlar üç tekerrürlü olacak şekilde 0,5 gram tartılarak üzerine 40 mL tamponlanmış rumen sıvısı ilave edilmiş ve 39 °C'de ayarlanmış su banyosuna yerleştirilmiştir. 24 saat fermantasyon sonunda körlerden elde edilen gaz ve metan değerleri ölçümlerden çıkartılarak rasyonlardan elde edilen net toplam gaz ve metan üretimleri belirlenmiştir. İnkübasyon sonunda açığa çıkan gazın metan içerikleri Infrared metan analiz cihazı kullanılarak belirlenmiştir (Goel ve Makkar 2008). Üretilen metan gaz miktarı aşağıdaki formülle hesaplanmıştır.

Metan (mL) = Gaz üretimi (mL) x metan (%)

Fermantasyon sonunda açığa çıkan gaz Menke ve Steingass (1988) belirttiği formüller kullanılarak rasyonların metabolik enerji ve dut yaprağının organik madde sindirim dereceleri belirlenmiştir. Rasyonun metabolik enerji ve organik madde sindirim dereceleri aşağıdaki formüller kullanılarak hesaplanmıştır (eşitlik 1 ve 2).

$$ME(MJ/kg\ KM) = 1,68 + 0,1418GÜ + 0,073\ HP + 0,217HY - 0,028HK \quad (1)$$

$$OMSD\ (\%) = 14,88 + 0,8893GÜ + 0,448HP + 0,651\ HK \quad (2)$$

GÜ: Gaz üretimi (40 ml/0.5 gram)
HP: Ham protein (%)
HY: Ham yağ (%)
HK: Ham kül (%)

Gaz ölçümlerinden sonra şırıngalarda kalan numüne behere koyulup üzerine 70 ml NDF eklenilerek 1 saat kaynatılmıştır. Kaynama işleminden sonra gooch por 1 krozelerden geçirilerek süzme işlemi yapılmıştır (Blümmel vd., 1997). Rasyonun gerçek sindirilebilebilir kuru madde (g) (GSKM), taksimat faktörü (TF), mikrobiyal protein (MP), mikrobiyal sentezleme etkinliği (MPSE), değerleri Blümmel vd., (1997)'nın bildirdiği formüllere göre hesaplanmıştır (eşitlik 3-5).

$$GSKM\ (mg) = İnkübe\ edilen\ KM\ (mg) - Kalan\ KM\ (mg) \quad (3)$$

$$MP\ (mg/g\ KM) = GSKM - (GÜ\ X\ 2,2\ mg/ml) \quad (4)$$

$$MPSE = (GSKM - (GÜ\ X\ 2,2\ mg/ml))/GSKM \quad (5)$$

2.4.İstatistiksel analiz

Çalışma sonucunda elde edilen veriler SPSS 20.0 (2011) paket programında varyans analize tabi tutulmuş ve ortalamalar arasındaki farklılıkların belirlenmesinde Duncan çoklu karşılaştırma testi kullanılmıştır (Duncan, 1955).

3. Bulgular ve Tartışma

3.1.Dut yapraklarının kimyasal kompozisyonu, *in vitro* gaz üretimi, metabolik enerji içeriği ve organik madde sindirim derecesi

Dut yapraklarının kimyasal kompozisyonu, *in vitro* gaz üretimi, metabolik enerji içeriği ve organik madde sindirim derecesi Tablo 2'de verilmiştir. Dut yapraklarının HK, HY, HP ve KT içerikleri sırasıyla %12,10, %3,77, %17,73, %0,82 olduğu belirlenmiş, ME değeri 808 MJ/kg KM ve OMSD değeri ise %66,36 olarak ölçülmüştür.

Tablo 2. Dut yapraklarının kimyasal kompozisyonu, *in vitro* gaz üretimi, metabolik enerji içeriği ve organik madde sindirim değerleri

	HK (%)	HY(%)	HP(%)	KT(%)	Gaz (ml)	ME (MJ/kg KM)	OMSD (%)
Dut yaprağı	12,10	3,77	17,73	0,82	38,29	8,88	66,36

HK= ham kül; HY= ham yağ; HP= ham protein; KT= kondanse tanen; ME= matabolik enerj; OMSD= organik madde sindirim derecesi.

Dut yapraklarının kompozisyonlarının daha önce yapılan çalışmalarla uyum içerisinde olduğu görülmüştür (Güven, 2012; Akçil ve Denek, 2013; Ulger vd., 2017, Özdemir ve Kaya, 2020; Cengiz ve Kamalak, 2020). Genel olarak bakıldığında, dut yapraklarının HP içerikleri ruminant hayvanların hem yaşama hem de verim payı ihtiyacını karşılayacak seviyede olduğu gözükmektedir.

Kuzu rasyonlarına farklı oranlarda dut yaprağı ilavesinin kimyasal analizlerine, *in vitro* gaz ve metan üretimi ile gerçek sindirim derecesi, taksimat faktörü, mikrobiyal protein ve mikrobiyal protein sentezleme etkinliğine etkisi belirlenmiş ve Tablo 3'te verilmiştir. Kuzu rasyonuna dut yaprağı ilavesinin metan (%) üretimine etkisi istatistiksel olarak %5 seviyesinde önemli olurken,

incelenen diğer özellikler üzerine etkisinin olmadığı bulunmuştur (P≥0.05).

Tablo 3'ten görüldüğü gibi gaz üretimi, rasyona eklenen dut yaprağı miktarına bağlı olarak 102.00 ml (0 g/kg) ile 106.00 ml (200 g/kg) arasında değişmiştir. Fermantasyon sonucunda açığa çıkan gaz miktarı fermente olabilen yem miktarına bağlıdır. Yani fermente olabilen yem ne kadar fazla ise fermantasyondan o kadar fazla gaz açığa çıkmaktadır (Blummel ve Orskov, 1993). Fakat bazı yemlerde bulunan tanen, esansiyel yağlar ve saponin gibi anti-besinsel faktörler fermantasyon sırasında çıkan gaz üretim miktarını ve gazın kompozisyonunu değiştirebilmektedir (Jafari vd., 2019). Bu anti-besinsel faktörler bakteriler ve metanojenler üzerinde doğrudan anti-mikrobiyal etkili olabildiği gibi yemlerle bileşik oluşturarak dolaylı bir şekilde fermantasyon sonucu açığa çıkan gaz miktarını ve kompozisyonunu etkilemektedir. Fakat bu çalışmada kullanılan dut yaprağının düşük kondense tanen içeriği gaz üretimi üzerinde herhangi bir etkisinin olmadığı bulunmuştur.

Tablo 3'den de görüldüğü gibi fermantasyon sonucu açığa çıkan gazın metan içeriği farklı şekilde ifade edilmiştir. Dut yaprağının rasyona ilavesi sadece oluşan gazın metan içeriğinde (%) küçük bir düşüşe neden olmasına rağmen dut yaprağının anti-metanojik özelliğe sahip olduğunu söylemek oldukça zordur. Çünkü metanın farklı şekillerde ifade edildiğinde metan üretimi kontrol grubuyla benzer bulunmuştur. Oysa daha önce yapılan bazı çalışmalarda Chen vd., (2015) ile Habib vd., (2016) dut yaprağının metan emisyonunu azaltıcı etkisini bildirmişlerdir.

Tablo 3. Dut yaprağının kuzu rasyonlarına ilavesinin sindirim derecesine ve bazı fermantasyon parametrelerine etkisi

Özellikler	Dut Yaprağının Katkı Oranları (g/Kg)					SEM	O.S
	0	50	100	150	200		
Gaz (ml)	102,00	103,25	102,00	103,50	106,00	1,609	0,137
CH_4(%)	14,93^{a}	14,70^{ab}	14,73^{a}	14,53^{ab}	13,97^{b}	0,242	0,013
CH_4(ml)	15,22	15,18	15,02	15,03	14,81	0,303	0,680
CH_4(ml/SK)	44,42	44,79	46,01	45,45	42,59	1,711	0,366
GSKM	67,75	67,24	64,43	65,68	68,87	2,108	0,288
TF	3,36	3,29	3,20	3,20	3,28	0,110	0,577
MP	118,47	113,05	102,25	103,72	115,10	11,058	0,521
MPSE	34,53	33,02	31,25	31,21	32,91	2,280	0,576
NH_3-N	47,88	48,33	49,30	48,56	48,62	0,815	0,550

^{abc}Aynı satırda farklı simgeye sahip ortalamalar farklıdır, GSKM= gerçek sindirim derecesi(%), TF= taksimat faktörü, MP= mikrobiyal protein (mg), MPSE= mikrobiyal protein sentezleme etkinliği(%).

Gerçek sindirim derecesi (GSKM), 100 g/kg oranında en düşük (%64,43), 200 g/kg oranında ise en yüksek (%68,87) değerleri almıştır. Bu durum, dut yaprağının rasyonun sindirilebilirliğine olumsuz bir etkisinin olmadığını göstermektedir. Mikrobiyal protein sentezi (MP) ve etkinliği (MPSE) değerlerinde belirgin bir fark gözlenmemesine rağmen, 0 g/kg katkı oranında MP 118,47 mg olarak en yüksek değeri göstermiştir. Bu sonuç, Olfaz vd. (2018) ile Kandylis vd. (2009) tarafından bildirilen bulgularla uyumlu bulunmuştur.

Taksimat faktörü (TF), dut yaprağı oranı artışıyla çok fazla değişmemiş olup, 100 g/kg ve 150 g/kg katkılarında 3,20 ile en düşük değeri gösterirken, 0 g/kg katkıda 3.36 ile en yüksek değeri göstermiştir. Bu durum, dut yaprağının rasyonun enerji ve protein dengesi üzerinde önemli bir bozulma yaratmadığını göstermektedir. Ek olarak, bu bulgu, Hassan vd. (2020) tarafından bildirilen benzer etkilerle uyumlu bulunmuştur. Mikrobiyal protein, 0 g/kg (118,47 mg) ile 100 g/kg (102,25 mg) arasında değişmiştir. Diğer araştırmacılar tarafından yapılan çalışmalarda mikrobiyal protein sentezleme etkinliğinin önemli parçası olan taksimat faktörü en uygun değerinin 2,75-4,41 arasında olduğu bildirilmektedir. (Blümmel vd., 1997; Blümmel ve Lebzien, 2001). Bildirilen değerler çalışmada elde dilen verilerin olumlu olduğunu göstermektedir.

4. Sonuç

İn vitro koşullarda yapılan çalışmada elde edilen bulgular dut yaprağının anti-metanojenik ve anti-proteolitik etkisinin olmadığını belirlemiştir. Rasyona dut yaprağının ilave edilmesinin fermantasyon parametreleri üzerinde olumsuz bir etkisinin olmaması ve dut yaprağının besin değerleri özellikle protein içeriğinin yüksek olmasından dolayı, ruminant hayvanların beslenmesinde kullanılan kaba yemlerin yeterince üretilmediği bölge ve mevsimlerde ucuz ve alternatif yem kaynağı olarak kullanılmasının kaba yem açığının giderilmesine katkıda bulunacağı düşünülmektedir.

Katkı Oranı Beyanı

Yazarların katkı yüzdeleri aşağıda verilmiştir. Yazarlar makaleyi incelemiş ve onaylamıştır.

	M.E	A.K
K	50	50
T	100	
Y		100
VTI	70	30
VAY	50	50
KT	70	30
YZ	60	40
KI	50	50
GR	60	40
PY	50	50
FA	50	50

K= kavram, T= tasarım, Y= yönetim, VTI= veri toplama ve/veya işleme, VAY= veri analizi ve/veya yorumlama, KT= kaynak tarama, YZ= Yazım, KI= kritik inceleme, GR= gönderim ve revizyon, PY= proje yönetimi, FA= fon alımı.

Çatışma Beyanı

Yazarlar bu çalışmada hiçbir çıkar ilişkisi olmadığını beyan etmektedirler.

Etik Onay Beyanı

Bu araştırmada hayvanlar ve insanlar üzerinde herhangi bir çalışma yapılmadığı için etik kurul onayı alınmamıştır.

Destek ve Teşekkür Beyanı

Bu Çalışma Kahramanmaraş Sütçü İmam Üniversitesi Bilimsel Araştırma Projeleri Birimi (Proje No: 2023/5-4 D) tarafından desteklenmiştir.

Kaynaklar

Akçil E, Denek N. 2013. Farklı seviyelerde okaliptus (Eucalyptus camaldulensis) yaprağının bazı kaba yemlerin in vitro metan gazı üretimi üzerine etkisinin araştırılması. Harran Univ Vet Fak Derg, 2(2): 75-81.

Akın G. 2006. Küresel ısınma, nedenleri ve sonuçları. Ankara Univ Dil Tarih Cog Fak Derg, 46(2): 29-43.

Aksay CS, Ketenoğlu O, Kurt L. 2005. Küresel ısınma ve iklim değişikliği. Selçuk Univ Fen Fak Fen Derg, 1(25): 29-42.

AOAC. 1990. Official method of analysis. 15th ed., Association of official analytical chemists, Washington, DC, USA, pp: 15.

Bilal Y, Kamalak A. 2022. Kuzu rasyonlarına meşe palamudu ilavesinin sindirim derecesine, metabolik enerjisine ve metan üretimine etkisinin in vitro gaz üretim tekniği ile belirlenmesi. KSÜ Tarım Doğa Derg, 25(Ek Sayı 2): 583-590.

Blümmel M, Lebzien P. 2001. Predicting ruminal microbial efficiencies of dairy rations by in vitro techniques. Livest Prod Sci, 68: 107-117.

Blümmel M, Makkar HPS, Chisanga G, Mtimuni J, Becker K. 1997. The prediction of dry matter intake of temperate and tropical roughages from in vitro digestibility/gas-production data. Anim Feed Sci Tech, 69(1-3): 131-141.

Blümmel M, Orskov ER. 1993. Comparison of in vitro gas production and nylon bag degradability of roughages in predicting feed intake in cattle. Anim Feed Sci Tech, 40: 109-119.

Cengiz T, Kamalak A. 2020. Farklı bölgelerde yetişen söğüt yapraklarının potansiyel besleme değerlerinin ve anti-metanojenik özelliklerinin belirlenmesi. KSÜ Tarım Doğa Derg, 23(5): 1351-1358.

Chen D, Chen X, Tu Y, Wang B, Lou C, Ma T, Diao Q. 2015. Effects of mulberry leaf flavonoid and resveratrol on methane emission and nutrient digestion in sheep. Anim Nutr, 1(4): 362-367.

de Morais JPG, Campana M, Gregorini P, Garcia TM, Minussi JFDA, Pereira SN, Del Valle TA. 2023. In vitro evaluation of potentially edible Brazilian trees and shrubs in ruminant nutrition. Animals, 13(23): 3703.

Duncan DB. 1955. Multiple range and multiple F tests. Biometrics, 11(1): 1-42.

Goel G, Makkar HP, Becker K. 2008. Effects of Sesbania sesban and Carduus pycnocephalus leaves and Fenugreek seeds and their extracts on partitioning of nutrients to methane. Anim Feed Sci Tech, 147(1-3): 72-89.

Guven I. 2012. Effect of species on nutritive value of mulberry leaves. Kafkas Univ Vet Fak Derg, 18(5).

Habib G, Khan NA, Sultan A, Ali M. 2016. Nutritive value of common tree leaves for livestock in the semiarid and arid rangelands of Northern Pakistan. Livest Sci, 184: 64-70.

Hassan FU, Arshad MA, Li M, Rehman MSu, Loor JJ, Huang J. 2020. Potential of mulberry leaf biomass and its flavonoids to improve production and health in ruminants. Animals, 10(1): 2076.

Jafari S, Ebrahimi M, Goh YM, Rajion MA, Jahromi MF, Al-Jumaili WS. 2019. Manipulation of rumen fermentation and methane gas production by plant secondary metabolites. Ann Anim Sci, 19(1): 3-29.

Johnson KA, Johnson DE. 1995. Methane emissions from cattle. J Anim Sci, 73(8): 2483-2492.

Kamalak A, Ozkan CO. 2021. Potential nutritive value and anti-methanogenic potential of some fallen tree leaves in Türkiye. Livest Res Rural Dev, 33(11): 132.

Kandylis K, Hadjigeorgiou I, Harizanis P. 2009. The nutritive value of mulberry leaves (Morus alba) as a feed supplement for sheep. Trop Anim Health Prod, 41: 17-24.

Kılıç HN, Boğa M. 2021. Hayvan besleme stratejileri ile metan emisyonunun azaltılması. Turk J Agric-Food Sci Technol, 9(9): 1700-1713.

Kutlu R, Görgülü M, Çelik LB. 2005. ZM-208 Genel Hayvan Besleme Ders Notu. URL: https://www.ruminantbesleme.com/wp-content/uploads/2018/09/GENEL-HAYVAN-BESLEME.pdf (accessed date: March 3, 2022).

Makkar HP, Blümmel M, Becker K. 1995. In vitro effects of and interactions between tannins and saponins and fate of tannins in the rumen. J Sci Food Agric, 69(4): 481-493.

Menke KH, Raab L, Salewski A, Steingass H, Fritz D, Schneider W. 1979. The estimation of the digestibility and metabolizable energy content of ruminant feedingstuffs from the gas production when they are incubated with rumen liquor in vitro. J Agric Sci, 93(1): 217-222.

Menke KH, Steingass H. 1988. Estimation of the energetic feed value from chemical analysis and in vitro gas production using rumen fluid. Anim Res Dev, 28: 7-55.

Olfaz M, Kilic U, Boga M, Abdi AM. 2018. Determination of in vitro gas production and potential feed value of olive, mulberry and sour orange tree leaves. Open Life Sci, 13(1): 269-278.

Özdemir Ö, Kaya A. 2020. Bazı ağaç yapraklarının in vitro gaz üretim tekniğiyle yem değerlerinin belirlenmesi. YYÜ J Agric Sci, 30(3): 454-461.

Selçuk B, Kamalak A. 2022. Biberiye yaprağı ekstraktının yonca otunun rumen fermentasyonu, metan ve mikrobiyal protein üretimine etkisi. KSÜ Tarım Doğa Derg, 25(3): 623-628.

SPSS. 2011. IBM SPSS statistics for Windows, version 20.0. New York: IBM Corp.

Tavendale MH, Meagher LP, Pacheco D, Walker N, Attwood GT, Sivakumaran S. 2005. Methane production from in vitro rumen incubation and effects of condensed tannin fractions. Anim Feed Sci Tech, 123-124: 403-419.

TÜİK. 2023. URL: https://data.tuik.gov.tr/Bulten/Index?p=Sera-Gazi-Emisyon-Istatistikleri-1990-2021-49672 (accessed date: June 24, 2025).

Ulger I, Kamalak A, Kurt O, Kaya E, Guven I. 2017. Comparison of chemical composition and anti-methanogenic potential of tree leaves using in vitro gas production technique. Cienc Investig Agrar, 44(1): 75-82.

Van Nevel CJ, Demeyer DI. 1996. Control of rumen methanogenesis. Environ Monit Assess, 42: 73-97.

Black Sea Journal of Engineering and Science
doi: 10.34248/bsengineering.1691203

Open Access Journal
e-ISSN: 2619 – 8991

Araştırma Makalesi (Research Article)
Cilt 8 - Sayı 5: 1313-1319 / Eylül 2025
Volume 8 - Issue 5: 1313-1319 / September 2025

YÜKLEME HIZININ DÖRT NOKTALI EĞİLME ETKİSİ ALTINDAKİ AAC LENTOLARIN EĞİLME PERFORMANSINA ETKİSİ

Yaşar ERBAŞ[1]*

[1]*Bartın University, Faculty of Engineering, Architecture and Design, Department of Civil Engineering, 74100, Bartın, Türkiye*

Özet: Bu çalışmada, farklı yer değiştirme kontrollü yükleme hızları altında dört noktadan eğilmeye tabi tutulan otoklavlanmış gaz beton (AAC) lentolarının eğilme özellikleri incelenmiştir. Toplamda beş adet lento deney elemanı, 2,5, 10, 20, 30 ve 40 mm/dakika hızlarında test edilmiştir. Temel yapısal performans parametreleri, maksimum yük kapasitesi, maksimum yükteki yer değiştirme, rijitlik, maksimum deformasyon ve enerji sönümleme kapasitesi gibi unsurlar yük-yer değiştirme eğrilerine dayanarak değerlendirilmiştir. Deney elemanları benzer hasar dağılımı ve genel eğilme davranışı göstermekle birlikte çalışma sonuçları yükleme oranının mekanik performans üzerindeki etkisinin sınırlı olduğunu göstermektedir. Maksimum yük değerleri 14,25 kN ile 16,77 kN arasında değişmiş olup, artan yükleme oranlarında tutarlı bir eğilim görülmemiştir. Benzer bir şekilde, sertlik ve şekil değiştirme kapasitesi dar bir aralıkta kalmış ve yükleme oranı ile arasında düzenli bir ilişki ortaya çıkmamıştır. Enerji dağılım değerlerinde bazı dalgalanmalar gözlemlenmiş olsada, bunlar arasında anlamlı bir ilişki kurulmamıştır. Bu sonuçlar, AAC lentolarının incelenen aralıktaki yükleme hızı değişikliklerinden büyük ölçüde etkilenmediğini ortaya koymaktadır. Yapısal özellik, yükleme hızından çok malzemenin içsel özellikleri ve üretim tutarlılığı tarafından yönlendiriliyor gibi görünmektedir. Bu yorum, AAC lentolarının performansında kayba sebep olmadan çeşitli yükleme durumlarına maruz kalabileceği pratik uygulamalar açısından özellikle önem taşımaktadır.

Anahtar kelimeler: Yığma, Gaz beton duvarlar, Yükleme hızı, Eğilme

Effect of Loading Rate on the Flexural Performance of AAC Lintels under Four-Point Bending

Abstract: This study investigates the flexural behavior of autoclaved aerated concrete (AAC) lintels subjected to four-point bending under varying displacement-controlled loading rates. A total of five lintel specimens were tested at loading rates of 2.5, 10, 20, 30, and 40 mm/min. Key structural performance parameters, including maximum load capacity, displacement at peak load, stiffness, maximum deformation, and energy absorption capacity were evaluated based on the load–displacement curves. The results indicate that while the specimens exhibited similar failure patterns and general flexural behavior, the influence of loading rate on mechanical performance was limited. Maximum load values ranged between 14.25 kN and 16.77 kN, with no consistent trend across increasing loading rates. Similarly, stiffness and deformation capacity varied within a narrow range and did not reveal a systematic dependency on the rate of loading. Although some fluctuation was observed in energy dissipation values, no significant correlation could be established. These findings suggest that the flexural response of AAC lintels is not substantially affected by loading rate variations within the examined range. The structural behavior appears to be governed more by intrinsic material characteristics and production consistency than by the speed of loading. This insight is particularly relevant for practical applications, where AAC lintels are exposed to various loading conditions without significant loss in performance.

Keywords: Masonry, AAC walls, Loading rate, Flexural bending

***Sorumlu yazar (Corresponding author):** Bartın University, Faculty of Engineering, Architecture and Design, Department of Civil Engineering, 74100, Bartın, Türkiye
E mail:yerbas@bartin.edu.tr (Y. ERBAŞ)
Yaşar ERBAŞ https://orcid.org/0000-0002-3475-9678

Gönderi: 04 Mayıs 2025 **Received:** May 04, 2025
Kabul: 13 Haziran 2025 **Accepted:** June 13, 2025
Yayınlanma: 15 Eylül 2025 **Published:** September 15, 2025
Cite as: Erbaş Y. 2025. Effect of loading rate on the flexural performance of AAC lintels under four-point bending. BSJ Eng Sci, 8(5): 1313-1319.

1. Giriş

Otoklavlanmış gazbeton (Autoclaved Aerated Concrete, AAC), gözenekli yapısı sayesinde yoğunluğu düşük, hafif bir yapı malzemesidir. Yaklaşık %80 oranında gözenek içeren bu hücresel beton, geleneksel betona kıyasla daha düşük kuruma büzülmesi ve ısı iletkenliğine sahiptir; ayrıca inşaat uygulamalarında kolaylık ve hız sağlamaktadır (Artino vd., 2019; Kamal, 2020; Raj, vd., 2020; Ferreti vd., 2021; Saad vd., 2022). Bu özellikleri sayesinde AAC bloklar yüksek ısıl dirençleriyle birlikte yapıda hem taşıyıcı duvar hem de yalıtım işlevini aynı anda görebilmekte, yani ek bir yalıtım tabakasına gerek kalmadan kullanılabilmektedir (Rafiza vd., 2022). Bunun yanı sıra, AAC tamamen inorganik bir malzeme olup A1 sınıfı yanmazlık özelliğine sahiptir; dolayısıyla yüksek yangın dayanımı ve güvenliği sunar. Bina açıklıklarının (kapı, pencere vb.) üstünde yer alan lentolar, açıklığın üzerindeki yükleri karşılayıp bu yükleri açıklığın her iki yanındaki duvar kısımlarına aktaran yatay taşıyıcı elemanlardır. Gaz beton malzemeden üretilen prefabrike lentolar ise duvar inşası sırasında yerine doğrudan yerleştirilebilen ve bünyesinde gömülü çelik donatı içeren kirişlerdir. Örneğin, Ytong Lento adıyla sunulan bu tür AAC lentoları montaja hazır olarak üretilmekte ve

sahada kalıp hazırlanmasına veya ayrı bir beton dökümüne gerek kalmadan duvarla birlikte hızlıca uygulanabilmektedir. AAC lentolarının, çevreleyen duvar bloklarıyla aynı malzemeden olmaları sayesinde termal ve mekanik uyum sağladıkları, böylece duvarda malzeme sürekliliği ile ısı köprüsü ve yoğuşma problemlerini önledikleri bilinmektedir (Ytong 2025).

Taşıyıcı yapı elemanlarının dayanımı kadar, eğilme altındaki davranış karakteristikleri de (çatlama durumu, süneklik düzeyi vb.) yapısal güvenlik açısından büyük önem taşımaktadır. Bir lentonun yeterli eğilme dayanımına sahip olması, üzerindeki duvar yüklerini güvenle taşıyabilmesi için gereklidir; bunun yanında, süneklik kabiliyeti elemanın beklenmedik aşırı yükler altında kırılmadan önce şekil değiştirebilmesine imkan tanıyarak ani göçme riskini azaltır (Abdel-Mooty vd., 2012; Ferreti vd., 2021; Malla vd., 2025). Yük altındaki sünek bir eleman, belli ölçüde plastik deformasyon yaparak ve enerji yutarak hasarı geciktirebilir; bu durum özellikle deprem gibi dinamik etkiler altında yapının enerji sönümleme kapasitesiyle doğrudan ilişkilidir (Akkaya vd., 2022; Mercimek vd., 2022; Mercimek, 2023; Erbaş vd., 2024, Kocaman vd, 2024; Yılmaz vd., 2024). Dolayısıyla, AAC gibi beton esaslı ve gözenekli bir malzemeden üretilen lentoların eğilme performansının (dayanım, süneklik ve enerji yutma özelliklerinin) anlaşılması, bu elemanların güvenli tasarımı ve kullanımı açısından kritik bir konudur.

Yükleme hızı, malzemelerin gözlenen mekanik performansı üzerinde etkili olabilen bir parametredir. Literatürde farklı yükleme hızlarında AAC malzemesi üzerinde yapılan çalışmalar, hem basınç hem de çekme dayanımlarının yükleme hızına duyarlı olduğunu göstermektedir. Devi vd. (2022) yükleme hızının 0.1 mm/dakikadan 10 mm/dakikaya yükseltilmesiyle AAC'nin basınç dayanımında yaklaşık 2,5 kat, çekme (yarma) dayanımında ise yaklaşık 1,5 kat artış gözlemlenmiştir. Benzer biçimde, AAC örneklerinin eğilme mukavemetinin de deplasman hızının artışıyla belirgin ölçüde (yaklaşık %50 oranında) yükseldiği rapor edilmiştir (Devi vd., 2024). Bununla birlikte, yüklemenin daha hızlı uygulanması malzemenin davranışını daha gevrek hale getirebilmektedir; başka bir deyişle, hızlı yükleme durumlarında tepe dayanımı artsa da, gerilme-eğilme eğrisinin düşüş bölümü daha dik olmakta ve kırılma davranışı daha ani gerçekleşmektedir (Wang vd., 2018).

Ancak, yükleme hızının AAC malzemeli yapı elemanlarının (örneğin lentoların) eğilme davranışına etkisi konusunda literatürde sistematik deneysel çalışma sayısı sınırlıdır. Bu çalışmada, söz konusu boşluğu doldurmak amacıyla, otoklavlanmış gazbeton lentoların dört noktalı eğilme düzeninde farklı deplasman hızları altındaki performansı deneysel olarak incelenmiştir. Belirlenen 2,5 mm/dk., 10 mm/dk., 20 mm/dk., 30 mm/dk. ve 40 mm/dk. olmak üzere beş farklı yükleme hızında gerçekleştirilen eğilme testleri ile her bir örneğin taşıma kapasitesi, sünek davranış özellikleri, enerji yutma kabiliyeti ve kırılma modu belirlenmiştir. Elde edilen veriler ışığında, yükleme hızı etkisinin AAC lentoların eğilme davranışına nasıl yansıdığı değerlendirilmiş ve bu kapsamda çalışmanın bulgularının, AAC lentoların tasarımı ve güvenliğine yönelik literatüre özgün bir katkı sunması hedeflenmiştir.

2. Materyal ve Yöntem

2.1. Deney Elemanları

Bu çalışmada, farklı yükleme hızlarının otoklavlanmış gazbeton (AAC) lentoların eğilme davranışına etkisini belirlemek amacıyla dört noktalı eğilme deneyleri gerçekleştirilmiştir. Toplam beş adet AAC lento numunesi hazırlanmış ve her biri farklı bir yükleme hızında test edilmiştir. Tüm numuneler 150 mm × 250 mm kesitine ve 2000 mm uzunluğa sahip olacak şekilde üretilmiştir.

Numuneler, dört noktalı eğilme düzeneğinde sırasıyla 2,5 mm/dk., 10 mm/dk., 20 mm/dk., 30 mm/dk. ve 40 mm/dk. yükleme hızlarında test edilmiştir. Deneysel çalışma kapsamında, yükleme hızının taşıma kapasitesi, rijitlik, kırılma modu ve enerji tüketimi gibi yapısal performans üzerindeki etkileri analiz edilmiştir. Deney numunelerine ilişkin yükleme türü, hızları ve boyutsal bilgileri Tablo 1'de özetlenmiştir.

Tablo 1. Deney elemanlarının özellikleri

Deney Elemanı	Yükleme Türü	Yükleme Hızı	Boyutlar
0	Dört Noktalı Eğilme	2,5 mm/dk.	150 mm x 250 mm x 2000 mm
1		10 mm/dk.	
2		20 mm/dk.	
3		30 mm/dk.	
4		40 mm/dk.	

2.2. Malzemeler

Deneylerde kullanılan tüm lento numuneleri, Türkiye'de yaygın olarak kullanılan ve TS EN 12602 standardına uygun olarak üretilmiş G3/0,45 sınıfı otoklavlanmış gazbeton (AAC) elemanlardan imal edilmiştir. Bu üretim sınıfı, 450 kg/m^3 kuru birim hacim ağırlığına ve ≥3,5 N/mm^2 ortalama basınç dayanımına sahiptir. Isıl iletkenlik değeri 0,15 W/mK olan bu malzeme, A1 sınıfı yangına tepki performansı ile yüksek düzeyde yangın güvenliği sunmaktadır. G3/0,45 sınıfı AAC malzeme, hem yapısal performansı hem de hafifliği nedeniyle yük taşıyan bölümlerde tercih edilmektedir. Bu çalışmada kullanılan lento elemanları, 150 mm genişlik, 250 mm yükseklik ve 2000 mm uzunluğa sahip olacak şekilde özel olarak kesilmiştir. Malzemelerin tasarım ve nakliye ağırlıkları sırasıyla 570 kg/m^3 ve 670 kg/m^3 olarak üretici tarafından belirtilmiştir. Tüm numuneler üretim

öncesinde görsel olarak incelenmiş ve yüzey kusuru ya da üretim hatası bulunmayan elemanlar seçilerek deney programına dâhil edilmiştir.

2.3. Deney Düzeneği ve Uygulanan Yükleme Protokolü

Bu çalışmada, AAC lento elemanlarının eğilme davranışını değerlendirmek amacıyla dört noktalı eğilme testleri gerçekleştirilmiştir. Deney düzeneği, iki mesnet ve iki eşit yükleme noktası içeren klasik dört nokta eğilme prensibine göre tasarlanmıştır. Numuneler, her iki ucundan 500 mm açıklıkla basit mesnetler üzerine yerleştirilmiş ve yükler, ortadaki iki noktadan 500 mm aralıklarla uygulanmıştır. Böylece, 500 mm uzunluğunda bir saf moment bölgesi elde edilmiştir (Şekil 1).

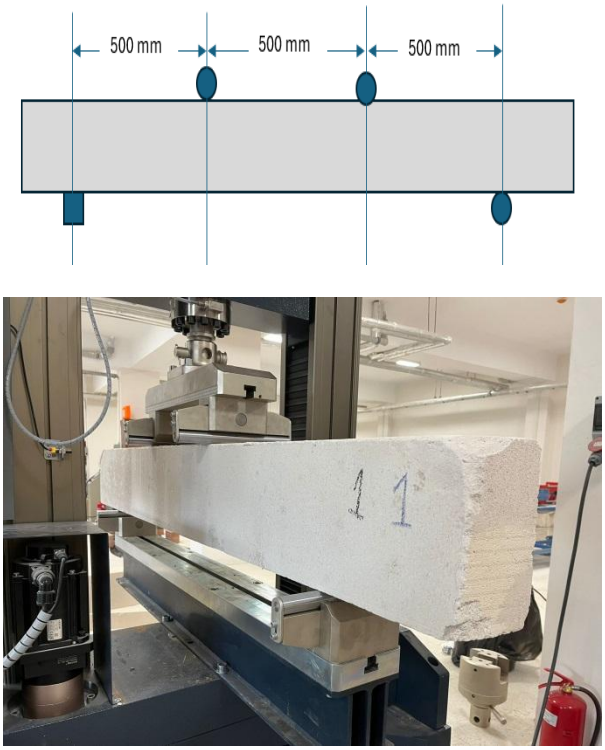

Şekil 1. Deney düzeneği.

Testler, 300 kN kapasiteli, deplasman kontrollü çalışan bir elektromekanik üniversal test cihazında gerçekleştirilmiştir. Elektromekanik yükleme sistemleri, özellikle gevrek davranış gösteren yapı malzemelerinde hassas ve düşük hızlarda yükleme imkânı sunarak daha doğru deneysel veri elde edilmesini sağlar. Yükleme, sabit deplasman hızlarıyla kontrol edilmiş ve her bir deney, Tablo 1'de verilen yükleme hızlarında (2.5 mm/dk., 10 mm/dk., 20 mm/dk., 30 mm/dk. ve 40 mm/dk.) gerçekleştirilmiştir.

Yük-deplasman verileri, cihazla entegre veri toplama sistemi aracılığıyla sürekli olarak kaydedilmiştir. Deney, maksimum yük seviyesinden sonra taşıma kapasitesinin %30 oranında azalması durumunda sonlandırılmıştır. Bu kriter, numunenin önemli bir taşıyıcılık kaybına uğradığını ve göçme davranışının başladığını göstermesi açısından tercih edilmiştir. Deneysel veriler, eğilme kapasitesi, rijitlik, süneklik ve enerji tüketimi gibi performans parametrelerinin değerlendirilmesinde kullanılmıştır.

3. Bulgular ve Tartışma

Bu bölümde, dört noktalı eğilme deneylerinden elde edilen yük-deplasman eğrileri üzerinden AAC lentoların mekanik performansı değerlendirilmiştir. Çalışmada beş farklı yükleme hızı (2.5, 10, 20, 30 ve 40 mm/dk.) uygulanmış ve her bir hız düzeyi için bir numune test edilmiştir. Performans değerlendirmesi, taşıma kapasitesi, maksimum deplasman, rijitlik ve enerji yutma kapasitesi gibi başlıca yapısal parametreler üzerinden gerçekleştirilmiştir.

3.1. Yük-Deplasman Davranışı

Şekil 2 ve Şekil 3'te sunulan yük-deplasman eğrileri incelendiğinde, tüm numunelerin benzer bir yapısal tepki verdiği görülmektedir. Elastik bölgede doğrusal davranışı takiben, tepe noktası civarında plastik deformasyon ve ardından ani dayanım kaybı meydana gelmiştir. Eğrilerin genel formu ve kırılma karakteristikleri arasında anlamlı bir fark gözlemlenmemiştir. Farklı yükleme hızlarında test edilen numunelerin maksimum taşıma kapasiteleri 14.25 kN ile 16.77 kN arasında değişmiştir. Bu fark yaklaşık %18 seviyesindedir ve deneysel tekrar sayısının sınırlı olması nedeniyle istatistiksel olarak anlamlı bir eğilim göstermemektedir. Örneğin, 2.5 mm/dk. ve 30 mm/dk. hızlarında test edilen numunelerin taşıma kapasiteleri birbirine çok yakın olup sırasıyla 16.28 kN ve 16.77 kN'dir. Buna karşın, 30 mm/dk. ve 40 mm/dk. hızlarında rijitlik değerlerinin daha düşük (sırasıyla 1.27 ve 1.25 kN/mm) olması, daha sünek bir davranış sergilendiğini ve deformasyon kabiliyetinin arttığını göstermektedir.

3.2. Rijitlik ve Deformasyon Davranışı

Numunelere ait başlangıç rijitlikleri, Şekil 4'te tanımlanan şekilde, yük-deplasman eğrisinin elastik doğrusal bölgesinden veya yaklaşık olarak maksimum yükün, o andaki deplasmana bölünmesiyle hesaplanmıştır. Bu yöntemle elde edilen rijitlik değerleri Tablo 2'de sunulmaktadır. Tüm numunelerin rijitlik değerleri 1.25 kN/mm ile 1.49 kN/mm aralığında kalmış, en yüksek rijitlik değeri 20 mm/dk. hızında elde edilen Numune-3'e (1.49 kN/mm) ait olmuştur. Ancak diğer hızlarda gözlenen değerler arasında sistematik bir artış ya da azalış eğilimi bulunmamaktadır.

Maksimum deplasman değerleri de benzer bir şekilde farklılık göstermekte; en yüksek değer 18.42 mm ile 20 mm/dk. hızındaki numunede, en düşük değer ise 10.88 mm ile 10 mm/dk. hızında elde edilmiştir. Ancak genel olarak bakıldığında, deformasyon kapasitesinde hızla ilişkili tutarlı bir değişim gözlenmemiştir. Bu durum, yükleme hızı arttıkça süneklik artar veya azalır gibi genel geçer bir yorum yapılmasını engellemektedir.

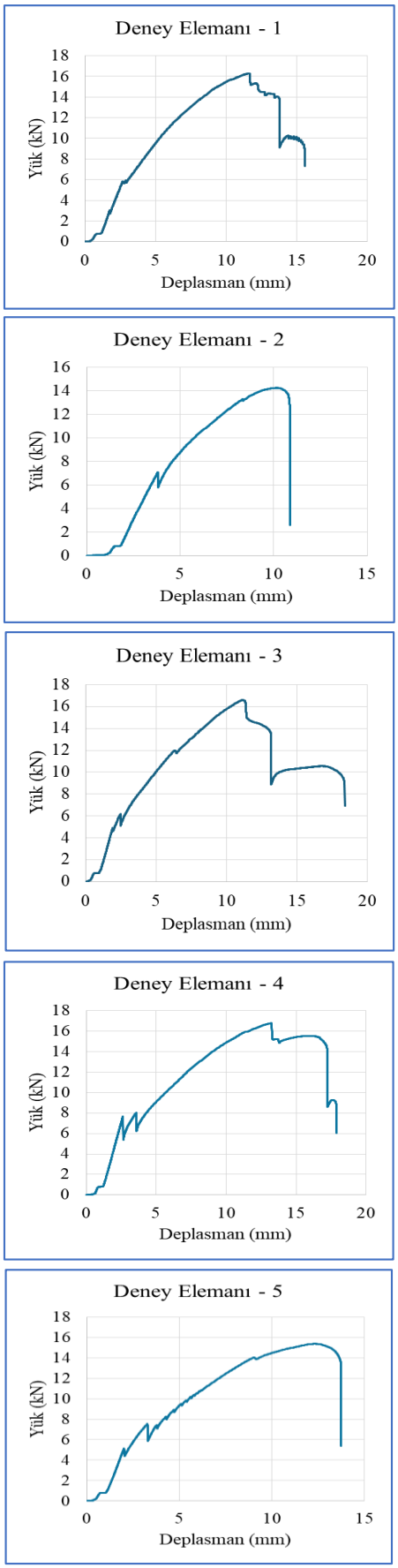

Şekil 2. Yük-deplasman grafikleri.

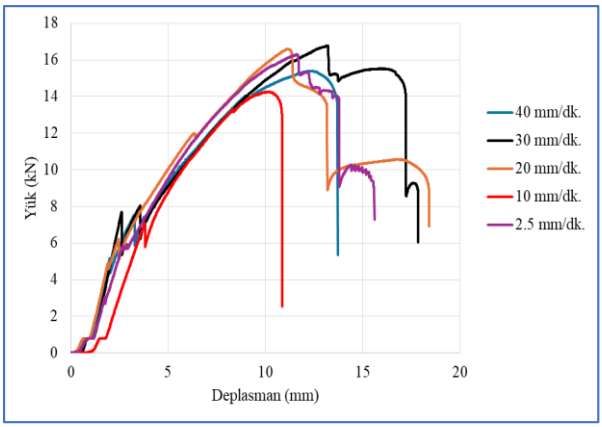

Şekil 3. Yük-deplasman grafikleri.

3.3. Enerji Yutma Kapasitesi

Şekil 4'te, yük-deplasman eğrisinin altında kalan alan olarak tanımlanan enerji yutma kapasitesinin hesaplama yaklaşımı sunulmaktadır. Her bir numune için sayısal entegrasyon yöntemiyle elde edilen bu değerler Tablo 2'de yer almaktadır. En yüksek enerji değeri 204 kN.mm ile 30 mm/dk. hızındaki Numune-4'te gözlenmiş, en düşük değer ise 90 kN.mm ile 10 mm/dk.'daki Numune-2'de elde edilmiştir. Diğer değerler (163, 193 ve 142 kN.mm), bu iki sınır arasında dağılmıştır.

Ancak dikkat çekici olan, enerji kapasitesinin yükleme hızına bağlı olarak düzenli bir artış ya da düşüş eğilimi göstermemesidir. Örneğin, 20 mm/dk. hızında test edilen Numune-3'teki enerji kapasitesi (193 kN.mm), daha yüksek hızdaki 40 mm/dk.'da (142 kN.mm) elde edilen değerden belirgin biçimde yüksektir. Bu da yükleme hızının enerji tüketimi üzerinde tek yönlü bir etkisi olmadığını göstermektedir.

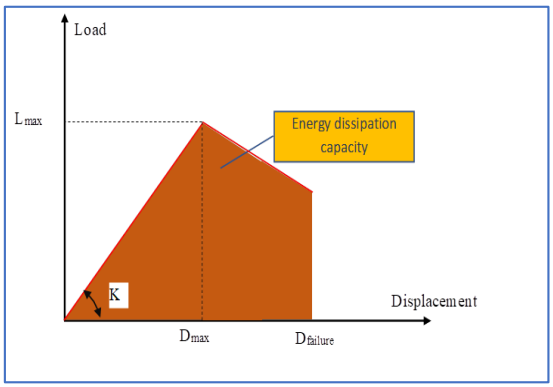

Şekil 4. Enerji Sönümleme Kapasitesi hesaplama yaklaşımı.

3.4. Kırılma Modu ve Gözlemler

Şekil 5'te sunulan hasar fotoğrafları incelendiğinde, tüm numunelerin eğilme bölgesinde tipik çatlama ve ezilme davranışları sergilediği görülmektedir. Farklı yükleme hızlarında gözlenen kırılma yüzeyleri arasında belirgin bir fark bulunmamaktadır. Çatlak ilerleme yönü ve kırılma tipi, tüm örneklerde benzer biçimde gelişmiştir.

3.5 Genel Değerlendirme

Elde edilen tüm veriler, AAC lentolarda yükleme hızının eğilme performansı üzerinde belirgin ve tutarlı bir etkisinin olmadığını ortaya koymaktadır. Maksimum taşıma kapasitesi, deformasyon kabiliyeti, rijitlik ve enerji yutma kapasitesi gibi parametrelerde yükleme hızına bağlı sistematik bir artış ya da azalma gözlemlenmemiştir. Bu durum, AAC gibi gözenekli ve gevrek karakterli malzemelerin eğilme davranışının, yükleme hızından ziyade malzeme homojenliği, iç boşluk yapısı ve üretim kalitesinden daha fazla etkilendiğini düşündürmektedir.

Tablo 2. Deney sonuçları

Deney Elemanı	Yükleme Hızı	Maks. Yük (kN)	Maks. Yükteki Deplasman (mm)	Rijitlik (kN/mm)	Maks. Deplasman (mm)	Enerji (kN.mm)
1	2,5 mm/dk.	16,28	11,58	1,41	15,61	163
2	10 mm/dk.	14,25	10,12	1,41	10,88	90
3	20 mm/dk.	16,60	11,15	1,49	18,42	193
4	30 mm/dk.	16,77	13,17	1,27	17,86	204
5	40 mm/dk.	15,39	12,34	1,25	13,73	142

Deney Elemanı -1

Deney Elemanı-2

Deney Elemanı -3

Deney Elemanı -4

Deney Elemanı -5

Şekil 5. Hasar fotoğrafları.

4. Sonuçlar

Bu çalışmada otoklavda işlenmiş gaz beton (AAC) lentoların dört noktalı eğilme altındaki yapısal tepkisi, değişik deplasman kontrollü yükleme hızları (2. 5, 10, 20, 30 ve 40 mm/dk.) çerçevesinde deneysel olarak incelenmiştir. Elde edilen sonuçlar doğrultusunda aşağıdaki bulgulara ulaşılmıştır:

- Yükleme hızının artması, AAC lentoların taşıma kapasitesi üzerinde belirgin ve sürekli bir etki yaratmamıştır. En yüksek yük değerleri 14. 25 kN ile 16. 77 kN arasında sınırlı bir değişim göstermiş ve sistematik bir artış veya azalma eğilimi göstermemiştir.
- Rijitlik değerleri (1. 25–1. 49 kN/mm) ile maksimum deplasman değerleri (10. 88–18. 42 mm) arasında yükleme hızıyla ilgili anlamlı bir ilişki bulunamamıştır. Bu durum, malzemenin başlangıç elastik tepkisi ve süneklik özelliklerinin yükleme hızına karşı duyarsız olduğunu ortaya koymaktadır.
- Enerji sönümleme kapasitesinin teorik olarak yükleme hızına göre değişebileceği düşünülse de, deney bulguları bu ilişkinin net bir şekilde ortaya konamadığını göstermiştir. En yüksek enerji kapasitesi (204 kN. mm) ile en düşük değer (90 kN. mm) arasındaki fark, deneysel tekrarsızlık ve örnek bazlı farklılıklarla açıklanabilir.
- Hasar incelemeleri, tüm örneklerde benzer kırılma şekillerinin ortaya çıktığını ve yükleme hızına bağlı olarak kırılma yöntemlerinde belirgin bir farklılık olmadığını göstermiştir.

Bu araştırma çerçevesinde yükleme hızının AAC lentoların eğilme özellikleri üzerindeki etkisi sınırlı kalmış ve istatistiksel olarak anlamlı bir yapısal fark göstermemiştir. Bu durum, AAC gibi gözenekli ve kırılgan özellikteki malzemelerde eğilme davranışının, yükleme hızından ziyade malzeme homojenliği, üretim standartları ve mikro yapı gibi unsurlara daha çok bağlı olabileceğini ortaya koymaktadır. Yapısal tasarım açısından incelendiğinde, standart yükleme koşulları altında AAC lentoların performansının hız değişikliklerinden belirgin şekilde etkilenmediği söylenebilir.

Katkı Oranı Beyanı

Yazarın katkı yüzdeleri aşağıda verilmiştir. Yazar makaleyi incelemiş ve onaylamıştır.

	Y. E.
K	100
T	100
Y	100
VTI	100
VAY	100
KT	100
YZ	100
KI	100
GR	100
PY	100
FA	100

K= kavram, T= tasarım, Y= yönetim, VTI= veri toplama ve/veya işleme, VAY= veri analizi ve/veya yorumlama, KT= kaynak tarama, YZ= Yazım, KI= kritik inceleme, GR= gönderim ve revizyon, PY= proje yönetimi, FA= fon alımı.

Çatışma Beyanı

Yazar bu çalışmada hiçbir çıkar ilişkisi olmadığını beyan etmektedirler.

Etik Onay Beyanı

Bu araştırmada hayvanlar ve insanlar üzerinde herhangi bir çalışma yapılmadığı için etik kurul onayı alınmamıştır.

Kaynaklar

Abdel-Mooty M, Hendam A, Fahmy E, Abou Zeid M, Haroun M. 2012. Experimental evaluation of lightweight AAC masonry wall prisms with ferrocement layers in compression and flexure. App Mech Mat, 166: 1730-1735.

Akkaya ST, Mercimek Ö, Ghoroubi R, Anil Ö, Erbaş Y, Yılmaz T. 2022. Experimental, analytical, and numerical investigation of punching behaviour of two-way RC slab with multiple openings. Struct, 43: 574-593.

Artino A, Evola G, Margani G, Marino EM. 2019. Seismic and energy retrofit of apartment buildings through autoclaved aerated concrete (AAC) blocks infill walls. Sustain, 11(14): 3939.

Devi NR, Dhir PK, Sarkar P. 2022. Influence of strain rate on the mechanical properties of autoclaved aerated concrete. J Build Eng, 57: 104830.

Devi NR, Dhir PK, Sarkar P. 2024. Influence of loading rate on bond shear strength of autoclaved aerated concrete masonry. Constr Build Mater, 416: 135072.

Erbaş Y, Mercimek Ö, Anıl Ö, Çelik A, Akkaya ST, Kocaman İ, Gürbüz M. 2024. Design deficiencies, failure modes and recommendations for strengthening in reinforced concrete structures exposed to the February 6, 2023 Kahramanmaraş Earthquakes (Mw 7.7 and Mw 7.6). Nat Hazards: 1-42.

Ferretti D, Michelini E. 2021. The effect of density on the delicate balance between structural requirements and environmental issues for AAC blocks: An experimental investigation. Sustain, 13(23): 13186.

Kamal MA. 2020. Analysis of autoclaved aerated concrete (AAC)

blocks with reference to its potential and sustainability. Build Mat Struct, 7(1): 76-86.

Kocaman İ, Mercimek Ö, Gürbüz M, Erbaş Y, Anıl Ö. 2024. The effect of Kahramanmaraş earthquakes on historical Malatya Yeni Mosque. Eng Fail Anal, 161: 108310.

Malla S, Dangol P, Gautam D. 2025. Experimental characterization and capacity assessment of GFRP retrofitted AAC block masonry. Eng Fail Anal: 109595.

Mercimek Ö, Ghoroubi R, Özdemir A, Anil Ö, Erbaş Y. 2022. Investigation of strengthened low slenderness RC column by using textile reinforced mortar strip under axial load. Eng Struct, 259: 114191.

Mercimek Ö. 2023. Experimental and analytical investigation of the effects of anchor types and strip shapes on shear-deficient reinforced concrete beams strengthened with TRM versus FRP. Int J Struct Civ Eng, 21(12): 1927-1950.

Mercimek Ö. 2023. Seismic failure modes of masonry structures exposed to Kahramanmaraş earthquakes (Mw 7.7 and 7.6) on February 6, 2023. Eng Fail Anal, 151: 107422.

Rafiza AR, Fazlizan A, Thongtha A, Asim N, Noorashikin MS. 2022. The physical and mechanical properties of autoclaved aerated concrete (AAC) with recycled AAC as a partial replacement for sand. Build, 12(1): 60.

Raj A, Borsaikia AC, Dixit US. 2020. Evaluation of mechanical properties of autoclaved aerated concrete (AAC) block and its masonry. Inst Eng (India): Ser A, 101: 315-325.

Saad AS, Ahmed TA, Radwan AI. 2022. In-plane lateral performance of AAC block walls reinforced with CFPR sheets. Build, 12(10): 1680.

Wang B, Wang H, Kang X, Duan L. 2018. Experimental study on autoclaved aerated concrete under uniaxial compression. In: 2018 7th Int Conf Energy Environ Sustain Dev (ICEESD 2018), pp: 779-783.

Yılmaz MC, Finner AAE, Mercimek Ö. 2024. Experimental investigation of out-of-plane behaviour of unreinforced masonry panels strengthened with TRM. Struct, 65: 106665.

Ytong. 2025. URL: https://ytong.com.tr/ (accessed date: April 18, 2025).

Black Sea Journal of Engineering and Science
doi: 10.34248/bsengineering.1690862

Open Access Journal
e-ISSN: 2619 – 8991

Research Article
Volume 8 - Issue 5: 1320-1327/ September 2025

DIFFERENTIABLE RAY TRACING-BASED ANALYSIS OF TRANSMITTER DEPLOYMENT STRATEGIES IN SITE-SPECIFIC SCENARIOS

Onem YILDIZ[1]*

[1]*Aydin Adnan Menderes University, Faculty of Engineering, Department of Electrical and Electronics Engineering, 09100, Aydin, Türkiye*

Abstract: Accurate modeling of wireless signal propagation in complex environments is essential for the efficient planning of next-generation communication networks. This study investigates the impact of transmitter placement and elevation on signal coverage and interference levels within a structured campus environment. Using Sionna ray tracing, a differentiable and GPU-accelerated ray tracing framework, realistic 3D models of the Aydin Adnan Menderes University main campus were constructed and simulated. Three transmitter deployment scenarios—distributed, centralized, and optimized—were evaluated in terms of path gain, Received Signal Strength (RSS), and Signal-to-Interference-plus-Noise Ratio (SINR). The simulation results reveal how different spatial configurations influence signal propagation, coverage uniformity, and interference. The findings provide valuable insights into strategic transmitter placement for enhanced network performance in real-world deployments.

Keywords: Ray tracing, Wireless propagation, Path gain, SINR, RSS, Sionna

***Corresponding author:** Aydin Adnan Menderes University, Faculty of Engineering, Department of Electrical and Electronics Engineering, 09100, Aydin, Türkiye
E mail: onem.yildiz@adu.edu.tr (O. YILDIZ)
Onem YILDIZ https://orcid.org/0000-0003-0675-6637

Received: May, 03 2025
Accepted: June, 11 2025
Published: September, 15 2025

Cite as: Yildiz O. 2025. Differentiable ray tracing-based analysis of transmitter deployment strategies in site-specific scenarios. BSJ Eng Sci, 8(5): 1320-1327.

1. Introduction

Large-scale environments including campuses, cities, and industrial complexes depend on dependable and efficient wireless communication. Optimizing coverage and controlling interference grow more difficult as wireless technologies move toward 5G and 6G. Accurate modeling of wireless propagation in realistic environments is indispensable to build networks fulfilling these needs.

Offering a degree of spatial consistency and environmental specificity that traditional models cannot match, ray tracing (RT) has become a powerful tool for simulating the intricate interactions of radio waves with their surrounds (Yun and Iskander, 2015; Egea-Lopez et al., 2021). By means of GPU-accelerated, flexible, and differentiable simulation tools, advanced frameworks such as NVIDIA's Sionna (Hoydis et al., 2023b) improve the capacity of RT even further. These developments enable high fidelity real-world wireless performance, so supporting more informed decisions in network planning and optimization.

Especially in relation to next-generation wireless systems, major efforts have been made recently to improve wireless channel modeling and network simulation by using the features of Sionna RT. Creating reasonable large-scale digital twins of metropolitan settings to enable accurate ray tracing simulations has become a main priority. In this sense, the BostonTwin project (Testolina et al., 2024) produced a comprehensive 3D model of Boston by combining actual cellular base station placements to support city-scale propagation investigations. Complementing this, the extension of RayMobtime with Sionna RT (Bastos et al., 2023) introduced dynamic scene modeling, including not only stationary buildings but also mobile objects such vehicles and pedestrians, so enabling the generation of realistic and mobility-aware wireless channel datasets.

Beyond broad environmental modeling, efforts have also focused on producing high-fidelity, site-specific digital twins for more localized but extremely detailed propagation analysis. Combining 3D mesh modeling with SUMO-based mobility traces and Sionna RT simulations, the study in (Noh and Choi, 2024) produces subcarrier-level MIMO-OFDM channel data appropriate for fine-grained system evaluations.

Parallel with advances in scene modeling, there is increasing interest in including physically consistent wireless channels into system-level network simulations. A major step in this direction is the development of (Zubow et al., 2024), which enables spatially and temporally coherent ray tracing-based channels inside the ns-3 network simulator. Particularly for indoor Wi-Fi and cellular systems, this integration lets evaluations of network performance under reasonable propagation conditions be more accurate.

Studies of comparative benchmarks have strengthened Sionna RT even more. Particularly in complex multi-link

and scattering situations, in (Zhu et al., 2024a) methodically compared several ray tracing solutions to show that Sionna RT provides high computational efficiency while preserving modeling accuracy. Likewise, for particular tasks such urban path loss prediction, the study in (Xia et al., 2024) showed that using accurate 3D propagation scene models with Sionna RT greatly increases prediction accuracy, especially in environments including dense vegetation and small-scale structures.

Deeper methodologically, the development of differentiable ray tracing capabilities inside Sionna RT (Hoydis et al., 2023a) has created fresh avenues for learning and direct environmental parameter optimization straight from data. Sionna RT promotes gradient-based optimization for applications including environment calibration and transmitter placement tuning by letting gradients be computed regarding material properties, antenna configurations, and node positions. Complementary to this, performance evaluations presented in (Zhu et al., 2024b) confirmed that Sionna RT, especially with GPU acceleration, achieves significant computational speed-ups, so enabling real-time large-scale wireless digital twin implementations. These developments together prove Sionna RT as a flexible and strong platform for both basic research and pragmatic design in next-generation wireless communication systems.

Although practical deployment strategies such as transmitter location and elevation greatly affect network performance due to architectural geometry, signal reflections, and LOS coverage, ray tracing precisely models wireless channel locations. This study contributes to the literature by examining the effect of transmitter placement and height on wireless communication performance in a real campus environment with detailed simulations based on ray tracing. In addition to scenarios created with real base station locations, centralized placement based on user density and optimization-oriented strategic placement alternatives were comparatively evaluated. It was shown that more homogeneous and fair coverage can be provided with fewer transmitters, and it was revealed that it is possible to balance infrastructure efficiency and service quality.

This paper is arranged mainly as follows: First, we examine closely the deployment scenarios and how they affect path gain. Subsequently, for every scenario, SINR and RSS distributions over campus are fully assessed. Finally, a comparative study emphasizes the performance trade-offs and advantages of strategic transmitter location, so offering information for best network design in challenging settings.

2. Materials and Methods

2.1. Sionna Ray Tracing

Using Sionna RT, an expansion of the open-source radio propagation simulation system Sionna, ray tracing simulations were conducted. Constructed atop Mitsuba 3 (Jakob et al., 2022) and TensorFlow (Martín et al., 2015), Sionna RT offers a GPU-accelerated, flexible, differentiable platform for high-fidelity radio propagation modeling. Operating natively in Python, the framework is completely compatible with Jupyter notebooks, so enabling reproducible and easily modifiable simulations.

Sionna RT lets the user create comprehensive simulation settings regarding the carrier frequency, bandwidth, antenna array geometries, material properties including relative permittivity, permeability, and conductivity. This information computes multipath components by following the propagation of electromagnetic waves across reflections, diffractions, and scattering events inside the 3D scene. Sionna RT generates complete channel information for every transmitter-receiver pair including path gains, propagation delays, angles of departure and arrival.

Using the open-source 3D modeling tool Blender (Blender Foundation, 2023), together with the Mitsuba-Blender plugin (Anonymous, 2023), scene models fit for Sionna RT are produced. The Blender-OSM add-on (Prochitecture, 2023) was used for realistic environmental modeling since it lets one import comprehensive geospatial data from OpenStreetMap (OpenStreetMap Foundation, 2023). This arrangement allows the quick creation of accurate and site-specific propagation simulations' realistic large-scale scenes.

2.2. Scene Setup

The central campus of Aydin Adnan Menderes University formed the basis for the simulation scene. Using the Blender-OSM plugin, OpenStreetMap's building layouts, road data, and vegetation information were imported into a thorough 3D model of the university. Blender helped the imported map data to be polished and corrected so that it faithfully portrayed important environmental elements including open spaces, surface materials, and building heights.

Common construction materials determined material properties for ground surfaces and buildings; relative permittivity and conductivity matched concrete, brick, metal, and ground. Exported in Mitsuba 3-compatible format, the built 3D scene was used in Sionna RT for the ray tracing simulations (Figure 1). Using this scene setup, multiple transmitter and receiver configurations were simulated to investigate the effects of transmitter placement and elevation on signal propagation across the campus environment (Figure 2).

Following the construction of the campus scene, three different transmitter deployment scenarios were designed to systematically analyze the effects of placement strategies on wireless signal propagation and network performance. These scenarios differ in terms of the number of transmitters, their spatial distribution across the campus, and their deployment heights. A summary of the scenarios considered is provided in Table 1, and the simulation parameters are shown in Table 2.

Figure 1. 3D scene of the campus in Sionna.

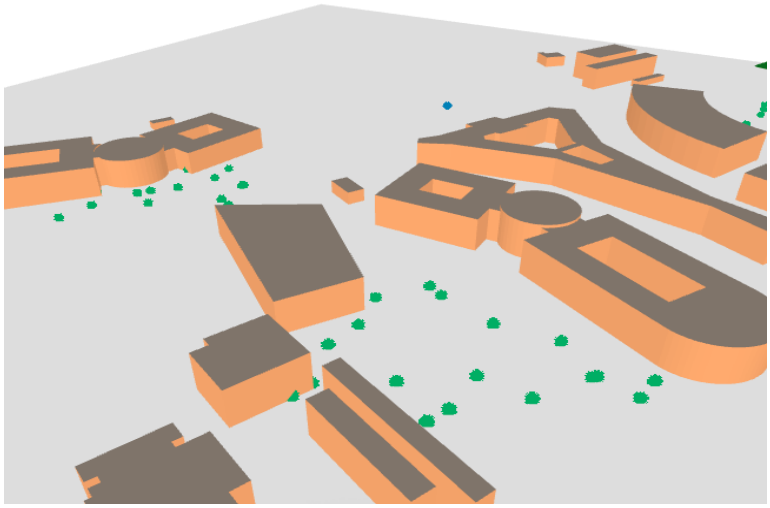

Figure 2. A transmitter (blue dot) and a receiver (green dot) representation in Sionna.

Table 1. Overview of transmitter deployment scenarios

Scenario	Number of Transmitters (TXs)	Transmitter Heights (m)	Deployment Type	Description
Scenario 1	4	1 TX: 40 m, 3 TXs: 30 m	Distributed	Real-world locations based on existing base stations within the campus
Scenario 2	3	All at 30 m	Centralized	Transmitters clustered in the central area of the campus
Scenario 3	3	All at 30 m	Optimized	Transmitters strategically placed for optimal campus-wide coverage

Table 2. Simulation parameters

Parameter	Value
Bandwidth	20 MHz
Number of users	60
Number of transmitters	Varies by scenario (see Table 1)
Transmitter array type	Planar array
Transmitter array pattern	TR 38.901 standard
Receiver array type	Planar array
Receiver array pattern	Dipole

The impact of transmitter placement and elevation on communication performance is evaluated by using ray tracing techniques. Table 2 indicates that Scenario 1 was designed by taking the real locations of the base stations located within the campus, while in Scenario 2, the transmitters were positioned in the center of the campus where the user density is high. In addition, the optimum placement scenario, Scenario 3, was determined through multiple simulation experiments to maximize the communication performance across the campus. The transmitter locations were optimized based on the signal strength and interference balance evaluated through RSS and SINR distributions. The selected configuration provides more homogeneous coverage and lower performance variance with fewer transmitters, thus increasing both efficiency and service fairness. For the simulation environment described, the methodology used to calculate key performance metrics such as path gain, SINR and RSS are described in detail.

To generate a coverage map for a given transmitter, path gain is calculated for each cell $C_{i,j}$ (equation 1). This represents the average signal strength across the cell.

$$g_{i,j} = \frac{1}{|C|}\int_{C_{i,j}} |h(s)|^2 ds \quad (1)$$

where $h(s)$ is the channel coefficients at position s(x,y), $C_{i,j}$ represents the specific cell in the map. This formula calculates the average path gain over the cell area by integrating the channel coefficients.

Path gain is converted to RSS by using equation 2. This represents the signal strength at the receiver for a specific cell.

$$RSS_{i,j} = P_{tx} g_{i,j} \quad (2)$$

where P_{tx} is the transmitter power (in dBm or Watts). RSS reflects the total signal power received at the receiver's location, which is critical for analyzing network coverage.

SINR (equation 3) is computed for every transmitter present in the scene to measure how much interference and noise influence the intended signal.

$$SINR_{i,j}^{k} = \frac{RSS_{i,j}^{k}}{N_0 + \sum_{k' \neq k} RSS_{i,j}^{k'}} \quad (3)$$

This formula shows that SINR treats signals from all other transmitters as interference while concentrating on the signal from the target transmitter. Thermal noise power N_0 (W) is computed using bandwidth, temperature, and Boltzmann's constant as in equation 4.

$$N_0 = B \times T \times k \quad (4)$$

where B is bandwidth (Hz), T is temperature (Kelvin) and k is Boltzmann constant 1.380649×10^{-23} J/K.

With the simulation setup and performance metrics defined, the following section provides a detailed analysis of the results, highlighting how transmitter placement and elevation influence wireless communication performance across the campus environment.

3. Results

This study analyzes the performance of path gain, SINR, and RSS in different transmitter deployments within Aydin Adnan Menderes University central campus environment. Three different scenarios (Table 1) are examined to investigate the impact of transmitter positions and heights on communication quality.

The effect of various placement techniques on coverage is clearly shown in Figure 3, which shows the placements of the transmitters (red dots), and their path gain distribution. In the first scenario (Figure 3a), the location of the transmitters in outer regions guarantees broad coverage but causes degraded signals in the inner sections of the campus. In the second scenario (Figure 3b), signal strength decreases toward the campus borders while the central placement of transmitters produces high path gain values in interior areas. In the third scenario (Figure 3c), strategic deployment results in a more homogeneous coverage distribution with less coverage gaps.

The cumulative distribution of path gain over the assessed scenarios (Figure 4) provides significant insights into signal quality and deployment efficiency. The distributed placement scenario (scenario 1), comprising four transmitters with one elevated to 40 meters, attains the maximum median path gain, surpassing the 50% cumulative probability at around -90 dB. Nonetheless, this incurs increased infrastructure complexity and expenditure. This arrangement demonstrates a considerable path gain range, spanning from -183 dB to -83 dB, signifying substantial spatial variation in signal strength throughout the area. The broad dynamic range indicates that although many users receive robust signal levels, others suffer from significantly impaired connectivity, compromising overall service consistency. The central placement (scenario 2) covers a broader range, from -200 dB to -82 dB, yielding the lowest median path gain, indicating suboptimal performance, particularly at the cell boundaries. Conversely, the ideal placement scenario (scenario 3), utilizing merely three transmitters positioned at a height of 30 meters, attains a median path gain of -100 dB with a more restricted range (-182 dB to -83 dB). This indicates a more uniform quality of coverage with diminished extreme weak areas. Despite its median being somewhat lower than that of scenario 1, the ideal configuration provides a superior equilibrium among deployment cost, simplicity, and fairness in user experience. Consequently, when evaluating both signal efficiency and implementation feasibility, the ideal placement emerges as the best balanced and efficient solution.

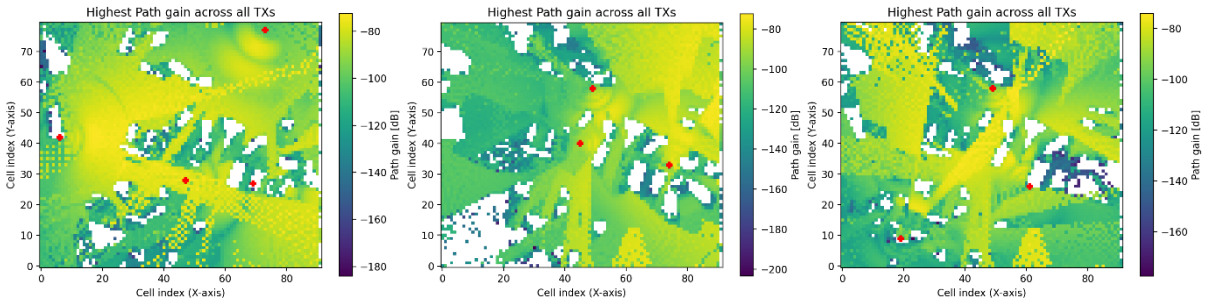

(a) (b) (c)

Figure 3. Highest path gain across all TXs for (a) scenario 1 (b) scenario 2 and (c) scenario 3.

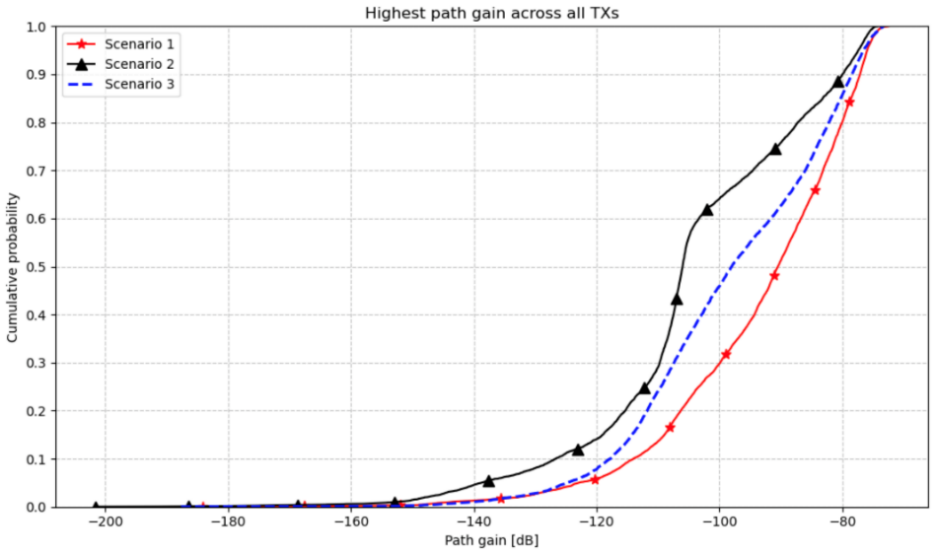

Figure 4. Cumulative probability distribution of highest path gain across all TXs for all scenarios.

The spatial distribution of SINR among the three deployment scenarios indicates significant disparities in interference management and coverage uniformity. In scenario 1 (Figure 5a), results in localized zones of higher SINR—surpassing 60 dB in certain areas—while also demonstrating considerable spatial variation, with many places, especially near the lower boundary, registering below 0 dB. This signifies variable service quality and inadequate interference dispersion despite elevated peak performance. Scenario 2 (Figure 5b), including centrally located transmitters, yields robust SINR in the central region but struggles to sustain satisfactory performance at the peripheries, where extensive areas of diminished SINR (often below -10 dB) arise due to restricted signal propagation and cumulative interference. Conversely, scenario 3 (Figure 5c), with an optimally distributed configuration with three transmitters at a consistent elevation, attains a well-balanced SINR distribution throughout the campus. The SINR values predominantly reside within the 20-70 dB range, with few regions exhibiting critically low levels. This suggests that the strategic positioning in scenario 3 provides more reliable and uniform signal quality, rendering it the most effective option regarding interference management and user experience consistency.

The cumulative distribution analysis of SINR values (Figure 6) demonstrates major differences in interference patterns and signal quality across the assessed transmitter setups. Scenario 2 demonstrates the poorest SINR performance, with values starting at -42 dB and a median SINR of roughly 13 dB. The significant increase in the lower SINR region suggests that a considerable number of users encounter severe signal degradation, especially at the cell edges, possibly attributable to concentrated interference and restricted spatial diversity. Scenario 1 provides modest enhancement with a median SINR of around 20 dB, due to the inclusion of an additional transmitter and expanded geographical coverage; yet, this results in elevated deployment costs and diminished SINR uniformity. Conversely, Scenario 3 attains superior SINR consistency throughout the network, exhibiting a median approximately at 27 dB and a more gradual increase in cumulative probability. This signifies enhanced overall signal quality and a more equal user experience, reducing the percentage of users exposed to low SINR circumstances. The results indicate that strategically planned transmitter positioning can surpass more resource-demanding options by enhancing SINR while maintaining deployment simplicity and cost-effectiveness.

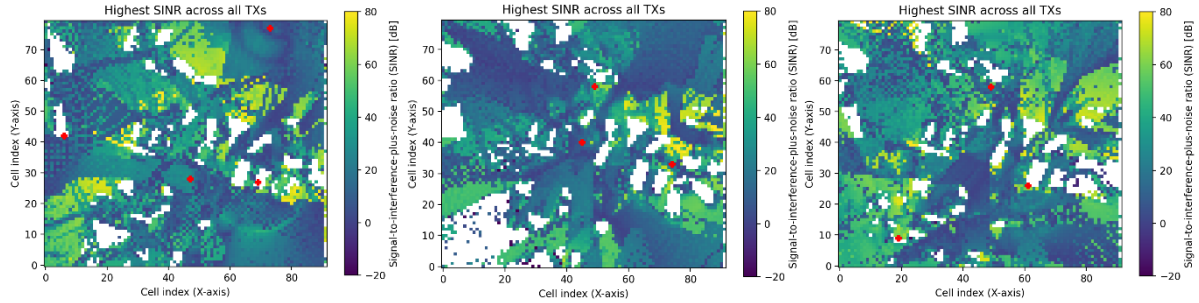

(a) (b) (c)

Figure 5. Highest SINR across all TXs for (a) scenario 1 (b) scenario 2 and (c) scenario 3.

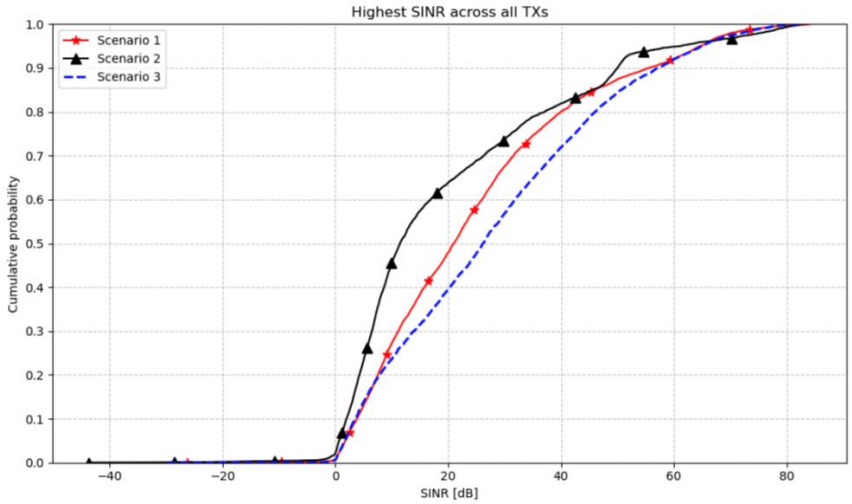

Figure 6. Cumulative probability distribution of highest SINR across all TXs for all scenarios.

The comparative examination of RSS distributions among the three deployment scenarios demonstrates significant variations in signal coverage and geographic homogeneity. Scenario 1 (Figure 7a) offers wide signal coverage with significant regions surpassing -60 dBm. Nonetheless, isolated areas with values below -100 dBm signify inconsistent transmission and fluctuation in coverage. Scenario 2 (Figure 7b) has robust RSS near the core but experiences rapid signal attenuation toward the periphery, resulting in notable coverage gaps. Conversely, scenario 3 (Figure 7c) attains a more uniform RSS distribution throughout the entire region. The diminished occurrence of weak-signal areas and the uniform coverage pattern indicate that strategic positioning not only elevates average signal strength but also augments equity in user experience throughout the network.

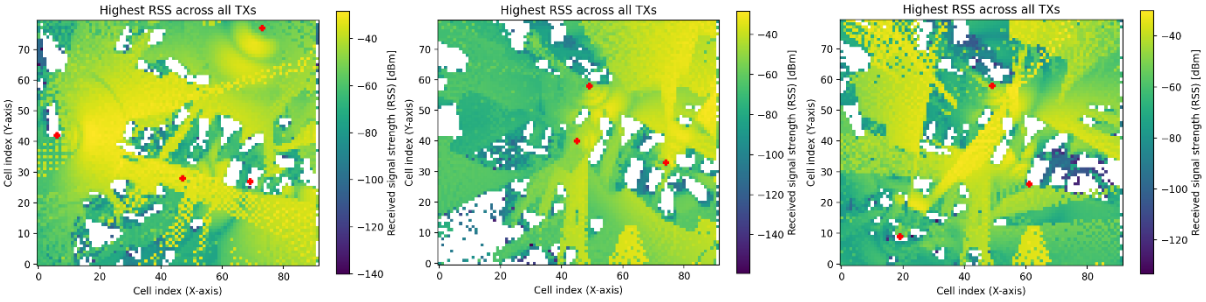

(a) (b) (c)

Figure 7. Highest RSS across all TXs for (a) scenario 1 (b) scenario 2 and (c) scenario 3.

The cumulative RSS distribution supports spatial RSS map findings (Figure 8). The highest median RSS performance is scenario 1 intersecting the 50% probability threshold near -47 dBm. However, the curve's wider spread suggests greater signal fluctuation over coverage. Scenario 2 has the lowest median RSS value at -62 dBm and a steeper slope, indicating rapid signal loss outside center locations. Scenario 3 balances strength

and consistency with a median RSS of roughly -55 dBm and a gentler slope. This improves signal homogeneity and coverage equity. Scenario 1 performs best in ideal locations, whereas scenario 3 has fewer weak-signal zones and better service quality, proving its efficiency and reliability.

An integrated evaluation of RSS and SINR outcomes indicates that elevated signal strength does not ensure communication quality without adequate interference management. Although scenario 1 provides superior RSS values, it experiences SINR inconsistency as a result of heightened interference. Scenario 3, though exhibiting marginally reduced RSS, attains the most uniform SINR distribution, signifying that deliberate transmitter positioning guarantees both effective coverage and dependable signal quality with diminished resources.

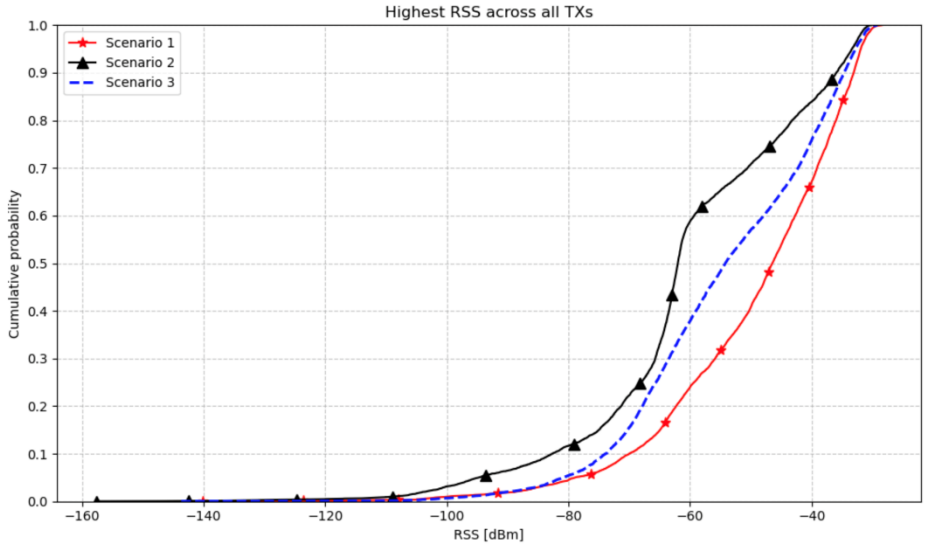

Figure 8. Cumulative probability distribution of highest RSS across all TXs for all scenarios.

4. Discussion

This work verifies that signal strength, interference distribution, and general network performance are much influenced by the location of the transmitter. Unlike many previous works that give coverage maximizing through more infrastructure top priority, our results show that a well-optimized deployment with less transmitters can produce more consistent and dependable signal quality. Especially, balanced SINR and RSS distributions found in the optimal scenario draw attention to the importance of strategic orientation above designs with only resource-intensive character. These results underline the need of including performance as well as deployment economy into network design. Moreover, the results provide a road for future integration of AI-based optimization models in which real-time system feedback and environmental data can be used to automate and improve placement decisions depending on machine learning.

5. Conclusion

The study shows that performance of wireless communication depends on the location of the transmitter, so influencing signal strength, interference management, and spatial coverage uniformity. It implies that a balance between power and interference avoidance is required since maximizing signal intensity by itself does not ensure dependable connectivity. While designs that evenly distribute RSS and SINR offer dependable and fair user experiences, excessive path gain and RSS variability can cause coverage discrepancies. Appropriate location can minimize infrastructure resources, so stressing the need of strategic and economical planning in the design of wireless networks.

Author Contributions

The percentages of the author' contributions are presented below. The author reviewed and approved the final version of the manuscript.

	O.Y.
C	100
D	100
S	100
DCP	100
DAI	100
L	100
W	100
CR	100
SR	100
PM	100
FA	100

C=Concept, D= design, S= supervision, DCP= data collection and/or processing, DAI= data analysis and/or interpretation, L= literature search, W= writing, CR= critical review, SR= submission and revision, PM= project management, FA= funding acquisition.

Conflict of Interest

The author declared that there is no conflict of interest.

Ethical Consideration

Ethics committee approval was not required for this study because of there was no study on animals or humans.

Acknowledgements

In memory of Prof. Radosveta Sokullu, whose earlier mentorship continues to inspire my research life, even after her passing.

References

Anonymous. 2023. Mitsuba Blender Add-on. URL: https://github.com/mitsuba-renderer/mitsuba-blender (accessed date: February 4, 2025).

Bastos S, Oliveira A, Suzuki, D, Gonçalves L, Sousa I, Klautau A. 2023. Generation of 5G/6G wireless channels using raymobtime with Sionna's ray-tracing. XLI Simpósio Brasileiro De Telecomunicações E Processamento De Sinais, pp:45-49.

Blender Foundation. 2023. Blender. URL: https://www.blender.org (accessed date: February 3, 2025).

Egea-Lopez E, Molina-Garcia-Pardo JM, Lienard M, Degauque P. 2021. Opal: An open source ray-tracing propagation simulator for electromagnetic characterization. Plos one, 16(11): e0260060.

Hoydis J, Aoudia FA, Cammerer S, Nimier-David M, Binder N, Marcus G, Keller A. 2023a. Sionna RT: Differentiable ray tracing for radio propagation modeling. 2023 IEEE Globecom Workshops (GC Wkshps), pp: 317–321.

Hoydis J, Cammerer S, Aoudia FA, Vem A, Binder N, Marcus G, Keller A. 2023b. Sionna: An open-source library for next-generation. Physical Layer Research, pp:45.

Jakob W, Speierer S, Roussel N, Vicini D. 2022. DR.JIT: A just-in-time compiler for differentiable rendering. ACM Transactions on Graphics, 41(4): 1–19.

Martín A, Ashish A, Paul B, Eugene B, Zhifeng C, Craig C, Greg SC, Andy D, Jeffrey D, Matthieu D. 2015. TensorFlow: Large-scale machine learning on heterogeneous systems, Mountain View, CA, USA, pp:1-19

Noh YJ, Choi KW. 2024. High-precision digital twin platform based on ray tracing simulation. 2024 15th International Conference on Information and Communication Technology Convergence (ICTC), pp: 1464–1465.

OpenStreetMap Foundation. 2023. OpenStreetMap. URL: https://www.openstreetmap.org (accessed date: February 1, 2025).

Prochitecture. 2023. Blender-OSM: OpenStreetMap and Terrain for Blender. URL: https://prochitecture.gumroad.com/l/blender-osm (accessed date: February 2, 2025).

Testolina P, Polese M, Johari P, Melodia T. 2024. Boston twin: The boston digital twin for ray-tracing in 6G networks. proceedings of the ACM. Multimedia Systems Conference 2024 on ZZZ, pp: 441–447.

Xia G, Zhou C, Zhang F, Cui Z, Liu C, Ji H, Zhang X, Zhao Z, Xiao Y. 2024. Path Loss prediction in urban environments with Sionna-RT based on accurate propagation scene models at 2.8 GHz. IEEE Transactions on Antennas and Propagation, pp:65-74.

Yun Z, Iskander MF. 2015. Ray tracing for radio propagation modeling: Principles and applications. IEEE Access, 3: 1089–1100.

Zhu M, Cazzella L, Linsalata F, Magarini M, Matteucci M, Spagnolini U. 2024a. On the digitization of the EM environment: a comparison of ray launching solutions. 2024 IEEE International Mediterranean Conference on Communications and Networking (MeditCom), pp: 85–90.

Zhu M, Cazzella L, Linsalata F, Magarini M, Matteucci M, Spagnolini U. 2024b. Toward real-time digital twins of em environments: computational benchmark for ray launching software. IEEE Open J Commun Soc, pp: 54.

Zubow A, Pilz Y, Rösler S, Dressler F. 2024. Ns3 meets sionna: using realistic channels in network simulation, pp: 41.

Black Sea Journal of Engineering and Science
doi: 10.34248/bsengineering.1673237

Open Access Journal
e-ISSN: 2619 – 8991

Research Article
Volume 8 - Issue 5: 1328-1338 / September 2025

CONTACTLESS DETECTION OF ELECTRICAL MACHINE BEARING FAULTS: A RADAR-BASED SOLUTION

Yunus Emre ACAR[1]*, Salih Bilal CETINKAL[2]

[1]*Selcuk University, Faculty of Technology, Department of Electrical and Electronics Engineering, 42075, Konya, Türkiye*
[2]*Selcuk University, Faculty of Technology, Department of Metallurgical and Materials Engineering, 42075, Konya, Türkiye*

Abstract: Bearing failures represent the most prevalent fault type in electrical machines, potentially leading to catastrophic consequences if not detected early. Conventional detection methods primarily rely on thermal, acoustic, and vibration sensors. Traditional vibration-based techniques have gained widespread adoption due to their stable and straightforward signal-processing capabilities. However, these approaches require direct motor mounting, introducing economic, temporal, and safety inefficiencies. This study presents the first investigation of contactless radar-based detection of bearing faults according to the authors' knowledge. The research employs the absolute value of complex signals derived from quadrature signals recorded by a 24 GHz radar transceiver as the vibration signal. Various defects like corrosion, improper oil levels, and scratches were deliberately introduced to the inner race, outer race, and balls of bearings, establishing 16 distinct fault classes. Classification performance was evaluated using both time-domain statistical features and frequency-domain PSD features. Multiple machine learning algorithms were applied to both approaches, consistently achieving accuracy rates exceeding 98%. This study validates the potential of radar-based systems for bearing fault diagnosis and introduces a novel paradigm for contactless bearing fault detection comprising radar signal data from 880 experiments. The results demonstrate that radar technology offers a promising alternative to traditional contact-requiring methods, enabling efficient and reliable bearing fault classification through non-invasive vibration detection.

Keywords: Bearing, Fault detection, Power spectral density, Radar, Time-domain features

***Corresponding author:** Selcuk University, Faculty of Technology, Department of Electrical and Electronics Engineering, 42075, Konya, Türkiye
E mail: yacar@selcuk.edu.tr (Y.E. ACAR)
Yunus Emre ACAR https://orcid.org/0000-0002-6809-9006
Salih Bilal CETINKAL https://orcid.org/0000-0001-6212-7670

Received: April 10, 2025
Accepted: June 17, 2025
Published: September 15, 2025
Cite as: Acar YE, Çetinkal SB. 2025. Contactless detection of electrical machine bearing faults: A radar-based solution. BSJ Eng Sci, 8(5): 1328-1338.

1. Introduction

Bearings are critical components in mechanical systems that minimize friction between moving parts, thereby reducing energy loss and increasing load-bearing capacity. These elements significantly enhance the efficiency and durability of systems by supporting rotational or linear motion through rolling elements positioned between inner and outer rings. The importance of bearings is further emphasized by their role in optimizing machine performance and reducing maintenance costs. Considering that approximately 40-50% of mechanical failures in rotating machinery stem from bearing faults, monitoring and maintaining these components plays a vital role (Zhang et al., 2020a). Bearing failures typically result from factors such as inadequate lubrication, contamination, improper installation, overloading, and material fatigue (Brito et al., 2022). These failures can manifest in various forms, including wear, fatigue cracks, corrosion, and surface damage.

Bearing fault detection utilizes various data types, each enabling distinct approaches with inherent advantages and disadvantages. Vibration analysis, owing to its high sensitivity and broad applicability, is prevalent for early fault detection (Qiao et al., 2020; Zhang et al., 2020b; Mueller et al., 2023). However, limitations include the criticality of sensor placement and susceptibility to noise interference. Acoustic emission, leveraging its capacity to capture high-frequency signals, offers advantages in early micro-crack detection, but remains susceptible to ambient noise (Pacheco-Cherrez et al., 2022; Glowacz et al., 2025). Current-based methods, exploiting existing motor current sensors, preclude the need for supplementary hardware; however, sensitivity can diminish in low-speed applications (Kao et al., 2018; Sabir et al., 2019). Thermal imaging, facilitating non-contact measurement of bearing temperature variations, necessitates expensive equipment and may exhibit reduced efficacy in incipient fault stages (Lopez-Perez and Antonino-Daviu, 2017; Mehta et al., 2021). Each approach contributes significantly to bearing fault detection within specific application scenarios and diverse industrial settings.

The detection of bearing faults has seen significant advancements in signal processing approaches and methods over time. Initially, in the earlier decades, basic frequency analysis techniques such as time-domain analyses and the Fast Fourier Transform (FFT) were employed. As the field progressed, the 1980s witnessed

the development and widespread adoption of envelope analysis techniques. Moving into the 1990s, more sophisticated signal processing and artificial intelligence methods, including wavelet analysis and neural networks, began to be utilized. In the subsequent years, adaptive signal processing techniques like Empirical Mode Decomposition (EMD) and the Hilbert-Huang Transform gained prominence (Akar et al., 2015). Recently, deep learning-based approaches have become increasingly prevalent. For instance, research by (Zhu et al., 2023) demonstrated the effectiveness of deep learning in bearing fault detection. Emerging trends in this area include multi-sensor fusion, transfer learning, and novel deep network architectures. The advantages of these methods include noise suppression capabilities, early fault detection, and automatic feature extraction.

In the field of bearing fault diagnosis, both synthetic and experimental data play crucial roles in the development and validation of diagnostic algorithms. Synthetic data, as utilized in various studies, allows researchers to simulate a wide range of fault conditions, providing a controlled environment to test the efficacy of machine learning models (Liu et al., 2020). Experimental data, such as that from the Case Western Reserve University Bearing Data Center, offers real-world insights and is instrumental in validating these models under practical conditions (Smith and Randall, 2015). The primary equipment used in these studies includes vibration sensors like accelerometers and acoustic emission sensors, which are essential for capturing the subtle signals indicative of bearing faults (Karabacak and Özmen, 2022; Ertarğın et al., 2023; Ercire and Ünsal, 2024; Kilic and Acar, 2024). However, contact-based sensors face challenges such as potential misalignment and the introduction of noise due to physical attachment. Non-contact measurement methods, such as laser-based ones, offer a compelling alternative by eliminating these issues, enabling accurate measurements even in challenging-to-access areas. Moreover, radar-based detection systems provide significant advantages over both laser and infrared systems. While laser and infrared technologies are effective in controlled environments, radar technology excels in harsh industrial conditions where dust, fog, vapors, and temperature variations can compromise measurement accuracy (Acar et al., 2021). Radar systems can penetrate protective covers and operate under various lighting conditions, providing measurements over longer distances and through obstructions. Unlike laser systems that require direct line-of-sight and careful surface preparation, radar sensors leverage the Doppler effect for direct velocity measurements while being resistant to electromagnetic interference. Additionally, a single radar sensor can simultaneously monitor multiple points, capturing not only vibration but also velocity, position, and structural deformation across various frequency bands. These capabilities make radar-based systems a more versatile and cost-effective solution for continuous monitoring in industrial applications where accessibility and environmental resilience are critical concerns.

In this study, we present significant contributions to the field of bearing fault diagnosis through the development of a comprehensive dataset specifically focused on bearing faults. A total of 880 data samples were generated, encompassing a diverse range of fault types. The experiments were conducted using bearings that were deliberately aged or deformed to simulate realistic fault conditions. Notably, the data were collected using a radar-based non-contact measurement system, marking the creation of the first dataset in the literature that encompasses bearing faults detected via radar technology. This pioneering dataset not only provides a valuable resource for future research but also demonstrates, for the first time, that bearing faults can be classified with very high accuracy using radar-based methods. This advancement opens new avenues for non-invasive and precise fault diagnosis in industrial applications. The subsequent sections of this paper will detail the dataset creation process, methodologies employed, and the results obtained, thereby elucidating the significance of this novel approach in the context of bearing fault diagnosis and its potential implications for industrial maintenance practices.

2. Materials and Methods

2.1. Radar-Based Vibration Estimation

The motion detection capability of continuous wave radars represents a fascinating phenomenon with diverse application domains in electrical engineering. The Doppler principle underpins a spectrum of applications, creating a methodological continuum that spans from detecting high-velocity objects like vehicles and aircraft to the subtle monitoring of vital physiological parameters—pulse rates and respiratory patterns—through the minute movements of the chest wall.

In these systems, a high-frequency RF signal generated via an oscillator is typically amplified through a power amplifier before radiating toward the target through an appropriate antenna. A portion of the oscillator signal, diverted immediately before the amplification stage, is mixed with the reflected signal through a mixer. The resulting low-frequency signal fundamentally represents the differential between transmitted and received signals. This low-frequency component encapsulates the target's motion information and enables target displacement determination after subsequent processing. Modern systems incorporate quadrature receiver sections to circumvent the inherent null point issue (Seflek et al., 2020) due to the trigonometric approaches to extract target displacement information. These radar configurations contain two mixer stages that combine the return signal with signals phase-shifted by 90 degrees from each other, thereby providing two baseband signals with a 90-degree phase difference. The fundamental block diagram of these IQ-demodulated radar structures is illustrated in Figure 1.

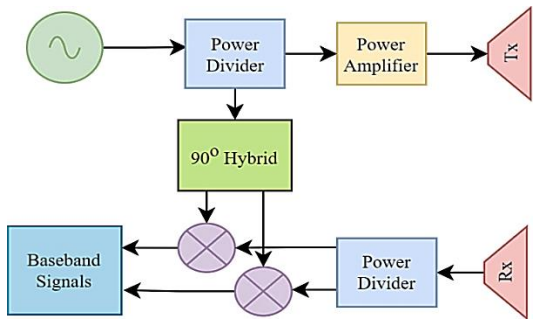

Figure 1. Block scheme of an IQ-demodulated radar.

The baseband signals $b_I(t)$ and $b_Q(t)$ provided by the IQ-demodulated radar structure can be expressed in sinusoidal forms as shown in equations 1 and 2, following elementary DC signal elimination processes. These orthogonal components constitute the fundamental representation of the target's motion characteristics.

$$b_I(t) = \cos\left(\frac{4\pi d_0}{\lambda_c} + \frac{4\pi x(t)}{\lambda_c}\right) = \cos(\theta) \quad (1)$$

$$b_Q(t) = \sin\left(\frac{4\pi d_0}{\lambda_c} + \frac{4\pi x(t)}{\lambda_c}\right) = \sin(\theta) \quad (2)$$

In this context, λ_c represents the operational wavelength of the radar, d_0 denotes the static distance between the radar and the target, and $x(t)$ signifies the target's displacement over time. The equations presented in equation 1.a and equation 1.b should theoretically incorporate residual phase noise terms. However, due to common source utilization, these terms become negligible (Gu et al., 2017) resulting in phase information θ being directly proportional to $d_0 + x(t)$.

Among the numerous methodologies proposed for phase information extraction, Differential Arctangent Cross Multiplication (DACM), Extended-DACM, Arctangent Demodulation (AD), and Complex Signal Demodulation (CSD) approaches predominate in practical applications. This study focuses on the CSD approach due to its superior immunity against high DC noise interference (Acar, 2024). This methodology utilizes the baseband signals as real and imaginary components of a complex signal. Following the Fourier transformation applied to this complex-valued signal, the frequency spectrum of the displacement signal is obtained. This spectrum can effectively substitute the vibration spectra traditionally employed in bearing fault diagnostics. The processes of complex signal formation and frequency spectrum generation are delineated in equation 3 and equation 4, respectively.

$$c[n] = b_I[n] + jb_Q[n] = e^{j\left(\frac{4\pi d_0}{\lambda_c} + \frac{4\pi x[n]}{\lambda_c}\right)} \quad (3)$$

$$C[k] = \frac{1}{N}\sum_{n=0}^{N-1} c[n]\, e^{-j2\pi kn/N} \quad (4)$$

Within this framework, $c[n]$ denotes the complex-valued signal, $C[k]$ represents the spectral information corresponding to the vibration, and N indicates the number of frequency points representing the spectrum.

2.2. Bearing Aging/Deforming Procedure

Bearing failures constitute the majority of motor failures occurring in industrial facilities. Different bearing models are employed based on varying load and operating conditions. This study focuses on 6205ZZ model bearings used in three-phase 1.1kW asynchronous motors. To simulate common bearing failures, bearing components (balls, cage, and outer rings) were supplied by ANADOLU RULMAN İMALAT SANAYİ VE TİCARET A.Ş. (ART). As part of the study, 16 bearings were prepared, including 15 defective bearings and a healthy bearing, to analyze three different failure types specified in Figure 2.

Lubricant Failures (LF): This bearing failure occurs due to the gradual reduction or performance degradation of lubricant within the bearing over time. During assembly, the ART company constructed the bearings with three different lubricant quantities (25%, 50%, and 75%) instead of the standard lubricant amount typically applied to a standard bearing.

Corrosion: Corrosions on the bearings occur with exposure to moisture or water under operating conditions. In this study, bearing components (balls, rings, and cages) were immersed in a laboratory-prepared aggressive acidic solution for a specific duration. After removal, we cleaned the components with alcohol and subjected them to ultrasonic cleaning. Thus, we have created three different corrosion damages: ball corrosion, ring corrosion, and cage corrosion.

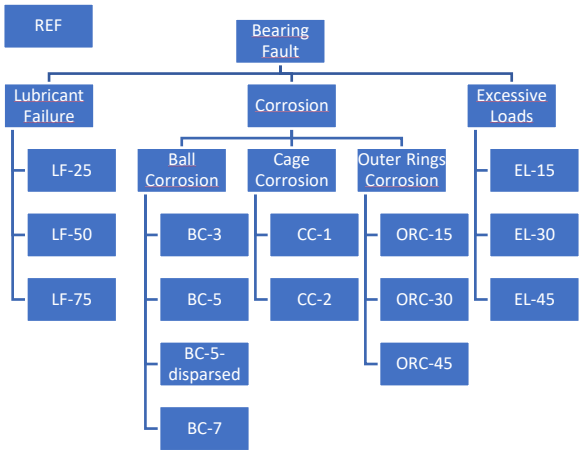

Figure 2. Prepared bearing types.

Ball Corrosion (BC-X): This type of failure occurs when all or some of the nine balls in a bearing are corroded. We have created different damage levels with varying numbers of corroded balls (3, 5, and 7) in each bearing. When assembling the bearings, some were corroded balls (Figure 3.b), and the rest were solid balls (Figure 3.c). The corroded balls were positioned adjacently (BC-3, BC-5, BC-7) or in a dispersed pattern (BC-5-dispersed).

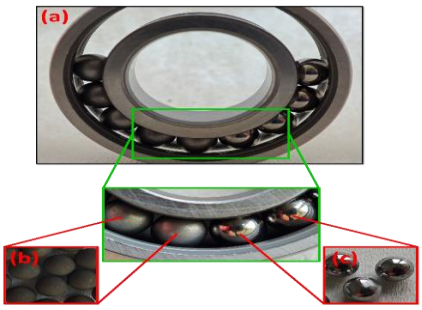

Figure 3. (a) The fabricated ball-corrosion specimen (BC-5), (b) corroded balls, (c) solid balls.

Outer Ring Corrosion (ORC-X): This failure originates from localized corrosion on the bearing's outer ring. We developed corrosion regions with distinct angular widths (15°, 30°, and 45°) on the interior surfaces of the outer rings. In Figure 4.a, the green-marked area represents the surface before acidic solution exposure, while the red-marked area indicates the surface following acidic solution treatment. As an outer ring defect, Figure 4.b is a magnified view of Figure 4.a to better illustrate the ORC-15 fault.

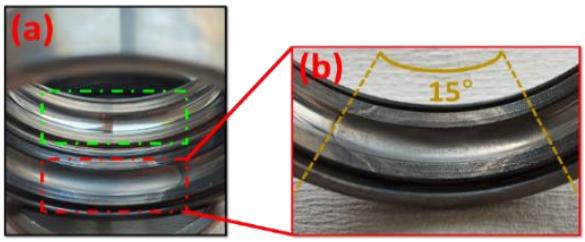

Figure 4. The fabricated outer-ring-corrosion specimen (ORC-15).

Cage Corrosion (CC-X): The wear of the cage surrounding the bearing balls causes these types of failures. We fabricated two distinct levels of failures with varying times the cages were immersed in the acidic solution. Figure 5 show cages of healthy and corroded specimens.

Figure 5. The cages of (a) healthy and (b, c) corroded specimens.

Excessive Load Failures (ELF-X): Wear damage occurs on the outer ring or ball surfaces due to excessive loads. We created three levels of damage by creating wear along different angles (15°, 30°, and 45°) on the ball path on the inner surface of the outer ring. In Figure 6.a, the part marked in green is the surface image where there is no wear, and the part marked in red is the surface image where there is wear. In Figure 6.b, the yellow arrow shows the close-up view of the ball-wear paths. Following the laboratory creation of these failure mechanisms, the ART assembled the bearings through their standard bearing assembly protocols.

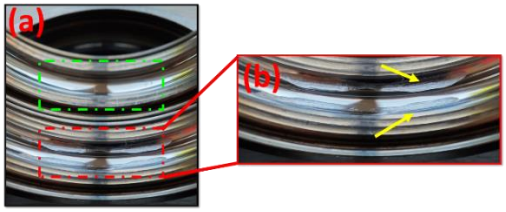

Figure 6. The created wear damage on the outer ring.

2.3. Experimental Setup and Data Acquisition

This study utilizes an experimental setup developed by Piritech to monitor bearing faults. The setup contains a single asynchronous motor coupled with a magnetic powder brake to load the motor. The setup also integrates a motor driver and a magnetic powder brake driver to control the rotational speed and load levels.

We have executed 55 experiments and stored the data for each bearing fault class. The motor operated at eleven equally spaced speed levels between 500 and 1500 rpm, and each speed level included five uniformly distributed load settings from 0 to 2.5 Nm. We have replaced the motor's bearing with an appropriately deformed one for each class.

We employed a straightforward Raspberry Pi–based hardware system to collect the radar data. We transmitted a 24.125 GHz signal toward the motor using the RFspace KLC5 transceiver and gathered the resulting low-frequency return signals. We then digitized the analog baseband signals at a 10 kHz sampling rate with the MCC118 device from Measurement Computing Corporation, saving them to an SD card through the Raspberry Pi. Our data set consists of 880 recordings distributed across 16 fault classes, and each recording contains 300,000 rows with two columns corresponding to the in-phase (I) and quadrature (Q) signals (Acar and Cetinkal, 2025). Figure 7 illustrates the experimental setup.

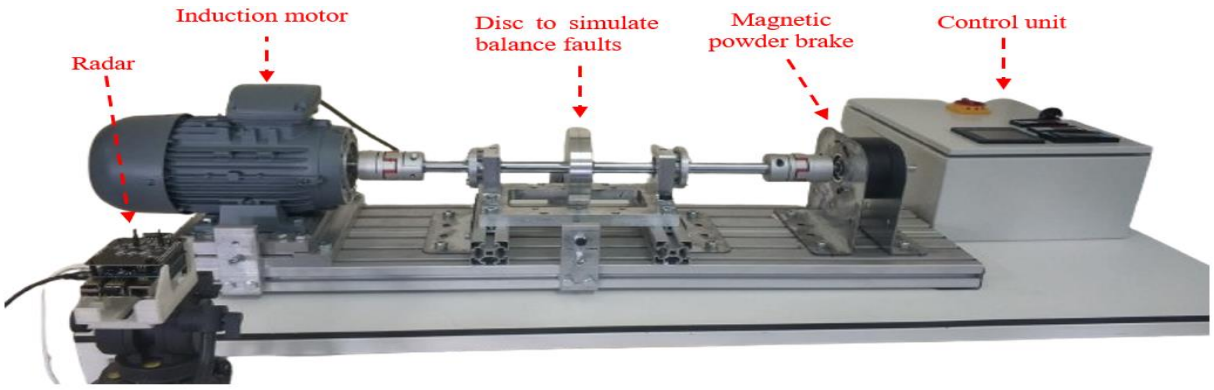

Figure 7. The experimental setup.

2.4. Data Processing

The discrete baseband signals recorded in the time domain constitute the dataset utilized in this research. By integrating these signals through complex signal demodulation techniques, we can effectively capture the micro-displacements of the target. This displacement signal, originating from motor vibrations, reflects the motor's oscillatory behavior in the time domain. The discrete signal, comprising 300.000 samples, is excessively lengthy for direct input into a classifier, necessitating additional feature extraction processes before implementation in machine learning algorithms. In this investigation, we executed feature extraction procedures in both temporal and frequency domains and conducted comparative analyses of the resultant outcomes.

2.4.1. Time-domain feature extraction

Engineers frequently analyze statistical characteristics of time-domain recordings when classifying bearing faults through vibration signals. Our research leverages 12 proven statistical features (Nayana and Geethanjali, 2017) extracted from the time domain. We first segment the input signal using sliding windows of length L with an overlap ratio O. We then apply all feature extraction techniques to these segments. We calculate the average of features across all segments to create the final feature representation. Figure 8 illustrates this extraction process clearly.

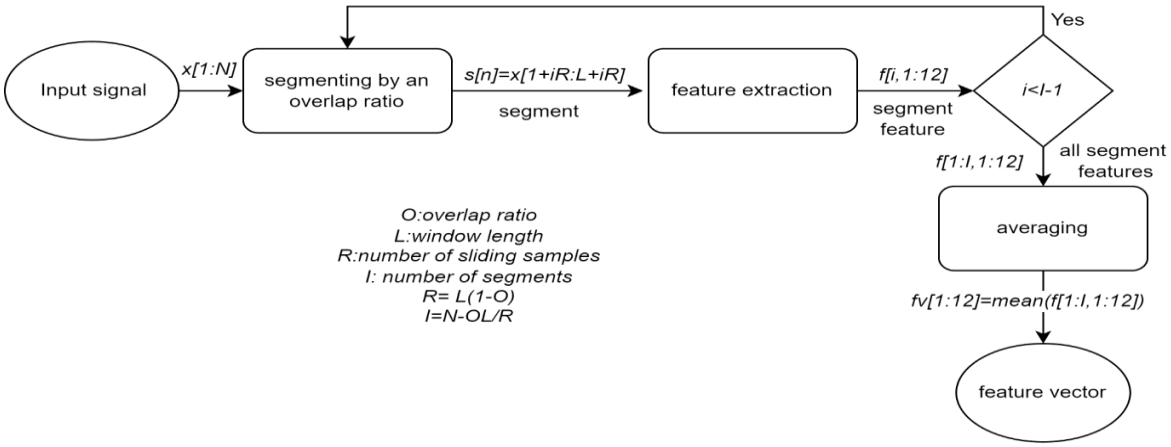

Figure 8. Time-domain feature extraction scheme.

Mean Absolute Value (MAV): This feature provides the mean of absolute values of samples within the segment and is calculated as shown in equation 5.

$$MAV = \frac{1}{L}\sum_{n=1}^{L}|x[n]| \quad (5)$$

Energy (E): This feature represents the segment's energy and is calculated as given in equation 6.

$$E = \sum_{n=1}^{L} x[n]^2 \quad (6)$$

Waveform Length (WL): This feature corresponds to the sum of absolute differences between consecutive samples. It represents the sum of absolute first-order derivatives, providing information about the signal's roughness, rate of change, and frequency characteristics for discrete signals. WL is calculated as shown in equation 7.

$$WL = \sum_{n=1}^{L}|x[n] - x[n-1]| \quad (7)$$

Willison Amplitude (WA): This feature compares the difference between consecutive samples against a threshold value and counts instances where this difference exceeds the threshold. WA is calculated using equation 8 and 9.

$$WA = \sum_{n=1}^{L} f|x[n] - x[n+1]| \quad (8)$$

$$f(x) = \begin{cases} 1 \; if \; x \geq \varepsilon \\ 0 \; otherwise \end{cases} \quad (9)$$

Zero Crossing (ZC): This feature determines the number of zero crossings within the segment. The expression in equation 10 identifies a zero crossing when consecutive values have different signs. To reject low-amplitude oscillations around zero, one can additionally check whether the difference between two samples exceeds a threshold value using the expression provided in equation 11.

$$ZC = \sum_{n=1}^{L} (x[n] \times x[n+1]) < 0 \quad (10)$$

$$(|x[n] - x[n+1]|) > \varepsilon \quad (11)$$

Slope Sign Change (SSC): This feature calculates the number of slope sign changes in the segment, effectively identifying points where the signal direction changes. These slope sign changes can be determined as shown in equation 12. To exclude minor fluctuations, one can only count instances where the difference between consecutive samples exceeds a threshold value, using the condition specified in equation 11.

$$SSC = \sum_{n=1}^{L} ((x[n+1] - x[n]) \times (x[n] - x[n-1])) < 0 \quad (12)$$

Root Mean Square (RMS): This feature calculates the square root of the mean square of the segment as given in equation 13.

$$RMS = \sqrt{\frac{1}{L}\sum_{n=1}^{L} x[n]^2} \quad (13)$$

Mean (μ): This feature calculates the average of the segment as given in equation 14.

$$Mean = \mu = \frac{1}{L}\sum_{n=1}^{L} x[n] \quad (14)$$

Variance (σ^2): This feature calculates the squared deviations from the mean value. The average of the squared deviations gives variance. The variance value for each segment is calculated as given in equation 15.

$$Variance = \sigma^2 = \frac{1}{L}\sum_{n=1}^{L} (x[n] - \mu)^2 \quad (15)$$

Standard Deviation (STD): This feature calculates the square root of the variance as in equation 16.

$$STD = \sigma = \sqrt{\frac{1}{L}\sum_{n=1}^{L} (x[n] - \mu)^2} \quad (16)$$

Skewness (SKW): This property is a measure of the symmetry of a distribution. It is zero for symmetric distribution. In an unsymmetric distribution, the sign of the skewness value can be positive or negative, depending on whether it is skewed to the right or left. The skewness of a segment is calculated as given in equation 17.

$$SKW = \frac{\frac{1}{L}\sum_{n=1}^{L} (x[n] - \mu)^3}{\sigma^3} \quad (17)$$

Kurtosis (KURT): This feature measures the sharpness or flatness of a distribution. The KURT value of a segment as shown in equation 18, provides a quantitative assessment of the signal's distribution shape relative to a normal distribution.

$$KURT = \frac{\frac{1}{L}\sum_{n=1}^{L} (x[n] - \mu)^4}{\sigma^4} \quad (18)$$

2.4.2. Power spectral density estimation

Power spectral density is a vital engineering tool that shows how power is distributed across frequency components. Engineers typically use two main approaches to calculate this density. For simple linear systems, parametric methods work well because they're easier to model. However, non-parametric methods like the Welch technique prove more effective where modeling becomes challenging.

The Welch method offers a practical Fourier-based approach to Power Spectral Density (PSD) estimation. The signal is first divided into equal-length segments, making a notable tradeoff: longer segments give better frequency resolution, while shorter ones provide better time resolution. By overlapping these segments, the number of segments is increased without changing their length. Then, the Fourier transform is applied to the segments after windowing to minimize the spectral leakage. Each segment's periodogram $P_m(f)$ is then calculated by squaring its Fourier transform as given in equation 19.

$$P_m(f) \cong \frac{1}{K}\left|\sum_{k=0}^{K-1} x_m(k) e^{\frac{-j2\pi fk}{K}}\right|^2 \quad (19)$$

Here, K represents the length of the Fourier transform, while $x_m(k)$ denotes the mth segment weighted by a window function $w(k)$. To achieve a specific overlap ratio, we perform a shift-and-window operation on the signal $x(k)$ by sliding R samples at a time, as illustrated in equation 20. This sliding window approach allows us to maintain consistent overlap between adjacent segments while processing the entire signal.

$$x_m(k) \cong w(k)x(k + mR), \quad (k = 0,1,2,\dots,K-1, m = 0,1,2,\dots,M-1) \quad (20)$$

The PSD of the entire signal is estimated by averaging the periodograms of all segments, as shown in equation 21. This averaging process helps reduce variance in the spectral estimate and produces a more reliable representation of the signal's frequency characteristics.

$$P_{Welch}(f) = \frac{1}{M}\sum_{m=0}^{M-1} P_m(f) \quad (21)$$

2.4.3. Machine learning classifiers and hyperparameters

In this study, we have employed traditional machine learning approaches to classify bearing faults. We tested K-Nearest Neighbors (KNN), Decision Tree (DT), Support Vector Machine (SVM), Linear Discriminant (LD), and several ensemble approaches with various parameters. Table 1 presents the optimal parameters for the best-performing methods, highlighting the configuration that delivered superior classification accuracy in our bearing fault diagnosis system.

Table 1. The ML methods and selected parameters

Method	Parameters
SVM	Kernel function: linear, quadratic, cubic box constraint level: 1 multiclass meth.: one vs one
KNN	# of neighbors: 1 distance metric: Euclidean distance weight: equal
DT	Max. # of splits: 100 split criterion: Gini diversity index
LD	Preset: Linear discriminant covariance structure: full
Subspace Discriminant	Ensemble method: Subspace learner type: Discriminant # of learners:30 subspace dimension:65
Subspace KNN	Ensemble method: Subspace learner type: nearest neighbors # of learners:30 subspace dimension:65

2.5. Performance Evaluation Metrics

When evaluating classification performance, we must understand how accurately a model identifies positive class examples and under what conditions it makes errors. In this context, True Positive (TP) indicates when a model correctly classifies a genuinely positive example as positive, demonstrating successful detection of target class instances. Conversely, False Positive (FP) occurs when the model incorrectly labels a non-positive example as positive. Finally, a False Negative (FN) happens when the model assigns a positive example to a negative or different class, showing that it missed detecting a positive case it should have captured.

Using these values as shown in equations 22-25, it is common to employ Accuracy, Recall, Precision, and F1-score metrics to assess classification performance. These metrics provide complementary insights into different aspects of the model's effectiveness in correctly identifying and distinguishing between classes.

$$Accuracy = (\Sigma\ TPs) / (All\ predictions) \quad (22)$$

$$Prec. = TP / (TP + FP) \quad (23)$$

$$Rec. = TP / (TP + FN) \quad (24)$$

$$F1\text{-}score = 2\ x\ (Prec.\ x\ Rec.) / (Prec. + Rec.) \quad (25)$$

In multi-class applications, these metrics are calculated on a per-class basis. In this study, we have presented the average of class-specific metrics to evaluate overall model performance. We also assess performance through additional practical considerations like training speed, prediction speed, and model size.

3. Results and Discussion

This section presents the classification results obtained by applying machine learning approaches to features extracted from time-domain analysis and frequency-domain PSD. The performances of different classifiers with these distinct feature sets to diagnose bearing faults are compared.

3.1. PSD-Based Approach

Table 2 presents the performance of various ML approaches with PSD inputs for both validation and test data sets. The performances of the methods are compared through accuracy, precision, recall, and F1 score.

Table 2. Classification performance of ML classifiers with PSD input

ML Meth.	Validation				Test			
	Accuracy (%)	Precision (%)	Recall (%)	F1 Score (%)	Accuracy (%)	Precision (%)	Recall (%)	F1 Score (%)
LD	98.9	98.9	98.9	98.9	97.7	97.8	97.7	97.7
Sub. KNN	98.6	98.6	98.6	98.6	98.9	98.9	98.9	98.9
Sub. Disc.	98.5	98.5	98.5	98.5	97.7	97.8	97.7	97.7
Quad. SVM	95.3	95.5	95.3	95.4	94.3	94.5	94.3	94.4
DT	85.5	86.2	85.5	85.8	90.9	91.2	90.9	91.1
KNN	76.9	79.3	76.9	78.1	84.1	85.3	84.1	84.7

According to Table 2 the LD model demonstrates superior performance with 98.86% accuracy on the validation set, while the Subspace KNN model excels on the test set with 98.86% accuracy. The Subspace Discriminant model also shows consistently high performance on both validation (98.48%) and test (97.73%) sets. A quick assessment based on accuracy clearly distinguishes these three methods from others.

The SVM algorithm exhibits moderate-to-high performance with accuracy rates of 95.33% and 94.32% on validation and test sets respectively, approaching the performance of the top three methods. DT and KNN

algorithms show comparatively lower performance; however, their higher accuracy rates on test sets versus validation sets indicate good generalization capabilities without overfitting issues.

The proximity of precision, recall, and F1 scores to accuracy values across all models suggests a balanced performance distribution among classes. Ensemble methods (Subspace KNN and Subspace Discriminant) outperforming standard algorithms demonstrate their effectiveness in complex classification problems.

Similar performance across methods necessitates additional application-specific selection criteria to determine the optimal approach. Prediction speed, training duration, and model size are the further metrics for real-time applications. Table 3 compares these methods in terms of testing speed, training duration, and model size.

Table 3 Prediction speed, training time, and model size of the models with PSD inputs

ML Meth.	Prediction Speed (obs/sec)	Training Time (sec)	Model size
LD	2700	8.62	332 kB
Sub. KNN	550	176.2	13 MB
Sub. Disc.	700	168.1	3 MB
Quad. SVM	840	57.3	3 MB
DT	6600	15.52	55 kB
KNN	3000	119.3	838 kB

Table 3 reveals that the DT algorithm possesses the highest prediction speed, processing 6600 observations per second with just a 15.52-second training period. It also stands out as the most compact model at only 55 kB. KNN and LD algorithms also show impressive prediction speeds, processing 3000 and 2700 observations per second, respectively. The LD model trains fastest at 8.62 seconds and maintains a compact 332 kB size.

In contrast, the Subspace KNN algorithm exhibits the lowest prediction performance at 550 observations per second and requires the longest training time at 176.2 seconds. It also demands the largest model size of 13 MB. SVM and Subspace Discriminant models show moderate prediction speeds and model sizes.

When evaluating classification metrics and computational performance parameters together, the LD algorithm offers the optimal balance. It achieves high classification performance (98.86% validation and 97.73% test accuracy) while demonstrating superior computational efficiency with 2700 observations processed per second, 8.62-second training time, and compact 332 kB size. Although the Subspace KNN model provides the highest test accuracy (98.86%), its low prediction speed (550 obs/sec), extended training time (176.2 seconds), and large model size (13 MB) create computational resource disadvantages. Despite having the fastest prediction performance (6600 obs/sec) and smallest model size (55 kB), The DT algorithm shows lower classification performance among other models.

3.2 Time-domain features-based approach

This section presents the experimental results of classifying bearing faults utilizing features extracted in the time domain. The features are extracted from the segments with duration of 1 second and an overlap ratio of 25%. Table 4 demonstrates the performance capabilities of the previously dis cussed machine learning methodologies with time-domain features.

Table 4 Classification performance of ML classifiers with time-domain features

ML Meth.	Validation				Test			
	Accuracy (%)	Precision (%)	Recall (%)	F1 Score (%)	Accuracy (%)	Precision (%)	Recall (%)	F1 Score (%)
LD	97.9	98.0	97.9	97.8	98.9	99.1	99.0	99.0
Sub. KNN	72.5	72.2	72.5	72.3	60.2	65.7	60.8	61.5
Sub. Disc.	98.4	98.4	98.4	98.3	100.0	100.0	100.0	100.0
Lin. SVM	99.9	99.9	99.9	99.9	100.0	100.0	100.0	100.0
DT	97.0	97.1	97.0	97.0	97.7	98.2	97.7	97.8
KNN	99.5	99.5	99.5	99.5	100.0	100.0	100.0	100.0

Upon examining the results in the validation and test sets presented in Table 5, the SVM algorithm demonstrates superior performance with an accuracy rate of 99.9% in the validation and 100% in the test sets. Similarly, KNN and Subspace Discriminant algorithms achieved 100% accuracy in the test set. LD and DT algorithms provide satisfactory test results with accuracy rates of 98.9% and 97.7%, respectively. The Subspace KNN algorithm, however, shows significantly lower performance with a test accuracy of 60.2%. To evaluate the computational performances, Table 5 provides the prediction speed, training duration, and model size of the methods operated with time-domain features.

According to Table 5, the Linear Discriminant algorithm stands out with a training duration of 3.1 seconds and a prediction speed of 18,000 observations/second. The DT algorithm also demonstrates efficient performance with a training duration of 13.5 seconds and a prediction speed of 13,000 observations/second. The SVM algorithm has the lowest prediction speed at 960 observations/second. In terms of model size, LD (11 kB) and DT (19 kB) offer the most compact models, while Subspace KNN (2 MB) exhibits the highest storage requirement.

Table 5. Prediction speed, training time, and model size of the models with time-domain features

ML Meth.	Prediction Speed (obs/sec)	Training Time (sec)	Model size
LD	18000	3.1	11 kB
Sub. KNN	1500	64.3	2 MB
Sub. Disc.	1800	61.1	215 kB
Lin. SVM	960	44.7	760 kB
DT	13000	13.5	19 kB
KNN	14000	50.7	98 kB

When considering Table 4 and Table 5 together, the performance-efficiency balance of the algorithms becomes more evident. Although SVM, KNN, and Subspace Discriminant algorithms demonstrate superior classification performance, they exhibit different computational efficiency profiles. The Linear Discriminant algorithm presents a remarkable balance with 98.9% test accuracy, the fastest training duration, high prediction speed, and minimal model size. These characteristics make the LD algorithm preferable in resource-constrained environments or real-time applications. The Subspace KNN algorithm, when used with time-domain features, is considered the most disadvantageous option in terms of both performance and efficiency.

3.3. Overall Evaluation

Table 2 and Table 4 confirm that radar-based systems can effectively diagnose bearing faults through vibration detection. The Linear Discriminant algorithm becomes the most efficient method across both approaches while maintaining high classification accuracy. Subspace Discriminant performs nearly as well as SVM in terms of both classification accuracy and computational efficiency. Despite their computational advantages, DT and KNN algorithms demonstrate significantly lower classification performance in the PSD-based approach than other methods. The Subspace KNN approach performed particularly poorly when using time-domain features.

Although the conventional PSD-based approach achieves high accuracy across various algorithms, it presents disadvantages in training duration, prediction speed, and model size compared to time-domain methods. This efficiency gap primarily stems from the dimensional difference: PSD methods utilize 129 features (representing frequency points across the spectrum), while time-domain approaches require only 12 features. Figure 9 provides a co mparative summary of all methods, evaluating classification performance based on validation accuracy and computational efficiency based on prediction speed.

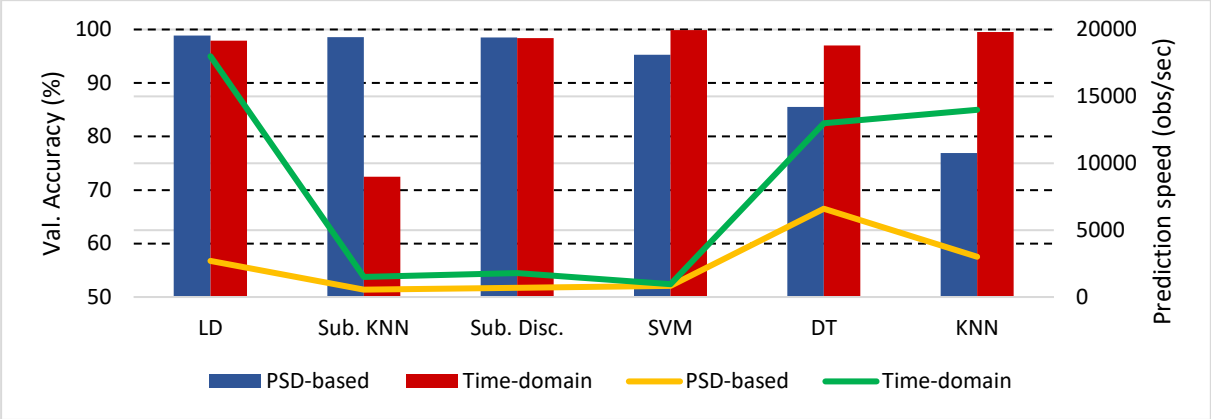

Figure 9 The overall comparison of the methods.

4.Conclusion

This study presents an innovative approach for radar-based diagnosis of bearing failures. Our research demonstrates that a 24 GHz radar system offers a non-contact detection of the bearing faults. Within the scope of this work, we have deliberately induced various defects in the inner race, outer race, and rolling elements of bearings. Corrosion, dust contamination, improper lubrication levels, and scratches are artificially generated with different severity levels and classified using a radar-based system.

PSD estimation and time-domain features with machine learning methodologies enabled the classification of these diverse bearing faults with accuracy exceeding 98%. These findings substantiate the capability of radar-based diagnostic techniques to differentiate various damage types in bearing components, offering a robust alternative to conventional contact-requiring methods.

Our investigation has contributed to the literature by providing radar signal data from 880 experiments encompassing 16 distinct classes. This dataset constitutes a valuable resource for future research endeavors. This pioneering study presents a new paradigm for non-contact fault diagnosis in bearing maintenance and monitoring processes.

Future research directions should examine the impact of different radar operating frequencies on performance, optimization of detection distance, and system reliability under various environmental conditions. Additionally, integration with real-time monitoring systems and

algorithms for detecting more complex fault types will contribute to advancements in this field.

Author Contributions

The percentages of the authors' contributions are presented below. All authors reviewed and approved the final version of the manuscript.

	Y.E.A.	S.B.Ç.
C	70	30
D	30	70
S	50	50
DCP	50	50
DAI	50	50
L	50	50
W	80	20
CR	50	50
SR	50	50
PM	50	50
FA	0	100

C=Concept, D= design, S= supervision, DCP= data collection and/or processing, DAI= data analysis and/or interpretation, L= literature search, W= writing, CR= critical review, SR= submission and revision, PM= project management, FA= funding acquisition.

Conflict of Interest

The authors declared that there is no conflict of interest.

Ethical Consideration

Ethics committee approval was not required for this study because of there was no study on animals or humans.

Acknowledgements

The authors gratefully acknowledge the ART company for their valuable contribution in supplying the bearing components and for their technical expertise in assembling the artificially aged bearing specimens essential for this research.

References

Acar YE, Cetinkal SB. 2025. SU RF Sensing Lab. Bearing Fault Diagnosis Dataset. Kaggle. https://www.kaggle.com/datasets/yunusemreacar1/su-rf-sensing-lab-bearing-fault-diagnosis-dataset (accesed date, March 15, 2025).

Acar YE. 2024. Radar-enabled non-contact speed estimation for rotating electrical machinery. Measurement, 235: 114989.

Acar YE, Saritas I, Yaldiz E. 2021. An S-band zero-IF SFCW through-the-wall radar for range, respiration rate, and DOA estimation. Measurement, 186: 110221.

Akar M, Hekim M, Orhan U. 2015. Mechanical fault detection in permanent magnet synchronous motors using equal width discretization-based probability distribution and a neural network model. Turk J Electr Eng Comput Sci, 23: 813–823.

Gu C, Huang TY, Li C, Lin J. 2017. Microwave and millimeter-wave radars for vital sign monitoring. In: Amin MG, editor. Radar for Indoor Monitoring. CRC Press, Florida, USA, pp: 199–226.

Brito LC, Susto GA, Brito JN, Duarte MA. 2022. An explainable artificial intelligence approach for unsupervised fault detection and diagnosis in rotating machinery. Mech Syst Signal Process, 163: 108105.

Ercire M, Ünsal A. 2024. Asenkron motor eş zamanlı çoklu arızalarının titreşim sinyalleri ile çok etiketli sınıflandırılması. Duzce Univ J Sci Technol, 12: 1296–1314.

Ertarğın M, Yıldırım Ö, Orhan A. 2023. Motor yataklarında meydana gelen arızaları tespit etmek için yeni bir tek boyutlu konvolüsyonel sinir ağı modeli. Firat Univ J Eng Sci, 35: 669–678.

Glowacz A, Sulowicz M, Zielonka J, Li Z, Glowacz W, Kumar A. 2025. Acoustic fault diagnosis of three-phase induction motors using smartphone and deep learning. Expert Syst Appl, 262: 125633.

Kao IH, Wang WJ, Lai YH, Perng JW. 2018. Analysis of permanent magnet synchronous motor fault diagnosis based on learning. IEEE Trans Instrum Meas, 68: 310–324.

Karabacak YE, Özmen NG. 2022. Rulmanlarda titreşim verilerinden durum izleme ve arıza teşhisi için derin öğrenme yönteminin uygulanması. Konya J Eng Sci, 10: 346–365.

Kilic ME, Acar YE. 2024. Performance evaluation of the time-frequency transformation methods on electrical machinery fault detection. Bitlis Eren Univ J Sci, 13: 1147–1157.

Liu W, Chen W, Zhang Z. 2020. A novel fault diagnosis approach for rolling bearing based on high-order synchrosqueezing transform and detrended fluctuation analysis. IEEE Access, 8: 12533–12541.

Lopez-Perez D, Antonino-Daviu J. 2017. Application of infrared thermography to failure detection in industrial induction motors: Case stories. IEEE Trans Ind Appl, 53: 1901–1908.

Mehta A, Goyal D, Choudhary A, Pabla B, Belghith S. 2021. Machine learning-based fault diagnosis of self-aligning bearings for rotating machinery using infrared thermography. Math Probl Eng, 2021: 9947300.

Mueller PN, Woelfl L, Can S. 2023. Bridging the gap between AI and the industry—a study on bearing fault detection in PMSM-driven systems using CNN and inverter measurement. Eng Appl Artif Intell, 126: 106834.

Nayana B, Geethanjali P. 2017. Analysis of statistical time-domain features effectiveness in identification of bearing faults from vibration signal. IEEE Sens J, 17: 5618–5625.

Pacheco-Cherrez J, Fortoul-Diaz JA, Cortes Santacruz F, Aloso Valerdi LM, Ibarra Zarate DI. 2022. Bearing fault detection with vibration and acoustic signals: Comparison among different machine learning classification methods. Eng Fail Anal, 139: 106515.

Qiao M, Yan S, Tang X, Xu C. 2020. Deep convolutional and LSTM recurrent neural networks for rolling bearing fault diagnosis under strong noises and variable loads. IEEE Access, 8: 66257–66269.

Sabir R, Rosato D, Hartmann S, Gühmann C. 2019. LSTM based bearing fault diagnosis of electrical machines using motor current signal. In: Proceedings of 18th IEEE International Conference on Machine Learning and Applications, December 16–19, Boca Raton, USA, pp: 613–618.

Seflek I, Acar YE, Yaldiz E. 2020. Small motion detection and non-contact vital signs monitoring with continuous wave Doppler radars. Elektron Elektrotech, 26: 54–60.

Smith WA, Randall RB. 2015. Rolling element bearing diagnostics using the Case Western Reserve University data: A benchmark study. Mech Syst Signal Process, 64: 100–131.

Zhang S, Zhang S, Wang B, Habetler TG. 2020a. Deep learning

algorithms for bearing fault diagnostics—A comprehensive review. IEEE Access, 8: 29857–29881.

Zhang Y, Xing K, Bai R, Sun D, Meng Z. 2020b. An enhanced convolutional neural network for bearing fault diagnosis based on time–frequency image. Measurement, 157: 107667.

Zhu Z, Lei Y, Qi G, Chai Y, Mazur N, An Y, Huang X. 2023. A review of the application of deep learning in intelligent fault diagnosis of rotating machinery. Measurement, 206: 112346.

Black Sea Journal of Engineering and Science
doi: 10.34248/bsengineering.1663621

Open Access Journal
e-ISSN: 2619 – 8991

Research Article
Volume 8 - Issue 5: 1339-1348 / September 2025

EVALUATION OF SALT STRESS TOLERANCE IN LETTUCE (*Lactuca sativa* L.) CULTIVARS UNDER HYDROPONIC CONDITIONS

Alim AYDIN[1]*

[1]*Kırsehir Ahi Evran University, Faculty of Agriculture, Department of Horticulture, 40100, Kırsehir, Türkiye*

Abstract:
Salt stress is one of the most important abiotic stress factors that significantly negatively affect plant growth and yield. This study evaluated the morphological and physiological responses of eight lettuce (*Lactuca sativa* L.) varieties to salt stress under hydroponic conditions. The lettuce varieties were grown in an aerated hydroponic system under control (1.8 dS/m) and salt stress (6.0 dS/m) conditions. The results showed that salt stress caused significant reductions in shoot biomass, particularly compared to root biomass characteristics. The varieties with the greatest reductions in biomass parameters under salt stress conditions were Chicarita, Triplex, and Levistro, while Baeza and Cherokee produced higher biomass. Morphological characteristics such as leaf number, stem diameter, plant height, and leaf area were also significantly affected by salt stress, with leaf area—the edible part of the lettuce—being the most affected by salt stress. As with other parameters, the Baeza, Kireve, and Cherokee varieties were more stable in these parameters. The Chicarita variety again showed the lowest performance in these parameters. Leaf color parameters such as L, a*, b*, chroma, and hue angle were significantly affected by salt stress. Under salt stress conditions, the Expedition and Kireve varieties had more vibrant colors than other varieties. Chlorophyll-a, chlorophyll-b, and total chlorophyll content increased in some varieties due to salt stress, while they decreased in others. Salt stress generally increased leaf sap EC and SSC values. The effect of salt stress on fruit juice pH was not statistically significant. In conclusion, salt stress negatively affected shoot parameters in lettuce varieties, while in some varieties it caused an increase in root morphology. These differences in response to salt stress are related to stress adaptation ability, so the parameters used in this study can be used as selection criteria for lettuce or other plants. Additionally, the varieties identified as salt-tolerant in this study can be used in breeding programs aimed at growing plants under saline conditions.

Keywords: Lettuce, Salt stress, Chlorophyll, Leaf color

***Corresponding author:** Kırsehir Ahi Evran University, Faculty of Agriculture, Department of Horticulture, 40100, Kırsehir, Türkiye
E mail: alim.aydin@ahievran.edu.tr (A. AYDIN)
Alim AYDIN https://orcid.org/0000-0002-9424-5556

Received: March 23, 2025
Accepted: June 24, 2025
Published: September 15, 2025

Cite as: Aydın A. 2025. Evaluation of salt stress tolerance in lettuce (*Lactuca sativa* L.) cultivars under hydroponic conditions. BSJ Eng Sci, 8(5): 1339-1348.

1. Introduction

Salt stress, one of the most harmful abiotic stress factors, causes physiological disorders in plants, which ultimately results in plant death and leads to a decrease in crop yield and quality. Salt stress is increasing from arid to semi-arid regions, thereby progressively limiting agricultural production (Sakadevan and Nguyen, 2010; Hussain et al., 2019; Rouphael et al., 2018). Due to excessive salt concentrations, approximately 2,000 hectares of arable land are lost every day worldwide (Shrivastava and Kumar, 2015). Salt concentration in irrigation water accumulates in the root zone of plants, causing stunted plant growth. In plants grown under saline conditions, sodium and chloride ion accumulation disrupts physiological balance by accumulating in plant cell compartments (Sakadevan and Nguyen, 2010; Muhammad et al., 2022). In addition, all soluble salts that contribute to soil salinity cause physiological stress in plants in arid and semi-arid regions (Chinnusamy et al., 2005; Hussain et al., 2019). To mitigate the adverse effects of salt stress on plants, it is necessary to adopt strategies for the more appropriate use of land and water resources (Yamaguchi and Blumwald, 2005). These strategies may enable vegetable production under saline conditions (Moncada et al., 2018; Moncada et al., 2021). The use of hydroponic cultivation systems helps overcome salt stress and other abiotic stresses and ensures more efficient and higher quality yields in some vegetable species (Settanni et al., 2013; Moncada et al., 2018; Moncada et al., 2021). In hydroponic systems, plants are supplied with a mineral nutrient solution, and their roots are supported by mineral or organic

substrates or floating panels (floating systems) that hold the plants above the nutrient solution. The water used to prepare nutrient solutions should have a particularly low salt concentration, as the addition of soluble mineral fertilizers can affect the electrical conductivity (EC) of the nutrient solution (Moncada et al., 2020). Hydroponics is one of the most promising systems in protected agriculture due to its simplicity, ease of operation, higher yield, economic feasibility and nutritionally superior products. Compared to traditional cultivation, hydroponics provides more efficient, early, high-quality and healthy products. In addition, water and fertilizer are used more efficiently than in traditional cultivation. Due to the widespread use of intensive agricultural practices in Mediterranean regions, excessive use of irrigation water has caused significant seawater leakage, which in turn has led to increased salinity in groundwater. The use of this water, which has a high EC value, in hydroponic systems can lead to nutrient solutions that exceed the tolerance thresholds of many vegetable species (Mariani and Ferrante, 2017). For these reasons, researchers have focused on understanding the adaptation mechanisms of plants to salt stress to increase the salt tolerance of vegetables (Rao et al., 2006). Lettuce (*Lactuca sativa* L.), which is rich in iron, which is essential for human health, is an important vegetable in terms of nutrition. It is mostly consumed as part of the daily diet in salads (Moncada et al., 2020). However, lettuce cultivation is quite sensitive to the adverse effects of salinity stress. Additionally, excessive accumulation of sodium and nitrate in vegetables is a particularly important issue for humans (Shi et al., 2022). Adverse soil conditions, challenging environmental factors, and irrigation with low-quality water severely limit lettuce production, significantly reducing its yield potential. Salt stress reduced seed germination, leaf water content, and chlorophyll content in lettuce plants, and reduced root and shoot growth in terms of biomass, while increasing sodium and chloride ion concentrations and lipid peroxidation in leaf tissues (Kaya et al., 2002; Barassi et al., 2006; Eraslan et al., 2007; Pérez-López et al., 2013Mohammadi and Khoshgoftarmanesh, 2014). Cultivated lettuce varieties are more sensitive to salt stress than wild species due to differences in root structure and varying uptake and accumulation of sodium. Lettuce production in soils and water with high salt concentrations can be increased by selecting salt-tolerant varieties through intraspecific genetic diversity (Wei et al., 2014).

The aim of this study is to determine the tolerance levels of eight different lettuce (*Lactuca sativa* L.) varieties to salt stress and to evaluate their physiological and morphological responses to salinity under static water culture conditions.

2. Materials and Methods

The experiment was conducted in a fully automated Venlo-type glass greenhouse at Kırşehir Ahi Evran University (38°08'02"N, 34°07'08"E) between January and April 2025. The seeds of the lettuce varieties (Table 1) were supplied by RIJK ZWAAN (Rijk Zwaan Seed Production and Seed Trade B.V.).

Table 1. provides information on lettuce varieties

Variety	Type
Levistro	Lollo type
Cencibel	Lollo type
Baeza	Mini Romaine
Kireve	Oak leaf lettuce
Expedition	Incised leaf sweet crisp frisée
Triplex	incised leaf sweet crisp frisée
Chicarita	Crunchy
Cherokee	Batavia

2.1. Sowing Seeds and Planting Seedlings

Seeds were sown on January 20, 2025, and seedlings were transplanted on February 17, 2025. Seed sowing was carried out in 128-cell pots filled with a 3:1 peat:perlite mixture. Transplanting was performed when the seedlings reached the 3-4 true leaf stage. Greenhouse climate control operations were carried out using an automation system.

2.2. Establishment of the Hydroponic System and Salt Stress Testing

Eight lettuce varieties were planted in a hydroponic system (130 L containers covered with aerated and perforated composite panels) according to a randomized plot design containing three replicates and three plants per replicate (9 control, 9 salt). The nutrient solution used in the hydroponic system consisted of 1500 µM $Ca(NO_3)_2$, 750 µM K_2SO_4, 650 µM $MgSO_4$, 500 µM KH_2PO_4, 10 µM H_3BO_3, 0.5 µM $MnSO_4$, 0.5 µM $ZnSO_4$, 0.4 µM $CuSO_4$, 0.4 µM Na_2MoO_4, and 80 µM Fe EDDHA, with a pH adjusted to 6.5. Salt application began two days after planting and gradually increased until reaching 6.00 dS/m on the sixth day. The salt level was adjusted by adding NaCl to the nutrient solution. The same genotypes were also grown under control conditions (1.8 dS/m) in addition to the saline water application. After reaching full salt concentration (6.00 dS/m), the plants were grown in the hydroponic system for 30 days, after which the experiment was terminated. Greenhouse cooling (fan-pad cooling) and humidification (high-pressure misting) were automated. When the temperature exceeded 27 °C, the cooling system was activated, and when the relative humidity dropped below 50%, misting continued until the humidity reached 65%. When the temperature dropped below 14°C, the geothermal heating system was activated.

2.3. Parameters Measured in Plants under Salt Stress Conditions

2.3.1. Determination of biomass parameters

The stem diameters of the plants were measured in

millimeters (mm) using a digital caliper just below the first leaves. The main stem length and canopy diameter were measured in centimeters (cm) using a tape measure. The number of leaves (number of leaves per plant) was recorded by counting all the leaves on the plant at the end of the experiment. The fresh weights of leaves and roots were determined by separating the plants into root and above-ground parts and weighing them during harvest (g). The dry weights of leaves and roots were obtained by drying fresh samples in an oven at 65°C for 48 hours (g). To determine root length (cm), diameter (mm), and volume (cm^3), 5 g fresh root material subsamples were collected from each treatment group. These root subsamples were scanned and analyzed using a root imaging system (WinRhizoRegular LA2400, Regent Instruments). The values obtained for 5 g of roots were then calculated proportionally to the total fresh root weight to determine the root length and root volume for each plant.

2.3.2. Determination of leaf sap electrical conductivity (EC), pH, and soluble solids content (SSC)

Leaf sap EC and pH were measured using an Extech EC meter and pH meter, respectively. Soluble solid content (SSC) was measured using a Hanna HI96801 digital refractometer.

2.3.3. Determination of hue angle value

Color parameters such as CIE L, a*, b*, chroma (C), and hue angle (h°) were measured using a Minolta CR-400 colorimeter (Konica Minolta, Japan). Measurements were taken at three different points for each lettuce leaf sample. The device was calibrated using a standard calibration plate prior to measurement (Özdemir, 2001). The hue angle was calculated using the following formula (equation 1):

$$\text{Hue angle } (h^\circ) = \left(\frac{180}{\pi}\right) \times \arctan\left(\frac{b^*}{a^*}\right) \quad (1)$$

The hue angle value indicates the color shade: 0° = red, 60° = yellow, 120° = green, 180° = cyan, 240° = blue, 300° = magenta, 360° or 0° = red.

2.3.4. Chlorophyll a, b, total chlorophyll, and carotenoid analysis

Total chlorophyll and carotenoid, chlorophyll a, and chlorophyll b contents were determined according to the Arnon, (1949) method. Measurements were performed using a spectrophotometer (Shimadzu Model 1208, Tokyo, Japan) for each process.

2.4. Statistical Analysis

Data obtained from the hydroponic experiment were analyzed using one-way analysis of variance (ANOVA) at a 5% significance level with the SPSS 18.0 statistical software package (IBM, Chicago, IL, USA). Differences between means were determined using Duncan's multiple range tests.

3. Results

Under control and salt stress conditions, the leaf and root weights (both fresh and dry) of lettuce plants were evaluated in Table 2. Salt stress caused a decrease in fresh leaf weight in all varieties, with the greatest decreases observed in the Chicarita (−58%), Levistro (−49%), and Triplex (−47%) varieties, respectively. The smallest decreases were observed in the Baeza (−7%) and Cherokee (−19%) varieties. Under control and salt stress conditions, the highest fresh leaf weight was determined in the Expedition variety. Leaf dry weight results showed a similar trend to fresh leaf weight results. In some varieties, an increase in root fresh weight was observed under salt stress conditions. Significant increases were observed in the Levistro (+12%), Baeza (+3%), Cencibel (+59%), Cherokee (+45%), Expedition (+24%), and Triplex (+17%) varieties. In the other two varieties, Chicarita (−29%) and Kireve (−13%), decreases were observed. As shown in Figure 1, despite the differences between varieties, the Kireve variety had the highest root fresh weight under both control and salt stress conditions.

Table 2. Effect of salt stress on leaf fresh weight, leaf dry weight, root fresh weight, root dry weight, and their percentage changes in lettuce varieties

Variety	Leaf Fresh Weight (g)			Leaf Dry Weight (g)			Root Fresh Weight (g)			Root Dry Weight (g)		
	Control	Salt	%C	Control	Salt	%C	Control	Salt	%C	Control	Salt	%C
Levistro	126.07cd	64.23de	-49	18.44cd	9.61de	-48	11.40bc	12.73abc	12	1.59bc	1.84abc	16
Cencibel	82.17e	56.80e	-31	12.12e	8.50e	-30	7.20d	11.47abc	59	1.15cd	1.52abc	32
Baeza	99.27de	91.90cd	-7	14.61de	13.51cd	-8	9.23cd	9.53bc	3	1.24cd	1.36bc	10
Kireve	205.47b	139.43ab	-32	29.78b	20.35ab	-32	21.83a	18.97a	-13	2.90a	2.62a	-9
Expedition	275.90a	169.60a	-39	39.79a	24.66a	-38	14.20b	17.63ab	24	2.03b	2.29ab	13
Triplex	136.57c	72.33de	-47	19.94c	10.71de	-46	8.73cd	10.20abc	17	1.18cd	1.44bc	23
Chicarita	106.30c-e	44.33e	-58	15.57c-e	6.76e	-57	6.77d	4.83c	-29	1.01d	0.77c	-24
Cherokee	140.27c	113.63bc	-19	20.47c	16.61bc	-19	9.80cd	14.2ab	45	1.39cd	2.03ab	46
P value	0.000	0.000		0.000	0.000		0.000	0.001		0.000	0.001	

%C= percentage change compared to the control. N.S= not significant. Means that do not share a letter are significantly different

(P<0.05).

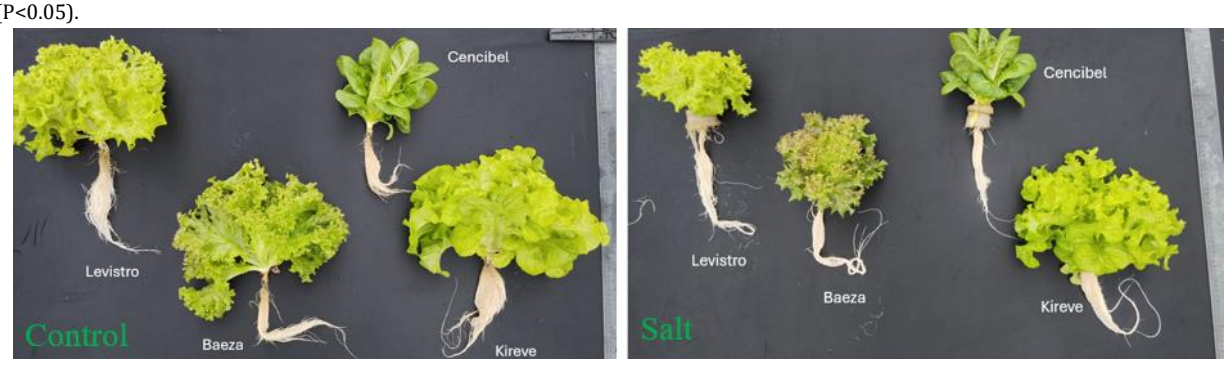

Figure 1. Effect of salt stress on growth and morphology of levistro, cencibel, baeza and kireve lettuce varieties.

Under control conditions, the highest number of leaves was observed in the Kireve variety, while the lowest number of leaves was observed in the Cencibel variety. Similarly, under salt stress conditions, the highest number of leaves was observed in the Kireve variety, as was the case under control conditions. Under salt stress, the lowest number of leaves was observed in the Cencibel and Levistro varieties. Salt stress had a statistically significant effect on stem diameter in all varieties (P< 0.001). Under both control and salt stress conditions, the tallest plants were measured in the Kireve variety, while the shortest plants were measured in the Triplex variety. Salt stress caused a reduction in plant height ranging from 11% to 31% depending on the variety. Leaf areas also decreased significantly in all varieties under salt stress. The greatest reduction in the leaf area was observed in the Chicarita variety (58%), while the lowest reduction was observed in the Baeza variety (7%) (Table 3). Despite the general decrease under salt stress conditions, the Expedition variety had the highest leaf area in both control and salt stress treatments (Figure 2).

Table 3. Effect of salt stress on number of leaves, main stem diameter, plant height, leaf area, and their percentage changes in lettuce varieties

Variety	Number of Leaves			Main Stem Diameter (mm)			Plant Height (cm)			Leaf Area (cm^2)		
	Control	Salt	%C	Control	Salt	%C	Control	Salt	%C	Control	Salt	%C
Levistro	13.67de	12.00d	-12	12.94a	7.51bc	-42	23.50a-c	18.67cd	-21	4724.00cd	2407.00de	-49
Cencibel	11.33e	11.33d	0	8.59c	7.29bc	-15	23.67a-c	17.00d	-28	3079.00e	2129.00e	-31
Baeza	20.33bc	22.67ab	11	11.76ab	13.61a	16	20.83bc	17.33d	-17	3719.90de	3443.80cd	-7
Kireve	26.67a	27.33a	2	10.48bc	9.99b	-5	26.83a	22.67a	-16	7700.00b	5225.10ab	-32
Expedition	21.33b	19.67bc	-8	9.49bc	9.45b	0	25.00ab	22.33ab	-11	10338.00a	6357.00a	-39
Triplex	17.00b-d	14.33cd	-16	8.37c	5.95c	-29	19.67c	16.67d	-15	5117.70c	2711.00de	-47
Chicarita	19.33bc	14.33cd	-26	10.10bc	8.11bc	-20	25.67ab	17.67d	-31	3983.50c-e	1661.30e	-58
Cherokee	15.67c-e	16.00cd	2	11.29ab	10.38ab	-8	25.00ab	20.33bc	-19	5256.00c	4258.3bc	-19
P value	0.000	0.000		0.000	0.000		0.003	0.000		0.000	0.000	

%C= percentage change compared to the control. N.S= not significant. Means that do not share a letter are significantly different (P<0.05).

Figure 2. Effect of salt stress on growth and morphology of expedition, triplex, chicarita and cherokee lettuce varieties.

A decrease in canopy diameter was observed in all lettuce varieties grown under salt stress. The highest canopy diameter under salt stress was measured in the Kireve variety. In terms of root length, the Kireve variety had the longest roots under both control and salt stress conditions, while the Chicarita variety had the shortest roots under salt stress. Under salt stress conditions, the highest root volume was observed in the Expedition variety (11.64 cm^3), followed by the Kireve (10.75 cm^3) and Levistro (10.02 cm^3) varieties. The lowest root volumes were observed in the Chicarita (3.83 cm^3) and Triplex (4.77 cm^3) varieties. Under salt stress, root diameter decreased in the Levistro, Cencibel, and Kireve varieties, while in other varieties, root diameter increased by 2% to 27% under salt conditions. Canopy diameter, root length, root volume, and root diameter were significantly influenced by genotype at the P< 0.001 level (Table 4).

Table 4. Effect of salt stress on canopy diameter, root length, root volume, root diameter, and their percentage changes in lettuce varieties

Variety	Canopy Diameter (cm)			Root Length (cm)			Root Volume (cm^3)			Root Diameter (mm)		
	Control	Salt	%C	Control	Salt	%C	Control	Salt	%C	Control	Salt	%C
Levistro	29.00bc	23.33bc	-20	3861.53b	4869.87b	26	8.26b	10.02a	21	0.52 ab	0.52a	-1
Cencibel	24.33cd	23.00c	-5	3062.31c	3557.58c	16	6.81b	6.16b	-10	0.53 ab	0.47b	-12
Baeza	18.00d	17.33cd	-3	3328.71c	3164.86c	-5	6.96b	7.08b	2	0.52 ab	0.53a	3
Kireve	37.00a	30.67a	-17	4255.52ab	4201.27b	-1	13.24a	10.75a	-19	0.63a	0.57a	-9
Expedition	32.67ab	29.67ab	-9	4545.95a	5514.79a	21	7.84b	11.64a	49	0.47 ab	0.52a	10
Triplex	24.00cd	19.00cd	-21	3998.28b	2318.25d	-42	4.50c	4.77c	6	0.40b	0.51a	27
Chicarita	19.67d	16.00d	-19	2980.23d	2293.28d	-23	4.77c	3.83c	-20	0.45 ab	0.46b	2
Cherokee	29.00bc	23.67bc	-18	3241.67c	4197.39b	29	6.70b	9.93a	48	0.51ab	0.55a	7
P value	0.000	0.000		0.000	0.000		0.000	0.000		0.000	0.000	

%C= percentage change compared to the control. N.S= not significant. Means that do not share a letter are significantly different (P<0.05).

In lettuce varieties, all leaf color parameters, including lightness (L), redness/greenness (a*), yellowness (b*), color (C), and color tone angle (°), were significantly affected by salt stress. (P< 0.05 or P< 0.001 depending on the parameter) (Table 5). The lightness value (L) decreased in most varieties under salt stress, resulting in a duller appearance of the leaves. The most pronounced decrease in L was observed in the Levistro (-13%) and Cencibel (-12%) varieties, while a significant increase (+17%) was detected in the Expedition variety. This variety exhibited lighter-colored leaves under salt stress conditions. The a* value, representing the red-green axis, decreased in most varieties, with the largest decrease observed in the Cencibel (-44%) variety, followed by the Triplex (-13%) variety. Interestingly, under salt stress conditions, the Expedition (+13%) and Kireve (+5%) varieties exhibited a redder color tone. The b* value decreased in the Triplex (-14%), Chicarita (-14%), and Cencibel (-13%) varieties due to salt stress, while the b* value increased in the Levistro (+8%), Expedition (+10%), and Kireve (+4%) varieties, which were more affected by salt stress and exhibited increased yellow pigmentation in their leaves. Under salt stress, the chroma values decreased in most varieties, with the greatest decrease observed in the Cencibel (-19%) and Triplex (-14%) varieties. However, the chroma values increased in the Expedition (+11%), Levistro (+6%), and Kireve (+4%) varieties, showing stronger color saturation under stress conditions. Regarding the color tone angle, which reflects the overall perceived color tone, salt stress had little effect on most varieties. The most significant decrease occurred in the Cencibel (-8%) variety. In the Baeza (+1%) and Chicarita (+2%) varieties, slight increases were observed. Under salt stress, the Kireve, Expedition, Triplex, and Cherokee varieties maintained relatively stable color tone angles.

Table 5. Effect of salt stress on leaf color parameters (l, a*, b*, chroma, hue angle) and their percentage changes in lettuce varieties

Variety	L			a*			b*			Chroma (C)			Hue Angle (°)		
	Control	Salt	%C	Control	Salt	%C	Control	Salt	%C	Control	Salt	%C	Control	Salt	%C
Levistro	56.69a	49.33a-d	-13	-17.81bc	-17.33cd	-3	30.52b	33.00b	8	35.27a-c	37.28b	6	120.08bc	117.70b	-2
Cencibel	46.00b	40.67d	-12	-15.00ab	-8.33a	-44	26.33b-d	23.00c	-13	30.33b-d	24.48cd	-19	119.57c	109.99c	-8
Baeza	45.67b	45.00b-d	-1	-15.67ab	-15.00bc	-4	23.00cd	21.00cd	-9	27.84cd	25.82cd	-7	124.29a	125.62a	1
Kireve	56.33a	57.33a	2	-21.33c	-22.33e	5	38.00a	39.67a	4	43.58a	45.53a	4	119.30c	119.37b	0
Expedition	46.00b	54.00ab	17	-18.33bc	-20.67de	13	29.67bc	32.67b	10	34.88bc	38.68b	11	121.75a-c	122.25ab	0
Triplex	45.67b	41.67d	-9	-16.00ab	-14.00bc	-13	28.67bc	24.67c	-14	32.83bc	28.38c	-14	119.17c	119.50b	0
Chicarita	43.33b	44.00cd	2	-13.00a	-12.00ab	-8	19.33d	16.67d	-14	23.30d	20.54d	-12	123.86ab	125.81a	2
Cherokee	56.00a	51.00a-c	-9	-19.00bc	-17.33cd	-9	33.00ab	31.00b	-6	38.08ab	35.53b	-7	119.90c	119.19b	-1
P value	0.000	0.000		0.001	0.000		0.000	0.000		0.000	0.000		0.001	0.000	

%C= percentage change compared to the control. N.S= not significant. Means that do not share a letter are significantly different (P<0.05).

The chlorophyll-a, chlorophyll-b, total chlorophyll, and total carotenoid contents and % changes of lettuce varieties under control and salt stress conditions are presented in Table 6. Salt stress causes significant differences in pigment contents among varieties. While all chlorophyll contents were significantly affected by salt stress (P< 0.05), the change in total carotenoid content was not statistically significant (P>0.05). Salt stress caused an increase in chlorophyll-a content in some lettuce varieties, while it caused a decrease in others. The most significant increase was observed in the Levistro variety (64%), followed by Baeza (37%) and Chicarita (14%). In contrast, chlorophyll-a content decreased significantly in the Triplex (-28%), Expedition (-25%), and Cherokee (-10%) varieties. When evaluating these results in response to salt stress, it can be concluded that Levistro and Baeza can increase chlorophyll-a accumulation, while other varieties are negatively affected by salt stress. Similar trends were observed in chlorophyll-b content as in chlorophyll-a content. Increases were observed in the Levistro (+50%), Baeza (+36%), and Chicarita (+21%) varieties under salt stress, while decreases were observed in the Triplex (-43%), Expedition (-26%), and Cencibel and Cherokee (-19%) varieties. Similar results to those observed in chlorophyll-a and b were obtained for total chlorophyll content. The Levistro variety showed the highest increase (+60%), while the Triplex variety showed the greatest decrease (-33%). Changes in total carotenoid content among varieties under control and salt stress conditions were not statistically significant.

Table 6. Effect of salt stress on chlorophyll-a, chlorophyll-b, total chlorophyll, total carotenoid contents, and their percentage changes in lettuce varieties (mg L^{-1})

Variety	Chlorophyll-a (mg l^{-1})			Chlorophyll-b (mg l^{-1})			Total Chlorophyll (mg l^{-1})			Total Carotenoid (mg l^{-1})		
	Control	Salt	%C	Control	Salt	%C	Control	Salt	%C	Control	Salt	%C
Levistro	0.28b	0.47ab	64	0.12b	0.17b	50	0.40c	0.64c	60	0.06a	0.09a	63
Cencibel	0.5ab	0.48ab	-4	0.24ab	0.20b	-19	0.74a-c	0.67c	-9	0.11a	0.09a	-11
Baeza	0.64ab	0.88a	37	0.45a	0.61a	36	1.10ab	1.50a	37	0.11a	0.08a	-11
Kireve	0.33b	0.33b	1	0.14b	0.14b	-1	0.47bc	0.48c	0	0.07a	0.08a	18
Expedition	0.64ab	0.48ab	-25	0.34ab	0.26b	-26	0.99a-c	0.74bc	-25	0.12a	0.07a	-36
Triplex	0.47ab	0.34b	-28	0.26ab	0.15b	-43	0.73a-c	0.49c	-33	0.08a	0.08a	-1
Chicarita	0.77a	0.87a	14	0.48a	0.58a	21	1.25a	1.45ab	16	0.11a	0.11a	-2
Cherokee	0.57ab	0.51ab	-10	0.24ab	0.20b	-19	0.82a-c	0.71bc	-13	0.11a	0.11a	-1
P value	0.008	0.004		0.004	0.000		0.006	0.001		0.075	0.141	

%C= percentage change compared to the control. N.S= not significant. Means that do not share a letter are significantly different (P<0.05).

The effects of salt stress on leaf sap electrical conductivity (EC), pH, and soluble solids content (SSC) in lettuce varieties are presented in Table 7. It shows that significant variety differences were observed in EC and SSC values (P< 0.05) and that pH was not statistically affected. Salt stress significantly increased EC in all varieties, representing increased ion accumulation in leaf tissue. The highest increase in EC was observed in the

Chicarita variety (+221%), followed by Triplex (+109%) and Cherokee (+106%). The lowest increase in EC was observed in the Kireve (+34%) and Baez (+49%) varieties. Leaf sap pH under control and salt stress conditions was not significantly different among varieties (P>0.05). The soluble solid content (SSC) in leaf sap was significantly affected by salt stress (P< 0.01). Salt stress increased SSC content in the Expedition (+78%), Baeza, Chicarita (+41%), and Cherokee (+30%) varieties. The lowest increase was observed in the Levistro (+7%) variety.

Table 7. Effect of salt stress on leaf sap electrical conductivity (ec), ph, soluble solids content (ssc), and their percentage changes in lettuce varieties

Variety	Leaf Sap EC (dS/m)			Leaf Sap pH			Leaf Sap Soluble Solids Content (%)		
	Control	Salt	%C	Control	Salt	%C	Control	Salt	%C
Levistro	4.57	8.06ab	76	6.59	6.52	-1	2.70a	2.90b	7
Cencibel	4.87	9.44a	94	6.81	6.39	-6	2.60a	3.20a	23
Baeza	4.24	6.33b	49	6.57	6.47	-2	2.20b	3.10ab	41
Kireve	5.15	6.89b	34	6.55	6.36	-3	2.40ab	2.90b	21
Expedition	4.17	7.47b	79	6.42	6.39	0	1.80c	3.20a	78
Triplex	4.08	8.51ab	109	6.54	6.58	1	1.90c	2.40c	26
Chicarita	2.07	6.64b	221	6.42	6.50	1	2.20b	3.10ab	41
Cherokee	4.55	9.39a	106	6.48	6.65	3	2.30b	3.00ab	30
P value	N.S	0.004		N.S	N.S		0.002	0.003	

4. Discussion

Salt stress inhibits plant growth and biomass accumulation by reducing water uptake, altering ion homeostasis, and disrupting metabolic activities (Aydın and Yetişir, 2022; Aydın, 2024; Munns and Tester, 2008). In the present study, salt stress significantly affected both shoot and root biomass in lettuce varieties, particularly causing notable decreases in leaf fresh and dry weights (Table 2). These findings are consistent with previous studies showing that salt stress inhibits shoot growth through osmotic stress and reduced cell expansion (Ashraf and Akram, 2009; Parida and Das, 2005). Leaf fresh weight decreased the most in the Baeza (−7%) and Cherokee (−19%) varieties, indicating that these varieties produced a more stable shoot biomass under salt stress. This relative tolerance mechanism may be associated with better osmotic adjustment or antioxidant capacity, which help maintain cellular functions under stress (Adhikari et al., 2021). The responses of varieties to root fresh weight were found to be different. Under salt stress, increases in root fresh weight were observed in the Cencibel (+59%), Cherokee (+45%), and Expedition (+24%) varieties. These varieties may have developed a tolerance mechanism by increasing root volume to enhance water uptake. Under salt stress, Chicarita (-29%) and Kireve (-13%) varieties showed decreases in root fresh weight. The low root development in these varieties may be due to reduced access to water and nutrients under salt stress. Root dry weight results are like root fresh weight results. These findings reflect the variability in genotype responses, as the Cherokee, Cencibel, and Expedition varieties showed superior root biomass performance under salt stress. Increased root development under saline conditions is a positive adaptive trait as it facilitates better water uptake and nutrient acquisition (Zhu, 2002; Munns and Gilliham, 2015). Overall, the findings indicate that the shoot biomass of 8 different lettuce varieties is more sensitive to salt stress than root biomass. While all varieties experienced reductions in shoot growth, some varieties were able to maintain or increase root growth under stress. Varieties such as Cherokee, Cencibel, and Expedition demonstrated greater adaptability to salt stress conditions due to their improved root performance, while the Chicarita variety was highly sensitive to salt stress, with significant reductions in both shoot and root growth. These responses of varieties to salt stress could serve as a useful selection criterion for breeding programs aimed at selecting salt-tolerant lettuce genotypes.

Salt stress caused significant changes in the parameters of leaf number, main stem diameter, plant height, and leaf area in lettuce varieties (Table 3). While most varieties showed a decrease in leaf number, some varieties showed an increase in leaf number. The most significant decreases in leaf number were observed in the Chicarita (-26%) and Triplex (-16%) varieties. These decreases are consistent with findings (Aydin, 2024) indicating that salt stress restricts leaf initiation and expansion due to osmotic and ionic stress. On the other hand, some varieties such as Baeza (+11%), Kireve (+2%), and Cherokee (+2%) maintained or increased their leaf count under salt stress. The variability in leaf count decreases and increases may be due to a potential genotype tolerance mechanism related to sustainable meristem activity. In plants under salt stress, stem diameter decreased significantly, particularly in the Levistro (-42%) and Triplex (-29%) varieties. This decrease may be due to salt stress affecting the development of the

vascular bundle and stem thickening through changes in cell turgor or lignin accumulation (Zhu, 2002). The Baeza variety, on the other hand, increased its stem diameter by 16% under salt stress conditions. While the plant heights of all lettuce varieties grown under salt stress decreased significantly, the highest decrease was observed in the Chicarita (-31%) variety. Similar findings regarding reduced plant height have been reported in other studies on lettuce and leafy vegetables (Ahmed et al., 2019; Adhikari et al., 2021). Among all the parameters examined, the leaf area was the trait most affected by salt stress. The greatest reductions were observed in the Chicarita (-58%), Triplex (-47%), and Levistro (-49%) varieties, respectively. This sharp reduction in leaf area may be attributed to the inhibitory effects of salt stress on cell growth and stomatal closure, which limit the photosynthetic surface area (Parida and Das, 2005). The Baeza (-7%) and Cherokee (-19%) varieties showed more stable decreases in leaf area compared to other varieties. These varieties may have the ability to tolerate efficient osmotic regulation and better tissue hydration. When all biomass parameters were considered, the morphological responses of the varieties to salt stress showed significant differences. Under salt stress conditions, lettuce varieties showed different responses in canopy diameter and root morphology parameters. The Expedition and Cherokee varieties increased root volume and diameter under stress. These findings suggest that salt-tolerant genotypes may have maintained or increased root development to improve water and nutrient uptake under saline conditions (Zhu, 2002; Munns and Tester, 2008;; Munns, 2011; Munns and Gilliham, 2015). Under salt stress conditions, some varieties attempted to maintain their biomass characteristics, which aligns with previous studies emphasizing the importance of morphological stability under stress conditions (Ashraf and Harris, 2013). It is thought that genetic diversity may affect the plant's response to salinity. Başak et al. 2025 reported that genotypes have different hormone levels in root and leaf tissues in saline conditions.

Overall, salt stress caused a decrease in L values (openness) in most varieties. The most significant decreases in L were observed in the Levistro (-13%) and Cencibel (-12%) varieties, while increases were observed in Expedition (+17%) and Kireve (+2%). Under salt stress, the a* value decreased significantly in Cencibel (-44%), Triplex (-13%), and Chicarita (-8%). This indicates a shift toward a greener leaf color under salt stress (Ashraf and Harris, 2013). Salt stress caused decreases in b* values in Cencibel (-13%) and Chicarita (-14%) varieties. This may be due to the loss of yellow pigments such as carotenoids (Parida and Das, 2005). Chroma, which represents color vibrancy, decreased in most varieties due to the effect of salt stress. The greatest decreases were observed in the Cencibel (-19%) and Triplex (-14%) varieties. However, Expedition (+11%) and Kireve (+4%) exhibited stronger colour saturation. Changes in colour tone were relatively minor among the varieties. These findings are consistent with previous studies (Ashraf and Harris, 2013; Zhao et al., 2017). Salt stress significantly affected the chlorophyll a, b, and total chlorophyll content in lettuce varieties ($P< 0.01$). The highest increases were observed in the Levistro, Baeza, and Chicarita varieties. These varieties may have activated pigment synthesis or retention mechanisms under saline conditions (Munns and Gilliham, 2015). In contrast, decreases in pigment levels were observed, particularly in the Triplex and Expedition varieties. In the study, total carotenoid content did not change statistically between control and salt stress conditions. Salt stress significantly increased leaf sap electrical conductivity (EC) and soluble solid content (SSC) in most lettuce varieties, particularly Chicarita, Triplex, and Cherokee, which may be related to enhanced ion accumulation and osmotic adjustment mechanisms under salt stress (Aydin, 2024).

5. Conclusion

In this study, the effects of salt stress on 8 different lettuce varieties on their morphological, physiological and biochemical properties were investigated. Salt stress had negative effects on all lettuce varieties. In the study, it was generally determined that the shoot mass decreased more than the decrease in root biomass. In addition, some varieties, especially those determined tolerant under salt stress conditions, either maintained or increased their root growth. In addition, in some varieties, leaf color parameters and pigment contents (chlorophyll-a, b and total chlorophyll) increased under the effect of salt stress, while in others they decreased. Salt stress caused a general increase in parameters such as leaf sap electrical conductivity (EC) and soluble solid content (SSC). In general, lettuce varieties gave different responses to salt stress. Cherokee, Cencibel, Baeza and Expedition varieties used in the study were determined to be more tolerant to salt than other varieties. These varieties can be starting materials for cultivation in saline environments and breeding studies to increase salt tolerance in lettuce.

Author Contributions

The percentages of the author' contributions are presented below. The author reviewed and approved the final version of the manuscript.

	A.A.
C	100
D	100
S	100
DCP	100
DAI	100
L	100
W	100
CR	100
SR	100
PM	100
FA	100

C=Concept, D= design, S= supervision, DCP= data collection and/or processing, DAI= data analysis and/or interpretation, L= literature search, W= writing, CR= critical review, SR= submission and revision, PM= project management, FA= funding acquisition.

Conflict of Interest

The authors declared that there is no conflict of interest.

Ethical Consideration

Ethics committee approval was not required for this study because of there was no study on animals or humans.

Acknowledgements

I would like to thank the JISTUAM – Geothermal Advanced Greenhouse Technologies and Production Techniques Research and Application Center, where this study was conducted.

References

Adhikari B, Olorunwa OJ, Wilson JC, Barickman TC, Di Toppi LS, Hasanuzzaman M, Adhikari T. 2021. Morphological and physiological response of different lettuce genotypes to salt stress. Stresses, 1(4): 285-304.

Ahmed S, Ahmed S, Roy SK, Woo SH, Sonawane KD, Shohael AM. 2019. Effect of salinity on the morphological, physiological and biochemical properties of lettuce (Lactuca sativa L.) in Bangladesh. Open Agric, 4(1): 361-373.

Arnon DI. 1949. Copper enzymes in isolated chloroplasts. Polyphenoloxidase in Beta vulgaris. Plant Physiol, 24(1): 1-15.

Ashraf M, Akram NA. 2009. Improving salinity tolerance of plants through conventional breeding and genetic engineering: An analytical comparison. Biotechnol Adv, 27(6): 744-752.

Ashraf M, Harris PJC. 2013. Photosynthesis under stressful environments: An overview. Photosynthetica, 51(2): 163-190.

Aydın A, Yetişir H. 2022. Rootstock effect of auto- and allotetraploid citron (Citrullus lanatus var. citroides) on hydroponically grown cucumber under salt stress. Gesunde Pflanzen, (in press): 1-14.

Aydın A. 2024. The growth, leaf antioxidant enzymes and amino acid content of tomato as affected by grafting on wild tomato rootstocks (S. pimpinellifolium and S. habrochaites) under salt stress. Sci Hortic, 325: 113843.

Barassi CA, Ayrault G, Creus CM, Sueldo RJ, Sobrero MT. 2006. Seed inoculation with Azospirillum mitigates NaCl effects on lettuce. Sci Hortic, 109(1): 8-14.

Başak H, Aydın A, Yetişir H, Turan M. 2025. Salt stress effects on hybrid bottle gourd (Lagenaria siceraria) rootstock candidates plant growth, hormones and nutrient content. J Crop Health, 77(1): 1-23.

Chinnusamy V, Jagendorf A, Zhu JK. 2005. Understanding and improving salt tolerance in plants. Crop Sci, 45(2): 437-448.

Eraslan F, Inal A, Savasturk O, Gunes A. 2007. Changes in antioxidative system and membrane damage of lettuce in response to salinity and boron toxicity. Sci Hortic, 114(1): 5-10.

Hussain S, Shaukat M, Ashraf M, Zhu C, Jin Q, Zhang J. 2019. Salinity stress in arid and semi-arid climates: Effects and management in field crops. Clim Change Agric. https://doi.org/10.5772/intechopen.87982

Kaya C, Higgs D, Sakar E. 2002. Response of two leafy vegetables grown at high salinity to supplementary potassium and phosphorus during different growth stages. J Plant Nutr, 25(12): 2663-2676.

Mariani L, Ferrante A. 2017. Agronomic management for enhancing plant tolerance to abiotic stresses—drought, salinity, hypoxia, and lodging. Horticulturae, 3(4): 5.

Mohammadi P, Khoshgoftarmanesh AH. 2014. The effectiveness of synthetic zinc (Zn)-amino chelates in supplying Zn and alleviating salt-induced damages on hydroponically grown lettuce. Sci Hortic, 172: 117-123.

Moncada A, Miceli A, Sabatino L, Iapichino G, D'Anna F, Vetrano F. 2018. Effect of molybdenum rate on yield and quality of lettuce, escarole, and curly endive grown in a floating system. Agronomy, 8(9): 171.

Moncada A, Miceli A, Vetrano F. 2021. Use of plant growth-promoting rhizobacteria (PGPR) and organic fertilization for soilless cultivation of basil. Sci Hortic, 275: 109714.

Moncada A, Vetrano F, Miceli A. 2020. Alleviation of salt stress by plant growth-promoting bacteria in hydroponic leaf lettuce. Agronomy, 10(10): 1523.

Muhammad HMD, Abbas A, Ahmad R. 2022. Fascinating role of silicon nanoparticles to mitigate adverse effects of salinity in fruit trees: a mechanistic approach. Silicon, 14(14): 8319-8326.

Munns R, Gilliham M. 2015. Salinity tolerance of crops – what is the cost? New Phytol, 208(3): 668-673.

Munns R, Tester M. 2008. Mechanisms of salinity tolerance. Annu Rev Plant Biol, 59: 651-681.

Munns R. 2011. Plant adaptations to salt and water stress: Differences and commonalities. Adv Bot Res, 57: 1-32.

Özdemir M. 2001. Mathematical analysis of color changes and chemical parameters of roasted hazelnuts. MSc Thesis, Fen Bilimleri Enstitüsü, Türkiye. http://hdl.handle.net/11527/16764

Parida AK, Das AB. 2005. Salt tolerance and salinity effects on plants: A review. Ecotoxicol Environ Saf, 60(3): 324-349.

Pérez-López U, Miranda-Apodaca J, Muñoz-Rueda A, Mena-Petite A. 2013. Lettuce production and antioxidant capacity are differentially modified by salt stress and light intensity under ambient and elevated CO2. J Plant Physiol, 170(17): 1517-1525.

Rao KVM, Raghavendra AS, Reddy KJ. 2006. Physiology and molecular biology of stress tolerance in plants. Physiol Mol Biol Stress Toler Plants, 1-345.

Rouphael Y, Petropoulos SA, Cardarelli M, Colla G. 2018. Salinity as eustressor for enhancing quality of vegetables. Sci Hortic, 234: 361-369.

Sakadevan K, Nguyen ML. 2010. Extent, impact, and response to soil and water salinity in arid and semiarid regions. Adv Agron, 109(C): 55-74.

Settanni L, Miceli A, Francesca N, Cruciata M, Moschetti G. 2013. Microbiological investigation of Raphanus sativus L. grown hydroponically in nutrient solutions contaminated with spoilage and pathogenic bacteria. Int J Food Microbiol, 160(3): 344-352.

Shi M, Gu J, Wu H, Rauf A, Emran T Bin, Khan Z, Mitra S, Aljohani ASM, Alhumaydhi FA, Al-Awthan YS, Bahattab O, Thiruvengadam M, Suleria HAR. 2022. Phytochemicals, nutrition, metabolism, bioavailability, and health benefits in lettuce – a comprehensive review. Antioxidants (Basel), 11(6): 1159.

Shrivastava P, Kumar R. 2015. Soil salinity: A serious environmental issue and plant growth promoting bacteria as one of the tools for its alleviation. Saudi J Biol Sci, 22(2): 123-131.

Wei Z, Julkowska MM, Laloë JO, Hartman Y, de Boer GJ, Michelmore RW, van Tienderen PH, Testerink C, Schranz ME. 2014. A mixed-model QTL analysis for salt tolerance in seedlings of crop-wild hybrids of lettuce. Mol Breed, 34(3): 1389-1400.

Yamaguchi T, Blumwald E. 2005. Developing salt-tolerant crop plants: Challenges and opportunities. Trends Plant Sci, 10(12): 615-620.

Zhao CY, Si JH, Feng Q, Deo RC, Yu TF, Li P, Du Y. 2017. Physiological response to salinity stress and tolerance mechanics of Populus euphratica. Environ Monit Assess, 189(11): 574.

Zhu JK. 2002. Salt and drought stress signal transduction in plants. Annu Rev Plant Biol, 53: 247-273.

Black Sea Journal of Engineering and Science
doi: 10.34248/bsengineering.1707841

Open Access Journal
e-ISSN: 2619 – 8991

Araştırma Makalesi (Research Article)
Cilt 8 - Sayı 5: 1349-1357 / Eylül 2025
Volume 8 - Issue 5: 1349-1357 / September 2025

BİNA ZARFININ RENK KOYULUĞUNUN BİNANIN TS 825'E GÖRE HESAPLANAN YILLIK ENERJİ İHTİYACI ÜZERİNDEKİ ETKİSİ

Abdullah Huzeyfe AKCA[1]*

[1]*Yıldız Technical University, Faculty of Civil Engineering, Department of civil Engineering, 34220, İstanbul, Türkiye*

Özet: Enerjiye olan talep her geçen gün arttığı için enerji kullanımını daha sürdürülebilir hale getirmek adına çalışmalar ve yönetmelikler yapılmaktadır. Binaların ısıtma ve soğutma enerjisi ihtiyacının karşılanması ciddi kaynak tüketimine ve çevresel sorunlara sebep olmaktadır. Bu sebeple binaların ısıtma ve soğutma enerjisi tüketiminin daha verimli ve sürdürülebilir olması için TS 825 – Binalarda Isı Yalıtımı Kuralları Standardı 2024 tarihinde güncellenmiştir. Son güncellemeyle yalıtım projelerine soğutma enerjisi talebi de dahil edilmiş olup bina zarfının renk koyuluğunun güneş enerjisi kazançları hesaplarında dikkate alınması istenmiştir. Bu çalışmada opak elemanların renk tercihinin bina enerji tüketimi üzerindeki etkilerinin incelenmesi hedeflenmiştir. Bunun için İzmir'deki ve Ankara'daki iki özdeş binanın farklı renk koyuluğu kombinasyonundaki yıllık ısıtma ve soğutma enerjisi talepleri hesaplanmıştır. Sonuçlar bina zarfının renk tonundaki koyulaşmanın toplam yıllık enerji tüketimini sıcak bölgede % 9,3'e kadar artırdığını göstermiştir. Renk koyulaşması ile soğutma enerjisi talebinin ısıtma enerjisindeki talebe göre daha çok arttığı anlaşılmıştır. Ayrıca duvar yüzeylerindeki renk koyulaşmasının çatı örtüsündeki renk koyulaşmasına göre enerji talepleri üzerinde daha belirgin bir etkisi olduğu görülmüştür.

Anahtar kelimeler: Bina renk tonu, TS 825, Isıtma enerjisi, Soğutma enerjisi

Effect of the Degree of the Color Darkness of the Building Envelope on the Annual Energy Requirement of the Building Calculated According to TS 825

Abstract: Since the energy demand is increasing day by day, researches and regulations are being carried out to make energy consumption more sustainable. Meeting the heating and cooling energy needs of buildings requires serious resource consumption and causes severe environmental problems. For this reason, TS 825 - Thermal insulation requirements for buildings was updated in 2024 in order to make the heating and cooling energy consumption of buildings more efficient and sustainable. The latest update requires calculations for the cooling energy need in thermal insulation projects and also requires that the degree of color darkness of the building envelope be taken into account in solar energy gain calculations. In this study, it was aimed to examine the effects of the color preference of opaque elements on building energy consumption. For this purpose, the annual heating and cooling energy demands of two identical buildings in Izmir and Ankara in different color combinations were calculated. The results showed that increase in the degree of color darkness of the building envelope increased the total annual energy consumption by up to 9.3% in the mild climate zone. The changes in the degree of color darkness affected the cooling energy demand more than the heating energy demand. It was also observed that the use of darker wall surfaces had a more significant effect on energy demands than the use of darker roof covering.

Keywords: Building color darkness, TS 825, Heating energy, Cooling energy

***Sorumlu yazar (Corresponding author):** Yıldız Technical University, Faculty of Civil Engineering, Department of Civil Engineering, 34220, İstanbul, Türkiye
E mail: aakca@yildiz.edu.tr (A.H. AKCA)
Abdullah Huzeyfe AKCA https://orcid.org/0000-0003-1151-5520

Gönderi: 28 Mayıs 2025 **Received:** May 28, 2025
Kabul: 02 Temmuz 2025 **Accepted:** July 02, 2025
Yayınlanma: 15 Eylül 2025 **Published:** September 15, 2025

Cite as: Akca AH. 2025. Effect of the degree of the color darkness of the building envelope on the annual energy requirement of the building calculated according to TS 825. BSJ Eng Sci, 8(5): 1349-1357.

1. Giriş

Binaların karakteristiğini belirleyen sağlamlık, işlevsellik, estetik gibi unsurlardan biri de binanın enerji tüketim performansıdır (Aydın, 2019). Binayı kullanan bireylerin konfor unsurlarını da gözeterek binada konaklamalarını, iş yaşantılarına devam etmelerini, çeşitli aktiviteleri ve çalışmaları yapabilmeleri için binanın detaylı ve düzgün hazırlanmış bir ısı yalıtım projesinin olması önem arz etmektedir (Bektaş vd., 2017). Binalar başta atmosferik koşulların etkisiyle olmak üzere kullanım amacına paralel olarak üretilen veya tüketilen enerjinin büyüklüğü ile iç ortam sıcaklığına ve nem seviyesine sahip olmaktadır (İZODER, 2017). Binanın ısı yalıtımının yeterliliği ve havalandırma sisteminin verimliliği binanın enerji tüketim performansını belirgin olarak etkilemektedir.

Türkiye İstatistik Kurumu tarafından 2022 yılında yayınlanan Hanehalkı Nihai Enerji Tüketim İstatistikleri'ne göre hanehalkının toplam enerji tüketiminin % 65,3'ü alan ısıtması amacıyla tüketilmiştir

(TÜİK, 2022). Bu sebeple 2008 yılı sonunda "Binalarda Enerji Performansı Yönetmeliği" yayınlanmıştır. Yönetmeliğin amacı "Binalarda enerjinin ve enerji kaynaklarının etkin ve verimli kullanılmasına, enerji israfının önlenmesine ve çevrenin korunmasına ilişkin usul ve esasları düzenlemektir." şeklinde belirtilmektedir (Binalarda Enerji Performansı Yönetmeliği, 2008). Yönetmelikle beraber mevcut yapılardaki tadilatlarda ve yeni yapılacak yapılarda ısı yalıtımı projesi gerekliliği belirtilmiştir.

Yönetmelik ısı yalıtımı projelerinde hesap yöntemi olarak TS 825 Binalarda Isı Yalıtımı Kuralları Standardı'nı işaret etmektedir. Standart, içeriğinde de belirttiği üzere, insan sağlığının ve binalarının ısı etkilerinden korunmasını ve yakıttan tasarruf konusunda gerekli kuralları kapsamaktadır. Bu minvalde TS 825 standardı 1989 yılından itibaren çeşitli revizyonlar geçirmiştir ve günümüzde standardın TS 825-2024 tarihli versiyonu geçerli durumdadır (TSE, 2024). Bir önceki standart TS 825-2013'e göre köklü değişiklikler yapılmış olan aktif standart özellikle soğutma enerjisi hesaplarının da dahil edilmesiyle birlikte çok daha kapsamlı bir hale gelmiştir. Güncellemeler ana hatlarıyla: Yıllık soğutma enerjisi ihtiyacının hesaplanması; derece gün bölgesi sayısının 5'ten 6'ya çıkarılması; toprak temaslı elemanlarda elemanların kullanım amacı ve geometrisine bağlı olarak farklı yöntemlerle ısı transfer katsayısının belirlenmesi; havalandırma yolu ile ısı kayıplarının, iç ısı kazançlarının ve güneş enerjisi kazançlarının hesap yöntemlerinin güncellenmesi; opak elemanların ısı kazançları hesaplarına dahil edilmesi şeklinde sıralanabilir. Güncellemeler incelendiğinde soğutma enerjisi hesaplarının ve opak elemanların ısı kazançları hesaplarının ilk defa hesap yöntemlerine dahil edildiği görülmektedir. Soğutma hesaplarında ısı akış yönünün dışarıdan binanın iç ortamına doğru olacağı prensibiyle ısıtma hesaplarına paralel olarak benzer işlemler yapılmaktadır.

Bilindiği üzere açık renkli malzemeler güneş ışınlarını yansıtırken koyu renkli malzemeler güneş ışınlarını tutmaktadır (Syuhada ve Maulana, 2018). Bu durum da malzemede ısı enerjisi depolanmasına sebep olur. (Paminto vd., 2021). Bu sebeple binayı çevreleyen yapı elemanlarında detaylı bir ısı yalıtımı tabakalandırmasının yanı sıra uygun renk seçiminin yapılması binanın enerji verimliliğini arttırabilir (Koçu ve Dereli, 2010). TS 825-2024'e göre opak elemanların ısı yalıtımı hesaplamalarına dahil edilmesi ise eşitlik 1 ile gösterildiği gibi aşağıdaki parametrelerle yapılmaktadır.

$$Q_{H/C;sol;op;k;m} = \alpha_{sol;k} \cdot R_{se;k} \cdot U_{c;op;k} \cdot A_{c;k} \cdot F_{sh;obst;k;m} \cdot H_{sol;k;m} - Q_{sky;k;m} \quad (1)$$

Eşitlik 1'deki parametreler: $\alpha_{sol;k}$ boyutsuz güneş ışınımı emme katsayısı (Kategori 1: Açık renk için 0,3, Kategori 2: Orta koyulukta renk için 0,6, Kategori 3: Koyu renk için 0,9 olarak alınır), $R_{se;k}$ Dış yüzey ısı direnci (m^2K/W), $U_{c;op;k}$ ısıl geçirgenlik (W/m^2K), $A_{c;k}$ izdüşüm alanı (m^2), $F_{sh;obst;k;m}$ dış engeller için boyutsuz gölgeleme azaltma faktörü, $H_{sol;k;m}$ İlgili eğim ve yönelme açısıyla elemanın birim alanına düşen aylık güneş ışınımı (kWh/m^2), $Q_{sky;k;m}$ gökyüzüne olan ısıl ışınım nedeniyle aylık ek ısı akışı (kWh) şeklindedir. $H_{sol;k;m}$ parametresindeki ilgili eğim ve yönelme açısı sırasıyla β_i ve γ_i şeklindedir. Eğim açısı yapı elemanın geometrik verilerinden elde edilen yataydan yukarıya doğru ölçülmüş açıdır. Yönelme açısı ise yapı elemanının geometrik verilerden elde edilen eğimli yüzeyin normalinin yatay iz düşümünün coğrafi azimut açısı şeklinde ifade edilir. eşitlik 1'deki $Q_{sky;k;m}$ parametresi ise ayrı bir denklem ile eşitlik 2'de gösterildiği gibi hesaplanır.

$$Q_{sky;k;m} = 0{,}001 \cdot F_{sky;k} \cdot R_{se;k} \cdot U_{c;op;k} \cdot A_{c;k} \cdot h_{re;k} \cdot \Delta\theta_{sky;m} \cdot \Delta t_m \quad (2)$$

Eşitlik 2'deki parametreler: $F_{sky;k}$ eleman ile gökyüzü arasındaki görme faktörü, $h_{re;k}$ dış yüzey uzun dalga ışınım ısı transfer katsayısı (W/m^2K), $\Delta\theta_{sky;m}$ görünür gökyüzü sıcaklığı ile hava sıcaklığı arasındaki ortalama fark (K), Δt_m ilgili ayın süresidir (saat).

İç ortam ile dış ortamı ayıran bina kabuğunu ifade eden bina zarfının renk seçimi daha çok estetik unsurlar ve çevre uyumu ile ilgili bir durumdur. Fakat görüldüğü üzere bina zarfındaki opak elemanlardan güneş enerjisi ile ısı akışı özellikle eleman rengine bağlı olarak belirlenen bir emme faktörüyle ve gökyüzüne olan ısıl ışınım faktörünün bileşkesine eşittir. Bu durumda bina zarfının rengi koyulaştıkça opak elemanlardan doğan ısı kazancı da değişmektedir. Bu sebeple bina zarfını çevreleyen elemanların renk tonları belirlenirken dikkate alınması amacıyla bu çalışmada İzmir'deki ve Ankara'daki 5 katlı (Bodrum katı + zemin katı + 3 normal kat) konut binalarının aynı yalıtım sistemiyle farklı tonlardaki dış cephe ve çatı örtüsüyle kaplanması durumundaki yıllık ısıtma enerjisi ihtiyacı farkı hesaplamaya alınmıştır. Böylece bu yeni hesap unsurunun enerji ihtiyacındaki payı değerlendirilmiştir.

2. Materyal ve Yöntem

TS 825-2024' e göre ısı yalıtımı hesapları İzmir'deki ve Ankara'daki 5 katlı konut amaçlı kullanılacak olan aynı özellikteki apartman binalarında yapılacaktır. Binaya ait cephe görselleri ve kat yükseklikleri Şekil 1, Şekil 2, Şekil 3 ve Şekil 4'te verilmiştir. Bina zarfında bulunan elemanların tabaka ve malzeme detayları ise Tablo 1'de verilmiştir.

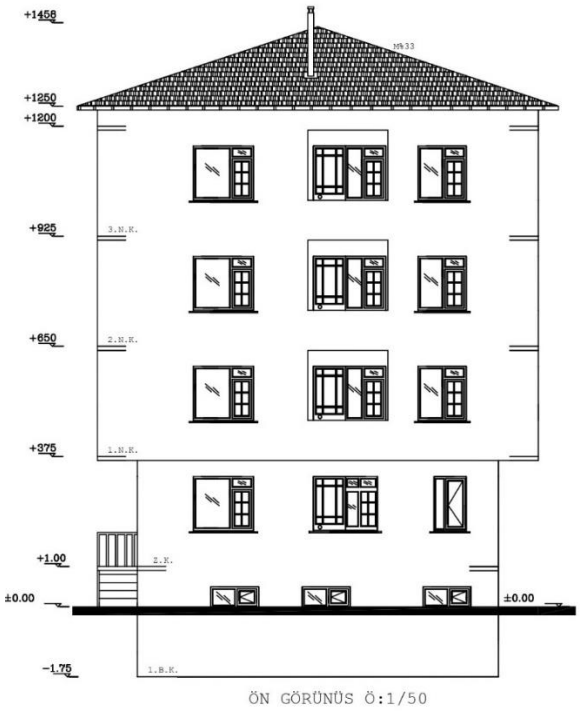

Şekil 1. Binanın ön cephesi.

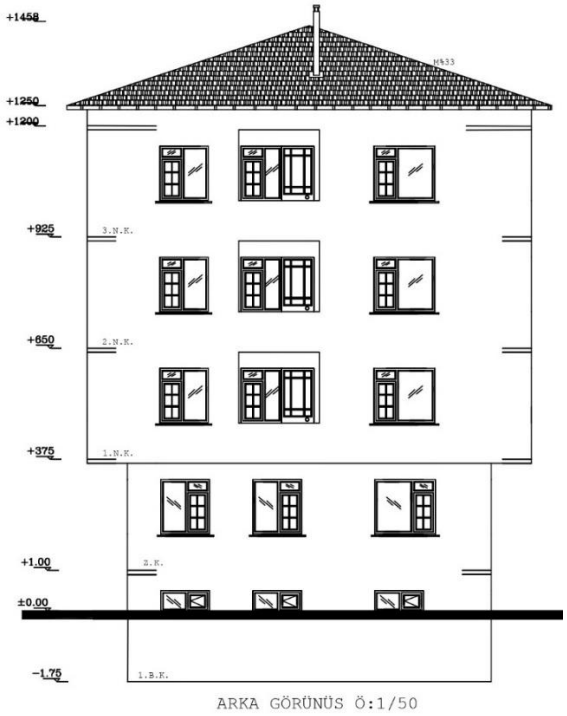

Şekil 3. Binanın arka cephesi.

Şekil 2. Binanın sol cephesi.

Şekil 4. Binanın sağ cephesi.

Tablo 1. Bina elemanlarının tabakaları

Bina elemanı	Tabakalar	Kalınlık (cm)	Isı iletim katsayısı (W/mK)
Çatı kaplaması	Su yalıtımı örtüsü	0,3	0,18
	Kontraplak	1,8	0,13
Çatı döşemesi	İç sıva	1	1
	Betonarme döşeme	15	2,5
	Isı yalıtımı	15	0,035
Duvar yüzeyleri	İç sıva	1	1
	Delikli tuğla	13,5	0,45
	Isı yalıtımı	15	0,035
	Dış sıva	1	1
Betonarme dikey yüzeyler (Kolon + Kiriş)	İç sıva	1	1
	Betonarme	25	2,5
	Isı yalıtımı	15	0,035
	Dış sıva	1	1
Betonarme konsol döşeme	Ahşap parke	1	1
	Şap betonu	5	2
	Betonarme	15	2,5
	Isı yalıtımı	15	0,035
	Dış sıva	1	1
Betonarme perde	İç sıva	1	1
	Betonarme	20	2,5
	Su yalıtımı örtüsü	0,5	0,5
	Isı yalıtımı	15	0,035
	Dış sıva	2	1
	Yüzey kaplaması	3	0,6
	Isı yalıtımı	10	0,035
	Betonarme	40	2,5
Taban	Su yalıtımı örtüsü	0,5	0,5

Binanın toprak üstü kotu 14,08 m olup toprak altındaki betonarme duvar yüksekliği 1,75 m'dir. Bodrum Kat taban boyutları 13 m uzunluk ve 9 m genişlik şeklindedir ve bina temeli 40 cm kalınlığındaki betonarme radye temeldir. 1. Kat Zemin Kat üzerine ön ve arka cephede 1,5 m, sol ve sağ cephede 1,0 m olacak şekilde çıkmalarla devam etmektedir. Normal katlarda ön ve arka cephelerdeki orta pencerelerde cephenin çıkma derinliği kadar genişliği olan birer balkon bulunmaktadır. Binanın üstünü çatı eğimi %33 olan soğuk kırma çatı örtmektedir. Binanın dış kapısı ahşap olup ısıl geçirgenliği $U_{kapı}$ =4,0 W/m²K'dir. Binada kullanılan pencereler yalıtımlı PVC doğramadan yapılmış olup hepsinin ısıl geçirgenliği U_{pen} =1,8 W/m²K'dir. TS 825-2024'e göre yapılacak olan ısıl hesaplamalarda $\alpha_{sol;k}$ boyutsuz güneş ışınımı emme katsayısı Tablo 2'de belirtilen bina tipleri için farklı olarak alınacaktır. Binada kolonlar 40x40 cm² boyutlarındadır. Bodrum ve Zemin Katlarda ön ve arka cephede bina zarfında olan kolon sayısı 4'tür, sol ve sağ cephede ise bina zarfında olan kolon sayısı 6'dır. Zemin katta bina zarfında bulunan kolonları birleştiren kirişlerin boyutları ise 25x50 cm²'dir. Bu sebeple bina zarfındaki döşemelerden, kolonlardan ve kirişlerden oluşan betonarme dikey yüzeylerin ısıl geçirgenliği hesaplanırken güvenli tarafta kalmak için tabaka kalınlığı ve dolayısıyla ısıl direnci en az olan kiriş elemanlar dikkate alınmış ve bu elemanlar için tek bir ısıl geçirgenlik değeri belirlenmiştir.

Tablo 2. Cephe ve çatı renk tonlarına göre bina kodları

Çatı	Dikey Cepheler		
	Açık	Orta	Koyu
Açık	RAA	RAO	RAK
Orta	ROA	ROO	ROK
Koyu	RKA	RKO	RKK

3. Bulgular

Binada TS 825-2024'e göre ısıl hesaplama yapabilmek için binadaki mevcut ölçü ve parametrelere göre bazı faktörlerin hesaplanması gerekmektedir. Bunlar çatı döşemesi için düzeltme faktörü, toprak temaslı döşeme karakteristik ölçüsü, toprak temaslı elemanların eş değer kalınlıkları, iletimle gerçekleşen ısı transfer katsayıları, havalandırma yoluyla gerçekleşen ısı transfer katsayısı, bina iç ısı kazançları ve bina güneş enerjisi kazançları şeklindedir. Bu veriler elde edildikten sonra binanın yıllık ısıtma ve soğutma enerjisi ihtiyacı hesaplanabilir.

3.1. Çatı Döşemesi Düzeltme Faktörü

Binanın üzerini kullanılmayan ve şartlandırılmayan soğuk kırma çatı örtmektedir. Çatı örtüsü çatı döşemesinden kaynaklanan ısı kaybını azaltacağı için çatı döşemesinin ısıl geçirgenliği bir düzeltme faktörü, b ile çarpılarak azaltılmalıdır. Düzeltme faktörü eşitlik 3 ile hesaplanabilir.

$$b = \frac{H_{ue}}{H_{ue} + H_{iu}} \tag{3}$$

Burada H_{ue} şartlandırılmayan mahalle dış ortam arasındaki ısı transfer katsayısıdır (W/mK) ve H_{iu} şartlandırılan mahal ile şartlandırılmayan mahal arasındaki doğrudan ısı transfer katsayısıdır (W/mK). Bu iki parametrenin hesaplanması eşitlik 4'te ve eşitlik 5'te gösterildiği gibi yapılır.

$$H_{ue} = H_{tr;ue} + H_{ve;ue} \tag{4}$$

$$H_{iu} = H_{tr;iu} + H_{ve;iu} \tag{5}$$

Şartlandırılmayan mahalle dış ortam arasındaki ısı transfer katsayısının iletimle ısı transferi bileşeni $H_{tr;ue}$'dir ve havalandırma yoluyla ısı transferi bileşeni ise

$H_{ve,ue}$'dir. Şartlandırılan mahal ile şartlandırılmayan mahal arasındaki doğrudan ısı transfer katsayısının iletimle ısı transferi bileşeni $H_{tr,iu}$'dir ve havalandırma yoluyla ısı transferi bileşeni ise $H_{ve,iu}$'dir. Binanın kullanılmayan çatısı ve şartlandırılan iç hacmi arasında hava akışı olmadığından $H_{ve,iu}$ = 0 W/K olarak belirlenir. Diğer parametreler sırasıyla eşitlik 6, eşitlik 7 ve eşitlik 8 ile hesaplanır.

$$H_{tr;ue} = U_{ue} \cdot A_{ue} \quad (6)$$

$$H_{ve;ue} = \rho \cdot c_p \cdot q_{ue} = 0{,}33 \times (\eta_{ue} \times V_{ue}) \quad (7)$$

$$H_{tr;iu} = U_T \cdot A_T \quad (8)$$

U_{ue} şartlandırılmayan mahal ile dış ortam arasındaki ısıl geçirgenlik olup tabaka kalınlıkları ve çatıda kullanılan malzemelerin ısıl iletim katsayılarından 3,08 W/m²K olarak hesaplanmıştır. A_{ue} çatı örtüsünün toplam alanı olup kırma çatı geometrisinden 213,6 m² olarak hesaplanmıştır. ρ havanın yoğunluğu (kg/m³), c_p havanın sabit basınçtaki özgül ısı kapasitesi (Wh/kgK) şeklinde olup $\rho \cdot c_p$ değerinin 0,33 (Wh/m³K) olarak alınması uygundur. Çatıda sabit havalandırma kanalları mevcut olduğundan hava değişim sayısı n_{ue}=3 1/h'tir. V_{ue} şartlandırılmayan çatı hacmi olup kırma çatı geometrisine göre 151,30 m³ olarak hesaplanmıştır. U_T şartlandırılan mahalle şartlandırılmayan mahal arasındaki ısıl geçirgenliktir. U_T değeri çatı döşemesi tabaka kalınlıkları ve kullanılan malzemelerin ısıl iletim katsayılarından 0,219 W/m²K olarak hesaplanmıştır. A_T çatı döşemesinin alanıdır ve 176 m²'dir. Bu durumda çatı döşemesi için düzeltme faktörü, b = 0,956 olarak hesaplanır.

3.2. Toprak Altı Döşeme Karakteristik Ölçüsü

Toprağa temas eden yapı elemanlarından iletimle gerçekleşen ısı transfer katsayısının hesaplanabilmesi için döşeme karakteristik ölçüsü, B'nin eşitlik 9'a göre belirlenmesi gerekmektedir.

$$B = \frac{A}{0{,}5 \times P} \quad (9)$$

A (m²) toprağa temas eden toplam döşeme alanını, P (m) ısıtılan bina ile dış ortamı ayıran dış duvarın toplam uzunluğu yani bina tabanının çevresidir. Buna göre döşeme karakteristik ölçüsü B=5,32 m'dir.

3.3. Eşdeğer Kalınlıklar

Toprağa temas eden döşemelerin iletimle gerçekleşen ısı transfer katsayısının hesaplanabilmesi için eşdeğer döşeme kalınlığı d_f, toprağa temas eden duvarların iletimle gerçekleşen ısı transfer katsayısının hesaplanabilmesi için eşdeğer duvar kalınlığı $d_{w;b}$ değerlerinin Eşitlik 10'a ve Eşitlik 11'e göre hesaplanması gerekmektedir.

$$d_f = d_{w;e} + \lambda_g \cdot \sum R_f \quad (10)$$

$$d_{w;b} = \lambda_g \cdot \sum R_{w;b} \quad (11)$$

Denklemlerdeki λ_g toprağın ısıl iletkenliğidir ve zemin cinsi, nem muhtevası gibi birçok parametreye bağlı olarak değişebilir (Xiong vd., 2023). TS 825-2024'e göre hesaplamalarda 2,0 W/mK olarak alınabilir (TSE, 2024). $d_{w;e}$ zemin seviyesindeki duvarların tüm katmanları içerecek şekilde toplam kalınlığını (m), ΣR_f toprağa basan döşemenin toplam ısıl direncini (m²K/W), $\Sigma R_{w;b}$ toprağa temas eden duvarın toplam ısıl direncini (m²K/W) ifade etmektedir. Bina tabanının tabaka kalınlıklardan ve kullanılan malzemelerin ısıl iletim katsayılarından yararlanarak $d_{w;e}$ = 0,385 m, ΣR_f = 3,25 m²K/W ve $\Sigma R_{w;b}$ = 4,54 m²K/W olarak hesaplanır. Bu durumda eşdeğer döşeme kalınlığı d_f = 6,88 m, eşdeğer duvar kalınlığı $d_{w;b}$ = 9,07 m olarak hesaplanır. Elde edilen eş değer kalınlıklar ile toprağa basan döşemenin ısıl geçirgenliği $U_{fg;b}$ = 0,196 W/m²K ve toprak temaslı duvarın ısıl geçirgenliği $U_{wg;b}$ = 0,180 W/m²K olarak hesaplanır.

3.4. Toplam Isı Transfer Katsayısı Çizelgesi

Tablo 1'de verilen malzeme parametreleri ve tabaka kalınlıkları doğrultusunda binanın toprak üstü ve toprak altı elemanlarının ısıl geçirgenlikleri hesaplanarak Tablo 3'te gösterilmiştir. Isıl geçirgenlikler ve yüzey alanları kullanılarak toprak temassız elemanların iletimle toplam ısı transfer katsayısı $\Sigma_k(H_{H/C;el;k;m})$ = 370,4 W/K olarak hesaplanır. Bu değere ısı köprülerinden dolayı meydana gelen kayıplar da eklenerek toprak temassız elemanların toplam ısı transfer katsayısı hesaplanabilir.

Tablo 3. Bina zarfındaki yapı elemanlarının ısıl geçirgenlikleri ve alanları

	Yapı Elemanı	U (W/m²K)	A (m²)
Toprak temassız	Çatı döşemesi	0,219	176,0
	Dış duvar	0,209	468,3
	Kolon+Kiriş	0,219	41,5
	Çıkma döşemesi	0,217	53,0
	Perde	0,219	37,5
	Pencere	1,800	108,8
	Kapı	4,000	2,7
Toprak temaslı	Perde	0,180	77,0
	Taban döşemesi	0,196	117,0

Binada çizgisel ısıl geçirgenlik katsayıları TS EN ISO 14683'e göre belirlenmiş olup çizgisel ısıl geçirgenlik katsayısı 0,10 W/mK'den küçük olan elemanlarda oluşan ısı köprüleri TS 825-2024'e göre ihmal edilebilir (TSE, 2017). Buna göre balkon döşemesi çevresinde oluşan ısı köprüsü kaybı 28,5 W/K, çatı döşemesi çevresinde oluşan ısı köprüsü kaybı 32,4 W/K ve bina taban çevresinde oluşan ısı köprüsü kaybı 26,4 W/K olarak belirlenmiştir. Toprak temaslı olmayan elemanların toplam ısı transfer katsayısı $H_{H/C;tr(excl.gf);ztc;m}$ = 431,3 W/K, toprak temaslı olan elemanların toplam ısı transfer katsayısı $H_{gr;an;ztc;m}$ = 63,2 W/K olarak hesaplanır.

3.5. Havalandırma Isı Transfer Katsayısı

Bina tipi apartman olduğu için şartlandırılmış döşeme alanı başına dış hava katsayısı TS 825-2024'e göre n_h = 0,7 m³/m²h olarak alınır. Bina geneli kullanılmayan çatı hariç şartlandırıldığından şartlandırılmış döşeme alanı balkon kullanım alanları hariç tüm kat alanları toplamına eşittir ve A_f = 744 m²'dir. Bu durumda havalandırma ısı transferi katsayısı $H_{H/C;ve;ztc;m}$ Eşitlik 12'ye göre hesaplanır ve 171,9 W/K olarak bulunur.

$$H_{H/C;ve;ztc;m} = \rho \cdot C_p \cdot A_f \cdot n_h \quad (12)$$

3.6. İç Isı Kazançları

Bina ortalama iç ısı kazançları $Q_{H/C;int;dir;zt;m}$ Eşitlik 13'e göre hesaplanır ve 4906 W olarak bulunur.

$$Q_{H/C;int;dir;zt;m} = A_f \cdot \left(Q_p/A_p + f_e \cdot q_e\right) \quad (13)$$

Q_p/A_p = 1,8 W/m² kişi başı alan başına metabolik ısı kazancı, f_E = %70 binanın şartlandırılmış bölümünde elektrik kullanımının kısmı ve q_E = 30 kWh/m² şartlandırılmış döşeme alanı başına yıllık elektrik kullanımı değerleri TS 825-2024'ten elde edilmiştir. Aylık ortalama günlük kullanım süresi bina kullanım amacına göre değişebilmektedir. TS 825-2024'e göre konut amaçlı kullanılan apartmanlar için GKS = 12 saat olarak alınabilir.

3.7. Güneş Enerjisi Kazançları

Güneş enerjisi kazançları binanın yönelim ve eğim açılarına göre değişmektedir. Binanın kapısı kuzey cephesine baktığı için yönlere bağlı bina saydam ve opak yüzey alanları Tablo 4'te verilmiştir. Mevsimlere göre güneş enerjisi kazanımı farklı olacağı için aylık güneş ışınımı şiddeti değerleri $H_{sol;wi;m}$ değerleri TS 825-2024'ten alınmış ve Tablo 5'te gösterilmiştir.

Tablo 4. Yönlere göre binanın saydam ve opak yüzey alanları dağılımı

Yön	Saydam Alanlar (m²)	Opak Alanlar (m²)
Kuzey	28,3	152,9
Doğu	28,0	96,8
Güney	24,5	156,7
Batı	28,0	96,8
Yatay	-	176,0

Tablo 5. İzmir ve Ankara için aylık güneş ışınımı şiddeti değerleri (W/m²) (TS 825-2024)

Aylar	Kuzey		Doğu		Güney		Batı		Yatay	
	İzmir	Ankara	İzmir	Ankara	İzmir	Ankara	İzmir	Ankara	İzmir	Ankara
Ocak	13,5	4,2	105,8	31,5	179,1	54,0	106,4	31,3	90,7	28,0
Şubat	15,0	7,7	117,2	61,9	153,8	76,8	119,0	62,0	112,1	57,2
Mart	21,2	8,1	161,5	60,4	154,5	57,6	158,0	61,0	163,0	62,2
Nisan	27,1	10,5	177,6	69,3	126,3	47,7	179,4	68,8	201,2	78,1
Mayıs	34,6	21,1	205,2	125,6	107,7	63,7	207,0	123,3	246,4	150,5
Haziran	50,6	41,8	235,2	194,9	107,6	85,1	238,0	192,5	291,4	239,6
Temmuz	44,2	30,5	248,6	173,6	131,1	86,9	253,0	171,8	304,3	209,8
Ağustos	39,1	28,4	237,4	171,7	168,2	118,9	237,9	171,5	272,0	198,0
Eylül	31,7	17,3	220,0	116,2	215,1	115,1	219,5	119,1	226,3	123,9
Ekim	21,0	8,3	157,9	60,5	201,5	78,3	156,8	60,0	148,5	59,3
Kasım	15,2	5,2	111,3	39,7	194,3	65,7	111,4	39,5	99,2	34,8
Aralık	12,5	4,7	95,7	34,7	183,0	67,6	91,3	36,1	78,3	30,0

Binanın her aydaki ilgili yöne ait güneş enerjisi kazancı $Q_{H/C;sol;dire;zt,m}$, saydam elemanların $\Sigma Q_{H/C;sol;wi;k}$ ve opak elemanların $\Sigma Q_{H/C;sol;op;k}$ güneş enerjisi kazançları toplanmıyla Eşitlik 14'e göre hesaplanır. Saydam elemanların güneş enerjisi kazancı $\Sigma Q_{H/C;sol;wi;k}$ Eşitlik 15'e göre aylık belirlenir.

$$Q_{H/C;sol;dire;zt,m} = \sum Q_{H/C;sol;wi;k} + \sum Q_{H/C;sol;op;k} \quad (14)$$

$$Q_{H/C;sol;wi;k;m} = g_{gl;wi;H/C;m} \cdot A_{wi} \cdot (1 - F_{fr;wi}) \cdot F_{sh;obst;wi;m} \cdot H_{sol;wi;m} - Q_{sky;k;m} \quad (15)$$

Binada pencereler çift camlı olduğu için camların güneş enerjisi geçirgenliği katsayısı $g_{gl;wi;H/C;m}$ = 0,675 olarak alınmıştır. A_{wi} ilgili yöne bakan pencere alanıdır ve Tablo 4'te saydam alanlar başlığı altında verilmiştir. Binadaki pencerelerin çerçeve kısmının toplam alandaki payı $F_{fr;wi}$ = 0,25 olarak belirlenmiştir. Binanın etrafı açık olduğu için dış engeller için boyutsuz gölgeleme azaltma faktörü $F_{sh;obst;wi;m}$ = 0,8 olarak alınmıştır.

3.8. Binanın Yıllık Isıtma Enerjisi İhtiyacı

Binanın yıllık ısıtma enerjisi ihtiyacı her ay için hesaplanan ısıtma enerjisi ihtiyaçlarını toplayarak bulunur. Bunun için aylık toplam ısı kayıplarının (Isıtma için iletimle toplam ısı transferi ve ısıtma için havalandırmayla toplam ısı transferi) ve toplam ısı

kazançlarının (Isıtma için iç ısı kazançları ve ısıtma için güneş enerjisi kazançları) belirlenmesi gerekir.

Isıtma enerjisi ihtiyacı iç ortam ve dış ortam sıcaklık farkının büyüklüğüyle doğru orantılı olarak artar veya azalır. Bina konut olarak kullanıldığından ısıtma enerjisi hesabında bina iç sıcaklığı $Q_{int;cal;H;ztc;m}$ = 20 °C olarak alınmıştır. İzmir ve Ankara için aylık dış ortam sıcaklıkları $\theta_{e;a;m}$ ve yıllık ortalama dış ortam sıcaklığı $\theta_{e;a;an}$ değerleri Tablo 6'da verilmiştir.

Tablo 6. İzmir ve Ankara için aylık ve yıllık ortalama dış ortam sıcaklıkları (TS 825-2024)

Aylar	Aylık (°C)		Yıllık (°C)	
	İzmir	Ankara	İzmir	Ankara
Ocak	4,00	-3,00	18,03	9,76
Şubat	4,40	-2,70	18,03	9,76
Mart	6,30	0,40	18,03	9,76
Nisan	11,25	6,38	18,03	9,76
Mayıs	19,40	14,00	18,03	9,76
Haziran	35,41	18,70	18,03	9,76
Temmuz	35,79	28,40	18,03	9,76
Ağustos	34,90	26,90	18,03	9,76
Eylül	32,41	17,20	18,03	9,76
Ekim	17,50	13,00	18,03	9,76
Kasım	10,10	-1,80	18,03	9,76
Aralık	4,88	-0,30	18,03	9,76

3.9. Binanın yıllık soğutma enerjisi ihtiyacı

Binanın yıllık soğutma enerjisi ihtiyacı her ay için hesaplanan soğutma enerjisi ihtiyaçlarını toplayarak bulunur. Bunun için aylık toplam ısı kayıplarının (Soğutma için iletimle toplam ısı transferi ve soğutma için havalandırmayla toplam ısı transferi) ve toplam ısı kazançlarının (Soğutma için iç ısı kazançları ve soğutma için güneş enerjisi kazançları) belirlenmesi gerekir.

Soğutma enerjisi ihtiyacı iç ortam ve dış ortam sıcaklık farkının büyüklüğüyle doğru orantılı olarak artar veya azalır. Bina konut olarak kullanıldığından soğutma enerjisi hesabında bina iç sıcaklığı $Q_{int;cal;C;ztc;m}$ = 26 °C olarak alınmıştır. Farklı renk tonu kombinasyonundaki binaların yıllık ısıtma enerjisi, soğutma enerjisi ve toplam enerji ihtiyacı Tablo 7'de verilmiştir.

Tablo 7. Yıllık ısıtma enerjisi, soğutma enerjisi ve toplam enerji ihtiyacı

Bina kodu	Yıllık ısıtma enerjisi ihtiyacı (kWh)		Yıllık soğutma enerjisi ihtiyacı (kWh)		Yıllık toplam enerji ihtiyacı (kWh)	
	İzmir	Ankara	İzmir	Ankara	İzmir	Ankara
RAA	8471	41056	37813	8339	46284	49395
ROA	8137	40620	39807	9186	47944	49806
RKA	7821	40192	41807	10038	49628	50230
RAO	8307	40862	38435	8573	46742	49435
ROO	7981	40428	40431	9421	48412	49849
RKO	7672	40003	42434	10275	50106	50278
RAK	8147	40668	39058	8808	47205	49476
ROK	7928	40238	41057	9657	48985	49895
RKK	7526	39815	43061	10512	50587	50327

4. Tartışma

Tablo 7 incelendiğinde opak elemanların enerji ihtiyaçları üzerindeki etkisi daha çok yaz aylarında olmaktadır. Bunun sebebi opak elemanların ısı akışı hesaplarında kullanılan parametrelerden biri olan güneş ışınımı şiddeti değerlerinin Tablo 5'te de görüldüğü üzere özellikle yaz aylarında daha yüksek değerlere ulaşmasıdır. Bu nedenle bina zarfındaki renk koyulaşmasının etkisi daha çok soğutma enerjisi ihtiyacında kendisini göstermektedir. Şekil 5'e ve Şekil 6'ya bakıldığında her iki şehirdeki bina için bina zarfının rengi koyulaştıkça ısıtma enerjisi ihtiyacı azalırken soğutma enerjisi ihtiyacındaki artış gözükmektedir. Bu sebeple renk tonundaki değişikliklerin toplam enerji ihtiyacındaki etkileri kısıtlanmıştır. En açık renk tonu kombinasyonun seçildiği RAA kodlu binanın toplam enerji ihtiyacı referans alındığında en koyu tonların seçildiği RKK kodlu binanın toplam enerji ihtiyacı İzmir'deki ve Ankara'daki bina için sırasıyla %9,3 ve % 1,9 oranında daha fazladır. Fakat aynı binada (RKK) ısıtma enerjisi ihtiyacı RAA kodlu binaya göre İzmir ve Ankara için sırasıyla % 4,9 ve % 3,0 oranında daha azken

soğutma enerjisi ihtiyacı İzmir ve Ankara için sırasıyla %9,3 ve % 26,1 oranında daha fazladır. Her ne kadar bu oranlar davranışı gösterse de, renk koyulaşmasından ötürü net enerji ihtiyacı artışı iki bölge arasındaki farkın anlaşılmasında faydalı olabilir. Yine Tablo 7'ye bakıldığında İzmir ve Ankara için toplam enerji ihtiyacının sırasıyla 4303 kWh ve 932 kWh olduğu, soğutma enerjisi ihtiyaçlarının ise sırasıyla 5248 kWh ve 2173 kWh olduğu görülmektedir. Sonuçların bu şekilde çıkmasında binaların bulunduğu bölgelerin iklim koşulları etkilidir. Ankara'daki ve İzmir'deki binalar karşılaştırıldığında daha sıcak bir bölgede olan binada bina zarfının renk koyuluğunun özellikle soğutma enerjisi ihtiyacı üzerinde önemli derecede etkili olduğu görülmektedir.

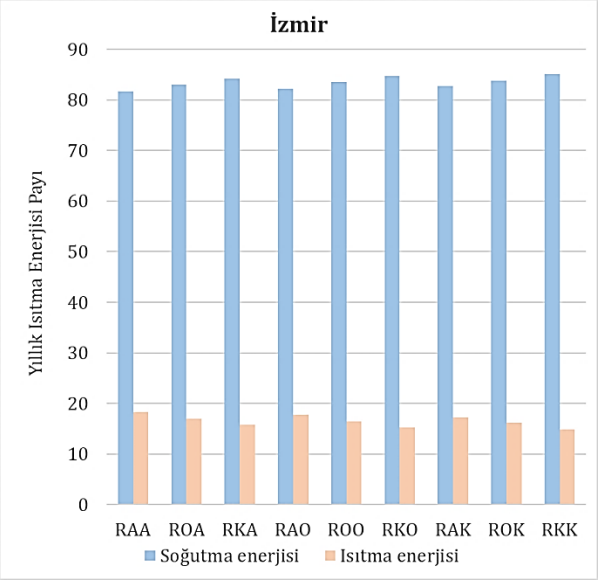

Şekil 5. İzmir'deki bina için soğutma ve ısıtma enerjilerinin yıllık enerji ihtiyacı içerisindeki dağılımları.

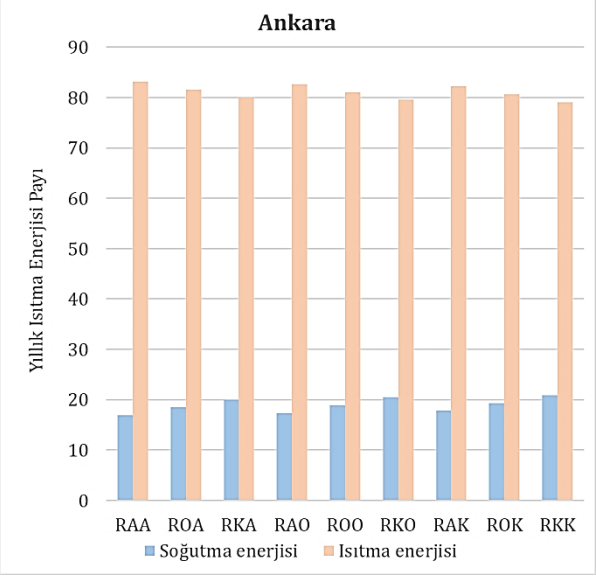

Şekil 6. Ankara'daki bina için soğutma ve ısıtma enerjilerinin yıllık enerji ihtiyacı içerisindeki dağılımları.

Çatı örtüsünün ve duvar yüzeylerinin renk koyuluğu ayrı ayrı değerlendirildiğinde duvar yüzeylerinin koyulaşmasının enerji ihtiyacı üzerindeki etkilerinin daha belirgin olduğu görülmektedir. Bunun nedeni toplam opak yüzey alanının duvar yüzeylerinde çatı alanına göre mertebece fazla (2,86 katı) olmasıdır.

Ankara'daki ve İzmir'deki binalar için bir önceki standarda (TS 825-2013) göre güneş enerjisi kazancı hesabı yapıldığında her iki bina için tek bir değer elde edilmektedir ve binanın güneş enerjisi kazancı 34217 kWh mertebesindedir (TSE, 2013). Bunun sebebi önceki standartta her derece gün bölgesi için tek bir güneş enerjisi kazanç tablosunun bulunmasıdır. Güncel standartta güneş enerjisi kazanç faktörleri bölgelere göre değişmektedir. Tablo 8'de görüldüğü üzere daha sıcak bölgede bulunan İzmir'de yıllık toplam güneş enerjisi kazancı 50607 kWh ile 59031kWh arasında değişmekteyken daha soğuk bölgede bulunan Ankara'da yıllık toplam güneş enerjisi kazancının 24333 kWh ile 29022 kWh arasında değiştiği görülmektedir. Bu durum bina zarfının renk tonunun değişmesinin güneş enerjisi kazancını ilgili bölgeler için %16'dan fazla etkilediğini göstermektedir.

Tablo 8. TS 825-2013'e ve TS 825-2024'e göre yıllık toplam güneş enerjisi kazançları

Bina kodu	TS 825-2013 (kWh)		TS 825-2024 (kWh)	
	İzmir	Ankara	İzmir	Ankara
RAA	34217	34217	50607	24333
ROA	34217	34217	53693	26090
RKA	34217	34217	56779	27847
RAO	34217	34217	51733	24920
ROO	34217	34217	54819	26677
RKO	34217	34217	57905	28434
RAK	34217	34217	52859	25508
ROK	34217	34217	55945	27265
RKK	34217	34217	59031	29022

4. Sonuç

Isınma ve soğutma için enerji tüketimi global olarak ciddi bir kaynak ihtiyacı doğurmaktadır. Bu sebeple binalarda ısı yalıtımının önemi uzun sürelerdir vurgulanmaktadır. Türkiye'de binalarda ısı yalıtımı esasları TS-825 standardı kapsamındadır ve standart son güncellemesinde enerji ihtiyacı hesaplamalarına opak elemanların renk koyuluğunun da dahil edilmesi gerektiğini belirtmiştir. Bu çalışmada sıcak ve soğuk bölgedeki iki şehir olan İzmir'de ve Ankara'da bulunan özdeş konut binalarının zarfının renk koyuluğunun değişiminin binaların yıllık enerji ihtiyacı üzerindeki etkileri araştırılmıştır.

Buna göre bina zarfının renk koyuluğun artması durumunda her şehirde ısıtma enerjisi ihtiyacında

azalma olurken soğutma enerjisi ihtiyacında artma olmuştur. Soğutma enerjisi talebindeki artış sıcak bölgedeki binada daha belirgin olmuştur. Bina duvar yüzeylerinin alanı çatı alanına göre daha fazla olduğu için duvar rengi koyuluğunun artması çatı rengi koyuluğunun artmasına göre enerji ihtiyacını daha fazla etkilemiştir. Standardın önceki versiyonuyla her iki şehirdeki bina için tek bir güneş enerjisi kazanç değeri hesaplanmaktayken güncel standart iklim koşullarına ve bina zarfının renk koyuluğuna göre değişen güneş enerjisi kazançları hesaplanması gerektiğini göstermektedir.

Sonuçlar ışığında yıllık enerji tüketiminde belirgin tasarruf edilebilmesi için özellikle sıcak bölgelerde yapılacak binaların duvar elemanlarının açık renk tonunda tercih edilmesinin önemi sayısal olarak ortaya konmuştur.

Katkı Oranı Beyanı

Yazarın katkı yüzdeleri aşağıda verilmiştir. Yazar makaleyi incelemiş ve onaylamıştır.

	A.H.A.
K	100
T	100
Y	100
VTI	100
VAY	100
KT	100
YZ	100
KI	100
GR	100
PY	100
FA	100

K= kavram, T= tasarım, Y= yönetim, VTI= veri toplama ve/veya işleme, VAY= veri analizi ve/veya yorumlama, KT= kaynak tarama, YZ= Yazım, KI= kritik inceleme, GR= gönderim ve revizyon, PY= proje yönetimi, FA= fon alımı.

Çatışma Beyanı

Yazar bu çalışmada hiçbir çıkar ilişkisi olmadığını beyan etmektedirler.

Etik Onay Beyanı

Bu araştırmada hayvanlar ve insanlar üzerinde herhangi bir çalışma yapılmadığı için etik kurul onayı alınmamıştır.

Kaynaklar

Aydın Ö. 2019. Binalarda enerji verimliliği kapsamında yapılan projelerin değerlendirilmesi: Türkiye örneği. Mimarlık Yaşam Derg, 4(1): 55-68.

Bektaş V, Çerçevik AE, Yerel Kandemir S. 2017. Binalarda ısı yalıtımının önemi ve ısı yalıtım malzemesi kalınlığının yalıtıma etkisi. Bilecik Şeyh Edebali Univ Fen Bilim Derg, 4(1): 36-42.

Bayındırlık ve İskân Bakanlığı. 2008. Binalarda enerji performansı yönetmeliği. Resmi Gazete, No: 27019.

İZODER. 2017. Isı yalıtımı bilgilendirme kitapçığı. URL: https://www.izoder.org.tr/dosyalar/2018-isi-yalitimi-genel-bilgi-almak-istiyorum.pdf (accessed date: May 27, 2025).

Koçu N, Dereli M. 2010. Dış duvarlarda ısı yalıtımı ile enerji tasarrufu sağlanması ve detaylarda karşılaşılan sorunlar (Konya kentinden öneriler). 5. Ulusal Çatı & Cephe Sempozyumu, Dokuz Eylül Üniversitesi, İzmir, Türkiye.

Paminto J, Fianti F, Yulianti I. 2021. The effect of surface color on the absorption of solar radiation. Phys Commun, 5(1): 27-32.

Syuhada A, Maulana MI. 2018. Heat transfer capability of solar radiation in colored roof and influence on room thermal comfort. AIP Conf Proc, 1931: 030054.

TS 825. 2013. Binalarda ısı yalıtım kuralları. Türk Standartları Enstitüsü, Ankara, Türkiye.

TS 825. 2024. Binalarda ısı yalıtım kuralları. Türk Standartları Enstitüsü, Ankara, Türkiye.

TS EN ISO 14683. 2017. Bina inşaatında termik köprüler - doğrusal ısı geçirgenliği - basitleştirilmiş yöntemler ve varsayılan değerler. Türk Standartları Enstitüsü, Ankara, Türkiye.

TÜİK. 2022. Hanehalkı nihai enerji tüketim istatistikleri. URL: https://data.tuik.gov.tr/Bulten/Index?p=Hanehalki-Nihai-Enerji-Tuketim-Istatistikleri-2022-53805 (accessed date: May 27, 2025).

Xiong K, Feng Y, Jin H, Liang S, Yu K, Kuang X, Wan L. 2023. A new model to predict soil thermal conductivity. Sci Rep, 10684.

Black Sea Journal of Engineering and Science
doi: 10.34248/bsengineering.1670833

Open Access Journal
e-ISSN: 2619 – 8991

Research Article
Volume 8 - Issue 5: 1358-1372 / September 2025

A BIBLIOMETRIC ANALYSIS ON UNIVERSITY CAMPUS DESIGN

Fazıl AKDAĞ[1]*, Fatma Betül KÜNYELİ[2], Murat Çağlar BAYDOĞAN[3]

[1]*Erciyes University, Institute of Science, Department of Architecture, 38039, Kayseri, Türkiye*
[2]*Erciyes University, Graduate School of Natural and Applied Sciences, Department of Architecture, 38039, Kayseri, Türkiye*
[3]*Erciyes University, Faculty of Architecture, Department of Architecture, 38039, Kayseri, Türkiye*

Abstract: This study provides an extensive bibliometric analysis of university campus design research, examining trends, collaborations, and thematic focuses through a systematic review of data from the Scopus database. A total of 5,753 publications from 1959 to 2024 were analyzed using VOSviewer and Biblioshiny. The results reveal a steady growth in scholarly attention to university campus design, particularly since 2007, with sustainability, digital transformation, and inclusivity emerging as dominant themes. Sustainability is highlighted as a central theme, focusing on energy-efficient materials, green infrastructure, and climate-responsive designs to address environmental challenges. For instance, life-cycle assessments underscore the importance of integrating sustainable practices during the planning stages to minimize long-term ecological impacts. Digital transformation, accelerated by the COVID-19 pandemic, is another critical trend, emphasizing the integration of hybrid learning environments, Internet of Things (IoT) technologies, and Building Information Modeling (BIM) for adaptive and data-driven campus designs. The analysis also reveals gaps in the field, such as limited research on modular and scalable designs to accommodate fluctuating populations and evolving technological needs. Additionally, the socio-cultural aspects of campus environments, including mental health, community integration and inclusivity, remain underexplored. By synthesizing past and current trends, this study provides a robust framework for advancing university campus design. It emphasizes the importance of interdisciplinary approaches, global collaboration, and innovative solutions to create campuses that are sustainable, adaptive, and inclusive, capable of meeting the evolving demands of the 21st century.

Keywords: University campus design, Bibliometric analysis, Scopus, VOSviewer, Biblioshiny

***Corresponding author:** Erciyes University, Faculty of Architecture, Department of Architecture, 38039, Kayseri, Türkiye
E mail: fazilakdag@erciyes.edu.tr (F. AKDAĞ)
Fazıl AKDAĞ https://orcid.org/0000-0002-3316-8104
Fatma Betül KÜNYELİ https://orcid.org/0000-0002-6189-5966
Murat Çağlar BAYDOĞAN https://orcid.org/0000-0002-7856-6712

Received: April 06, 2025
Accepted: July 09, 2025
Published: September 15, 2025
Cite as: Akdağ F, Künyeli FB, Baydoğan MÇ. 2025. A Bibliometric analysis on university campus design. BSJ Eng Sci, 8(5): 1358-1372.

1. Introduction

The word 'university' carries a rich historical significance, borrowed into Western languages from the Latin 'Universitas,' which means 'all, whole.' After the establishment of the republic, it was further enriched by the French 'universitè,' which signifies an institution open to the whole society and where all knowledge is taught. The Latin term 'Universitas' originally referred to a community of persons with independent legal personalities and shared interests (guilds) in the Middle Ages, the origin of the first universities (Sönmezler, 2003). Universities, whose first establishment dates back to the 12th century, have come to the present by continuously developing and increasing their social value. Kortan (1981) defines universities as 'Universitas magistrorum et scholarium,' meaning the union of teachers and students, and the living spaces of individuals or groups dealing with the fields of science, and 'Universitas Literarum,' meaning the union of sciences today. The origin of the word campus is French; 'campus' (Turner, 1990).

A campus is an accessible area reserved for an educational institution, university, or college (Paker, 2016). University campuses are living cities in terms of their functional complexity. A university campus usually includes facilities for education, training, research, administration, housing, sports and recreation, and social and auxiliary activities (Begeç, 2002).

Initially established as a single building within the city, universities evolved to meet new requirements. Different faculties were established in various parts of the city, leading to students needing to travel to multiple points in the city. To address this, universities in Rome and London were planned around the city. In contrast, universities in the US were planned as campuses outside the city. The first examples of the campus approach in the USA, inspired by the 'castra' (camps) of the Roman era, were the Universities of New York in 1813 and Virginia in 1817-1826 (Figure 1) (Kortan, 1981) and Princeton University in the second half of the 19th century (Türeyen, 2002).

In the 20th century, as the number and population of universities increased, it became difficult for campuses to find a place in the city. This situation has led to the establishment of 'university cities' which are established outside the cities and are candidates to become cities instead of the traditional 'city universities' in Europe. The conventional location of universities in the center of the city, as in Europe, has many benefits, such as the student's social integration with the city dwellers and the

completion of their development through 'non-formal education' in the city, while the city dwellers benefit from the educational and intellectual environment of the university and its facilities such as libraries, auditoriums, sports halls, etc.

Figure 1. University of Virginia campus, one of the first campus examples (Kortan, 1981).

Until the last quarter of the 20th century, when a rapid increase in the number of campuses was observed, research on university campus designs mainly addressed the issue of campus design from a more general framework. At the same time, more recent studies have focused on more specialized issues (sustainability, accessibility, etc.). In addition, while the number of users of university campuses (students-academics-administrative staff) is increasing every year, campus designs do not sufficiently focus on future growth and flexibility scenarios, and campuses with insufficient spatial adaptability to new conditions emerge. From this point of view, comprehensive research on the 'planning and design of university campuses' constitutes the motivation of this study. University campus design is a multidimensional issue that is not limited to the arrangement of physical spaces but also has direct effects on the quality of education, social interaction, and the psychological well-being of users. Well-designed campuses can provide positive outcomes such as enhancing academic performance, strengthening students' sense of belonging, and increasing the work motivation of faculty and administrative staff. Additionally, campuses designed in accordance with environmental sustainability principles can increase energy efficiency, reduce their ecological footprint, and thereby contribute to global environmental goals. Therefore, research on university campus design is of great importance in today's architecture and urban planning practice, as it enables the creation of learning environments that support academic success and the development of healthier, more inclusive, and sustainable university environments.

This research seeks to answer the research questions (RQs) listed below through bibliometric and systematic analysis conducted via the Scopus database.

RQ1. What are the publication trends?

RQ2. What are the average publications and citations per year?

RQ3. What are the most popular keywords and their clustering relations?

RQ4. What are the most relevant authors, sources, and publications?

RQ5. What are the current research limitations and future directions?

2. Materials and Methods

Manual reviews of existing studies, which refer to traditional literature review methods where researchers individually read and interpret relevant studies by noting key concepts, methodologies, and findings based on their subjective perspectives, can be limited, particularly in broad research areas with a substantial number of publications, due to being time-consuming and prone to personal interpretation biases (He et al., 2017). Moreover, manual review in scientific analysis studies tends to be biased and limited in subjective interpretation (Yalçınkaya and Singh, 2015). This necessitates using a mixed-method systematic review to synthesize the literature on a topic 'to increase the depth and breadth of understanding' (Heyvaert et al., 2016). Mixed-method systematic review studies combine quantitative and qualitative methods to integrate and analyze existing literature on a topic (Harden and Thomas, 2010). In this context, the 'bibliometric analysis method,' one of the scientific analysis and mapping methods frequently used in recent academic studies and adopted as a literature review approach, was used to reveal the relationships and the effects of the data obtained in the study.

The scientific analysis and mapping method aims to produce bibliometric maps and visuals that explain the way a scientific dataset is studied in different research fields (Van Eck and Waltman, 2010) and is used as a descriptive approach to academic studies (Tijssen and Van Raan, 1994). The bibliometric analysis method produces maps of the interrelationships between research areas and helps to identify gaps and prominent topics. This helps to fill the gap in the literature and thus enables more original studies to be conducted (Cobo et al., 2011).

In the study, the software tool for the analysis technique was first decided. Search criteria and keywords for the search query were determined. The bibliographic record data of the scientific articles obtained were taken from the Scopus database. VOSviewer and Biblioshiny are used to map these data in terms of countries, years of study, branches of science, etc., and the gaps in the research were analyzed through graphs. Afterward, the findings were evaluated, and the study was finalized by addressing the future directions. The bibliometric analysis method process for the research is shown below (Figure 2).

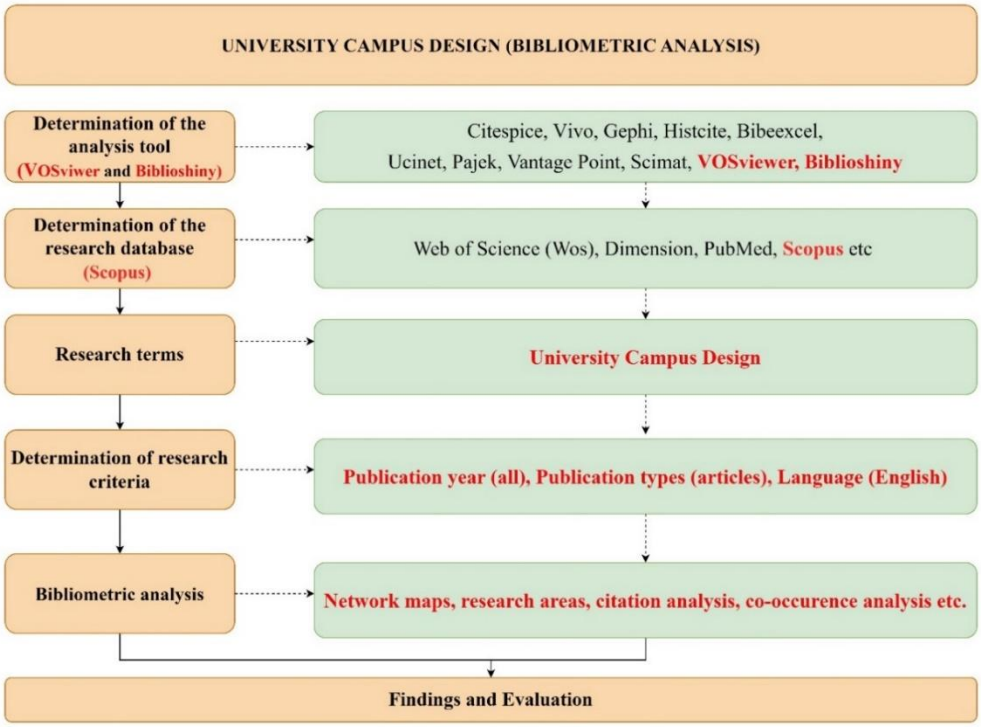

Figure 2. Bibliometric analysis workflow.

3. Bibliometric Analysis and Findings

Various software tools exist for bibliometric mapping and analysis of large-scale scientific datasets (Cobo et al., 2011). Citespice, Vivo, Gephi, Histcite, Bibeexcel, Biblioshiny, Ucinet, Pajek, Vantage Point, Scimat, and VOSviwer are the prominent ones among these tools, but VOSviewer and Biblioshiny are the most intensively used in scientific studies (Van Eck and Waltman, 2010; 2014). In this study, "university campus design" was determined as the keyword for bibliometric analysis, and this search term was analyzed in VOSviewer and Biblioshiny based on their practicality and prevalence. Both applications need information obtained from common databases in order to analyze scientific datasets. They can transform this information with relevant tools and produce maps and content for analysis.

A search in the Scopus database on 02.01.2025 conducted and 9800 studies published between 1959 and 2024 containing the words "University Campus Design" in the title, abstract, or keywords are found (Figure 3).

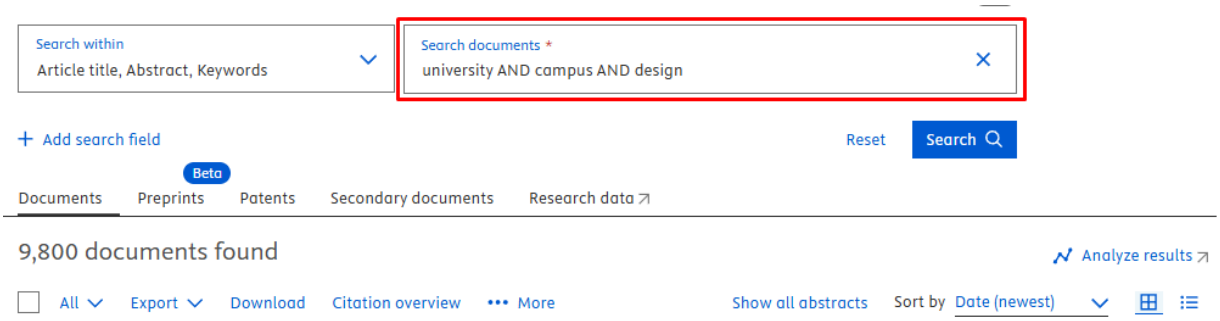

Figure 3. Search in the Scopus database.

Some of these studies were excluded from the evaluation to make a meaningful and holistic analysis and evaluation. For the studies included in the evaluation, the criteria of being conducted after 2010, having English as the language of publication, and being a research article as the publication type were determined. Under the filter of these criteria, 9800 studies were reduced to 5753, and network maps were produced based on these studies. General information related to the search outcomes can be found at Figure 4. On the other hand, The PRISMA2020 app used for facilitating the creation of flow diagrams for systematic reviews (Haddaway et al., 2022). The Preferred Reporting Items for Systematic Reviews and Meta-Analyses (PRISMA) is a globally recognized framework designed to enhance the transparency and quality of systematic reviews and meta-analyses. PRISMA provides researchers with a standardized checklist and a flow diagram to ensure that every aspect of the review

process is thoroughly documented (Moher et al., 2009). PRISMA ensures transparency throughout the systematic review process, from study selection to data synthesis. It emphasizes the need to clearly outline how studies were identified, the criteria used to select them, and the methodology for analyzing the data. This approach allows readers to fully understand the scope, methods, and results of the review (Page et al., 2021). In this scope, PRISMA workflow of the research is shown at Figure 5.

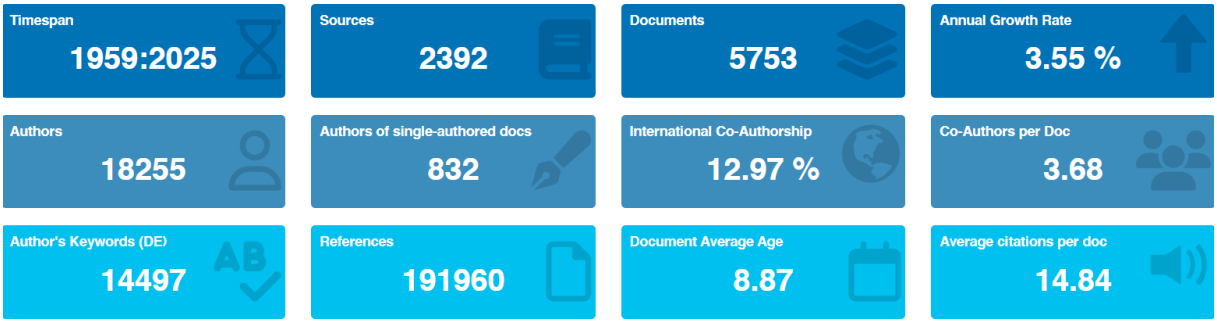

Figure 4. Main general information obtained via Biblioshiny.

According to the information obtained from Biblioshiny, a total of 5753 articles from 2392 sources were reached as a result of the relevant research between 1959-2025. The total number of authors of these articles is 18,255, the number of single-author publications is 832, and the average number of authors per publication is 3.68. The total rate of publications with international authors is 12.97% and the annual increase rate in the number of publications is 3.55%. The total number of keywords used in these publications is 14,497 and the total number of sources used is 191,960. The average age of the publications is 8.87 and the average number of citations per publication is 14.84.

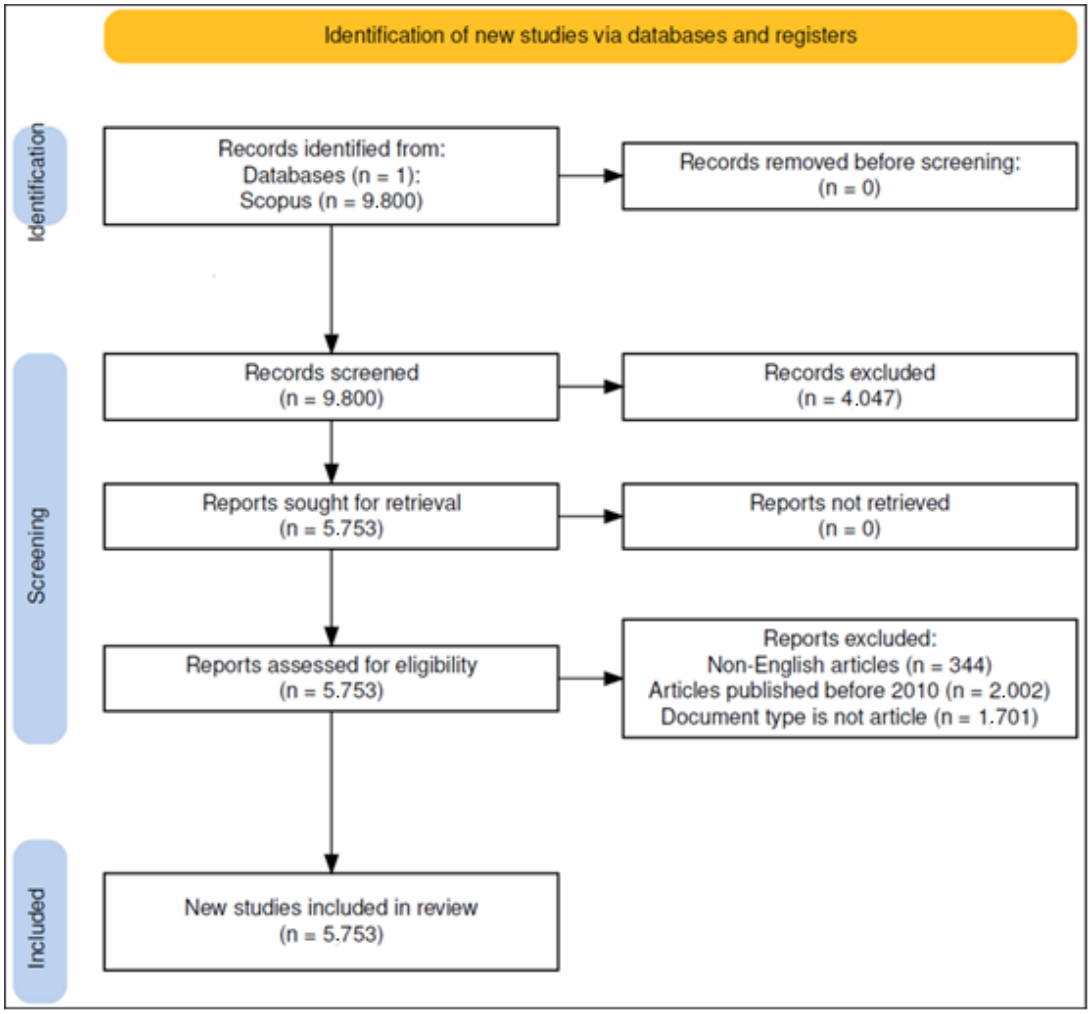

Figure 5. PRISMA workflow for the inclusion and exclusion of the research items.

In the mapping process, the publications containing the "University Campus Design" concept with at least five citations were evaluated, and total number of articles count 5753 was reduced to 2965 for the VOSviewer process. Then, the studies produced in the countries that produced at least five publications and those that received at least five citations were subjected to the final evaluation. As a result of the evaluation, the following results and findings emerged:

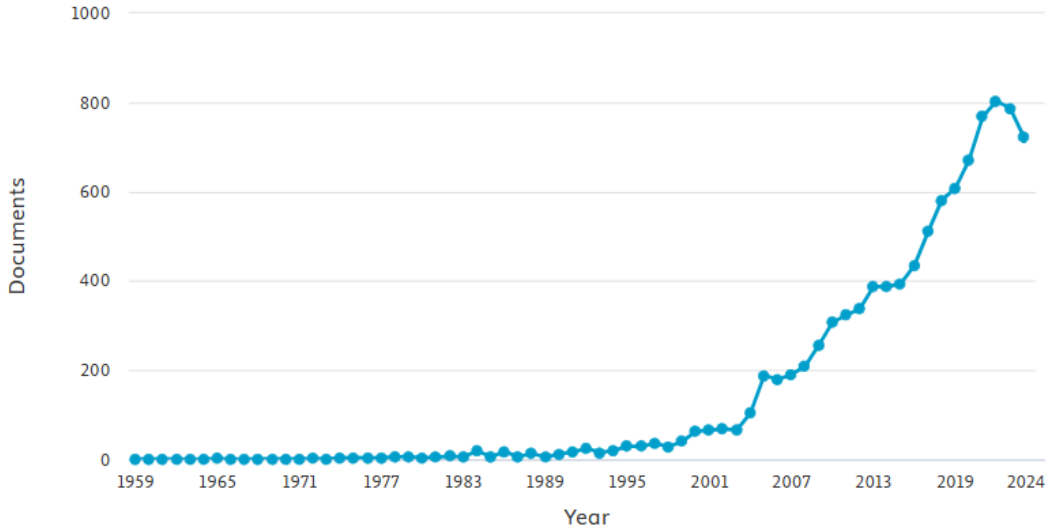

Figure 6. Distribution of publications on research terms by years.

Figure 6 shows the years of publication of the studies in the Scopus database and a significant acceleration in the research on the related topic, especially after 2007. According to the information in the graph, the number of studies on the subject shows a significant increase every year. From this point of view, it can be easily observed that university campus designs are accepted as a research area that attracts academic attention, and studies are increasingly intensifying. Since the search in Scopus was made on January 2, 2025, the number of publications in 2025 is quite low and not included in the Figure 6.

According to Figures 7 and 8, USA produces more publications on university campus design than any other country. USA, China, Australia, and the United Kingdom stand out as the countries with the most research in this field.

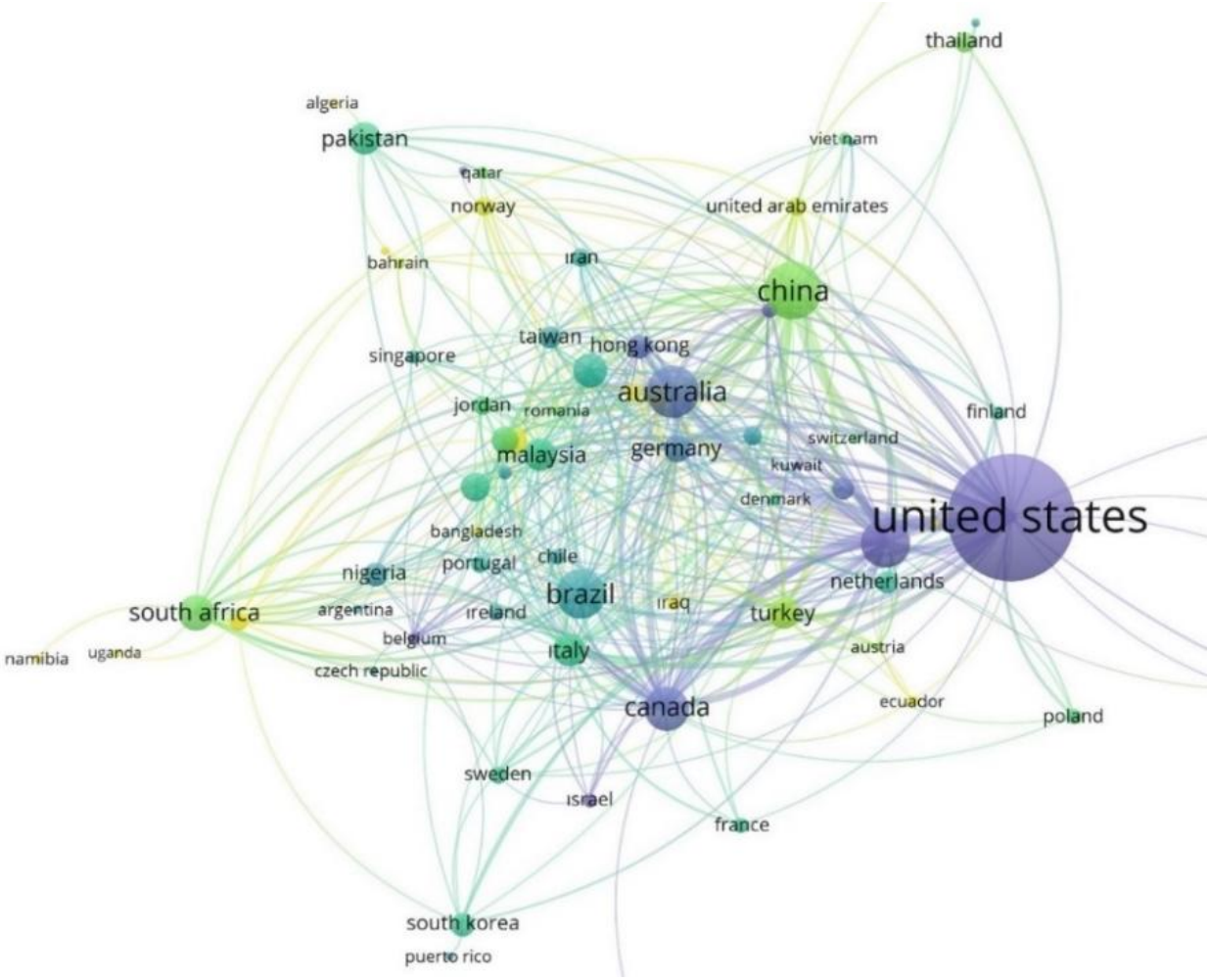

Figure 7. Most productive countries and their relations (Network map from VOSviewer).

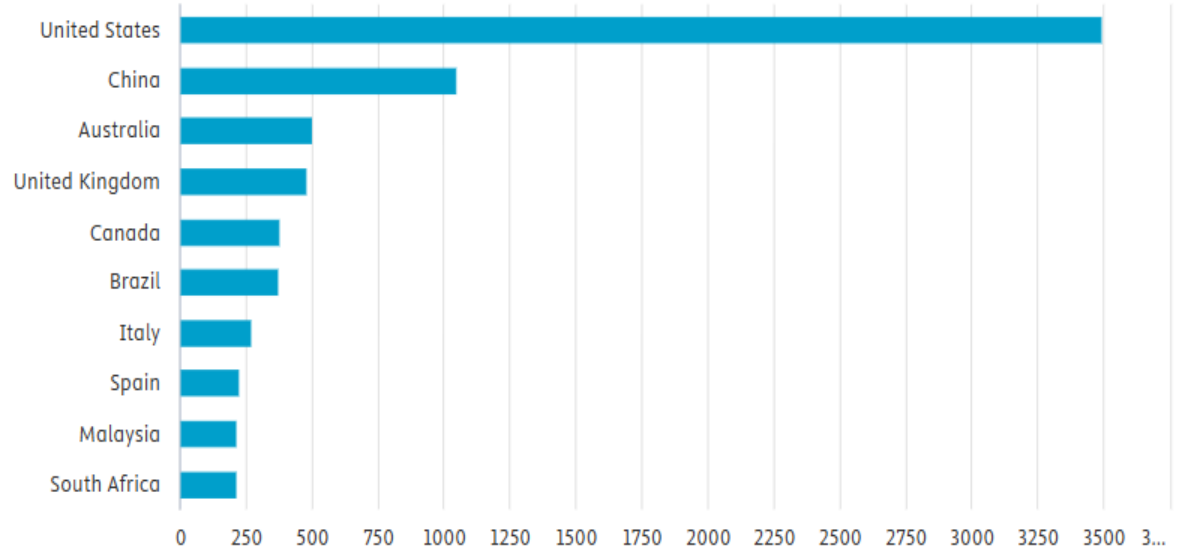

Figure 8. Countries producing the most publications on "university campus design.

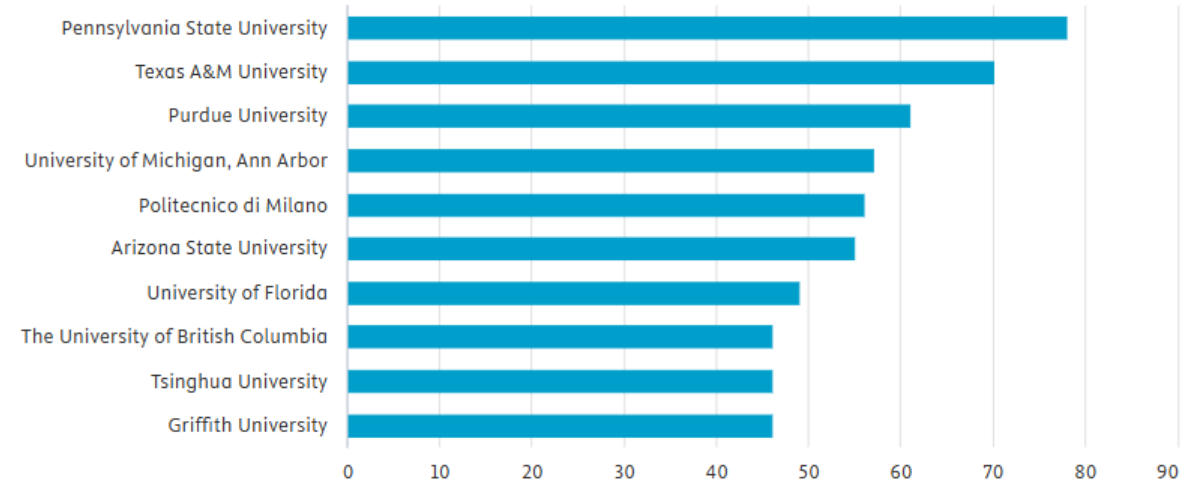

Figure 9. Universities and institutions producing the highest number of publications on research terms.

Figure 9 lists the universities and institutions that produce the most publications. Pennsylvania State University ranks first. Texas A&M University, Purdue University, and the University of Michigan follow this university. As a result of the data obtained, it is seen that US universities and institutions are also prominent in this field.

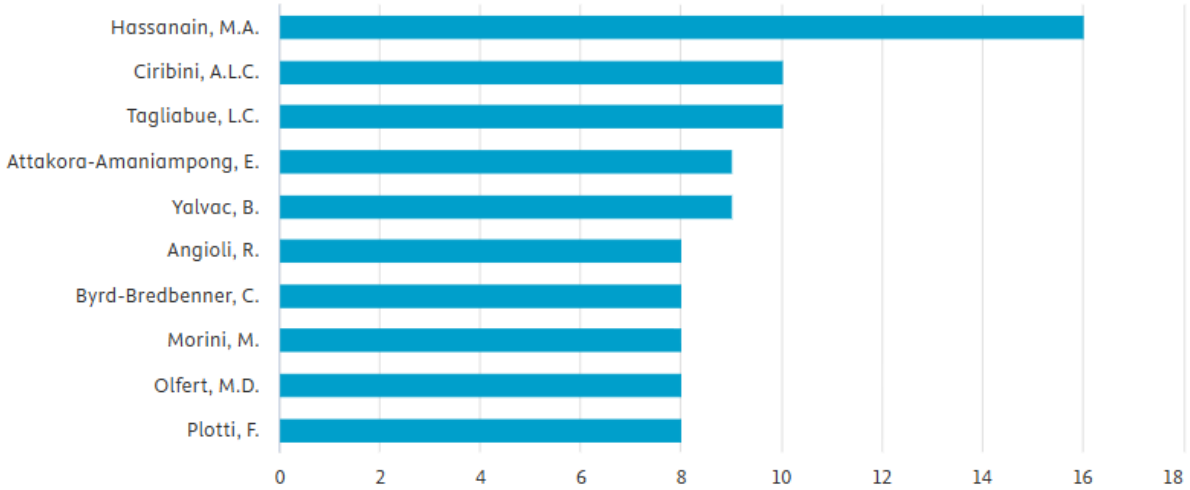

Figure 10. Researchers who produced the most publications on university campus design.

Figure 10 shows the researchers who produced the most publications on "university campus design". (Hassanain 2024; 2023; 2022; 2016; Ciribini 2021; 2017; 2016; 2015; Tagliabue 2022; 2021; 2019; 2016; 2015) stand out as researchers on the related topic. Their studies focus on sustainability, energy efficiency, and building information systems on university campuses.

Three-field chart countries (left), authors (middle), and keywords (right) is shown in Figure 11. The size of the rectangular nodes in the graph reflects the collaboration network of a particular country, author, and keyword. In this graph, the width of the lines between the nodes indicates the number of connections. According to the data in the Figure 11, China is the country with most connections followed by USA and Brazil. "University campus", "Covid 19", "college students", "higher education" and, "students" are the most common keywords in order according to the date obtained from Biblioshiny app.

When the types of publications produced on university campus design are analyzed as in Figure 12, articles have the most significant percentage, followed by conference proceedings and book chapters.

According to the Figure 13, social sciences stand out in the distribution of research fields on "university campus design", followed by engineering sciences, computer sciences, and other disciplines.

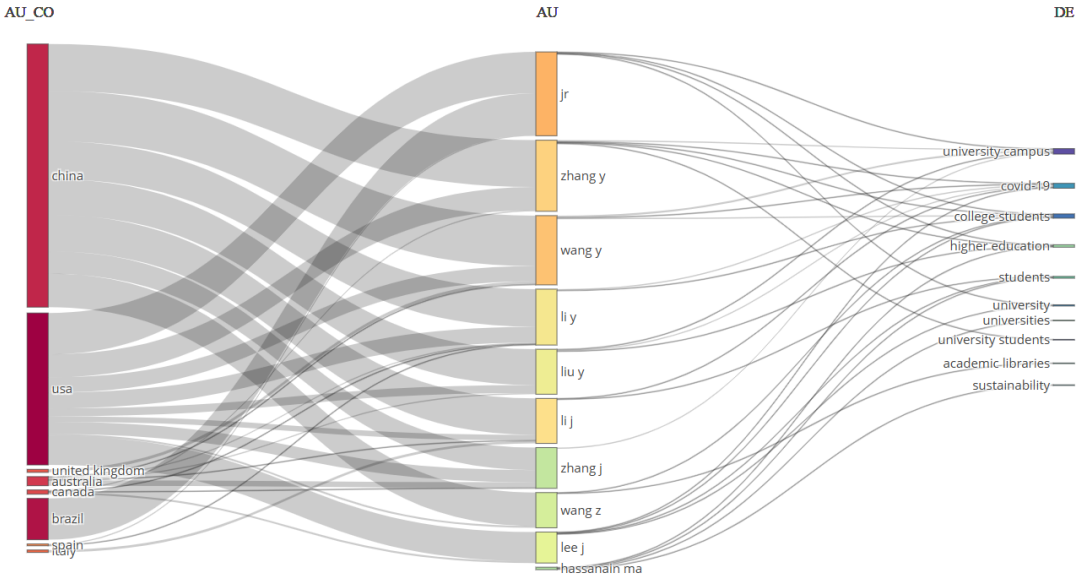

Figure 11. Three-Field Plot produced with Biblioshiny.

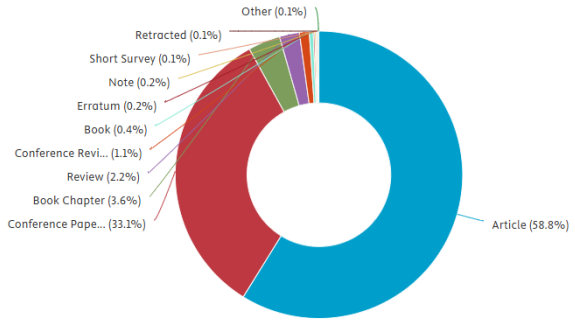

Figure 12. Distribution of types of publications produced on research terms.

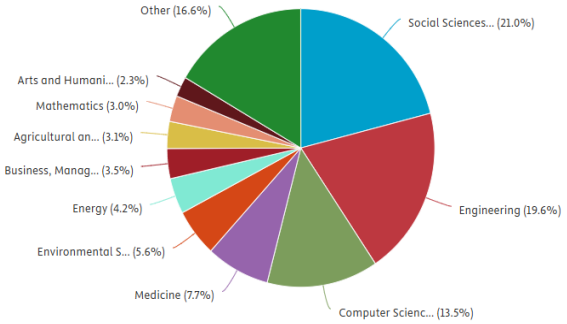

Figure 13. Distribution of publications on research terms according to research fields.

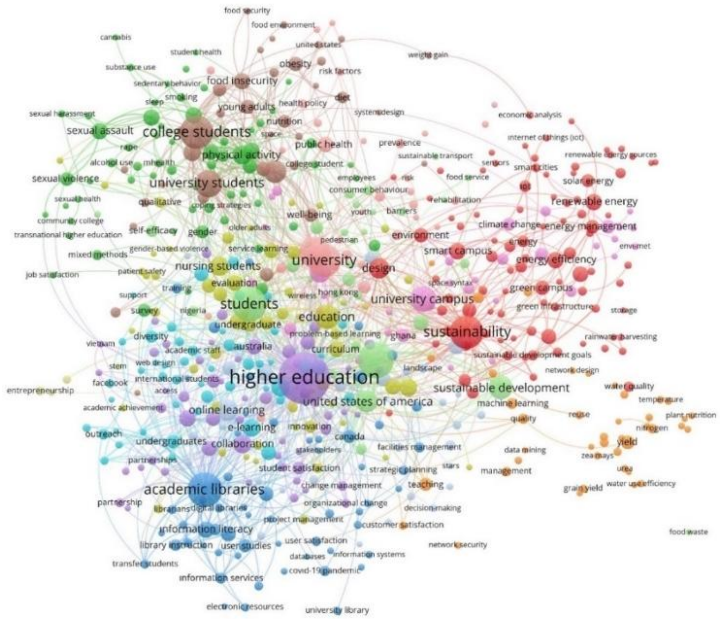

Figure 14. Interaction network map from VOSviewer related to research terms.

Keyword	Occurrences	Total link strength
higher education	304	596
universities	148	386
students	137	335
academic libraries	135	311
sustainability	128	282
university	127	271
covid-19	111	208
college students	127	204
united states of america	54	168
education	70	158
university students	85	136
mental health	58	134
sustainable development	63	131
university campus	77	121
design	47	100
college	31	94
campus	51	92
online learning	50	89
learning	38	85
depression	37	83

Figure 15. Keywords with which research terms interact most intensively.

According to the information in the network map in Figure 14 and data table in the Figure 15, the research areas and keywords that studies on university campus design focus on are 'higher education, universities, students, academic libraries, and sustainability' in order of interaction.

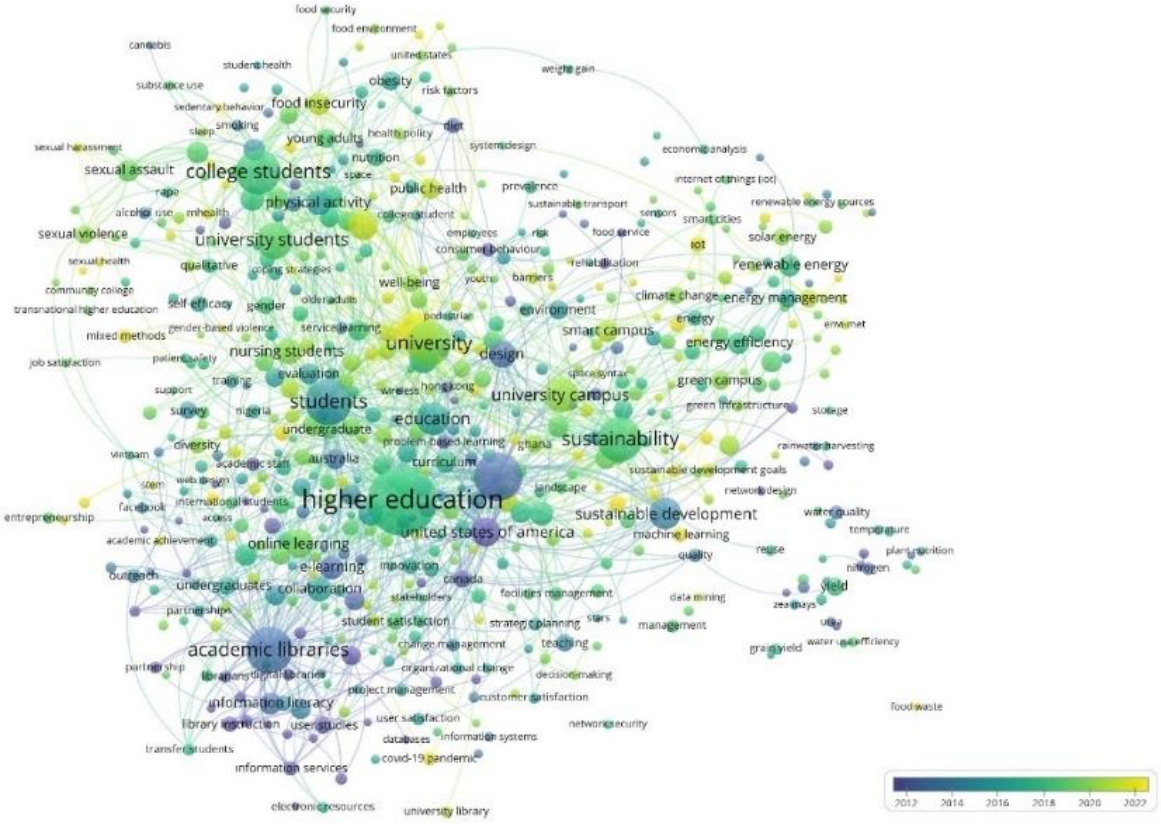

Figure 16. Distribution map of publications on research terms by years.

According to Figure 16, when the publications produced in the last 15 years covering 2010-2025 are evaluated, it is seen that the publications produced between 2016-2020 stand out. However, studies focusing on different topics on the subject are concentrated in different years. For example, research focused on 'higher education' was mainly produced between 2018-2020, while research focused on 'sustainability' was mainly produced between 2020-2022. Studies in areas that are not as popular as other topics, such as 'academic libraries,' are concentrated in earlier years.

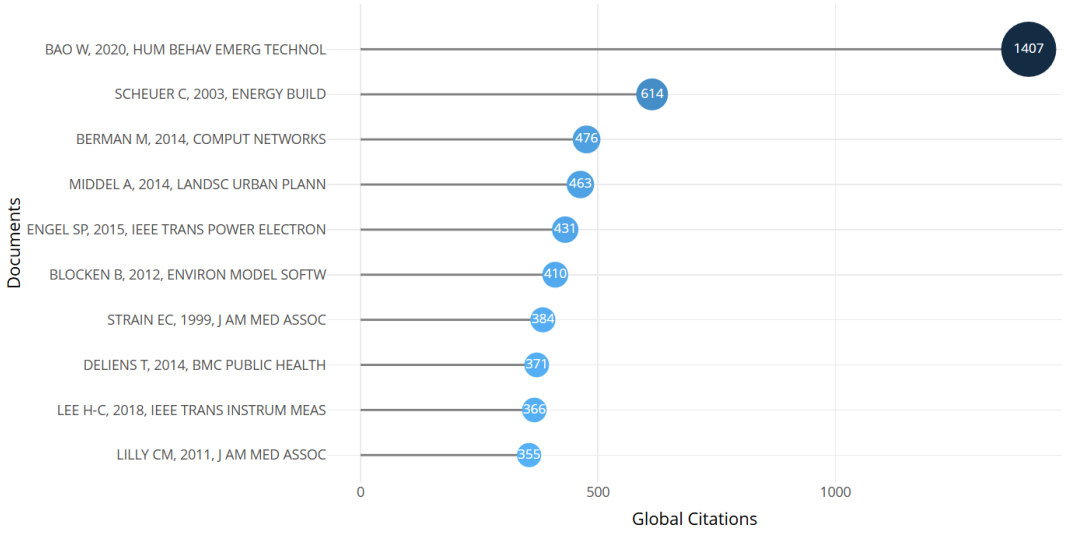

Figure 17. Most cited articles.

Figure 17 shows the top 10 most cited authors with the exact citation numbers. Bao, (2020) is the most cited author with 1407 total citations followed by Scheuer (2003) with 614 citations and Berman (2014) with 476 citations. Table 1 shows these 10 most cited articles' details regarding of their topics and methodologies.

Table 1. Summary of top 10 most cited articles

Title	Topic	Method	Reference
COVID-19 and online teaching in higher education: A case study of Peking University	COVID-19 and Online Teaching in Higher Education: A Case Study of Peking University	Analyzes instructional strategies and principles for effective online education during the COVID-19 pandemic, focusing on design, delivery, and contingency plans for higher education.	Bao, 2020 (Human Behavior and Emerging Technologies)
Life cycle energy and environmental performance of a new university building: modeling challenges and design implications	Life Cycle Energy and Environmental Performance of a New University Building	Utilizes life cycle assessment to evaluate energy consumption, material use, and environmental impact across a building's lifespan, highlighting challenges in sustainable design.	Scheuer et al., 2003 (Energy and Buildings)
GENI: A federated testbed for innovative network experiments	GENI: A Federated Testbed for Innovative Network Experiments	Describes the design and deployment of GENI as a virtual testbed for advanced networking experiments, including SDN and distributed computing innovations.	Berman et al., 2014 (Computer Networks)
Impact of urban form and design on mid-afternoon microclimate in Phoenix Local Climate Zones	Impact of Urban Form and Design on Microclimate in Phoenix Local Climate Zones	Uses ENVI-met simulations to study how urban design influences mid-afternoon microclimate conditions, identifying effective cooling strategies for semi-arid cities.	Middel et al., 2014 (Landscape and Urban Planning)
Comparison of the Modular Multilevel DC Converter and the Dual-Active Bridge Converter for Power Conversion in HVDC and MVDC Grids	Comparison of Modular Multilevel DC Converter and Dual-Active Bridge Converter	Benchmarks two power converter types for HVDC and MVDC grids, evaluating efficiency, cost, and scalability in renewable energy applications.	Engel et al., 2014 (IEEE Transactions on Power Electronics)

Table 1. Summary of top 10 most cited articles (continuing)

CFD simulation for pedestrian wind comfort and wind safety in urban areas: General decision framework and case study for the Eindhoven University campus	CFD Simulation for Pedestrian Wind Comfort and Safety in Urban Areas	Develops a framework using CFD to evaluate wind flow, safety, and comfort in urban environments, validated with field measurements and applied to Eindhoven University.	Blocken et al., 2012 (Environmental Modelling & Software)
CFD simulation for pedestrian wind comfort and wind safety in urban areas: General decision framework and case study for the Eindhoven University campus	Moderate- vs High-Dose Methadone in the Treatment of Opioid Dependence	Conducts a randomized trial comparing efficacy and retention rates of moderate- and high-dose methadone for opioid dependence treatment.	Strain et al., 1999 (JAMA)
Determinants of eating behaviour in university students: a qualitative study using focus group discussions	Determinants of Eating Behaviour in University Students: A Qualitative Study	Explores factors influencing eating behaviors through focus groups, offering tailored recommendations for promoting healthy eating in a university setting.	Deliens et al., 2014 (BMC Public Health)
Monitoring of Large-Area IoT Sensors Using a LoRa Wireless Mesh Network System: Design and Evaluation	Monitoring of Large-Area IoT Sensors Using LoRa Wireless Mesh Network System	Designs and evaluates a LoRa mesh network for IoT sensor monitoring, demonstrating enhanced packet delivery ratio and cost efficiency.	Lee and Ke, 2018 (IEEE Transactions on Instrumentation and Measurement)
Hospital Mortality, Length of Stay, and Preventable Complications Among Critically Ill Patients Before and After Tele-ICU Reengineering of Critical Care Processes	Hospital Mortality, Length of Stay, and Preventable Complications with Tele-ICU	Analyzes the impact of tele-ICU systems on critical care outcomes, emphasizing adherence to best practices and reduction in preventable complications.	Lilly et al., 2011 (JAMA)

According to the Table 1, The top 10 most-cited publications address a variety of themes, such as sustainability, microclimate effects, user comfort, and the integration of digital technologies in campus design. The studies employ diverse methodologies, including case studies, simulations, experimental data, and qualitative research, offering a wide range of perspectives on campus design challenges. Sustainability and digitalization emerge as key trends in campus design, reflecting the growing need for energy-efficient and technologically advanced infrastructure. Following section indicates importance and insights of each research;

COVID-19 and Online Teaching in Higher Education: A Case Study of Peking University (Bao, 2020)

Importance: This study highlights how the sudden shift to online education during the pandemic required campuses to adapt their technological and spatial infrastructure to support remote learning.

Insight: It underscores the importance of flexible spaces and digital infrastructure in campus design to accommodate hybrid education models.

Life Cycle Energy and Environmental Performance of a New University Building (Scheuer et al., 2003)

Importance: This research uses life cycle assessment to evaluate the energy consumption and environmental impacts of university buildings, providing actionable insights for sustainable design.

Insight: The study emphasizes integrating energy-efficient materials and processes into the planning stages to reduce long-term environmental impacts.

GENI: A Federated Testbed for Innovative Network Experiments (Berman et al., 2014)

Importance: This publication discusses the development of a testbed for networking innovations, which has implications for building digital ecosystems within campus environments.

Insight: It showcases the role of campus networks as hubs for research and innovation, advocating for robust and scalable digital infrastructure.

Impact of Urban Form and Design on Microclimate in Phoenix Local Climate Zones (Middel et al., 2014)

Importance: This study uses ENVI-met simulations to examine how urban form and landscape design influence microclimates, particularly in hot, arid environments.

Insight: It offers practical recommendations for mitigating urban heat island effects through thoughtful spatial arrangements and green infrastructure in campus design.

Comparison of Modular Multilevel DC Converter and Dual-Active Bridge Converter (Engel et al., 2014)

Importance: By comparing two types of power converters, the study provides insights into renewable energy systems suitable for campus applications.

Insight: The findings can inform the integration of scalable and cost-effective renewable energy solutions into campus infrastructure.

CFD Simulation for Pedestrian Wind Comfort and Safety in Urban Areas (Blocken et al., 2012)

Importance: The study develops a framework using computational fluid dynamics (CFD) to evaluate pedestrian wind comfort and safety, with a case study focused on a university campus.

Insight: It provides a methodological foundation for assessing the aerodynamic impact of high-rise buildings and open spaces on campus comfort and usability.

Moderate- vs High-Dose Methadone in the Treatment of Opioid Dependence (Strain et al., 1999)

Importance: While primarily focused on healthcare, this study indirectly highlights the role of campus-based health services in addressing public health issues like opioid dependence.

Insight: The findings can inform the design of campus health centers with specialized facilities for mental health and addiction recovery.

Determinants of Eating Behaviour in University Students: A Qualitative Study (Deliens et al., 2014)

Importance: This qualitative study explores the factors influencing eating behaviors among university students, such as social networks, time constraints, and campus food environments.

Insight: The research suggests designing affordable and accessible dining options on campuses to promote healthy eating habits.

Monitoring of Large-Area IoT Sensors Using LoRa Wireless Mesh Network System (Lee and Ke, 2018)

Importance: This publication investigates the application of IoT technologies for large-scale monitoring, providing valuable insights for smart campus initiatives.

Insight: It highlights the potential of IoT-based solutions for real-time monitoring of environmental and operational conditions across campus facilities.

Hospital Mortality, Length of Stay, and Preventable Complications with Tele-ICU (Lilly et al., 2011)

Importance: The study examines the impact of tele-ICU systems on healthcare outcomes, showcasing the role of remote monitoring and digital health technologies in critical care.

Insight: It advocates for incorporating telemedicine and remote care systems into campus-based medical facilities.

Summary the findings in the table:

Sustainability as a Priority: Sustainable energy systems, efficient materials, and climate-responsive designs are central to modern campus planning.

Digital Transformation: The integration of advanced digital systems, from IoT networks to hybrid learning platforms, is essential for creating adaptive and future-proof campuses.

Human-Centric Design: Catering to the physical, social, and psychological needs of students and staff such as healthy dining, safe pedestrian zones, and access to health services enhances campus usability and inclusivity.

4. Discussion and Conclusion

This study provides a comprehensive bibliometric analysis of university campus design research, offering an in-depth exploration of its trends, gaps, and future directions. By analyzing a dataset of 9800 publications from 1959 to 2024, sourced from the Scopus database, the study reveals the dynamic evolution of this interdisciplinary field in response to global challenges such as sustainability, digital transformation, and inclusivity. The analysis, conducted using VOSviewer and Biblioshiny, maps relationships between disciplines, institutions, and thematic priorities, providing a robust framework for advancing the discourse in campus design.

The findings demonstrate a notable increase in scholarly activity post-2007, with peak growth observed between 2016 and 2020. This corresponds to the heightened global emphasis on sustainability, digitalization, and accessibility. The annual growth rate of publications is 3.55%, reflecting sustained academic engagement. With an average citation count of 14.84 per publication, the field continues to attract attention, though its dissemination and influence can be further enhanced.

Sustainability emerges as the dominant theme in campus design research, reflecting the urgency to address climate change and resource efficiency. Life-cycle energy assessments, green infrastructure, and energy-efficient materials feature prominently in the literature. For instance, Scheuer et al. (2003), one of the most-cited articles with 614 citations, underscores the importance of early-stage sustainable design to minimize long-term environmental impacts. Middel et al. (2014) explores the role of microclimate-sensitive designs in mitigating urban heat islands, offering actionable strategies for enhancing ecological balance and campus comfort.

Digital transformation has become a pivotal trend, further accelerated by the COVID-19 pandemic. The most-cited article in the dataset, Bao (2020), with 1407 citations, highlights the need for adaptable digital infrastructures to support hybrid learning models. Technologies such as Building Information Modeling (BIM) and the Internet of Things (IoT) are revolutionizing campus planning, enabling data-driven decision-making and enhancing operational efficiency. These innovations represent a paradigm shift towards adaptive, future-ready campus environments that integrate physical and digital spaces seamlessly.

The interdisciplinary nature of the field is evident, with major contributions from social sciences (40%), engineering (25%), and computer sciences (15%). Topics like "higher education," "academic libraries," and "students" dominate the discourse, reflecting the multifaceted priorities of campus design. However, the field still faces significant gaps. Research on flexible and scalable campus designs remains limited, leaving universities ill-equipped to address fluctuating student populations, evolving technological advancements, and shifting pedagogical needs. Similarly, the social and psychological dimensions of campus design, including its impact on mental health, social engagement, and inclusivity, are underexplored. For example, Deliens et al. (2014), with 53 citations, highlights the role of campus environments in shaping student behaviors, emphasizing the need for accessible and user-friendly designs.

Geographically, the United States leads in research output and citation impact, contributing 18.35% of total publications. Other major contributors include China, Australia, and the United Kingdom. However, developing nations like Türkiye remain underrepresented, with international co-authorship accounting for only 12.97% of publications. This highlights the need for greater global collaboration and the inclusion of diverse socio-economic and geographic perspectives. According to the analysis results, it has been observed that campus design research is concentrated in academic centers sourced from developed countries such as the USA, UK, and Australia. At the core of this regional focus are the strong academic networks, funding opportunities, and access to effective platforms in international publications that universities in developed countries possess. Additionally, the findings we observed, where campus design increasingly focuses on themes such as digitalization, sustainability, and scalability, may hinder the representation of universities in developing countries in international publications because these universities tend to concentrate more on practical applications and short-term solutions to concrete local needs. Therefore, it is crucial to promote interdisciplinary collaborations and integrate digital-sustainable innovations with local applications to enhance the international visibility of campus design studies in universities of developing countries.

Institutions such as Pennsylvania State University, Texas A&M University, and Purdue University dominate in research output, reflecting a concentration of high-impact studies in resource-rich academic centers.

The insights from the most-cited articles provide valuable perspectives on core themes:

- Bao (2020) underscores the shift toward hybrid education, advocating for robust digital infrastructures that support both virtual and physical learning.
- Scheuer et al. (2003) highlights sustainability, emphasizing the importance of integrating energy-efficient materials during planning stages.
- Middel et al. (2014) offers practical solutions for urban heat mitigation, showcasing the role of green infrastructure in improving campus microclimates.
- Blocken et al. (2012) introduces a framework for assessing wind comfort and safety in campus spaces, contributing to user-centric design approaches.
- Deliens et al. (2014) examines the environmental factors affecting student eating behaviors, recommending accessible and health-conscious dining facilities.

Despite these advancements, significant research gaps persist:

- Regional Imbalances: The concentration of research in developed nations limits the applicability of findings to diverse contexts. Developing regions require tailored solutions to address their unique challenges.
- Modularity and Scalability: Static campus designs fail to accommodate fluctuating user needs and technological advancements, necessitating adaptive and reconfigurable models.
- Physical-Digital Integration: Hybrid campuses that seamlessly combine physical and virtual infrastructures remain underexplored, especially in light of post-pandemic educational demands.
- Social and Community Integration: The interplay between campuses and their surrounding urban environments requires further study to foster mutual benefits in social, cultural, and economic domains.

To address these gaps, future research should focus on:

- Developing cost-effective, localized sustainability strategies that incorporate renewable energy systems and climate-resilient features.
- Prioritizing modular, scalable, and adaptable campus designs to accommodate changing demographics and technological advancements.
- Expanding the integration of smart campus technologies, such as IoT, AI, and big data, to optimize operations and enhance user experiences.
- Exploring designs that support hybrid learning environments, ensuring compatibility between physical and digital infrastructures.
- Strengthening global research networks to promote knowledge sharing and bridge regional disparities.
- Emphasizing user-centric approaches that enhance accessibility, inclusivity, and well-being, creating welcoming and innovative environments.

University campuses are no longer merely physical spaces

for education but dynamic ecosystems that integrate academic, technological, environmental, and social considerations. By addressing existing limitations and leveraging interdisciplinary approaches, the field can evolve toward creating campuses that are resilient, inclusive, and future-ready. This study provides a foundational framework for advancing campus design research, underscoring the transformative potential of universities to act as pioneers of innovation, sustainability, and societal progress in the 21st century.

Author Contributions

The percentages of the authors' contributions are presented below. All authors reviewed and approved the final version of the manuscript.

	F.A.	F.B.K.	M.Ç.B.
C	25	50	25
D	25	50	25
S	25	50	25
DCP	25	50	25
DAI	25	50	25
L	25	50	25
W	25	50	25
CR	25	50	25
SR	25	50	25
PM	25	50	25
FA	25	50	25

C=Concept, D= design, S= supervision, DCP= data collection and/or processing, DAI= data analysis and/or interpretation, L= literature search, W= writing, CR= critical review, SR= submission and revision, PM= project management, FA= funding acquisition.

Conflict of Interest

The authors declared that there is no conflict of interest.

Ethical Consideration

Since this study did not involve any studies on animals or humans, ethics committee approval was not obtained

References

Bao W. 2020. COVID-19 and online teaching in higher education: A case study of Peking University. Hum Behav Emerg Technol. 2(2): 113-115. https://doi.org/10.1002/hbe2.191

Begeç H. 2002. Üniversitelerde kampus yerleşme biçimleri. Yapı Derg, 252: 57-63.

Berman M, Chase JS, Landweber L, Nakao A, Ott M, Raychaudhuri D, Ricci R, Seskar I. 2014. GENI: A federated testbed for innovative network experiments. Comput Netw, 61: 5-23. https://doi.org/10.1016/j.bjp.2013.12.037

Blocken B, Janssen WD, van Hooff T. 2012. CFD simulation for pedestrian wind comfort and wind safety in urban areas: General decision framework and case study for the Eindhoven University campus. Environ Model Softw, 30: 15-34. https://doi.org/10.1016/j.envsoft.2011.11.009

Cobo MJ, López-Herrera AG, Herrera-Viedma C, Herrera F. 2011. Science mapping software tools: Review, analysis, and cooperative study among tools. J Am Soc Inf Sci Technol, 62(7): 1382-1402. (accessed date: October 20, 2024). https://doi.org/10.1002/asi.21525

Deliens T, Clarys P, De Bourdeaudhuij I, Deforche B. 2014. Determinants of eating behaviour in university students: A qualitative study using focus group discussions. BMC Public Health, 14(1): 53. https://doi.org/10.1186/1471-2458-14-53

Engel SP, Stieneker M, Soltau N, Rabiee S, Stagge H, De Doncker RW. 2014. Comparison of modular multilevel DC converter and dual-active bridge converter for power conversion in HVDC and MVDC grids. IEEE Trans Power Electron, 30(1): 124-137. https://doi.org/10.1109/TPEL.2014.2310656

Haddaway NR, Page MJ, Pritchard CC, McGuinness LA. 2022. PRISMA2020: An R package and Shiny app for producing PRISMA 2020-compliant flow diagrams, with interactivity for optimised digital transparency and open synthesis. Campbell Syst Rev, 18(2): e1230. https://doi.org/10.1002/cl2.1230

Harden A, Thomas J. 2010. Mixed methods and systematic reviews: Examples and emerging issues. In: Tashakkori A, Teddlie C (Eds.), SAGE handbook of mixed methods in social & behavioral research (2nd ed., pp: 749-774). SAGE Publications, (accessed date: December 10, 2024). https://methods.sagepub.com/book/sage-handbook-of-mixed-methods-social-behavioral-research

He Q, Wang G, Luo L, Shi Q, Xie J, Meng X. 2017. Mapping the managerial areas of Building Information Modeling (BIM) using scientometric analysis. Int J Project Manag, 35(4): 670-685. (accessed date: November 15, 2024). https://doi.org/10.1016/j.ijproman.2016.08.001

Heyvaert M, Hannes K, Onghena P. 2016. Using mixed methods research synthesis for literature reviews: The mixed methods research synthesis approach (Vol. 4). Sage Publications, pp: 344. (accessed date: October 13, 2024). https://doi.org/10.4135/9781483399935

Kortan E. 1981. Çağdaş üniversite kampusları tasarımı. ODTÜ, Mimarlık Fakültesi, Mimarlık Bölümü, Ankara. pp: 196.

Lee HC, Ke KH. 2018. Monitoring of large-area IoT sensors using LoRa wireless mesh network system: Design and evaluation. IEEE Trans Instrum Meas, 67(9): 2177–2187. https://doi.org/10.1109/TIM.2018.2814082

Lilly CM, Cody S, Zhao H, Landry K, Baker SP, McIlwaine J, Chandler MW, Irwin RS. 2011. Hospital mortality, length of stay, and preventable complications among critically ill patients before and after tele-ICU reengineering of critical care processes. JAMA, 305(21): 2175-2183. https://doi.org/10.1001/jama.2011.697

Middel A, Häb K, Brazel AJ, Martin CA, Guhathakurta S. 2014. Impact of urban form and design on mid-afternoon microclimate in Phoenix Local Climate Zones. Landsc Urban Plan, 122: 16-28. https://doi.org/10.1016/j.landurbplan.2013.11.004

Moher D, Liberati A, Tetzlaff J, Altman DG, The PRISMA Group. 2009. Preferred reporting items for systematic reviews and meta-analyses: The PRISMA statement. PLOS Med, 6(7): e1000097. https://doi.org/10.1371/journal.pmed.1000097

Page MJ, McKenzie JE, Bossuyt PM, Boutron I, Hoffmann TC, Mulrow CD, … Moher D. 2021. PRISMA 2020 explanation and elaboration: Updated guidance and exemplars for reporting systematic reviews. BMJ, 372: n160. https://doi.org/10.1136/bmj.n160

Paker N. 2016. Üniversite-kampüs ilişkisinin tarihsel gelişimi üzerine bir okuma. Mimarlık Kültür Dergisi, Mimarist, 16(1): 44-49.

Scheuer C, Keoleian GA, Reppe P. 2003. Life cycle energy and environmental performance of a new university building:

Modeling challenges and design implications. Energy Build, 35(10): 1049-1064. https://doi.org/10.1016/S0378-7788(03)00066-5

Sönmezler K. 2003. Modern mimarinin kentsel deney alanı: Üniversite tasarımı. PhD thesis, Mimar Sinan Fine Arts University, Institute of Science, İstanbul. pp: 115.

Strain EC, Bigelow GE, Liebson IA, Stitzer ML. 1999. Moderate- vs high-dose methadone in the treatment of opioid dependence: A randomized trial. JAMA, 281(11): 1000-1005. https://doi.org/10.1001/jama.281.11.1000

Tijssen RJW, Van Raan AFJ. 1994. Mapping changes in science and technology: Bibliometric co-occurrence analysis of the R&D literature. Eval Rev, 18(1): 98–115. (accessed date: October 13, 2024). https://doi.org/10.1177/0193841X9401800110

Turner PV. 1990. Some thoughts on history and campus planning. Plan High Educ, 16(3): 1–28. (accessed date: September 11, 2024). https://eric.ed.gov/?id=EJ372294

Türeyen MN. 2002. Yükseköğretim kurumları: Kampuslar. Tasarım Yayın Grubu. İstanbul, Türkiye, pp: 66-94.

Van Eck NJ, Waltman L. 2010. Software survey: VOSviewer, a computer program for bibliometric mapping. Scientometrics, 84(2): 523–538. (accessed date: September 11, 2024). https://doi.org/10.1007/s11192-009-0146-3

Van Eck NJ, Waltman L. 2014. Visualizing bibliometric networks. In: Ding Y, Rousseau R, Wolfram D (Eds.), Measuring scholarly impact: Methods and practice. Springer, pp: 285–320. (accessed date: October 17, 2024). https://doi.org/10.1007/978-3-319-10377-8_13

Yalçınkaya M, Singh V. 2015. Patterns and trends in building information modeling (BIM) research: A latent semantic analysis. Autom Constr, 59: 68–80. (accessed date: December 21, 2024). https://doi.org/10.1016/j.autcon.2015.07.012

Black Sea Journal of Engineering and Science
doi: 10.34248/bsengineering.1699472

Open Access Journal
e-ISSN: 2619 – 8991

Research Article
Volume 8 - Issue 5: 1373-1400 / September 2025

A CONTEMPORARY APPROACH TO SOLVING SELECTION PROBLEMS: THE ENTROPY-BASED PERFORMANCE MEASUREMENT METHOD

Furkan Fahri ALTINTAŞ[1]*

[1]*Aydın Provincial Gendarmerie Command, Ata OSB, 09010, Efeler, Aydın, Türkiye*

Abstract: In this study, the applicability of the widely used entropy method traditionally employed for calculating criterion weights in the Multi-Criteria Decision-Making (MCDM) literature is investigated as a novel approach for measuring the performance of alternatives. The proposed method, termed Entropy-Based Performance Measurement (EBPM), is grounded in the principle of continuously increasing uncertainty inherent in both natural and social systems. The primary motivation of this approach is to demonstrate, through sensitivity, comparative, and simulation analyses, that the method can produce ideally sensitive, reliable, consistent, stable, and robust results. The study aims to expand the application domain of the entropy method and to contribute to both the MCDM and entropy literature. EBPM is theoretically based on entropy's inherent capability to quantify and enhance informational performance. Without manipulating the original entropy equation, the entropy function is reformulated into a positively increasing structure, enabling it to measure the performance of alternatives. In the methodology section, the characteristics of 15 widely recognized MCDM methods are introduced, the theoretical and mathematical foundations of the proposed approach are explained, and its applicability is demonstrated using the innovation performance data of seven countries selected from the 2024 Global Innovation Index. In the results and discussion section, the quantitative findings and comprehensive explanations of the proposed method are presented in detail. Thus, this study aims to broaden the potential of the entropy method within the field of MCDM and to offer a novel perspective for decision-making processes.

Keywords: MCDM, Entropy, EBPM

***Corresponding author:** Aydın Provincial Gendarmerie Command, Ata OSB, 09010, Efeler, Aydın, Türkiye
E mail: furkanfahrialtintas@yahoo.com (F.F. ALTINTAŞ)
Furkan Fahri ALTINTAŞ https://orcid.org/0000-0002-0161-5862

Received: May 14, 2025
Accepted: July 09, 2025
Published: September 15, 2025

Cite as: Altıntaş FF. 2025. A contemporary approach to solving selection problems: The entropy-based performance measurement method BSJ Eng Sci, 8(5): 1373-1400.

1. Introduction

The development of new Multi-Criteria Decision-Making (MCDM) methods is of critical importance for overcoming the limitations of existing approaches and offering solutions to a wider range of problem types (Ćirovic and Pamučar, 2022). While traditional methods may be effective under certain criteria, they often fall short when addressing complex and dynamic challenges. Overcoming these limitations enables more accurate and reliable decision-making outcomes. Innovative MCDM approaches enhance the accuracy of decision support processes and strengthen overall decision-making efficiency (Lopez et al., 2023).

Therefore, the discovery and development of novel MCDM methods can provide effective solutions to increasingly complex problems and allow for more refined decisions through the interaction of multiple criteria. This is especially significant in addressing contemporary critical issues such as sustainability, resource management, and risk analysis. One of the core components of MCDM methods characteristic quantitative superiority objectively reveals the relative dominance of alternatives across multiple criteria (Thakkar, 2021).

Such an approach renders the decision-making process more rational and consistent under prevailing conditions, thus enabling decision-makers to make more reliable and defensible choices. Characteristic quantitative superiority enhances the credibility of decision support systems and clarifies the distinctions between alternatives, thereby contributing to scientifically grounded solutions (Owen, 2023).

In this context, the study proposes a novel method for evaluating the performance of alternatives based on the Entropy method, which is frequently employed in the MCDM literature for calculating the weight values of criteria. This method, referred to as the Entropy-Based Performance Measurement (EBPM), aims to extend the applicability of entropy beyond traditional weight determination, offering a performance evaluation mechanism of alternatives within the broader MCDM framework.

The primary motivation of this research is to demonstrate that the proposed method possesses ideal

sensitivity through sensitivity analyses, yields credible and reliable outcomes in comparative analyses, and proves to be stable and robust under simulation conditions. An additional motivation is to expand the application scope of the entropy method, thereby contributing to both the MCDM literature and entropy-based analytical approaches.

The theoretical foundation of the EBPM method is grounded in the frequently cited notion in the literature that entropy and by extension, uncertainty exhibits a continuously increasing and positively oriented behavior in both natural and social systems (Shankar, 2014). The second theoretical foundation of the method is based on the assumption that the presence of entropy reduces the existing information performance of the systems it influences and consequently increases their information requirements. Accordingly, low levels of entropy imply high information performance, whereas high levels of entropy indicate reduced information performance (Aksakal and Çalışkan, 2020). Within the framework of these two theoretical premises, the entropy function is employed without modifying the original entropy equation, thereby establishing a positively progressive structure that effectively measures the performance of alternatives.

In the methodology section, the study first introduces the characteristics of 15 widely used MCDM methods, each with distinct structural features. Subsequently, the theoretical and mathematical foundations of the proposed EBPM method are comprehensively detailed. Finally, the performance of seven countries selected from the 2024 Global Innovation Index is evaluated using the proposed method based on innovation performance criteria. The discussion section elaborates on the quantitative results.

2. Materials and Methods

2.1. Some MCDM Methods and Their Properties

MCDM methods play a fundamental role in complex decision-making processes, particularly in selecting the most appropriate solution among various alternatives and evaluating the performance of each alternative based on specific criteria (Munier, 2024). In today's decision-making landscape, decision-makers are often faced with a wide array of alternatives possessing diverse attributes, making it essential to identify the optimal choice (Munier, 2021). This process becomes especially crucial in contexts characterized by high uncertainty and complexity, where considering multiple criteria enables more comprehensive and balanced decisions compared to single-criterion evaluations (Zardari et al., 2014).

The literature offers a wide range of MCDM methods, each grounded in different computational techniques. These methods contribute to decision support processes by analyzing alternative performance according to their unique structural frameworks (Thanh, 2021). Such approaches allow decision-makers to assess the strengths and weaknesses of each alternative while maintaining a balance among criteria. The significance of MCDM lies in its ability to facilitate more effective and informed decisions across various spheres of life. From business and public administration to education and healthcare, MCDM methods serve as valuable tools for solving complex problems and achieving optimized outcomes. Moreover, these methods are critical for the efficient allocation of resources, minimizing risks, and promoting sustainable decision-making practices. As such, MCDM methodologies are indispensable in contemporary decision-making environments where complexity, diversity, and uncertainty are inherent.

As a result, it is commonly observed that researchers make extensive use of methods such as Simple Additive Weighting (SAW) (Azadfallah, 2025), the Weighted Product Method (WPM) (Fan et al., 2025), the Technique for Order of Preference by Similarity to the Ideal Solution (TOPSIS) (Paradhita et al., 2025), the Weighted Aggregated Sum Product Assessment (WASPAS) (Chen et al., 2025), the Measurement of Alternatives and Ranking according to Compromise Solution (MARCOS) (Roshanravan et al., 2025), the multi-attributive border approximation area comparison (MABAC) (Mehdiabadi, et al., 2025), CRADIS (Aghamammadli et al., 2024), the Multiple Attribute Utility Theory (MAUT) (Permata et al., 2025), the range of value (ROV) (Anđić, 2024), the Complex Proportional Assessment (COPRAS) (Ballamudi, 2024) the ranking of alternatives through functional mapping of criterion sub-intervals into a single interval (RAFSI) (Trung et al., 2022), the combined compromise solution (COCOSO) (Lendvai et al., 2025), the proximity indexed value (PIV) (Ersoy, 2024), the multi attributive ideal-real comparative analysis (MAIRCA) (Öztaş and Öztaş, 2024), and the additive ratio assessment (ARAS) (Aydemir, 2025).

The SAW method, also known as the scoring method, is applicable exclusively to numerical and comparable data sets (Demirci, 2020). The quantitative performances of the alternatives are evaluated based on normalized and weighted values corresponding to the criteria (Sutoyo et al., 2025). The method begins with the construction of a decision matrix. Subsequently, the data are normalized, and the normalized values are multiplied by the respective criterion weights to obtain the weighted normalized decision matrix (Ciardiello and Genovese, 2023). In the final step, the overall score for each alternative is calculated. These scores are then ranked in descending order, thereby facilitating the selection process and concluding the decision-making procedure (Ciardiello and Genovese, 2023)

The WPM evaluates each decision alternative by computing the product of the normalized values corresponding to each criterion, raised to the power of the respective criterion weights (Kaya and Karaşan, 2020). In this context, the quantitative performance of alternatives is based on weighted normalized values

(Chinnasamy et al., 2023). The method involves the following steps: constructing the decision matrix, normalizing the matrix, and then applying exponential weighting to the normalized values using the corresponding criterion weights (Chinnasay et al., 2023). In the final step, the weighted values for each criterion are multiplied for each alternative to obtain the overall performance score. These scores are then ranked in descending order to complete the decision-making process (Alali et al., 2023).

The TOPSIS evaluates decision alternatives based on their proximity to a positive ideal solution and their distance from a negative ideal solution (Başdar, 2019; Çankaya Kurnaz, 2025). The positive ideal solution represents the best values for each criterion, whereas the negative ideal solution represents the worst (Aktaş et al., 2015). In this context, the quantitative superiority of alternatives is associated with being closer to maximum values for benefit-oriented criteria and farther from minimum values (Kaymaz et al., 2020). The TOPSIS method involves several steps: constructing the decision matrix, normalizing the data, and generating the weighted decision matrix by multiplying normalized values with corresponding criterion weights (Çelikbilek, 2018). Subsequently, the ideal (positive) and anti-ideal (negative) values are determined, and the Euclidean distances of each alternative to these reference points are calculated (Tepe, 2021; Han et al., 2025). In the final step, the relative closeness of each alternative to the positive ideal solution is computed, and the alternatives are ranked in descending order according to these scores (Chaipetch et al., 2025: Han et al., 2025; Alqoud et al., 2025).

The WASPAS method is an integrated multi-criteria decision-making technique that combines the principles of the SAW and WPM approaches (Özdemir, 2018; Chen et al., 2025). The methodology involves the construction of a decision matrix, normalization of the input data, and subsequent calculation of relative importance scores using both SAW and WPM formulations (Arisantoso et al., 2023; Radomska-Zalas, 2023). In the final step, a composite optimality score is computed for each alternative. These scores are then ranked in descending order to determine the most suitable alternative (Zavadskas et al., 2012; Handayani et al., 2023).

The MARCOS method evaluates decision alternatives through a compromise-based approach that considers their proximity to the ideal (AI) and anti-ideal (AAI) solutions (Ecer, 2020). The alternative that is closest to the ideal solution and farthest from the anti-ideal solution is regarded as the most preferable option (El-Araby et al., 2024). The method begins with the normalization of the decision matrix, followed by the application of weights, and then the computation of criterion total for each alternative (Muni et al., 2024). The quantitative superiority of alternatives is associated with their closeness to ideal values and distance from anti-ideal values, particularly in benefit-oriented criteria (Trung, 2021). Utility degrees are determined by relating these totals to both the ideal and anti-ideal solutions. In the final step, performance scores are calculated using a ratio-based approach that simultaneously considers both reference points (Munier et al., 2024; Andrejic and Vukasin, 2025).

The MABAC method is an evaluation approach based on the distance of each alternative from the boundary approach area of the criterion functions (Ecer, 2020). In the first three steps, a decision matrix is created, normalized, and the weighted normalized decision matrix is obtained (Keleş, 2023). In the fourth step, the boundary approach area matrix is determined, and in the fifth step, the distances of the alternatives to this area are calculated (Akmaludin et al., 2024). The quantitative performance of the alternatives is related to the height of the weighted normalized values and their distance to the boundary approach values of the criteria (Bektaş, 2023). In the final step, the distance values of each alternative across all criteria are summed, and the performance scores are ranked in descending order. (Doković and Doljanica, 2023; Yadav et al., 2025).

The CRADIS method is MCDM approach that evaluates alternatives based on their deviations from the ideal, anti-ideal, and optimal solutions through a utility function (Çilek and Şeyranlıoğlu, 2025). The method begins with the creation, normalization, and weighting of the decision matrix. Subsequently, the ideal and anti-ideal solution values are determined, and deviations from these values are calculated (Puška et al., 2023). The utility functions for the alternatives are derived based on these deviation levels. In the final step, both the ideal and anti-ideal solutions are equally weighted, and the average performance of each alternative is determined. In this context, the quantitative superiority of the alternatives depends on the low deviation levels from the ideal and anti-ideal solutions (Özekenci, 2024).

The MAUT method is an approach aimed at maximizing total utility through real-valued utility functions in decision problems involving multiple, conflicting criteria (Atan and Altan, 2020). Preferences are expressed through the utility functions defined for each criterion (Begam, 2024). The method begins with the creation of the decision matrix and the normalization of the data (Çetinkaya et al., 2023). The normalized values are integrated into the exponential form of the base of the natural logarithm, e, and then the ratio of 1 minus this value to 1.71 is calculated, allowing the marginal utility scores of the alternatives to be determined. The quantitative superiority of the alternatives is related to the magnitude of these marginal utility values based on the exponential values (Ecer, 2020). Finally, the total utility score for each alternative is determined by summing the weighted marginal utilities, and the alternatives are ranked in descending order based on these scores (Özkaya, 2024).

The ROV method begins with the creation of the decision matrix, similar to the SAW method (Turan and Bulak, 2023). In the second step, the matrix values are normalized, and in the third step, the normalized values are weighted, with benefit and cost-oriented criteria summed separately (Madić and Radovanović, 2015). In the final step, the averages of these sums are calculated to determine the performance scores of the alternatives (Madić et al., 2016). In this method, the quantitative superiority of the alternatives is directly related to the magnitude of the weighted normalized criterion values (Ulutaş and Topal, 2020).

The COPRAS method provides a percentage-based analysis by separately considering benefit- and cost-oriented criteria in the evaluation of decision alternatives (Goswami et al., 2021). The method begins with the construction of the decision matrix, followed by normalization of the data and application of the criterion weights. Based on the weighted normalized values, the benefit and cost criteria are aggregated separately (Taherdoost and Mohebi, 2024). The relative significance of each alternative is determined using these values, and performance indices are then calculated. In this context, higher values for benefit criteria and lower values for cost criteria indicate the quantitative superiority of the alternatives (Paksoy, 2017). Finally, the alternatives are ranked in descending order according to their performance indices (Organ and Yalçın, 2016).

The RAFSI method diverges from conventional normalization processes by introducing a distinctive standardization approach capable of transforming data variations within the decision matrix across any subinterval. This feature aims to fulfill the conditions of ideal decision-making (Alossta et al., 2021). The method begins with the construction of the decision matrix. In the second step, the matrix values are matched with their corresponding criterion weights. In the third step, both arithmetic and harmonic means are calculated for each alternative (Žižovic et al., 2020). Subsequently, a normalized decision matrix is derived based on these averages. In the final step, the criterion functions for each alternative are aggregated to determine their overall performance scores (Demir, 2021).

The COCOSO method, developed through the integration of the SAW and WPM techniques, offers a unified compromise decision-making strategy by combining two distinct aggregation logics. Accordingly, the quantitative superiority of alternatives aligns with the dominance structures inherent in both SAW and WPM approaches (Ecer, 2020). The method begins with the construction of the decision matrix, followed by the formation of the normalized decision matrix. In the third step, the sum of the weighted normalized values (S) and the product of the exponential weighted values (P) are calculated (Rasoanaivo et al., 2024). In the fourth step, three distinct evaluation strategies are applied based on the magnitude of the S and P values. In the final step, the arithmetic and geometric means of these strategies are used to derive the performance scores of the alternatives. In this context, higher values of S and P indicate greater quantitative superiority of the alternatives (Tesic et al., 2023).

The PIV method is based on the principle that the best decision alternatives should be closest to the positive ideal solution. In this method, the proximity index is used to measure the deviations of the normalized values of the alternatives from the ideal values, which vary according to whether the criteria are benefit or cost-oriented (Goswami et al., 2022). These indices are calculated by incorporating the weights of the criteria and are linearly aggregated across all attributes to determine the overall proximity value of each alternative. Within this framework, the alternative with the greatest total weighted normalized proximity is considered the optimal decision alternative (Trung and Tan, 2023). The procedure involves the following steps: construction of the decision matrix, generation of the normalized decision matrix, formation of the weighted normalized decision matrix, calculation of the Weighted Proximity Index for each alternative, and finally, the evaluation of the Overall Proximity Values of the alternatives (Khan et al., 2019).

The MAIRCA method is based on determining the discrepancy between the theoretical solution and the actual outcomes. In this method, the total deviation of each alternative from the expected performance for each criterion is considered (Aksoy, 2021). Accordingly, alternatives with the smallest difference between the theoretical and actual evaluations are deemed to have the greatest quantitative superiority. The procedure begins with the construction of the decision matrix in the first step, followed by the formulation of the preference values for the alternatives in the second step (Zolfani et al., 2020). In the third step, a theoretically derived matrix is developed, while in the fourth step, the actual evaluation matrix is constructed (Işık et al., 2025). Subsequently, a deviation matrix is obtained, and finally, the functional values or performance scores for each alternative are calculated in the last step (Ulutaş, 2019).

In the ARAS method, decision alternatives are evaluated based on their benefit levels, and the optimality value of each alternative is compared with a reference alternative (Altın, 2020). The process begins with the construction of the decision matrix and the normalization of the data. Subsequently, the normalized values are weighted, and the optimality function value for each alternative is calculated accordingly (Arslan, 2017). In the final stage, these values are compared to the reference alternative to determine the performance levels of all alternatives, which are then ranked in descending order (Özbek and Erol, 2017). Therefore, in this method, the quantitative superiority of the alternatives is directly associated with the magnitude of their weighted normalized values (Özbek, 2019).

2.2. Proposed Method: ENTROPY-Based Performance Measurement (EBPM)

Shannon entropy, one of the fundamental concepts of information theory, was introduced by Claude E. Shannon in 1948 (Krippendorff, 2019). First defined in his seminal work "A Mathematical Theory of Communication", this concept aims to quantitatively measure the level of uncertainty contained within a system or probability distribution (Nanda, 2020). Moreover, entropy is widely employed to determine the average amount of information conveyed by a message or dataset (Robinson, 2008). In this context, the entropy formula is presented in equation 1 (Cincotta et al., 2021).

$$E = -\sum_{i=1}^{m} \left(p_{ij} * In(p_{ij})\right) \quad (1)$$

In the entropy equation presented in Equation 1, E denotes the total entropy (i.e., the information content or degree of uncertainty); p_{ij}represents the probability of occurrence of the $i-th$ event in the $j-th$ condition; ln refers to the natural logarithm (logarithm to the base e); and m indicates the number of data points. Accordingly, the fundamental assumption of Shannon entropy is that events or communication processes occur with specific probabilities (Stevenson, 2021). In this context, low-probability (low entropy) events are considered to carry more information, whereas high-probability (high entropy) events are assumed to provide less information. This characteristic renders the entropy measure an effective indicator for evaluating the overall informational potential of a system by taking into account the probability distribution of events (Bahadır and Türkmençalıkoğlu, 2021).

However, some limitations of Shannon entropy have also been highlighted in the literature. Particularly in systems involving continuous variables, the entropy value may yield negative results or possess units with ambiguous physical interpretations. Such issues complicate the practical applicability of the method (Rudnicki, 2011). Despite these challenges, Shannon entropy remains one of the most fundamental and widely accepted measures for quantitatively assessing information content in the field of information theory (van Stokkum, 2024). In summary, Shannon entropy serves as a critical tool for quantitatively evaluating the uncertainty or unpredictability inherent in a random variable or probability distribution. Within the framework of information theory, it plays a significant role in assessing the informational potential of systems and is extensively applied across various decision-making domains (Zaeemzadeh and Tononi, 2024).

The principal aim of Shannon entropy is to quantitatively measure the "amount of information" conveyed by a random variable. When the probabilities associated with a variable are characterized by high uncertainty meaning that each outcome has an equal likelihood of occurring the entropy value becomes high. This indicates a low level of existing informational performance and suggests that more information is required to adequately describe the system (Mishra et al., 2019). Conversely, when the outcomes of a variable are more distinct and predictable such that one particular outcome has a much higher probability than the others the entropy value is low. This implies that there is already sufficient informational performance to understand or describe the system, and less additional information is needed (Sharma et al., 2015).

In information theory, entropy is generally associated with concepts such as "uncertainty," "disorder," or "randomness." It is also directly related to "information content," as the realization of an uncertain (i.e., high-entropy) event introduces new information. In cases where entropy is high, the informational performance is low, meaning that each observed event contributes substantially to new knowledge. In contrast, when entropy is low, the information performance per event is considered adequate, or only a limited amount of new information is required. This underscores the notion that enhancing the potential to gain information about an event is only feasible by reducing the uncertainty surrounding that event. High entropy reflects increased complexity or disorder, and the occurrence of low-probability (high-entropy) events is typically associated with a need for greater information acquisition (Aksakal and Çalışkan, 2020).

In the MCDM literature, Shannon entropy is commonly utilized in the criterion weighting process (Ecer, 2020). In this context, entropy emerges as a crucial tool for ensuring a more objective and balanced weighting when evaluating different alternatives (Ayçin, 2019). By considering the uncertainties and diversity among the criteria, entropy serves as a method that contributes to the decision-making process (Dinçer, 2019). The entropy equation used in criterion weighting is detailed in equation 2 (Öztel and Alp, 2020). Subsequently, equation 3 is utilized to measure the importance weights of the criteria within the scope of MCDM (Öztel and Alp, 2020).

$$E_j = -\frac{1}{In(m)} \sum_{i=1}^{m} \left(p_{ij} * In(p_{ij})\right) \quad (2)$$

$$w_j = 1 - E_j \quad (3)$$

Within the framework of Equation 2, the criterion exhibiting the lowest entropy value corresponds to the one possessing the least uncertainty and, consequently, the highest information capacity (Uludağ and Doğan, 2021). This observation leads to the inference that such a criterion represents the most significant factor, thereby commanding the highest weight. In this context, Shannon entropy, as a quantifier of uncertainty, effectively serves as an indicator of information-carrying potential (Demir

et al., 2021). Accordingly, entropy, or uncertainty, can be conceptualized as an independent variable, while the performance related to information acquisition may be treated as the dependent variable.

In the MCDM literature, the application of entropy is predominantly confined to its role as an independent variable within the criterion weighting process. However, a notable gap exists in the extant literature, as no studies have been identified that mathematically model the influence of entropy itself representing the inherent information potential on the performance evaluation of the alternatives. Consequently, it is postulated that, analogous to the utilization of Shannon entropy as an independent variable for criterion weighting, the information capacity signified by entropy should also be considered a pertinent factor potentially influencing the performance outcomes of the alternatives.

Conventionally within MCDM literature, entropy is employed almost exclusively as an independent variable for the purpose of deriving weights (Bircan, 2020; Baş, 2021). Nevertheless, a mathematical framework that explicitly models the information potential engendered by uncertainty, within the scope of entropy throughout the decision-making process, remains conspicuously absent. It is therefore proposed that, just as entropy serves as an independent variable for criterion weighting in MCDM methodologies, low entropy indicative of high information potential associated with alternatives could be recognized as a factor that positively modulates their information-based performance capabilities. In this regard, the entropy method can be regarded as a potent instrument within decision-making paradigms, contributing significantly to the clarification and refinement of the information presented to the decision-maker (Öztel and Alp, 2020).

Stated differently, when the decision-making process is conceptualized as an information processing sequence, decision-pertinent information characterized by low uncertainty, which impacts the alternatives, is conveyed, perceived, and processed via the inherent attributes of these alternatives. Within this paradigm, the attributes of the alternatives constitute the fundamental conduits of information. The comprehensiveness and diversity of the information presented through these attributes under conditions of low entropy at the critical decision point directly correlate with the magnitude of their influence on the final decision (Chakraborty et al., 2015).

From an alternative viewpoint, the concept of entropy, or information content, can be defined as the capacity to generate signals possessing communication potential. The principal objective herein is the faithful transmission of the intended information or information content without degradation or loss. Indeed, the necessity for information concerning an event arises only when uncertainty pervades that event. Therefore, if an event exhibits a low probability of occurrence, corresponding to high entropy, it implies that the available information potential is diminished, necessitating the acquisition of further information (Uludağ and Doğan, 2021). In this context, the information performance of alternatives is amenable to quantification through an entropy-based approach, potentially utilizing the entropy method itself.

It is well-established that the standard Entropy method, particularly when applied using normalized data constrained to the [0, 1] interval, exhibits a non-monotonic behaviour initially increasing and subsequently decreasing. This characteristic is inconsistent with the inherent expectation within the MCDM context of achieving quantitative superiority when evaluating alternative performance. For instance, in methods such as SAW, WPM, COCOSO, and WASPAS, the quantitative dominance of alternatives is directly proportional to the magnitude of the criterion weights and the normalized performance values; as these values increase, the overall performance scores of the alternatives correspondingly rise (Thakkar, 2021).

Conversely, other MCDM techniques, including TOPSIS, MARCOS, and ARAS, assess alternative performance based on their proximity to ideal solutions (maximum for benefit criteria, minimum for cost criteria) (Munier, 2024). In light of these divergences, it can be asserted that, particularly within the framework of Multi-Criteria Decision-Making (MCDM) utilizing [0, 1] normalized values, the Entropy method exhibits inconsistent behavior in reflecting the quantitative superiority derived from the magnitudes of criterion weights and normalized data when assessing the performance of alternatives.

Conversely, the monotonically increasing nature of Shannon entropy provides a more robust and widely accepted metric for information measurement. This aligns with the established principle, observed across natural and social-sciences, that entropy tends perpetually towards an increase. A prime exemplification of this is Heisenberg's Uncertainty Principle, which stipulates that the position and momentum of a particle cannot be simultaneously determined with absolute precision. This limitation arises not from an inability to measure the momentum transferred during, for instance, a photon-electron collision, but rather from the inherent constraints of the measurement process itself (Köksal and Köseoğlu, 2010). In quantum mechanics, predicting both the position and momentum of an electron with certainty is impossible; an increase in the uncertainty of a particle's position corresponds to a decrease in the uncertainty (entropy) related to its momentum, and vice versa. Consequently, nature exhibits an inherent tendency towards increasing entropy (Apaydın, 2004; Sakurai and Napolitano, 2012).

Similarly, the Second Law of Thermodynamics defines entropy and dictates its directionality in thermal processes, asserting that the entropy of the universe is constantly increasing (Shankar, 2014). Furthermore, Boltzmann's H-Theorem, which examines the statistical

behavior of gas molecules, mathematically substantiates the monotonic increase of entropy over time (Gressman and Strain, 2010). The Clausius inequality offers another mathematical perspective, asserting that entropy cannot decrease in any cyclic process; rather, it is constrained to increase or remain constant (Narang et al., 2024). From a social science perspective, Gini (2000) posits that human interactions within social systems perpetually augment entropy. Moreover, considering the principle of information conservation alongside the non-additive nature of information and the additive property of entropy collectively underscores the continuity and persistent increase of entropy within isolated systems (Zhang, 2008). The continuous formation of Shannon entropy can be achieved without manipulating the entropy equation, but by ensuring that the process operates under equal conditions for all values, thereby maintaining the continuity of the entropy function's increase. In this context, the proposed method ensures the continuous increasing position of the entropy function in order to establish quantitative superiority in measuring the performance of alternatives within the MCDM framework. Initially, the weighted normalized values and their original entropy simulation positions are presented in Table 1, while their graphical representation is illustrated in Figure 1.

Table 1. Entropy values of the weighted normalized values

(wd_{ij}^{*})	m=2	m=3	m=4	m=5
0.1	0.332193	0.209590	0.166096	0.143068
0.2	0.464386	0.292995	0.232193	0.200000
0.3	0.521090	0.328771	0.260545	0.224421
0.4	0.52877124	0.33361751	0.26438562	0.22772938
0.400001	0.52877112	0.33361743	0.26438556	0.22772932
0.5	0.500000	0.315465	0.250000	0.215338
0.6	0.442179	0.278984	0.221090	0.190436
0.7	0.360201	0.227262	0.180101	0.155130
0.8	0.257542	0.162491	0.128771	0.110918
0.9	0.136803	0.086313	0.068401	0.058918
0.999999	0.0000014	0.0000009	0.0000007	0.0000005
(wd_{ij}^{*})	m=6	m=7	m=8	m=9
0.1	0.12851	0.11833	0.11073	0.10480
0.2	0.17965	0.16542	0.15480	0.14650
0.3	0.20159	0.18562	0.17370	0.16439
0.4	0.20455664	0.18835212	0.17625708	0.16680875
0.400001	0.20455659	0.18835207	0.17625704	0.16680872
0.5	0.19343	0.17810	0.16667	0.15773
0.6	0.17106	0.15751	0.14739	0.13949
0.7	0.13934	0.12831	0.12007	0.11363
0.8	0.09963	0.09174	0.08585	0.08125
0.9	0.05292	0.04873	0.04560	0.04316
0.999999	0.0000055	0.0000055	0.0000055	0.0000055

m: number of components

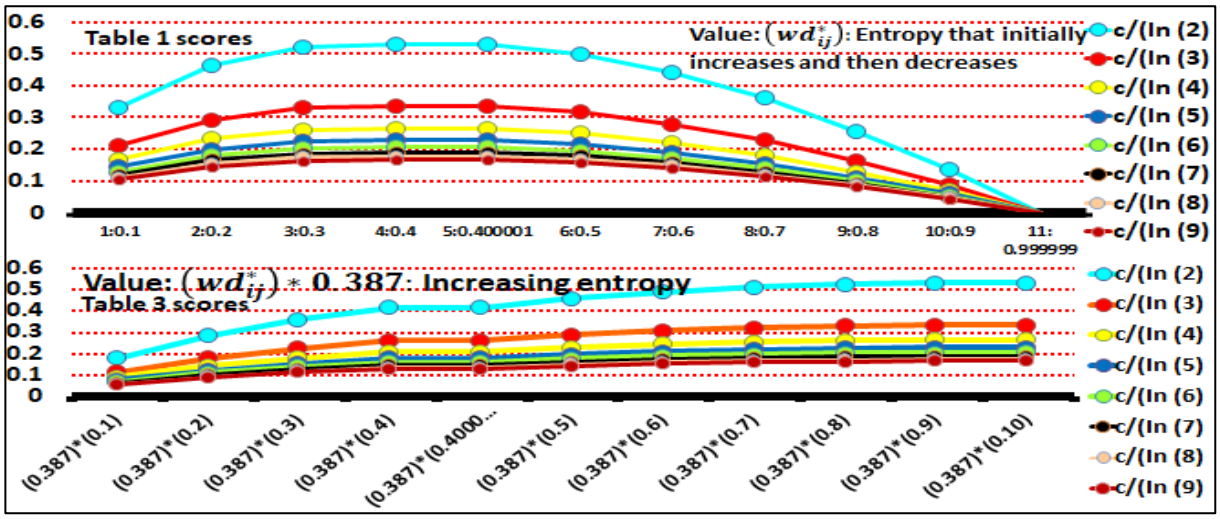

Figure 1. Positions of entropy values.

When Table 1 and Figure 1 are examined together, it is observed that the values of wd_{ij}^{*}, representing the weighted normalized scores of each criterion corresponding to each alternative, fall within the range of 0 to 1, as required by the structural nature of MCDM methods. In the simulation analysis, based on Equation 3, it was found that when the wd_{ij}^{*} value reached 0.4 in the fourth scenario, the entropy attained its maximum value. However, beyond this point, the entropy began to exhibit a decreasing trend. Accordingly, when the weighted normalized decision matrix contains values exceeding 0.4, the decreasing behavior of the entropy function introduces a contradiction regarding the quantitative superiority of alternatives within the framework of MCDM methodologies.

In contrast, the proposed method, similar to widely used MCDM approaches such as SAW, WPM, COCOSO, and WASPAS, assumes that the quantitative superiority of alternatives is positively correlated with both the magnitude of the criteria weights (w) and the normalized values (d_{ij}^{*}). In this context, for the entropy function to demonstrate a monotonically increasing behavior, it is necessary to constrain the weighted normalized values within the interval $0 < wd_{ij}^{*} \leq 0.387$. When each wd_{ij}^{*} value is multiplied by the coefficient 0.387, the entropy function becomes strictly increasing, thereby allowing the decision matrix to be standardized in alignment with the proposed approach, as illustrated in Table 2 and Figure 1.

In various simulation experiments, when the wd_{ij}^{*} values were standardized using the coefficient 0.4, it was observed also reflected in Table 3 that the wd_{ij}^{*}value initially increased up to approximately 0.939, after which it began to decline. Consequently, through extensive simulations, it was determined that the wd_{ij}^{*} value that yields a strictly increasing entropy function within the [0,1] interval is approximately 0.387. In each of these scenarios, the weighted normalized values standardized by the coefficient 0.387 consistently exhibited a monotonically increasing trend (Table 2 and Figure 1). The proposed result has been repeatedly tested and validated across a wide range of scenario sets, including simulations where the number of alternatives (m) reached up to 1,000. In each scenario, the entropy value was consistently observed to increase monotonically in a positive direction. This indicates that the method remains stable even under large-scale data conditions and is capable of producing computationally reliable outcomes. Therefore, under such conditions, the proposed method (EBPM) transforms into a continuously increasing entropy function, thereby ensuring consistency in reflecting the quantitative superiority of alternatives.

Table 2. Standardization entropy scores of weighted normalized values ((wd_{ij}^{*}) *0.387)

$(wd_{ij}^{*}) * 0.387$	m=2	m=3	m=4	m=5
0.03870 (0.1*0.387)	0.182	0.115	0.091	0.182
0.07740 (0.2*0.387)	0.286	0.180	0.143	0.286
0.11610 (0.3*0.387)	0.361	0.228	0.180	0.361
0.15480000 (0.4*0.387)	0.4166477	0.2628754	0.20832385	0.4166477
0.15480004 (0.400001*0.387)	0.4166478	0.2628755	0.20832388	0.4166478
0.19350 (0.5*0.387)	0.459	0.289	0.229	0.459
0.23220 (0.6*0.387)	0.489	0.309	0.245	0.489
0.27090 (0.7*0.387)	0.510	0.322	0.255	0.510
0.30960 (0.8*0.387)	0.524	0.330	0.262	0.524
0.34830 (0.9*0.387)	0.529	0.3343	0.264	0.529
0.38700 (0.999999*0.387)	0.530	0.3344	0.265	0.530
$(wd_{ij}^{*}) * 0.387$	m=6	m=7	m=8	m=9
0.03870 (0.1*0.387)	0.078	0.070	0.065	0.061
0.07740 (0.2*0.387)	0.123	0.111	0.102	0.095
0.11610 (0.3*0.387)	0.155	0.140	0.128	0.120
0.15480000 (0.4*0.387)	0.17944040	0.16118133	0.14841291	0.13888257
0.15480004 (0.400001*0.387)	0.17944042	0.16118135	0.14841292	0.13888258
0.19350 (0.5*0.387)	0.197	0.177	0.163	0.153
0.23220 (0.6*0.387)	0.211	0.189	0.174	0.163
0.27090 (0.7*0.387)	0.220	0.197	0.182	0.170
0.30960 (0.8*0.387)	0.226	0.203	0.187	0.175
0.34830 (0.9*0.387)	0.22825	0.20502	0.18878	0.17666
0.38700 (0.999999*0.387)	0.22827	0.20504	0.18880	0.17667

m= number of components

Table 3. Standardization entropy scores of weighted normalized values ((wd_{ij}^{*}) *0.4)

$(wd_{ij}^{*}) * 0.4$	m=2	m=3	m=4	m=5
0.04 (0.1*0.4)	0.186	0.117	0.093	0.080
0.08 (0.2*0.4)	0.292	0.184	0.146	0.126
0.12 (0.3*0.4)	0.367	0.232	0.184	0.158
0.16 (0.4*0.4)	0.42301699	0.26689401	0.21150850	0.18218350
0.16000004 (0.41*0.4)	0.42301704	0.26689404	0.21150852	0.18218352
0.2 (0.5*0.4)	0.464	0.293	0.232	0.200
0.24 (0.6*0.4)	0.494	0.312	0.247	0.213
0.28 (0.7*0.4)	0.51422	0.324437	0.257110	0.221463
0.32 (0.8*0.4)	0.52603	0.331890	0.263017	0.226551
0.36 (0.9*0.4)	0.53061	0.334781	0.265308	0.228524
0.3756 (0.4*0.9390)	0.530622	0.334785	0.2653109	0.228526
0.37564 (0.4*0.9391)	0.530621	0.334784	0.2653103	0.228525
$(wd_{ij}^{*}) * 0.4$	m=6	m=7	m=8	m=9
0.04 (0.1*0.4)	0.072	0.066	0.062	0.059
0.08 (0.2*0.4)	0.113	0.104	0.097	0.044
0.12 (0.3*0.4)	0.142	0.131	0.122	0.055
0.16 (0.4*0.4)	0.16364531	0.1506816	0.14100566	0.06380966
0.16000004 (0.41*0.4)	0.16364533	0.1506817	0.14100568	0.06380967
0.2 (0.5*0.4)	0.180	0.165	0.155	0.070
0.24 (0.6*0.4)	0.191	0.176	0.165	0.075
0.28 (0.7*0.4)	0.198928	0.183169	0.171407	0.162218
0.32 (0.8*0.4)	0.203498	0.187377	0.175345	0.165945
0.36 (0.9*0.4)	0.205270	0.189009	0.176872	0.167390
0.3756 (0.4*0.9390)	0.2052725	0.189011	0.1768739	0.1673925
0.37564 (0.4*0.9391)	0.2052721	0.189010	0.1768735	0.1673922

m= number of components

As illustrated in Table 3 and Figure 1, a noticeable upward trend in entropy values has been observed following the standardization process applied to ensure that the entropy values or the entropy function attain a monotonically increasing structure. Specifically, this standardization involves multiplying the weighted normalized values by a coefficient of 0.387.

Within this context, the Entropy method demonstrates the capability to distinguish between criteria during the weighting phase, and as emphasized in the literature [45], it enhances the discriminative power of the criteria. Similarly, by transforming the entropy function into a monotonically increasing form, it is considered that the performance levels of alternatives can be more clearly differentiated based on their own intrinsic quantitative superiority. In line with this, the implementation steps of the proposed method are systematically presented below.

ALT: Alternative

CRT: Criteria

$CRTi$: $i-th$ evaluation criterion

m: number of criteria

n: number of alternative

d_{ij}: value of the $j-th$ alternative according to the $i-th$ evaluation criterion

w_j: weight of the $i-th$ evaluation criterion ($i = 1, 2, \dots, m$)

$max(d_{ij})$: maximum value of the alternative according to the $i-th$ criterion

$\min(d_{ij})$: minimum value of the alternative according to the $i-th$ criterion.

Step 1. Obtaining Decision Matrix (DM)

In the first step of the proposed method, the decision matrix is constructed using equation 4.

$$DM = \left[d_{ij}\right]_{mxn} = \begin{matrix} ALT \\ CRT_1 \\ CRT_2 \\ \vdots \\ CRT_m \end{matrix} \begin{bmatrix} ALT_1 & ALT_2 & \dots & ALT_n \\ d_{11} & d_{12} & \dots & d_{1n} \\ d_{21} & d_{22} & \dots & d_{2n} \\ \vdots & \vdots & \dots & \vdots \\ d_{m1} & d_{m2} & \dots & d_{mn} \end{bmatrix} \quad (4)$$

Step 2. Obtaining Normalized Decision Matrix (DM^*)

In the second phase of the methodology, the decision matrix is normalized by applying Equation 5 for benefit-type criteria and equation 6 for cost-type criteria. Following this step, the normalized decision matrix is constructed in accordance with equation 7, taking into account the nature (i.e., orientation) of each criterion.

For benefit-oriented criteria:

$$d_{ij}^* = \frac{d_{ij}}{\max(d_{ij})} \quad (5)$$

For cost-oriented criteria:

$$d_{ij}^* = \frac{\min(d_{ij})}{d_{ij}} \quad (6)$$

Normalized matrix:

$$DM^* = \left[d_{ij}\right]^*_{mxn} = \begin{matrix} ALT \\ CRT_1 \\ CRT_2 \\ \vdots \\ CRT_m \end{matrix} \begin{bmatrix} ALT_1 & ALT_2 & \dots & ALT_n \\ d^*_{11} & d^*_{12} & \dots & d^*_{1n} \\ d^*_{21} & d^*_{22} & \dots & d^*_{2n} \\ \vdots & \vdots & \dots & \vdots \\ d^*_{m1} & d^*_{m2} & \dots & d^*_{mn} \end{bmatrix} \quad (7)$$

Step 3. Obtaining Weighted Normalized Decision Matrix (wDM^*)

In this step, the normalized values corresponding to each criterion for a given alternative, as presented in equation 8, are multiplied by the respective criterion weights. Subsequently, the weighted normalized decision matrix is obtained using equation 9.

$$wd^*_{ij} = w * d^*_{ij} \quad (8)$$

$$wDM^* = \left[d_{ij}{}^*\right]_{mxn} = \begin{matrix} ALT \\ CRT_1 \\ CRT_2 \\ \vdots \\ CRT_m \end{matrix} \begin{bmatrix} ALT_1 & ALT_2 & \dots & ALT_n \\ wd^*_{11} & wd^*_{12} & \dots & wd^*_{1n} \\ wd^*_{21} & wd^*_{22} & \dots & wd^*_{2n} \\ \vdots & \vdots & \dots & \vdots \\ wd^*_{m1} & wd^*_{m2} & \dots & wd^*_{mn} \end{bmatrix} \quad (9)$$

Step 4. Construction of the Standardized Matrix ($SwDM^*$)

In this step, the weighted normalized values are scaled by a factor of 0.387, based on the rationale provided in Table 3, to ensure that none of the values exceed the specified threshold. As a result of this transformation, the entropy function defined in equation 10 is converted into a structure that increases monotonically. Subsequently, the standardized matrix is constructed using equation 11.

$$Swd^*_{ij} = 0.387 * wd^*_{ij} \quad (10)$$

$$SwDM^* = \left[Swd^*_{ij}\right]_{mxn} = \begin{matrix} ALT \\ CRT_1 \\ CRT_2 \\ \vdots \\ CRT_m \end{matrix} \begin{bmatrix} ALT_1 & ALT_2 & \dots & ALT_n \\ Swd^*_{11} & Swd^*_{12} & \dots & Swd^*_{1n} \\ Swd^*_{21} & Swd^*_{22} & \dots & Swd^*_{2n} \\ \vdots & \vdots & \dots & \vdots \\ Swd^*_{m1} & Swd^*_{m2} & \dots & Swd^*_{mn} \end{bmatrix} \quad (11)$$

Step 5. Measurement of entropy score of alternatives (E_j)

In this step, based on Equation 1, entropy values of each alternative are measured using Equation 2, within the framework of the increasing entropy function defined in Equation 12. According to the theoretical foundation of entropy in the literature, an increase in entropy implies a decrease in existing information performance and, consequently, a rise in information requirements. Conversely, a lower entropy value indicates higher information performance. Following this step, the

performance values are ranked from the lowest to the highest (equation 12).

$$E_j = -\frac{1}{In(m)} * \sum_{i=1}^{m} \left(Swd^*_{ij} * In\left(Swd^*_{ij}\right)\right) \quad (12)$$

Step 6. The knowledge performances of the alternatives (KP_j)

In this step, in order to achieve a quantitative superiority ranking of the alternatives from highest to lowest, the information performances of the alternatives are calculated as shown in equation 13, by subtracting their entropy values from 1, similar to the approach used for determining criterion weights in Equation 3 of the entropy method. Accordingly, the higher the value obtained by subtracting the entropy from 1, the greater the information performance of the alternative.

$$KP_j = 1 - E_j \quad (13)$$

When the proposed method is examined, it offers several notable advantages from multiple perspectives. First, unlike traditional MCDM approaches, the EBPM method evaluates the information contribution of alternatives to the decision-maker directly through an entropy-based function, thereby providing a more qualified decision support mechanism. By preserving the structural integrity of Shannon entropy, the method integrates scientific rigor into the decision-making process through information generation.

Second, the method emphasizes objectivity in the evaluation process, as it does not rely on subjective weighting and operates based on a predefined threshold value. This feature minimizes decision-maker biases and enables consistent and systematic analysis.

Third, due to its mathematically simple structure and straightforward data processing steps, EBPM is highly applicable to large datasets and across various sectors. Another advantage is its capacity to prevent excessive data dispersion during the standardization phase. As a result, extreme values within the decision matrix are brought under control, and the influence of such values is appropriately considered within the proposed method.

Despite its advantages, the proposed method also has certain limitations. The first limitation arises from the logarithmic computation involved in the method, which makes it sensitive to zero and negative values. In this context, Zhang et al. (2014) emphasized that the decision matrix should be positively oriented and free from zero values, which can be ensured through Z-score standardization. The second limitation pertains to the formation of the standardized matrix, where a significant reduction in values can lead to excessive sensitivity. The inclusion of these highly sensitive values in the computational process may complicate the calculation steps. Moreover, when the original data points are very close to each other, the sensitivity of the standardized values increases, potentially affecting the overall stability and robustness of the method.

The proposed method, when compared with certain MCDM methods, demonstrates similarities in terms of the computational logic underlying the evaluation of alternatives. Specifically, methods such as SAW (Radulescu and Radulescu, 2024). WPM (Özbek, 2019), WASPAS (Chakraborty et al., 2015), COCOSO (Yazdani et al., 2019), MAUT (Keeney and Raiffa, 1976), ROV (Yakowitz et al., 1993), ARAS (Zavadskas and Turskis, 2010) and COPRAS (Zavadskas et al., 1994) share a common foundation with the proposed approach, in that the quantitative superiority of alternatives is based on the relationship between the weighted normalized values and the numerical magnitude of the criterion weights. This resemblance highlights the fact that these methods adopt a similar calculation framework in determining the performance of alternatives. In contrast, the computational logic of the proposed method significantly differs from that of methods such as TOPSIS (Hwang and Yoon, 1981), MARCOS (Stević et al., 2020), MABAC (Pamućar and Ćirović, 2015) CRADIS (Taşcı, 2024), PIV (Goswami et al., 2022), MAIRCA (Pamućar et al., 2018), and RAFSI (Alossta et al., 2021). In these methods, the performance or quantitative dominance of alternatives is determined based on their proximity to an ideal solution point (either maximum or minimum reference values). Therefore, while these methods rely on an evaluation approach grounded in the distance of alternatives from the ideal solution, the proposed method emphasizes the direct quantitative contribution and the effect of weighted normalized score.

When compared to other MCDM methods, the proposed approach offers several notable advantages. Firstly, the EBPM method does not merely evaluate the overall performance of the alternatives; it also quantifies their respective information potentials. This dual functionality allows for a more comprehensive assessment of alternatives beyond conventional performance metrics. Secondly, from the perspective of entropy analysis, the theoretical foundation of the proposed method is inherently associated with both natural and social sciences. This interdisciplinary foundation enhances the applicability of the method in real-world decision-making contexts, particularly when the decision matrix includes criteria drawn from diverse scientific fields. Thirdly, unlike many other MCDM methods, the proposed approach is grounded in the entropy equation, which has previously been employed in both natural and social sciences and is recognized for its validity and reliability in the literature. Accordingly, the theoretical basis of the method is indirectly supported by a broader range of academic disciplines, reinforcing its scientific credibility and cross-disciplinary relevance.

2.3. Data Set

In this study, a dataset was constructed within the scope of a sample application to demonstrate that the

performance of alternatives in decision-making problems can be evaluated using the entropy method, and thereby to validate the applicability of the proposed approach. The dataset consists of the 2024 Global Innovation Index (GII) criterion values of seven selected countries exhibiting varying levels of performance (World Intellectual Property Organization, 2024). These countries were deliberately chosen to prevent the criterion values from dominating the overall performance outcomes and to ensure that the differences among alternatives are not excessively large. Accordingly, there are no dominant values for any alternative within the dataset. Through this approach, the proposed method aims to reveal an ideal differentiation in the performance of alternatives. For the sake of clarity, the abbreviations of the countries and GII criteria are provided in Table 4.

Table 4. Data set

GII Criteria	Abbreviations
Institutions	CRT1
Human Capital and Research	CRT2
Infrastructure	CRT3
Market Sophistication	CRT4
Business Sophistication	CRT5
Knowledge and Technology Outputs	CRT6
Creative Outputs	CRT7
Countries/Alternatives	Abbreviations
Saudi Arabia	ALT1
Romania	ALT2
Qatar	ALT3
Brazil	ALT4
Chile	ALT5
Serbia	ALT6
Philippines	ALT7

3. Results

3.1. Computational analysis

In the study, the decision matrix was initially constructed using Equation 4. Subsequently, in the second step of the proposed method, the normalized decision matrix was obtained by applying Equation 5 and Equation 7 to the decision matrix values. In this context, the corresponding values are presented in Table 5.

In the third step of the method, the normalized values were weighted using the Entropy method as defined in equation 8, and the weighted normalized decision matrix was constructed using equation 9. All procedural steps related to the calculation of criterion weights within the scope of the entropy method are presented in detail in Appendix A in a systematic and transparent manner. This appendix enhances the traceability of the computational process and provides concrete support for the practical applicability of the method. In this context, the weighted normalized values are explained in Table 6.

Table 5. Decision and normalized decision matrix

Decision Matrix							
CRT	ALT1	ALT2	ALT3	ALT4	ALT5	ALT6	ALT7
CRT1	64.9	42.2	73.4	31.8	56.3	46.5	47.2
CRT2	43.4	30.8	36.6	33.9	33.5	35.7	26.2
CRT3	46.1	51.4	50.2	45.5	45.6	52.3	34.3
CRT4	48.7	32.4	34.7	38.2	38.6	42.2	29.7
CRT5	23.7	31.1	25.7	36.2	30.5	22.2	36.7
CRT6	20.6	29.9	17.5	24.5	21.2	29.6	28.7
CRT7	24.4	28.5	25.9	32.3	27.5	17.9	26.2
Normalized Decision Matrix							
CRT	ALT1	ALT2	ALT3	ALT4	ALT5	ALT6	ALT7
CRT1	1.000	0.821	1.000	0.699	1.000	0.889	1.000
CRT2	0.669	0.599	0.499	0.745	0.595	0.683	0.555
CRT3	0.710	1.000	0.684	1.000	0.810	1.000	0.727
CRT4	0.750	0.630	0.473	0.840	0.686	0.807	0.629
CRT5	0.365	0.605	0.350	0.796	0.542	0.424	0.778
CRT6	0.317	0.582	0.238	0.538	0.377	0.566	0.608
CRT7	0.376	0.554	0.353	0.710	0.488	0.342	0.555

Table 6. Weighted normalized decision matrix

CRT	ALT1	ALT2	ALT3	ALT4	ALT5	ALT6	ALT7
C1 *294	0.294	0.241	0.294	0.205	0.294	0.261	0.294
C2 *093	0.062	0.056	0.046	0.069	0.055	0.063	0.052
C3 *071	0.050	0.071	0.049	0.071	0.058	0.071	0.052
C4 *110	0.083	0.069	0.052	0.092	0.075	0.089	0.069
C5 *153	0.056	0.093	0.054	0.122	0.083	0.065	0.119
C6 *163	0.052	0.095	0.039	0.088	0.061	0.092	0.099
C7 *117	0.044	0.065	0.041	0.083	0.057	0.040	0.065

In the fourth step, the uncertainty values of each decision alternative were ensured to be an increasing function, thereby enhancing their information levels. To achieve this, the matrix was standardized using Equation 10, and the newly standardized matrix was constructed using Equation 11. Consequently, the standardized matrix values are presented in Table 7.

In the fifth step of the proposed method, the ENTROPY values representing the information capacity of each alternative were calculated using Equation 12. Subsequently, the information performance of the alternatives was determined using Equation 13. The performance rankings of the alternatives were arranged from the highest to the lowest value. In this context, the entropy and information performance values of the alternatives are presented in the Table 8.

Table 7. Standardized matrix

ALT	ALT1	ALT2	ALT3	ALT4	ALT5	ALT6	ALT7
CRT1	0.114	0.093	0.114	0.080	0.114	0.101	0.114
CRT2	0.024	0.022	0.018	0.027	0.021	0.025	0.020
CRT3	0.020	0.027	0.019	0.027	0.022	0.027	0.020
CRT4	0.032	0.027	0.020	0.036	0.029	0.034	0.027
CRT5	0.022	0.036	0.021	0.047	0.032	0.025	0.046
CRT6	0.020	0.037	0.015	0.034	0.024	0.036	0.038
CRT7	0.017	0.025	0.016	0.032	0.022	0.015	0.025

Table 8. Performance scores of alternatives

ALT	Entropy Score	Performance Score	Rank
ALT1	0.388	0.612	2
ALT2	0.428	0.572	5
ALT3	0.351	0.649	1
ALT4	0.455	0.545	7
ALT5	0.412	0.588	3
ALT6	0.418	0.582	4
ALT7	0.442	0.558	6

In order to further concretize the proposed method, the mathematical calculation of the performance value of the ALT1 alternative is presented below.

Step 2. Obtaining Normalized Decision Matrix (DM^*)

$Equation$ 5: $d^*_{CRT1-ALT1} = \frac{64.9}{64.9} = 1$

Step 3. Obtaining Weighted Normalized Decision Matrix (wDM^*)

$Equation$ 8: $wd^*_{CRT1-ALT1} = 0.294 * 1 = 0.294$

Step 4. Construction of the Standardized Matrix ($SwDM^*$)

$Equation$ 10: $Swd^*_{CRT1-ALT1} = 0.387 * 0.294 = 0.114$

Step 5. Meuserement of entropy score of alternatives (E_j)

$Equation$ 12: E_{ALT1}

$= (0.114 * -2.174) + (0.024 * -3.727)$
$+(0.020 * -3.996) + (0.032 * -3.444)$
$+(0.022 * -3.834) + (0.020 * -3.911)$
$+(0.017 * -4.073) = -7.5438$

$E_{ALT1} = \frac{-7.5438}{-1.9469} = 0{,}3877$

Step 6. Meuserement of performance score of alternatives (KP_j)

$KP_{ALT1} = 1 - 0.388 = 0.612$

Upon examining Table 8, it can be observed that the obtained ENTROPY values range between 0.649 and 0.545. In this context, the alternative with the highest ENTROPY value, ALT3 (0.649), is the option that provides the most information to the decision-maker. This is followed by ALT1 (0.612), ALT5 (0.588), ALT6 (0.582), ALT2 (0.572), ALT7 (0.558), and ALT4 (0.545). This ranking reflects the contribution of the alternatives to the decision-making process, i.e., their potential for generating information. The results obtained demonstrate that the Entropy-based information

measurement approach objectively reveals the distinctiveness of each alternative within the system and the value of the information it provides to the decision-maker. In this context, a low Entropy value indicates that the alternatives have high information performance.

Consequently, an increase in entropy (uncertainty) suggests high information performance, while a high entropy value indicates low information performance. Therefore, entropy contributes to assisting the decision-maker in making a selection. For instance, the fact that ALT3 has the highest information value indicates that this alternative possesses a stronger and clearer performance profile compared to others under the given alternative, thus providing the decision-maker with more meaningful information. These results demonstrate that the EBPM method yields consistent outcomes both theoretically and mathematically.

3.2. Sensitivity Analysis

Assessing the robustness of MCDM approaches frequently necessitates the deliberate alteration of the decision environment either through the integration of additional criteria or by eliminating criteria deemed less competitive within the initial evaluation scope. In such scenarios, it is expected that a resilient MCDM framework will demonstrate a high level of methodological stability, particularly by maintaining a consistent ordinal structure among the ranked entities. This characteristic is vital to ensuring the reliability and validity of the decision outcomes, even in the face of modifications to the input dataset (Demir and Arslan, 2022).

To investigate this dimension of methodological robustness, a comprehensive sensitivity analysis was carried out. The process began with the progressive exclusion of those criteria which, according to the proposed weighting methodology, exhibited the lowest relative significance. By incrementally removing these less influential parameters, the analysis aimed to explore the extent to which the ranking of alternatives remained unaffected or fluctuated under varying model configurations. The corresponding values are presented in Table 9, and the graphical representation of the sensitivity analysis is illustrated in Figure 2.

Table 9. Rank reversal score

Alternatives	S0	S1	S2	S3	S4	S5
ALT6	7	7	7	7	7	7
ALT7	6	6	6	6	6	6
ALT4	5	5	5	5	5	5
ALT2	4	4	4	4	4	4
ALT5	3	2	3	3	3	3
ALT3	2	3	2	2	2	2
ALT1	1	1	1	1	1	1

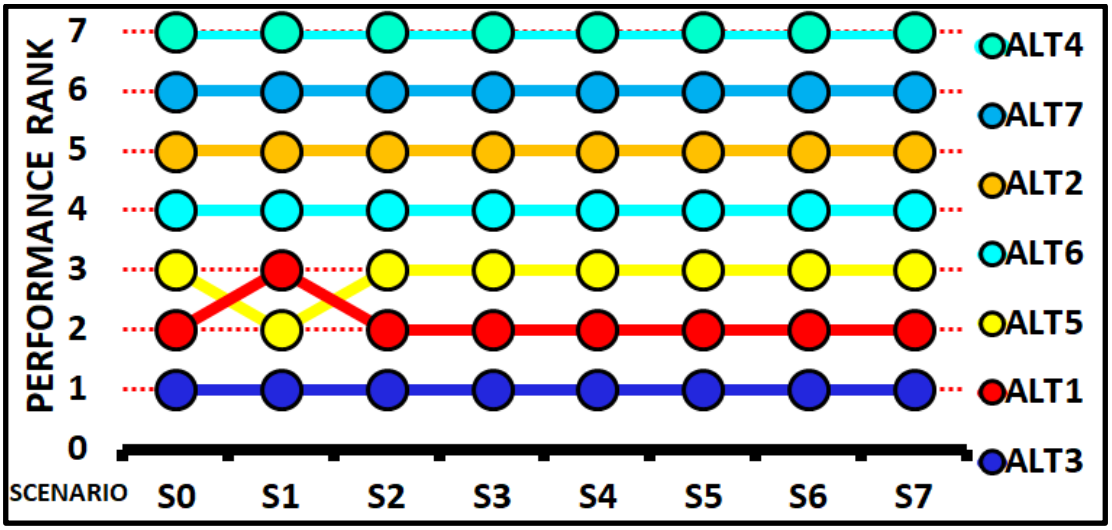

Figure 2. Rank reversal graph.

A simultaneous examination of Figure 2 and Table 9 clearly reveals that the proposed decision-making method, EBPM, exhibits a high level of structural stability in terms of sensitivity. As part of the sensitivity analysis, eight scenarios—ranging from S0 to S7 were systematically evaluated to assess the model's performance under varying sets of criteria. In each scenario, the number of criteria included in the model was gradually reduced; specifically, the criterion with the lowest weight was sequentially eliminated from the decision model, and the resulting impact on the ranking of alternatives was meticulously analyzed. While Table 9 provides the numerical representation of alternative rankings under each scenario, Figure 2 offers a visual

depiction of these variations. The base scenario, S0, represents the inclusion of all criteria within the model. Accordingly, the ability to trace changes in rankings holds critical importance for evaluating the model's sensitivity.

According to the findings, a limited change in ranking was observed only in the first scenario (S1), during which CRT3 the criterion with the lowest weight based on the ENTROPY method was removed from the model. Specifically, the alternative ALT1 dropped from second to third place, while ALT5 advanced from third to second. Apart from this exceptional case, the rankings of all other alternatives remained unchanged across subsequent scenarios. In the following steps, CRT2 (6th), CRT4 (5th), CRT7 (4th), CRT5 (3rd), CRT6 (2nd), and finally CRT1 (1st) were removed from the model, yet none of these eliminations resulted in any further modifications to the ranking structure.

Particularly notable is the consistent performance of ALT4, which maintained its first-place position throughout all scenarios, thereby underscoring its dominant and stable standing in the decision-making context. Similarly, the rankings of ALT2, ALT3, ALT6, and ALT7 also remained entirely unaffected during the sensitivity analysis, indicating their robustness against structural changes in the set of criteria. This consistency highlights the model's capacity for effectively distinguishing between both dominant and marginal alternatives. The fact that a ranking shift occurred solely between ALT1 and ALT5, and only within a single scenario, demonstrates the strong rank-preserving capability of the proposed method. As depicted in Figure 2, the graphical representation clearly illustrates this singular deviation, while the horizontally stable lines of the remaining alternatives further emphasize the structural resilience of the approach. In conclusion, the EBPM method demonstrates a high level of resistance to variations in the set of decision criteria and is capable of preserving the ranking stability of alternatives under different structural conditions. This characteristic confirms the method's theoretical consistency and practical applicability. Therefore, EBPM can be regarded as a reliable, robust, and methodologically stable decision-support tool with superior rank-preserving capabilities in MCDM problems.

3.3. Comparative Analysis

This comparative investigation aims to systematically evaluate the interconnections and relative alignment of the proposed method approach in relation to several well-established techniques within the MCDM domain. The principal objective is to substantiate the effectiveness, dependability, and methodological coherence of the proposed framework by highlighting its alignment with traditional MCDM procedures and its statistically significant and positive correlation with alternative models, as emphasized by Keshavarz-Ghorabaee et al. (2021).

To initiate this comparative analysis, a comprehensive set of benchmark 15 MCDM methods (SAW, WPM, TOPSIS, WASPAS, MARCOS, MABAC, CRADIS, MAUT, ROV, COPRAS, RAFSI, COCOSO, PIV, MAIRCA, ARAS) applied to determine the performance scores of alternatives. These methods were specifically selected due to their widespread adoption and methodological rigor in MCDM literature. The computed scores, along with the corresponding alternative rankings derived from each method, are systematically illustrated in Table 10, Table 11 and visually represented in Figure 3 and Figure 4.

A comprehensive examination of Table 8, Table 10, Table 11, along with Figures 3 and 4, reveals that the proposed method (EBPM) exhibits a high level of consistency and robustness in ranking decision alternatives. According to the EBPM results, ALT3 emerges as the top-performing alternative, followed by ALT1 and ALT5, indicating that the method offers a balanced and discriminative structure from both statistical and decision-making perspectives.

Table 11 presents a comparative ranking analysis, where the performance trends derived from EBPM both increases and decreases closely resemble those produced by widely used MCDM methods such as SAW, WPM, TOPSIS, WASPAS, MARCOS, CRADIS, COPRAS, PIV (adjusted by 180 degrees due to reverse ranking logic), and ARAS. This strong similarity indicates that EBPM not only maintains internal consistency but also generates externally valid rankings that align with conventional methods frequently applied in decision science.

Importantly, a complete rank concordance is observed between EBPM and the MARCOS method. The exact matching of rankings across all alternatives suggests a substantial structural and mathematical alignment between the underlying logic of MARCOS and the formulation of the EBPM model. This harmony not only validates the theoretical foundation of EBPM but also enhances its practical credibility and applicability in real-world decision-making problems. The findings presented in Table 10 further support this assertion. The performance scores generated by EBPM show a high level of correlation with results from other dominant MCDM techniques such as SAW, WPM, TOPSIS, WASPAS, MARCOS, CRADIS, COPRAS, PIV, and ARAS. For example, the top-ranked position of ALT5 is similarly supported by SAW, WPM, TOPSIS, WASPAS, MARCOS, CRADIS, COPRAS, PIV and ARAS.

The findings presented in Table 10 further support this assertion. The performance scores generated by EBPM show a high level of correlation with results from other dominant MCDM techniques such as SAW, WPM, TOPSIS, WASPAS, MARCOS, CRADIS, COPRAS, PIV, and ARAS. For example, the top-ranked position of ALT5 is similarly supported by SAW, WPM, TOPSIS, WASPAS, MARCOS, CRADIS, COPRAS, PIV and ARAS.

Table 10. Performance score in scope of methods

ALT	SAW	WPM	TOPSIS	WASPAS	MARCOS
ALT1	0.824	0.814	0.699	0.819	0.474
ALT2	0.773	0.756	0.348	0.764	0.404
ALT3	0.815	0.800	0.743	0.807	0.480
ALT4	0.749	0.712	0.260	0.730	0.379
ALT5	0.788	0.786	0.569	0.787	0.438
ALT6	0.747	0.730	0.392	0.738	0.406
ALT7	0.762	0.747	0.421	0.754	0.403
ALT	MABAC	CRADIS	MAUT	ROV	COPRAS
ALT1	0.114	1.000	0.629	0.296	0.152
ALT2	0.045	0.929	0.586	0.262	0.140
ALT3	0.065	0.986	0.624	0.272	0.151
ALT4	0.013	0.895	0.581	0.246	0.135
ALT5	0.044	0.949	0.519	0.261	0.145
ALT6	-0.021	0.893	0.559	0.229	0.136
ALT7	-0.003	0.914	0.574	0.238	0.139
ALT	RAFSI	COSOSO	PIV	MAIRCA	ARAS
ALT1	6.934	3.568	0.069	0.058	0.827
ALT2	6.335	1.814	0.107	0.068	0.764
ALT3	6.504	2.023	0.075	0.065	0.820
ALT4	6.048	2.745	0.126	0.073	0.738
ALT5	6.320	1.609	0.094	0.068	0.787
ALT6	5.753	1.382	0.099	0.078	0.742
ALT7	5.914	2.196	0.106	0.075	0.758

Table 11. Performance ranks in scope of methods

ALT	SAW	WPM	TOPSIS	WASPAS	MARCOS
ALT1	1	1	2	1	2
ALT2	4	4	6	4	5
ALT3	2	2	1	2	1
ALT4	6	7	7	7	7
ALT5	3	3	3	3	3
ALT6	7	6	5	6	4
ALT7	5	5	4	5	6
ALT	MABAC	CRADIS	MAUT	ROV	COPRAS
ALT1	1	1	1	1	1
ALT2	3	4	3	3	4
ALT3	2	2	2	2	2
ALT4	5	6	4	5	7
ALT5	4	3	7	4	3
ALT6	7	7	6	7	6
ALT7	6	5	5	6	5
ALT	RAFSI	COSOSO	PIV	MAIRCA	ARAS
ALT1	1	1	1	1	1
ALT2	3	5	6	3	4
ALT3	2	4	2	2	2
ALT4	5	2	7	5	7
ALT5	4	6	3	4	3
ALT6	7	7	4	7	6
ALT7	6	3	5	6	5

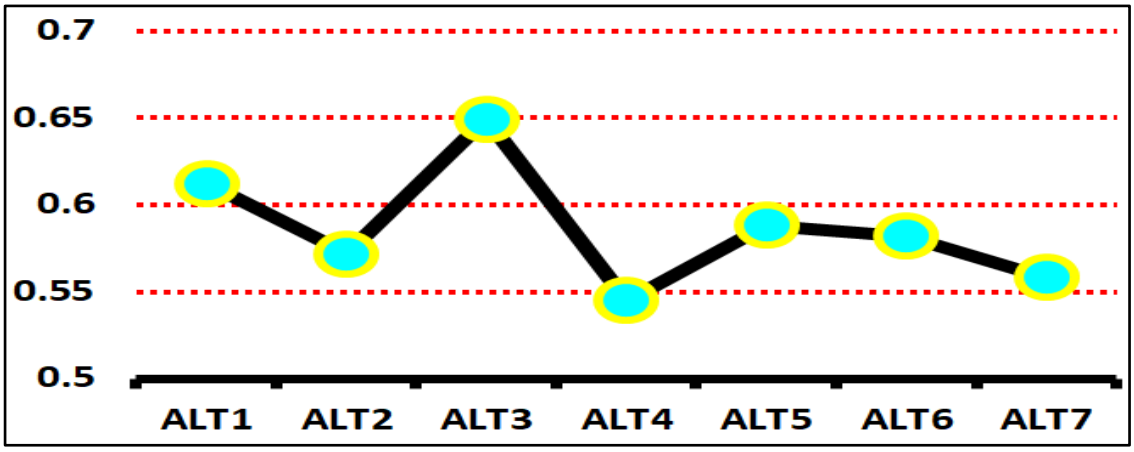

Figure 3. Position of EBPM method.

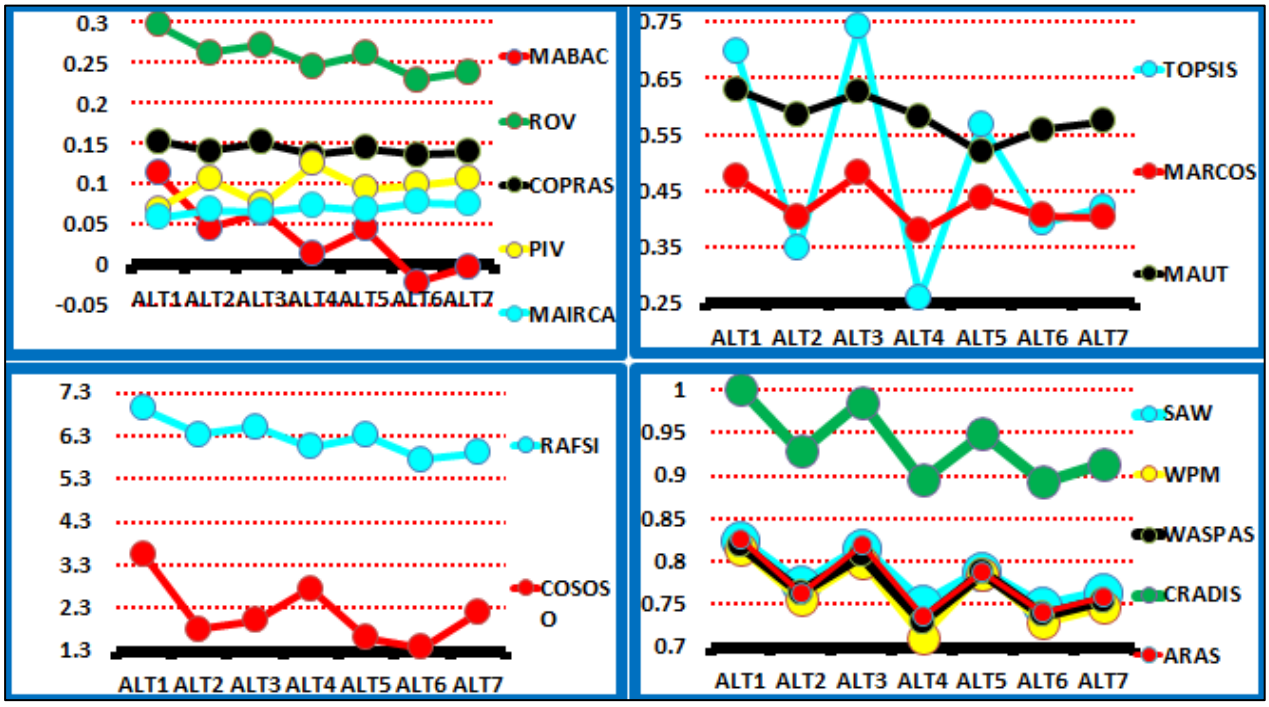

Figure 4. Position of other methods.

A comprehensive examination of Table 8, Table 10, Table 11, along with Figures 3 and 4, reveals that the proposed method (EBPM) exhibits a high level of consistency and robustness in ranking decision alternatives. According to the EBPM results, ALT3 emerges as the top-performing alternative, followed by ALT1 and ALT5, indicating that the method offers a balanced and discriminative structure from both statistical and decision-making perspectives.

Table 11 presents a comparative ranking analysis, where the performance trends derived from EBPM both increases and decreases closely resemble those produced by widely used MCDM methods such as SAW, WPM, TOPSIS, WASPAS, MARCOS, CRADIS, COPRAS, PIV (adjusted by 180 degrees due to reverse ranking logic), and ARAS. This strong similarity indicates that EBPM not only maintains internal consistency but also generates externally valid rankings that align with conventional methods frequently applied in decision science.

Importantly, a complete rank concordance is observed between EBPM and the MARCOS method. The exact matching of rankings across all alternatives suggests a substantial structural and mathematical alignment between the underlying logic of MARCOS and the formulation of the EBPM model. This harmony not only validates the theoretical foundation of EBPM but also enhances its practical credibility and applicability in real-world decision-making problems.

The findings presented in Table 10 further support this assertion. The performance scores generated by EBPM show a high level of correlation with results from other dominant MCDM techniques such as SAW, WPM, TOPSIS, WASPAS, MARCOS, CRADIS, COPRAS, PIV, and ARAS. For example, the top-ranked position of ALT5 is similarly supported by SAW, WPM, TOPSIS, WASPAS, MARCOS, CRADIS, COPRAS, PIV and ARAS.

Visual interpretations in Figure 3 clearly illustrate the relative distances among alternatives based on EBPM scores, with ALT3 exhibiting a distinctly higher performance level. In contrast, Figure 4, which includes the output distributions of other methods, reveals more pronounced performance fluctuations, suggesting that these conventional approaches may offer less stable or consistent rankings compared to EBPM. In summary, the EBPM method demonstrates a strong capability in producing stable, interpretable, and reliable rankings across decision alternatives. Its close alignment with methods like MARCOS not only confirms its theoretical soundness but also establishes it as a practical, data-driven alternative within the MCDM landscape.

Consequently, the performance rankings obtained through the EBPM method exhibit a high degree of consistency when compared with both directly proportional and inversely oriented MCDM methods. In particular, a joint evaluation of Figure 3 and Figure 4 reveals that the performance fluctuations of the alternatives are highly aligned with those derived from methods such as SAW, WPM, TOPSIS, WASPAS, MARCOS, CRADIS, COPRAS, PIV and ARAS. This strong alignment indicates that the EBPM method demonstrates a positively strong correlation with these widely recognized MCDM approaches. In support of this conclusion, the correlation coefficients reflecting the degree of association between the EBPM method and the aforementioned MCDM techniques are presented in Table 12.

Table 12. Correlation scores

M	SAW	WPM	TOPSIS	WASPAS	MARCOS
S	0.834**	0.820**	0.920**	0.832**	0.943**
M	MABAC	CRADIS	MAUT	ROV	COPRAS
S	0.631**	0.834**	0.508*	0.631**	0.869**
M	RAFSI	COSOSO	PIV	MAIRCA	ARAS
S	0.631**	0.063*	-0.904**	-0.631**	0.866**

P**<01, P*<.05, M=method, S= score

As presented in Table 12, the EBPM method exhibits strong and statistically significant correlations with widely recognized and frequently applied multi-criteria decision-making (MCDM) techniques such as SAW, WPM, TOPSIS, WASPAS, MARCOS, CRADIS, COPRAS, and ARAS. This high level of correlation indicates that the performance rankings derived from EBPM are largely consistent with those produced by well-established MCDM approaches. A particularly noteworthy point is that the PIV and MAIRCA methods employ a reverse ranking structure, in which alternatives are ordered from the worst to the best, i.e., in ascending order of performance. Accordingly, the negative but statistically significant correlation coefficients observed between these methods and EBPM are expected and can be interpreted as an indication of methodological consistency. In other words, these inverse correlations reflect the intrinsic ranking logic of the PIV and MAIRCA methods, and despite the opposite direction of the association, they confirm the existence of a strong and meaningful relationship. In addition, the relationships between EBPM and the MABAC, RAFSI, MAIRCA, MAUT, and ROV methods were found to be moderately significant. This suggests that the proposed method achieves an acceptable level of agreement with these techniques, indicating a moderate degree of methodological compatibility.

On the other hand, although the correlation coefficient between EBPM and the COCOSO method is relatively lower than those observed with other methods, it remains statistically significant. This finding implies that, despite some divergence in the computational frameworks of the two methods, there is limited alignment in terms of decision-making outcomes.

In conclusion, the correlation analysis demonstrates that the EBPM method not only produces stable and consistent rankings but also establishes a methodologically coherent and statistically verifiable relationship with a broad range of mainstream MCDM methods. These findings strongly support the validity and reliability of EBPM in addressing complex decision-making problems.

Overall, the correlation analysis reveals that the EBPM method demonstrates strong associations with both positively and inversely ranked MCDM methods. This not only confirms the statistical robustness of the proposed approach but also underscores its capacity to distinguish between alternatives in alignment with decision-maker preferences. Taken together, the findings suggest that EBPM is a reliable and valid performance assessment tool that yields highly compatible results with prominent methods in the MCDM literature. Hence, considering all comparative analyses, the EBPM method proves to be a trustworthy and effective technique in terms of capturing decision-makers' preferences and discriminating between alternatives.

3.4. Simulation analysis

To evaluate the reliability and consistency of the proposed method, a simulation-based study was carried out by constructing alternative decision matrices through the assignment of diverse input values. As the number of simulated scenarios increases, it is anticipated that the discrepancy between the proposed technique and other objective MCDM methods will become more apparent. In

this regard, it is expected that the correlation between the performance scores derived from the proposed method and those obtained from other MCDM techniques will gradually decrease. Such a trend would serve as evidence of the proposed method's enhanced capability to differentiate between criteria based on their relative significance. Moreover, the homogeneity observed in the variance distribution across all scenarios would further substantiate the stability and robustness of the proposed weighting mechanism (Keshavarz-Ghorabaee et al., 2021).

As part of this analysis, ten distinct scenarios were developed in the form of decision matrices and subsequently categorized into two separate groups for comparative purposes (Group 1: Scenario 1, Scenario 2, Scenario 3; Group 2: Scenario 4 through Scenario 10). Moreover, although the scenarios utilized in this study were constructed based on randomly generated datasets, particular attention was paid to avoiding excessively dominant values in order to more effectively reveal performance differences among alternatives within the proposed EBPM framework. Instead, alternatives with relatively close values were deliberately selected to enable a more accurate and meaningful assessment of the method's discriminative capacity. Furthermore, the dataset was designed to exhibit statistical normality, thereby ensuring a balanced distribution of data across criteria. This methodological approach not only provides a sound foundation for conducting sensitivity analyses but also demonstrates that the proposed method does not rely on artificially exaggerated contrasts. Rather, it delivers a performance evaluation based on realistic and substantively meaningful distinctions among alternatives. Following this categorization, correlation coefficients were computed to assess the degree of alignment between the proposed EBPM method and other established weighting approaches across the defined scenarios. The outcomes of these correlation analyses are comprehensively illustrated in Table 13 and Figure 5.

Table 13. Correlation scores

Methods	SAW	WPM	TOPSIS	WASPAS	MARCOS
Scenario1	0.861**	0.833**	0.965**	0.863**	0.973**
Scenario2	0.933**	0.888**	0.981**	0.901**	0.993**
Scenario3	0.958**	0.905**	0.988**	0.905**	0.996**
Scenario4	0.829**	0.814**	0.912**	0.849**	0.955**
Scenario5	0.817**	0.803**	0.905**	0.831**	0.943**
Scenario6	0.791**	0.779**	0.888**	0.823**	0.932**
Scenario7	0.768**	0.753**	0.874**	0.807**	0.925**
Scenario8	0.744**	0.729**	0.869**	0.800**	0.915**
Scenario9	0.726**	0.718**	0.852**	0.779**	0.907**
Scenario10	0.711**	0.703**	0.829**	0.759**	0.903**
Methods	MABAC	CRADIS	MAUT	ROV	COPRAS
Scenario1	0.655**	0.873**	0.551*	0.654**	0.899**
Scenario2	0.693**	0.913**	0.579*	0.693**	0.903**
Scenario3	0.601**	0.927**	0.491*	0.604**	0.927**
Scenario4	0.633**	0.869**	0.444*	0.631**	0.876**
Scenario5	0.719**	0.855**	0.429*	0.616**	0.867**
Scenario6	0.608**	0.839**	0.417*	0.612**	0.859**
Scenario7	0.591*	0.826**	0.404*	0.593*	0.845**
Scenario8	0.582*	0.817**	0.391*	0.579*	0.839**
Scenario9	0.567*	0.808**	0.376*	0.569*	0.819**
Scenario10	0.559*	0.800**	0.359*	0.559*	0.808**
Methods	RAFSI	COSOSO	ARAS	PIV	MAIRCA
Scenario1	0.655**	0.071	0.894**	-0.956**	-0.657**
Scenario2	0.695**	0.091	0.900**	-0.978**	-0.698**
Scenario3	0.674**	0.099	0.923**	-0.963**	-0.679**
Scenario4	0.636**	0.084	0.871**	-0.921**	-0.643**
Scenario5	0.615**	0.077	0.864**	-0.908**	-0.617**
Scenario6	0.604**	0.075	0.854**	-0.889**	-0.609**
Scenario7	0.594*	0.071	0.842**	-0.881**	-0.600**
Scenario8	0.586*	0.067	0.833**	-0.876**	-0.589*
Scenario9	0.563*	0.061	0.815**	-0.873**	-0.568*
Scenario10	0.555*	0.049	0.805**	-0.869**	-0.561*

P**<0.01, P*<0.05.

When Table 13 and Figure 5 are examined jointly, it is generally observed that the correlation values between the EBPM method and other MCDM methods tend to decline as the number of scenarios increases. This trend suggests that increasing the number of scenarios reveals greater evaluation differences among the methods. Notably, methods such as TOPSIS, MARCOS, and PIV maintained high correlation levels despite changes in scenario structures, thereby exhibiting consistent and stable performance evaluations. In contrast, methods such as COCOSO demonstrated relatively lower correlation values, indicating a higher sensitivity to scenario variations. Meanwhile, the PIV and MAIRCA methods continued to yield negative correlation coefficients, which is consistent with their reverse ranking logic, wherein lower numerical values indicate better performance. These inverse correlations are not anomalies but rather expected outcomes aligned with the inherent evaluation structures of the respective methods. Additionally, the statistical significance of the correlation coefficients presented in Table 13 is marked at the $p < .01$ and $p < .05$ levels. This reinforces the notion that the observed relationships are not coincidental but are statistically valid and meaningful. This analysis offers valuable insights into the sensitivity and consistency of different MCDM methods when subjected to varying decision-making scenarios. The fact that the EBPM method gradually diverges from other methods as the number of scenarios increases, and thereby becomes more distinguishable, highlights its ability to characterize and preserve stability in complex decision environments. Such findings emphasize the robustness and reliability of the proposed EBPM method in multi-scenario decision-making contexts, further enhancing its value as a dependable and structured performance evaluation tool.

In the concluding stage of the simulation analysis, the uniformity of variance in the performance scores determined through the EBPM methodology was rigorously evaluated using Levene's test. This statistical procedure offers a visual and analytical tool for assessing the consistency of variances across different groups. The graphical representation is structured around three essential components: the overall mean Avarage Decision Metric (ADM), derived from the Analysis of Means (ANOM) for variances based on Levene's test, which acts as the central reference line; and the Upper Decision Limit (UDL) and Lower Decision Limit (LDL), which delineate the acceptable bounds for variance fluctuation. When the variance of a particular group or cluster exceeds these decision thresholds, it indicates a statistically significant deviation from the overall mean ADM, suggesting the presence of variance heterogeneity. Conversely, if the variances of all clusters fall within the UDL and LDL range, this supports the assumption of variance homogeneity. Such consistency reinforces the robustness, reliability, and methodological stability of the proposed methodological framework by confirming the homogeneity of variances under diverse simulation scenarios (Keshavarz-Ghorabaee et al., 2021). In this context, Figure 6 presents the graphical results of the ADM-based analysis, offering visual confirmation of these findings, while Table 14 complements and substantiates the interpretation by providing the detailed numerical outcomes underpinning the graphical assessment (Levene Test).

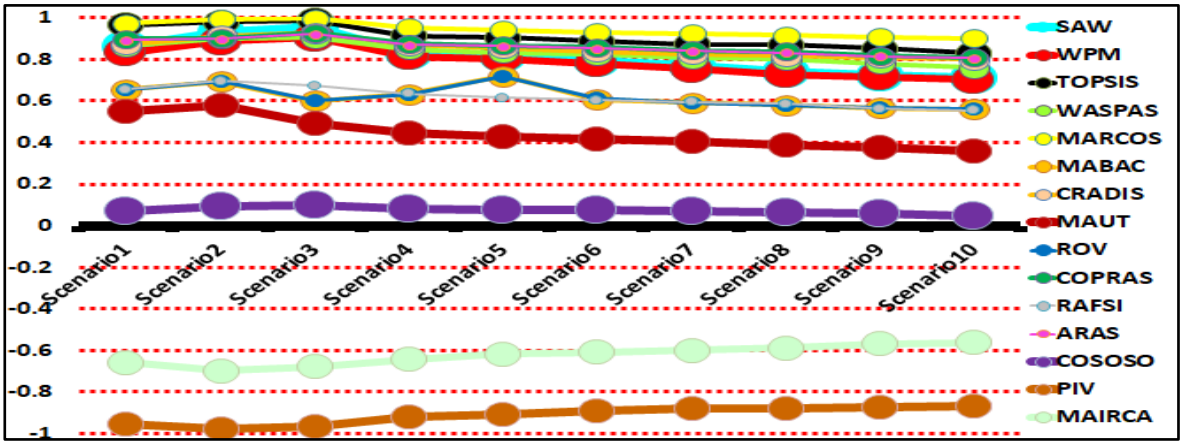

Figure 5. Correlation positions of EBPM with other MCDM methods.

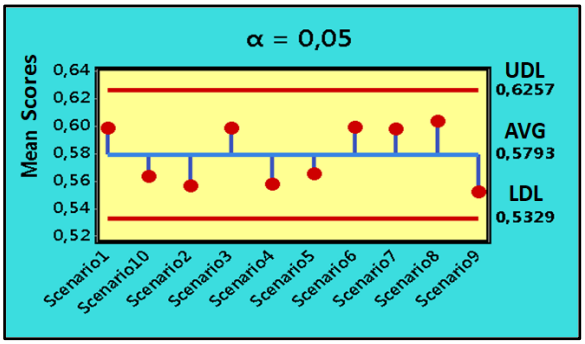

Figure 6. ADM graph.

Figure 6 presents a visual summary of the Analysis of Means (ANOM) for the variances of the Average Decision Metric (ADM) weights calculated under different scenarios at a significance level of α = 0.05. This analysis is based on the Levene's test, which is used to assess the homogeneity of variances. On the graph, the horizontal axis represents the different scenarios (from Scenario 1 to Scenario 10), while the vertical axis displays the Average ADM Weights.

The central blue line (AVG) indicates the overall average of ADM performance scores across all scenarios (0.5793), serving as the main reference point for the variance analysis. The upper red line (0.6257) and the lower red line (0.5329) represent the Upper Decision Limit (UDL) and Lower Decision Limit (LDL), respectively, indicating the boundaries within which the variance is considered acceptable. The yellow dots depict the calculated Average ADM Weights for each individual scenario. As shown in Figure 6, all the scenario-specific ADM scores lie within the range defined by the UDL and LDL. This clearly demonstrates that the variances of ADM scores across different scenarios are homogeneous, and there is no statistically significant deviation from the mean. Such homogeneity validates the robustness, reliability, and methodological consistency of the proposed framework. This finding aligns with the assertion of Keshavarz-Ghorabaee et al. (2021), who emphasized that preserving variance homogeneity across simulation scenarios is of critical importance in ensuring methodological consistency.

In conclusion, Figure 6 provides a clear visual depiction of the ANOM analysis based on Levene's test, effectively confirming the homogeneity of variances in ADM performance scores under varying scenarios. This statistical homogeneity reinforces the consistency and credibility of the proposed methodological approach, indicating that the results are built upon a solid foundation. This visual analysis, in conjunction with the numerical findings presented in Table 14, significantly strengthens the validity and reliability of the overall methodological framework. Moreover, based on the results of the ADM diagram and Levene's test, the homogeneity of performance scores generated by the proposed method across random different scenarios has been empirically validated. In this context, the Levene statistics obtained from scenario datasets exhibiting normal distribution are comprehensively reported in Table 14.

Table 14. Correlation scores

Levene Statistic	df1	df2	Sig. (p)
0.167	2	10	0.249

P*<0.05

Upon examining Table 14, it is observed that the significance level (p = 0.241) is greater than 0.05. This finding indicates that the variances of the performance scores obtained through the EBPM method across ten different scenarios are homogeneous, thereby supporting the outcomes derived from the ADM analysis. In other words, since there is no statistically significant difference in the variances of the scores obtained under different scenarios, it can be inferred that the model demonstrates consistent performance in terms of variance stability. From a broader perspective, when the quantitative findings of all simulation analyses are considered collectively, it can be concluded that the EBPM method possesses a stable and robust structure. This statistical consistency underscores the method's reliability in multi-scenario decision-making environments and reinforces its potential for practical application in complex decision contexts.

4. Discussion

MCDM methods are systematic and analytical tools developed to solve multidimensional problems in today's increasingly complex decision-making environments [2]. Although existing MCDM methods offer significant advantages, the growing demand for information-based decision-making has exposed certain limitations of these techniques [1]. In this context, the development of novel MCDM approaches not only aims to overcome the constraints of existing models but also paves the way for innovative evaluation techniques grounded in alternative paradigms [4]. In particular, the creation of models that effectively provide informative value to decision-makers and reduce uncertainty highlights a critical, yet unmet, need within the MCDM literature.

Within the scope of this study, the proposed EBPM method introduces a novel evaluation framework based on the informational potential of entropy. The theoretical foundation of the method is built upon two core principles. The first is the continuous tendency of entropy to increase in both natural and social systems [5,107]. The second is the premise that such an increase enhances the information performance of these systems [6]. Without introducing any structural modifications to the Shannon entropy formula, the method transforms the entropy function into a theoretically justified and literature-consistent monotonically increasing structure by rescaling the weighted normalized values based on a predefined threshold. This approach not only offers a

theoretically consistent model but also introduces an original dimension for performance evaluation in decision analysis grounded in information theory.

In the application of the EBPM method to the 2024 Global Innovation Index dataset, the model has been rigorously tested in terms of ranking stability, reliability, and sensitivity. In the sensitivity analysis, even when specific criteria were systematically removed from the decision matrix, no significant changes were observed in the ranking of alternatives. The results of the comparative analysis demonstrate that EBPM exhibits a high degree of correlation with widely used MCDM methods such as SAW, WPM, TOPSIS, WASPAS, MARCOS, CRADIS, COPRAS, PIV, and ARAS, thereby confirming its reliability and credibility as a decision-making tool. On the other hand, the observation that the proposed EBPM method exhibits only moderate correlation with certain MCDM techniques such as MAUT, MABAC, RAFSI, and MAIRCA, and a relatively low correlation with the COCOSO method, can be attributed to the conceptual and computational divergence between these approaches. Fundamentally, this discrepancy arises from the differences in how each method interprets and computes the performance of alternatives. While EBPM directly evaluates the information contribution of each alternative through an entropy-based performance framework, methods like MAUT, MABAC, RAFSI, and MAIRCA adopt diverse structural models based on utility theory, approximation areas, or ideal-theoretical deviations. As a result, the divergence in evaluation paradigms naturally leads to differentiated correlation levels. Specifically, the COCOSO method aggregates performance scores through additive and multiplicative synthesis based on SAW and WPM principles, which conceptually misaligns with the continuously increasing entropy-based formulation of EBPM. Thus, the lower correlation with COCOSO does not indicate a methodological deficiency, but rather reflects the distinctive theoretical foundation and originality of the EBPM approach. These differences underscore EBPM's unique contribution to the MCDM literature, offering an alternative perspective independent of traditional ranking logics.

Furthermore, simulation analyses conducted under various correlation and homogeneity-based scenarios revealed a consistently high level of ranking stability, indicating that EBPM possesses a stable and robust structure.

A key distinguishing advantage of the method lies in its capacity to assess performance not merely based on numerical magnitudes but also on the informational contribution it offers to the decision-maker. Unlike conventional MCDM techniques such as SAW (Radulescu and Radulescu, 2024), WPM (Özbek and Erol, 2017), WASPAS (Zawadskas et al., 2012), COCOSO (Yazdani et al., 2019), MAUT (Keeney and Raiffa, 1976), ROV (Yakowitz et al., 1993), ARAS (Zawadskas et al., 2010), and COPRAS (Zawadskas et al., 1994), which primarily emphasize the magnitude of normalized values and criterion weights (i.e., quantitative superiority), the EBPM method considers both quantitative dominance and the information-generating capacity of alternatives, thereby enabling a more qualitative and nuanced evaluation.

Moreover, in contrast to proximity-to-ideal-solution-based methods such as TOPSIS (Hwang and Yoon, 1981) MARCOS (Stević et al., 2020), MABAC (Pamućar and Ćirović, 2015), CRADIS (Puška et al., 2023), PIV (Goswami et al., 2022), MAIRCA (Pamucar et al., 2018), and RAFSI (Žižovic et al., 2020), EBPM evaluates each alternative according to its intrinsic information potential, rather than its closeness to an ideal maximum or minimum reference point. Notably, its negative correlation with methods such as MAIRCA and PIV, which operate under a reverse-ranking mechanism, not only reveals the ranking coherence across models but also underlines EBPM's capacity to maintain comparative compatibility with existing methods.

In addition, the entropy-based foundation of EBPM grants it an inherently multi-disciplinary character, making it potentially more usable and insightful for decision-makers across various domains. Nevertheless, the proposed method presents certain limitations when compared to other multi-criteria decision-making (MCDM) techniques. In particular, the EBPM method is sensitive to zero and negative values, which may limit its flexibility in certain application domains. In such cases, the application of Z-standardization scores, as suggested by Zhang et al. (2014), is recommended. In other words, by transforming the values in the decision matrix into Z-standardization scores, all data can be converted into positive numbers, thereby preserving the applicability of the EBPM method. Another significant limitation emerges when the standardized criterion values of alternatives are very close to one another. Under such circumstances, the method's discriminative capacity and computational precision may diminish, making it more challenging to identify meaningful differences between alternatives. To address this issue, it is advisable to employ high-precision numerical operations within the scope of advanced mathematical computation. This would allow for the clearer detection of subtle differences between alternatives, thereby enhancing the method's discriminative performance.

Moreover, this study offers significant contributions to the MCDM literature from several perspectives. Firstly, while the entropy method has traditionally been utilized as a tool for weighting criteria, this research introduces a novel application by employing it directly to measure the performance of alternatives, thus providing a new perspective to the literature. This approach broadens the application potential of the entropy method in decision-making problems.

Furthermore, by integrating information theory and the concept of entropy into MCDM methodology, this study presents an innovative framework that evaluates alternatives not only based on their quantitative

attributes but also on the informational value they provide. The proposed method (EBPM) constitutes an original methodology that assesses the knowledge-generating capacity of alternatives, thereby enabling decision-makers to perform more comprehensive and qualitative analyses. Additionally, the use of entropy as the foundation of the method introduces an interdisciplinary perspective to the MCDM field, facilitating the integration of knowledge from diverse disciplines into decision-making processes.

Furthermore, by integrating information theory and the concept of entropy into MCDM methodology, this study presents an innovative framework that evaluates alternatives not only based on their quantitative attributes but also on the informational value they provide. The proposed method (EBPM) constitutes an original methodology that assesses the knowledge-generating capacity of alternatives, thereby enabling decision-makers to perform more comprehensive and qualitative analyses. Additionally, the use of entropy as the foundation of the method introduces an interdisciplinary perspective to the MCDM field, facilitating the integration of knowledge from diverse disciplines into decision-making processes.

Although the present study demonstrates the potential of the proposed EBPM method in the MCDM domain, it also offers several avenues for future research. First, addressing the current limitations of the method may constitute a major focus for subsequent studies. Specifically, solutions can be sought for issues such as the method's sensitivity to zero and negative values, and the diminished discriminatory power when the criterion values of alternatives are closely aligned. In this regard, the adoption of alternative normalization techniques or the development of methodological modifications may be considered. Second, testing the method across various application domains would provide greater insight into its effectiveness and generalizability. Implementing the method with data from different sectors and decision-making problems could help to more clearly identify its strengths and weaknesses. Third, integrating the EBPM method into decision support systems could enable decision-makers to utilize the approach more easily and effectively, thereby enhancing its dissemination and impact on decision-making processes. Fourth, improving visualization techniques to better present the method's outcomes is essential; effective visualization tools can assist decision-makers in interpreting results more intuitively and integrating them into their decision-making processes.

The proposed EBPM is not merely a theoretical tool grounded in the concept of entropy; it also creates a tangible impact on real-world decision-making processes by offering high informational performance to decision-makers. In this context, EBPM reduces the level of uncertainty encountered during the evaluation of alternatives, thereby enabling decisions to be made based on high-quality, information-rich foundations rather than relying on intuition or subjective judgments. For instance, in the context of policy development, EBPM provides an objective assessment of the informative value of policy alternatives, guiding decision-makers in identifying which option possesses greater strategic impact potential. Similarly, in business strategy formulation, it facilitates the information-based comparison of investment projects or market offerings, allowing organizations to make more rational, data-driven, and sustainable strategic decisions. Therefore, EBPM is not merely an abstract decision-support model but a practical method that enhances the strategic orientation of decision-makers by grounding their choices in measurable, reliable, and information-rich foundations.

5. Conclusion

This study proposes the EBPM method, which provides an information-based alternative performance measurement for MCDM problems. The developed method transforms the classical Shannon Entropy function into a continuously increasing structure through a specific standardization, without manipulating the original entropy function, and measures the potential of alternatives to provide information accordingly. The EBPM method has demonstrated stable and reliable results both in simulation analyses and comparative evaluation studies. Particularly, its high sensitivity, ranking stability, and structural flexibility across various scenarios have led to strong performance from both theoretical and practical perspectives.

The high correlation of the method with different MCDM techniques enhances the validity of EBPM in the current literature and enables integrated analyses between methods. Additionally, its information measurement-based approach provides a multi-dimensional evaluation by considering not only the criterion weights but also the informative value that alternatives present to the decision-maker.

In conclusion, the EBPM method can be considered as an innovative MCDM approach that provides objective, stable, and information-based decision support, contributing both theoretically and methodologically to the literature. Future studies could further increase the method's validity by applying it across different sectors and facilitating its integration into decision support systems.

Although the present study demonstrates the potential of the proposed EBPM method in the MCDM domain, it also offers several avenues for future research. First, addressing the current limitations of the method may constitute a major focus for subsequent studies. Specifically, solutions can be sought for issues such as the method's sensitivity to zero and negative values, and the diminished discriminatory power when the criterion values of alternatives are closely aligned. In this regard, the adoption of alternative normalization techniques or

the development of methodological modifications may be considered. Second, testing the method across various application domains would provide greater insight into its effectiveness and generalizability. Implementing the method with data from different sectors and decision-making problems could help to more clearly identify its strengths and weaknesses. Third, integrating the EBPM method into decision support systems could enable decision-makers to utilize the approach more easily and effectively, thereby enhancing its dissemination and impact on decision-making processes. Fourth, improving visualization techniques to better present the method's outcomes is essential; effective visualization tools can assist decision-makers in interpreting results more intuitively and integrating them into their decision-making processes. Finally, exploring the potential integration of the EBPM method with other MCDM approaches may lead to the development of more comprehensive and robust decision-making frameworks.

The scope of the EBPM method can be further expanded through future research endeavors. For instance, applying the EBPM approach to decision-making problems in various domains such as healthcare, energy, environmental management, supply chain optimization, and sustainable development could provide valuable insights into its interdisciplinary applicability. Moreover, integrating EBPM with uncertainty-based MCDM approaches—such as fuzzy logic, grey system theory, rough set theory, or D-numbers—has the potential to enhance its methodological flexibility in decision environments characterized by ambiguity. Another promising research direction involves adapting the method to group decision-making processes or multi-layered (hierarchical) decision models. Additionally, evaluating the method's computational efficiency, processing time, and algorithmic performance when applied to large-scale datasets is crucial for assessing its practical scalability. Finally, conducting parameter sensitivity analyses on components such as normalization techniques, entropy coefficients, and weighting strategies will contribute to a deeper understanding of the method's behavior across different data structures and decision contexts.

Author Contributions

The percentages of the author' contributions are presented below. The author reviewed and approved the final version of the manuscript**.**

	F.F.A.
C	100
D	100
S	100
DCP	100
DAI	100
L	100
W	100
CR	100
SR	100
PM	100

C=Concept, D= design, S= supervision, DCP= data collection and/or processing, DAI= data analysis and/or interpretation, L= literature search, W= writing, CR= critical review, SR= submission and revision, PM= project management.

Conflict of Interest

The author declared that there is no conflict of interest.

Ethical Consideration

Ethics committee approval was not required for this study because of there was no study on animals or humans.

References

Aghamammadli F, Toptancı Ş, Karamaşa Ç. 2024. Analyzing the energy consumption of OECD countries through an interval-valued circular intuitionistic fuzzy AHP-based CRADIS. Res Square, 1(1):1-31. https://doi.org/10.21203/rs.3.rs-6283480/v1

Akmaludin, Suriyanto AD, Iriadi N, Widianto K. 2024. Integrated MCDM-AHP and MABAC for selection head of branch offices. Sinkron J Penelit Tek Inform, 8(4):2335-2344. https://doi.org/10.33395/sinkron.v8i4.13669

Aksakal E, Çalışkan E. 2020. Olimpiyatlarda aday şehirlerin seçim sürecinde dikkate alınacak kriterlerin entropi yönetimi ile değerlendirilmesi. In: Kabak M, Çınar Y, editors. Çok kriterli karar verme yöntemleri MS Excel çözümlü uygulamalar. Nobel, Ankara, Türkiye, pp: 169-179.

Aksoy E. 2021. An analysis on Türkiye's merger and acquisition activities: MAIRCA method. Gümüşhane Univ Sos Bilim Enst Elektron Derg, 12(1):1-11

Aktaş R, Doğanay MM, Türen U, Gazibey Y, Gökmen Y. 2015. Sayısal karar verme yöntemleri. Beta Yayınları, İstanbul, Türkiye, pp: 412.

AlAli AM, Salih A, Hassaballa A. 2023. Geospatial-based analytical hierarchy process (AHP) and weighted product model (WPM) techniques for mapping and assessing flood susceptibility in the Wadi Hanifah Drainage Basin, Riyadh Region, Saudi Arabia. Water, 15(1943):1-130. https://doi.org/10.3390/w15101943

Alossta A, Elmansouri O, Badi I. 2021. Resolving a location selection problem by means of an integrated AHP-RAFSI

approach. Rep Mech Eng, 2(1):135-142. https://doi.org/10.31181/rme200102135a

Alqoud A, Milisavljevic-Syed J, Salonitis K. 2025. Multi-criteria decision making in evaluating digital retrofitting solutions: Utilizing AHP and TOPSIS. Procedia CIRP, 132:184-190. https://doi.org/10.1016/j.procir.2025.01.031

Altın H. 2020. ARAS ve MOOSRA yöntemlerinin performans sonuçlarının karşılaştırılması: Amerika kıtası ülkeleri. Pressacademia J Econ Finance Account, 7(2):173-186

Anđić D. 2024. Comparison of a tower geodetic micro-network optimization results obtained using the MABAC, MAIRCA, COCOSO and ROV methods with those obtained applying the VIKOR method. Int J Eng Res Dev, 20(10):81-95

Andrejic M, Vukasin P. 2025. Integrated BWM–QFD–MARCOS framework for strategic decision-making in cold chain logistics. J Oper Strateg Anal, 3(1):23-33. https://doi.org/10.56578/josa030103

Apaydın F. 2004. Kuantum fiziği. Hacettepe Üniversitesi Yayınları, Ankara, Türkiye, pp: 356.

Arisantoso, Somaida MH, Sanwasih M, Shalahudin MI. 2023. Multi-criteria decision making using the WASPAS method in webcam selection decision support systems. Int J Informatics Comput Sci, 7(1):1-11. https://doi.org/10.30865/ijics.v7i1.6001

Arslan HM. 2017. Determination of optimal vehicle selection of logistics companies with AHP-ARAS hybrid method. Alphanumeric J, 5(2):272-281. https://doi.org/10.17093/alphanumeric.339476

Atan M, Altan Ş. 2020. Örnek uygulamalarla çok kriterli karar verme yöntemleri. Gazi Kitapevi, Ankara, Türkiye, pp: 276.

Ayçin E. 2019. Çok kriterli karar verme. Nobel Yayın, Ankara, Türkiye, pp: 198.

Aydemir MF. 2025. Evaluation of foreign direct investment attractiveness of BRICS-T countries: The CRITIC-LOPCOW based ARAS approach. Polit Ekonomik Kuram, 9(1):372-392. https://doi.org/10.30586/pek.1613421

Azadfallah M. 2025. Incorporating negative values into the simple additive weighting (SAW) under uncertain conditions: An application in project manager selection problem. In: Strang KD, Vajjhala NR, editors. International program and project management — best practices in selected industries. Springer, Cham, Switzerland, pp: 1-12.

Bahadır O, Türkmençalıkoğlu H. 2021. Shannon entropy and its applications in information theory. Eur J Sci Technol, (32):491-498. https://doi.org/10.31590/ejosat.1039771,

Ballamudi S. 2024. Evaluating IoT platforms: An approach using the COPRAS method. J Data Sci Inform Technol, 2:55-65

Baş F. 2021. Çok kriterli karar verme yöntemlerinde kriter ağırlıklarının belirlenmesi. Nobel Bilimsel, Ankara, Türkiye, pp: 144.

Başdar C. 2019. Finansal performans ve çok kriterli karar verme teknikleri. Ekin Yayınevi, Bursa, Türkiye, pp: 232.

Begam S. 2024. Identification of groundwater recharge zone in periurban watershed with the help of MAUT and MEREC techniques. Res Square, 1(1):1-29. https://doi.org/10.21203/rs.3.rs-4178085/v1

Bektaş S. 2023. MEREC ve MABAC yöntemleri ile BİST 100'de işlem gören enerji firmalarının finansal performanslarının değerlendirilmesi. Dokuz Eylül Univ İşletme Fakültesi Derg, 24(2):115-128

Bircan H. 2020. Çok kriterleri karar verme problemlerinde kriter ağırlıklandırma yöntemleri. Nobel Akademik, Ankara, Türkiye, pp: 184.

Chaipetch P, Amprayn C, Pawan P, Vatanavongs R. 2025. A multi-criteria decision support system for prioritizing road maintenance: Integrating AHP and TOPSIS with a focus on low-volume roads. IOP Conf Ser Earth Environ Sci, 1450(1):1-11. https://doi.org/10.1088/1755-1315/1450/1/012004

Chakraborty S, Zavadskas EK, Antucheviciene J. 2015. Applications of WASPAS method as a multi-criteria tool. Econ Comput Econ Cybern Stud Res, 49(1):5-22

Chen LC, Chang KH, Hung JF. 2025. WASPAS-based natural language processing method for handling content words extraction and ranking issues: An example of SDGs corpus. Information, 16(198):1-19. https://doi.org/10.3390/info16030198

Chinnasamy S, Ramachandran M, Rajkumar S, Sivaji C. 2023. A survey on transportation system using the WPM method. Build Mater Eng Struct, 1(2):37-44. http://doi.org/10.46632/bmes/1/2/5

Chinnasay S, Ramachandran M, Sravanan V. 2023. Analysis of blast resistant buildings using the WPM method. REST J Emerg Trends Model Manuf, 9(1):26-36. https://doi.org/10.46632/jemm/9/1/4

Ciardiello F, Genovese A. 2023. A comparison between TOPSIS and SAW methods. Ann Oper Res, 325:967-994. https://doi.org/10.1007/s10479-023-05339-w

Cincotta PM, Giordano CM, Silva RA, Beaugé C. 2021. Shannon entropy diffusion estimates: Sensitivity on the parameters of the method. Celest Mech Dyn Astron, 133(7):1-20. https://doi.org/10.1007/s10569-021-10006-y

Ćirovic G, Pamučar D. 2022. Multiple-criteria decision making. MDPI AG, Basel, Switzerland, pp: 244.

Çankaya Kurnaz S. 2025. Çok kriterli karar verme yöntemlerinden TOPSIS ile AB ülkelerinin e-devlet performanslarının karşılaştırılması. Sos Bilim EKEV Akad Derg, 101:149-173. https://orcid.org/my-orcid?orcid=0000-0001-6977-300X

Çelikbilek Y. 2018. Çok kriterli karar verme yöntemleri. Nobel Akademik Yayıncılık, Ankara, Türkiye, pp: 212.

Çetinkaya C, Erbaş M, Kabak M, Özceylan E. 2023. A mass vaccination site selection problem: An application of GIS and entropy-based MAUT approach. Socio Econ Plan Sci, 85:1-11. https://doi.org/10.1016/j.seps.2022.101376,

Çilek A, Şeyranlioğlu O. 2025. Measuring the financial performance of reinsurance companies in Türkiye with LODECI, CRADIS and AROMAN MCDM methods. Int J Bus Econ Stud, 7(1):1-18. https://doi.org/10.54821/uiecd.1587675

Demir G. 2021. Özel sermayeli mevduat bankalarında performans analizi: RAFSI bütünleşik model uygulaması. Atatürk Univ İktisadi İdari Bilim Derg, 35(4):1359-1382

Demir G, Arslan R. 2022. Sensitivity analysis in multi-criteria decision-making problems. Ankara Hacı Bayram Veli Univ İktisadi İdari Bil Fak Derg, 24(3):1025-1056

Demir G, Özyalçın AT, Bircan H. 2021. Çok kriterli karar verme yöntemleri ve ÇKKV yazılımı ile problem çözümü. Nobel, Ankara, Türkiye, pp: 198.

Demirci A. 2020. Sağlık hizmetleri yönetiminde çok kriterli karar verme teknikleri. Gazi Kitapevi, Ankara, Türkiye, pp: 224.

Dinçer SE. 2019. Çok kriterli karar alma. Gece Akademi, Ankara, Türkiye, pp: 164.

Doković L, Doljanica D. 2023. Application of AHP and MABAC methods in the framework of multi criteria decision making in the selection of investment projects. J Process Manag New Technol, 11(3-4):105-114, pp: 105-114.

Ecer F. 2020. Çok kriterli karar verme. Seçkin Yayıncılık, Ankara, Türkiye, pp: 186.

El-Araby A, Sabry I, El-Assal A. 2024. Ranking performance of

MARCOS method for location selection problem in the presence of conflicting criteria. Decis Mak Adv, 2(1):148-162. https://doi.org/10.31181/dma21202435

Ersoy N. 2024. Assessing renewable energy impact in Nordic-Baltic region: Sensitivity analysis and MCDM approach. Renew Energy Res Appl, 6(1):47-60. https://doi.org/10.22044/rera.2023.13416.1238

Fan J, Yao X, Wu M. 2025. Extended WPA CRITIC WASPAS model based on picture fuzzy soft sets for green building materials selection. Int J Fuzzy Syst, 1(1):1-15. https://doi.org/10.1007/s40815-025-01982-6

Gini A. 2000. What happens if work goes away. Bus Ethics Q, 10(1):181-188. https://doi.org/10.2307/3857704

Goswami SS, Behera DK, Afzal A, Kaladgi AR, Khan SA, Rajendran P, Asif M. 2021. Analysis of a robot selection problem using two newly developed hybrid MCDM models of TOPSIS-ARAS and COPRAS-ARAS. Symmetry, 13(1331):1-35. https://doi.org/10.3390/sym13081331

Goswami SS, Mohanty SK, Behera DK. 2022. Selection of a green renewable energy source in India with the help of MEREC integrated PIV MCDM tool. Mater Today, 52(3):1152-1160. https://doi.org/10.1016/j.matpr.2021.11.019

Gressman PT, Strain RM. 2010. Global classical solutions of the Boltzmann equation with long-range interactions. Proc Natl Acad Sci USA, 107(13):5744-5749. https://doi.org/10.1073/pnas.1001185107

Han F, Alkhawaji RN, Shafieezadeh MM. 2025. Evaluating sustainable water management strategies using TOPSIS and fuzzy TOPSIS methods. Appl Water Sci, 15(4):1-13. https://doi.org/10.1007/s13201-024-02336-7

Handayani N, Heriyani N, Septian F, Alexander AD. 2023. Multi-criteria decision making using the WASPAS method. J Teknoinfo, 17(1):260-270

Hwang CL, Yoon K. 1981. Multiple attribute decision making - methods and applications. Springer Verlag, Berlin, Germany, pp: 357.

Işık Ö, Çalık A, Shabir M. 2025. A consolidated MCDM framework for overall performance assessment of listed insurance companies based on ranking strategies. Comput Econ, 65:271-312. https://doi.org/10.1007/s10614-024-10578-5

Kaya İ, Karaşan A. 2020. Çok kriterli karar verme. Umuttepe Yayınları, Kocaeli, Türkiye, pp:15-56.

Kaymaz ÇK, Kızılkan Y, Birinci S. 2020. Ordu ili turizm merkezlerinin çok kriterli karar verme yöntemlerine göre analizi. Kriter Yayınevi, İstanbul, Türkiye, pp:25-45.

Keeney R, Raiffa H. 1976. Decision with multiple objectives: Preferences and value trade off. John Wiley & Sons, New York, USA, pp:14,16.

Keleş N. 2023. Uygulamalarla klasik ve güncel karar verme yöntemleri. Nobel Bilimsel, Ankara, Türkiye, pp:45-49.

Keshavarz-Ghorabaee, M, Amiri M, Zavadskas EK, Turskis Z, Antucheviciene J. 2021. Determination of objective weights using a new method based on the removal effects of criteria (merec). Symmetry, 13(525): 1-21. https://doi.org/10.3390/sym13040525.

Khan NZ, Ansari TA, Siddiquee AN, Khan ZA. 2019. Selection of e-learning websites using a novel proximity ındexed value (piv) mcdm method. J Comput Educ 6: 241-256. https://doi.org/10.1007/s40692-019-00135-7.

Köksal K, Köseoğlu R. 2010. Fenciler için kuantum mekaniği. Nobel Yayın, Ankara, Türkiye, pp:14-16.

Krippendorff K. 2009. Mathematical theory of communication. In: Encyclopedia of communication theory, SW. Littlejohn, KA. Foss Editors. Sage, Los Angeles: USA, pp: 614-618.

Lendvai L, Jakab S, Singh T. 2025. Optimal design of agroresidue filled poly(lactic acid) biocomposites using an integrated critic-cocoso multi-criteria decision-making approach. Sci Rep, 15(11586): 1-18. https://doi.org/10.1038/s41598-025-92724-z.

Lopez LM, Ishizaka A, Qin J. 2023. Multi criteria decision making sorting methods: Applications to real world., Acad Press, Cambridge-Massachusetts, USA, pp:56-78.

Madić M, Radovanović M. 2015. Ranking of some most commonly used nontraditional machining processes using rov and critic methods. U.P.B. Sci Bull D, 72(2): 193-204.

Madić M, Radovanović M, Manić, M. 2016. Application of the rov method for the selection of cutting fluids. Dec SciLett5: 245–254.

Mehdiabadi A, Sadeghi A, Yazdi AK, Tan Y. 2025. Sustainability service chain capabilities in the oil and gas industry: A fuzzy hybrid approach swara-mabac. Spectr Oper Res, 2(1): 92-112. https://doi.org/10.31181/sor21202512.

Mishra S, Ayyub, BM. 2019. Shannon entropy for quantifying uncertainty and risk in economic disparity. Risk Anal., 39(10): 2160-2181. https://doi.org/10.1111/risa.13313.

Muni GD, Sudipa G, Meinarni NS, Wiguna, IA, Sandhiyasa, IS. 2024. Comparison of magıq, mabac, marcos, and moora methods in multi-criteria problems. Sinkron : Jurnal dan Penelitian Teknik Informatika, 8(3): 1286-1303. https://doi.org/10.33395/sinkron.v8i3.13639.

Munier N. 2021. Mathematical modelling of decision problems. Springer Cham., Gewerbestrasse, Switzerland, pp:45-46.

Munier N. 2024. Strategic Approach in multi criteria decision making. Springer Int Pub AG, Gewerbestrasse, Switzerland, pp:47-89

Nanda A. 2020. Shannon's entropy and ıts generalisations towards statistical ınference in last seven decades: Review on entropy. Int Stat Rev, 87(11): 167-186 https://doi.org/10.1111/insr.12374

Narang V, Rai R, Johal RS. 2024. Clausius' theorem and the Second law in the process of isoenergetic thermalization. arXiv:1-17 https://doi.org/10.1103/PhysRevE.110054103

Organ A, Yalçın E. 2016. Performance evaluation of research assistants by copras method. Eur Sci J Spec Issue: 102-109

Owen C. 2023. Multiple-criteria decision making: techniques, analysis and applications. States Acad Press, New York, USA, pp:15-56

Özbek A. 2019. Çok kriterli karar verme yöntemleri ve excel ile problem çözümü kavram-teori-uygulama. Seçkin Yayıncılık, Ankara, Türkiye, pp:45-49

Özbek A, Erol E. 2017. Ranking of factoring companies in accordance with aras and copras. Int J Acad Res Acc Financ Manag Sci, 2(7): 105-116 http://dx.doi.org/10.6007/IJARAFMS/v7-i2/2876

Özdemir M. 2018. Çok kriterli karar verme yöntemleri. Nobel Yayımcılık, Ankara, Türkiye, pp:35-37

Özekenci SY. 2024. Financial performance measurement of companies in the bıst sustainability 25 ındex with lbwa and merec-based cradis methods. J Mehmet Akif Ersoy Univ Econ Admin Sci Fac, 11(24): 1184-1211 https://doi.org/10.30798/makuiibf.1465069

Özkaya G. 2024. An analysis of the circular economy in europe through comparative research employing the crıtıc-based maut and copras methods. Verimlilik Derg, 58(3): 337-358 https://doi.org/10.51551/verimlilik.1462098

Öztaş T, Öztaş GZ. 2024. Innovation performance analysis of g20 countries: a novel ıntegrated lopcow-maırca mcdm approach ıncluding the covıd-19 period. J Prod Spec Issue: Productivity for Innovations: 1-20

https://doi.org/10.51551/verimlilik.1320794
Öztel A, Alp İ. 2020. Çok kriterli karar verme seçiminde yeni bir yaklaşım. Kriter Yayıncılık, İstanbul, Türkiye, pp:15-16
Paksoy S. 2017. Çok kriterli karar vermede güncel yaklaşımlar. Karahan Kitapevi, Adana, Türkiye, pp:265-258
Pamućar DS, Tarle SP, Parezanovic T. 2018. New hybrid multi-criteria decision-making dematel-mairca sustainable selection of a location for the development of multimodal logistics centre. 31(1): 1641-1665 https://doi.org/10.1080/1331677X.2018.1506706
Pamućar D, Ćirović G. 2015. The selection of transport and handling resources in logistics centers using multi-attributive border approximation area comparison. Expert Syst Appl, 42: 3016–3028
Paradhita AN, Fajariyanti Y, Amanda MT, Puspitasari A, Sulistyowati V. 2025. Implementation of topsıs method to assist the process of accepting new employees in the company. People Behav Anal, 3(1): 35-48 https://doi.org/10.31098/pba.v3i1.3135
Permata KI, Putri DS, Sasmita GA. 2025. Multi-criteria decision support system for web-based credit approval: a study of topsıs, mabac, waspas, and maut methods. J Penelit Teknol Inform Dan Sains, 3(1): 114-130 https://doi.org/10.54066/jptis.v3i1.3152
Puška A, Božanić D, Mastilo Z, Pamučar D. 2023. A model based on merec-cradis objective decision-making methods and the application of double normalization: A case study of the selection of electric cars. Res Square, pp: 2-19 https://doi.org/10.21203/rs.3.rs-2092146/v1
Radomska-Zalas A. 2023. Application of the waspas method in a selected technological. Procedia Comput Sci, 225: 177–187 https://doi.org/10.1016/j.procs.2023.10.002
Radulescu CZ, Radulescu M. 2024. A hybrid group multi-criteria approach based on saw,topsıs, vıkor, and copras methods for complex IoT selection problem. Electronics, 13(789): 1-27 https://doi.org/10.3390/electronics13040789
Rasoanaivo RG, Yazdani M, Zaraté P, Fateh A. 2024. Combined compromise for ıdeal solution (CoCoFISo): A multi-criteria decision-making based on the CoCoSo method algorithm. Expert Syst Appl, pp: 1-35 https://doi.org/10.1016/j.eswa.2024.124079
Robinson DW. 2008. Entropy and uncertainty. Entropy, 10: 493-506 https://doi.org/10.3390/e10040493
Roshanravan B, Kreuzer OP, Buckingham A. 2025. BWM-MARCOS: A new hybrid mcdm approach for mineral potential modelling. J Geochem Explor, 269: 1-13 https://doi.org/10.1016/j.gexplo.2024.107639
Rudnicki L. 2011. Shannon entropy as a measure of uncertainty. J Russ Laser Res, 32: 393–399 https://doi.org/10.1007/s10946-011-9227-x
Sakurai JJ, Napolitano J. 2012. Modern kuantum mekaniği. (Translated by G. Önengüt). Palme Yayınevi, Ankara, Türkiye, pp:45-49
Shankar R. 2014. Thermodynamics II. In: Fundamentals of Physics: Mechanics, relativity, and thermodynamics. Yale University Press, New Haven, USA, pp:65-68
Sharma LP, Patel N, Ghose MK, Debnath P. 2015. Development and application of Shannon's entropy integrated information value model for landslide susceptibility assessment and zonation in Sikkim Himalayas in India. Nat Hazards, 75: 1555–1576 https://doi.org/10.1007/s11069-014-1378-y
Stevenson D. 2021. Application of shannon entropy metrics to cultural diversity and language evaluation. Academia Lett, 2503: 1-7 https://doi.org/10.20935/AL2503
Stević Ž, Pamučar D, Puškac A, Chatterjee P. 2020. Sustainable supplier selection in healthcare ındustries using a new mcdm method: measurement of alternatives and ranking according to compromise solution (MARCOS). Comput Ind Eng, 140: 1-15
Sutoyo MN, Paliling A. 2025. The Integration of dematel and saw methods for developing a research performance assessment model for lecturers. J Appl Data Sci, 6(2): 1026-1036 https://doi.org/10.47738/jads.v6i2.550
Taherdoost H, Mohebi A. 2024. A Comprehensive guide to the copras method for multi-criteria decision making. J Manag Sci Eng Res, 7(2): 1-11 https://doi.org/10.30564/jmser.v7i2.6280
Taşcı MZ. 2024. Merec ve cradis yöntemlerini içeren entegre bir çkkv modeli ile dask özelinde bir uygulama. Doğuş Univ Derg, 25(1): 35-53 https://doi.org/10.31671/doujournal.1294336
Tepe S. 2021. Örnek uygulamalarla çok kriterli karar verme yöntemleri. Akademisyen Kitapevi, Ankara, Türkiye, pp:36-123
Tesic D, Bozanic D, Radovanovic M, Petrovski A. 2023. Optimising assault boat selection for military operations: an application of the dibr ii-bm-cocoso mcdm model. J Intell Manag Dec, 2(4): 160-171 https://doi.org/10.56578/jimd020401
Thakkar JJ. 2021. Multi criteria decision making. Springer Singapore, Singapore, Singapore, pp:45-59
Thanh NV. 2021. Multi criteria decision making model for supply change management. Eliva, Chişinău, Moldovia, pp:63-68
Trung D. 2021. Application of edas, marcos, topsıs, moora and pıv methods for multi-criteria decision making ın milling process. J Mech Eng, 71(2): 69-84
Trung DD, Tan TN. 2023. Combination of doe and pıv methods for multi-criteria decision making. J Appl Eng Sci, 21(1): 361-373 https://doi.org/10.5937/jaes0-41482
Trung D, Thinh HX, Ha LD. 2022. Comparison of the rafsi and piv method in multi-criteria decision making: application to turning processes. Int J Metrol Qual Eng, 13(14): 1-9 https://doi.org/10.1051/ijmqe/2022014
Turan H, Bulak ME. 2023. An application of multi criteria methods in choosing location for disaster logistics. Meriç Uluslar Sos Sos Stratej Araştır Derg, 7(Special Issue): 78-93
Uludağ AS, Doğan H. 2021. Üretim yönetiminde çok kriterli karar verme. Nobel, Ankara, Türkiye, pp:48-98
Ulutaş A. 2019. Swara ve mairca yöntemleri ile catering firması seçimi. BMIJ, 7(4): 1467-1479
Ulutaş A, Topal A. 2020. Bütünleştirilmiş çok kriterli karar verme yöntemlerinin üretim sektörü uygulamaları. Akademisyen Kitapevi, Ankara, Türkiye, pp:58-69
van Stokkum R. 2024. An information measure of ınstitutional complexity for social psychology. Adv Soc Sci Res J, 11(2): 33-53 https://doi.org/10.14738/assrj.112.16387
World Intellectual Property Organization (WIPO) 2024. Global innovation index 2024: Unlocking the promise of social entrepreneurship. WIPO, Geneva, Switzerland, pp:45-49
Yadav A, Kant R, Kumar V. 2025. Evaluation and ranking of solutions to mitigate Industry 4.0 adoption risks in manufacturing: A hybrid spherical fuzzy fucom-mabac approach. Int J Comput Integr Manuf, 1-27 https://doi.org/10.1080/0951192X.2025.2503315
Yakowitz DS, Lane LJ, Szidarrovszky F. 1993. Multi-attribute decision making: dominance with respect to an importance order of the attributes. Appl Math Comput, 54(2-3): 167-181
Yazdani M, Zarate P, Zavadskas E, Turskis Z. 2019. A combined compromise solution (CoCoSo) method for multi-criteria decision-making problems. Manag Dec, pp: 1-19

Zaeemzadeh A, Tononi G. 2024. Shannon information and integrated information: Message and meaning. arXiv: 1-26 https://doi.org/10.48550/arXiv.2412.10626

Zardari NH, Ahmed K, Shirazi SM, Yusop ZB. 2014. Weighting methods and their effects on multi criteria decision making model outcomes in water resources management. Springer Nature, Berlin, Germany, pp:47-132

Zavadskas EK, Turskis Z. 2010. A new addiadditive ratio assessment (aras) method in multicriteria decision-making. Technol Econ Dev Econ, 16(2): 159–172

Zavadskas EK, Kaklauskas A, Šarka V. 1994. The new method of multicriteria complex proportional assessment of projects. Technol Econ Dev Econ, 1(3): 131-139

Zavadskas EK, Turskis Z, Antucheviciene J, Zakarevičius A. 2012. Optimization of weighted aggregated sum product assessment. Elektronika ir Elektrotechnika, 6(122): 3-6

Zhang QR. 2008. A general information theoretical proof for the second law of thermodynamics. Int J Mod Phys E, pp: 531-537 https://doi.org/10.1142/S0218301308009859

Zhang X, Wang C, Li E, X C. 2014. Assessment model of ecoenvironmental vulnerability based on ımproved entropy weight method. Sci World J, pp: 1-7 http://dx.doi.org/10.1155/2014/797814

Žižovic M, Pamucar D, Albijanic M, Chatterjee P, Pribicevi. 2020. Eliminating rank reversal problem using a new multi-attribute model: The rafsi method. Mathematics, 8: 1-16 https://doi.10.3390/math8061015

Zolfani SH, Ecer F, Pamučar D, Raslanas S. 2020. Neighborhood selection for a newcomer via a novel bwm-based revised mairca ıntegrated model: A case from the coquimbo-la serena conurbation, Chile. Int J Strateg Prop Manag, 24(2): 102-118 https://doi.org/10.3846/ijspm.2020.11543

Black Sea Journal of Engineering and Science
doi: 10.34248/bsengineering.1708610

Open Access Journal
e-ISSN: 2619 – 8991

Research Article
Volume 8 - Issue 5: 1401-1405 / September 2025

HELMINTH EGGS CONTAMINATION OF COMMONLY CONSUMED LEAFY GREEN VEGETABLES IN KIRŞEHİR PROVINCE, TÜRKİYE

Nuri ERCAN[1]*

[1]*Kırşehir Ahi Evran University, Kaman Vocational School, Department of Food Processing, 40300 Kaman, Kırşehir, Türkiye*

Abstract: Safe food is crucial for human health and well-being. Fruit and vegetables are essential for human diet as they provide providing vitamins, minerals, phytochemicals, and fibre, which are associated with a lower risk of cardiovascular disease and obesity. However, they are also a potential source of microbial contamination that can lead to food-borne infections. The aim of this study was to reveal the helminth egg contamination of leafy green vegetables for sale to humans in Kırşehir province. A total of 60 fresh leafy green vegetable samples (parsley, rocket, peppermint, purslane, and spinach) obtained from markets and bazaars were examined microscopically. Helminth eggs were detected in 3 (5%) of the 60 vegetables, specifically in rocket (1/12), spinach (1/12), and purslane (1/12) samples. These results highlight that unwashed or poorly washed leafy green vegetables pose a risk of parasite egg exposure and emphasize the importance of consumers adhering to proper hygiene practices before consumption. This study provides the first data on parasitic contamination of leafy green vegetables sold in markets and bazaars in Kırşehir province, Türkiye.

Keywords: Helminth eggs, Vegetables, Public health, Kırşehir

***Corresponding author:** Kırşehir Ahi Evran University, Kaman Vocational School, Department of Food Processing, 40300 Kaman, Kırşehir, Türkiye
E mail: nuri.ercan@ahievran.edu.tr (N. ERCAN)
Nuri ERCAN https://orcid.org/0000-0001-6039-3510

Received: May 29, 2025
Accepted: July 22, 2025
Published: September 27, 2025

Cite as: Ercan N. 2025. Helminth eggs contamination of commonly consumed leafy green vegetables in Kırşehir province, Türkiye BSJ Eng Sci, 8(5): 1401-1405.

1. Introduction

Vegetables and fruit are an important part of the human diet all around the globe. They provide important nutrients, such as vitamins, minerals, dietary fiber, and phytochemicals, and offer protection against chronic diseases (Mazzoni et al., 2021; Erol et al., 2023; Irma et al., 2023). A diet rich in vegetables is closely associated with to improved gastrointestinal health and vision, as well as a lower risk of heart disease, stroke, diabetes, certain cancers, and protects and promotes mental well-being (Dias, 2012; Fismen et al., 2024). Moreover, the growing demand for easy and quick-to-eat, high-quality, and organic food has led to an increase in raw food consumption of vegetables (Li et al., 2020; Alneyadi et al., 2024). For example, the consumption of lettuce in the USA has increased significantly in the last decade (12.0 kg/person/year) (Esmael et al., 2023).

Food contaminated with harmful levels of pathogens and chemical or physical substances can cause acute or chronic illnesses – including more than 200 diseases (WHO, 2020). Despite all these benefits, fresh leafy green produce is susceptible to contamination throughout the entire process, from production to consumption (Esmael et al., 2023). The main routes of pathogenic contamination during vegetable production include farm and municipal waste, as well as irrigation water sources contaminated with human or animal feces (wild or domestic animals) (Bilgiç et al., 2023). Among these pathogens, several protozoal cysts (*Entamoeba* spp., *Giardia intestinalis*, *Blastocystis* spp.), oocysts (*Cryptosporidium parvum*, *Cyclospora* spp., *Isospora* spp., *Toxoplasma* spp.), and helminth eggs and larvae (*Strongyloides* spp, *Trichuris trichiura*, *Enterobius vermicularis*, *Fasciola hepatica*, *Ascaris lumbricoides*, *Toxocara* spp., *Taenia* spp.) play an important role in contamination (Balali et al., 2020). Despite the dominance of bacteria in foodborne diseases, neglected parasitic foodborne diseases can be serious and even fatal (Bosch et al., 2018; Robertson, 2018). In addition, helminth-borne diseases affect a quarter of the world's population and cause significant health problems (Jourdan et al., 2018).

To date, the presence of vegetable-borne pathogenic diseases has been reported from many different countries, including Türkiye. However, no study has been conducted to determine the parasitic contamination of vegetables sold in Kırşehir. In this context, the present study aimed to determine the contamination of fresh vegetables with helminth eggs, sampled from local markets and bazaars in the Kırşehir province.

2. Materials and Methods

2.1. Study Area

This study was carried out in Kırşehir province, located in the Central Anatolian Region of Türkiye. Kirsehir province has cold, snowy winters and hot, dry summers. The average annual temperature is +11.3 °C, and the annual

rainfall is less than 400 mm (http://www.kirsehir.gov.tr). Agriculture and animal husbandry are the primary economic activities in this region.

2.2. Sample Collection

A total of 60 unwashed and pre-washed vegetables, including parsley (n=12), rocket (n=12), peppermint (n=12), purslane (n=12), and spinach (n=12) samples (Figure 1) were taken from local markets and bazaars between March to June in 2024 (Table 1). To prevent cross-contamination, each sample was placed in a separate nylon bag and immediately transported to the laboratory for examination. No human or animal ethics approval was required for the completion of this study.

Table 1. Distribution of samples that are obtained from market and bazaar

	Parsley	Rocket	Peppermint	Purslane	Spinach
Market	5	4	4	10	-
Bazaar	7	8	8	2	12
Total	12	12	12	12	12

2.3. Processing samples for helminthological examination

The samples were included in the study as purchased and without prior treatment. A sample of each vegetable was weighed (~200 g) and placed in an Erlenmeyer flask with physiological saline solution (0.9% NaCl). The flask was placed on the orbital shaker plate and shaken for two hours at 130 rpm at room temperature. The vegetable leaves were discarded, and the resulting solution was allowed to settle overnight. The supernatant was then carefully decanted, ensuring minimal disturbance to the sediment. Approximately 50 mL of the sediment was transferred to a Falcon tube and centrifuged for 10 min at 2500×g (M'rad et al., 2020). After centrifugation, the supernatant was decanted, and a portion of the resulting sediment was then examined for the presence of trematode eggs. The remaining sediment was transferred to a 15 mL glass tube, mixed with a saturated salt solution, and a glass coverslip was placed on top. After 15 minutes, the coverslip was examined at 10x and 40x magnification for the presence of cestode and nematode eggs. To ensure quality, three slides per sample were analysed.

Figure 1. Vegetable Samples. A. Rockets, B. Purslane, C. Parsley, D. Spinach.

3. Results

Helminth egg contamination in the examined vegetables, including parsley, peppermint, rocket, spinach, and purslane is presented in Table 2. Helminth eggs were detected in 3 (5%) of 60 vegetables, including purslane (1/12), rocket (1/12), and spinach (1/12). Morphological analysis of the detected helminth eggs revealed them to be of the ascarid type (Figure 2). Although other helminth eggs or larvae (e.g., *Toxocara*, *Strongyloides*) have been reported in similar studies, only ascarid-type eggs were observed in our samples.

Table 2. Distribution of helminths eggs contamination in vegetable samples in Kırşehir

Vegetables	No. of Positive (%)	No. of Negative	Total
Parsley	-	12	12
Rocket	1 (8.3)	11	12
Peppermint	-	12	12
Spinach	1 (8.3)	11	12
Purslane	1 (8.3)	11	12
Total	3 (5)	57	60

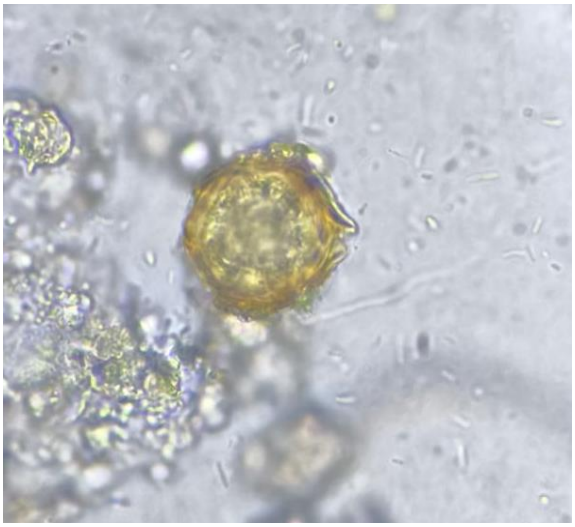

Figure 2. The identified helminth egg in purslane sample in this study (40X magnification).

4. Discussion

Despite health advances and preventive measures, foodborne diseases remain unexpectedly high in both developed and developing countries. The World Health Organisation (WHO) estimates that 600 million people worldwide fall ill each year after consuming contaminated food (WHO, 2022). While there are many benefits to eating fruit and vegetables, eating raw or insufficiently washed fruit and vegetables carries the risk of contracting pathogen-borne diseases (Tangi et al., 2023). In our study, very few helminth eggs were identified with a low contamination rate (5%). Compared to previous findings in Türkiye, this result is relatively similar to those of Kozan et al. (2005) [5.9%], Avcioglu et al., (2011) [3.0%], Adanir and Tasci (2013) [6.3%] and Erol et al. (2023) [9.1%], but significantly lower than those of Bilgiç et al. (2023) [26.2%], Erez et al., (2022) [13.5%] and Kartal et al. (2024) [16.6%], and slightly higher than that of Aydenizoz et al. (2017) [1.0%]. Ulukanligil et al. (2001) conducted a comprehensive study in Şanlıurfa and found high levels of helminth contamination (59.5%) in fecal samples from farmers, irrigation water, soil samples, and locally grown vegetables. These observations could be due to differences in the sensitivity of the techniques used in the different studies, as well as differences in geographical location, sample size, origin and type of vegetable samples, and the seasons in which the samples were collected. When local climatic conditions are unfavourable, the demand for green vegetables in Kırşehir is met by imports from other regions. In the late spring and summer, however, locally grown produce from rural areas and villages is sold at local markets and bazaars, alongside imported vegetables. The origin and growing conditions of the samples used in this study are unknown.

Ascarids are widespread nematodes that primarily infect the small intestine of their hosts, which include several domestic animals, wildlife species, and humans. Especially in humans, ascariasis can have acute and chronic manifestations, the latter being associated with significant nutritional and growth deficits (Else et al., 2020). In addition to the physical effects, recent investigations have also indicated that *Ascaris* infections can affect mental processing in some school children (O'lorcain and Holland, 2000; Drake et al., 2020). From this perspective, ascariasis is an important but neglected disease (Holland et al., 2022). The results of our study reinforce the understanding that foodborne pathogens pose a threat to public health, especially for children and immunocompromised individuals.

The contamination of vegetables by microbial agents can occur at any point in the production chain (Balali et al., 2020). Gil et al. (2015) categorised the sources of contamination into two broad groups: pre-harvest and post-harvest. Pre-harvest sources of contamination include the soil in which the vegetables are grown, irrigation water, dust, improperly composted manure, and human interaction with the product. In addition to irrigation water, rain also contaminates leafy vegetables with soil particles (da Costa Dantas et al., 2023). Post-harvest contamination sources include feces, harvesting and packaging equipment, human handling, insect vectors, and rinsing water. All of this information highlights the risks associated with consuming raw fruit and vegetables without proper washing and emphasises the need to strictly adhere to washing procedures.

5. Conclusion

To summarise, this study is the first to reveal parasitic contamination of green vegetables sold in Kırşehir province. It is crucial for producers and consumers to comply with the required maximum hygiene standards. In addition, the relevant state institutions must take the necessary measures to raise public awareness and municipalities should prioritise public health in the disposal of solid and liquid waste.

Author Contributions

The percentages of the author' contributions are presented below. The author reviewed and approved the final version of the manuscript.

	N.E.
C	100
D	100
S	100
DCP	100
DAI	100
L	100
W	100
CR	100
SR	100
PM	100
FA	100

C=Concept, D= design, S= supervision, DCP= data collection and/or processing, DAI= data analysis and/or interpretation, L= literature search, W= writing, CR= critical review, SR= submission and revision, PM= project management, FA= funding acquisition.

Conflict of Interest

The author declared that there is no conflict of interest.

Ethical Consideration

Ethics committee approval was not required for this study because of there was no study on animals or humans.

Acknowledgements

The author would like to thank the editor and blind reviewers for their comments and contributions to the manuscript.

References

Adanir R, Tasci F. 2013. Prevalence of helminth eggs in raw vegetables consumed in Burdur, Türkiye. Food Control, 31(2): 482-484.

Alneyadi KSS, Almheiri MSB, Tzortzakis N, Di Gioia F, Ahmed Z FR. 2024. Organic-based nutrient solutions for sustainable vegetable production in a zero-runoff soilless growing system. J Agric Food Res, 15:101035.

Avcioglu H, Soykan E, Tarakci U. 2011. Control of helminth contamination of raw vegetables by washing. Vector-Borne Zoonotic Dis, 11(2): 189-191.

Aydenizoz M, Gokpinar S, Gazyagci AN. 2017. Investigation of parasitological contamination in leafy vegetables in Kırıkkale of Türkiye. Anim Health Prod Hyg, 6(1): 463-467.

Balali GI, Yar DD, Afua Dela VG, Adjei-Kusi P. 2020. Microbial contamination, an increasing threat to the consumption of fresh fruits and vegetables in today's world. Int J Microbiol, 2020:3029295.

Bilgiç F, Ozturk E, Babat S, Babaoğlu A, Erdoğan D, Korkmaz M. 2023. Determination of parasitic contamination in vegetables collected from local markets in İzmir province, Türkiye. Türkiye Parazitoloji Derg, 47(2).

Bosch A, Gkogka E, Le Guyader FS, Loisy-Hamon F, Lee A, Van Lieshout L, Phister T. 2018. Foodborne viruses: Detection, risk assessment, and control options in food processing. Int J Food Microbiol, 285: 110-128.

da Costa Dantas LM, de Medeiros Maia CM, da Silva Chaves Damasceno KSF, Mont'Alverne Jucá Seabra L, Chaves G, de Assis CF, de Sousa Júnior FC. 2023. Prevalence of helminths in fresh vegetables: a narrative literature review. J Sci Food Agric, 103(8): 3761-3765.

Dias JS. 2012. Nutritional quality and health benefits of vegetables: A review. Food Nutr Sci, 3(10): 1354-1374.

Drake LJ, Jukes MCH, Sternberg RJ, Bundy DAP. 2000. Geohelminth infections (ascariasis, trichuriasis, and hookworm): cognitive and developmental impacts. Sem Pediatr Infect Dis, 11(4): 245-251.

Else KJ, Keiser J, Holland CV, Grencis RK, Sattelle DB, Fujiwara RT, Cooper PJ. 2020. Whipworm and roundworm infections. Nat Rev Dis Primers, 6(1): 44.

Erez MS, Kozan E, Göksu A. 2022. Detection of helminth egg contamination on raw vegetables in Afyonkarahisar, Türkiye. Kocatepe Vet J, 15(4): 374-380.

Erol U, Altay K, Şahin ÖF, Urhan OF. 2023. Helminth contamination of commonly consumed raw vegetables in sivas province in the central part of Türkiye: First molecular detection of human pathogenic Toxocara canis eggs in raw vegetables. Acta Vet Eurasia, 49(1).

Esmael A, Al-Hindi RR, Albiheyri RS, Alharbi MG, Filimban AA, Alseghayer MS, Teklemariam AD. 2023. Fresh produce as a potential vector and reservoir for human bacterial pathogens: Revealing the ambiguity of interaction and transmission. Microorganisms, 11(3): 753.

Fismen AS, Aarø LE, Thorsteinsson E, Ojala K, Samdal O, Helleve A, Eriksson C. 2024. Associations between eating habits and mental health among adolescents in five nordic countries: a cross-sectional survey. BMC Public Health, 24(1): 2640.

Gil MI, Selma MV, Suslow Jacxsens L, Uyttendaele M, Allende A. 2015. Pre-and postharvest preventive measures and intervention strategies to control microbial food safety hazards of fresh leafy vegetables. Crit Rev Food Sci Nutr, 55(4): 453-468.

Holland C, Sepidarkish M, Deslyper G, Abdollahi A, Valizadeh S, Mollalo A, Rostami A. 2022. Global prevalence of Ascaris infection in humans (2010–2021): a systematic review and meta-analysis. Infect Dis Poverty, 11(1): 113.

Irma KNG, Thierry EBJ, Isaka KN, Vanelle WS, Efietngab AN, Emilie TT, Lucia N. 2023. Parasitological assessment of some fruits and vegetables commonly sold in retail outlets in the Mfoundi Division of Cameroon. Parasite Epidem Cont, 22:e00313.

Jourdan PM, Lamberton PH, Fenwick A, Addiss DG. 2018. Soil-transmitted helminth infections. Lancet, 391(10117): 252-265.

Kartal K, Eser M, Güzel H. 2024. The prevalence of helminth eggs in raw vegetables from street markets in Eskişehir, Türkiye. Eur J Life Sci, 3(1): 1-8.

Kozan E, Gonenc B, Sarimehmetoglu O, Aycicek H. 2005. Prevalence of helminth eggs on raw vegetables used for salads. Food Control, 16(3): 239-242.

Li J, Wang Z, Karim MR, Karim MR, Zhang L. 2020. Detection of human intestinal protozoan parasites in vegetables and fruits: a review. Parasit Vectors, 13:380.

Mazzoni L, Ariza Fernández MT, Capocasa F. 2021. Potential health benefits of fruits and vegetables. Appl Sci, 11(19): 8951.

M'rad S, Chaabane-Banaoues R, Lahmar I, Oumaima H, Mezhoud H, Babba H, Oudni-M'Rad M. 2020. Parasitological contamination of vegetables sold in Tunisian retail markets with helminth eggs and protozoan cysts. J Food Prot, 83(7):

1104-1109.

O'lorcain P, Holland CV. 2000. The public health importance of Ascaris lumbricoides. Parasitology, 121(S1): S51-S71.

Robertson LJ. 2018. Parasites in food: from a neglected position to an emerging issue. Adv Food Nutr Res, 86: 71-113.

Tangi FB, Arnauld TGB, Koye B. 2023. Parasitic contamination of commonly consumed fresh fruits sold at Tiko and Limbe Municipality Markets, South West Region of Cameroon. Food Sci Nutr Res, 6(1): 1-7.

Ulukanligil M, Seyrek A, Aslan G, Ozbilge H, Atay S. 2001. Environmental pollution with soil-transmitted helminths in Sanliurfa, Türkiye. Mem inst oswaldo cruz, 96: 903-909.

World Health Organization (WHO). 2020. Key facts: food safety. (accessed date: April 15, 2025).

World Health Organization (WHO). 2022. WHO global strategy for food safety 2022–2030: towards stronger food safety systems and global cooperation: executive summary. World Health Organization. (accessed date: April 15, 2025).

Black Sea Journal of Engineering and Science
doi: 10.34248/bsengineering.1703012

Open Access Journal
e-ISSN: 2619 – 8991

Research Article
Volume 8 - Issue 5: 1406-1414 / September 2025

CHAOTIC SPEED CONTROL OF A DC MOTOR USING THE SPROTT-A SYSTEM FOR ROBOTIC END-EFFECTOR APPLICATIONS

Yusuf HAMİDA EL NASER[1]*, Berk DEMİRSOY[2], Kenan ERİN[3], Mert Süleyman DEMİRSOY[1]

[1]*Sakarya University of Applied Sciences, Faculty of Tecnology, Department of Mechatronic Engineering, 54050, Sakarya, Türkiye*
[2]*Kormas Electric Motor inc., TOSB OSB, 41420, Kocaeli, Türkiye*
[3]*Tarsus University, Faculty of Engineering, Department of Mechanical Engineering, 33400, Mersin, Türkiye*

Abstract: This study investigates the use of chaotic speed control, based on the Sprott-A chaotic system, for improving the performance and stability of DC motor-driven robotic end-effector mixers. The chaotic differential equations were implemented and numerically solved in MATLAB/Simulink using the fourth-order Runge–Kutta method, and the resulting time series were analyzed. Among the variables generated, the X_t signal was selected for pulse-width modulation (PWM) due to its smooth dynamic characteristics. This signal was scaled to match the 0–100% duty cycle range and applied to the motor driver as a control input. The chaotic control system was realized both through analog circuit simulation in OrCAD and experimentally using an STM32F407 microcontroller. Time series, phase portraits, and oscilloscope outputs confirmed the consistency between simulation and hardware implementations. Compared to chaotic Y_t and Z_t signals, the chaotic X_t based PWM control reduced motor vibrations and provided more stable speed regulation. These results demonstrate the feasibility and effectiveness of chaotic dynamics for real-time motor control in robotic mixing applications, offering a robust alternative to traditional deterministic methods.

Keywords: Robotics, Chaos theory, Motor speed control, PWM

***Corresponding author:** Sakarya University of Applied Sciences, Faculty of Tecnology, Department of Mechatronic Engineering, 54050, Sakarya, Türkiye
E mail: yusufelnaser@subu.edu.tr (Yusuf HAMİDA EL NASER)
Yusuf HAMİDA EL NASER https://orcid.org/0000-0003-4757-6288
Berk DEMİRSOY https://orcid.org/0009-0003-3489-7346
Kenan ERİN https://orcid.org/0000-0003-4714-1161
Mert Süleyman DEMİRSOY https://orcid.org/0000-0002-7905-2254

Received: May 20, 2025
Accepted: July 23, 2025
Published: September 15, 2025

Cite as: Hamida El Naser Y, Demirsoy B, Erin K, Demirsoy MK. 2025. Chaotic speed control of a dc motor using the sprott-a system for robotic end-effector applications. BSJ Eng Sci, 8(5): 1406-1414.

1. Introduction

The precise regulation of mixer speed in robotic and industrial applications remains a cornerstone of process efficiency, particularly in fields such as food engineering, pharmaceuticals, and advanced materials. As the demand for uniformity, adaptability, and energy efficiency intensifies, control methodologies have evolved from deterministic frameworks to encompass nonlinear and chaotic dynamics, particularly within robotic systems.

Variable-speed mixers have demonstrated superior performance across diverse mixing scenarios. Simanjorang et al. showed that maintaining consistent stirring speeds enables uniform viscosity during nanoparticle dispersion (Simanjorang et al., 2022) Brushless DC (BLDC) motors further enhance this stability with high efficiency and reduced energy losses, as observed by Nayak and Shivarudraswamy (Nayak and Shivarudraswamy, 2020). Feedback-enhanced control architectures are increasingly employed to improve real-time mixer response. Shih et al. introduced a vision-based feedback system capable of adjusting DC motor speed based on material visual cues (Shih et al., 2017).

Recent advances in Cartesian robotic systems have highlighted the growing importance of integrating intelligent control strategies, particularly in applications involving dynamic environments and complex manipulation tasks. Among the most widely applied techniques, impedance and admittance control frameworks have proven effective for achieving compliant motion and safe physical interactions. Mayr and Salt-Ducaju introduced a Cartesian impedance controller that stabilizes motion under contact-rich conditions, while Yang et al. demonstrated the benefits of admittance control in dual-arm robots for facilitating human-robot interaction (Yang et al., 2019; Mayr and Salt-Ducaju, 2022). Complementing these approaches, Portillo-Vélez et al. developed an optimization-based impedance regulation method to maintain operational safety within force boundaries (Portillo-Vélez et al., 2015). To manage uncertainties and dynamic variability, adaptive control methodologies have gained prominence. Al Khudir and De Luca focused on acceleration level control by exploiting kinematic redundancy, and Kazemipour et al. addressed time-varying constraints through real-time adaptive

kinematic adjustments (Al Khudir and De Luca, 2018; Kazemipour et al., 2022). Fuzzy logic-based control has further expanded the adaptability of robotic systems, as seen in the work of Li et al. and Chen et al., who demonstrated fuzzy controller designs that enhance trajectory tracking and resilience against environmental disturbances (Li et al., 2017 and Chen et al., 2022). In the domain of robotic manipulators, ILC has been successfully integrated with servo motors to enhance tracking accuracy in cyclic operations, such as robotic welding, pick-and-place tasks, and repetitive force control. Studies have shown that combining ILC with conventional Proportional-Integral-Derivative (PID) or model-based controllers leads to faster convergence and robustness against model uncertainties. For instance, adaptive ILC schemes have been proposed to address parameter variations and nonlinearities in actuator dynamics, enabling consistent performance even under fluctuating load conditions (Demirsoy et al. 2024). This capability becomes especially valuable in visual servoing tasks, where image-based feedback is incorporated to adjust the robot's end-effector trajectory in real time (El Naser et al., 2024). In such cases, the synergy between ILC and computer vision algorithms allows for the compensation of visual disturbances, delays, or occlusions, leading to improved spatial accuracy and adaptive behavior in unstructured environments.

Addressing high-dimensional and redundant systems, Flacco et al. proposed strategies for managing hard joint constraints without compromising task execution (Flacco et al., 2015). Liu et al. advanced motion generation using dynamic movement primitives (DMPs) with embedded feedback to achieve adaptive and human-like motions (Liu et al., 2020). A growing body of research explores chaos theory as a powerful framework for robotic control. Miranda-Colorado et al. introduced chaotic modulation in flexible joint manipulators, revealing improved maneuverability through nonlinear trajectories (Miranda-Colorado et al., 2018). Ren et al. (2015) applied multiple chaotic central pattern generators (CPGs) for legged locomotion, enabling adaptive fault compensation. Zang et al. systematically reviewed chaos-based robotic applications, highlighting its potential for navigation, exploration, and unpredictable motion planning (Zang et al., 2016). Chaos stabilization techniques such as the OGY method and Hamiltonian energy feedback further illustrate how nonlinear control enhances system robustness (Huang et al., 2016; Ahrabi and Kobravi, 2019). Li et al. proposed Lorenz-based bounded coverage strategies for mobile robots, affirming the utility of chaos in task diversification (Li et al., 2016). In parallel, the control of robotic end-effectors in mixing applications has evolved to incorporate novel actuator technologies and sensor-driven feedback systems. Tanaka et al. designed pneumatic suction-based end-effectors for depalletizing tasks, and Telegenov et al. introduced an underactuated gripper with breakaway clutch mechanisms for adaptive manipulation (Telegenov et al., 2015; Tanaka et al., 2020). Xiang et al. integrated soft robotics into end-effector design, enabling delicate and responsive material handling (Xiang et al., 2019). Zhao et al. implemented vision-based trajectory compensation to enhance flexibility in manufacturing robots, while Khan et al. proposed a virtual force-tracking impedance control scheme for precise trajectory tracking in mixing contexts (Zhao et al., 2024; Khan et al., 2025). These studies outline a multidimensional research landscape where impedance control, adaptive strategies, fuzzy logic, and chaos-informed models converge to address the challenges of dynamic robotic manipulation. The integration of chaotic dynamics into speed control and motion generation represents a promising direction for future robotic mixers, especially in environments demanding flexibility, responsiveness, and control robustness.

Recent experimental work demonstrated the integration of chaotic speed control with robotic mixing systems, where chaotic signals derived from the Halvorsen, Newton-Leipnik, Hadley, and Sprott A attractors were used to modulate the DC motor speed of a Cartesian robot's end-effector mixer (Yagmur and Kutlu, 2024). Furthermore, the application of chaotic speed modulation has also been extended to bioreactor systems, where a hybrid shaft mixer controlled by chaotic algorithms (Hadley, Halvorsen, Lorenz, and Sprott-A) significantly enhanced methane production and combustion quality compared to conventional fixed-speed methods (Sarıkaya et al., 2025). These findings confirm the practical relevance of chaos-based speed modulation in robotic mixing applications and support its further investigation within Cartesian robotic frameworks.

Despite the extensive body of research on mixer speed control using classical techniques such as PID controllers, fuzzy logic, and sliding mode control, significant limitations persist, particularly in environments characterized by nonlinearity, variable material properties, and dynamic operational constraints. Existing studies primarily focus on deterministic control methods that assume relatively stable mixing conditions and do not adequately address the performance fluctuations observed in complex, time-varying mixing tasks. Furthermore, while the application of chaotic dynamics to motor control has been explored at a theoretical level (particularly in the context of chaotization and stability control of standalone DC motors) the integration of chaos theory into robotic end-effector systems performing mixing tasks remains largely unexplored.

This study aims to address these gaps by proposing a novel approach in which a DC motor, mounted as an end-effector on a Cartesian robotic system, performs the mixing operation with its speed dynamically modulated based on scaled outputs from the Sprott-A chaotic differential equations. Unlike traditional speed profiles, the use of chaotic signals introduces non-repetitive, yet bounded variations in motor speed, thereby enhancing turbulence and improving fluid mixing efficiency. This method bridges the domains of nonlinear dynamics,

robotic control, and process engineering by embedding chaos-derived trajectories into the actuator control loop. Through simulation-based validation, the proposed system is expected to enhance mixing performance in terms of homogeneity and process speed, particularly in scenarios involving high-viscosity or heterogeneous mixtures. The study contributes a novel intersection between chaos theory and robotic mixing applications, filling a critical gap in the literature and offering a foundation for future experimental and industrial deployment.

2. Materials and Methods

In this study, the speed control of the DC motor integrated into the robotic end-effector was performed by chaotically modulating the PWM (Pulse Width Modulation) signal based on the z-component of the "A" system presented by J. C. Sprott in his 1994 paper titled *"Some Simple Chaotic Flows"* (Sprott, 1994). The corresponding differential equation system is provided in equation 1, with initial conditions defined as x(0)=0, y(0)=1 and z(0)=0.

$$\begin{aligned} \dot{x} &= y \\ \dot{y} &= yz - x \\ \dot{z} &= 1 - y^2 \end{aligned} \tag{1}$$

2.1. Dynamic analysis and stability assessment of the system

When analyzing the behavior of the system in the vicinity of the point (0,0,0), the differential equations constituting the system are set equal to zero, as shown in equation 2, in order to identify possible equilibrium points. However, upon attempting to solve the system of equations simultaneously, it becomes evident that no valid solution exists near this point. Consequently, the system does not exhibit a critical (equilibrium) point at (0,0,0).

$$\dot{x} = y = 0, \dot{y} = yz - x = 0, \dot{z} = 1 - y^2 = 0 \tag{2}$$

The Jacobian matrix of the system, as presented in equation 3, is analyzed to investigate the local stability characteristics of the system around potential equilibrium points.

$$J = \begin{vmatrix} 0 & 1 & 0 \\ -1 & z & y \\ 0 & -2y & 0 \end{vmatrix} \tag{3}$$

To examine the conservativeness of the system, the elements along the main diagonal of the Jacobian matrix are summed, as shown in equation 4, which represents the volumetric divergence of the system. However, due to the absence of an identifiable equilibrium point, conservativeness cannot be conclusively determined through this method alone.

$$\nabla . \vec{F} = \frac{\partial \dot{x}}{\partial x} + \frac{\partial \dot{y}}{\partial y} + \frac{\partial \dot{z}}{\partial z} = 0 + z + 0 = z \tag{4}$$

Therefore, further analysis such as evaluating the Kaplan–Yorke dimension is necessary to draw a definitive conclusion (Sarıkaya et al., 2024). Owing to these distinctive characteristics, the Sprott-A chaotic system is considered a special case and has been selected for use in this study.

The MATLAB/Simulink model of the Sprott-A chaotic system is presented in Figure 1.

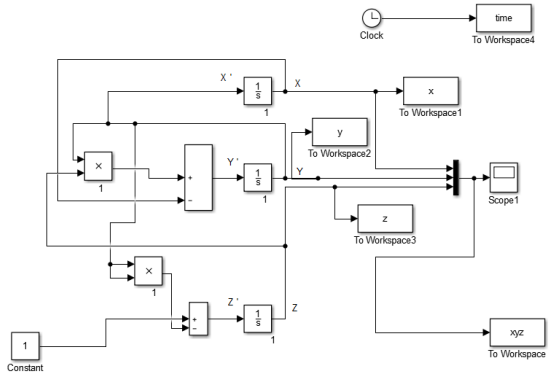

Figure 1. Modeling of the sprott-a chaotic system using simulink.

The Lyapunov exponents of the system are calculated using the formula given in equation 5.

$$\lambda_Y = \lim_{n\to\infty} \frac{1}{n} \sum_{k=0}^{n-1} ln \left| \frac{x_k - y_k}{x_0 - y_0} \right| \tag{5}$$

The Lyapunov exponent graph, plotted based on the expression in Equation 5, is shown in Figure 2.

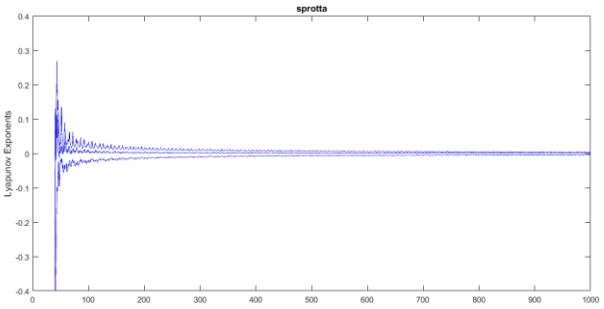

Figure 2. Determination of the system's Lyapunov exponents.

According to the results, the Lyapunov exponents are approximately calculated as λ_1=0.004, λ_2=0 and λ_3=−0.004. Based on these values, the Kaplan–Yorke (Lyapunov) dimension is computed as in equation 6.

$$\lambda_{KY} = j + \frac{\lambda_1 + \lambda_2}{|\lambda_3|} = 2 - \frac{0.004}{|-0.004|} = 3 \tag{6}$$

In three-dimensional chaotic systems, the Kaplan–Yorke dimension typically lies between 2 and 3. However, obtaining an exact value of 3 indicates that the system is conservative, meaning it does not exhibit volumetric contraction over time. Instead, the system tends to fill the entire three-dimensional phase space as time approaches infinity. Furthermore, based on this interpretation, the equality expressed in equation 7 can also be derived.

$$\frac{1}{V}\frac{dV}{dt} = \frac{\partial \dot{x}}{\partial x} + \frac{\partial \dot{y}}{\partial y} + \frac{\partial \dot{z}}{\partial z} = \lambda_1 + \lambda_2 + \lambda_3 = 0 \qquad (7)$$

Variations in the parameters of a nonlinear system of differential equations can directly influence the system's dynamic behavior. Depending on the nature and extent of these changes, the system may exhibit different types of stability characteristics, including point stability, limit cycle behavior, quasi-periodic or quasi-chaotic responses, fully developed chaos, or even instability. The influence of parameter variations (particularly on the system's transition to chaos) can be effectively analyzed using bifurcation diagrams, which provide a visual representation of how the system's qualitative behavior changes with respect to key parameter values.

The bifurcation diagram shown in Figure 3 illustrates the variation in the system's chaotic behavior with respect to changes in the coefficient of the y parameter in Equation 1 ($\dot{x} = y$), as it varies within the range [0,3].

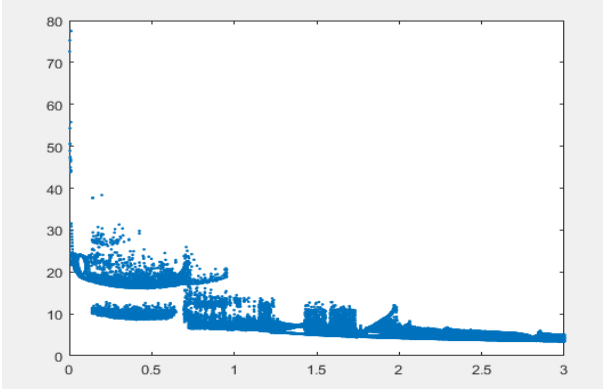

Figure 3. Effect of varying the coefficient of the y parameter in Equation 1 within the range [0,3] on the system's behavior.

The bifurcation diagram presented in Figure 4 illustrates in Figure 4 how the system's chaotic behavior varies with changes in the constant term added to the $-y^2$ expression in Equation 1 ($\dot{z} = 1 - y^2$), as this constant is varied within the range [0,3].

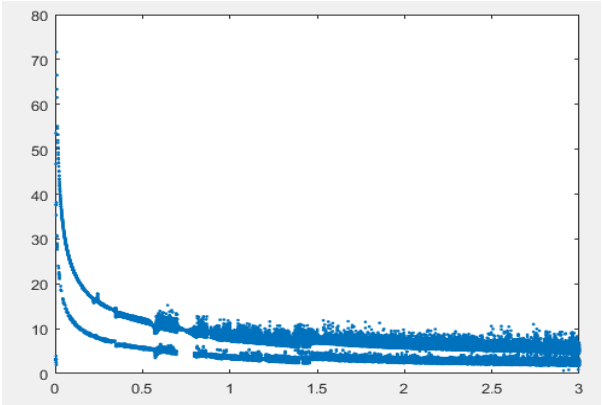

Figure 4. Effect of varying the constant added to the $-y^2$ term in Equation 1 within the range [0,3] on the system's behavior.

3. Results and Discussion

This section presents the analog implementation of the chaotic system to verify its dynamic characteristics in a physical environment.

In order to validate the numerical behavior of the system under real conditions, an analog circuit implementation was carried out. This implementation enables the observation of the system's dynamic response through physical measurements. Time series, phase portraits, and oscilloscope outputs were obtained to analyze the temporal and state-space behavior of the chaotic system. These experimental signals not only verify the theoretical simulations but also provide insight into the circuit-level realizability of the chaotic dynamics. The use of an oscilloscope facilitates real-time monitoring of the system's variables, allowing for a visual comparison of analog trajectories with simulated results. The results obtained in this section serve as an essential step toward confirming the physical feasibility and consistency of the Sprott-A chaotic system. The system's analog realizations in the simulation environment are presented in Figure 5, while the experimental (hardware-based) implementation is shown in Figure 6.

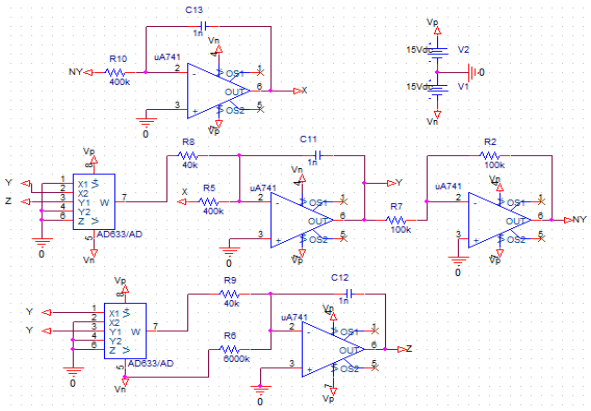

Figure 5. Analog simulation of the system in OrCAD.

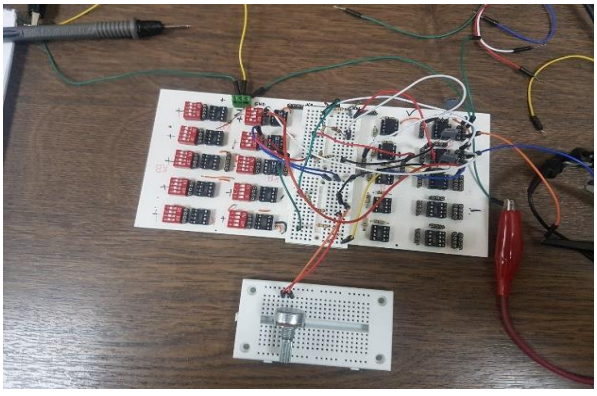

Figure 6. Experimental observation of the system's analog implementation.

The time series outputs obtained from the PSpice software are presented in Figure 7, while the corresponding results from the MATLAB software are shown in Figure 8.

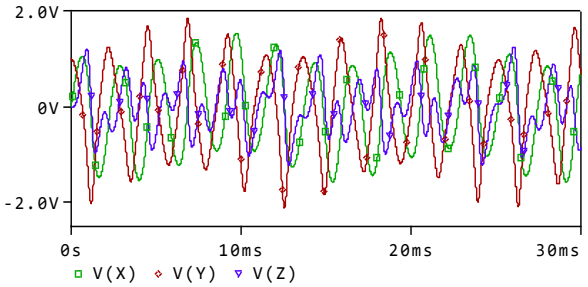

Figure 7. Time series outputs of the system obtained from PSpice software

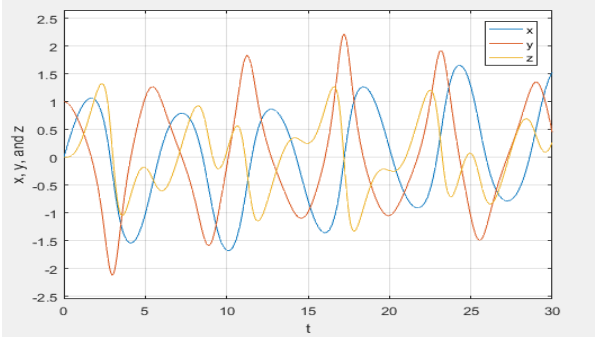

Figure 8. Time series outputs of the system obtained from MATLAB software.

The DAC channels of the STM32F407 microcontroller were configured to output the computed x, y and z signals in real time. These outputs were connected to an oscilloscope, enabling direct observation of the phase relationships between the chaotic variables. Additionally, the z signal was scaled and mapped to generate a PWM signal through one of the timer modules on the microcontroller. This PWM output was then used to control the speed of a DC motor connected to the robotic end-effector.

The two-dimensional phase portraits are presented in Figure 9, and the oscilloscope outputs are shown in Figure 10.

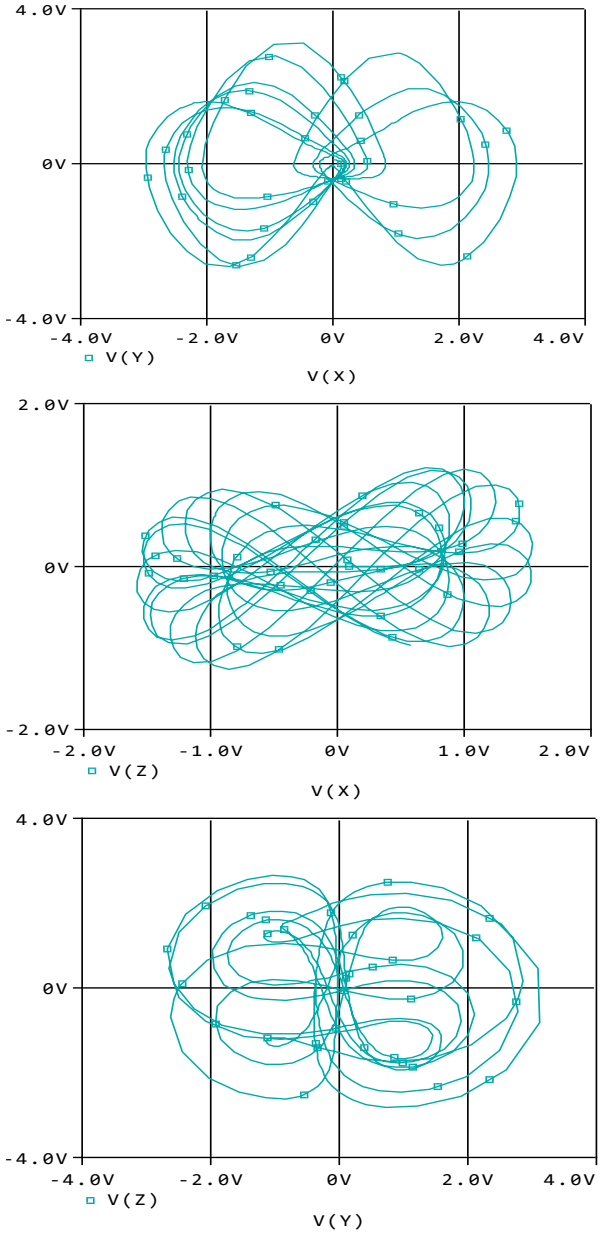

Figure 9. Phase portraits of the system obtained from PSpice outputs.

Figure 10. Oscilloscope images of the system's phase portraits.

The microcontroller-based hardware implementation of the Sprott-A chaotic system was used to control the speed of the DC motor mounted on the robotic end-effector. The system of differential equations defining the Sprott-A attractor was solved in the MATLAB environment, and the resulting time series data for the variables x, y and z were transferred to the microcontroller. For this implementation, the STM32F407 Discovery board, based on a 32-bit ARM Cortex-M4 processor, was used as shown in Figure 11. This microcontroller was selected due to its high processing speed and ease of integration with MATLAB/Simulink, enabling code generation and deployment without the need for manual programming.

Figure 11. STM32F407 Discovery development board.

In this study, the Sprott-A chaotic differential equation system was first implemented in the MATLAB/Simulink software. The Runge–Kutta 4th-order (RK4) algorithm was employed to numerically solve the system. After solving the equations, the resulting chaotic signals were used to generate phase diagrams (specifically X–Y, Y–Z, and X–Z plots) which were visualized on an oscilloscope using the DAC outputs of the microcontroller. Among the generated time series signals (X, Y, and Z), the Z signal was further utilized as a PWM input to control the speed of a DC motor. The MATLAB/Simulink block diagram used for programming the microcontroller is shown in Figure 12.

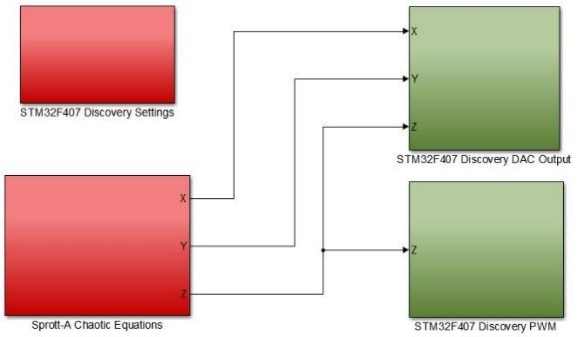

Figure 12. MATLAB/Simulink block diagram for the STM32F407 Discovery board.

The time series of the Sprott-A chaotic system analyzed in the MATLAB software are shown, upon examination of these time series, it was observed that the X_t signal exhibits smoother rising and falling transitions compared to the Y_t and Z_t signals. For this reason, the X_t signal was selected as the basis for generating the PWM (Pulse Width Modulation) signal used in motor speed control. When the Y_t and Z_t signals were applied as PWM inputs, the rapid fluctuations in their amplitude caused the motor to exhibit excessive vibration due to frequent and abrupt changes in speed.

A closer analysis of the X_t signal revealed that its amplitude ranges approximately between 4.3 and –3.9. However, this range is not directly suitable for PWM-based motor control, where the duty cycle typically needs to vary within a 0–100% interval. Therefore, the X_t signal was first scaled mathematically to fit within this interval. The scaling formula used for this purpose is provided in equation 8.

$$PWM = (X + 3.9) * 12 \quad (8)$$

According to this transformation, the resulting PWM duty cycle varies between 0% and approximately 98.4% depending on the instantaneous value of X_t. This mapping enables smoother motor operation with significantly reduced vibration compared to the use of the other chaotic signals.

After the mathematical operations of the chaotic system were performed in MATLAB/Simulink, the system was implemented and controlled on a microcontroller. The resulting PWM signal was used to drive a DC motor equipped with an encoder. The experimental setup is shown in Figure 13. In this setup, the L298N motor driver was used to interface the microcontroller with the motor.

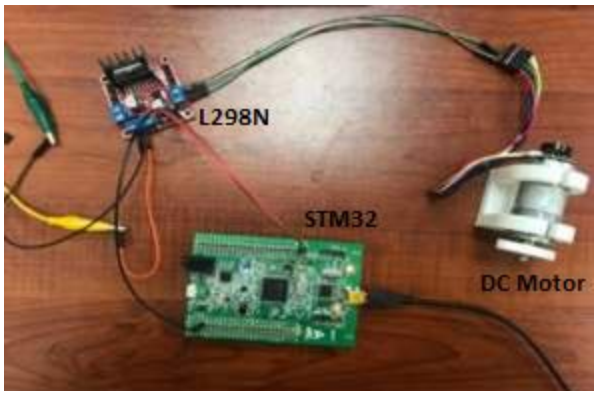

Figure 13. The experimental setup.

The motor speed was controlled chaotically by converting the X_t time series into a PWM signal. The duty cycle of the generated PWM signal was examined using an oscilloscope, and the corresponding waveform is presented in Figure 14.

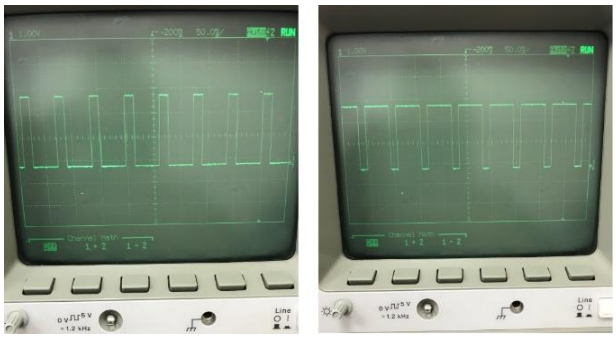

Figure 14. The generated PWM signal.

The findings of this study confirm the practical benefits of implementing chaos-based speed control in robotic mixing systems. By using the X_t component of the Sprott-A chaotic system (scaled appropriately to generate a PWM signal) the motor speed was modulated in a non-repetitive yet bounded manner. This led to significantly smoother motor behavior with reduced mechanical vibration, especially when compared to PWM signals derived from the Y_t and Z_t time series. The superior performance of the X_t driven control signal is attributed to its gradual transitions and lower frequency oscillations, which reduce abrupt torque fluctuations and thus contribute to mechanical stability.

The findings of this study provide compelling evidence supporting the practical benefits of chaotic speed modulation in robotic mixer applications. By employing the X_t signal from the Sprott-A chaotic attractor as a basis for PWM signal generation, a more stable and vibration-free control of the DC motor was achieved, particularly in comparison to PWM signals derived from Y_t and Z_t signals. This outcome is consistent with previous studies suggesting that non-repetitive, smooth input signals can enhance actuator performance by minimizing torque fluctuations and mechanical resonance (Miranda-Colorado et al., 2018; Khan et al., 2025). Unlike conventional fixed-speed or deterministically controlled mixing systems, the chaotic control paradigm introduces bounded yet dynamically rich variations in motor speed. This facilitates enhanced turbulence and material dispersion, which are known to be critical for achieving homogeneity in high-viscosity or multi-phase mixtures (Simanjorang et al., 2022; Nayak & Shivarudraswamy, 2020). The observed improvements in motor stability and responsiveness are especially significant in the context of robotic end-effectors, where frequent changes in position and load may otherwise destabilize conventional controllers. Moreover, the successful implementation of the Sprott-A system in analog (OrCAD), numerical (MATLAB), and real-time (STM32 microcontroller) environments underscores the feasibility of embedding chaos-based control into physical systems. This multi-level verification aligns with findings in the literature demonstrating the practical realizability of chaotic control models when implemented with appropriate scaling and feedback mechanisms (Zang et al., 2016; Ahrabi & Kobravi, 2019).

The integration of chaos theory into mixer speed control addresses several limitations observed in classical control approaches such as PID or fuzzy logic, which often assume time-invariant system dynamics and linear responses (Li et al., 2017; Chen et al., 2022). While these methods offer satisfactory performance under nominal conditions, they lack the adaptability required for dynamic environments—particularly in mixing scenarios involving fluctuating material properties or non-Newtonian fluids. The chaotic control strategy used in this study overcomes these shortcomings by embedding variability directly into the control signal without compromising boundedness or

stability. Additionally, the analog and oscilloscope-based observations confirm that chaotic signals maintain structural coherence even after hardware conversion and digital-to-analog transformation. This result is particularly relevant for control systems relying on real-time feedback, where signal fidelity is crucial for achieving deterministic outcomes from nonlinear dynamics (Huang et al., 2016; Portillo-Vélez et al., 2015).

The results of this study also resonate with recent experimental investigations into chaos-driven robotic mixing systems (Yagmur & Kutlu, 2024) and chaotic modulation in bioreactor configurations (Sarıkaya et al., 2025), which have shown improved process outcomes such as enhanced biogas yield and reduced energy consumption. These findings collectively support the broader applicability of chaos-informed control strategies across various sectors including biotechnology, materials science, and autonomous robotics. Nevertheless, some limitations remain. The current implementation focused solely on the speed control aspect of the mixing mechanism. Future studies could extend this approach by integrating chaotic trajectory modulation for robotic arms, as proposed in central pattern generator (CPG)-based locomotion studies (Ren et al., 2015), or by applying hybrid chaotic controllers that combine force and position control (Mayr & Salt-Ducaju, 2022; Khan et al., 2025). Additionally, a comparative evaluation between different chaotic attractors (e.g., Lorenz, Rössler, Halvorsen) may reveal further insights into system responsiveness and mixing efficiency.

4. Conclusion

This study demonstrated the applicability of the Sprott-A chaotic system in various domains by developing its MATLAB-based numerical model, analog circuit implementation in OrCAD, and microcontroller-based real-time control application. By solving the system's differential equations, time series data corresponding to the variables X_t, Y_t and Z_t were obtained. Among these, the X_t signal was selected for generating a PWM control signal due to its smoother dynamic behavior. When applied to a DC motor, the X_t based PWM signal enabled more stable motor speed regulation and significantly reduced mechanical vibration, which is typically observed when using the more abrupt Y_t or Z_t signals. The successful analog and embedded realizations validate the physical feasibility of chaos-based control for robotic mixer applications. Moreover, the findings support the potential of chaotic signals as a superior alternative to traditional deterministic controllers, especially in nonlinear, time-sensitive, and high-precision systems. The approach serves as a foundational step for extending chaos-informed control techniques into more complex robotic mixing architectures.

In summary, the study demonstrates that chaotic control can be practically implemented on microcontroller-based systems to improve mixer behavior in robotic end-effectors. The approach not only enhances performance and energy efficiency but also provides a robust control alternative suitable for nonlinear, high-viscosity, or dynamically changing environments.

In future studies, the design of an industrial mixing system using a delta robot and chaos-based control strategies is planned, with two distinct control approaches to be investigated. The first approach involves transmitting chaotic time series to the servo motors controlling the delta robot's three axes, thereby inducing chaotic variation in the spatial position of the end-effector. This motion is expected to create a dynamically shifting mixing pattern across the workspace. In the second approach, rather than modulating the robot's position, the focus will shift to directly altering the speed of the mixing motor using a chaotic signal. This aims to achieve efficient mixing through speed variability while maintaining a fixed spatial trajectory. Both strategies will be comparatively evaluated to determine their impact on mixing homogeneity, energy efficiency, and control robustness in industrial settings.

Author Contributions

The percentages of authors' contributions are given below. All authors have reviewed and approved the article.

	Y.H.E.N.	B.D.	K.E.	M.S.D.
C	25	30	25	20
D	40	30	10	10
S	10	10	40	40
DCP	25	25	25	25
DAI	25	25	25	25
L	20	30	30	20
W	30	40	15	15
CR	40	40	10	10
SR	10	40	40	10
PM	20	20	40	20
FA	10	30	30	30

C=Concept, D= design, S= supervision, DCP= data collection and/or processing, DAI= data analysis and/or interpretation, L= literature search, W= writing, CR= critical review, SR= submission and revision, PM= project management, FA= funding acquisition.

Conflict of Interest

The authors declare that they have no conflict of interest in this study.

Ethical Approval Statement

Since this study did not involve any studies on animals or humans, ethics committee approval was not obtained.

References

Ahrabi AR, Kobravi H. 2019. Chaos control in chaotic dynamical systems via auto-tuning Hamilton energy feedback. Turk J Forecast, 3(2): 47-53.

Al Khudir K, De Luca A. 2018. Faster motion on Cartesian paths exploiting robot redundancy at the acceleration level. IEEE Robot Autom Lett, 3(4): 3553-3560.

Chen R, Wang C, Wei T, Liu C. 2022. A composable framework for policy design, learning, and transfer toward safe and efficient industrial insertion. In: 2022 October–2022 IEEE/RSJ Int Conf Intell Robots Syst (IROS), Kyoto, Japan, pp: 8894-8901.

Demirsoy MS, El Naser YH, Sarıkaya MS, Peker NY, Kutlu M. 2024. Development of elbow rehabilitation device with iterative learning control and internet of things. Turk J Eng, 8(2): 370-379.

El Naser YH, Karayel D, Demirsoy MS, Sarıkaya MS, Peker NY. 2024. Robotic arm trajectory tracking using image processing and kinematic equations. Black Sea J Eng Sci, 7(3): 436-444.

Flacco F, De Luca A, Khatib O. 2015. Control of redundant robots under hard joint constraints: Saturation in the null space. IEEE Trans Robot, 31(3): 637-654.

Huang Y, Huang Q, Wang Q. 2016. Chaos and bifurcation control of torque-stiffness-controlled dynamic bipedal walking. IEEE Trans Syst Man Cybern Syst, 47(7): 1229-1240.

Khan H, Lee MC, Suh J, Kim R. 2025. Enhancing robot end-effector trajectory tracking using virtual force-tracking impedance control. Adv Intell Syst, 7(2): 2400380.

Kazemipour A, Khatib M, Al Khudir K, Gaz C, De Luca A. 2022. Kinematic control of redundant robots with online handling of variable generalized hard constraints. IEEE Robot Autom Lett, 7(4): 9279-9286.

Li C, Song Y, Wang F, Wang Z, Li Y. 2016. A bounded strategy of the mobile robot coverage path planning based on Lorenz chaotic system. Int J Adv Robot Syst, 13(3): 107.

Li S, Xu M, Quo J, Wang B, Hong Y. 2017. Design of fuzzy cross coupling controller for Cartesian robot. In: 2017 Int Conf Appl Math Model Stat Appl (AMMSA), Atlantis Press, pp: 427-431.

Liu N, Zhou X, Liu Z, Wang H, Cui L. 2020. Learning peg-in-hole assembly using Cartesian DMPs with feedback mechanism. Assembly Autom, 40(6): 895-904.

Mayr M, Salt-Ducaju JM. 2022. A C++ implementation of a Cartesian impedance controller for robotic manipulators. arXiv preprint arXiv:2212.11215 (accessed date: September 2, 2025).

Miranda-Colorado R, Aguilar LT, Moreno-Valenzuela J. 2018. A model-based velocity controller for chaotization of flexible joint robot manipulators: Synthesis, analysis, and experimental evaluations. Int J Adv Robot Syst, 15(5): 1729881418802528.

Nayak DS, Shivarudraswamy R. 2020. Solar fed BLDC motor drive for mixer grinder using a buck-boost converter. Bull Electr Eng Inform, 9(1): 48-56.

Portillo-Vélez RDJ, Rodriguez-Angeles A, Cruz-Villar CA. 2015. An optimization-based impedance approach for robot force regulation with prescribed force limits. Math Probl Eng, 2015:918301.

Ren G, Chen W, Dasgupta S, Kolodziejski C, Wörgötter F, Manoonpong P. 2015. Multiple chaotic central pattern generators with learning for legged locomotion and malfunction compensation. Inf Sci, 294:666-682.

Sarıkaya MS, El Naser YH, Kaçar S, Yazıcı İ, Derdiyok A. 2024. Chaotic-based improved Henry gas solubility optimization algorithm: Application to electric motor control. Symmetry, 16(11): 1435.

Sarıkaya MS, Demirel O, Kaçar S, Derdiyok A. 2025. Modelling and chaotic based parameter optimization of sliding mode controller. J Math Sci Model, 8(2): 42-54.

Shih CL, Hsu JH, Chang CJ. 2017. Visual feedback balance control of a robot manipulator and ball-beam system. J Comput Commun, 5(9): 8-18.

Simanjorang MR, Susanto H, Bukhori ML. 2022. Design and construction of mixer with variable speed for manufacturing nanoparticle composite materials. Teknika STTKD J Tek Electron Eng, 8(2): 257-266.

Sprott JC. 1994. Some simple chaotic flows. Phys Rev E, 50(2): R647.

Tanaka J, Ogawa A, Nakamoto H, Sonoura T, Eto H. 2020. Suction pad unit using a bellows pneumatic actuator as a support mechanism for an end effector of depalletizing robots. ROBOMECH J, 7: 1-30.

Telegenov K, Tlegenov Y, Hussain S, Shintemirov A. 2015. Preliminary design of a three-finger underactuated adaptive end effector with a breakaway clutch mechanism. J Robot Mechatron, 27(5): 496-503.

Xiang C, Guo J, Rossiter J. 2019. Soft-smart robotic end effectors with sensing, actuation, and gripping capabilities. Smart Mater Struct, 28(5): 055034.

Yagmur D, Kutlu M. 2024. 3D chaotic mixing application for polymer production. Phys Scr, 99(4): 045210.

Yang J, Xie Y, Feng M, Li J. 2019. Design and implementation of admittance control for a dual-arm robot under space limitation. In: MATEC Web Conf, 256: 02010.

Zang X, Iqbal S, Zhu Y, Liu X, Zhao J. 2016. Applications of chaotic dynamics in robotics. Int J Adv Robot Syst, 13(2): 60.

Zhao N, Murakami K, Yamakawa Y. 2024. Vision-based trajectory dynamic compensation system of industrial robot. Int J Adv Manuf Technol, 131(12): 6013-6026.

Black Sea Journal of Engineering and Science
doi: 10.34248/bsengineering.1700159

Open Access Journal
e-ISSN: 2619 – 8991

Araştırma Makalesi (Research Article)
Cilt 8 - Sayı 5: 1415-1428 / Eylül 2025
(Volume 8 - Issue 5: 1415-1428 /September 2025)

KAMU BİNALARINDA ENERJİ YÖNETİMİ İÇİN MAKİNE ÖĞRENMESİ YAKLAŞIMLARI

Vildan ARSLANTÜRK[1], Betül TURANOĞLU ŞİRİN[1]*

[1]*Atatürk University, Faculty of Engineering, Department of Industrial Engineering, 25240, Erzurum, Türkiye*

Özet: Modern yaşamın getirdiği yüksek refah standartları, elektrik enerjisini günlük yaşamın vazgeçilmez bir unsuru haline getirmiştir. Enerji politikalarının başarıya ulaşması, enerji talebinin doğru bir şekilde planlanması ve yönetilmesini zorunlu kılmaktadır. Elektrik arz güvenliğinin sağlanması, enerji verimliliğinin artırılması ve buna bağlı olarak enerji maliyetlerinin ekonomik etkisinin azaltılması, doğru enerji talep tahminleri ve etkin karar alma süreçleriyle mümkün olmaktadır. Bu durum, enerji tüketim tahminlerinin stratejik önemini bir kez daha ortaya koymaktadır. Bu çalışmada, Erzurum ilindeki üç farklı kaymakamlık binasının yıllık elektrik tüketimi; uzun dönemli tahmin modelleri (LSTM), k-en yakın komşu (KNN), gradyan destekli karar ağaçları (GBDT), rastgele orman (RF) ve aşırı gradyan artırma (XGBoost) gibi çeşitli makine öğrenmesi teknikleri kullanılarak modellenmiştir. Her bir bina için hesaplanan kök ortalama kare hata (Root Mean Square Error-RMSE), ortalama mutlak hata (Mean Absolute Error- MAE) ve ortalama mutlak yüzde hata (Mean Absolute Percentage Error- MAPE) performans metrikleri, yöntemlerin doğruluğu ve etkinliği açısından karşılaştırmalı bir analiz sunmaktadır. Elde edilen sonuçlar, bazı yöntemlerin yüksek tahmin performansı sergilediğini ve kamu binalarındaki enerji yönetimi süreçlerine önemli katkılar sağlayabileceğini göstermektedir. Bu çalışma, yalnızca kaymakamlık binaları için değil, aynı zamanda diğer kamu binalarında enerji yönetimine yönelik politikaların geliştirilmesine ve uygulanmasına rehberlik edebilecek nitelikte bir örnek teşkil etmektedir.

Anahtar kelimeler: Enerji verimliliği, Enerji yönetimi, Elektrik tüketim tahmini, Makine öğrenmesi yaklaşımları

Machine Learning Approaches for Energy Management in Public Buildings

Abstract: The high standards of welfare achieved in modern life have made electrical energy an indispensable element of daily activities. The success of energy policies depends on accurate planning and effective management of energy demand. Ensuring electricity supply security, improving energy efficiency, and reducing the economic impact of energy costs all rely on precise energy demand forecasts and efficient decision-making processes. This underscores the strategic importance of energy consumption forecasting. In this study, the annual electricity consumption of three district governorship buildings in Erzurum province was modeled using various machine learning techniques, including long short-term memory (LSTM), k-nearest neighbor (KNN), gradient-boosted decision trees (GBDT), random forest (RF), and extreme gradient boosting (XGBoost). Performance metrics such as Root Mean Square Error (RMSE), Mean Absolute Error (MAE), and Mean Absolute Percentage Error (MAPE) were calculated for each building, offering a comparative analysis of the accuracy and efficiency of these methods. The results demonstrate that certain methods achieve high forecasting performance, providing valuable insights for energy management processes in public buildings. This study serves as an example that can inform the development and implementation of energy management policies not only for district governorship buildings but also for other public facilities.

Keywords: Energy efficiency, Energy management, Electricity consumption prediction, Machine learning approaches

***Sorumlu yazar (Corresponding author):** *Atatürk University, Faculty of Engineering, Department of Industrial Engineering, 25240, Erzurum, Türkiye*
E mail: b.turanoglu@atauni.edu.tr (B. TURANOĞLU ŞİRİN)
Vildan ARSLANTÜRK https://orcid.org/0009-0005-7349-6099
Betül TURANOĞLU ŞİRİN https://orcid.org/0000-0002-7910-6312

Gönderi: 16 Mayıs 2025 **Received:** May 16, 2025
Kabul: 26 Temmuz 2025 **Accepted:** July 26, 2025
Yayınlanma: 15 Eylül 2025 **Published:** September 15, 2025
Cite as: Arslantürk V, Turanoğlu Şirin B. 2025. Machine learning approaches for energy management in public buildings. BSJ Eng Sci. 8(5): 1415-1428.

1. Giriş

Enerji ihtiyacı her geçen gün kritik ihtiyaçlar listesinde üst sıralara doğru ilerlemektedir. Artan enerji ihtiyacını karşılamak üzere yeni enerji kaynakları bulunması gerekliliğinin yanı sıra, enerjinin üretilmesi, güvenle iletilmesi ve son kullanıcıya kadar ulaştırılan enerjinin verimli kullanılması son derece önemlidir.

Enerji açısından verimli ve sürdürülebilir binaların inşa edilmesi, çevrenin korunması açısından elzem hale gelmiştir. Çünkü binalardaki verimsizlik, dünya genelindeki enerji tüketiminin ve sera gazı emisyonlarının önemli bir kısmına neden olmaktadır. Binalar tarafından tüketilen yüksek miktardaki enerji; iklim değişikliği, hava kirliliği ve termal kirlilik gibi ciddi çevre sorunlarına yol açmakta, bu da insanlığın varlığı üzerinde önemli etkiler yaratmaktadır. Son yıllarda, nüfus artışı ve hızlı kentleşme nedeniyle binalardaki enerji talebi önemli ölçüde artmıştır (Olu-Ajayi vd., 2022).

Bina enerji verimliliğini daha iyi anlamaya yönelik çalışmalar, birçok araştırmacının ilgisini çekmiş ve makine öğrenmesi aracılığıyla yeni gelişmelerin ortaya çıkmasına neden olmuştur. Bina enerji tüketimi tahmini, enerji tasarrufu sağlamak ve enerji kullanımını azaltmak için daha iyi kararlar alınmasında büyük önem

taşımaktadır. Ancak, hava koşulları, binanın fiziksel özellikleri ve kullanıcıların enerji kullanım alışkanlıkları gibi pek çok faktör enerji tüketimini etkilediğinden, enerji tahmini hâlâ karmaşık bir süreç olmaya devam etmektedir (Olu-Ajayi vd., 2022).

Doğru elektrik tüketimi tahmini, ulusal veya bölgesel düzeyde elektrik arz ve talep dengesi ile enerji üretim tesislerinin planlanması açısından oldukça önemlidir. Bu tahminler, gereksiz enerji üretimini ve olası güç kesintilerini önlemeye yardımcı olabilir. Örneğin; elektrik talebi olduğundan fazla tahmin edilirse, gereksiz enerji üretim tesislerinin kurulmasına ve dolayısıyla israf edilen kaynaklara yol açabilir. Öte yandan, elektrik talebinin olduğundan az tahmin edilmesi durumunda, yetersiz üretim kapasitesi güç kıtlığına ve elektrik kesintilerine neden olabilir (Hwang vd., 2020).

Hem ev ekonomisinde hem de ülke ekonomisinde enerji maliyetleri önemli bir yere sahiptir. Cumhurbaşkanlığı tarafından 17.05.2024 tarihli ve 32549 sayılı Resmî Gazete 'de yayımlanarak yürürlüğe giren 2024/7 sayılı ve "Tasarruf Tedbirleri" konulu Genelge ile enerji alımları ile ilgili maddeler de yer almaktadır. Enerjiyi verimli kullanmak için atılacak ilk adım enerji ihtiyacının bilinmesi ve doğru bir planlama yapılmasıdır.

Literatürde elektrik enerjisi tahmini yapılan birçok çalışma mevcuttur. Voronin ve Partanen (2014) tarafından yapılan çalışmada dalgacık dönüşümleri, ARIMA modelleri ve yapay sinir ağlarını (YSA) birleştirerek elektrik talebini ve fiyatını eş zamanlı tahmin eden bir model ortaya koymuştur. Cao vd. (2014) destek makinesi regresyonu (SVR) ile kuantum davranışlı parçacık sürüsü optimizasyonu (PSO) metotları birleştirilmiş ve ekonomiyle ilgili sekiz adet girdi kullanan bir enerji talep tahmin modeli önermişlerdir. Başoğlu ve Bulut (2017) elektrik tüketim tahmini için Türkiye'nin piyasa ve mevsim koşullarını da dikkate alan yapay sinir ağları ile uzman sistemlerin birlikte kullanıldığı bir hibrit model geliştirmişlerdir. Çayır vd. (2018) tarafından yapılan çalışmada, Londra'da bulunan 30 farklı evden Kasım 2011 ile Şubat 2014 zaman aralığında alınan yarım saatlik tüketim verilerinden oluşan ve bir milyon adet gözlem içeren bir veri kümesi ile yapay sinir ağları, destek vektör makineleri ve rassal orman modellerini kullanarak kısa vadeli bir tüketim tahmini yapılmıştır. He ve Lin (2018) Çin'in enerji yapısı ve talebini tahmin eden en uygun modeli saptamak amacıyla ADLeMIDAS isimli yaklaşımı geliştirmişlerdir. Wang vd. (2019) tarafından yapılan çalışmada, gerçek ısıtma enerjisi verileri ile rastgele orman (RF), aşırı gradyan artırma (XGBoost), gradyan artırma karar ağacı (GBDT), yapay sinir ağı (YSA) ve destek vektör regresyonu (SVR) uygulanarak tahmin modelleri oluşturulmuştur. Li ve Jones (2019) trafo merkezinin maksimum talebini modellemek için; müşteri sayısı, ortalama talep ve kurulu fotovoltaik kapasite faktörlerinin bir eğilim fonksiyonu olarak aşırı değer teorisinden hareketle bir nokta süreci modeli önermişlerdir. Kazemzadeh vd. (2020) araştırmalarında, enerji talebi tahmini için zaman serisi ve veri madenciliği tekniğine dayalı uzun vadeli hibrit bir tahmin modeli geliştirmişlerdir. Wang vd. (2020) bina enerji tüketimini tahmin etmeyi sağlayacak iyileştirilmiş hibrit bir makine öğrenmesi (Machine Learning-ML) modeli önermişlerdir. Nebati vd. (2021), Türkiye'nin 1970-2019 yılları arasındaki yıllık frekanstaki elektrik tüketim verilerini kullanarak regresyon analizi ve ARIMA'nın IMA modeli ile tüketim tahmini yapmışlardır. Filippov vd. (2021) sistem analizi yöntemlerine dayalı bir enerji talebi tahmin modeli geliştirmişlerdir. Iftikhar vd. (2023) çalışmalarında, saatlik elektrik talep tahmininin detaylı bir analizini sunmak üzere yeni ayrıştırma metotlarını çeşitli tek değişkenli ve çok değişkenli zaman serisi yöntemleriyle kıyaslamışlardır. Zhou vd. (2023) hem güç üretimini hem de güç tüketimini tahmin etmek amacıyla arz-talep etkileşimi olan verimli bir model geliştirmişlerdir. Li vd. (2024) önerdikleri genetik algoritma tabanlı destek vektör makinesi yöntemiyle elektrik talep tahmini yapmışlardır. Nikseresht ve Amindavar (2024) çalışmalarında, enerji tüketim tahmini için istatistiksel yöntemlerden faydalanarak ARFIMA temelli yeni bir hibrit model sunmuşladır. Li vd. (2024), elektrik tüketim tahmini için CatBoost ve XGBoost yöntemlerini hibrit olarak kullanmış ve oldukça yüksek doğrulukla tahmin değerleri elde etmişlerdir. Lei vd. (2024), bina enerji tüketimi tahmini için EWKM, rastgele orman, SSA ve BiLSTM tabanlı evrimsel bir derin öğrenme modeli önermişlerdir. Cui vd. (2024), makine öğrenmesi ve SHAP kullanarak farklı konut bina tipleri için enerji tüketimi tahmini ve hane halkı özellik analizi yapmışlardır. Grveón vd. (2024), elektrik tüketim tahmini için klasik istatistik ve makine öğrenmesi algoritmalarını melez olarak kullanmışlardır. MAPE değeri olarak %3,2'nin altında bir tahmin doğruluğu elde etmişlerdir. Hsu vd. (2025), binalarda değişken soğutucu akışlı (VRF) sistemlerin güç tüketimi tahmini için LSTM ve ANN modellerinin karşılaştırmalı analizine dayalı bir çalışma yapmışlardır. Uddin vd. (2025), enerji tüketim tahmini için ajan tabanlı modelleme ve makine öğrenmesi yaklaşımını içeren hibrit bir yaklaşım önermişlerdir. Wang vd. (2025), küçük veri kümelerinde özellik seçimi ve elektrik tüketimi tahmini yapmak için LSTM tabanlı bir çerçeve geliştirmişlerdir. Kim vd. (2025) çalışmalarında, farklı yapay sinir ağı modelleri kullanılarak bir binadaki elektrik tüketiminin tahmin edilmesinde veri normalleştirme yöntemlerinin etkisini araştırmışlardır. Dong vd. (2025), mekansal-zamansal korelasyon ve elektrik tüketim davranışı bilgilerine dayalı elektrik yükü tahmini için LSTM tabanlı yeni bir yöntem geliştirmişlerdir. Botman vd. (2025), bireysel hanelerin elektrik tüketiminin kısa vadeli tahmini için global olasılıksal bir yaklaşım önermişlerdir.

Yukarıda açıklanan tüm çalışmalar, Tablo 1'de özet olarak gösterilmiştir.

Tablo 1. Literatürde incelenen çalışmalar

Yazar(lar)	Yıl	Çalışma Konusu	Yöntem
Voronin ve Partanen	2014	Elektrik talebi ve fiyatının eş zamanlı tahmini	Dalgacık dönüşümleri + ARIMA + YSA
Cao vd.	2014	Enerji talep tahmini	SVR + Kuantum davranışlı PSO
Başoğlu ve Bulut	2017	Türkiye için elektrik tüketimi tahmini	YSA + Uzman Sistem
Çayır vd.	2018	Londra'daki evlerde kısa vadeli tüketim tahmini	YSA, SVM, Rassal Orman
He ve Lin	2018	Çin enerji yapısı ve talep tahmini	ADLeMIDAS modeli
Wang vd.	2019	Isıtma enerjisi talep tahmini	RF, XGBoost, GBDT, YSA, SVR
Li ve Jones	2019	Trafo merkezi maksimum talep modellemesi	Nokta süreci modeli + EVT
Kazemzadeh vd.	2020	Uzun vadeli enerji talep tahmini	Zaman serisi + Veri madenciliği (Hibrit)
Wang vd.	2020	Bina enerji tüketimi tahmini	Geliştirilmiş hibrit ML modeli
Nebati vd.	2021	Türkiye için elektrik tüketim tahmini	Regresyon + ARIMA (IMA modeli)
Filippov vd.	2021	Enerji talebi tahmini	Sistem analizi yöntemleri
Iftikhar vd.	2023	Saatlik elektrik talep tahmini	Yeni ayrıştırma + zaman serisi yöntemleri
Zhou vd.	2023	Güç üretim ve tüketim tahmini	Arz-talep etkileşimli model
Li vd.	2024	Elektrik talep tahmini	Genetik algoritma + SVM
Nikseresht ve Amindavar	2024	Enerji tüketimi tahmini	ARFIMA temelli hibrit model
Li vd.	2024	Elektrik tüketim tahmini	CatBoost + XGBoost (Hibrit)
Lei vd.	2024	Bina enerji tüketimi tahmini	EWKM + RF + SSA + BiLSTM
Cui vd.	2024	Konut tipi tüketim tahmini ve özellik analizi	ML + SHAP
Grveón vd.	2024	Elektrik tüketim tahmini	Klasik istatistik + ML
Hsu vd.	2025	VRF sistemlerinde güç tüketimi tahmini	LSTM ve ANN
Uddin vd.	2025	Enerji tüketimi tahmini	Ajan tabanlı modelleme + ML
Wang vd.	2025	Küçük veri ile tahmin & öznitelik seçimi	LSTM tabanlı çerçeve
Kim vd.	2025	Normalleştirme yöntemlerinin YSA'ya etkisi	Farklı YSA modelleri
Dong vd.	2025	Elektrik yükü tahmini	LSTM + mekansal-zamansal korelasyon
Botman vd.	2025	Hane bazlı kısa vadeli tüketim tahmini	Global olasılıksal model

Bu çalışmada; kamuya ait kaymakamlık binalarının elektrik enerjisi ihtiyacını isabetli bir şekilde tahmin etmek, yapılan tahmin ile karar alma süreçleri için kaynak oluşturmak ve kamu kaynaklarının verimli kullanılmasını teşvik etmek amaçlanmıştır. Bu amaca ulaşmak için uzun dönemli tahmin modelleri (LSTM), k-en yakın komşu (KNN), gradyan destekli karar ağaçları (GBDT), rastgele orman (RF) ve XGBoost gibi makine öğrenmesi teknikleri kullanılmıştır.

Bu çalışmanın ana katkıları aşağıdaki gibi sıralanabilir:

- LSTM, KNN, GBDT, RF ve XGBoost gibi modellerin performansları, üç farklı kaymakamlık binası üzerinden değerlendirilmiştir.
- Elde edilen tahmin sonuçlarıyla, bazı makine öğrenmesi yöntemlerinin kamu binalarında yüksek doğrulukla enerji tahmini yapabildiği ortaya konmuştur. Bu da karar vericilere daha etkili enerji yönetimi stratejileri geliştirme fırsatı sunmaktadır.
- Kamu binalarının enerji yönetiminde makine öğrenmesi tabanlı yaklaşımların uygulanabilirliğini göstermiş ve bu alanda politika geliştirme süreçlerine katkı sağlamıştır.
- Yerel düzeyde (Erzurum ili) gerçekleştirilen uygulama ile Türkiye'deki benzer kamu yapıları için genellenebilir örnek bir model oluşturulmuştur.

2. Materyal ve Yöntem

2.1. Veri Seti

Bu çalışmada kullanılan veri seti, Erzurum ilinde bulunan üç farklı kaymakamlık binasının 2013-2023 yılları arasındaki aylık elektrik tüketim değerleri, Erzurum iline ait ısıtma derece gün (HDD) değerleri ve aylık ortalama bulut kapalılığı (8 Okta cinsinden) değerlerinden oluşmaktadır. Toplamda 132 adet örnekten oluşan bu veri setinde tespit edilen birkaç eksik veri sütun ortalaması ile giderilmiştir. Kullanılan makine öğrenmesi yöntemlerinde veri setinin %80'lik kısmı eğitim için, %20'lik kısmı ise test için ayrılmıştır.

2.2. Makine Öğrenmesi Yöntemleri

Bu çalışmada, veri setine birden fazla makine öğrenmesi yöntemi uygulanmıştır. Bunlar; uzun dönemli tahmin modelleri (LSTM), k-en yakın komşu (KNN), gradyan destekli karar ağaçları (GBDT), rastgele orman (RF) ve aşırı gradyan artırma (XGBoost) yöntemleridir. Bu yöntemlerin tamamı, gözetimli öğrenme algoritmalarıdır. Söz konusu yöntemler, geçmişe ait etiketli verilerden (girdi özellikleri ve karşılık gelen enerji tüketimi değerleri) öğrenerek gelecekteki enerji tüketimini tahmin etmeye yönelik olarak eğitilmiştir.

2.2.1. Uzun dönemli tahmin modelleri (Long Short Term Memory-LSTM)

Yinelemeli sinir ağları (Recurrent Neural Networks-RNN), art arda dizilmiş olan sinir ağları arasında geçmiş ve geleceğe ilişkin bilgi akışının sağlandığı, bu akışın sürekli olarak tekrarlandığı ve böylece geçmişe ait veriler ile geleceğe yönelik tahmin çalışmalarında kullanılan elverişli bir yapay sinir ağı modelidir (Akkurt ve Sarıçiçek, 2024). Ancak RNN'de uzun zaman serilerinin eğitiminde kaybolan veya patlayan gradyan problemleri ortaya çıkmaktadır. Bu sorunu çözmek amacıyla, Hochreiter ve Schmidhuber (1996) tarafından sınırlı veri setlerindeki uzun süreli bağımlılıkları öğrenme yeteneği bulunan ve RNN'nin özel bir türü olan LSTM (Long Short Term Memory) yöntemi önerilmiştir (Hochreiter ve Schmidhuber, 1997; Goodfellow vd. 2016).

LSTM, tekrarlayan bir sinir ağı uzantısı olup uzun vadeli bilgileri hatırlamak üzere tasarlanmış bir hafıza hücresi içermektedir. Bu hücre, bilgiyi uzun bir süre muhafaza etmek üzere kullanılan bir depo görevi görmektedir. LSTM bellek hücresi, bilgiyi 0-1 arasında bir sayıya dönüştürerek bileşenlere verilecek bilgileri açıklayan bir sigmoid katmanı ve bir çarpandan müteşekkil hücre haline bilgi ekleme ve çıkarma kabiliyetine sahip olan kapıları birleştirmektedir. Sigmoid katmanı çıktısının 0 olması hiçbir bilginin geçişine izin verilmeyeceği, 1 olması ise tüm bilgilerin geçişine izin verileceği anlamı taşımaktadır (Yazıcı, 2021).

2.2.2. K-en yakın komşu (K-Nearest Neighbor-KNN) algoritması

KNN algoritması, mevcut veri setine katılan yeni veriyi en yakınındaki komşularına göre sınıflayan basit, güçlü ve parametrik olmayan bir yöntemdir (Peterson, 2009). KNN yönteminde, veri kümesine gelen yeni bir verinin ait olduğu sınıfı saptamak için sınıfı belli olan k adet komşusuna olan yakınlığı ölçülür (Özkan, 2008). Örnekler arasındaki mesafenin hesaplanmasında genellikle Öklid, Manhattan ve Chebyschev uzaklık ölçütleri esas alınır (Peker vd., 2017). Uzaklık ölçütü yardımıyla yeni verinin veri setinde yer alan tüm gözlem değerlerine olan yakınlığının hesaplanmasından sonra yakınlıklar sıralanır, en yakın k adet gözlem dikkate alınarak değerlendirilir ve yeni değer ile sınıflandırılmış veri arasındaki benzerliğe göre bir karara varılır. k değeri sınıflandırmada dikkate alınacak olan komşu sayısıdır. Veri setinin büyüklüğüne göre değişmekle birlikte 3, 5 ve 7 en sık tercih edilen k değerleridir (Silahtaroğlu, 2008). k değerinin tek sayı seçilmesindeki amaç eşitlik durumu olmasını önlemektir (Balaban ve Kartal, 2018). k değerine karar verilmesinde farklı yöntemler bulunmakla birlikte, en basit yöntem algoritmanın farklı k değerleriyle bir çok kez çalıştırılması sonucunda performansı yüksek olanın seçilmesidir (Guo vd., 2003). Veri boyutu büyüdükçe KNN algoritmasının ihtiyaç duyduğu bellek kapasitesi artacağı için daha az sayıda veri ve ilgili değişken ile sınıflandırma yapılması tavsiye edilmektedir. k değeri büyüdükçe karar sınırları düzgünleşir, ancak hesaplama yükü de artar. k değeri küçüldükçe de algoritmanın çalışma hızı yükselir, ancak bu durum gürültülü veriye hassasiyeti arttırır (Taşcı ve Onan, 2016). KNN yöntemi her bir verinin sınıfını belirlemek için tüm verileri taradığı için işlem süresi uzundur. (Khan vd., 2002). Eğitim aşamasının bulunmaması yöntemin avantajı, sınıfı belirlenecek veri için tüm verinin taranması ise dezavantajıdır (Gök, 2017). Küçük ve orta büyüklükteki veri kümelerinde tercih edilerek bu dezavantaj bertaraf edilebilir. Yöntemin uygulanmasının kolay olması ve basit bir matematiksel temele dayanması tahmin çalışmalarında oldukça farklı alanlardaki kullanımını yaygınlaştırmıştır.

2.2.3. Gradyan destekli karar ağaçları (Gradient-Boosted Decision Trees-GBDT)

Karar ağaçları, hesaplama maliyetlerinin düşük ve kolay yorumlanabilir olması dolayısıyla sınıflandırma ve tahmin çalışmalarında oldukça sık kullanılmaktadır (Yazıcı, 2021). GBDT, tahminlerini kademeli bir şekilde sırasıyla yapan ve zayıf öğreniciler tarafından yapılan tahminleri birleştirerek güçlü bir son tahmin elde etmeyi amaçlayan bir topluluk algoritmasıdır (Hastie vd., 2009; Balta, 2024). Genellikle ilk öğrenici ortalama bir değeri veya yaygın bir sınıfı temsil eden basit bir tahmin yapar ve sonraki her bir yeni ağaç son ağacın hatalarını düzeltmeye odaklanarak öğrenmeye devam eder. Böylece her adımda daha isabetli tahminler yapılır (Mercan, 2023; Gür vd., 2024). Belirli sayıda iterasyona ulaşılıncaya veya tahmin edilen ile gerçek değer arasındaki fark (hata) eşik değerin altına düşünceye dek bu işlem tekrar edilir (Mayr vd., 2014). GBDT yöntemi, tek bir karar ağacına göre büyük ve karmaşık veri setlerini işleme esnekliği, tahmin hızı ve doğruluğu gibi güçlü yönleri ile öne çıkmaktadır (Aydın, 2023). Sınıflandırma ve regresyon problemlerinde etkili olan yöntem düşük hata oranları sağlarken yüksek yorumlamaya da olanak tanımaktadır (Wang ve Mamo, 2020).

2.2.4. Rastgele orman (Random Forest-RF)

RF yöntemi, karar ağacı temelli bir denetimli öğrenme yöntemidir. (Gültepe, 2019). RF, tek bir karar ağacı ile bir sonuç elde etmek yerine birden çok karar ağacı oluşturmakta ve böylece zayıf öğrenicilerden güçlü bir öğreniciye vararak çok daha isabetli sonuçlar üretmektedir (Dev ve Eden, 2019). Bu yöntem, her bir karar ağacından bağımsız tahminler elde eder ve bu özellik yöntemin belli bir özelliğe çok güvenmesinin önüne geçerek tüm özelliklerin adil bir şekilde kullanılmasını sağlar (Breiman, 2001; Nacar ve Erdebilli, 2021). Karar ağaçlarından ayrı ayrı elde edilen sonuçlar

birleştirilerek orman adına tek ve daha güvenilir bir karar verilir (Gök, 2017). Nihai tahmin ormandaki her bir ağacın gerçekleştirdiği tahminlerin ortalaması alınmak suretiyle elde edilmektedir (Kulkarni ve Sinha, 2012).

RF yönteminin aşırı öğrenme problemi yoktur. Büyük boyutlu veri kümelerine uygulanabilir olup gürültülü, aykırı veya eksik verilere karşı da oldukça güçlüdür (Sinap, 2024). Ayrıca, çok hızlıdır ve istenilen ağaç sayısı ile çalıştırılabilir.

2.2.5. Aşırı gradyan artırma (Extreme Gradient Boosting-XGBoost)

Chen ve Guestrin (2016) tarafından önerilen XGBoost yöntemi, sınıflandırma ve regresyon problemlerinde yaygın bir şekilde kullanılan gradyan temelli bir karar ağacı algoritmasıdır. XGBoost, klasik gradyan artırma algoritmasının yapılan bazı düzenlemelerle optimize edilmiş bir versiyonudur ve daha yüksek performansla çalışmaktadır.

XGBoost, temel sınıflandırıcıları doğrusal olarak üst üste bindirerek sıralı bir karar ağacı oluştur ve birden fazla zayıf öğreniciden faydalanarak güçlü bir model ortaya koyar (Mercan, 2023). Yapısında yer alan zayıf öğreniciler verinin alt kümeleri üzerinde eğitilir, modelin hatalarını azaltmak üzere her adımda yeni bir model ekler ve böylece güçlü bir öğrenici meydana getirilir (Man vd., 2023). XGBoost, amaç fonksiyonunu genişleterek algoritmanın hem doğruluğunu hem de hızını arttırır (Chen ve Guestrin, 2016).

Bu yöntemin temeli, kayıp fonksiyonunu mümkün olduğunca azaltmaya ve daha iyi bir karar ağacı oluşturmaya dayanmaktadır. Bu durum yöntemi alternatiflerine göre daha etkili ve hızlı kılmaktadır (Demolli vd., 2019; Yelgeç ve Bingöl, 2022). Klasik yöntemlere göre daha uzun bir eğitim süresine ihtiyaç duymakla birlikte, büyük boyutlu verilerde ve karmaşık problemlerde gösterdiği yüksek performans XGBoost'u yüksek ölçekli proje ve veri bilimi uygulamalarında popüler hale getirmektedir (Eşidir, 2025). Diğer avantajları ise aşırı öğrenmeye dirençli olması, boş/kayıp verileri doğru yönetebilmesi ve hızlı olmasıdır. (Aydın, 2023).

2.3. Performans Metrikleri

Tahmin modellerinden birini seçerken yaygın olarak kabul edilen önemli kriterlerden biri, modelin verilere uygunluğu ve tahmin başarısının yüksek olmasıdır. Bu doğrultuda, modellerin tahmin doğruluklarını karşılaştırmak için çeşitli istatistiksel yöntemler kullanılmaktadır (Sofyalıoğlu ve Öztürk, 2013).

Tahmin doğruluğunu değerlendirmede sıklıkla başvurulan temel ölçütler ise şunlardır (Sofyalıoğlu ve Öztürk, 2013):

- Kök Ortalama Kare Hata (Root Mean Squared Error - RMSE)
- Ortalama Mutlak Hata (Mean Absolute Error - MAE)
- Ortalama Mutlak Yüzde Hata (Mean Absolute Percentage Error -MAPE)

$$RMSE = \sqrt{(1/n \, \Sigma \, (y_i - \hat{y}_i)^2)} \quad (1)$$

$$MAE = (1/n) \, \Sigma \, |y_i - \hat{y}_i| \quad (2)$$

$$MAPE \, (\%) = (1/n) \, \Sigma \, |(y_i - \hat{y}_i) / y_i| \times 100 \quad (3)$$

Burada;

y_i: Gerçek değer

$\hat{y}_i$: Tahmin edilen değer

n: Veri sayısı

Tahmin etkinliğini değerlendirmek için kullanılan tüm ölçütlerde hedef, en düşük RMSE, MAE ve MAPE değerlerine sahip bir tahmin modeline ulaşmaktır (Çuhadar, 2006). Bu ölçütler arasında, tahmin hatalarını yüzde olarak ifade etmesi nedeniyle MAPE'nin tek başına anlamlı bir değerlendirme kriteri olması, diğer ölçütlere göre bir avantaj sağlamaktadır.

Witt ve Witt (1991), MAPE değerine göre tahmin modellerini şu şekilde sınıflandırmıştır: %10'un altındaki değerler "yüksek doğruluk", %10 ile %20 arasındaki değerler ise "doğru tahmin" kategorisine girmektedir. (Witt ve Witt, 1991; Sofyalıoğlu ve Öztürk, 2013).

Bu çalışmada, kullanılan bütün yöntemlerin etkinliği RMSE, MAE ve MAPE değerlerine göre hesaplanmıştır.

3. Bulgular ve Tartışma

Bu çalışmada, Erzurum ilinde bulunan üç farklı kaymakamlık binası (Bina-1, Bina-2 ve Bina-3) için 2013-2023 yılları arasındaki aylık elektrik tüketim değerleri, aylık ortalama ısıtma derece gün (HDD) değerleri ve aylık ortalama bulut kapalılığı (8 Okta cinsinden) değerleri kullanılarak elektrik tüketim tahmini yapılmıştır. Tahminde kullanılan makine öğrenmesi yaklaşımları LSTM, KNN, GBDT, RF ve XGboost yöntemleridir. Bu yöntemler, varsayılan parametre ayarlarını kullanmak için scikit-learn Python paketinde kodlanmış ve çalıştırılmıştır. Elde edilen sonuçlar Tablo 2, Tablo 3 ve Tablo 4'te verilmiştir. Bu tablolarda, tüm yöntemlere ait RMSE, MAE ve MAPE değerleri bulunmaktadır. Ayrıca Şekil 1, kullanılan metodolojinin akış şemasını göstermektedir.

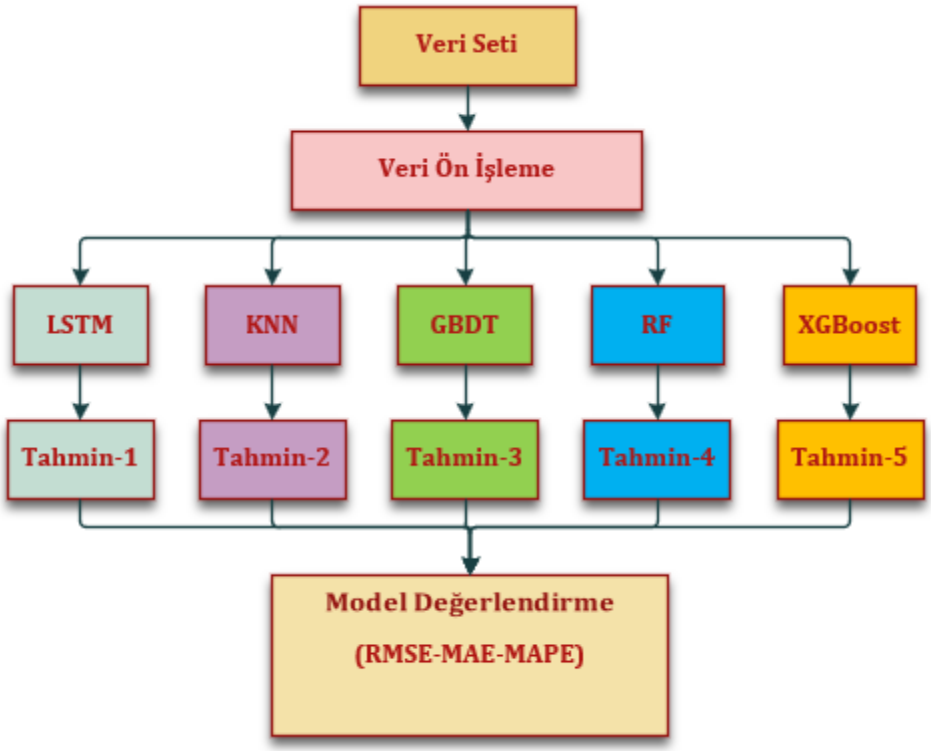

Şekil 1. Kullanılan metodolojinin akış şeması.

Tablo 2. Bina-1 için yöntemlerin performans karşılaştırması

Yöntemler	RMSE	MAE	MAPE (%)
LSTM	490,66	439,64	8,34
KNN (k=3)	1194,55	927,14	13,08
GBDT	1277,71	1008,4	14,11
RF	1267,61	1009,38	14,29
XGBoost	1344,41	1049,70	15,34

Tablo 3. Bina-2 için yöntemlerin performans karşılaştırması

Yöntemler	RMSE	MAE	MAPE (%)
LSTM	2792,74	2387,44	8,58
KNN (k=6)	7041,25	4891,49	12,50
GBDT	5381,97	4059,40	10,70
RF	8226,91	5867,01	14,84
XGBoost	8759,37	6158,82	15,94

Tablo 4. Bina-3 için yöntemlerin performans karşılaştırması

Yöntemler	RMSE	MAE	MAPE (%)
LSTM	924,36	861,48	11,18
KNN (k=4)	1004,72	745,68	9,64
GBDT	970,27	731,46	9,48
RF	1065,47	811,58	10,42
XGBoost	1316,85	948,19	11,90

Tablo 2'de görüldüğü gibi, Bina-1 için en iyi performansı özellikle zaman serisi verilerinde güçlü olan LSTM modeli göstermiştir. KNN algoritması, LSTM'ye kıyasla daha düşük bir performans sergilerken, ağaç tabanlı yöntemler (GBDT, RF, XGBoost) daha yüksek hata değerleriyle geride kalmıştır. Bu durum, elektrik tüketiminin geçmiş verilere dayalı zaman serisi yapısını yansıtırken, LSTM'nin bu tür verilere olan üstünlüğünü ortaya koymaktadır. Genel olarak, LSTM'nin Bina-1'in elektrik tüketim tahmini için en uygun model olduğu söylenebilir.

Tablo 3'de Bina-2 için çalıştırılan yöntemlerin sonuçları gösterilmiştir. Bu sonuçlara göre, yine LSTM yöntemi diğer yöntemlere kıyasla en düşük hatayı sağlayarak en iyi performansı sergilemiştir. GBDT yöntemi, daha düşük doğruluğa sahip olsa da LSTM'nin hemen ardından gelmiştir. KNN, RF ve XGBoost ise tahmin performansı açısından diğerlerinden geride kalmıştır. Özellikle RF ve XGBoost'un yüksek hata metrikleri, bu modellerin bu bina için daha az etkili olduğunu ortaya koymaktadır.

Tablo 4 ise, Bina-3 için kullanılan yöntemlerin performansını göstermektedir. Bu tablodaki sonuçlar, tahmin doğruluğu açısından diğer binalara göre farklı bir dengeyi ortaya koymaktadır. LSTM, RMSE ve MAE açısından diğer yöntemlere yakın değerler sunarken, MAPE (%11.18) ile özellikle göreceli hata oranında daha düşük performans göstermiştir. Bu kez GBDT (%9.48) ve KNN (%9.64) MAPE açısından daha iyi sonuçlar vererek dikkat çekmiştir. Ancak RF ve özellikle XGBoost, daha yüksek hata metrikleriyle diğer yöntemlerin gerisinde kalmıştır.

Şekil 2 ve Şekil 3'deki grafikler, sırasıyla Bina-1 ve Bina-2 için en düşük hata değerine sahip olan LSTM modelinin tahminlerini göstermektedir. Bu tahminlerin

genel olarak gerçek tüketim değerlerini iyi takip ettiği görülse de, ani dalgalanmalardan kaynaklı sapmalar mevcuttur. Geleceğe yönelik tahminler daha stabil bir yapı sergilemekte, ancak uzun vadeli mevsimsellik ve trendleri yeterince yansıtmadığı dikkat çekmektedir. Bunların temel nedeni, veri setindeki tüketim verilerinin mevsimsellik dışında başka faktörlerden de etkilenebileceğini göstermektedir. Örneğin; hava durumu, ekonomik koşullar, pandemi gibi olağanüstü durumlar tüketimde ciddi dalgalanmalara yol açabilir. Bazı ayların değerleri aşırı yüksek veya düşük olabilir, bu da modelin genelleme yeteneğini zorlaştırabilir.

Şekil 4 ise, Bina-3 için en düşük hata değerini veren GBDT modelinin test setindeki elektrik tahmin sonuçlarını göstermektedir. Buna göre, GBDT modelinin genel eğilimleri yakalamakta başarılı olduğu söylenebilir. Özellikle bazı zirve noktalarında tahminlerin gerçek değerlere oldukça yakın olduğu dikkat çekmektedir. Ancak, model bazı durumlarda dalgalanmaları tam olarak yakalayamamıştır. Bu durum, modelin uç değerlere yeterince duyarlı olmadığını göstermektedir. Buna rağmen, GBDT ile yapılan tahminler gerçek değerlerin ortalamasına doğru yakınsama eğilimindedir.

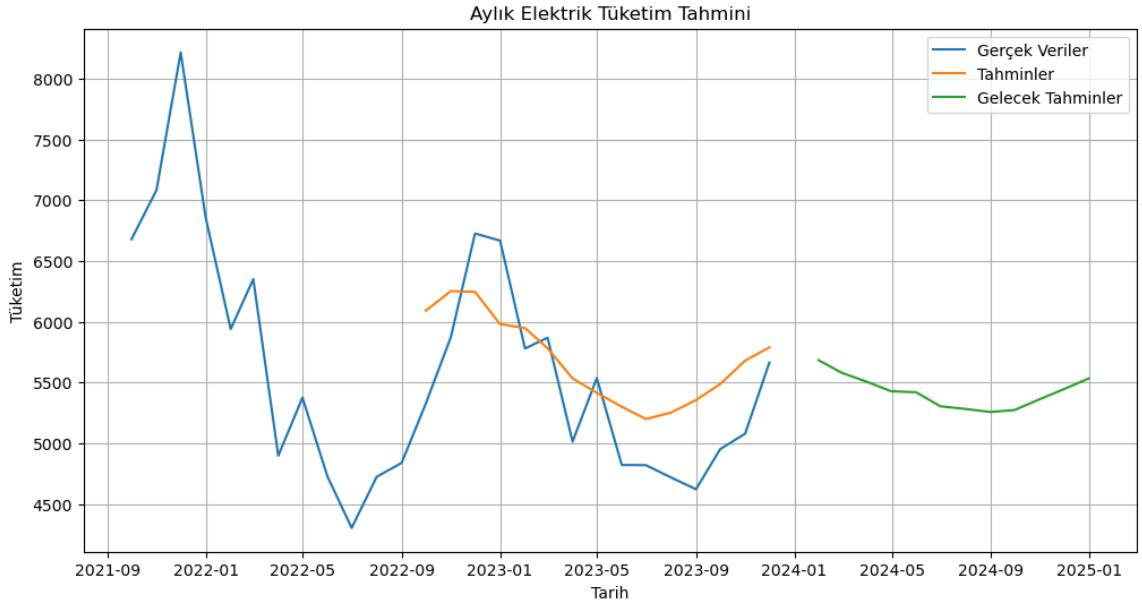

Şekil 2. Bina-1'in LSTM yöntemine göre aylık elektrik tüketim tahmini.

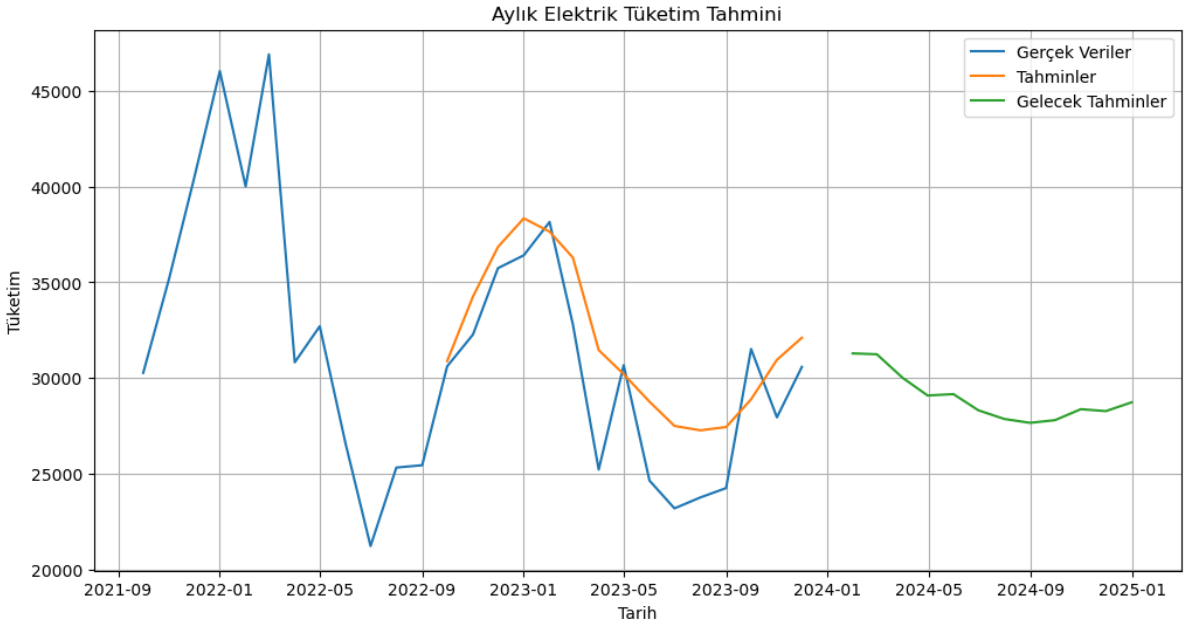

Şekil 3. Bina-2'nin LSTM yöntemine göre aylık elektrik tüketim tahmini.

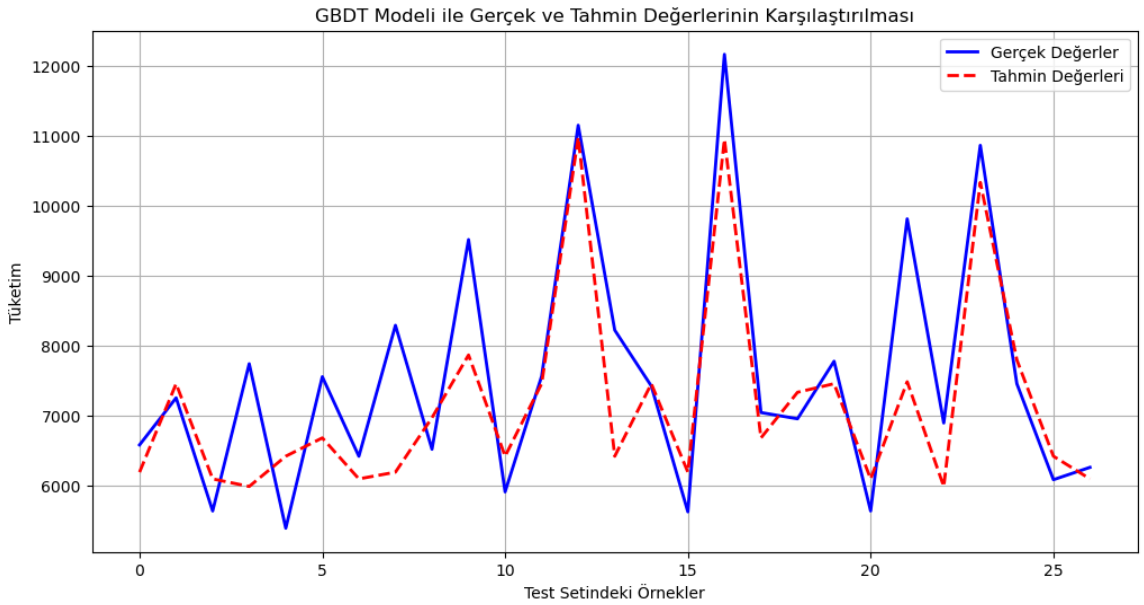

Şekil 4. Bina-3'ün GBDT yöntemi ile test setindeki elektrik tüketim tahmini sonuçları.

Şekil 5, Şekil 6 ve Şekil 7, sırasıyla Bina-1, Bina-2 ve Bina-3 için test setindeki gerçek değerler ile tahmin değerlerin RF, KNN, GBDT ve XGboost yöntemlerine göre karşılaştırılmasını göstermektedir. Bu şekillere bakıldığında genel olarak, söz konusu yöntemlerin tahmin değerleri birbirlerine oldukça yakındır. Bunun dışında gerçek değerler ile tahmin değerleri arasında, bazı noktalar hariç diğer noktalarda önemli bir fark olmadığı söylenebilir.

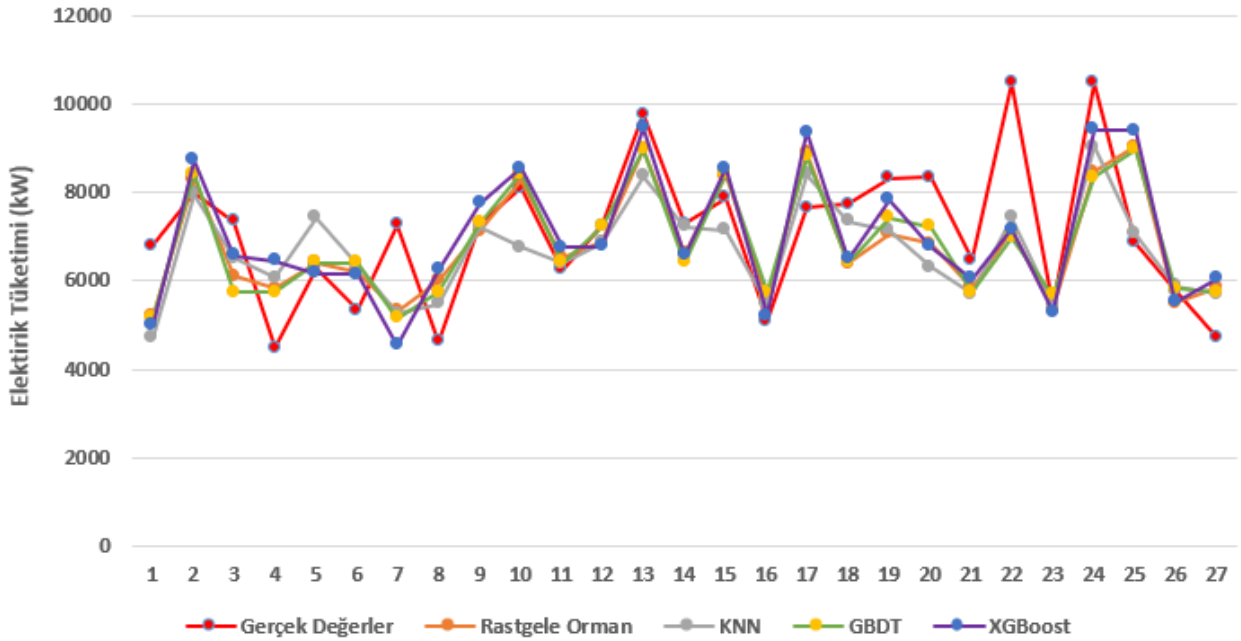

Şekil 5. Bina-1 için test setindeki gerçek değerler ile tahmin değerlerinin yöntemlere göre karşılaştırılması.

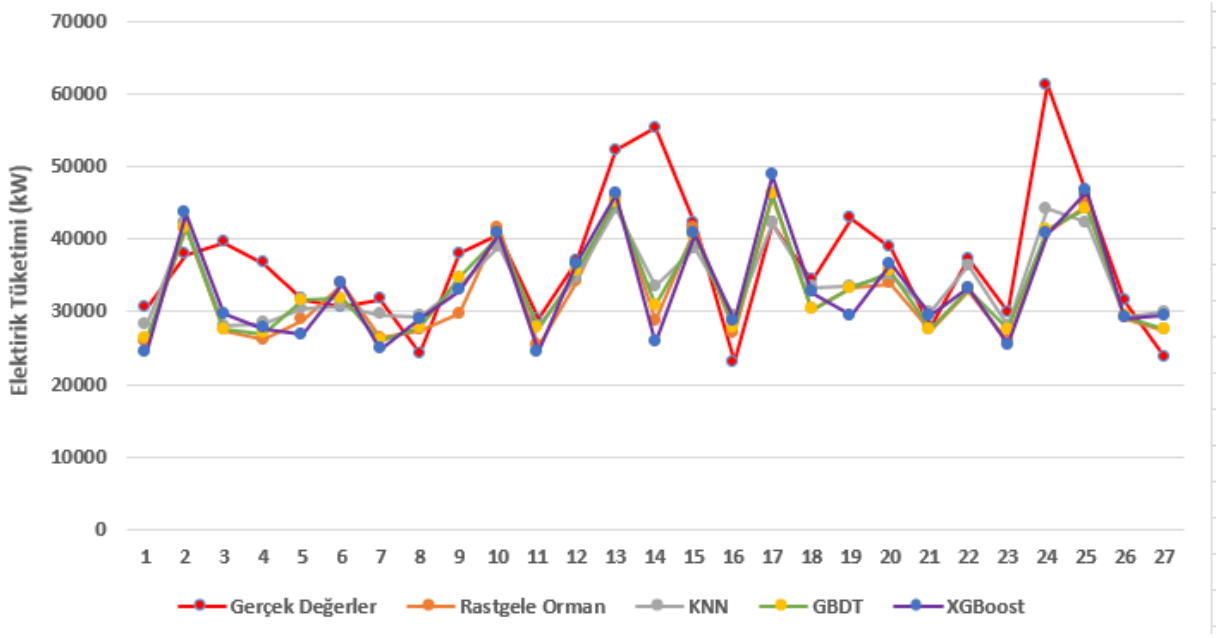

Şekil 6. Bina-2 için test setindeki gerçek değerler ile tahmin değerlerinin yöntemlere göre karşılaştırılması.

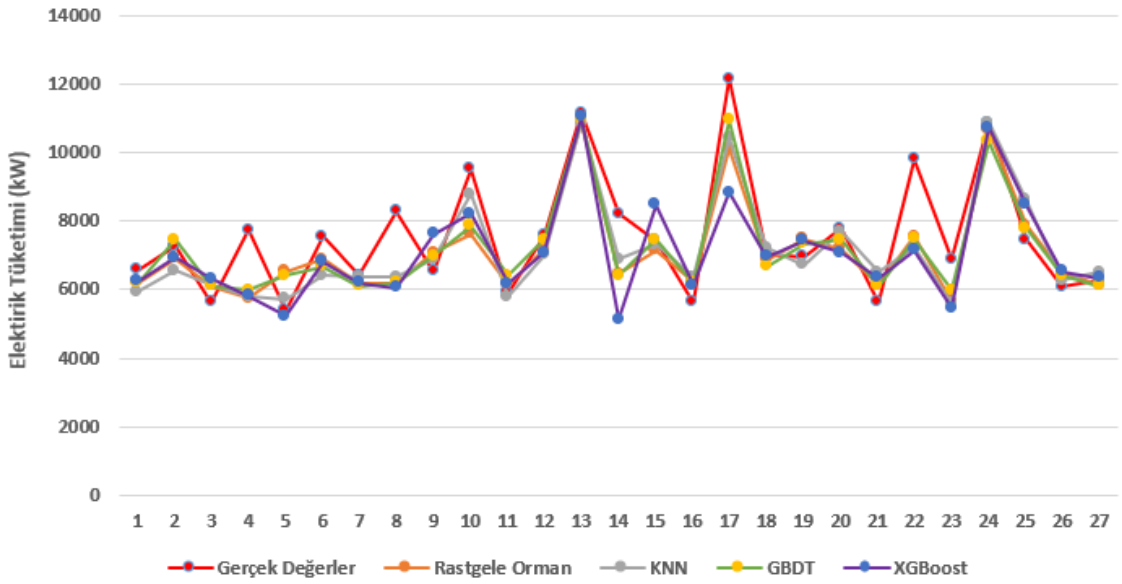

Şekil 7. Bina-3 için test setindeki gerçek değerler ile tahmin değerlerinin yöntemlere göre karşılaştırılması.

Şekil 8, Şekil 9 ve Şekil 10, sırasıyla Bina-1, Bina-2 ve Bina-3 için tüm yöntemlerin performans metriklerine göre karşılaştırılmasını göstermektedir. Şekil 8'e göre, Bina-1 için en iyi yöntem olan LSTM modeli ile diğer yöntemlere göre oldukça düşük performans değerleri elde edildiği söylenebilir. Şekil 9'a göre, Bina-2 için yine en iyi performans değerleri LSTM modeli ile elde edilmiştir. Bu modele en yakın değerler, GBDT yöntemi tarafından üretilmiştir. Şekil 10'a bakıldığında ise, Bina-3 için kullanılan tahmin modellerine ait performans metriklerinden özellikle MAPE değerinin tüm yöntemlerde birbirine çok yakın olduğu görünmektedir. Fakat yine en iyi MAPE değeri (%9,48), GBDT yöntemi ile elde edilmiştir. Bu değere en yakın MAPE değeri ise %9,64 ile KNN yöntemi olmuştur. Bu sonuçlara göre, Bina-3'e ait verilerin Bina-1 ve Bina-2'den daha tutarlı olduğunu söylenebilir.

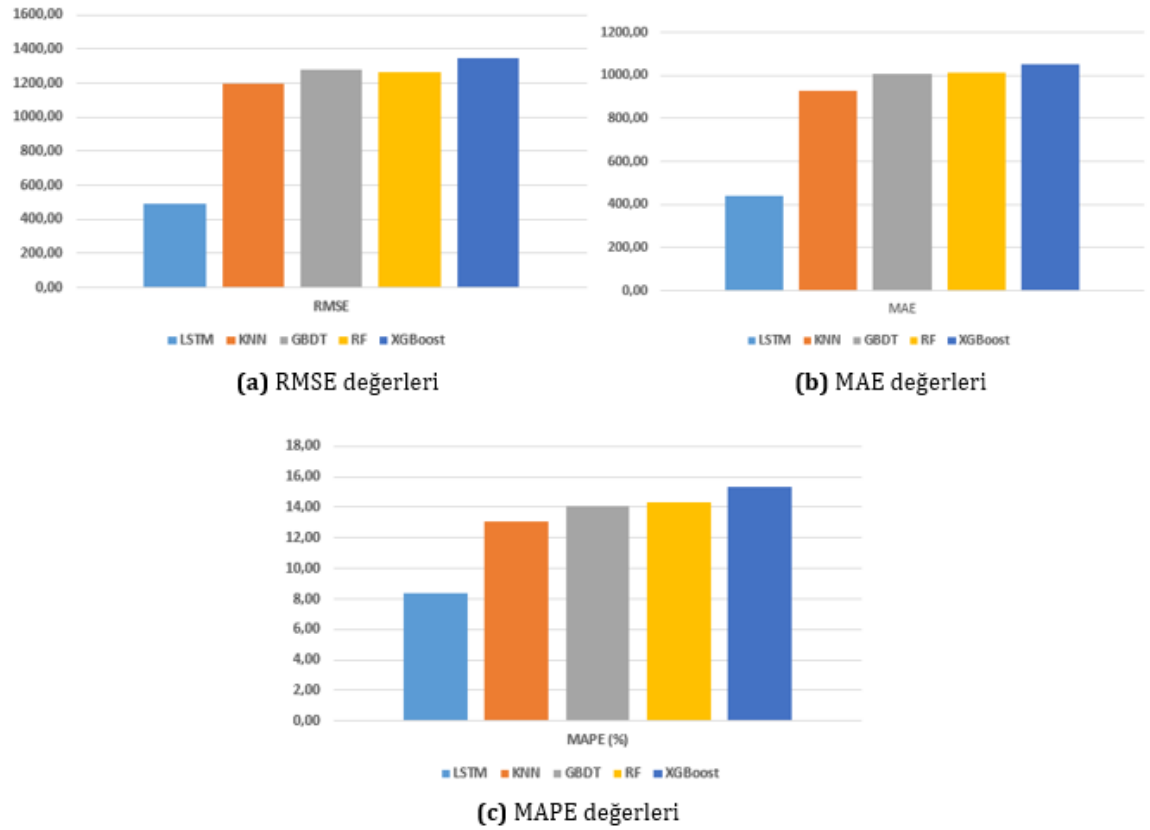

Şekil 8. Bina-1 için yöntemlerin performans metriklerine göre karşılaştırılması.

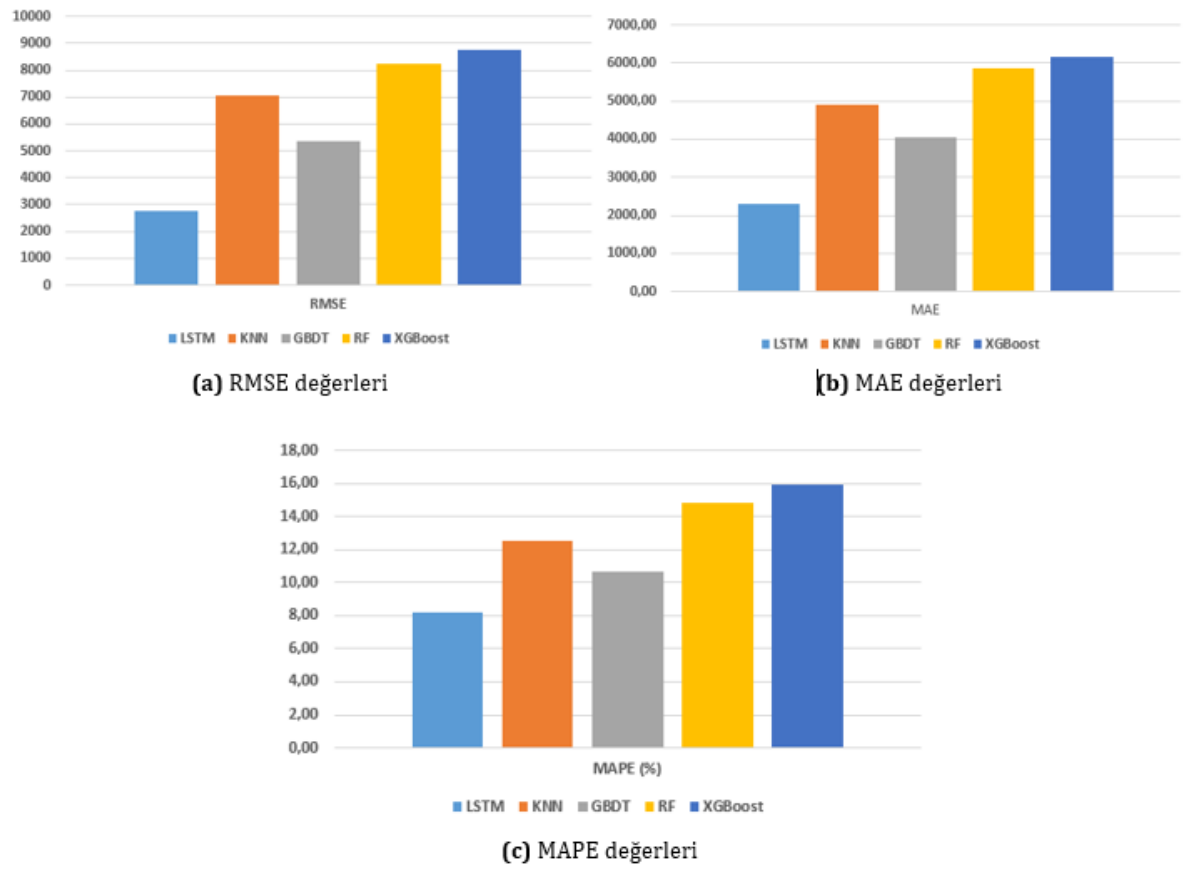

Şekil 9. Bina-2 için yöntemlerin performans metriklerine göre karşılaştırılması.

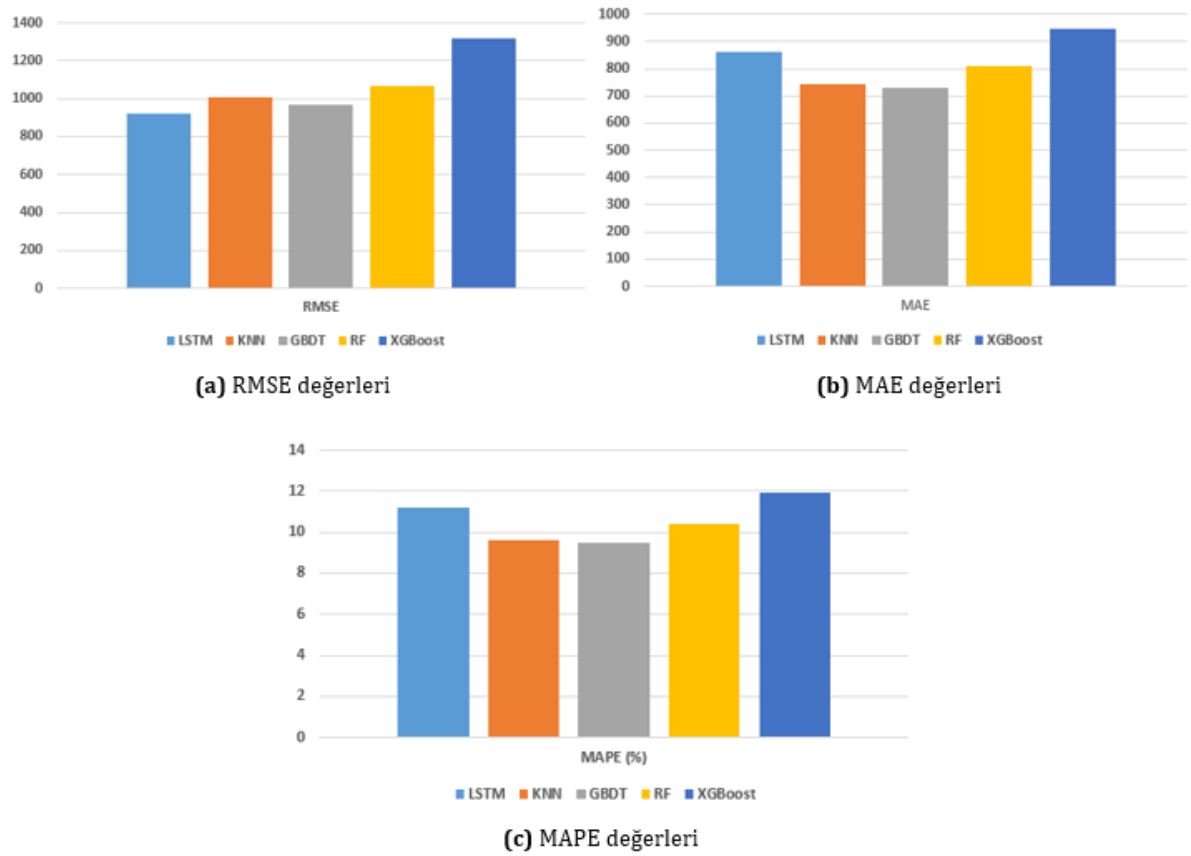

Şekil 10. Bina-3 için yöntemlerin performans metriklerine göre karşılaştırılması.

Bu çalışmada, kullanılan makine öğrenmesi yöntemleri (LSTM, KNN, GBDT, RF, XGBoost), kamu binalarının elektrik tüketim tahmininde farklı performanslar göstermiştir. Elde edilen RMSE, MAE ve MAPE değerleri üzerinden yapılan karşılaştırmalar sonucunda, özellikle LSTM ve GBDT modellerinin daha başarılı tahminler sunduğu görülmüştür. Benzer şekilde, Wang vd. (2020) tarafından yapılan bir çalışmada, RF, GBDT, SVR, KNN ve XGBoost yöntemleri bina enerji tüketiminin tahmini için kullanılmış; MAPE değerleri sırasıyla %9,71, %8,72, %11,20, %8,47 ve %9,30 olarak rapor edilmiştir. Bu bulgular, çalışmamızda GBDT ve KNN'nin başarılı sonuçlar üretmesiyle örtüşmektedir. Ayrıca, Liu vd. (2020) kamu binalarına yönelik gerçekleştirdikleri çalışmada SVM modelini kullanarak aylık tüketim verileriyle yaklaşık %97 R^2 değeri elde etmişlerdir. Bu durum, kamu binalarında makine öğrenmesi tabanlı yöntemlerin yüksek doğrulukla tahmin yapabildiğini göstermektedir. Dash vd. (2021), ev içi enerji tahmini için RNN-GBRT yöntemini önermiş ve yüksek tahmin başarısı rapor etmiştir. Bu çalışma, melez modellerin enerji tüketim tahmininde etkili olduğunu ortaya koymuştur. Bu bağlamda, çalışmamızda LSTM gibi zaman serisi modellerinin güçlü performans sergilemesi literatürdeki eğilimlerle paralellik göstermektedir. Öte yandan, Soyler ve Izgi (2022), İstanbul'daki hastaneler için gerçekleştirdikleri enerji tahmin çalışmasında, lineer regresyon modeli ile yaklaşık %9,87 MAPE değeri elde etmişlerdir. Bu sonuç, daha karmaşık modellerin doğruluğunu test etmek için referans bir temel sağlamaktadır.

Tüm bu çalışmalara bakıldığında, çalışmamızda kullanılan yöntemlerin bu değerlere benzer şekilde MAPE değerleri sunması, modellerin doğruluk seviyesini ortaya koymaktadır. Yapılan karşılaştırmalar, kullanılan yöntemlerin doğruluğunu desteklemekte ve literatürdeki önceki çalışmalarla genel bir uyum içerisinde olduğunu göstermektedir. Bununla birlikte, farklı veri kümeleri, frekans düzeyleri (günlük, haftalık, aylık) ve bina türleri gibi değişkenler, tahmin performansındaki farklılıkların temel nedenleri arasında değerlendirilebilir.

4. Sonuç

Bu çalışma, Erzurum ilindeki üç farklı kaymakamlık binasının elektrik tüketim tahmininde farklı makine öğrenmesi yöntemlerinin performansını karşılaştırmıştır. Elde edilen sonuçlar, zaman serisi verilerinde güçlü bir performans sergileyen LSTM modelinin, özellikle Bina-1 ve Bina-2 için en düşük hata değerlerini sağlayarak diğer yöntemlere kıyasla daha üstün olduğunu göstermiştir. Bina-3'te ise göreceli hata oranı (MAPE) açısından GBDT ve KNN modelleri LSTM'ye göre daha başarılı sonuçlar elde etmiş, bu da farklı binaların tüketim dinamiklerinin model seçiminde önemli bir rol oynadığını ortaya koymuştur.

LSTM'nin genel üstün performansı, elektrik tüketimi gibi zaman serisi yapısına sahip verilerde daha yüksek doğrulukla çalışabildiğini ve enerji yönetimi süreçlerinde etkili bir araç olduğunu kanıtlamaktadır. Bununla birlikte, GBDT ve KNN gibi yöntemlerin belirli durumlarda daha düşük hata oranları sunabilmesi, farklı veri yapıları ve özelliklerin dikkate alınmasının model seçimini nasıl etkilediğini vurgulamaktadır.

Sonuçlar, model performanslarının, tüketim verilerindeki mevsimsellik dışında, hava durumu, ekonomik koşullar veya olağanüstü durumlar gibi dış etkenlere de duyarlı olduğunu göstermektedir. Bu durum, tahmin doğruluğunu artırmak için veri setlerinin daha geniş bir değişken yelpazesiyle zenginleştirilmesi gerektiğini işaret etmektedir. Özellikle ani dalgalanmalar veya uç değerler, tüm modeller için önemli bir zorluk teşkil etmiş ve gelecekte bu zorlukları aşmak için hibrit modeller veya veri ön işleme tekniklerinin kullanımı önerilmiştir.

Bu çalışma, yalnızca incelenen kaymakamlık binaları için değil, diğer kamu binalarındaki enerji yönetimi uygulamalarına da rehberlik edebilecek bir perspektif sunmaktadır. Tahmin modellerinin seçimi ve uygulanması, enerji verimliliğini artırma, maliyetleri düşürme ve sürdürülebilirlik hedeflerine ulaşma açısından kritik bir öneme sahiptir. Gelecek çalışmalar, daha geniş veri setleri ve değişkenlerle birlikte enerji tüketimini etkileyen faktörlerin kapsamlı analizine odaklanabilir. Böylelikle, kamu binalarındaki enerji yönetimi politikalarının daha sağlam temellere oturtulması sağlanabilir.

Katkı Oranı Beyanı

Yazarların katkı yüzdeleri aşağıda verilmiştir. Yazarlar makaleyi incelemiş ve onaylamıştır.

	V.A.	B.T.Ş.
K	50	50
T	40	60
Y	30	70
VTI	90	10
VAY	50	50
KT	70	30
YZ	50	50
KI	50	50
GR	30	70
PY	50	50
FA	50	50

K= kavram, T= tasarım, Y= yönetim, VTI= veri toplama ve/veya işleme, VAY= veri analizi ve/veya yorumlama, KT= kaynak tarama, YZ= Yazım, KI= kritik inceleme, GR= gönderim ve revizyon, PY= proje yönetimi, FA= fon alımı.

Çatışma Beyanı

Yazarlar bu çalışmada hiçbir çıkar ilişkisi olmadığını beyan etmektedirler.

Etik Onay Beyanı

Bu araştırmada hayvanlar ve insanlar üzerinde herhangi bir çalışma yapılmadığı için etik kurul onayı alınmamıştır.

Destek ve Teşekkür Beyanı

Bu çalışma, Atatürk Üniversitesi Bilimsel Araştırma Projeleri Koordinasyon Birimi tarafından 14678 numaralı yüksek lisans projesi ile desteklenmiştir.

Kaynaklar

Akkurt T, Sarıçiçek İ. 2024. Derin öğrenme teknikleri kullanılarak üretim sistemlerinde KPI tabanlı performans tahminleme. Gazi Univ Müh Mim Fak Derg, 39(3): 1499-1508.

Aydın R. 2023. Satış adedini etkileyen değişkenlerin keşfi ve duyarlılık analizi uygulaması: E-ticaret örneği. Yüksek Lisans Tezi, İstanbul Teknik Univ, Lisansüstü Eğitim Enstitüsü, İstanbul, Türkiye, pp: 45-46.

Balaban ME, Kartal E. 2018. Veri madenciliği ve makine öğrenmesi temel algoritmaları ve r dili ile uygulamaları. Çağlayan Kitabevi, İstanbul, Türkiye, 2. Baskı, pp: 56-59.

Balta M. 2024. Rulman titreşim verilerinden derin öğrenme tabanlı hata tespiti. Yüksek Lisans Tezi, Maltepe Univ, Lisansüstü Eğitim Enstitüsü, İstanbul, Türkiye, pp: 45-85.

Başoğlu B, Bulut M. 2017. Kısa dönem elektrik talep tahminleri için yapay sinir ağları ve uzman sistemler tabanlı hibrit sistem geliştirilmesi. Gazi Univ Müh Mim Fak Derg, 32(2): 575-583.

Botman L, Lago J, Becker T, Vanthournout K, De Moor B. 2025. A global probabilistic approach for short-term forecasting of individual households electricity consumption. Appl Energy, 382: 125168.

Breiman L. 2001. Random forests, machine learning. Kluwer Academic Publ, Dordrecht, Netherlves, 45(1): 5-32.

Cao Z, Yuan P, Ma YB. 2014. Energy demand forecasting based on economy-related factors in China. Energy Sources Part B, 9(2): 214-219.

Chen T, Guestrin C. 2016. XGBoost: A scalable tree boosting system. In Proc 22nd ACM SIGKDD Int Conf Knowl Discov Data Min, 13-17 Aug 2016, San Francisco, CA, USA, pp: 785–794.

Cui X, Lee M, Koo C, Hong T. 2024. Energy consumption prediction and household feature analysis for different residential building types using machine learning and SHAP: Toward energy-efficient buildings. Energy Build, 309: 113997.

Çayır A, Yenidoğan I, Dağ H. 2018. Konutların günlük elektrik güç tüketimi tahmini için uygun model seçimi. Fırat Univ Müh Bil Derg, 30(3): 15-21.

Çuhadar M. 2006. Turizm sektöründe talep tahmini için yapay sinir ağları kullanımı ve diğer yöntemlerle karşılaştırmalı analizi (Antalya ilinin dış turizm talebinde uygulama). Doktora Tezi, Süleyman Demirel Univ, Sosyal Bilimler Enstitüsü, Isparta, Türkiye, pp: 45-87.

Dash SK, Roccotelli M, Khansama RR, Fanti MP, Mangini AM. 2021. Long term household electricity demand forecasting based on RNN-GBRT model and a novel energy theft detection method. Appl Sci, 11(18): 8612.

Demolli H, Dokuz AS, Ecemis A, Gokcek M. 2019. Wind power forecasting based on daily wind speed data using machine learning algorithms. Energy Convers Manag, 198: 111823.

Dev VA, Eden MR. 2019. Formation lithology classification

using scalable gradient boosted decision trees. Comput Chem Eng, 128: 392-404.

Dong X, Luo Y, Yuan S, Tian Z, Zhang L, Wu X, Liu B. 2025. Building electricity load forecasting based on spatiotemporal correlation and electricity consumption behavior information. Appl Energy, 377: 124580.

Eşidir KA. 2025. Makine öğrenimi modelleri ile yetişkin eğitimi analizi: modellerin karşılaştırmalı performansı. Elektronik Sosyal Bilimler Dergisi, 24(2): 946-964.

Filippov SP, Malakhov VA, Veselov FV. 2021. Long-term energy demand forecasting based on a systems analysis. Thermal Eng, 68: 881-894.

Goodfellow I, Bengio Y, Courville A. 2016. Deep Learning. MIT Press, Cambridge, UK, pp: 800.

Gök M. 2017. Makine öğrenmesi yöntemleri ile akademik başarının tahmin edilmesi. Gazi Univ J Sci Part C: Des Technol, 5(3): 139-148.

Grveón TG, Schwenzer J, Steens T, Breuing J. 2024. Electricity demand forecasting with hybrid classical statistical and machine learning algorithms: Case study of Ukraine. Appl Energy, 355: 122249.

Guo G, Wang H, Bell D, Bi Y, Greer K. 2003. KNN model-based approach in classification. In OTM Confederated Int Conf, Catania, Sicily, Italy, 3-7 Nov 2003, pp: 986-996.

Gültepe Y. 2019. Makine öğrenmesi algoritmaları ile hava kirliliği tahmini üzerine karşılaştırmalı bir değerlendirme. Avrupa Bilim Teknol Derg, 16: 8-15.

Gür YE, Eşidir KA, Şimşek Aİ. 2024. Sağlık istatistiklerinin veri madenciliği teknikleri ile analizi: makine öğrenmesi algoritmaları kullanılarak genel sağlık durumunun sınıflandırılması. Afyon Kocatepe Univ Fen Müh Bil Derg, 24(06): 1364-1381.

Hastie T, Tibshirani R, Friedman J. 2009. The elements of statistical learning: data mining, inference, and prediction. Springer Sci & Bus Media, New York, 2nd ed, pp: 758.

He Y, Lin B. 2018. Forecasting China's total energy demand and its structure using ADL-MIDAS model. Energy, 151: 420-429.

Hochreiter S, Schmidhuber J. 1996. LSTM can solve hard long time lag problems. In Advances in Neural Inf Process Syst, 2-5 Dec 1996, Denver, CO, USA, 9: 473-479.

Hochreiter S, Schmidhuber J. 1997. Long short-term memory. Neural Comput, 9(8): 1735-1780.

Hsu PC, Gao L, Hwang Y. 2025. Comparative study of LSTM and ANN models for power consumption prediction of variable refrigerant flow (VRF) systems in buildings. Int J Refrig, 169: 55-68.

Hwang J, Suh D, Otto MO. 2020. Forecasting electricity consumption in commercial buildings using a machine learning approach. Energies, 13(22): 5885.

Iftikhar H, Turpo-Chaparro JE, Canas Rodrigues P, López-Gonzales JL. 2023. Day-ahead electricity demand forecasting using a novel decomposition combination method. Energies, 16(18): 6675.

Kazemzadeh MR, Amjadian A, Amraee T. 2020. A hybrid data mining driven algorithm for long term electric peak load and energy demand forecasting. Energy, 204: 117948.

Khan M, Ding Q, Perrizo W. 2002. K-nearest neighbor classification on spatial data streams using P-trees. Adv Knowl Discov Data Min, 2336: 517-528.

Kim YS, Kim MK, Fu N, Liu J, Wang J, Srebric J. 2025. Investigating the impact of data normalization methods on predicting electricity consumption in a building using different artificial neural network models. Sustain Cities Soc, 118: 105570.

Kulkarni V, Sinha PK. 2012. Pruning of random forest classifiers: a survey and future directions. In 2012 Int Conf Data Sci Eng (ICDSE), IEEE, 18-20 Jul 2012, Cochin, India, pp: 64-68.

Lei L, Shao S, Liang L. 2024. An evolutionary deep learning model based on EWKM, random forest algorithm, SSA and BiLSTM for building energy consumption prediction. Energy, 288: 129795.

Li X, Jiang M, Cai D, Song W, Sun Y. 2024. A hybrid forecasting model for electricity demand in sustainable power systems based on support vector machine. Energies, 17(17): 4377.

Li X, Wang Z, Yang C, Bozkurt A. 2024. An advanced framework for net electricity consumption prediction: Incorporating novel machine learning models and optimization algorithms. Energy, 296: 131259.

Li Y, Jones B. 2019. The use of extreme value theory for forecasting long-term substation maximum electricity demand. IEEE Trans Power Syst, 35(1): 128-139.

Liu Y, Chen H, Zhang L, Wu X, Wang XJ. 2020. Energy consumption prediction and diagnosis of public buildings based on support vector machine learning: A case study in China. J Clean Prod, 272: 122542.

Man H, Huang H, Qin Z, Li Z. 2023. Analysis of a sarima-xgboost model for hand, foot, and mouth disease in xinjiang, china. Epidemiol Infect, 151: 200.

Mayr A, Binder H, Gefeller O, Schmid M. 2014. The evolution of boosting algorithms. Methods Inf Med, 53(6): 419-427.

Mercan V. 2023. Metinsel veriler için çok sınıflı problemlere hata düzelten kod tabanlı kolektif öğrenme yönteminin uygulanması. Yüksek Lisans Tezi, İstanbul Sabahattin Zaim Univ, Lisansüstü Eğitim Enstitüsü, İstanbul, Türkiye, pp: 54.

Nacar EN, Erdebilli B. 2021. Makine öğrenmesi algoritmaları ile satış tahmini. Endüstri Müh, 32(2): 307-320.

Nebati EE, Taş M, Ertaş G. 2021. Türkiye'de elektrik tüketiminde talep tahmini: zaman serisi ve regresyon analizi ile karşılaştırma. Avrupa Bilim Teknol Derg, 31: 348-357.

Nikseresht A, Amindavar H. 2024. Energy demand forecasting using adaptive ARFIMA based on a novel dynamic structural break detection framework. Appl Energy, 353: 122069.

Olu-Ajayi R, Alaka H, Sulaimon I, Sunmola F, Ajayi S. 2022. Building energy consumption prediction for residential buildings using deep learning and other machine learning techniques. J Build Eng, 45: 103406.

Özkan Y. 2008. Veri madenciliği yöntemleri. Papatya Yayıncılık, İstanbul, Türkiye, pp: 45-65.

Peker M, Özkaraca O, Kesimal B. 2017. Enerji tasarruflu bina tasarımı için ısıtma ve soğutma yüklerini regresyon tabanlı makine öğrenmesi algoritmaları ile modelleme. Bilişim Teknol Derg, 10(4): 443-449.

Peterson LE. 2009. K-nearest neighbor. Scholarpedia, 4(2): 1883.

Silahtaroğlu G. 2008. Kavram ve algoritmalarıyla temel veri madenciliği. Papatya Yayıncılık, İstanbul, Türkiye, pp: 65-96.

Sinap V. 2024. Perakende Sektöründe Makine Öğrenmesi Algoritmalarının Karşılaştırmalı Performans Analizi: Black Friday Satış Tahminlemesi. Selçuk Univ Sos Bil Meslek Yüksekok Derg, 27(1): 65-90.

Sofyalıoğlu Ç, Öztürk Ş. 2013. Bir çimento firması için dönemsel satış miktarlarının tahmininde bulanık zaman serisi modellerinin karşılaştırılması. Süleyman Demirel Univ İktisadi İdari Bil Fak Derg, 18(3): 161-186.

Soyler I, Izgi E. 2022. Electricity demand forecasting of hospital buildings in Istanbul. Sustainability, 14(13): 8187.

Taşcı E, Onan A. 2016. K-en yakın komşu algoritması parametrelerinin sınıflandırma performansı üzerine etkisinin incelenmesi. Akademik Bilişim, 1(1): 4-18.

Uddin MN, Lee M, Cui X, Zhang X. 2025. Predicting occupant energy consumption in different indoor layout configurations using a hybrid agent-based modeling and machine learning approach. Energy Build, 328: 115102.

Voronin S, Partanen J. 2014. Forecasting electricity price and demand using a hybrid approach based on wavelet transform, ARIMA and neural networks. Int J Energy Res, 38(5): 626-637.

Wang FK, Mamo T. 2020. Gradient boosted Regresyon model for the degradation analysis of prismatic cells. Comput Ind Eng, 144: 106494.

Wang R, Lu S, Feng W. 2020. A novel improved model for building energy consumption prediction based on model integration. Appl Energy, 262: 114561.

Wang R, Lu S, Li Q. 2019. Multi-criteria comprehensive study on predictive algorithm of hourly heating energy consumption for residential buildings. Sustain Cities Soc, 49: 101623.

Wang W, Shimakawa H, Jie B, Sato M, Kumada A. 2025. BE-LSTM: An LSTM-based framework for feature selection and building electricity consumption prediction on small datasets. J Build Eng, 102: 111910.

Witt SF, Witt CA. 1991. Tourism forecasting: Error magnitude, direction of change error, and trend change error. J Travel Res, 30(2): 26-33.

Yazıcı K. 2021. Makine öğrenmesi yöntemleri kullanılarak kısa dönem rüzgâr gücü tahmini. Yüksek Lisans Tezi, Sakarya Univ, Fen Bil Enstitüsü, Sakarya, Türkiye, pp: 72.

Yelgeç MA, Bingöl O. 2022. Ayrık dalgacık dönüşümü ve Xgboost ile rüzgâr gücü tahmini. Uluslararası Teknol Bilim Derg, 14(2): 58-65.

Zhou K, Chu Y, Hu R. 2023. Energy supply-demand interaction model integrating uncertainty forecasting and peer-to-peer energy trading. Energy, 285: 129436.

Black Sea Journal of Engineering and Science
doi: 10.34248/bsengineering.1695801

Open Access Journal
e-ISSN: 2619 – 8991

Research Article
Volume 8 - Issue 5: 1429-1439 / September 2025

ANALYSING THE CHANGE OF ABOVEGROUND BIOMASS DENSITY USING EARTH OBSERVATION AND MACHINE LEARNING TECHNOLOGY: ALANYA CASE

Ercüment AKSOY[1]*

[1]*Akdeniz University, Technical Sciences Vocational School, Technical Sciences Vocational School, Department of Geographical Informations Systems, 07070, Antalya, Türkiye*

Abstract: Aboveground biomass (AGB) is a key parameter in assessing forest carbon stocks, ecosystem productivity, and the global carbon cycle. This study aims to model the annual AGB change between 2019 and 2024 in Alanya, Türkiye, using remote sensing (RS) technologies and open-source datasets. Sentinel-2 surface reflectance data, slope data derived from the Copernicus GLO-30 Digital Elevation Model (DEM), and GEDI L4A biomass data were utilized. As GEDI point data cannot be directly used for mapping, it was employed as a reference for model training. Spectral bands and vegetation indices from Sentinel-2 imagery were modeled using the Random Forest algorithm. Model performance was evaluated using the coefficient of determination (R^2) and root mean square error (RMSE). The highest total AGB was observed during the 2022–2023 period, while the lowest occurred between 2019–2020. The findings indicate that biomass dynamics in the region are influenced not only by climatic conditions but also significantly by anthropogenic activities. The study presents a remote sensing-based approach to support carbon-neutral strategies through accurate biomass monitoring.

Keywords: Geographic information systems, Remote sensing, Earth observation, Biomass, Above ground biomass (AGB)

***Corresponding author:** Akdeniz University, Technical Sciences Vocational School, Technical Sciences Vocational School, Department of Geographical Informations Systems, 07070, Antalya, Türkiye
E mail: ercumentaksoy@akdeniz.edu.tr (E. AKSOY)
Ercüment AKSOY https://orcid.org/0000-0001-7313-0891

Received: May 09, 2025
Accepted: July 28, 2025
Published: September 15, 2025

Cite as: Aksoy E. 2024. Analysing the change of aboveground biomass density using earth observation and machine learning technology: Alanya case. BSJ Eng Sci, 8(5): 1429-1439.

1. Introduction

Although there are many definitions of biomass, it generally refers to the mass of plant organisms that grow and develop by photosynthesis per unit area. Biomass, which is formed as a result of plants storing solar energy by converting it into chemical energy through photosynthesis, is also considered as organic carbon for this reason (Kim et al., 2004).

Forest biomass is an important raw material for building materials, pulp and paper production and energy production as fuel. However, forests are also recognised as an important regulator of the world's climate because they capture and store large amounts of carbon in their woody biomass (De et al., 2025).

Forest ecosystems provide many goods and services to society when planned and managed sustainably. Forests have many economic functions as well as important ecological and environmental functions such as climate regulation, water conservation, soil conservation and biodiversity conservation. Recently, high consumption of fossil fuels, deforestation and changes in land use and land cover have caused serious changes in the atmosphere resulting in climate change and global warming all over the world. Forest ecosystems store CO^2 in their biomass and in the soil for a longer period of time in the context of mitigating global climate change (Evrendilek et al., 2004). Forest ecosystems are an important component of the global carbon budget in terrestrial ecosystems and there is a need to accurately determine the amount of carbon they store (Sharma et al., 2008). Biomass estimation is crucial for determining carbon budgets (Güverçin, 2022). For this purpose, many methods are used to determine the biomass in a spesific area (Ravindranath and Ostwald, 2007).

Originating from the United Nations Framework Convention on Climate Change (UNFCCC), the Kyoto Protocol sets legally binding targets for industrialized countries to reduce their greenhouse gas emissions or remove them from the atmosphere. The Protocol was adopted in 1997 and finally entered into force in February 2005. The protocol aimed to reduce overall greenhouse gas emissions by at least 5 per cent below current 1990 levels during the commitment period from 2008 to 2012. To achieve this, industrialized member states have set different binding targets ranging from -8% to +10% of 1990 emissions. The EU has set a 'bubble'

target of -8 per cent by 2010 and -20 per cent by 2020, redistributed based on the EU agreement (UNFCCC). The UK's reduction target is set at 20 per cent below 1990 levels by 2010, with a further legally binding reduction target of 26-32 per cent below 1990 levels for 2020. In the face of growing concerns that national CO^2 emission reduction targets cannot be met by emission reduction strategies alone, industrialised countries are keen to find alternative ways to reduce atmospheric CO^2 concentrations.

An important mechanism for removing CO^2 from the atmosphere is carbon sequestration in growing vegetation. The Clean Development Mechanism (CDM) initiative under the Kyoto Protocol, among other things, envisages forestry projects for carbon sequestration. This allows industrialized countries to offset atmospheric carbon emissions by financing such projects in developing countries.

However, the viability of carbon sequestration programmers relies on both a scientific understanding of how CO^2 is captured and stored as vegetative biomass and the development of operational techniques to measure standing biomass globally.

The largest impact on the global carbon cycle comes from human activities through the burning of biomass and fossil fuels and extraction of vegetation, especially forests (Watson et al., 2000). It is estimated that about 75% of CO^2 emissions to the atmosphere are from combustion, with the remainder contributed by land use change through the removal of carbon sinks (Prentice et al., 2001). It is therefore regrettable that the CDM currently excludes tropical forest conservation projects. Ongoing discussions culminated at the UN Climate Change Conference in Bali (COP 13 December 2007) with a call for the future inclusion of Reduced Emissions from Deforestation in Developing Countries (REDD), now commonly referred to as Reduced Emissions from Deforestation and Degradation. Therefore, in addition to estimating global forest biomass, forest monitoring is needed by quantifying deforestation and other potential sources of atmospheric CO^2 emissions, such as fire damage from forest areas. Earth observation techniques are ideal for such mapping and monitoring activities as they offer the ability to repeat data capture frequently and cover large areas that may be difficult to reach for field measurements.

With the increasing importance of forestry-based carbon sequestration initiatives and global forest monitoring, there is a need for accurate information at regional and national scales on the spatial extent, condition, biomass and growth potential of forests and woodlands with canopy cover as low as 10 per cent. Earth observation (EO) techniques are more suitable for biomass estimation than traditional in situ methods. The latter involves laborious fieldwork, often based on destructive sampling (Gilreath et al., 1994). While regional biomass estimates based on in situ methods are unlikely to accurately depict the heterogeneity of the landscape, those based on EO data produce updatable biomass estimates that more accurately represent the spatial heterogeneity of the landscape. Depending on spatial and temporal resolution, EO can detect differences in the spatial distribution of biomass density, such as the occurrence of forest gaps and land cover changes and provides systematic observations at scales ranging from local to global while improving monitoring of inaccessible areas (Aaslyng et al., 2003).

Accurate land cover mapping from EO data combined with known biomass estimates for each land cover class is a relatively simple use of EO for biomass estimation. RadarRI methods such as Synthetic Aperture Radar (SAR) interferometry (InSAR) used for canopy height retrieval in closed canopy forests can be used in combination with allometric equations to estimate AG biomass (Askne et al., 1997). In addition, SAR backscattering has been statistically correlated with forest biomass up to a certain level depending on the radar wavelength (Le et al., 1992).

The most accurate and reliable methods for estimating above-ground biomass are terrestrial measurements. The above-ground biomass is accurately estimated using allometric equations obtained with the help of terrestrial data. This method is time consuming, labour intensive and difficult to implement. It is especially difficult to do in large areas (Lu et al., 2005). Biomass estimation with GIS is not a widely used method because it requires a large, accurate, reliable database and quality relationships between these data. Remote sensing method is preferred for estimating above-ground biomass especially in hard-to-reach areas due to the ease of data collection, rapid data evaluation, high correlations between band brightness values, vegetation indices and texture values (Nelson et al., 1988; Sader et al., 1989; Franklin and Hiernaux, 1991; Steininger, 2000; Foody et al., 2001; Santos et al., 2003; Zheng et al., 2004).

The above-ground forest biomass potential (carbon stock) is classically calculated on the basis of values obtained from field measurements. An alternative method to this labour-intensive and time-consuming method should be estimated with the support of Geographic Information Systems (GIS) and Remote Sensing (RS) techniques, which provide a new and efficient approach. RS is based on the qualitative and quantitative evaluation of electromagnetic radiation emitted or reflected from an object without a mechanical connection and the remote detection and measurement of the properties of the object (Khan et al., 2024). Thanks to RS techniques, the earth and earth objects can be imaged by means of measuring instruments placed on platforms in the atmosphere or space at a certain distance from the earth (Al, 2022).

Developments in the field of RS have opened a new and efficient way to estimate forest biomass. Pixel-based and object-based (segmentation) image classification techniques, which are performed to interpret the images produced by RS techniques and to obtain information

from these images, provide faster and more practical results than approaches such as field measurement. The increase in image resolution in RS gives more importance to segmentation methods together with pixel-based classification techniques.

Recently, studies have been carried out to estimate above-ground biomass in large forested areas using remote sensing data (Houghton et al., 2009; Gallaun et al., 2010). In particular, Landsat satellite images, the first natural resource satellite, are used both in small areas and in large forested areas. However, there are many studies in the literature on estimating aboveground biomass using different satellite images (Muukkonen and Heiskanen, 2005; Eckert et al., 2012). Moreover, studies have also been carried out on the estimation of AGB using radar and lidar data, and it is stated that the model estimation results obtained from these studies give better results than the model estimation results obtained from optical satellite images (Lu et al., 2005; Houghton et al., 2009).

Lidar and radar satellite data have been used to estimate AGB in different forest ecosystems (Zhao et al., 2016; Keleş et al., 2024). It has been stated that especially long wavelength radar data can be used to estimate AGB in mixed forest ecosystems (Zimble et al., 2003).

A preliminary research study was carried out using the bibliometric analysis technique based on quantitative data and numerical measurement indicators of previous studies on the subject of biomass and Earth Observation technology including remote sensing and GIS technology. After searching for "earth observation" and "biomass" on Web of Science, Martin Herold was detected as the most cited author with 592 citations, Ian Mccallum with 527 citations, and A. Uwe Schneider with 510 citations.

When countries are considered in terms of the criteria of publishing at least 1 work and receiving 1 citation, the countries with the most citations are the USA (7513 citations), the UK (6590 citations) and Germany (5017 citations). In terms of total connectivity, two of these three countries are in the top three. The other country in the top three in terms of connectivity and in third place is Canada. In terms of the number of works, the ranking is England (151 publications), America (126 publications) and China (122 publications). These results are shown in the Figure 1. Citation Links of Countries below

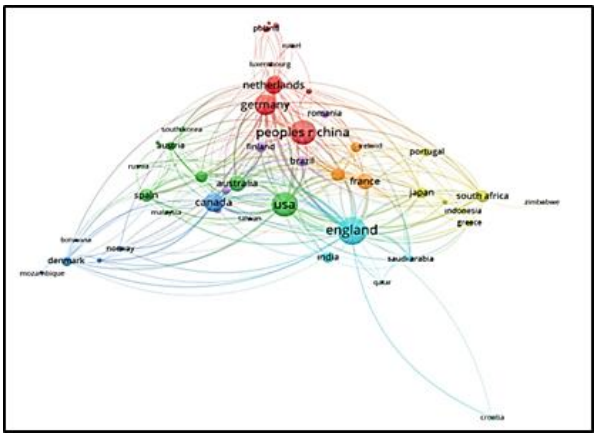

Figure 1. Citation links of countries.

Institutional structures make the most important contributions to biomass and Earth observation studies. In order to examine the work of institutions in the field and to identify institutions that are intensively active, the criteria of at least 1 work being published and 1 citation being received were examined. While the Chinese Academy of Sciences (45 works), Plymouth Marine Laboratory (33 works), and University of Leicester (28 works) were represented by works, the institutions addressing the most cited publications were the Chinese Academy of Sciences (1211 citations), the National Oceanic and Atmospheric Administration (1194 citations), and Plymouth Marine Laboratory (1081 citations). This institutional citation link relationship is shown in Figure 2. Citation Links of Institutions.

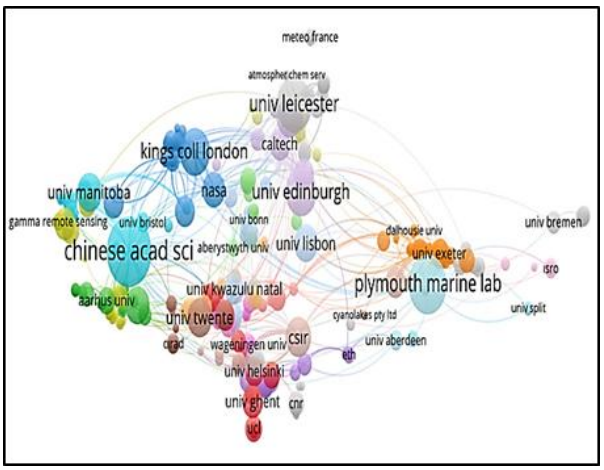

Figure 2. Citation links of institutions.

When we look at the most frequently used keywords in biomass and Earth observation publications, the most frequently used expressions are remote sensing (ground tracking) with 60 repetitions, lidar (sensor) with 35 repetitions, sentinel-2 (satellite) with 32 repetitions, modus (a type of radiometer developed by NASA) with 23 repetitions and phytoplankton (photo-plankton) with 20 repetitions. This keyword link information is shown in Figure 3. Most Frequently Used Keyword links below.

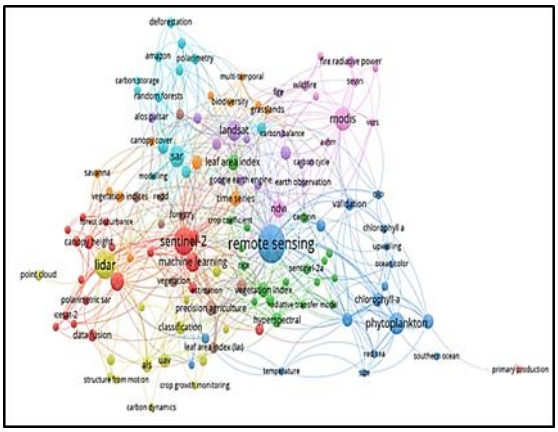

Figure 3. Most Frequently Used Keyword Links

Figure 4. Geolocation.

In biomass studies, total Aboveground Biomass (AGB) data are primarily derived from GEDI observations. Utilizing laser technology, GEDI maps vegetation in the vertical dimension, enabling three-dimensional modeling of biomass distribution, particularly in tropical and temperate forest ecosystems (Duncanson et al., 2022). The mission has been instrumental in tracking annual forest carbon changes at a spatial resolution of 1 km (Potapov et al., 2021). In the Amazon Basin, combining GEDI data with Sentinel-2 satellite imagery has achieved high biomass estimation accuracy, reaching up to 82%. This accuracy has been further enhanced in steep and densely forested areas (Silveira et al., 2023). Similarly, GEDI-based validation studies in western U.S. forests have yielded strong correlation coefficients (R^2 = 0.90) and low error rates (RMSE = 32.62 Mg/ha) (Cao et al., 2023). Comparable results have also been reported in boreal forests in Norway.

This study proposes a high-accuracy biomass estimation methodology based on remote sensing and open-access datasets. The integration of image processing techniques and index-based models allows for rapid and precise analysis over large areas. The use of publicly available data not only minimizes operational costs but also enhances sustainability by enabling frequent analysis and retrospective access to long-term time series datasets. These aspects represent major advantages of the proposed approach in supporting data-driven forest carbon monitoring.

2. Materials and Methods

Study Area Alanya. 36'30'07‘ and 36'36'31’ north latitudes and 31'38'40‘ and 32'32'02’ east longitudes, 135 km from the city centre within the borders of Antalya province on the Mediterranean coast of Türkiye. The study area is shown in the following Figure 4.

Alanya district, which is the study area, is the district with the most fertile soil richness of the region due to its location and climate characteristics. District forests account for 0.5% of Türkiye's forest size. Afforestation works are carried out in the region. An average area of 750 hectares is afforested annually.

While the mountainous areas of the region have larch and cedar trees, the coastal areas have red pine tree type. Due to banana and citrus production, which brings significant income to the region, these tree types are intensively present (Turgut and Günlü, 2022). These trees are generally located in the coastal area. While Avacado and Kiwi trees can be observed in every area, Quince, Pear and Apple trees are found in mountainous areas due to their cold resistance. Recently, as a result of the planting of Eucalyptus trees as a method in the marsh drying works, these types of trees are found in the region for ornamental purposes. As can be seen in the light of the above information, the region contains a rich green area type due to its different characteristics. The green area information of the study area is given in the area and percentage information with the Pie Slice Image in Figure 5.

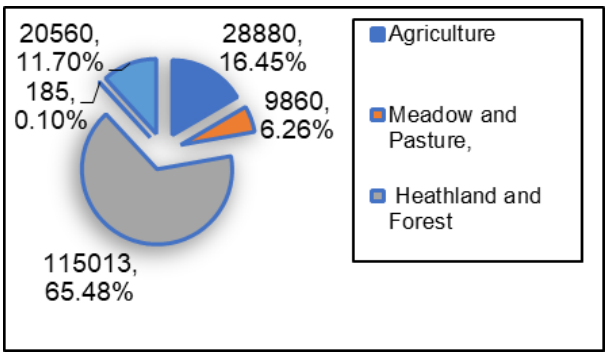

Figure 5. Green area information (Alanya Governorship).

All procedures carried out in the study were itemized and presented in the form of a workflow diagram. The flowchart is shown in the following Figure 6.

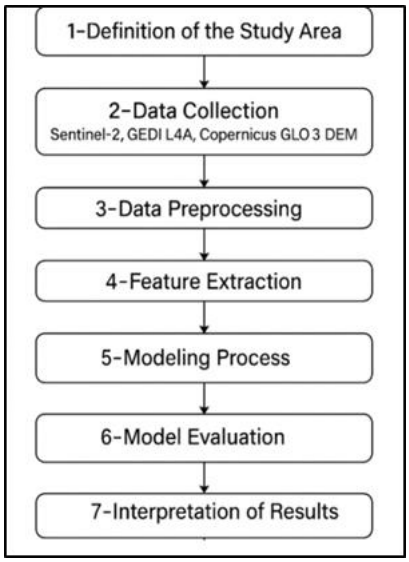

Figure.6. Flowchart.

Climatically, when the study area is examined, the region has arid and hot summers. It has been determined that the winters are rainy and mild. The breeze wind coming from the sea reduces the heat effect in summer. Table 1 below, contains information that helps to deduce the average climatic characteristics of the province where the study area is located between 1930 and 2024.

17.05.2020 measurement was determined as 41.7 ºC, 06.06.2000 measurement was determined as 45 ºC, 01.10.2022 measurement was determined as 41.2 ºC and 06.06.2024 measurement was determined as 45 ºC. For the generation of climate data, 30-year data of 220 stations were used.

Table.1. Average climatic characteristics between 1930 and 2023

Month	AT	AHT	AMT	AST	ANRD	MTRA	1930 - 2023	
							*HT (°C)	*LT (°C)
1	10	14.9	6	5.1	12.5	234.5	23.9	-4.3
2	10.7	15.6	6.4	5.8	10.45	150.2	26.7	-4.6
3	12.9	18	8.1	6.7	8.63	92.1	28.6	-1.6
4	16.4	21.4	11.3	8	6.51	49	36.4	1.4
5	20.6	25.7	15.3	9.8	5.22	34.3	41.7	6.7
6	25.3	30.7	19.7	11.4	2.56	11	44.8	11.1
7	28.6	34.2	22.8	11.8	0.53	4.4	45	14.8
8	28.4	34.1	22.8	11.3	0.55	4.3	44.6	13.6
9	25.3	31.2	19.5	9.8	1.71	16.9	42.5	10.3
10	20.6	26.6	15.3	7.9	5.45	70.9	41.2	4.9
11	15.5	21.3	10.9	6.3	7.49	129.7	33	0
12	11.7	16.7	7.7	4.9	11.91	256.1	25.4	-1.9
13	18.8	24.2	13.8	8.2	73.5	1053.4	45	-4.6

HT=highest temperature; LT=lowest temperature; AT=average temperature; AHT=average highest temperature; AMT=average minimum temperature; AST=average sunbathing time (hours); ANDR=average number of rainy days; MTRA=monthly total rainfall average (mm).

First, Preparation of Data Sets was performed., upland biomass density modelling was performed using Sentinel-2 (S2) and GEDI L4A data. In addition, GLO-30 Digital Elevation Model (DEM) data was also used for slope calculations. In the study, time series from 2019 to 2024, which is the temporal data intersection time of the layers, were used. In the study, the time series from 2019 to 2024, which is the temporal data intersection time of the layers, was used.

The datasets used in the study and their corresponding characteristics are presented in the Table.2 below. The process steps are as follows: Sentinel-2 data were filtered to the region and time interval specified for the year 2022. Then, various quality controls and band scaling operations were performed on the images. Besides, various vegetation and surface indices such as NDVI, MNDWI, NDBI, EVI and BSI have been added. GEDI L4A data was used for biomass density estimations and improved with filters such as data quality and slope. Areas sloping more than 30 degrees were masked. Elevation and slope bands were calculated using DEM data and these data were added to the system as additional variables to be used in biomass estimation.

As the second step, Data Processing and Filtering process was performed. Quality control filters were applied on Sentinel-2 and GEDI data. For Sentinel-2 data, images with low cloudiness values were selected using 'Cloud Score Plus' and the spatial resolution of the images was scaled to 10 metres. GEDI data Quality was controlled with 'l4_quality_flag' and 'degrade_flag' variables and masked with variables such as slope and error rate. As the third step, Model Training process was performed.

Sentinel-2 and DEM data were used to model the biomass density to be estimated:

Random Forest regression algorithm was preferred for modelling biomass density. The model was trained to estimate the aboveground biomass density (AGBD) for each pixel. The training data was limited to 1000 samples and these samples were determined by stratified sampling method. In the training process, Sentinel-2 image bands and DEM bands were used as 'predictors' and GEDI data was included in the model as 'predicted' values.

As the fourth step, Model Evaluation process was performed. The performance of the model was evaluated using the root mean square error (RMSE). Furthermore, a scatter plot visualising the relationship between the predicted biomass density values and the observed values was created. In the graph, the predicted and observed biomass values are compared and a linear trend line is added on the graph. As a result of this analysis, biomass density was estimated and Total AGB (Mg), which is the total amount of biomass in the identified land classes, was extracted. Graphs, results and explanations are given under the heading of findings below.

As the fifth step, Findings process was performed. In order to examine the relationship between the biomass density values estimated on an annual basis in the time interval between 2019 and 2023 and the observed values, each year is considered separately. Figure 7. below shows a certain slope in the Regression line graph between Observed and Aboveground Biomass Density between 2019-2020. A linear relationship was found between the predicted Aboveground Biomass Density values (y-axis) and the Observed values (x-axis).

Table 2. Data sets

SENTINEL-2	
Resolution	Detail
Spectral	13 bands (443–2190 nm), covering visible, NIR, red edge, and SWIR regions.
Radiometric	12-bit resolution, reflectance range 0–4095, enabling high sensitivity.
Spatial	10 m:B2–B4 (Vis),B8 (NIR);20 m: B5–B8A(RedEdge),B11–12(SWIR);60 m: B1, B9–B10 (Atmospheric).
Temporal	Revisit time ~5 days, varies by weather and location.
GEDI L4A employs an active LiDAR system operating in a single near-infrared wavelength band.	
Spectral	GEDI L4A uses active LiDAR in a single NIR band.
Radiometric	16-bit resolution captures backscatter with high accuracy for detailed vertical structure.
Spatial	Footprint: ~25 m; spacing: 60 m nadir, ~600 m globally.
Temporal	45-day revisit (ISS-dependent); limited global coverage due to orbit.
GLO-30 Digital Elevation Model-DEM	
Spectral	LiDAR wavelength: 1064 nm (NIR).
Radiometric	16-bit precision ensures accurate LiDAR backscatter measurement.
Spatial	Footprint: ~25 m; spacing: 60 m nadir, ~600 m globally.
Temporal	45-day revisit (ISS-dependent); coverage limited to orbital track

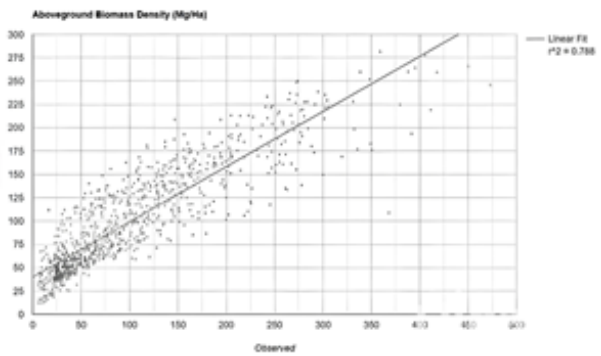

Figure 7. 2019-2020 regression graph.

R-square (r^2), 0.788 was obtained. This value reveals that the observed value, which is the independent variable of the model, explains the predicted biomass density, which is the dependent variable, at a high rate of 78.8%. Although the model cannot be called a perfect model, it is shown to be compatible with this value.

In satellite-based biomass estimation studies, numerous factors such as atmospheric effects, sensor noise, topographic variability, and vegetation diversity directly influence model performance. Despite these challenges, a high explanatory power of 78.8% (R^2 = 0.788) demonstrates both the statistical reliability and practical

applicability of the model. In this regard, the model provides a strong and reliable foundation for large-scale spatial biomass monitoring, offering a fast, scalable, and cost-effective approach.

The data are mostly distributed close to the regression line. This revealed the existence of a linear relationship. This graph reveals that the biomass density increases with increasing observed value.It has been observed that as the observed value increases, the deviations from the regression line increase. The 300-400 range is the range where this deviation is intense. A deviation from the regression line above 300 values was detected on the Observed (x-axis).

This reveals the deviation from the estimate.The reasons for this are also analysed and inferences are made. They will be explained in detail in the following sections of the study.The Regression line graph shows a certain slope in the same way as 2020-2021 shown in Figure.8 below.A linear relationship was found between the predicted Aboveground Biomass Density values (y-axis) and Observed values (x-axis)

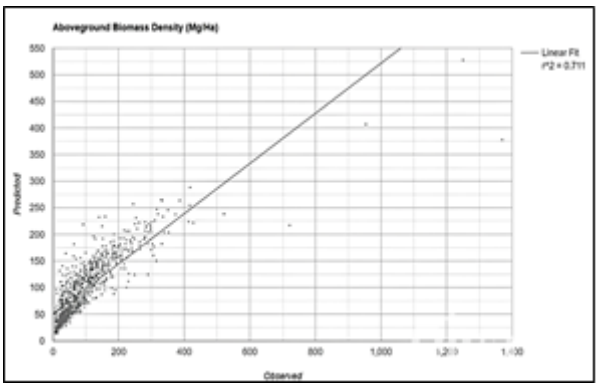

Figure 8. 2019-2020 Regression Graph.

R-square (r^2), 0.793 was obtained. This value reveals that the observed value, which is the independent variable of the model, explains the predicted biomass density, which is the dependent variable, at a high rate of 79.3%.

Although the model cannot be called a high accuracy model, it is shown to be compatible with this value. The data mostly show a distribution close to the regression line. It has been revealed that these two variables change proportionally and there is a linear relationship. This graph reveals that biomass density increases with the increase in the observed value.

It was observed that as the observed value increased, the deviations from the regression line increased. While it is in harmony up to the range of 300-400, the deviations intensifies above 400. It has been determined that there are deviations from the model.

A significant deviation from the regression line was detected above 400 values of Observed (x-axis). In the observations after 500 values, these deviation values are at large rates. After these values, the model does not represent the observations well and reveals a bias away from the prediction. The reasons for this were also analysed and inferences were made. They will be explained in detail in the following sections of the study.

In the analysis for the years 2021-2022 shown in Figure 9 below, a linear relationship was found between the Estimated Above Ground Biomass Density values (y-axis) and the Observed (x-axis) values.

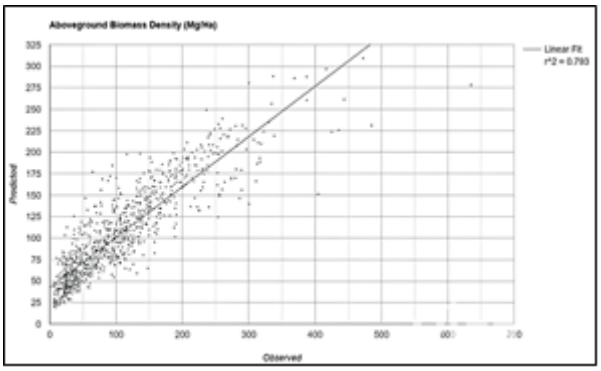

Figure 9. 2021-2022 Regression Graph.

R-square (r^2), 0.814 was obtained. This value reveals that the observed value, which is the independent variable of the model, explains the estimated biomass density, which is the dependent variable, at a high rate with a value of 81.4%.

The data was mostly close to the regression line. It was determined that the increase in biomass occurs when the amount of observation increases. While there is a distribution close to the regression line between 300-400, it was determined that the deviations from the model starting with the value of 400 and increasing with 500.

A linear relationship was found between the estimated Aboveground Biomass Density values (y-axis) and Observed values (x-axis) for the years 2022-2023 as shown in Figure 10 below.

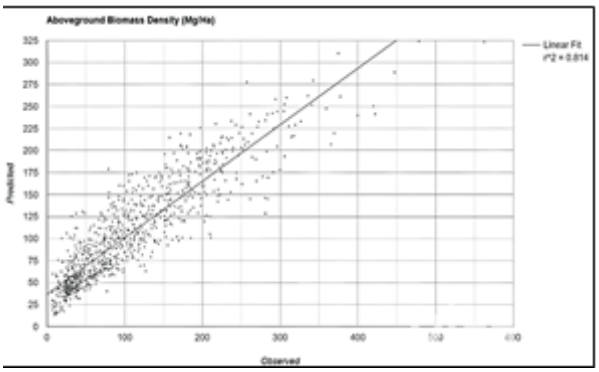

Figure.10. 2022-2023 Regression Graph.

R-square (r^2), 0.711 was obtained. This value reveals that the observed value, which is the independent variable of the model, explains the predicted biomass density, which is the dependent variable, to a high extent with a value of 71.1%. The data were generally observed close to the regression line. It has been determined that The observed increase in biomass appears to correlate with increased sampling density The observed increase in

biomass appears to correlate with increased sampling density. Especially after the value of 600, anomalies were detected to a great extent.

R-square (r^2), 0.711 was obtained. This value reveals that the observed value, which is the independent variable of the model, explains the predicted biomass density, which is the dependent variable, to a high extent with a value of 71.1%. The observed increase in biomass appears to correlate with increased sampling density. Especially after the value of 600, anomalies were detected to a great extent.

In the interpretation of the linear regression analysis graph between Observed and Aboveground Biomass Density between 2023-2024 shown in Figure 11 below, the following conclusions were obtained. A linear relationship was found between the predicted Aboveground Biomass Density values (y-axis) and the Observed values (x-axis).

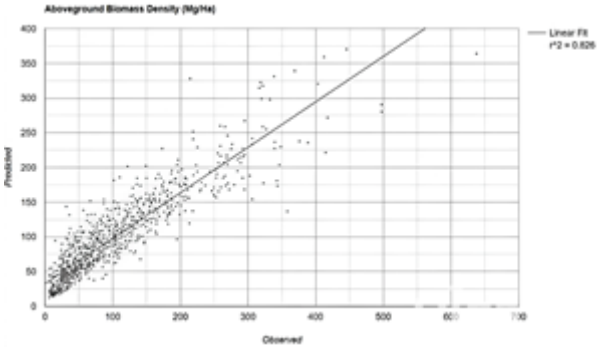

Figure.11. 2023-2024 Regression Graph.

R-square (r^2), 0.826 was obtained. This value shows that the observed value, which is the independent variable of the model, explains the estimated biomass density, which is the dependent variable, to a high extent with a value of 82.6%. The distribution of the data is generally close to the regression line. As the amount of observations increases, the biomass increases. Especially after the value of 300, anomalies were detected to a great extent.

In the study, Aboveground Biomass Density and the Root Mean Square Error RMSE value of the model were calculated separately for each year in the time interval from 2019 to 2024. The results obtained are shown in Table.3 below.

Table.3. Total AGB and RMSE by years

Time Interval	Total AGB(Mg)	RMSE
2019-2020	14043214.68	40.97
2020-2021	14638570.78	41
2021-2022	14339747.88	37.04
2022-2023	15029798.83	60.12
2023-2024	14658066.64	37.65

The following Figure.8. Annual Total AGB (Mg) graph was created by utilising the data in Figure.12 above. The lowest Total AGB(Mg) value in the study year range was 2019-2020 with the value 14043214.68, while the highest Total AGB(Mg) value was 2022-2023. A decrease was observed between 2023-2024, the last measurement interval.

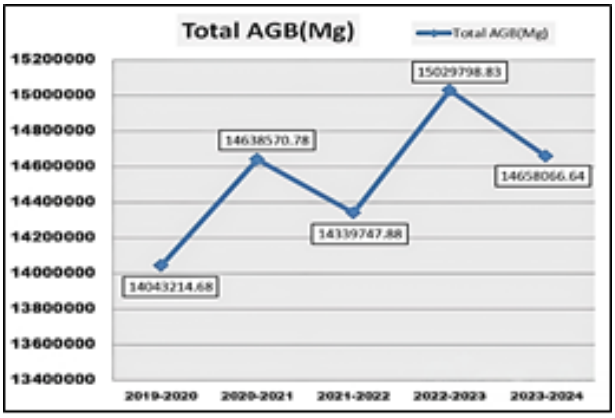

Figure.12. Total AGB by years.

The processes such as creating a data set for the study area, standardisation of the data, creating the data in the form of layers in the GIS platform environment, modelling the data, obtaining the estimated Total AGB (Mg) values were completed and the findings were obtained. In the light of these findings, discussion and conclusions are explained in detail below.

Increases in biomass observed over the years can be attributed to forest regeneration, insect outbreaks, land use changes, a decrease in wildfires, and post-fire forest restoration activities during these periods.

3. Results and Discussion

A negative situation such as climate change, soil degradation, soil erosion, urban growth, industrial pollution, decrease in water resources, decrease in biodiversity and natural disasters threaten the carbon sinks on the earth. With the decrease in these areas, diseases that threaten human health increase and living conditions become more difficult.

The reduction in forested areas is the most important variable that increases this amount. Forests are destroyed by harmful activities such as settlement, fires, conversion to agricultural land and stubble burning. In addition to being an indicator of negativity, forest enhancement activities in forests make a significant contribution to the increase in biomass in forest improvement activities. The study in the upper basin of the Göksu River in the Eastern Mediterranean found that the total above-ground stand carbon content increased by 47.6 thousand tons and this increase was achieved by forest improvement works (Günlü et al., 2019).

It was revealed that there will be a 6.62% decrease in plant biomass density in the study area Alanya until the end of 2030 in the projection of 2018 data (İşler et al., 2024). It has been determined that the region is under the threat of losing its natural carbon deposits due to urbanization pressure as well as climate change. The

common point in the studies reveals that urbanization pressure is associated with forest fires. The negative impact of urban growth pressure on vegetation was obtained due to the strong link between EVI and NDBI (Sharma et al., 2022; Zhang et al., 2004).

The transformation of green areas into urban areas, which can be characterized as irreversible actions in the ecosystem, or the negativities caused by human activities in urban areas reduce the biomass storage areas of the earth.

Tourism is an important economic income sector among human activities for the study area. Although this situation creates opportunities to increase economic income, it causes uncontrolled and unplanned urbanization and the reduction of natural land covers and natural landscape areas.

With this study, the change in Biomass Density in Alanya has been addressed in the year time interval. Forest above ground biomass (AGB) calculation with forecasting methodology was modelled with a dataset covering the time interval between 2019 and 2023 in order to guide local managers and planners. Spectral indices and bands data (Sentinel-2 Surface Reflectance) used as data set independent variable, cloudlessness mask data (CloudScore+) due to the consideration of cloud factor to improve the quality of the data, Digital Elevation Model data (Copernicus GLO-30 DEM) containing Slope and Elevation information used as independent variables of the model, and Real-time Aboveground Biomass Density (GEDI L4A Raster Aboveground Biomass Density) data which is Raster data were included in the model in the study. This methodology demonstrates the applicability of AGBD estimation at both temporal and spatial scales using earth observation technology.

Global Ecosystem Dynamics Investigation (GEDI), produces Light Detection and Ranging (LIDAR) data with 60 m range and 30 m spatial resolution. The data obtains three-dimensional positional data of plants in the vertical direction. A solution was developed using the regression model, which is a machine learning method, as an indirect solution technique for converting point-based data into spatial data. In general, compared to other years, the 2023–2024 period experienced fewer wildfires and higher rainfall amounts. Therefore, the observed increase in aboveground biomass during this period can be attributed to these favorable environmental conditions.

In the application of the model over the years, the lowest Total AGB(Mg) value was 14043214.68 in the 2019-2020 time period and the highest Total AGB(Mg) value was 15029798.83 in the 2022-2023 time period. Here, the highest time interval was determined as the 2022–2023-time interval with the highest error value of RMSE value 60.12. For this reason, it was determined that additional variables should be included in the model in future studies.

In the modeling process, the Random Forest algorithm was used to capture nonlinear relationships between variables. Its ability to reduce overfitting and provide high generalization performance makes it a prominent method. In comparison, Linear Regression is more effective for identifying linear relationships, while Support Vector Regression (SVR) can be less efficient on large datasets and is sensitive to parameter tuning. Random Forest was preferred in this study due to its flexibility, robustness, and ability to produce accurate results with minimal parameter configuration.

In this study, the hyperparameters of the Random Forest algorithm were selected manually. Instead of a systematic optimization approach, parameters were chosen using a trial-and-error-based method. This represents one of the key areas for improvement in future work.

With the model presented in this study, a feasible model with low image processing load but high accuracy has been presented.

In future studies to strengthen the model, it is suggested that adding new variables to the model by dividing it into subgroups such as humidity rate, soil type, plant species will reduce the amount of outline values in the model and increase the accuracy of the model. In the future, more diverse and rich studies can be produced by trying different regression models with linear regression models and new variables. There is a possibility that the approach of detecting complex relationships will make the model more powerful. After the findings that are suggestions for further studies, the fact that the model accuracy is close to high rates with the least variable input clearly reveals the success of the model in the study.

Since climate characteristics cause many effects on humans and nature, the subject of the study has emerged as an important variable in the decrease and increase of biomass. İşler et al. (2023) showed in their study that despite the population increase, biomass change is positive and the climate characteristics of the region have a positive effect on plant health. It has been found that the factors causing vegetation change are proportional to the relationship between urbanization and climate. It shows that climate conditions should be taken into consideration in determining positive proactive environmental planning and policies.

Another noteworthy result of the study is the emphasis on the critical role of the interaction between climate conditions and urbanization in shaping vegetation dynamics. In particular, despite higher levels of urbanization, Alanya exhibits a more favorable vegetation status, indicating the contribution of more favorable climatic conditions and positive proactive environmental policies.

Obtaining Total AGB(Mg) indirectly, which is difficult to obtain directly using Earth Observation technology, offers more practical and accurate solutions. Since it has become difficult to find biomass change with high accuracy due to economic and technical limitations, this methodology has provided decision makers and planners

with a solution-oriented contribution to the process by revealing the spatial and temporal biomass change of the region. In order to advance and develop the study, additional variables should be included in the model and studies should be carried out to improve the accuracy quality of opensource data.

Author Contributions

The percentages of the author' contributions are presented below. The author reviewed and approved the final version of the manuscript.

	E.A.
C	100
D	100
S	100
DCP	100
DAI	100
L	100
W	100
CR	100
SR	100
PM	100
FA	100

C=Concept, D= design, S= supervision, DCP= data collection and/or processing, DAI= data analysis and/or interpretation, L= literature search, W= writing, CR= critical review, SR= submission and revision, PM= project management, FA= funding acquisition.

Conflict of Interest

The author declared that there is no conflict of interest.

Ethical Consideration

Ethics committee approval was not required for this study because of there was no study on animals or humans.

References

Aaslyng JM, Lund JB, Ehler N, Rosenqvist E. 2003. IntelliGrow: a greenhouse component-based climate control system. Environ Model Softw, 18(7): 657–666.

Al Saud MM. 2022. Space techniques for earth observation. in: applications of space techniques on the natural hazards in the MENA Region, 1: 3–14.

Askne JI, Dammert PB, Ulander LM, Smith G. 1997. C-band repeat-pass interferometric SAR observations of the forest. IEEE Trans Geosci Remote Sens, 35(1): 25–35.

Cao L, Dubayah R, Zhang Z, Armston J. 2023. Validation of GEDI biomass estimates in Western U.S. forests using field inventory data. Remote Sens Environ, 295: 113630.

Da Silveira F, Da Silva SLC, Machado FM, Barbedo JGA, Amaral FG. 2023. Farmers' perception of the barriers that hinder the implementation of agriculture 4.0. Agric Syst, 208: 103656.

De Araujo V, Pramreiter M, Christoforo A. 2025. A global policy framework for the circular use of forest biomass as building materials. Nat Rev Mater, 3: 1–3.

Duncanson L, Kellner JR, Armston J, Dubayah R, Minor DM, Hancock S, Healey S. 2022. Aboveground biomass density models for NASA's GEDI L2A data. Environ Res Lett, 17(9): 095001.

Eckert S. 2012. Improved forest biomass and carbon estimations using texture measures from WorldView-2 satellite data. Remote Sens, 4(4): 810–829.

Evrendilek F, Celik I, Kilic S. 2004. Changes in soil organic carbon and other physical soil properties along adjacent Mediterranean forest, grassland, and cropland ecosystems in Turkey. J Arid Environ, 59(4): 743–752.

Foody GM, Cutler ME, McMorrow J, Pelz D, Tangki H, Boyd DS, Douglas IA. 2001. Mapping the biomass of Bornean tropical rain forest from remotely sensed data. Glob Ecol Biogeogr, 10(4): 379–387.

Franklin J, Hiernaux PH. 1991. Estimating foliage and woody biomass in Sahelian and Sudanian woodlands using a remote sensing model. Int J Remote Sens, 12(6): 1387–1404.

Gallaun H, Zanchi G, Nabuurs GJ, Hengeveld G, Schardt M, Verkerk PJ. 2010. EU-wide maps of growing stock and above-ground biomass in forests based on remote sensing and field measurements. For Ecol Manag, 260(3): 252–261.

Gilreath JP, Jones JP, Overman AJ. 1994. Soil-borne pest control in mulched tomato with alternatives to methyl bromide. 156–159.

Günlü A, Göl C, Sariçam F. 2019. The evaluation of temporal and spatial change of aboveground stand carbon: a case study of upstream of the Göksu river basin. 352–359.

Güverçin İ. 2022. Estimation of aboveground biomass in pure red pine stands using Sentinel-1A and Landsat 8 OLI satellite images (Anamur forest sub-district directorate example). PhD thesis, Çankırı Karatekin University, Institute of Science, Çankırı, pp: 65-66.

Houghton RA, Hall F, Goetz SJ. 2009. Importance of biomass in the global carbon cycle. J Geophys Res Biogeosci. 114(G2).

İşler B, Aslan Z, Sunar F, Güneş A, Feoli E, Gabriels D. 2023. Evaluation of prediction performance of vegetation biomass density for two different case study areas in Turkey with hybrid wavelet and artificial neural network method, pp:56-59.

İşler B, Aslan Z, Sunar F, Güneş A, Feoli E, Gabriels D. 2024. Hybrid model-based prediction of biomass density in case studies in Türkiye. Ecol Inform, 79: 102439.

Keleş NN, Tepebaş B, Keleş S. 2024. Analysis of the temporal changes in the amount of carbon stored and oxygen produced in forest trees. Anat J For Res, 10(2): 16–21.

Khan MN, Tan Y, Gul AA, Abbas S, Wang J. 2024. Forest aboveground biomass estimation and inventory: Evaluating remote sensing-based approaches. Forests, 15(6): 1055.

Kim CK, Chung JD, Park SH, Burrell AM, Kamo KK, Byrne DH. 2004. Agrobacterium tumefaciens-mediated transformation of Rosa hybrida using the green fluorescent protein (GFP) gene. Plant Cell Tissue Organ Cult, 78: 107–111.

Le Toan T, Beaudoin A, Riom J, Guyon D. 1992. Relating forest biomass to SAR data. IEEE Trans Geosci Remote Sens, 30(2): 403–411.

Lu D, Batistella M. 2005. Exploring TM image texture and its relationships with biomass estimation in Rondônia, Brazilian Amazon. Acta Amazon, 35: 249–257.

Muukkonen P, Heiskanen J. 2005. Estimating biomass for boreal forests using ASTER satellite data combined with standwise forest inventory data. Remote Sens Environ, 99(4): 434–447.

Nelson R, Krabill W, Tonelli J. 1988. Estimating forest biomass and volume using airborne laser data. Remote Sens Environ, 24(2): 247–267.

Potapov P, Li X, Hernandez-Serna A, Tyukavina A, Hansen MC, Kommareddy A. 2021. Mapping global forest canopy height through integration of GEDI and Landsat data. Remote Sens, pp: 52-58.

Prentice IC, Farquhar GD, Fasham MJ, Goulden ML, Heimann M, Jaramillo VJ, Kheshgi HS, Le Quéré C, Scholes RJ, Wallace DW, Archer D. 2001. The carbon cycle and atmospheric carbon dioxide. In: Climate change 2001: The scientific basis. Intergovernmental Panel on Climate Change, pp:45-59.

Protocol K. 1997. United Nations framework convention on climate change. Kyoto Protocol. Kyoto, 19(8): 1–21.

Ravindranath NH, Ostwald M. 2007. Carbon inventory methods: handbook for greenhouse gas inventory, carbon mitigation and roundwood production projects. Springer, pp: 3.

Sader SA, Waide RB, Lawrence WT, Joyce AT. 1989. Tropical forest biomass and successional age class relationships to a vegetation index derived from Landsat TM data. Remote Sens Environ, 28: 143–198.

Santos JR, Freitas CC, Araujo LS, Dutra LV, Mura JC, Gama FF, Soler LS, Sant'Anna SJ. 2003. Airborne P-band SAR applied to the aboveground biomass studies in the Brazilian tropical rainforest. Remote Sens Environ, 87(4): 482–493.

Sharma RK, Sankhayan PL, Hofstad O. 2008. Forest biomass density, utilization and production dynamics in a western Himalayan watershed. J For Res, 3: 171–180.

Sharma V, Ghosh S, Singh S, Vishwakarma DK, Al-Ansari N, Tiwari RK, Kuriqi A. 2022. Spatial variation and relation of aerosol optical depth with LULC and spectral indices. Atmosphere, 13(12): 1992.

Steininger MK. 2000. Satellite estimation of tropical secondary forest above-ground biomass: data from Brazil and Bolivia. Int J Remote Sens, 21(6-7): 1139–1157.

Turgut R, Günlü A. 2022. Estimating aboveground biomass using Landsat 8 OLI satellite image in pure Crimean pine (Pinus nigra JF Arnold subsp. pallasiana (Lamb.) Holmboe) stands: a case from Turkey. Geocarto Int, 37(3): 720–734.

Watson RT, Noble IR, Bolin B, Ravindranath NH, Verardo DJ, Dokken DJ. 2000. Land use, land use change, and forestry, pp:1-373.

Zhang P, Liu H, Li H, Yao J, Chen X, Feng J. 2023. Using enhanced vegetation index and land surface temperature to reconstruct the solar-induced chlorophyll fluorescence of forests and grasslands across latitude and phenology. Front For Glob Change, 6: 1257287.

Zhao P, Lu D, Wang G, Liu L, Li D, Zhu J, Yu S. 2016. Forest aboveground biomass estimation in Zhejiang Province using the integration of Landsat TM and ALOS PALSAR data. Int J Appl Earth Obs Geoinf, 53: 1–5.

Zheng D, Rademacher J, Chen J, Crow T, Bresee M, Le Moine J, Ryu SR. 2004. Estimating aboveground biomass using Landsat 7 ETM+ data across a managed landscape in northern Wisconsin, USA. Remote Sens Environ, 93(3): 402–411.

Zimble DA, Evans DL, Carlson GC, Parker RC, Grado SC, Gerard PD. 2003. Characterizing vertical forest structure using small-footprint airborne LiDAR. Remote Sens Environ, 87(2-3): 171–182.

Black Sea Journal of Engineering and Science
doi: 10.34248/bsengineering.1664037

Open Access Journal
e-ISSN: 2619 – 8991

Research Article
Volume 8 - Issue 5: 1440-1449 / September 2025

UNVEILING ANTIBODY-MEDIATED ALLOSTERY IN INTERLEUKIN-1ß VIA CONFORMATIONAL SAMPLING AND MACHINE LEARNING

Arzu UYAR[1]*

[1]*İzmir Institute of Technology, Faculty of Engineering, Department of Bioengineering, 35433, İzmir, Türkiye*

Abstract: Human interleukin-1β (IL-1β), a pivotal proinflammatory cytokine, is a therapeutic target in autoimmune and inflammatory diseases. While antibodies blocking IL-1β signaling are effective, their allosteric mechanisms remain poorly understood. This study investigates how four distinct antibodies induce long-range allosteric effects in IL-1β, leveraging computational approaches to map allosteric communication and identify critical sites. Ensembles of apo and antibody-bound IL-1β states were generated using the enhanced conformational sampling technique ClustENMD, followed by the application of two different dimensionality reduction methods in machine learning (principal component analysis, PCA; linear discriminant analysis, LDA) to the generated conformers. PCA highlighted how diverse ensembles ClustENMD generated, while LDA revealed antibody-specific allosteric effects on the human IL-1β. By integrating conformational dynamics with machine learning, this work advances a predictive framework for engineering antibodies with tailored allosteric properties. The discovery of binding sites on IL-1β might further open avenues for drug design.

Keywords: Antibody, Allostery, Conformational sampling, ClustENMD, Machine learning

***Corresponding author:** İzmir Institute of Technology, Faculty of Engineering, Department of Bioengineering, 35433, İzmir, Türkiye
E mail: arzuuyar@iyte.edu.tr (A. UYAR)
Arzu UYAR https://orcid.org/0000-0003-2357-1941

Received: March 24, 2025
Accepted: July 23, 2025
Published: September 15, 2025

Cite as: Uyar A. 2025. Unveiling antibody-mediated allostery in Interleukin-1 β via conformational sampling and machine learning. BSJ Eng Sci, 8(5): 1440-1449.

1. Introduction

The human interleukin-1 β (IL-1β) is a potent pro-inflammatory cytokine that plays a critical role in immune response. Changes in IL-1β regulation have been linked to many diseases, such as autoinflammatory diseases, type II diabetes mellitus, cardiovascular events, gout, amyotrophic lateral sclerosis, as well as cancer (Dinarello, 2014; Guo et al., 2016; Ridker et al., 2017a; Ridker et al., 2017b; Wong et al., 2020; Diwanji et al., 2023). Therefore, IL-1β is one of the targets in the drug discovery field.

IL-1β is a monomeric protein with 269 residues (~31 kDa). It becomes active after the caspase-1 cleaves the structure. The resulting structure is the mature form of the IL-1β and contains 154 amino acids (~17 kDa). The mature form consists of 12 antiparallel beta-strands forming a β-barrel. Some of the loops connecting the β-strands in the IL-1β structure are responsible for the IL-1β receptor (IL-1βR) binding, and they form sites A and B as shown in Figure 1. Therefore, both sites are a focus of IL-1β drug discovery studies, and currently, 26 small-molecules have been discovered targeting those sites in IL-1β (Berman et al., 2000).

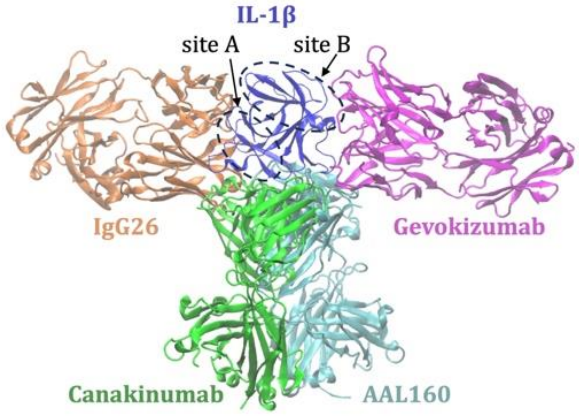

Figure 1. 3D structures of the IL-1β:IgG26 (orange), IL-1β:AAL160 (cyan), IL-1β:Canakinumab (green), and IL-1β:Gevokizumab (magenta). Only the IL-1β (dark blue) in the Gevokizumab-bound complex is shown for clarity. The figure is prepared using VMD (Humphrey et al., 1996).

In addition to small molecules, another way to regulate a protein structure is to develop antibodies that specifically bind to the target of interest. Antibodies are Y-shaped proteins and are increasingly preferred in the pharmaceutical sector due to their properties, such as

high specificity and affinity for their targets and reduced side effects. Currently, five different fragment antigen-binding (Fab) structures have been specifically developed to target IL-1β. Four of them, namely IgG26, AAL160, Canakinumab, and Gevokizumab, have a full 3D structure. On the other hand, the fifth antibody, IgG26A, has missing residues and is an IgG26-derivative (Kuo et al., 2021).

IgG26 binds to the IL-1β epitope (site A) and simultaneously inhibits IL-1βR and IL-1βR accessory protein (IL-1RAcP) binding (PDB ID: 7chy) (Kuo et al., 2021). Also, AAL160 and Canakinumab interact with the IL-1β from a site with a slight overlap with the IgG26-binding site; however, their binding poses are different than that of IgG26. AAL160 acts on a site in IL-1β different than the IL-1βR recognition site and interacts with some of the residues in site A (PDB ID: 7z4t) (Fischman et al., 2023). Similarly, the Canakinumab-bound crystal structure (PDB ID: 4g6j) indicates that the heavy-chain of the antibody binds to IL-1β from site A (Blech et al., 2013). On the other hand, Gevokizumab (PDB ID: 4g6m) binds to IL-1β from site B (Blech et al., 2013). It is claimed to be a regulatory therapeutic antibody that modulates IL-1β bioactivity by reducing the affinity for its IL-1βRI:IL-1βRAcP signaling complex (Owyang et al., 2011).

Interactions at the antibody:IL-1β interfaces were identified and explained in detail in the articles related to corresponding crystal structures (Blech et al., 2013; Owyang et al., 2011; Kuo et al., 2021; Fischman et al., 2023). However, elucidating long-range allosteric effects on IL-1β upon antibody binding was so far not available. Here, in this computational study, a comparison between four different antibody-bound IL-1β complexes and apo IL-1β was performed in atomistic detail using conformational sampling and machine learning. Several conformers for the bound complexes and apo IL-1β were generated using ClustENMD (Kaynak et al., 2021), a conformational sampling method. Then, these conformers were subjected to two different machine learning methods, Principal Component Analysis (PCA) and Linear Discriminant Analysis (LDA), to analyze the diversity of ensembles and detect any differences between antibody-bound and apo IL-1β conformers.

2. Materials and Methods

2.1. Human IL-1β Crystal Structures

Figure 1 shows the crystal structures of human IL-1β used in this study. Only one IL-1β structure (Gevokizumab-bound form, 4g6m) is shown for clarity because there is no big structural difference in the antigen part of four different antibody-bound human IL-1β. In Figure 1, each antibody is colored differently, and well-known binding sites A and B are shown with dashed circles. The resolution values of each structure are as follows: Gevokizumab-bound (4g6m): 1.81 Å; Canakinumab (4g6j): 2.03 Å; IgG26 (7chy): 2.65 Å; AAL160 (7z4t): 3.30 Å. None of the structures has a mutation.

2.2. ClustENMD: Unbiased Conformational Sampling

The ClustENMD (Kaynak et al., 2021) provides an unbiased sampling of biomolecular structures such as proteins, protein-protein, and protein-nucleic acid complexes. It is a hybrid method that combines the Anisotropic Network Model (ANM) (Doruker et al., 2000; Atilgan et al., 2001), an Elastic Network Model, with molecular dynamics (MD) simulation. In ClustENMD, the initial structure is deformed along the linear combination of the slowest (softest) modes obtained from ANM, and several different conformers are generated. Then, the structural similarity values between these conformers are calculated using the root-mean-square deviation (RMSD) value, and this metric is used in hierarchical clustering of all conformers. Each cluster is represented by a cluster member. A short energy minimization is applied to each cluster member using OpenMM, an open-source MD program (Eastman et al., 2017; Eastman and Pande, 2010). The energetically minimized cluster members are subjected to the same process applied to the initial conformation, and thus, new generations (gens) are produced. Eventually, an ensemble of conformers is obtained for one ClustENMD run. In this study, a ClustENMD run is performed for each antibody-bound and apo IL-1β. The five slowest modes are used in ANM to generate nearly 2000 conformers from 10 generations in ClustENMD runs. Thus, all conformers are used in PCA and LDA analyses. The total number of conformers is higher than the number of features used in PCA and LDA analyses (see next section for details),

2.3. Principal Component Analysis (PCA)

Principal component analysis (PCA) (Amadei et al., 1993) is applied separately to the apo and antibody-bound IL-1β ensembles to extract essential modes (principal components, PCs). Only Cα coordinates of all residues in the apo and antibody-bound IL-1β ensembles were extracted and used in PCA calculations. Each conformer is considered when calculating the covariance matrix in PCA. Eigenvector sets representing the first and second PCs are obtained for both apo and antibody-bound forms and used in projection calculations.

2.4. Linear Discriminant Analysis (LDA)

Linear Discriminant Analysis (LDA) is a supervised machine learning technique used for dimensionality reduction within multiclass data and class prediction of a new data point. LDA constructs a set of projection variables that aim to minimize the intra-class variance while simultaneously maximizing the inter-class separation.

In the context of protein dynamics, LDA serves as a valuable tool for discerning differences between various datasets and predicting the class index of novel conformations (Sakuraba and Kono, 2016; Uyar et al., 2018; Uyar and Dickson, 2021). In this study, two specific classes of IL-1β conformations, named “apo” and “complex”, are used in LDA training and testing. Here, the features are the x, y, and z coordinates of all Cα atoms in the apo and complex classes. LDA is applied to the data

sets using the Scikit-learn library (Pedregosa et al., 2011). The generated LDA models provide an LDA vector that separates two classes. The component of the LDA vector provides high fluctuating residues and, therefore, highlights the significant differences between classes.

3. Results

3.1. ClustENMD Conformers

Ensembles of unbiased ClustENMD conformers for the apo (Ab-removed) and antibody-bound IL-1β were shown in Figure 2. Here, IgG26 was colored in orange, whereas ALL160 was in cyan, Canakinumab in green, Gevokizumab in magenta, and the apo IL-1β in blue. Every 50th conformer (gray cartoons) for each studied system was shown for clarity from the front and side views.

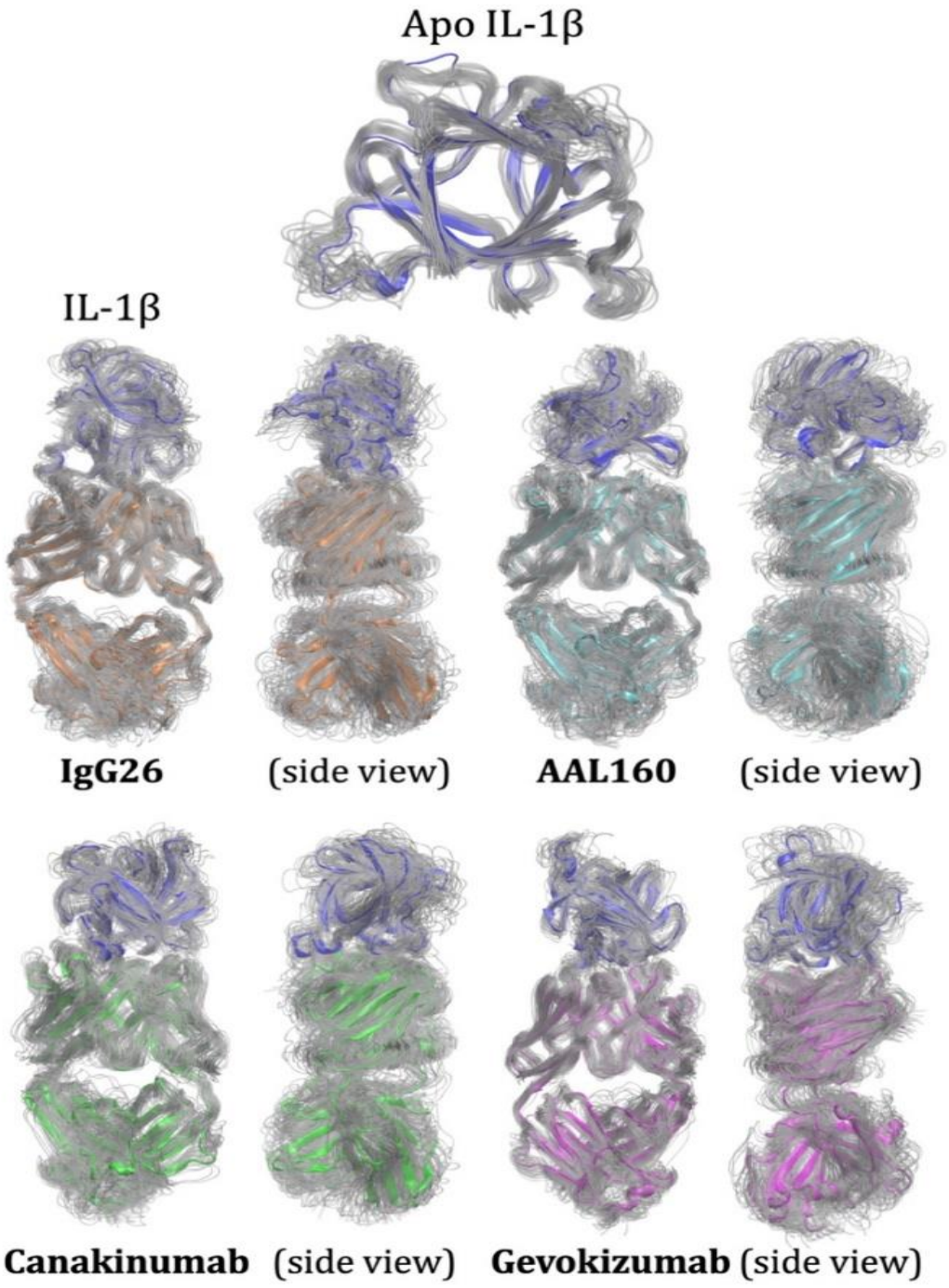

Figure 2. ClustENMD ensembles for the apo IL-1β (dark blue), IL-1β:IgG26 (orange), IL-1β:AAL160 (cyan), IL-1β:Canakinumab (green), and IL-1β:Gevokizumab (magenta). Every 50th conformer is shown for each structure for clarity. The figure is prepared using VMD (Humphrey et al., 1996).

RMSD values with respect to the initial conformer were calculated for each conformer (without skipping any frame), and their median and maximum RMSD values were given in Table 1 for each studied system. The conformers generated for the apo IL-1β reached near 3.5 Å. Antibody-bound forms were more flexible and produced higher RMSD values between 10.2-12.7 Å.

Table 1. The median and maximum RMSDs with respect to the initial conformer for each studied system for IL-1β.

System (PDB ID)	Median RMSD (Å)	Max RMSD (Å)
Ab-removed IL-1β (4g6m)	1.66	3.45
IgG26:IL-1β (7chy)	2.85	10.57
AAL160:IL-1β (7z4t)	2.97	12.71
Canakinumab:IL-1β (4g6j)	2.94	11.02
Gevokizumab:IL-1β (4g6m)	2.97	10.20

A similar RMSD calculation was done for each generation and is given in Figure 3. Here, the figure shows the minimum (min), mean, and maximum (max) RMSD of the conformers in each generation with respect to the initial conformation where the min is in orange, the mean in cyan, and the max in magenta. As expected, it can be seen that the RMSD values increased when the number of generations used in the ClustENMD calculation was increased.

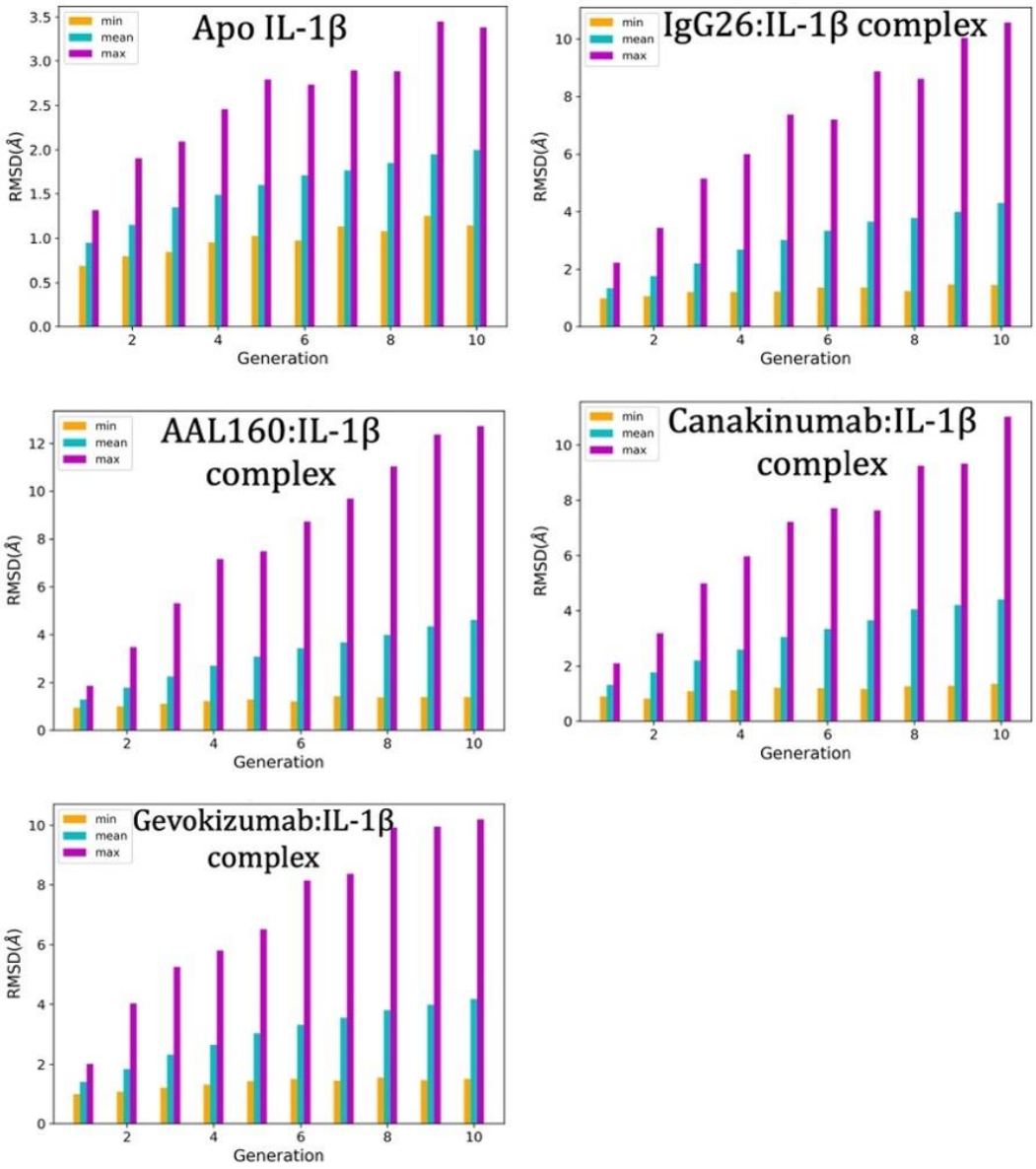

Figure 3. The min, mean, and max RMSD of the conformers in each generation with respect to the initial conformation of IL-1β.

3.2. PCA Analysis

Progression of the apo conformers in generations is shown by projecting them onto PC1 and PC2 (top panel in Figure 4). Here, the initial conformation of the apo IL-1β is highlighted with a red star, whereas the apo conformers coming from 10 different generations are colored differently. It was observed that most conformers were grouped in similar regions; however, gen 5 and later generations produced distinct conformers, which sampled different spots in the conformational space.

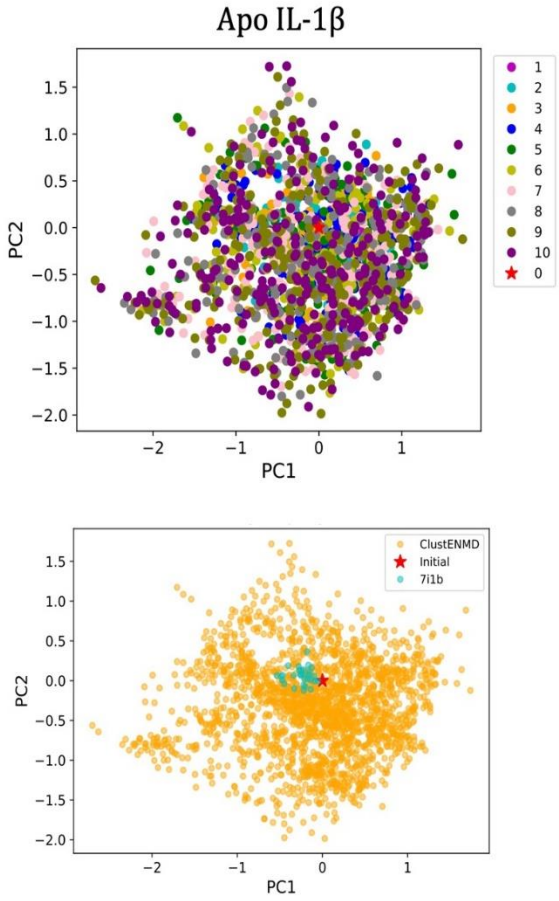

Figure 4. Projection of IL-1β conformers onto the PC1 and PC2. In the top panel, a projection of apo IL-1β conformers obtained from 10 generations is given. The red star represents the initial structure. Each generation is shown in different colors. A projection of the NMR structure of IL-1β (PDB ID: 7i1b) having 32 conformers (cyan) is also given in the bottom panel.

An NMR structure for IL-1β is available and has 32 conformers. These NMR conformers were also projected onto the same two principal components to see if the unbiased ClustENMD conformers yield structures similar to those of the NMR ensemble (bottom panel in Figure 4). Here, the unbiased ClustENMD conformers for the apo structure are in orange, and NMR conformers are in cyan dots. It was observed that ClustENMD produced conformers similar to the NMR conformers in addition to distinct conformers that are pretty different than the NMR conformers.

PCA analysis was also performed for each antibody-bound IL-1β structure. Here, the initial conformation of each antibody-bound IL-1β is highlighted with a red star, whereas the conformers in different generations are colored differently. Again, it was observed that most of the conformers were near the initial complex structure; however, generations after gen 5 produced distinct antibody-bound conformers for IL-1β that were in the different regions of the conformational space.

PCA is an unsupervised machine learning method and is suitable for maximizing the variance in data. However, PCA is not very effective in comparing two distinct classes, such as apo and antibody-bound ensembles. Therefore, next, another machine learning method, Linear Discriminant Analysis (LDA), was applied to ClustENMD conformers.

3.3. LDA Analysis

All conformers from the apo and IL-1β part of each antibody-bound IL-1β ensemble were merged into two sets, apo and bound. Thus, four different apo-bound set pairs were obtained. LDA was separately applied to all pairs to detect significant differences in each set. The yielded first LDA mode vectors that separate the two data sets were used for projection. The densities of the projection values were calculated and given in Figure 6, where the apo IL-1β is in blue and antibody-bound in orange. All apo and complex conformers were well separated using the corresponding first LDA mode vector, except Gevokizumab-bound IL-1β, where slight overlap was observed between the apo and complex conformers.

Next, the first LDA mode vectors obtained from each LDA analysis were used to calculate residue displacements in IL-1β for each structure. Figure 7 shows the residue fluctuations of IL-1β in each antibody-bound complex. Here, in each panel, the IL-1β structure is colored according to the residue fluctuation values obtained from the corresponding LDA mode vector using a rainbow color code. The high fluctuating residues are represented by red and orange, and the lowest fluctuating residues are in dark blue. The corresponding antibody binding sites are also marked with dashed dark gray circles in Figure 7. The IL-1β residue fluctuations in the first LDA mode vectors showed that the LDA analysis for the IgG26- and Canakinumab-bound IL-1β structures revealed very dominant single residues (one for each structure). K109 near site B is the only key residue revealed from the LDA analysis for the IgG26-bound (7chy) structure (top left in Figure 7). Clearly, the dominance of K109 in LDA fluctuations suppresses the other residues. In fact, eight more residues, N129 and P131 in the binding site A; L110 in site B; as well as S17, Y24, E111, F112, and V132 contribute to the conformational differences between the apo and antibody-bound IL-1β when the high fluctuating K109 is omitted in the calculation (top center in Figure 7). In the case of Canakinumab, L67 appears as the only key residue (bottom left in Figure 7). Similar to the IgG26, single residue dominance is present in the LDA mode.

When the dominant L67 is omitted, it is observed that K65, N66, K109 (near site B), and D145 also contribute to the conformational difference in IL-1β conformers (bottom center in Figure 7). Here, only K65 is an antibody-interacting residue, which makes both H-bond and non-bonded interactions with the heavy chain of Canakinumab.

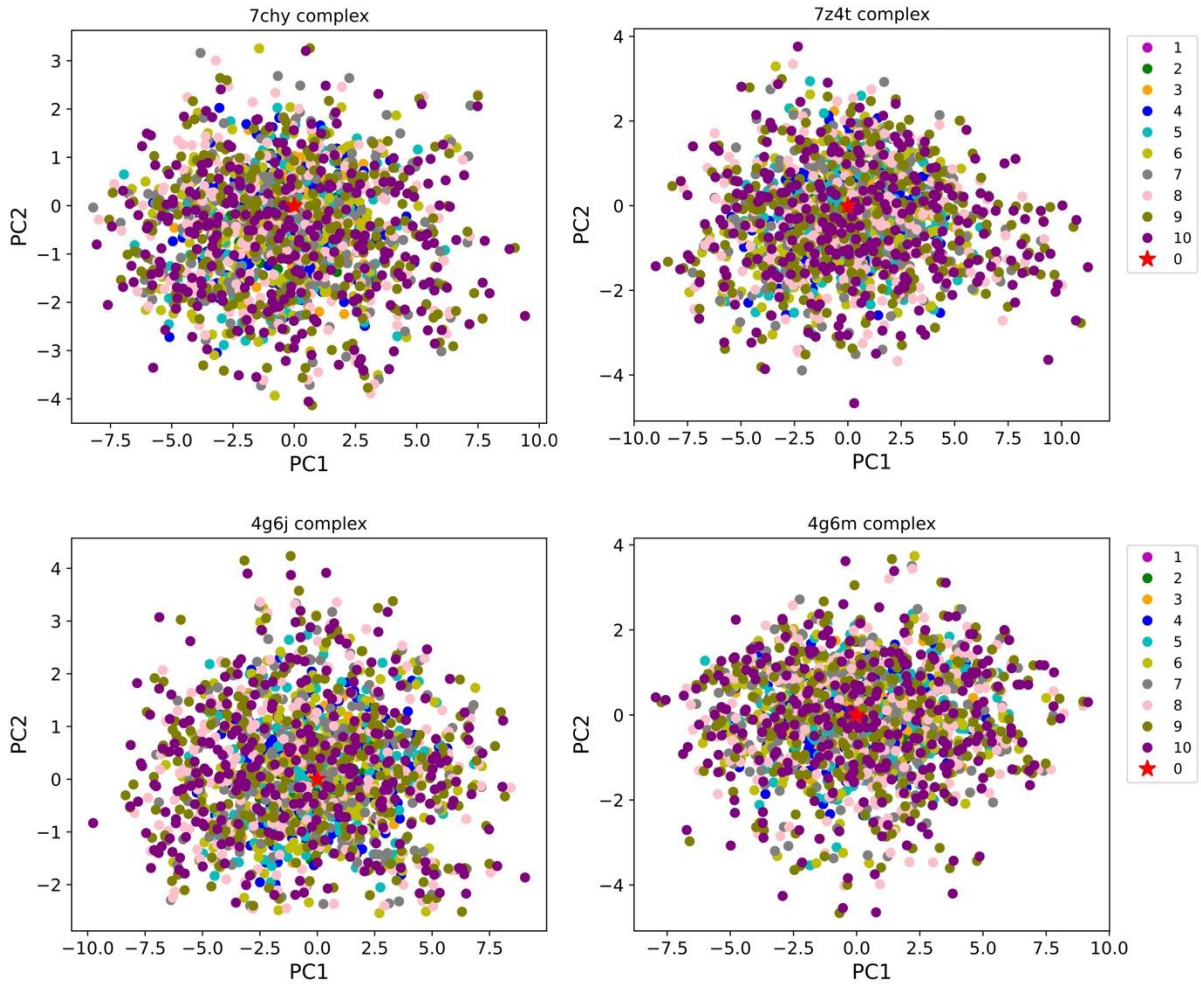

Figure 5. Projection of the antibody-bound (complex) IL-1β conformers: IgG26: 7chy, AAL160: 7z4t, Canakinumab: 4g6j, and Gevokizumab: 4g6m. Conformers in different generations are colored differently, as shown in the color legend. The red star represents the initial structure.

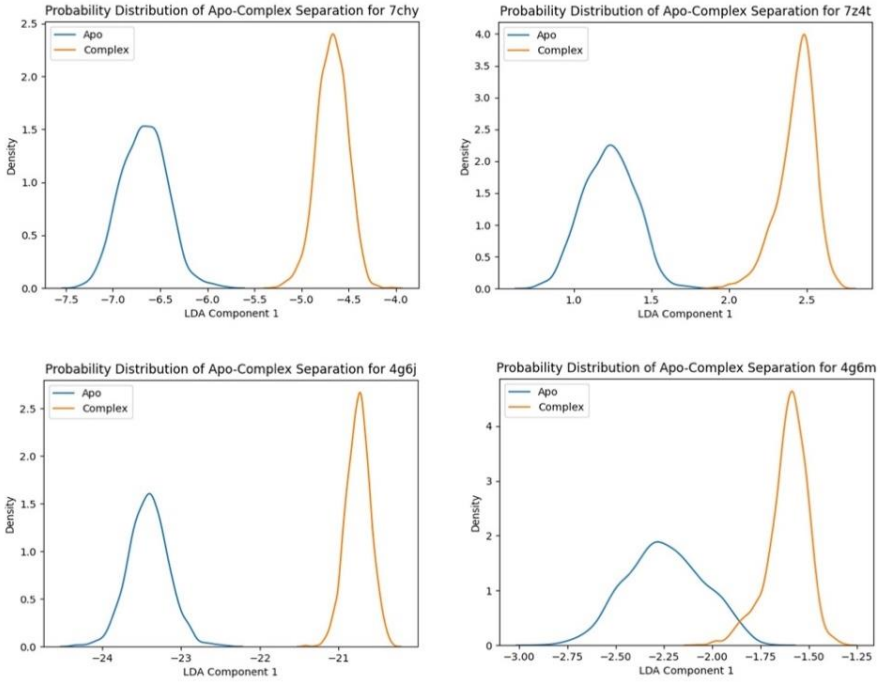

Figure 6. Distributions of the LDA projections of four antibody-bound IL-1β conformers. IgG26: 7chy, AAL160: 7z4t, Canakinumab: 4g6j, and Gevokizumab: 4g6m.

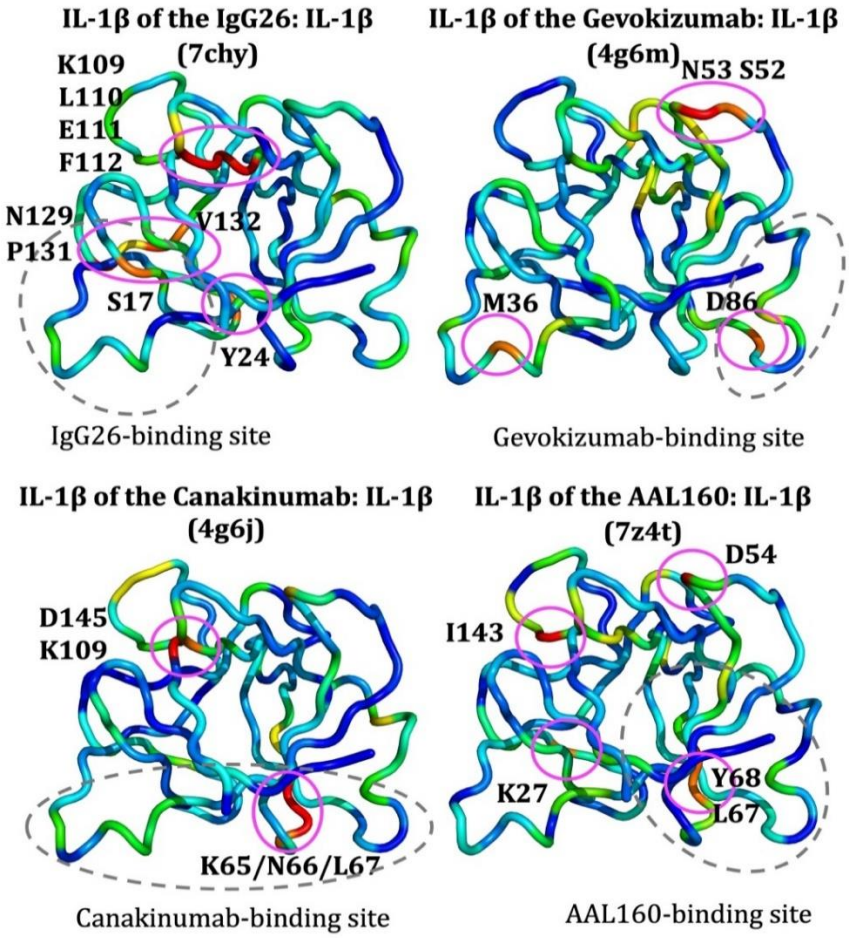

Figure 7. Residue fluctuations in the first LDA mode vectors for the corresponding structures. The structures are colored individually according to the residue fluctuation values using a rainbow color code. Red represents the highest fluctuating residues, whereas dark blue represents the lowest fluctuating residues. High fluctuating residues (red and orange) are marked with magenta circles, and their one-letter codes are written on each structure. The corresponding antibody binding sites are marked with dashed dark gray circles. The figure is prepared using PyMOL (DeLano, 2020).

On the other hand, Gevokizumab and AAL160 antibodies revealed more key residues in their first LDA mode, showing conformational differences in IL-1β conformers. In the Gevokizumab-bound IL-1β (top right in Figure 7), the most critical residue is N53, which is far from the antibody binding site; however, this residue is one of the residues in site B. Its neighbor S52 was also revealed as important. In addition, Gevokizumab-bound conformers yielded two more key residues: D86 in the Gevokizumab-binding site and M36 in site A. In Gevokizumab, the critical residues N53 and S52 are within the 4.5 Å of the IL-1β receptor in its crystal structure with IL-1β (PDB ID: 1itb) (Vigers et al., 1997). N53 makes non-bonded contacts with the receptor. D86 in the antibody binding site makes H-bond and non-bonded interactions with IL-1β.

In the case of antibody AAL160-bound IL-1β (bottom right in Figure 7), the key residues showing the highest fluctuations are D54 in the receptor binding site B and I143, which are far from the antibody binding site. In addition to these residues, K27, which is in site A, appears as a key residue. Moreover, L67 in the AAL160 binding site and its neighbor Y68 are also significant. Here, L67 makes non-bonded contact with the heavy chain of the antibody. Also, K27 is a very critical residue that makes H-bond, non-bonded contact, as well as a salt bridge with the IL-1β receptor.

4. Discussion

This computational study investigated the effect of four different antibodies binding to IL-1β. The aim of the study is to reveal critical residues that are affected by antibody binding to IL-1β and determine any allosteric effect of studied antibodies on IL-1β. For this aim, four antibody-bound crystal structures of IL-1β and its apo form were first subjected to the ClustENMD unbiased enhanced sampling method to generate diverse conformers. Then, these conformers were used in two different machine learning methods. PCA was used to analyze the diversity in IL-1β ensembles. PCA results indicate that the total number of generations used in ClustENMD analysis is critical in producing diverse ensembles, and more generations would yield more distinct conformers.

Later, LDA was used to detect differences in apo and antibody-bound IL-1β ensembles. The computational investigation of four different antibodies binding to IL-1β using LDA revealed long-range allosteric effects on the IL-1β cytokine. Three of these antibodies, namely IgG26, Canakinumab, and AAL160, directly interact with the IL-1β from its receptor binding sites A or B. Only Gevokizumab binds IL-1β far from its receptor binding site. Some of the critical residues determined using LDA pinpoint either site A or B, which are the IL-1β receptor interaction sites, or another antibody's binding site, showing long-range allosteric effects of these antibodies.

In another crystal structure of IL-1β, a local but large conformational change (near 11 Å) exists on the loop (comprising residues 47-55, PDB ID: 8c3u) (Hommel et al., 2023). Interestingly, both Gevokizumab and AAL160 binding affect a few residues on this loop (comprising residues 47-55), which is far from their binding site.

On the other hand, LDA results for the IgG26- and Canakinumab-bound IL-1β highlight the region comprising residues 109-112 and 145. The residue K109 makes a salt bridge and non-bonded contacts with the IL-1β receptor accessory protein (PDB ID: 3o4o) (Wang et al., 2010), and E111 has non-bonded contacts, whereas D145 makes a hydrogen bond. This region is also a binding site in another cytokine, IL-36, which is a member of the IL-1 family and structurally quite similar to IL-1β. A recently discovered antagonist molecule binds IL-36 and is shown to inhibit psoriasis in a 3D human skin model with psoriasis (PDB ID: 6p9e) (Todorović et al., 2019). This region might be a potential binding site for the modulation of human IL-1β and needs further investigation.

The human IL-1β cytokine also plays a role in different types of cancer. When the mutation data on IL-1β using the cBioPortal web server (Cerami et al., 2012; de Bruijn et al., 2023; Gao et al., 2013), where users can access critical mutations in 10,953 cancer patients, is analyzed, it was revealed that three key residues from LDA, namely N129 (from IgG26-bound) and K65 (from Canakinumab-bound), are the missense mutations observed in patients with uterine endometrioid carcinoma whereas Y68 (from AAL160-bound) is a nonsense mutation observed in a lung adenocarcinoma patient. Thus, further investigation of the interactions between the mutant forms of IL-1β and corresponding antibodies might enlighten the effect of the mutation on their modulatory mechanism and help develop better antibodies for the patients having this specific mutation, serving in personalized medicine.

The experimental studies focused on the combination therapies of two anti-IL-1β antibodies, namely Gevokizumab and Canakinumab, showed their better modulatory effectiveness on IL-1β compared to single antibody treatment (Diwanji et al., 2023). Notably, the LDA results for these antibodies pinpoint distinct affected regions on IL-1β. Therefore, this might be one of the reasons why combination therapies of these antibodies are more effective on IL-1β, and further analysis is needed on the dynamics of IL-1β in complex with both antibodies.

This study reveals novel insights into the antibody-mediated modulation of IL-1β. Critical residues, which pinpoint potential binding sites in human IL-1β, are determined using ClustENMD and LDA. The findings of the study underscore the role of computational tools in unraveling complex allosteric networks, offering mechanistic insights to optimize antigen-targeted biologics.

Author Contributions

The percentages of the author' contributions are presented below. The author reviewed and approved the final version of the manuscript.

	A.U.
C	100
D	100
S	100
DCP	100
DAI	100
L	100
W	100
CR	100
SR	100
PM	100
FA	100

C=Concept, D= design, S= supervision, DCP= data collection and/or processing, DAI= data analysis and/or interpretation, L= literature search, W= writing, CR= critical review, SR= submission and revision, PM= project management, FA= funding acquisition.

Conflict of Interest

The author declared that there is no conflict of interest.

Ethical Consideration

Ethics committee approval was not required for this study because there was no study on animals or humans.

Acknowledgements

AU acknowledges the financial support from the projects at İzmir Institute of Technology (Project no: AUDP-2022-İYTE-3-0041). Google Colab free computing resources are also used in this study.

References

Amadei A, Linssen ABM, Berendsen HJC. 1993. Essential dynamics of proteins. Proteins, 17(4).

Atilgan AR, Durell SR, Jernigan, RL, Demirel MC, Keskin O, Bahar I. 2001. Anisotropy of fluctuation dynamics of proteins with an elastic network model. Biophys J, 80(1): 505–515.

Berman HM, Westbrook J, Feng Z, Gilliland G, Bhat TN, Weissig H, Shindyalov IN, Bourne PE. 2000. The Protein Data Bank. Nucleic Acids Res, 28 (1).

Blech M, Peter D, Fischer P, Bauer MMT, Hafner M, Zeeb M, Nar H. 2013. One Target - Two Different Binding Modes: Structural Insights into Gevokizumab and Canakinumab Interactions to Interleukin-1β. J Mol Biol, 425(1).

Cerami E, Gao J, Dogrusoz U, Gross BE, Sumer SO, Aksoy BA, Jacobsen A, Byrne CJ, Heuer ML, Larsson E, Antipin Y, Reva B, Goldberg AP, Sander C, Schultz N. 2012. The cBio Cancer Genomics Portal: An open platform for exploring multidimensional cancer genomics data. Cancer Discov, 2(5).

de Bruijn I, Kundra R, Mastrogiacomo B, Tran TN, Sikina L, Mazor T, Li X, Ochoa A, Zhao G, Lai B, Abeshouse A, Baiceanu D, Ciftci E, Dogrusoz U, Dufilie A, Erkoc Z, Lara EG, Fu Z, Gross B, Haynes C, Heath A, Higgins D, Jagannathan P, Kalletla K, Kumari P, Lindsay J, Lisman A, Leenknegt B, Lukasse P, Madela D, Madupuri R, van Nierop P, Plantalech O, Quach J, Resnick AC, Rodenburg SYA, Satravada BA, Schaeffer F, Sheridan R, Singh J, Sirohi R, Sumer SO, van Hagen S, Wang A, Wilson M, Zhang H, Zhu K, Rusk N, Brown S, Lavery JA, Panageas KS, Rudolph JE, LeNoue-Newton ML, Warner JL, Guo X, Hunter-Zinck H, Yu TV, Pilai S, Nichols C, Gardos SM, Philip J, Kehl KL, Riely GJ, Schrag D, Lee J, Fiandalo MV, Sweeney SM, Pugh TJ, Sander C, Cerami E, Gao J, Schultz N. 2023. Analysis and visualization of longitudinal genomic and clinical data from the AACR project GENIE Biopharma Collaborative in cBioPortal. Cancer Res, 83(23).

DeLano WL. 2020. The PyMOL molecular graphics system, version 2.3. In Schrödinger LLC, New York , USA, pp: 14-45.

Dinarello CA. 2014. An expanding role for interleukin-1 blockade from gout to cancer. Molecular Medicine, 20.

Diwanji R, O'Brien NA, Choi JE, Nguyen B, Laszewski T, Grauel AL, Yan Z, Xu X, Wu J, Ruddy DA, Piquet M, Pelletier MR, Savchenko A, Charette LS, Rodrik-Outmezguine V, Baum J, Millholland JM, Wong CC, Martin AM, Dranoff G, Pruteanu-Malinici I, Cremasco V, Sabatos-Peyton C, Jayaraman P. 2023. Targeting the IL1b pathway for cancer immunotherapy remodels the tumor microenvironment and enhances antitumor immune responses. Cancer Immunol Res, 11(6).

Doruker P, Atilgan AR, Bahar, I. 2000. Dynamics of proteins predicted by molecular simulations and analytical approaches: Application to α-amylase inhibitor. Proteins: Structure, Function and Genetics, 40(3): 512–524.

Eastman P, Pande VS. 2010. OpenMM: A hardware-independent framework for molecular simulations. Comput Sci Eng, 12(4).

Eastman P, Swails J, Chodera JD, McGibbon RT, Zhao Y, Beauchamp KA, Wang LP, Simmonett AC, Harrigan MP, Stern CD, Wiewiora RP, Brooks BR, Pande VS. 2017. OpenMM 7: Rapid development of high performance algorithms for molecular dynamics. PLoS Comput Biol, 13(7).

Fischman S, Levin I, Rondeau JM, Štrajbl M, Lehmann S, Huber T, Nimrod G, Cebe R, Omer D, Kovarik J, Bernstein S, Sasson Y, Demishtein A, Shlamkovich T, Bluvshtein O, Grossman N, Barak-Fuchs R, Zhenin M, Fastman Y, Twito S, Vana T, Zur N, Ofran Y. 2023. Redirecting an anti-IL-1β antibody to bind a new, unrelated and computationally predicted epitope on hIL-17A. Commun Biol, 6(1).

Gao J, Aksoy BA, Dogrusoz U, Dresdner G, Gross B, Sumer SO, Sun Y, Jacobsen A, Sinha R, Larsson E, Cerami E, Sander C, Schultz N. 2013. Integrative analysis of complex cancer genomics and clinical profiles using the cBioPortal. Sci Signal, 6(269).

Guo B, Fu S, Zhang J, Liu B, Li Z. 2016. Targeting inflammasome/IL-1 pathways for cancer immunotherapy. Sci Rep, 6.

Hommel U, Hurth K, Rondeau JM, Vulpetti A, Ostermeier D, Boettcher A, Brady JP, Hediger M, Lehmann S, Koch E, Blechschmidt A, Yamamoto R, Tundo Dottorello V, Haenni-Holzinger S, Kaiser C, Lehr P, Lingel A, Mureddu L, Schleberger C, Blank J, Ramage P, Freuler F, Eder J, Bornancin F. 2023. Discovery of a selective and biologically active low-molecular weight antagonist of human interleukin-1β. Nat Commun, 14(1).

Humphrey W, Dalke A, Schulten K. 1996. VMD: Visual molecular dynamics. J Mol Graph, 14(1).

Kaynak BT, Zhang S, Bahar I, Doruker P. 2021. ClustENMD: efficient sampling of biomolecular conformational space at atomic resolution. Bioinformatics, 37(21).

Kuo WC, Lee CC, Chang YW, Pang W, Chen HS, Hou SC, Lo SY, Yang AS, Wang AHJ. 2021. Structure-based development of human Interleukin-1β-specific antibody That Simultaneously Inhibits Binding to Both IL-1RI and IL-1RAcP. J Mol Biol, 433(4).

Owyang AM, Issafras H, Corbin J, Ahluwalia K, Larsen P, Pongo E, Handa M, Horwitz AH, Roell MK, Haak-Frendscho M, Masat L.

2011. XOMA 052, a potent, high-affinity monoclonal antibody for the treatment of IL-1β-mediated diseases. MAbs, 3(1).

Pedregosa F, Varoquaux G, Gramfort A, Michel V, Thirion B, Grisel O, Blondel M, Prettenhofer P, Weiss R, Dubourg V, Vanderplas J, Passos A, Cournapeau D, Brucher M, Perrot M, Duchesnay É. 2011. Scikit-learn: Machine learning in Python. J Machine Learning Research, 12.

Ridker PM, Everett BM, Thuren T, MacFadyen JG, Chang WH, Ballantyne C, Fonseca F, Nicolau J, Koenig W, Anker S.D, Kastelein JJP, Cornel JH, Pais P, Pella D, Genest J, Cifkova R, Lorenzatti A, Forster T, Kobalava Z, Vida-Simiti L, Flather M, Shimokawa H, Ogawa H, Dellborg M, Rossi PRF, Troquay RPT, Libby P, Glynn RJ. 2017. Antiinflammatory therapy with canakinumab for atherosclerotic disease. New England J Med, 377(12).

Ridker PM, MacFadyen JG, Thuren T, Everett B, Libby P, Glynn RJ, Lorenzatti A, Krum H, Varigos J, Siostrzonek P, Sinnaeve P, Fonseca F, Nicolau J, Gotcheva N, Genest J, Yong H, Urina-Triana M, Milicic D, Cifkova R, Vettus, R, Koenig W, Anker S. D, Manolis A. J, Wyss F, Forster T, Sigurdsson A, Pais P, Fucili A, Ogawa H, Shimokawa H, Veze I, Petrauskiene B, Salvador L, Kastelein J, Cornel JH, Klemsdal T. O, Medina F, Budaj A, Vida-Simiti L, Kobalava Z, Otasevic P, Pella D, Lainscak M, Seung K. B, Commerford P, Dellborg M, Donath M, Hwang J. J, Kultursay H, Flather M, Ballantyne C, Bilazarian S, Chang W, East C, Forgosh L, Harris B, Ligueros M, Bohula E, Charmarthi B, Cheng S, Chou S, Danik J, McMahon G, Maron B, Ning M. M, Olenchock B, Pande R, Perlstein T, Pradhan A, Rost N, Singhal A, Taqueti V, Wei N, Burris H, Cioffi A, Dalseg A. M, Ghosh N, Gralow J, Mayer T, Rugo H, Fowler V, Limaye A. P, Cosgrove S, Levine D, Lopes R, Scott J, Hilkert R, Tamesby G, Mickel C, Manning B, Woelcke J, Tan M, Manfreda S, Ponce T, Kam J, Saini R, Banker K, Salko T, Nandy P, Tawfik R, O'Neil G, Manne S, Jirvankar P, Lal S, Nema D, Jose J, Collins R, Bailey K, Blumenthal R, Colhoun H, Gersh B. 2017. Effect of interleukin-1β inhibition with canakinumab on incident lung cancer in patients with atherosclerosis: exploratory results from a randomised, double-blind, placebo-controlled trial. The Lancet, 390(10105).

Sakuraba S, Kono H. 2016. Spotting the difference in molecular dynamics simulations of biomolecules. J Chem Physics, 145(7).

Sims JE, Smith DE. 2010. The IL-1 family: Regulators of immunity. In Nature Reviews Immunology,10 (2).

Todorović V, Su Z, Putman CB, Kakavas SJ, Salte KM, McDonald HA, Wetter JB, Paulsboe SE, Sun Q, Gerstein CE, Medina L, Sielaff B, Sadhukhan R, Stockmann H, Richardson PL, Qiu W, Argiriadi MA, Henry RF, Herold J. M, Shotwell JB, McGaraughty SP, Honore P, Gopalakrishnan SM, Sun CC, Scott VE. 2019. Small molecule IL-36γ antagonist as a novel therapeutic approach for plaque psoriasis. Sci Rep, 9(1).

Uyar A, Dickson A. 2021. Perturbation of ACE2 structural ensembles by SARS-CoV-2 spike protein binding. J Chem Theory Comput, 17(9).

Uyar A, Karamyan VT, Dickson A. 2018. Long-range changes in neurolysin dynamics upon inhibitor binding. J Chem Theory Comput, 14(1).

Vigers GPA, Anderson LJ, Caffes P, Brandhuber BJ. 1997. Crystal structure of the type-I interleukin-1 receptor complexed with interleukin-1β. Nature, 386(6621).

Wang D, Zhang S, Li L, Liu X, Mei K, Wang X. 2010. Structural insights into the assembly and activation of IL-1β 2 with its receptors. Nat Immunol, 11(10).

Wong CC, Baum J, Silvestro A, Beste MT, Bharani-Dharan B, Xu S, Wang YA, Wang X, Prescott MF, Krajkovich L, Dugan M, Ridker, PM, Martin AM, Svensson EC. 2020. Inhibition of IL1β by canakinumab may be effective against diverse molecular subtypes of lung cancer: An exploratory analysis of the CANTOS trial AC. Cancer Res, 80(24).

Black Sea Journal of Engineering and Science
doi: 10.34248/bsengineering.1696059

Open Access Journal
e-ISSN: 2619 – 8991

Research Article
Volume 8 - Issue 5: 1450-1459 / September 2025

PRECLINICAL EVALUATION OF BRIGIMADLIN (BI 907828) AS A NOVEL MDM2 INHIBITOR IN ACUTE LYMPHOBLASTIC LEUKEMIA

Erhan APTULLAHOĞLU[1,2]*

[1]*Bilecik Şeyh Edebali University, Faculty of Science, Department of Molecular Biology and Genetics, 11100, Bilecik, Türkiye*
[2]*Bilecik Şeyh Edebali University, Biotechnology Application and Research Centre, 11100, Bilecik, Türkiye*

Abstract: Acute lymphoblastic leukemia (ALL) is a genetically heterogeneous malignancy that frequently retains wild-type *TP53* at diagnosis, rendering it a potential candidate for therapies targeting upstream regulators of p53 such as MDM2. Brigimadlin (BI 907828) is a next-generation, orally bioavailable MDM2-p53 antagonist with established activity in solid tumors, yet its therapeutic potential in hematologic malignancies remains underexplored. In this study, the *in vitro* effects of brigimadlin were investigated using a panel of ALL cell lines with a defined *TP53* status. Cell viability assays demonstrated potent, dose-dependent growth inhibition in *TP53* wild-type cell lines Nalm-6 and RS4;11, with low nanomolar IC_{50} values (38 nM and 18 nM, respectively). In contrast, the *TP53*-mutant CCRF-CEM line displayed resistance, with minimal viability loss even at micromolar concentrations. Microscopic analysis corroborated these findings, showing marked cytotoxicity in *TP53*-functional cell lines but not in *TP53*-deficient one. Quantitative RT-PCR analysis revealed strong induction of p53 target genes, including *CDKN1A*, *PUMA*, *BAX*, and *MDM2*, in wild-type Nalm-6 cells following treatment, consistent with reactivation of p53-mediated transcriptional signature. No gene induction was observed in the *TP53*-mutant cell line, supporting the specificity of brigimadlin's action. Taken together, these findings highlight brigimadlin's potential to selectively target p53-functional ALL cells and provide foundational preclinical evidence for its continued investigation. *In vivo* studies in *TP53* wild-type models are warranted to assess its translational relevance, and future research may explore its integration into combination regimens or biomarker-guided therapeutic strategies.

Keywords: Acute lymphoblastic leukaemia, MDM2-p53 antagonists, MDM2, p53, Brigimadlin (BI 907828)

***Corresponding author:** Bilecik Şeyh Edebali University, Faculty of Science, Department of Molecular Biology and Genetics, 11100, Bilecik, Türkiye
E mail: erhan.aptullahoglu@bilecik.edu.tr (E. APTULLAHOĞLU)
Erhan APTULLAHOĞLU https://orcid.org/0000-0002-9400-0938

Received: May 09, 2025
Accepted: August 06, 2025
Published: September 15, 2025

Cite as: Aptullahoğlu E. 2025. Preclinical evaluation of Brigimadlin (BI 907828) as a novel MDM2 inhibitor in acute Lymphoblastic Leukemia. BSJ Eng Sci, 8(5): 1450-1459.

1. Introduction

Acute lymphoblastic leukemia (ALL) is a heterogeneous hematologic malignancy with diverse genetic alterations and clinical outcomes (Terwilliger and Abdul-Hay, 2017). Despite advances in multi-agent chemotherapy (Specchia et al., 2005; Farooq et al., 2019), targeted agents (Malagola et al., 2016), immunotherapies (Maude et al., 2018; Chitadze et al., 2020), and stem cell transplantation (Thomas et al., 2004; Sun and Huang, 2022), treatment resistance and relapse remain significant challenges, especially in adult patients and those with high-risk features (Pulte et al., 2014; Schwartz and Muffly, 2024). While *TP53*, the gene encoding the tumor suppressor protein p53 (a key regulator of DNA repair, cell cycle arrest, and apoptosis), is typically intact in most ALL cases and generally associated with a more favorable prognosis, a subset of patients with wild-type *TP53* still exhibit resistance to standard therapies. In such cases, wild-type *TP53* may represent a therapeutic opportunity, as pharmacologic reactivation of p53 through MDM2 inhibition offers a mechanistically rational approach to overcoming treatment resistance.

The p53 protein orchestrates essential cellular processes, including DNA repair, cell cycle arrest, and apoptosis, in response to genomic stress (Ozaki and Nakagawara, 2011). Loss of p53 function, either through mutation (Chen et al., 2022) or regulatory inactivation (Kubbutat et al., 1997; Garcia-Cano et al., 2020; Chen et al., 2021), disrupts these pathways, thereby promoting unchecked cell proliferation and survival. Although *TP53* mutations are a defining feature in approximately half of all human cancers (Hollstein et al., 1991) and represent a well-established focus in cancer drug development (Wiman, 2006; Wu et al., 2022), they are relatively rare in ALL. These mutations are detected in fewer than 10% of cases at diagnosis (Chiaretti et al., 2013; Stengel et al., 2014) and rise to approximately 30-40% at relapse (Irving et al., 2016; Yu et al., 2020), with an especially low prevalence in pediatric cases. These data suggest that in ALL, particularly in the *TP53* wild-type subset, alternative mechanisms such as post-translational regulation of p53

may play a more critical role in leukemogenesis.

Among the primary regulators of p53 is MDM2, an E3 ubiquitin ligase that binds to p53, represses its transcriptional activity, and targets it for proteasomal degradation (Oliner et al., 1992). Overexpression of MDM2 has been documented in various malignancies (Hou et al., 2019), including hematologic cancers such as ALL (Zhou et al., 1995; Gustafsson et al., 1998), where it contributes to p53 inactivation (Nag et al., 2013) despite the absence of *TP53* mutations. This has catalyzed interest in pharmacologically targeting the MDM2-p53 interaction to restore p53's tumor suppressor function. The development of small-molecule MDM2 antagonists began with Nutlin-3 (Vassilev, 2004) and has extended to newer-generation compounds such as RG7388 (Ding et al., 2013), HDM201 (Furet et al., 2016), AMG232 (Rew and Sun, 2014), DS-3032 (Arnhold et al., 2018), ASTX295 (Willmore et al., 2024), and MI-77301 (Wang et al., 2014). These agents have demonstrated promising preclinical efficacy, including in models of leukemia and lymphoma (Ciardullo et al., 2016; Wu et al., 2018; Ciardullo et al., 2019; Ghotaslou et al., 2022; Aptullahoglu, Ciardullo, et al., 2023; Johansson et al., 2023; Bell et al., 2024; Gungordu and Aptullahoglu, 2024; Aptullahoglu et al., 2025). Many of these inhibitors are currently under investigation in clinical trials, both as single-agent therapies (Stein et al., 2022; Koyama et al., 2023) and in combination with other treatments (Abdul Razak et al., 2022; Daver et al., 2022; Konopleva et al., 2022).

While MDM2 inhibitors are supported by a strong mechanistic rationale, many early clinical candidates have failed to translate this promise into meaningful clinical efficacy and have been associated with significant hematologic toxicity (Pi et al., 2019). Thrombocytopenia and neutropenia, in particular, have been identified as dose-limiting toxicities that restrict their therapeutic potential (Pi et al., 2019). Moreover, clinical investigations have largely concentrated on solid tumors with high mutational burdens or refractory phenotypes. In contrast, leukemias may be more biologically suited to benefit from MDM2-targeted therapy due to the frequent retention of wild-type *TP53*. This positions these diseases as rational targets for MDM2 inhibition.

Brigimadlin (BI 907828) is a next-generation, orally bioavailable MDM2-p53 antagonist that has demonstrated potent antitumor activity in preclinical models, particularly in *TP53* wild-type, MDM2-amplified cancers such as dedifferentiated liposarcoma (DDLPS) (Rudolph et al., 2018; Cornillie et al., 2020; Gollner et al., 2024). The compound exhibits favorable pharmacokinetic characteristics, including high oral bioavailability and dose-proportional exposure (Sarkaria et al., 2024). The compound is presently undergoing evaluation in several phase I and II clinical trials, predominantly in patients with advanced solid tumors (Clinical Trial Identifiers: NCT05376800, NCT06619509, NCT03449381, and NCT05512377). Among the broad array of MDM2 inhibitors developed to date, BI 907828 stands out due to its optimized balance of pharmacologic efficacy and clinical tolerability. While first-generation compounds such as nutlin-3a were instrumental in elucidating the biological role of MDM2 inhibition, their clinical utility was limited by suboptimal pharmacokinetics. Similarly, second-generation agents like idasanutlin showed promising on-target effects but were hampered by gastrointestinal toxicity and limited clinical benefit in AML trials (Yee et al., 2021; Konopleva et al., 2022). In contrast, BI 907828 was specifically engineered to allow intermittent, high-dose administration, a strategy that enhances therapeutic impact while minimizing cumulative toxicity. Preclinical studies have demonstrated robust p53 pathway activation at nanomolar concentrations and significant tumor regression in xenograft models (Hao et al., 2023; Gollner et al., 2024). Early-phase clinical data further support its favorable safety, pharmacokinetic profile, and durable on-target activity under less frequent dosing regimens (LoRusso et al., 2023).

However, its efficacy in hematologic malignancies, and in ALL in particular, remains largely uncharacterized. This study was designed to assess the *in vitro* therapeutic potential of BI 907828 in ALL cells with defined *TP53* status.The findings may help inform the future clinical utility of MDM2 inhibition strategies in hematologic cancers.

2. Materials and Methods

2.1. Cell lines and Compound

The human ALL cell lines Nalm-6, RS4;11, and CCRF-CEM, sourced from authenticated cell line repositories (ATCC), were cultured in RPMI-1640 medium (Gibco), supplemented with 10% fetal bovine serum (FBS) (Gibco) and 100 U/mL penicillin/streptomycin (Sigma-Aldrich). The cells were maintained in appropriate culture vessels (Labselect) at 37°C in a CO2 incubator (Esco) with a 5% CO2 atmosphere. Cell viability, morphology, and potential contamination were carefully monitored on a daily basis. The cell panel included two cell lines with wild-type *TP53*, Nalm-6 and RS4;11, as well as one cell line with a mutated *TP53*, CCRF-CEM, which harbors missense mutations at codons 175 and 248. These mutations affect the DNA-binding domain of p53 in the CCRF-CEM cell line (Gungordu and Aptullahoglu, 2024). Brigimadlin (BI 907828), purchased from Selleckchem, was dissolved in dimethyl sulfoxide (DMSO, Sigma-Aldrich) and used at a final concentration of 0.5% (v/v) DMSO for experimental purposes.

2.2. Cell Viability Assay

Cells were plated in 96-well plates (Labselect) at a density of 100 µL of complete medium per well, 24 hours prior to treatment with the inhibitor. The optimal initial cell density of 2.5×10^5 cells/mL, established from growth curve analysis for each cell line, ensured at least two doubling times over the 72-hour treatment period, and was used in subsequent XTT assays. On the following day,

the cells were exposed to BI 907828, with the final concentration of DMSO maintained at 0.5% (v/v) across all treatment and control groups, and incubated for 72 hours. Treatment concentrations were selected based on preliminary optimization studies using a wide dose range to capture the sensitivity profiles of each cell line. Additionally, published IC_{50} values for brigimadlin in *TP53* wild-type and mutant tumor models were considered to define a relevant starting range (Gollner et al., 2024). A 72-hour incubation period was chosen to allow sufficient time for cumulative cytotoxic effects to manifest. Cell viability was evaluated using the XTT assay kit (Cayman Chemical Company), which quantifies mitochondrial activity (Scudiero et al., 1988). Viability percentages were calculated by comparing the treated cells to the DMSO control wells. The half-maximal inhibitory concentration (IC50) values were derived from at least three independent experiments, where IC50 is defined as the concentration required to inhibit mitochondrial activity by 50%.

2.3. Cell Imaging Post-Treatment with BI 907828

After a 72-hour incubation period following treatment with the vehicle control (VC), 50 nM, and 500 nM concentrations of BI 907828, cell morphology and confluence were assessed using an inverted phase-contrast microscope. Final DMSO concentration was maintained at 0.5% (v/v) across all treatment and control groups. Images were captured from multiple fields of view per well to ensure representative sampling of the entire well surface. For each condition, at least three independent replicate wells were imaged to ensure reproducibility. The captured images were analyzed qualitatively to evaluate cell confluence, indicative of cytotoxicity or treatment effects.

2.4. RNA Extraction and Quantitative Real-Time PCR (qRT-PCR) Analysis

Cells were seeded at a density of 1×10^6 cells/mL in 12-well plates (Labselect) and treated with BI 907828 for 24 hours. Final DMSO concentration was maintained at 0.5% (v/v) across all treatment and control groups. The 24-hour time point was selected based on previous studies (Ohtani et al., 2004; Ciardullo et al., 2019), which demonstrated that transcriptional changes in p53 pathway-associated downstream genes are most prominently captured at this interval, making it a suitable time frame for assessing p53-mediated gene expression responses. Total RNA was isolated using the Aurum™ Total RNA Mini Kit (Bio-Rad). RNA integrity and concentration were determined using a spectrophotometer. Complementary DNA (cDNA) synthesis was carried out with the Promega reverse transcriptase kit. Quantitative real-time PCR (qRT-PCR) was performed using SYBR Green Master Mix (Life Technologies, Thermo Fisher Scientific) according to the manufacturer's protocol. Each qRT-PCR reaction was carried out with 20 ng of cDNA in a final volume of 10 µL, employing standard cycling conditions. Amplification products were monitored in real-time using a Roche LightCycler 480® system. PCR primers (listed in Table 1) were designed based on cDNA sequences (GenBank™) to assess alterations in gene expression. Gene expression levels were quantified using the $2^{-\Delta\Delta CT}$ method (also known as the comparative CT method). In this approach, the threshold cycle (CT) values of target genes were first normalized to the CT value of the reference (housekeeping) gene GAPDH to obtain ΔCT ($\Delta CT = CT_{TARGET} - CT_{GAPDH}$). These ΔCT values were then compared between treated and corresponding untreated (DMSO control) samples to calculate ΔΔCT ($\Delta\Delta CT = \Delta CT_{TREATED} - \Delta CT_{CONTROL}$). Finally, the relative gene expression was calculated as $2^{-\Delta\Delta CT}$, representing the fold change in gene expression relative to the control group. A no-template control was included to rule out contamination with external DNA.

Table 1. Forward and reverse primer sequences used for quantitative real-time PCR.

Genes	Forward Primers (5'-3')	Reverse Primers (5'-3')
GAPDH	CGACCACTTTGTCAAGCTCA	GGGTCTTACTCCTTGGAGGC
CDKN1A	TGTCCGCAGAACCCATGC	AAAGTCGAAGTTCCTCGCTC
BAX	CCCGAGAGGTCTTTTTCCGAG	CCAGCCCATGATGGTTCTGAT
PUMA (BBC3)	ACCTCAACGCACAGTACGA	CTGGGTAAGGGCAGGAGTC
CASP3	ATGGAAGCGAATCAATGGA	TGTACCAGACCGAGATGTC
BCL-2	GGTGGGGTCATGTGTGTGG	CGGTTCAGGTACTCAGTCATCC
MDM2	AGTAGCAGTGAATCTACAGGGA	CTGATCCAACCAATCACCTGAAT
TP53	TGCGTGTGGAGTATTTGGAT	GGTACAGTCAGAGCCAACCTC

2.5. Statistical Analysis

Data from the repeated experiments were presented as mean±standard error of the mean (SEM) unless otherwise stated. Statistical tests were carried out using GraphPad Prism 6 software (version 8.0.1). Comparisons between each treatment and its matched DMSO control were made using paired t-tests (*P<0.05; **P<0.01; ***P<0.001; ****P<0.0001*).* Given the limited number of biological replicates (n=3), formal normality testing was not performed; nevertheless, the paired t-test was chosen as a standard method for matched-sample comparisons in similar preclinical studies. qRT-PCR data were analyzed using the Roche LightCycler 480 Software (version 1.5), according to the manufacturer's instructions, and subsequently visualized using GraphPad Prism 6 software (version 8.0.1).

3. Results

Three ALL cell lines were treated with increasing concentrations of the MDM2 inhibitor BI-907828 to evaluate its cytotoxic effects. Cell viability was measured 72 hours post-treatment using the XTT assay, and results were normalized to the vehicle control (0 nM DMSO). BI-907828 treatment resulted in a dose-dependent reduction in viability in two *TP53* wild-type cell lines, Nalm-6 and RS4;11, with respective IC_{50} values of 38 ± 5 nM and 18 ± 7 nM (Figure 1, Table 2), indicating high sensitivity to MDM2 inhibition. In contrast, the CCRF-CEM cell line, which carries two missense mutations within the DNA-binding domain of the *TP53* gene, exhibited marked resistance to BI-907828, with an IC_{50} value exceeding 3000 nM (Figure 1, Table 2).

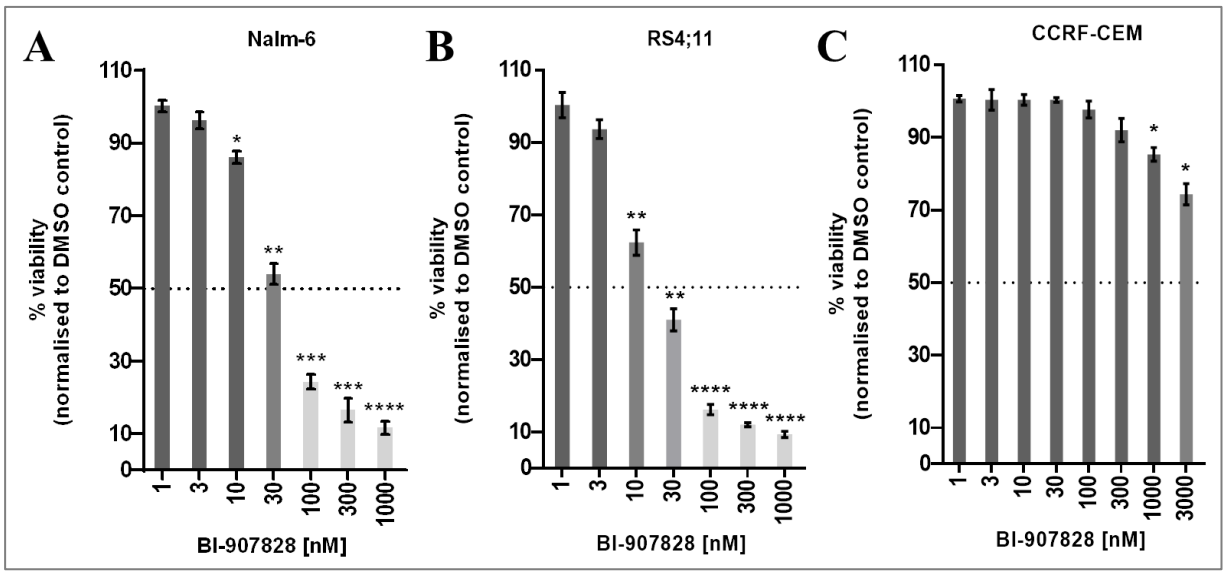

Figure 1. Dose-dependent reduction in cell viability induced by BI-907828 in three distinct ALL cell lines. The ALL cell lines Nalm-6 (A), RS4;11 (B), and CCRF-CEM (C) were exposed to increasing concentrations of BI-907828, ranging from 1 to 1000 nM (up to 3000 nM for CCRF-CEM). Following 72 hours of treatment, cellular metabolic activity was evaluated using the XTT assay. Viability was normalized to the DMSO-treated control and expressed as a percentage. Results are shown as the mean ± standard error of the mean (SEM) from three independent biological replicates. For each concentration, statistical comparison with the control was performed using paired t-tests. Statistically significant differences are indicated on the graphs as follows: **P*<0.05; ***P*<0.01; ****P*<0.001; *****P*<0.0001.

Table 2. *TP53* status and BI-907828 sensitivity in ALL cell lines used in this study.

Cell lines	Cell type	* *TP53* Status	** BI 907828 (nM)
Nalm-6	B cell ALL	WT	38 ± 5
RS4;11	B cell ALL	WT	18 ± 7
CCRF-CEM	T cell ALL	Mutant (Heterozygous) c.524G>A;p.R175H & c.743G>A;p.R248Q	>3000

**TP53* gene mutational status were taken from COSMIC (Catalogue of Somatic Mutations in Cancer) database. **The IC_{50} values shown represent the mean of at least n=3 independent repeats±SEM. WT: wild-type; nM: nanomolar; ALL: acute lymphoblastic leukemia.

Following a 72-hour incubation with vehicle control (VC), 50 nM, or 500 nM of BI-907828, cell morphology and confluence were examined using inverted phase-contrast microscopy. Qualitative analysis of the images revealed dose-dependent reductions in cell confluence for the *TP53* wild-type cell lines, Nalm-6 and RS4;11(Figure 2). Notably, RS4;11 cells showed a marked decrease in cell density even at 50 nM, which became more pronounced at 500 nM. A similar, though slightly less dramatic, effect was observed in Nalm-6 cells. In contrast, the *TP53*-mutant CCRF-CEM cell line exhibited no observable changes in cell confluence or morphology, even at the highest concentration tested, suggesting resistance to BI-907828–induced cytotoxicity (Figure 2).

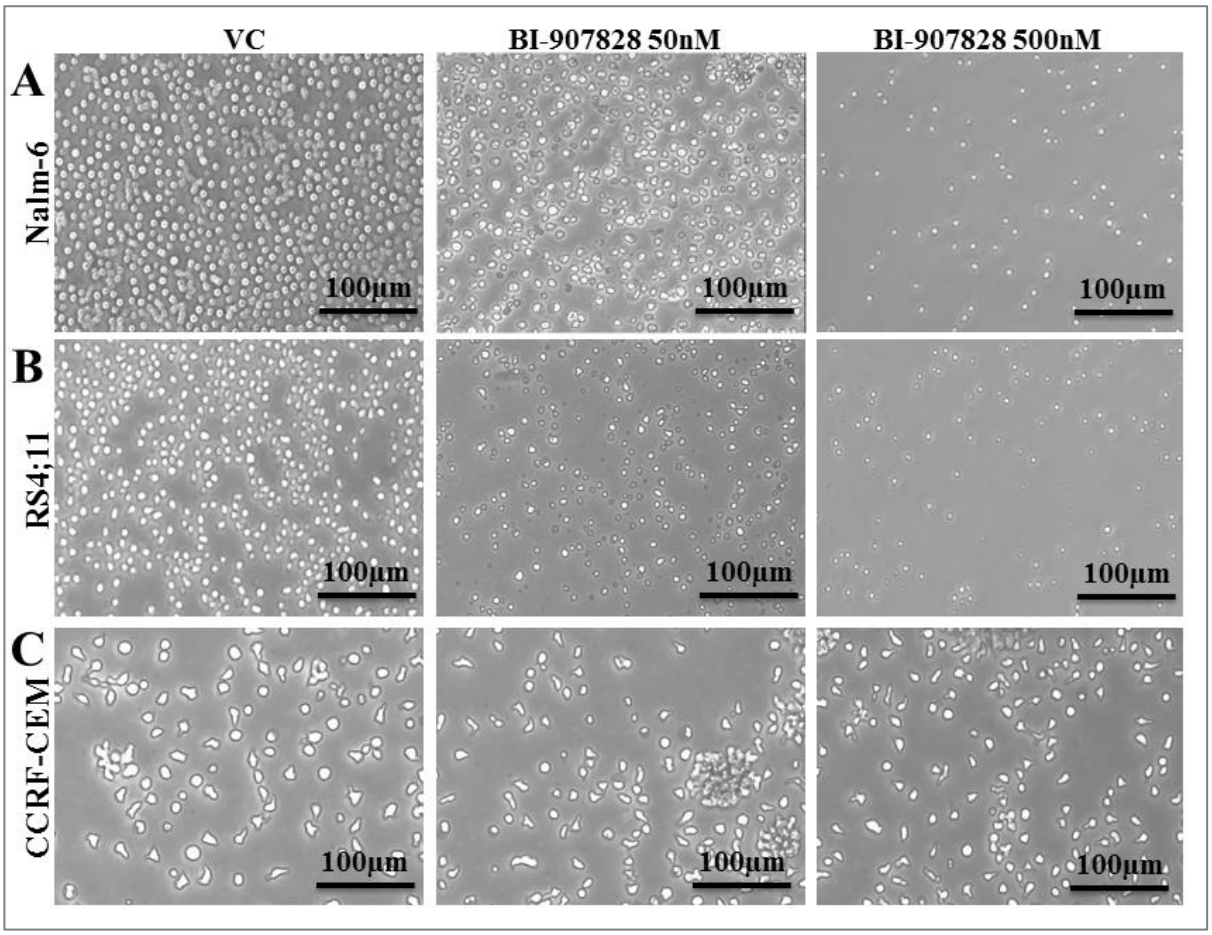

Figure 2. Effects of BI-907828 on the proliferation of Nalm-6 (A), RS4;11 (B), and CCRF-CEM (C) cells. Changes in cell density were observed following treatment with BI-907828. Cells were incubated for 72 hours with 0 nM (vehicle control, VC), 50 nM, or 500 nM of BI-907828 and imaged using phase-contrast microscopy. Imaging was performed in three independent biological replicates, and representative images are presented. Scale bar: 100 µm. nM: nanomolar.

To test the hypothesis that inhibition of the p53 negative regulator MDM2 activates p53-dependent signaling pathways leading to cell death in ALL cells, the mRNA expression levels of several canonical p53 target genes involved in cell cycle arrest, apoptosis, and auto-regulation were quantitatively assessed using qRT-PCR. Quantitative RT-PCR was performed on two ALL cell lines treated with 100 nM and 300 nM of BI-907828, with an additional 1000 nM dose included for the CCRF-CEM cell line. Gene expression was normalized to GAPDH and compared to the DMSO-treated control.

In the *TP53* wild-type Nalm-6 cell line, BI-907828 treatment significantly upregulated multiple p53 transcriptional targets. Among these, *CDKN1A* (encoding p21), a key mediator of p53-induced cell cycle arrest, and *MDM2*, which participates in the negative feedback regulation of p53, showed robust increases in expression (Figure 3A). Furthermore, treatment with 300 nM BI-907828 induced marked upregulation of pro-apoptotic genes, including *PUMA* (7.3-fold), *BAX* (3.4-fold), and *CASP3* (2.2-fold), indicating activation of the apoptotic pathway. Concurrently, a modest downregulation of the anti-apoptotic gene *BCL2* was observed, supporting a shift toward a pro-apoptotic transcriptional profile. As expected, no significant changes in *TP53* mRNA levels were detected, consistent with the mechanism of MDM2 inhibitors, which stabilize existing p53 protein rather than increasing its transcription.

In contrast, the CCRF-CEM cell line, which harbors two missense mutations in the DNA-binding domain of *TP53* and was previously shown to be resistant to BI-907828-induced cytotoxicity (Figure 1C), did not exhibit any significant transcriptional activation of p53 target genes at any tested concentration (Figure 3B).

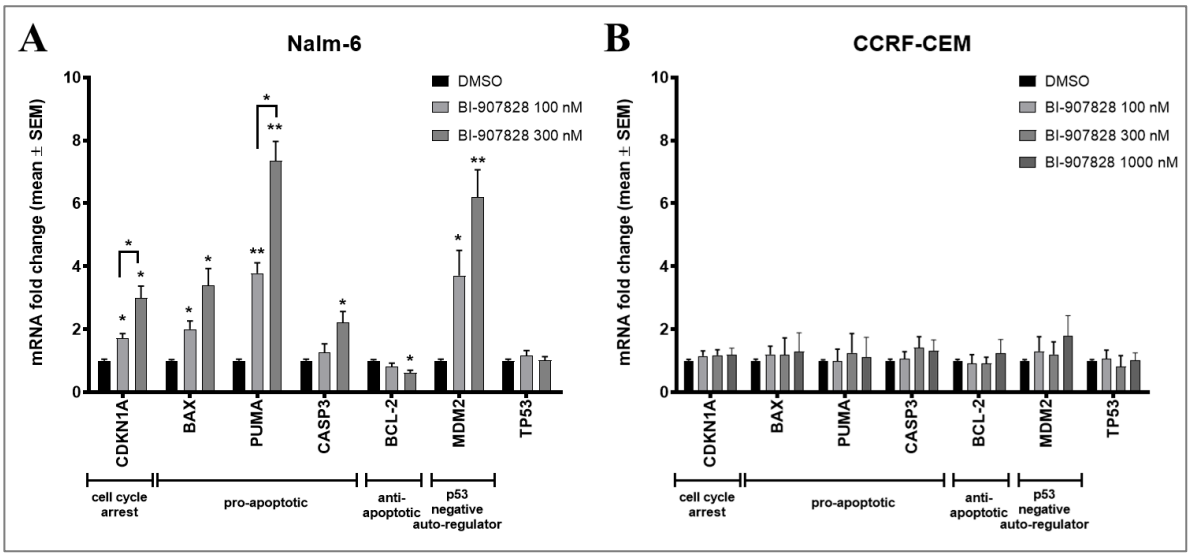

Figure 3. Fold change in mRNA expression of p53 target genes following BI-907828 treatment, measured by qRT–PCR. mRNA levels of p53-regulated target genes were quantified after 24-hour treatment with 100 nM or 300 nM of the MDM2 inhibitor BI-907828 (with an additional 1000 nM dose applied in CCRF-CEM cells). Gene expression was normalized to GAPDH and compared to the DMSO vehicle control in Nalm-6 (A) and CCRF-CEM (B) cell lines. Statistical significance was determined using paired t-tests (*P<0.05; ** P<0.01) and is indicated above the bars for comparisons versus the DMSO control. Differences between BI-907828 doses are marked above the horizontal lines, with only statistically significant values (P<0.05) shown. Data represent the mean ± standard error of the mean (SEM) from three independent biological replicates. nM: nanomolar.

4. Discussion

This study evaluated the anti-leukemic efficacy of the novel, orally bioavailable MDM2-p53 antagonist brigimadlin in a panel of ALL cell lines with defined *TP53* status. The results provide compelling evidence that brigimadlin exerts potent cytotoxic activity in *TP53* wild-type ALL cells by reactivating p53-dependent signaling pathways, while *TP53*-mutant cells remain largely unresponsive, underlining the importance of functional p53 in mediating the therapeutic response to MDM2 inhibition.

The dose-dependent inhibition of proliferation observed in Nalm-6 and RS4;11 cells—both harboring wild-type *TP53*—with IC_{50} values in the low nanomolar range, highlights brigimadlin's high potency and therapeutic potential in p53-intact leukemic contexts. These results align with prior studies of MDM2 inhibitors such as RG7388 and HDM201, which similarly demonstrated selective cytotoxicity in p53-functional hematologic malignancies (Ciardullo et al., 2019; Gungordu and Aptullahoglu, 2024; Aptullahoglu et al., 2025). Notably, RS4;11 cells exhibited particularly high sensitivity, suggesting possible cell line–specific factors that enhance responsiveness, such as MDM2 amplification or differences in basal p53 activity. In contrast, CCRF-CEM cells, which harbor dual missense mutations in the DNA-binding domain of *TP53* (R175H and R248Q) (see Table 2), exhibited profound resistance to brigimadlin, consistent with a loss of transcriptionally active p53 and impaired engagement of downstream apoptotic pathways.

Microscopy-based morphological assessments corroborated these findings, revealing clear reductions in confluence in *TP53* wild-type cells following treatment, while *TP53*-mutant cells remained morphologically unchanged with no alteration in cell density. These phenotypic observations reinforce the central role of functional p53 in mediating the biological response to MDM2 antagonism and are consistent with brigimadlin's mechanism of action: disrupting the MDM2-p53 interaction, thereby stabilizing and activating endogenous p53.

Mechanistically, quantitative real-time PCR analyses further confirmed the activation of canonical p53 transcriptional targets following brigimadlin treatment in *TP53* wild-type cells. Upregulation of *CDKN1A* (encoding p21 protein) and *MDM2* indicates intact p53-mediated cell cycle regulation and autoregulatory feedback loops. Additionally, the significant induction of apoptotic effectors such as *PUMA*, *BAX*, and *CASP3*, coupled with the downregulation of anti-apoptotic *BCL2*, suggests a robust pro-apoptotic transcriptional shift, consistent with p53-driven intrinsic apoptosis. These transcriptional changes were completely absent in CCRF-CEM cells at all tested concentrations, supporting the idea that p53 functionality is essential for brigimadlin's activity.

Collectively, these data position brigimadlin as a promising candidate for targeted therapy in *TP53* wild-type ALL. Given the relatively low prevalence of *TP53* mutations in newly diagnosed ALL (Stengel et al., 2014; Irving et al., 2016) and the increasing interest in precision oncology, brigimadlin may represent a viable therapeutic strategy for a substantial subset of ALL patients.

Importantly, the differential sensitivity observed based on *TP53* mutational status supports the development of predictive biomarkers to guide patient selection in future clinical trials.

Combination strategies may further enhance the therapeutic impact of brigimadlin. For instance, MDM2 inhibitors have previously been shown to synergize with DNA-damaging agents such as cytarabine (Shabashvili et al., 2022) or with other targeted therapies (Aptullahoglu, Ciardullo, et al., 2023; Bell et al., 2024) by enhancing p53-mediated apoptosis. Similarly, co-targeting anti-apoptotic BCL2 with agents like venetoclax has demonstrated synergism with p53 reactivation in lymphoid and myeloid malignancies (Lehmann et al., 2016; Hohtari et al., 2022), potentially lowering the apoptotic threshold in resistant clones. Furthermore, given p53's emerging role in modulating immune checkpoint expression and tumor immunogenicity (Munoz-Fontela et al., 2016), combining MDM2 inhibitors with immunotherapeutic agents (Fang et al., 2019; Tolcher et al., 2019) may provide additional clinical benefit, particularly in settings where immune evasion contributes to disease persistence.

To better understand both sensitivity and potential resistance, comprehensive molecular profiling including whole transcriptome and exome sequencing should be employed. These approaches may uncover predictive biomarkers of response or resistance (e.g., *MDM2* amplification, alternative splicing (Aptullahoglu, Wallis, et al., 2023), or deregulation of p53 co-factors) and inform patient stratification in future clinical trials.

Nonetheless, certain considerations should be acknowledged. This study was limited to *in vitro* analyses of established ALL cell lines and may not fully reflect the heterogeneity of patient-derived leukemias or the influence of the bone marrow microenvironment. The lack of *in vivo* validation restricts the clinical applicability of these findings, particularly with respect to drug absorption, distribution, metabolism, and potential immunological interactions. Although the current study did not identify any acquired resistance, the scope was limited to a small panel of established cell lines. It remains possible that in a more heterogeneous patient-derived setting, intrinsic or adaptive resistance mechanisms could emerge as observed in some preclinical studies based on MDM2 inhibition (Aptullahoglu et al., 2024). Additionally, although the study clearly demonstrates that brigimadlin's activity is p53-dependent, the molecular underpinnings of the differential sensitivity between Nalm-6 and RS4;11 warrant further investigation. Factors such as MDM2 expression levels, alterations in upstream regulators (e.g., ARF, ATM), or differential expression of pro-survival factors may modulate the cellular response and should be systematically evaluated. Also, reliance on single end-point measurements of gene expression precludes insight into temporal response dynamics; incorporating longitudinal sampling or single-cell transcriptomic approaches in future work would provide a more detailed understanding of treatment kinetics. Lastly, although the data emphasize a strict requirement for functional p53 in mediating brigimadlin's cytotoxicity, possible off-target effects were not systematically evaluated, which merits further investigation through comprehensive mechanistic assays or high-throughput combination screens. Finally, while gene expression changes were evaluated at the mRNA level via qRT-PCR, corresponding protein-level analyses were not performed. Given that mRNA abundance does not always correlate with protein expression due to post-transcriptional and translational regulation, validating key findings at the protein level (e.g., via western blot or flow cytometry) would strengthen the biological relevance of the results.

5. Conclusion

This study provides the first comprehensive preclinical evidence of brigimadlin's potent and selective anti-leukemic activity in *TP53* wild-type ALL cells. Using a combination of viability assays, morphological assessments, and transcriptional profiling, this study demonstrates that brigimadlin effectively suppresses proliferation and activates canonical p53 target genes involved in cell cycle arrest and apoptosis, in a strictly p53-dependent manner. The complete absence of transcriptional responses in *TP53*-mutant cells confirms the compound's on-target mechanism and underscores the critical role of functional p53 in mediating its cytotoxic effects. These findings highlight the therapeutic potential of brigimadlin as a precision medicine targeting the MDM2–p53 axis in genetically defined subsets of ALL and support its further clinical investigation in hematologic malignancies characterized by intact p53 signaling.

Author Contributions

The percentages of the author' contributions are presented below. The author reviewed and approved the final version of the manuscript.

	E.A.
C	100
D	100
S	100
DCP	100
DAI	100
L	100
W	100
CR	100
SR	100
PM	100
FA	100

C=Concept, D= design, S= supervision, DCP= data collection and/or processing, DAI= data analysis and/or interpretation, L= literature search, W= writing, CR= critical review, SR= submission and revision, PM= project management, FA= funding acquisition.

Conflict of Interest

The author declared that there is no conflict of interest.

Ethical Consideration

Ethics committee approval was not required for this study because of there was no study on animals or humans.

Acknowledgements

This study was supported by the TÜBİTAK R&D projects numbered 121S986 and 323S070, both led by the author. We gratefully acknowledge Prof. Şehime Gülsün Temel and Adem Alemdar from Bursa Uludağ University for conducting the STR profiling of the ALL cell lines.

References

Abdul Razak AR, Bauer S, Suarez C, Lin CC, Quek R, Hutter-Kronke ML, Cubedo R, Ferretti S, Guerreiro N, Jullion A, Orlando EJ, Clementi G, Sand Dejmek J, Halilovic E, Fabre C, Blay JY, Italiano A. 2022. Co-targeting of MDM2 and CDK4/6 with siremadlin and ribociclib for the treatment of patients with well-differentiated or dedifferentiated liposarcoma: results from a proof-of-concept, phase Ib study. Clin Cancer Res, 28: 1087-1097.

Aptullahoglu E, Ciardullo C, Wallis JP, Marr H, Marshall S, Bown N, Willmore E, Lunec J. 2023. Splicing modulation results in aberrant ısoforms and protein products of p53 pathway genes and the sensitization of B cells to non-genotoxic MDM2 Inhibition. Int J Mol Sci, 24(3): 2410.

Aptullahoglu E, Howladar M, Wallis JP, Marr H, Marshall S, Irving J, Willmore E, Lunec J. 2025. Targeting the MDM2-p53 ınteraction with siremadlin: a promising therapeutic strategy for treating TP53 wild-type chronic lymphocytic leukemia. cancers (Basel), 17(2): 274.

Aptullahoglu E, Nakjang S, Wallis JP, Marr H, Marshall S, Willmore E, Lunec J. 2024. RNA sequencing reveals candidate genes and pathways associated with resistance to MDM2 antagonist ıdasanutlin in TP53 wild-type chronic lymphocytic leukemia. Biomedicines, 12(7): 1388.

Aptullahoglu E, Wallis JP, Marr H, Marshall S, Bown N, Willmore E, Lunec J. 2023. SF3B1 Mutations are associated with resistance to non-genotoxic MDM2 ınhibition in chronic lymphocytic leukemia. Int J Mol Sci, 24(12): 11335.

Arnhold V, Schmelz K, Proba J, Winkler A, Wunschel J, Deubzer HE, Kunkele A, Eggert A, Schulte JH, Hundsdoerfer P. 2018. Reactivating TP53 signaling by the novel MDM2 inhibitor DS-3032b as a therapeutic option for high-risk neuroblastoma. Oncotarget, 9: 2304-2319.

Bell HL, Blair HJ, Jepson Gosling SJ, Galler M, Astley D, Moorman AV, Heidenreich O, Veal GJ, van Delft FW, Lunec J, Irving JAE. 2024. Combination p53 activation and BCL-x(L)/BCL-2 inhibition as a therapeutic strategy in high-risk and relapsed acute lymphoblastic leukemia. Leukemia, 38: 1223-1235.

Chen X, Zhang T, Su W, Dou Z, Zhao D, Jin X, Lei H, Wang J, Xie X, Cheng B, Li Q, Zhang H, Di C. 2022. Mutant p53 in cancer: from molecular mechanism to therapeutic modulation. Cell Death Dis, 13: 974.

Chen Y, Hao Q, Wang S, Cao M, Huang Y, Weng X, Wang J, Zhang Z, He X, Lu H, Zhou X. 2021. Inactivation of the tumor suppressor p53 by long noncoding RNA RMRP. Proc Natl Acad Sci, 118(29): e2026813118.

Chiaretti S, Brugnoletti F, Tavolaro S, Bonina S, Paoloni F, Marinelli M, Patten N, Bonifacio M, Kropp MG, Sica S, Guarini A, Foa R. 2013. TP53 mutations are frequent in adult acute lymphoblastic leukemia cases negative for recurrent fusion genes and correlate with poor response to induction therapy. Haematologica, 98: e59-61.

Chitadze G, Laqua A, Lettau M, Baldus CD, Bruggemann M. 2020. Bispecific antibodies in acute lymphoblastic leukemia therapy. Expert Rev Hematol, 13: 1211-1233.

Ciardullo C, Aptullahoglu E, Woodhouse L, Lin WY, Wallis JP, Marr H, Marshall S, Bown N, Willmore E, Lunec J. 2019. Non-genotoxic MDM2 inhibition selectively induces a pro-apoptotic p53 gene signature in chronic lymphocytic leukemia cells. Haematologica, 104: 2429-2442.

Ciardullo C, Woodhouse L, Aptullahoglu E, Wallis JP, Marr HJ, Marshall SR, Bown N, Willmore E, Lunec J. 2016. The p53-MDM2 antagonist RG7388 activates p53 and ınduces a predominantly pro-apoptotic gene expression signature in chronic lymphocytic leukemia. Blood, 128(22): 893.

Cornillie J, Wozniak A, Li H, Gebreyohannes YK, Wellens J, Hompes D, Debiec-Rychter M, Sciot R, Schoffski P. 2020. Anti-tumor activity of the MDM2-TP53 inhibitor BI-907828 in dedifferentiated liposarcoma patient-derived xenograft models harboring MDM2 amplification. Clin Transl Oncol, 22: 546-554.

Daver NG, Dail M, Garcia JS, Jonas BA, Yee KWL, Kelly KR, Vey N, Assouline S, Roboz GJ, Paolini S, Pollyea DA, Tafuri A, Brandwein JM, Pigneux A, Powell BL, Fenaux P, Olin RL, Visani G, Martinelli G, Onishi M, Wang J, Huang W, Green C, Ott MG, Hong WJ, Konopleva MY, Andreeff M. 2022. Venetoclax and idasanutlin in relapsed/refractory AML: a non-randomized, open-label phase 1b trial. Blood, 141(11): 1265-1276.

Ding Q, Zhang Z, Liu JJ, Jiang N, Zhang J, Ross TM, Chu XJ, Bartkovitz D, Podlaski F, Janson C, Tovar C, Filipovic ZM, Higgins B, Glenn K, Packman K, Vassilev LT, Graves B. 2013. Discovery of RG7388, a potent and selective p53-MDM2 inhibitor in clinical development. J Med Chem, 56: 5979-5983.

Fang DD, Tang Q, Kong Y, Wang Q, Gu J, Fang X, Zou P, Rong T, Wang J, Yang D, Zhai Y. 2019. MDM2 inhibitor APG-115 synergizes with PD-1 blockade through enhancing antitumor immunity in the tumor microenvironment. J Immunother Cancer, 7: 327.

Farooq MU, Mushtaq F, Farooq A, Khan DH, Mir MA. 2019. FLAG vs FLAG-IDA: outcomes in relapsed/refractory acute leukemias. Cancer Chemother Pharmacol, 83: 1191-1193.

Furet P, Masuya K, Kallen J, Stachyra-Valat T, Ruetz S, Guagnano V, Holzer P, Mah R, Stutz S, Vaupel A, Chene P, Jeay S, Schlapbach A. 2016. Discovery of a novel class of highly potent inhibitors of the p53-MDM2 interaction by structure-based design starting from a conformational argument. Bioorg Med Chem Lett, 26: 4837-4841.

Garcia-Cano J, Sanchez-Tena S, Sala-Gaston J, Figueras A, Vinals F, Bartrons R, Ventura F, Rosa JL. 2020. Regulation of the MDM2-p53 pathway by the ubiquitin ligase HERC2. Mol Oncol, 14: 69-86.

Ghotaslou A, Samii A, Boustani H, Kiani Ghalesardi O, Shahidi M. 2022. AMG-232, a New Inhibitor of MDM-2, enhance doxorubicin efficiency in pre-B acute lymphoblastic leukemia cells. Rep Biochem Mol Biol, 11: 111-124.

Gollner A, Rudolph D, Weyer-Czernilofsky U, Baumgartinger R, Jung P, Weinstabl H, Ramharter J, Grempler R, Quant J, Rinnenthal J, Perez Pitarch A, Golubovic B, Gerlach D, Bader G, Wetzel K, Otto S, Mandl C, Boehmelt G, McConnell DB, Kraut N, Sini P. 2024. Discovery and characterization of brigimadlin, a novel and highly potent MDM2-p53 antagonist suitable for ıntermittent dose schedules. Mol Cancer Ther, 23: 1689-1702.

Gungordu S, Aptullahoglu E. 2024. Targeting MDM2-mediated suppression of p53 with idasanutlin: a promising therapeutic

approach for acute lymphoblastic leukemia. Invest New Drugs, 42: 603-611.

Gustafsson B, Stal O. 1998. Overexpression of MDM2 in acute childhood lymphoblastic leukemia. Pediatr Hematol Oncol, 15: 519-526.

Hao X, Bahia RK, Cseh O, Bozek DA, Blake S, Rinnenthal J, Weyer-Czernilofsky U, Rudolph D, Artee Luchman H. 2023. BI-907828, a novel potent MDM2 inhibitor, inhibits glioblastoma brain tumor stem cells in vitro and prolongs survival in orthotopic xenograft mouse models. Neuro Oncol, 25: 913-926.

Hohtari H, Kankainen M, Adnan-Awad S, Yadav B, Potdar S, Ianevski A, Dufva O, Heckman C, Sexl V, Kytola S, Mustjoki S, Porkka K. 2022. Targeting apoptosis pathways with BCL2 and MDM2 ınhibitors in adult B-cell acute lymphoblastic leukemia. Hemasphere, 6: e701.

Hollstein M, Sidransky D, Vogelstein B, Harris CC. 1991. p53 mutations in human cancers. Science, 253: 49-53.

Hou H, Sun D, Zhang X. 2019. The role of MDM2 amplification and overexpression in therapeutic resistance of malignant tumors. Cancer Cell Int, 19: 216.

Irving JA, Enshaei A, Parker CA, Sutton R, Kuiper RP, Erhorn A, Minto L, Venn NC, Law T, Yu J, Schwab C, Davies R, Matheson E, Davies A, Sonneveld E, den Boer ML, Love SB, Harrison CJ, Hoogerbrugge PM, Revesz T, Saha V, Moorman AV. 2016. Integration of genetic and clinical risk factors improves prognostication in relapsed childhood B-cell precursor acute lymphoblastic leukemia. Blood, 128: 911-922.

Johansson KB, Zimmerman MS, Dmytrenko IV, Gao F, Link DC. 2023. Idasanutlin and navitoclax induce synergistic apoptotic cell death in T-cell acute lymphoblastic leukemia. Leukemia, 37: 2356-2366.

Konopleva MY, Rollig C, Cavenagh J, Deeren D, Girshova L, Krauter J, Martinelli G, Montesinos P, Schafer JA, Ottmann O, Petrini M, Pigneux A, Rambaldi A, Recher C, Rodriguez-Veiga R, Taussig D, Vey N, Yoon SS, Ott M, Muehlbauer S, Beckermann BM, Catalani O, Genevray M, Mundt K, Jamois C, Fenaux P, Wei AH. 2022. Idasanutlin plus cytarabine in relapsed or refractory acute myeloid leukemia: results of the MIRROS trial. Blood Adv, 6: 4147-4156.

Koyama T, Shimizu T, Kojima Y, Sudo K, Okuma HS, Shimoi T, Ichikawa H, Kohsaka S, Sadachi R, Hirakawa A, Yoshida A, Ando RM, Ueno T, Yanagaki M, Matsui N, Nakamura K, Yamamoto N, Yonemori K. 2023. Clinical activity and exploratory resistance mechanism of milademetan, an MDM2 ınhibitor, in ıntimal sarcoma with MDM2 Amplification: An open-label phase Ib/II study. Cancer Discov, 13: 1814-1825.

Kubbutat MH, Jones SN, Vousden KH. 1997. Regulation of p53 stability by Mdm2. Nature, 387: 299-303.

Lehmann C, Friess T, Birzele F, Kiialainen A, Dangl M. 2016. Superior anti-tumor activity of the MDM2 antagonist idasanutlin and the Bcl-2 inhibitor venetoclax in p53 wild-type acute myeloid leukemia models. J Hematol Oncol, 9: 50.

LoRusso P, Yamamoto N, Patel MR, Laurie SA, Bauer TM, Geng J, Davenport T, Teufel M, Li J, Lahmar M, Gounder MM. 2023. The MDM2-p53 Antagonist brigimadlin (BI 907828) in patients with advanced or metastatic solid tumors: results of a phase ıa, first-in-human, dose-escalation study. Cancer Discov, 13: 1802-1813.

Malagola M, Papayannidis C, Baccarani M. 2016. Tyrosine kinase inhibitors in Ph+ acute lymphoblastic leukaemia: facts and perspectives. Ann Hematol, 95: 681-693.

Maude SL, Laetsch TW, Buechner J, Rives S, Boyer M, Bittencourt H, Bader P, Verneris MR, Stefanski HE, Myers GD, Qayed M, De Moerloose B, Hiramatsu H, Schlis K, Davis KL, Martin PL, Nemecek ER, Yanik GA, Peters C, Baruchel A, Boissel N, Mechinaud F, Balduzzi A, Krueger J, June CH, Levine BL, Wood P, Taran T, Leung M, Mueller KT, Zhang Y, Sen K, Lebwohl D, Pulsipher MA, Grupp SA. 2018. Tisagenlecleucel in children and young adults with B-cell lymphoblastic leukemia. N Engl J Med, 378: 439-448.

Munoz-Fontela C, Mandinova A, Aaronson SA, Lee SW. 2016. Emerging roles of p53 and other tumour-suppressor genes in immune regulation. Nat Rev Immunol, 16: 741-750.

Nag S, Qin J, Srivenugopal KS, Wang M, Zhang R. 2013. The MDM2-p53 pathway revisited. J Biomed Res, 27: 254-271.

Ohtani S, Kagawa S, Tango Y, Umeoka T, Tokunaga N, Tsunemitsu Y, Roth JA, Taya Y, Tanaka N, Fujiwara T. 2004. Quantitative analysis of p53-targeted gene expression and visualization of p53 transcriptional activity following intratumoral administration of adenoviral p53 in vivo. Mol Cancer Ther, 3: 93-100.

Oliner JD, Kinzler KW, Meltzer PS, George DL, Vogelstein B. 1992. Amplification of a gene encoding a p53-associated protein in human sarcomas. Nature, 358: 80-83.

Ozaki T, Nakagawara A. 2011. Role of p53 in cell death and human cancers. Cancers (Basel), 3: 994-1013.

Pi L, Rooprai J, Allan DS, Atkins H, Bredeson C, Fulcher AJ, Ito C, Ramsay T, Shorr, Stanford WL, Sabloff M, Christou G. 2019. Evaluating dose-limiting toxicities of MDM2 inhibitors in patients with solid organ and hematologic malignancies: A systematic review of the literature. Leuk Res, 86: 106222.

Pulte D, Jansen L, Gondos A, Katalinic A, Barnes B, Ressing M, Holleczek B, Eberle A, Brenner H, Group GCSW. 2014. Survival of adults with acute lymphoblastic leukemia in Germany and the United States. PLoS One, 9: e85554.

Rew Y, Sun D. 2014. Discovery of a small molecule MDM2 inhibitor (AMG 232) for treating cancer. J Med Chem, 57: 6332-6341.

Rudolph D, Gollner A, Blake S, Rinnenthal J, Wernitznig A, Weyer-Czernilofsky U, Haslinger C, Garin-Chesa P, Quant J, McConnell DB, Moll J, Norbert K. 2018. A novel, potent MDM2 inhibitor that is suitable for high-dose intermittent schedules. Cancer Research, 78(13_Supplement): 4868-4868.

Sarkaria JN, Mrugala MM, Jaeckle KA, Burns TC, Vaubel RA, Parney IF, Chaichana K, Clement PM, Martinez-Garcia M, Sanchez JMS, Omuro AMP, Pronk L, Ross H, Teufel M, Hesse R, Grempler R, Galanis E. 2024. A phase (Ph) 0/Ia study of brigimadlin concentration in brain tissue and a non-randomized, open-label, dose escalation study of brigimadlin in combination with radiotherapy (RT) in patients (pts) with newly diagnosed glioblastoma (GBM). 19th Meeting of the European Association of Neuro-Oncology, October 17-20, Glasgow, UK, pp: 42.

Schwartz MS, Muffly LS. 2024. Predicting relapse in acute lymphoblastic leukemia. Leuk Lymphoma, 65: 1934-1940.

Scudiero DA, Shoemaker RH, Paull KD, Monks A, Tierney S, Nofziger TH, Currens MJ, Seniff D, Boyd MR. 1988. Evaluation of a soluble tetrazolium/formazan assay for cell growth and drug sensitivity in culture using human and other tumor cell lines. Cancer Res, 48: 4827-4833.

Shabashvili DE, Feng Y, Kaur P, Venugopal K, Guryanova OA. 2022. Combination strategies to promote sensitivity to cytarabine-induced replication stress in acute myeloid leukemia with and without DNMT3A mutations. Exp Hematol, 110: 20-27.

Specchia G, Pastore D, Carluccio P, Liso A, Mestice A, Rizzi R, Ciuffreda L, Pietrantuono G, Liso V. 2005. FLAG-IDA in the treatment of refractory/relapsed adult acute lymphoblastic leukemia. Ann Hematol., 84: 792-795.

Stein EM, DeAngelo DJ, Chromik J, Chatterjee M, Bauer S, Lin CC,

Suarez C, de Vos F, Steeghs N, Cassier PA, Tai D, Kiladjian JJ, Yamamoto N, Mous R, Esteve J, Minami H, Ferretti S, Guerreiro N, Meille C, Radhakrishnan R, Pereira B, Mariconti L, Halilovic E, Fabre C, Carpio C. 2022. Results from a first-in-human phase I study of siremadlin (HDM201) in patients with advanced wild-type TP53 solid tumors and acute leukemia. Clin Cancer Res, 28: 870-881.

Stengel A, Schnittger S, Weissmann S, Kuznia S, Kern W, Kohlmann A, Haferlach T, Haferlach C. 2014. TP53 mutations occur in 15.7% of ALL and are associated with MYC-rearrangement, low hypodiploidy, and a poor prognosis. Blood, 124: 251-258.

Sun W, Huang X. 2022. Role of allogeneic haematopoietic stem cell transplantation in the treatment of adult acute lymphoblastic leukaemia in the era of immunotherapy. Chin Med J, 135: 890-900.

Terwilliger T, Abdul-Hay M. 2017. Acute lymphoblastic leukemia: a comprehensive review and 2017 update. Blood Cancer J, 7: e577.

Thomas X, Boiron JM, Huguet F, Dombret H, Bradstock K, Vey N, Kovacsovics T, Delannoy A, Fegueux N, Fenaux P, Stamatoullas A, Vernant JP, Tournilhac O, Buzyn A, Reman O, Charrin C, Boucheix C, Gabert J, Lheritier V, Fiere D. 2004. Outcome of treatment in adults with acute lymphoblastic leukemia: analysis of the LALA-94 trial. J Clin Oncol, 22: 4075-4086.

Tolcher AW, Karim R, Tang YF, Ji J, Wang HB, Meng LC, Kaiser A, Coe J, Liang E, Rosas C, Yang DJ, Zhai YF. 2019. Phase Ib study of a novel MDM2 inhibitor APG-115, in combination with pembrolizumab in patients with metastatic solid tumors in US. Molec Cancer Therap, 18(12): A086-A086.

Vassilev LT. 2004. Small-molecule antagonists of p53-MDM2 binding: research tools and potential therapeutics. Cell Cycle, 3: 419-421.

Wang SM, Sun W, Zhao YJ, McEachern D, Meaux I, Barrière C, Stuckey JA, Meagher JL, Bai LC, Liu L, Hoffman-Luca CG, Lu JF, Shangary S, Yu SH, Bernard D, Aguilar A, Dos-Santos O, Besret L, Guerif S, Pannier P, Gorge-Bernat D, Debussche L. 2014. SAR405838: An optimized ınhibitor of MDM2-p53 ınteraction that ınduces complete and durable tumor regression. Cancer Res, 74: 5855-5865.

Willmore E, Ahn M, Kyle S, Zhao Y, Thomas H, Rankin KS, Bevan L, Fazal L, Hearn K, Wilsher N, Kucia-Tran J, Ferrari N, Wallis N, Thompson N, Lyons J, Miller D, Cano C, Noble ME, Hardcastle IR, Howard S, Chessari G, Lunec J, Newell DR, Wedge SR. 2024. Targeting the MDM2-p53 interaction: Time- and concentration-dependent studies in tumor and normal human bone marrow cells reveal strategies for an enhanced therapeutic index. Cancer Res, 84: 3333.

Wiman KG. 2006. Strategies for therapeutic targeting of the p53 pathway in cancer. Cell Death Differ, 13: 921-926.

Wu CE, Chen CP, Huang WK, Pan YR, Aptullahoglu E, Yeh CN, Lunec J. 2022. p53 as a biomarker and potential target in gastrointestinal stromal tumors. Front Oncol, 12: 872202.

Wu CE, Esfandiari A, Ho YH, Wang N, Mahdi AK, Aptullahoglu E, Lovat P, Lunec J. 2018. Targeting negative regulation of p53 by MDM2 and WIP1 as a therapeutic strategy in cutaneous melanoma. British J Cancer, 118: 495-508.

Yee K, Papayannidis C, Vey N, Dickinson MJ, Kelly KR, Assouline S, Kasner M, Seiter K, Drummond MW, Yoon SS, Lee JH, Blotner S, Jukofsky L, Pierceall WE, Zhi J, Simon S, Higgins B, Nichols G, Monnet A, Muehlbauer S, Ott M, Chen LC, Martinelli G. 2021. Murine double minute 2 inhibition alone or with cytarabine in acute myeloid leukemia: Results from an idasanutlin phase 1/1b study small star, filled. Leuk Res, 100: 106489.

Yu CH, Chang WT, Jou ST, Lin TK, Chang YH, Lin CY, Lin KH, Lu MY, Chen SH, Wu KH, Wang SC, Chang HH, Su YN, Hung CC, Lin DT, Chen HY, Yang YL. 2020. TP53 alterations in relapsed childhood acute lymphoblastic leukemia. Cancer Sci, 111: 229-238.

Zhou M, Yeager AM, Smith SD, Findley HW. 1995. Overexpression of the MDM2 gene by childhood acute lymphoblastic leukemia cells expressing the wild-type p53 gene. Blood, 85: 1608-1614.

Black Sea Journal of Engineering and Science
doi: 10.34248/bsengineering.1654579

Open Access Journal
e-ISSN: 2619 – 8991

Research Article
Volume 8 - Issue 5: 1460-1467 / September 2025

CUSTOMER LIFETIME VALUE PREDICTION IN MOBILE GAMING INDUSTRY: FUZZY LOGIC APPROACH

Ahmet Tezcan TEKİN[1]*

[1]*Istanbul Technical University, Faculty of Management, Department of Management Engineering, 34367, İstanbul, Türkiye*

Abstract: The Customer Lifetime Value (CLV) is an essential metric in customer relationship management (CRM), allowing companies to identify valuable customers and refine their advertising strategies. Traditional customer lifetime value prediction methods, including regression and machine learning techniques, frequently depend on accurate and predictable input data, making them less effective at capturing the inherent uncertainty and unpredictability in customer behavior. This research presents a fuzzy logic-based Customer Lifetime Value prediction model that integrates Recency, Frequency, and Monetary Value (RFM) as essential input factors. The proposed approach utilizes fuzzy membership functions and fuzzy inference systems (FIS), enabling consumers to possess partial membership in different CLV categories, hence offering a more adaptable and comprehensible framework for CLV calculation. A rule-based IF-THEN fuzzy system is established to categorize clients into various CLV segments, and defuzzification methods are employed to derive a precise CLV score. Experimental results indicate that the fuzzy logic model adeptly manages uncertainty and imprecision, outperforming traditional hard-segmentation methods by providing a continuous and adaptable strategy for CLV prediction. This research underscores the benefits of fuzzy logic in customer analytics, offering enterprises an easy and flexible instrument for customer segmentation, retention strategies, and revenue optimization.

Keywords: Customer lifetime value (CLV), Fuzzy logic, Fuzzy inference system, Customer segmentation, Recency-frequency-monetary (RFM) model

***Corresponding author:** Istanbul Technical University, Faculty of Management, Department of Management Engineering, 34367, İstanbul, Türkiye
E mail: tekina@itu.edu.tr (AT. TEKİN)
Ahmet Tezcan TEKIN https://orcid.org/0000-0002-1792-6622

Received: March 10, 2025
Accepted: August 06, 2025
Published: September 15, 2025

Cite as: Tekin A.T. 2025. Customer lifetime value prediction in mobile gaming industry: Fuzzy logic approach. BSJ Eng Sci, 8(5): 1460-1467.

1. Introduction

Predicting Customer Lifetime Value is essential in contemporary marketing, allowing organizations to optimize resource distribution, tailor customer interactions, and ultimately improve profitability (Pollak, 2021). Conventional approaches to Customer Lifetime Value (CLV) prediction frequently depend on statistical and econometric models, which may falter in addressing the intrinsic uncertainties and ambiguities linked to customer behavior and preferences. These models commonly presume accurate data and well-defined relationships, assumptions that seldom reflect reality, where consumer data is usually inadequate, inconsistent, or open to subjective interpretations (Hızıroğlu et al., 2018). Furthermore, the fluidity of customer connections, shaped by numerous factors, including market trends, competitive pressures, and individual client situations, affects the accuracy of CLV prediction. Fuzzy logic techniques have emerged as a potent alternative to tackle these difficulties, providing a flexible and resilient framework for modeling the uncertainties and imprecision inherent in customer and data behavior (Marin Diaz, 2025). Fuzzy logic, capable of managing ambiguous and subjective data, offers a more realistic and flexible method for predicting Customer Lifetime Value (CLV), enabling organizations to make better-informed decisions amid uncertainty (Burelli, 2019).

Fuzzy logic is characterized by using fuzzy sets and membership functions to denote degrees of truth, in contrast to the binary logic of conventional sets (Zadeh, 1994). This functionality facilitates the depiction of language characteristics, such as 'high value' or 'low risk,' as exemplified by linguistic variables (Zadeh, 1975). Moreover, fuzzy logic enables the integration of expert knowledge and qualitative insights into the modeling process, enhancing the analysis with significant contextual information that may be challenging to quantify through conventional methods. Fuzzy inference systems facilitate the development of rule-based models that emulate human thinking, converting qualitative descriptions of customer behavior into quantitative customer lifetime value forecasts. The variance related to a customer's anticipated CLV is a crucial element to evaluate, as it signifies the level of uncertainty in the estimates (McCarthy et al., 2016). By elucidating the subtleties of customer behavior and integrating expert insights, fuzzy logic models can yield a more thorough and accurate evaluation of client value, resulting in enhanced marketing strategies and superior customer relationship management.

Recent studies have increasingly integrated fuzzy logic with machine learning to address challenges related to data uncertainty, interpretability, and decision flexibility. Fuzzy logic, with its ability to model partial truth using fuzzy sets and membership functions, complements the data-driven strengths of ML by introducing linguistic reasoning and approximate inference capabilities. For instance, Abo El-Hamd et al. (2012) employed a fuzzy Q-learning framework to predict customer lifetime value under uncertain environments, demonstrating improved decision robustness over traditional reinforcement learning. Similarly, Tekin et al. (2022) developed a fuzzy clustering-based ensemble for lifetime value prediction in the gaming industry, enhancing prediction accuracy by integrating fuzzy rules with machine-learned outcomes. In healthcare, fuzzy-neuro models, such as ANFIS (Adaptive Neuro-Fuzzy Inference System), have been optimized using particle swarm optimization to enhance the accuracy of medical diagnoses (Rajabi et al., 2019). These hybrid models utilize fuzzy logic to interpret human-centric attributes (e.g., "high risk" or "moderate loyalty") while employing machine learning for pattern discovery and model training, thereby offering a balance between accuracy and transparency in predictive modeling. Additionally, Dalar and Egrioglu noted that the hybridization of ML and FL provides a robust, flexible, and interpretable framework, which is particularly compelling when handling uncertain or fuzzy real-world data, surpassing traditional ML in both practical performance and explainability (Dalar and Egrioglu, 2025).

In recent years, there has been a growing interest in applying fuzzy logic to predict customer lifetime value (CLV), with researchers investigating various strategies and methodologies to enhance forecast accuracy and model interpretability (Aeron et al., 2010). Fuzzy clustering algorithms have been utilized to categorize customers according to their behavioral patterns and attributes, facilitating the recognition of distinct customer segments with differing CLV profiles. Fuzzy rule-based systems, utilizing fuzzy inference methods, have been created to simulate the correlations between customer qualities and customer lifetime value (CLV), enabling the production of tailored CLV predictions based on distinct customer profiles. Furthermore, hybrid methodologies that integrate fuzzy logic with other machine learning techniques, including neural networks and evolutionary algorithms, have demonstrated the potential to enhance prediction accuracy and robustness. These hybrid models leverage the advantages of fuzzy logic and machine learning, combining the interpretability of fuzzy rules with the learning capabilities of neural networks and the optimization efficiency of genetic algorithms. CRM necessitates cultivating enduring relationships with consumers and deploying resources to sustain these connections (Aeron et al., 2010).

The advantages of fuzzy logic in Customer Lifetime Value prediction include heightened accuracy, better interpretability, and greater resilience. The capacity of fuzzy logic to manage imprecise data and subjective information enhances the accuracy of Customer Lifetime Value forecasts, especially in contexts with poor data quality or significant variability in customer behavior. Furthermore, the rule-based framework of fuzzy inference systems enhances model interpretability, allowing marketers to understand the determinants of CLV projections and identify significant client categories with substantial potential value. Integrating expert knowledge and qualitative insights enhances the modeling process, resulting in more substantial and actionable outcomes. Customer Lifetime Value (CLV) is assessed at the individual customer or segment level, enabling the distinction between more and less profitable customers (Chen, 2018). Moreover, fuzzy logic models exhibit intrinsic robustness to outliers and noisy data, ensuring steady and reliable CLV predictions despite data defects.

Notwithstanding the numerous advantages, obstacles persist in implementing fuzzy logic for CLV prediction, including the need for meticulous selection of membership functions, the risk of rule explosion, and the computational complexity of specific fuzzy inference methods. Choosing suitable membership functions is crucial for accurately representing the uncertainty and ambiguity associated with customer qualities, requiring a meticulous evaluation of domain knowledge and data characteristics. The quantity of fuzzy rules may increase exponentially with the number of input variables, resulting in a rule explosion issue that can impede model interpretability and computational efficiency. Confronting these issues necessitates meticulous model design, feature selection, and optimization methodologies. The difficulty resides in forecasting future gains when the timing and advantages of forthcoming transactions remain uncertain (Chen, 2018).

On the other hand, machine learning algorithms, especially ensemble learning algorithms such as Extreme Gradient Boosting (Chen and Guestrin, 2016), Catboost (Prokhorenkova et al., 2018), and Random Forest (Breiman, 2001), have an essential place in the literature for predicting CLV. Numerous studies are in the literature for predicting CLV (Asadi et al., 2024; Kumari et al., 2024; Todupunuri, 2024; Tudoran et al., 2024; Haddadi and Hodjat, 2025). However, fuzzy logic has an advantage in terms of interpretability of results, computational time, and resources.

This study consists of five main sections. The first section highlights the significance of fuzzy logic in predicting CLV, offering a comprehensive review of the relevant literature. The second section shows the preliminaries of Fuzzy Logic. The third section details the dataset and methodology employed in this study, and the performance of fuzzy logic in the calculation stage is evaluated using actual values of CLV. Finally, the last section discusses the study's recommendations, limitations, and suggestions for future research.

2. Materials and Methods

In mobile gaming, predicting CLV is crucial for optimizing marketing strategies, player retention, and monetization (Tekin et al., 2022). However, player behavior is highly uncertain and nonlinear, making traditional CLV prediction models ineffective. Fuzzy logic offers a robust framework for handling uncertainty by incorporating degrees of membership rather than rigid classifications. This section introduces the fundamental concepts of fuzzy logic and its application to CLV prediction in mobile games.

Customer Lifetime Value (CLV) represents the total revenue a company expects to earn from a player throughout their engagement with the game (Tsai et al., 2013). Unlike traditional retail models, CLV in mobile gaming is influenced by:

- In-App Purchases (IAPs) – Direct revenue from item purchases.
- Ad Revenue – Revenue from watching rewarded ads.
- Session Length & Frequency – Indicators of long-term engagement.
- Retention Rate – Probability of a player staying active over time.

A general CLV model for mobile games is given in equation 1:

$$CLV = \sum_{t=0}^{T} \frac{(IAP_t + AdRev_t)x\ P_t}{(1+d)^t} \quad (1)$$

where:

IAP_t = In-app purchase revenue at time t,

$AdRev_t$= Ad revenue generated at time t,

P_t = Probability of the player being active at t,

d = Discount rate,

T= Predicted player lifespan.

Uncertain player behavior, sparse transactions, and nonlinear progression in mobile games cause challenges in predicting CLV in mobile games. Fuzzy logic provides a way to handle these uncertainties by categorizing players into fuzzy segments rather than rigid groups.

Fuzzy logic, introduced by Zadeh (1965), is a mathematical approach for handling imprecise data. Unlike classical binary logic (true/false), fuzzy logic assigns degrees of truth between 0 and 1.

A fuzzy set A in a universal set X is defined by a membership function. It is given in equation 2:

$$\mu_A : X \rightarrow [0,1 \quad (2)$$

where:

$\mu_A(x)$ represents the degree of membership of x in set A.

Values closer to 1 indicate strong membership; values near 0 indicate weak membership.

Membership functions define how crisp values (e.g., session length, spending) are mapped into fuzzy values. Common types include:

The Triangular Membership Function is given in equation 3:

$$\mu_A(x) = \begin{cases} 0, & x \le a \text{ or } x \ge c \\ \dfrac{x-a}{b-a}, & a < x \le b \\ \dfrac{c-x}{c-b}, & b < x < c \end{cases} \quad (3)$$

The Triangular membership function is shown in Figure 1.

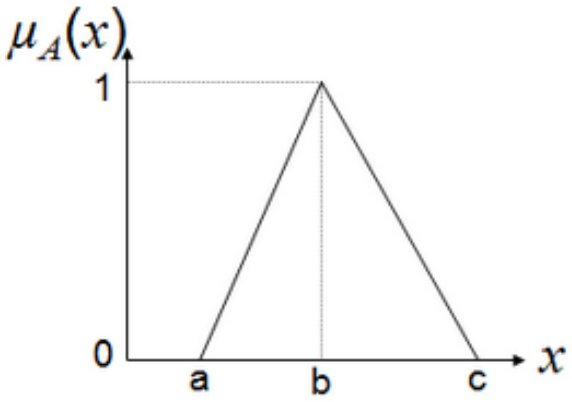

Figure 1. Triangular membership function.

The Trapezoidal Membership Function is given in equation 4:

$$\mu_A(x) = \begin{cases} 0, & x \le a \text{ or } x \ge d \\ \dfrac{x-a}{b-a}, & a < x \le b \\ 1, & b < x \le c \\ \dfrac{d-x}{d-c}, & c < x < d \end{cases} \quad (4)$$

The Trapezoidal membership function is shown in Figure 2.

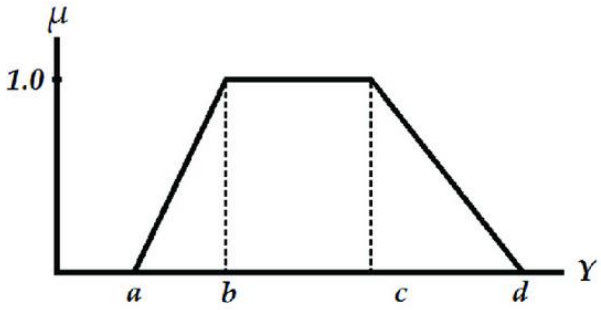

Figure 2. Trapezoidal membership function.

Gaussian Membership Function is given in equation 5:

$$\mu_A(x) = \exp\left(-\frac{(x-c)^2}{2\sigma^2}\right) \quad (5)$$

The Gaussian membership function is shown in Figure 3.

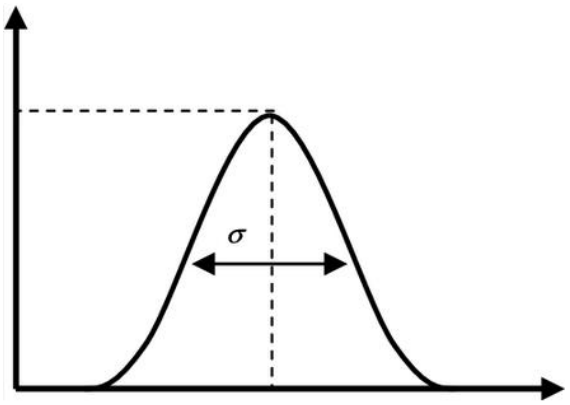

Figure 3. Gaussian membership function.

A Fuzzy Inference System (FIS) maps input variables (Recency, Frequency, Monetary) to an output variable (CLV) using IF-THEN rules. Input variables and their fuzzy categories are shown in Table 1.

Table 1. Input variables and fuzzy categories

Input Variables	Fuzzy Categories
Recency (R) days	Recent, Medium, Inactive
Frequency (F) (sessions/week)	Low, Medium, High
Monetary Value (M) ($spent)	Low, Medium, High

The output variables and their corresponding fuzzy categories are presented in Table 2.

Table 2. Output variables and fuzzy categories

Output Variable	Fuzzy Categories
Customer Lifetime Value (CLV)	Low, Medium, High

Fuzzy Rule Base:
Rules define relationships between inputs and CLV.
Example IF-THEN Rules

- IF Frequency is High AND Monetary is High, THEN CLV is High.
- IF Frequency is Medium AND Recency is Recent, THEN CLV is Medium.
- IF Frequency is Low AND Monetary is Low, THEN CLV is Low.

Each rule is evaluated using fuzzy logic operators:

- AND = Minimum (min) function.
- OR = Maximum (max) function.
- Implication (firing strength) = Apply rule strength to CLV membership.

After applying fuzzy rules, we get a fuzzy CLV value. To convert it into a crisp CLV estimate, we use defuzzification. Common defuzzification methods are shown below.
The Centroid function is given in equation 6:

$$CLV = \frac{\sum(\mu(x).\, x\,)}{\sum \mu(x)} \quad (6)$$

The Mean of the Maximum function is given in equation 7:

$$CLV = \frac{x_{max1} + x_{max2}}{2} \quad (7)$$

3. Results

Customer Lifetime Value (CLV) is one of the key metrics used in customer relationship management to estimate the total revenue a company can expect from a customer in their lifetime. CLV consists of two major components in a mobile game. These are in-app Revenue Streams triggered in the Google Play Store and Apple App Store, as well as in-ad revenue streams triggered by an ad the user sees within the game. Accurate CLV estimation helps companies optimize their marketing strategies, resource allocation, and customer churn prevention efforts. However, predicting CLV is complex due to the uncertainty and variability in customer behavior, as well as demographic differences.
Traditional approaches to CLV prediction, such as machine learning algorithms (Sun et al., 2023; Bauer and Jannach, 2021), regression models, and Markov chains (Cheng et al., 2012; Mzoughia and Limam, 2015; Ekinci et al., 2014), often work with customer behavior following deterministic or probabilistic patterns. These models can predict well in structured and predictable data, but they struggle to deal with imprecise real-world customer interactions.
Fuzzy logic provides a more realistic and flexible approach to CLV prediction by handling uncertainty and modeling imprecise customer behaviors. Fuzzy logic provides partial membership in multiple categories instead of hard classes like low-value or high-value customers. Challenges in traditional CLV prediction models are explained below.

3.1. Challenges in Traditional CLV Prediction

3.1.1. Uncertainty and variability in customer behavior

Customers can interact with businesses in different ways. Two customers can have similar histories but behave differently in the future. It makes it challenging to predict customers' future behavior. Because statistical models rely on fixed rules and assumptions, some customers make small monetary values while others make them infrequently, but they can create high monetary values. Additionally, some customers may suddenly churn, despite having a history of consistent transactions in the system. Therefore, it enables their CLV to be predicted using traditional methods. For example, Customer A plays the game daily, but they can only create one dollar in a month. Customer B plays the game weekly but can make five dollars in one month.
A traditional regression-based CLV model might classify Customer A as a low-value user and Customer B as a high-value user. However, Customer B's behavior introduces high uncertainty and makes inaccurate classifications.

3.1.2. Hard segmentation in traditional models

Many traditional models rely on hard segmentation, assigning customers to distinct strict groups. For example, if the user creates five dollars, he can be assigned to high-value users, and the other users will be assigned to a low-value user group. This approach ignores gradual transitions between customer categories. For example, if a customer creates $4.9, he may behave like a high-value customer but be assigned to a low-value user group. Fuzzy logic will eliminate this issue by allowing customers to have partial membership in multiple categories. For example, if a customer spends 4.5 dollars, he could be 70% in the Medium CLV category and 30% in the High CLV category instead of being assigned to one group.

3.1.3. Difficulty in handling multi-dimensional factors

Traditional CLV models often rely on a few key variables such as Recency, Frequency, and Monetary value. However, these models struggle to integrate additional qualitative factors such as Customer Engagement, Customer Satisfaction, and Churn probability. Fuzzy logic can handle multiple dimensions by incorporating additional input variables without increasing model complexity.

Given these challenges, fuzzy logic provides an alternative approach that more effectively captures real-world customer behavior. It allows customers to have partial membership in multiple CLV categories instead of hard classes. So, it handles uncertainty in CLV calculation. Also, fuzzy logic uses IF-THEN rules to capture human-like decision-making, so it incorporates expert knowledge. On the other hand, fuzzy logic can integrate multiple qualitative and quantitative factors into the prediction model, so it adapts to complex patterns.

3.2. Proposed Methodology

3.2.1. Membership Functions Overview

The Python programming language and the skfuzzy library were used in the application phase, and Microsoft SQL Server was used in the data preparation phase in the study.

Three input and one CLV output variable are defined with their respective fuzzy sets. Three different fuzzy rules were created for each input variable and output variable. These rules were obtained based on the mobile game's specific geographical distribution of actual users' Recency, Frequency, and Monetary values. Additionally, the actual customer lifetime of these users was calculated based on their one-year generated revenue. As Jang (2013) stated, the Sugeno fuzzy inference system supports numerical output generation by combining fuzzy rules with learning capability; therefore, the Sugeno fuzzy inference system was applied in the methodology. The input variables and output variables, along with their Corresponding Fuzzy Sets, are defined in Table 3 and Table 4.

Table 3. Input variables and fuzzy sets

Variable	Fuzzy Sets (Categories)	Range
Recency (R) days	Recent, Medium, Inactive	0-60
Frequency (F) (sessions/week)	Low, Medium, High	0-20
Monetary Value (M) ($spent)	Low, Medium, High	0-5

Table 4. Output variables and fuzzy sets

Variable	Fuzzy Sets (Categories)	Range
Customer Lifetime Value (CLV)($)	Low, Medium, High	0-50

3.2.2. Membership functions for input variables

3.2.2.1. Recency (days since last play)

- Recent (0-30 days)
- Medium (20-50 days)
- Inactive (40-60 days)

Mathematical Definitions

Recent (Triangular Membership Function):

$$\mu_{Recent}(x) = \begin{cases} 1, x = 0 \\ \dfrac{30 - x}{30}, 0 < x \leq 30 \\ 0, x > 30 \end{cases}$$

Medium (Triangular Membership Function):

$$\mu_{Medium}(x) = \begin{cases} \dfrac{x - 20}{50 - 20}, 20 \leq x \leq 50 \\ 0, \quad otherwise \end{cases}$$

Inactive (Triangular Membership Function):

$$\mu_{Inactive}(x) = \begin{cases} 0, x < 40 \\ \dfrac{x - 40}{60 - 40}, 40 \leq x \leq 60 \\ 1, x > 60 \end{cases}$$

3.2.2.2. Frequency (sessions per week)

- Low (0-5 sessions)
- Medium (5-15 sessions)
- High (10-20 sessions)

Mathematical Definitions

Low (Triangular Membership Function):

$$\mu_{Low}(x) = \begin{cases} 1, x = 0 \\ \dfrac{5 - x}{5}, 0 < x \leq 5 \\ 0, x > 5 \end{cases}$$

Medium (Trapezoidal Membership Function):

$$\mu_{Medium}(x) = \begin{cases} \dfrac{x - 5}{10 - 5}, \ 5 \leq x \leq 10 \\ 1, \quad 10 < x < 15 \\ \dfrac{20 - x}{20 - 15}, 15 \leq x \leq 20 \\ 0, x > 20 \end{cases}$$

High (Triangular Membership Function):

$$\mu_{High}(x) = \begin{cases} 0, x < 10 \\ \dfrac{x - 10}{20 - 10}, 10 \leq x \leq 20 \\ 1, x > 20 \end{cases}$$

Fuzzy Membership Functions for Session Frequency are shown in Figure 4.

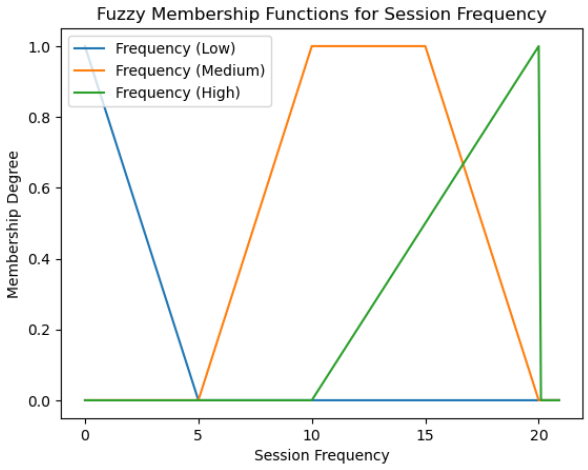

Figure 4. Fuzzy membership functions for session frequency.

3.2.2.3. Monetary value ($ spent)

- Low (0-2 dollars)
- Medium (1-3 dollars)
- High (2.5-5 dollars)

Mathematical Definitions

Low (Triangular Membership Function):

$$\mu_{Low}(x) = \begin{cases} 1, x = 0 \\ \frac{2-x}{2}, 0 < x \leq 2 \\ 0, x > 2 \end{cases}$$

Medium (Triangular Membership Function):

$$\mu_{Medium}(x) = \begin{cases} \frac{x-1}{3-1}, 1 \leq x \leq 3 \\ 0, \quad otherwise \end{cases}$$

High (Gaussian Membership Function):

$$\mu_{High}(x) = \exp\left(-\frac{(x-4)^2}{2\,x\,1^2}\right)$$

3.2.3. Membership functions for output variable (CLV)

- Low (0-20 dollars)
- Medium (15-35 dollars)
- High (30-50 dollars)

Mathematical Definitions

Low (Triangular Membership Function):

$$\mu_{Low}(x) = \begin{cases} 1, x = 0 \\ \frac{20-x}{20}, 0 < x \leq 20 \\ 0, x > 20 \end{cases}$$

Medium (Triangular Membership Function):

$$\mu_{Medium}(x) = \begin{cases} \frac{x-15}{35-15}, 15 \leq x \leq 35 \\ 0, \quad otherwise \end{cases}$$

High (Triangular Membership Function):

$$\mu_{High}(x) = \begin{cases} 0, x < 30 \\ \frac{x-30}{50-30}, 30 \leq x \leq 50 \\ 1, x > 50 \end{cases}$$

3.2.4. Calculating customer lifetime value (CLV) using fuzzy membership functions

This section provides a step-by-step calculation of Customer Lifetime Value using fuzzy membership functions, fuzzy rules, and defuzzification.

Let's assume we have a mobile game player with the following attributes. His recency is 10 days, his frequency is eight sessions per week, and his monetary value is $ 1.20.

3.2.4.1. Fuzzification (convert crisp values into fuzzy sets)

Each crisp input value is mapped into fuzzy sets using the membership functions we defined.

Recency (10 days) – Membership Calculation:

Fuzzy Sets for Recency:

- Recent (0-30 days) -> Triangular MF
- Medium (20-50 days) -> Triangular MF
- Inactive (40-60 days) -> Triangular MF

Calculate Membership Values:

Recent (0-30 days):

$$\mu_{Recent}(10) = \frac{30-10}{30} = 0.67$$

Medium (20-50 days):

$$\mu_{Medium}(10) = 0\ (since\ 10 < 20)$$

Inactive (40-60 days):

$$\mu_{Inactive}(10) = 0$$

The recency fuzzification results are 0.67 Recent, 0 Medium, and 0 Inactive.

Frequency (8 sessions per week) – Membership Calculation:

Fuzzy Sets for Frequency:

- Low (0-5 sessions) -> Triangular MF
- Medium (5-15 sessions) -> Trapezoidal MF
- High (10-20 sessions) -> Triangular MF

Calculate Membership Values:

Low (0-5 sessions):

$$\mu_{Low}(8) = 0\ (since\ 8 > 5)$$

Medium (5-15 sessions):

$$\mu_{Medium}(8) = \frac{8-5}{10-5} = 0.6$$

High (10-20 sessions):

$$\mu_{High}(8) = 0\ (since\ 8 < 10)$$

The frequency fuzzification results are 0.6 Medium, 0 High, and 0 Low.

Fuzzy Sets for Monetary Value:

- Low (0-2 dollars) -> Triangular MF
- Medium (1-3 dollars) -> Triangular MF
- High (2.5-5 dollars) -> Gaussian MF

Calculate Membership Values:

Low (0-2 dollars):

$$\mu_{Low}(1.2) = \frac{2-1.2}{2} = 0.4$$

Medium (1-3 dollars):

$$\mu_{Medium}(1.2) = \frac{1.2-1}{3-1} = 0.1$$

High (2.5-5 dollars):

$$\mu_{High}(1.2) = 0$$

The monetary values fuzzification results are 0.4 Low, 0.1 Medium, and 0 High.

Applied fuzzy rules to determine which CLV categories get activated are shown in Table 5.

Table 5. Fuzzy rules and category activation

Rule	IF Conditions	THEN CLV	Firing Strength
R1	Recency is Recent (0.67) & Frequency is Medium (0.6) & Monetary is Low (0.4)	Medium CLV	min(0.67, 0.6, 0.4) = 0.4
R2	Recency is Recent (0.67) & Frequency is Medium (0.6) & Monetary is Medium (0.1)	Medium CLV	min(0.67, 0.6, 0.1) = 0.1

Thus, the CLV fuzzy output is Medium CLV at a strength of 0.4 and Medium CLV at a strength of 0.1. The firing strengths were determined according to the and operator. In the next step, defuzzification was applied to the dataset, and fuzzy outputs were converted into Crisp CLV Values. This conversion was applied with Sugeno's weighted average output method.

CLV Fuzzy Sets and their representative values are shown in Table 6.

Table 6. Fuzzy sets and representative values

CLV Set	Range	Representative Value
Low	0-20	10
Medium	15-35	25
High	30-50	40

The centroid function shown in Equation 6 is used to predict CLV.

$$CLV = \frac{(0.4\ X\ 25) + (0.1\ X\ 25)}{0.4 + 0.1} = 25$$

Thus, the predicted CLV for the player is 25 dollars.

The proposed methodology was applied to a dataset consisting of 10,000 unique users who downloaded the game within a specific period. These users have different demographic characteristics. After applying the proposed methodology, the predicted CLV was compared to the actual CLV. The obtained results have an R-squared value of 0.91 and a Root Mean Squared Error (RMSE) of 0.08. The applied method shows promising results, and instead of applying more complex methods for a machine learning-based prediction model, this model can be applied in the prediction stage. Because fuzzy logic handles ambiguity and models imprecise customer behaviors, the forecasts offer a more flexible and realistic approach to CLV prediction.

4. Discussion and Conclusion

In this study, CLV was estimated using fuzzy logic to optimize user acquisition strategies for lower cost and apply custom strategies to increase the mobile game industry's income. Fuzzy Logic was applied to the dataset acquired by a mobile game published in the Google Play Store and Apple App Store. Before applying the model, each user's recency, frequency, and monetary values were determined and grouped according to the selected boundaries. Due to the fuzzy logic nature, the results can be interpreted easily, and the calculation time and resource usage were optimized when we compared applying machine learning models. The estimations of the applied model were evaluated by calculating MAE and R-squared values according to the users' actual CLV values. The results indicate that fuzzy logic can be effectively utilized in estimating CLV values and enhancing marketing strategies.

This study has two primary limitations. First, the demographic information of the users not used in the study effect the CLV of the users. Second, before applying the model, a broader range of periods for the data can improve the group boundary selection stage.

Future research can expand on the findings of this study in several ways. First, the model can be applied according to users' demographic information in different clusters. Therefore, the boundaries can be adjusted, and more accurate results can be obtained in the estimation process. Second, hybrid fuzzy models with machine learning can enhance accuracy and adaptability in dynamic business environments. Third, the applied model can be tested in different mobile games, generating different values according to the game's retention values.

Author Contributions

The percentages of the author' contributions are presented below. The author reviewed and approved the final version of the manuscript.

	A.T.T.
C	100
D	100
S	100
DCP	100
DAI	100
L	100
W	100
CR	100
SR	100
PM	100
FA	100

C=Concept, D= design, S= supervision, DCP= data collection and/or processing, DAI= data analysis and/or interpretation, L= literature search, W= writing, CR= critical review, SR= submission and revision, PM= project management, FA= funding acquisition.

Conflict of Interest

The author declared that there is no conflict of interest.

Ethical Consideration

Ethics committee approval was not required for this study because of there was no study on animals or humans.

References

AboElHamd E, Abdel-Basset M, Shamma H M, Saleh M, El-Khodary I. 2021. Modeling customer lifetime value under uncertain environment. Neutrosophic Sets Syst, 39(1): 2.

Aeron H, Kumar A, Janakiraman M. 2010. Application of data mining techniques for customer lifetime value parameters: a review. Int J Bus Inf Syst, 6(4): 514-529.

Asadi Ejgerdi N, Kazerooni M. 2024. A stacked ensemble learning method for customer lifetime value prediction. Kybernetes, 53(7): 2342-2360.

Bauer J, Jannach D. 2021. Improved customer lifetime value prediction with sequence-to-sequence learning and feature-based models. ACM Trans Knowl Discov Data, 15(5): 1-37.

Breiman L. 2001. Random forests. Mach Learn, 45: 5-32.

Burelli P. 2019. Predicting customer lifetime value in free-to-play games. data analytics applications in gaming and entertainment, auerbach publications, Boca Raton, FL, USA, pp: 79-107.

Chen S. 2018. Estimating customer lifetime value using machine learning techniques. Data Mining. IntechOpen, London, UK, pp: 17-34.

Chen T, Guestrin C. 2016. Xgboost: A scalable tree boosting system, Proc 22nd ACM SIGKDD Int Conf Knowl Discov Data Min, San Francisco, August 13-17, 2016, USA, pp: 785-794.

Cheng C J, Chiu S W, Cheng C B, Wu J Y. 2012. Customer lifetime value prediction by a Markov chain based data mining model: Application to an auto repair and maintenance company in Taiwan. Scientia Iranica, 19(3): 849-855.

Dalar AZ, Egrioglu E. 2025. Blending traditional and novel techniques: Hybrid type-1 fuzzy functions for forecasting. Eng Appl Artif Intell, 148: 110445.

Ekinci Y, Ülengin F, Uray N, Ülengin B. 2014. Analysis of customer lifetime value and marketing expenditure decisions through a Markovian-based model. Eur J Oper Res, 237(1): 278-288.

Haddadi AM, Hamidi H. 2025. A hybrid model for ımproving customer lifetime value prediction using stacking ensemble learning algorithm. Comput Hum Behav Rep, 100616, pp: 100616.

Hızıroğlu A, Sisci M, Cebeci H I, Seymen Ö F. 2018. An empirical assessment of customer lifetime value models within data mining. Ankara Türkiye, pp: 15-26.

Jang J S. 1993. ANFIS: adaptive-network-based fuzzy inference system. IEEE Trans Syst Man Cybern, 23(3): 665-685.

Kumari D A, Siddiqui M S, Dorbala R, Megala R, Rao K T V, Reddy N S. 2024. Deep learning models for customer lifetime value prediction in E-commerce, Proc 5th Int Conf Recent Trends Comput Sci Technol (ICRTCST), Chennai, April 2024, India, pp: 227-232.

McCarthy D, Fader P, Hardie B. 2016. V (CLV): Examining variance in models of customer lifetime value. SSRN, Available online: https://ssrn.com/abstract=2739475 (accessed date: September 1, 2024).

Marín Díaz G. 2025. A Fuzzy-XAI framework for customer segmentation and risk detection: Integrating RFM, 2-tuple modeling, and strategic scoring. Mathematics, 13: 2141.

Mzoughia MB, Limam M. 2015. An improved customer lifetime value model based on Markov chain. Appl Stoch Models Bus Ind, 31(4): 528-535.

Prokhorenkova L, Gusev G, Vorobev A, Dorogush AV, Gulin A. 2018. CatBoost: unbiased boosting with categorical features. Adv Neural Inf Process Syst, 31: 6638-6648.

Pollak Z. 2021. Predicting Customer Lifetime Values—e-commerce use case. arXiv preprint arXiv:2102.05771 (accessed date: September 1, 2024).

Rajabi M, Sadeghizadeh H, Mola-Amini Z, Ahmadyrad N. 2019. Hybrid adaptive neuro-fuzzy inference system for diagnosing the liver disorders. arXiv preprint arXiv:1910.12952 (accessed date: September 4, 2024).

Sun Y, Liu H, Gao Y. 2023. Research on customer lifetime value based on machine learning algorithms and customer relationship management analysis model. Heliyon, 9(2): e13432.

Tekin AT, Kaya T, Cebi F. 2022. Customer lifetime value prediction for gaming industry: fuzzy clustering based approach. J Intell Fuzzy Syst, 42(1): 87-96.

Todupunuri A. 2024. Develop machine learning models to predict customer lifetime value for banking customers, helping banks optimize services. Int J All Res Educ Sci Methods, 12(10): 10-56025.

Tsai CF, Hu Y H, Hung CS, Hsu YF. 2013. A comparative study of hybrid machine learning techniques for customer lifetime value prediction. Kybernetes, 42(3): 357-370.

Tudoran AA, Thomsen C H, Thomasen S. 2024. Understanding consumer behavior during and after a Pandemic: Implications for customer lifetime value prediction models. J Bus Res, 174: 114527.

Zadeh LA. 1965. Fuzzy sets. Inf Control, 8(3): 338-353.

Zadeh LA. 1975. The concept of a linguistic variable and its application to approximate reasoning-III. Inf Sci, 9(1): 43-80.

Zadeh LA. 1994. Soft computing and fuzzy logic. IEEE Softw, 11(6): 48-56.

Black Sea Journal of Engineering and Science
doi: 10.34248/bsengineering.1739684

Open Access Journal
e-ISSN: 2619 – 8991

Research Article
Volume 8 - Issue 5: 1468-1477 / September 2025

APPLICATION OF GIS IN FLOOD RISK ANALYSIS AND MITIGATION STRATEGIES: THE CASE OF ULUOVA AND IKITEPE STREAMS

Muhammed UYMAZ[1], Meral KORKMAZ[1]*

[1]*Munzur University, Faculty of Engineering, Department of Civil Engineering, 62000, Tunceli, Türkiye*

Abstract: In recent years, the frequency and severity of floods have increased significantly due to the effects of global climate change, leading to serious economic and social losses, particularly in agricultural production areas. Floods not only damage cultivated lands but also negatively affect the livelihoods and socio-economic structures of local communities. This situation necessitates accurate identification of flood risk in agricultural areas and timely implementation of appropriate mitigation measures. In this study, flood risk was investigated in agricultural lands surrounding the Uluova Stream located between Doğankuş, Karşıbağ, and the Keban Dam and the İkitepe Stream, which flows through the center of Mollakendi in Elazığ Province, Türkiye. These areas are characterized by intensive agricultural activities. Using Geographic Information Systems (GIS), seven key parameters distance to streams, land use, aspect, slope, soil structure, precipitation, and geological features were analyzed, and corresponding thematic maps were generated. Flood risk levels were determined through spatial analysis and classification of these parameters using ArcGIS software. Based on the results, areas with high flood risk were identified, and both structural and non-structural mitigation measures were proposed for these zones. The findings offer valuable insights to support sustainable agricultural production and rural development by minimizing potential flood damages and reducing associated economic risks in the region.

Keywords: ArcGIS, Flood management, Flood mitigation strategies, Flood risk, Geographic information systems (GIS)

***Corresponding author:** Munzur University, Faculty of Engiineering, Department of Civil Engineering, 62000, Tunceli, Türkiye
E mail: meralkorkmaz@munzur.edu.tr (M. KORKMAZ)
Muhammed UYMAZ https://orcid.org/0009-0009-0095-2064
Meral KORKMAZ https://orcid.org/0000-0001-5689-2560

Received: July 11, 2025
Accepted: August 08, 2025
Published: September 15, 2025

Cite as: Uymaz M, Korkmaz M. 2025. Application of GIS in flood risk analysis and mitigation strategies: The case of Uluova and İkitepe streams. BSJ Eng Sci, 8(5): 1468-1477.

1. Introduction

In recent years, climate change has emerged as one of the most significant drivers of the increasing frequency and severity of natural disasters worldwide. Among these disasters, floods stand out as a serious natural hazard that causes loss of life and property, threatens agricultural production, and disrupts sustainable development processes, affecting both rural and urban areas (IPCC, 2022). Floods occurring in agricultural areas not only result in production losses but also lead to decreased soil fertility, increased erosion, and deterioration of the rural economic structure (FAO, 2021). In rural regions, livelihoods are largely dependent on agriculture and agri-food activities. Therefore, accurately analyzing disasters such as erosion, drought, and floods in agricultural areas and developing effective prevention strategies are of great importance for the protection of these lands (FAO, 2021).

Due to their geographical locations and topographical characteristics, agricultural areas are often among the regions most exposed to flood risk. In countries like Türkiye, where agriculture plays a major role in the economy, the damages caused by floods affect not only farmers but also food security and rural development directly (FAO, 2023; Turkish Statistical Institute, 2023). In this context, determining flood risk and developing applicable strategies to minimize this risk are essential for maintaining agricultural sustainability. New approaches to flood risk emphasize multi-dimensional evaluations, considering not only the hydrological aspects but also the broader socio-economic and environmental impacts of floods, including their effects on people, infrastructure, agricultural lands, economic activities, and ecosystems (Mshelia and Belle, 2024).

In many countries, especially those frequently exposed to flooding, integrated flood risk management systems have been developed based on Geographic Information Systems (GIS), hydrological modeling, and remote sensing technologies. For instance, the Netherlands has implemented a comprehensive flood defense strategy through spatial planning and dike reinforcement (Jongman et al., 2012), while the United Kingdom uses risk-based flood mapping supported by LiDAR data and probabilistic models (Bates et al., 2010).

In addition, Kaya and Çelik (2025) demonstrated the effectiveness of integrating GIS with Analytic Hierarchy

Process (AHP) and Fuzzy AHP methods for flood risk assessment in the Upper Tigris Basin, highlighting how such multi-criteria approaches can enhance decision-making under uncertainty and be adapted for global applications.

Disasters can be defined as events caused by human activities or natural factors that result in loss of life and property, environmental damage, and disruptions to daily life (Singh et al., 2021). Among these, floods occupy an important place. Floods occur when water flow exceeds the physical capacity of riverbeds. Chow (1959) and Smith and Ward (1998) define floods as "the overflowing of a water source beyond its capacity, spreading to surrounding land areas." Globally, floods have put millions of lives at risk and resulted in significant fatalities. The possibility of flood recurrence has led to the development of flood frequency analysis methodologies to better understand and manage such events.

Floods are not limited to the physical transport of water but also have severe impacts on human health and infrastructure. Floods are natural phenomena in which excessive water overflows riverbeds, affecting nearby settlements, agricultural lands, and natural environments (Longley et al., 2015; Altın et al., 2024). Beyond their hydrological dimension, floods are also considered as disasters with significant economic, social, and environmental consequences. The frequency, intensity, and impact of floods vary depending on the geographical region, precipitation patterns, and local hydrological and topographical characteristics (Zhou et al., 2021).

It has been demonstrated that changes in land use, such as urbanization and deforestation, intensify water flow and reduce soil infiltration capacity, thereby increasing flood damage. Additionally, land use changes and urbanization within watershed areas directly affect surface runoff and groundwater recharge capacity. Such structural changes disrupt the natural water cycle, increase the frequency and severity of floods, and exacerbate the negative effects of climate change. Furthermore, natural climate variability and extreme weather events, especially severe storms, make flood prediction and management processes more complex and less predictable (Alobid et al., 2024; Dharmarathne et al., 2024).

Floods frequently cause significant economic losses, particularly in infrastructure and settlements. It is a natural event in which rivers, lakes, or seas overflow, damaging surrounding areas due to excessively rising water levels (Zhou et al., 2021; Alharbi, 2024). Floods cause considerable economic and social damage, especially in agricultural areas. In Türkiye, after earthquakes, floods are the second most damaging natural disaster in terms of economic losses. Agricultural floods are particularly concentrated along riverbanks, alluvial plains, and areas where water flow paths are located. These regions are intensely used for agricultural production due to their fertile soils. However, floods in these areas cause severe damage not only to crops but also to agricultural infrastructure such as irrigation channels, drainage systems, and field roads (Republic of Türkiye, Ministry of Agriculture and Forestry, 2017). Agricultural flood disasters can result in:

-Crop losses due to inundated agricultural lands

-Soil erosion and degradation of soil structure

-Damage to agricultural irrigation and drainage infrastructure

-Negative impacts on livestock production (e.g., damage to animal shelters and barns)

-Material damage to agricultural machinery and equipment

If floods occur close to the harvest period, economic losses increase significantly (Republic of Türkiye, Ministry of Agriculture and Forestry, 2017).

2. Materials and Methods

Today, thanks to rapidly developing technologies and information systems, access to accurate and up-to-date data is much easier and faster, and the obtained data can be analyzed and evaluated effectively. These advancements in science and technology form the foundation of the information age and have led to significant transformations, especially in sectors where location-based activities are carried out. Geographic Information Systems (GIS), which have emerged as an essential part of this transformation process, stand out as a powerful technological tool that enables the collection, storage, management, analysis, and visualization of spatial data (Yomralıoğlu, 2003).

GIS technologies, with their ability to integrate with modern information systems, are widely used in both public institutions and the private sector, contributing significantly to decision-making processes. In this study, GIS infrastructure was utilized to spatially determine and analyze flood risk. The ArcGIS Desktop software used within the scope of the study contains comprehensive tools and modules for the creation, management, visualization, and analysis of GIS data. Developed by ESRI, ArcGIS is widely used around the world in the fields of spatial analysis and mapping (Tanrıverdi, 2019).

The project area selected as the research site includes the region between Doğankuş, Karşıbağ, and Keban Dam, located within the borders of Mollakendi town in Elazığ province, which is known for its high flood risk. The study area also covers the Uluova Stream and the İkitepe Stream, which originates from the downstream of İkitepe district and flows through the center of Mollakendi. Photographs taken in the project area were integrated into the program with the help of Google Earth, and a flow route was created (Figure 1). Based on these generated flow routes, cross-sections of the terrain were systematically created. Within this scope, data were organized using ArcGIS software, and the necessary maps were produced to prepare the flood risk map.

Figure 1. General location of the study area and representation of the stream route on Google Earth image.

In this direction, topographic data, hydrological network structure, stream routes, slope, aspect, soil properties, land use, and precipitation data of the study area were obtained. The collected data were integrated holistically in the ArcGIS environment and analyzed. Using GIS infrastructure, spatial analyses were carried out to identify flood risk areas in the region, and flood risk maps were generated. Based on the obtained data and analyses, vulnerable areas in terms of flood risk were identified, and recommendations were developed to mitigate the potential impacts of possible floods. The operational steps of the methodology followed in the study are shown in Figure 2.

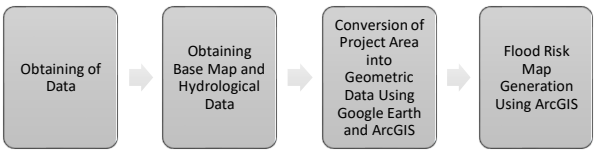

Figure 2. Data collection and GIS-based flood risk mapping process.

The GIS-based method used in the study enables both the improvement of spatial accuracy in flood risk analysis and the provision of fast and effective information to decision-makers. Thus, a significant infrastructure has been established for the early identification of flood risk and the implementation of necessary measures.

2.1. Study Area

The project area is located in Mollakendi, one of the southern towns of Elazığ city center, situated in the Upper Euphrates Section of the Eastern Anatolia Region of Türkiye. The study area, shown in Figure 3, is evaluated within the zoning boundaries of Mollakendi town. The general route of the field survey lies predominantly on flat terrain with a low hydraulic slope. Within the boundaries, the project area includes Uluova Stream (also known as Karingeç Stream), which flows between Doğankuş, Karşıbağ, and Keban Dam, and the İkitepe Stream, which starts its flow from the downstream of İkitepe district and passes through the center of Mollakendi.

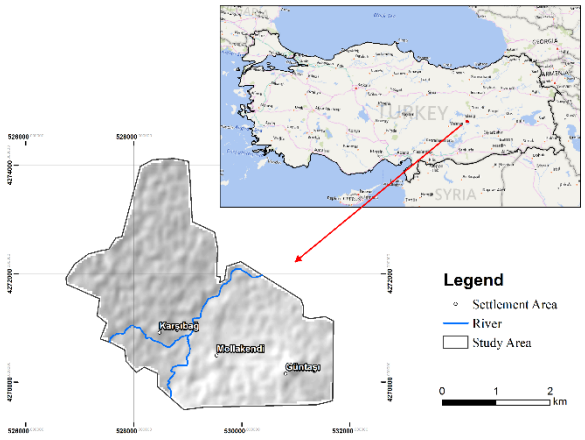

Figure 3. Location and route of the study area within the zoning boundaries.

Mollakendi is located in the Eastern Anatolia Region of Türkiye and is characterized by a continental climate. Summers in the region are hot and dry, while winters are cold and snowy. According to the Köppen Climate Classification, the area falls within the Bsk (Semi-Arid Steppe Climate) zone. Based on long-term meteorological data, the annual average temperature of Mollakendi is 13.2°C, and the annual average total precipitation is 420.2 mm (Figure 4). According to the temperature analysis, the highest temperatures are observed in July, with extreme values reaching up to 42.4°C, while the lowest temperatures are recorded in January, with minimum values dropping to -22.6°C. Regarding the precipitation regime, it has been determined that the highest rainfall occurs during the spring months, with April having the highest monthly average precipitation of 63.4 mm. Conversely, August is identified as the driest month of the year, with an average precipitation of only 1.8 mm (Figures 4-5).

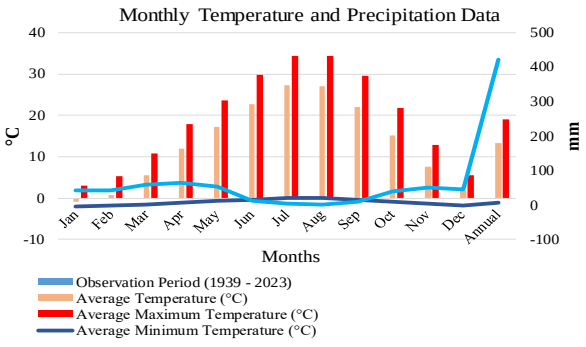

Figure 4. Meteorological data of Mollakendi district between 1939 and 2023 (MGM, 2024).

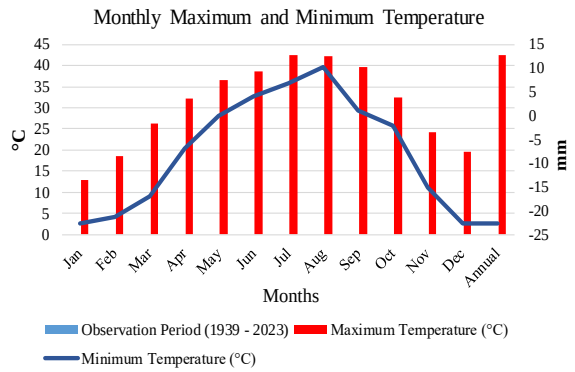

Figure 5. Monthly maximum and minimum temperature data for Mollakendi district between 1939 and 2023 (MGM, 2024).

2.2. Examination of the Stream Course and Current Conditions

The Uluova Stream and the İkitepe Tributary, which are within the project area, generally continue their flow along agricultural lowland areas in the region (Figure 6). Field measurements and analyses reveal that the bed slope of the upstream section of Uluova Stream is approximately 0.00273, while it increases to approximately 0.00366 in the downstream section. The width of the stream channel at the top of the banks varies between 20 and 25.5 meters. For the İkitepe Tributary, the longitudinal bed slope (thalweg slope) is approximately 0.00371, and the stream width reaches up to 10 meters at certain sections.

Figure 6. Geographical course of Uluova stream and İkitepe tributary.

It has been determined that, due to floods that occurred in previous years, significant anthropogenic interventions and deformations have been observed along the stream courses (Figure 5). Visual inspections reveal the presence of algae growth in certain parts of the stream banks and bed. Furthermore, the substrate of the area consists largely of sandy and gravelly material, and the natural bed structure has been significantly disrupted due to bed erosion and sediment transport from the upstream areas. This situation is one of the major factors negatively affecting the flow capacity of the stream.

Based on current measurements, it has been calculated that the discharge capacity of the Uluova Stream along the route varies between 80 and 100 m^3/s, with a safety capacity of approximately 75 m^3/s. In contrast, it has been identified that the İkitepe Tributary, particularly in its downstream sections, has a severely limited capacity, with bed capacity varying between 10 and 15 m^3/s and a safety capacity limited to only 11 m^3/s, which is insufficient.

Figure 7. Overview of Uluova and İkitepe streams.

Observations along the route indicate that sediment transport (gravel, sand, and similar materials) originating from the upstream catchment area occurs partially. The large size of the Uluova Stream's drainage basin suggests that the flood risk may increase in the coming years. Therefore, in addition to immediate mitigation measures to be taken downstream, it is recommended that upstream flood reduction measures also be implemented, depending on budgetary possibilities.

It has been determined that the streambed material along the Uluova Stream route generally consists of sandy and gravelly materials, originating both from the natural characteristics of the floodplain and from sediment transport from the upstream areas. The İkitepe Tributary, on the other hand, has a smaller drainage basin and includes a channel in its upper reaches that collects slope runoff. Therefore, no significant sediment transport issue has been observed along the İkitepe Tributary. However, due to its limited capacity and anthropogenic interventions, the route is exposed to flood risk (Figure 7).

2.3. Flood Protection Structures and Engineering Structures

There are no dedicated flood protection structures along the Uluova Stream and the İkitepe Tributary within the study area to mitigate flood risk. However, various engineering structures have been constructed along the stream courses to facilitate transportation. In this context, a total of four bridges have been identified along the Uluova Stream, and one bridge along the İkitepe Tributary. Additionally, at the downstream connection point where the İkitepe Tributary joins the Uluova Stream, a culvert with insufficient capacity and significant structural damage has been observed (Figure 8).

Figure 8. Culvert structure at the junction of Uluova and İkitepe streams.

Field investigations reveal that many of the existing engineering structures have lost their functionality over time due to various reasons. Significant sediment accumulation has occurred within the streambeds, negatively affecting the natural water flow. Capacity limitations and structural damage to these constructions are among the key factors contributing to increased flood risk. It has also been reported that floodwaters occasionally exceed the banks, causing damage along the route. In particular, in the curved sections of the streams, floodwaters surpass the banks due to insufficient channel capacity and backwater effects.

In addition to field observations, a basic hydrological evaluation was also conducted to support the assessment of structural adequacy. Considering the contributing catchment area, precipitation data, and average runoff coefficients, the estimated peak discharges for a 10-year and 25-year return period were calculated for both Uluova and İkitepe Streams. It was observed that, particularly in the İkitepe Tributary, the design capacities of existing structures fall below the estimated peak flows, indicating that these structures are insufficient to safely convey floodwaters during significant storm events. This further emphasizes the need for rehabilitation or replacement of under-capacity structures in flood-prone segments.

A detailed assessment of the engineering structures along the Uluova Stream is presented in Table 1.

Table 1. General assessment of engineering structures along Uluova stream

Uluova Stream Hydraulic Structures	Type (Width × Height)	Observations
0+316.33	3-Span 12*2m	Significant accumulation of bed material. Hydraulic capacity is sufficient.
1+531.91	3-Span 12*4.5m 12*4.5m 13*3.5m	Accumulated bed material; one span is partially blocked due to slope gradient. Capacity is sufficient.
2+792.88	3-Span 7*4.5 m 5.5*4.5m 5*3.5m	Spans are relatively functional. Minor material accumulation. One span has an arched structure.

3. Results and Discussion

In order to prevent flood and inundation disasters, protect against them, and reduce associated damages, it is essential to establish and analyze a comprehensive database that includes the basin's geomorphological, lithological, hydrographic, climatic, soil, vegetation, and land use characteristics (Turoğlu and Özdemir, 2005). Within this scope, parameters affecting flood risk were evaluated using maps prepared in the GIS environment. All data were transferred into ArcGIS software and analyzed accordingly.

3.1. River Proximity Map

One of the most significant environmental factors to be considered in flood risk analysis is the distance to the nearest watercourse. As highlighted in the literature, flood risk increases as the distance to rivers decreases and diminishes as the distance increases (Şen, 2009). In this context, the River Proximity Map prepared for the study area illustrates different distance zones using a color scale (Figure 9).

Upon examining Figure 9, it is evident that areas within 0–200 meters are shown in dark blue and represent zones with very high flood risk. Areas between 200–400 meters fall within the moderate-high risk group, while regions 400–600 meters away are classified as low-risk zones. Zones located beyond 800 meters, illustrated in light green tones, represent the safest areas in terms of flood risk.

It was determined that a significant portion of the Mollakendi settlement is located within the 400–600 meter distance range, placing it in the moderate flood risk category. Particularly, the proximity of agricultural areas and residential zones to high-risk areas (0–200 m) increases vulnerability to flooding. It is critically important to prioritize the areas near watercourses in Mollakendi for preventive planning efforts.

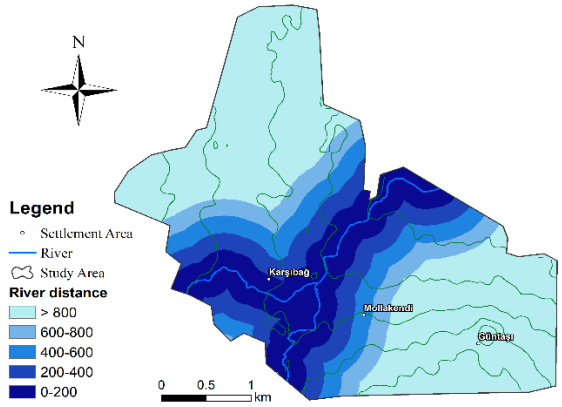

Figure 9. River proximity map for flood risk assessment.

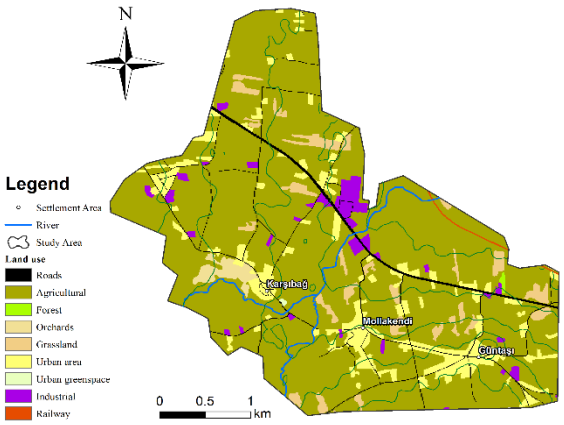

Figure 10. Land use map of the study area.

3.2. Land Use Map

Land use characteristics are among the most crucial factors influencing flood occurrence. Land use directly affects the surface runoff regime, which can either increase or reduce flood risk (Turoğlu and Özdemir; Özdemir, 2005). As emphasized in the literature, in areas where vegetation cover is sparse, slopes are steep, and land use is inappropriate, rainfall rapidly transforms into surface runoff, accelerating flood formation. Conversely, in regions with dense vegetation and controlled land use, surface runoff decreases, leading to a lower flood risk (Özdemir, 2007; Engman and Schultz, 2000).

The Land Use Map prepared for the study area reveals that the stream beds in Mollakendi and its surroundings predominantly pass through agricultural lands (Figure 10). Agricultural areas are considered the most vulnerable land use class regarding flood risk due to reduced surface permeability and soil disturbance from farming activities. According to reports, between 1975 and 2011, 820 flood events occurred in Türkiye, resulting in the loss of 660 lives, approximately 872 km^2 of agricultural land being affected by floods, and an estimated annual economic loss of 150 million TL (DMİ, 2016). These figures highlight the vulnerability of agricultural areas to flood hazards.

The extensive agricultural lands surrounding streams in the Mollakendi region increase the area's fragility concerning flood risk. Therefore, implementing appropriate protection measures in agricultural areas located within flood zones and relocating settlements and production activities away from high-risk regions is essential.

3.3. Aspect Map

Aspect refers to the directional orientation of a slope or terrain, which directly influences hydrological processes, vegetation development, evapotranspiration, and surface runoff. Given Türkiye's geographical location in the Northern Hemisphere, different aspect characteristics are observed on north- and south-facing slopes.

Generally, north-facing slopes receive less sunlight, retain soil moisture for extended periods, and promote vegetation development. In contrast, south-facing slopes are exposed to sunlight at steeper angles, resulting in increased evapotranspiration rates and quicker soil moisture loss. Therefore, vegetation is typically sparse and drought-tolerant on south-facing slopes, while denser, moisture-loving vegetation is common on north-facing slopes (Özdemir, 2007).

The Aspect Map prepared for the study area indicates that the slopes surrounding Uluova Stream predominantly face west, south, and east. This suggests the presence of areas along Uluova Stream, especially on the south-facing slopes, where soil moisture is low, and surface runoff may increase. More balanced conditions are observed on the west- and east-facing slopes. For İkitepe Stream, the slopes generally face northwest, north, southeast, and partially west. North- and northwest-facing slopes are likely to experience reduced surface runoff and prolonged soil moisture retention, leading to relatively lower flood risk in these areas. Conversely, southeast-facing slopes, characterized by lower soil moisture, are prone to increased surface runoff and relatively higher flood risk (Figure 11).

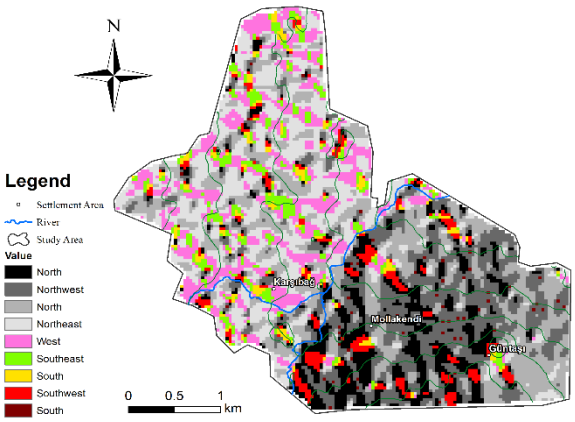

Figure 11. Aspect map of the study area.

3.4. Slope Map

Slope is one of the most critical geomorphological factors influencing flood formation. Slope affects surface runoff, soil infiltration capacity, and erosion, playing a vital role in flood risk assessment (Özcan, 2008). According to widely accepted understanding, in steep areas, the retention time of water on the surface decreases, resulting in faster runoff, but the risk of flooding may be relatively lower. Conversely, in areas with gentle slopes, runoff slows down, water accumulates, and the likelihood of flooding increases.

It was determined that the Uluova Stream corridor largely falls within the first slope group, meaning it passes through very gently sloping areas. The İkitepe Stream corridor is predominantly located within the second slope group, corresponding to gently sloping areas (Figure 12).

The inverse relationship between slope and flood risk is frequently emphasized in the literature. As slope decreases, water tends to accumulate on the surface, thereby increasing flood risk. In this context, low-slope areas around Uluova and İkitepe Streams are considered more vulnerable to flooding within the study area.

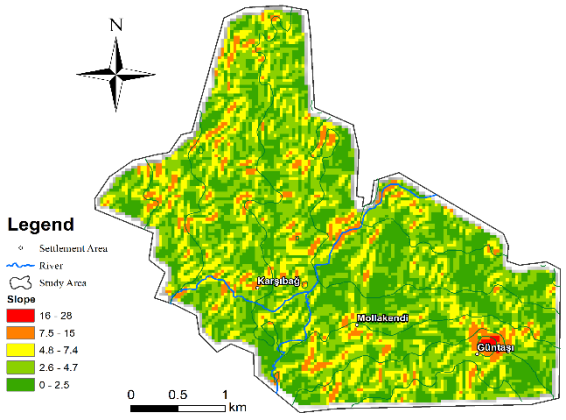

Figure 12. Slope map of the study area.

3.5. Soil Map

Soil characteristics, particularly infiltration capacity, play a crucial role in the formation of floods and inundations. Factors such as soil surface features, existing soil moisture, water-holding capacity, temperature, structural properties, and water movement within the soil directly affect infiltration. Soils with good drainage characteristics allow water accumulated on the surface to quickly infiltrate the ground, thereby significantly reducing the risk of floods and inundations (Turoğlu and Özdemir, 2005).

Other critical factors affecting soil drainage capacity include soil texture (proportions of sand, clay, and silt), structure, precipitation amount, environmental seepage, the presence of impermeable layers, salt content and type, groundwater level, and the general physical structure of the soil profile. Additionally, soil type indirectly affects flood and inundation risk by determining vegetation growth conditions. Dense and healthy vegetation reduces surface runoff, limits sediment transport, and increases water infiltration. Conversely, areas lacking vegetation experience increased surface runoff and elevated flood risk.

The Soil Map prepared for the study area reveals that alluvial soils are widespread throughout the region (Figure 13). Alluvial soils are formed by the accumulation of sand, clay, gravel, and similar sediments transported by rivers. These soils are highly permeable but are considered vulnerable to floods and inundations due to their susceptibility to erosion and sediment transport. Alluvial soils are commonly found in plains, riverbeds, and floodplains, where they amplify the impacts of flood events (Oğuz et al., 2022).

The widespread presence of alluvial soils in the region increases the flood vulnerability of the study area and enhances the potential for river overflows.

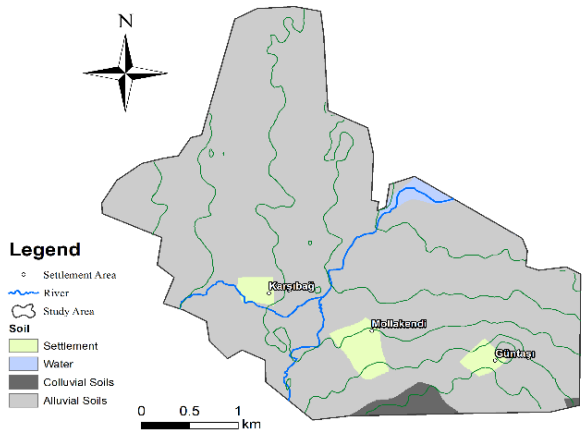

Figure 13. Soil map of the study area.

3.6. Precipitation Map

Precipitation is among the most influential factors in the formation of floods and inundations. The amount, intensity, and distribution of precipitation directly affect surface runoff, soil infiltration capacity, and groundwater recharge. In regions where precipitation is high or concentrated over short periods, the likelihood of floods and flash floods significantly increases (Turoğlu and Özdemir, 2005).

The Precipitation Map prepared for the study area reveals that annual precipitation ranges between 519 mm and 538 mm (Figure 14). Higher precipitation values are concentrated in the eastern sections of the study area, particularly around the Guntaşı settlement, while lower precipitation values are observed towards the west and northwest.

The spatial distribution of precipitation aligns with the region's semi-arid (Bsk) steppe climate, characterized by low overall annual rainfall but significant local variability. Areas receiving more than 535 mm of precipitation annually are considered higher flood risk zones due to the increased likelihood of surface runoff.

The precipitation characteristics of the region, combined with other environmental parameters such as slope, soil type, and land use, must be evaluated holistically to accurately assess flood risk.

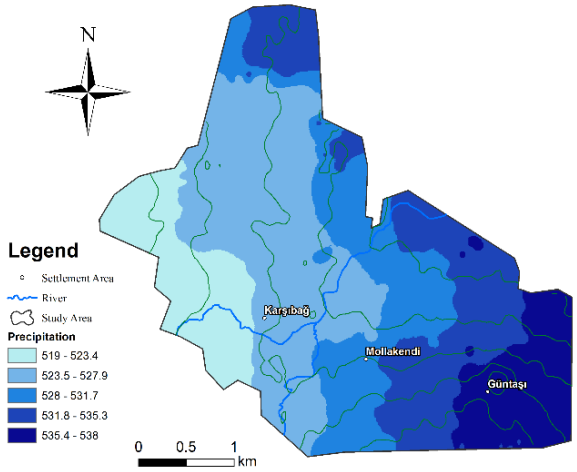

Figure 14. Precipitation map of the study area.

Within the scope of this study, the flood risk in Uluova Stream (Karingeç Creek) and İkitepe Stream, located within the borders of Mollakendi Town in Elazığ Province, was comprehensively evaluated. In this context, seven key geographic parameters, including slope, land use, soil, aspect, geology, precipitation, and proximity to watercourses, were analyzed within the Geographic Information Systems (GIS) environment, and a flood risk map was produced (Figure 15).

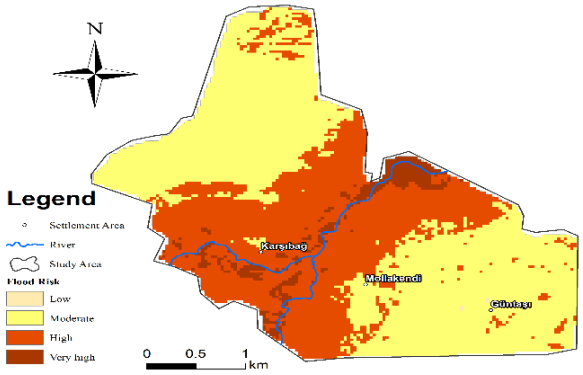

Figure 15. Flood risk map.

The generated flood risk map has clearly revealed the spatial distribution of risk within the study area. The map indicates that areas close to stream beds, low-slope regions, zones with extensive alluvial soils, and agricultural areas are among the most vulnerable zones with a high flood risk. Moreover, considering the region's topographical structure and current land use characteristics, it is evident that flood risk is not only driven by natural factors but also significantly exacerbated by unplanned and uncontrolled human activities.

When the Land Use Map and the Flood Risk Map are examined together, it becomes clear that a significant portion of the high-risk areas overlaps with agricultural lands and settlement zones. In particular, the proximity of extensive agricultural areas to the Uluova and İkitepe Stream beds increases surface runoff and facilitates flood formation. In these areas, characterized by insufficient vegetation cover and soils with low permeability, the water infiltration capacity of the soil is significantly reduced, further aggravating flood risk.

Additionally, industrial zones and residential areas are also observed to be located close to stream beds in the region. This situation poses a serious threat not only to natural areas but also to economic activities and human life.

The literature clearly emphasizes that unplanned land use and improper site selection significantly increase flood risk (Turoğlu and Özdemir, 2005; Özdemir, 2007). The findings obtained from this study concretely demonstrate this situation specifically for the Mollakendi region. It was determined that land use decisions in Mollakendi have largely been made without considering flood risk maps, which increases the potential for future floods to create significant impacts on the local economy and social life.

The Flood Risk Map provides concrete guidance for decision-makers, local administrators, and the local community, enabling the identification of risky areas in advance and the implementation of necessary precautions. Therefore, it is essential that this map is not only regarded as an academic output but also actively utilized in local planning and disaster management processes.

5. Conclusion and Recommendations

In this study, the flood risk for Uluova Stream (Karingeç Creek) and İkitepe Stream, located within the administrative boundaries of Mollakendi Town in Elazığ Province, was evaluated using Geographic Information Systems (GIS) technologies. Within the scope of the study, seven key geographic parameters—slope, land use, soil, aspect, geology, precipitation, and proximity to the stream—were analyzed through ArcGIS software, and a flood risk map was produced based on these parameters (Figure 16).

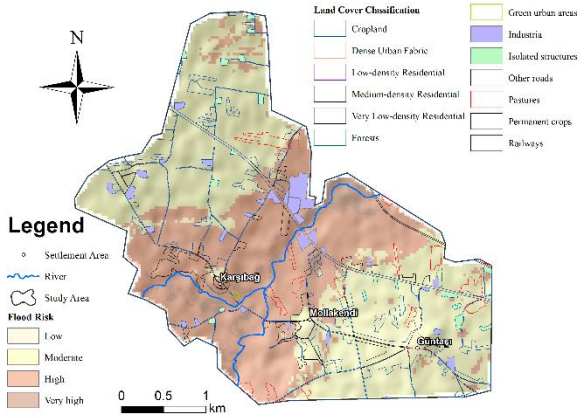

Figure 16. Flood risk and land use map of Mollakendi region (2018).

The flood risk analysis revealed areas within the study site with varying levels of risk. Particularly, areas close to stream beds, low-slope regions, locations with dominant alluvial soil, agricultural lands, and regions with high precipitation were identified as having the highest flood risk. These vulnerable areas also overlap with residential zones, industrial areas, and fertile agricultural lands, indicating that potential future flood events may cause significant economic, environmental, and social damage.

The evaluation clearly shows that land use decisions made in the Mollakendi region to date have largely ignored the realities of flood risk. In particular, the widespread agricultural activities and residential settlements located in proximity to stream beds significantly increase the region's vulnerability to floods.

To reduce the risk of floods and minimize potential losses, the following measures are recommended:

Land use within flood-prone areas should be strictly regulated, and settlements and agricultural activities should be relocated away from high-risk zones.

Natural vegetation cover must be preserved and reinforced to reduce surface runoff and erosion.

Stream beds should be rehabilitated, and flood protection structures such as embankments, culverts, and bridges should be systematically planned and implemented.

Engineering solutions appropriate to soil characteristics, especially in alluvial soil zones, should be developed to enhance flood resilience.

The integration of flood risk maps into local planning processes should be made mandatory.

Early warning systems should be improved, and public awareness efforts should be increased to enhance preparedness.

Through these measures, the continuity of agricultural production in rural areas where agriculture is the primary livelihood source will be secured, employment opportunities will be preserved, and the risk of income loss to the regional economy will be minimized, creating significant social and economic benefits.

5.1. Suggested Academic Warning Statement for Project Planning

The findings of this study clearly reveal that previous land use and development projects within the study area have been implemented without adequate consideration of flood risk. To prevent potential future disasters and economic losses, it is strongly recommended that the integration of flood risk analyses into all zoning, construction, and development projects be made compulsory. Neglecting this obligation will significantly increase the vulnerability of both human settlements and economic activities to flood hazards.

Author Contribution

The percentages of the authors' contributions are presented below. All authors reviewed and approved the final version of the manuscript.

	M.U.	M.K.
K	50	50
T	50	50
Y	50	50
VTI	50	50
VAY	50	50
KT	50	50
YZ	50	50
KI	50	50
GR	50	50
PY	50	50
FA	50	50

C= Concept, D= Design, S= Supervision, DCP= Data Collection and/or Processing, DAI= Data Analysis and/or Interpretation, LR= Literature Review, W= Writing, CR= Critical Review, SR= Submission and Revision, PA= Project Administration, FA= Funding Acquisition

Conflict of Interest

The authors declare that there is no conflict of interest regarding this study.

Ethical Consideration

Since this study did not involve research on humans or animals, ethical committee approval was not required.

Acknowledgement

The authors would like to express their sincere gratitude to OpenAI's ChatGPT language model for providing

language editing and technical writing assistance during the preparation of this study.

The authors also gratefully acknowledge the General Directorate of State Hydraulic Works (DSİ) for providing access to the necessary data that significantly contributed to this research.

This research did not receive any specific grant from funding agencies in the public, commercial, or not-for-profit sectors.

References

Alharbi T. 2024. A weighted overlay analysis for assessing urban flood risks in arid lands: a case study of Riyadh, Saudi Arabia. Water, 16(3): 397.

Alobid M, Chellai F, Szűcs I. 2024. Trends and drivers of flood occurrence in Germany: a time series analysis of temperature, precipitation, and river discharge. Water, 16(18): 2589.

Altın G, Taşkın S, Yurtal R, Aköz MS. 2024. Kuru derelerde taşkın risk analizi; Kebendibi deresi örneği. Çukurova Üniv Müh Fak Derg, 39(1): 221-229.

Bates PD, Horritt MS, Fewtrell TJ. 2010. A simple inertial formulation of the shallow water equations for efficient two-dimensional flood inundation modelling. J Hydrol, 387(1-2): 33-45.

Chow VT. 1959. Determination of hydrologic frequency factor. J Hydraul Div, 85(7): 93-98.

Dharmarathne G, Waduge AO, Bogahawaththa M, Rathnayake U, Meddage DPP. 2024. Adapting cities to the surge: A comprehensive review of climate-induced urban flooding. Results Eng, 102123.

DMİ. 2016a. Doğal afetler. devlet meteoroloji işleri genel müdürlüğü. URL: http://www.mgm.gov.tr/arastirma/dogal-afetler.aspx?s=taskinlar (accessed date: December 9, 2016).

Engman ET, Schultz GA. 2000. Future perspectives. In: Remote sensing in hydrology and water management. Springer Berlin Heidelberg, Berlin, Germany, pp: 445-457.

FAO. 2021. The state of food and agriculture 2021: Making agrifood systems more resilient to shocks and stresses. Food and Agriculture Organization of the United Nations.

FAO. 2023. The impact of disasters on agriculture and food security 2023: Avoiding and reducing losses through investment in resilience. Food and Agriculture Organization of the United Nations.

IPCC. 2022. Climate Change 2022: Impacts, adaptation and vulnerability. Intergovernmental Panel on Climate Change.

Jongman B, Ward PJ, Aerts JC. 2012. Global exposure to river and coastal flooding: Long term trends and changes. Glob Environ Change, 22(4): 823-835.

Kaya B, Çelik R. 2025. Dynamic and scalable flood risk assessment using GIS, AHP, and novel fuzzy AHP: A case study of the upper tigris basin. Preprint, Research Square, https://doi.org/10.21203/rs.3.rs-5776107/v1

Longley PA, Goodchild MF, Maguire DJ, Rhind DW. 2015. Geographic information science and systems. John Wiley and Sons, New York, US, pp: 517.

Meteoroloji Genel Müdürlüğü Resmi Veri Sayfası. 2024. https://mgm.gov.tr (accessed date: July 2024).

Mshelia ZH, Belle JA. 2024. A systematic flood risk assessment of Bloemfontein Watershed, South Africa. Geom Nat Hazards Risk, 15(1): 2423739.

Oğuz E, Oğuz K, Öztürk K. 2022. Düzce bölgesi taşkın duyarlılık alanlarının belirlenmesi. Geomatik, 7(3): 220-234.

Özcan O. 2008. Evaluation of flood risk analysis in Sakarya sub basin by using remote sensing and GIS. MSc Thesis, İstanbul Technical University, Institute of Information, İstanbul, Türkiye, pp: 72.

Özdemir H. 2007. SCS CN Yağış-akış modelinin CBS ve uzaktan algılama yöntemleriyle uygulanması: Havran Çayı Havzası örneği (Balıkesir). Coğrafi Bil Derg, 5(2): 1-12.

Republic of Türkiye, Ministry of agriculture and forestry, general directorate of water management. 2017. Flood Management Book, Ankara, Türkiye, pp:1-160.

Singh S, Dhote PR, Thakur PK, Chouksey A, Aggarwal SP. 2021. Identification of flash-floods-prone river reaches in Beas river basin using GIS-based multi-criteria technique: validation using field and satellite observations. Nat Hazards, 105: 2431-2453.

Smith K, Ward R. 1998. Floods: Physical processes and human impacts. John Wiley & Sons, Chichester, UK, pp: 12-382.

Solin L, Skubincan P. 2013. Flood risk assessment and management: review of concepts, definitions and methods. Geogr J, 65: 23-44.

Şen Z. 2009. Taşkın afet ve modern hesaplama yöntemleri. Su Vakfı, Ankara, Türkiye, pp: 1-20.

Tanriverdi M. 2019. Determination of flood areas of Şanlıurfa provincial center by multi-criteria decision analysis based on geographic information systems (GIS). PhD Thesis, Harran University, Institute of Science, Şanlıurfa, Türkiye, pp: 74.

Turkish Statistical Institute. 2023. Agricultural statistics of Türkiye, 2023. Turkish Statistical Institute.

Turoğlu H, Özdemir H. 2005. Bartın'da Sel ve Taşkınlar: Sebepler, Etkiler, Önleme ve Zarar Azaltma Önerileri. Çantay Kitabevi, İstanbul, Türkiye, pp:45-59.

Yomralıoğlu T. 2003. Coğrafi Bilgi Sistemi Politikası. TUJK 2003 Yılı Bilimsel Toplantısı, Coğrafi Bilgi Sistemleri ve Jeodezik Ağlar Çalıştayı, 24-26 Eylül 2003, Konya, Türkiye, pp:15-19.

Zhou Q, Su J, Arnbjerg-Nielsen K, Ren Y, Luo J, Ye Z, Feng J. 2021. A GIS-based hydrological modeling approach for rapid urban flood hazard assessment. Water, 13(11): 1483.

Black Sea Journal of Engineering and Science
doi: 10.34248/bsengineering.1697455

Open Access Journal
e-ISSN: 2619 – 8991

Araştırma Makalesi (Research Article)
Cilt 8 - Sayı 5: 1478-1492 / Eylül 2025
(Volume 8 - Issue 5: 1478-1492/September 2025)

TÜRKİYE'NİN BİLGİSAYAR, ELEKTRONİK VE OPTİK ÜRÜNLERİ DIŞ TİCARETİNİN MAKİNE ÖĞRENMESİ İLE TAHMİNLENMESİ

Tolga HASTAOĞLU[1]*, Tolga AYDIN[1]

[1]*Ataturk University, Faculty of Engineering, Department of Computer Engineering, 25100, Erzurum, Türkiye*

Özet: Bu çalışmanın amacı, Türkiye'nin bilgisayar, elektronik ve optik ürünleri dış ticaretinin dinamiklerini anlamak ve makine öğrenmesi tekniklerini kullanarak bu ürünlerin dış ticaret verilerini tahmin etmektir. Çalışma, dış ticaret stratejilerinin geliştirilmesine katkıda bulunmayı ve Türkiye'nin uluslararası ticaret pazarındaki rekabet gücünü artırmak için veri odaklı karar verme süreçlerinin önemine vurgu yapmayı hedeflemektedir. Çalışma kapsamında öncelikle veri setindeki anomali gözlemler İzolasyon Ormanı (Isolation Forest) yöntemi ile tespit edilmiştir. Daha sonra Minimum Redundancy Maximum Relevance (MRMR) ve Recursive Feature Elimination (RFE) yöntemleri kullanılarak en etkili değişkenler belirlenmiştir. Kümeleme aşamasında, veri setindeki örüntüleri belirlemek amacıyla K-Ortalamalar (K-Means) ve CLARANS algoritmaları kullanılmıştır. Son olarak, tahminleme modelleri olarak XGBoost, LightGBM ve Rastgele Orman Regresörü (Random Forest Regressor) uygulanarak dış ticaret verilerinin gelecekteki eğilimleri öngörülmüştür. Bu yöntemlerden üç farklı model oluşturulmuştur. İlk modelde, Isolation Forest algoritması ile anomali tespiti yapılmış, ardından özellik seçimi için MRMR ve RFE yöntemleri kullanılmış ve sonuç olarak Random Forest Regressor, XGBoost ve LightGBM regresyon modelleri uygulanmıştır. İkinci modelde, yine özellik seçimi yapılmış, sonrasında CLARANS ve K-means kümeleme algoritmaları uygulanmış ve ardından regresyon analizi gerçekleştirilmiştir. Üçüncü modelde ise, anomali tespiti için Isolation Forest kullanılmış, özellik seçimi yapılmış, kümeleme algoritmaları uygulanmış ve regresyon modelleri ile sonuçlar değerlendirilmiştir. Elde edilen sonuçlar karşılaştırılarak, dış ticaret verileri üzerinde makine öğrenmesinin etkinliği ortaya konulmuştur Kullanılan metriklere göre en iyi sonuç model 2 (Clarans+MRMR+Random Forest) modeli ile R^2=0,8322 olacak şekilde elde edilmiştir.

Anahtar kelimeler: Dış ticaret, Makine öğrenmesi, Regresyon

Prediction of Türkiye's Foreign Trade of Computer, Electronic and Optical Products with Machine Learning

Abstract: The objective of this study is to understand the dynamics of Türkiye's foreign trade in computer, electronic, and optical products and to predict the trade data of these products using machine learning techniques. The study aims to contribute to the development of foreign trade strategies and emphasizes the importance of data-driven decision-making processes to enhance Türkiye's competitiveness in the international trade market. In this study, anomalous observations in the dataset were first identified using the Isolation Forest method. Subsequently, the most effective variables were determined using the Minimum Redundancy Maximum Relevance (MRMR) and Recursive Feature Elimination (RFE) methods. In the clustering phase, K-Means and CLARANS algorithms were employed to identify patterns within the dataset. Finally, prediction models, including XGBoost, LightGBM, and Random Forest Regressor, were applied to forecast future trends in foreign trade data. Three different models were developed using these methods. In the first model, anomaly detection was performed using the Isolation Forest algorithm, followed by feature selection using MRMR and RFE, and subsequently, Random Forest Regressor, XGBoost, and LightGBM regression models were applied. In the second model, feature selection was again conducted, followed by the application of CLARANS and K-Means clustering algorithms, and regression analysis was performed. In the third model, the Isolation Forest was used for anomaly detection, feature selection was conducted, clustering algorithms were applied, and results were evaluated using regression models. The results obtained were compared to demonstrate the effectiveness of machine learning on foreign trade data. According to the metrics used, the best result was achieved with Model 2 (CLARANS + MRMR + Random Forest) with an R^2 value of 0.8322.

Keywords: Foreign trade, Machine learning, Regression

***Sorumlu yazar (Corresponding author):** Ataturk University, Faculty of Engineering, Department of Computer Engineering, 25100, Erzurum, Türkiye
E mail: tolga.hastaoglu@icloud.com (T.HASTAOĞLU)
Tolga HASTAOĞLU https://orcid.org/0009-0001-0444-1167
Tolga AYDIN https://orcid.org/0000-0002-8971-3255

Gönderi: 12 Mayıs 2025 **Received:** May 12, 2025
Kabul: 14 Ağustos 2025 **Accepted:** August 14, 2025
Yayınlanma: 15 Eylül 2025 **Published:** September 15, 2025

Cite as: Hastaoglu T, Aydin T. 2025. Prediction of Türkiye's foreign trade of computer, electronic and optical products with machine learning BSJ Eng Sci, 8(5): 1478-1492.

1.Giriş

Dış ticaret verileri, büyüme ve kalkınma süreci olarak ülkelerin ekonomik göstergelerinde çok önemli bir yere sahiptir. 1970'li yıllarda ortaya çıkan küreselleşme süreci kısa bir dönemde tüm dünyayı etkilemiştir. 1980 ve 1990'lı yıllarda ise küreselleşme finans piyasalarında çok daha önemli bir boyuta ulaşmıştır (Aytekin, 2013). küreselleşmenin artışıyla birlikte, ülkelerin ihracat ve ithalat hacmi ekonomik istikrar ve sürdürülebilir büyüme açısından kritik hale gelmiştir. Dış ticaret bir ülkeden diğerine ihraç veya ithal edilen mal ve hizmetlerin değeridir, bu değer uluslararası ticaret politikaları ve

ticaretin yapıldığı her iki ülkenin iç ekonomi politikalarını etkiler. Ayrıca ülkelerdeki politika yapıcılar ve o ülkenin ekonomistleri için de gösterge niteliğindedir (Circlaeys vd., 2017).

Türkiye, stratejik konumu ve üretim kapasitesi ile bölgesel bir ticaret merkezi konumunda olup, özellikle son yıllarda dış ticaret hacmini önemli ölçüde arttırmıştır. Bu nedenle, Türkiye'nin dış ticaret performansını tahmin etmek, ekonomik karar alıcılar ve politika yapıcılar için değerli bilgiler sunmaktadır. Şekil 1 ve Şekil 2'de Türkiye Dış Ticaret verilerinin yıllara göre ithalat ve ihracat verileri verilmiştir. Şekillerde de görüldüğü üzere 2020 yılında bütün dünyayı etkileyen COVİD 19 pandemisi ile dış ticaret hacmi düşmüş, 2021 ve 2022'de ise artışa geçmiştir.

Şekil 3 ve Şekil 4 ise çalışma kapsamında ele alınan Bilgisayarların, Elektronik ve Optik Ürünlerin imalatı için ithalat ve ihracat Şekilleri verilmiştir. Bu tür teknolojik ürünlerin ithalatının, ihracatına göre yaklaşık 6 kat daha büyük olduğu görünmekte ve ilgili sektörde dış ticaret açığı olduğu açıkça görünmektedir.

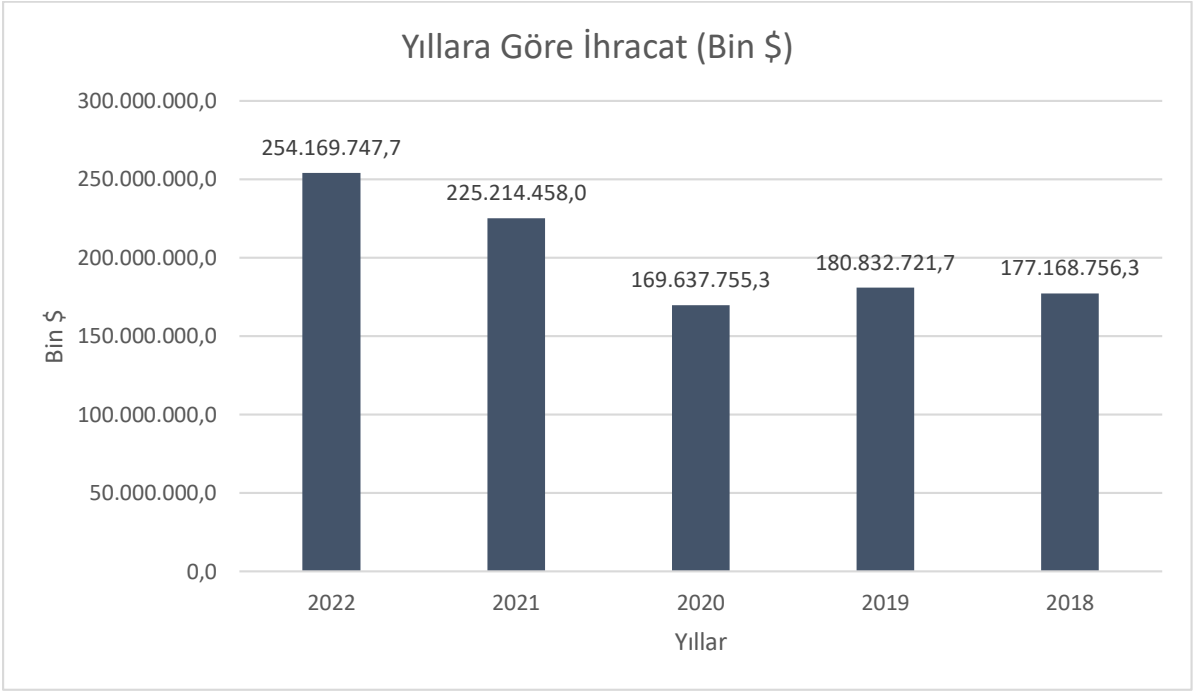

Şekil 1. Türkiye toplam ihracat grafiği

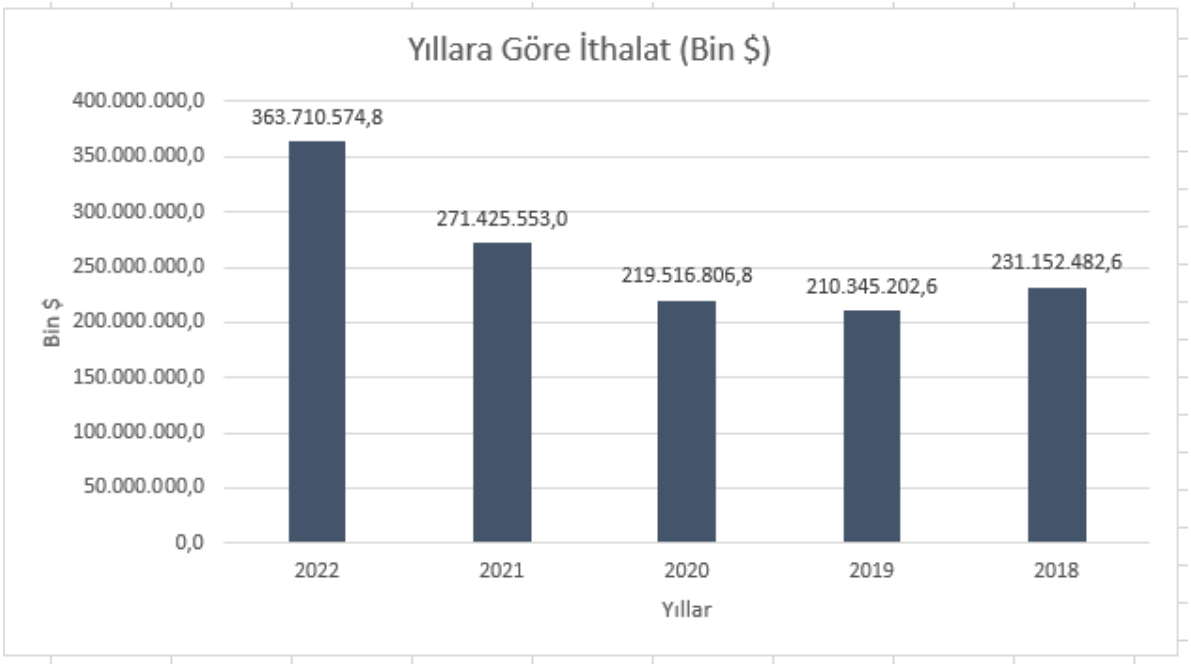

Şekil 2. Türkiye toplam ithalat grafiği

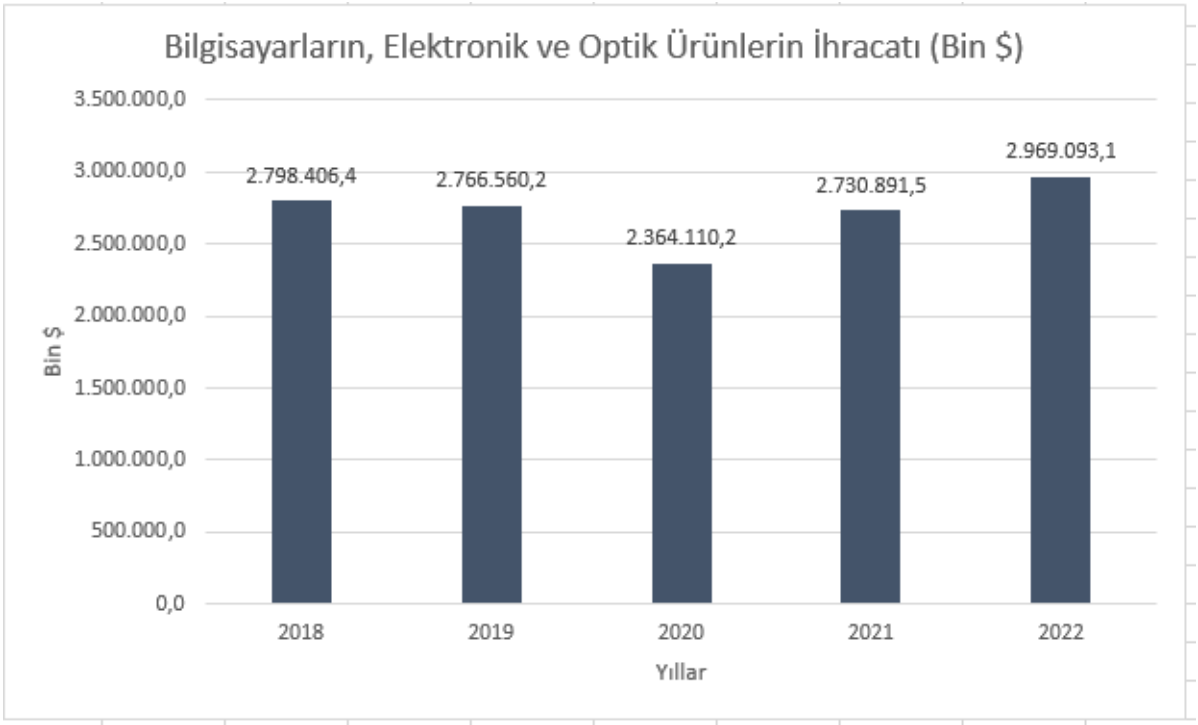

Şekil 3. Bilgisayarların, elektronik ve optik ürünlerin imalatı ihracat grafiği

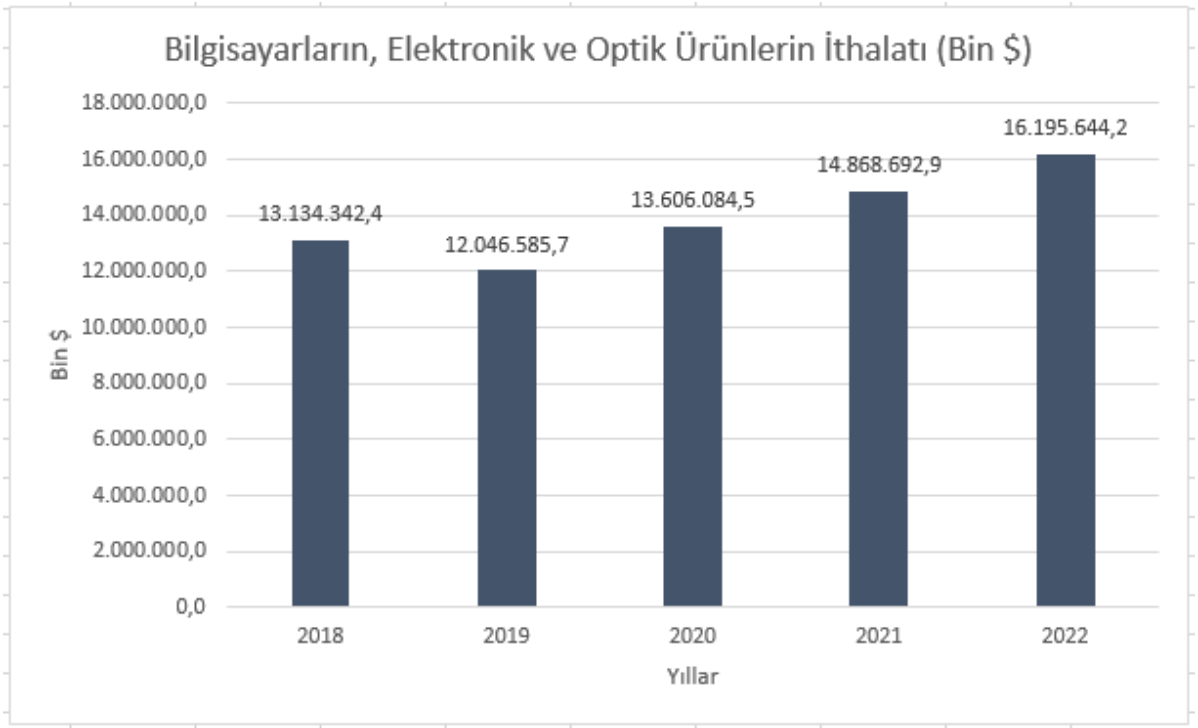

Şekil 4. Bilgisayarların, elektronik ve optik ürünlerin imalatı ithalat grafiği

Dış ticaret verilerinde geleneksel olarak yer çekimi modeli kullanılmaktadır. Newton'un yerçekimi yasasından yola çıkılan bu yöntemde Reçus ve Timbergen (1964) iki ülke arasındaki ticaret akışını ülkelerin Gayri Safi Yurt İçi Hasılası ve ülkeler arasındaki mesafe ile kurmuştur. Bu model ampirik olarak güçlü olduğu için çok yoğun bir şekilde yıllarca kullanılmıştır. Anderson (2021) bu model için teorik ve çok ayrıntılı bir litaratür hazırlamıştır. Ancak geleneksel tahmin yöntemleri, dış ticaret gibi büyük hacimli ve karmaşık verilerle çalışırken sınırlı kalabilmektedir (Aktan, 2018). Bu nedenle büyük hacimli ve karmaşık verilerin çözümü için makine öğrenmesi tabanlı modellemeler ön plana çıkmaktadır.

Torkul vd. (2017)'ne göre "Makine öğrenmesi mantıksal işlemler gerçekleştirebilen makinelerin, gözlem ve ölçüm yöntemleriyle elde edilen verileri tecrübe olarak kabul etmesi ve bu tecrübelerden matematiksel algoritmalar aracılığıyla anlamlı ilişkiler üretmesi sürecidir".

Öğrenmenin amacı elimizde bulunan veriler ile bilgisayarların karar verebilme yeteneğinin kullanılmasıdır. Makine öğrenmesi uygulamalarında üç çeşit öğrenme yöntemi vardır. Bu yöntemler denetimli öğrenme, denetimsiz öğrenme ve yarı denetimli öğrenme şeklindir.

Sınıflandırma, regresyon, karar ağaçları için denetimli öğrenme kullanılır. Bu öğrenme algoritmasında hem giriş hem de çıkış verileri sisteme verilir. Giriş verileri kullanılarak çıkış verileri tahminlenmeye ya da öğrenmeye çalışılır. Araştırmada kullanılan giriş ve çıkış verileri bu sistemdeki algoritmaya işlenerek performansı ölçülür ve araştırmada kullanılan çıkış verileri tahmin edilmeye çalışılır. Denetimsiz öğrenmede sisteme giriş verileri verilerek çıktıyı kendi keşfedebilmektedir. Veriler arasındaki örüntüyü makinenin keşfetmesi ve ilişki ağını kendisinin bulması beklenir. Boyut azaltma, kümeleme gibi çalışmalarda denetimsiz öğrenme kullanılır. Son olarak yarı denetimli öğrenme ise kullanılan verilerin içerisinde az sayıda işaretlenmiş veri olduğu ve işaretlenmemiş çok sayıda verinin tahmini ve sınıflandırılması yapılmaktadır (Gökalp, 2022).

Hem denetimli hem de denetimsiz öğrenmenin kullanıldığı bu çalışmada, makine öğrenmesi yöntemlerinin bu tür çok boyutlu ve dinamik veriler üzerindeki güçlü tahmin performansından faydalanarak, Türkiye'nin dış ticaret verileri üzerinde üç farklı tahmin modeli önerilmiştir. Önerilen modeller, dış ticaret verilerindeki anomalilerin tespiti, öznitelik seçim yöntemleri ile veri boyutunun azaltılması, veri kümelerinin yapısına uygun kümeleme yöntemleri ve çeşitli regresyon teknikleri ile elde edilen sonuçların analizini kapsamaktadır. Bu kapsamda çalışma litaratüre katkı sağlamaktadır. Çalışma dört bölümden oluşmaktadır. Birinci bölümde teorik çerçeve ele alınmıştır. İkinci bölümde konu kapsamında litaratür araştırması ile veri seti ve modelin tahmin yöntemi tanıtılmaktadır. Üçüncü bölümde tahmin edilen modelden elde edilen bulgular kısmı, dördüncü bölümde bulgular ışığında elde edilmiş sonuçları ile çalışmanın kısıtları ve gelecek çalışmalar için tavsiyelerden bahsedilmiştir.

2. Materyal ve Yöntem

Veri Seti Türkiye İstatistik Kurumu A grubu mikro veri setlerinden dış ticaret istatistikleri mikro veri setidir. Veriler TÜİK Erzurum Bölge Müdürlüğü Veri Araştırma Merkezi'nde kullanılabilmektedir. Veriler Veri Araştırma Merkezi dışına çıkarılamadığından burada sağlanmış olan bilgisayar ile algoritmalar çalıştırılmıştır. Bütün sektörleri içeren kayıtlar incelenmiş ve çalışmanın konusu olacak şekilde Nace Rev2 26 (Bilgisayarların, elektronik ve optik ürünlerin imalatı) sektörü verileri içerisinden 2018-2022 yılları için tam sayım olacak şekilde 817500 veri işleme alınmıştır.

Bu çalışma kapsamında elimizde bulunan veri için en iyi algoritma bulunmaya çalışılmıştır. 3 farklı model ile yapılan çalışmalarda 30 farklı sonuç elde edilmiş bu sonuçlar ışığında en iyi model seçilmiştir.

2.1. Literatür Taraması

Dış ticaret akışlarının modellenmesi ve öngörülmesinde makine öğrenmesi yöntemlerinin kullanımı, son yıllarda artan bir ilgi görmektedir. Bu bağlamda Nuroğlu (2014) geleneksel yerçekimi yöntemi ile yapay sinir ağları modellerini karşılaştırmıştır. Bu modellerde yapay sinir ağlarının girdi ve çıktıların arasındaki ilişkileri öğrenme ve açıklama yeteneğinin daha iyi olduğu gözlemlenmiştir. Bayrak (2020) ise medikal cihazların dış ticareti için makine öğrenme yöntemlerini kullanmış ve DVM yöntemi ile R^2=0,974 performans yakalamıştır. Nummelin ve Hanninen (2016) Birleşmiş Milletler FAO verilerinikullanarak kütük dış ticareti tahminlemesi için makine öğrenmesi yöntemleri kullanmışlardır.

Bu çalışmaya benzer olarak yurtdışında Filimnova vd. (2021) makalesinde Rusya'nın dış ticaret verilerini kullanırken kümeleme analizinin tahminleme gücüne etkisini ölçmeye çalışmıştır. Huang vd. (2020) Çin ve 5 merkez Asya ülkelerinin ihracat hacmi tahminlemesinde çok fazla faktör olduğunda klasik istatistik yöntemleri ile karar ağaçları gibi çok değişkenli regresyon analizini kullanmışlardır. Jošić ve Žmuk (2022) Hırvatistan Dış Ticaret verileri için gaussian yöntemler, lineer regresyon ve çok katmanlı perceptron kullanarak çalışmışlardır.

Gopinath vd. (2021) Amerika Birleşik Devletlerinde tarım dış ticareti için yapay sinir ağları kullanarak makine öğrenmesi modelleri kullanmıştır. Jia vd. (2019) Latin Amerikada yapılan yakıt ihracatının yönünü belirlemek için karar ağaçları, rasgele ormanlar ve Boosting ağaç yöntemini kullanmışlardır. Shen vd. (2021) ise 10 ülkenin dış ticaretini ölçmek için zaman serileri verileri ile LSTM modeli kullanmıştır.

Baxter ve Srisaeng (2018) yapay sinir ağları kullanarak Avusturalya'nın hava kargoculuğu ile yapacağı ihracatı tahmin çalışması yapmıştır. CHAN vd. (2021) çalışmasında Amerika Birleşik Devletleri ile 15 Asya ülkesi arasında yapılan kıyafet ticaretini çoklu regresyon ve yapay sinir ağları modelleri ile tahminlemeye çalışmıştır. Burada klasik çoklu regresyona göre yapay sinir ağları modelinin daha yüksek R^2 değerine sahip olduğu görülmüştür.

Dumor ve Yao (2019) çalışmasında Çin'in Belt and Road inisiyatifi ile ortak ülkeleri olan Kenya, Burundi, Rwanda, Tanzanya, Uganda ve Cibuti ile yaptığı ticareti yapay sinir ağları ile tahminlemeye çalışmıştır. Çalışma kapsamında yerçekimi modeli sonuçları ile yapay sinir ağları modeli karşılaştırılmış ve yapay sinir ağları modelinin daha düşük RMSE sahip olduğu görülmüştür.

Micocci ve Rungi (2023) derin öğrenme algoritmaları olan LOGIT, LOGIT-LASSO, CART, Random Forest, BART ve BART-MIA kullanarak Fransa'nın dış ticaret verileri hesaplamaya çalışılmış ve en iyi sonuç BART-MIA modeli ile alınmıştır.

Gupta ve Kumar (2022) Hindistan'ın dış ticaretini ölçmek için Doğrusal Regresyon, DVM, Karar Ağaçları ve Rasgele Orman algoritmalarını kullanmıştır. Bu algoritmalar arasında en iyi sonucu Karar Ağacı algoritmaları vermiştir.

Eşidir (2025) Türkiye'nin kimyasal madde ithalatını ölçmek için doğrusal regresyon, rasgele orman, rasyonel kuadratik regresyon, DVM ve XGBOOST regresyon modellerini kullanmıştır. Burada XGBOOST algoritması en iyi sonuçları vermiştir.

Ay vd. (2024) Türkiye ve Türk Cumhuriyetleri (Azerbaycan, Kazakistan, Kırgızistan, Özbekistan ve Türkmenistan) arasındaki ticareti ölçmek için lineer regresyon, gauss süreç regresyonu ve çok katmanlı algılayıcılar gibi farklı makine öğrenme algoritmaları kullanmış, en iyi sonuca çok katmanlı algılayıcılar algoritması ile ulaşmıştır.

Gür ve Eşidir (2024) Türkiye'nin hurda demir çelik ithalatını ölçmek için LTSM, MLP, Random Forest, DVM, XGBOOST ve doğrusal regresyon modellerini kullanmış, LTSM modeli ile en iyi sonuçlara ulaşmıştır.

Soydal vd (2024) Türkiye ve Balkan ülkeleri üzerine çekim modeli uygulaması yapmış ve her ülke değişkeni için en iyi sonuçları veren yöntemleri çalışmasında yayınlamıştır.

2.2. Veri Seti

Öncelikle kullanılacak sektör için veriler SAS Enterprise uygulaması ile 5 yıllık çekilmiştir. Daha sonrasında aynı paket program aracılığıyla birleştirilmiştir. Veri işleme için Jupyter Notebook kullanılmıştır. Önce veri temizleme yapılmıştır. Veri temizleme yapılırken eksik ve tekrarlayan veriler silinmiştir. Bu işlem sonucunda 15 satır mükerrer veri ve 22 satır veri ürün kodu ve parasal değeri eksik olduğu için yanlılık olmaması adına silinmiştir, Silinen verinin toplam veriye oranı 0,00005'dir. Daha sonra metin verileri kodlanmıştır. Bu işlemler ithalat ve ihracat verileri için ayrı ayrı yapılmış, veriler birleştirilmiştir.

5 yıllık veri seti 18 öznitelikten oluşmaktadır. Bu öznitelikler aşağıdaki şekilde açıklanmıştır

IHRITH: İhracat ve İthalat ayrımını gösterir.

YIL: Yıl bilgisini içerir.

ISTPOZ: Gümrük Tarifesi İstatistik Pozisyonu 12 dijit (GTİP)

ULKE: İhracat/İthalat yapılan ülke kodlarını içerir. (Ülke bilgisi ithalatta menşei ülke, ihracatta malın gideceği bilinen son ülkeyi ifade eder)

OLCU: GTİP'lerin ölçü kodlarını içerir.

IL_KODU: Dış ticaret yapan firmanın merkezinin bulunduğu il kodu

ODEME_SEKLI: Alıcı ve satıcı arasındaki ödemenin ne şekilde yapıldığını ifade eder.

DOVIZ_KODU: Yapılan dış ticaretin para biriminin kodu

YOL: Taşıma şeklinin kodu

GCGUMRUK: Giriş çıkış gümrük kodu

SOZLESME_KODU: Alıcı ve satıcı arasındaki ticari sözleşme türlerini ifade eder.

KONTEYNER: Malın konteynerle mi konteynersiz mi taşındığını belirten kodlardır.

BEC: Geniş ekonomik gruplar sınıflaması

NACE: Avrupa Topluluğunda Ekonomik Faaliyetlerin İstatistiki Sınıflaması, Rev.2 (4 dijitlidir)

CPA: Avrupa Topluluğunda Ekonomik Faaliyete Göre Ürünlerin İstatistiki Sınıflaması, 2008 versiyonu (4 dijitlidir)

MIKTAR_1: Ürünlerin kilogram bilgisini ifade eder. (doğalgaz, elektrik hariç)

MIKTAR_2: Yardımcı ölçü birimini ifade eder. (adet m^3, m^2 gibi)

DOLAR: ABD para birimi cinsinden dış ticareti ifade eder.

EURO: Avrupa Birliği para birimi cinsinden dış ticareti ifade eder.

Çalışma bütününde test veri setleri %20, %25 ve %30 olarak çalıştırılmış en iyi sonuç %20 test, %80 train veri setinde ulaşılmış bu nedenle bütün çalışmada bu şekilde çalışılmıştır.

Burada uygulanan modele göre öznitelik seçimi algoritmaları uygulanmış ve bu algoritmalar sonucunda çıkan öznitelik önemliliğine göre seçilerek model sonuçları alınmıştır. Öznitelik önemliliği için MRMR ve RFE algoritmaları uygulanmıştır.

2.3. Anomali Tespit

2.3.1. Isolation forest

Literatürde, "Anomali Tespiti" ile aynı veya benzer anlamlara sahip farklı terimler kullanılmaktadır. Bunlar arasında olay tespiti, yenilik tespiti, (nadir) olay tespiti, sapma keşfi, değişim noktası tespiti, arıza tespiti, izinsiz giriş tespiti ve kötüye kullanım tespiti yer almaktadır (DA, 2013). Esasında farklı görünen bu terimler aynı amacı anlatmak istemektedir. Veri dağılımından belirgin bir şekilde sapmış veri noktalarını tespit etmek. Anomali gücünün bir ölçüsü genellikle sapma miktarı üzerinden değerlendirilir veya stokastik olarak, bir anomali olma ihtimali anlamına gelen "anomali skoru" olarak tanımlanır.

İzolasyon ormanı algoritması ile verideki aykırı değerleri tespit etmek için rastgele oluşturulmuş izolasyon ağaçlarından oluşan bir orman oluşturulur. Her ağaç, analiz edilen veri kümesinin bir alt kümesi olan bağımsız olarak alınmış örneklere dayanarak büyütülür. Bu ağaçlar, analiz edilen uzayı özyinelemeli olarak bölerek ayrı noktalar yapraklarında izole edilene veya derinlik sınırına ulaşılana kadar işleyen "izole edici" ağaçlar olarak adlandırılır. Aykırı değer tespiti, verilerin oluşturulan ormana gönderilmesi ve her bir veri noktası için bir anomali ölçüsünün üretilmesiyle gerçekleştirilir. Bu çalışmada Python programlama dilinde Sklearn Kütüphanesinde IsolationForest kullanılmıştır.

2.4. Öznitelik Seçimi

2.4.1. MRMR öznitelik seçim algoritmasi

MRMR algoritması sınıf etiketleriyle en ilişkili öznitelikleri seçmeye çalışırken, seçilen öznitelikler arasındaki artıklığı, fazlalığı minimize etmeye çalışan bir literatür yöntemidir (Ding ve Peng, 2005). Öznitelik kümesini seçerken, seçilmek istenilen kümenin seçilebilecek en iyi küme olması için iki koşul vardır, birincisi minimum ortaklık, ikincisi maksimum ilişkidir. Bu çalışmada Python programlama dilinde MRMR kütüphanesinden mrmr_classif yöntemi kullanılmıştır.

2.4.2. RFE öznitelik seçim algoritmasi

Geriye dönük öznitelik seçimi olan RFE öznitelik

seçiminde öncelikle bir model oluşturulur. Bu modelde her özniteliğe bir önem puanmı vermektedir. Sonraki aşamalarda en düşük önem puanındaki öznitelikler silinerek yeniden hesaplanır ve istenilen sayıda öznitelik sayısına ulaşılır. (Emanet vd., 2021)

Çalışma kapsamında Python programlama dilinde Sklearn Kütüphanesinde RFEkullanılmıştır.

2.5. Kümeleme Algoritmaları

2.5.1. Clarans algoritmasi

K-medoids, her kümenin merkezini küme içerisindeki gerçek bir gözlem noktası (medoid) olarak belirler. CLARANS ise K-Medoids'in daha gelişmiş versiyonudur ve klasik k-medoids algoritması, veri seti büyüdükçe daha maliyetlidir. CLARANS ise küresel en iyi çözüme daha yakın bir sonuç elde etmeyi amaçlayan rastgeleleştirilmiş bir arama prosedürü uygular.

CLARANS'ın temel fikri, küme merkezlerinin komşuluk uzayında rastgele araştırılması ve bu süreçte maliyeti düşüren komşuların kabul edilmesidir. Bu yönüyle CLARANS, kısmi bir rastgele optimizasyon algoritması olarak da değerlendirilebilir. (Ng ve Han, 2002)

2.5.2. K-Means algoritmasi

K-Means algoritması, gözetimsiz öğrenme (unsupervised learning) kapsamında en yaygın kullanılan merkez-temelli (centroid-based) kümeleme yöntemlerinden birisidir. Amaç, gözlemleri, her biri kendi merkezine (centroid) en yakın olacak şekilde k adet kümeye ayırmaktır. Bu merkezler, kümelerin geometrik temsilcileridir ve kümeler arası farklılıkları en üst düzeye çıkarırken, kümeler içi benzerlikleri en üst düzeye çıkarmayı hedefler. (Demiralay ve Çamurcu, 2005)

K-Means algoritmasının en önemli özelliği büyük veri setlerinde hızlı ve etkili olmasıdır. Bunun yanında çok boyutlu veri kümelerine uygulama kolaylığı nedeniyle de çalışma kapsamında seçilmiştir.

2.6. Regresyon Algoritmaları

2.6.1. XGBOOST algoritmasi

Çok boyutlu büyük veri analizinde etkin olarak kullanılabilen XGBOOST algoritmasının bir çok regresyon modeline göre kullanımı ve skorları daha yüksek çıkmaktadır. Model, ardışık ağaçlar inşa ederek bu hatayı minimize etmeye çalışır. Ayrıca, erken durdurma (early stopping), çapraz doğrulama (cross-validation) ve hiperparametre optimizasyonu ile yüksek doğruluk ve genelleme sağlanabilir. (Abar, 2020)

Ağaç tabanlı yöntemler arasında en yüksek skorları veren ve Gradyan Boosting temeline kurulmuş XGBOOST algoritması aşırı öğrenmeyi kontrol etmek için L1 (lasso) ve L2 (ridge) cezalarını kullanır. (Carmona vd., 2019)

2.6.2. LightGBM algoritmasi

LİghtGBM modeli XGBOOST ile benzer prensiplerle çalışmasıyla birlikte büyük ölçekli veri setlerinde daha hızlı modelleme ve daha düşük bellek kullanımı yapısal optimizasyon içerir. Bu optimizasyonları ağaç dallarını dikey bir şekilde değil, yatay bir şekilde dallanma yoluan gitmesi ile gerçekleştirir. Bu sayede daha düşük ram kullanımı sağlar. Ancak LightGBM regresyon modelinin zaafı aşırı öğrenmeye (overfitting) meyilli olmasıdır. Bu nedenle model kurulduktan sonra hiperparametre optimizasyonuna çok büyük rol düşmektedir. (Ke vd., 2017)

2.6.3. Random forest regresyon algoritmasi

Random Forest Regresyonu hem sınıflandırma hem de regresyon problemlerinde kullanılan topluluk öğrenme yöntemlerinden bir tanesidir. Veri seti rastgele parçalanarak küçük parçalara ayrılır. Bu küçük parçalardan oluşmuş tahminlerin ortalaması alınarak sonuç ortaya çıkarır. Model küçük parça sonuçları üzerine kurulu olduğu için hem aşırı öğrenmenin (overfitting) önüne geçmekte hem de veri gürültüsüne karşı dayanıklılığı artmaktadır. Zaman serilerinde de yüksek başarılı sonuçlar sağlamaktadır. (Akşehir ve Kılıç, 2019)

Veri setimiz 5 yıllık verilerden oluşmakta ve random forest algoretimesı daha başarılı sonuçlar verdiği için random forest regresyon yöntemi de modellerimizde kullanılacaktır.

2.7. Hiperparametre Optimizasyonu

2.7.1. GridSearchCv ile hiperparametre optimizasyonu

Grid Search (Izgara Arama), hiperparametre ayarlaması için kullanılan bir yöntemdir ve hiperparametrelerin tüm olası kombinasyonlarını sistematik olarak değerlendirir. Bu yöntem, önceden belirlenmiş hiperparametre değerlerinin Kartesyen çarpımını oluşturarak her bir kombinasyon için modeli eğitir. Model performansı, çapraz doğrulama yöntemi kullanılarak ölçülür; bu sayede modelin veri kümesindeki anlamlı desenleri öğrenmesi sağlanır.

Grid Search yöntemi şu adımları içerir:

1. Her bir hiperparametre için makul bir değer kümesi tanımlanır.
2. Model, hiperparametrelerin tüm olası kombinasyonları ile eğitilir.
3. Her kombinasyonun performansı, çapraz doğrulama veya ayrı bir doğrulama seti kullanılarak değerlendirilir.
4. En iyi sonuç veren kombinasyon seçilerek nihai modelde kullanılır.

Her ne kadar Grid Search, en uygun hiperparametre kombinasyonunu bulmayı garanti etse de, yüksek hesaplama maliyeti önemli bir dezavantajdır. Hiperparametre sayısının artmasıyla birlikte kombinasyon sayısı üstel olarak çoğalır, O(nk) karmaşıklığına sahip olduğu için geniş arama alanları için verimsiz hale getirmektedir (Ahmad vd., 2022)

2.7.2. RandomSearchCv ile hiperparametre optimizasyonu

Önceki bölümde belirtildiği üzere, Grid Search (Izgara Arama), model seçimi için kapsamlı bir arama yöntemidir. Bu yöntemde, hiperparametre değerlerinden oluşan bir ızgara kurulur; her kombinasyon için model eğitilir ve test verileri üzerinde performans skorları hesaplanır. Bu süreç, özellikle yüksek boyutlu arama alanlarında ciddi verimsizliklere yol açabilir. Örneğin, beş hiperparametre için her biri 10 farklı değerin test edilmesi durumunda 100.000 deneme gerçekleştirilir. Eğer 10 katlı çapraz doğrulama kullanılırsa, bu durum 1.000.000 model

eğitimi ve 1.000.000 tahmine denk gelir; dolayısıyla hem hesaplama gücü hem de zaman açısından önemli maliyetler doğurmaktadır.

Buna karşılık, Random Search arama alanını örnekleyerek belirli bir olasılık dağılımından hiperparametre setlerini değerlendirir. Kısaca, bu yöntem, üzerinde çalışılan model için en uygun çözümü bulmak amacıyla hiperparametrelerin rastgele kombinasyonlarını kullanır. Örneğin, tüm 100.000 denemenin değerlendirilmesi yerine yalnızca 1000 rastgele seçilen hiperparametre seti incelenir. Random Search'te gerçekleştirilecek deneme sayısı, hiperparametre optimizasyon süreci başlamadan önce belirlenir; bu nedenle, n denemenin yapıldığı durumlarda yöntem, O(n) hesaplama karmaşıklığına sahiptir. Ancak, Random Search algoritmasının önemli bir dezavantajı, önceki denemelerden elde edilen bilgileri kullanarak bir sonraki denemeyi yönlendirmemesi ve sonraki denemeyi öngörmek için stratejik bir yaklaşım benimsememesidir (Elgeldawi vd., 2021).

Çalişma kapsamında hem GridSearchCv hem de RandomSearchCv hiperparametre optimizasyomu algoritmaları uygulanmıştır. Her iki optimizasyon algoritması sonuçları regresyon modellerine uygulanmış ve en yüksek R^2 ve en düşük MSE ve RMSE sonuçlarına göre ortaya çıkan en iyi hiperparametre sonuçları aşağıda bulunan tablolarda her alt kırılım için verilmiştir.

Tablo 1. Modellere göre XGBOOST en iyi hiperparametreler

Model Seçimi	Öznitelik Seçimi	Kümeleme Modeli	Regresyon Seçimi	Hiperparametre
Model1	MRMR	-	XGBOOST	colsample_bytree': 0.535, 'gamma': 0.387, 'learning_rate': 0.0413, 'max_depth': 11, 'min_child_weight': 6, 'n_estimators': 878, 'reg_alpha': 0.451, 'reg_lambda': 0.113, 'subsample': 0.992
Model2	MRMR	CLARANS	XGBOOST	'learning_rate': 0.2, 'max_depth': 5, 'n_estimators': 200, 'subsample': 1.0
Model2	MRMR	K-Means	XGBOOST	'learning_rate': 0.1, 'max_depth': 5, 'n_estimators': 200, 'subsample': 0.8
Model3	MRMR	CLARANS	XGBOOST	'learning_rate': 0.2, 'max_depth': 5, 'n_estimators': 200, 'subsample': 1.0
Model3	MRMR	K-Means	XGBOOST	'learning_rate': 0.1, 'max_depth': 5, 'n_estimators': 200, 'subsample': 0.8
Model1	RFE	-	XGBOOST	colsample_bytree': 0.878, 'gamma': 0.234, 'learning_rate': 0.0912, 'max_depth': 9, 'min_child_weight': 2, 'n_estimators': 537, 'reg_alpha': 0.772, 'reg_lambda': 0.520, 'subsample': 0.926
Model2	RFE	CLARANS	XGBOOST	'learning_rate': 0.1, 'max_depth': 5, 'n_estimators': 200, 'subsample': 0.8
Model2	RFE	K-Means	XGBOOST	'learning_rate': 0.2, 'max_depth': 5, 'n_estimators': 200, 'subsample': 1.0
Model3	RFE	CLARANS	XGBOOST	'learning_rate': 0.1, 'max_depth': 5, 'n_estimators': 200, 'subsample': 0.8
Model3	RFE	K-Means	XGBOOST	'learning_rate': 0.1, 'max_depth': 5, 'n_estimators': 200, 'subsample': 0.8

Tablo 2. Modellere göre LightGBM en iyi hiperparametreler

Model Seçimi	Öznitelik Seçimi	Kümeleme Modeli	Regresyon Seçimi	Hiperparametre
Model1	MRMR	-	LightGBM	colsample_bytree': 0.745, 'gamma': 0.667, 'learning_rate': 0.0175, 'max_depth': 11, 'min_child_weight': 6, 'n_estimators': 878, 'reg_alpha': 0.41, 'reg_lambda': 0.153, 'subsample': 0.992
Model2	MRMR	CLARANS	LightGBM	boosting_type': 'gbdt', 'learning_rate': 0.2, 'n_estimators': 200, 'num_leaves': 31, 'subsample': 0.7}
Model2	MRMR	K-Means	LightGBM	{'boosting_type': 'gbdt', 'learning_rate': 0.2, 'n_estimators': 200, 'num_leaves': 100, 'subsample': 0.7}
Model3	MRMR	CLARANS	LightGBM	{'boosting_type': 'gbdt', 'learning_rate': 0.2, 'n_estimators': 200, 'num_leaves': 100, 'subsample': 0.7}
Model3	MRMR	K-Means	LightGBM	boosting_type': 'gbdt', 'learning_rate': 0.2, 'n_estimators': 200, 'num_leaves': 100, 'subsample': 0.7
Model1	RFE	-	LightGBM	colsample_bytree': 0.836, 'gamma': 0.453, 'learning_rate': 0.0221, 'max_depth': 8, 'min_child_weight': 6, 'n_estimators': 658, 'reg_alpha': 0.141, 'reg_lambda': 0.533, 'subsample': 0.889
Model2	RFE	CLARANS	LightGBM	'boosting_type': 'gbdt', 'learning_rate': 0.2, 'n_estimators': 200, 'num_leaves': 31, 'subsample': 0.7
Model2	RFE	K-Means	LightGBM	'boosting_type': 'gbdt', 'learning_rate': 0.2, 'n_estimators': 200, 'num_leaves': 50, 'subsample': 0.7
Model3	RFE	CLARANS	LightGBM	boosting_type': 'dart', 'learning_rate': 0.2, 'n_estimators': 200, 'num_leaves': 31, 'subsample': 0.7
Model3	RFE	K-Means	LightGBM	'boosting_type': 'gbdt', 'learning_rate': 0.2, 'n_estimators': 200, 'num_leaves': 100, 'subsample': 0.7

Tablo 3. Modellere göre random forest en iyi hiperparametreler

Model Seçimi	Öznitelik Seçimi	Kümeleme Modeli	Regresyon Seçimi	Hiperparametre
Model1	MRMR	-	Random Forest Regressor	colsample_bytree': 0.786, 'gamma': 0.578, 'learning_rate': 0.0963, 'max_depth': 9, 'min_child_weight': 6, 'n_estimators': 864, 'reg_alpha': 0.248, 'reg_lambda': 0.312, 'subsample': 0.910
Model2	MRMR	CLARANS	Random Forest Regressor	'learning_rate': 0.2, 'max_depth': 5, 'n_estimators': 200, 'subsample': 1.0
Model2	MRMR	K-Means	Random Forest Regressor	'learning_rate': 0.1, 'max_depth': 5, 'n_estimators': 200, 'subsample': 0.8
Model3	MRMR	CLARANS	Random Forest Regressor	'learning_rate': 0.2, 'max_depth': 5, 'n_estimators': 200, 'subsample': 1.0
Model3	MRMR	K-Means	Random Forest Regressor	'learning_rate': 0.1, 'max_depth': 5, 'n_estimators': 200, 'subsample': 0.8
Model1	RFE	-	Random Forest Regressor	colsample_bytree': 0.965, 'gamma': 0.479, 'learning_rate': 0.0847, 'max_depth': 11, 'min_child_weight': 6, 'n_estimators': 744, 'reg_alpha': 0.146, 'reg_lambda': 0.132, 'subsample': 0.787
Model2	RFE	CLARANS	Random Forest Regressor	'learning_rate': 0.1, 'max_depth': 5, 'n_estimators': 200, 'subsample': 0.8
Model2	RFE	K-Means	Random Forest Regressor	'learning_rate': 0.2, 'max_depth': 5, 'n_estimators': 200, 'subsample': 1.0
Model3	RFE	CLARANS	Random Forest Regressor	'learning_rate': 0.1, 'max_depth': 5, 'n_estimators': 200, 'subsample': 0.8
Model3	RFE	K-Means	Random Forest Regressor	'learning_rate': 0.1, 'max_depth': 5, 'n_estimators': 200, 'subsample': 0.8

2.8. Çalışmada Kullanılan Modeller

Bu çalışmada kullanılan algoritmaların seçimi, veri setinin büyüklüğü, karmaşıklığı ve yapısal çeşitliliği dikkate alınarak yapılmıştır. Dış ticaret verileri; yüksek boyutlu, öznitelik bakımından heterojen ve yıl, ülke, ürün ve firma gibi çok sayıda kategorik ve sayısal değişken içeren bir yapı arz etmektedir. Bu nedenle hem anlamlı özniteliklerin seçilmesi, hem de karmaşık örüntülerin çıkarılması açısından farklı aşamalarda farklı algoritmaların birlikte kullanılması uygun görülmüştür.

Regresyon aşamasında XGBoost, LightGBM ve Random Forest Regressor algoritmaları tercih edilmiştir. Bu üç algoritma, ağaç tabanlı yöntemlerin farklı varyasyonlarını temsil etmekte olup, yüksek doğruluk ve genelleme gücü ile literatürde başarısı kanıtlanmış modellerdir. Özellikle: XGBoost, gradyan artırma temelli bir yöntem olarak karmaşık örüntüleri modelleme başarısı ile öne çıkmaktadır.

LightGBM, benzer prensiplere dayanmakla birlikte daha düşük bellek kullanımı ve hız avantajı nedeniyle yüksek hacimli verilerde tercih edilmiştir.

Random Forest, çok sayıda karar ağacının ortalaması ile overfitting'e karşı dayanıklı sonuçlar üretmektedir. Özellikle zaman serilerine benzer dönemsel dış ticaret verilerinde başarılı performansı sayesinde bu çalışmaya dahil edilmiştir.

Ayrıca, özellik seçimi (MRMR ve RFE) ile modelin boyutu azaltılarak hesaplama yükü minimize edilmiş, yalnızca anlamlı değişkenlerin kullanılması sağlanmıştır. Kümeleme algoritmaları olarak ise K-Means ve CLARANS kullanılmıştır. K-Means'in hızlı ve etkili olması ile CLARANS'ın küresel minimumlara daha yakın çözümler sunması bu seçimi desteklemiştir.

Model eğitimi süreci, hiperparametre optimizasyonu da içerecek şekilde, GridSearchCV ve RandomSearchCV yöntemleri ile sistematik olarak gerçekleştirilmiştir. Eğitim ve test veri setleri 80:20 oranında ayrılmış, farklı model bileşenlerinin etkisini gözlemleyebilmek adına üç temel model mimarisi oluşturulmuştur. Böylece her algoritmanın, farklı ön işleme aşamalarıyla nasıl performans sergilediği detaylı biçimde test edilmiştir.

Çalışma boyunca 3 farklı model oluşturulmuş ve sonuçlar bu modellerden çıkan R^2, MSE ve RMSE değerlerine göre karşılaştırılmıştır.

2.8.1. Model 1: Anomali tespiti, öznitelik seçimi ve regresyon

Bu modelde, önce Isolation Forest yöntemi kullanılarak anomali tespiti yapılmıştır. Anomaliler çıkarıldıktan sonra öznitelik seçimi için Minimum Redundancy Maximum Relevance (MRMR) ve Recursive Feature Elimination (RFE) yöntemleri kullanılmıştır. Son olarak, tahmin için XGBoost, LightGBM ve Random Forest Regressor yöntemleri uygulanmıştır. Modelin detaylı Şekil 5'de de gösterildiği üzere aşağıdaki gibidir.

- Anomali Tespiti: Isolation Forest
- Öznitelik Seçimi: MRMR ve RFE
- Regresyon: XGBoost, LightGBM, Random Forest Regressor.

<table>
<tr><td colspan="3">Model 1</td></tr>
<tr><td>Veri Alınması</td><td>Veri Önişleme</td><td>Anomali Tespiti</td></tr>
<tr><td>TÜİK VAM ile 2018-2022 yılları arası 26 Bilgisayarların, elektronik ve optik ürünlerin imalatı sektörü verileri 817500 veri</td><td>*Veri Temizliği
*Kayıp Veri analizi
*Veri Sınıflamaları, Kodlamaları
*Uluslarası Sınıflamalara Göre Faaliyet Kodlaması yapılması</td><td>Isolation Forest Algoritması kullanılarak anomali tespiti yapılması</td></tr>
<tr><td colspan="2">Öznitelik Seçimi</td><td>Regresyon Modelleri</td></tr>
<tr><td colspan="2">*MRMR (Minimum Redundancy Maximum Relevance)
*RFE (Recursive Feature Elimination)</td><td>*XGBOOST
*LightGBM
*Random Forest Regressor</td></tr>
</table>

Şekil 5. Model 1 akış diyagramı.

2.8.2. Model 2: Kümeleme, öznitelik seçimi ve regresyon

Bu modelde, veri kümeleme işlemi ile analiz edilmiştir. K-means ve CLARANS algoritmaları ile kümeler oluşturulmuş, ardından öznitelik seçimi için MRMR ve RFE yöntemleri kullanılmıştır. Kümelenmiş veri setleri üzerinden regresyon uygulanmıştır. Akış diyagramı Şekil 6'de gösterilmiştir.

- Kümeleme: K-means, CLARANS
- Öznitelik Seçimi: MRMR ve RFE
- Regresyon: XGBoost, LightGBM, Random Forest Regressor.

Model 2		
Veri Alınması	Veri Önişleme	Öznitelik Seçimi
TÜİK VAM ile 2018-2022 yılları arası 26 Bilgisayarların, elektronik ve optik ürünlerin imalatı sektörü verileri 817500 veri	*Veri Temizliği *Kayıp Veri analizi *Veri Sınıflamaları, Kodlamaları *Uluslarası Sınıflamalara Göre Faaliyet Kodlaması yapılması	*MRMR (Minimum Redundancy Maximum Relevance) *RFE (Recursive Feature Elimination)
Kümeleme Algoritması		Regresyon Modelleri
*CLARANS Kümeleme Algoritması *K-Means Kümeleme Algoritması		*XGBOOST *LightGBM *Random Forest Regressor

Şekil 6. Model 2 akış diyagramı.

2.8.3. Model 3: Anomali tespiti, kümeleme, öznitelik seçimi ve regresyon

Bu modelde ise, önce anomali tespiti yapılmış, ardından kümeleme uygulanmış ve son olarak öznitelik seçimi ile regresyon uygulanmıştır. Modelin detaylı Şekil 7'te de gösterildiği üzere aşağıdaki gibidir.

- Anomali Tespiti: Isolation Forest
- Öznitelik Seçimi: MRMR ve RFE
- Kümeleme: K-means, CLARANS
- Regresyon: XGBoost, LightGBM, Random Forest Regressor.

Model 3			
Veri Alınması	Veri Önişleme	Anomali Tespiti	Öznitelik Seçimi
TÜİK VAM ile 2018-2022 yılları arası 26 Bilgisayarların, elektronik ve optik ürünlerin imalatı sektörü verileri 817500 veri	*Veri Temizliği *Kayıp Veri analizi *Veri Sınıflamaları, Kodlamaları *Uluslarası Sınıflamalara Göre Faaliyet Kodlaması yapılması	Isolation Forest Algoritması kullanılarak anomali tespiti yapılması	*MRMR (Minimum Redundancy Maximum Relevance) *RFE (Recursive Feature Elimination)
Kümeleme Algoritması		Regresyon Modelleri	
*CLARANS Kümeleme Algoritması *K-Means Kümeleme Algoritması		*XGBOOST *LightGBM *Random Forest Regressor	

Şekil 7. Model 3 Akış Diyagramı

2.9. Çalışmada Kullanılan Metrikler

Çalışmada kullanılan modeller R^2, MSE ve RMSE metriklerine göre karşılaştırılmıştır.

2.9.1. Determinasyon katsayısı (R^2)

Yağmur (2022) Makalesinde R^2 tanımını "Korelasyon katsayısının karesi olan determinasyon katsayısı, bağımlı değişkendeki değişkenliğin ne kadarının bağımsız değişkenlerdeki değişkenlikle açıklanabildiğini ifade eder. İki değişken arasındaki doğrusal ilişkinin gücünü belirleyen determinasyon katsayısı 0-1 aralığında değer almakta olup ilişkinin gücü 1'e yaklaştıkça artmaktadır. R^2 'nin 1'e eşit olması regresyon tahminlerinin gerçekleşen değerlere tam olarak uyduğu anlamına gelmektedir." şeklinde yapmaktadır (eşitlik 1).

$$R^2 = \frac{\sum_{i=1}^{x}(y_i - \overline{y})^2 - \sum_{i=1}^{x} \mathrm{e}_i^2}{\sum_{i=1}^{x}(y_i - \overline{y})^2} \quad (1)$$

Yi : Y gerçek değerlerini göstermektedir.
Y : Yi değerlerinin ortalama değerlerini göstermektedir.
ei : Y gerçek değeleri ile tahmin değerleri arasındaki farkı göstermektedir

2.9.2. Mean squared error MSE (karesel ortalama hata)

Modeller sonucu algoritmanın elde ettiği değerler ile gerçek değerler arasındaki farkın karesinin ortalaması MSE değerini vermektedir. Burada yapılan tahminin gerçek değerden ne kadar saptığı elde edilmektedir (eşitlik 2).

$$MSE = \frac{1}{n}\sum_{i=1}^{n} \mathrm{e}_i^2 \quad (2)$$

Yi : Y gerçek değerlerini göstermektedir.
Y : Yi değerlerinin ortalama değerlerini göstermektedir.
ei : Y gerçek değeleri ile tahmin değerleri arasındaki farkı göstermektedir.

2.9.3. Root mean squared error rmse (karesel ortalama hataların kökü)

Burada kullanılan metrik ise elde edilen MSE değerinin karekökünü almaktadır. MSE değerinde karesel olarak hesaplanan için gerçek veriden sapma değeri RMSE ile hesaplanmaktadır (eşitlik 3).

$$RMSE = \sqrt{\frac{1}{n}\sum_{i=1}^{n} \mathrm{e}_i^2} \quad (3)$$

3. Bulgular ve Tartışma

Bu makale Türkiye'nin dış ticaret verileri kullanılarak bir model ortaya çıkarmak amacıyla yazılmıştır. Yapılan çalışmada veriler A grubu mikro veriler olduğu için kurum dışına çıkartılamamış, TÜİK VAM bilgisayarı üzerinde kullanılmıştır. Burada kullanılan bilgisayarın CPU ve ram özellikleri yeterli olmadığı için bütün veriler kullanılamamış, 2018-2022 yılları arasında NACE 26 "Bilgisayarların, elektronik ve optik ürünlerin imalatı" faaliyetinde bulunulan 817500 veri kullanılmıştır.

Çalışmamızda Türkiye'nin bilgisayar, elektronik ve optik ürünler dış ticaretine ilişkin verileri kullanarak üç farklı makine öğrenmesi modeli oluşturulmuş ve performansları değerlendirilmiştir. Model 1'de Anomali Tespiti (Isolation Forest), Özellik Seçimi (MRMR, RFE) ve Regresyon (XGBoost, LightGBM, Random Forest Regressor) yöntemleri uygulanmıştır. Model 2'de Kümeleme (K-Means, CLARANS), Özellik Seçimi (MRMR, RFE) ve Regresyon (XGBoost, LightGBM, Random Forest Regressor) süreçleri gerçekleştirilmiştir. Model 3'te ise Anomali Tespiti, Kümeleme, Özellik Seçimi ve Regresyon yöntemleri entegre edilerek daha kapsamlı bir tahminleme süreci yürütülmüştür.

Öncelikle, veri seti üzerinde gerçekleştirilen izolasyon ormanı yöntemi ile anomali tespiti sonucunda belirlenen aykırı gözlemler çıkarılmış ve bu işlem veri kalitesini artırmıştır. Anomali tespit işlemi sonrası, MRMR ve RFE yöntemleri ile en etkili değişkenler seçilmiş ve modelin hesaplama yükü azaltılmıştır. Modelin tahmin başarısını artıran ve aşağıda detaylıca açıklanan özniteliklerin yıl, ülke, il, NACE Rev2 dörtlüsü, CPA 2.1 dörtlüsü, ürün miktarı, ithalat-ihracat ayrımı ve gümrük sınıflamaları olduğu görülmüştür.

Yıl: Makroekonomik faktörler (resesyonlar, pandemi etkisi, döviz kuru dalgalanmaları vb.) ve politika değişiklikleri (gümrük vergileri, teşvikler vb.) ile doğrudan ilgilidir, ayrıca yıllara göre ürün fiyatı dalgalanmaları olacağından yıl özniteliğinin modelde bulunması hayati önem taşımaktadır.

Ülke: Bazı ülkelerle ticaret yapısı teknoloji ithalatı ağırlıklı iken, bazılarıyla hammadde ihracatı gibi farklılıklar gösterebilmektedir. Örneğin Avrupa Birliği ülkelerine yapılan ihracat, katma değeri yüksek ürünler açısından farklı bir dinamik sunar. Bu farklılıkların modelin tahmin doğruluğunu artırmada önemli rol oynayacağı düşünülmektedir.

İl: İller ve bölgeler arası üretim kapasitesi, teşvik politikaları ve liman erişimi gibi faktörler dış ticaret hacmini ve ticaret yapılan ürün cinsini doğrudan etkilemektedir. Bu nedenle il bazlı ayrımın kümeleme ve regresyon aşamalarında belirleyici rol oynadığı düşünülmektedir.

Nace Rev2: Ekonomik faaliyet kodu olan NACE bazında 26 sektörü seçilmiştir. Ancak 26 sektöründe 10 farklı dörtlü bulunmaktadır. Bu ayrım çalışılan sektör içinde farklı faaliyet alanları için tahmin yapılabilmesini sağlamaktadır.

CPA 2.1: Ürün sınıflaması olan CPA bazında da aynı NACE'de olduğu gibi 26 sektörü alınmaktadır. Burada 116 farklı altılı bulunmakta ve 116 farklı ürün için tahminleme yapılabilmektedir.

Ürün Miktarı: Birim fiyat değişimlerinin izlenmesi, dış ticaret karlılığı ve verimliliği gibi önemli göstergelerin hesaplanmasını sağlar.

İthalat-İhracat Ayrımı: Model için temel belirleyici unsurdur. Bu ayrım ile hem Türkiye'nin ithalat hem de ihracat değeri tahminelenecektir. 26 sektörü için dış ticaret açığı ya da fazlası tahmini bu değişken ile kontrol edilebilecektir.

Gümrük Sınıflamaları: Burada kullanılan sınıflama CPA sınıflamasına benzer şekilde ürün sınıflamasıdır. En net farkı ise sekizli sınıflama olduğundan daha alt kırılımda ürünler için hesaplama yapılabilme yeteneğini modele kazandırmasıdır.

Kümeleme aşamasında, K-Means ve CLARANS yöntemleri kullanılarak veri gruplara ayrılmıştır. K-Means yönteminde en uygun küme sayısını belirlemek için Dirsek Yöntemi ve Silhouette Skoru kullanılmıştır. CLARANS yöntemi ise büyük veri kümelerinde daha esnek bir kümeleme sağladığı için tercih edilmiştir. Kümeleme

sonuçları, farklı dış ticaret eğilimleri gösteren grupların belirlenmesine yardımcı olmuştur.

Regresyon modellerinin performanslarını karşılaştırmak amacıyla R-Kare (R^2), Karesel Ortalama Hata (MSE) ve Kök Ortalama Kare Hata (RMSE) gibi değerlendirme metrikleri kullanılmıştır. Yapılan analizler sonucunda, Model 2'ün (Kümeleme + Özellik Seçimi + Regresyon) en yüksek doğruluk oranına sahip olduğu görülmüştür. Özellikle Random Forest algoritmasının diğer regresyon yöntemlerine kıyasla daha düşük hata oranlarına ve daha yüksek determinasyon katsayısına sahip olduğu belirlenmiştir. Bununla birlikte, kümeleme yöntemlerinin tahmin başarısını önemli ölçüde artırdığı ve belirli kümelerde regresyon modellerinin daha başarılı tahminler ürettiği gözlemlenmiştir.

Ayrıca, ithalat ve ihracat verilerinin yıllık bazda tahmin edilmesi sonucunda, Türkiye'nin bilgisayar, elektronik ve optik ürünler sektöründe belirli yıllarda ihracatın arttığı, ancak küresel ekonomik krizler ve tedarik zinciri problemleri gibi dış faktörlerin dış ticaret üzerinde dalgalanmalara yol açtığı belirlenmiştir. Özellikle 2020 yılında COVID-19 pandemisinin ticaret hacmi üzerinde olumsuz etkiler yarattığı, ancak sonraki yıllarda ihracatta toparlanmalar yaşandığı görülmüştür. Makine öğrenmesi modelleri ile yapılan tahminler, gelecekteki dış ticaret eğilimlerini anlamada önemli bilgiler sağlamaktadır.

Her bir regresyon algoritması için Model1 3 fold ve 100 deneme için çalıştırılmış ve sonuç olarak optimum sonuçlar alınmıştır. Model2 ve Model3 için ise her regresyon modeli ayrı ayrı kümeleme algoritmaları için 3 fold 34 deneme için çalıştırılmış, çıkan sonuçlar kümelere göre ayrı ayrı alınmıştır. Kümelere göre alınan sonuçlar küme ağırlıkları kullanılarak ağırlıklı ortalama yöntemine göre hesaplanarak R^2, MSE ve RMSE sonuçları hesaplanmıştır.

Elde edilen sonuçlar IBM SPSS versiyon 20 paket program (Statistical Package for Social Sciences v.21, IBM, Chicago, IL) paket programı kullanılarak gruplar arası fark testine tabi tutulmuştur. Üç grup için Kruskal Wallis ve İkili gruplar için Mann-Whitney U fark testi uygulanmış, bütün P değerler 0,05 değerinden büyük olduğu için gruplar arası istatistiki olarak anlamlı fark olmadığı görülmüştür. Gruplar arası anlamlı bir fark olmadığından en yüksek R^2 değeri kullanılarak en yüksek tahmin değeri bulunulmak istenilmiştir.

Kullanılan verileri göre en yüksek R^2 0,8322 ile MRMR öznitelik seçimi, Clarans kümelemesi ve Random Forest Regressor kullanılan ve makalede model 2 olarak adlandırılan modelde elde edilmiştir. Aynı modelde MSE değeri 21683120914,9233 ve RMSE değeri 144269,018 çıkmıştır.

En düşük MSE değeri 26317190,429, RMSE değeri 4627,3104 ile Model 3 modellemesinde olmuştur. Bu model 3 uygulamasında öncelikle Isolation Forest ile anomali tespiti yapılmış, K-Means ile kümeleme yapılmış, MRMR yöntemi ile öznitelik seçilmiş ve LightGBM Regresyon algoritması ile model tamamlanmıştır. Düşük hata değeri olsa dahi bu modelin R^2 değeri 0,7857'dir.

Çıkan sonuçlar karşılaştırılıdığında Model3'te daha düşük hatalar olmasına rağmen Model2'nin daha yüksek R^2'ye sahip olması, izolasyon ormanı ve kümeleme algoritması kullanımın varyansı azalttığı ancak determinasyon katsayısını sınırladığı şeklinde yorumlanabilmektedir.

Sonuç olarak, bu çalışma, Türkiye'nin bilgisayar, elektronik ve optik ürünler dış ticaretinin makine öğrenmesi ile tahmin edilmesinde farklı yöntemlerin karşılaştırmalı analizini sunarak, en başarılı model kombinasyonlarını ortaya koymuştur.

Tablo 4. Modellere Göre XGBOOST Algoritma Sonuçları

Model Seçimi	Öznitelik Seçimi	Kümeleme Modeli	Regresyon Seçimi	R^2	MSE	RMSE
Model1	MRMR	-	XGBOOST	0,7861	227.725.704,3	15.090,6
Model2	MRMR	CLARANS	XGBOOST	0,6704	74.339.256.508,0	242.739,3
Model2	MRMR	K-Means	XGBOOST	0,7589	51.721.079.447,0	162.545,1
Model3	MRMR	CLARANS	XGBOOST	0,7605	198.861.827,3	13.876,3
Model3	MRMR	K-Means	XGBOOST	0,7436	210.449.067,8	14.478,6
Model1	RFE	-	XGBOOST	0,7925	166.904.775,1	12.919,2
Model2	RFE	CLARANS	XGBOOST	0,7357	166.550.000.000,0	300.934,4
Model2	RFE	K-Means	XGBOOST	0,7602	60.180.218.688,0	165.537,5
Model3	RFE	CLARANS	XGBOOST	0,7417	130.135.895,9	10.371,7
Model3	RFE	K-Means	XGBOOST	0,7454	209.001.603,9	14.431,0

Tablo 5. Modellere Göre LightGBM Algoritma Sonuçları

Model Seçimi	Öznitelik Seçimi	Kümeleme Modeli	Regresyon Seçimi	R^2	MSE	RMSE
Model1	MRMR	-	LightGBM	0,7925	179.618.006,5	13.402,2
Model2	MRMR	CLARANS	LightGBM	0,6401	88.900.885.650,0	258.405,1
Model2	MRMR	K-Means	LightGBM	0,7642	40.932.954.877,0	155.975,1
Model3	MRMR	CLARANS	LightGBM	0,7927	171.511.277,3	12.894,9
Model3	MRMR	K-Means	LightGBM	0,7857	26.317.190,4	4.627,3
Model1	RFE	-	LightGBM	0,7904	171.185.487,4	13.083,8
Model2	RFE	CLARANS	LightGBM	0,7278	180.678.000.000,0	303.949,6
Model2	RFE	K-Means	LightGBM	0,7804	41.065.577.372,0	152.402,4
Model3	RFE	CLARANS	LightGBM	0,7832	112.450.066,9	9.705,3
Model3	RFE	K-Means	LightGBM	0,7894	172.676.279,9	13.116,0

Tablo 6. Modellere Göre Random Forest Algoritma Sonuçları

Model Seçimi	Öznitelik Seçimi	Kümeleme Modeli	Regresyon Seçimi	R^2	MSE	RMSE
Model1	MRMR	-	Random Forest Regressor	0,7593	192.266.701,4	13.866,0
Model2	MRMR	CLARANS	Random Forest Regressor	0,8322	21.683.120.915,0	144.269,0
Model2	MRMR	K-Means	Random Forest Regressor	0,8142	16.350.213.943,0	123.714,6
Model3	MRMR	CLARANS	Random Forest Regressor	0,7618	197.867.193,7	13.838,8
Model3	MRMR	K-Means	Random Forest Regressor	0,7522	203.010.840,9	14.221,8
Model1	RFE	-	Random Forest Regressor	0,8018	189.454.067,4	13.764,2
Model2	RFE	CLARANS	Random Forest Regressor	0,8225	21.683.120.915,0	144.269,0
Model2	RFE	K-Means	Random Forest Regressor	0,8145	16.572.497.458,0	124.399,2
Model3	RFE	CLARANS	Random Forest Regressor	0,7503	127.765.522,2	10.340,8
Model3	RFE	K-Means	Random Forest Regressor	0,7548	201.162.104,9	14.155,7

4. Sonuç

Bu çalışmada, 2018-2022 yılları arası Türkiye Dış Ticaret verileri kullanılarak Türkiye için Nace Rev2 26 (Bilgisayarların, elektronik ve optik ürünlerin imalatı) sektörü ihracat ve ithalat verileri makine öğrenmesi teknikleriyle tahmin edilmesine yönelik bir analiz gerçekleştirilmiştir. Anomali tespiti, değişken seçimi, kümeleme ve regresyon yöntemlerinin entegre edilmesiyle üç farklı model geliştirilmiş ve karşılaştırmalı performans analizi yapılmıştır. Elde edilen bulgular, dış ticaret tahminlerinde makine öğrenmesi yöntemlerinin etkinliğini ortaya koymuş ve en başarılı model kombinasyonlarını belirlenmeye çalışılmıştır.

Tablo 4 'de XGBOOST regresyon modeli kullanılarak oluşturulmuş modeller görülmektedir. Burada en yüksek R^2 0,7925 ile model 1 RFE öznitelik seçimi ile olmuştur. Tablo 5'de ise LightGBM regresyon modeli için sonuçlar listelenmiştir. Burada en yüksek R^2 0,7925 ile model 1 MRMR özniteliği seçeneğindedir.

Kullanılan metriklere göre en iyi R^2 değeri veren sonuç Tablo 6'da görüldüğü üzere model 2 (Clarans + MRMR + Random Forest) modeli ile elde edilmiştir. İleride yapılacak çalışmalarda sonuçlar diğer NACE ikililerinde de test edilerek dış ticaret verileri için en uygun model tespit edilebilecek ve ekonomik anlamda ülkenin ihtiyaç duyduğu projeksiyon rakamları elde edilebilecektir

Tablo 6 'da görüldüğü üzere en yüksek R^2 en düşük RMSE eşleşmesinde ise en iyi sonuç model 1 (Isotaliton Forest+ RFE+Random Forest) ile elde edilmiştir. Ulaşılmaya çalışılan verilerde hata oranında düşüklükte istenildiği için bu modelin kullanımın da uygun olacağı düşünülmüştür.

Çalışmanın bulguları, mevcut literatürle karşılaştırıldığında birden fazla açıdan özgün katkılar sunmaktadır. Mevcut çalışmalarda çoğunlukla dış ticaret tahminlerinde klasik regresyon ya da yapay sinir ağı tabanlı tekil modellemeler kullanılmışken, bu çalışmada çok aşamalı ve modüler bir makine öğrenmesi mimarisi önerilmiştir. Özellikle, anomali tespiti, kümeleme ve öznitelik seçimi gibi işlemlerin tahmin başarısına etkisi

detaylı biçimde analiz edilmiştir.

En yüksek R^2 değeri Model 2'de (CLARANS + MRMR + Random Forest) elde edilmiştir (R^2 = 0,8322). Bu durum, aşağıdaki nedenlerle açıklanabilir:

CLARANS algoritması, geleneksel K-Means'e kıyasla daha esnek ve küresel optimuma yakın kümeler üretmiş; bu da alt gruplar üzerinde uygulanan regresyon modellerinin daha homojen ve doğru tahminler yapmasına imkan tanımıştır.

Random Forest algoritması, ensemble yapısı sayesinde örüntü farklılıklarını etkili şekilde modellemiş, veri setindeki bölgesel, yıllık ve ürün bazlı farklılıkları yakalamada avantaj sağlamıştır.

MRMR öznitelik seçimi, gereksiz ve korelasyonlu değişkenleri filtreleyerek sadece tahmini güçlendiren değişkenleri modele dahil etmiştir. Bu durum, özellikle Random Forest gibi çok sayıda karar ağacı kullanan modellerde model karmaşıklığını azaltarak performansı artırmıştır.

Model 3 ise, düşük MSE ve RMSE değerlerine ulaşmasına rağmen (MSE=26.317.190, RMSE=4.627,3), R^2 değerinin görece düşük kalması (R^2=0,7857) dikkat çekicidir. Bu durum, modelin bazı veri noktalarını oldukça isabetli tahmin ettiğini (düşük hata), ancak veri setinin tamamı üzerindeki varyansı yeterince iyi açıklayamadığını göstermektedir. Bunun başlıca nedeni:

Anomali tespit ve kümeleme sonrası, modelin daha "sadeleşmiş" bir veri yapısı üzerinden eğitilmesi ve veri çeşitliliğinin kısmen azaltılmasıdır. Bu da modelin varyansı daha dar bir aralıkta öğrenmesine neden olmuş olabilir.

Ayrıca LightGBM modelinin aşırı öğrenmeye meyilli yapısı, düşük hata verirken genelleme kabiliyetini azaltmış olabilir.

Bu bulgular, yalnızca hata oranlarının değil, determinasyon katsayısının da tahmin kalitesinin çok boyutlu bir ölçüsü olarak değerlendirilmesi gerektiğini ortaya koymaktadır.

Elde edilen sonuçlar, politika yapıcılar ve sektör temsilcileri için önemli karar destek mekanizmaları sunmaktadır. Veri kaynağı olan TÜİK aynı zamanda Türkiye'de resmi istatistik programı kapsamında veri toplayan, yayınlayan ve dağıtımını yapan kamu kurumudur. Çalışma sonucunda ortaya çıkan projeksiyonlar resmi istatistik programı kapsamında yayınlanan dış ticaret istatistikleri için katkı sağlayacaktır. Ayrıca çalışma neticesinde çıkan sonuçlar bütün sektörlere yayılarak bütün sektörler için dış ticaret tahminleri oluşturabilecektir. Bununla birlikte Ticaret Bakanlığı sitesinde bu tür istatistikler için TÜİK bağlantısı kullanmaktadır. Yapılacak projeksiyonlar ile ürün ve faaliyet bazlı dış ticaret teşviği, vergi iade politikaları ve dış ticaret açığına neden olan eksik parçalar tahmin edilebilecektir.

Makine öğrenmesi tabanlı tahmin modelleri, ihracat ve ithalat politikalarının planlanmasında, kaynak tahsisinde ve sektörel stratejilerin geliştirilmesinde kullanılabilir. Özellikle hızlı değişen küresel ticaret dinamiklerine uyum sağlamak adına, tahminleme süreçlerinin sürekli güncellenmesi ve yeni veri kaynaklarıyla desteklenmesi önerilmektedir.

4.1 Çalışmanın Kısıtları ve Önerileri

Gelecek çalışmalarda aynı modellerin Türkiye'nin en çok dış ticaretine konu olan hazır giyim ve tekstil, otomotiv ve gıda sektörlerinde uygulanmasını yapılması tavsiye edilmektedir. Bu çalışmada en büyük kısıt kullanılan verilerin TÜİK Veri Araştırma Merkezi dışına çıkarılamaması ve bu nedenle yüksek işlemcili bilgisayarlarda kullanılamaması olmuştur. Sektör değişiklikleri ile farklı yöntemler de denenerek bu kısıt altında daha iyi sonuçlara ulaşmak mümkün olacaktır.

Sonuç olarak bu çalışma Türkiye'nin bilgisayar, elektronik ve optik ürünler dış ticaret tahmininde makine öğrenmesi yöntemlerinin kullanımına ilişkin kapsamlı bir analiz sunmaktadır. Anomali tespiti, kümeleme, değişken seçimi ve regresyon aşamalarının birlikte ele alınması, tahmin performansını artırmada aldığı rol bu çalışma ile herüstik olarak incelenmiştir. Gelecekteki çalışmaların, daha geniş veri setleri ve farklı makine öğrenmesi algoritmalarını içerecek şekilde genişletilmesi, dış ticaret tahminlerinde daha yüksek doğruluk oranlarına ulaşılmasını sağlayacağı düşünülmektedir.

Katkı Oranı Beyanı

Yazarların katkı yüzdeleri aşağıda verilmiştir. Yazarlar makaleyi incelemiş ve onaylamıştır.

	T.H.	T.A.
K	60	40
T	60	40
Y	40	60
VTI	60	40
VAY	60	40
KT	60	40
YZ	60	40
KI	60	40
GR	60	40
PY	50	50

K= kavram, T= tasarım, Y= yönetim, VTI= veri toplama ve/veya işleme, VAY= veri analizi ve/veya yorumlama, KT= kaynak tarama, YZ= Yazım, KI= kritik inceleme, GR= gönderim ve revizyon, PY= proje yönetimi

Çatışma Beyanı

Yazarlar bu çalışmada hiçbir çıkar ilişkisi olmadığını beyan etmektedirler.

Etik Onay Beyanı

Bu araştırmada hayvanlar ve insanlar üzerinde herhangi bir çalışma yapılmadığı için etik kurul onayı alınmamıştır.

Teşekkür ve Bilgilendirme

Bu çalışma Doç. Dr. Tolga AYDIN danışmanlığında Tolga HASTAOĞLU'nun hazırladığı "Türkiye'nin Dış Ticaret Verilerinin Makine Öğrenmesi Yöntemleri ile Analizi ve

Tahmini" isimli yayınlanmamış yüksek lisans tezinden türetilmiştir. Bu makalede elde edilen bulgu ve değerlendirmeler yazarın kişisel görüşleri olup, verilerin temin edildiği Türkiye İstatistik Kurumunu hiçbir şekilde bağlamamaktadır.

Kaynaklar

Abar H. 2020. Xgboost ve Mars yöntemleriyle altın fiyatlarının kestirimi. Ekev Akad Derg, 2020(83): 427-446.

Ahmad G N, Fatima H, Ullah S, Saidi A S. 2022. Efficient medical diagnosis of human heart diseases using machine learning techniques with and without GridSearchCV. IEEE Access, 10: 80151-80173.

Akşehir Z D, Kılıç E. 2019. Makine öğrenmesi teknikleri ile banka hisse senetlerinin fiyat tahmini. Türkiye Bilisim Vakfı Bilgisayar Bilim Müh Derg, 12(2):30-39.

Aktan E. 2018. Büyük veri: Uygulama alanları, analitiği ve güvenlik boyutu. Bilgi Yönetimi, 1(1): 1-22.

Anderson J E. 2011. The gravity model. Annu Rev Econ, 3(1):133-160.

Ay A, Soydal H, Ay M. 2024. Çekim modeli çerçevesinde ticaret tahmininde makine öğrenmesi yöntemlerinin performans karşılaştırması: Türkiye ve Türk Cumhuriyetleri örneği. Yönetim Ekon Derg, 31(3): 439-459.

Aytekin İ. 2013. Küreselleşme ve ekonomik küreselleşme. Bitlis Eren Üniv Sos Bilim Derg, 1(2): 123-134.

Baxter G, Srisaeng P. 2018. The use of an artificial neural network to predict Australia's export air cargo demand. Int J Traffic Transp Eng, 8(1): 15-30.

Bayrak T. 2020. A machine-learning-based model for forecasting medical device foreign trade. Eskisehir Tech Univ J Sci Technol A-Appl Sci Eng, 21(4): 477-485.

Carmona P, Climent F, Momparler A. 2019. Predicting failure in the US banking sector: An extreme gradient boosting approach. Int Rev Econ Finance, 61: 304-323.

Chan E M, Ho D C, Tsang C W. 2021. Estimating United States-Asia clothing trade: Multiple regression vs. artificial neural networks. J Asian Finance Econ Bus, 8(7): 403-411.

Circlaeys S, Kanitkar C, Kumazawa D. 2017. Bilateral trade flow prediction. Unpublished manuscript. Available at: http://cs229.stanford.edu/proj2017/final-reports/5240224.pdf (accessed date: September 28, 2024).

Da M. 2014. Outlier detection for temporal data. Berlin, Germany, pp: 45-65.

Demiralay M, Çamurcu A Y. 2005. Cure, agnes ve k-means algoritmalarındaki kümeleme yeteneklerinin karşılaştırılması. İstanbul Tic Univ Fen Bilim Derg, 4(8): 1-18.

Ding C, Peng H. 2005. Minimum redundancy feature selection from microarray gene expression data. J Bioinform Comput Biol, 3(2): 185-205.

Dumor K, Yao L. 2019. Estimating China's trade with its partner countries within the Belt and Road Initiative using neural network analysis. Sustainability, 11(5): 1449.

Elgeldawi E, Sayed A, Galal A R, Zaki A M. 2021. Hyperparameter tuning for machine learning algorithms used for Arabic sentiment analysis. Informatics, 8(4): 79.

Emanet S, Baydoğmuş G K, Demir Ö. 2021. Öznitelik seçme yöntemlerinin makine öğrenmesi tabanlı saldırı tespit sistemi performansına etkileri. Dicle Univ Müh Fak Müh Derg, 12(5): 743-755.

Eşidir K A. 2025. Türkiye'nin kimyasal madde ithalatının gelecek tahmini: Makine öğrenmesi ve topluluk öğrenme yöntemleri performans analizi. Fırat Univ J Soc Sci, 35(1): 261-278.

Filimonova M, Kislyakov A, Tikhonyuk N. 2021. Structural and dynamic modelling of the regions' foreign trade profile based on graph cluster analysis. Strategica: Shaping the future of business and economy, Bucharest, Romania, pp: 34-49.

Gopinath M, et al. 2021. International agricultural trade forecasting using machine learning. Data Policy, 3:e1.

Gökalp Ö M. 2022. Makine öğrenmesi. Gazi Univ, Gazi Bilisim Enstitüsü, Adli Bilisim Bölümü, Ankara, Türkiye, pp: 1-14.

Gupta V, Kumar E. 2022. Evaluation of machine learning models for predicting exports of India, Proc 7th Int Conf Comput Eng Technol (ICCET), Goa, February 2022, India. IET, pp: 47-52.

Gür Y E, Eşidir K A. 2024. Türkiye hurda demir çelik ithalatının gelecek değerlerinin derin öğrenme, makine öğrenmesi ve topluluk öğrenme yöntemleri ile öngörülmesi. Alanya Akad Bakış, 8(3): 885-908.

Huang R, et al. 2020. Forecasting trade potential between China and the five Central Asian countries: under the background of Belt and Road Initiative. Comput Econ, 55: 1233-1247.

Jia H, Adland R, Wang Y. 2019. Latin American oil export destination choice: A machine learning approach, Proc IEEE Int Conf Ind Eng Eng Manag (IEEM), Macao, December 2019, pp: 345-348.

Jošić H, Žmuk B. 2022. A machine learning approach to forecast international trade: The case of Croatia. Bus Syst Res, 13(3): 144-160.

Ke G, et al. 2017. LightGBM: A highly efficient gradient boosting decision tree. Adv Neural Inf Process Syst, 30: 3146-3154.

Micocci F, Rungi A. 2023. Predicting exporters with machine learning. World Trade Rev, 22(5): 584-607.

Ng R T, Han J. 2002. CLARANS: A method for clustering objects for spatial data mining. IEEE Trans Knowl Data Eng, 14(5): 1003-1016.

Nummelin T, Hänninen R. 2016. Model for international trade of sawnwood using machine learning models. Helsinki, Finland, pp: 154-168.

Nuroğlu E. 2014. Estimating and forecasting trade flows by panel data analysis and neural networks. İstanbul Univ İktisat Fak Mec, 64(1): 85-111.

Reçus L, Tinbergen J. 1962. Shaping the world economy. Suggestions for an international economic policy. The Twentieth Century Fund, New York. Rech Econ Louvain, 30(2): 157.

Shen M L, Lee C F, Liu H H, Chang P Y, Yang C H. 2021. Effective multinational trade forecasting using LSTM recurrent neural network. Expert Syst Appl, 182: 115199.

Soydal H, Ay M, Koç S. 2024. Makine öğrenimi ile ticaretin öngörülmesi: Türkiye ve Balkan ülkeleri üzerine çekim modeli analizi. Selçuk Univ Sos Bil Meslek Yüksekokulu Derg, 27(2): 746-765.

Torkul O, Gülseçen S, Uyaroğlu Y, Çağıl G, Uçar M K. 2017. Mühendislikte yapay zeka ve uygulamaları. Ankara, Türkiye, pp: 156-158.

Yağmur E Ç. 2022. Atmosferik partikül maddelerin makine öğrenmesi ile tahmini: Beşiktaş, İstanbul örneği. Konya J Eng Sci, 10(4): 807-826.

Black Sea Journal of Engineering and Science
doi: 10.34248/bsengineering.1687682

Open Access Journal
e-ISSN: 2619 – 8991

Research Article
Volume 8 - Issue 5: 1493-1503 / September 2025

OPTIMIZING ACCURACY OF ABRASIVE WATERJET CUTTING SYSTEM: A COMPREHENSIVE STUDY ON MECHANICAL AND SOFTWARE COMPENSATION STRATEGIES ON 5-AXIS CNC WATERJET CUTTING MACHINE AND ANALYSIS USING DESIGN FMEA

Uğur ŞİMŞİR[1]*

[1]*Milteksan CNC A.S., Basibuyuk Mh. Sureyyapasa Basibuyuk Yolu Sk. No:4/1, 34854, Istanbul Türkiye*

Abstract: Abrasive Waterjet cutting technology is more environmentally friendly than other methods like plasma and laser cutting. As a cold cutting method, it does not use flammable gases. Furthermore, it uses water and natural garnet as abrasive materials. The amount of waste is significantly lower compared to other methods. This study aims to increase cutting speed and efficiency while lowering carbon emissions by controlling the taper angle and enhancing machine sensitivity. The primary objective of this study was to optimize errors caused by the kerf and the taper angle in a waterjet cutting machine, both mechanically and during the cutting process. The goal of increasing precision was achieved successfully. A 10 mm thick SS314 Steel was processed using a CNC waterjet cutting device. Mechanical compensation was performed using a laser-based algorithm that measured and compensated for values at 10 mm intervals along the X and Y axes. After determining the waterjet's taper angle, the 5-axis cutting head was aligned perpendicular to the edge to ensure accuracy. The most efficient cutting parameters were found to be a pressure of 3.750 bar, an abrasive flow rate of 0.4 kg/m, a 1.02 mm nozzle, a 0.35 mm orifice, and 80 mesh garnet abrasive. The cutting speed was set at 300 mm/min. The taper angle was 1 degree, and the 5-axis machining head was positioned perpendicularly to the material's edge. Cutting was performed by tilting the head by 1 degree to effectively eliminate the taper angle effect. Design FMEA, as defined by the FMEA Tables of the IATF 16949 Automotive Standard, is typically used to identify the most critical characteristics. The patent for this original study is registered with the Patent Office (Patent no: TR 2018 20101). The improvements in cutting angle and precision have increased machine efficiency, which in turn has led to higher cutting speeds and reduced carbon emissions. By controlling the cutting angle, a thinner kerf is created, which leads to a reduction in waste.

Keywords: Taper angle, High precision, Compensation, Sustainability, Automation, Machine design

***Corresponding author:** Milteksan CNC A.S., Basibuyuk Mh. Sureyyapasa Basibuyuk Yolu Sk. No:4/1, 34854, Istanbul Türkiye
E mail: ugur.simsir@milteksan.com (U. SIMSIR)
Ugur ŞİMŞİR https://orcid.org/0000-0002-0948-6364

Received: April 30, 2025
Accepted: August 16, 2025
Published: September 15, 2025

Cite as: Şimşir U. 2025. Optimizing accuracy of abrasive waterjet cutting system: A comprehensive study on mechanical and software compensation strategies on 5-axis CNC waterjet cutting machine and analysis using design FMEA. BSJ Eng Sci, 8(5): 1493-1503.

1. Introduction

Automation and digital transformation are critical for the success of manufacturing firms. Accordingly, the formulation of strategies and the translation of strategic objectives into concrete, actionable initiatives in this domain are of paramount importance (Oner et al., 2024).

Using the abrasive water-jet cutting method, all types of materials can be cut efficiently without thermal effects or the need for equipment changes (Ibaraki and Knapp, 2014). The cutting process is performed by directing water, with or without an abrasive onto the material (Rajamani et al., 2022). The water is pressurised by pumps to create high-pressure jet. During the cutting process, a consistent standoff distance between the nozzle and the material, as well as a stable feed rate, must be maintained. For this purpose, cutting machines are integrated with automatic feed rate control.

Water jet technology was invented in the late 1800s for pressure-water washing in the mining industry. in the early 1900s, experiments were conducted to cut rocks using pressurized water which led to the development of a 500 bar waterjet. Equipment capable of generating 2.750 bar pressure was developed in the 1970s, leading to the first industrial waterjet cutting system in 1972.

Since then, abrasive material has been added to the pressurized water stream, allowing for more efficient cutting of hard materials. Today, waterjet systems can generate pressures up to 6.200 bar.

There are two major cutting methods in waterjet technology: pure waterjet and abrasive waterjet. In pure waterjet cutting, no additional material is added to the

water sprayed onto the workpiece. This method is used for cutting materials with relatively low hardness. In abrasive waterjet cutting, an abrasive (such as garnet) is added to the water stream. This method is used for very hard and thick materials, including titanium-tungsten alloys, carbon steels, and stainless steels. It is also used for soft metals like aluminum, copper, brass, and lead, as well as for hard non-metallic materials like glass, marble, granite, and ceramic.

The physical mechanisms of the abrasive waterjet cutting (AWJ) process are largely imperceptible to operators. In brief, AWJ flow theory describes the jet as a supersonic, three-phase flow consisting of a fluid (water and air).

During cutting and drilling operations, this complex flow is rapidly confined to a limited area. Boundary conditions fluctuate, and pressurized water exhibits approximately 15% compressibility at 400 MPa.

The hydraulic power (P), required to produce a high-velocity water jet through an orifice is directly proportional to the product of the pressure (p) and the flow rate (Q) (equation 1):

$$P = p\,\frac{Q}{c} \tag{1}$$

In this equation, c is a constant equal to 60, where P is expressed in kilowatts (kW), p in megapascals (MPa), and Q in liters per minute (l/min). For instance, the flow rate can be determined using Bernoulli's principle. The flow rate through an orifice with cross-sectional area A is given by equation 2.

$$Q = c_d A \sqrt{2p/\rho} \tag{2}$$

Where A = d2/4, with d denoting the orifice diameter, cd representing the discharge coefficient (typically 0.65), p indicating the pressure, and ρ denoting the density of water.

According to the KMT waterjet manual and operation book, waterjet technology can meet the cutting needs of various industries and handle complex shapes. Abrasive waterjet cutting systems integrated with CNC (computer numerical controlled) systems can easily perform cutting procedures involving numerous zigzags, sharp edges, very narrow angles, and very small diameters (Hsu and Lei, 2003; Lianjun et al., 2014; Polzer et al., 2014; Lu et al., 2020)

The primary benefit of waterjet technology is its nature as a cold cutting process. Because the material experiences neither mechanical nor thermal stress during cutting, no post-cutting stress relief treatments are required. Any material can be cut without creating a thermal effect (Ibaraki and Ota, 2014). Thus, undesired hardening, burns, deformations, any droplets, molten metal residues and poisonous gas on the material are eliminated. Moreover, the sandwich materials and the material pairs with different combustion points or melting temperatures, which cannot be cut using laser or plasma technology, can be cut with a water jet (Rajamani et al., 2022).

Krajcarz D. discusses the comparison of waterjet cutting with laser and plasma cutting. This reference could be cited in the introduction when discussing environmental benefits and cold cutting nature of waterjet technology are mentioned, particularly in sentences like "Metal Cutting technology with Abrasive Waterjet is more environmentally friendly than other plasma and laser cutting methods and is a cold cutting method that does not use flammable gases." or "Moreover, the sandwich materials and the material pairs with different combustion points or melting temperatures, which cannot be cut using laser or plasma technology, can be cut with a water jet". (Krajcarz D. 2014)

Wan L at al. examine the sustainable and clean applications of steel slag for abrasive waterjet machining. It could be cited when discussing the study's objectives related to sustainability and carbon emission reduction. Relevant sentences include "With this study, it is aimed to increase the cutting speed by controlling the taper angle and increasing the machine sensitivity, and to increase efficiency and lower carbon emission." or "Since there is an improvement in cutting angle and cutting precision, the machine efficiency is increased, therefore the cutting speed is increased and carbon emission is reduced. (Wan et al., 2023)

Yun et al. (2019) focus on optimizing energy consumption with hybrid laser-waterjet. It can be cited when discussing energy efficiency and carbon emission reduction in your paper. A suitable place for this reference would be in the conclusion, for example, after the sentence "Thanks to patented mechanical improvements and software compensation with taper angle control to achieve the desired precision edge cutting quality, the cutting speed has been increased by approximately 30%, which means that the work is done 30% faster and 30% energy is saved."

Wang et al. (2019) present a comprehensive kinematic error compensation strategy for a double swivel head used in five-axis abrasive water jet (AWJ) machining systems. The authors develop a mathematical model to quantify the kinematic errors resulting from rotary axis deviations and mechanical imperfections. Using a multi-body system approach, the compensation algorithm significantly improves the accuracy of the cutting head's motion, leading to enhanced cutting precision and surface quality. Experimental validation demonstrates that the proposed compensation method reduces angular errors and improves geometric consistency in complex 3D cutting operations.

Chen et al. (2019) address the persistent issue of shape inaccuracies in the cut-in and cut-out regions during abrasive water jet cutting processes. The paper proposes a correction model that accounts for dynamic changes in jet pressure and traverse speed at the beginning and end of the cutting path. By modifying toolpath parameters and introducing predictive error modeling, the authors successfully mitigate edge deformation and discontinuities. Experimental results confirm that the

approach reduces shape deviations, particularly in high-precision applications involving intricate geometries.

Lin et al., focuse on the visualization and evaluation of spatial kinematic rotation errors in five-axis abrasive water jet cutting heads. Lin et al., propose a novel method using coordinate measuring techniques and spatial analysis to capture rotational inaccuracies in real time. The study highlights how cumulative errors in the A and C rotary axes affect the final tool orientation and cutting quality. The visualized error distributions provide critical insights for calibration and compensation strategies, ultimately leading to more accurate five-axis AWJ machining (Lin et al. 2021.)

Since no material combustion or melting occurs during the cutting process, no chemical pollution arises. Due to this advantage, there is no need for additional investment such as gas suction, treatment or filtration. The waterjet does not create any direct pressure effect on the material being cut. The mechanical reaction involved in the cutting process operates at a micro-molecular level, preventing material deformation and the formation of burrs, even though the "water jet" carries a high amount of "kinetic energy."

In the waterjet cutting process, the cutting edges have an astonishing clarity, eliminating the need for a deburring process, which would create an additional cost. Due to the very small cutting mark (max 1.1 mm), material losses are minimized. It is possible to cut narrow or sharp edges, depending on the diameter of the waterjet beam. Without any modifications, the same cutting tool can be used to cut materials of different thicknesses simply by changing the cutting speed.

Waterjet cutting experiments were conducted and the results on the response properties of the process variables and second order regression models were evaluated. In addition, statistical multiple response optimization was performed to improve the cutting quality properties.

FMEA is an important technique used by many quality systems. FMEA is a powerful analysis technique for preventing errors by estimating risks. It is based on the principle that the problem arising from the occurrence of the error is perceived as the customer. In FMEA studies, probability, severity and detectability are estimated for all identified faults. Accordingly, actions that should be taken, planned or ignored are evaluated.

Benefits of FMEA:

- It is an important opportunity to make fundamental changes successfully.
- It enhances the product or service's quality, reliability, and safety.
- It boosts the company's image and strengthens its competitiveness.
- It contributes to enhancing customer satisfaction.
- It cuts down on product development time and costs.
- Sets priorities in design development activities.
- Helps initiate corrective and preventive actions.
- Lists potential defects and their effects.

FMEA is performed by a team; it cannot be performed by a single person. This team may consist of 3 to 7 people (preferably 5), and an interdisciplinary approach is useful. The team is led by a team leader, who should be selected from individuals who have received FMEA training.

The FMEA team leader is a guarantor of the method's application and organizes the team's work, including setting the meeting agenda, guiding the meeting, preparing the meeting report, and ensuring the work continues.

Since the aim of FMEA is to prevent known or possible failures are identified before they reach the customer, some predictions need to be made. Prioritization is one of the most important points of the method and there are three criteria for this.

- Probability refers to the frequency at which failure occurs.
- Severity is the seriousness and effects of the error
- Detectability: The ability to detect the error before it reaches the customer

The value of these criteria ranges from 1 to 10. Priority is established based on the Risk Priority Number(RPN), which is determined by evaluating these three criteria.

Once an FMEA is initiated, it becomes a living document. It should be updated whenever there are significant changes in the design and process. A design FMEA can be considered complete when it is approved for production and a start date is given. (Karacan et al., 2021)

A process FMEA is considered complete once all operations have been identified and evaluated, and critical and important features are incorporated into the quality control plans.

One of the most competitive sectors is the automotive industry. The FMEA technique is explained much more effectively in the IATF 16949 standard, which is the automotive quality management system. The basic functions of the product are defined as special characteristics in this standard and in this framework, special characteristics are definitely addressed in quality studies. In addition, unlike the classical FMEA, corrective action is not only initiated when the risk priority number is above 100, but also when the severity value is 8 and above. In order to calculate the probability severity and detectability values more accurately, the relevant tables have been prepared in a much more understandable way in this standard. For these reasons, the FMEA developed for the automotive quality standard was used in our study (Table 1).

Table 1. FMEA Scoring Criteria Based on IATF 16949

PFM	PFE	Sev	Prob.	Det.	RPN	Prevention/Action	Responsible/ Termin	Sev.	Prob.	Det.	RPN
Taper angel	All products can be scrap.	8	5	4	160	A axis mut be calibrated	U. Simsir	8	2	4	64
Cutting edge quality	Some products can be scrap.	8	4	4	128	Cutting pressure and sutting speed must be calirated	U. Simsir, Software developer, R&D Manager	8	2	4	64
Nozzle Size	Cutting velocity may be low	7	4	4	112	Nozzle size must be checked and changed	U. Simsir, R&D Manager	7	2	4	56
Orifice size	Cutting pressure may be low	7	3	3	63	Orifice failure must be checked and may need to change orifice	No Corrective action is required				
Abrasive grade	Cost may be increased	6	3	3	54	Abrasive mesh size must be checked and may need to change abrasive	No Corrective action is required				

PFM= potential failure mode, PFE= potential failure effect

The flowchart of the developed system is as follows:

1. The distance of the material from the nozzle is measured.
2. The material type and thickness are input into the CNC software.
3. The software selects the cutting pressure and cutting speed.
4. The taper angle is calculated based on the distance from the nozzle tip to the lowest surface of the material.
5. The taper angle is compensated with the 5th axis (A-axis) to be perpendicular to the material's cut surface.
6. Mechanical errors in the X and Y axes are compensated by the volumetric error software.
7. While the X, Y, and C axes work interpolated during cutting, the A-axis is automatically positioned to remain perpendicular to the cut material surface.

The patent of this original study is registered by the Turkish Patent Office (Simsir and Bicer, 2018 Patent no: TR 2018 20101)

2. Operating principles and functionalty of water jet cutting systems

In water jet cutting systems, a high-pressure pump produces a water pressure of 4.000-6.000 bar. This pressurized water is driven through steel pipes to the pneumatic valve on the machine's cutting head. Using the valve control, the pressurized water in the cutting head is transferred through the orifice and mixed with the abrasive. The material is then cut by the water exiting the nozzle. This process is referred to as a "water jet" because the flow rate of water passing through the orifice is increased to approximately three times the speed of sound. The inner diameter of the orifice typically ranges from 0.20 mm to 0.35 mm. The selection of the orifice size, which depends on the pump capacity and the amount of water transferred, is a crucial factor for ensuring a high-quality cutting process (Figure 1). Garnet abrasive with a particle size of 80–120 mesh is transported along with the water exiting the orifice through the nozzle, which has an inner diameter typically ranging from 0.60 mm to 1.02 mm. Approximately 2–3 mm is maintained between the tip of the nozzle and the material, and cutting is performed by the water exiting the nozzle. Abrasive carrying systems are used not only to transport the abrasive by creating a vacuum with the waterjet exiting the orifice but also to achieve a more uniform flow. The abrasive-infused waterjet, propelled by the nozzle, must move forward at a consistent speed.

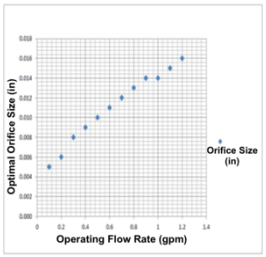

Orifice Size (in)	Orifice size (SI)
0.004	0.10
0.006	0.15
0.008	0.20
0.010	0.25
0.012	0.30
0.014	0.35

Figure 1. The connection between orifice diameter and flow rate min (Liu et al., 1998).

3. Materials and Methods

3.1. Nozzle Movability and Cutting Speed Selection Experiments

During the cutting process, if the surface geometry is uneven — for example, if there are dips or bulges — the distance between the nozzle and the surface changes. This variation negatively affects the cutting quality, as consistent stand-off distance is critical for optimal results. Ideally, the nozzle should maintain a constant distance of 2–3 mm from the surface. To address this, an obstacle detection sensor is used to detect any

irregularities in the surface. When a hole or a raised area is detected, the sensor adjusts the nozzle's position accordingly to maintain a consistent cutting height.

The nozzle ability to move adaptively offers several advantages, including:

i. improved quality of cutting
ii. reduces costs (e.g. lower garnet and energy consumption)
iii. reduced time loss
iv. increased the cutting speed

Cutting speed varies depending on the purpose. In this case, because the cutting surface quality of the material was not a primary concern and the goal was simply to separate the parts, the fastest cutting speed (rough cut) was selected. In addition, the nozzle-orifice combination and abrasive flow rate were selected based on experiments conducted for this application to achieve the optimum cutting speed. Nozzles with inner diameter of 0.60-1.02mm and sapphire orifices with a beam diameter of 0.20mm (0.008") and 0.35mm (0.014") were used. Tests conducted at different pressures and flow rates determined that the optimum cutting process is achieved with a pressure of 3.750 bar and abrasive flow rate 0.4kg/m a 1.02mm nozzle diameter and 0.35mm orifice beam diameter. The results are presented in Figure 2.

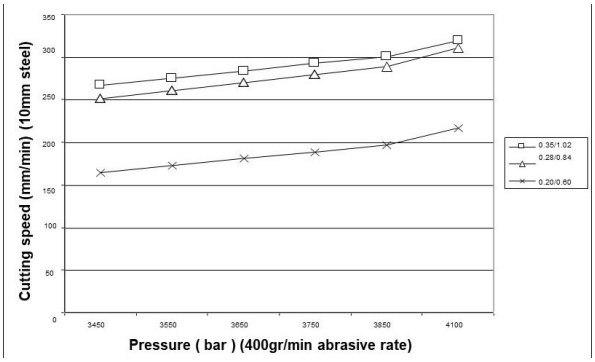

Figure 2: Cutting speeds for 10mm thickness of SS314 steel with different orifice-nozzle combinations and abrasive flow rates.

The waterjet's taper angle was aligned perpendicular to the cutting edge using a 5-axis cutting head. The conic angle of the waterjet was set to 1 degree and oriented to compensate for taper formation. By tilting the cutting head precisely by 1 degree, the taper effect was effectively eliminated, resulting in a perpendicular cut profile. Accordingly, the most efficient cutting level parameters are shown in Figure 3.

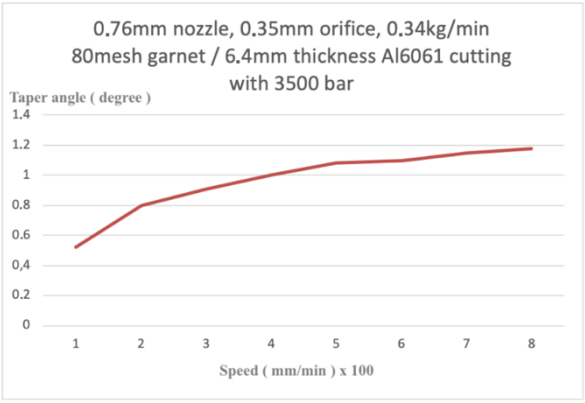

Figure 3. Taper angle as a function of speed.

3.2. Volumetric Compensation

In the aviation industry, automation systems are required for the high accuracy of the workpieces and machines. Complex 5-axis machines are used for machining large workpieces and their accuracy depends on the tolerances determined during production and the temperature created during the machining. Volumetric compensation has become a fundamental necessity in especially in the aviation industry to meet these demands (Bohez, 2001; Givi and Mayer, 2014).

3.3. Improvement of Machining Tolerances

Machining errors can occur for many reasons, including design, kinematics, and assembly-related features. Volumetric compensation is a feature used for correcting machining errors (Ibaraki et al., 2012; Harnicarova et al., 2013;). The best way to correct some of these errors is to design the machine correctly, but this is not always possible or economical. The C and A axes of the machine designed to adjust the taper angle are shown in Figure 4.

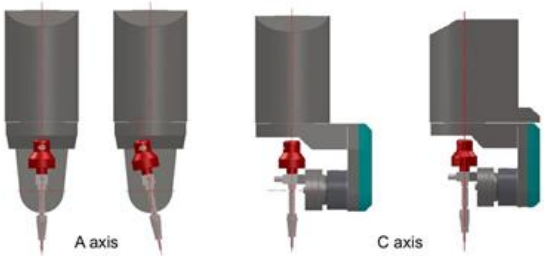

Figure 4. Nozzle structure C and A axes.

Figure 5 shows that the taper angle is adjusted to be perpendicular to the material's edge using these axes.

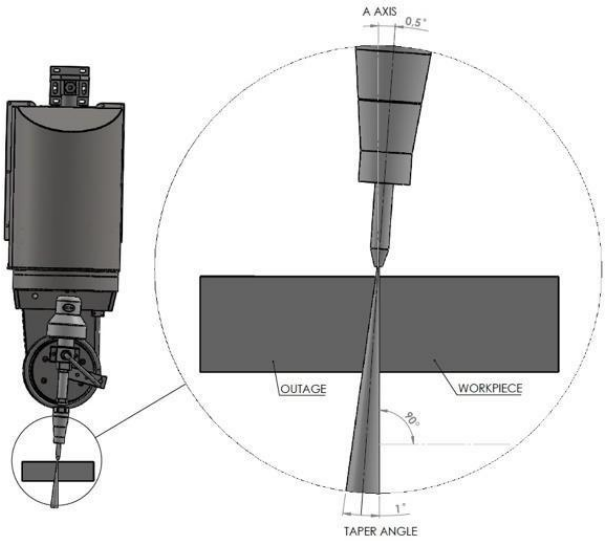

Figure 5. Tapering angle of Nozzle and correction.

3.4. Easy Volumetric Compensation

Machining errors may have various reasons related to design, kinematics or assembly. "Easy Volumetric Compensation" allows the correction of machining errors. The best way to fix some of these errors is to design the machine correctly. However, sometimes this may not alwats be possible or economical. It may also be impossible or unacceptably expensive to increase the hardness for medium- or large-sized machines. For this reason, classical error correction instruments should be integrated with more advanced instruments that allow adaptation to different machine designs, even with certain kinematics. In general, "Easy Volumetric Compensation" requires the identification of 25 control points per axis. For this reason, the calibration of points and their integration into the CNC are much faster. This process improves machine accuracy and is more economical because it eliminates the need to hire third-party companies to perform the measurements. Much more accurate and reliable improvements are achieved in many machines, even without achieving the accuracy levels of Standard Volumetric Compensation (Figure 9) (Lianjun et al., 2014). The waterjet cutting machine used in this study is shown in Figure 6. Since the appropriate temperature conditions were selected, no temperature compensation was performed.

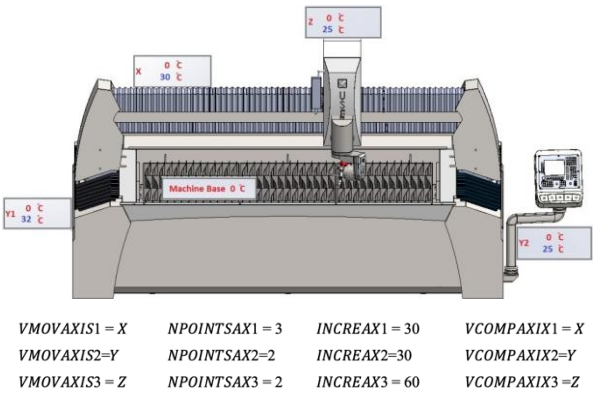

Figure 6. Waterjet Cutting machine structure and axes.

Volumetric compensation is a method used to improve the accuracy of CNC machine tools by correcting geometric and kinematic deviations. Depending on the machine size and required precision, different levels of volumetric compensation can be applied. This section classifies them as small, medium, and large, based on the complexity and calibration requirements.

3.5. Small-Scale Volumetric Compensation

This is the simplest and fastest volumetric compensation method, generally applied to compact machines or systems requiring basic correction. The compensation volume is defined using 25 control points.

It corrects basic transmission and alignment errors.

Compensation tables are generated by the calibration software and can be manually edited on the CNC interface. The machine manufacturer must define essential parameters such as the axes involved, position ranges, and compensation limits.

Although this method allows for rapid calibration, it is less accurate than more advanced techniques.

3.6 Medium-ScaleVolumetric Compensation (Volumes >10 m^3)

Medium-scale compensation is suitable for larger machines where more complex geometric deviations must be corrected.

It targets compensation volumes larger than 10 m^3.

A total of 21 geometric errors are corrected, including axis misalignments, squareness deviations, and rotational shifts.

Compensation tables are generated by the calibration software but cannot be edited through the CNC interface.

The manufacturer only needs to specify the relevant axes. All other parameters are embedded within the calibration application by default.

This method provides higher accuracy compared to small-scale compensation but requires a longer calibration process.

3.7. Large-Scale Volumetric Compensation (Very Large Machines)

Large-scale compensation follows the same methodology as medium-scale, but is applied to machines with significantly greater working volumes and higher demands on geometric accuracy.

Applicable for machine volumes well above 10 m^3, typically in aerospace or heavy-industry equipment.
All 21 geometric error types are compensated in greater detail.
Calibration and compensation are fully handled through dedicated software, with minimal manual input on the CNC side.
Provides the highest level of geometric correction, but requires the most time-intensive calibration process.
Volumetric compensation, when properly implemented, allows manufacturers to significantly reduce geometric deviations. By classifying compensation methods based on machine size and complexity, users can select the most appropriate approach to ensure optimal machine accuracy.
The main reasons for the lack of “accuracy”, and “precision” in a “machine tool” might arise from the geometrical failures that might originate from production montage, misuse and the production machine wearing that might cause early deformation (Liu et al., 1998; Liu et al., 2014; Öner et al., 2024). Volumetric compensation chart is shown in Figure 7.

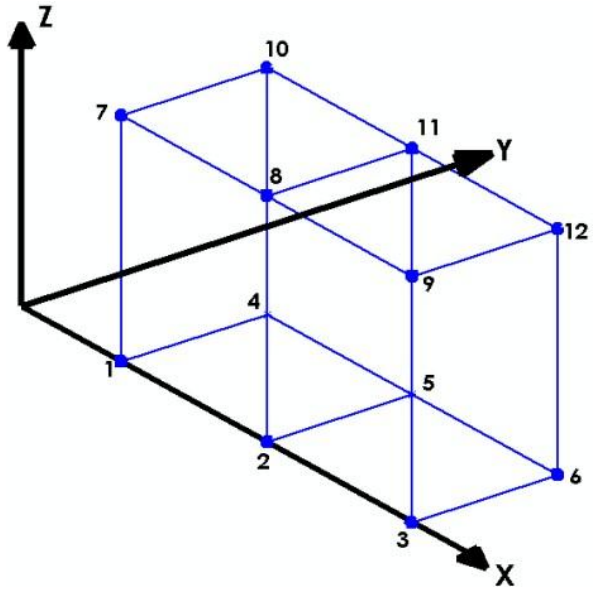

	1	2	3	4	5	6	7	8	9	10	11	12
ErrorX	-0.1684	-0.1440	-0.1550	-0.1632	-0.1646	-0,1860	-0.1780	-0.1566	-0.1577	-0.0018	-0.0091	-0.0285
ErrorY	0.0703	0.0932	0.0964	0.0904	0.0952	0.0993	0.0090	0.1150	0.1145	0.0542	0.0930	0.0895
ErrorZ	-0.0135	-0.0109	-0.0009	-0.0028	0.0080	-0.2230	0.0013	0.0012	0.0012	-0.0235	-0.0162	-0.0033

Figure 7. Volumetric compensation chart.

"Volumetric compensation" corrects geometric errors by enhancing the accuracy and reproducibility of machines. The volume to be compensated is defined as a point cluster, where the error is measured and corrected at each point.
Standard volumetric compensation can be costly, as it requires significant time and expensive equipment to collect and apply all the compensation points to the CNC. While this cost is generally accepted for large, high-performance machine tools, it is harder to justify for smaller or medium-sized machines. Therefore, depending on the end-user’s needs, a simpler volumetric compensation algorithm can be employed. This algorithm simplifies the process and is adaptable to any machine (Lianjun et al., 2014; Patel and Ehman, 1997; Polzer et al., 2014; Veldhuis and Elbestawi, 1995).
Easy volumetric compensation limits the number of points to 25 per axis, making calibration faster and integration into the CC simpler. It significantly improves accuracy while being quicker and easier to implement, which is a key benefit for small-sized machines.
Although traditional ball screw and cavity compensation can still be used, it is not necessary, as volumetric compensation already addresses these errors. However, these compensation tables can also be used and automatically integrated into the CNC compensation matrix (Liu et al., 1998).

4. Modeling the volumetric errors

In modeling the volumetric errors of machines, a "1 error twist" is applied to each "component error" of the driver. After aligning the twist bends with the working space, they are processed through the "kinematic model" of the "five-axis machine" as described in (Bohez, 2001; Bohez 2002; Feng et al., 2019; Rajamani et al., 2022).

4.1.Measurement and representation of geometric error for 5 axis machine

An unconstrained rigid object has six degrees of freedom (DOF) in space. As a result, any linear axis is associated

with six error components corresponding to these six DOFs. For example, a linear motion along the X-axis can cause three translational errors (δx(x), δy(x) δz(x)) in the X, Y, and Z directions and three rotational errors (εx(x), εy(x) εz(x)) about the X, Y, and Z axes. In the 5-axis machine, the rotation of the Cutting Head about z is defined as the C-axis, and the rotation about x and y axes is defined as the B-axis as shown in Figure 8. These six errors are also called position-dependent geometric errors (PDGEs). As a result, for a typical 5-axis machine tool, there are a total of twenty-one geometric error components, including three squareness errors (Sxy, Sxz, Syz) caused by assembly imperfections between the three linear axes. These errors are measured and compensated by the software. The three squareness errors are constant regardless of the command position of the linear axes and are also called position-independent geometric errors (PIGEs) (Hsu and Wang, 2007; Polzer et al., 2014; Okafor and Ertekin, 2000; Ramesh et al., 2000; Schwenke et al, 2008).

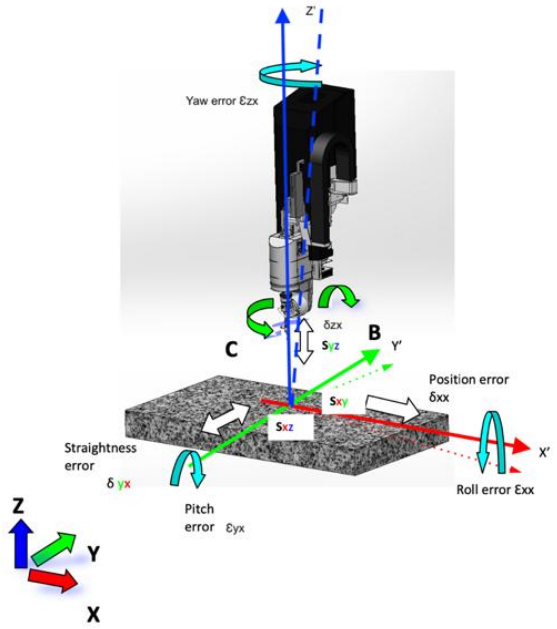

Figure.8. Position-dependent geometric errors (PDGEs).

4.2. Error twists (ξe)

The "geometric errors" between the "tool-tip" and the "workpiece" are represented using error twists. Consider that the "machine" is ideally positioned at "Pd" and that the "linear axis" or "rotational axis" of the "rotary drive" is ideally directed along "ωd." However, the "actual machine position" might be at "P," and the "axis" could exhibit an "angular error" denoted by "θe." The "ideal twist" (ξd) and the "actual twist" (ξ), which include these geometric errors, are expressed as follows equation 3:

$$\xi_d = [q_d \times \omega_d \omega_d]^T, \xi = [q \times \omega\omega]^T \quad (3)$$

The conversion from the "ideal twist" ξd to the "actual twist" ξ results from an "error motion" represented by (e^ξ θe). The "error twist" (ξe) includes both an "angular geometric error" (θe), which lies along the "common perpendicular" between the "ideal" and "actual axis lines," and a "linear positional error" (d) of the "axis." The "error twist" is expressed as ξe = [Ve ωe]^T (equations 4 and 5).

$$\omega_e = \frac{\omega_d \times \omega}{\sin\theta_e}, h_e = \frac{d}{\theta_e} = \frac{|q - q_d|}{\theta_e} \quad (4)$$

$$v_e = \frac{q \times (\omega_d \times \omega)}{\sin\theta_e} + h_e \frac{\omega_d \times \omega}{\sin\theta_e} = \frac{q_d \times q}{d} + \frac{q - q_d}{\theta_e} \quad (5)$$

If the "angular geometric error" is zero (θe = 0), the "actual axis line" becomes parallel to the "ideal axis line." As a result, the "twist vector" consists solely of "translational errors" (ωe = 0, he = ∞), and the "error twist" simplifies to equation 6:

$$\xi_e = \begin{bmatrix} q - q_d \\ d \\ 0 \end{bmatrix} \quad (6)$$

When “d = 0,” meaning “he = 0” and “q = qd,” the “actual” and “ideal axes” align perfectly with no “linear errors.” Consequently, the “error twist” reflects only “angular errors.” (equation 7).

$$\xi = \begin{bmatrix} v_e \\ \omega_e \end{bmatrix} = \begin{bmatrix} q \times (\omega_d \times \omega) & \omega_d \times \omega \\ \sin\theta_e & \sin\theta_e \end{bmatrix}^T \quad (7)$$

For example, if the “rotary drive” (C) has a “tilt error” (εyc) about the “Y-axis,” the “coordinate system” of the “C drive” is defined in the “MCS” as “q = [Ox Oy Oz]^T”. According to equation 8, “ω_e” and “ve” are given as follows:

$$\omega_e = [0\ 1\ 0]^T$$

$$v_e = q \times \omega_e = \begin{bmatrix} O_x \\ O_y \\ O_z \end{bmatrix} \times \begin{bmatrix} 0 \\ 1 \\ 0 \end{bmatrix} \quad (8)$$

As a result, this leads to the formation of the “error twist” expressed as "ξ_e = [v_e ω_e]^T". The “geometric errors” for all “axes” can be described similarly Table 2 presents the “geometric errors” of the “AC axis table” that provides tilting for the “five-axis machine tool”. (Xiang and Altintas, 2016; Yang and Altintas, 2013; Yang et al., 2015).

Table 2. Error twist components for the AC axis of the five-axis rotary table

X- axis	Y- axis	Z- axis	Squareness Error	A- axis	C- axis	PIGEs Rotary axes
δxx	*δyy*	*εzz*	*Sxy*	*δxa*	*Δxc*	*δxoc Sboa*
δyx	*δxy*	*εxz*	*Syz*	*δya*	*Δyc*	*δyoc Scoa*
δzx	*δzy*	*εyz*	*Sxz*	*δza*	*Δzc*	*δyoa Saoc*
εxx	*εxy*	*εxz*		*εxa*	*Exc*	*Δzoa Sboc*
εyx	*εyy*	*εyz*		*εya*	*Eyc*	(ISO 230-7)
εzx	*εzy*	*εzz*		*εza*	*Ezc*	

5. Results

The squareness measurement results made before and after the improvements are shown in Figure 9 and Figure 10 and. The measurement and software precision improvement results made before and after the improvements are shown in Figures 11, 12, 13 and 14.

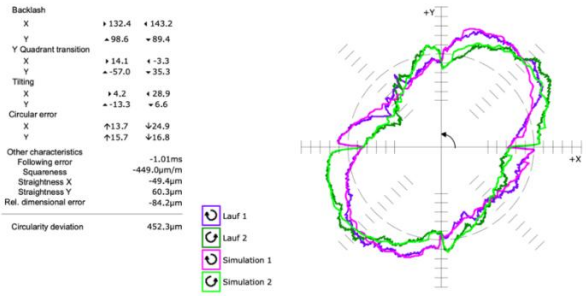

Figure 9. Squareness test, before compensation.

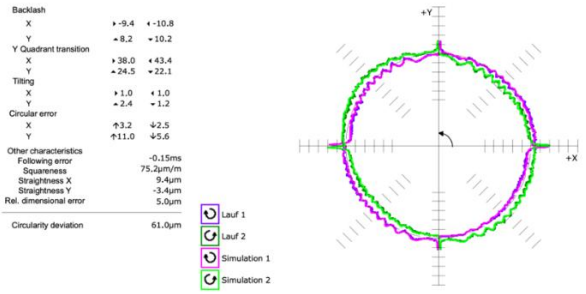

Figure 10. Squareness test, after compensation.

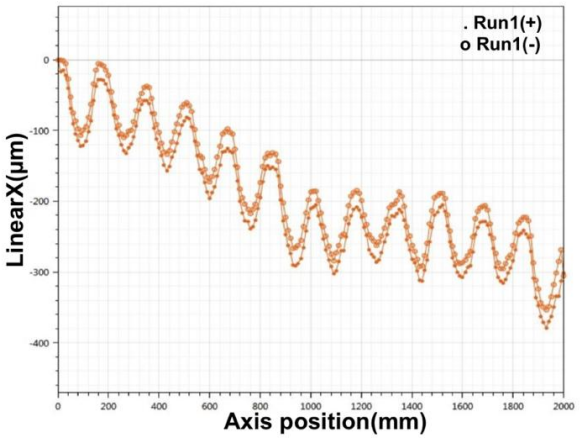

Figure 11. X axis, before software compensation.

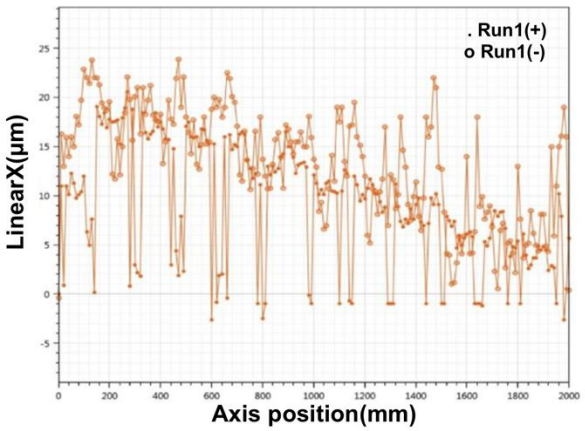

Figure 12. X axis, after software compensation.

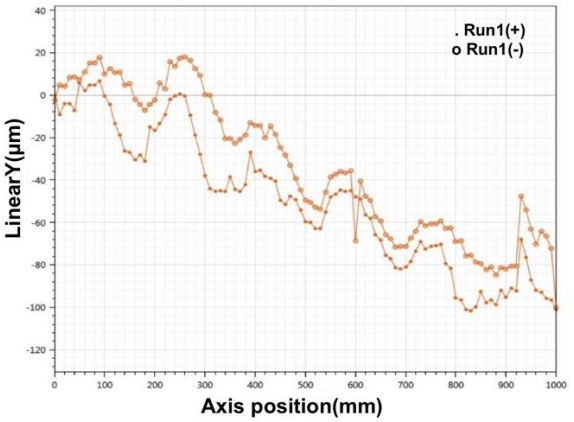

Figure 13. Y axis, before software compensation.

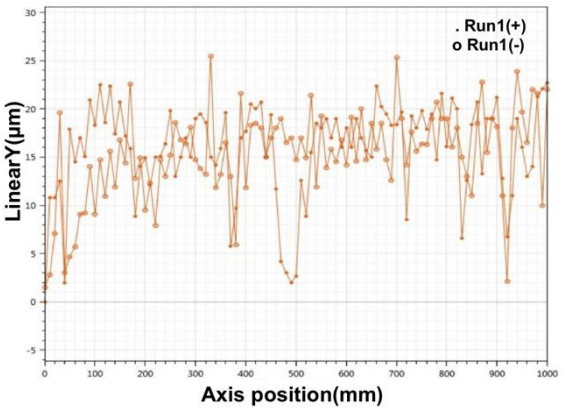

Figure 14. Y axis, after software compensation.

Scanning Electron Micrograph Experiments showed that for higher cut surface quality with abrasive waterjet, there is a need to reduce the cutting speed of the material with more precise positioning. In this study, the results were compared by making the tapering angle perpendicular to the cutting edge on a 5-axis CNC waterjet machine. This machine was chosen as the workpiece material and its mechanical sensitivity was increased by compensation.

Cuts were made on a sample in three different ways: with taper and without compensation, with taper and with compensation, and with vertical and with compensation. The optimum control parameter settings were: water pressure = 3.500 bar, abrasive flow rate = 400 g/min, nozzle inner size = 1.01 mm, and orifice = 0.35 mm. Scanning electron microscopic (SEM) results of the cutting surface are shown in Figure 15. The experimental results definitively demonstrate the success of this application, yielding a significantly improved surface quality, with Ra values improving from Ra=400 µm (a) to Ra=25 µm (c). A more precise measurement tolerance was achieved, leading to superior edge cutting quality at higher speeds and a notable increase in machine efficiency.

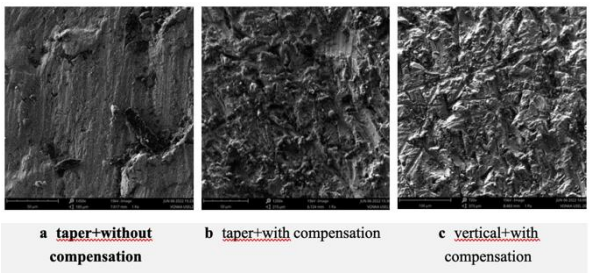

Figure 15. SEM photographs of the "cutting surface".

From the scanning electron micrographs, it is understood that when the abrasive hits the hard steel workpiece with high pressure, brittle fracture occurs and the surface is not fully worn during the angled and inaccurate positioning cut. It has been observed that fracture and abrasion are better in cutting by making perpendicular and precise positioning to the cutting surface.

6. Conclusion

The widespread adoption of waterjet cutting machines globally is often hindered by inefficiencies stemming from the waterjet's inherent taper angle. This taper angle significantly compromises cutting surface quality as cutting speed increases. This study successfully addressed these limitations by implementing a novel approach: orienting the conical water jet exiting the nozzle perpendicularly to the cutting surface and incorporating mechanical compensation to enhance machining tolerances in waterjet systems.

The experimental results definitively demonstrate the success of this application, yielding a significantly improved surface quality. A more precise measurement tolerance was achieved, leading to superior edge cutting quality at higher speeds and a notable increase in machine efficiency. The utilization of a 5-axis nozzle, coupled with axis compensation, proved highly effective, reducing the cutting tolerance from 400µm to a remarkable 25µm. This breakthrough in achieving more precise cutting at elevated speeds significantly expands the application areas for waterjet cutting machines.

Furthermore, the patented mechanical improvements and software compensation with taper angle control, which enable the desired precise edge cutting quality, have resulted in approximately a 30% increase in cutting speed. This translates directly to a 30% reduction in processing time and a corresponding 30% energy saving. Additionally, the reduction in kerf due to controlled cutting angles has led to a decrease in waste and material savings. As a future endeavor, further studies could explore optimizing process duration by experimenting with various taper angle values under pressures up to 6.000 bar.

Author Contributions

The percentages of the author' contributions are presented below. The author reviewed and approved the final version of the manuscript.

	U.Ş.
C	100
D	100
S	100
DCP	100
DAI	100
L	100
W	100
CR	100
SR	100
PM	100
FA	100

C=Concept, D= design, S= supervision, DCP= data collection and/or processing, DAI= data analysis and/or interpretation, L= literature search, W= writing, CR= critical review, SR= submission and revision, PM= project management, FA= funding acquisition.

Conflict of Interest

The author declared that there is no conflict of interest.

Acknowledgements

The author would like to thank Prof. Dr. Ufuk Cebeci for his valuable comments and support.

Ethical Consideration

Ethics committee approval was not required for this study because of there was no study on animals or humans.

References

Bohez ELJ. 2001. Compensating for systematic errors in 5-axis NC machining. Comput-Aided Des, 34: 391–403.

Bohez ELJ. 2002. Five-axis milling machine tool kinematic chain design and analysis. Int J Mach Tools Manuf. 42(4): 505–520.

Chen, et al., 2019. Correcting shape error located in cut in/cut out region in abrasive water jet cutting process. Int J Adv Manuf Technol, 2019: 102.

Feng S, Huang C, et al., 2019. Surface quality evaluation of single crystal 4H-SiC wafer machined by hybrid laser-waterjet: Comparing with laser machining. Mater Sci Semicond Process, 93: 238-251.

Givi M, Mayer JRR. 2014. Validation of volumetric error compensation for a five-axis machine using surface mismatch producing tests and on-machine touch probing. Int J Mach Tools Manuf, 87: 89-95.

Harničárová M, Valíček J, et al., 2013. Comparison of non-traditional technologies for material cutting from the point of view of surface roughness. Int J Adv Manuf Technol, 69: 81-91.

Hsu YY, Lei WT. 2003. Accuracy enhancement of five-axis CNC machines through real-time error compensation. Int J Mach Tools Manuf, 43: 871-877.

Hsu YY, Wang SS. 2007. A new compensation method for geometry errors of five-axis machine tools. Int J Mach Tools Manuf, 47: 352-360.

Ibaraki S, Iritani T, Matsushita T. 2012. Calibration of location errors of rotary axes on five-axis machine tools by on-the-machine measurement using a touch-trigger probe. Int J Mach Tools Manuf, 58: 44-53.

Ibaraki S, Knapp W. 2012. Indirect measurement of volumetric accuracy for three-axis and five-axis machine tools: a review. Int J Autom Technol, 6(2): 110-124.

Ibaraki S, Ota Y. 2014. A machining test to calibrate rotary axis error motions of five-axis machine tools and its application to thermal deformation test. Int J Mach Tools Manuf, 86: 81-88.

Karacan İ, Erdoğan İ, İğdil M, Cebeci U. 2021. Machine vision supported quality control applications in rotary switch production by using both process FMEA and design FMEA. Nat Appl Sci J, 4(2): 16-31.

KMT Waterjet Manual and Operation Books. UK, London, UK, pp: 25-26.

Krajcarz D. 2014. Comparison metal water jet cutting with laser and plasma cutting. Procedia Eng, 69: 838-843.

Lianjun Z, Chunli H, Guangjun C. 2014. Application of tool compensation in CNC machining. Mater Sci Forum, 800–801: 435-439.

Lin W, Lei Y, Zhang S, Wu Z. 2021. Visualization and evaluation of the spatial kinematic rotation error of a five axis abrasive water jet cutting head. Int J Adv Manuf Technol, 114: 3217-3228.

Liu HT, Miles P, Veenhuizen SD. 1998. CFD and physical modeling of UHP AWJ. Jenny Stanford Publishing, Singapore, pp: 121-137.

Liu ZF, Li DD, Liu ZZ. 2014. Gantry machining tool assembly method and predictive optimization based on multi-body system. Comput Integr Manuf Syst, 20: 394-400.

Lu H, Cheng Q, Zhang X, Liu Q, Qiao Y, Zhang Y. 2020. A novel geometric error compensation method for gantry-moving CNC machine regarding dominant errors. Processes, 8(8): 906.

Okafor AC, Ertekin YM. 2000. Derivation of machine tool error models and error compensation procedure for three axes vertical machining center using rigid body kinematics. Int J Mach Tools Manuf, 40: 1199-1213.

Öner M, Cebeci U, Doğan O. 2024. BSC-based digital transformation strategy selection and sensitivity analysis. Mathematics, 12(2): 225.

Patel AJ, Ehman KF. 1997. Volumetric error analysis of a stewart platform-based machine tool. Ann CIRP. 46(1).

Polzer A, Piska M, Dufkova K. 2014. On the modern CNC milling with a compensation of cutting tools deflections. DAAAM Int Sci Book, 2014: 311-322.

Rajamani D, Balasubramanian E, Dilli Babu G, Ananthakumar K. 2022. Experimental investigations on high precision abrasive waterjet cutting of natural fibre reinforced nano clay filled green composites. J Ind Text, 51(3_suppl): 3786-3810.

Ramesh R, Mannan MA, Poo AN. 2000. Error compensation in machine tools: a review. Int J Mach Tools Manuf, 40(9): 1235-1256.

Schwenke H, Knapp W, Haitjema H, Weckenmann A, Schmitt R, Delbressine F. 2008. Geometric error measurement and compensation of machines: an update. CIRP Ann, 57: 660-675.

Simsir U, Biçer K. 2018. Patent no: TR 2018 20101 B CNC waterjet cutting machine with six-axis movement capability. Turkish Patent and Trademark Office, Ankara, Türkiye, pp:15-25.

Veldhuis SC, Elbestawi MA. 1995. A strategy for the compensation of errors in five-axis machining. Ann CIRP, 44(1): 373-377.

Wan L, Xiong J, et al., 2023. Feasible study on the sustainable and clean application of steel slag for abrasive waterjet machining. J Clean Prod, 420: 138378.

Wang, et al., 2019. Kinematic error compensation of a double swivel head in five axis abrasive water jet machine tool. Int J Adv Manuf Technol, 103: 2783-2793.

Xiang S, Altintas Y. 2016. Modeling and compensation of volumetric errors for five-axis machine tools. Int J Mach Tools Manuf, 101: 65-78.

Yang J, Altintas Y. 2013. Generalized kinematics of five-axis serial machines with non-singular tool path generation. Int J Mach Tools Manuf, 75: 119-132.

Yang J, Mayer JRR, Altintas Y. 2015. A position independent geometric errors identification and correction method for five-axis serial machines based on screw theory. Int J Mach Tools Manuf, 95: 52-66.

Yun H, Zou B, Wang J, Huang C, Li S. 2019. Optimization of energy consumption in coating removal for recycling scrap coated cemented carbide tools using hybrid laser-waterjet. J Clean Prod, 229: 104-114.

Black Sea Journal of Engineering and Science
doi: 10.34248/bsengineering.1723258

Open Access Journal
e-ISSN: 2619 – 8991

Research Article
Volume 8 - Issue 5: 1504-1513 / September 2025

THE EFFECT OF COMMON-MODE NOISE IN QUADRATURE RADAR SYSTEMS: ROTATING DISC IMBALANCE ESTIMATION

Yunus Emre ACAR[1]*

[1]*Selcuk University, Faculty of Technology, Department of Electrical and Electronics Engineering, 42075, Konya, Türkiye*

Abstract: Accurate and robust detection of imbalance in rotating machinery is critical for ensuring operational reliability in industrial environments. This study experimentally investigates the impact of common-mode noise (CN) on feature-based classification performance in quadrature radar systems, estimating the imbalance level in a rotating disk. The proposed methodology utilizes a homodyne radar architecture to acquire in-phase (I) and quadrature (Q) baseband signals, from which time-domain features are extracted. A Hilbert transform-based denoising approach is implemented to address the detrimental effects of CN caused by electromagnetic interference and hardware imperfections. The extracted features, both from raw and denoised signals, are evaluated using various machine learning classifiers, including Decision Trees, Support Vector Machines, k-nearest Neighbors, Artificial Neural Networks, and ensemble methods. Experimental results demonstrate that CN significantly degrades classification accuracy, particularly for features derived from the amplitude and phase of complex-valued signals. The application of the proposed denoising technique yields a substantial improvement in classification metrics, with k-nearest Neighbors and Support Vector Machines achieving over 97% accuracy on the denoised data. The findings highlight the importance of effective noise mitigation in radar-based condition monitoring pipelines and establish the practical viability of quadrature radar systems for non-contact, high-precision imbalance detection in rotating machinery.

Keywords: Classification, Fault diagnosis, Feature extraction, Noise removal, Radar, Vibration

***Corresponding author:** Selcuk University, Faculty of Technology, Department of Electrical and Electronics Engineering, 42075, Konya, Türkiye
E mail: yacar@selcuk.edu.tr (Y.E. ACAR)
Yunus Emre ACAR https://orcid.org/0000-0002-6809-9006

Received: June 19, 2025
Accepted: August 16, 2025
Published: September 15, 2025

Cite as: Acar YE. 2025. The effect of common-mode noise in quadrature radar systems: rotating disc imbalance estimation. BSJ Eng Sci, 8(5): 1504-1513.

1. Introduction

Fault diagnosis and monitoring of rotating machinery are crucial for maintaining production efficiency and extending equipment lifespan within industrial settings (Li et al., 2023; Zhao et al., 2025). The imbalance, among the prevalent faults, is a significant concern, potentially leading to detrimental outcomes such as bearing damage, excessive vibration, energy wastage, and catastrophic machinery failures if not identified promptly (Cho et al., 2018). This issue substantially contributes to increased maintenance expenditures and unforeseen operational downtimes in rotating machinery.

While traditionally identified through contact-based vibration sensors, this approach faces several practical limitations, including susceptibility to sensor wear and degradation, challenges in sensor installation and maintenance in confined or inaccessible locations, signal interference from mechanical couplings, and reduced reliability in environments characterized by high temperatures, excessive contamination, or hazardous operating conditions. Consequently, non-contact measurement techniques have garnered considerable attention promptly (Goyal et al., 2020; Liu et al., 2025; Xu et al., 2025). In this regard, radar systems present a compelling alternative for industrial applications, owing to their inherent capabilities in target detection, tracking, and identification (Hansen et al., 2022; Acar, 2024).

Radar-based non-contact measurement methodologies promise reliable imbalance detection, even within demanding industrial environments. Contemporary radar systems frequently employ signals derived from quadrature demodulation for classification tasks. The cooperative use of in-phase (I) and quadrature (Q) signals, which exhibit a 90-degree phase difference, ensures the preservation of both amplitude and phase information integral to their complex-valued representation. This complex signal structure offers a rich dataset for applications such as discerning varying levels of imbalance in rotating machinery.

Nevertheless, common-mode noise (CN) presents a substantial challenge in such radar systems (Du et al., 2022). CN concurrently affects both I and Q signals acquired through IQ demodulation, degrading overall system performance. Key sources of this noise, particularly prevalent in industrial contexts, include electromagnetic interference, power supply fluctuations, and hardware imperfections. The presence of CN can introduce distortions in complex-valued signal parameters, complicating the accurate classification of different imbalance severities.

Although the existing literature describes various noise mitigation techniques (Ge et al., 2025; Park et al., 2025), there is a lack of studies on the specific impact of CN on imbalance detection within industrial radar applications. This study systematically handles the effect of CN in quadrature radar signals on the performance of classifiers using features derived from complex-valued radar data and evaluates the impact of CN reduction. Although various noise reduction methods are available in the literature, the study examines a practical Hilbert transform-based CN elimination approach. It contributes by demonstrating the negative effect of CN on classification accuracy and determining to what extent the selected methods successfully reduce this impact, especially in the complex feature framework. This analysis highlights the importance of CN removal in radar processing chains.

Our methodological approach begins with experimentally acquired radar signals known to contain CN. We then subject these signals to a CN denoising process. Following the noise reduction step, we extract discriminative features from the complex-valued $I + jQ$ signals, for both the original noisy signals (as a baseline) and the processed, denoised signals. These features are chosen based on their effectiveness in classification literature (Nayana and Geethanjali, 2017). In the final stage, these feature sets become the input for training and rigorously testing standard machine learning classifiers, such as Decision Tree (DT), Support Vector Machine (SVM), Kth Nearest Neighbors (KNN), Artificial Neural Network (ANN), and some ensemble ones. The core of our analysis involves quantitatively evaluating and comparing the resulting classification performance and assessing the impact of each denoising technique.

The rest of the study is structured as follows. Section 2 provides detailed information on the experimental setup, dataset, mathematical background, feature extraction, classification, and evaluation criteria. Section 3 presents the experimental findings and a comprehensive assessment. Finally, the last section concludes the study.

2. Materials and Methods

2.1. The experimental Setup

This section details the experimental apparatus used for this investigation. A versatile test rig designed by PiriTech was employed. This setup enables the simulation of common industrial faults such as winding defects, bearing failures, rotor bar damage, shaft misalignment (horizontal and vertical), and mechanical imbalance. Our research utilizes this platform to focus on imbalance faults intentionally introduced at different severity levels.

A 1.1 kV three-phase asynchronous motor rotated a metal disc at different speeds and loads. Imbalance levels were systematically created by attaching weights to threaded mounting points on the disc: 0 g (normal), 10 g (slight imbalance), 20 g (moderate imbalance), and 30 g (severe imbalance). Figure 1 illustrates the experimental configuration, and Table 1 lists the key components.

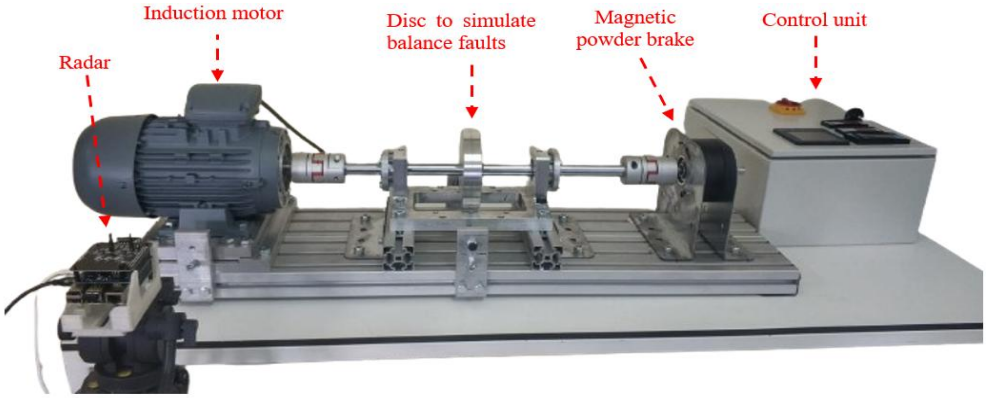

Figure 1. The experimental setup.

Table 1. Key components of the experimental test rig

Component	Specifications	Explanation
Volt VM 90S-4 Induction motor	1.1 kW, 1500 rpm, 3-phase	the monitored motor
ABB ACS150-01E-07A5-2 motor driver	50/60 Hz, 220V, 1.5 kW	controls the motor speed
EMF ABTF02 mag. powd. brake	15 Nm, 24 W, 24 V_{in}	load for the motor
EMF TFD-02 mag. powd. brake driver	12-48 VDC, operation options (4-20 mA, 0-10V)	drives the load

A radar system based on the RFBEAM KLC5 transceiver module was employed. The module features a Homodyne receiver architecture, which directly provides baseband I and Q signals. Following the manufacturer's recommended circuit design, I/Q signal outputs were amplified by approximately 40 dB. Subsequently, the amplified signals were digitized using a Measurement Computing MCC118 Data Acquisition (DAQ) card. The Raspberry Pi 4 managed the data logging process, saving the acquired digital data into a CSV file format. Figure 2 illustrates this compact, Raspberry Pi-based data acquisition setup.

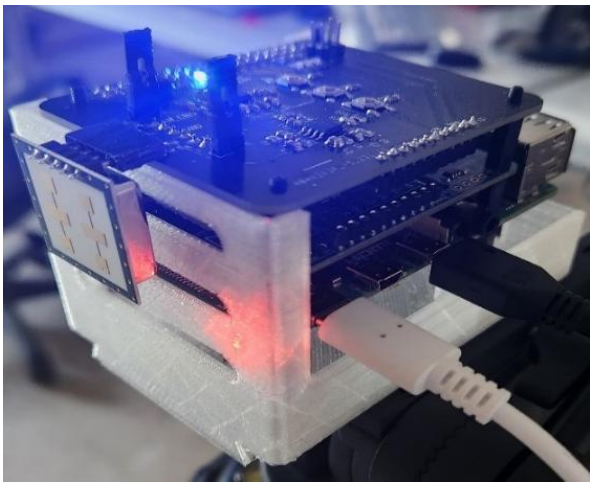

Figure 2. The radar hardware for data acquisition.

2.2. The Dataset

For this four-class classification problem, encompassing the normal operating condition and three distinct levels of imbalance fault, a total of 1802 experimental trials were conducted. Each trial resulted in a 30-second data recording. The radar module, directed towards the motor from a distance of 30 cm, sampled the I/Q signals at a rate of 10 kSPS. The raw acquired data and a version processed to remove CN have been made publicly accessible to the research community via the KAGGLE platform (Acar,2025). Table 2 provides a detailed breakdown of the amount of data recordings obtained for each of the four classes.

Table 2. Class distribution in the dataset

Class Name	# of data
normal	462
slight imbalance	464
moderate imbalance	413
severe imbalance	463

In constructing the dataset for each classification category, we systematically varied the operational parameters of the motor. The rotational speed was incrementally adjusted across a comprehensive range from 500 to 1500 rpm, with precise 100 rpm intervals between test conditions. We implemented a methodical variation in mechanical loading conditions for each speed level. The load modulation was precisely controlled via a magnetic powder brake mechanism, varying from minimal loading (0%) to quarter-capacity loading (25% of the maximum 15 Nm torque capacity). We conducted repeated measurement sessions at different intervals to enhance statistical robustness and monitor temporal variations in system response.

2.3. IQ Demodulation

Homodyne, or Direct-Conversion (Zero-IF), receiver architectures offer significant advantages in radar system design primarily because they simplify the overall structure. By eliminating the need for an Intermediate Frequency (IF) stage, these architectures reduce component count, lower power consumption, decrease cost, and readily support monolithic integration onto a single chip. These factors make homodyne designs attractive for cost-sensitive, low-power, or highly integrated radar applications, such as automotive sensors or short-range presence detection.

Within this simplified framework, quadrature (IQ) demodulation, performed directly at the baseband, provides a key technique for extracting crucial target information, particularly velocity direction. Modern radar systems employing these homodyne architectures utilize IQ demodulation to directly convert the received Radio Frequency (RF) echo signal into its baseband I and Q components. The demodulation process maintains these components in phase quadrature (a 90-degree phase separation).

In this architecture, the Local Oscillator (LO) signal operates at the same frequency (f_c) as the transmitted carrier signal . The system derives this LO signal directly from the transmitter's frequency source for phase coherence. A power splitter then divides the LO signal to generate the two reference signals in phase quadrature as in equation 1 and equation 2.

$$I_{ref} = \cos 2\pi f_c t \tag{1}$$

$$Q_{ref} = sin2\pi f_c t \tag{2}$$

The antenna captures the RF echo signal reflected from the vibrating target. This received signal, $S_r(t)$, carries the phase modulation imparted by the target's time-varying displacement $x(t)$. Its phase relative to the transmitted signal can be expressed as equation 3

$$\phi(t) = \phi_0 + \frac{4\pi x(t)}{\lambda} \tag{3}$$

where λ is the carrier wavelength (c/f_c) and ϕ_0 represents the static phase shift due to the average target distance and system delays. The received signal is thus (equation 4):

$$S_r(t) \approx A_R cos(2\pi fct + \phi_0 + \frac{4\pi x(t)}{\lambda}) \tag{4}$$

where A_R is the received signal amplitude.

The receiver front-end directly mixes this incoming RF signal $S_r(t)$ independently with both the I and Q reference signals. Two parallel low-pass filters then reject the high-frequency mixing, yielding the baseband I and Q signals (equation 5.1 and 5.2)**:**

$$I(t) = K\ cos(\phi_0 + \frac{4\pi x(t)}{\lambda}) \tag{5.1}$$

$$Q(t) = K\ sin(\phi_0 + \frac{4\pi x(t)}{\lambda}) \tag{5.2}$$

Here, K represents the overall gain and amplitude factors. These I/Q signals encode the target's vibration information within their relative phase. By treating the outputs as a complex baseband signal $C(t) = I(t) + jQ(t)$,

one can robustly extract the instantaneous phase angle (equation 6):

$$arctan2(Q(t), I(t)) = \phi_0 + \frac{4\pi x(t)}{\lambda} \quad (6)$$

The $arctan2$ function resolves phase ambiguities across the 360-degree range. Subsequent processing involves unwrapping this phase angle (if necessary) and removing the static phase offset ϕ_0 (often achieved through high-pass filtering or baseline subtraction). Finally, we recover the target's vibration displacement waveform $x(t)$ by scaling the dynamic phase component (equation 7):

$$x(t) = \frac{\lambda}{4\pi} \times (arctan2(C(t)) - \phi_0) \quad (7)$$

This homodyne IQ demodulation scheme allows direct conversion of the target's micro-scale motion $x(t)$ into measurable baseband phase variations, forming the basis for our vibration analysis. Figure 3 illustrates the described receiver architecture.

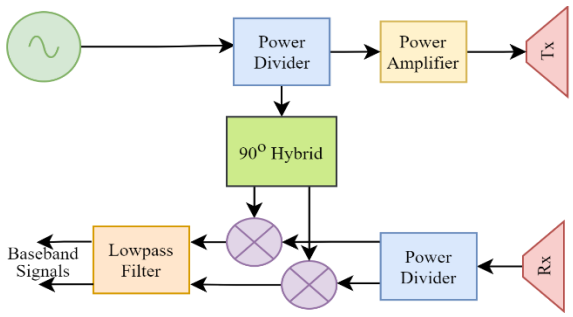

Figure 3. Block scheme of an IQ demodulated CW radar.

2.4. CN Removal

CN can be expressed for IQ demodulated receivers as noise that affects both quadrature signals equally, as shown in equations 8.a and 8.b.

$$I_n(t) = K\ cos\left(\phi_0 + \frac{4\pi x(t)}{\lambda}\right) + noise \quad (8.a)$$

$$Q_n(t) = K\ sin\left(\phi_0 + \frac{4\pi x(t)}{\lambda}\right) + noise \quad (8.b)$$

System performance can be considerably compromised by CN in hardware configurations where dedicated CN elimination mechanisms are absent or in architectures with simplified complexity.

This research employs a methodology centered on Hilbert transformation techniques to extract CN-removed I and Q signals. The Hilbert transform represents a mathematical operation that generates a phase-quadrature version of the original signal, shifted by precisely 90 degrees. In formal mathematical terms, when applied to a signal $f(t)$, the Hilbert transform $H\{f(t)\}$ is characterized as the convolution integral of the signal with the function $1/(\pi t)$. In this approach, the difference between the noisy signals, $D(t)$, is initially obtained as expressed in equation 9.

$$\begin{aligned} D(t) &= I_n(t) - Q_n(t) \\ &= K[cos(\phi(t)) - sin(\phi(t))] \end{aligned} \quad (9)$$

When the Hilbert transform is applied to this difference signal, the $D_q(t)$ signal is obtained as presented in equation 10.

$$\begin{aligned} D_q(t) &= H\{D(t)\} \\ &= K[sin(\phi(t)) + cos(\phi(t))] \end{aligned} \quad (10)$$

The noise-free baseband signals $I(t)$ and $Q(t)$ are recovered through the combined utilization of these signals as formulated in equation 11 and equation 12.

$$I(t) = \frac{D(t) + D_q(t)}{2} = Kcos(\phi(t)) \quad (11)$$

$$Q(t) = \frac{D_q(t) - D(t)}{2} = Ksin(\phi(t)) \quad (12)$$

2.5. Feature Extraction

Feature extraction is a critical stage in machine learning-based classification applications. Numerous studies have demonstrated effective feature extraction methods in both time and frequency domains for applications like vibration-based machine health monitoring and fault diagnosis (Zhao et al., 2023; Jiao et al., 2025). While frequency domain features obtained through time-frequency transformations often improve classification performance (Kilic and Acar, 2024), time domain feature extraction offers simplicity and superior capability in capturing transient events. Direct usage of time domain signals reduces complexity across many applications (Wang et al., 2022).

This study focuses on time domain features with proven classification efficacy from windowed signals. We constructed the complex signal $C(t)$ from 30-second recordings and divided its amplitude and phase components into 1-second windows with 50% overlap. For each signals, we calculated 12 features by averaging the values extracted from individual windows. We applied this extraction methodology to raw signals and those processed with the CN reduction approach. Equations 13-24 present the mathematical formulations of these extracted features.

Mean Absolute Value (MAV): Equation 13 demonstrates the calculation method for this particular feature, which represents the arithmetic average of absolute sample magnitudes within the analyzed segment.

$$MAV = \frac{1}{L}\sum_{n=1}^{L} |x[n]| \quad (13)$$

Energy (E): The segment's power content is quantified by this feature, with its mathematical computation presented in equation 14.

$$E = \sum_{n=1}^{L} x[n]^2 \quad (14)$$

Waveform Length (WL): This feature corresponds to the sum of absolute differences between consecutive samples. It represents the sum of absolute first-order derivatives,

providing information about the signal's roughness, rate of change, and frequency characteristics for discrete signals. WL is calculated as shown in equation 15.

$$WL = \sum_{n=1}^{L} |x[n] - x[n-1]| \quad (15)$$

Willison Amplitude (WA): This metric evaluates sequential sample variations against a predetermined threshold, tallying occurrences where the differential surpasses this boundary value. The quantification process utilizes the mathematical framework outlined in equations 16.a and 16.b.

$$WA = \sum_{n=1}^{L} f|x[n] - x[n+1]| \quad (16.a)$$

$$f(x) = \begin{cases} 1 \; if \; x \geq \varepsilon \\ 0 \; otherwise \end{cases} \quad (16.b)$$

Zero Crossing (ZC): This parameter quantifies the frequency of axis intersections throughout the segment. The mathematical formulation in equation 17.a identifies an axis crossing when adjacent values exhibit sign reversal. An additional verification can eliminate insignificant fluctuations near the zero line and confirm that the magnitude difference between consecutive samples exceeds a defined threshold, as formulated in equation 17.b.

$$ZC = \sum_{n=1}^{L} (x[n] \times x[n+1]) < 0 \quad (17.a)$$

$$(|x[n] - x[n+1]|) > \varepsilon \quad (17.b)$$

Slope Sign Change (SSC): This metric counts directional reversals in the signal trajectory throughout the segment. Equation 18 provides the mathematical framework for identifying these gradient sign changes. Only instances where consecutive sample differences exceed a defined threshold are counted, following the criterion specified in equation 17.b.

$$SSC = \sum_{n=1}^{L} ((x[n+1] - x[n]) \times (x[n] - x[n-1])) < 0 \quad (18)$$

Root Mean Square (RMS): Equation 19 presents the mathematical formulation for this feature, which computes the square root of the average of squared values across the segment.

$$RMS = \sqrt{\frac{1}{L}\sum_{n=1}^{L} x[n]^2} \quad (19)$$

Mean (μ): This parameter determines the arithmetic average across all points within the segment, computed according to the formula presented in equation 20.

$$Mean = \mu = \frac{1}{L}\sum_{n=1}^{L} x[n] \quad (20)$$

Variance (σ^2): This metric evaluates the dispersion of values by measuring squared deviations from the central tendency. The mathematical average of these squared differentials yields the variance parameter. Equation 21 presents the computational framework for determining this statistical dispersion value for each analyzed segment.

$$Variance = \sigma^2 = \frac{1}{L}\sum_{n=1}^{L} (x[n] - \mu)^2 \quad (21)$$

Standard Deviation (STD): This parameter quantifies the degree of dispersion by extracting the square root of the variance value, as mathematically formulated in equation 22.

$$STD = \sigma = \sqrt{\frac{1}{L}\sum_{n=1}^{L} (x[n] - \mu)^2} \quad (22)$$

Skewness (SKW): This attribute quantifies distributional asymmetry characteristics. For perfectly symmetric distributions, it yields a zero value. In asymmetric cases, the parameter's sign indicates directional bias—positive values denote rightward skewing while negative values indicate leftward skewing. Equation 23 provides the mathematical framework for calculating this distributional asymmetry metric for each segment.

$$SKW = \frac{\frac{1}{L}\sum_{n=1}^{L}(x[n] - \mu)^3}{\sigma^3} \quad (23)$$

Kurtosis (KURT): This parameter evaluates the peakedness or flatness characteristics of a distribution profile. As formulated in equation 24, the KURT value for each segment offers a numerical assessment of the distribution's morphology compared to the Gaussian curve.

$$KURT = \frac{\frac{1}{L}\sum_{n=1}^{L}(x[n] - \mu)^4}{\sigma^4} \quad (24)$$

Feature extraction procedures were applied separately to amplitude and phase signals, and by combining the extracted features, a total of 24 features were generated for each data sample to be input into the classifier.

2.6. Classification

The four-class imbalance detection problem was addressed by well-known machine learning approaches with the dataset comprising 1802 experiments. The performance of these methods was validated using 5-fold cross-validation. The hyperparameters of the classifiers were optimized through a systematic grid search methodology. This process involved evaluating all possible hyperparameter combinations within predefined ranges at specific incremental steps. Performance metrics were assessed for each parameter configuration, enabling the identification of the optimal hyperparameter set that maximizes the model's generalization capability. Table 3 summarizes the parameter searching ranges for the preferred classifiers.

2.7. Performance Metrics

The effectiveness of the classifiers is evaluated through confusion matrices. These matrices are tabular representations that show how the model's predictions align with each class, functioning as an assessment tool for model performance. Figure 4 illustrates a multi-class confusion matrix.

Table 3. Hyperparameter searching ranges for the classifiers

Method	Parameters
SVM	*Kernel function:* linear, quadratic, cubic *box constraint level:* 0.001-1.0 *multiclass meth.:* one vs one, one vs all
KNN	*number of neighbors:* 1-901 *distance metric:* Euclidean, Chebyshev, cosine, Hamming, cubic. *distance weight:* equal, inverse, squared inverse.
DT	*Max. # of splits:* 1-1801 *split criterion:* Gini diversity index, twoing rule, maximum deviance reduction.
Ensemble	*Ensemble method*: Bag, AdaBoost, RUSBoost. *# of learners:*10-50 *learning rate:*0.001-1.0 *max. # of splits:* 1-1801
ANN	*# of fully connected layer: 1-3* *activation func.: sigmoid, tanh, ReLU, none.* *lambda:* 5×10^{-9} −50 *first layer size:*1-300 *second layer size:*1-300 *third layer size:*1-300

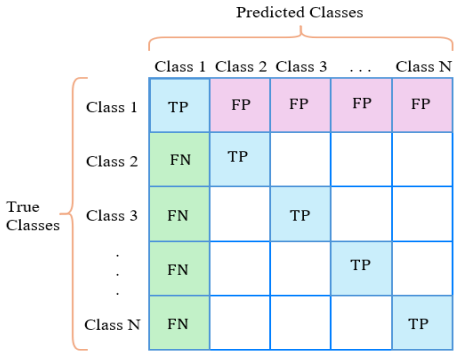

Figure 4. A multi-class confusion matrix.

The confusion matrix's True Positive (TP), False Positive (FP), and False Negative (FN) values are used to compute various assessment metrics. equations 25 through 28 present the metrics and formulas employed.

$$Accuracy = (\Sigma\, TPs) / (All\ predictions) \quad (25)$$

$$Precision = TP / (TP + FP) \quad (26)$$

$$Recall = TP / (TP + FN) \quad (27)$$

$$F1\ score = 2 \times (Precision \times Recall) / (Precision + Recall) \quad (28)$$

Within formulas (25)-(28), TP values indicate successful classification for individual classes. Accuracy represents the proportion of total TP values, showing how well the model correctly classifies the issue. Precision reflects the accuracy of the positive predictions, emphasizing its capability to reduce FP values. The Recall metric, meanwhile, gauges how effectively the model identifies actual positives, showcasing its ability to minimize FN values.

In the context of the four-class imbalance detection problem, precision and recall metrics have been calculated discretely for each class. This calculation methodology yields four distinct precision and recall values corresponding to the four classes. For the final metric values in the analysis, we have implemented an averaging approach of the class-wise precision and recall metrics. The F1 score, the harmonic means of the average precision and recall metrics, has been utilized to evaluate the equilibrium between these metrics through collective assessment.

3. Results and Discussion

This section presents the classification results obtained using different input configurations. The performance of the classifiers is reported both without and with CN removal. Table 4 summarizes the classification results obtained by directly using the radar baseband signals without applying CN removal. In Table 4, the feature set F_I refers to the 12 features extracted solely from the I signal, F_Q denotes the features extracted exclusively from the Q signal, F_{abs} represents the features derived from the amplitude of the complex-valued signal formed by the I and Q components, and F_{angle} corresponds to the features extracted from the phase of the complex-valued signal. The [·] operator indicates that the respective feature sets are used in combination. Each classifier was trained and evaluated separately with these different input sets, and the classification performance is reported in terms of accuracy, precision, recall, and F1 score. The complexity analysis of the models is conducted based on model size and prediction speed.

Table 4. The classification results without CN removal

Model Name	Input signal	Accuracy (%)	Precision (%)	Recall (%)	F1 Score (%)	Prediction Speed (obs/s)	Model Size (kb)
DT	F_I	88.62	88.61	88.58	88.58	16000	36
	F_Q	82.74	82.52	82.49	82.5	21000	48
	$[F_I\ F_Q]$	88.9	88.89	88.8	88.84	36000	35
	F_{abs}	81.63	81.68	81.59	81.63	54000	46
	F_{angle}	83.02	82.9	82.9	82.9	48000	49
	$[F_{abs}\ F_{angle}]$	87.85	87.82	87.82	87.82	52000	39
SVM	F_I	93.23	93.38	93.12	93.21	13000	387
	F_Q	93.4	93.4	93.34	93.35	20000	124
	$[F_I\ F_Q]$	95.56	95.52	95.54	95.52	15000	155
	F_{abs}	93.4	93.45	93.37	93.4	33000	225
	F_{angle}	88.79	88.68	88.68	88.68	45000	131
	$[F_{abs}\ F_{angle}]$	95.12	95.12	95.14	95.1	43000	156
KNN	F_I	91.51	91.67	91.46	91.53	19000	216
	F_Q	91.24	91.22	91.16	91.16	14000	216
	$[F_I\ F_Q]$	91.51	91.59	91.48	91.51	4000	395
	F_{abs}	91.45	91.54	91.5	91.49	15000	216
	F_{angle}	90.23	90.28	90.28	90.25	5000	218
	$[F_{abs}\ F_{angle}]$	94.12	94.13	94.16	94.12	15000	386
NN	F_I	94.40	94.47	94.36	94.40	88000	18
	F_Q	92.79	92.73	92.77	92.75	67000	169
	$[F_I\ F_Q]$	96.89	96.89	96.9	96.9	38000	32
	F_{abs}	91.62	91.63	91.59	91.6	44000	37
	F_{angle}	91.95	91.91	91.89	91.89	52000	110
	$[F_{abs}\ F_{angle}]$	96.84	96.79	96.86	96.81	47000	74
Ensemble	F_I	94.89	94.89	94.85	94.86	730	23000
	F_Q	89.62	89.54	89.43	89.46	620	32000
	$[F_I\ F_Q]$	96.45	96.43	96.45	96.44	400	20000
	F_{abs}	86.51	86.56	86.54	86.54	23000	824
	F_{angle}	89.96	89.9	89.92	89.88	13000	2200
	$[F_{abs}\ F_{angle}]$	96.12	96.09	96.16	96.12	1700	7000

When examining the classification results obtained from non-denoised data, the NN model with the $[F_I\ F_Q]$ combination demonstrates superior performance, achieving an accuracy rate of 96.89%. This model also excels in other classification metrics, showing balanced precision (96.89%), recall (96.9%), and F1 score (96.9%), indicating its robust performance across all evaluation criteria. The NN model using the [abs angle] combination follows closely with 96.84% accuracy, 96.79% precision, 96.86% recall, and 96.81% F1 score, demonstrating consistent performance across metrics. From a model complexity perspective, NN models stand out not only for their high accuracy but also for their remarkably compact model sizes (18-169 kb) and rapid prediction speeds (38,000-88,000 observations per second). In contrast, Ensemble models, while achieving comparable accuracy levels (96.45%) and balanced precision (96.43%), recall (96.45%), and F1 score (96.44%), require substantially larger model sizes (7,000-32,000 kb) and operate at significantly slower prediction speeds (400-1,700 observations per second). SVM models demonstrate good performance with moderate model sizes (124-387 kb) and prediction speeds (13,000-45,000 observations per second), maintaining consistent precision, recall, and F1 scores that closely track their accuracy values. Despite being the smallest and fastest, the decision tree model yields the lowest accuracy rates and corresponding classification metrics. These findings highlight the critical importance of model selection and signal feature combination strategies in quadrature signal classification. Notably, NN models emerge as the most suitable option for real-time applications by offering an optimal balance between computational efficiency and comprehensive classification performance across all evaluation metrics. Examining the classification results after CN removal reveals significant performance improvements across models as tabulated in Table 5. The KNN model with the $[F_{abs\_c}\ F_{angle\_c}]$ combination achieves the highest accuracy at 97.45%, with corresponding precision (97.43%), recall (97.42%), and F1 score (97.41%) values demonstrating exceptional balance across metrics.

Table 5. The classification results with CN removal

Model Name	Input signal	Accuracy (%)	Precision (%)	Recall (%)	F1 Score (%)	Prediction Speed (obs/s)	Model Size (kb)
DT	F_{I_c}	83.24	83.08	83.09	83.07	64000	52
	F_{Q_c}	83.24	83.15	83.11	83.13	6600	50
	$[F_{I\_c}\ F_{Q\_c}]$	85.96	85.89	85.9	85.89	37000	43
	F_{abs_c}	85.18	85.17	85.12	85.13	56000	45
	F_{angle_c}	81.47	81.4	81.42	81.38	56000	53
	$[F_{abs\_c}\ F_{angle\_c}]$	90.57	90.5	90.59	90.52	39000	38
SVM	F_{I_c}	92.79	92.64	92.7	92.66	20000	144
	F_{Q_c}	92.73	92.63	92.63	92.61	25000	149
	$[F_{I\_c}\ F_{Q\_c}]$	93.9	93.82	93.85	93.82	42000	166
	F_{abs_c}	91.73	91.71	91.69	91.67	45000	98
	F_{angle_c}	93.45	93.37	93.32	93.33	9900	237
	$[F_{abs\_c}\ F_{angle\_c}]$	97.29	97.26	97.28	97.26	30000	152
KNN	F_{I_c}	85.13	85.16	85.17	85.09	20000	216
	F_{Q_c}	84.24	84.16	84.18	84.15	3500	218
	$[F_{I\_c}\ F_{Q\_c}]$	86.9	86.85	86.9	86.86	9900	386
	F_{abs_c}	92.06	92.09	92.12	92.06	14000	216
	F_{angle_c}	92.45	92.38	92.36	92.37	8100	216
	$[F_{abs\_c}\ F_{angle\_c}]$	97.45	97.43	97.42	97.41	14000	386
NN	F_{I_c}	93.51	93.41	93.46	93.4	57000	70
	F_{Q_c}	94.4	94.32	94.27	94.28	65000	193
	$[F_{I\_c}\ F_{Q\_c}]$	95.23	95.17	95.19	95.17	26000	284
	F_{abs_c}	95.89	95.87	95.89	95.87	74000	163
	F_{angle_c}	93.78	93.69	93.69	93.67	64000	46
	$[F_{abs\_c}\ F_{angle\_c}]$	97.34	97.3	97.32	97.3	86000	19
Ensemble	F_{I_c}	91.73	91.65	91.65	91.64	7200	3000
	F_{Q_c}	90.95	90.95	90.89	90.9	910	24000
	$[F_{I\_c}\ F_{Q\_c}]$	94.17	94.12	94.15	94.13	630	16000
	F_{abs_c}	92.01	92.05	92.0	92.02	810	25000
	F_{angle_c}	88.57	88.45	88.46	88.46	850	21000
	$[F_{abs\_c}\ F_{angle\_c}]$	95.06	95.04	95.02	95.01	13000	891

This performance is closely followed by the SVM model using the same feature combination (97.29% accuracy) and the NN model (97.34% accuracy), showing similarly balanced precision, recall, and F1 scores.

The relationship between model complexity and performance also presents interesting patterns in the noise-removed scenario. Despite their previously modest performance, KNN models show remarkable improvement with noise removal, particularly with the $[F_{abs\_c}\ F_{angle\_c}]$ combination, while maintaining moderate model sizes (386 kb) and reasonable prediction speeds (14,000 obs/s). NN models continue to offer an excellent balance of high accuracy and computational efficiency with small model sizes (19-284 kb) and impressive prediction speeds (26,000-86,000 obs/s). SVM models demonstrate substantial improvement with noise removal while maintaining moderate resource requirements.

The most striking transformation occurs in the effectiveness of signal features. While $[F_I\ F_Q]$ combinations dominated in the non-denoised scenario, the $[F_{abs\_c}\ F_{angle\_c}]$ combination consistently outperforms all other feature combinations after noise removal across nearly all models. Additionally, individual F_{abs_c} and F_{angle_c} features show marked improvement compared to their non-denoised counterparts.

Comparing the Table 4 and Table 5 highlights the critical importance of CN noise removal in quadrature signal classification. The overall accuracy ceiling rises from 96.89% to 97.45%, but more importantly, the performance distribution across models and features changes significantly. The noise removal process enhances the discriminative power of amplitude and phase information, making the $[F_{abs\_c}\ F_{angle\_c}]$ combination superior to the previously dominant $[F_I\ F_Q]$ combination. This transformation suggests that CN disproportionately affects signal characteristics, and its removal allows previously obscured patterns to emerge.

Furthermore, the improved performance of simpler models like KNN after noise removal indicates that much of the classification challenge in the original data stemmed from noise rather than inherent signal complexity. These findings emphasize that implementing effective noise removal techniques can be as crucial as model selection in achieving optimal classification performance, potentially allowing computationally lighter models without sacrificing accuracy in practical applications. The heatmap presented in Figure 5 visually summarizes the impact of CN removal on classification accuracy.

Figure 5. The impact of the CN-removal for each model and input type.

The heat map visualization presents a comprehensive comparative analysis of classification accuracy across multiple dimensions: machine learning models, signal feature combinations, and noise conditions. This multifactorial representation effectively illustrates the interaction between model selection and feature engineering in noisy and noise-removed scenarios.

The color gradient reveals a clear performance stratification, with the highest accuracy values (>97%) concentrated in the noise-removed $[F_{abs\_c}\ F_{angle\_c}]$ combinations for KNN, SVM, and NN models. This pattern suggests a significant interaction between noise removal and the discriminative power of combined amplitude and phase information. The visualization demonstrates that while $[F_I\ F_Q]$ combinations generally outperform other feature sets in normal conditions, the CN removal fundamentally alters this relationship, elevating $[F_{abs\_c}\ F_{angle\_c}]$ combinations to superior performance.

The heat map also effectively captures the differential impact of noise removal across models. The dramatic improvement in KNN performance with noise-removed amplitude and phase features (from 94.12% to 97.45%) represents a particularly noteworthy transition, suggesting that this model's classification boundaries become substantially more effective when the CN is eliminated. Conversely, the relatively modest improvements in some DT model configurations indicate potential limitations in the model's ability to leverage enhanced signal quality.

From a methodological perspective, this visualization provides valuable insights for optimizing classification pipelines in quadrature signal processing applications. It demonstrates that optimal model selection may differ significantly between noisy and clean signal conditions, challenging the assumption that more complex models necessarily yield better performance. The heat map also indicates that appropriate noise removal techniques potentially allow simpler, computationally efficient models to achieve performance comparable to or exceeding that of more complex alternatives in noisy environments.

4. Conclusion

This study investigated the classification of quadrature radar signals using machine learning methods and the impact of CN removal on classification performance. The results demonstrate that radar-based systems offer an effective solution for detecting imbalance in rotating machinery.

The elimination of CN noise led to significant transformations in classification performance. The most striking improvement was observed in the KNN model with the $[F_{abs\_c}\ F_{angle\_c}]$ combination, where accuracy increased from 94.12% to 97.45%. Furthermore, the noise

removal process fundamentally altered the effectiveness of signal features, elevating the [abs angle] combination to superiority over the [F_I F_Q] combination.

The superiority of radar-based solutions lies in their ability to detect imbalance from a safe distance without requiring physical intervention with machinery. The capability of radar signals to detect movements with millimeter precision enables early-stage detection of imbalance.

Accuracy rates exceeding 97% confirm that radar-based systems represent a high-performance solution for imbalance detection. The combined use of noise-removed amplitude and phase information demonstrates the effectiveness of radar signals in capturing imbalance characteristics.

Unlike conventional vibration sensor-based approaches, radar systems enable simultaneous monitoring of multiple machines, offering a cost-effective monitoring solution for industrial facilities.

Future research will explore the capability of radar-based systems to detect imbalance location and provide automatic correction recommendations. This development transforms radar technology from a passive monitoring tool into an active troubleshooting solution.

Author Contributions

The percentages of the author' contributions are presented below. The author reviewed and approved the final version of the manuscript.

	Y.E.A.
C	100
D	100
S	100
DCP	100
DAI	100
L	100
W	100
CR	100
SR	100
PM	100
FA	100

C=Concept, D= design, S= supervision, DCP= data collection and/or processing, DAI= data analysis and/or interpretation, L= literature search, W= writing, CR= critical review, SR= submission and revision, PM= project management, FA= funding acquisition.

Conflict of Interest

The author declared that there is no conflict of interest.

Ethical Consideration

Ethics committee approval was not required for this study because of there was no study on animals or humans.

References

Acar YE. 2024. Radar-enabled non-contact speed estimation for rotating electrical machinery. Meas, 235: 114989.

Acar YE. 2025. Radar data for rotational mass imbalance detection. URL: https://www.kaggle.com/datasets/yunusemreacar1/radar-data-for-machine-fault-detection (accessed date: August 11, 2025).

Cho S, Gao Z, Moan T. 2018. Model-based fault detection, fault isolation and fault-tolerant control of a blade pitch system in floating wind turbines. Renew Energy, 120: 306-321.

Du M, Zhong P, Cai X, Bi D. 2022. DNCNet: Deep radar signal denoising and recognition. IEEE Trans Aerosp Electron Syst, 58(4): 3549-3562.

Ge Y, Wang R, Zeng X. 2025. Robust and accurate eye-blink detection using a 24-GHz CW radar. IEEE Trans Instrum Meas, 74: 1-10.

Goyal D, Dhami SS, Pabla BS. 2020. Non-contact fault diagnosis of bearings in machine learning environment. IEEE Sens J, 20(9): 4816-4823.

Hansen S, Bredendiek C, Briese G, Froehly A, Herschel R, Pohl N. 2022. A SiGe-chip-based D-band FMCW-radar sensor with 53-GHz tuning range for high resolution measurements in industrial applications. IEEE Trans Microw Theory Tech, 70(1): 719-731.

Jiao H, Sun W, Wang H, Wan X. 2025. Comprehensive exploitation of time- and frequency-domain information for bearing fault diagnosis on imbalanced datasets via adaptive wavelet-like transform general adversarial network and ensemble learning. Sensors, 25(7): 2328.

Kilic ME, Acar YE. 2024. Performance evaluation of the time-frequency transformation methods on electrical machinery fault detection. Bitlis Eren Univ J Sci, 13: 1147-1157.

Li H, Wu X, Liu T, Li S. 2023. Rotating machinery fault diagnosis based on typical resonance demodulation methods: A review. IEEE Sens J, 23(7): 6439-6459.

Liu H, Ji D, Lin J, Liu Z, Li H. 2025. Residual angular speed analysis based on laser Doppler vibrometer and its application in planetary gearbox diagnosis. Meas, 250: 116987.

Nayana BR, Geethanjali P. 2017. Analysis of statistical time-domain features effectiveness in identification of bearing faults from vibration signal. IEEE Sens J, 17(17): 5618-5625.

Park JE, Lee GH, Lee IS, Yang JR. 2025. Heart rate extraction technique with mitigation of respiration harmonic for bio-radar sensors. IEEE Sens J, 25(1): 929-939.

Wang H, Sun W, He L, Zhou J. 2022. Rolling bearing fault diagnosis using multi-sensor data fusion based on 1D-CNN model. Entropy, 24(5): 573.

Xu W, He J, Li G, Wu C, Lv J, Qian C. 2025. Progressive orthogonal matching pursuit and adaptive modal screening for fault diagnosis of rotating machinery components using acoustic signals. Meas, 252: 117345.

Zhao N, Zhang J, Mao Z, Jiang Z, Li H. 2023. Time-frequency feature extraction method of the multi-source shock signal based on improved VMD and bilateral adaptive Laplace wavelet. Chin J Mech Eng, 36(1): 36.

Zhao Y, Yang X, Huang J, Gao J, Zhou X, Zhang T. 2025. Ensemble targeted stacked denoising autoencoders with mutual information constraint for rotating machinery fault diagnosis. IEEE Trans Ind Inform, 21(2): 1329-1338.

Black Sea Journal of Engineering and Science
doi: 10.34248/bsengineering.1745277

Open Access Journal
e-ISSN: 2619 – 8991

Araştırma Makalesi (Research Article)
Cilt 8 - Sayı 5: 1514-1524 / Eylül 2025
(Volume 8 - Issue 5: 1514-1524 /September 2025)

HAVALİMANLARINDA YOLCU TAŞIMACILIĞININ KARBON EMİSYONLARINA ETKİSİ: SCHİPHOL HAVALİMANI ÖRNEĞİ

Firdevs Didem GÖÇMEN[1]*

[1]*University of Turkish Aeronautical Association Aeronautical Vocational School of Higher Education, Civil Air Transportation Management, 06790, Ankara, Türkiye*

Özet: Havalimanı kaynaklı emisyonların yönetimi, yalnızca uçuş operasyonlarıyla sınırlı kalmayıp havalimanına erişimde kullanılan ulaşım modlarının da değerlendirilmesini gerekli kılmaktadır. Literatürde, özellikle özel otomobil ve taksi gibi karayolu modlarının, toplam emisyonların anlamlı bir bölümünü oluşturduğu ve bu emisyonların çoğunlukla dolaylı kaynaklar arasında sınıflandırıldığı ifade edilmektedir. Bu çalışmada, havalimanına erişimde karayolu taşımacılığının, karbon emisyonlarına etkisi değerlendirilmiş ve Amsterdam Schiphol Havalimanı örneği üzerinden erişim modlarının, emisyon üretimi üzerindeki dağılımı analiz edilmiştir. Erişim modları içerisinde raylı sistemlerin yoğun olarak kullanıldığı, buna rağmen toplam erişim emisyonlarının büyük bir bölümünden özel otomobillerin sorumlu olduğu tespit edilmiştir. Elde edilen bulgular, havalimanı yönetimlerinin erişim modlarına yönelik stratejiler geliştirmesi gerektiğini ortaya koymaktadır. Yolcu davranışlarını yönlendiren uygulamalar, gerçek zamanlı veri erişimi, raylı sistem entegrasyonu, toplu taşıma altyapısının genişletilmesi, park yönetimi, düşük emisyonlu araçlara yönelik teşvikler, erişim temelli emisyonların azaltımında kullanılabilecek yönetsel araçlar olarak görülmektedir. Erişim kaynaklı emisyonların ölçülmesi ve yönetimi, havalimanlarının sürdürülebilirlik hedeflerine ulaşmasında temel bir unsur olarak ele alınmalıdır.

Anahtar kelimeler: Havalimanı yönetimi, Karayolu taşımacılığı, Demiryolu taşımacılığı, Karbon emisyonları, Sürdürülebilir ulaşım

The Impact of Passenger Transportation on Carbon Emissions in Airports: The Case of Schiphol Airport

Abstract: The management of airport-related emissions should not be limited solely to flight operations but must also encompass an assessment of the transport modes used to access the airport. The literature indicates that, in particular, road-based modes such as private cars and taxis account for a significant share of total emissions, and that these emissions are predominantly classified among indirect sources. In this study, the impact of road transport on carbon emissions in airport access was evaluated, and the distribution of emissions generated by different access modes was analysed using the case of Amsterdam Schiphol Airport. Although rail systems are extensively used among access modes, it was determined that private cars account for a substantial share of total access-related emissions. The findings reveal that airport managements should develop strategies targeting access modes. Practices that influence passenger behaviour, real-time data access, rail system integration, expansion of public transport infrastructure, parking management, and incentives for low-emission vehicles are considered managerial tools that can be utilised in reducing access-based emissions. The measurement and management of access-related emissions should be regarded as a fundamental component in achieving airports' sustainability objectives.

Keywords: Airport management, Road transportation, Rail Transport, Carbon emissions, Sustainable transportation

***Sorumlu yazar (Corresponding author):** University of Turkish Aeronautical Association Aeronautical Vocational School of Higher Education, Civil Air Transportation Management, 06790, Ankara, Türkiye
E mail: dgocmen@gmail.com (F.D. GÖÇMEN)
Firdevs Didem GÖÇMEN https://orcid.org/0000-0002-3939-441X

Gönderi: 17 Temmuz 2025 **Received:** July 17, 2025
Kabul: 20 Ağustos 2025 **Accepted:** August 20, 2025
Yayınlanma: 15 Eylül 2025 **Published:** September 15, 2025
Cite as: Göçmen FD. 2025. The impact of passenger transportation on carbon emissions in airports: The case of Schiphol Airport's. Eng Sci, 8(5): 1514-1524.

1. Giriş

Küresel iklim değişikliğiyle mücadele, sera gazı emisyonlarının azaltılmasına yönelik çalışmaları arttırmış; bu süreçte ulaşım sektörü, özellikle de hava taşımacılığı, çevresel sürdürülebilirlik politikalarının geliştirilmesinde öncü olarak rol almıştır. Hava taşımacılığı, doğrudan ve dolaylı faaliyetleriyle küresel sera gazı (GHG) salımlarına yaklaşık %2 ile % 3 arasında etki etmektedir (Gössling ve Humpe, 2024). Havalimanları ise bu sistemin yapısal bileşenleri arasında yer almakta yalnızca uçuş operasyonları ile değil; enerji tüketimi, yer hizmetleri, atık yönetimi ve kara yolu yolcu taşımacılığı gibi faaliyetleriyle geniş bir emisyon profiline sahip olmaktadır.

Havalimanı yolcu erişimi kaynaklı taşımacılık faaliyetleri, doğrudan uçuş operasyonları dışındaki emisyon bileşenlerinin içinde değerlendirilmekte ve çoğunlukla Scope 3 (Kapsam 3) kapsamında sınıflandırılmaktadır. Scope 3, bir işletmenin doğrudan kontrolü altında olmayan ancak faaliyetleriyle dolaylı olarak ilişkili sera gazı emisyonlarını ifade eden en geniş kapsamlı karbon ayak izi kategorisidir (Schneider vd., 2024). Özellikle havalimanı gibi büyük ölçekli tesislerde, yolcu ve çalışan ulaşımı, tedarik zinciri süreçleri, atık yönetimi, iş seyahatleri ve sermaye malları gibi uçuş operasyonları dışındaki birçok faaliyet Scope 3 kapsamına girmektedir.

Bu tür emisyonlar, genellikle havalimanı yönetimlerinin doğrudan denetimi dışında kalan ancak operasyonel süreklilik ve hizmet erişimi açısından sistematik biçimde bağlantılı süreçlerden kaynaklanmaktadır. Karayolu yolcu taşımacılığı ise, özellikle özel araç ve taksi kullanımı aracılığıyla terminale erişimde, Scope 3 emisyonlarının önemli bir bileşenini oluşturmaktadır. Hernández ve Padrón (2021) tatil seyahati özelinde kara yolu erişiminin ulaşım kaynaklı toplam emisyonların %8'ine kadar çıkabileceğini göstermekte bazı bölgelerde bu oranın çok daha yüksek olabileceğini de belirtmektedirler. Benzer şekilde, Miyoshi ve Mason (2013), kara yolu taşımacılığının toplam karbon emisyonuna olan maliyet etkisini hesaplayarak erişim sürecinin havacılık dışı ancak doğrudan ilişkili bir çevresel yük oluşturduğunu belirtmişlerdir. Postorino ve Mantecchini (2014) ise kara yolu erişiminin toplam ulaşım kaynaklı emisyonlar üzerindeki etkisinin ihmal edilemeyecek düzeyde olduğunu göstermiştir. Çalışmalar, erişim modlarının emisyon hesaplamalarında dışsal değil, sistem içi bir değişken olarak ele alınması gerektiğini ortaya koymaktadır.

Havalimanı yönetimi, hizmet alanı içerisinde şekillenen ulaşım davranışlarını yönlendirme kapasitesine sahiptir. Toplu taşıma entegrasyonu, elektrikli araç altyapısı, paylaşım temelli ulaşım sistemleri gibi uygulamalar, bu alandaki yönetsel müdahale alanlarını genişletmektedir. Postorino ve Mantecchini (2020), havalimanı karbon ayak izinin doğru değerlendirilebilmesi için erişim modları ile terminal operasyonları arasındaki ilişkilerin çok boyutlu biçimde analiz edilmesini önermektedir. Literatürde giderek artan sayıda çalışma, karar destek sistemleri, kentsel bağlantı tasarımı ve paydaşlar arası koordinasyonun, havalimanı yönetimlerinin dolaylı emisyonlar üzerindeki etkisini artırdığına işaret etmektedir (Greer vd., 2020; Meindl vd., 2024).

Yolcu taşımacılığına bağlı emisyonlar, kullanılan ulaşım moduna, seyahat mesafesine ve yolcu doluluk oranlarına göre değişkenlik göstermektedir. Özel araç ve taksi kullanımı, yolcu başına düşen karbon salımı açısından toplu taşıma sistemlerine kıyasla çok daha yüksek değerlere sahiptir (Qiao vd., 2021). Ayrıca, yaş grubu, seyahat amacı, gelir düzeyi gibi demografik faktörler ulaşım tercihlerinde belirleyici rol oynamakta; bu durum, farklı yolcu profillerine yönelik özelleştirilmiş ulaşım yönetimi politikalarının geliştirilmesini zorunlu kılmaktadır (Nijen, 2024).

Amsterdam Schiphol Havalimanı, sürdürülebilir havalimanı yönetimi uygulamaları açısından Avrupa'da örnek havalimanlarından biridir. Terminale entegre edilmiş demiryolu ağı, elektrikli taksi ve otobüs filoları, bisiklet altyapısı ve düşük karbonlu erişim modellerinin yaygınlaştırılması gibi uygulamalarla yolcu taşımacılığı kaynaklı karbon emisyonlarının azaltılmasına yönelik stratejik adımlar atmaktadır (Dijkstra, 2010; Meindl vd., 2024). Schiphol özelinde karayolu yolcu taşımacılığına bağlı dolaylı (Scope 3) emisyonların azaltılmasına yönelik önerilen stratejiler arasında; elektrikli araçlara dayalı kapıdan kapıya servislerin sübvanse edilmesi (Smirti, 2008), toplu taşıma bağlantılarının erişilebilirlik ve sıklık açısından güçlendirilmesi (Qiao vd., 2021), emisyon temelli vergilendirme politikalarının uygulanması ve paylaşımlı mobilite çözümlerinin yaygınlaştırılması (Cerasi ve Yaman, 2024) yer almaktadır. Elektrikli araçlar için şarj altyapısının genişletilmesi, bu geçişin teknik olarak mümkün ve kullanıcı açısından cazip hale getirilmesini sağlayacak önemli bir yapı taşıdır (Meindl vd., 2024; Morch vd., 2024). Havalimanı erişiminin incelendiği birçok çalışmada raylı sistemlerin yaygın kullanımına yönelik öneriler gelmesine rağmen iş seyahati yapan, fazla bagaj taşıyan ya da yaş ortalaması yüksek yolcu gruplarında, özel araç ve taksi kullanımının hala yüksek seviyelerde sürdüğü de görülmektedir.

Bu durum, havalimanı yönetimlerinin sadece altyapı yatırımlarıyla değil, aynı zamanda ulaşım politikaları, bilinçlendirme kampanyaları, teşvik mekanizmaları ve paydaş koordinasyonuyla davranışsal dönüşüm sağlaması gerektiğini ortaya koymaktadır (Greer vd., 2020). Ayrıca, erişim tercihlerinin şehir bazında analiz edilmesi, uzak mesafelerde karayolu tercihinin arttığını; buna karşın güçlü tren entegrasyonu bulunan bölgelerde demiryolu kullanımının yaygın olduğunu göstermektedir. Bu bulgular, havalimanı yönetimi için bölgesel ölçekte hedeflenen, coğrafi ve demografik temelli ulaşım stratejileri geliştirilmesinin gerektiğini göstermektedir.

Bu çalışma, Amsterdam Schiphol Havalimanı özelinde yolcu taşımacılığı faaliyetlerinin karbon emisyonlarına olan etkisini analiz etmeyi amaçlamaktadır. Analizde, erişim modlarının dağılımı, emisyon profilleri ve havalimanı yönetimi uygulamaları değerlendirilerek; sürdürülebilir havalimanı ulaşım stratejilerine katkı sağlayacak politika önerileri sunulmaktadır.

2. Kavramsal Çerçeve: Havalimanı Erişiminde Yolcu Taşımacılığının Emisyon Dinamikleri

Havalimanlarının karbon ayak izi değerlendirmelerinde geleneksel olarak uçuş operasyona ait emisyonlar, karbon ayak izinin ana kaynağı olarak algılansa da kara tarafı ulaşım bağlantılarının, emisyonlar üzerindeki etkisi giderek daha çok araştırma tarafından tartışılmaktadır. Li ve Merkert (2023), kapıdan kapıya karbon emisyon hesaplamalarında kara tarafının uçuş bazlı emisyonlara kıyasla %22'ye varan bir etkisi olduğunu belirterek bu alandaki karbon azaltım potansiyeline dikkat çekmektedir. Bu durum, havalimanına erişim modlarının karbon azaltım süreçlerine entegre bir parça olarak dahil edilmesi gerekliliğini ortaya koymaktadır. Özellikle özel araç, taksi ve servis kullanımı gibi karayolu temelli ulaşım modları, toplam havalimanı emisyon düzeylerini önemli ölçüde artırabilmektedir. Matheys vd. (2009) tarafından Brüksel Havalimanı'nda yapılan bir çalışmada, yolcu ve çalışanların erişiminde kullanılan karayolu modlarının toplam havalimanı emisyonlarının %30'una kadar artışa neden olabileceği saptanmıştır. Benzer şekilde,

Hernández ve Padrón (2021), turistik seyahatlerin bir parçası olarak karayolu ulaşımının toplam emisyonların %8'ini oluşturabileceğini ortaya koymuştur. Havalimanına yolcu erişiminin toplam karbon emisyonlarındaki payının, bağlama göre geniş bir aralıkta değişebildiği de görülmektedir.

Yolcuların havalimanına ulaşırken tercih ettiği ulaşım modu, oluşan karbon emisyonu miktarını belirleyen bir faktördür. Özel otomobiller ve taksiyle bırakma gibi düşük doluluk oranlı veya tek yolculu taşıma türleri, yolcu başına düşen emisyonu artırmaktadır. Taksi veya yakınlar tarafından bırakma durumunda aracın genellikle gidiş-dönüş yapması gerektiğinden, tek bir yolcu için kat edilen mesafe ve dolayısıyla karbon salımı iki katına çıkmaktadır (Hernández ve Padrón, 2021). Almanya'da 2008 verilerine göre havalimanı yolcularının %51,6'sı taksi veya bırakma yöntemiyle erişim sağlarken, bu araçların gidiş dönüş yapması nedeniyle erişim kaynaklı mesafe/emisyon etkisi ikiye katlanmaktadır. Aynı yılda özel araçla uzun süreli park ederek seyahat edenlerin oranı %19,2, toplu taşıma (otobüs) kullanımı %10,1 ve raylı sistem kullanımı %19,1 olarak raporlanmıştır. Ortalama bir fosil yakıtlı araba yolcu-km başına yaklaşık 176 gram CO_2 salarken, otobüs 104 g, elektrikli otomobiller 35 g, elektrikli trenler ise yaklaşık 41 g CO_2 salmaktadır (Hernández ve Padrón, 2021). Bu veriler, toplu taşımanın karbon verimliliğini göstermekte ve mod tercihlerinin emisyon üzerindeki etkisini ortaya koymaktadır.

Havalimanına yolcu erişiminin emisyon boyutu, literatürde yeterince ön plana çıkmamış bir konudur. Greer, Rakas ve Horvath (2020), 2009–2019 yılları arasında yapılan akademik yayınları inceledikleri çalışmalarında, yolcu erişimi konusunun havalimanı sürdürülebilirliği literatüründe merkezi bir yer tutmadığını belirtmişlerdir. Uçak emisyonları üzerine odaklanan çoğu çalışma, yolcuların havalimanına ulaşım tercihlerinden kaynaklanan emisyonları ikincil kaynak olarak görme eğilimi göstermiştir. Pasha ve Hickman (2016) yaptıkları literatür taramasında, yolcu mod tercihlerinin çevresel etkileri konusunda daha derinlemesine çalışmalara ihtiyaç olduğuna dikkat çekmiş ve çalışan erişiminin dahi yeterince incelenmediğini vurgulamışlardır. Alandaki güncel çalışmalar karayolu erişiminin ikincil değil; aksine müdahale edilebilir bir kaynak olduğunu ortaya koymaktadır. Bologna Havalimanı'nda yapılan bir çalışma, erişimin karbon ayak izi içindeki payının %41,4'e ulaşabildiğini göstermiş ve uçuş emisyonlarının ise %49,3 oranında bir paya sahip olduğunu ortaya koymuştur (Postorino ve Mantecchini, 2014). Benzer şekilde, Gatwick Havalimanı (2021) verilerine göre toplam havalimanı kaynaklı CO_2 emisyonlarının %33'ünün yolcu ve personel erişiminden kaynaklandığı bildirilmiştir (London Gatwick Airport, 2021).

Karayolu tabanlı yolcu taşımacılığına ilişkin modlar ve emisyon profilleri detaylı biçimde değerlendirildiğinde, özel otomobillerin, içten yanmalı motorlara olan bağımlılıkları nedeniyle CO2, NOx ve PM gibi kirleticileri yüksek oranda saldığı görülmektedir. Brüksel Havalimanı'nda yapılan bir çalışmada, hibrit ve elektrikli araçların devreye alınmasıyla %30'dan fazla CO_2 emisyon azaltımı sağlanabileceği ortaya konmuştur (Matheys vd., 2009). Benzer şekilde, Thomas ve Serrenho (2024), özel otomobil kullanımının %27 oranında azaltılmasının, demiryolu gibi verimli modlara yönelimin toplam emisyonları %30 oranında azaltabileceğini ifade etmektedir.

Bireysel araçlardan sonra en çok tercih edilen modlardan biri olan taksiler ise şehir içi yoğun trafik koşullarında çalışmaları ve çoğunlukla boş sefer gerçekleştirmeleri nedeniyle emisyon kaynakları arasında öne çıkmaktadır. Liu (2024), taksi kaynaklı emisyonların ticaret merkezleri ve havalimanı çevresinde yoğunlaştığını belirtmiş elektrikli filo dönüşümünün çevresel etkileri azaltmada etkin rol oynayabileceğini vurgulamıştır. Sperling ve Henao (2020) da benzer şekilde taksi filolarının elektrifikasyonunun hem emisyon hem de maliyet avantajı sağlayabileceğini ortaya koymuştur. Araç ve yolculuk paylaşımı uygulamaları da bu sistematik içerisinde karmaşık çevresel etkileri ile değerlendirilmektedir. Zhang et al. (2023), algoritmik olarak optimize edilen eşleştirme sistemlerinin, tekil yolculuklara kıyasla %34,52 oranında CO_2 azaltımı sağlayabildiğini belirtmiş; ancak Zhang et al. (2024), rota örtüşmesinin zayıf olduğu durumlarda bu sistemlerin emisyonları artırabileceğini ifade etmiştir.

Taşıma modlarına ilişkin tüm bu çevresel etkiler değerlendirildiğinde, karayolu erişiminin, sera gazı (GHG) salımlarına etkisinin, sürdürülebilirlik açısından belirleyici bir unsur olduğu görülmektedir. Matheys et al. (2009) ve Higgins (1994), genel havalimanı emisyonlarının %30'una kadarının kara erişiminden kaynaklanabileceğini belirtmiştir. Bunun yanında, NOx, VOC ve PM gibi yerel hava kirleticilerinin özellikle yoğun yolcu trafiği alanlarında birikim gösterdiği ve hava kalitesini olumsuz etkilediği de ifade edilmektedir (Liu, 2024). Ayrıca, Sun et al. (2021), taksi yörünge verilerine dayanarak sabah ve akşam saatlerinde emisyon yoğunlaşmasının arttığını; bu emisyonların mekânsal olarak da belli bölgelerde kümelendiğini belirtmektedir.

Emisyonların azaltımına yönelik sunulan stratejiler ise üç ana başlık altında şekillenmektedir. İlk olarak, teknolojik yenilikler çerçevesinde elektrikli ve otonom araç sistemlerinin entegrasyonu önem kazanmaktadır. Hájnik et al. (2021), bu sistemlerin hem trafik tıkanıklığını hem de karbon emisyonlarını azaltmada etkili olduğunu belirtmektedir. İkinci olarak, politika araçları üzerinden geliştirilen vergi teşvikleri, öncelikli park imkânları ve toplu taşıma yatırımları gibi mekanizmaların, mod tercihini daha sürdürülebilir yönlere kaydırabildiği ifade edilmektedir (Matheys et al. ,2009; Ryley et al. ,2013). Üçüncü olarak davranışsal düzeyde yürütülen stratejilerin de etkili olduğu görülmektedir. Shao et al. (2023), çevresel farkındalığın yüksek olduğu durumlarda ve seyahat süresi belirsizliğinin düşük olduğu senaryolarda, yolcuların daha

sürdürülebilir ulaşım seçeneklerine yöneldiğini ayrıca karbon bilinci kampanyalarının yolcuların ulaşım modu tercihleri üzerinde etkili olduğunu belirtmektedir. Mahesh ve Calvert (2025), teknik ve yönetimsel açıdan bütüncül bir yaklaşım olarak kara tarafı ulaşım süreçlerinin seyahat davranışı, ulaşım altyapısı, politika yaklaşımları ve alan sürdürülebilirliği olmak üzere dört temel başlıkta analiz edilmesini önermektedir.

Tüm bu bulgular, vaka çalışmaları üzerinde de görülebilmektedir. Higgins (1994), Kaliforniya'daki büyük havalimanlarında karayolu erişiminden kaynaklanan emisyonları yolcu hacmi, araç tipi ve yolculuk mesafesi gibi parametrelerle modellemiş; elektrikli araç kullanım oranının artırılması ve çalışanlara yönelik ulaşım stratejilerinin, emisyonları anlamlı şekilde düşürdüğünü belirlemiştir. Avogadro et al. (2024), Milan-Bergamo Havalimanı'nda yaptıkları çalışmada, mod seçim modellemesi ile trafik simülasyonunu birleştirerek otopark yönetimi, paylaşım teşvikleri ve toplu taşıma yatırımlarının emisyon azaltımına katkısını ortaya koymuştur. Shao et al. (2023) ise Xi'an Xianyang Havalimanı'na yönelik analizlerinde, yolcuların karbon azaltımı yönündeki farkındalığı ile seyahat süresi belirsizliğinin mod tercihlerinde belirleyici olduğunu ortaya koymuş ve psikolojik faktörlerin altyapısal müdahalelerle birlikte değerlendirilmesi gerektiğini savunmuştur. Benzer şekilde Zhang et al. (2023), Chengdu ve Xi'an'daki çalışmalarında, yolculuk paylaşımının tekil sürüşlere göre %13,4 ila %34,5 oranında emisyon azaltımı sağladığını; ancak bu etkinin eşleştirme verimliliğine bağlı olduğunu vurgulamıştır. Liu (2024) tarafından New York'ta yürütülen çalışmada ise yüksek taksi yoğunluğuna sahip bölgelerde hava kalitesinin ciddi şekilde bozulduğu, coğrafi bilgi sistemleri (GIS) ve büyük veri analitiği ile rota planlamasının optimize edilmesinin emisyonları ve boş seyir oranlarını azalttığı gösterilmiştir. Havalimanına erişimde karayolu tabanlı yolcu taşımacılığının emisyon dinamikleri çok katmanlı, zamansal ve mekânsal olarak değişkenlik gösteren, teknik olduğu kadar yönetsel müdahale gerektiren bir konu olarak öne çıkmaktadır. Ison, Merkert ve Mulley (2014), farklı ülke bağlamlarında geliştirilen ulaşım politikalarının etkililiğine dikkat çekmiş ve yerel bağlamların stratejik planlamaya entegre edilmesinin önemini vurgulamıştır. Dolayısıyla, havalimanlarının karbon azaltım hedeflerine ulaşabilmesi için teknolojik dönüşüm, politika mekanizmaları ve davranışsal müdahalelerin birlikte ve entegre bir biçimde ele alınması gerekmektedir.

Bu çalışmada kavramsal çerçevede ortaya konan emisyon dinamiklerinin havalimanı erişim süreçlerindeki etkisini somutlaştırmak amacıyla Amsterdam Schipholl havalimanı üzerinden analizler gerçekleştirilmiştir.

3. Materyal ve Yöntem

Araştırmada ikincil veri analizi benimsenmiştir. Schiphol Havalimanı'na yolcu erişiminde kullanılan ulaşım modlarına ilişkin veriler, resmî istatistikler, literatür kaynakları ve çevrimiçi veri setleri üzerinden toplanmıştır. Kaynaklar, veri seti ile birlikte metin içinde verilmiştir. Ulaşım modlarının yolcu oranları, ortalama mesafeleri ve karbon emisyon faktörleri dikkate alınarak kişi başı CO_2 emisyonları hesaplanmış ve toplam erişim kaynaklı karbon ayak izi tahmini yapılmıştır. Ayrıca analiz kapsamında çeşitli şehirler, demografik gruplar ve seyahat türlerine göre ulaşım tercihleri değerlendirilmiş; karayolu ulaşımının emisyon üzerindeki etkisi ortaya konmuştur.

4. Bulgular

Amsterdam Schiphol Havalimanı'nda, 2024 yılı verilerine göre yaklaşık olarak seyahat eden 66 milyon yolcunun yarısının (%50) havalimanına trenle ulaştığı görülmektedir (Royal Schiphol Group, 2025; Statista, 2023; Statista, 2024; Boersma ve Toet, 2024).

Entegre tren istasyonu ve sık seferlerin de etkisiyle havalimanında demiryolu kullanım seviyesi oldukça yüksektir. Trenle gelen yolcuların, toplam yolcuların yarısını oluşturduğu değerlendirildiğinde, geriye kalan yaklaşık 33 milyon yolcunun diğer ulaşım modları (özel araç -kendi aracıyla gelen veya bir yakını tarafından bırakılan-, otel/hizmet servisleri (shuttle), toplu taşıma, taksi ve bisiklet/yaya) ile havalimanına eriştiği görülmektedir. 2019 verilerine göre Schiphol yolcularının %47 kadarı tren ve otobüs gibi toplu taşıma kullanırken yaklaşık %20'si bir araçla bırakılmayı tercih etmektedir (Statista, 2023; Boersma ve Toet, 2024). Bu oranın 2024'te tren kullanımının artmasıyla birlikte biraz daha değişime uğradığı değerlendirilebilir. Mevcut literatür verileri ve raporlar ışığında 2024 yılı için tahmini yolcu erişim dağılımı Tablo 1'de gösterilmiştir.

Tablo 1. Schiphol Havalimanı'na erişim modlarına göre yolcu dağılımı ve yıllık CO_2 emisyonları (2024)

Ulaşım Modu	Yolcu Oranı (%)	Yıllık Yolcu (Milyon)	Tek Yön Mesafe (km)	CO_2 Emisyon Faktörü (g/kişi-km)	Yıllık CO_2 Emisyonu (ton)	Varsayım ve Kaynaklar
Tren (demiryolu)	50%	33,0	~50 km (ülke içi ort.) (NS Annual Report, 2022)	~14 (elektrikli tren) (AmsterdamTips, 2025)	~23,100	Yolcuların ~yarısı trenle gelmektedir (Statista, 2023; Boersma ve Toet, 2024). Hollanda'da elektrikli trenlerin CO_2 emisyonu çok düşüktür (~14–17 g/pkm) (Greenreporting ,2023). Mesafe ort. ~50 km varsayılmıştır.
Özel Araç (*kendi aracıyla gelen veya bıraktırılan*)	~30%	~20,5	~60 km (araçlı yolcular)	~120 (benzin/dizel araç)(9)	~147,300	Toplam ~%30 (2019'da ~%20 bırakılma + ~%10 (3) park etme). Yerli yolcuların özel araç kullanma eğilimi yüksektir (Nijen, 2024n). Mesafe ~60 km; araç başına ~150 g/km ve ~1.2 yolcu varsayımıyla ~120 g/kişi-km alınmıştır(Greenreporting ,2023).
Taksi (*ticari taksi, Uber vb.*)	~10%	~6,6	~30 km (çoğu yakın çevre)	~120 (fosil yakıtlı, rölanti dahil)	~23,760	Yaklaşık %10'luk pay (özellikle iş seyahati ve turist segmenti) (Statista, 2023). Nijen (2024) çalışmasına göre yaşlı ve iş seyahatinde olan yolcular taksiye daha yatkındır. Mesafe ~30 km (Amsterdam ~17 km, çevre kentler ~30–50 km) varsayılmıştır(NS Annual Report, 2022). Emisyon faktörü özel araçla benzer (~120 g/kişi-km) kabul edilmiştir.
Toplu Taşıma (Otobüs)	~5%	~3,3	~20 km (bölgesel hatlar)	~96 (dizel otobüs) (10)	~6,336	Düşük bir yolcu payı (~%5) vardır. Amsterdam Airport Express otobüsü vb. çoğunlukla yakın bölgelere hizmet verir. Mesafe kısa (genelde ~15–20 km) alınmıştır. Dizel otobüslerin emisyon faktörü ~96 g/pkm (ortalama dolulukta) olarak kullanılmıştır.
Shuttle (otel servisleri)	~3%	~2,0	~30 km (tahmini ort.)	~100 (minibüs/servis)	~5,940	Küçük bir kesim (~%3) otel shuttle veya tur servisi gibi paylaşımlı transferleri kullanır. Mesafe ortalama ~30 km varsayılmıştır. Minibüs/servis araçların ~100 g/kişi-km emisyon değerine sahip olduğu öngörülmüştür (doluluk oranına göre).
Bisiklet/Yaya	~1%	~0,7	~5 km (yakın mesafe)	0 (doğrudan emisyon yok) (7).	~0	Havalimanına yakın yerleşimlerden bazı yolcular bisiklet veya yaya gelmektedir. Araç kaynaklı doğrudan karbon emisyonu olmadığından 0 g/kişi-km olarak alınmıştır.

Schiphol Havalimanı'nın toplam emisyon düzeyi incelendiğinde, 2024 yılında Schiphol yolcularının havalimanına ulaşımının yaklaşık 206 bin ton CO_2 emisyonuna yol açtığı görülmektedir. En büyük emisyon payı, büyük oranda fosil yakıtlı araçların kullanımından kaynaklanan özel araç kategorisindedir. Toplam ulaşım

emisyonu açısından tren kaynaklı emisyonların çok düşük olduğu görülmektedir (%11'i). Demiryolu taşımacılığının başarısı görülmekle birlikte aynı yıl içerisinde özel araç ve taksi kullanan yolcuların yaklaşık %41 oranında olması, karayolu erişiminin, toplam emisyonların yaklaşık %82'sini oluşturmasına neden olmaktadır. Kalan küçük dilimlerde ise otobüs (%5), otel servisleri gibi shuttle araçlar (%3) ve bisiklet/ yaya (%1) ile gelen yolcular yer almaktadır; bu grupların emisyon katkıları da görece düşüktür (Şekil 1)

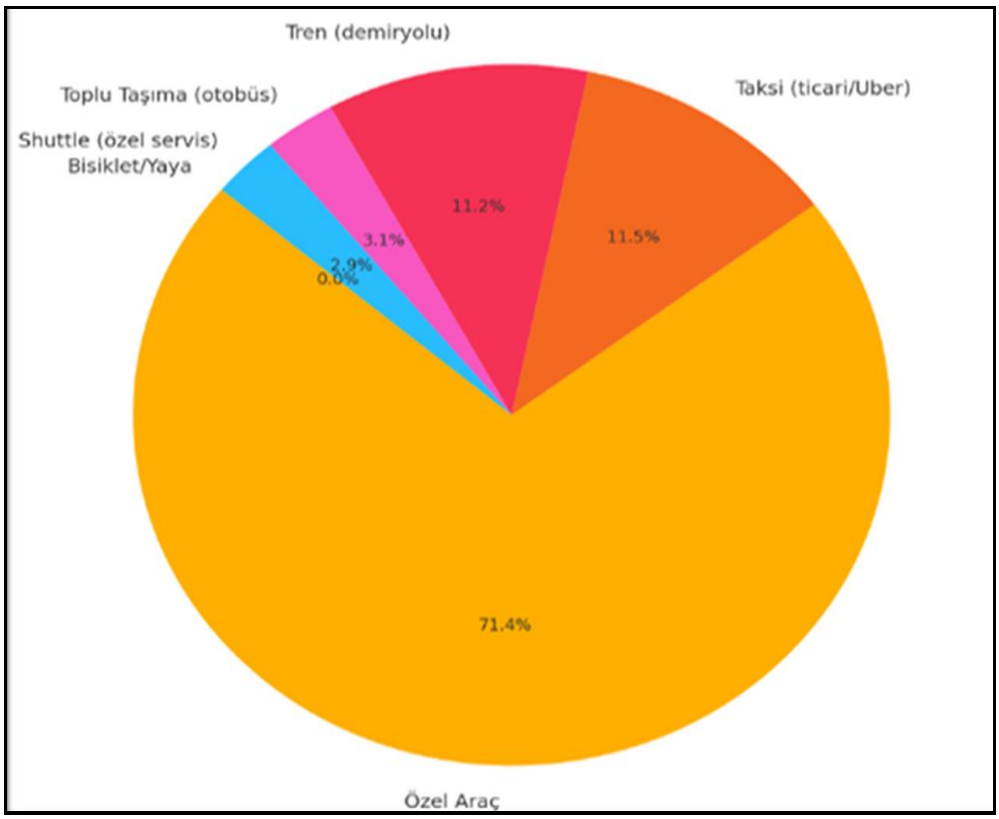

Şekil 1. Schiphol havalimanı yıllık karbon emisyon dağılımı.

Toplam emisyon oranları incelendiğinde özel araçla yolculuğun yolcu payı her ne kadar %30 civarında olsa da emisyonların yaklaşık %71'ini oluşturduğu görülmektedir. Benzer şekilde taksi ve özel araç toplamı, yolcuların %41'ini taşıyarak karayolu erişim emisyonlarının yaklaşık %82'sini üretmektedir. Trenle gelen yaklaşık %50'lik yolcu ise toplam emisyonun sadece %11'inden sorumludur, zira elektrikli trenlerin emisyon faktörü son derece düşüktür. Bu nedenle, tren kullanım oranının artırılması, havalimanı erişiminden kaynaklanan karbon emisyonlarını azaltmada önemlidir.

Sürdürülebilir ulaşım modlarına (özellikle demiryolu ve toplu taşıma) yönelimi artırmak havalimanının, toplam karbon emisyonlarını düşürmede en etkili stratejilerden biridir. Bununla birlikte tren kullanım oranı mesafe ve bağlantı imkanlarına göre de değişmektedir; örneğin iyi tren bağlantısı olan Amsterdam şehrinden dahi yolcuların yaklaşık %20'si özel araç/taksi ile gelmeyi tercih etmektedir. Daha uzak bir şehir olan Eindhoven'dan ise karayolu tercihi %50'ye ulaşabilmektedir. Bu durum, mesafe arttıkça ve doğrudan tren bağlantısı zorlaştıkça karayolu kullanım oranının yükseldiğini göstermekte; karayolu kaynaklı emisyonların mutlak yükünü artırmaktadır. Bu nedenle önemli şehirlerden gelen yolcuların erişim tercihleri de analizde dikkate alınmıştır. Schiphol Havalimanı'nın yolcu potansiyeli büyük ölçüde Amsterdam metropolü ve Randstad bölgesi şehirlerinden beslenmektedir. Bunun yanı sıra ülkenin farklı bölgelerinden ve bazı durumlarda komşu ülkelerden de yolcular karayolu veya demiryolu ile Schiphol'e ulaşmaktadır. Önemli şehirlerden havalimanına uzaklıklar ve tahmini karayolu (özel araç, taksi, otobüs) kullanım oranları içeren bilgiler, doğrudan kamusal kaynaklardan sunulmadığından güncel çalışmalardan (Statista, 2023; Nijen, 2024; Amsterdamtips, 2025) elde edilen genel eğilimler ile demiryolu bağlantısı, yolculuk süresi ve trafik koşulları gibi ölçülebilir parametrelere dayalı tahmini oranlar Tablo 2'de sunulmuştur.

Tablo 2. Schiphol'e erişimde önemli şehirlerin mesafeleri ve tahmini tren vs. karayolu kullanım oranları

Şehir	Havalimanına Mesafe (km)	Tren Kullanımı (%)	Karayolu Kullanımı (%)	Açıklama/Notlar
Amsterdam (merkez)	~17 km	~70-80%	~20-30 %	Şehir içi trafik ve park zorlukları nedeniyle tren tercih ediliyor.
Rotterdam	~60 km	~60%	~40%	Intercity Direct ile hızlı tren bağlantısı (~25-30 dk).
Den Haag (Lahey)	~45 km	~60-70%	~30-40%	Özellikle diplomatik ve iş çevreleri tren kullanıyor.
Utrecht	~50 km	~60%	~40%	Aile ve bagajlı yolcular arasında özel araç kullanımı yaygın.
Haarlem	~15 km	~80%	~20%	Tren ve otobüsle erişim 15-20 dk, özel araç kullanımı düşük.
Almere	~40 km	~50%	~50%	Aktarmalı tren (~50-60 dk), grup seyahatlerinde araç tercih ediliyor.
Amersfoort	~70 km	~50% (	~50%	Trenle aktarmalı (~1 saat), otoyolla ~45 dk. Araç ve tren yarı yarıya.
Eindhoven	~120 km	~40-50%	~50-60 %	Uzak mesafe. Gece tren yoksa araçla erişim daha yaygın.

Tablo 2. de yer alan şehir bazlı değerlendirmeler incelendiğinde, Schiphol kaynaklı karayolu trafiğinin önemli bir kısmının Amsterdam ve çevresinden gelen araçlar olduğu, uzak mesafeli şehirlerden ise belirli oranda karayolu akışı bulunduğu görülmektedir. Amsterdam gibi çok iyi tren bağlantısı olan ve yakın mesafedeki bir şehirden bile hâlâ ~%20 oranında yolcu karayolunu kullanmaktadır. Karayolunu kullanan grubun büyük bölümünü üst gelir grubu veya iş amacıyla seyahat eden taksi müşterileri ve ailece seyahat eden, fazla bagajı olan tatilciler oluşturmaktadır. Eindhoven gibi daha uzak şehirlerde ise tren süresinin uzunluğu ve sefer sıklığı gibi etkenlerle karayolu tercihinin %50'yi bulabildiği görülmektedir. Dolayısıyla, mesafe arttıkça ve doğrudan tren bağlantısı zorlaştıkça karayolu kullanım oranı yükselmektedir. Bu durum, gelecekte hızlı tren entegrasyonunun geliştirilmesi halinde uzak şehirlerden de tren kullanımının artırılabileceğini göstermektedir.

Diğer yakın/orta mesafeli şehirler olan Rotterdam, Den Haag (Lahey) ve Utrecht için de tren kullanım oranları %70-75 civarında yüksek oranda seyretmekte, ancak bu şehirlerden gelen yolcuların yaklaşık %25-30'luk bir kesimi karayolunu kullanmaktadır. Mesafe arttıkça trenle erişim süresi uzadığından, daha uzak şehirlerde karayolu tercihinin yükseldiği görülmektedir. Örneğin; Eindhoven (120 km mesafe, 1.5 saat tren yolculuğu) yolcularının tren kullanımı %40-50 düzeyinde kalırken, karayolu ile gelenlerin oranı %50-60 bandına çıkabilmektedir. Gece seferi olmaması gibi nedenlerle özellikle çok erken saatte uçuşu olanlar, uzak şehirlerden kendi araçlarıyla gelmeyi tercih edebilmektedir. Ayrıca Eindhoven bölgesinde ayrı bir uluslararası havalimanının bulunması da buradan

Schiphol'e gelen yolcu potansiyelini sınırlamaktadır.

Schiphol kaynaklı karayolu trafiğinin önemli bir bölümünü, Amsterdam ve çevresinden gelen araçların oluşturduğu görülmektedir. Buna karşın uzak mesafeli şehirlerden de belirli oranda karayolu akışı mevcuttur. Mesafe arttıkça ve doğrudan hızlı tren bağlantıları kısıtlı oldukça özel araç/taksi ile havalimanına gitme eğilimi artmaktadır. Havalimanına olan mesafe ve ulaşım kapasitesi haricinde yolcuların ulaşım tercihlerinde yaş grubu ve seyahat amacı da önemli bir değişken olarak rol oynamaktadır.

Nijen, (2024), yaşı 61 üzeri olan yolcuların taksi kullanmaya daha yatkın olduğunu ortaya koymuştur; buna karşın özellikle 11-20 ve 21-30 yaş gruplarını içeren genç yolcular özel araçla gelmeye daha az meyilli olup toplu taşımayı daha fazla tercih etmektedirler. Bu durumun muhtemel sebepleri arasında genç yolcular arasında araç sahipliğinin daha düşük olması ve toplu taşımanın ekonomik bir seçenek olması sayılabilir. İş seyahati amacıyla yolculuk yapanlar arasında taksi veya araç kiralama kullanım oranı görece daha yüksek bulunmuştur. Buna karşılık tatil/gezi amaçlı yolcuların bir yakını tarafından arabayla bırakılma oranı daha düşüktür. Örneğin, iş insanı kategorisindeki yolcuların havalimanına ulaşımda taksi veya kiralık araç kullanma eğilimi yüksek tir. Tatil amaçlı seyahat edenler ise genellikle daha uzun süreli seyahat ettiklerinden, uzun süreli park ücretinden kaçınmak veya daha ekonomik olduğu için toplu taşımayı tercih edebilmektedirler. Ayrıca yurt içinden (yerli) gelen yolcuların kendi araçlarıyla gelip park etme eğiliminin, yurt dışından gelen uluslararası yolculara kıyasla daha yüksek olduğu gözlemlenmiştir. Demografik kırılımlar da belirli gruplara yönelik hedefli ulaşım politikaları geliştirilmesi gerektiğine işaret etmektedir.

5. Tartışma ve Sonuç

Havalimanı işletmeleri açısından sürdürülebilirlik hedeflerine ulaşmak, yalnızca operasyonel verimliliği değil, aynı zamanda karbon emisyonlarının kapsamlı şekilde yönetilmesini de zorunlu kılmaktadır. Özellikle küresel iklim politikaları doğrultusunda, havalimanlarının toplam emisyon envanterinde yer alan tüm kaynakların sistematik biçimde izlenmesi ve raporlanması önem kazanmaktadır. Bu doğrultuda, yolcuların havalimanına erişiminde tercih ettikleri ulaşım türlerinin oluşturduğu emisyonlar da değerlendirme kapsamına alınmakta; bu emisyonlar genellikle dolaylı nitelikte olup Scope 3 kategorisinde sınıflandırılmaktadır. Literatürde, erişim modlarının karbon ayak izi üzerindeki etkisinin ayrıntılı incelenmesi, sürdürülebilir ulaşım stratejilerinin geliştirilmesinde temel referanslardan biri olarak ele alınmaktadır. Bu çalışma, Amsterdam Schiphol Havalimanı örneği üzerinden, yolcu erişiminde kullanılan ulaşım modlarının emisyon düzeylerini karşılaştırmalı olarak analiz etmekte ve belirli yolcu segmentlerine göre değişen tercihler üzerinden değerlendirmeler sunmaktadır.

Yapılan segment bazlı hesaplamalara göre 2024 yılında Schiphol Havalimanı yolcularının havalimanına ulaşımı sonucunda yaklaşık 206 bin ton CO_2 emisyonu oluşturduğu görülmektedir (Tablo 1). Emisyonlara ait en büyük payın, özel araç kullanımı sonucu oluştuğu görülmektedir (%71). Özel araçla gelen yolcuların sayısı trenle gelenlerin üçte ikisinden az olmasına rağmen, fosil yakıtlı bireysel motorlu araçların karbon yoğunluğu yüksek olduğu için toplam emisyonun büyük bir kısmını oluşturmaktadırlar. Taksi kullanımı, yolcu payı içindeki %10'luk dilime rağmen emisyonların yaklaşık %11.5'ini üretmektedir. Toplu taşıma otobüsleri ve shuttle servisleri, birlikte yolcuların %8 kadarını taşıyıp emisyonların yaklaşık %6'sını oluşturmakta; görece daha verimli bir seçenek olduklarını göstermektedirler. Bisiklet ve yaya ulaşımı, yolcu sayısı bakımından ihmal edilebilir düzeyde olsa da emisyonlara katkısı sıfıra yakın olduğundan sürdürülebilir ulaşımın en çevreci şeklidir. Yolcuların yarısını taşıyan trenler (elektrikli) için hesaplanan emisyonlar, toplam emisyonların yalnızca %11'ini oluşturmaktadır. Hollanda Demiryolları (NS) 2017'den itibaren çekiş enerjisinde %100 yenilenebilir elektrik kullandığını bildirmektedir. Dolayısıyla, burada hesaplanan tren kaynaklı 23 bin ton CO_2, fosil kaynaklı elektrik üzerinden belirlenen değerdir; gerçekte yenilenebilir enerji anlaşmaları sayesinde bu değerin nötrlenmesi mümkündür. Nitekim NS resmi verilerine göre tren yolculukları iklim nötr olarak işletilmektedir. Bu nedenle havaalanı erişiminde sürdürülebilir ulaşım modlarına, özellikle demiryolu ulaşımına ve toplu taşımaya yönelimin artırılması, havalimanının toplam karbon ayak izini düşürmek için en etkili stratejilerden biri olmaktadır.

Schiphol Havalimanı'nda yapılan bu analiz, yolcuların yaklaşık yarısının tren ile havalimanına eriştiğini ve bunun sonucunda karayolu trafiği ve emisyonlarının önemli ölçüde azaldığını göstermektedir. Kalan yolcu segmentinin dağılımında özel araç ve taksi kullanımının, özellikle belirli demografik gruplar ve seyahat türlerinde hâlâ yüksek bir paya sahip olduğu görülmektedir. Yaşlı ve iş amaçlı yolcular, oransal olarak daha fazla taksi/araç kullanırken, genç ve tatil amaçlı yolcular toplu taşımaya daha fazla yönelmektedir. Bu farklılıklar, ulaşım politikalarının hedeflenmesinde önem taşımaktadır. İş seyahati yolcularını taksi yerine trene yönlendirmek için şirketlerle teşvik programları geliştirilmesi veya fazla bagajlı tatilciler için havalimanı yakınlarında park et ve trenle devam et (park and ride) imkanlarının artırılması, bölgesel hızlı tren projelerinin hayata geçirilerek uzak mesafeli yolcuların da karayolu yerine demiryolunu seçmesi, halihazırda önceliklendirilen demiryolu ulaşım ağına destek önerilerdir. Bununla birlikte bu araştırmanın ortaya koyduğu üzere hala büyük emisyon kaynağı olan karayolu ulaşımına ilişkin stratejik planlamaların yapılması da önem arz etmektedir.

Analiz verilerine göre yolcu erişiminde tren altyapısının güçlü olması, karayolu trafiğini ve emisyonlarını önemli ölçüde azaltmaktadır Bununla birlikte, belirli demografik segmentler ve şehirler için karayolu kullanımı hâlâ yüksek

bir paya sahiptir. Özellikle yaşlı ve iş amaçlı yolcuların oransal olarak daha fazla özel araç/taksi kullandığı, genç ve tatil amaçlı yolcuların ise toplu ulaşıma daha meyilli olduğu tespit edilmiştir. Bu farklılıklar göz önüne alındığında, havalimanının yolcu ulaşımından kaynaklanan emisyonlarını azaltmaya yönelik çözüm önerileri şu alt başlıklarda özetlenebilir:

Yolcu Ulaşım Verilerinin Doğrudan Toplanması: Birçok havalimanında yolcuların havalimanına ulaşım tercihleri belirli aralıkla yapılan anketler aracılığıyla toplanmakta fakat anlamlı çıkarımlar yapabilmek için verinin sistematik hale getirilmesi gerekmektedir. Bu nedenle havalimanına gelen yolcuların erişim modlarına dair verilerin doğrudan yolculardan toplanması önerilmektedir. Havayolları ile paydaşlığın geliştirilerek yolcuların ulaşım şeklinin online checkin işlemleri sırasında sorulması ve teşvik için koltuk seçimi sırasında indirimler, mil puanı veya diğer ödüllerin yolcuya sunulması değerlendirilebilir. Gönüllülük esaslı toplanacak gerçek zamanlı veriler, emisyon hesaplamalarının gerçekçi bir zemine oturmasına ve havalimanının yıllık emisyon envanterinde kapsam 3 hesaplamalarını daha sağlıklı ölçmesine yardımcı olacaktır.

Paylaşımlı VIP Araç ve Transfer Hizmetleri: Tren bağlantısının sınırlı olduğu veya karayolu tercihinin yüksek olduğu güzergâhlarda, bireysel araç yerine kullanılabilecek paylaşımlı VIP araç servisleri teşvik edilmelidir. Bu hizmetler konforlu ve güvenilir bir alternatif olarak sunularak özellikle üst gelir grubu ve iş insanlarının taksi yerine bu paylaşımlı araçları kullanması sağlanabilir.

Şirketlerle İş Birliği ve Teşvik Programları: İş seyahati yapan yolcuların, taksi yerine treni tercih etmesini teşvik için şirketlerle ortak programlar geliştirilmelidir. Şirket çalışanlarına tren biletinde indirim, iş gezisi masraflarının tren kullanımına göre karşılanması gibi uygulamalar örnek olarak verilebilir.

Tatilcilere Yönelik Park ve Ride İmkânları: Tatil/gezi amaçlı yolcular, uzun süreli seyahatlerde yüksek park ücreti nedeniyle özel araçtan kaçınma eğilimindedir. Bu yolcular için havalimanı çevresinde güvenli "Park et ve Trenle Devam Et" alanları genişletilebilir. Yolcuların özel araçlarını şehir dışındaki bu noktalara park edip kalan mesafeyi tren veya toplu taşıma ile tamamlaması emisyon düzeylerinin azalmasına katkı sağlayacaktır.

Toplu Taşıma ve Tren Teşvikleri: Havalimanına direkt hizmet veren otobüs hatları ve tren seferleri arttırılarak; bilet entegrasyonu, konfor iyileştirmeleri ve gerekirse ücret sübvansiyonu ile daha fazla yolcunun bu modlara yönelmesi sağlanabilir. Özellikle gece uçuşu olanlar için geç saatlerde toplu ulaşım alternatifleri geliştirmek de karayolu bağımlılığını azaltacaktır.

Elektrikli/Hibrit Araç Destekleri: Havalimanına erişimde kullanılan karayolu araç filosunun daha temiz hale gelmesi için elektrikli ve hibrit araç kullanımının teşviki de önemlidir. Havalimanı otoparklarında ev şarj istasyonları yaygınlaştırılmalı, elektrikli taksi ve indirimli park, öncelikli bekleme alanları gibi transfer araçlarına yönelik ayrıcalıklar tanınmalıdır.

Havalimanı Yer Seçimi, Erişim Planlaması ve Yerel Yönetimlerin Sorumlulukları: Havalimanlarının yer seçimi, mania planlaması, şehir, havalimanı mesafesi ve ulaşım bağlantıları, erişim kaynaklı karbon emisyonlarının oluşumunu doğrudan etkilemektedir. Uygun olmayan yer seçimi, kentsel merkezlere uzak konumlandırma veya yetersiz toplu taşıma bağlantıları, karayolu kullanımını artırmakta ve buna bağlı olarak CO_2 salımlarını yükseltmektedir (Budd ve Ison, 2017). Bu nedenle, yerel yönetimler kentsel gelişim planlarını havalimanı erişimi ile entegre ederek düşük karbonlu ulaşım modlarını teşvik etmeli ve erişim mesafelerinden kaynaklanan çevresel etkileri ~~en aza indirmeye~~ azaltmaya yönelik stratejiler geliştirmelidirler. Ulaşım politikalarının başarısı, farklı bölgelerde yerel koşulların stratejik planlamaya ne ölçüde entegre edildiğine bağlı olarak da değişkenlik göstermektedir.

Schiphol Havalimanı örneğinde analiz edilen veriler, yolcuların karayolu ulaşımının mutlak emisyon yükü açısından hala önemli olduğunu göstermektedir. Bu çalışmada yolcu ulaşımı esas alınmakla birlikte sonraki araştırmalarda çalışan ulaşımının da değerlendirmeye dahil edilmesi alan yazına katkı sağlayacaktır. Ayrıca, uzun bekleme sürelerine sahip transit yolcuların terminal içi faaliyetleri ve bekleme süresini şehir merkezine giderek değerlendirmeye yönelik ulaşım tercihlerinin, erişim kaynaklı dolaylı emisyonlar üzerindeki potansiyel etkilerinin incelenmesi de konunun kapsamının genişletilmesine katkı sunacaktır. Tren ve toplu taşıma kullanımını artırmaya yönelik altyapı ve teşvikler sürerken karayolu kaynaklı emisyonları azaltmaya odaklanan yenilikçi çözümler havalimanı yönetim stratejilerinde devreye alınmalıdır. Veri tabanlı izleme, paylaşımlı araç hizmetleri, demografik kıstasların önceliklendirilmesi ve teşvikler gibi öneriler paketinin, havalimanlarının sürdürülebilirlik hedeflerine ulaşmasına katkı sağlaması beklenmektedir.

Katkı Oranı Beyanı

Yazarın katkı yüzdeleri aşağıda verilmiştir. Yazar makaleyi incelemiş ve onaylamıştır.

	F.D.G.
K	100
T	100
Y	100
VTI	100
VAY	100
KT	100
YZ	100
KI	100
GR	100
PY	100
FA	100

K= kavram, T= tasarım, Y= yönetim, VTI= veri toplama ve/veya işleme, VAY= veri analizi ve/veya yorumlama, KT= kaynak tarama, YZ= Yazım, KI= kritik inceleme, GR= gönderim ve revizyon, PY= proje yönetimi, FA= fon alımı.

Çatışma Beyanı

Yazar, bu çalışmada hiçbir çıkar ilişkisi olmadığını beyan etmektedirler.

Etik Onay Beyanı

Bu araştırmada hayvanlar ve insanlar üzerinde herhangi bir çalışma yapılmadığı için etik kurul onayı alınmamıştır.

Kaynaklar

Avogadro M, Colovic A, Rossi M. 2024. Assessing airport ground access interventions: An integrated simulation approach. J Air Transp Manag, 119: 102451.

Boersma K, Toet A. 2024. The future is multimodal. Airport World, 25 Mar 2024. https://airport-world.com/the-future-is-multimodal/ (accessed date: June 02, 2025).

Budd L, Ison S, Budd T. 2016. Improving the environmental performance of airport surface access in the UK: The role of public transport. Res Transp Econ, 59: 185-195.

Cerasi C Ç, Yaman F. 2024. Luggage management system in order to reduce carbon emissions and ensure sustainability. Darnios Aplinkos Vystymas. 2024: 1-6. https://doi.org/10.52320/dav.v21i1.303

Dijkstra A. 2010. Mapping and reducing CO_2 emissions at Amsterdam Airport Schiphol: Developing a model to assess CO_2 reduction at Amsterdam Airport Schiphol [Master's thesis, TU Delft]. TU Delft Repository, Amsterdam, Netherlands, pp: 56-59.

Gössling S, Humpe A, Sun Y-Y. 2024. Are emissions from global air transport significantly underestimated? Curr Issues Tour, 28(5): 695-708. https://doi.org/10.1080/13683500.2024.2337281

Greenreporting.nl. 2023. De CO2-uitstoot per vervoersmiddel: wat je moet weten. https://greenreporting.nl/co2-uitstoot-per-vervoersmiddel/ (accessed date: June 01, 2025)

Greer F, Rakas J, Horvath A. 2020. Airports and environmental sustainability: A comprehensive review. Environ Res Lett, 15(10): 103007. https://doi.org/10.1088/1748-9326/abb42a

Hájnik A, Harantová V, Kalašová A. 2021. Use of electromobility and autonomous vehicles at airports in Europe and worldwide. Transp Res Procedia, 55: 71-78.

Hernández-Martín R, Padrón-Ávila H. 2021. The carbon footprint of airport ground access as part of an outbound holiday trip. Sustainability, 13(16): 9085. https://doi.org/10.3390/su13169085

Higgins TJ. 1994. California Airports: Ground Access Vehicle Trips, Emissions And Emission Reduction Strategies. Aviation Crossroads, California, USA, pp: 54-96.

Ison S, Merkert R, Mulley C. 2014. Policy approaches to public transport at airports—Some diverging evidence from the UK and Australia. Transp Policy, 35(C): 265-274.

Li DC, Merkert R. 2023. "Door-to-door" carbon emission calculation for airlines–Its decarbonization potential and impact. Transp Res Part D: Transp Environ, 121: 103849.

Liu K. 2024. Comprehensive Analysis of Taxi Service Distribution, Demand Hot spots, and Air Pollution Impact: A GIS and Big Data Approach. Appl Comput Eng, 110: 188-194.

London Gatwick Airport. 2021. Decade of Change Performance Summary. Gatwick Airport Ltd, Crawley, UK, pp: 56-75.

London Heathrow Airport. 2022. ULEZ consultation summary report. Heathrow Airport Ltd., London, UK, pp: 26-63.

Mahesh R, Calvert SC. 2025. Decarbonizing airport ground access: A framework of user behavior, infrastructure, and policy. Transp Res Part D: Transp Environ, In press, pp: 54-55.

Matheys J, Van Autenboer W, Timmermans H. 2009. Improvement of the CO_2 balance of the landside accessibility of Brussels Airport through implementation of electric vehicles and general policy measures. J Asian Electr Veh, 7(1): 1265-1271.

Meindl M, De Ruiter C, Marciello V, Di Stasio M, Saavedra Rubio K, Laurent A, Ruocco M, Maerz M. 2024. Greening Regional Airports: A Vision for Carbon Neutral Infrastructure. In: RY Qassim (Ed.), Contemporary Perspective on Sci, Technol and Res, 3: 165-201.

Milieu Centraal. 2020. CO2-uitstoot fiets, ov en auto. (Bisiklet, toplu taşıma ve araba CO2 karşılaştırması), Amsterdam, Netherlands, pp: 45-46.

Miyoshi C, Mason KJ. 2013. The damage cost of carbon dioxide emissions produced by passengers on airport surface access: The case of Manchester Airport. J Transp Geogr, 28: 137-143. https://doi.org/10.1016/j.jtrangeo.2012.12.003

Morch A, Laveneziana L, Erga I, Foss M, Wolden HK, Hennig M. 2024. Electrification of airports and air transport: Airports becoming integrated energy systems. Proc 21st Int Conf European Energy Market (EEM), Held 27-29 May 2025, Lisbon, Portugal, pp: 63. https://doi.org/10.1109/eem60825.2024.10608967

Nijen N. 2024. Explaining Access Mode Choice for Passengers and Personnel travelling to Schiphol Airport. Yüksek Lisans Tezi, Univ Twente, Enschede, Netherlands, pp:54-65.

NS Annual Report. 2022. https://2022.nsannualreport.nl/annual-report-2021/our-activities-and-achievements-in-the-netherlands/performance-on-sustainability (accessed date: June 12, 2025)

Pasha MM, Hickman M. 2016. Airport ground accessibility: Review and assessment. 38th Australasian Transp Res Forum (ATRF), pp: 1-12.

Postorino MN, Mantecchini L. 2014. A transport carbon footprint methodology to assess airport carbon emissions. J Air Transp Manag, 37: 76-86.

Qiao B, He J, Yan X, Chen H, Liu Y, Zhang J. 2021. Assessing emission reduction effects from shifts of urban passenger transport modes by implementing targeted emission tax considering the whole fuel cycle. Environ Sci Pollut Res, 28(9):

11758-11775. https://doi.org/10.1007/s11356-021-14226-5

Risby J, Guest S, Warnock-Smith D. 2022. A critical analysis of Bristol Airport's ground access strategy in a post-COVID context. Case Stud Transp Policy, 10(4): 2161-2170.

Rome2Rio. 2023. Amsterdam Airport to Rotterdam – Distance and travel options. https://www.rome2rio.com/map/Amsterdam-Airport-Schiphol/Rotterdam (accessed date: May 15, 2025)

Royal Schiphol Group. 2025. 2024 Yılı Faaliyet Raporu (Yolcu ve Ulaşım İstatistikleri). Amsterdam: Schiphol Group, Amsterdam, Netherlans, pp: 24-26.

Ryley T, Burchell J, Davison L. 2013. Valuing air transportation and sustainability from a public perspective: Evidence from the United Kingdom and the United States. Res Transp Bus Manag, 7: 114-119.

Schneider A, Stern C, Sachdeva N, Dar Z. 2024. Can airports be a catalyst for reducing aviation's effect on the climate? One Earth, 7(6): 695-709. https://doi.org/10.69554/oibc8419

Shao M, Chen C, Lu Q, Zuo X, Liu X, Gu X. 2023. The Impacts of Low-Carbon Incentives and Carbon-Reduction Awareness on Airport Ground Access Mode Choice under Travel Time Uncertainty: A Hybrid CPT-MNL Model. Sustainability, 15(16): 12610.

Smirti M. 2008. Modeling and measuring greenhouse gas reduction from low carbon airport access modes [Research report]. Research Papers in Economics, pp: 156-169.

Sperling J, Henao A. 2020. Electrification of high-mileage mobility services in cities and at airports. Intell and Eff Transp Syst, 65: 1-15.

Statista. 2023. Choice of transport to and from Amsterdam Airport Schiphol 2015–2019. Statista Research Department. https://www.statista.com/statistics/688080/choice-of-transport-to-and-from-amsterdam-airport-schiphol-the-netherlands/ (accessed date: March 13, 2025)

Statista. 2024. Number of passengers utilizing Amsterdam Airport Schiphol (2024). https://www.statista.com/statistics/652766/number-of-passengers-utilizing-amsterdam-airport-schiphol/ (accessed date: May 08, 2025)

Sun M, Xue C, Cheng Y, Zhao L, Long Z. 2021. Analyzing spatiotemporal daily travel source carbon emissions based on taxi trajectory data. IEEE Access, 9: 107012-107023.

Thomas H, Serrenho A. 2024. Using different transport modes: An opportunity to reduce UK passenger transport emissions? https://doi.org/10.17863/CAM.104214

Travelmath. 2023. Driving distance from AMS to Amersfoort, NL. https://www.travelmath.com (accessed date:June 24, 2025)

Yılmaz O, Frost M, Timmis A, Ison S. 2023. Investigation of employee-related airport ground access emissions. Transp Res Procedia, 64: 350-359.

Zhang Z, Peng ZR, He HD, Yang JM, Gao K, Jia R. 2024. Environmental impacts of ridesplitting considering modal substitution and associations with built environment. Transp Res Part D: Transp Environ, 130: 104160. https://doi.org/10.1016/j.trd.2024.104160

Zhang Z, Gao K, He HD, Yang JM, Jia R, Peng ZR. 2023. How do travel characteristics of ridesplitting affect its benefits in emission reduction? Evidence from Chengdu. Transp Res Part D: Transp Environ, 123: 103912.

Black Sea Journal of Engineering and Science
doi: 10.34248/bsengineering.1618933

Open Access Journal
e-ISSN: 2619 – 8991

Research Article
Volume 8 - Issue 5: 1525-1530 / September 2025

OPPORTUNITIES FOR THE USE OF AGRIVOLTAIC SYSTEMS IN ANIMAL BARNS: A CASE STUDY OF WATER BUFFALO BARNS

Elif TÜRKBOYLARI[1]*, Ahmet Nedim YÜKSEL[2]

[1]*Tekirdağ Namık Kemal University, Vocational School of Technical Sciences, Department of Plant and Animal Production, 59030, Tekirdağ, Türkiye*
[2]*Tekirdağ Namık Kemal University, Faculty of Agriculture, Department of Biosystem Engineering, 59030, Tekirdağ, Türkiye*

Abstract: The utilization of fossil fuels has accelerated with technological advancements and population growth. The increase in harmful gas emissions from non-renewable energy sources is a significant contributor to climate change. To mitigate this threat, there has been a shift towards renewable energy sources, particularly solar energy. The placement of solar panel systems on agricultural land has given rise to agrivoltaic systems, which combine energy production and agricultural use of the same land. However, the installation of agrivoltaic systems often requires considerable agricultural land. In livestock farming, such as water buffalo barns, solar panels can be installed on barn roofs or over cooling ponds used by buffaloes, thus preventing the loss of agricultural land. For a closed water buffalo barn with a floor area of 588.3 m^2 (11.1 × 53.0 m), housing 70 animals, 13 fans with a capacity of 9500 m^3 h^{-1} are required for ventilation and cooling. Additionally, 23.5 m^2 of cooling pads and a circulation pump with a 0.2 kWh capacity are necessary. A solar panel system of 14–15 kWh can meet the energy requirements for ventilation and cooling. When controlled, the panel system would occupy 156 m^2 of land, which expands to 312 m^2 if designed as an agrivoltaic system. Installing solar panels over buffalo cooling ponds can significantly reduce water loss caused by evaporation in summer.

Keywords: Agrivoltaic, Anatolian water buffalo barn, Solar panel system, Ventilation, Cooling

***Corresponding author:** Tekirdağ Namık Kemal University, Vocational School of Technical Sciences, Department of Plant and Animal Production, 59030, Tekirdağ, Türkiye
E mail: eyuksel@nku.edu.tr (E. TÜRKBOYLARI)
Elif TÜRKBOYLARI https: //orcid.org/0000-0003-4658-8068
Ahmet Nedim YÜKSEL http: //orcid.org/0000-0002-0278-7498

Received: January 13, 2025
Accepted: August 22, 2025
Published: September 15, 2025

Cite as: Türkboyları E, Yüksel AN. 2025. Opportunities for the use of agrivoltaic systems in animal barns: A case study of water buffalo barns BSJ Eng Sci, 8(5): 1525-1530.

1. Introduction

Human life depends on the fulfillment of fundamental needs such as clean air, water, food, and energy. Among these essentials, energy is particularly critical, as it not only supports daily activities but also plays a central role in economic development, technological progress, and environmental sustainability. To address their energy needs, people have turned to fossil energy sources, as they are the most accessible and convenient to use. However, the production and use of fossil-based energy bring significant environmental problems. The environmental damage caused by fossil fuels increases with each passing day (Karaağaç et al., 2020). The greenhouse gases released into the atmosphere as a result of fossil fuel use, particularly the accumulation of CO_2 in the troposphere, leading to a greenhouse effect, contribute to rising air temperatures and global warming. Developed countries, where industrialization and technological advancement progress rapidly, through increasingly threatening the ecological balance of the planet through the emission of gases such as CO_2 and CH_4.

With the increasing global population, the demand for energy and food is also rising. Food security necessitates an increase in arable land to meet the growing demand for food. Generally, the predicted trend of rising temperatures in the lower troposphere and surface air layers contributes to an accelerated and intensified hydrological cycle. This situation indicates that the frequency and severity of extreme weather and climate events may increase in many regions of the world. Extreme events such as heatwaves, floods, and droughts, resulting from these intensified and undesirable weather phenomena, could disrupt the stability of food supply (Türkeş, 2020).

Policies adopted to reduce fossil fuel-based energy production, which contributes to climate change, are increasing investments in renewable energy. Investments in renewable energy require the use of more land for energy production purposes. Among renewable energy investments, solar energy is the fastest-growing sector, and as a result, solar panels significantly impact land use (Adeh et al., 2018).

The dimensions of solar panels to be used in agrivoltaic systems are 1.67 m^2 (1.67 m x 1.00 m = 1.67 m^2). The panel thickness is 32 mm, and its maximum power output is approximately 275 W. When two panels are placed one on top of the other lengthwise, 4 panels

generate 1 kWh of electricity. If the panels are placed on the ground at a 40° angle, 4 panels occupy a land area of 2 m x 3.2 m = 6.4 m^2. A 5 kWh panel array occupies a land surface of 10.0 m x 3.2 m = 32.0 m^2. At least a 2 m wide path should be left at the front of the panel rows. This path serves two purposes: facilitating panel maintenance and preventing shading of the subsequent panel row, which could reduce energy production. For a 1 kWh panel system, the area occupied by this path is 2.0 m x 2.0 m = 4.0 m^2. For a 10 kWh system, this value increases to 20.0 m x 2.0 m = 40.0 m^2. Therefore, the total land area occupied by a 10 kWh panel system, including the path, is 64.0 m^2 + 40.0 m^2 = 104.0 m^2. If the panels are arranged with spacing suitable for agrivoltaic farming, the system occupies a total land area of 208.0 m^2. Since the planned panel system is 14–15 kWh, the required area for the panel system and the access path is 156 m^2. If the system is arranged in an agrivoltaic layout, the required area is calculated as 312 m^2.

Agrivoltaic systems are systems that combine photovoltaic panels placed on agricultural land to produce energy while allowing agricultural products to grow underneath the panels. The solar panels in agrivoltaic systems provide shade over plants, helping to preserve soil moisture, reduce heat-induced plant stress, and promote growth (Kırbaş, 2023).

However, a disadvantage of cultivating crops under solar panels is a reported yield reduction ranging from 5% to 20%, depending on the cultivated product. Additionally, the elevated installation of the panel system significantly increases the costs of support structures and wiring. This leads to extra expenses compared to traditional panel systems (Toledo and Scognamiglio, 2021).

There is no existing system to protect such investments in agricultural production areas. Panel systems utilize valuable equipment, such as panels, inverters, and chargers. These devices, located in open fields like farms, are always at risk of theft (Ağır et al., 2023).

Another issue is the transfer of energy produced by the solar panel system to the operation center. Direct current requires cables with a thick cross-section for transmission. Furthermore, significant energy loss occurs during the transmission of direct current. Therefore, the generated direct current should first be converted into alternating current using a charge regulator and an inverter before attempting to transfer it.

However, in solar energy electricity production systems equipped with photovoltaic technology planned to be established in various regions of our country, the production of electricity at the point of consumption offers high feasibility outcomes. Considering all the results obtained, it is stated that investors should prioritize investments where electricity is produced at the point of consumption, as this represents the most profitable investment (Bakır and Yılancı, 2023).

1.1. Placement Areas of Solar Panels in Crop Production

Agricultural production is divided into two main categories: crop production and livestock production, forming the foundation of food security. In agrivoltaic systems utilized in crop production, areas designated for electricity generation and agricultural production often overlap. The land is typically shared between the panel system and crop cultivation on a 50-50 basis. The key factor here is the equitable distribution of photons from sunlight. While this division may result in reduced agricultural yield, it is highlighted as a system that supports food security by mitigating climate change and provides an additional income stream to producers through electricity generation (Ağır et al., 2023).

The best locations for installing solar energy systems without losing agricultural land are water surfaces such as lakes, reservoirs, and ponds. Inactive areas not utilized for activities such as transportation or shipping can accommodate floating solar panels. A notable example in this context is Türkiye's first floating solar power plant installed on Büyükçekmece Lake (Yılmaz and Can-Öziç, 2018). Large energy systems established in these locations can be effectively protected against damage, theft, and other security risks.

In climate change scenarios, Türkiye and the Mediterranean basin are among the regions most affected by rising temperatures, posing significant challenges. A major issue here is the evaporation losses caused by elevated air temperatures. Approximately 55% of the country's water resources are lost to evaporation into the atmosphere. Among these losses, reservoirs, lakes, and rivers account for nearly 90% of the total. However, with floating panel systems installed over water surfaces, it is possible to reduce evaporation losses by approximately 60%, while simultaneously generating electricity (Korkmaz, 2015).

The impact of wind, another factor that increases evaporation from water surfaces, is also mitigated by solar panels. With reduced wind effect on water surfaces, evaporation rates decrease.

On the other hand, a regulation introduced by the General Directorate of Agricultural Research and Policies under the Ministry of Agriculture and Forestry has imposed restrictions on installing solar panels on agricultural land.

1.2. Placement of Solar Panels in Livestock Production Areas

In livestock farming, the other form of agricultural production besides crop farming, there is no conflict between agricultural production areas and solar panel system locations. In livestock facilities, solar panels can be installed on the roofs of animal barns and feed storage areas. Energy can also be generated from locations unsuitable for any other purpose. By placing panels in elevated positions, potential damage from animals or agricultural machinery and equipment can be prevented.

In this study, solar panel systems were designed for

buffalo barns among various types of animal housing.

Buffaloes are water-dependent animals. Particularly during the summer and warmer seasons, their semi-aquatic nature requires access to water for cooling. Therefore, having a pond or water source near the barn is beneficial (Koyuncu et al., 2021).

Using the water surfaces around buffalo barns as locations for solar panel placement can be highly advantageous. Solar panels installed over water bodies near barns can generate electricity for the farm. Additionally, placing panels on the water surface significantly reduces water evaporation. At the same time, the panels block excessive sunlight from reaching the water surface, thereby protecting buffaloes from intense heat and sunlight.

1.3. Buffalo Farming

Buffaloes are known globally as water buffaloes, and in our country as the Anatolian water buffalo. The Anatolian water buffalo, a subspecies of river buffalo originating from the Mediterranean buffalo, is raised in various regions. Knowledge about buffalo farming is limited, and practices generally known for cattle farming are often applied to buffalo farming as well (Satılmış and Kul, 2024).

In Türkiye, Anatolian water buffalo farming is typically carried out on a pasture-based system within traditional family farms (Satılmış and Kul, 2024). Buffaloes can be kept in wetlands throughout the year, where cattle cannot sustain life. Regions with an abundance of marshes, wetlands, and reed-covered pastures are suitable for buffalo farming. Due to their thick and dark skin with limited sweat glands, buffaloes are highly sensitive to heat. In hot weather, they avoid reduced productivity by cooling off in water. Maximum productivity from buffaloes is achieved in areas like seas, lakes, ponds, rivers, and marshes (Koyuncu et al., 2021). When buffaloes are kept in barns during summer and hot seasons, effective ventilation and humidity control must be ensured to prevent them from being affected by the heat.

Buffaloes are economically valuable animals in the regions where they are found worldwide. While raised for meat and milk production, their hide, horns, and manure are also utilized. Additionally, in some countries like those in Southeast Asia, buffaloes are used as draft animals in agriculture. With these characteristics, buffalo farming can play a significant role in rural development as an economically viable branch of farming (Kul et al., 2018).

Some of the key advantages of buffaloes include their ability to produce higher levels of protein, superior weight gain, resistance to diseases, and high load-carrying capacity. Furthermore, they are long-lived animals and make better use of low-quality roughage compared to cattle (Koyuncu et al., 2021).

In recent years, buffalo farming has been significantly supported by the Ministry of Agriculture and Forestry. Through support for projects such as the "On-Farm Improvement of Anatolian Buffalo" program, interest in buffalo products has increased as part of efforts to promote healthy nutrition among the population. This has raised awareness about the production and consumption of buffalo products in recent years (Koyuncu et al., 2021).

In this study, it was aimed to provide the energy required for the fan-pad system used for ventilation and cooling in a 70-head closed buffalo barn with an area of 588.3 m^2 under the conditions of Tekirdağ province, using solar panel systems installed on the barn roof and over the water pool.

2. Materials and Methods

2.1. Material

The project area, Tekirdağ province, is located north of the Sea of Marmara on the Thrace Peninsula. The Thrace Peninsula is the part of Türkiye situated on the European continent. It is bordered by the Black Sea to the north, the Bosphorus Strait to the east, the Sea of Marmara and the Dardanelles Strait to the south, and the Aegean Sea to the west.

The research area, Tekirdağ province, is strategically situated in the Marmara Region between the longitudes of 26°41' and 28°10' east, and latitudes of 40°35' and 41°35' north. Tekirdağ covers an area of 6,313 km^2, with an elevation ranging from 0 to 200 meters above sea level. Its terrain is slightly undulating, with no high mountains, steep slopes, or deep valleys. The geological structure is relatively young. Tekirdağ has a semi-humid climate type based on its overall humidity conditions. It is windy during both summer and winter seasons (MCT, 2024).

There are many buffalo barns located to the west of Istanbul and around Tekirdağ. These producers supply buffalo milk, yogurt, cream, and butter to confectioneries, patisseries, and restaurants in Istanbul and the surrounding areas.

To ensure that buffaloes, which are highly sensitive to heat, do not experience productivity losses, ventilation and cooling systems must be implemented in buffalo barns in Tekirdağ and its vicinity. Appropriate ventilation and cooling for all seasons require mechanical ventilation in the animal barns.

The barn where the project will be implemented accommodates 70 buffalo, arranged in double rows. The dimensions of this barn are approximately 588.3 m^2 (11.1 m x 53.0 m = 588.3 m^2) (Avcı, 2015).

2.2. Method

The internal temperature of animal barns can be reduced through various water-based methods. Cooling systems for buffalo barns may include misting systems, mini-sprinkler nozzles, or fan-pad systems. These systems or sprinkler nozzles are used to wet the walkways, structural elements, and the buffalo inside the barn. When water evaporates from these moist surfaces, the latent heat of vaporization is drawn from the surfaces and the air. This principle is based on the fact that, during

evaporation, 1 g of water absorbs approximately 598 calories (≈2500 J) of latent heat from its surroundings. The designed fan-pad system likewise utilizes water evaporation to cool the air and lower the barn's indoor temperature.

A pad is installed on one wall of the barn, while fans are placed on the opposite wall. The fans exhaust the indoor air, while humidified and cooled air that passes through the pad enters the barn. Consequently, the indoor air temperature decreases.

For a closed buffalo barn measuring 11.1 m × 53.0 m = 588.3 m^2 and housing 70 buffalo, a fan-pad cooling system and a solar photovoltaic (PV) system were designed.

2.3. Solar Energy Potential in Türkiye

Due to its geographical location, Türkiye benefits from an average annual sunlight duration of 7.5 hours, which is significantly higher than that of many countries. Regarding solar energy potential, the annual total sunshine duration is approximately 2.741 hours, and the total solar energy yield is about 1.527 kWh m^{-2} $year^{-1}$ (with a daily average of 4.18 kWh m^{-2}) (MENR, 2024). These factors make Türkiye highly suitable for utilizing solar energy.

The radiation intensity in Tekirdağ province, where the project was implemented, is 1.450 kWh m^{-2} $year^{-1}$ (3.97 kWh m^{-2} day^{-1}), which is close to Türkiye's average. The adequacy of solar energy encourages electricity use in agricultural enterprises in rural areas. In barns, electricity generated by solar panel systems is utilized for lighting, ventilation, cooling, and milking operations.

Solar panels, which consist of solar cells, directly convert sunlight into electricity. Most solar cells are made from inorganic materials, with an efficiency rate of approximately 15-20% (Grätzel, 2009).

2.4. Ventilation and Cooling of Buffalo Barns Using a Fan-Pad System

Buffaloes are physiologically different from other large ruminants. Their thick, dark skin and insufficient sweat glands make them highly susceptible to heat stress. Indoor air temperature is critical for buffaloes, as their limited sweat glands make it challenging for them to regulate their body temperature. The air temperature in the barn significantly impacts milk production and lactation duration (Kocaman and Kurç, 2018). A rapid deterioration of air quality within the barn induces stress in buffaloes, resulting in notable decreases in both meat and milk productivity (Avcı, 2015).

To design a fan-pad cooling system for buffalo barns, certain dimensions and parameters of the barn need to be considered. Ventilation requirements are calculated based on either the volume of the barn or the number of animals. Generally, calculations focus on the number of animals. The barn in this project houses 70 buffalo. The total floor area of the barn is 588.3 m^2 with a height of 3 m.

For water-cooled barns, it is required to have 1 m^2 of pad area per 25 m^2 of floor space (Yüksel and Yüksel Türkboyları, 2018). Based on this ratio, the required pad area for the barn is calculated as follows (equation 1):

$$588.3/25 = 23.5\ m^2 \quad (1)$$

In addition to managing excess heat and humidity, harmful gases from the animals' metabolism must also be removed from the environment (Koç and Şahin, 2023). Thus, the ventilation requirements of the fan-pad system need to be determined. Along with pad area, the number of fans (ventilators) should be calculated. Ventilation capacity varies depending on the season and the live weight of the animals. For buffaloes, this value is approximately 1.925 m^3 h^{-1} kg^{-1} (Wathes and Charles, 1994). The average live weight of Anatolian buffaloes is 500 kg (Atasever and Erdem, 2008). Therefore, the ventilation volume required for a barn housing 70 buffaloes of average 500 kg each is calculated as follows (equation 2):

$$1.925\ m^3h^{-1}kg^{-1} \times 500\ kg \times 70\ heads = 67375\ m^3h^{-1} \quad (2)$$

Fan systems should be designed to operate both individually and collectively. For quiet operation, fans with a diameter of 60 cm are preferred. These fans have a capacity of 9500 m^3 h^{-1}, a power of 0.75 kW, a speed of 1400 rpm (dd^{-1}), and operate on a single-phase 230 V power source (Anonymous, 2024a). The number of fans needed to ensure proper ventilation is calculated as follows (equation 3):

$$67375\ m^3h^{-1}/9500\ m^3h^{-1} = 7.1\ fans \quad (3)$$

Due to the barn's length exceeding 30 m (it is 53 m), fans should also be placed within the barn at 15–17 m intervals for effective ventilation (Yüksel and Yüksel Türkboyları, 2018). At least two sets of ventilators should be installed at these intervals to increase ventilation efficiency. Including six additional fans for interior placement, the total number of fans required for the system is 13. The system will use 13 fans with a power of 0.75 kW each and a circulation pump for pad wetting with a power of 0.2 kW. The total energy demand of the system is calculated as follows (equation 4):

$$13 \times 0.75\ kWh + 0.2\ kWh = 9.95\ kWh \quad (4)$$

3. Results and Discussion

Data obtained for the ventilation and cooling systems planned for a closed barn housing 70 Anatolian water buffaloes are presented in Table 1.

Table 1 provides the project details for the solar panel system designed for a closed buffalo barn with a capacity of 70 buffalo. To achieve the desired environmental conditions within the barn, a solar panel system with a capacity of 9.95 kWh is required. This system necessitates 13 ventilators, each 60 cm in diameter, to ensure ventilation at a rate of 67375 m^3 h^{-1}. Additionally, a pad area of 23.5 m^2 is required for cooling, along with a

circulation pump of 0.2 kWh to supply water to the pad. The floor plan of the ventilation and cooling system for a closed buffalo barn with a capacity of 70 head is presented in Figure 1.

Climatic conditions may hinder the expected efficiency of the solar panel system. Factors such as dirty solar panel surfaces, extreme hot or cold temperatures, the oblique angle of sunlight during morning and evening hours, cloudy weather, or night hours without sunlight could prevent the system from generating the desired amount of energy (Anonymous, 2024b). To ensure the system delivers optimal performance, a system with a capacity of 14-15 kWh—25-30% higher than the calculated 9.95 kWh—should be selected. When the system operates at full capacity, the excess energy produced can be stored in batteries. This stored energy can be utilized during times without sunlight, and for other equipment and lighting within the barn (Yüksel and Türkboyları, 2021).

The 15 kWh solar panel system planned for this buffalo barn requires an area of 156 m^2. If designed as an agrivoltaic structure, the necessary land area doubles to 312 m^2. Installing this system at a height of 3-4 meters would be costly due to the need to accommodate the operation of agricultural machinery underneath (Toledo and Scognamiglio, 2021). Since agricultural production is carried out beneath the panels, the operation of agricultural machinery and equipment should be enabled (Kırbaş, 2023).

For solar panels intended for buffalo barns, the most suitable installation locations are identified as above the water pool or on the barn roof (Figure 2). One advantage of installing the panels above the water pool is reducing water evaporation and loss, as the panels provide shade over the pool (Korkmaz, 2015). Furthermore, during the summer, the panels shield buffaloes in the pool from excessive sunlight, enhancing their comfort and well-being (Koyuncu et al., 2021).

Table 1. Ventilation and cooling system data for a 70-head Anatolian buffalo barn

Pad Area (m^2)	Ventilation Volume (m^3 h^{-1})	Number of Fans (units)	Energy Requirement (kWh)
23.5	67375	13	9.95

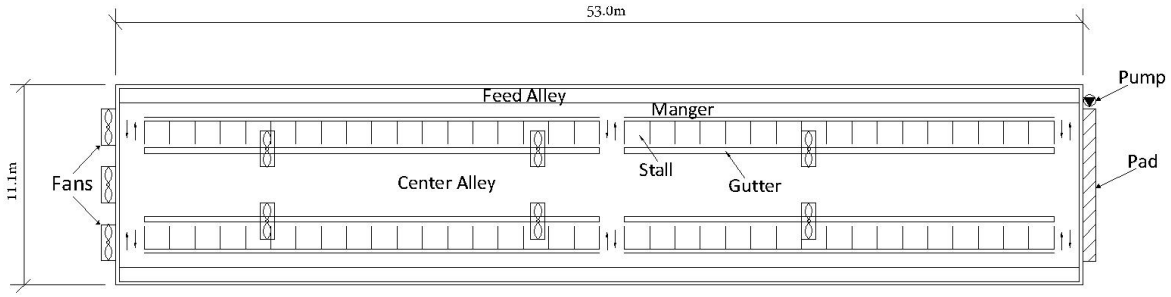

Figure 1. Floor plan of the ventilation and cooling system for a closed buffalo barn with a capacity of 70 head.

Figure 2. Placement of solar panels on the roof of the barn and over the water pool in the buffalo barn (OpenAI's ChatGPT platform generated this image).

4. Conclusion

The increased use of renewable energy sources, particularly solar panel systems, in agriculture has been causing a loss of arable land. In agricultural areas, conflicts can arise between energy production and crop cultivation. However, in livestock production, the use of solar panels does not result in land loss. In this context, the roofs of livestock barns and feed storage facilities can be utilized to contribute to energy generation.

In buffalo barns, the roof of the barn and the top of the water pools used by the buffalo for cooling can also be utilized as installation areas for solar panels. This approach avoids the use of arable land for panel systems, as seen in agrivoltaic systems. The energy generated by these systems can be used for ventilating and cooling buffalo barns. Ventilation systems help remove excessive heat, humidity, harmful gases, and dust from the barn. If ventilation is inadequate, the development and productivity of buffalo's decline. Proper ventilation and cooling conditions in buffalo barns can only be achieved through mechanical ventilation systems. The energy

required for operating these systems can be supplied by solar panel energy systems.

In rural areas lacking access to electricity grids, renewable energy systems can meet the energy demands of agricultural operations. Solar panel systems not only fulfill energy needs but also provide backup power during outages and help reduce energy costs for the operation.

Author Contributions

The percentages of the authors' contributions are presented below. All authors reviewed and approved the final version of the manuscript.

	E.T.	A.N.Y.
C	50	50
D	50	50
S	60	40
DCP	60	40
DAI	60	40
L	60	40
W	60	40
CR	60	40
SR	60	40
PM	60	40
FA	60	40

C=Concept, D= design, S= supervision, DCP= data collection and/or processing, DAI= data analysis and/or interpretation, L= literature search, W= writing, CR= critical review, SR= submission and revision, PM= project management, FA= funding acquisition.

Conflict of Interest

The authors declared that there is no conflict of interest.

Ethical Consideration

This study did not involve human participants or animal; therefore, ethics committee approval was not required.

References

Adeh EH, Selker JS, Higgins CW. 2018. Remarkable agrivoltaic influence on soil moisture, micrometeorology and water-use efficiency. PLoS ONE, 13(11): e0203256. https: //doi.org/10.1371/journal.pone.0203256

Ağır S, Derin-Güre P, Şentürk B. 2023. Türkiye'de Tarım ve Enerjinin Kesişimi, TarımFV: Güncel Yazın Işığında Bir Ön Değerlendirme. Hacettepe Univ İktisadi ve İdari Bil Sci Fac Derg, 41(Tarım özel sayısı): 1-22. https: //doi.org/10.17065/huniibf.1250434

Anonymous. 2024a. URL: www.fansanmarket.com (accessed date: October 10, 2024)

Anonymous. 2024b. Güneş enerji sistemlerinin (GES) güç çıkışını etkileyen faktörler URL: https: //mirsolar.com.tr/gunes-paneli-cikisini-ne-etkiler/ (accessed date: October 17,2024)

Atasever S, Erdem H. 2008. Manda yetiştiriciliği ve Türkiye'deki geleceği. OMÜ Zir Fak Derg, 23(1): 59-64.

Avcı H. 2015. İstanbul ili Avrupa yakasındaki manda işletmelerinin yapısal ve mekansal özelliklerinin belirlenmesi üzerine bir çalışma. Yüksek lisans tezi, Namık Kemal Univ Fen Bil Enst, Tekirdağ, Türkiye, pp: 69.

Bakır C, Yılancı A. 2023. Türkiye'deki farklı iller için şebekeye bağlı arazi ve çatı tipi lisanssız fotovoltaik güç santrallerinin tekno-ekonomik analizi. Mühendis ve Makina, 63(709): 560-584. https: //doi.org/10.46399/muhendismakina.114780

Grätzel M. 2009. Recent advances in sensitized mesoscopic solar cells. Acc Chem Res, 42(11): 1788-1798.

Karaağaç MO, Oğul H, Bardak S. 2020. Güneş enerji sistemi tasarımı: kanatlı hayvan çiftliği örneği. Düzce Univ J Sci Technol, 8(1): 711-722. https: //doi.org/10.29130/dubited.490154

Kırbaş İ. 2023. Agrivoltaik sistemler ve tarım alanlarının hibrit kullanımı. Uluslar Müh Tasarım Teknol Derg, 5(1-2): 9-19.

Kocaman İ, Kurç HC. 2018. A research on the determination of lactation length and milk yield of Anatolian water buffaloes under different environmental conditions. J Sci Eng Res (JSER), 5(8): 39-44.

Koç K, Şahin O. 2023. Bitlis ili, Güroymak ilçesi, Gölbaşı beldesindeki Anadolu mandası işletmelerinde barınak içi karbondioksit (CO2) emisyonu üzerine barınak hacmi ve sürü büyüklüğünün etkisi. J Anim Sci Econ, 2(2): 44-52. https: //doi.org/10.5152/JASE.2023.1224595

Korkmaz MS. 2015. Buharlaşma kayıplarının yüzer fotovoltaik paneller ile azaltılması. Yüksek lisans tezi, İstanbul Teknik Univ Fen Bil Enst, İstanbul, Türkiye, pp: 89.

Koyuncu M, Çetin İ, Sargın HG, Çetin E. 2021. Bursa ili Mustafakemalpaşa ilçesi manda yetiştiriciliği "Karaoğlan mahallesi örneği". Hayvansal Üretim, 62(1): 25-34. https: //doi.org/10.29185/hayuretim.820358

Kul E, Filik G, Şahin A, Çayıroğlu H, Uğurlutepe E, Erdem H. 2018. Effects of some environmental factors on birth weight of Anatolian buffalo calves. Turk J Agric-Food Sci Technol, 6(4): 444-446. https: //doi.org/10.24925/turjaf.v6i4.444-446.1716

MCT (Republic of Türkiye Ministry of Culture and Tourism). 2024. https: //tekirdag.ktb.gov.tr/TR-75726/genel-bilgiler.html (accessed date: October 03,2024)

MENR (Republic of Türkiye Ministry of Energy and Natural Resources). 2024. https: //enerji.gov.tr/eigm-resources-en (accessed date: October 08, 2024)

Satılmış AS, Kul E. 2024. Herd management practices in water buffalo enterprises in Amasya province: Feeding, milking and health protection. Turk J Agric-Food Sci Technol, 12(5): 753-762. https: //doi.org/10.24925/turjaf.v12i5.753-762.6593

Toledo C, Scognamiglio A. 2021. Agrivoltaic systems design and assessment: A critical review, and a descriptive model towards a sustainable landscape vision (three-dimensional agrivoltaic patterns). Sustainability, 13(12): 6871. https: //doi.org/10.3390/su13126871

Türkeş M. 2020. İklim değişikliğinin tarımsal üretim ve gıda güvenliğine etkileri: bilimsel bir değerlendirme. Ege Coğrafya Derg, 29(1): 125-149.

Yılmaz EA, Can Öziç H. 2018. Türkiye'nin yenilenebilir enerji potansiyeli ve gelecek hedefleri. ODÜ SOBİAD, 8(3): 525-535.

Yüksel AN, Türkboyları E. 2021. Use of solar panels in water buffalo barns for providing climatic environmental conditions. Iğdır Int Appl Sci Congr, April 14-15, Iğdır, Türkiye, pp: 301-310.

Yüksel AN, Yüksel-Türkboyları E. 2018. Using the photovoltaic cells for ventilation and cooling of the animal barns. 1st Int 14th Natl Cong Agric Struct Irrig (ICASI-2018), 26-28 September, Antalya, Türkiye, pp: 49-55.

Wathes CM, Charles DR. 1994. Livestock housing. CAB Int: Wallingford, Oxon, UK, pp: 428.

Black Sea Journal of Engineering and Science
doi: 10.34248/bsengineering.1697543

Open Access Journal
e-ISSN: 2619 – 8991

Research Article
Volume 8 - Issue 5: 1531-1536 / September 2025

PRODUCTION AND CHARACTERIZATION OF SPOROPOLLENIN REINFORCED ALGINATE-BASED COMPOSITE FILMS

Bahar AKYUZ YILMAZ[1]*

[1]*Aksaray University, Faculty of Arts and Sciences, Department of Molecular Biology and Genetics, 68100 Aksaray, Türkiye*

Abstract: Sporopollenin is a natural biomaterial that offers great potential for various applications due to its biocompatibility, biodegradability, non-toxicity, durability, and high thermal stability. In this study, sporopollenin was extracted from *Pinus nigra* pollen and incorporated into alginate-based films to utilize these advantageous properties. Sporopollenin samples were added to 100 mL of 1% alginate solution at different concentrations of 0, 5, 10, and 50 mg. Both sporopollenin-free alginate films and sporopollenin-enriched films were comprehensively characterized using FT-IR, TGA, SEM, and MTT analysis methods. The results revealed that sporopollenin obtained from *P. nigra* pollen was successfully incorporated into the alginate-based films. Furthermore, an increase in the amount of sporopollenin led to enhanced surface roughness. MTT test results also confirmed that the films were non-toxic. The aim of this work is to investigate the potential of sporopollenin as a functional additive in alginate films and to highlight its importance in developing sustainable and biocompatible biomaterials. These findings suggest that sporopollenin holds promise as an innovative biomaterial for various applications, such as food packaging.

Keywords: Alginate, Biodegradable, Composite, Cytotoxicity

***Corresponding author:** Aksaray University, Faculty of Arts and Sciences, Department of Molecular Biology and Genetics, 68100 Aksaray, Türkiye
E mail: baharakyuzylmaz@gmail.com (B. AKYUZ YILMAZ)
Bahar AKYUZ YILMAZ https: //orcid.org/0000-0001-9760-9856

Received: May 12, 2025
Accepted: August 23, 2025
Published: September 15, 2025

Cite as: Akyuz Yilmaz B. 2025. Production and characterization of sporopollenin reinforced alginate-based composite films. BSJ Eng Sci, 8(5): 1531-1536.

1. Introduction

Recently, consumer demand for high-quality fruits and vegetables has been increasing day by day. This increasing demand has led to protecting foods with appropriate preservation techniques and extending their shelf-life by using various packaging. The use of synthetic and non-biodegradable packaging brings environmental problems. For this reason, scientists have turned to the research of edible films consisting of biopolymers or their composites obtained by using natural, edible, and biodegradable polymers for food preservation and shelf-life extension. These edible films and coatings create a semi-permeable safety barrier around vegetables and fruits, reducing the loss of quality attributes. Biopolymers such as starch, pectin, chitosan, carrageenan, alginate, xanthan gum, and gelatine are commonly used to produce these films (Martins et al., 2024).

Alginates are natural biopolymers found in the cell wall of brown seaweeds. It is structurally known as a linear copolymer containing (1 → 4)-linked β-d-mannuronate (M) and α-l-guluronate (G) residues (Dekamin et al., 2018). Alginates have attracted attention in many fields thanks to their biological properties, making them suitable for many applications in the medical, food, cosmetic, pharmaceutical, and surgical sectors (Tallis, 1950). It offers non-toxic properties such as thickening, stabilizing, suspending, film forming, gel forming, and emulsion stabilizing (Rahman et al., 2024). Thanks to its excellent film-forming ability and low cost, sodium alginate is widely applied in edible packaging. Although alginate edible films form strong films, they show poor resistance to water due to their hydrophilic nature (Pathak et al., 2008). Moreover, single alginate films have poor mechanical properties and low additional functionalities. It is more effective to improve the properties of alginate films when composite with other polymers or different inorganic, organic materials. Adding sporopollenin, known as the apple of the plant world, to alginate films can also improve film properties.

Sporopollenins are microcapsules that form the protective outer layer of plant spores and pollen grains and are obtained by removing the genetic materials, oils, and proteins of pollen with chemicals such as acid, base, and chloroform. They are cross-linked biopolymers that are mechanically robust, chemically inert, very high thermally stable, non-allergenic, and can remain intact in nature for thousands of years (Tønnesen and Karlsen, 2002). Sporopollenin microcapsules have attracted great interest as microencapsulation materials due to their environmentally friendly nature and uniform micron-scale size. Therefore, due to their mechanical and thermal durability, sporopollenin exine capsules have become a promising material for drug delivery, electronics, and food packaging applications (Alshehri et al., 2016; Martău

et al., 2019; Mohammed et al., 2021). Accordingly, composite materials reinforced with hollow sporopollenin microcapsules from different plant spores were developed (Mujtaba et al., 2022; Lingait et al., 2024).

In this study, sporopollenin particles obtained from *P. nigra* pollen were incorporated into alginate-based composite films, and their physicochemical properties were analyzed using Fourier Transform Infrared Spectroscopy (FTIR), Scanning Electron Microscopy (SEM), and Thermogravimetric Analysis (TGA). In addition, the cytotoxicity of all films was investigated by MTT assay. The effects of sporopollenin added at different ratios to alginate-based films were evaluated.

2. Materials and Methods

2.1. Materials and chemicals

In this study, *Pinus nigra* pollen was collected from Aksaray University Campus, Aksaray, Türkiye. They were then left to dry at room temperature for 3 days. Then, to remove dust and other unwanted particles, they were first sieved through a sieve with a pore diameter of 10 µm and then through a sieve with a pore diameter of 100 µm to remove large particles. Pollen samples were stored in sealed tubes at -20°C for further experiments. The chemicals used for sporopollenin extraction; HCl, NaOH, Chloroform and Methanol were purchased from Sigma-Aldrich (St. Louis, Missouri, USA). Glycerol, the plasticizing agent, was obtained from Sigma-Merck, USA. Distilled water was used in all experimental stages.

2.2. Isolation of Sporopollenin from *P. Nigra* Pollen

For the isolation of sporopollenin, the obtained *P. nigra* pollen was treated with acid for demineralization, base for deproteinization, and chloroform/methanol/water solution for depigmentation. Briefly, for demineralization, 10 g of *P. nigra* pollen was treated with 4 M HCl solution for 2 h at 50°C. Then, the samples were filtered with a Whatman filter paper with a pore size of 110 µm and then washed with distilled water to neutral pH. For deproteinization, the samples were incubated with 4M NaOH solution for 6 hours at 150°C using a magnetic stirrer with a heating system. The treated samples were then filtered using Whatman filter paper and washed extensively with distilled water to neutral pH. The demineralization and deproteinization processes were repeated 4 times to ensure complete removal of genetic and cellulosic materials in the pollen. Acid and base treated pollen samples were then kept in chloroform/methanol/water solution (4: 2: 1 v: v: v) for 1 h at room temperature. Finally, sporopollenin samples were washed thoroughly with distilled water and dried in an oven at 60°C for 48 hours. Figure 1a shows the isolation stages of sporopollenin schematically.

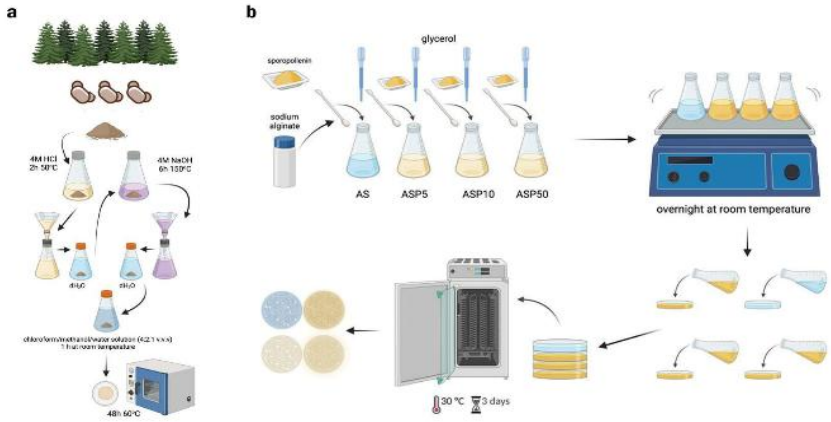

Figure 1. Schematic representation of the isolation steps of sporopollenin (a) and preparation of sporopollenin reinforced of alginate-based films (b).

2.3. Preparation of Films

Four different types of alginate-based films were prepared to investigate the effects of sporopollenin on film properties. Initially, a 1% (w/v) sodium alginate solution was prepared by dissolving sodium alginate in distilled water. For flexibility enhancement, 5 mg of glycerol was added as a plasticizer to each solution. The control film, containing only alginate and glycerol without sporopollenin, was labeled AS. To prepare the other film samples, sporopollenin was added to three alginate solutions at concentrations of 5 mg, 10 mg, and 50 mg, creating samples labeled ASP5, ASP10, and ASP50, respectively. The use of different concentrations was adapted from the method of previous study (Kaya et al., 2017). After adding glycerol and different amounts of sporopollenin, each solution was stirred overnight at room temperature using a magnetic stirrer at 100 rpm. This gentle stirring was done to ensure homogeneity and prevent fragmentation of the sporopollenin. The mixed solutions were then poured into plastic petri dishes and left to dry at 30 °C for three days. Figure 1b schematically shows the preparation of sporopollenin reinforced films. The original camera images of all films are shown in Figure 2. Film thickness was measured with a digital micrometer (Mitutoyo, China). For each film, measurements were taken at ten random points, and the average thickness was calculated.

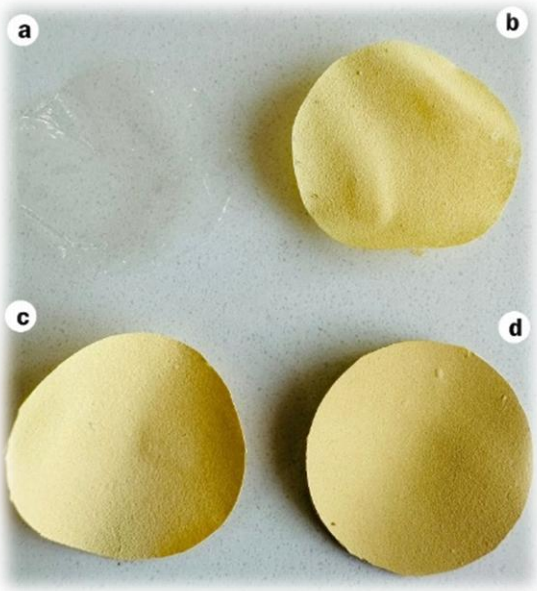

Figure 2. Original camera images of alginate-based control film (a), and sporopollenin-alginate composite films; ASP5 (b), ASP10 (c), ASP50 (d).

2.4. Physicochemical Characterization

2.4.1. Fourier transform infrared spectroscopy (FTIR)

Infrared spectra of sodium alginate-based films (AS, ASP5, ASP10, and ASP50) reinforced with sporopollenin obtained from *P. nigra* pollen were recorded in the wavelength range of 4000-400 cm^{-1} using Perkin Elmer Spectrum Two FT-IR Spectrometer.

2.4.2. Thermogravimetric analysis (TGA)

The thermal stability of AS, ASP5, ASP10 and ASP50 film samples was determined by EXSTAR S11 7300 thermogravimetric analyzer. The samples were tested by heating at a constant temperature of 10 ˚C min^{-1} from 30 ˚C to 700 ˚C under a nitrogen atmosphere.

2.4.3. Scanning electron microscopy (SEM)

The surface morphologies of *P. nigra* pollen, sporopollenin isolated from pollen samples, and all film samples were analyzed with FEI Quanta FEG 250 Scanning Electron Microscopy device at different magnifications between 500X-50.000X. With the help of these images, the surface morphologies of the samples were investigated.

2.5. MTT Assay

Within the scope of the study, biocompatibility assessments of biomaterials with physicochemical characterizations were conducted using healthy mouse fibroblast cells (L929) (HUKUK, Sap Institute). For the relevant analysis, cells were briefly cultured in Dulbecco's Modified Eagle Medium (DMEM) containing 10% fetal bovine serum (FBS), penicillin (100 units/ml), and streptomycin (100 µg/ml) at 37°C in a 5% CO_2 atmosphere. When cells reached 70% confluency, they were trypsinized and passaged at a 1: 4 dilution twice a week. Cell viability was monitored with trypan blue during procedures, and experiments proceeded only if the viability level was above 90%. Suspended cells obtained after passaging were prepared for the MTT assay by adjusting the cell density to 3 x 10^4 cells/mL per well and were seeded into 96-well culture plates. The culture plates were incubated at 37°C in a 5% CO_2 atmosphere for 24 hours. After 24 hours, pre-sterilized 2x2 mm samples were added to each well, and the cultures were further incubated under the previously mentioned conditions for incubation periods of 24, 48, and 72 hours without any medium change. For biocompatibility assessments, control cells were maintained in growth medium only, without any treatment, for the same durations. The cytotoxicity of the materials on cells was evaluated using the standard MTT assay. After the incubation period, the materials were removed from the wells, and 10 µL of MTT solution (final concentration 0.5 mg/mL) was added to all test and control wells. The plates were then incubated in the dark at 37°C for 3 hours. Next, the reaction mixture was removed from the wells, and 100 µL of DMSO solution was added to dissolve the formazan crystals. The plates were left for 5 minutes to stabilize the color, and the absorbance was measured at 492 nm using a ChroMate® ELISA reader. The viability of untreated cells without any material was considered 100%. The cell viability percentage (%) was calculated using the following equation 1:

$$\%\, Viability\ = \frac{(Abs_{sample})}{(Abs_{control})} x100 \qquad (1)$$

2.6. Statistical Analysis

Data analysis was performed using version 5 of GraphPad Prism software (GraphPad Software®). Data is presented as the mean ± standard error of the mean (SEM). Statistical differences were evaluated by one-way ANOVA followed by Tukey's post-hoc test (95% confidence interval). p-values of $P<0.05$ were considered statistically significant.

3. Results and Discussion

3.1. Transparency and Thickness

Stereo microscopy images of all films are presented in Figure 2. The surface of the AS control film has a uniform and smooth morphology due to the absence of sporopollenin. With the addition of sporopollenin, significant roughness was observed on the surface. It is also observed that the surface roughness becomes more pronounced as the concentration of sporopollenin in the alginate matrix increases. The thickness of the films was measured as 0.109 ± 0.0145 mm, 0.053 ± 0.0017 mm, 0.0537 ± 0.0006 mm, and 0.086 ± 0.0047 mm for AS, ASP5, ASP10, and ASP50, respectively. These results show that there is a significant increase in the thickness of the films with an increasing amount of sporopollenin.

3.2. FTIR

FT-IR spectra of AS, ASP5, ASP10, and ASP50 films were recorded (Figure 3). The broad peak observed at 3279.17

cm^{-1} in the spectrum of the alginate-based control film (AS) was attributed to -OH groups forming intermolecular hydrogen bonds. Two peaks at 2929.5 and 2107.8 cm^{-1} were associated with aliphatic C-H stretching vibrations. The sharp peak at 1600.2 cm^{-1} indicated the presence of sodium ions attached to the carboxylate (COO^-) group in the structure of sodium alginate, and the peak around 1407.3 cm^{-1} indicated aliphatic C-H bending vibrations. The peak at 1025.6 cm^{-1} indicated C-O-C sugar ring groups and showed that alginate has a polysaccharide structure. These spectra show the structural and chemical properties of the AS film. The 3239.59 cm^{-1} peak in the spectrum of the 0.05% sporopollenin-alginate composite film (ASP5) is attributed to intermolecular OH bonding. The 2924.34 cm^{-1} peak is produced by aliphatic C-H stretching vibrations. 1599.12 cm^{-1} peak is aliphatic C=C stretching vibrations. 1406.7 cm^{-1} are aliphatic C-H bends. 1025.91 cm^{-1} peak is produced by C-O-C group (Figure 3). The FTIR spectrum reveals the characteristic functional groups and structural features of sporopollenin. The broad OH bond peak at 3400.1 cm^{-1} indicates the presence of hydroxyl groups present in the structure of sporopollenin (Tønnesen and Karlsen, 2002). The peak observed at 1678.5 cm^{-1} indicates the presence of a carbonyl (C=O) group. The aromatic C=C stretching band at 1516.2 cm^{-1} is one of the features that supports the durable, chemically and biologically degradation-resistant structure of sporopollenin. The presence of aromatic rings can provide structural stability and rigidity to sporopollenin (Kaya et al., 2017; Martău et al., 2019).

Some changes were observed when comparing the AS spectrum with the FT-IR spectra of ASP5, ASP10, and ASP50 alginate sporopollenin films. In general, peaks at higher wavelengths were observed as the sporopollenin ratio increased and because of intermolecular interactions. As the amount of sporopollenin increased, the OH bond shifted to 3324.92 cm^{-1} and gave a broader peak. The intensity of aliphatic C-H stretching vibration peaks increased due to the increase in aliphatic C-H bonds because of the combination of sporopollenin with sodium alginate. It was observed that the C-O-C group shifted from 1025 cm^{-1} in the control to 1032 cm^{-1} in the presence of sporopollenin (ASP50). The results obtained from FT-IR analysis demonstrated the successful incorporation of *P. nigra* sporopollenin into alginate films.

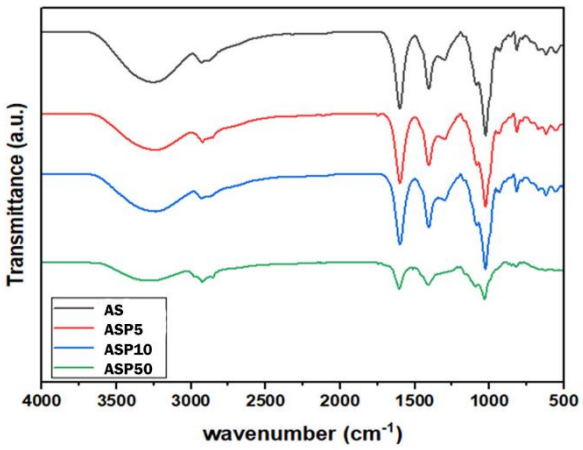

Figure 3. FT-IR spectra of AS and sporopollenin-alginate composite films (ASP5, ASP10, and ASP50).

3.3. TGA

The thermograms of all films are presented in Figure 4. For the AS film, only three mass loss stages were observed, whereas for ASP5, ASP10, and ASP50 films, the mass loss occurred in three distinct stages. In all films, the first mass loss corresponds to the evaporation of adsorbed water (Tavassoli-Kafrani et al., 2016). The second mass loss is attributed to the decomposition of glycerol (nearly 200 °C), as reported in the literature. The third mass loss is associated with the degradation of the polymeric structure of alginate (between 335-480 °C) (Chiappe et al., 2017). The third mass loss, observed between 370-550°C (DTGmax, °C), is attributed to the degradation of the sporopollenin structure. The mass loss during the third stage increased progressively with the increasing sporopollenin content in the films. The degradation temperatures of both alginate and sporopollenin were close, giving a single broad degradation step. These findings suggest that sporopollenin is successfully incorporated into the alginate matrix.

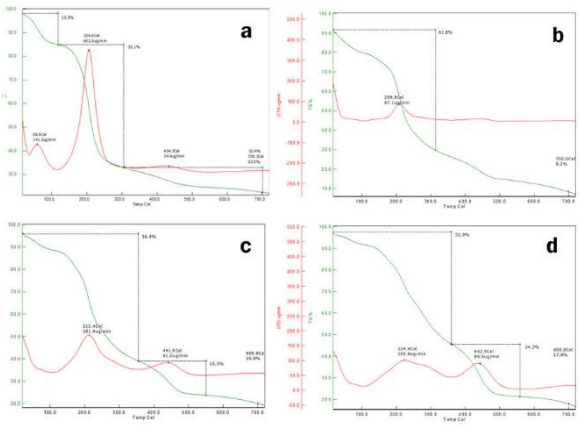

Figure 4. Thermograms of a) Control film; AS and sporopollenin-alginate composite films; b) ASP5, c) ASP10, and d) ASP50 films.

3.4. SEM

Scanning electron micrographs of dry *P. nigra* pollen, sporopollenin microcapsules are presented in Figure 5. As observed in Figure 5, the structure of sporopollenin is approximately 20-25 µm. In the extraction of sporopollenin, the genetic material and the inner part of the pollen were removed and sporopollenin microcapsules were obtained. As a result of heavy chemical treatments, no breakage of sporopollenin structures was observed and the pore openings formed are approximately 0.7-1 µm.

Figure 6 shows SEM images of alginate control film (AS) and alginate-based composite films to which sporopollenin was added at different ratios (ASP5, ASP10, and ASP50). It was observed that the AS film had a smooth structure (Figure 6a), while the roughness of the films increased with increasing sporopollenin concentration (Figures 6b-d). The homogeneous distribution of sodium alginate and glycerol to form a film matrix and the presence of H bonds between them are the main reasons for the smooth structure of the AS film. According to the SEM images, sporopollenin is trapped in the film, but in homogeneously distributed. Increasing the sporopollenin concentration increased the roughness by disrupting the integrity of the film matrix. Moreover, the breakage of H bonds between alginate and glycerol and the formation of new interactions with sporopollenin caused the film to become more brittle. In conclusion, SEM analysis shows that sporopollenin was successfully integrated into the alginate film.

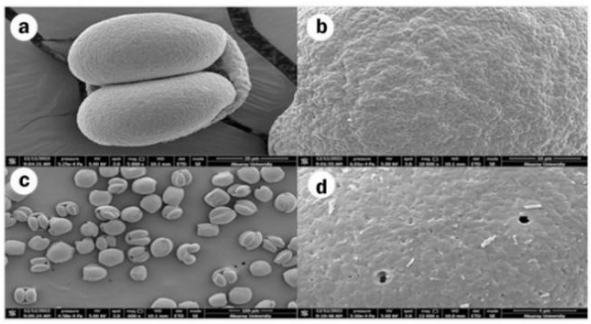

Figure 5. SEM images of *P. nigra* pollen (a-b), sporopollenin microcapsules (c-d).

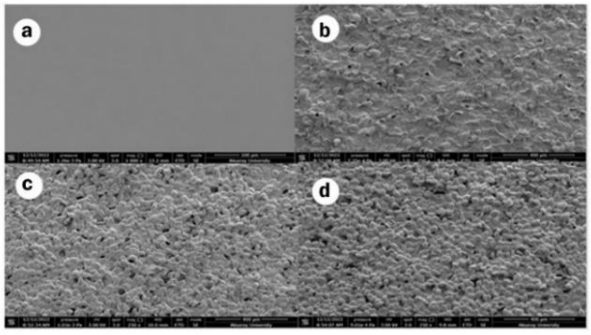

Figure 6. SEM images of a) AS, b) ASP5, c) ASP10, and d) ASP50 films.

3.5. MTT Assay

The main purpose of the MTT assay is to measure cell viability in connection with the activity of mitochondrial dehydrogenase enzymes. In living cells, ongoing mitochondrial activity reduces the MTT salt, forming formazan crystals. When these formazan crystals dissolve in solvents such as DMSO, they produce a purple color with intensity proportional to cell viability. The resulting coloration is then evaluated spectrophotometrically to obtain the MTT assay results.

MTT assays were performed at 24, 48, and 72 hours for the relevant biomaterials (Figure 7). As a control group, cells without any material, containing only DMEM culture medium, were selected. The percentage cell viabilities of the film samples compared to the control group at 24 h, 48 h, and 72 hours are shown in Figure 7. The cell viability results (MTT results) indicate that all 2x2 mm diameter samples did not exhibit cytotoxic effects on L929 cells at 24, 48, and 72 hours (values > ~70%). Additionally, at 72 hours, ASP50 showed a significant level of proliferation compared to samples ASP5 and ASP10 (**; $P<0.01$). These findings are consistent with previous studies reporting the biocompatibility of sporopollenin-based materials. Dyab et al. (2018) demonstrated that sporopollenin microcapsules preserved cell viability and maintained excellent cytocompatibility even after antibiotic encapsulation. Similarly, Akyuz Yilmaz et al. (2021) showed that chitosan–fungal spore blend films did not adversely affect cell viability. Together with our results, these studies reinforce the cytocompatible nature of sporopollenin composites and highlight their strong potential for safe biomedical applications.

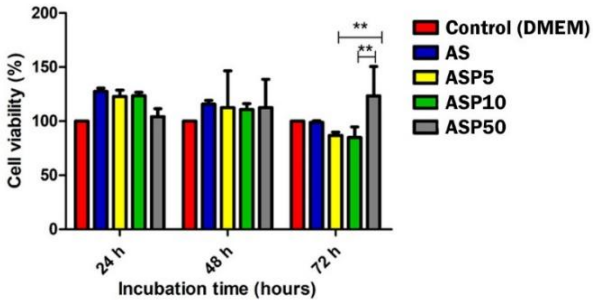

Figure 7. Cell viability assays of L929 cells after cultured on sporopollenin-alginate composite films for 24 h and 72 h (Bar represent mean of cell viability ± SEM; n = 3 statistical difference is showed as **$p < 0.05$).

4. Conclusion

In this study, sporopollenin grains isolated from *P. nigra* were used in the design of alginate-based composite films. It has been reported that mixing sporopollenin with alginate improves the thermal stability and acid-base resistance of the alginate film. Sporopollenin reinforced alginate-based composite films can be used in application areas such as material science and food

industry. Sporopollenin used in the study was obtained from *P. nigra* pollen. It is thought that microcapsules of sporopollenin obtained by removing the genetic material can be used as an ideal biomaterial in different application areas. Especially for the design of food coating, drug delivery and biomedical materials.

Author Contributions

The percentages of the author' contributions are presented below. The author reviewed and approved the final version of the manuscript.

	B.A.Y.
C	100
D	100
S	100
DCP	100
DAI	100
L	100
W	100
CR	100
SR	100
PM	100
FA	100

C=Concept, D= design, S= supervision, DCP= data collection and/or processing, DAI= data analysis and/or interpretation, L= literature search, W= writing, CR= critical review, SR= Submission and revision, PM= project management, FA= funding acquisition.

Conflict of Interest

The author declared that there is no conflict of interest.

Ethical Consideration

Ethics committee approval was not required for this study because there was no study on animals or humans.

References

Akyuz Yilmaz B, Karaduman T, Cicek M, Akata I, Kaya M. 2021. Production and characterization of nontoxic and biodegradable chitosan–ectomycorrhizal fungi spores blend films. Waste Biomass Valor, 12(11): 5899-5908.

Alshehri SM, Al-Lohedan HA, Chaudhary AA, Al-Farraj E, Alhokbany N, Issa Z, Ahamad T. 2016. Delivery of ibuprofen by natural macroporous sporopollenin exine capsules extracted from Phoenix dactylifera L. Eur J Pharm Sci, 88: 158-165.

Chiappe C, Demontis GC, Di Bussolo V, Douton MJR, Rossella F, Pomelli CS, Caporali S. 2017. From pollen grains to functionalized microcapsules: a facile chemical route using ionic liquids. Green Chem, 19(4): 1028-1033.

Dekamin MG, Karimi Z, Latifidoost Z, Ilkhanizadeh S, Daemi H, Naimi-Jamal MR, Barikani M. 2018. Alginic acid: A mild and renewable bifunctional heterogeneous biopolymeric organocatalyst for efficient and facile synthesis of polyhydroquinolines. Int J Biol Macromol, 108: 1273-1280.

Dyab AK, Mohamed MA, Meligi NM, Mohamed SK. 2018. Encapsulation of erythromycin and bacitracin antibiotics into natural sporopollenin microcapsules: antibacterial, cytotoxicity, in vitro and in vivo release studies for enhanced bioavailability. RSC Adv, 8(58): 33432-33444.

Kaya M, Akyuz L, Sargin I, Mujtaba M, Salaberria AM, Labidi J, Ceter T. 2017. Incorporation of sporopollenin enhances acid–base durability, hydrophobicity, and mechanical, antifungal and antioxidant properties of chitosan films. J Ind Eng Chem, 47: 236-245.

Lingait D, Sethy LK, Kumar A. 2024. Biopolymer sporopollenin reinforced pectin/PVA composite films for sustainable packaging application. Sustain Chem Pharm, 41: 101711.

Martău GA, Mihai M, Vodnar DC. 2019. The use of chitosan, alginate, and pectin in the biomedical and food sector—biocompatibility, bioadhesiveness, and biodegradability. Polym, 11(11): 1837.

Martins VF, Pintado ME, Morais RM, Morais AM. 2024. Recent highlights in sustainable bio-based edible films and coatings for fruit and vegetable applications. Foods, 13(2): 318.

Mohammed ASY, Dyab AK, Taha F, Abd El-Mageed I. 2021. Encapsulation of folic acid (vitamin B9) into sporopollenin microcapsules: Physico-chemical characterisation, in vitro controlled release and photoprotection study. Mater Sci Eng C, 128: 112-271.

Mujtaba M, Yilmaz BA, Cansaran-Duman D, Akyuz L, Yangın S, Kaya M, Khawar KM. 2022. Newly isolated sporopollenin microcages from Cedrus libani and Pinus nigra as carrier for Oxaliplatin; xCELLigence RTCA-based release assay. Polym Bull, 79(1): 519-540.

Pathak TS, Kim JS, Lee SJ, Baek DJ, Paeng KJ. 2008. Preparation of alginic acid and metal alginate from algae and their comparative study. J Polym Environ, 16: 198-204.

Rahman MM, Shahid MA, Hossain MT, Sheikh MS, Rahman MS, Uddin N, Hossain I. 2024. Sources, extractions, and applications of alginate: a review. Discov Appl Sci, 6(8): 443.

Tallis E. 1950. The structure of alginate fibres. J Text Inst Trans, 41(4): 151-158.

Tavassoli-Kafrani E, Shekarchizadeh H, Masoudpour-Behabadi M. 2016. Development of edible films and coatings from alginates and carrageenans. Carbohydr Polym, 137: 360-374.

Tønnesen HH, Karlsen J. 2002. Alginate in drug delivery systems. Drug Dev Ind Pharm, 28(6): 621-630.

Black Sea Journal of Engineering and Science
doi: 10.34248/bsengineering.1748071

Open Access Journal
e-ISSN: 2619 – 8991

Research Article
Volume 8- Issue 5: 1537-1547 / September 2025

THE EFFECTS OF DEVELOPMENTS IN DIGITAL TECHNOLOGIES ON THE ACTIVITIES OF MARITIME BUSINESSES AND SHIPS

Murat SAKA[1]*, Tayfun ACARER[1]

[1]*Piri Reis University, Maritime Vocational High School, Department of Maritime Transportation and Management, 34940, Istanbul, Türkiye*

Abstract: In the era of digitalization, record-breaking leaps in information and communication technologies (ICT) are revolutionizing industries worldwide, including the maritime transport sector. The theme of this research is to examine the effects of digitalization on maritime business models and ships. Utilizing a qualitative, explanatory, and applied research design, the study reviews secondary data and literature to explain how digital technologies such as broadband systems, wireless networks, and Internet of Things (IoT) are transforming maritime communication, navigation, and ship management systems. Results show that digitalization powerfully enhances operational efficiency, reduces manpower requirements, and introduces new economics paradigms like the use of cryptocurrencies. However, it also has its downsides in the shape of heightened cyber threats, particularly with the introduction of autonomous ships. The discussion stresses the need for updated training, robust cybersecurity measures, and the adoption of next-generation satellite communication technologies (like Starlink, Iridium) to preserve the industry's flexibility and security. The report finds that adjusting digital means and policies is paramount to the competitiveness, efficiency, and security of maritime players with a more data-focused world economy.

Keywords: Information and communication technologies, Digital technologies, Maritime business, Maritime communication, Ship management

***Corresponding author:** Piri Reis University, Maritime Vocational High School, Department of Maritime Transportation and Management, 34940, Istanbul, Türkiye
E mail: msaka@pirireis.edu.tr (M. SAKA)
Murat SAKA https://orcid.org/0000-0002-8637-0736
Tayfun ACARER https://orcid.org/0000-0003-2407-5552

Received: July 23, 2025
Accepted: August 26, 2025
Published: September 15, 2025

Cite as: Saka M, Acarer T. 2025. The effects of developments in digital technologies on the activities of maritime businesses and ships. BSJ Eng Sci, 8(5): 1537-1547.

1. Introduction

In today's world where oil pipelines are turning into fiber cables and oil into data, the IT sector is increasing its influence in both individual and corporate areas. Presently, the IT sector and digitalization are advancing at such a rapid pace that numerous individuals and organizations are struggling to keep pace. Today, there is no area left where the IT sector has not had an impact, both individually and institutionally. Because all technological developments in this sector also affect other sectors affected by IT to varying degrees (Tekin et al., 2006). The primary catalyst for recent developments in this sector is digitalization. Digitalization signifies real-time sophistication, and consequently, it has become the focal point of data-driven ecosystems due to new technological advancements and the resultant changes in business models. In the information technology sector, numerous definitions have been proposed regarding this subject; however, the most widely accepted definition pertains to technology utilizing binary number systems. The decimal system, characterized by ten digits, remains prevalent in everyday life, encompassing numbers from 0 to 9. This system facilitates the expression of various measurements, such as length, weight, distance, and time, using ten digits. Conversely, computer systems employ a binary number system, consisting of two digits, known as "bits," which are represented by "0" and "1." In other words, everything is very clear in the 2-digit number system. Something either exists or it doesn't. It is either black or white. In this way, uncertainty is eliminated in digital systems, and everything is defined very clearly (Acarer, 2017). The 2-digit number system, also defined as the "binary system", forms the basis of digital technology. All devices produced in this system are considered digital technology and carry the advantages of the binary number system.

Progress in digitalization has substantially advanced the IT sector, and the profound transformation within this sector impacts all industries to varying extents. Digital technology facilitates the recording of diverse system data, compression (zipping) to conserve space, data transfer, enhancement, and optional modification. The binary number system further enables device miniaturization, accelerates data communication, and enhances system capabilities. A notable manifestation of digitalization is the reduced demand for human resources in the production of these systems.

Maritime transportation is the backbone of the global

trade. Today, about 80% of global trade by volume is carried via sea (Kodak and İstikbal, 2021). A notable manifestation of digitalization in recent years has been observed in the maritime sector. This transformation is evident across various domains, including ship structures, marine communication systems, ship equipment, and maritime transportation. This evolution is encapsulated in concepts such as next-generation ships, electronic commerce, unmanned ships, and Maritime Trade 4.0. Although these concepts encompass diverse expressions, they all fundamentally stem from the differentiation introduced by digitalization in maritime contexts.

The reliance on manual or semi-automatic systems has diminished with digitalization, as exemplified in the maritime sector, where ship management has evolved. Historically, smaller tonnage ships required 35 to 40 crew members, whereas contemporary large tonnage vessels can be operated with 15 to 20 personnel. This transition has resulted in substantial savings, particularly in ship operating costs. Additionally, significant changes have occurred in ship loads and loading areas, accompanied by notable reductions in fuel expenses.

Today, technological and digital innovations frequently alter the competitive landscape, providing strategic implications and new market dynamics for companies (Saygılı, 2021). Digital technology exerts a profound influence across various sectors, significantly impacting the economy. The advancement of digital technology has led to a decline in the traditional economy. The transition between the traditional and digital economy over the 20-year period from 2005 to 2025 is illustrated graphically in Figure 1. The digital economy, whose share of global GDP has increased from 11% to 15% over the last 10 years, is expected to account for 24% of global GDP by 2025 (Huawei and Oxford Economics, 2017).

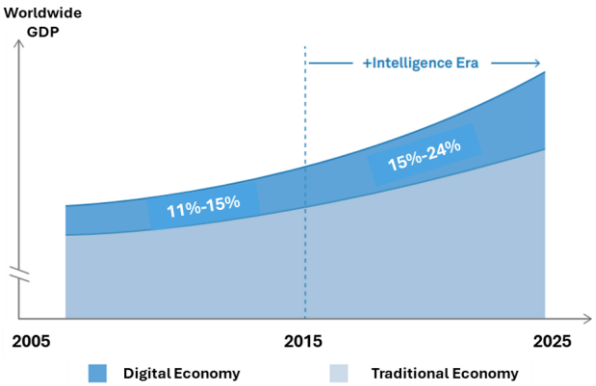

Figure 1. Projected growth in global digital economy (Huawei and Oxford Economics, 2017).

The rapid evolution of electronic commerce continues unabated. Both corporate and individual trade are increasingly transitioning to electronic platforms, significantly altering the nature of commerce. A primary driver of this transformation is the pervasive integration of mobile devices into daily life. These devices facilitate a wide range of functions, from photography to internet access, effectively becoming indispensable tools. Consequently, mobile phones have emerged as essential items in daily life (Acarer, 2020). Beyond voice communication, mobile phones now serve as critical instruments for data exchange, functioning akin to portable computers. Many individuals and organizations utilize mobile phones for mobile payments in commercial transactions, a trend that is gaining momentum. Currently, 73% of consumers are capable of making payments across various domains using their smartphones (Türkiye Bankalar Birliği, 2020). Concurrently, the increased utilization of technology, juxtaposed with a rapid decline in trust in technology, brings cryptology to the forefront. The advent of virtual currencies, which are increasingly recognized as digital money, is propelling digital economies forward. Although Bitcoin, a prominent digital currency, is a relatively recent innovation, it addresses age-old economic challenges (Koçoğlu, 2016). Over time, numerous cryptocurrencies have emerged (Tasca, 2015). Cryptocurrencies other than Bitcoin are commonly referred to as altcoins, a term derived from "alternative" and "coin" (Lee, 2015). Presently, the majority of payments and money transfers occur online, a preference that is strengthening globally due to the acceleration of digitalization and the proliferation of social networks and digital enterprises. Similar advancements are evident in the maritime sector, which demands expedited decision-making and transaction processes. The maritime industry capitalizes on digital systems to enhance its competitive edge. The adoption of digital currencies facilitates the development of payment systems and fosters faster, more secure commercial interactions. Over 2.8 billion people worldwide use mobile payment services on a regular basis as of 2024, which backs the shift towards a fully digitized economy (Statista, 2024). The annual global mobile payment transaction volume has increased over the years in parallel with the number of users. The protection of information has been a persistent challenge since antiquity, with numerous solutions devised for its safeguarding. Cryptology has emerged as the most widely accepted solution to date, effectively preventing unauthorized access to information (Yılmaz, 2007).

Currently, the United Nations estimates an economic volume of 10 trillion dollars globally. The proliferation of internet tools and the development of new payment methods significantly contribute to this figure. According to research commissioned by Google from the Boston Consulting Group (BCG), a substantial portion of this increase is attributed to the more widespread use of mobile devices and mobile phones in recent years. Because mobile equipment is one of the devices we use most frequently in our daily lives (Aktan, 2018).

In contemporary times, the most significant advancements in communication infrastructures are observed in wireless systems. Progress in 3G (Third Generation) and 4G (Fourth Generation) infrastructures continues to enhance this process. Notably, recent technological advancements have precipitated a rapid

increase in broadband data communication. Consequently, many forms of communication that were previously unattainable are now readily achievable. Figure 2 illustrates the advancements in wireless communication systems in recent years. The share of mobile connections on 4G reached its highest level in 2023, approaching 60%, but then this share began to gradually decrease as 5G became more widespread.

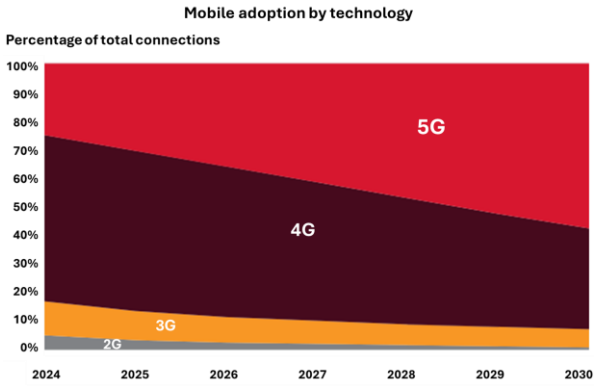

Figure 2. Development of technology investments (GSMA, 2025).

As of December 2024, 305 operators in 121 markets have launched commercial 5G mobile services, with 5G's share reaching 25%. 5G adoption is projected to catch up with 4G adoption in 2028 and approach 60% by 2030. Specifically, developments in mobile communication systems are increasingly facilitating communication from any location at any time. This has also contributed to the development and simplification of maritime trade in recent years. Today, advancements in wireless systems are not confined to mobile networks but extend to short-range systems such as Bluetooth, RFID, and NFC. This has facilitated faster and more efficient communication. Furthermore, the types and coverage areas of various wireless communication systems are comparatively depicted in Figure 3.

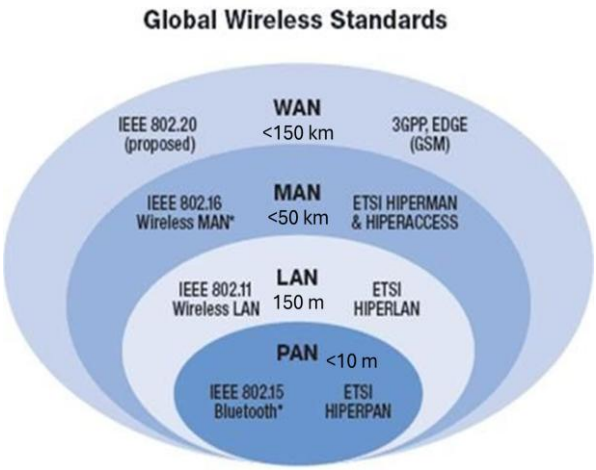

Figure 3. Wireless Networks (Cisco, 2014).

Data speed in wireless systems is increasing with each successive generation. The data speed, which reached 168 Mbps in 3G, was elevated to 300 Mbps in the initial phase with the LTE standard of 4G, and further to 1 Gbps with LTE-A (LTE - Advanced). A new era in mobile communication was inaugurated by establishing a fully IP (Internet Protocol) based communication infrastructure with 4G (Acarer, 2017).

The aim of this study is to examine the effects of developments in digital technologies on the operational frameworks, efficiency, and strategic management of maritime businesses and ships and propose conceptual, system-based solutions to problems resulting from this transformation.

2. Problems and Study Areas

2.1. The Effects of Digital Technology on Maritime

Recent technological advancements have significantly impacted various sectors, including the maritime industry, facilitating substantial changes and developments. The influence of these technological advancements on maritime operations is evident in three primary areas:

- Changes in the systems used on ships,
- Changes in ship communication systems,
- Differences in communication between maritime businesses, agencies, cargo authorities and public institutions related to maritime.

2.2. Systems Used on Ships

The reflections of technological developments on ships are mostly seen in navigation systems. Automation and especially remote-control possibilities in these systems, which are of great importance in terms of the dispatch and management of ships, have led to significant changes in the quality and quantity of personnel required on ships. In recent years, notable advancements have been made in radar systems, Ecdis, and other navigation devices, as well as ship machinery systems. These developments have introduced significant changes and conveniences in the dispatch and management of ships.

In recent years, the information technology sector has increasingly focused on the opportunities afforded by digital technology's most significant feature, the “binary system”. This includes data storage, processing, seamless sharing with other systems, and the interpretation of large datasets. Consequently, effective data communication is now feasible among interconnected devices on ships, such as Autopilot, Ecdis, AIS, and Log systems. These advancements are progressively enhancing ship dispatch and management.

The evolution of ship navigation systems is ongoing, with the ultimate goal being the development of Autonomous Ships. Another domain where technological advancements are markedly impacting ship systems is machinery systems. Innovations in ship machinery systems not only enhance their efficiency but also enable substantial labor savings. As a result, the number of machinery personnel on ships is decreasing, and

significant progress is being made in ship automation. This automation allows for remote operation of ship machinery, monitoring of malfunctions, and status observation without the need to enter the engine room. Today, it has become possible to operate and control the machinery systems of new generation ships from the bridge or other locations, to monitor system alarms from different locations and to troubleshoot problems other than mechanical malfunctions via remote control (Acarer, 2023a). The positive impacts of technological advancements in ship machinery systems continue, and further significant developments are anticipated in the near future.

2.2.1. Changes in Ship Communication Systems

Ship communication systems can be categorized into ship-internal and ship/land, ship/ship communication systems (Ekinalan, 2020). In shipboard communication systems, numerous conveniences have been introduced, particularly with the advancement of wireless communication systems. These developments have gained importance as ship sizes increase. Consequently, each extended cable offers significant maintenance and repair convenience rather than cost, as each additional cable represents a potential failure point. As the volume of information from various devices and systems on ships increases, so does the amount of cabling required to connect these devices to the central evaluation unit, typically an advanced computer system or server. With the growing prevalence of automatic systems on ships, data from sensors, detectors, and various systems is also increasing. If cables are used to transmit this data, a substantial amount of cabling becomes inevitable.

Wireless communication systems offer effective solutions to these challenges. They are particularly cost-effective for data transfer within ships and provide significant advantages in fault detection and maintenance. However, one persistent issue with wireless systems is the propagation of electromagnetic waves in enclosed metal areas, as described by the "Faraday cage" principle. To address this, relay systems are currently employed.

In recent years, numerous systems have been developed, particularly in the realm of maritime communication between ships and with terrestrial stations. Significant advancements have been achieved in wide-band data communication through these systems, which are entirely digital in nature. Currently, maritime communication is conducted via two primary platforms: satellite and terrestrial communication systems (Acarer, 2023b). Terrestrial systems include VHF and HF, while satellite systems encompass Inmarsat, Cospas Sarsat, and Iridium, among others.

A crucial component of the satellite systems currently employed on ships is the Inmarsat devices. Devices such as Inmarsat C and Inmarsat F77 are optionally available on ships undertaking long-distance voyages due to GMDSS obligations (Yılmaz and Acarer, 2014). The widespread adoption of digital technology within these systems has facilitated significant communication opportunities. Recent digital enhancements by the Inmarsat organization (International Mobile Satellite Organization – IMSO) have led to substantial reductions in communication costs and notable increases in data transmission speeds. These developments offer considerable opportunities for communication between ships and with terrestrial stations.

In the short term, the most significant changes in ship-to-ship and ship-to-land communication are anticipated with the deployment of Starlink satellites. The widespread adoption of this system, currently utilized by some large-tonnage ships and yachts, is expected to bring about substantial opportunities and transformations in maritime communication. The low installation costs and affordable communication fees associated with the Starlink satellite system are pivotal factors in its anticipated widespread adoption. Furthermore, the system's capability to facilitate wideband data communication is expected to drive its rapid adoption in marine vessels in the near future.

2.2.2. Changes in Ship Navigation Systems

It is possible to collect the navigation devices that are required to be installed on ships under the following headings.

- Radar,
- Arpa Radar
- Electronic Map (Ecdis),
- AIS
- Auto Pilot,
- Eco Sounder,
- GPS, etc.

Regarding changes in ship navigation systems, radars remain the most critical navigation devices on ships, playing a vital role in ensuring the safe navigation of vessels of all sizes. Other navigation devices serve distinct functions to ensure safe navigation.

Recent technological advancements have led to significant changes and enhancements in both the technical features and navigation-related functions of these devices. Notably, the capabilities of devices such as AIS and Ecdis, which are among the new navigational aid equipment, play a crucial role in advancing ships towards an autonomous structure. The digitalization of navigation-related data now allows for the efficient processing, analysis, interpretation, and sharing of big data with other relevant navigation systems. As a consequence of digitalization, significant advancements have been made in the development of unmanned ships in recent years. Although still in its nascent stages, the production of small-sized and low-tonnage autonomous marine vehicles has commenced. With the advent of new opportunities afforded by digitalization in navigation and communication technologies over the next decade, the proliferation of autonomous ships appears inevitable. Furthermore, recent years have witnessed substantial improvements in the remote monitoring, dispatch, and management of ships, as well as in communication between land units and ship officers. As technological advancements persist, it is

anticipated that the evolution and development of navigation systems, dispatch, and management of ships will continue.

2.2.3. The Impact of Digitalization on Ship Machinery Systems

In recent years, there have been profound changes in the machinery systems utilized on ships. Initially, steam turbine engines were employed; however, contemporary ship engines have evolved significantly in both size and functionality, becoming more technologically advanced. Recently, the machinery installed on ships is predominantly operated via remote control, with many functions being monitored remotely. Indeed, certain malfunctions can be rectified through remote intervention in these systems. Computer systems facilitate remote access to ship machinery systems, and the capabilities provided by these systems have rendered the maintenance and repair of ship engines more efficient and expedient than previously possible. Despite the substantial conveniences afforded in the operation and maintenance/repair functions of ships, which result in significant savings in personnel and time, they also pose considerable risks. This is because the structure of ships is vulnerable to cyber-attacks that could potentially render all machinery systems uncontrollable. Consequently, it is imperative to safeguard remote control systems with security measures against potential cyber threats, both internal and external.

2.3. Changes in Ship Types and Cargo Carried

One of the most significant manifestations of developments in the IT sector in recent years is the widespread use of the internet and broadband data communication. Today, the pervasive use of the internet has transformed the world into a global market.

Consequently, organizations situated in disparate locations can now communicate effortlessly, irrespective of location and time. Concurrently, there have been substantial changes in cargo transportation methods. Container transportation has been on the rise, particularly to expedite the handling of diverse cargo and minimize the risk of spoilage. The widespread adoption of this transportation method has led to significant changes in ship design, capacity enlargement, port handling times, and the structure and characteristics of ports in recent years.

In contemporary container transportation, a critical issue is the requirement for seamless and rapid internet communication among carriers, shippers, cargo authorities, and port authorities. While the duration of loading and unloading operations in container transportation has decreased, it remains essential to ensure the efficient logistics of both the containers and the cargo they carry. Specifically, the appropriate storage of containers, whether empty or full, at ports is a fundamental aspect of this transportation mode. This function necessitates a robust technological infrastructure and uninterrupted internet connectivity.

2.4. The Importance of Digitalization in the Activities of Maritime Companies

When time is not a constraint, maritime transport offers the lowest unit transportation cost among mass transportation methods (Kodak and Acarer, 2021). Currently, 85% of cargo in global trade and 97% of energy transportation are conducted via sea routes. Consequently, approximately 75% of the global population resides in coastal or near-coastal areas (Usluer, 2015).

Digitalization presents numerous opportunities to enhance the productivity, efficiency, and sustainability of the maritime industry (Heilig et al., 2017). Beyond its positive impact on ship operations, digitalization also fosters improvements in the interactions among organizations involved in maritime trade. Numerous businesses participate in the process from the initial transportation order to the final delivery to the recipient. Indeed, the transportation of cargo to ships often involves multiple transportation systems, such as railways and roads, in a combined transportation approach.

Additionally, support services, including insurance, logistics, and agency services, are utilized during cargo transportation. Coordination with various relevant organizations, particularly port authorities, is required from the point of cargo arrival at the ship to its delivery to the intended recipient. Minimizing disruptions in these processes is crucial to ensuring timely transportation activities. Therefore, establishing a fast and reliable communication network among carriers, shippers, and logistics companies is of paramount importance in contemporary maritime activities. As previously mentioned, the IT sector, a domain characterized by rapid technological advancements, has recently provided significant opportunities and conveniences. This progress continues to facilitate the establishment of communication networks with the desired features among relevant maritime organizations. In the context of technological advancements, the ability to communicate with all cargo-related organizations from any location and at any time is becoming increasingly crucial for the operations of these entities. It is anticipated that enhancements in this area will continue to grow in the foreseeable future. Consequently, it can be asserted that technological developments significantly contribute to the efficiency of maritime transportation and trade, thereby fostering the growth of maritime commerce.

2.5. Cyber Attacks on Shipping Companies

The recent wave of digitalization has impacted all sectors, including the maritime industry, leading to substantial changes and differentiations. These transformations are evident not only in the operations of maritime businesses but also in various aspects, ranging from cargo handling to navigation and machinery equipment on ships. Furthermore, new systems are emerging in ship-to-land communication, with automatic and broadband data communication becoming increasingly prevalent. These advancements, while enhancing the quality and quantity

of ship personnel, also expose unprecedented risks of cyber-attacks. Such attacks target not only land-based maritime businesses, cargo operators, agencies, and port authorities but also ships, particularly in recent years. This situation presents a heightened risk in the current era, where ships are becoming more automated and the production of autonomous ships is under consideration.

According to Pawelski (2023), cyber-attacks on the maritime transportation sector increased tenfold between 2017 and 2020. Successful cyberattacks on the maritime industry could have catastrophic consequences (Ahmed and Gkioulos, 2022). Autonomous ships are more vulnerable to cyber threats than conventional ships (Yousaf et al., 2024) and necessitate robust countermeasures (Symes et al., 2024).

Presently, cyber-attacks pose significant threats to both ships and land-based maritime organizations. Therefore, it is imperative to address this issue separately and draw the attention of all stakeholders involved in maritime activities.

3. Materials and Methods

This study adopts a design science research (DSR) approach, which is directed towards identifying real-world problems and developing novel, system-based solutions. The research process includes four phases:

(1) Conceptual Foundation: Literature review of the phenomenon of digitalization, its grounding in binary logic, and its implications for maritime information systems.

(2) Sectoral Impact Analysis: Examination of the effects of digital technologies on labor composition, cost-effectiveness, and operational patterns in maritime logistics.

(3) Technology Mapping: Identification and assessment of key ICT innovations, including wireless networks, mobile generations, broadband infrastructure, and IoT, and their relevance to maritime transformation.

(4) Problem–Solution Synthesis: Recognition of communication gaps, cybersecurity threats, and coordination problems, followed by conceptual solutions such as satellite internet systems and blockchain-enabled authentication.

The section of "Problems and Study Areas" maps out the findings to identify key challenges and trouble areas in ship operation and maritime enterprise. This section indicates the effects of digitalization on the maritime sector, the opportunities it provides in ship equipment, and new opportunities in the activities of maritime businesses and their communications with their ships. In the meantime, attention is drawn to the increasing Cyber Attacks in recent years, and the importance of this issue for businesses and ships is explained.

The "Results and Discussion" section evaluates the feasibility and relevance of the envisaged systems within the framework of the shipping industry and includes topics that can provide solutions to the problems experienced in response to the many opportunities provided by digitalization. This section also draws attention to the positive developments that digitalization has caused in the activities of maritime businesses, as well as the risks experienced, and compares them with examples.

The study uses secondary data sources, including academic literature, industry reports, and technology roadmaps, to create a contextual backdrop of digitalization of maritime operations. In this study, various conceptual solutions have been proposed for the problems addressed.

4. Results and Discussion

The Information Technology sector, internationally recognized as Information and Communication Technology (ICT), comprises two fundamental components: communication and content (Acarer, 2017). Although distinct, these components are interdependent; as communication advances, content becomes richer, necessitating further communication development. Communication, a sub-element of informatics, is categorized into fixed and wireless sub-structures (Acarer, 2021). Additionally, satellite infrastructure is identified as a separate element, constituting the wireless communication framework.

The advancements in wireless communication systems have significantly enhanced maritime communication systems and, consequently, communication between ships and land. Additionally, communication between ship operators, cargo operators, agencies, and official authorities in maritime trade has become more rapid and reliable. As a result, there has been a marked increase in international maritime trade in recent years. In the digitalized maritime sector, relevant institutions are in much greater communication with each other, allowing for the development of commercial relations at every opportunity.

4.1. Developments in Broadband Data Systems

The most tangible outcomes of advancements in information systems are evident in broadband data communication. This is because developments in data communication lead to greater differentiation in other sectors compared to other communication modes. Furthermore, significant differentiation and opportunities are provided in voice over data (Voice over Internet Protocol - VoIP), image, and media communication. Another common feature of mobile communication systems is the increasing demand for higher data communication speeds by both individual and corporate customers. To meet this demand, bandwidth must be progressively increased. Technically, achieving higher speeds in data communication necessitates more bandwidth. Consequently, having more bandwidth has become a technical imperative in every new mobile communication system. This era is characterized by the processing and interpretation of data. Figure 4 shows the increase in data traffic over the years. The increase in total data usage started with the use of LTE Advance (4.5G)

systems and then continued at an increasing rate. However, it is estimated that the real increase in data usage will come with the start of the use of 5G systems. Because the bandwidth and therefore the speed of 5G systems will be much higher than other mobile systems. International Data Corporation (IDC) forecasts the Global Datasphere to grow to 163 zettabytes by 2025.

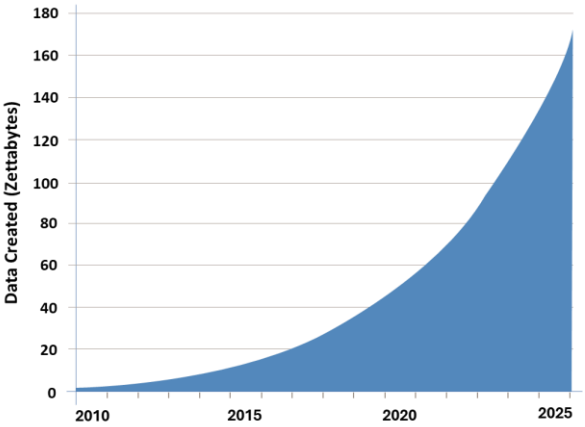

Figure 4. Annual size of the global datasphere (IDC, 2018).

The primary factor in the advancement of broadband data communication is the expansion of data communication channels, with a concurrent aim to progressively reduce latency. Consequently, the latency of 5G systems is anticipated to be lower than that of 4G, while data capacity and connection density are expected to be higher (Bass et al., 2017). As the bandwidth expands, data speed increases, resulting in a proportional increase in the amount of data transmitted per unit of time. Given the substantial data speeds achieved today, the delay in transmitting data generated by sensors and objects to central processing units has been reduced to milliseconds (Acarer, 2021).

The aggregation of data from sensors, the Internet of Things, websites, social media, mobile platforms, and organizational data has led to the emergence of the concept of "big data" (Goes, 2014). Big data analytics is employed to analyze large datasets to extract information that informs decision-making (Gandomi and Haider, 2015). The expansion of bandwidth has facilitated the emergence of various forms of communication that were previously unfeasible with narrowband, thereby providing new communication opportunities for businesses and individuals.

4.2. Developments in the Internet of Things

With the increasing developments in the software and hardware sector, there is a great increase in the amount of addressable objects and devices, and this process continues in the same way (Çavdar and Öztürk, 2018). Developments in the Internet of Things (IoT) have become increasingly prevalent in recent years. IoT, defined as communication between objects, primarily operates on wireless network technologies (Li et al., 2015). It encompasses a global network that connects physical and virtual objects, enabling dynamic communication among them (Sullivan et al., 2020). IoT facilitates the remote monitoring of equipment status (Ichimura et al., 2022). The proliferation of IoT has been further augmented by advancements in mobile access generations (IDC, 2018). Notably, in 4th generation mobile communication systems, it is possible to connect to 50 users and, consequently, 50 objects simultaneously, with download speeds of up to 1 Gbps, upload speeds of 400 Mbps, and capacity values of 100 GByte. This development has presented significant opportunities for mobile access (Acarer, 2020).

4.3. Use of Communication Systems Capable of New Generation Wideband Data Communication in Maritime Communication

To fully capitalize on the opportunities presented by digitalization within the maritime sector, the implementation of next-generation systems is paramount. These systems, characterized by the binary number system and commonly referred to as the binary system in the information technology sector, offer substantial labor and time efficiencies. They also significantly enhance the dispatch and management of ships. As digitalization advances, ship navigation systems have become increasingly technological, simplifying ship operations. In contemporary settings, particularly with the digitalization of new vessels, it is feasible to operate numerous systems, notably machinery systems, via remote control. To maximize the benefits of digitalization for maritime enterprises and vessels, it is essential to employ systems that facilitate broadband data communication between ships and land. As elucidated in section 4.1, modern communication predominantly occurs in the form of data. With broadband data communication, the transfer of substantial information volumes can occur with minimal delay, enabling many ship functions to be executed remotely. Furthermore, numerous functions related to ship activities and system operations can be easily monitored. Additionally, it is imperative to utilize fixed and mobile communication systems with broadband capabilities for communications among businesses, agencies, cargo operators, and port operators on the land side of maritime operations. It is particularly crucial for maritime organizations to optimize the use of mobile communication systems with increasingly advanced broadband features. Based on these assessments, the systems identified for use between ships and land to facilitate broadband maritime communication include the Iridium satellite system, Starlink satellite system, and Inmarsat F77 system. Moreover, satellite systems such as Global Star and Amazon are anticipated to be employed on ships in the near future, enabling broadband data communication through these systems.

4.4. Enhancing Cybersecurity Awareness Among Maritime Personnel and Organizations

Cybersecurity represents a highly specialized domain, necessitating targeted awareness training for employees. It is imperative to deliver cybersecurity training to cargo officers and port personnel within maritime enterprises,

agencies, and liaison offices, focusing on the systems they utilize. Furthermore, integrating information security courses and practices into the training programs for ship personnel, particularly officers, has become essential. This topic should be urgently incorporated into the training curriculum, with current officers receiving relevant information and orientation sessions.

Safeguarding communication systems on ships from external cyber threats is another critical concern. Attention should be directed towards implementing diverse protective measures for communication systems, including mandatory deployment of systems such as firewalls across all communication platforms. This requirement extends to both shipboard systems and land-based entities such as companies and agencies. Establishing cybersecurity laboratories within universities or related institutions is another significant measure to protect ship communication and navigation systems from cyber threats. These laboratories will facilitate security testing of systems intended for ship use. Employing personnel with expertise in both ship communication and navigation systems and cybersecurity will enable comprehensive security assessments. Consequently, expert personnel will be able to evaluate the resilience of navigation and communication systems on existing ships and those planned for new installations against cyber threats.

4.5. Use of Cryptocurrency in Different Payments of Maritime Businesses

While businesses derive substantial benefits from technological advancements, it is crucial to implement stringent safeguards against individuals and organizations that may exploit these technological opportunities for malicious purposes. In recent years, numerous organizations have adopted cryptocurrencies in payment systems that entail monetary risks. Cryptocurrencies represent an increasingly prevalent system, distinguished by the enhanced security of their transmission and accounts compared to conventional monetary systems. For an asset to be classified as money, it must be portable, durable, divisible, universally accepted, and finite in supply. Cryptocurrencies, derived from the combination of the words "crypto" and "currency" (Turan, 2018), represent encrypted money. This form of currency is a novel type of currency pair that is internet-based and decentralized (Yaktıyol, 2018). In essence, cryptocurrency is defined as "digital values that facilitate secure transactions and additional virtual money supply in an encrypted manner." Consequently, cryptocurrency serves as a novel alternative currency designed as an alternative medium of exchange (Chohan, 2022). It is both digital and virtual (Schueffel, 2017) and operates independently of the traditional banking system. Cryptocurrency (crypto asset) employs cryptography to secure transactions (Zohuri et al., 2022), which are conducted on a system known as blockchain. Cryptocurrencies should be distinctly separated from currencies not produced by governments or companies and, therefore, not issued by central banks (Çarkacıoğlu, 2016). Thus, crypto assets are entirely decentralized, in contrast to centralized banking systems (Allison, 2015). Given the mechanisms, algorithms, computer software, and hardware they utilize, cryptocurrencies are pertinent to the fields of mathematics and information technologies (Gültekin and Bulut, 2016). The proliferation of cryptocurrencies has been increasing in recent years, paralleling advancements in these scientific domains. Presently, the supply of most cryptocurrencies increases at a predetermined rate, immune to alteration by any central authority. Generally, the majority of research on cryptocurrencies has focused specifically on Bitcoin. Bitcoin and alternative cryptocurrencies have profoundly impacted various markets, particularly financial markets. They offer significant advantages, such as 24/7 trading capability, low commission fees, and high transaction speed. These features confer an advantage over traditional intermediary institutions and compel businesses engaged in trading with existing financial instruments to modify their business models (Karaoğlan, 2018). Recent developments in the Internet, notably the ability to access it ubiquitously via mobile devices, have diminished the significance of borders in trade. Cryptocurrencies are a product of this development and exemplify how technological advancements transform the financial system (Çağlar, 2007). Consequently, it is inevitable that the Internet will emerge as a formidable force diminishing the role of governments in the near future, and digital currencies will proliferate globally (Wegdell and Andersson, 2014).

The features in question regarding cryptocurrencies ensure that they are an extremely secure payment system for maritime businesses, whose activities generally involve international relations. In this way, maritime businesses can benefit from the developments in the internet and technology to the maximum extent and can also use a very secure payment system.

With the advent of the Internet, the process of accessing information has accelerated and evolved significantly. In the current Fourth Industrial Revolution, data and data-driven ecosystems are increasingly gaining prominence. Recent years have witnessed substantial growth in both the speed and capacity demands of the Internet, particularly in the realm of mobile Internet (Acarer, 2017). In the contemporary business landscape, where enterprises are progressively transitioning to online platforms, advancements in internet technology are positively influencing the structure of commerce. The Internet and various digital platforms afford businesses the capability to provide real-time feedback, facilitating seamless two-way communication between customers and enterprises (Akadal, 2019). Presently, the majority of payments and money transfers are conducted online, a trend driven by the speed and connectivity afforded by digitalization. This phenomenon enables digital enterprises to expand and strengthen their global presence. Consequently, the emerging ecosystem of

cryptocurrencies warrants attention in the field studies of economic and administrative sciences. In alignment with the opportunities presented by information systems, cryptocurrencies utilized via the Internet have emerged as a digital cash system (Nair and Motwani, 2018). This development offers significant advantages for organizations, such as maritime businesses, that require rapid and secure financial transactions.

5. Conclusion

The proliferation of digitalization is inducing profound transformations across various sectors, including maritime. Beyond the core components of the maritime sector, such as carriers, shippers, and cargo, numerous ancillary entities provide logistical support to these transportation activities. Therefore, ensuring seamless information exchange among relevant organizations is crucial for profitable and successful maritime transportation operations. Despite the acceleration of ship dispatch and management through technological advancements, numerous challenges persist. To fully leverage developing technology, it is imperative to enhance user qualifications progressively. Consequently, the number of certifications required from seafarers for ship operations is increasing, with many of these training programs necessitating periodic renewal. Digitalization is also driving significant changes in ship equipment, a process that remains ongoing. As a result, the size of ship equipment is gradually decreasing, while their interconnectivity is increasing, allowing ships to operate with reduced personnel.

One of the ultimate advancements in the digitalization of maritime vessels is the development of autonomous ships. In the operation of these autonomous, or unmanned, ships, data is collected not only from numerous sensors, detectors, and internal components but also from external sources such as positional information, weather conditions, and environmental data. This comprehensive data is processed by an advanced onboard computer system, thereby enabling the technical feasibility of unmanned ship navigation. Furthermore, various communication platforms are employed for the remote monitoring, control, and dispatch of these vessels, with satellite systems being paramount. To date, different Inmarsat terminal satellites have been utilized for this purpose. However, the use of Starlink and similar low Earth orbit satellite systems, which have rapidly advanced in recent years, is becoming increasingly prevalent in land-to-ship communications. Notably, recent amendments to the GMDSS regulations by the International Maritime Organization (IMO) have necessitated the inclusion of Iridium satellite terminals among the essential systems for ships. As digitalization in maritime operations progresses, the emergence of cyber-attacks as a novel challenge is inevitable. Although the concept of cyber-attacks is not entirely new, having been a significant issue in the IT sector for approximately 25 years, it is increasingly manifesting within the maritime industry. These attacks, which have been observed in land-based maritime entities such as shipping companies, agencies, and port authorities, particularly over the past five years, pose a substantial risk to ships as they become more automated and autonomous. Consequently, it is imperative that both the terrestrial components of the maritime sector and the ships themselves, which are among the primary beneficiaries of digital technology, prepare for potential cyber threats. Therefore, the issue of cyber-attacks warrants serious consideration and should be regarded as a distinct area of study. As in many other domains, the IT sector offers significant advancements and benefits to individuals and businesses through cryptocurrencies. In an era where time is increasingly valuable and speed is a critical factor in business competition; it is essential to rigorously evaluate the positive developments that cryptocurrencies bring to payment systems across all management frameworks. Thus, it is advantageous for maritime enterprises to consider the integration of cryptocurrencies into their commercial activities. Recent innovations in payment systems and methods can substantially enhance business opportunities. Accordingly, it is crucial for businesses to monitor the impact of IT sector developments on payment systems and cryptocurrency processes sensitively.

Author Contributions

The percentages of the authors' contributions are presented below. All authors reviewed and approved the final version of the manuscript

	M.S.	T.A.
C	40	60
D	40	60
S	60	40
DCP	40	60
DAI	50	50
L	50	50
W	40	60
CR	60	40
SR	60	40
PM	60	40
FA	50	50

C=Concept, D=design, S=supervision, DCP=data collection and/or processing, DAI=data analysis and/or interpretation, L=literature search, W=writing, CR=critical review, SR=submission and revision, PM=project management, FA=funding acquisition.

Conflict of Interest

The authors declared that there is no conflict of interest.

Ethical Consideration

Ethics committee approval was not required for this study because there was no study on animals or humans.

References

Acarer T. 2017. Bilgi ve iletişim sistemlerinde eğilim kitabı. Boyut Yayıncılık ve Tic. A.Ş., İstanbul, Türkiye, ss: 63.

Acarer T. 2020. Yeni nesil mobil erişim sistemlerinin KOBİ'lerin

finansal işlerinde sunduğu değişimler ve yeni fırsatlar. Soc Sci Res J, 9(3): 124-132.

Acarer T. 2021. Developments in the IT sector and new communication opportunities for the management of businesses. Gece Kitaplığı, Ankara,Türkiye, pp: 45-54.

Acarer T. 2023a. Endüstrideki gelişmelerin denizcilik işletmelerine ait gemilerin yönetiminde temin ettiği yeni olanaklar ve insansız gemiler. Mersin Univ Denizcilik Lojistik Araş Derg, 5(2): 122-153. https://doi.org/10.54410/denlojad.1364567

Acarer T. 2023b. VHF kısa mesafe deniz haberleşmesinin data iletişimine dönüşmesinin deniz işletmelerinin gemi yönetimleri için temin edeceği olanaklar. Den Araş Derg: Amfora, 2(3): 15-31.

Ahmed A, Gkioulos V. 2022. Utilizing AIS for command and control in maritime cyber attacks. In: Computer Security - ESORICS. Springer, London, UK, pp: 535-553. https://doi.org/10.1007/978-3-031-17143-7_26

Akadal B. 2019. Dijital pazarlamaya giriş 101. İstanbul: Eren Akademi, İstanbul, Türkiye, pp: 41-49.

Aktan E. 2018. Büyük veri: Uygulama alanları, analitiği ve güvenlik boyutu. Bilgi Yön, 1(1): 1-22. https://doi.org/10.33721/by.403010

Allison I. 2015. Nick Szabo: If banks want benefits of blockchains they must go permissionless. Int Bus Times. URL: https://www.ibtimes.co.uk/nick-szabo-if-banks-want-benefits-blockchains-they-must-go-permissionless-1518874 (accessed date: July 09, 2024).

Bass M, Berg M, Dhingra V. 2017. Drivers and path to 5G. Bell Labs Consulting, London, UK, pp: 56.

Chohan UW. 2022. Cryptocurrencies: A brief thematic review. SSRN. http://dx.doi.org/10.2139/ssrn.3024330 (accessed date: July 09, 2024).

Cisco. 2014. Network types: LAN, WAN, PAN and MAN. Available at: https://ciscorouterswitch.over-blog.com/article-network-types-lan-wan-pan-and-man-123597502.html (accessed date: July 21, 2024).

Çağlar Ü. 2007. Elektronik para: Enformasyon teknolojisindeki gelişmeler ve yeni ödeme sistemleri. Manas Univ Sos Bil Derg, 9(17): 177-186.

Çarkacıoğlu A. 2016. Kripto-para Bitcoin. Sermaye Piyasası Kurulu Araştırma Dairesi, Ankara, Türkiye.

Çavdar T, Öztürk E. 2018. A novel architecture design for internet of things. Sakarya Univ J Sci, 22(1): 39-48. https://doi.org/10.16984/saufenbilder.285444

Ekinalan TT. 2020. GMDSS el kitabı. Elif Reklam Basım Sanatları, İstanbul, Türkiye, pp: 25-29.

Gandomi A, Haider M. 2015. Beyond the hype: Big data concepts, methods, and analytics. Int J Inf Manage, 35: 137-144. https://doi.org/10.1016/j.ijinfomgt.2014.10.007

Goes PB. 2014. Big data and IS research. MIS Q, 38: III-VIII.

GSMA. 2025. The Mobile Economy 2025. URL: https://www.gsma.com/solutions-and-impact/connectivity-for-good/mobile-economy/wp-content/uploads/2025/04/030325-The-Mobile-Economy-2025.pdf (accessed date: July 21, 2024).

Gültekin Y, Bulut Y. 2016. Bitcoin ekonomisi: Bitcoin eko-sisteminden doğan yeni sektörler ve analizi. Adnan Menderes Univ Sos Bil Enst Derg, 3(3): 82-92. https://doi.org/10.30803/adusobed.288167

Heilig L, Lalla-Ruiz E, Voß S. 2017. Digital transformation in maritime ports: Analysis and a game theoretic framework. Netnomics, 18(2): 227-254.

Huawei, Oxford Economics. 2017. Digital spillover - Measuring the true impact of the digital economy. Huawei Technologies Co., Ltd. URL: https://www.huawei.com/minisite/gci/en/digital-spillover/files/gci_digital_spillover.pdf (accessed date: July 10, 2025).

Ichimura Y, Dalaklis D, Kitada M, Christodoulou A. 2022. Shipping in the era of digitalization: Mapping the future strategic plans of major maritime commercial actors. Digital Bus, 2(1): 100022. https://doi.org/10.1016/j.digbus.2022.100022

IDC. 2018. Data Age 2025: The digitization of the world. URL: https://www.seagate.com/files/www-content/our-story/trends/files/dataage-idc-report-final.pdf (accessed date: July 21, 2025).

Karaoğlan SA. 2018. Türkiye'de kripto para farkındalığı ve kripto para kabul eden işletmelerin motivasyonları. İşletme İktisat Çalış Derg, 6(2): 15.

Koçoğlu ŞÇ. 2016. Bitcoin piyasalarının etkinliği, likiditesi ve oynaklığı. İşletme Araş Derg, 8(2): 77-97.

Kodak G, Acarer T. 2021. İstanbul Boğazı'nda deniz trafik düzenlemelerinin kaza oranına etkisinin değerlendirmesi. Aquatic Res, 4(2): 181-207. https://doi.org/10.3153/AR21015

Kodak G, İstikbal C. 2021. A suggestion to improve navigational safety in the Strait of Istanbul (Bosphorus): Patrol tugs. J Black Sea, 27(3): 294-316.

Lee K. 2015. Handbook of digital currency: Bitcoin, innovation, financial instruments, and big data.: Elsevier, Amsterdam, the Netherland, pp: 63.

Li S, Xu LD, Zhao S. 2015. The internet of things: A survey. Inf Syst Front, 17: 243-259. https://doi.org/10.1007/s10796-014-9492-7

Nair J, Motwani DA. 2018. Currency: Bubble or boom. Int J Adv Res Comput Sci Manag Stud, 6(1): 35-42.

Pawelski J. 2023. Cyber threats for present and future commercial shipping. TransNav, 17(2): 261-267. https://doi.org/10.12716/1001.17.02.01

Saygılı MS. 2021. Logistics operation challenges of digital organizations. In: Ozturk I (ed.). Dark Side of Digital Organization. Peter Lang, Berlin, Germany, pp: 42.

Schueffel P. 2017. The concise fintech compendium. School of Management, Fribourg, Switzzerland, pp: 65-69.

Statista. 2024. Mobile payment transactions worldwide. URL: https://www.statista.com/statistics/1234567/mobile-payment-transactions-worldwide/ (accessed date: July 21, 2024).

Sullivan BP, Desai S, Sole J, Rossi M, Ramundo L, Terzi S. 2020. Maritime 4.0 - Opportunities in digitalization and advanced manufacturing for vessel development. Procedia Manuf, 42: 246-253. https://doi.org/10.1016/j.promfg.2020.02.078

Symes S, Blanco-Davis E, Graham T, Wang J, Shaw E. 2024. Cyberattacks on the maritime sector: A literature review. J Mar Sci Appl, 23: 689-706. https://doi.org/10.1007/s11804-024-00443-0

Tasca P. 2015. Digital currencies: Principles, trends, opportunities, and risks. SSRN. https://doi.org/10.2139/ssrn.2657598 (accessed date: July 21, 2024).

Tekin M, Güleş HK, Öğüt A. 2006. Değişim çağında teknoloji yönetimi. Nobel Yayın Dağıtım, Ankara, Türkiye, pp: 67.

Turan Z. 2018. Kripto paralar, Bitcoin, blockchain, Petro Gold, dijital para ve kullanım alanları. Ömer Halisdemir Üniv İİBF Derg, 11(3): 1-5.

Türkiye Bankalar Birliği. 2020. İnternet bankacılığı ve mobil bankacılık istatistikleri. Türkiye Bankalar Birliği, İstanbul, Türkiye, pp: 75.

Usluer HB. 2015. Liman planlama ve geliştirmede deniz bilimlerinin önemi. II. Ulusal Liman Kongresi, November 2-3,

İzmir, Türkiye, pp: 330-343.

Wegdell A, Andersson G. 2014. Prospects of Bitcoin - An evaluation of its future. MSc Thesis. Lund University, Lund, Swedish. http://lup.lub.lu.se/student-papers/record/4462711

Yaktıyol EP. 2018. Dijitalleşen dünyada: Kripto paralar. BESFİN, Ankara, Türkiye.

Yılmaz L, Acarer T. 2014. Küresel denizde tehlike ve emniyet sistemi (GMDSS), Genel Telsiz Operatör Ehliyeti (GOC). Akademi Yayınları, İstanbul, Türkiye, pp: 65-75.

Yılmaz Y. 2007. Kriptoloji uygulamalarında hukuki boyut. Marmara Univ Huk Fak Huk Araş Derg, 13(1-2): 137-147.

Yousaf A, Amro A, Kwa PTH, Li M, Zhou J. 2024. Cyber risk assessment of cyber-enabled autonomous cargo vessel. Int J Crit Infrastruct Prot, 46: 100695. https://doi.org/10.1016/j.ijcip.2024.100695

Zohuri B, Nguyen HT, Moghaddam M. 2022. What is the cryptocurrency? Is it a threat to our national security, domestically and globally? Int J Theor Comput Phys, 3(1): 1-14.

Black Sea Journal of Engineering and Science
doi: 10.34248/bsengineering.1746982

Open Access Journal
e-ISSN: 2619 – 8991

Research Article
Volume 8 - Issue 5: 1548-1555 / September 2025

EXPLORING THE ADSORPTION PERFORMANCE OF EGGSHELL POWDER FOR METHYLENE BLUE REMOVAL FROM WASTEWATER

Emine KAYHAN[1]*

[1]*Usak University, Usak University Quality Coordinatorship Department, 64000, Uşak, Türkiye*

Abstract: This study investigates the potential of eggshell (ES) powder as a sustainable and low-cost adsorbent for the removal of methylene blue (MB) dye from aqueous solutions. Batch adsorption experiments were conducted using an initial MB concentration of 20 mg/L and ES powder with an average particle size of 5.49 µm ($D_{0.5}$). The effects of pH (2, 7, and 12), contact time (0–45 minutes), and adsorbent dosage (0–40 g/L) on MB removal efficiency were evaluated. The ES powder was prepared through drying, grinding, and ball milling, and characterized using SEM, FTIR, and particle size analysis. UV–Vis spectrophotometric measurements indicated that MB adsorption was highly pH-dependent, with removal efficiency of 98% observed at pH 12, 10 g/L ES dosage, and 5 minutes contact time. The adsorption efficiency increased rapidly in the first 5 minutes, followed by a gradual plateau as equilibrium was approached. FTIR spectra confirmed interactions between MB and ES, particularly under alkaline conditions, supporting the role of electrostatic attraction. Compared to previous ES-based adsorbents, this study demonstrates improved removal efficiency at lower contact times without thermal or chemical pre-treatment, highlighting its novelty. Overall, the findings demonstrate that ES is an effective, eco-friendly adsorbent for MB removal, especially under basic pH, making it a promising candidate for wastewater treatment applications.

Keywords: Methylene blue, Eggshell powder, Adsorption, Wastewater treatment, pH-dependent removal

***Corresponding author:** Usak University, Usak University Quality Coordinatorship Department, 64000, Uşak, Türkiye
E mail: emine.kayhan@usak.edu.tr (E. KAYHAN)
Emine KAYHAN https://orcid.org/0000-0002-3015-4188

Received: July 20, 2025
Accepted: August 26, 2025
Published: September 15, 2025

Cite as: Kayhan E. 2025. Exploring the adsorption performance of eggshell powder for methylene blue removal from wastewater. BSJ Eng Sci, 8(5): 1548-1555.

1. Introduction

The presence of textile dyes, such as methylene blue (MB), poses serious environmental and public health concerns by reducing water quality, increasing biochemical and chemical oxygen demand, inhibiting photosynthesis, and causing risks of bioaccumulation, mutagenicity, and carcinogenicity (Abdulla et al., 2019; Lellis et al., 2019). Due to the recalcitrant nature of many azo dyes, conventional removal approaches often fail to achieve complete degradation, underscoring the need for innovative, eco-friendly treatment strategies (Wu, 2017; Kayhan et al., 2024; Kayhan, 2025a; M. Kayhan, 2025b).

Among available techniques, adsorption is recognized for its high efficiency, operational simplicity, and cost-effectiveness (Younis et al., 2021; Strebel et al., 2024). By contrast, many physical and chemical methods—such as coagulation, advanced oxidation, and microbial degradation—often require substantial capital investment, produce secondary pollutants, or result in complex sludge management issues (Hussain et al., 2019; Mubarak et al., 2021; Badri et al., 2022; Kathing and Saini, 2022). Although biotechnological applications, including fungal-mediated degradation, show potential for complete mineralization (Raliya et al., 2017; Nawaz et al., 2023), the chemical complexity and xenobiotic character of synthetic dyes often necessitate supplementary methods, particularly adsorption using novel, eco-friendly materials (Ajmal et al., 2014; Das et al., 2015; Rathour et al., 2019; Shah, 2019; Ledakowicz and Paździor, 2021; Yusoff et al., 2021; Selvam, 2023).

MB is a widely used cationic dye in textiles, paper production, pharmaceuticals, and medical diagnostics, yet its release into aquatic environments is problematic due to its non-biodegradable and toxic nature (Hashemi and Kaykhaii, 2022; Howland, 2022). Even though it is not acutely toxic, prolonged exposure can harm aquatic ecosystems and human health, highlighting the urgent need for efficient remediation strategies (Malekbala et al., 2015; Vassileva et al., 2023). Adsorption offers a versatile solution for MB removal, relying on the affinity between dye molecules and adsorbent surfaces (J. Fendi and A. Naser, 2018; Chkirida et al., 2021).

In recent years, attention has turned toward biomass-derived adsorbents as a means of combining waste valorization with pollution control, reflecting circular economy principles (Aragaw and Bogale, 2021; Kamath Miyar et al., 2021; Badri et al., 2022; Ferkous et al., 2022). Biowastes such as eggshells (ES) are particularly attractive due to their high calcium carbonate ($CaCO_3$) content, surface alkalinity, porosity, and abundance as

food industry by-products (Hameed, 2009; Manyatshe and Sibali, 2025). ES typically contains over 94% $CaCO_3$ along with trace organic components, providing abundant reactive sites for dye molecules (Gupta et al., 2023; Salah et al., 2025). Their eco-friendly nature, biocompatibility, and suitability for surface modification further enhance their applicability in dye removal.

Previous studies have reported promising results for ES-based adsorbents. For example, Hasan et al. (2019) employed a composite of ES and palm oil fuel ash to remove MB, achieving a 17.78% removal efficiency with calcined ES. Abdel-Khalek et al. (2017) demonstrated that thermally treated ES could achieve over 90% removal under optimized conditions. Such evidence underscores the feasibility of ES as a low-cost, sustainable, and effective adsorbent for dye-contaminated wastewater.

The present study investigates the adsorption performance of ES for MB removal from aqueous solutions, with a focus on assessing its potential as an eco-friendly and economically viable wastewater treatment material. The novelty of the present work lies in achieving higher MB removal efficiency without such pre-treatment, using only mechanically ground ES with defined particle size distribution.

2. Materials and Methods

2.1. Preparation of Adsorbent

Waste ES were collected from household kitchens. The collected shells were first manually cleaned to remove any residual organic matter and then vigorously washed with tap water, followed by thorough rinsing with distilled water to eliminate surface impurities.

After the cleaning step, the ES were dried in an oven at 110 °C for 24 hours to remove residual moisture. The dried shells were then crushed and ground into fine powder using a planetary ball mill (Optosense Opt-Qxmcm-2) at 500 rpm for 120 minutes in a zirconia jar.

The prepared powdered ES adsorbent was stored in airtight containers at room temperature prior to further characterization and adsorption experiments.

2.2. Preparation of Dye Solutions

MB solutions with an initial concentration of 20 ppm were prepared by dissolving the appropriate amount of dye in distilled water. The pH of the dye solutions was adjusted to desired values of 2, 7, and 12 using 0.1 M HCl or 0.1 M NaOH solutions and measured using a calibrated pH meter.

2.3. MB Adsorption Behavior Evaluation of ES

Batch adsorption experiments were conducted to evaluate the removal efficiency of MB using ES under varying experimental conditions, including pH, contact time, and adsorbent dosage.

In the initial set of experiments, 1 g of ES powder was added to 50 mL of MB solution at three different pH values: 2, 7, and 12. The mixtures were stirred continuously at room temperature (~25 °C) using a magnetic stirrer to ensure uniform mixing throughout the adsorption process.

The adsorption process was monitored using a UV–Visible spectrophotometer (PerkinElmer Lambda 35). An initial absorbance spectrum was recorded at 0 minutes. Subsequently, absorbance readings were taken at 5, 10, 20, 30, and 45 minutes to investigate the influence of contact time on MB removal at each pH condition. Spectral data were collected within the wavelength range of 450–750 nm to quantify the change in MB dye concentration over time and to calculate the corresponding adsorption efficiency.

After identifying the optimal pH and contact time conditions, the effect of adsorbent dosage on MB removal was systematically investigated. In this phase, different quantities of ES powder (0, 0.25 g, 0.50 g, 1 g, and 2 g) were added into separate beakers containing 50 mL of MB solution at the previously determined optimal pH and contact time. To maintain consistency, all solutions were stirred under the same mixing and temperature conditions, and their absorbance spectra were collected using a UV–Vis spectrophotometer.

The experimental results were analyzed by plotting UV–Vis absorbance and adsorption efficiency versus contact time for each pH condition. Additionally, comparative analyses of MB removal performance at varying adsorbent dosages were carried out to determine the optimal dosage for maximum dye adsorption.

2.4. Characterization of the Adsorbent

To investigate the structural and surface changes in the ES before and after the MB adsorption process, Fourier-transform infrared (FTIR) spectroscopy in the range of 400–4000 cm^{-1} using an ATR-equipped spectrometer (Spectrum Two, Perkin Elmer) was employed. FTIR spectra were recorded for four different samples: ES and ES after MB adsorption at pH 2, 7, and 12.

The average particle size of the ES was characterized by particle size distribution analyzer (Horiba LA-350 Partica).

Surface morphology of the ES was examined using scanning electron microscopy (SEM) equipped with a CeB_6 electron source (Phenom ProX SEM) both before and after dye adsorption to observe any morphological changes and surface interactions related to the adsorption process.

3. Results and Discussion

The surface morphology of ES was examined using SEM, as shown in Figure 1. At 5000× magnification, the ES surface appears highly irregular and heterogeneous, consisting of aggregated particles with varying sizes in the micron and submicron range. The presence of cracks, crevices, and interparticle voids indicates a rough and granular morphology, which enhances the availability of sites for dye molecule interaction. At 15000× magnification, a closer inspection reveals the fine-scale roughness of individual ES particles. The high-resolution image shows nanoscale protrusions and ridges across the surface, further confirming the presence of numerous active sites for adsorption. This rough texture contributes

to enhanced dye adsorption capacity by facilitating molecular diffusion and increasing the effective contact area between the adsorbent and the adsorbate.

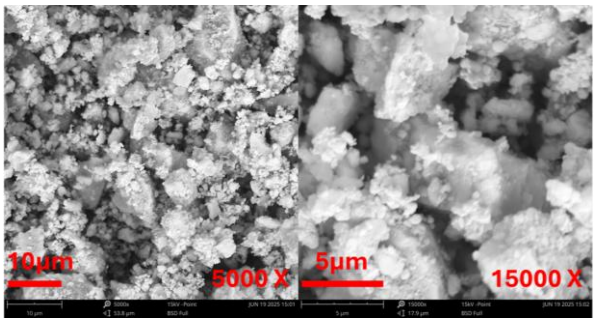

Figure 1. SEM images of ES at magnification of 5000X and 15000X.

In accordance with the particle size distribution analysis, the majority of the ground ES particles fall within the 1–12 µm range, with D(v,0.1), D(v,0.5), and D(v,0.9) measured as 1.50 µm, 5.49 µm, and 11.70 µm, respectively (Figure 2). The SEM images visually support this size distribution, as many particles observed lie within this dimensional scale. Furthermore, the relatively narrow distribution and the presence of fine particles confirm the efficiency of the grinding process. The combination of appropriate particle size and high surface roughness is expected to significantly enhance the adsorption efficiency of the ES powder in dye removal applications.

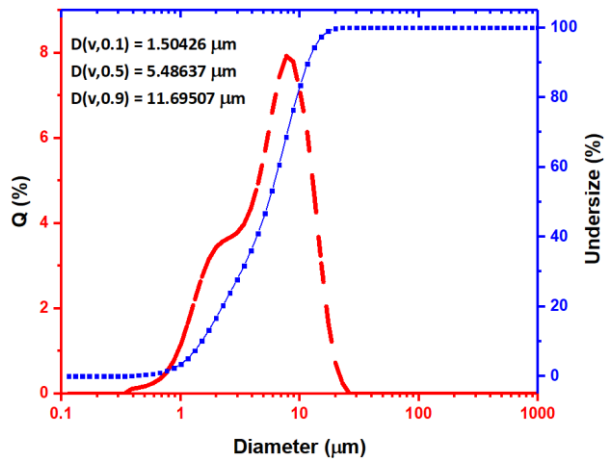

Figure 2. Particle size distribution of ground ES measured by laser diffraction of particle size distribution analysis. The red dashed line represents the differential volume distribution (Q%), while the blue solid line indicates the cumulative undersize distribution.

The UV-Vis absorption spectra of MB during the adsorption process using ES at three different pH values (2, 7, and 12) over various contact times (0, 5, 10, 20, 30, and 45 minutes) are shown in Figure 3. The characteristic absorbance peak of MB is observed around 664 nm, which corresponds to the π–π* transition of the aromatic rings in the dye molecule. The pH of the solution is a critical parameter that influences the surface charge of the adsorbent, ionization of functional groups, and speciation of dye molecules.

As evident from the UV-Vis spectra; at pH 2 (acidic conditions), the adsorption of MB was relatively low. The absorbance at 664 nm decreased slightly with time, indicating limited dye removal. This can be attributed to the high concentration of H^+ ions in acidic media, which compete with cationic MB molecules for the active adsorption sites on the ES surface. Furthermore, under acidic conditions, the surface of the ES (mainly composed of $CaCO_3$) becomes protonated, leading to electrostatic repulsion with MB, which also carries a positive charge. On the other hand, at pH 7 (neutral conditions), a moderate decrease in absorbance was observed over time, indicating improved adsorption efficiency compared to pH 2. At neutral pH, the competition from H^+ ions are reduced, and more surface sites on the ES are available for MB binding. Electrostatic interactions and possible physical adsorption contribute to the removal of dye. In contrast, at pH 12 (alkaline conditions), the most significant decrease in absorbance was observed at this pH. After 45 minutes, the MB absorbance peak was drastically reduced, indicating a high adsorption efficiency. This can be explained by the deprotonation of the ES surface under basic conditions, which leads to a negatively charged surface that strongly attracts the cationic MB molecules through electrostatic interactions. Additionally, the high pH may enhance the porosity or activation of the ES material, facilitating greater dye uptake.

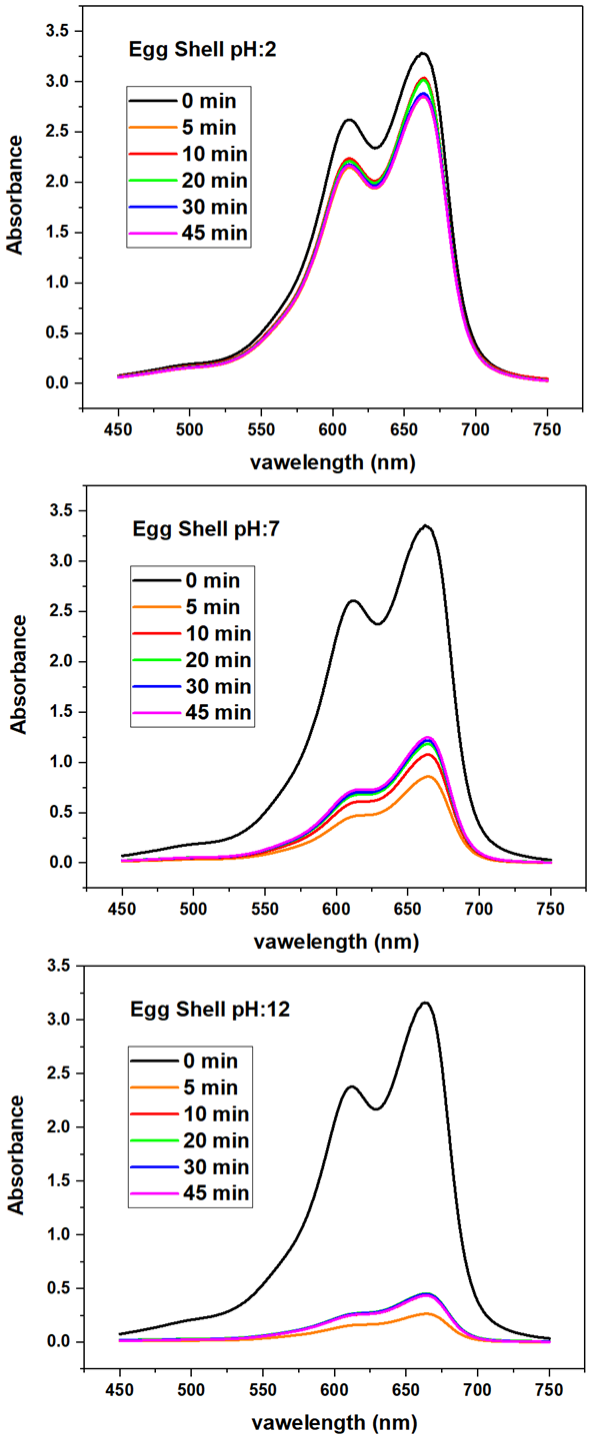

Figure 3. UV–Vis spectra of MB at pH 2, 7, and 12 after adsorption by ES over time intervals of 0 to 45 minutes.

Removal of MB at pH 2, pH 7 and pH 12 by ES is calculated by using equation 1 which is given below; Adsorption efficiency,

$$AE\% = ((C_0 - C_e) / C_0) \times 100 \quad (1)$$

where C_0 and C_e (mg/L) are the initial and equilibrium concentrations.

Adsorption efficiency versus contact time of ES with MB at pH 2, pH 7 and pH 12 is plotted in Figure 4. For all pH values, the intensity of the MB peak at 664 nm decreased with increasing contact time, confirming the time-dependent two stages of adsorption behavior (Lou et al., 2019; Savcı and Karadağ, 2020) (Figure 3). The rate of adsorption was initially rapid, particularly in the first 5 minutes, likely due to the abundance of available active sites on the ES surface. As the contact time progressed, the adsorption rate slowed down, reaching a near-equilibrium state by 30–45 minutes. This plateau indicates the saturation of active binding sites on the adsorbent surface. In the absence of strong chemisorptive forces, some MB molecules initially adsorbed onto the surface may undergo desorption. As a result, the adsorption efficiency slightly decreases after the first 5 minutes, until a dynamic equilibrium is established between adsorption and desorption processes.

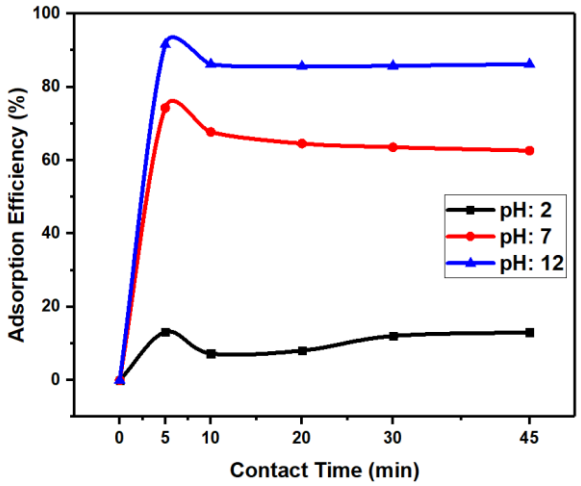

Figure 4. Contact time vs MB adsorption efficiency of ES with different starting pH values measured at an eggshell dosage of 20 g/L.

These results collectively suggest that the adsorption of MB onto ES is highly pH-dependent, with maximum efficiency achieved at pH 12. The observed trends align with typical adsorption mechanisms involving electrostatic interactions and highlight the potential of ES as a low-cost, environmentally friendly adsorbent for dye removal under alkaline conditions.

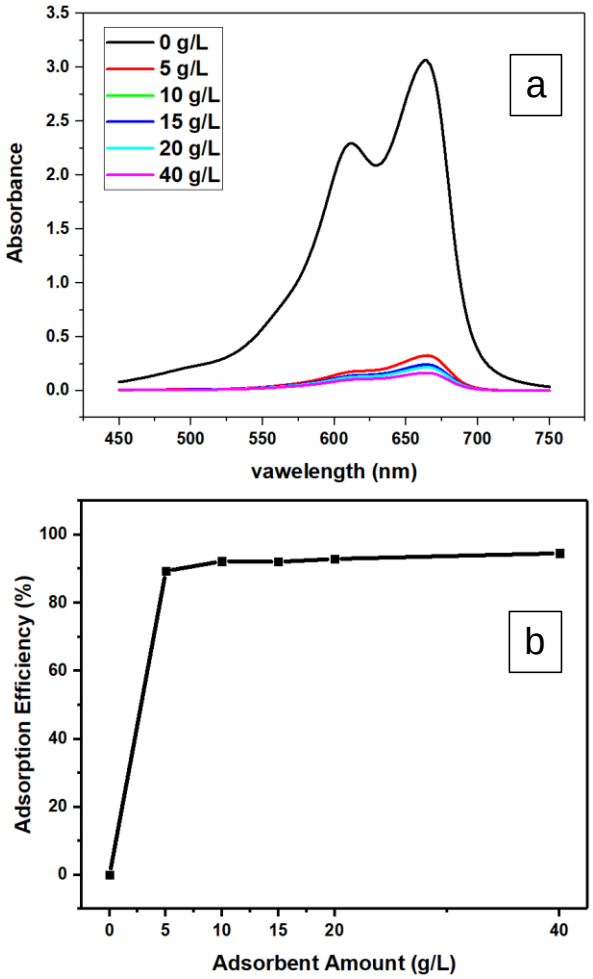

Figure 5. a. UV-Vis spectra of MB with different adsorbent amounts at pH 12, **b.** adsorption efficiency versus adsorbent amount at pH 12.

The influence of ES dosage on the adsorption of MB was investigated by varying the amount of adsorbent from 0 to 40 g/L, and the results are shown in Figure 5. Figure 5a displays the UV-Vis absorbance spectra of MB after the adsorption process for different dosages, while Figure 5b shows the corresponding adsorption efficiency.

When no ES is added (at 0 g/L adsorbent) on MB solution, the absorbance peak of MB at 664 nm is very high, confirming the presence of a high dye concentration in solution (Figure 5a). As the amount of ES increased, a gradual and significant decrease in absorbance was observed, indicating effective removal of MB. Even at a low dosage of 5 g/L, a substantial reduction in absorbance was noted, and further increases in adsorbent concentration (10, 15, 20, and 40 g/L) continued to reduce the intensity of the MB peak. The peak almost disappeared at higher dosages, demonstrating efficient dye adsorption by the ES. The plot of adsorption efficiency % versus adsorbent dosage reveals that the efficiency increased sharply with increasing dosage up to 10 g/L (Figure 5b). At 5 g/L, the adsorption efficiency reached nearly 90%, and at 10 g/L and above, it approached a plateau near 95–98%. This trend suggests that increasing the adsorbent dose provides more active sites for dye molecules to bind, leading to higher removal efficiency. Beyond 10 g/L, the adsorption efficiency increment becomes marginal, indicating that the system has reached near saturation and the available dye molecules are almost completely removed. Excess adsorbent beyond a certain point does not significantly improve performance due to the fixed initial dye concentration and limited number of dye molecules available for adsorption.

Compared to previous studies utilizing ES as a low-cost adsorbent for MB removal, the present work demonstrates significantly enhanced performance under simplified conditions. For instance, Putra et al. (2025) reported a maximum removal efficiency of 97.34% using duck eggshell powder at pH 8 and 30 minutes contact time, with complete removal only achieved in medical wastewater under specific conditions. Similarly, Hassan and Salih (2013) observed removal efficiencies ranging from 73% to 84% depending on MB concentration and contact time, with equilibrium reached after 60 minutes. In contrast, our study achieved 98% removal efficiency within just 5 minutes at pH 12 and 10 g/L ES dosage, without requiring energy-intensive pre-treatment or chemical modification. This superior performance can be attributed in part to the mechanical treatment of the eggshell using a ball mill, which effectively reduced the material into finer particles, thereby increasing surface area and enhancing adsorption efficiency.

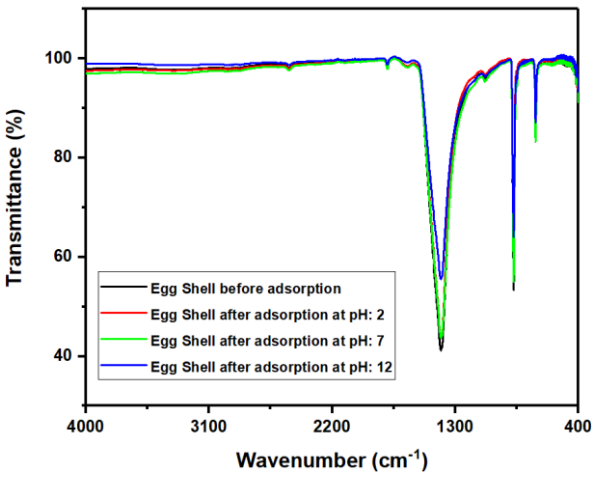

Figure 6. Comparison of FTIR spectra of ES before and after adsorption of MB, measured over the wavenumber range of 4000 to 400 cm^{-1}.

The FTIR spectra of ES before and after MB adsorption at different pH values (2, 7, and 12) are presented in Figure 6. The characteristic peaks observed around 1400–1450 cm^{-1} and 870 cm^{-1} correspond to the symmetric stretching and out-of-plane bending vibrations of carbonate ions (CO_3^{2-}), respectively, confirming the calcium carbonate-rich composition of the ES. Peaks below 720 cm^{-1} are attributed to lattice vibrations in calcite. Minor absorptions in the region above 3000 cm^{-1} can be attributed to O–H stretching vibrations of surface-adsorbed moisture or organic components.

After adsorption, notable changes in the intensity and

position of the carbonate peaks were observed, particularly at higher pH. The sample treated at pH 12 exhibited the most significant spectral alterations, including slight shifts and intensity reductions in the 1400–870 cm^{-1} region, suggesting enhanced interaction between the dye molecules and the ES surface. These changes may result from electrostatic attraction between the negatively charged ES surface and the cationic MB molecules under alkaline conditions.

Conversely, minimal spectral changes were observed in the sample treated at pH 2, indicating limited adsorption at acidic pH due to electrostatic repulsion. At neutral pH 7, moderate peak variations were recorded, reflecting intermediate adsorption behavior. Overall, the FTIR results corroborate the pH-dependent adsorption efficiency, confirming that electrostatic interactions play a critical role in the MB adsorption mechanism onto ES, with maximum adsorption occurring at pH 12. These findings are consistent with the observed increase in adsorption efficiency as the pH rises from 2 to 12, as shown in Figure 4.

5. Conclusion

The present study demonstrates the effectiveness of ES as a low-cost and environmentally friendly adsorbent for MB removal from aqueous solutions. The adsorption process was found to be strongly influenced by pH, with optimal performance observed under alkaline conditions (pH 12) due to favorable electrostatic interactions. Adsorption efficiency increased significantly within the first 5 minutes, indicating rapid uptake, and reached near equilibrium by 45 minutes. Moreover, increasing the ES dosage enhanced the removal efficiency up to a threshold, beyond which further improvements were negligible due to saturation. The optimal conditions were pH 12, 10 g/L ES dosage, and 5 min contact time, achieving 98% removal efficiency. FTIR and SEM analyses supported the adsorption mechanism and revealed structural interactions between MB molecules and the ES surface. These results highlight the potential of ES-derived adsorbents as a sustainable alternative for dye removal in wastewater treatment processes, particularly in regions where cost and material availability are critical concerns. Compared to previous studies, this work achieves high efficiency without chemical pre-treatment, emphasizing its novelty and practical applicability.

Author Contributions

The percentages of the author' contributions are presented below. The author reviewed and approved the final version of the manuscript.

	E.K.
C	100
D	100
S	100
DCP	100
DAI	100
L	100
W	100
CR	100
SR	100
PM	100
FA	100

C=Concept, D= design, S= supervision, DCP= data collection and/or processing, DAI= data analysis and/or interpretation, L= literature search, W= writing, CR= critical review, SR= submission and revision, PM= project management, FA= funding acquisition.

Conflict of Interest

The author declared that there is no conflict of interest.

Ethical Consideration

Ethics committee approval was not required for this study because of there was no study on animals or humans.

References

Abdel-Khalek MA, Abdel Rahman MK, Francis AA. 2017. Exploring the adsorption behavior of cationic and anionic dyes on industrial waste shells of egg. J Environ Chem Eng, 5(1): 319-327. https://doi.org/10.1016/j.jece.2016.11.043

Abdulla NK, Siddiqui SI, Tara N, Hashmi AA, Chaudhry SA. 2019. Psidium guajava leave-based magnetic nanocomposite γ-Fe2O3@GL: A green technology for methylene blue removal from water. J Environ Chem Eng, 7(6): 103423. https://doi.org/10.1016/j.jece.2019.103423

Ajmal A, Majeed I, Malik RN, Idriss H, Nadeem MA. 2014. Principles and mechanisms of photocatalytic dye degradation on TiO2 based photocatalysts: A comparative overview. RSC Adv, 4(70): 37003-37026. https://doi.org/10.1039/C4RA06658H

Aragaw TA, Bogale FM. 2021. Biomass-based adsorbents for removal of dyes from wastewater: A review. Front Environ Sci, 9: 764958. https://doi.org/10.3389/fenvs.2021.764958

Badri AF, Juleanti N, Mohadi R, Mardiyanto M, Lesbani A. 2022. The efficiency of Mg-Al/biochar for methyl orange and methyl red removal. Ecol Eng Environ Technol, 23(1): 202-211. https://doi.org/10.12912/27197050/142971

Chkirida S, Zari N, Achour R, Hassoune H, Lachehab A, Qaiss AE, Bouhfid R. 2021. Highly synergic adsorption/photocatalytic efficiency of alginate/bentonite impregnated TiO2 beads for wastewater treatment. J Photochem Photobiol A Chem, 412: 113215. https://doi.org/10.1016/j.jphotochem.2021.113215

Das D, Samal DP, Meikap BC. 2015. Preparation of activated carbon from green coconut shell and its characterization. J

Chem Eng Process Technol, 6: 248. https://doi.org/10.4172/2157-7048.1000248

Fendi WJ, Naser JA. 2018. Adsorption isotherms study of methylene blue dye on membranes from electrospun nanofibers. Orient J Chem, 34(6): 2884-2894. https://doi.org/10.13005/ojc/340628

Ferkous H, Rouibah K, Hammoudi NEH, Alam M, Djilani C, Delimi A, Laraba O, Yadav KK, Ahn HJ, Jeon BH, Benguerba Y. 2022. The removal of a textile dye from an aqueous solution using a biocomposite adsorbent. Polymers, 14(12): 1-6. https://doi.org/10.3390/polym14122396

Gupta A, Vennila T, Andiyappan K, Shreepad S, Sathiyamoorthy M, Gopala Gupta ASALG. 2023. Characterization of the hydroxyapathite obtained from chicken egg shell applied in bioceramics. Mater Today Proc: 2023: 1-8. https://doi.org/10.1016/j.matpr.2023.09.079

Hameed BH. 2009. Evaluation of papaya seeds as a novel non-conventional low-cost adsorbent for removal of methylene blue. J Hazard Mater, 162(2): 939-944. https://doi.org/10.1016/j.jhazmat.2008.05.120

Hasan R, Chong CC, Setiabudi HD, Jusoh R, Jalil AA. 2019. Process optimization of methylene blue adsorption onto eggshell-treated palm oil fuel ash. Environ Technol Innov, 13: 62-73. https://doi.org/10.1016/j.eti.2018.10.004

Hashemi SH, Kaykhaii M. 2022. Chapter 15-Azo dyes: Sources, occurrence, toxicity, sampling, analysis, and their removal methods. In: Dalu T, Tavengwa NT (eds). Emerging freshwater pollutants. Elsevier, London, UK, pp: 267-287. https://doi.org/10.1016/B978-0-12-822850-0.00013-2

Hassan AA, Salih ZA. 2013. Methylene blue removal from aqueous solution by adsorption on eggshell bed. Euphrates J Agric Sci, 5(2): 11-23. https://cdnx.uobabylon.edu.iq/research/E2d3HngqjUWTB76yse1BaQ.pdf

Howland MA. 2022. Chapter 3.3-Methylene blue. In: Woolf AD (ed). History of modern clinical toxicology. Academic Press, UK, London, pp: 231-241. https://doi.org/10.1016/B978-0-12-822218-8.00052-1

Hussain S, Khan S, Gul S, Khan N, Khan H. 2019. Contamination of water resources by food dyes and its removal technologies. In: Eyvaz M, Yüksel E (eds). Water chemistry. IntechOpen, London, UK, pp: 84. https://doi.org/10.5772/intechopen.90331

Kamath Miyar H, Pai A, Goveas LC. 2021. Adsorption of malachite green by extracellular polymeric substance of Lysinibacillus sp. SS1: Kinetics and isotherms. Heliyon, 7(6): e07169. https://doi.org/10.1016/j.heliyon.2021.e07169

Kathing C, Saini G. 2022. A review of various treatment methods for the removal of dyes from textile effluent. Recent Prog Mater, 4(4): 028. https://doi.org/10.21926/rpm.2204028

Kayhan E. 2025a. Temperature-controlled synthesis of bismuth tungstate with enhanced photochromic properties. Int J Appl Ceram Technol, 22(3): e15079. https://doi.org/10.1111/ijac.15079

Kayhan M. 2025b. Comparative study of photochromic behavior of bismuth tungstate via different surfactants. Ceram Int, 51(14): 19579-19588. https://doi.org/10.1016/j.ceramint.2025.02.133

Kayhan M, Aksoy M, Kayhan E. 2024. A facile synthesis of photocatalytic Fe(OH)3 nanoparticles for degradation of phenol. ChemistrySelect, 9(23): e202401367. https://doi.org/10.1002/slct.202401367

Ledakowicz S, Paździor K. 2021. Recent achievements in dyes removal focused on advanced oxidation processes integrated with biological methods. Molecules, 26(4): 1185. https://doi.org/10.3390/molecules26040870

Lellis B, Fávaro-Polonio CZ, Pamphile JA, Polonio JC. 2019. Effects of textile dyes on health and the environment and bioremediation potential of living organisms. Biotechnol Res Innov, 3(2): 275-290. https://doi.org/10.1016/j.biori.2019.09.001

Lou T, Yan X, Wang X. 2019. Chitosan coated polyacrylonitrile nanofibrous mat for dye adsorption. Int J Biol Macromol, 135: 919-925. https://doi.org/10.1016/j.ijbiomac.2019.06.008

Malekbala MR, Khan MA, Hosseini S, Abdullah LC, Choong TSY. 2015. Adsorption/desorption of cationic dye on surfactant modified mesoporous carbon coated monolith: Equilibrium, kinetic and thermodynamic studies. J Ind Eng Chem, 21: 369-377. https://doi.org/10.1016/j.jiec.2014.02.047

Manyatshe A, Sibali LL. 2025. A review on egg waste-based adsorbents for the removal of organic and inorganic contaminants from aqueous solution. Heliyon, 11(3): e42278. https://doi.org/10.1016/j.heliyon.2025.e42278

Mubarak HA, Kubba MA, Hashim K, Al-Janabi A, Safaa KH. 2021. A short review on dyes removal from water and wastewaters. IOP Conf Ser Mater Sci Eng, 1184(1): 012017. https://doi.org/10.1088/1757-899X/1184/1/012017

Nawaz M, Muhammad Afzaal D, Shahid Z, Jam M, Ahmad S, Nawaz H. 2023. Studies on the role of fungal strains in bioremediation of dyes isolated from textile effluents. Int J Econ Environ Geol, 12: 32-37. https://doi.org/10.46660/ijeeg.v12i2.100

Putra A, Fitri WE, Yuniko F, Handayani T, Hidayat H, Ighalo JO. 2025. Evaluating the potential of duck egg shell for methylene blue adsorption in medical laboratory wastewater. Pollution, 11(3): 828-845. https://journals.ut.ac.ir/article_101002_884371d4dade3fab98cfd2ceeb4277c4.pdf

Raliya R, Avery C, Chakrabarti S, Biswas P. 2017. Photocatalytic degradation of methyl orange dye by pristine titanium dioxide, zinc oxide, and graphene oxide nanostructures and their composites under visible light irradiation. Appl Nanosci, 7(5): 253-259. https://doi.org/10.1007/s13204-017-0565-z

Rathour R, Jain K, Madamwar D, Desai C. 2019. Microaerophilic biodegradation of raw textile effluent by synergistic activity of bacterial community DR4. J Environ Manage, 250: 109549. https://doi.org/10.1016/j.jenvman.2019.109549

Salah SB, Attia A, Ben Amar R, Heran M. 2025. Eggshell waste as a sustainable adsorbent for effective removal of direct dyes from textile wastewater. ChemistrySelect, 10(16): e202500149. https://doi.org/10.1002/slct.202500149

Savcı S, Karadağ F. 2020. Fast adsorption of methylene blue by filter coffee waste. NWSA Acad J, 15(4): 111-120. https://doi.org/10.12739/nwsa.2020.15.4.5a0138

Selvam K. 2023. Recent trends in agro-waste based activated carbons for the removal of emerging textile pollutants. Int J Environ Anal Chem, 103(17): 5142-5158. https://doi.org/10.1080/03067319.2021.1935910

Shah MP. 2019. Chapter 6-Bioremediation of azo dye. In: Shah MP, Rodriguez-Couto S (eds). Microbial wastewater treatment. Elsevier, London, UK, pp: 103-126. https://doi.org/10.1016/B978-0-12-816809-7.00006-3

Strebel A, Behringer M, Hilbig H, Machner A, Helmreich B. 2024. Anionic azo dyes and their removal from textile wastewater through adsorption by various adsorbents: A critical review. Front Environ Eng, 3: 1347981. https://doi.org/10.3389/fenve.2024.1347981

Vassileva P, Tumbalev V, Kichukova D, Voykova D, Kovacheva D, Spassova I. 2023. Study on the dye removal from aqueous solutions by graphene-based adsorbents. Materials, 16(17):

5754. https://doi.org/10.3390/ma16175754

Wu Y. 2017. Chapter 16-The removal of methyl orange by periphytic biofilms: Equilibrium and kinetic modeling. In: Wu Y (ed). Periphyton. Elsevier, London, UK, pp: 367-387. https://doi.org/10.1016/B978-0-12-801077-8.00016-8

Younis SA, Serp P, Nassar HN. 2021. Photocatalytic and biocidal activities of ZnTiO2 oxynitride heterojunction with MOF-5 and g-C3N4: A case study for textile wastewater treatment under direct sunlight. J Hazard Mater, 410: 124562. https://doi.org/10.1016/j.jhazmat.2020.124562

Yusoff NA, Yee LY, Iberahim NI, Zainol NA, Abdullah S, Zailani SN. 2021. Synthesis and characterization of carboxymethyl cellulose derived from office paper waste for methylene blue dye removal. IOP Conf Ser Earth Environ Sci, 646(1): 012008. https://doi.org/10.1088/1755-1315/646/1/012008

Black Sea Journal of Engineering and Science
doi: 10.34248/bsengineering.1746300

Open Access Journal
e-ISSN: 2619 – 8991

Research Article
Volume 8 - Issue 5: 1556-1560 / September 2025

A CHAIN RULE FOR REDUCED FUNCTIONAL DIFFERENTIAL INCLUSIONS AND STABILITY THEOREMS

Nurgül GÖKGÖZ[1,2]*

[1]*Çankaya University, Faculty of Arts and Sciences, Department of Computer Science, 06815, Ankara, Türkiye*
[2]*Çankaya University, Faculty of Arts and Sciences, Department of Mathematics, 06815, Ankara, Türkiye*

Abstract: In order to represent real-world problems, modeling and stability concepts of a system are two essential steps, and functional differential inclusions become favorable among other methods because of their flexibility and robustness to handle those problems. Thus, functional differential inclusions (FDIs) provide a solid foundation for engineering problems, and the calculation of their derivatives becomes an important issue in checking the stability of them. Especially, to check the Lyapunov stability, various chain rules for FDIs are defined in the literature. In this work, a new chain rule is introduced in terms of the reduction procedure, a comparison with another one is represented, and the stability theorems in terms of Lyapunov are extended to the reduced functional differential inclusions.

Keywords: Functional differential inclusions, Set-valued analysis, Convex analysis, Stability

***Corresponding author:** Çankaya University, Faculty of Arts and Sciences, Department of Mathematics, 06815, Ankara, Türkiye
E mail: nurgul.gokgoz@gmail.com (N. GÖKGÖZ)
Nurgül GÖKGÖZ https://orcid.org/0000-0002-9640-4194

Received: July19, 2025
Accepted: August 29, 2025
Published: September 15, 2025

Cite as: Gökgöz, N. 2025. A chain rule for reduced functional differential inclusions and stability theorems. BSJ Eng Sci, 8(5): 1556-1560.

1. Introduction

Functional differential inclusions (FDIs), a sophisticated branch of mathematical analysis, have emerged as a versatile framework for modeling and analyzing complex dynamical systems that exhibit intricate interactions between time-dependent variables and their histories. These powerful mathematical tools, which generalize the classic concept of differential equations, have proven invaluable in capturing the nuanced behaviors of systems that are influenced both by their current state and past trajectories. Functional differential inclusions are particularly valuable when modeling systems where the rate of change depends not only on the current state but also on the history of the state variables. These inclusions generalize functional differential equations so that they allow multi-valued right-hand sides. This allows the derivative to belong to a set of possible values rather than being uniquely defined. This property makes FDIs particularly useful for modeling systems with uncertainty, non-smooth dynamics, or control constraints. They provide benefits from different perspectives such as flexibility (FDIs handle non-uniqueness in solutions, making them suitable for systems with inherent ambiguity or multiple possible trajectories) or robustness (they model systems under uncertainty effectively, providing a framework for robust analysis and synthesis). They play a vital role in several domains such as control systems and optimization, modeling uncertainty, non-smooth and hybrid systems, population dynamics and biological models, material Science and mechanics, economics and finance in economic modeling. FDIs are widely applied in control theory, particularly in optimal control and differential games where the system's dynamics are influenced by control actions that may vary within a range of admissible values. This is common in situations with bang-bang control or state-dependent constraints (Aubin and Cellina, 1984). FDIs are used to model systems with uncertainty in the dynamics, such as when the exact form of the derivative is unknown but is known to lie within a specified set. This is critical in engineering and economics, where systems are influenced by external disturbances or imprecise measurements (Filippov, 1988). Hybrid systems that involve both continuous dynamics and discrete transitions often exhibit non-smooth behavior. FDIs can describe such systems' evolution by accommodating jumps, switches, and other discontinuities (Clarke et al., 1998). In population dynamics and epidemiology, FDIs may be used to account for time delays in reproduction or infection processes and to model systems with uncertain growth rates or carrying capacities. In economic modeling, FDIs may be used to represent markets where decisions depend on historical trends or delayed responses to changes in economic indicators. These applications align with the foundational works by Hale (1977) and Kolmanovskii and Myshkis (1992) in functional differential equations.

Apart from the previously mentioned works, recent studies on functional differential inclusions have

advanced the theory and applications significantly. In (Aitalioubrahim and Raghib, 2023), explored existence results for inclusions driven by maximal monotone operators with nonconvex perturbations are explored, broadening classical frameworks. In (Bokalo et al., 2024), strong nonlinear functional-differential variational inequalities without initial conditions are focused on, addressing dynamic processes beyond fixed starts. Research on optimal control of hereditary differential inclusions has provided insights into systems with memory effects (Mahmudov and Mastaliyeva, 2024). Additionally, the topological properties of solution sets have been studied to better understand stability and robustness (Haddad, 1981b). These studies reflect a dynamic research front, bridging advanced mathematics with applications in areas such as engineering and the sciences.

In this work, a new chain rule for functional differential inclusions is obtained by the reduction procedure defined in (Kamalapurkar et al., 2020), a comparison with the chain rule in (Liu et al., 2015) is done and the stability theorems for the reduced functional differential inclusion are obtained. The paper's structure can be summarized as the following. In Section 2, preliminaries are mentioned and the necessary definitions and theorems in order to be utilized in Sections 5.1, 5.2 and 5.3 are given. In sections 3 and 4 a new chain rule is defined and a comparison between two chain rules is considered. In Sections 5.1, 5.2 and 5.3 stability theorems for autonomous and nonautonomous systems and Razumikhin type theorems are given, respectively.

2. Functional Differential Inclusions

Observe the functional (delay) differential inclusion;

$$\dot{x} \in \mathcal{F}(t, x_t) \tag{1}$$

where $\mathcal{F}: R_{\geq 0} \times D \rightrightarrows R^n$ is a functional that is set valued and moreover, it is bounded on closed bounded subsets of D. The solutions of equation (1) are assumed to satisfy basic assumptions in (Liu et al., 2016, p. 3216) and the property (Liu et al., 2016, Theorem 1). The definitions for solution, precompact solution, maximal solution can be found in (Surkov, 2007; Kamalapurkar et al., 2020). The definitions of weakly invariant set and strongly forward invariant set can be found in (LaSalle, 1976; Surkov, 2007; Kamalapurkar et al., 2020). The set-valued functional F satisfies the, $\mathcal{F}$ is upper semi-continuous and $\mathcal{F}(\phi)$ is nonempty, compact, and convex for each $\phi \in D$ where $D \subset C_r$ is an open set containing the origin and C_r is the collection of continuous functions from $[-r, 0]$ to $\mathcal{R}^n$, with the norm $\|\phi\|_r = max_{-r \leq s \leq 0} |\phi(s)|$ and $\phi \in C([-r, 0]; R^n)$. With the given basic assumptions there exists at least a solution for (1) on the interval $[t_0 - r, T]$ for some $T > 0$ (Liu et al., 2016, Haddad, 1981a). The chain rule for delay differential inclusion (1) is given by as the following in (Liu et al., 2016). A locally absolutely continuous function x is called a solution for 2.1 if it is a solution of 2.1 and verifies $x_{t_0} = \phi$. In this case, the solution will be represented by $x(t, t_0, \phi)$ where t_0 is the initial time and $\phi \in C_r$ is the initial value. The definitions of weakly forward invariant set, strongly forward invariant set, precompactness of solutions, the conditions that admits local solutions can be found in (Liu et al., 2015).

3. Set-Valued Derivatives

Proposition 3.1. Observe the functional (delay) differential inclusion (1). Let $V: R_{\geq 0} \times R \times \mathcal{C}_r \rightarrow R_{\geq 0}$ is a functional that is locally Lipschitz and moreover the following conditions hold (Liu et al., 2016):

(1) Functional V is composite locally absolutely continuous;

(2) For each point $(\alpha, \beta) \in (R_{\geq 0} \times R) \times \mathcal{C}_r$ it is possible to find the invariant directional derivative;

(3) $V'(\alpha, \beta, z) = V^o(\alpha, \beta, z)$ for each $(\alpha, \beta) \in (R_{\geq 0} \times R) \times \mathcal{C}_r$ and $z \in R_{\geq 0} \times R$

Then for any solution $x: [t_0 - r, T]$ of (1), it holds that for almost all $t \in [t_0, T)$

$$\dot{V}(t, x(t), x_t) \in \dot{\tilde{V}}(t, x(t), x_t)$$
$$where\ \dot{\tilde{V}}(t, x(t), x_t) = \cap_{\xi \in \partial V(\alpha, x_t)} \xi \begin{bmatrix} 1 \\ \mathcal{F}(t, x_t) \\ 1 \end{bmatrix}\ and\ \alpha = (t, x(t)). \tag{2}$$

Since the chain rule in (Liu et al., 2016) represents an analogy of the chain rule defined in (Paden and Sastry, 1987) for the functional differential inclusions, then it is possible to define a chain rule analogous to the one defined in (Bacciotti, and Ceargioli, 1999).

Definition 3.2. For a locally Lipschitz functional $V: R_{\geq 0} \times R \times \mathcal{C}_r \rightarrow R_{\geq 0}$ that satisfies the conditions of (Liu et al., 2016, Proposition 1) (given in proposition 3.1), the set valued derivative of V with respect to 2.1 is defined as

$$\dot{\tilde{V}}(t, x(t), x_t) = \left\{ a \in \mathbb{R} : \exists \psi \in \mathcal{F}(t, x_t) \text{ such that } \xi^T \begin{bmatrix} 1 \\ \psi \\ 1 \end{bmatrix} = a, \forall \xi \in \partial V(t, x(t), x_t) \right\}. \tag{3}$$

Proposition 3.3. Suppose that the set valued functional $\mathcal{F}: R_{\geq 0} \times D$ is upper semicontinuous, with compact, nonempty, and convex values. If V is a locally Lipschitz functional which satisfies properties of (Liu et al., 2016, Proposition 1) (given in proposition 3.1) and $\max \dot{\tilde{V}} \leq 0$ or $\max \dot{\tilde{V}} \leq 0$, then the trivial solution of (1) is stable.

Proof. It is straightforward to verify the proof using results of (Shevitz and Paden, 1994; Bacciotti and Ceragioli, 1999).

4. Construction of Reduced Functional Differential Inclusions and Generalized Time Derivatives

Definition 4.1. For any regular, locally Lipschitz function $U: R_{\geq 0} \times R \times C_r \to R$ and the set-valued functional $H: R_{\geq 0} \times D \rightrightarrows R^n$, the reduction $R_U^H: R_{\geq 0} \times D \rightrightarrows R^n$ is define as.

$$R_U^H(t,x(t),x_t) = \{\psi \in \mathcal{F}(t,x_t) | \xi^T \begin{bmatrix} 1 \\ \psi \\ 1 \end{bmatrix} = 0, \forall \xi \in \partial V(t,x(t),x_t)\}. \quad (4)$$

By using 4.1, the chain rule 3.2 can be written as follows.

$$\max \dot{\overline{V}}(t,x(t),x_t) = \min_{p \in \partial V(t,x(t),x_t)} \max_{q \in R_V^{\mathcal{F}}(t,x_t)} \xi^T [1;\psi;1]. \quad (5)$$

Proposition 4.2. Suppose that $\mathcal{F}: R_{\geq 0} \times D \rightrightarrows R^n$ *is a functional which is upper semi-contiuous and takes nonempty, convex and compact values. Let* $V: R_{\geq 0} \times R \times C_r \to R$ be a locally Lipschitz functional with the conditions c1, c2 and c3 of (Liu et al., 2016, Proposition 1) and V : R≥0 × R × Cr → R be a regular functional. If then the trivial solution of 2.1 is stable.

$$\min_{\xi \in \partial V(t,x(t),x_t)} \max_{\psi \in R_U^{\mathcal{F}}(t,x_t)} \xi^T [1;\psi;1] \leq 0, \quad (6)$$

Proof. Using theorem 4.4 of this paper, one may prove the stability and global asymptotic stability of equation 5.1. Then the statement of the proposition is concluded. □

Definition 4.3. Let $\mathcal{U} = \{U_i\}_{i=1}^{\infty} where \{U_i\}_{i=1}^{\infty}$ where $\{U_i\}_{i=1}^{\infty}$ is a collection of real-valued locally Lipschitz regular functions. $\mathcal{F}: R \times C_r$ is defined as

$$\mathcal{F}_U(t,x_t) = \mathcal{F}(t,x_t) \cap (\cap_{i=1}^{\infty} R_{U_i}^{\mathcal{F}}(t,x_t)). \quad (7)$$

Theorem 4.4. *Let U be defined as in Definition 4.3 and* $x(t): \mathcal{I}_{\mathcal{D}} \to R$ *is a solution of 2.1. Then,* $\dot{x}(t) \in \mathcal{F}_{\mathcal{U}}(t,x_t)$ *for almost all* $t \in \mathcal{I}_{\mathcal{D}}$.

Proof. By using the fact that x(t) is locally absolutely continuous and $U(t,x(t),\beta)$ is composite locally absolutely continuous, $U_i(t,x(t),x_t)$ is locally absolutely continuous. If E_0 is the set of measure zero such that x(t) and $U_i(t,x(t),x_t)$ are not differentiable. By following the steps in (Shevitz and Paden, 1994; Liu et al., 2016, Kamalapurkar et al., 2020) it can be verified that the right derivative of $U_i(t,x(t),x_t)$ is equal to

$$\dot{U}_i(t,x(t),x_t) = \max\{\xi \begin{bmatrix} 1 \\ \mathcal{F}(t,x_t) \\ 1 \end{bmatrix} | \xi \in \partial U_i(w,x_t)\}. \quad (8)$$

With a similar approach, the left derivative of $U_i(t,x(t),x_t)$ is equal to

$$\dot{U}_i(t,x(t),x_t) = \min\{\xi \begin{bmatrix} 1 \\ \mathcal{F}(t,x_t) \\ 1 \end{bmatrix} | \xi \in \partial U_i(w,x_t)\}. \quad (9)$$

The remaining steps follow from (Kamalapurkar et al., 2020, Theorem 1) and therefore $\dot{x}(t) \in \mathcal{F}_{\mathcal{U}}$

Generalized time derivative definitions are given as follows.

Definition 4.5. The U-generalized time derivative of V , $\dot{\overline{V}}_{\mathcal{U}}$, whenever V is regular, is equal to

$$\dot{\overline{V}}_{\mathcal{U}} := \min_{\xi \in \partial V(t,x(t),x_t)} \max_{\psi \in \tilde{\mathcal{F}}_{\mathcal{U}}(t,x_t)} \xi^T [1;\psi;1]. \quad (10)$$

The U-generalized time derivative of V , $\dot{\overline{V}}_{\mathcal{U}}$, whenever V is not regular, is equal to

$$\dot{\overline{V}}_{\mathcal{U}} := \max_{\xi \in \partial V(t,x(t),x_t)} \max_{\psi \in \tilde{\mathcal{F}}_{\mathcal{U}}(t,x_t)} \xi^T [1;\psi;1]. \quad (11)$$

Definition 4.6. If V is locally Lipschitz, positive definite and if $\dot{\overline{V}}_{\mathcal{U}} \leq 0$, then V is called a U-generalized Lyapunov function for 2.1.

Theorem 4.7. *If* $V \in Lip(C_r, R)$, *then* $\forall x(\cdot) \in \mathcal{S}(\Omega)$,

$$\dot{V}(t,x(t),x_t) \in (\partial V(t,x(t),x_t))^T \begin{bmatrix} 1 \\ \mathcal{F}_{\mathcal{U}}(t,x_t) \\ 1 \end{bmatrix} \quad (12)$$

for almost all $t \in \mathcal{I}_{\mathcal{D}}$. *Moreover, if there exists a function* $W: \Omega \to R$ *such that* $\dot{\overline{V}}_{\mathcal{U}}(t,x(t),x_t) \leq W(t,x(t),x_t)$, $\forall (t,x(t),x_t) \in \Omega$ *then* $\dot{V}_{\mathcal{U}}(t,x(t),x_t) \leq W(t,x(t),x_t)$, *for almost all* $t \in \mathcal{I}_{\mathcal{D}}$.

Proof. Investigate two cases: when V is regular or not. If regular, the result follows from (Bacciotti, and Ceargioli, 1999). If not regular, then the result is obtained from (Shevitz and Paden, 1994). □

5. Stability Theorems for Reduced Functional Differential Inclusions

5.1. Stability of Autonomous Systems

Consider the functional differential inclusion;

$$\dot{x} \in \mathcal{F}(x_t) \tag{13}$$

Theorem 5.1. *Let V be a functional such that* $V: \mathcal{C} \to R$ *and* $\dot{\overline{V}}_{\mathcal{U}} \leq 0$ *for all* $\phi \in G$ *and* $f \in F(\phi)$*. Moreover, assume that x(t) is precompact and* x_t *remains in G for all* $t \geq 0$*. Then, for some c,* x_t *approaches* $M_v \cap V^{-1}(c)$*.*

Proof. Two cases are investigated. If V is regular then the result follows from (Liu et al., 2015, Theorem 1) and from very well-known Arzela-Ascoli theorem, omega limit set is compact. If V is not regular, then the result follows from (Kamalapurkar et al., 2020, Theorem 19) and (Moreau and Valadier, 1987).

5.2. Stability of Nonautonomous Systems

Definition 5.2. The differential inclusion (1) is said to be uniformly stable at x = 0 if $\forall \epsilon > 0$ $\exists \delta > 0$ such that if $x(\cdot) \in \overline{\mathcal{B}}(0,\delta) \times \mathcal{R}_{\geq 0}$, then $x(\cdot)$ is complete and $x(t) \in \overline{B}(0,\epsilon)$, $\forall t \geq t_0$.

Theorem 5.3. Consider (1). Let $V: R_{\geq 0} \times \mathcal{C}_r \to R_{\geq 0}$ be a locally Lipschitz functional. If there exist positive definite functions u, v , w that is positive for s > 0, and u(0) = v(0) = 0. If the following condition is satisfied

$$u(|\phi(0)|) \leq V(t,\phi) \leq v(|\phi|) \tag{14}$$

$$\dot{\overline{V}}_{\mathcal{U}}(t,\phi) \leq -w(|\phi(0)|) \tag{15}$$

then the solution $x = 0$ *of (2.1) is uniformly stable.*

Proof. Investigation of two cases is enough to prove the theorem. If $\dot{\overline{V}}_{\mathcal{U}}$ is regular follow (Liu et al., 2016, Theorem 3). If $\dot{\overline{V}}_{\mathcal{U}}$ is not regular follow similar steps to (Kamalapurkar et al., 2020, Theorem 19) and (Moreau and Valadier, 1987).

5.3. Razumikhin Theorem

The chain rule will be defined by reduced Lyapunov functions in this case. More specifically, the chain rule will be defined as

$$\dot{\overline{V}}(t,x(t)) = \{a \in \mathbb{R} : \exists \psi \in \mathcal{F}(t,x_t) \text{ such that } \xi^T \begin{bmatrix} 1 \\ \psi \end{bmatrix} = a, \forall \xi \in \partial V(t,x(t))\}. \tag{16}$$

Theorem 5.4. Observe the equation (1). $u, v, w: R^+ \to R^+$ such that u, v, w are continuous functions and they are non-decreasing, u(s), v(s) positive whenever s > 0 and u(0) = v(0) = 0. Moreover, v is strictly increasing. Assume that a continuous function $V: R \times R^n \to R$, with the following conditions

$$u(|x|) \leq V(t,x) \leq v(|x|), \quad t \in \mathbb{R}, x \in \mathbb{R}^n, \tag{17}$$

and

$$\dot{\overline{V}}_{\mathcal{U}}(t,\phi(0)) \leq -w(|\phi(0)|) \text{ if } V(t+\theta,\phi(\theta)) \leq V(t,\phi(0)), \tag{18}$$

exist for $\theta \in [-r,0]$*. Then the trivial solution,* $x = 0$*, of (2.1) is uniformly stable.*

Proof. Start by choosing some variable θ_0 from [−r,0]. Check the cases where $\theta_0 < 0$ and θ_0. Then use of theorem 5.3 for non-autonomous case of this paper. This finishes the proof of uniform stability.

6. Conclusion

In summary, the chain rule and stability theorems constitute fundamental analytical tools for functional differential inclusions, offering a robust framework for the investigation of intricate system behaviors and the verification of solution dependability. The chain rule, particularly in its generalized forms applicable to set-valued mappings and non-smooth analysis, facilitates the computation of derivatives along solution trajectories, thereby enabling the characterization of system sensitivity to perturbations and parameter variations. Stability theorems, encompassing Lyapunov-like approaches and fixed-point methodologies, furnish criteria for ascertaining the qualitative properties of solutions, including boundedness, convergence, and robustness in the face of uncertainties. These theoretical underpinnings are not merely abstract mathematical constructs but have tangible implications across various scientific and engineering disciplines. Functional differential inclusions, which inherently incorporate memory effects and hereditary characteristics, demand sophisticated mathematical techniques for their analysis, where the chain rule allows for the effective propagation of derivative information through the functional arguments of the inclusion, while stability theorems provide a rigorous basis for assessing the long-term behavior of solutions, ensuring that the system's response remains within acceptable bounds.

Future investigations may extend the reduction-based chain rule to stochastic and more general classes of functional differential inclusions, broadening its theoretical scope. At the same time, integrating these analytical advances with computational techniques could facilitate the stability assessment of complex systems, reinforcing the connection between abstract analysis and applied practice.

Author Contributions

The percentages of the author' contributions are presented below. The author reviewed and approved the final version of the manuscript.

	N.G.
C	100
D	100
S	100
DCP	100
DAI	100
L	100
W	100
CR	100
SR	100

C=Concept, D= design, S= supervision, DCP= data collection and/or processing, DAI= data analysis and/or interpretation, L= literature search, W= writing, CR= critical review, SR= submission and revision.

Conflict of Interest

The author declared that there is no conflict of interest.

Ethical Consideration

Authors of this manuscript follow all ethical guidelines including authorship, citation, data reporting, and publishing original research.

References

Aitalioubrahim M, Raghib T. 2023. Functional differential inclusions with maximal monotone operators and nonconvex perturbations. Filomat, 37(20): 6793-6811.

Aubin JP, Cellina A. 1984. Differential inclusions: Set-valued maps and viability theory. Springer, Berlin, Germany, pp: 56-59.

Bacciotti A, Ceragioli F. 1999. Stability and stabilization of discontinuous systems and nonsmooth Lyapunov functions. ESAIM Control Optim Calc Var, 4: 361-376.

Bokalo M, Skira I, Bokalo T. 2024. Strong nonlinear functional-differential variational inequalities: Problems without initial conditions. Front Appl Math Stat, 10: 54-61.

Clarke FH, Ledyaev YS, Stern RJ. 1998. Nonsmooth analysis and control theory. Springer, New York, USA, pp: 48-59.

Filippov AF. 1988. Differential equations with discontinuous right-hand sides. Kluwer Academic Publishers, Dordrecht.

Haddad G. 1981a. Monotone viable trajectories for functional differential inclusions. J Differ Equ, 42: 1-24.

Haddad G. 1981b. Topological properties of the sets of solutions for functional differential inclusions. Nonlinear Anal Theory Methods Appl, 5(12): 1349-1366.

Hale JK. 1977. Theory of functional differential equations. Springer, New York, USA, pp: 152-159.

Kamalapurkar R, Dixon W, Teel AR. 2020. On the reduction of differential inclusions and Lyapunov stability. ESAIM Control Optim Calc Var, 26: 24.

Kolmanovskii VB, Myshkis AD. 1992. Applied theory of functional differential equations. Kluwer Academic Publishers, Copenhagen, Netherlands, pp: 45-49.

LaSalle JP. 1976. The stability of dynamical systems. SIAM, Philadelphia,USA, pp: 65-69.

Liu KZ, Sun XM, Wang W, Liu J. 2015. Invariance principles for delay differential inclusions. Chin Control Decis Conf (CCDC): 123-135.

Liu KZ, Sun XM, Liu J, Teel AR. 2016. Stability theorems for delay differential inclusions. IEEE Trans Autom Control, 61(10): 3215-3220.

Mahmudov EN, Mastaliyeva D. 2024. Optimal control of second order hereditary functional-differential inclusions with state constraints. J Ind Manag Optim, 20(11): 3562-3579.

Moreau JJ, Valadier M. 1987. A chain rule involving vector functions of bounded variation. J Funct Anal, 74:333-345.

Paden BE, Sastry SS. 1987. A calculus for computing Filippov's differential inclusion with application to the variable structure control of robot manipulators. IEEE Trans Circuits Syst, 34(1): 73-82.

Shevitz D, Paden B. 1994. Lyapunov stability theory of nonsmooth systems. IEEE Trans Autom Control, 39(9): 1910-1914.

Surkov AV. 2007. On the stability of functional-differential inclusions with the use of invariantly differentiable Lyapunov functionals. Differ Equ, 43(8): 1079-1087.

Black Sea Journal of Engineering and Science
doi: 10.34248/bsengineering.1754321

Open Access Journal
e-ISSN: 2619 – 8991

Research Article
Volume 8 - Issue 5: 1561-1576 / September 2025

EFFECT OF WORMHOLE DEFECTS ON ELECTRIC FIELD DISTRIBUTION UNDER COMPOSITE VOLTAGE

Emre TUNÇ[1], Murat FİDAN[1]*

[1]*Bolu Abant Izzet Baysal University, Faculty of Engineering, Department of Electrical and Electronics Engineering, 14030, Bolu, Türkiye*

Abstract: The reliability of electrical insulation systems is critical to the continuity of energy transmission and distribution systems. Structural defects that occur in polymer-based insulating materials can affect the distribution of electric fields, leading to partial discharges and subsequently serious failures such as breakdowns. In this study, the effects of wormhole structures with different diameters in cross-linked polyethylene (XLPE) insulators on electric field distribution under alternating current (AC), direct current (DC), and composite voltage (AC+DC) components were numerically investigated using COMSOL Multiphysics software. In the system modeled under a needle-plane electrode configuration, significant increases in both volumetric and surface electric field intensities were observed as the diameter of the wormhole increased. Among all cases, composite voltage conditions resulted in the highest field concentrations, indicating increased electrical stress on the insulation. Additionally, higher field intensities were observed under negative polarity than under positive polarity in all cases. The findings highlight the importance of considering wormhole-type defects in the design of insulating systems and analyzing the electrical stress caused by composite voltage conditions.

Keywords: Wormhole, Composite voltages, Electric field, High voltage

***Corresponding author:** Bolu Abant Izzet Baysal University, Faculty of Engineering, Department of Electrical and Electronics Engineering, 14030, Bolu, Türkiye
E mail: mfidan@ibu.edu.tr (M. FİDAN)
Emre TUNÇ https://orcid.org/0000-0002-1264-8571
Murat FİDAN https://orcid.org/0000-0003-2181-070X

Received: July 31, 2025
Accepted: September 02, 2025
Published: September 15, 2025

Cite as: Tunç E, Fidan M. 2025. Effect of wormhole defects on electric field distribution under composite voltage: a COMSOL Multiphysics-based approach. BSJ Eng Sci, 8(5): 1561-1576.

1. Introduction

Today's advancing technology and increasing energy needs make it essential for electrical energy systems to operate more efficiently, reliably, and sustainably (Kadim et al., 2021). In this context, the quality of the insulation systems used is as important as the mechanical and electrical integrity of the production, transmission, and distribution systems. Electrical insulators play a crucial role in preventing failures in transmission and distribution equipment, directly affecting the continuity, safety, and economic operation of energy systems (Ispirli et al., 2022a; Freitas-Gutierres et al., 2024). Deterioration in the performance of insulators can result in serious consequences, such as short circuits, arc formation, or complete failure of equipment functionality (Kavanagh et al., 2020; Tunç and Fidan, 2023; Park et al., 2024). This may impair the integrity of the energy system and pose risks to both system components and connected devices.

Insulation systems operate under increasingly complex electrical stresses in modern systems, where more compact designs are being adopted and higher voltage levels are preferred (Adhikari and Ghassemi, 2024). Insulators operating under high voltage must withstand not only normal operating conditions but also high-frequency pulses (Borghei and Ghassemi, 2022), harmonic voltages (Fidan and Ismailoglu, 2017), composite voltages (Li et al., 2019), transient states (Annadi and Patsa, 2020), and environmental effects such as temperature and humidity (Roggendorf and Schnettler, 2012; Negari and Moghadam, 2024). Under these conditions, the electrical endurance limits of insulators can be significantly reduced, particularly due to defects in their internal structures or surfaces. Therefore, characterizing defects in insulation systems and quantitatively determining their effects on electric field distribution is crucial for enhancing system reliability and reducing the risk of failure.

Air gaps are among the defects frequently observed in insulating materials (Qiu et al., 2015). Microcracks are also frequently reported in the literature (Dissado and Fothergill, 1992; Stone et al., 2014; Kavanagh et al., 2020). Bubbles and irregular geometric structures can also be considered among other important defects (Tian et al., 2017; Zheng et al., 2021; Zhao et al., 2024). These defects can form during the material's production process or operation and can further intensify the electric field, especially in areas where the electric field is concentrated, such as sharp-tipped electrodes. These field intensifications can lead to the formation of electrical treeing and partial discharge over time (Ghassemi, 2018; Zhang et al., 2021; Adhikari and Ghassemi, 2024). This accelerates the degradation process of the insulating material (Borghei and Ghassemi, 2022; Kavanagh et al., 2020). As a result, permanent damage to the insulation

structure may occur. This can reduce the reliability of power systems and cause serious operational issues.

The wormhole effect (Zhao, 2022), which has been increasingly discussed in the literature in recent years, has been found to be closely related to the formation of partial discharges in insulating materials (Li et al., 2017; Li et al., 2019; Wu et al., 2024). A wormhole is a structural defect in an insulator characterized by the formation of thin, long, channel-like gaps or cracks (Rosenberg et al., 2010; Zhao et al., 2013; Gong et al., 2020). Such structures can cause excessive concentration of the electric field in certain areas, leading to insulation failures such as breakdown, partial discharge, or thermal degradation (Zhao et al., 2013; Li et al., 2017). In this context, the numerical and experimental investigation of the effects of wormhole defects on electric field distribution is of significant importance for enhancing the reliability of insulation systems.

Li et al. (2017) investigated the effect of temperature on partial discharges under DC using an oil-paper insulation model in a configuration with a needle plane electrode. The study also investigated the breakdown characteristics of the insulation material under the wormhole effect. In the study conducted to experimentally verify the wormhole effect (Zhao et al., 2013), bulk breakdown and surface discharge properties were investigated on organic glass and polystyrene samples by applying different pulse durations (10 ns and 7 μs) at different voltage levels (100 kV, 130 kV, and 170 kV). Theoretical evaluations of the fundamental physical mechanisms underlying the wormhole effect were presented by analyzing the surface discharge threshold and delay time. In addition to the wormhole effect, which has been discussed only limitedly in the literature, there are also different studies conducted under non-homogeneous electric fields.

In a study conducted by Lin et al. (2024) the effects of mixed voltage components on the channel discharge formation mechanism were investigated using a 3-electrode configuration consisting of a needle electrode and a pair of parallel plates. Hamidieh and Ghassemi (2024) computationally investigated the effect of different needle electrodes with conical cross-sections on negative corona discharge. The study particularly focuses on Trichel current pulses, which are regular and repetitive small current pulses observed during negative corona discharge. Dordizadeh et al. (2017) presented an experimental study investigating Trichel pulses in a needle-plane electrode geometry. In this study, the effects of parameters such as corona voltage, gap distance, and tip radius on the characteristics of Trichel pulses were investigated.

Saini and Prasad (2024) investigated the surface charging characteristics of polymeric insulators under AC corona discharge at low pressure conditions. Discharge generation was performed under different electrode configurations, including single-needle, double-needle, and triple-needle configurations. Zhao et al. (2017) investigated the discharge characteristics of CF_3I/N_2 gas mixtures under standard lightning impulse voltage in needle-plane and sphere-plane electrode configurations, which are important for CF_3I and its mixtures used in electrical equipment. Chen et al. investigated the breakdown characteristics of the SF_6/N_2 gas mixture under an extremely non-uniform electric field using an experimental setup isolated from external influences (Chen et al., 2022). In another study, Chen et al. (2019) conducted an experimental study on negative corona discharges under a needle-plane electrode configuration in a container where gas humidity and pressure could be precisely controlled. In this study, the transition characteristics of discharge modes were examined in detail under the influence of electrode curvature radius, humidity, and pressure.

The behavior of wormhole-type structural internal defects in insulating materials under complex stresses remains an area that has yet to be explored in the literature. This study aims to numerically investigate the effects of wormhole structures with different diameters on the electric field distribution under composite voltage conditions consisting of AC and DC components. Simulation analyses performed in the COMSOL Multiphysics environment were used to evaluate how volumetric and surface electric field intensities vary depending on the presence and size of structural defects in the material. The obtained results are expected to contribute to the existing knowledge on the behavior of insulation systems and provide a foundation for future experimental or theoretical studies.

2. Materials and Methods

2.1. Composite Voltages

Electrical insulation systems are often subjected not only to a single type of voltage stress but to the simultaneous influence of multiple voltage components (Ispirli et al., 2022a). In the literature, insulation systems have been investigated under AC conditions (Hu et al., 2022; Yang et al., 2022). Similarly, there are investigations conducted under DC (Beroual et al., 2013; Muppala and Reddy, 2021). Moreover, in some studies, insulation systems have been evaluated solely under the influence of impulse voltage. (Liang et al., 2020; Reddy et al., 2023). However, in real operating conditions, especially in modern power systems, these voltage components may occur together. The AC + DC composite voltage resulting from the simultaneous application of AC and DC components can cause stress beyond standard test conditions, significantly affecting the voltage withstand capability of insulation systems. In this case, the resulting electric field distribution differs from that formed under AC or DC alone, which may cause regional field concentrations and early insulation degradation.

The widespread adoption of HVDC technologies has increased the need for AC–DC conversion in power transmission and has led to the widespread use of power electronics-based systems. In parallel with these developments, it has become more likely for electrical

equipment to operate under composite voltages, including both AC and DC components. Therefore, tests conducted under single voltages alone may be insufficient to represent the actual operating conditions of the systems. In particular, when the positive or negative component of the DC voltage combines with the AC voltage, the electrical discharge mechanism and breakdown voltage behavior can vary significantly depending on the polarity (Ispirli et al., 2022b).

In this context, examining the effects of composite voltages on insulation systems is important not only from a theoretical perspective but also in terms of understanding performance under real-world conditions. In particular, a detailed assessment of insulation behavior under composite voltages consisting of AC and DC components plays a critical role in the design and validation processes of new-generation power systems.

2.2 Geometrical and Electrical Configuration of the Test System

This section presents a simulation study of wormhole structures modeled in insulating material under a non-uniform electric field at different voltage levels and types. The needle-plane electrode configuration was modeled using the COMSOL Multiphysics program. In the study, the electric field distribution in the insulation system was analyzed in detail using COMSOL Multiphysics software for different wormhole diameters. The Electric Currents module was used for the electric field distribution analysis.

The structural features and electrical parameters of the system modeled in the COMSOL Multiphysics environment are presented in Table 1.

A stainless steel disc with a thickness of 5 mm and a diameter of 300 mm was modeled as the plane electrode. The diameter of the plane electrode was determined based on similar studies in the literature (Lan et al., 2012). Stainless steel was selected as the electrode material due to its high electrical conductivity, corrosion resistance, and experimental repeatability, which is also a preferred approach in (Timoshkin et al., 2009).

The needle electrode was modeled with a curvature radius of 100 μm and a length of 50 mm using stainless steel material due to these advantages. The material and dimensional specifications of the needle electrode were determined based on similar studies in the literature (Liu et al., 2013; Rubinetti et al., 2024). In the COMSOL Multiphysics environment, the gap between the electrodes was set to 2 mm. XLPE is widely used as a cable insulation material due to its excellent insulation performance, favorable electrical and mechanical properties, and cost-effectiveness (Dong et al., 2019). Therefore, XLPE with dimensions of 2 × 400 × 400 mm (thickness × width × length) was selected as the insulating material in this study. Wormhole channels with various diameters were introduced within the volume of the insulating material. The entire test model was constructed using COMSOL's built-in CAD tools, and tetrahedral mesh elements with a maximum size of 5 mm were used. Visual representations of the model's geometric dimensions are presented in Figure 1.

The electric field distribution of the insulator and electrode configuration modeled in the COMSOL Multiphysics environment was analyzed under different voltage levels and types. The voltage waveforms used in the study were generated by the IEC 60060-1:2010 standard. This standard defines the technical principles for high-voltage testing under composite voltage conditions (Dedeoglu and Merev, 2023; IEC 60060-1:2010 - High-Voltage Test Techniques - Part 1: General Definitions and Test Requirements, 2010). These voltage levels and types are listed in Table 2.

Table 1. Structural features of the modeled test system

Parameter	Description / Value
Electrode Configuration	Needle–Plane Electrode (Stainless Steel Material)
Needle Electrode Size	r_{tip}= 100 μm, h= 50 mm
Plane Electrode Size	r=300 mm, thickness= 5 mm
Insulating MaterialSize and Type	2 x 400 x 400 mm (thickness × width × length) XLPE ($\varepsilon_{XLPE} = 2.4$)
Wormhole Channel Diameter	0 μm ,50 μm, 75 μm, 100 μm, 150 μm, 200 μm

Table 2. Voltage types applied to the test model along with associated mathematical expressions

Voltage Type	Mathematical Expression of Voltage
AC	$V_{AC} = 170000\sin(2\pi ft)\ V$
DC	$V_{DC} = 85000$ V
Composite Voltage	$V_{composite} = 170000\sin(2\pi ft) + 85000\ V$

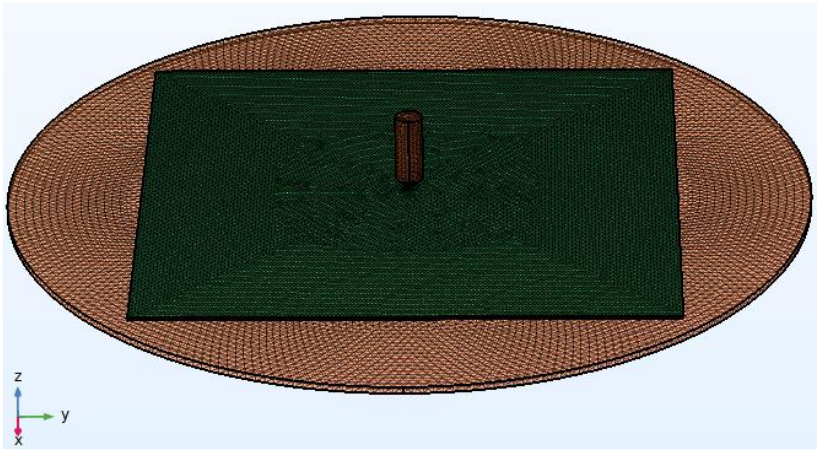

(a)

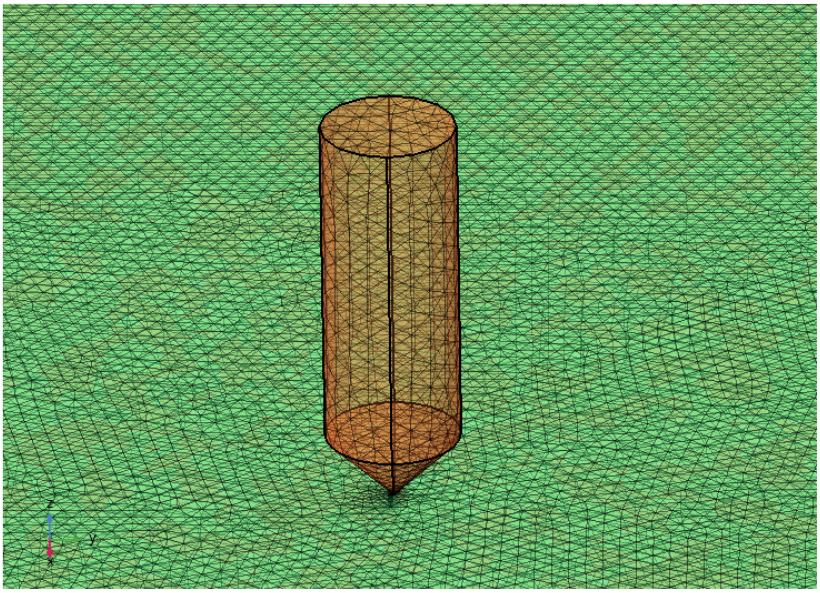

(b)

Figure 1. The designed model: (a) the network architecture, (b) a detailed view of the network architecture.

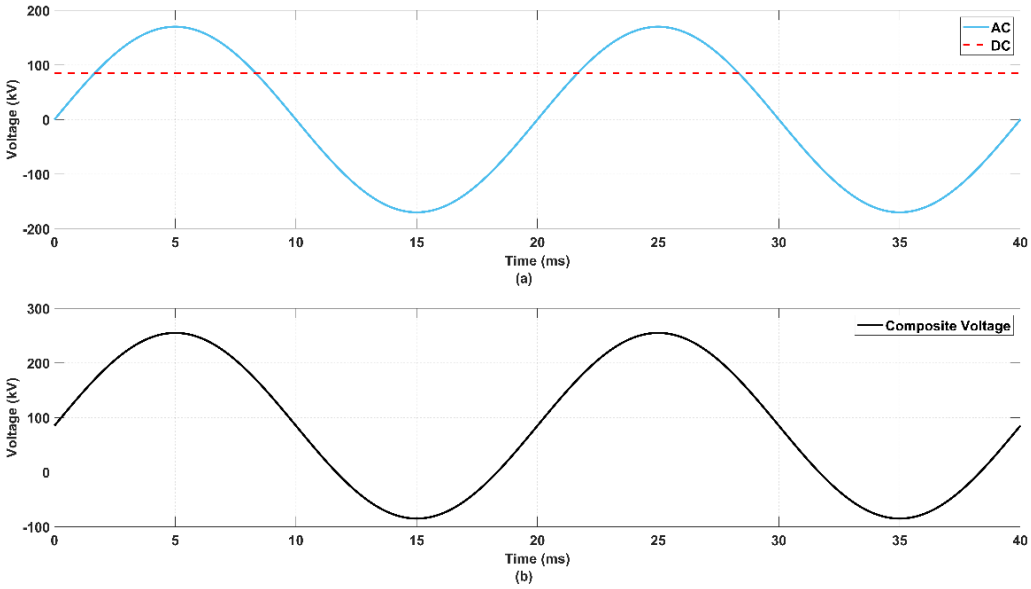

Figure 2. (a) The AC and DC voltage waveforms generated using MATLAB/Simulink, (b) the composite voltage waveform.

In order to analyze the test model designed in the COMSOL Multiphysics environment under composite voltage conditions, the required voltage waveforms were generated in the MATLAB/Simulink environment and then transferred to COMSOL Multiphysics. The time-dependent variations of the generated AC, DC, and composite voltage signals in MATLAB/Simulink are presented in Figure 2.

Although there is no standardized ratio for the application of AC–DC composite voltages in the literature, various ratios have been investigated in different studies. In this context, some studies have preferred a 1:1 ratio so that the amplitudes of the AC and DC components are equal (Li et al., 2025; Zhou et al., 2020). Additionally, ratios such as 1:3, 1:5, and 1:7 have also been examined to evaluate the effects of different DC levels (Zhou et al., 2020). In other studies, the DC component has been applied at levels corresponding to 1%, 3%, 5%, and 10% of the AC peak value (Ispirli et al., 2021a). Furthermore, a wide range of ratios have been tested using a constant 5 kV AC voltage combined with DC voltages varying from −25 kV to +20 kV (Ispirli et al., 2022b).

This variety indicates that system behavior is sensitive to the AC–DC ratio and that a specific standard has not yet been established. Accordingly, in this study, a 2:1 ratio was adopted, and a composite voltage consisting of a 170 kV peak AC at 50 Hz and an 85 kV DC was simultaneously applied to the electrodes in the COMSOL Multiphysics environment. The 170 kV AC peak value was determined based on the voltage levels commonly preferred in similar studies in the literature (Zhao et al., 2013). This voltage level was selected to enable a clear observation of the effects of AC and DC components on the insulating material, as well as to allow comparisons with different ratios presented in the literature.

In electric power systems, overvoltage-induced failures can vary depending on the amplitude of the operating voltage. In this study, to analyze the most critical conditions in the power system, the electric field distribution was examined based on the peak values of both AC and composite voltages. For this reason, the electric field distribution within the test model was analyzed at two specific time instances: t = 0.005 s (corresponding to the voltage maximum) and t = 0.015 s (corresponding to the voltage minimum). The test model, designed in the COMSOL Multiphysics environment, was evaluated under six different cases: five with varying wormhole channel diameters and one without any wormhole effect. The types of voltage signals applied to the electrodes in these six cases are presented in Table 3.

Table 3. Voltage waveforms applied to the test model for six different cases

Case	Voltage Type	Mathematical Expression of Voltage	Wormhole Diameter
Case 1	AC	V_{AC}=170000sin(wt)	No wormhole
	DC	V_{DC}= 85000	
	Composite Voltage	$V_{composite}$ =170000sin(wt)+85000	
Case 2	AC	V_{AC}=170000sin(wt)	50 µm
	DC	V_{DC}= 85000	
	Composite Voltage	$V_{composite}$ =170000sin(wt)+85000	
Case 3	AC	V_{AC}=170000sin(wt)	75 µm
	DC	V_{DC}= 85000	
	Composite Voltage	$V_{composite}$ =170000sin(wt)+85000	
Case 4	AC	V_{AC}=170000sin(wt)	100 µm
	DC	V_{DC}= 85000	
	Composite Voltage	$V_{composite}$ =170000sin(wt)+85000	
Case 5	AC	V_{AC}=170000sin(wt)	150 µm
	DC	V_{DC}= 85000	
	Composite Voltage	$V_{composite}$ =170000sin(wt)+85000	
Case 6	AC	V_{AC}=170000sin(wt)	200 µm
	DC	V_{DC}= 85000	
	Composite Voltage	$V_{composite}$ =170000sin(wt)+85000	

3. Results and Discussion

3.1 Simulation Results

This section presents the results of electric field analyses under composite voltage components for the test model designed using the COMSOL Multiphysics program. Detailed electric field distribution analyses were performed for six different cases of XLPE material under a needle-plane electrode configuration. For the cases specified in Table 3, the simulation duration in COMSOL Multiphysics was set to 20 ms, with a time resolution of 10^{-4} seconds. The analysis results for Case 1 are presented in Figure 3.

In the simulation studies conducted without the influence of the wormhole effect, a maximum volumetric electric field intensity (E_{maxvol}) of 2282.76 kV/cm was observed

within the volume of the insulating material under AC at t = 0.005 s. At the negative peak value of the AC (at t = 0.015 s), the E_{maxvol} in the insulating material volume was 2288.09 kV/cm. In the first case, which was conducted without the wormhole effect and under DC, the electric field intensity within the insulating material volume reached 1141.38 kV/cm. Under composite voltage, the electric field intensity within the volume of the insulating material was calculated as 3423.08 kV/cm at t = 0.005 s and 1139.90 kV/cm at t = 0.015 s, respectively. On the surface of the XLPE material near the needle electrode, the maximum surface electric field intensities ($E_{maxsurf}$) under AC, DC, and composite voltages at t = 0.005 s were obtained as 45.0348 V/cm (Figure 3.b), 22.5175 V/cm (Figure 3.d), and 67.5316 V/cm (Figure 3.f), respectively.

The results obtained for Case 2 are presented in Figure 4. In the analysis conducted for the wormhole condition with a diameter of 50 μm, the E_{maxvol} within the insulating material under AC voltage was obtained as 14014.2 kV/cm at t = 0.005 s. At t = 0.015 s, corresponding to the negative peak of the AC, the E_{maxvol} was observed to be 14038.1 kV/cm. Under the influence of DC, the E_{maxvol} was obtained as 7024.71 kV/cm. The E_{maxvol} values obtained under composite voltage were 21670.5 kV/cm at t = 0.005 s and 7182.66 kV/cm at t = 0.015 s, respectively. On the surface of the XLPE material near the high-voltage electrode, the $E_{maxsurf}$ at t = 0.005 s under AC, DC, and composite voltages were obtained as 2704.91 V/cm (Figure 4.b), 1763.45 V/cm (Figure 4.d), and 3724.38 V/cm (Figure 4.f), respectively.

The results for Case 3 are presented in Figure 5. For the wormhole structure with a diameter of 75 μm, the E_{maxvol} under AC was obtained as 14926.8 kV/cm at t = 0.005 s. At t = 0.015 s, this value was calculated as 14941.3 kV/cm under the same conditions. Under DC, the E_{maxvol} was found to be 7463.76 kV/cm. In the case of composite voltage, the E_{maxvol} values were determined as 22384.3 kV/cm and 7463.70 kV/cm at t = 0.005 s and t = 0.015 s, respectively. On the surface of the insulating material facing the needle electrode in the test model, the $E_{maxsurf}$ values at t = 0.005 s under AC, DC, and composite voltage were calculated as 2422.42 V/cm (Figure 5.b), 1542.17 V/cm (Figure 5.d), and 3632.66 V/cm (Figure 5.f), respectively.

The results for Case 4 are presented in Figure 6. For the wormhole structure with a diameter of 100 μm, the E_{maxvol} under AC was obtained as 15176.9 kV/cm and 15211.5 kV/cm at t = 0.005 s and t = 0.015 s, respectively. Under DC, the E_{maxvol} was found to be 7891 kV/cm. In the case of composite voltage, the E_{maxvol} was observed to be 22737.2 kV/cm and 7513.01 kV/cm at t = 0.005 s and t = 0.015 s, respectively. For XLPE material, the $E_{maxsurf}$ values under AC, DC, and composite voltage at t = 0.005 s were calculated as 2376.11 V/cm (Figure 6.b), 1302.19 V/cm (Figure 6.d), and 3508.31 V/cm (Figure 6.f), respectively.

The results for Case 5 are presented in Figure 7. For the wormhole structure with a diameter of 150 μm, the E_{maxvol} under AC was observed as 15382.4 kV/cm and 15403 kV/cm at t = 0.005 s and t = 0.015 s, respectively. Under DC, the E_{maxvol} was found to be 8325.27 kV/cm. Under composite voltage, the E_{maxvol} values were obtained as 23068.2 kV/cm and 7691.31 kV/cm at t = 0.005 s and t = 0.015 s, respectively. On the surface of the XLPE material near the high-voltage electrode for Case 5, the $E_{maxsurf}$ values at t = 0.005 s under AC, DC, and composite voltage were calculated as 2257.6 V/cm (Figure 7.b), 1128.89 V/cm (Figure 7.d), and 3385.61 V/cm (Figure 7.f), respectively.

The results for Case 6 are presented in Figure 8. For the wormhole structure with a channel diameter of 200 μm, the E_{maxvol} under AC was obtained as 18375.9 kV/cm and 18400.9 kV/cm at t = 0.005 s and t = 0.015 s, respectively. Under DC, the E_{maxvol} was observed to be 9188.67 kV/cm for the same channel diameter.

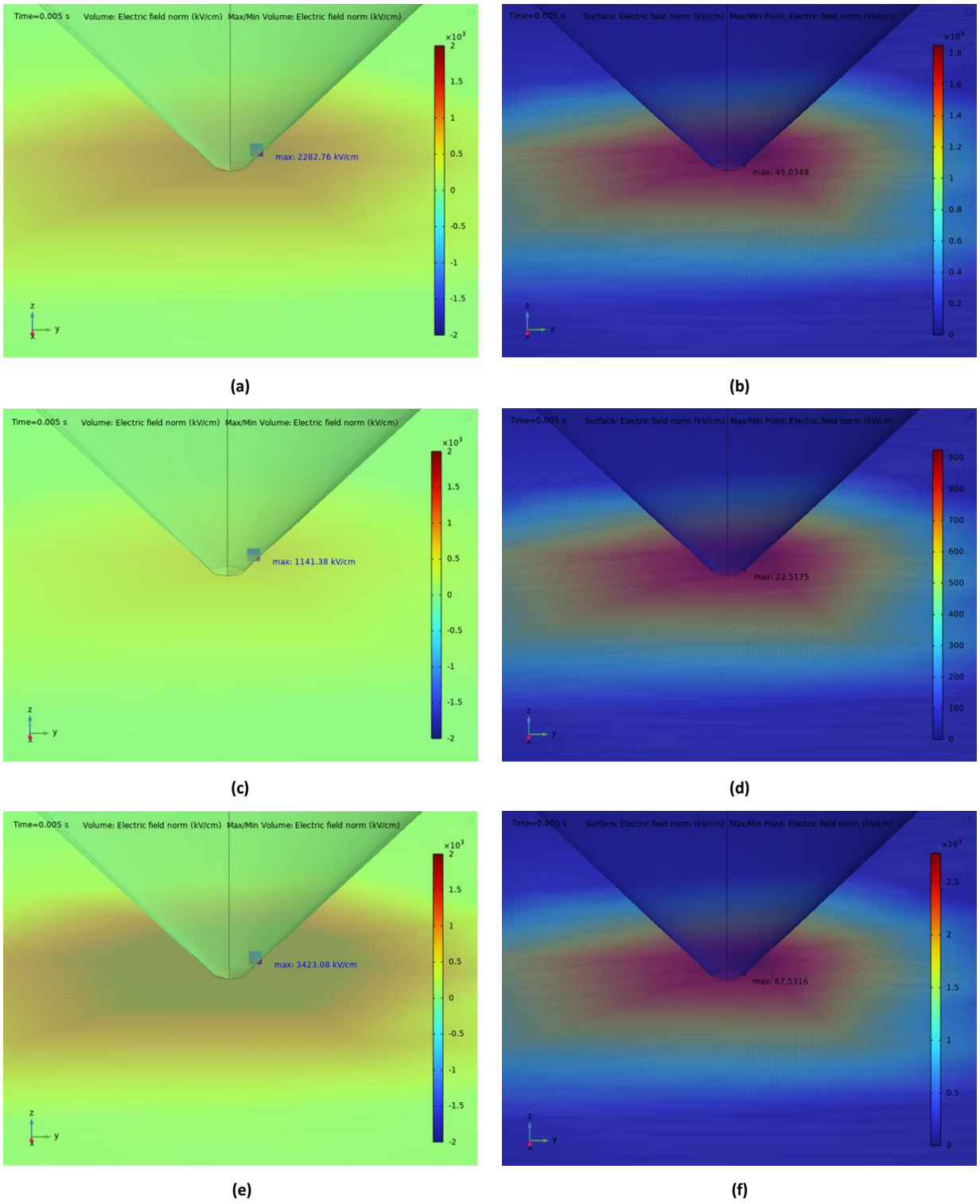

Figure 3. Volumetric (a), (c), (e) and surface (b), (d), (f) electric field distributions obtained for Case 1.

In the test model where a composite voltage was applied, the E_{maxvol} was obtained as 27557.4 kV/cm and 9187.88 kV/cm at t = 0.005 s and t = 0.015 s, respectively. On the surface of the XLPE material near the needle electrode, the $E_{maxsurf}$ values at t = 0.005 s under AC, DC, and composite voltage were calculated as 2145.74 V/cm (Figure 8.b), 1072.96 V/cm (Figure 8.d), and 3217.87 V/cm (Figure 8.f), respectively.

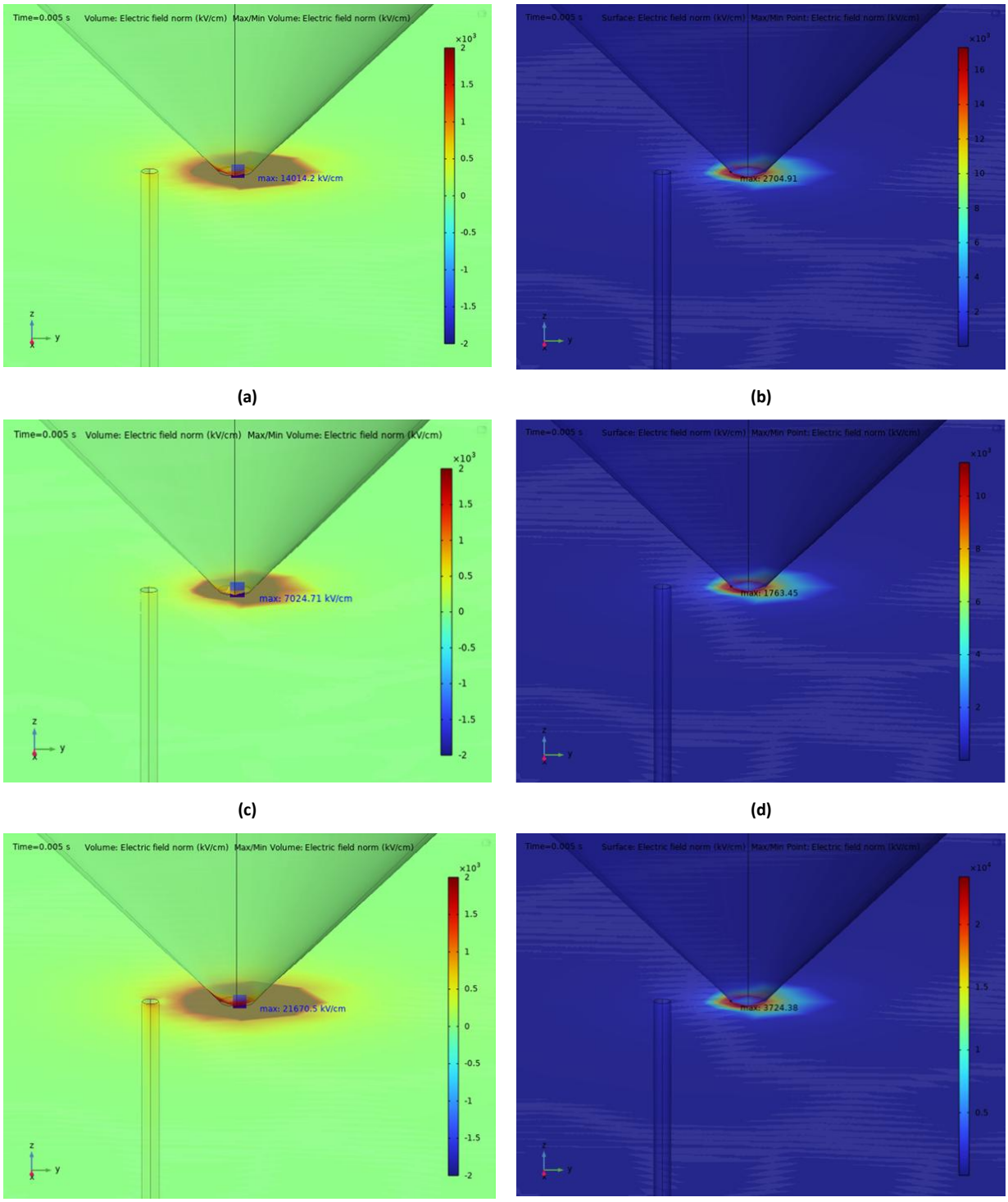

Figure 4. Volumetric (a), (c), (e) and surface (b), (d), (f) electric field distributions obtained for Case 2 (wormhole diameter: 50 μm).

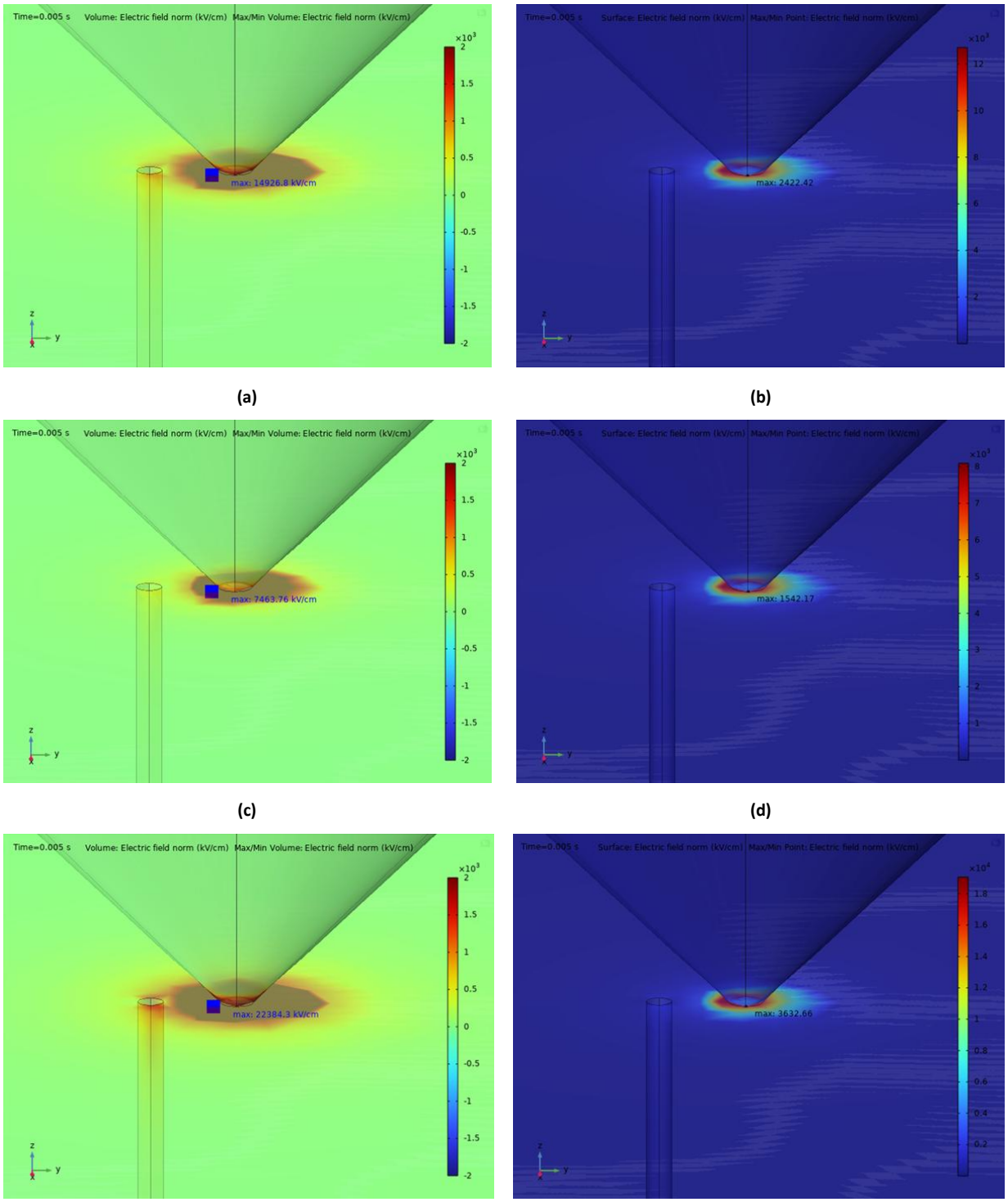

Figure 5. Volumetric (a), (c), (e) and surface (b), (d), (f) electric field distributions for Case 3 (wormhole diameter: 75 μm).

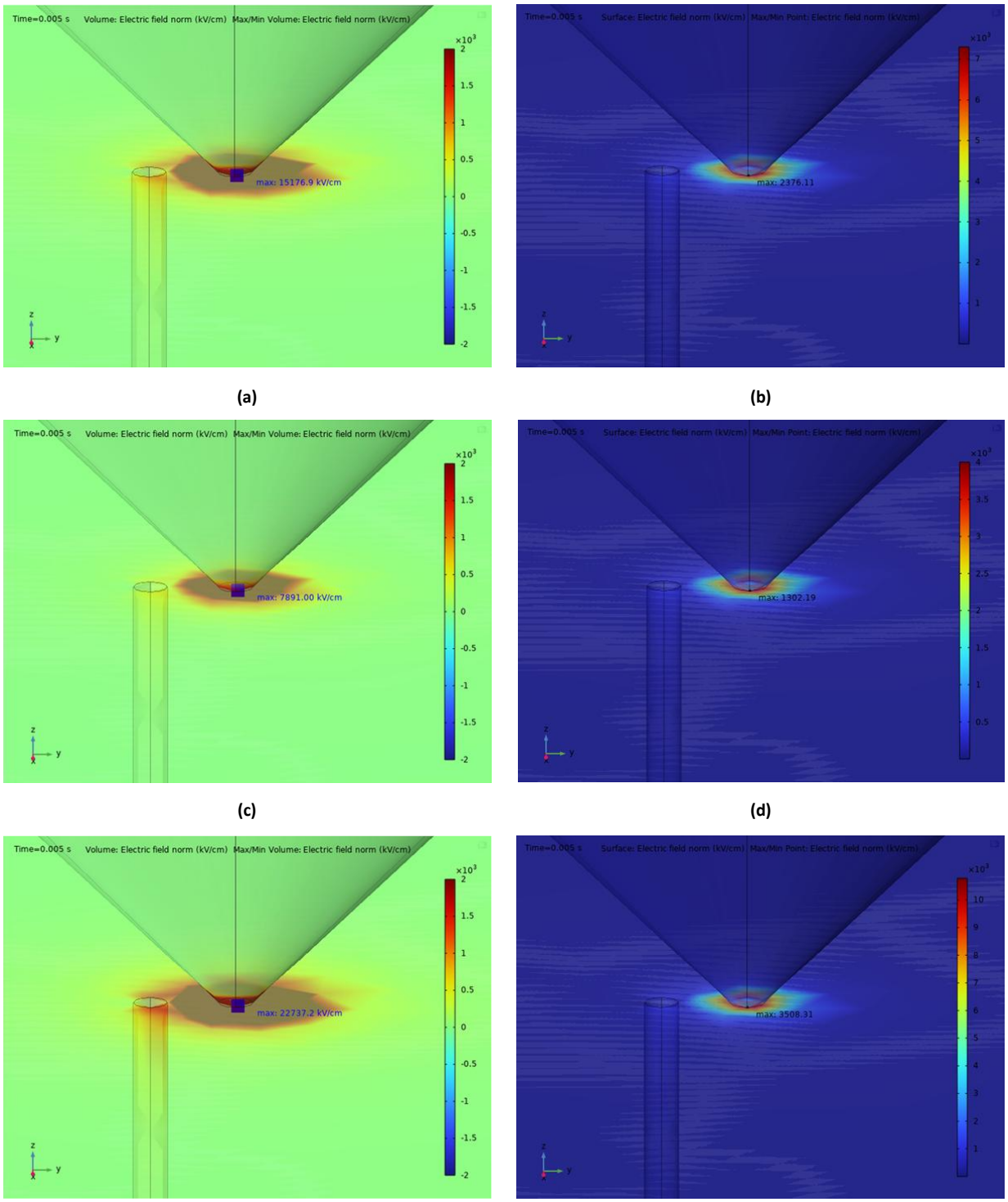

Figure 6. Volumetric (a), (c), (e) and surface (b), (d), (f) electric field distributions obtained for Case 4 (wormhole diameter: 100 μm).

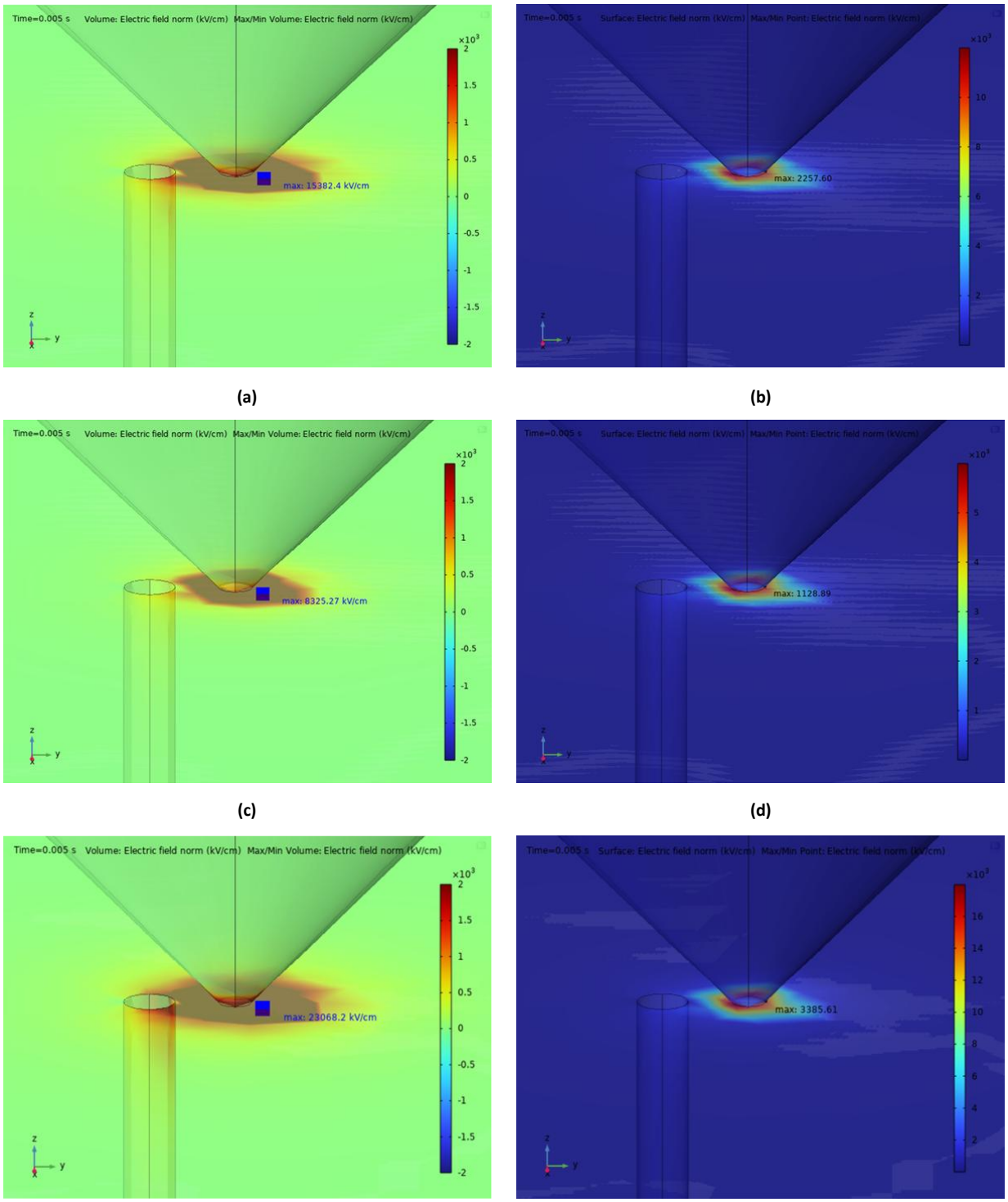

Figure 7. Volumetric (a), (c), (e) and surface (b), (d), (f) electric field distributions for Case 5 (wormhole diameter: 150 μm).

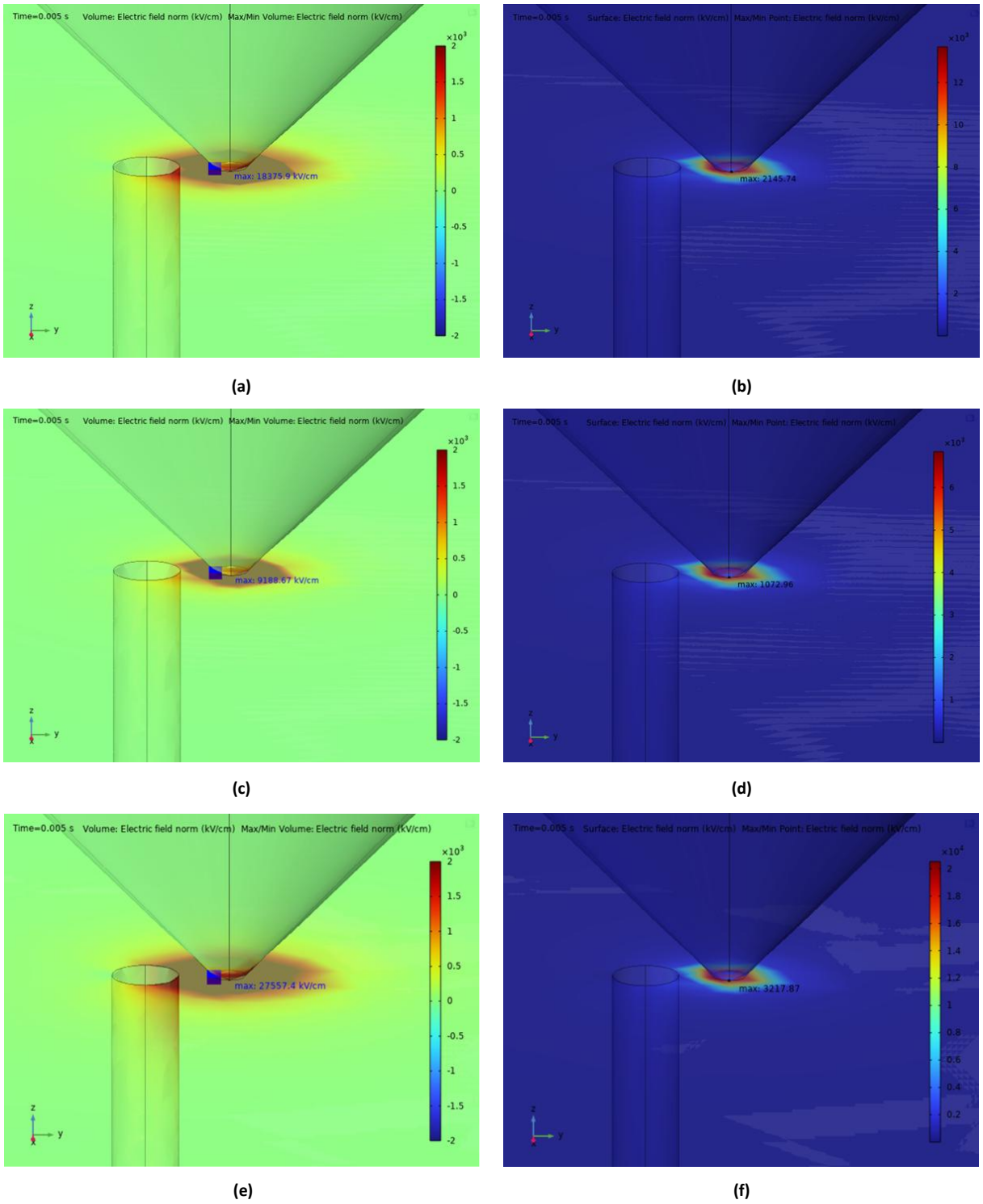

Figure 8. Volumetric (a), (c), (e) and surface (b), (d), (f) electric field distributions obtained for Case 6 (wormhole diameter: 200 μm).

3.2 Analysis and Comparison of the Results

The test model designed in the COMSOL Multiphysics environment was analyzed under AC, DC, and composite voltage signals. The resulting electric field distributions within the volume and on the surface of the XLPE are presented in Table 4.

The results presented in Table 4 indicate that both the wormhole structures with different diameters and the various voltage types (AC, DC, and composite voltage) significantly influence the electric field distribution in the XLPE insulating material. In the reference case without any wormhole defects (Case 1), the E_{maxvol} under composite voltage was obtained as 3423.08 kV/cm. In contrast, the $E_{maxsurf}$ remained limited to 67.5316 V/cm. This situation indicates that in an insulating environment without any structural damage, the electric field distribution is more regular and the field concentration is limited.

Table 4. Electric field intensities obtained in the volume and on the surface of the insulating material for six different cases

Case 1 – No Wormhole			
Voltage Type	E_{maxvol} kV/cm		$E_{maxsurf}$ V/cm
	t=0.005 s	t=0.015 s	t=0.005 s
AC	2282.76	2288.09	45.0348
DC	1141.38	1141.38	22.5175
Composite Voltage	3423.08	1139.90	67.5316
Case 2 – Wormhole Diameter = 50 μm			
Voltage Type	E_{maxvol} kV/cm		$E_{maxsurf}$ V/cm
	t=0.005 s	t=0.015 s	t=0.005 s
AC	14014.2	14038.1	2704.91
DC	7024.71	7024.71	1763.45
Composite Voltage	21670.5	7182.66	3724.38
Case 3 – Wormhole Diameter = 75 μm			
Voltage Type	E_{maxvol} kV/cm		$E_{maxsurf}$ V/cm
	t=0.005 s	t=0.015 s	t=0.005 s
AC	14926.8	14941.3	2422.42
DC	7463.76	7463.76	1542.17
Composite Voltage	22384.3	7463.70	3632.66
Case 4 – Wormhole Diameter = 100 μm			
Voltage Type	E_{maxvol} kV/cm		$E_{maxsurf}$ V/cm
	t=0.005 s	t=0.015 s	t=0.005 s
AC	15176.9	15211.5	2376.11
DC	7891.00	7891.00	1302.19
Composite Voltage	22737.2	7513.01	3508.31
Case 5 – Wormhole Diameter = 150 μm			
Voltage Type	E_{maxvol} kV/cm		$E_{maxsurf}$ V/cm
	t=0.005 s	t=0.015 s	t=0.005 s
AC	15382.4	15403	2257.6
DC	8325.27	8325.27	1128.89
Composite Voltage	23068.2	7691.31	3385.61
Case 6 – Wormhole Diameter = 200 μm			
Voltage Type	E_{maxvol} kV/cm		$E_{maxsurf}$ V/cm
	t=0.005 s	t=0.015 s	t=0.005 s
AC	18375.9	18400.9	2145.74
DC	9188.67	9188.67	1072.96
Composite Voltage	27557.4	9187.88	3217.87

However, the inclusion of the wormhole defect in the system resulted in a significant increase in both volumetric and surface electric field values. In this context, for the case with a 50 μm diameter wormhole (Case 2), the E_{maxvol} under composite voltage reached 21670.5 kV/cm, representing an approximately 6.5-fold increase compared to the reference case. Likewise, the $E_{maxsurf}$ increased nearly 55 times, reaching 3724.38 V/cm. These results indicate that even small-scale defects can severely disrupt the electric field distribution. It was also observed that as the wormhole diameter increased, the E_{maxvol} showed a rising trend. For the largest diameter of 200 μm (Case 6), the maximum electric field under composite voltage reached 27557.4 kV/cm, representing the highest value among all simulation scenarios. This increase demonstrates that larger wormhole diameters lead to greater local intensification of the electric field. Similarly, a significant increase in surface electric field strength was observed compared to the reference case. The $E_{maxsurf}$ obtained in this scenario reached 3217.87 V/cm, indicating a considerable degree of field concentration.

The values obtained under AC resulted in higher field strengths in all cases compared to the values obtained under DC. This difference can be explained by the higher peak value of the AC and its time-varying nature, which contribute more significantly to field intensification. Since the DC component does not vary with time, it leads to a more stable field distribution with lower maximum values. Furthermore, it was observed that the E_{maxvol} was higher during the negative half-cycle of the AC waveform than during the positive half-cycle. Especially in negative polarity, since the mobility and acceleration tendency of free electrons are higher, channel formation can begin at lower field strengths in high-field regions.

The increased electric field during the negative half-cycle, combined with the non-uniform field distribution and localized intensifications around wormhole defects, supports the initiation of channel discharges. Under negative polarity, the higher mobility and acceleration of free electrons enable channel formation to begin at lower field strengths in high-field regions. This explains the more significant increase in peak electric field values observed near defects under negative polarity compared to positive polarity. Furthermore, polarity has a notable impact on breakdown voltage in non-uniform electric fields (Özkaya, 2008; Ispirli et al., 2022b; Küchler, 2017) Therefore, polarity should be considered a critical factor influencing field intensification and material stress.

Under composite voltage conditions, the combined effect of DC and AC components results in the highest electric field intensities. This is particularly important for the design of insulation systems in HVDC applications, where such mixed electrical stresses can accelerate insulation degradation by exceeding the material's stress-handling capacity.

4. Conclusion

In this study, the electric field distribution caused by wormhole structures of varying diameters within XLPE insulation under alternating current AC, direct current DC, and composite voltage components was numerically investigated using COMSOL Multiphysics software. Under a needle-plane electrode configuration, field intensifications occurring particularly under non-uniform electric field conditions were analyzed in detail.

The analysis results revealed that wormhole structures significantly increase the local electric field intensity within the insulation. In the reference case without a wormhole (Case 1), the E_{maxvol} under composite voltage was 3423.08 kV/cm. With a 200 μm diameter wormhole, it increased to 27557.4 kV/cm. This represents an almost eightfold increase in electric field intensity. Furthermore, in all cases involving wormhole defects, the surface electric field intensity was observed to reach substantially higher values compared to the reference case.

The results also revealed significant differences in terms of the impact of voltage types on electric field distribution. The maximum electric field values observed under AC were considerably higher than those observed under DC. This can be mainly attributed to the higher amplitude of the AC voltage and its continuous variation over time, which causes higher stress on the insulation. In composite voltage applications, the combined effect of both components resulted in more intense and irregular electric field patterns. In particular, the electric field distribution at t = 0.005 s corresponds to the moment when the voltage level reaches its peak under composite voltage, representing the condition of highest electrical stress.

Due to the effect of the negative half-cycle, higher electric field intensities were recorded in all cases compared to the positive half-cycle. This is attributed to the fact that free electrons accelerate more easily under negative voltage. Under negative polarity, electrons are subjected to a stronger electric field, allowing them to gain higher energy. As a result, electrons may move more effectively in defect regions, potentially initiating the discharge process. This can trigger the channel discharge mechanism earlier in regions where the electric field is concentrated. Consequently, the breakdown voltage threshold of the insulation may decrease, increasing the risk of electrical breakdown.

As the diameter of the wormhole defects increases, not only the magnitude but also the distribution characteristics of the electric field were observed to change. Larger channels caused a sharper field concentration around the defect region, potentially creating critical zones that may facilitate partial discharges or electrical breakdown. This finding highlights the importance of defect control, particularly during the manufacturing processes of insulating materials.

In conclusion, this study provides important findings regarding: (i) the electrical risks induced by wormhole defects depending on their size, (ii) the comparative effects of AC, DC, and composite voltages, and (iii) the influence of polarity on field concentration in non-uniform electric field distributions under high voltage stress. The results obtained contribute to the literature and provide an important perspective on the fundamental parameters that must be considered in terms of the design and reliability of insulation systems.

Author Contributions

The percentages of the authors' contributions are presented below. All authors reviewed and approved the final version of the manuscript.

	E.T.	M.F.
C	50	50
D	50	50
S	0	100
DCP	50	50
DAI	50	50
L	60	40
W	40	60
CR	30	70
SR	50	50
PM	50	50

C=Concept, D= design, S= supervision, DCP= data collection and/or processing, DAI= data analysis and/or interpretation, L= literature search, W= writing, CR= critical review, SR= submission and revision, PM= project management.

Conflict of Interest

The authors declared that there is no conflict of interest.

Ethical Consideration

Ethics committee approval was not required for this study because of there was no study on animals or humans.

References

Adhikari P, Ghassemi M. 2024. Navigating strategies to mitigate insulation issues within high power density (U)WBG power module packages: A comprehensive review emphasizing alternative encapsulation materials. IEEE Transact Industry Applicat, 2024: 1–22. https://doi.org/10.1109/tia.2024.3520096

Annadi RR, Patsa CS. 2020. Estimation of switching surge flashover rate of 1200-kV UHVAC transmission line considering switching overvoltage waveshape. Electr Eng, 102(2): 953–966. https://doi.org/10.1007/s00202-020-00918-7

Beroual A, Dang V-H, Perrier C. 2013. Investigation on creeping discharges propagating over pressboard immersed in mineral and vegetable oils under AC, DC and lightning impulse voltages. IEEE Trans Dielectr Electr Insul, 20(5): 1-6.

Borghei M, Ghassemi M. 2022. Separation and classification of corona discharges under low pressures based on deep learning method. IEEE Trans Dielectr Electr Insul, 29(1): 319–326. https://doi.org/10.1109/TDEI.2022.3146608

Chen Q, Wu Z, Liu F, Yun F, Liu D, Fan J, … Gao C. 2022. The discharge mode of SF6N2Gas mixture in extremely inhomogeneous electric field under power frequency voltage. Conference on Electrical Insulation and Dielectric Phenomena, CEIDP, 13-16 November, pp: 560–563. Institute of Electrical and Electronics Engineers Inc. https://doi.org/10.1109/CEIDP55452.2022.9985344

Chen S, Li K, Wang F, Sun Q, Zhong L. 2019. Effect of humidity and air pressure on the discharge modes transition characteristics of negative DC corona. IET Sci Meas Technol, 13(8): 1212–1218. https://doi.org/10.1049/iet-smt.2019.0032

Dedeoglu S, Merev A. 2023. Realization of the reference composite voltage waveforms for lightning impulse (LI) voltages superimposed over DC and AC signals. Mapan J Metrol Soc India, 38(3): 597–606. https://doi.org/10.1007/s12647-023-00634-0

Dissado LA, Fothergill JC. 1992. Electrical degradation and breakdown in polymers (1st ed.). Institution of Engineering and Technology. London, UK, pp: 54-98.

Dong W, Wang X, Tian B, Liu Y, Jiang Z, Li Z, Zhou W. 2019. Use of grafted voltage stabilizer to enhance dielectric strength of cross-linked polyethylene. Polymers, 11(1): 1-6. https://doi.org/10.3390/POLYM11010176

Dordizadeh P, Adamiak K, Castle GSP. 2017. Experimental study of the characteristics of Trichel pulses in the needle-plane negative corona discharge in atmospheric air. J Electrostat, 88: 49–54. https://doi.org/10.1016/j.elstat.2016.12.013

Fidan M, Ismailoglu H. 2017. Harmonik kaynaklı gerilim bozulmalarının elektriksel kısmi boşalmalar üzerindeki etkilerinin incelenmesi. J Fac Eng Archit Gazi Univ, 32(3): 929–939. https://doi.org/10.17341/gazimmfd.337646

Freitas-Gutierres LF, Maresch K, Morais AM, Nunes MVA, Correa CH, Martins EF, … Oliveira AL. 2024. Framework for decision-making in preventive maintenance: Electric field analysis and partial discharge diagnosis of high-voltage insulators. Electr Power Syst Res, 233: 1-6. https://doi.org/10.1016/j.epsr.2024.110447

Ghassemi M. 2018. PD measurements, failure analysis, and control in high-power IGBT modules. High Volt, 3(3): 170–178. https://doi.org/10.1049/hve.2017.0186

Gong M, Lu M, Liu H, Jiang H, Sun QF, Xie XC. 2020. Transport study of the wormhole effect in three-dimensional topological insulators. Phys Rev B, 102(16): 1-6. https://doi.org/10.1103/PhysRevB.102.165425

Hamidieh M, Ghassemi M. 2024. Conic cross-sectional electrodes and their influence on negative corona discharge and trichel pulse characteristics. IEEE Trans Dielectr Electr Insul, 31(4): 2064–2073. https://doi.org/10.1109/TDEI.2024.3385751

Hu K, Li G, Gu Z, Zhang F, Wei Y, Lei Q. 2023. Analysis of influence factors on ac breakdown characteristics of rod-barrier gap and electric field simulation. J Electr Eng Technol, 18(3): 2189–2197. https://doi.org/10.1007/s42835-022-01259-0

IEC 60060-1:2010. High-voltage test techniques - Part 1: General definitions and test requirements. 2010: 68.

Ispirli MM, Kalenderli Ö, Seifert F, Rock M, Oral B. 2022b. Investigation of impact of DC component on breakdown characteristics for different electric fields under composite AC and DC voltage. High Volt, 7(2): 279–287. https://doi.org/10.1049/hve2.12185

Ispirli MM, Oral B, Kalenderli Ö. 2022a. Electric field analysis of 66 kV and 110 kV SiR insulators under combined AC–DC voltages. Energy Rep, 8: 361–368. https://doi.org/10.1016/j.egyr.2021.11.149

Kadim EJ, Noorden ZA, Adzis Z, Azis N. 2021. Nanoparticles application in high voltage insulation systems. IEEE Trans Dielectr Electr Insul, 28(4): 1380–1399. https://doi.org/10.1109/TDEI.2021.009531

Kavanagh DF, Gyftakis KN, Mcculloch MD. 2020. Thermal degradation phenomena of polymer film on magnet wire for electromagnetic coils. IEEE Trans Ind Appl, 57(1): 458–467. https://doi.org/10.1109/TIA.2020.3040201

Küchler A. 2017. High voltage engineering. Springer eBooks, London, UK, pp: 168. https://doi.org/10.1007/978-3-642-11993-4

Lan G, Bo L, Huanchao C, Jinzhong Li. 2012. Breakdown characteristics of typical model in transformer oil under AC and DC mixed voltage. 2012 October 14–17, 2012 Annual Report Conference on Electrical Insulation and Dielectric Phenomena. IEEE, Ottawa, Canada, pp: 68.

Li Y, Zhang Q, Zhao Y, Wang T, Liu G, Wang K. 2017. The influence of temperature on Partial Discharges and wormhole effect of oil-paper insulation under DC voltage. 2017 June 11–14 IEEE Electrical Insulation Conference (EIC). IEEE, Montreal, Canada.

Li Y, Zhou K, Zhu GY, Zhang QG. 2019. Effect of DC discharges in mineral oil on degradation characteristics of oil-impregnated pressboard. IEEE Trans Dielectr Electr Insul, 26(5): 1701–1708. https://doi.org/10.1109/TDEI.2019.008256

Li Z, He D, Ren F, Li S, Wu H, Sun Y, … Li Q. 2025. Effect of temperature on the internal electric field distribution and discharge mechanism of converter transformer under AC–DC composite voltage. IEEE Trans Dielectr Electr Insul, 32(2): 1084–1093. https://doi.org/10.1109/TDEI.2024.3435815

Liang H, Du B, Li J. 2020. Non-Intrusive measurement of transient electric field distribution under AC and impulse voltages. IEEE Sens J, 20(18): 10898–10902. https://doi.org/10.1109/JSEN.2020.2994246

Lin L, Meng X, Mei H, Wang L. 2024. Influence of AC and DC composite voltage on positive streamer discharge. IEEE Trans Dielectr Electr Insul, 31(2): 779–785. https://doi.org/10.1109/TDEI.2023.3325421

Liu L, Zhang Z, Peng Z, Ouyang J. 2013. Comparison of point-to-plane corona in different gases. J Phys Conf Ser, 418(1): 1-6. Institute of Physics Publishing. https://doi.org/10.1088/1742-6596/418/1/012092

Muppala P, Reddy CC. 2021. Electric field and DC breakdown voltage of multi-layer dielectrics in parallel-plane geometry.

IEEE Trans Dielectr Electr Insul, 28(1): 257–265. https://doi.org/10.1109/TDEI.2020.008830

Negari S, Moghadam DE. 2024. A novel approach towards parametric assessment of reliability and resilience of high voltage mica-based insulation systems by statistical analysis of experimental failure data. High Volt, 9(2): 495–507. https://doi.org/10.1049/hve2.12431

Özkaya M. 2008. Yüksek gerilim tekniği. Birsen Yayınevi, Cilt I, İstanbul, Türkiye, ss: 68.

Park C, Lee K, Kim K, Lim H, Park Y. 2024. Evaluation of Time-Based arc flash detection with non-contact UV sensor. J Electr Eng Technol, 19(3): 1983–1992. https://doi.org/10.1007/s42835-023-01555-3

Qiu Z, Ruan J, Huang D, Pu Z, Shu S. 2015. A prediction method for breakdown voltage of typical air gaps based on electric field features and support vector machine. IEEE Trans Dielectr Electr Insul, 22(4): 2125–2135. https://doi.org/10.1109/TDEI.2015.004887

Reddy BST, Wani SA, Amizhtan SK, Naresh C, Sarathi R. 2023. Understanding the surface discharge activity with nano oil-pressboard insulation under AC and lightning impulse voltages. IEEE Trans Dielectr Electr Insul, 31(2): 889–896. https://doi.org/10.1109/TDEI.2023.3334245

Roggendorf C, Schnettler A. 2012. Accelerated hydrothermal aging of epoxy resin based syntactic foams with polymeric microspheres. IEEE Trans Dielectr Electr Insul, 19(3): 973–980. https://doi.org/10.1109/TDEI.2012.6215102

Rosenberg G, Guo HM, Franz M. 2010. Wormhole effect in a strong topological insulator. Phys Rev B, 82(4): 1-6. https://doi.org/10.1103/PhysRevB.82.041104

Rubinetti D, Iranshahi K, Onwude DI, Nicolaï BM, Xie L, Defraeye T. 2024. Energy-saving discharge needle shape for electrohydrodynamic airflow generation. J Electrostat, 127: 1-6. https://doi.org/10.1016/j.elstat.2023.103876

Saini S, Prasad SD. 2024. Quasi-static ac surface charging of polymeric insulators at low pressure. IEEE Trans Ind Appl, 60(4): 5663–5670. https://doi.org/10.1109/TIA.2024.3397773

Stone G, Boulter EA, Culbert I, Dhirani H. 2014. Electrical insulation for rotating machines. Design, Evaluation, Aging, Testing, and Repair, London, UK, pp:59-67.

Tian H, Liu L, Guo Z, Wang H, Shi R, Peng Z. 2017. Research on electrical field distribution of tri-post insulator and distortion effect by defects. 2017 IEEE Conference on Electrical Insulation and Dielectric Phenomenon (CEIDP). IEEE, 22-25 October, Fort Worth, Texas, USA, pp: 82.

Timoshkin IV, Given MJ, Macgregor SJ, Wilson MP, Lehr JM. 2009. Pre-breakdown currents in insulating liquids stressed with non-uniform DC electric field. 2009 June 12–14 IEEE Pulsed Power Conference, Washington DC, USA, pp: 63.

Tunç E, Fidan M. 2023. Residual voltage tests of 4.5 kV metal oxide surge arrester. 14th International Conference on Electrical and Electronics Engineering, ELECO 2023 - Proceedings. November 30-December 2, Bursa, Türkiye, pp: 18. https://doi.org/10.1109/ELECO60389.2023.10415938

Wu Z, Xu H, Zhou J, Chen Y, Zhang Z, Zhang Q. 2024. Accumulative effect of bipolar oscillation impulse voltage on interturn insulation of transformer winding. IEEE Trans Dielectr Electr Insul, 32(2): 1-6. https://doi.org/10.1109/TDEI.2024.3446768

Yang Y, Gao K, Bi J, Ding L, Yuan S, Wang G. 2022. Influence of micro-water on AC breakdown characteristics of C4F7N/CO2 gas mixture under non-uniform electric field. High Volt, 7(6): 1059–1068. https://doi.org/10.1049/hve2.12215

Zhang B, Ghassemi M, Zhang Y. 2021. Insulation materials and systems for power electronics modules: A review identifying challenges and future research needs. IEEE Trans Dielectr Electr Insul, 28(1): 290–302. https://doi.org/10.1109/TDEI.2020.009041

Zhao L, Su J, Zhang X, Pan Y, Wang L, Fang J, … Cheng J. 2013. An experimental and theoretical investigation into the “wormhole” effect. J Appl Phys, 114(6): 1-6. https://doi.org/10.1063/1.

Zhao L. 2022. A unified formula for five basic forms of discharge in an electric field under short pulses. IEEE Trans Plasma Sci, 50(10): 3400–3411. https://doi.org/10.1109/TPS.2022.3169602

Zhao T, Liu Y, Liu Y, Yang C, Zheng Y, Zhu W, Gu Z. 2024. Bubble motion characteristics in the transformer oil gap at the top of HV Winding. IEEE Transact Dielectrics Electrical Insulat, 1: 3361848. https://doi.org/10.1109/tdei.2024.3361848

Zhao X, Li B, Xiao D, Deng Y. 2017. Breakdown characteristics of CF3I-N2 gas mixtures in a needle-plate geometry. IEEE Transact Dielectrics Electrical Insulation, 24(2): 869–875. https://doi.org/10.1109/tdei.2017.006089

Zheng Y, Zhao T, Tong Y, Chao N. 2021. Simulation of the movement characteristics of micro-bubbles in the oil gap of transformer. 2021 Electrical Insulation Conference, EIC 2021, June 7-28, online, pp: 141–144. https://doi.org/10.1109/EIC49891.2021.9612265

Zhou Y, Huang X, Zhang L, Zhang Y, Zhou Z, Teng C, . . . Huang M. 2020. Space charge characteristics of oil-paper under AC/DC composite voltage. 2022 IEEE Conference on Electrical Insulation and Dielectric Phenomena (CEIDP), September 14-17, Manchester, United Kingdom, pp: 308–311. https://doi.org/10.1109/ceidp49254.2020.9437530

Black Sea Journal of Engineering and Science
doi: 10.34248/bsengineering.1733519

Open Access Journal
e-ISSN: 2619 – 8991

Research Article
Volume 8 - Issue 5: 1577-1584 / September 2025

ENHANCED PHOTOCATALYTIC DEGRADATION OF METHYL RED DYE VIA HYDROTHERMALLY SYNTHESIZED MANGANESE TUNGSTATE

Mehmet KAYHAN[1]*

[1]*Usak University, Usak University Scientific Analysis, Technological Application and Research Center, 64000, Uşak, Türkiye*

Abstract: In this study, $MnWO_4$ nanoparticles were successfully synthesized via a CTAB-assisted hydrothermal method and evaluated for their photocatalytic degradation performance against Methyl Red (MR) dye under UV-C irradiation. Structural and morphological characterizations were performed using XRD, FTIR, SEM, and UV-DRS techniques, confirming the formation of highly crystalline monoclinic $MnWO_4$ with defect-rich surfaces. The photocatalytic experiments were conducted under UV-C light (254 nm) with a catalyst dosage of 0.5 g/L, initial MR concentration of 20 mg/L, and solution pH of 6.5. The synthesized $MnWO_4$ exhibited excellent degradation efficiency, achieving 98% MR removal within 90 minutes, outperforming several conventional photocatalysts. This work addresses a critical gap in the literature by demonstrating the enhanced activity of CTAB-modified $MnWO_4$ under UV-C light, offering a promising route for azo dye remediation. The findings suggest that morphology control and surface defect engineering significantly influence photocatalytic performance, making $MnWO_4$ a viable candidate for environmental applications.

Keywords: Manganese tungstate, Hydrothermal synthesis, Methyl red, UV-C photocatalysis, Azo dye degradation, Band gap engineering

***Corresponding author:** Usak University, Usak University Scientific Analysis, Technological Application and Research Center, 64000, Uşak, Türkiye
E mail: mehmet.kayhan@usak.edu.tr (M. KAYHAN)
Mehmet KAYHAN https://orcid.org/0000-0002-4581-2657

Received: July 03, 2025
Accepted: September 08, 2025
Published: September 15, 2025

Cite as: Kayhan M. 2025. Enhanced photocatalytic degradation of methyl red dye via hydrothermally synthesized manganese tungstate. BSJ Eng Sci, 8(5): 1577-1584.

1. Introduction

Industrial dyes, particularly azo dyes such as Methyl Red (MR), pose serious threats to aquatic ecosystems and human health due to their toxic, carcinogenic, and non-biodegradable nature (Ahmad et al., 2015; Ahmad et al., 2019; Alharbi et al., 2024). The uncontrolled discharge of dye-laden effluents from industries such as textiles, leather processing, and printing significantly contributes to water pollution, adversely affecting photosynthetic activity and ecological balance (He et al., 2010; Berradi et al., 2019; Allabakshi et al., 2025). The visible coloration of even trace amounts in water can inhibit photosynthesis by obstructing light penetration, leading to ecological imbalances (He et al., 2010). Conventional wastewater treatment methods, including coagulation, adsorption, and biological degradation, often fail to adequately remove such persistent organic contaminants (Shivaganga et al., 2023; Shamshad and Ur Rehman, 2025). So, the rapid release of these dyes into water necessitates the development of effective and sustainable wastewater treatment technologies.

To address these concerns advanced oxidation processes (AOPs), particularly semiconductor-based photocatalysis, has emerged as a green, sustainable, and cost-effective approach for degrading organic dyes under light irradiation among alternative methods (Kayhan et al., 2024; Shalini et al., 2024; Nagaraja et al., 2025; Nezzari et al., 2025; Rastin et al., 2025). This method utilizes semiconductor materials that generate reactive oxygen species (ROS), leading to the breakdown of complex dye molecules into harmless byproducts such as CO_2 and H_2O (Kumar et al., 2021; Jayakumar et al., 2024). The success of photocatalysis depends significantly on the optical and structural properties of the catalyst used.

In this context, among various semiconductors, transition metal tungstates (Kayhan, 2025a; Kayhan, 2025b), and particularly manganese tungstate ($MnWO_4$), have drawn increasing attention due to their favorable optical and electronic properties. $MnWO_4$, a monoclinic wolframite-type oxide, possesses a favorable bandgap energy (~1.75–2.8 eV) that facilitates visible-light-driven photocatalytic reactions (He et al., 2010; Kumar et al., 2021; Jayakumar et al., 2024). In addition to its stability and cost-effectiveness, $MnWO_4$ exhibits unique physicochemical properties, including high photostability, versatile electronic properties, magnetic behavior and multiferroicity, which further enhance its versatility for environmental (Khaksar et al., 2015; Kumar et al., 2021). These properties make $MnWO_4$ an attractive candidate not only in photocatalysis but also in electrocatalysis, gas

sensing, and energy storage systems (Khaksar et al., 2015; Vosoughifar, 2017).

Previous studies have demonstrated the effectiveness of $MnWO_4$ in degrading organic dyes such as methyl orange and methylene blue under UV and visible light sources (Vosoughifar, 2017; Shivaganga et al., 2023; Kayhan and Kayhan, in press). The photocatalytic performance of $MnWO_4$ is greatly influenced by factors such as synthesis parameters such as pH, temperature, and precursor concentration, particle morphology and surface area (Wu et al., 2012; Jayakumar et al., 2024). For instance, $MnWO_4$ exhibits nanorod or needle-like morphologies that promote efficient charge separation, enhancing photocatalytic performance (Vosoughifar, 2017; Kayhan Kayhan, in press).

Several studies have explored $MnWO_4$-based composite materials to enhance photocatalytic performance by facilitating charge separation and extending light absorption range. For example, $MnWO_4$–TiO_2 nanoflower composites have demonstrated superior degradation efficiency of methyl orange under visible light, attributed to the formation of heterojunctions that promote effective electron-hole separation (Hassan et al., 2015). Additionally, incorporation of conductive materials like reduced graphene oxide (RGO) has shown to enhance surface area and charge carrier mobility, further improving photocatalytic activity (Siahsahlan et al., 2025). Despite this growing body of research and promising results in the degradation of dyes like methylene blue and methyl orange, research specifically focused on the visible-light-driven degradation of Methyl Red using the standalone performance of hydrothermally synthesized pure $MnWO_4$ remains underexplored. Therefore, given MR's recalcitrant nature and environmental significance, this study aims to synthesize $MnWO_4$ nanoparticles via a controlled hydrothermal method, characterize their structural and optical properties, and evaluate their photocatalytic performance against MR dye under UV-light.

2. Materials and Methods

2.1. Materials

The chemicals used in the synthesis such as Sodium tungstate dihydrate ($Na_2WO_4.2H_2O$, 99+% ACS Reagent purity from Thermo Scientific) and Manganese chloride tetrahydrate ($MnCl_2.4H_2O$, analytical grade from Thermo Scientific), Hexadecyltrimethylammonium bromide (CTAB, 99+% purity from Thermo Scientific), methyl red were ACS reagent grade purchased from Supelco and they were used without any purification.

2.2. Synthesis of Manganese Tungstate

To initiate the synthesis, 2.0 g of sodium tungstate dihydrate ($Na_2WO_4 \cdot 2H_2O$) was accurately weighed and dissolved in distilled water to obtain 100 mL of stock solution using a volumetric flask. A 10 mL aliquot of this solution was then transferred into a 100 mL glass beaker and diluted with an additional 40 mL of distilled water. Subsequently, 150 mg of cetyltrimethylammonium bromide (CTAB) was added as a surfactant to assist in controlling particle growth and morphology.

The resulting mixture was stirred magnetically for 5 minutes to ensure complete dissolution of the CTAB. Thereafter, 485 mg of manganese(II) chloride tetrahydrate ($MnCl_2 \cdot 4H_2O$) was gradually introduced into the solution under continuous stirring. The reaction mixture was further stirred for 40 minutes to allow for homogeneous mixing and precursor interaction.

Following the mixing step, the solution was transferred into a Teflon-lined stainless steel autoclave and subjected to hydrothermal treatment at 140 °C for 24 hours. Upon completion of the reaction, the resulting precipitates were collected by vacuum filtration, thoroughly rinsed with distilled water to remove residual ions and surfactant, and subsequently dried at ambient temperature overnight.

2.3. Characterization

The crystalline structure and phase composition of the hydrothermally synthesized $MnWO_4$ samples were analyzed using X-ray diffraction (XRD) with Cu Kα radiation, scanned over a 2θ range of 10° to 65° (Rigaku Miniflex X-Ray Diffractometer). Functional groups and chemical bonding characteristics were examined via Fourier-transform infrared (FTIR) spectroscopy in the range of 400–4000 cm^{-1} using an ATR-equipped spectrometer (Spectrum Two, Perkin Elmer). Optical properties and band gap estimation were obtained through UV–Visible Diffuse Reflectance Spectrophotometer (UV-DRS) within the 300–800 nm wavelength range (SHIMADZU 2600i). The surface morphology and microstructural features of the materials were observed using a scanning electron microscope (SEM) equipped with a CeB_6 electron source (Phenom ProX SEM).

2.4. Photocatalytic Behavior Evaluation of Manganese Tungstate

Photocatalytic performance was evaluated using a custom-fabricated reactor system consisting of a cylindrical quartz vessel surrounded by six symmetrically arranged 8 watt UV-C lamps positioned at a distance of 25 mm from the quartz reactor. The configuration was designed to ensure uniform irradiation of the reaction medium. Throughout the experiments, the solution inside the reactor was continuously stirred with a magnetic stirrer, while a steady flow of air was bubbled into the system to maintain both oxygenation and solution homogeneity at 25±2°C. To mitigate any thermal effects induced by prolonged UV exposure, the reactor's outer chamber was cooled by ambient air circulation.

The model pollutant, Methyl Red (MR), was initially prepared as a 400 mg/L stock solution in a solvent mixture of ethanol and distilled water (40:60, v/v). This stock solution was then diluted with distilled water to obtain a 10 mg/L working solution in a total volume of 500 mL. The pH of the solution was adjusted to 1.5 using hydrochloric acid (HCl) to simulate acidic conditions favorable for MR degradation.

For each experiment, 200 mg of the synthesized

manganese tungstate catalyst was added to the dye solution. Prior to irradiation, the suspension was stirred and aerated for 30 minutes in the dark to establish adsorption–desorption equilibrium between the catalyst surface and the dye molecules.

Photocatalytic degradation of MR was monitored using a UV-Visible spectrophotometer (PerkinElmer Lambda 35). An initial absorbance spectrum was recorded at 0 minutes following the adsorption phase. Thereafter, the reactor was exposed to UV-C illumination, and absorbance measurements were taken at 15-minute intervals for a total irradiation duration of 180 minutes. Spectral data were collected in the 300–650 nm wavelength range to track the progressive decomposition of MR over time.

3. Results and Discussion

The manganese tungstate photocatalyst was successfully synthesized via a hydrothermal method. In order to comprehensively investigate its structural properties, XRD analysis was performed.

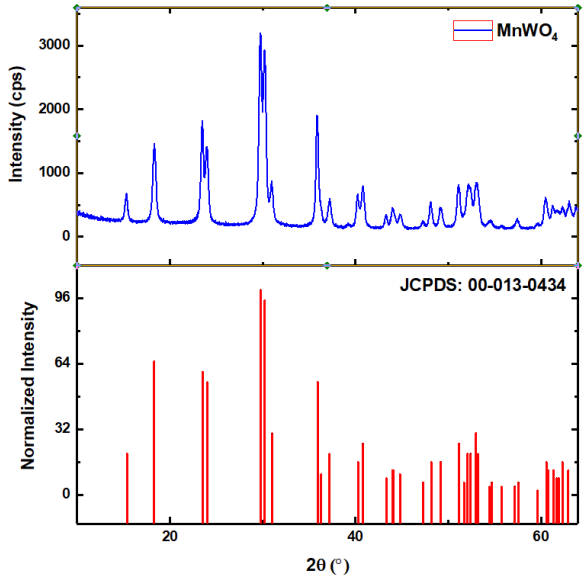

Figure 1. XRD pattern of $MnWO_4$.

The crystallographic structure of the hydrothermally synthesized manganese tungstate ($MnWO_4$) was confirmed by X-ray diffraction (XRD) analysis (Figure 1). The diffraction peaks observed in the XRD pattern correspond precisely to those of monoclinic phase with a wolframite-type crystal structure of $MnWO_4$ and are in excellent agreement with the standard data from the Joint Committee on Powder Diffraction Standards (JCPDS Card No. 00-013-0434). No secondary or impurity phases were detected, indicating the high phase purity of the product. The sharp and well-defined diffraction peaks suggest the formation of a well-crystallized structure. This result confirms that the hydrothermal method employed in this study is effective in producing phase-pure $MnWO_4$ with the desired crystalline characteristics. The absence of extraneous peaks also implies that no residual precursors or unintended by-products are present in the final material.

Figure 2 presents SEM micrographs of hydrothermally synthesized $MnWO_4$ particles prepared in the presence of CTAB surfactant, recorded at magnifications of 10,000× (Figure 2A) and 30,000× (Figure 2B). The images clearly reveal that the $MnWO_4$ particles exhibit predominantly spherical to sub-spherical morphologies with a relatively uniform size distribution. Unlike the needle-like structures typically observed in $MnWO_4$ synthesized via coprecipitation routes (Kayhan and Kayhan, in press), the use of CTAB during hydrothermal synthesis appears to suppress anisotropic growth, promoting more isotropic and equiaxed particle formation.

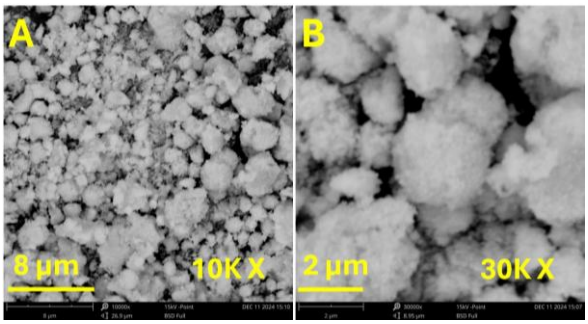

Figure 2. SEM images of hydrothermally synthesized $MnWO_4$.

This suggests that the synthesis conditions—particularly the presence of surfactants—play a crucial role in directing the formation of highly controlled and uniform nanoparticles, rather than the aggregated structures commonly associated with hydrothermal processes (Wang et al., 2020). The observed morphological transition can be attributed to the surface-active nature of CTAB, which likely adsorbs preferentially on specific crystal facets, thereby modulating the relative growth rates and favoring spherical particle assembly (Rao and Cölfen, 2017). Mild particle agglomeration is also observed, which is typical for hydrothermally derived oxides due to Van der Waals interactions during the drying stage (Grass et al., 2006). Nevertheless, the overall microstructure indicates good homogeneity and potential for enhanced surface reactivity. The selective adsorption of CTAB facilitates fine-tuning of particle morphology by controlling surface energies, enabling the formation of structures not typically achievable through conventional growth mechanisms (Maya-Johnson et al., 2017).

The morphological findings are in strong agreement with the XRD results, which confirmed the formation of monoclinic $MnWO_4$ with high crystallinity and no detectable secondary phases. The absence of sharp anisotropic features in the SEM images is consistent with the broadened but symmetrical diffraction peaks in the XRD patterns, suggesting that the particles are nanocrystalline and structurally uniform across different orientations.

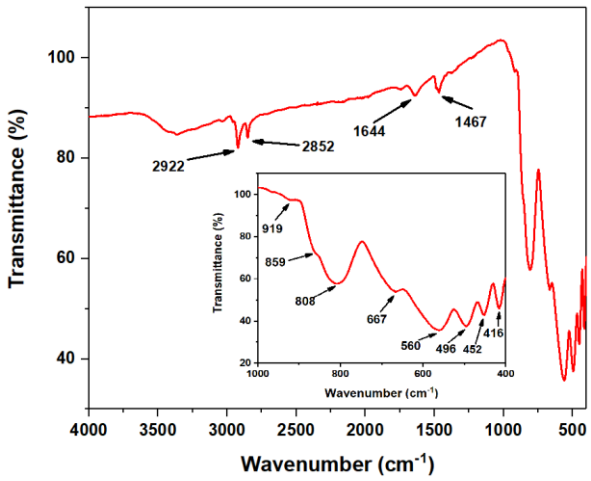

Figure 3. FTIR spectrum of $MnWO_4$. Inset shows the bands in the range of 1000-400cm-1.

The FTIR spectrum of hydrothermally synthesized $MnWO_4$ is presented in Figure 3, with an inset highlighting the fingerprint region between 1000 and 400 cm^{-1}. The observed spectral bands confirm the formation of $MnWO_4$ and the successful incorporation of CTAB as a structure-directing agent during synthesis. Characteristic CH_2 stretching vibrations of the amine group were identified at 2922 cm^{-1} (asymmetric) and 2852 cm^{-1} (symmetric), accompanied by a CH_3 bending vibration at 1467 cm^{-1}, N–H bending (from CTAB) at 1644 cm^{-1} which are in agreement with previous reports on CTAB-assisted metal tungstates (Xue et al., 2007; Kayhan M, 2025). These features indicate the possible presence of residual CTAB molecules or their interaction with the oxide surface.

In the lower wavenumber region, several distinct peaks were observed between 1000 and 400 cm^{-1}. The sharp band at 919 cm^{-1} is assigned to the stretching vibration of terminal W=O bonds, while the bands at 859 cm^{-1} and 808 cm^{-1} correspond to the symmetric and asymmetric stretching modes of W–O bonds in the WO_4 tetrahedra (Pirhashemi et al., 2018; Kayhan and Kayhan, in press). A band at 667 cm^{-1} is associated with the asymmetric stretching of W–O bonds in the $(W_2O_4)_n$ structural network. Additional peaks at 560 cm^{-1} and 496 cm^{-1} are attributed to Mn–O stretching vibrations, confirming the integration of manganese into the oxide framework (Zheng et al., 2013; Muthamizh et al., 2015). A weak peak at 452 cm^{-1} is linked to the in-plane deformation of the longest W–O bond, while the band at 416 cm^{-1} is assigned to the bending mode of W–O in the WO_2 terminals (Muthamizh et al., 2015).

Moreover, CTAB-assisted $MnWO_4$ exhibited minor shifts in the Mn–O stretching region, which may be indicative of subtle structural perturbations. These shifts could possibly reflect weak substitutional effects or partial coordination involving bromine species, such as Mn–Br, as suggested in similar CTAB-mediated tungstate systems (Luo et al., 2018; Zargazi and Entezari, 2019). This could possibly suggest the formation of disordered $[WO_{6-x}Br_{2x}]$ species due to the presence of bromide ions, which disturb the local coordination geometry of tungsten. Such distortion may facilitate the creation of electron traps or oxygen vacancies, forming active surface sites that contribute to enhanced properties in photocatalytic or photochromic responses (Kayhan E, 2025; Kayhan M, 2025).

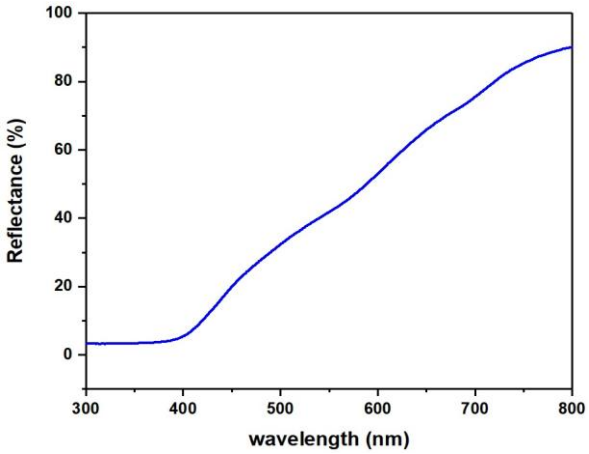

Figure 4. Reflectance data of MnWO4 via UV-DRS.

The optical properties of the synthesized $MnWO_4$ sample were investigated using UV–visible diffuse reflectance spectroscopy (UV-DRS), as shown in Figure 4. A sharp absorption edge exhibits near 395 nm, indicative of a band gap characteristic of tungstate-based semiconductors. The reflectance gradually increases with wavelength, reaching approximately 90% at 800 nm. A weak reflectance shoulder peak was detected at approximately 512 nm, which is attributed to the electronic transition from O-2p to Mn-3d states within the $MnWO_4$ structure. In addition to this, a weaker yet distinct absorption band was observed near 640 nm, which is assigned to the spin-forbidden electronic transition between the e_g and t_{2g} orbitals of the Mn-3d states (Nogami et al., 2008). These transitions are characteristic of Mn^{2+} ions in a distorted octahedral coordination, as expected for wolframite-type $MnWO_4$, and are in good agreement with the XRD results confirming the formation of a single-phase monoclinic structure with high crystallinity.

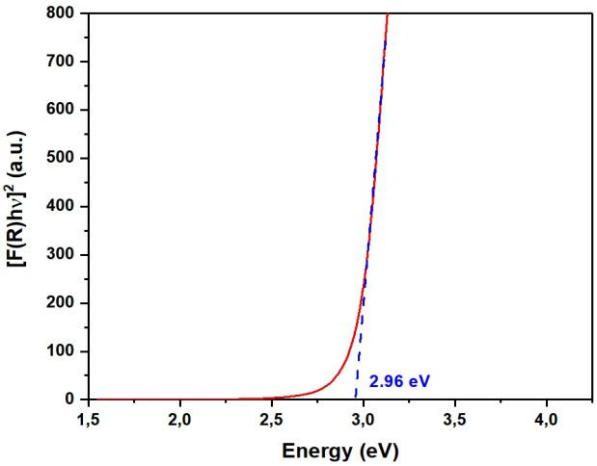

Figure 5. Direct band gap of $MnWO_4$.

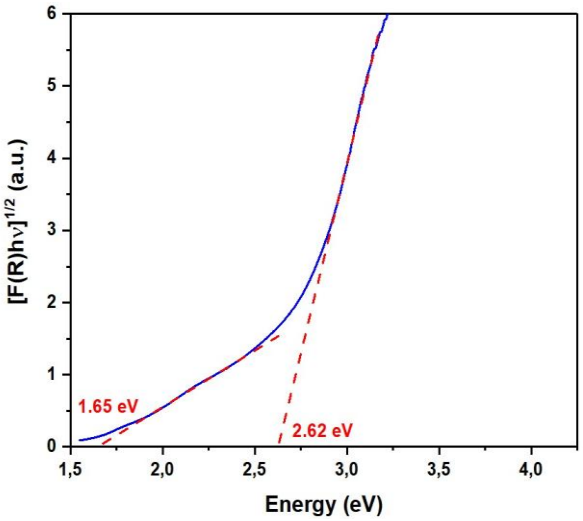

Figure 6. Indirect band gap of $MnWO_4$.

The optical band gap (E_g) of the synthesized $MnWO_4$ nanostructures was estimated using the Tauc method, based on the Kubelka–Munk transformation of diffuse reflectance data. The Tauc plot was constructed by plotting $[F(R)h\nu]^n$ versus photon energy ($h\nu$), where F(R) denotes the Kubelka–Munk function, h is Planck's constant, and ν is the frequency of the incident light. The value of the exponent *n* in the Tauc relation depends on the nature of the electronic transition, with $n = ½$ for indirect allowed transitions and $n = 2$ for direct allowed transitions. The optical band gap was determined by extrapolating the linear region of the plot to the energy axis, where $[F(R)h\nu]^n = 0$.

In the present study, the Tauc plots revealed both an indirect and a direct band gap for $MnWO_4$, consistent with the semiconducting nature of tungstate-based oxides. The indirect band gap was found to be approximately 1.65 eV and 2.62 eV (Figure 6), whereas the direct band gap was estimated to be around 2.96 eV (Figure 5). These values align well with previously reported band gaps of $MnWO_4$ nanostructures synthesized via hydrothermal and microwave-assisted routes (Almeida et al., 2012; Chakraborty et al., 2012). The presence of both direct and indirect transitions suggests that the optical behavior of $MnWO_4$ may be influenced by its microstructure, crystallite size, or surface states induced during synthesis, particularly in the presence of surfactants like CTAB.

Compared to our earlier work in which $MnWO_4$ was synthesized via a conventional solid-state route (Kayhan and Kayhan, in press), the hydrothermal method used in this study yielded lower band gap values. In the previous study, indirect band gaps were determined as 1.72 eV and 2.76 eV, while the direct band gap was measured at 3.18 eV. This downward shift in energy levels is indicative of enhanced light absorption in the visible range. Such narrowing of the band gap may arise not only from morphological and crystallinity differences, but also from structural disorder introduced during synthesis, as evidenced by FTIR analysis. Specifically, the CTAB-assisted $MnWO_4$ exhibited subtle shifts in the Mn–O stretching region and signatures of bromine-influenced $[WO_{6-x}Br_{2x}]$ species. These features suggest that bromide ions may have partially substituted oxygen within the coordination sphere of tungsten, thereby inducing local distortions and creating electron traps or oxygen vacancies (Luo et al., 2018; Zargazi and Entezari, 2019). Such defect-related states are known to facilitate charge carrier separation and enhance the generation of reactive species under illumination.

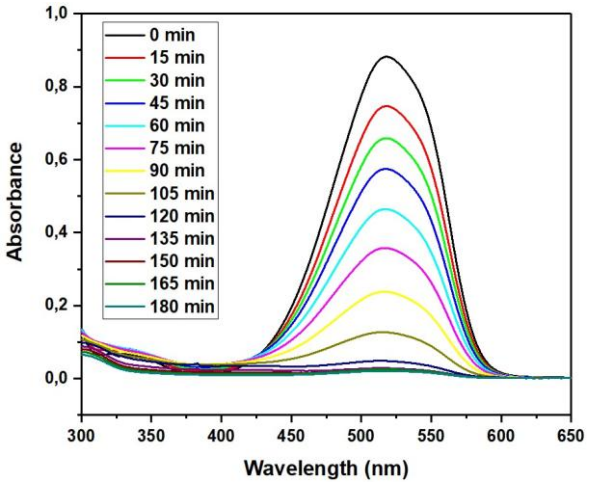

Figure 7. UV–Vis spectra of methyl red solution during photocatalytic degradation by $MnWO_4$ over 180 minutes.

Figure 7 shows the change in absorbance of methyl red using hydrothermally synthesized MnWO4 as a photocatalyst over time at every 15 minutes within the time interval of 0–180 minutes.

The initial spectrum (black line at 0 min) shows a strong absorbance peak around 518 nm is associated with the azo chromophore (–N=N–) group of methyl red, corresponding to the characteristic absorption of methyl red (MR) in aqueous solution. As time elapses, the intensity of this peak decreases steadily, indicating the progressive breakdown of the MR dye molecules. The degradation efficiency increases rapidly during the first 120 minutes, reaching over 90%. Between 135–180 minutes, the curve plateaus near 95–97%, suggesting a saturation point or equilibrium. The near-complete degradation (close to 100%) highlights the high photocatalytic activity of $MnWO_4$. After 180 minutes, the absorbance at 518 nm is nearly zero, suggesting almost complete degradation of methyl red.

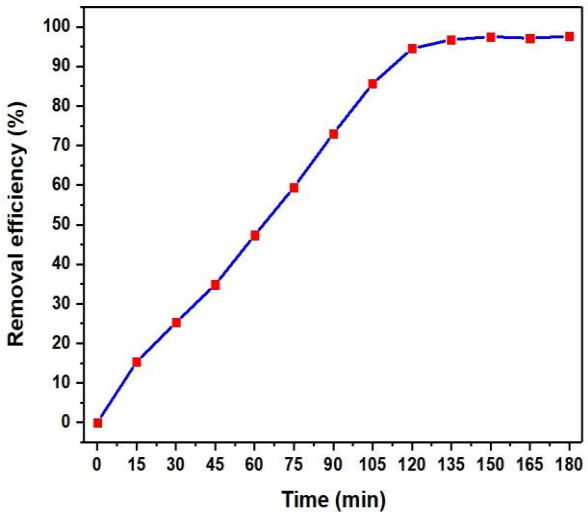

Figure 8. Removal efficiency of MnWO4 on the photodegradation of Methyl Red dye.

The improvement in optical properties directly translated into superior photocatalytic activity. While the solid-state-derived $MnWO_4$ achieved only ~60% degradation of methylene blue after 180 minutes, the hydrothermally synthesized counterpart reached 98% under identical conditions (Figure 8). These findings highlight the synergistic effect of controlled synthesis, defect engineering, and surfactant-assisted structural modulation on the functional performance of $MnWO_4$-based photocatalysts. The near-complete degradation (close to 100%) highlights the high photocatalytic activity of $MnWO_4$.

The superior photocatalytic performance of $MnWO_4$ synthesized via the CTAB-assisted hydrothermal method can be attributed to its controlled morphology and defect-rich surfaces, which enhance charge separation and light absorption. Compared to conventional photocatalysts such as TiO_2 and ZnO under different light sources, the $MnWO_4$ system demonstrated significantly higher degradation efficiency under UV-C irradiation. For instance, TiO_2 achieved 85% methyl red removal in 120 minutes under UV-A light (Zhang et al., 2021), while ZnO reached only 54% removal under sunlight in 180 minutes (Gaim et al., 2019). Recent studies on g-C_3N_4 and its composites have also explored azo dye degradation under sunlight, reporting efficiencies of 97% for pristine g-C_3N_4 in 120 minutes (Sahoo et al., 2024) and 95% for g-C_3N_4/$MnWO_4$ heterojunctions in 120 minutes (Li et al., 2025). Similarly, $MnWO_4$-based composites such as $MnWO_4$/WO_3 have shown 88% methyl orange removal in 120 minutes under sunlight (Jayakumar et al., 2024). Moreover, $MnWO_4$ ceramic nanomaterials demonstrated excellent performance, achieving 98% methylene blue degradation under visible light in 120 minutes (Shivaganga et al., 2023). Although these systems demonstrate good sunlight activity, their performance strongly depends on solar irradiation and longer treatment times. While previous $MnWO_4$-based systems have shown promising results, they generally reported lower efficiencies under UV-C. For example, a closely related study reported only 60% methyl red removal after 180 minutes without CTAB modification (Kayhan and Kayhan, in press). In contrast, the current $MnWO_4$ system achieved 98% degradation within 90 minutes under UV-C, highlighting its potential as a more effective alternative. Thus, this work clearly differentiates itself by demonstrating enhanced performance through surfactant-assisted synthesis, validating the role of CTAB in improving photocatalytic activity. These comparative results are summarized in Table 1, highlighting the superior performance of CTAB-assisted $MnWO_4$ relative to conventional and previously reported photocatalysts.

Table 1. Comparative photocatalytic performance of $MnWO_4$ and benchmark catalysts (TiO_2, ZnO, g-C_3N_4, Bi_2WO_6) for azo dye degradation under various light sources. The enhanced efficiency of CTAB-assisted $MnWO_4$ under UV-C irradiation is highlighted relative to previously reported systems

Photocatalyst	Light Source	Dye Type	Degradation Efficiency (%)	Time (min)	Reference
TiO_2	UV-A	Methyl Red	85	120	(Zhang et al. 2021)
ZnO	Sunlight	Methyl Red	54	180	(Gaim et al. 2019)
g-C_3N_4	Sunlight	Methyl Red	97	120	(Sahoo et al. 2024)
g-C_3N_4/$MnWO_4$ heterojunction	Sunlight	Azo dyes (CR, MB)	95	120	(Li et al. 2025)
$MnWO_4$/WO_3 nanocomposite	Sunlight	Methyl Orange	88	120	(Jayakumar et al. 2024)
$MnWO_4$ ceramic nanomaterial	Visible	Methylene Blue	98	120	(Shivaganga et al. 2023)
$MnWO_4$	UV-C	Methyl Red	60	180	(Kayhan and Kayhan, in press)
$MnWO_4$	UV-C	Methyl Red	98	90	This study

5. Conclusion

In conclusion, $MnWO_4$ nanoparticles synthesized via CTAB-assisted hydrothermal method demonstrated remarkable photocatalytic efficiency, achieving 98% degradation of Methyl Red dye under UV-C irradiation. This high performance is attributed to the controlled morphology and defect-rich surfaces, which enhance light absorption and charge separation. The structural features confirmed by XRD, SEM, FTIR, and UV-DRS analyses directly correlate with the observed photocatalytic activity. These findings highlight the potential of $MnWO_4$ as a cost-effective and efficient photocatalyst for azo dye remediation. Given its strong degradation capability and reproducible synthesis, $MnWO_4$ may be considered for future environmental applications, particularly in wastewater treatment technologies.

Author Contributions

The percentages of the author' contributions are presented below. The author reviewed and approved the final version of the manuscript.

	M.K.
C	100
D	100
S	100
DCP	100
DAI	100
L	100
W	100
CR	100
SR	100
PM	100
FA	100

C=Concept, D= design, S= supervision, DCP= data collection and/or processing, DAI= data analysis and/or interpretation, L= literature search, W= writing, CR= critical review, SR= submission and revision, PM= project management, FA= funding acquisition.

Conflict of Interest

The author declared that there is no conflict of interest.

Ethical Consideration

Ethics committee approval was not required for this study because of there was no study on animals or humans.

References

Ahmad MA, Ahmad N, Bello OS. 2015. Modified durian seed as adsorbent for the removal of methyl red dye from aqueous solutions. Appl Water Sci, 5(4): 407–423. https://doi.org/10.1007/s13201-014-0208-4

Ahmad MA, Ahmed NB, Adegoke KA, Bello OS. 2019. Sorption studies of methyl red dye removal using lemon grass (Cymbopogon citratus). Chem Data Collect, 22: 100249. https://doi.org/10.1016/j.cdc.2019.100249

Alharbi AA, Aldaghri O, El-Badry BA, Ibnaouf KH, Alfadhl F, Albadri A, Modwi A. 2024. Degradation of methyl red dye via fabricated Y_2O_3–MgO/g-C_3N_4 nanostructures: modification of band gap and photocatalysis under visible light. Opt Mater, 152: 115443. https://doi.org/10.1016/j.optmat.2024.115443

Allabakshi SM, Srikar PSNSR, Gangwar RK, Maliyekkal SM. 2025. Nonthermal plasma technology for degradation of dyes in wastewater. In: Hamdaoui O (Ed.), Innovative and Hybrid Advanced Oxidation Processes for Water Treatment. Elsevier, pp: 255–278. https://doi.org/10.1016/B978-0-443-14100-3.00001-6

Almeida MAP, Cavalcante LS, Varela JA, Li MS, Longo E. 2012. Effect of different surfactants on the shape, growth and photoluminescence behavior of $MnWO_4$ crystals synthesized by the microwave-hydrothermal method. Adv Powder Technol, 23(1): 124–128. https://doi.org/10.1016/j.apt.2011.10.004

Berradi M, Hsissou R, Khudhair M, Assouag M, Cherkaoui O, El Bachiri A, El Harfi A. 2019. Textile finishing dyes and their impact on aquatic environs. Heliyon, 5(11): e02711. https://doi.org/10.1016/j.heliyon.2019.e02711

Chakraborty AK, Ganguli S, Kebede MA. 2012. Photocatalytic degradation of 2-propanol and phenol using Au loaded $MnWO_4$ nanorod under visible light irradiation. J Cluster Sci, 23(2): 437–448. https://doi.org/10.1007/s10876-012-0450-6

Gaim YT, Tesfamariam GM, Nigussie GY, Ashebir ME. 2019. Synthesis, characterization and photocatalytic activity of N-doped Cu_2O/ZnO nanocomposite on degradation of methyl red. J Compos Sci, 3(4): 93. https://doi.org/10.3390/jcs3040093

Grass RN, Tsantilis S, Pratsinis SE. 2006. Design of high-temperature, gas-phase synthesis of hard or soft TiO_2 agglomerates. AIChE J, 52(4): 1318–1325. https://doi.org/10.1002/aic.10739

Hassan MS, Amna T, Al-Deyab SS, Kim HC, Khil MS. 2015. Monodispersed 3D $MnWO_4$–TiO_2 composite nanoflowers photocatalysts for environmental remediation. Curr Appl Phys, 15(6): 753–758. https://doi.org/10.1016/j.cap.2015.03.022

He HY, Huang JF, Cao LY, Wu JP. 2010. Photodegradation of methyl orange aqueous on $MnWO_4$ powder under different light resources and initial pH. Desalination, 252(1): 66–70. https://doi.org/10.1016/j.desal.2009.10.024

Jayakumar P, Palani S, Nallathambi M, Kuppusamy K. 2024. Evaluation of $MnWO_4$ nanomaterial for enhanced photocatalytic degradation activity over methyl orange. Lett Appl NanoBioSci, 13(1): 1. https://doi.org/10.33263/lianbs131.001

Kayhan E. 2025a. Temperature-controlled synthesis of bismuth tungstate with enhanced photochromic properties. Int J Appl Ceram Technol, 22(3): e15079. https://doi.org/10.1111/ijac.15079

Kayhan M, Aksoy M, Kayhan E. 2024. A facile synthesis of photocatalytic $Fe(OH)_3$ nanoparticles for degradation of phenol. ChemistrySelect, 9(23): e202401367. https://doi.org/10.1002/slct.202401367

Kayhan M. 2025b. Comparative study of photochromic behavior of bismuth tungstate via different surfactants. Ceram Int, 51(14): 19579–19588. https://doi.org/10.1016/j.ceramint.2025.02.133

Khaksar M, Boghaei DM, Amini M. 2015. Synthesis, structural characterization and reactivity of manganese tungstate nanoparticles in the oxidative degradation of methylene blue. C R Chim, 18(2): 199–203. https://doi.org/10.1016/j.crci.2014.04.004

Kumar KS, Vaishnavi K, Venkataswamy P, Ravi G, Ramaswamy K, Vithal M. 2021. Photocatalytic degradation of methylene blue over N-doped $MnWO_4$ under visible light irradiation. J Indian Chem Soc, 98(10): 100140. https://doi.org/10.1016/j.jics.2021.100140

Li R, Du Y, Tang C, Huang Y, Han G. 2025. Photocatalytic degradation of azo dye wastewater by thermal stripping of g-C_3N_4. In: Al-Majali Y, Wisner B, Mastorakos IN, Hunyadi Murph SE, Paramsothy M (eds) Advances in Sustainable Composites. TMS 2025. Springer, Cham. https://doi.org/10.1007/978-3-031-81057-2_17

Luo S, Ke J, Yuan M, Zhang Q, Xie P, Deng L, Wang S. 2018. $CuInS_2$ quantum dots embedded in Bi_2WO_6 nanoflowers for enhanced visible light photocatalytic removal of contaminants. Appl Catal B Environ, 221: 215–222. https://doi.org/10.1016/j.apcatb.2017.09.028

Maya-Johnson S, Gracia L, Longo E, Andres J, Leite ER. 2017. Synthesis of cuboctahedral CeO_2 nanoclusters and their assembly into cuboid nanoparticles by oriented attachment. ChemNanoMat, 3(4): 228–232. https://doi.org/10.1002/cnma.201700005

Muthamizh S, Suresh R, Giribabu K, Manigandan R, Praveen Kumar S, Munusamy S, Narayanan V. 2015. $MnWO_4$ nanocapsules: synthesis, characterization and its electrochemical sensing property. J Alloys Compd, 619: 601–609. https://doi.org/10.1016/j.jallcom.2014.09.049

Nagaraja K, Mallika B, Arunpandian M, Ravindran E, Tae Hwan O. 2025. Green synthesis of gold-decorated $BaTiO_3$-ZnO nanocomposites using Arabic gum polymer for efficient photocatalytic degradation of emerging textile dyes, antimicrobial, and toxicological evaluation. Int J Biol Macromol, 311: 143396. https://doi.org/10.1016/j.ijbiomac.2025.143396

Nezzari A, Medina S, Khane Y, Boublenza H, Guezzoul M, Zoukel A, Amrani B. 2025. Photocatalytic degradation of brilliant green dye using Cu_2NiSnS_4 thin films under ultraviolet irradiation. Inorg Chem Commun, 174: 114021. https://doi.org/10.1016/j.inoche.2025.114021

Nogami A, Suzuki T, Katsufuji T. 2008. Second harmonic generation from multiferroic $MnWO_4$. J Phys Soc Jpn, 77(11): 115001. https://doi.org/10.1143/JPSJ.77.115001

Pirhashemi M, Habibi-Yangjeh A. 2018. Fabrication of novel ZnO/$MnWO_4$ nanocomposites with p-n heterojunction: visible-light-induced photocatalysts with substantially improved activity and durability. J Mater Sci Technol, 34(10): 1891–1901. https://doi.org/10.1016/j.jmst.2018.01.014

Rao A, Cölfen H. 2017. Facet control in nanocrystal growth. In: Atwood JL (Ed.), Comprehensive Supramolecular Chemistry II. Elsevier, UK, London, pp: 129–156. https://doi.org/10.1016/B978-0-12-409547-2.12638-1

Rastin H, Dell'Angelo D, Sayede A, Badawi M, Habibzadeh S. 2025. Green and sustainable metal-organic frameworks (MOFs) in wastewater treatment: a review. Environ Res, 282: 122087. https://doi.org/10.1016/j.envres.2025.122087

Sahoo S, Reddy GBT, Mahamallik P. 2024. Sunlight-assisted photocatalytic degradation of methyl red using g-C_3N_4 as metal-free photocatalyst. In: Mazumder D (ed.) Sustainable Advanced Technologies for Environmental Management. Springer Proc Earth Environ Sci. Springer, Cham, London, UK, pp: 62. https://doi.org/10.1007/978-3-031-64006-3_1

Shalini S, Sasikala T, Tharani D, Venkatesh R, Muthulingam S. 2024. Novel green CQDs/ZnO binary photocatalyst synthesis for efficient visible light irradiation of organic dye degradation. J Mol Liq, 410: 125525. https://doi.org/10.1016/j.molliq.2024.125525

Shamshad J, Ur Rehman R. 2025. Innovative approaches to sustainable wastewater treatment: a comprehensive exploration of conventional and emerging technologies. Environ Sci Adv, 4(2): 189–222. https://doi.org/10.1039/D4VA00136B

Shivaganga GS, Parameswara P, Mallikarjunaswamy C, Kumar KCS, Soundarya TL, Nagaraju G, Ranganatha VL. 2023. Green, nonchemical route for the synthesis of $MnWO_4$ nanostructures: photocatalytic and electrochemical performance. J Mater Sci Mater Electron, 34(25): 1791. https://doi.org/10.1007/s10854-023-11190-3

Siahsahlan M, Mohammadi Aref S, Naghshara H, Azmayesh R. 2025. The effects of reduced graphene oxide amount on the photocatalytic performance of TiO_2 nanoparticles for hydrogen evolution. Int J Hydrogen Energy, 142: 318–329. https://doi.org/10.1016/j.ijhydene.2025.05.411

Vosoughifar M. 2017. Preparation, characterization, and morphological control of $MnWO_4$ nanoparticles through novel method and its photocatalyst application. J Mater Sci Mater Electron, 28(2): 2135–2140. https://doi.org/10.1007/s10854-016-5777-6

Wang G, Xu J, Sun Z, Zheng S. 2020. Surface functionalization of montmorillonite with chitosan and the role of surface properties on its adsorptive performance: a comparative study on mycotoxins adsorption. Langmuir, 36(10): 2601–2611. https://doi.org/10.1021/acs.langmuir.9b03673

Wu W, Qin W, He Y, Wu Y, Wu T. 2012. The effect of pH value on the synthesis and photocatalytic performance of $MnWO_4$ nanostructure by hydrothermal method. J Exp Nanosci, 7(4): 390–398. https://doi.org/10.1080/17458080.2010.533293

Xue W, He H, Zhu J, Yuan P. 2007. FTIR investigation of CTAB–Al–montmorillonite complexes. Spectrochim Acta A Mol Biomol Spectrosc, 67(3): 1030–1036. https://doi.org/10.1016/j.saa.2006.09.024

Zargazi M, Entezari MH. 2019. Sonochemical versus hydrothermal synthesis of bismuth tungstate nanostructures: photocatalytic, sonocatalytic and sonophotocatalytic activities. Ultrason Sonochem, 51: 1–11. https://doi.org/10.1016/j.ultsonch.2018.10.010

Zhang D, Otitoju TA, Ouyang Y, Shoparwe NF, Wang S, Li S. 2021. A review on metal ions modified TiO_2 for photocatalytic degradation of organic pollutants. Catalysts, 11(9): 1039. https://doi.org/10.3390/catal11091039

Zheng M, Zhang H, Gong X, Xu R, Xiao Y, Dong H, Liu Y. 2013. A simple additive-free approach for the synthesis of uniform manganese monoxide nanorods with large specific surface area. Nanoscale Res Lett, 8(1): 166. https://doi.org/10.1186/1556-276X-8-166

Black Sea Journal of Engineering and Science
doi: 10.34248/bsengineering.1759120

Open Access Journal
e-ISSN: 2619 – 8991

Research Article
Volume 8 - Issue 5: 1585-1594 / September 2025

NUMERICAL INVESTIGATION OF HYDROFOIL CAVITATION USING OPENFOAM: EFFECT OF THICKNESS AND CAMBER

Mehmet Numan KAYA[1]*

[1]*Necmettin Erbakan University, Faculty of Engineering, Department of Mechanical Engineering, Konya, Türkiye*

Abstract: Cavitation is a critical phenomenon in hydrodynamic applications, significantly influencing the performance and durability of hydrofoils. This study presents a numerical investigation of cavitation over hydrofoils, focusing on the effects of thickness and camber, using the interPhaseChangeFoam solver within the OpenFOAM framework. The numerical setup was validated against experimental data for the NACA66(mod) hydrofoil. Simulations were performed at a fixed angle of attack of 4° under two cavitation numbers, σ = 0.84 and σ = 0.91 using the Schnerr–Sauer cavitation model with a vapor pressure of 2420 Pa. To assess thickness effects, symmetric hydrofoils NACA0012, NACA0016, and NACA0020 were analyzed, while camber effects were examined using hydrofoils of identical thickness but varying camber, NACA0012, NACA2412, and NACA4412. Results show that cambered and thicker hydrofoils develop more extensive cavitation regions. Increasing the cavitation number generally leads to higher lift coefficients, with the effect more pronounced for cambered profiles. Greater camber promotes earlier cavitation inception, a larger cavity extent, and higher lift, with NACA4412 achieving the highest lift coefficients of approximately C_L = 0.74 and 0.79 at σ = 0.84 and 0.91, respectively. Increased thickness also enlarges the cavitation region but generally results in lower lift, as observed for NACA0020, which exhibited lift coefficients of approximately C_L = 0.31 and 0.34 at σ = 0.84 and 0.91, respectively. Increasing the cavitation number from σ = 0.84 to 0.91 reduced drag for all profiles by up to about 23% while preserving lift in cambered foils.

Keywords: Cavitation, Hydrofoil, Thickness, Camber, CFD, OpenFOAM

***Corresponding author:** Necmettin Erbakan University, Faculty of Engineering, Department of Mechanical Engineering, Konya, Türkiye
E mail: mnkaya@erbakan.edu.tr (M.N. KAYA)
Mehmet Numan KAYA https://orcid.org/0000-0003-3116-9442

Received: August 05, 2025
Accepted: September 09, 2025
Published: September 15, 2025

Cite as: Kaya MN. 2025. Numerical investigation of hydrofoil cavitation using openfoam: Effect of thickness and camber. BSJ Eng Sci, 8(5): 1585-1594.

1. Introduction

Cavitation, the rapid phase change from liquid to vapor when local pressure drops below the vapor-pressure threshold, remains one of the most critical, and still incompletely understood, phenomena in the hydrodynamic performance and durability of lifting surfaces such as hydrofoils (Adil et al., 2025). In practical applications, cavitation can trigger drastic lift/drag fluctuations, high-amplitude pressure pulses, broadband noise, and material erosion, thereby limiting operating envelopes and shortening service life (Qiu et al., 2025). As performance targets tighten and design margins shrink, a predictive, physics-based understanding of cavitation on hydrofoils has become indispensable.

Numerical investigations have systematically examined how multiple physical and operating parameters govern cavitation on hydrofoils. Early investigations by Kang et al. (2014) showed, for a Clark-Y profile, that both cavity length and lift/drag increase monotonically with angle of attack over several cavitation numbers. Karim et al. (2018) carried out finite-volume RANS calculations on NACA 0012/0021 foils, independently sweeping cavitation number (σ) and angle of attack (α), and their results showed that cavity length and lift–drag trends are more sensitive to α at fixed σ. Guo et al. (2023) extended parameter studies through a combined experimental/CFD effort with viscous oil, varying velocity, pressure, temperature, and α, revealing that pressure had the strongest influence on vapor-volume growth while temperature effects were secondary. The interaction of cavitation with flow dynamics has been shown to be crucial for understanding hydrofoil performance. The nucleation and dynamics of cavitation bubbles have been investigated by Huang et al. (2014) , who revealed that bubble formation and interaction with hydrofoil surfaces can lead to material degradation, erosion, and performance loss, with flow conditions directly influencing cavitation erosion intensity. Peng et al. (2016) demonstrated the effectiveness of combining experimental observations with numerical simulations in advancing cavitation understanding, providing critical insights into cloud cavitation and its associated flow structures while validating numerical model reliability. Recently, Chen and Escaler (2024) conducted numerical investigations of cavitation effects on wake dynamics behind a blunt trailing edge NACA 0009 hydrofoil, finding that cavitation development enhances vortex shedding frequency while decreasing streamwise inter-vortex spacing, with substantial increases in both lift (C_L) and drag (C_D) coefficients observed as vortex cavitation size

grows. Kumar et al. (2024) introduced passive geometric controls, a rectangular pimple and finite trailing edge, on a cambered NACA 4412 and demonstrated that the pimple suppressed cloud shedding and postponed the onset of supercavitation relative to the baseline foil. Usta et al. (2025) performed numerical simulations to investigate the effects of leading-edge tubercles and surface corrugations on twisted hydrofoils, finding that tubercles delayed stall and reduced cavitation formation. Gallegos and Luo (2024) performed a 3-D RANS study of a circular-leading-edge hydrofoil in which σ, Reynolds number, and three turbulence closures were systematically varied. They concluded that the MSST-PANS model best reproduced the cloud-cavitation regime and its shedding frequency. Mostafa et al. (2016) adopted a bubble-dynamics cavitation model and compared three RANS turbulence closures across multiple σ–α combinations, finding that the SST k-ω scheme captured unsteady sheet-to-cloud transitions most faithfully. Wang et al. (2025) coupled an implicit LES with the Schnerr–Sauer model to probe how an upstream cylinder wake, together with changes in σ and α, modifies vortex-induced pressure fluctuations on a downstream hydrofoil, highlighting the pivotal role of wake shedding frequency in cloud-cavitation dynamics.

Collectively, these studies underscore that cavitation behaviour is highly multi-parametric: turbulence modelling, cavitation number, Reynolds number, inflow unsteadiness, geometric modifications including thickness and camber variations all interact to dictate inception thresholds, cavity topology, and associated hydrodynamic loads. Despite these comprehensive investigations, the individual and isolated effects of thickness and camber on cavitation characteristics remain insufficiently explored. The present study addresses this gap by conducting a systematic numerical investigation using OpenFOAM's interPhaseChangeFoam solver with the Schnerr-Sauer cavitation model to examine the individual contributions of thickness and camber variations on cavitation, thereby offering fundamental, parameter-isolated understanding of the role of thickness and camber in governing cavitation behaviour, which can directly support both theoretical modelling and practical hydrofoil design.

2. Materials and Methods

2.1. Numerical Approach

Computational Fluid Dynamics (CFD) was employed to simulate cavitating flow over hydrofoils using the open-source OpenFOAM framework. The governing equations 1 and 2 are based on the finite volume discretization of the incompressible Reynolds-Averaged Navier–Stokes (RANS) equations, coupled with a volume-of-fluid (VOF) formulation to capture the liquid-vapor interface. The equations of mass and momentum conservation are expressed as (Canlı et al., 2020; Kaya et al., 2025; Manolesos et al., 2024; Zhou and Wang, 2008):

$$\frac{\partial \rho}{\partial t} + \nabla \cdot (\mathbf{V}\rho) = 0 \tag{1}$$

$$\frac{\partial (\rho \mathbf{V})}{\partial t} + \nabla \cdot (\rho \mathbf{V}\mathbf{V}) = -\nabla p + \nabla(\mu \nabla \mathbf{V}) + \rho \mathbf{g} \tag{2}$$

where ρ is the local density depending on vapor volume fraction, $\mathbf{V}$ is the velocity vector, p is pressure, μ is dynamic viscosity, and g is gravitational acceleration. The turbulence was modeled using the standard k-ε model, governed by the following transport equations 3 and 4 for turbulent kinetic energy (k) and turbulent dissipation (ε):

$$\frac{\partial (\rho k)}{\partial t} + \nabla \cdot (\rho \mathbf{V} k) = \nabla \cdot \left[\left(\mu + \frac{\mu_t}{\sigma_k} \right) \nabla k \right] + P_k - \rho \varepsilon \tag{3}$$

$$\frac{\partial (\rho \varepsilon)}{\partial t} + \nabla \cdot (\rho \mathbf{V} \varepsilon) = \nabla \cdot \left[\left(\mu + \frac{\mu_t}{\sigma_\varepsilon} \right) \nabla \varepsilon \right] + C_{\{1\varepsilon\}} \left(\frac{\varepsilon}{k} \right) P_k - C_{\{2\varepsilon\}} \rho \left(\frac{\varepsilon^2}{k} \right) \tag{4}$$

where P_k is the production of turbulent kinetic energy, and μ_t is the eddy viscosity. The standard k–ε turbulence model was selected for its reliability in cavitating flow simulations and its ability to provide stable, accurate results without the need for excessive near-wall refinement. The model also produced results in good agreement with experimental validation data, as presented in section 2.4. In this study, y^+ values were maintained within the range of approximately 30–100, which is consistent with the recommended range for this turbulence model.

2.2. Cavitation Modelling

Cavitation was simulated using the interPhaseChangeFoam solver in OpenFOAM, which solves the incompressible two-phase flow using the VOF method with mass transfer between liquid and vapor phases. The Schnerr–Sauer cavitation model was adopted to model the phase change process (Schnerr and Sauer, 2001). The mass transfer source term ṁ in the continuity equation is defined based on bubble dynamics as (Arndt, 2012; Kubota et al., 1992):

$$\dot{m} = C_v \cdot \frac{3\alpha_l (1-\alpha_l)\rho_l}{R_b} \sqrt{\left[\frac{2}{3} \cdot \frac{p_v - p}{\rho_l} \right]}, if\ p < p_v \tag{5}$$

$$\dot{m} = C_c \cdot \frac{3\alpha_v (1-\alpha_v)\rho_v}{R_b} \sqrt{\left[\frac{2}{3} \cdot \frac{p - p_v}{\rho_l} \right]}, if\ p > p_v \tag{6}$$

where vapor pressure of water is p_v=2420, bubble diameter is $R_b = 2 \times 10^{-6}$ m, α_l and α_v are liquid and vapor volume fractions, evaporation and condensation coefficients are C_v=1 and $C_c = 1$, ρ_l and ρ_v are liquid and vapor densities. equation 5 represents the evaporation process, activated when the local pressure p is below p_v, while equation 6 models condensation, occurring when p exceeds p_v. The cavitation number is calculated as (equation 7):

$$\sigma = \frac{p_\infty - p_v}{0.5 \cdot \rho \cdot U^2} \tag{7}$$

where σ=0.84 and 0.91 were selected to represent moderate and weak cavitation regimes, respectively.

Time-dependent simulations were run over 20 seconds of physical time, and the last 5 seconds were used to average liftand drag coefficients, ensuring steady-state behavior and statistical convergence. The simulation setup, including boundary conditions, mesh parameters, and solver settings, was chosen to ensure a balance between numerical accuracy and computational efficiency, providing a reproducible framework for similar cavitation studies. BaramFlow was used as the graphical user interface for OpenFOAM simulations.

2.3. Tested Hydrofoils

To investigate the effects of geometric parameters on cavitation behavior, two separate hydrofoil groups were analyzed: one focusing on thickness and the other on camber.

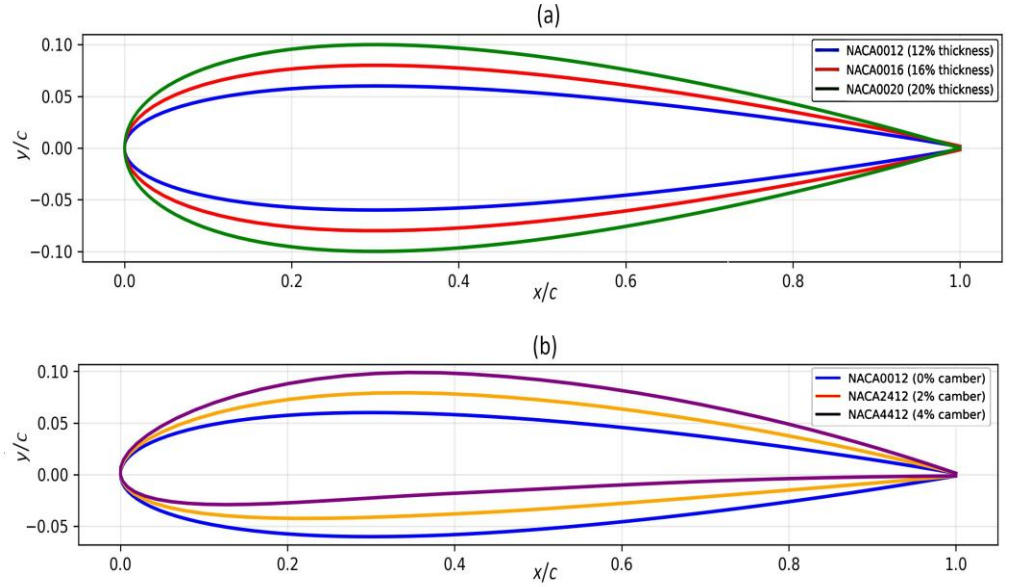

Figure 1. Hydrofoil geometries used in the simulations: (a) NACA0012, NACA0016, NACA0020 (b) NACA0012, NACA2412, NACA4412.

For the thickness effect, symmetric NACA hydrofoils, NACA 0012, NACA 0016, and NACA 0020 were selected, with maximum thicknesses of 12%, 16%, and 20% of the chord, respectively, and zero camber. To examine the effect of camber, three hydrofoils with identical thickness (12%) but varying camber values were studied: NACA 0012 (symmetric), NACA 2412 (2% camber), and NACA 4412 (4% camber). All hydrofoils have the same chord length and were simulated under the same operating conditions to enable a consistent comparison. Geometries of the hydrofoils are presented in Fig. 1.

2.4. Mesh Independence and validation

Three mesh resolutions were generated: coarse, medium, and fine, with 72380, 103148, and 162162 cells, respectively. The numerical results from all three meshes, together with the experimental data (Kim et al., 2010; Shen and Dimotakis, 1989), are compared in Figure 2.

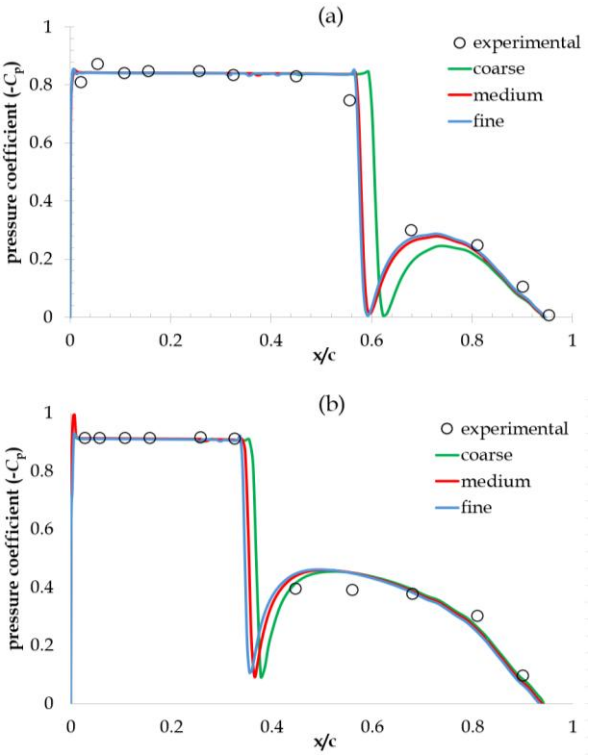

Figure 2. Mesh independence study and validation based on pressure coefficient (C_p) distribution over the NACA66(mod) hydrofoil at an angle of attack of 4° for (a) $\sigma = 0.84$ (b) $\sigma = 0.91$.

For σ = 0.84 (Figure 2a), the onset of the pressure drop occurs at approximately $x/c \approx 0.60$ for the fine and medium meshes, while the coarse mesh shows a slight delay of about $\Delta x/c \approx 0.02$. For σ = 0.91 (Figure 2b), the pressure drop begins earlier at around $x/c \approx 0.38$ for all meshes, with the coarse mesh exhibiting a marginal delay of less than $\Delta x/c \approx 0.01$. These results confirm that the medium mesh provides mesh-independent performance while ensuring computational efficiency; therefore, it was selected for further analysis. Images of the selected medium mesh are presented in Figure 3. All simulations were performed with a Courant number (CFL) of 1. Validation was carried out using the NACA66(mod) hydrofoil at a 4° angle of attack under both cavitation numbers, showing strong agreement in both pressure distribution and cavity extent, confirming the reliability of the numerical setup.

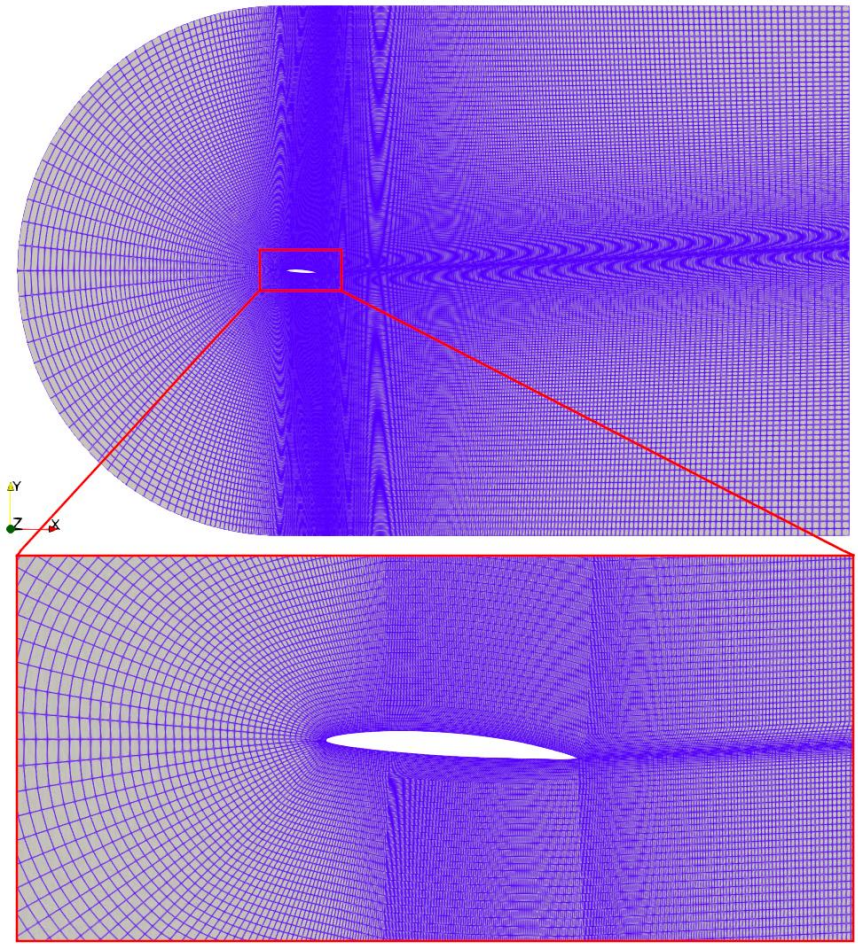

Figure 3. Medium-resolution computational grid selected for further analysis. The illustration shows the overall computational domain (top) and a zoomed-in view around the hydrofoil (bottom).

3. Results and Discussion

This section presents the cavitation characteristics obtained from unsteady simulations performed using the interPhaseChangeFoam solver. The spatial evolution of cavitation structures over the hydrofoil surface for each geometry was analyzed for cavitation number σ=0.84, captured at four nondimensional time instances: t* = 0.1, 0.4, 0.7, and 1.0 and presented in Figure 4. The time-dependent development of cavitation is illustrated through contours of the liquid water volume fraction (α_{water}) at selected nondimensionalized time instances. Time normalization was carried out using a reference time of t_R = 10 seconds, i.e., $t/t_R = t^*$.

The cavitation development over time differs significantly between symmetric and cambered airfoils. In general, cavitation begins near the leading edge and gradually extends downstream with time. The cambered profiles, NACA2412 and NACA4412, exhibit stronger and more pronounced cavitation clouds, especially during the mid-to-late stages (t/t_R = 0.4–1.0). In addition, increase in camber caused to extension of cavitation clouds. In contrast, symmetric airfoils such as NACA0012, NACA0016, and NACA0020 tend to show more localized and stable cavitation patterns. The thickness of the airfoil also increases the extent of cavitation, as observed in the increasing coverage from NACA0012 to NACA0020. Moreover, the asymmetric profiles demonstrate earlier cavitation inception and a broader cavity region due to their higher suction peak near the leading edge. Figure 5 presents the distribution of the liquid water volume fraction on the hydrofoil surfaces for two different cavitation numbers.

The top two rows correspond to the more aggressive cavitating condition at σ = 0.84 while the bottom two rows show results for a milder condition at σ=0.91. The comparison highlights the role of cavitation number in determining cavity extent and shape. As expected, lower σ results in more developed vapor regions and longer attached cavity structures, particularly for thicker or cambered hydrofoils.

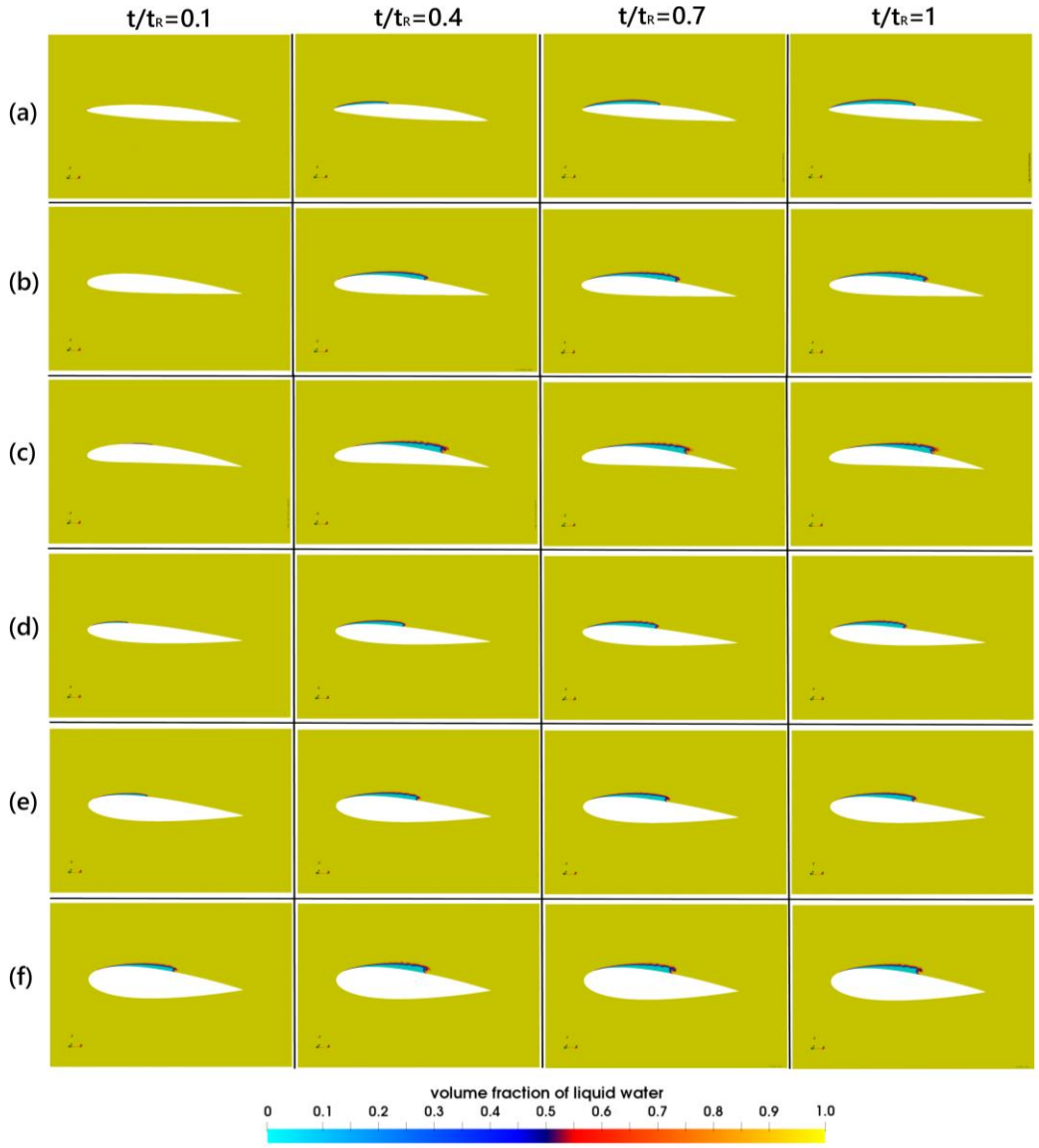

Figure 4. Time evolution of cavitation structures for different airfoils at a cavitation number of σ = 0.84. From top to bottom: (a) NACA66, (b) NACA2412, (c) NACA4412, (d) NACA0012, (e) NACA0016, and (f) NACA0020. The snapshots correspond to nondimensional time instances t/t_R = 0.1, 0.4, 0.7, and 1.0 from left to right. Color contours represent the volume fraction of liquid water.

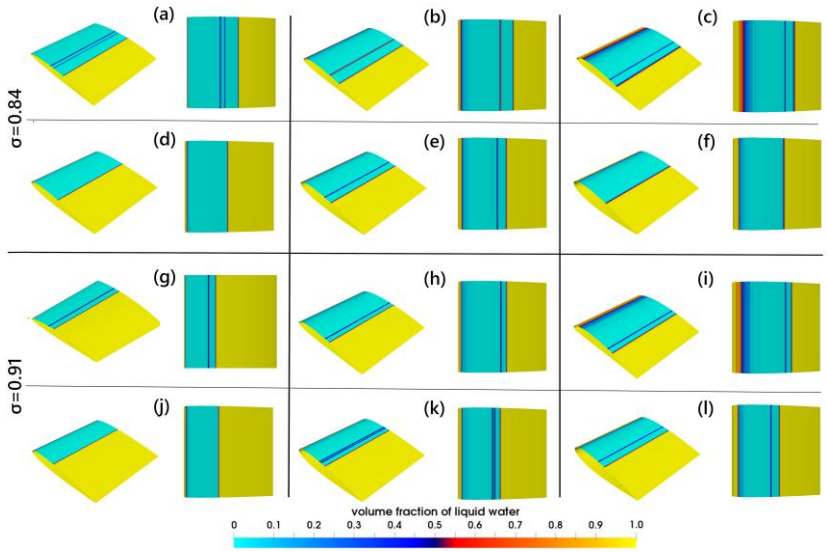

Figure 5. Distribution of liquid water volume fraction over various hydrofoils at two cavitation numbers. The top two rows, (a,b,c,d,e,f), correspond to σ = 0.84, and the bottom two rows, (g,h,i,j,k,l), correspond to σ = 0.91. The hydrofoils are (a,g) NACA66, (b,h) NACA2412, (c,i) NACA4412, (d,j) NACA0012, (e,k) NACA0016, and (f,l) NACA0020.

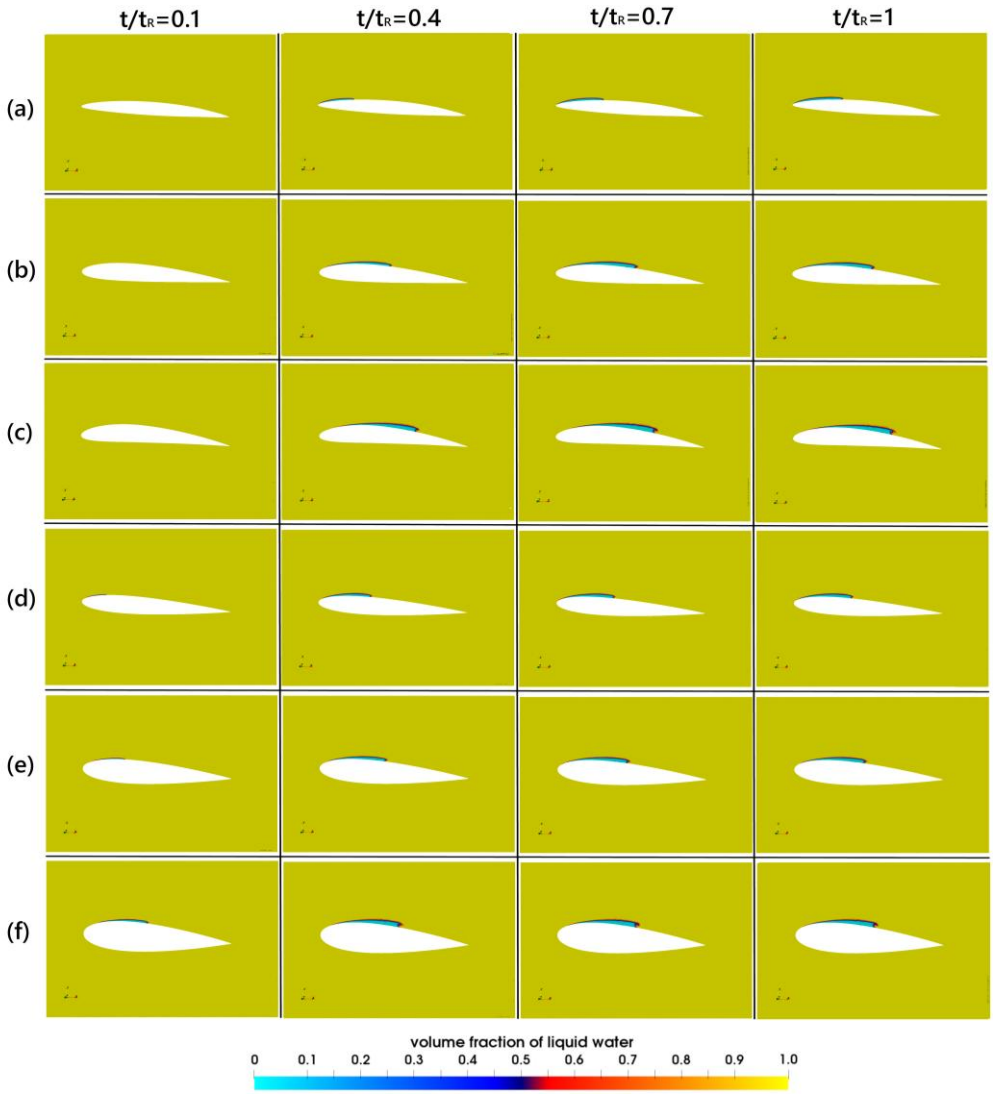

Figure 6. Time evolution of cavitation structures for different airfoils at a cavitation number of σ = 0.91. From top to bottom: (a) NACA66, (b) NACA2412, (c) NACA4412, (d) NACA0012, (e) NACA0016, and (f) NACA0020. The snapshots correspond to nondimensional time instances t/t_R = 0 .1, 0.4, 0.7, and 1.0 from left to right. Color contours represent the volume fraction of liquid water.

To further examine unsteady effects, Figure 6 displays the time-dependent cavitation development for σ = 0.91 at the same nondimensional time instants as in Figure 4. Although cavitation is less pronounced than at σ = 0.84, unsteady cavity dynamics are still evident, especially for thicker and cambered profiles. These results support the conclusion that both thickness and camber significantly influence cavitation inception and evolution.

To evaluate the influence of airfoil geometry on cavitation inception and development, pressure coefficient (C_p) contours were analyzed at two different cavitation numbers σ = 0.84 and 0.91. As shown in Figure 7 at σ=0.84, strong low-pressure zones emerge on cambered hydrofoils, especially near the leading edge, due to enhanced suction effects. This pressure drop increases the risk of cavitation formation. The symmetric profiles exhibit relatively moderate pressure drops.

When the cavitation number is increased to σ = 0.91, as seen in Figure 8 the pressure minima weaken across all profiles, which correlates with delayed cavitation onset and less severe cavity formation. Figure 9 visualizes the surface distribution of pressure coefficient over the hydrofoil surfaces. The upper two rows show results for σ = 0.84, and the lower two rows for σ = 0.91. The color gradients indicate the spatial variation of local pressure, and distinct patterns are visible between cambered and symmetric foils. Cambered foils such as NACA66(mod) and NACA4412 exhibit sharper and more extensive low-pressure zones, which are potential sites for cavitation inception.

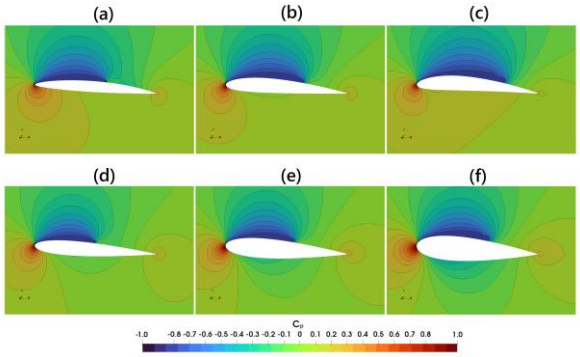

Figure 7. Pressure coefficient (C_p) contours σ =0.84 for (a) NACA66(mod), (b) NACA2412, (c) NACA4412, (d) NACA0012, (e) NACA0016, and (f) NACA0020.

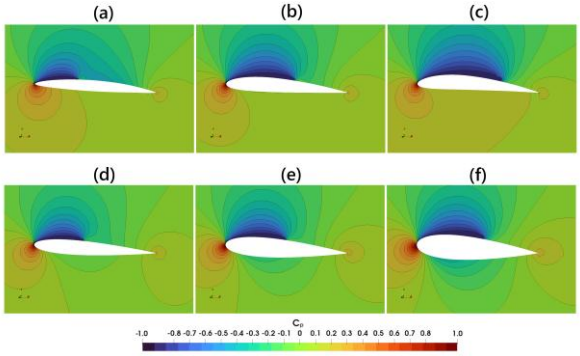

Figure 8. Pressure coefficient (C_p) contours σ =0.91 for (a) NACA66(mod), (b) NACA2412, (c) NACA4412, (d) NACA0012, (e) NACA0016, and (f) NACA0020.

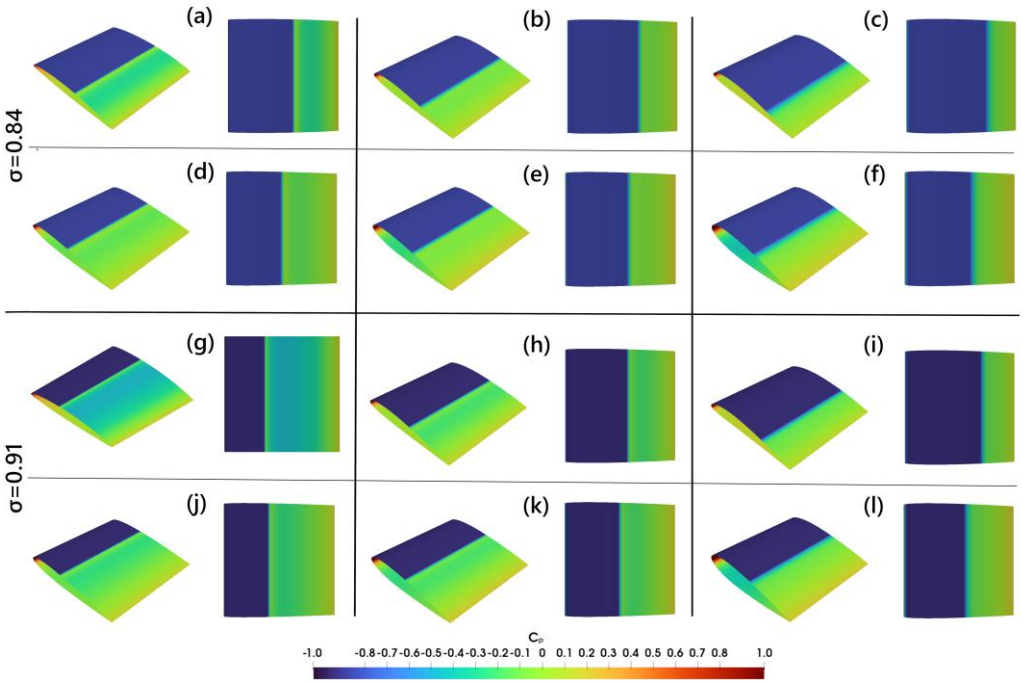

Figure 9. Surface pressure coefficient distributions for all hydrofoils. The upper two rows correspond to σ = 0.84, and the bottom two rows to σ = 0.91. Each two shows (a, g) NACA66(mod), (b, h) NACA2412, (c, i) NACA4412, (d, j) NACA0012, (e, k) NACA0016, and (f, l) NACA0020.

The pressure coefficient distributions presented in Figure 10 demonstrate the significant influence of airfoil geometry parameters on cavitation behavior under different flow conditions. For symmetric airfoils (NACA0012, NACA0016, NACA0020), the thickness effect becomes evident as thicker profiles exhibit more extensive low-pressure regions and increased susceptibility to cavitation, particularly at higher cavitation numbers. At σ = 0.84, all symmetric profiles show similar cavitation inception patterns around x/c = 0.5, while the NACA0012 demonstrates the most pronounced pressure recovery compared to the thicker NACA0016 and NACA0020 profiles. This thickness-dependent behavior intensifies at σ = 0.91, where the NACA0020 profile maintains the most extensive low-pressure zone, confirming that increased thickness ratio promotes cavitation development. The camber effect analysis reveals equally significant influences on cavitation characteristics, where cambered airfoils (NACA2412, NACA4412) exhibit distinctly different pressure distributions compared to the symmetric NACA0012. The highly cambered NACA4412 profile consistently maintains lower pressure coefficients over broader chord ranges at both cavitation numbers, indicating enhanced cavitation inception likelihood and extended cavitation regions on the suction side. The comparison between σ = 0.84 and σ = 0.91 conditions reveals that higher cavitation numbers lead to more extensive cavitation regions and deeper pressure drops across all airfoil geometries, confirming the fundamental relationship between cavitation number and cavitation intensity in hydrofoil applications.

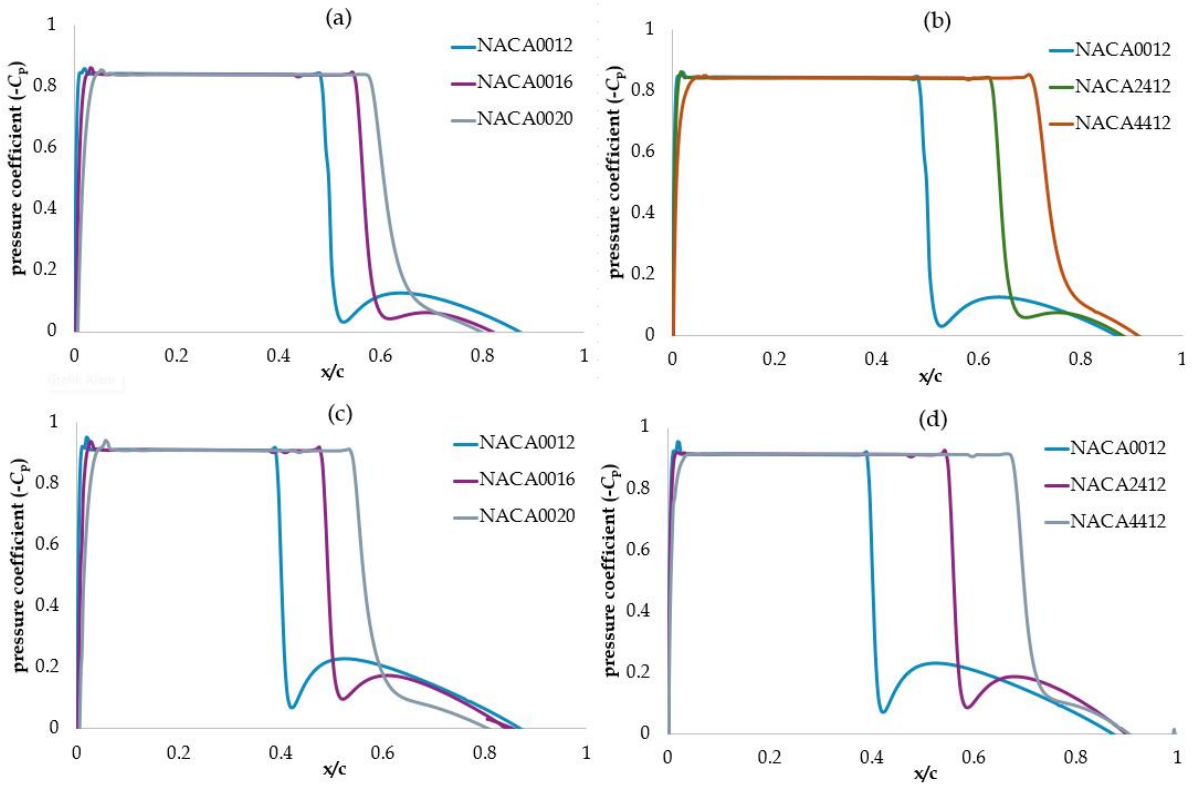

Figure 10. Pressure coefficient distributions on the suction surfaces of hydrofoils at (a,b) σ = 0.84 and (c,d) σ = 0.91.

Table 1 compares the lift and drag coefficients of different hydrofoils under two cavitation conditions. At σ =0.84, cambered hydrofoils like NACA4412 and NACA66 exhibit higher lift coefficients compared to symmetric ones. The drag increases with increasing thickness and camber. When the cavitation number increases to 0.91, the overall drag decreases for all airfoils, while the lift generally remains stable or increases slightly for cambered profiles. This indicates that cavitation has a notable influence on aerodynamic performance, particularly for thin or symmetric hydrofoils.

Table 1. Lift and drag coefficients of the hydrofoils at cavitation numbers σ = 0.84 and σ = 0.91

Hydrofoil	σ = 0.84		σ = 0.91	
	C_L	C_D	C_L	C_D
NACA66	0.698	0.019	0.640	0.016
NACA2412	0.617	0.030	0.624	0.023
NACA4412	0.743	0.039	0.792	0.033
NACA0012	0.423	0.025	0.413	0.020
NACA0016	0.376	0.029	0.385	0.023
NACA0020	0.313	0.039	0.343	0.032

5. Conclusions

This study numerically investigates the cavitation behavior of hydrofoils with varying camber and thickness using the interPhaseChangeFoam solver of OpenFOAM. Two cavitation numbers, σ = 0.84 and 0.91, were considered under a fixed angle of attack of 4°. Time-dependent simulations were performed to assess the influence of geometrical parameters on cavitation dynamics. The results show that both camber and thickness significantly affect cavitation development. Cambered hydrofoils generate higher lift and exhibit earlier onset and wider extent of cavitation compared to symmetric profiles. Increasing thickness tends to delay cavitation inception but leads to more pronounced sheet cavitation. For example, the NACA4412 achieved lift coefficients of approximately C_L = 0.74 and 0.79 at σ = 0.84 and 0.91, while the thick symmetric NACA0020 yielded the lowest lift coefficient of approximately C_L =0.31. Furthermore, increasing the cavitation number to 0.91 reduced drag for all profiles by up to about 23%, while preserving lift in cambered foils. Pressure distribution and vapor volume fraction contours further support these observations, indicating stronger low-pressure regions on cambered foils. Time-resolved analyses revealed that cavitation structures grow and detach more rapidly at lower σ, especially for cambered geometries. These findings suggest that for applications where minimizing cavitation-induced performance degradation is critical, moderate camber with reduced thickness may offer a balance between lift generation and cavitation resistance. In high-lift-demand applications, cambered profiles may be preferred, while thicker symmetric sections could be more suitable for durability in high-load conditions despite their lower lift performance.

Author Contributions

The percentages of the author' contributions are presented below. The author reviewed and approved the final version of the manuscript.

	M.N.K.
C	100
D	100
S	100
DCP	100
DAI	100
L	100
W	100
CR	100
SR	100
PM	100
FA	100

C=Concept, D= design, S= supervision, DCP= data collection and/or processing, DAI= data analysis and/or interpretation, L= literature search, W= writing, CR= critical review, SR= submission and revision, PM= project management, FA= funding acquisition.

Conflict of Interest

The author declared that there is no conflict of interest.

Ethical Consideration

Ethics committee approval was not required for this study because there was no study on animals or humans.

References

Adil S, Hussien HA, Othman SA. 2025. Detect cavitation in centrifugal hydraulic pumps: A Review. Iraqi J Oil Gas Res, 5(1): 1–19.

Arndt REA. 2012. Some remarks on hydrofoil cavitation. J Hydrodyn, 24(3): 305–314.

Canlı E, Ates A, Bilir Ş. 2020. Derivation of dimensionless governing equations for axisymmetric incompressible turbulent Flow Heat Transfer Based on Standard k-ϵ Model. Afyon Kocatepe Univ J Sci Eng, 20(6): 1096–1111.

Chen J, Escaler X. 2024. Numerical investigation of the cavitation effects on the wake dynamics behind a blunt trailing edge hydrofoil. Ocean Eng, 302: 117599.

Gallegos DP, Luo X. 2024. 3D study of cloud cavitation on a circular leading-edge hydrofoil using RANS approaches. ASME Fluids Eng Div Summer Conf Proc, pp:45-64.

Guo M, Liu C, Ke Z, Yan Q, Zuo Z, Khoo BC. 2023. Effects of flow conditions on the cavitation characteristics of viscous oil around a hydrofoil. Phys Fluids, 35: 1-15.

Huang B, Zhao Y, Wang G. 2014. Large Eddy Simulation of turbulent vortex-cavitation interactions in transient sheet/cloud cavitating flows. Comput Fluids, 92: 113-124.

Kang T, Park W, Jung C. 2014. Cavitation flow analysis of hydrofoil with change of angle of attack. J Comput Fluids Eng, 19: 17-23.

Karim M, Rahman M, Hai MA, Shimul MM, Sudhi SH. 2018. Numerical investigation of flow around cavitating hydrofoil using finite volume method. AIP Conf Proc, 1980: 40018.

Kaya MN, Satcunanathan S, Meinke M, Schröder W. 2025. Leading-edge noise mitigation on a rod–airfoil configuration using regular and irregular leading-edge serrations. Appl Sci, 15(14): 7822.

Kim SE, Schroeder S, Jasak H. 2010. A multi-phase CFD framework for predicting performance of marine propulsors. Proc 13th Int Symp Transport Phenomena Dyn Rotating Mach: 4–7.

Kubota A, Kato H, Yamaguchi H. 1992. A new modelling of cavitating flows: a numerical study of unsteady cavitation on a hydrofoil section. J Fluid Mech, 240: 59–96.

Kumar P, Sharma N, Pattanayek SK, Garg A. 2024. Computational comparison of passive control for cavitation suppression on cambered hydrofoils in sheet, cloud, and supercavitation regimes. Phys Fluids, 36: 1-18.

Manolesos M, Celik Y, Ramsay H, Karande R, Wood B, Dinwoodie I, Masters I, Harrold M, Papadakis G. 2024. Performance improvement of a Vestas V52 850kW wind turbine by retrofitting passive flow control devices. J Phys Conf Ser, 2767(2): 022027.

Mostafa N, Karim M, Sarker M. 2016. Numerical prediction of unsteady behavior of cavitating flow on hydrofoils using bubble dynamics cavitation model. J Appl Fluid Mech, 9: 1829-1837.

Peng XX, Ji B, Cao Y, Xu L, Zhang G, Luo X, Long X. 2016. Combined experimental observation and numerical simulation of the cloud cavitation with U-type flow structures on hydrofoils. Int J Multiph Flow, 79: 10-22.

Qiu Q, Gu Y, Ren Y, Mou C, Hu C, Ding H, Wu D, Wu Z, Mou J. 2025.

Research progress in hydrofoil cavitation prediction and suppression methods. Phys Fluids, 37: 011301.

Schnerr GH, Sauer J. 2001. Physical and numerical modeling of unsteady cavitation dynamics. Proc 4th Int Conf Multiph Flow, New Orleans, USA, pp: 1–12.

Shen Y, Dimotakis P. 1989. Viscous and Nuclei Effects on Hydrodynamic Loadings and Cavitation of a NACA 66 (MOD) Foil Section. J Fluids Eng Trans ASME, 111: 306–316.

Usta O, Öksüz S, Çelik F. 2025. Effect of leading-edge tubercles and surface corrugations on the performance and cavitation characteristics of twisted hydrofoils. Ocean Eng, 335: 121663.

Wang F, Zhu B, Zhang W, Zhang H. 2025. Cylinder wake effect on cavitation flow field around a downstream hydrofoil. Phys Fluids, 37: 1-15.

Zhou L, Wan Z. 2008. Numerical simulation of cavitation around a hydrofoil and evaluation of a RNG κ-ε model. J Fluids Eng Trans ASME, 130(1): 011302.

Black Sea Journal of Engineering and Science
doi: 10.34248/bsengineering.1766799

Open Access Journal
e-ISSN: 2619 – 8991

Research Article
Volume 8 - Issue 5: 1595-1604 / September 2025

OPTIMIZATION OF COAGULATION PROCESS PARAMETERS FOR REACTIVE RED 120 DYE USING FERRIC CHLORIDE VIA RESPONSE SURFACE METHODOLOGY

Sevtap TIRINK[1]*

[1]*Iğdır University, Health Services Vocational School, Department of Medical Services and Techniques, 76000, Iğdır, Türkiye*

Abstract: In this study, the removal of Reactive Red 120, a dye commonly present in textile wastewater, was investigated using Ferric Chloride ($FeCl_3$) as a coagulant. Process optimization was carried out through Response Surface Methodology based on a four-factor experimental design, considering initial pH (2–12), coagulant dose (100–500 mg/L), mixing speed (50–250 rpm), and initial dye concentration (25–250 mg/L). A second-order polynomial model was developed and evaluated by ANOVA to assess the individual and interactive effects of these parameters on color removal efficiency. The maximum removal efficiency of 96.28% was obtained at pH 3, coagulant dose 400 mg/L, mixing speed 100 rpm, and dye concentration 200 mg/L. The Response Surface Methodology model showed good agreement with the experimental data and predicted a theoretical maximum efficiency of 98.33% under optimized conditions. Overall, the results confirm that $FeCl_3$-based coagulation, when optimized by Response Surface Methodology, is a robust and scalable pretreatment option for textile wastewater, capable of achieving near-complete decolorization and providing practical operating ranges for implementation.

Keywords: Reactive red 120, Response surface methodology, Parameter optimization, Color removal, $FeCl_3$, Jar test

***Corresponding author:** Iğdır University, Health Services Vocational School, Department of Medical Services and Techniques, 76000, Iğdır, Türkiye
E mail: sevtap.tirink@igdir.edu.tr (S. TIRINK)
Sevtap TIRINK https://orcid.org/0000-0003-0123-0054

Received: Agust 16, 2025
Accepted: September 09, 2025
Published: September 15, 2025

Cite as: Tırınk S. 2025. Optimization of coagulation process parameters for reactive red 120 dye using ferric chloride via response surface methodology. BSJ Eng Sci, 8(5): 1595-1604.

1. Introduction

The textile industry is one of the largest producers of wastewater worldwide due to its high-water consumption and intensive use of chemicals. Approximately 100,000 different dyes have been identified, with an estimated annual production of about 700,000 tons. These dyes generate large volumes of wastewater not only during their application but also throughout production processes. During dyeing and finishing operations, 10–60% of dyes are discharged into water as waste, leading to an annual release of around 280,000 tons of dyes into textile effluents (Kusumlata et al., 2024). Textile wastewater represents a serious source of pollution for aquatic ecosystems due to its high color intensity, chemical oxygen demand (COD), and toxic chemical components (Yılmaz and Yılmaz, 2019). Containing both organic and inorganic pollutants, such effluents cause toxicity in aquatic organisms, disrupt the food chain through bioaccumulation, and pose carcinogenic, mutagenic, and allergenic risks to human health (Rauf and Ashraf, 2009; Holkar et al., 2016; Argun, 2025). The direct discharge of untreated effluents into receiving environments leads to contamination of drinking water resources, inhibition of photosynthetic activity due to reduced light penetration, and deterioration of ecosystem balance (Verma et al., 2012). Moreover, the recalcitrant nature of dyes limits the effectiveness of conventional biological treatment methods (Robinson et al., 2001).

Although physical, chemical, and biological methods are used for wastewater treatment, chemical coagulation–flocculation is widely preferred because of its rapid applicability, high removal efficiency, and relatively low operating cost (Yılmaz and Yılmaz, 2019; Ramadan, 2023; Kopan, 2023). Coagulation destabilizes colloidal particles and dissolved pollutants, facilitating the formation and subsequent settling of larger flocs. Commonly used coagulants include metal salts such as aluminum sulfate and ferric chloride (Bratby, 2016). Several recent studies have explored alternative adsorbents for dye removal from wastewater (Sözüdoğru et al., 2015; İrdemez et al., 2022; Tırınk and Kulakcı, 2025). Beyond textile dye effluents, the effectiveness of metal-salt coagulants has also been demonstrated in other high-strength industrial wastewaters; for instance, chemical pretreatment of pistachio-processing effluents identified suitable coagulant choices under optimized pH conditions (Tırınk et al., 2020). Ferric chloride ($FeCl_3$) stands out as an effective coagulant for the removal of color, turbidity, and organic matter due to the high charge density of Fe^{3+} ions, which rapidly destabilize colloidal particles. In particular,

its strong hydrolysis products and high performance over a wide pH range make $FeCl_3$ advantageous compared to aluminum-based coagulants for the treatment of reactive dyes (Papić et al., 2000). Literature reports indicate that $FeCl_3$ can achieve color removal efficiencies exceeding 90% under optimal conditions, along with significant reductions in COD and suspended solids (Islam and Mostafa, 2018). However, process performance is highly dependent on operational parameters such as pH, coagulant dose, mixing speed, and initial pollutant concentration.

Therefore, statistical optimization of these parameters is critical for achieving high removal efficiencies while minimizing chemical consumption and operating costs (Koç and Kaymak-Ertekin, 2009). Response Surface Methodology (RSM), as a multivariate experimental design approach, provides a powerful tool to analyze parameter interactions and identify optimal conditions (Myers et al., 2016). However, studies optimizing the coagulation of reactive dyes with $FeCl_3$ using RSM remain limited in the literature. This study aims to address this gap by investigating the performance of $FeCl_3$ in the removal of RR120 dye and optimizing key process parameters—pH, coagulant dose, mixing speed, and initial dye concentration—via RSM to determine the maximum achievable color removal efficiency.

In this study, the performance of $FeCl_3$ in the coagulation of RR120 dye was systematically investigated and optimized using Response Surface Methodology. The findings revealed that pH was the most critical factor controlling removal efficiency, with acidic conditions leading to the highest performance. Under optimized parameters, a maximum experimental color removal of 96.28% was achieved, while the RSM model predicted a theoretical maximum efficiency of 98.33%. These results confirm that $FeCl_3$ coagulation, when optimized through RSM, can provide a robust and scalable pretreatment option for textile wastewater.

2. Materials and Methods

2.1. Dye and Coagulant

In this study, the anionic dye RR120 was used as the model pollutant. The chemical structure of the dye is presented in Figure 1. The dye was obtained in analytical grade and employed in the preparation of synthetic wastewater solutions for the experiments. $FeCl_3$ was selected as the coagulant. $FeCl_3$ is a commonly used metal salt coagulant in chemical coagulation processes and is known to provide high color removal efficiency (Bratby, 2016).

For the experiments, 1 g of RR120 was dissolved in distilled water and diluted to a final volume of 1000 mL to prepare a 1000 mg/L stock solution. Working solutions of desired concentration were obtained by diluting this stock solution. Standard solutions of 0 ppm, 1 ppm, 2.5 ppm, 5 ppm, 7.5 ppm, 10 ppm, 20 ppm, 30 ppm, 40 ppm, 50 ppm, 75 ppm, and 100 ppm were also prepared from the stock solution, and their absorbance values were measured at the maximum wavelength to construct the calibration curve of RR120. The maximum wavelength (λ_{max}) for RR120 was determined as 536 nm (Figure 2), and the calibration curve is presented in Figure 3.

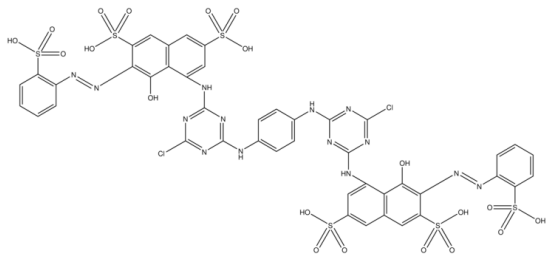

Figure 1. Chemical structure of RR120 dye.

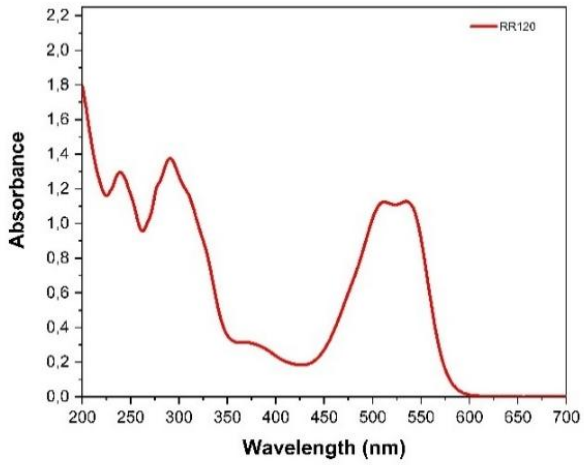

Figure 2. Determination of Wavelengths for Absorbance Measurements of RR120 Dye.

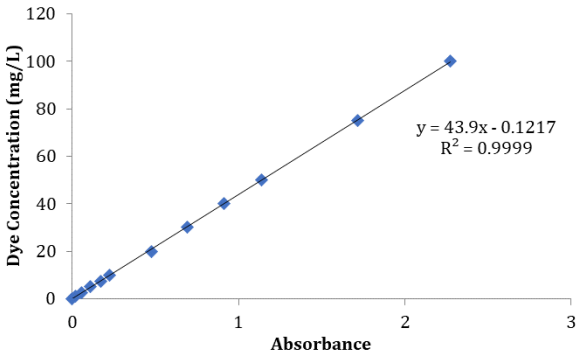

Figure 3. Calibration curve of RR120.

2.2. Experimental Setup

Coagulation/flocculation experiments were carried out using a six-paddle, variable-speed jar test apparatus (WiseStir Jar Tester JT-M6C) (Figure 4). The unit is equipped with six 1 L glass beakers, and the working sample volume was 500 mL. For pH adjustments, 0.1 N HCl and 0.1 N NaOH solutions were used.

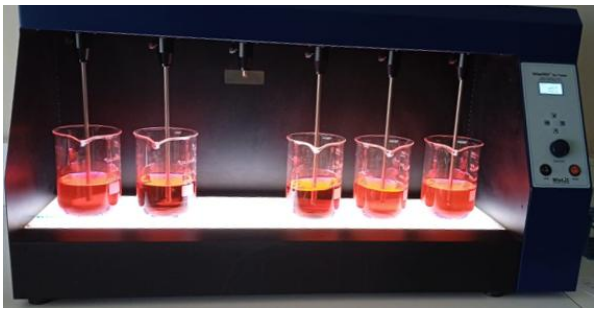

Figure 4. Jar test system.

2.3. RSM and Experimental Design

In this study, RSM and Central Composite Design (CCD) were applied to optimize process parameters for the removal of RR120 dye using $FeCl_3$ as the coagulant (Myers et al., 2016). The independent variables were defined as pH (X_1), coagulant dose (mg/L) (X_2), mixing speed (rpm) (X_3), and initial dye concentration (mg/L) (X_4). The response variable (Y) was selected as color removal efficiency (%).

The experimental design consisted of four factors, each with five levels. The factor levels were determined based on preliminary tests and optimum ranges reported in the literature. The factor levels are presented in Table 1. A total of 30 experimental runs were conducted within the design. In each experiment, rapid mixing (50–250 rpm, 5 min) followed by slow mixing (40 rpm, 20 min) was performed at the specified pH value (Verma et al., 2012). After mixing, the samples were allowed to settle for 30 minutes, and absorbance measurements of the supernatant were carried out using an OPTIZEN-POP UV-Vis spectrophotometer (λ_{max} = 536 nm).

Table 1. Factors and levels used in the experimental design for the $FeCl_3$ coagulation process

Independent Variables	Levels				
	-2	-1	0	1	2
Initial pH	2	3	7	11	12
Coagulant dosage (mg/L)	100	200	300	400	500
Stirring speed (rpm)	50	100	150	200	250
Initial dye concentration (mg/L)	25	50	100	200	250

The color removal efficiency was calculated using the experimental data according to equation 1:

$$\% \text{ Removal efficiency} = \frac{C_0 - C_t}{C_0} \times 100 \quad (1)$$

where C_0 represents the initial dye concentration (mg/L), and C_t denotes the residual dye concentration (mg/L) measured after sedimentation.

The experimental data were modeled using a second-order polynomial model (equation 2), and the model coefficients were tested by analysis of variance (ANOVA):

$$\hat{y}_n = \beta_0 + \sum_{i=1}^{n} \beta_i x_i + \sum_{i=1}^{n} \beta_{ii} x_i^2 + \sum_{i=1}^{n} \sum_{j=i+1}^{n} \beta_{ij} x_i x_j + \varepsilon \quad (2)$$

Here, Y represents the color removal efficiency; X_i and X_j are the coded independent variables; and β_0, β_i, β_{ii}, and β_{ij} represent the constant, linear, quadratic, and interaction coefficients, respectively. The validity of the model was evaluated using R^2, adjusted R^2 (Radj^2), and p-values (<0.05). The predictive ability of the model was confirmed through residual analysis and cross-validation.

2.4. Statistical Analysis

The experimental data were analyzed using RSM with CCD. ANOVA was employed to determine the significance of model terms, and regression coefficients (R^2 and adjusted R^2) were calculated to evaluate model adequacy. A p-value < 0.05 was considered statistically significant. All statistical analyses were performed using Minitab 16.0 software.

3. Results and Discussion

This section presents the experimental findings on the removal of RR120 dye through $FeCl_3$ coagulation, along with the modeling results obtained via RSM. Initially, the individual effects of pH, coagulant dose, mixing speed, and initial dye concentration were examined, followed by an evaluation of model adequacy, ANOVA results, and surface contour analyses.

The experimental results demonstrated that $FeCl_3$ coagulation achieved significantly higher color removal efficiencies under acidic conditions. The hydrolysis of Fe^{3+} ions at low pH leads to the formation of $Fe(OH)_3$ flocs, which are more effective in removing dye molecules from suspension (Verma et al., 2012). Similarly, Yılmaz and Yılmaz (2019) reported that optimal pH ranges are critical for achieving maximum removal in magnesium and alum coagulation processes. Increasing the coagulant dose up to 400 mg/L enhanced color removal efficiency; however, no significant improvement was observed beyond this dosage. Excessive dosing may cause restabilization of flocs and subsequently reduce removal efficiency, as also reported in the literature (Bratby, 2016). With respect to mixing speed, the optimal value was determined as 100 rpm. At lower speeds, floc formation was insufficient, while at higher speeds, the flocs tended to break apart. Furthermore, an increase in the initial dye concentration resulted in a decrease in removal efficiency. At high dye concentrations, the available Fe^{3+} ions may be insufficient to bind all dye molecules, indicating that under such conditions higher coagulant doses may be required (Robinson et al., 2001).

The statistical evaluation conducted using RSM confirmed the influence of pH, coagulant dose, mixing speed, and initial dye concentration on color removal efficiency. Based on the CCD, 30 experimental runs were carried out,

yielding a maximum removal efficiency of 96.282%. The optimal conditions were determined as pH 3, coagulant dose 400 mg/L, mixing speed 100 rpm, and initial concentration 200 mg/L.

The color removal efficiency obtained from the experiments ranged between 0.04% and 96.28%. The relationship between the experimental results and model predictions is presented in Figure 5.

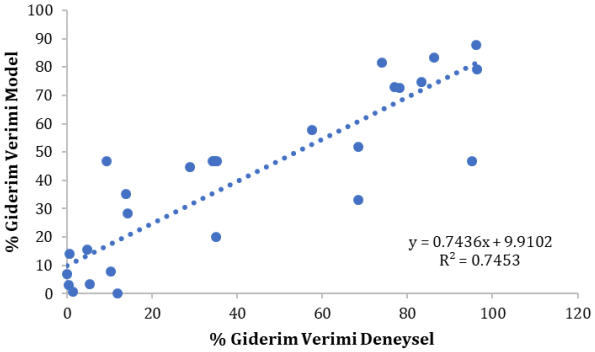

Figure 5. Correlation graph between experimental and model data.

As shown in Figure 5, a significant correlation was achieved between the experimental and model data (R^2 0.7453). This indicates that the developed model is capable of predicting color removal performance with reasonable accuracy. Under maximum removal conditions, the model yielded R^2 and adjusted R^2 (R^2adj) values of 74.53% and 50.76%, respectively.

The difference between R^2 and adjusted R^2 can be explained by the structure of the model and the number of experimental runs. The central composite design involved 30 runs, whereas the second-order model included 14 terms (four linear, four quadratic, and six interaction). In relatively small samples, the adjusted R^2 penalizes the inclusion of multiple terms more strongly, which accounts for the decrease from 0.7453 to 0.5076 (Adj. $R^2 = 1 - (1-R^2)\cdot(n-1)/(n-p-1)$, with n = 30 and p = 14). Despite this reduction, the model was statistically significant (ANOVA: F = 3.14, p = 0.018), and the lack-of-fit was not significant (p = 0.581), confirming that the model was consistent with the data. Moreover, the bounded nature of the response variable (0–100%) and the wide experimental domain (0.04–96.28%) contributed to the "moderate" overall fit. Importantly, pH was highly significant (P<0.001), and the model predictions were in close agreement with the experimental optimum (predicted 98.33% vs. observed 96.28%). These findings demonstrate that, although the overall fit is moderate, the model is sufficiently robust for optimization and for identifying the dominant factors governing the coagulation process.

By processing the experimental data into the model, an equation for calculating the percentage removal efficiency was derived, which is presented in equation 3. Using the equations obtained from the RSM, the percentage removal efficiency can be estimated without the need for additional experiments.

$$\begin{aligned} \%\, Removal\ efficiency\ =\ & 91 - 7.8\,X_1 + 0.058\,X_2 \\ & -0.127\,X_3 + 0.264\,X_4 + 0.025\,X_1 * X_1 \\ & -0.000565\,X_2 * X_2 + 0.00015\,X_3X_3 \\ & -0.00117\,X_4 * X_4\ + 0.0109\,X_1 * X_2 \\ & -0.0145\,X_1 * X_3 - 0.0172\,X_1 * X_4 \\ & +0.00065\,X_2 * X_3 + 0.000861\,X_2 * X_4 \\ & -\ 0.00047\,X_3 * X4 \end{aligned} \tag{3}$$

To evaluate the influence of the independent variables in the experimental study, an ANOVA was conducted based on the percentage removal efficiency data. The ANOVA results for color removal efficiency are presented in Table 2. According to the analysis, the developed model was found to be statistically significant (p = 0.018). Among the factors, pH was identified as the most influential parameter on color removal efficiency (P<0.001), while the other variables individually exhibited no statistically significant effects. The quadratic terms and two-way interactions did not provide a significant contribution to the model. Furthermore, the lack-of-fit test was not significant (p = 0.581), indicating that the model was consistent with the experimental data.

According to the Pareto chart of standardized effects presented in Figure 5, only the pH factor exceeded the significance threshold (α = 0.05) and was found to have a statistically significant influence on color removal efficiency. Coagulant dose, mixing speed, initial concentration, as well as their interaction and quadratic terms, were not significant. This finding, consistent with the ANOVA results, confirms that pH is the dominant parameter governing the efficiency of the coagulation process.

The analysis of three-dimensional surface and contour plots obtained within the scope of RSM provides a more detailed illustration of the effects of process parameters on color removal efficiency (Figures 7–12).

Table 2. ANOVA analysis for percentage removal efficiency

	Degrees of Freedom (DF)	Sum of Squares (SS)	Mean Square (MS)	F-Value	P-Value
	14	25157.4	1797	3.14	0.018
Linear	4	22311.7	5577.9	9.73	0
Initial pH	1	22108.6	22108.6	38.58	0
Coagulant dosage (mg/L)	1	30.3	30.3	0.05	0.821
Stirring speed (rpm)	1	159	159	0.28	0.606
Initial dye concentration (mg/L)	1	14	14	0.02	0.878
Square	4	1310.7	327.7	0.57	0.687
Initial pH * Initial pH	1	1.3	1.3	0	0.963
Coagulant dosage (mg/L)*Coagulant dosage (mg/L)	1	901.5	901.5	1.57	0.229
Stirring speed (rpm)*Stirring speed (rpm)	1	3.8	3.8	0.01	0.936
Initial dye concentration (mg/L)*Initial dye concentration (mg/L)	1	410.1	410.1	0.72	0.411
2-Way Interaction	6	1783.9	297.3	0.52	0.785
Initial pH *Coagulant dosage (mg/L)	1	305.4	305.4	0.53	0.477
Initial pH *Stirring speed (rpm)	1	135.1	135.1	0.24	0.634
Initial pH *Initial dye concentration (mg/L)	1	431.8	431.8	0.75	0.399
Coagulant dosage (mg/L)*Stirring speed (rpm)	1	168.8	168.8	0.29	0.595
Coagulant dosage (mg/L)*Initial dye concentration (mg/L)	1	691.8	691.8	1.21	0.289
Stirring speed (rpm)*Initial dye concentration (mg/L)	1	51.1	51.1	0.09	0.769
Error	15	8596.9	573.1		
Lack-of-Fit	10	5550.6	555.1	0.91	0.581
Pure Error	5	3046.3	609.3		
Total	29	33754.2			

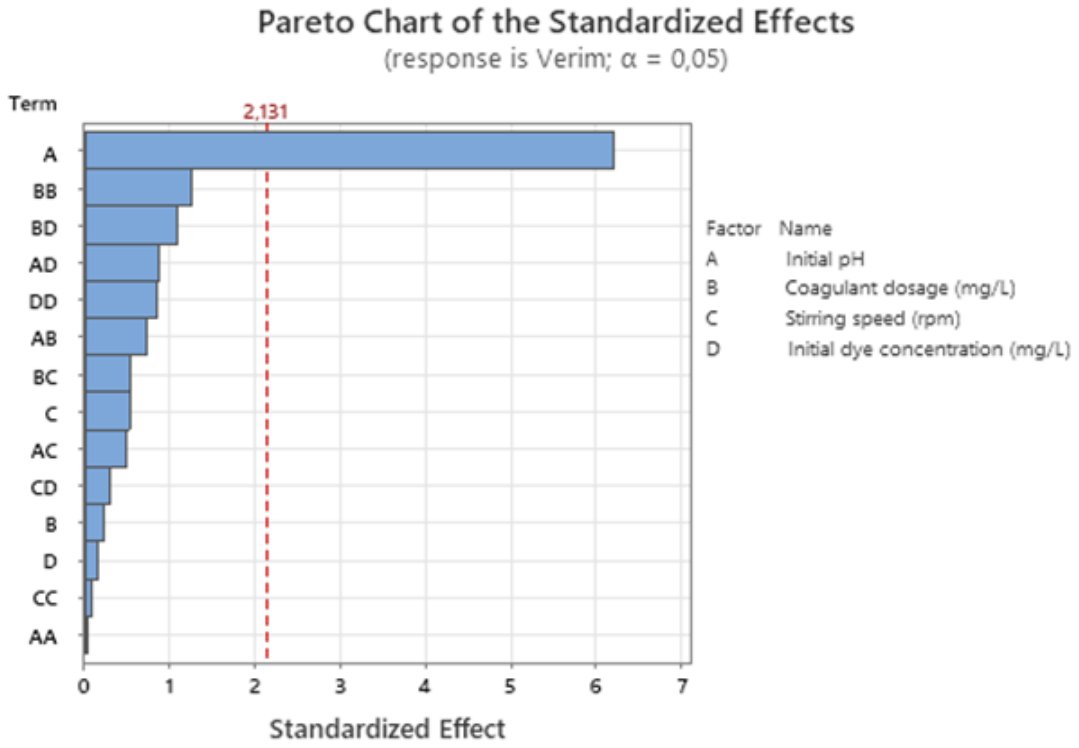

Figure 6. Pareto chart.

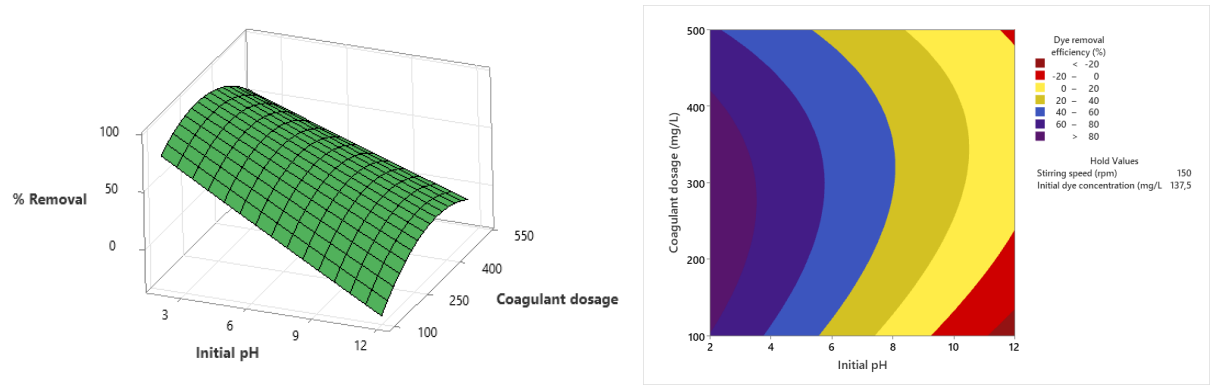

Figure 7. Surface (a) and contour (b) plots of % removal efficiency as a function of pH and coagulant dose (mg/L).

Figure 7 illustrates the interaction between pH and coagulant dose. As shown, pH is the dominant factor influencing removal efficiency. The highest efficiency was achieved under low pH conditions (pH 3–4) and at high coagulant doses. At higher pH levels, the removal efficiency decreased regardless of the coagulant dose. This behavior can be attributed to the formation of more effective hydrolysis products of $FeCl_3$ under acidic conditions. Papić et al. (2000) reported that optimal removal efficiency is achieved under low pH.

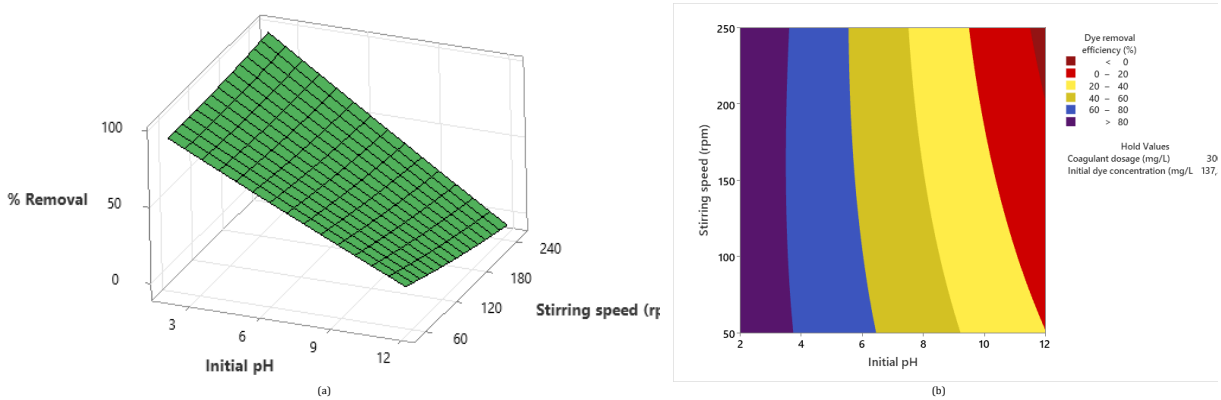

(a) (b)

Figure 8. Surface (a) and contour (b) plots of % removal efficiency as a function of pH and mixing speed (rpm).

Figure 8 presents the relationship between pH and mixing speed. As observed, high removal efficiencies were obtained under acidic conditions, while variations in mixing speed had no significant effect. At higher pH levels, the efficiency remained low regardless of mixing speed. This finding indicates that pH is a more decisive factor compared to mixing speed. The literature also emphasizes that pH is among the most critical parameters in the coagulation process, whereas mixing speed plays only a secondary role, primarily influencing floc formation and stability (Bratby, 2016).

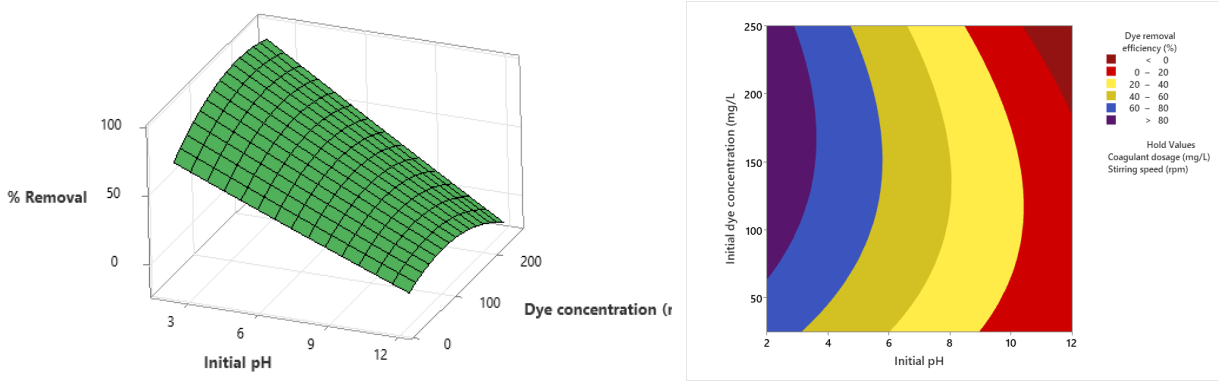

(a) (b)

Figure 9. Surface (a) and contour (b) plots of % removal efficiency as a function of pH and initial dye concentration (mg/L).

Figure 9 illustrates the interaction between pH and initial dye concentration. As shown, under low-pH conditions, removal efficiency remained relatively stable at high levels even as the initial dye concentration increased. In

contrast, at higher pH values, removal efficiency was consistently low regardless of dye concentration. These results demonstrate that pH is a much more dominant parameter than initial dye concentration. Similarly, Islam and Mostafa (2018) reported that pH is a stronger determinant than concentration in the coagulation of reactive dyes with $FeCl_3$.

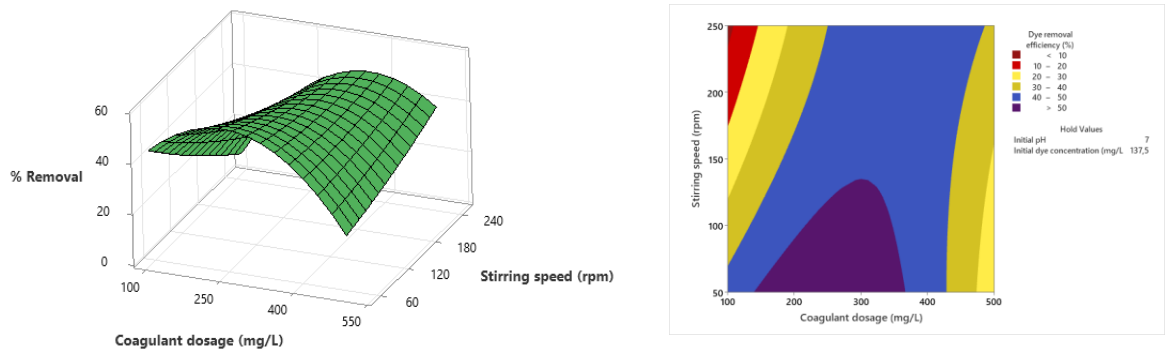

(a) (b)

Figure 10. Surface (a) and contour (b) plots of % removal efficiency as a function of mixing speed (rpm) and coagulant dose (mg/L).

Figure 10 illustrates the interaction between mixing speed and coagulant dose. The plot shows that removal efficiency increased at low mixing speeds with high coagulant doses, but this effect was limited compared to the influence of pH. At very high mixing speeds, the efficiency decreased, likely due to the breakup of floc structures. This observation is consistent with the findings of Verma et al. (2012), who also reported that moderate mixing speeds should be preferred to achieve optimal coagulation.

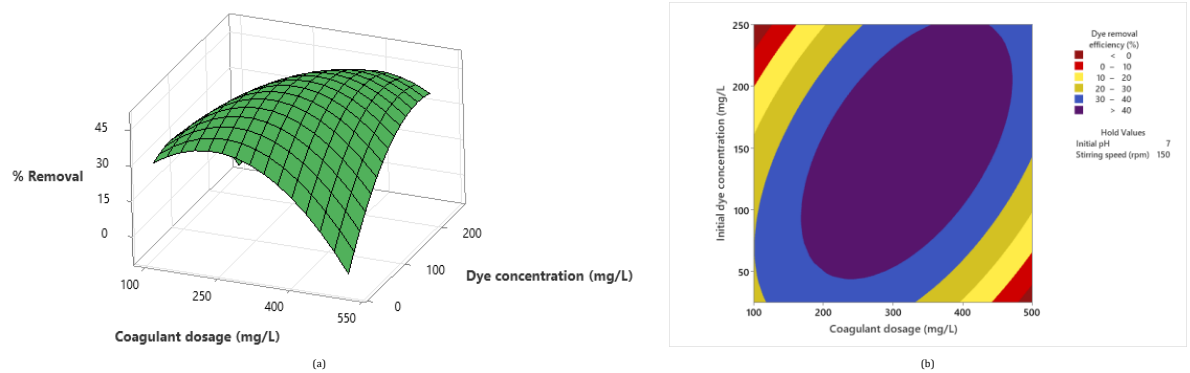

(a) (b)

Figure 11. Surface (a) and contour (b) plots of % removal efficiency as a function of initial dye concentration (mg/L) and coagulant dose (mg/L).

Figure 11 depicts the relationship between initial dye concentration and coagulant dose. As observed, increasing the coagulant dose enhanced removal efficiency at lower concentrations; however, this effect became limited as dye concentration increased. This finding indicates that applying $FeCl_3$ beyond the optimum dose increases chemical consumption without providing additional benefits. Li et al. (2013) also reported that at high initial concentrations, coagulant doses above the optimum level contributed only marginally to removal efficiency.

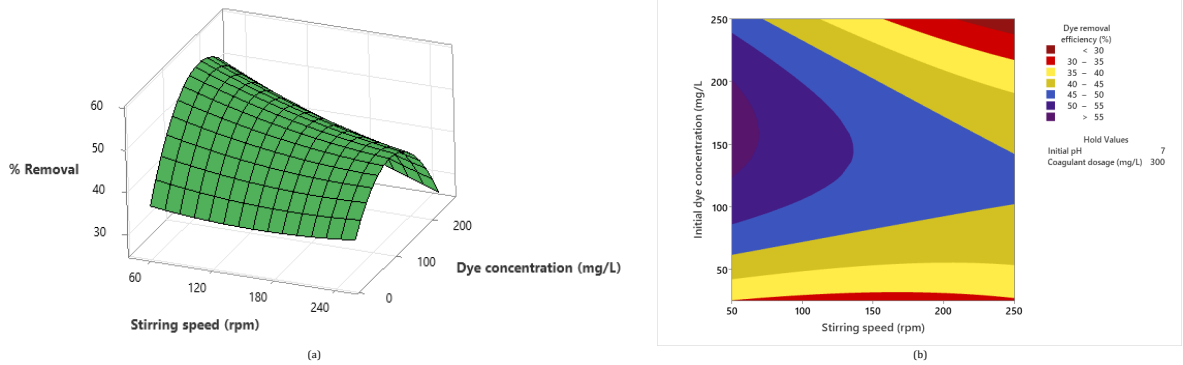

(a) (b)

Figure 12. Surface (a) and contour (b) plots of % removal efficiency as a function of mixing speed (rpm) and initial dye concentration (mg/L).

Figure 12 examines the interaction between mixing speed and initial dye concentration. As shown, relatively higher efficiencies were obtained at low initial concentrations and moderate mixing speeds. The interaction between these two parameters was limited, and due to the dominant influence of pH, their combined effect was not decisive for overall removal efficiency.

When all the surface and contour plots presented in Figures 7–12 are evaluated, pH emerges as the most critical parameter governing color removal, while the other factors—coagulant dose, mixing speed, and initial concentration—provide only limited contributions. These findings are consistent with the results of the ANOVA analysis and the Pareto chart.

The literature also reports that while the interactions among process parameters are generally limited, defining the optimum conditions is critical for maximizing efficiency (Islam and Mostafa, 2018). Similarly, Argun et al. (2023) reported that combined treatment processes can effectively enhance the removal of azo dyes from wastewater, supporting the potential of integrated approaches for improving color removal performance. These findings highlight the dominant influence of pH but also suggest that optimizing the other factors can further enhance overall system performance. Unlike previous studies, which generally investigated $FeCl_3$ coagulation through one-factor-at-a-time experiments, the present work systematically applied RSM to model and optimize the removal of RR120 dye. This represents one of the first attempts to develop a predictive regression model for this specific dye, validated against experimental results, and highlights the dominant role of pH under varying operational conditions. Optimization is a technique aimed at identifying the most suitable levels of influential parameters to achieve the desired process outcomes. In dye removal processes, the primary goal of optimization is to define the conditions that maximize color removal efficiency (Karimifard and Moghaddam, 2018). In addition, UV/Fe^{3+} photolysis has been optimized for RR120 removal using RSM, as demonstrated by Dhruv and Abhipsa (2020), further confirming the applicability of statistical modeling in dye decolorization processes.

In this context, the optimum conditions predicted by the model, along with model estimations and validation experiments conducted under these conditions, are presented in Figure 13. As shown, the optimum color removal efficiency was calculated as 98.33%. This maximum efficiency was achieved under the following conditions: pH 2.0, coagulant dose 350.51 mg/L, mixing speed 250 rpm, and initial dye concentration 177.27 mg/L.

The enhanced efficiency at low pH can be explained by the formation of more effective hydrolysis products of $FeCl_3$ under acidic conditions, which promote rapid flocculation (Papić et al., 2000; Islam and Mostafa, 2018). The determination of an optimum coagulant dose at an intermediate level indicates that overdosing is not only economically disadvantageous but may also negatively affect floc stability (Al-Sameraiy, 2015). The relatively high optimal mixing speed reflects the need for sufficient turbulence to ensure effective mass transfer and floc growth; however, excessive turbulence may lead to floc breakage, thereby reducing efficiency (Verma et al., 2012). Finally, the optimum efficiency observed at moderate dye concentrations suggests that at high concentrations the available active sites may be insufficient, while at very low concentrations floc formation may not occur effectively.

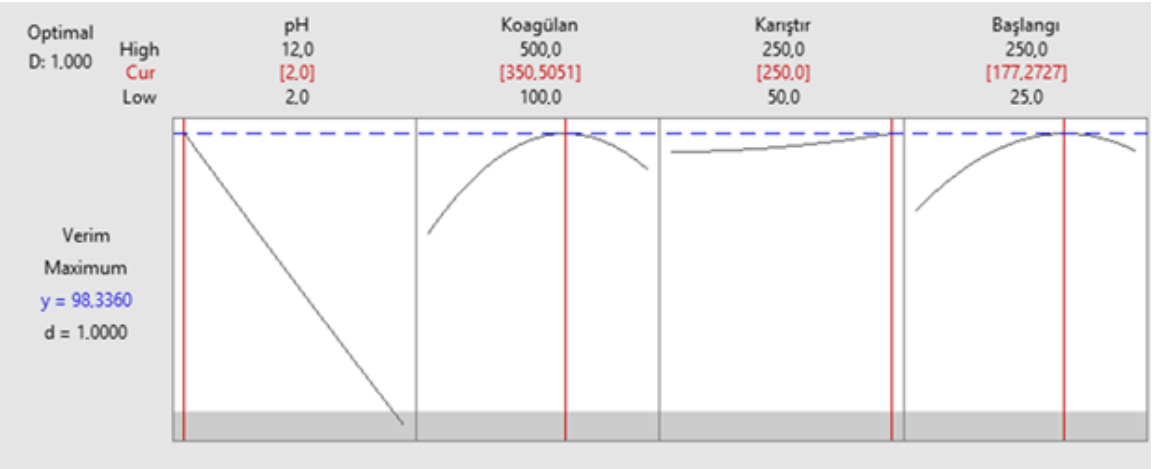

Figure 13. Optimum process parameters and maximum color removal efficiency determined by RSM.

In addition, previous optimization studies on $FeCl_3$ coagulation have also emphasized the effectiveness of RSM. For example, Kumar and Bishnoi (2017) reported color removal efficiencies as high as 99.6% in landfill leachate models, with high R^2 values confirming the reliability of the model. Sadri Moghaddam et al. (2010) likewise achieved a removal efficiency of 96.5% for the AR119 dye using an iron-based sludge known as FCS and highlighted the critical role of low pH in achieving high efficiency. These findings from the literature are

consistent with the pH-driven optimum conditions and high removal efficiencies observed in the present study, further reinforcing the validity of the model and the reliability of the optimization approach. Electrocoagulation has also been applied for the removal of RR120, and Gautam et al. (2020) achieved high efficiency while optimizing process conditions through a multivariate approach, combined with an economic and sludge characterization analysis. In addition to coagulation-based studies, alternative approaches such as biosorption have also been applied for the removal of RR120. Çakmakcı (2025) reported that *Suillus collinitus* mushroom achieved an adsorption capacity of 56.82 mg/g for RR120 at pH 2, with the adsorption process best described by the Freundlich isotherm. This confirms that low pH conditions are critical not only for coagulation but also for adsorption-based processes.

4. Conclusion

In this study, the removal of RR120 dye using $FeCl_3$ as a coagulant was optimized with respect to pH, coagulant dose, mixing speed, and initial dye concentration through RSM. The experimental findings demonstrated that pH was the most influential factor affecting coagulation efficiency, whereas coagulant dose, mixing speed, and initial dye concentration had secondary effects.

The CCD experiments yielded a maximum removal efficiency of 96.28% under the conditions of pH 3, coagulant dose 400 mg/L, mixing speed 100 rpm, and initial dye concentration 200 mg/L. Furthermore, RSM optimization predicted a maximum efficiency of 98.33% at pH 2.0, coagulant dose 350.51 mg/L, mixing speed 250 rpm, and initial dye concentration 177.27 mg/L.

These results indicate that $FeCl_3$ coagulation, under suitable conditions, can achieve near-complete removal of RR120 and provides a scalable and reliable pretreatment option. The findings confirm that $FeCl_3$ is particularly effective under acidic conditions and can serve as a practical method for textile wastewater treatment. Moreover, RSM proved to be a powerful tool for parameter optimization in multivariable systems, providing results consistent with experimental validation.

Taken together, the findings revealed that pH was the most critical factor controlling removal efficiency, with acidic conditions leading to the highest performance. Under optimized parameters, a maximum experimental color removal of 96.28% was achieved, while the RSM model predicted a theoretical maximum efficiency of 98.33%. These results confirm that $FeCl_3$ coagulation, when optimized through RSM, can provide a robust and scalable pretreatment option for textile wastewater.

In conclusion, the combined use of $FeCl_3$ coagulation and RSM optimization offers both scientifically robust and industrially applicable potential for dye removal from textile wastewater.

Author Contributions

The percentages of the author' contributions are presented below. The author reviewed and approved the final version of the manuscript.

	S.T.
C	100
D	100
S	100
DCP	100
DAI	100
L	100
W	100
CR	100
SR	100
PM	100
FA	100

C=Concept, D= design, S= supervision, DCP= data collection and/or processing, DAI= data analysis and/or interpretation, L= literature search, W= writing, CR= critical review, SR= submission and revision, PM= project management, FA= funding acquisition.

Conflict of Interest

The author declared that there is no conflict of interest.

Ethical Consideration

Ethics committee approval was not required for this study because of there was no study on animals or humans.

References

Al-Sameraiy M. 2015. A new approach using coagulation rate constant for evaluation of turbidity removal. Appl Water Sci, 7: 1439–1448. https://doi.org/10.1007/s13201-015-0341-8

Argun YA, Tırınk S, Çakmakcı Ö. 2023. Treatment of wastewater containing azo dyes by combined processes. Eng Sci Issues Oppor Res, 2023: 65.

Argun YA. 2025. Investigation of the adsorption of anionic and cationic dyes in the textile industry using tinder fungus (Fomes fomentarius) as a natural adsorbent. Int J Environ Res, 19(5): 1-6. https://doi.org/10.1007/s41742-025-00856-x

Bratby J. 2016. Coagulation and flocculation in water and wastewater treatment. 3rd ed. IWA Publishing, London, UK, pp: 54. https://doi.org/10.2166/9781780407500

Çakmakcı Ö. 2025. Removal kinetics, thermodynamics and adsorption mechanism of anionic and cationic textile dyes using Suillus collinitus mushroom. Chem Pap, 2025: 2-18. https://doi.org/10.1007/s11696-025-04272-5

Dhruv B, Abhipsa M. 2020. UV/Fe^{3+} photolysis process optimization using response surface methodology for decolorization of Reactive Red 120 dye simulated wastewater. In: Recent Trends in Civil Engineering: Select Proceedings of ICRTICE 2019. Singapore: Springer, Singapore, Singapore, pp: 847–865.

Gautam K, Kamsonlian S, Kumar S. 2020. Removal of Reactive Red 120 dye from wastewater using electrocoagulation: Optimization using multivariate approach, economic analysis, and sludge characterization. Sep Sci Technol, 55(18): 3412–3426. https://doi.org/10.1080/01496395.2019.1695744

Holkar CR, Jadhav AJ, Pinjari DV, Mahamuni NM, Pandit AB. 2016. A critical review on textile wastewater treatments: Possible approaches. J Environ Manage, 182: 351–366. https://doi.org/10.1016/j.jenvman.2016.07.090

İrdemez Ş, Özyay G, Ekmekyapar Torun F, Kul S, Bingül Z. 2022. Comparison of Bomaplex Blue CR-L removal by adsorption using raw and activated pumpkin seed shells. Ecol Chem Eng S, 29(2): 199–216. https://doi.org/10.2478/eces-2022-0015

Islam MR, Mostafa MG. 2018. Removal of a Reactive Dye from Synthetic Wastewater Using PAC and $FeCl_3$ Coagulants. Life Earth Sci, 13: 39–44.

Karimifard S, Moghaddam MRA. 2018. Application of response surface methodology in physicochemical removal of dyes from wastewater: A critical review. Sci Total Environ, 640–641: 772–797. https://doi.org/10.1016/j.scitotenv.2018.05.355

Koç B, Kaymak-Ertekin F. 2009. Yanıt yüzey yöntemi ve gıda işleme uygulamaları. Gida, 34(3): 185–192.

Kopan M. 2023. Endüstriyel atıksu arıtımında zeytin çekirdeği tozunun doğal pıhtılaştırıcı olarak kullanılabilirliğinin belirlenmesi. Yüksek Lisans Tezi. Karabük Üniversitesi, Lisansüstü Eğitim Enstitüsü, Karabük, Türkiye, ss: 63.

Kumar A, Bishnoi NR. 2017. Coagulation of landfill leachate by $FeCl_3$: Process optimization using Box–Behnken design (RSM). Appl Water Sci, 7(4): 1943–1953. https://doi.org/10.1007/s13201-015-0372-1

Kusumlata ., Gautam S, Kumar A, & Ambade B. 2024. Sustainable Solutions: Reviewing the Future of Textile Dye Contaminant Removal with Emerging Biological Treatments. Limnol. Rev, 24(2), 126–149. https://doi.org/10.3390/limnolrev24020007

Li JZ, Xuyin Y, Ming T, Hao J, Jiang W. 2013. Decolorization of reactive brilliant red x-3b simulated dye water by novel coagulants. Mater Sci Forum, 743–744: 665–668. https://doi.org/10.4028/www.scientific.net/MSF.743-744.665

Myers RH, Montgomery DC, Anderson-Cook CM. 2016. Response surface methodology: Process and product optimization using designed experiments. 4th ed. Wiley, London, UK, pp: 63.

Papić S, Koprivanac N, Božić AL, Meteš A. 2000. Removal of reactive dyes from wastewater using Fe(III) coagulant. Color Technol, 116(11): 352–358. https://doi.org/10.1111/j.1478-4408.2000.tb00013.x

Ramadan HAA. 2023. Çam kozalığından elde edilen doğal koagülant kullanılarak endüstriyel atıksuların arıtılması. Yüksek Lisans Tezi, Karabük Üniversitesi, Lisansüstü Eğitim Enstitüsü, Karabük, Türkiye, ss: 63.

Rauf MA, Ashraf SS. 2009. Fundamental principles and application of heterogeneous photocatalytic degradation of dyes in solution. Chem Eng J, 151(1–3): 10–18. https://doi.org/10.1016/j.cej.2009.02.026

Robinson T, McMullan G, Marchant R, Nigam P. 2001. Remediation of dyes in textile effluent: A critical review on current treatment technologies with a proposed alternative. Bioresour Technol, 77(3): 247–255. https://doi.org/10.1016/S0960-8524(00)00080-8

Sadri Moghaddam M, Moghaddam MRA, Arami M. 2010. Coagulation/flocculation process for dye removal using sludge from water treatment plant: Optimization through response surface methodology. J Hazard Mater, 175(1–3): 651–657. https://doi.org/10.1016/j.jhazmat.2009.10.058

Sözüdoğru O, Fil BA, Boncukcuoğlu R, Aladağ E, Kul S. 2015. Adsorptive removal of cationic (BY2) dye from aqueous solutions onto Turkish clay: Isotherm, kinetic, and thermodynamic analysis. Part Sci Technol, 34(1): 103–111. https://doi.org/10.1080/02726351.2015.1052121

Tırınk S, Kulakcı A S. 2025. Natural and biosorbent adsorbents for decolorization of azo dyes: a bibliometric analysis of global research trends. Mühendislik Alanında Multidisipliner Araştırma ve Değerlendirmeler, Özgür Yayınları, Harran, Türkiye, pp: 87-112. https://doi.org/10.58830/ozgur.pub776.c3232

Tırınk S, Nuhoğlu A, Kul S. 2020. Characterization of pistachio processing industry wastewater and investigation of chemical pretreatment. Environ Res Technol, 3(4): 209–216. https://doi.org/10.35208/ert.800721

Verma AK, Dash RR, Bhunia P. 2012. A review on chemical coagulation/flocculation technologies for removal of colour from textile wastewaters. J Environ Manage, 93(1): 154–168. https://doi.org/10.1016/j.jenvman.2011.09.012

Yılmaz K, Yılmaz T. 2019. Tekstil atıksuyu ve sentetik boyarmadde çözeltilerinden renk ve KOİ gideriminde alüm ve magnezyum klorürün karşılaştırılması. KSÜ J Eng Sci, 22(4): 270–280.

Black Sea Journal of Engineering and Science
doi: 10.34248/bsengineering.1710797

Open Access Journal
e-ISSN: 2619 – 8991

Research Article
Volume 8 - Issue 5: 1605-1616 / September 2025

DESIGN AND DEVELOPMENT OF TOPOLOGICALLY OPTIMIZED EARLY FIRE DETECTION MOBILE ROBOT

Hilmi Saygın SUCUOĞLU[1]*

[1]*Aydin Adnan Menderes University, Faculty of Engineering, Department of Mechanical Engineering, 09010, Aydin, Türkiye*

Abstract: In this study, the comprehensive design, development, topology optimization, and power analysis of a mobile early fire detection robot were conducted. All subcomponents and the full assembly model were created using computer-aided design (CAD) tools. Electronic hardware-including RGB and thermal cameras, Raspberry Pi, and motor drivers-was selected, and corresponding mounting parts were designed to integrate the components into the structure. Finite element analyses (FEA) were performed to evaluate structural strength and stability. Topology optimization was applied to reduce the overall weight and energy consumption of the system. A specialized power analysis tool was developed to compare the energy usage of the non-optimized and optimized designs. The FEA and power analysis results confirmed that the optimized structure achieved a 25% weight reduction and an 11% decrease in energy consumption, demonstrating improved efficiency in the mobile fire detection robot.

Keywords: CAD-based fire detection robot, Computer-aided engineering, Energy-efficient mobile robot, Finite element analysis, Power analysis, Topology optimization

***Corresponding author:** Aydin Adnan Menderes University, Faculty of Engineering, Department of Mechanical Engineering, 09010, Aydin, Türkiye
E mail: hilmisucuoglu@adu.edu.tr (H. S. SUCUOGLU)
Hilmi Saygın SUCUOĞLU https://orcid.org/0000-0002-2136-6015

Received: May 31, 2025
Accepted: September 09, 2025
Published: September 15, 2025
Cite as: Sucuoglu HS. 2025. Design and development of topologically optimized early fire detection mobile robot. BSJ Eng Sci, 8(5): 1605-1616.

1. Introduction

Fire represents a category of disaster that causes harm in a variety of settings, including residential areas, industrial zones, and forest lands. Despite the inherently dangerous nature of firefighting, which encompasses tasks such as fire extinguishment and victim rescue, the work is still conducted by human operators, thereby placing firefighters at risk. Once a fire has spread, it is impossible to control, and the process of recovery in a damaged area is inherently challenging. Consequently, the optimal approach to firefighting is to identify and locate the fire before it reaches a point of no return (Sucuoglu, 2015; Sucuoglu, et al., 2018; Sucuoglu et al., 2019; Saeed et al., 2020; Sucuoglu, 2020). A multitude of devices and systems have been designed and developed with the objective of facilitating early fire detection. Optical flame and smoke detectors, camera systems equipped with fire detection algorithms and capabilities represent the various types of early fire detection devices. These systems have certain disadvantages, including high cost, the necessity of fixing, and inflexibility. This situation gives rise to the utilization of effective technologies such as artificial intelligence, image processing methods and mobile systems for the purpose of early fire detection (He et al., 2022; Khan et al., 2022).

A significant approach in the field of early fire detection is the development and utilization of video-based systems. Those types of the systems utilize spatial-temporal flame modelling and dynamic texture analysis. Dimitropoulos et al. (2014) developed a method using the video-based system. They achieved a high frame rate for early fire detection. One of the most important parameters of the video-based fire detection systems is the development of a precise filtering system. This filtering is required to decrease the level of environmental noise and thus false alarm rates.

Madsen et al. (2018) proposed a method including the usage of chemical markers for early fire detection. They used laevulose as an indicator for early detection of fires burning in cellulose-based material as an improvement of the video-based detection systems. Although their method is seen as promising, it is limited to detect certain types of fires.

Zamal et al. (2017) developed a multi-sensor early fire detection. They equipped the system with GSM technology. They proposed real time monitoring and analysis of indicators such as smoke level and temperature changes. While the structure is effective for detection of flaming and non-flaming fire types, it has disadvantages such as high sensor costs, calibration and maintenance requirements.

One of the important problems and challenges of the usage of sensor-based detection systems is the effects of the environmental factors. Those factors cause noises and fail detections. For instance, smoke and heat detectors might be confused via increasing level of

ambient noise and complexity.

Zhang and Du (2010) emphasized that smoke detectors frequently fail to detect and cause false alarms in the operations of early fire detection. As a solution they proposed more sophisticated detection algorithms and developed a hybrid model to consider many different parameters.

Biase and Laneve (2018) investigated the SFIDE algorithm. This algorithm uses remote sensing satellite imagery technology for early fire detection, especially in forest fires. Their system includes ground-based sensors and image processing techniques to monitor forest fires in real time to decrease the rates of the false alarms. Their system achieved highly effective detection. However, it has some disadvantages such as high investments costs.

Wei et al. (2014) developed a fire detection system based on wireless sensor network and artificial intelligence (AI) based structure to enhance accuracy as a significant contribution. Their system is adaptable to dynamic environmental conditions. By this way it decreases the false and failed alarms.

Frizzi et al. (2016) proposed an AI based system using CNN (convolutional neural networks) for early fire detection. They combined convolution and maximum pooling methods to create a model to enhance the data training efficiency and to decrease the risk of false alarms.

Zhong et al. (2018) developed a fire detection system based on CNN using video sequences. Their structure passes a fire image based on the RGB model through three convolution layers with kernel sizes of 11x11, 5x5, and 3x3, respectively. Then adapts a maximum pooling window of size 3x3 to reduce the cost of the computational function. Their structure aims to reduce the computational load during the detection processes.

Zhao and Ban (2022) studied and demonstrated the significant accuracy improvement effects of the deep learning models for forest fire detection. They have used the analyses of the time series data from the geostationary satellites.

Abdusalomov et al. (2021) studied the application of convolutional neural networks for fire detection. They developed a model to improve the classification and identification of fire events.

Li and Zhao (2020) proposed an image fire detection algorithm based on the advanced object detection CNN models of Faster-RCNN, R-FCN, SSD, and YOLO v3. They proved that developed algorithms could achieve 28 FPS and 83.7% accuracy in real-time fire detection applications.

Yang et al. (2024) developed an image fire algorithm based on YOLOv3 to detect smoke and flame simultaneously. They then enhanced the early fire detection capability of the algorithm by making various improvements. Tests and benchmarks demonstrated that the developed structure can be used for real-time detection.

Ahn et al. (2023) developed a computer vision-based early fire detection model. They used closed-circuit television (CCTV) surveillance. Their model facilitates rapid fire detection through the acquisition of data from authentic fire tests.

Biswas et al. (2023) modified the third version of the Inception Convolutional Neural Network (Inception-V3). They integrated images including smoke into the dataset and optimized the functions to reduce the computational load.

Rahayu et al. (2023) emphasized the significance of IOT for the development of synchronized automatic early fire detection systems. Proposed structure could perform early fire detection operations with the help of continuous monitoring, data collection, and the analysis of the collected data.

Currently, topology optimization is an important tool in product design processes. It is used in a wide range of industries such as automotive and aerospace. Additive manufacturing technologies also have expanded their applications. There is a strong and useful relation between topology optimization and additive manufacturing to increase the prototyping efficiency to decrease the production time.

Topology optimization is technique that can be explained as general as optimizing material distribution within a designated design space, considering specific loads, boundary conditions, and constraints. The objective is to reduce the weight of the structure while keeping or improving its strength and natural frequencies. One of the main aims of optimization is to determine the appropriate material usage within the specified design area to achieve the desired structural performance. In the process, the designed volume is divided into smaller elements, a FEA model is created, and boundary conditions are applied to perform the FEA. During the analysis, the elements exhibit intermediate density values. These values approach 1 or 0 by employing penalization techniques such as the power law to penalize higher-density elements. This process ensures convergence towards

solid and void regions to build the final structure.

The optimization process uses an iterative updating of the material density by the optimization algorithm to converge to a solution. By this way it tries to achieve the optimal performance and design volume. The final structure is determined by ensuring a smooth transition between solid and void regions.

Two commonly preferred methods for determining the distribution of elements in topology optimization are Solid Isotropic Material Penalization (SIMP) and the Evolutionary Structural Optimization Technique (ESO) (Yurdem et al., 2019). The mathematical equations 1 and 2 of the SIMP method can be written as (Zhu et al., 2016):

$$E(\rho_e) = \rho_e^{\rho} E_0 \quad (1)$$

$$C_{ijkl} = \rho\, C^{0}_{ijkl}, 0 \le \rho(x) \le 1, Vol = \int_{\Omega}^{1} \rho(x) d\Omega \quad (2)$$

The SIMP interpolation and generalized schemes are shown in Figures 1 and 2.

Figure 1. Interpolation scheme used in the SIMP method for topology optimization, illustrating the relationship between material density and stiffness.

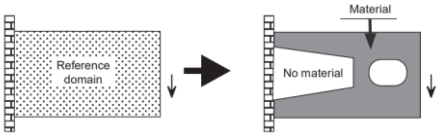

Figure 2. Generalized SIMP scheme demonstrating the penalization approach for differentiating solid and void regions during optimization.

Barbieri and Muzzupappa (2022) conducted a comparative study to compare the mechanical performance results of topology-optimized and generatively designed rocker arms and brake pedals for the Formula Student race car. Their results demonstrated that both optimized and generatively designed structures yielded effective outcomes.

Meng et al. (2020) studied a comprehensive account of the entire process of a bracket for the aviation industry, from topology optimization to additive manufacturing. The authors created and published a valuable guide for researchers engaged in topology optimization.

Cavazzuti et al. (2020) conducted studies involving optimization techniques for automotive chassis design. Their target of the optimization process was to reduce the weight of the chassis while ensuring structural performance constraints, as defined by Ferrari standards, were met. Their objective was to create the optimum chassis configuration by combining topology, size optimization and FEA. They used the structural performance of the Ferrari F458 as a reference point. They achieved a significant reduction in weight along with the creation of an optimized chassis structure.

Today, computer-based tools are essential for the design and analysis of structures. Solid modelling using CAD (Computer Aided Design) methods allows designers to define parts and assemblies and utilize geometry for simulations, analysis and prototyping. CAE methods enable virtual prototype simulations and static, kinematic and dynamic analysis (Sucuoglu et al., 2020; Demir et al., 2021a; Demir et al., 2021b).

In this study, a mobile early fire detection robotic structure was designed and developed. All sub parts and assembly model were created using Computer Aided Design tools. The electronic hardware (Rgb - thermal camera, raspberry pi, motor drivers and etc.) were selected, the mounting parts were designed and that hardware integrated into the structure. Required (FEA) finite element analyses were applied to check the structural strength and stability of the system. Then, topology optimization was conducted to decrease the weight and energy consumption of the mobile robot. A proper power analyses tool was developed to calculate and to compare the energy consumption of the non-optimized and optimized structures.

2. Materials and Methods

2.1. Design of the Robotic Structure

n this phase of the project, the robotic structure was designed using Fusion 360 CAD software. All subcomponents, including the top and bottom frames, motor connectors, and hardware mounts—were modeled and assembled accordingly. The mounting parts for electronic hardware were custom-designed and integrated into the chassis. Aluminum 6061 was selected as the structural material due to its favorable strength-to-weight ratio and machinability. The chassis was designed with pre-defined placement holes to ensure modularity and ease of assembly. The fully assembled robotic system is illustrated in Figure 3.

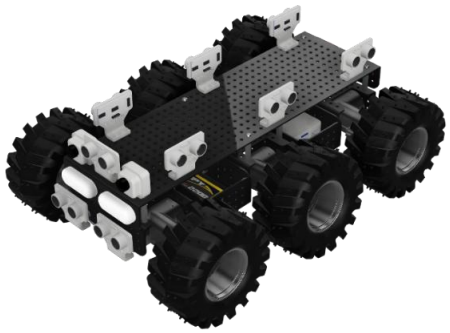

Figure 3. Assembled structure of the robotic system.

Following the 3D design process, a comprehensive part list, exploded view, and detailed engineering drawings—including general dimensions—were generated. These documents facilitated component selection and procurement. The robotic system was equipped with six DC motors and corresponding wheels, along with appropriate mounting elements. To enable path planning and obstacle avoidance, nine HC-SR04 ultrasonic sensors were integrated. For early fire detection, both RGB and thermal cameras were incorporated. Key hardware components, including a Li-Po battery, Raspberry Pi 5 (as the main controller), and motor drivers, were selected and embedded into the structure. The part list, exploded view, and engineering drawings are presented in Figure 4.

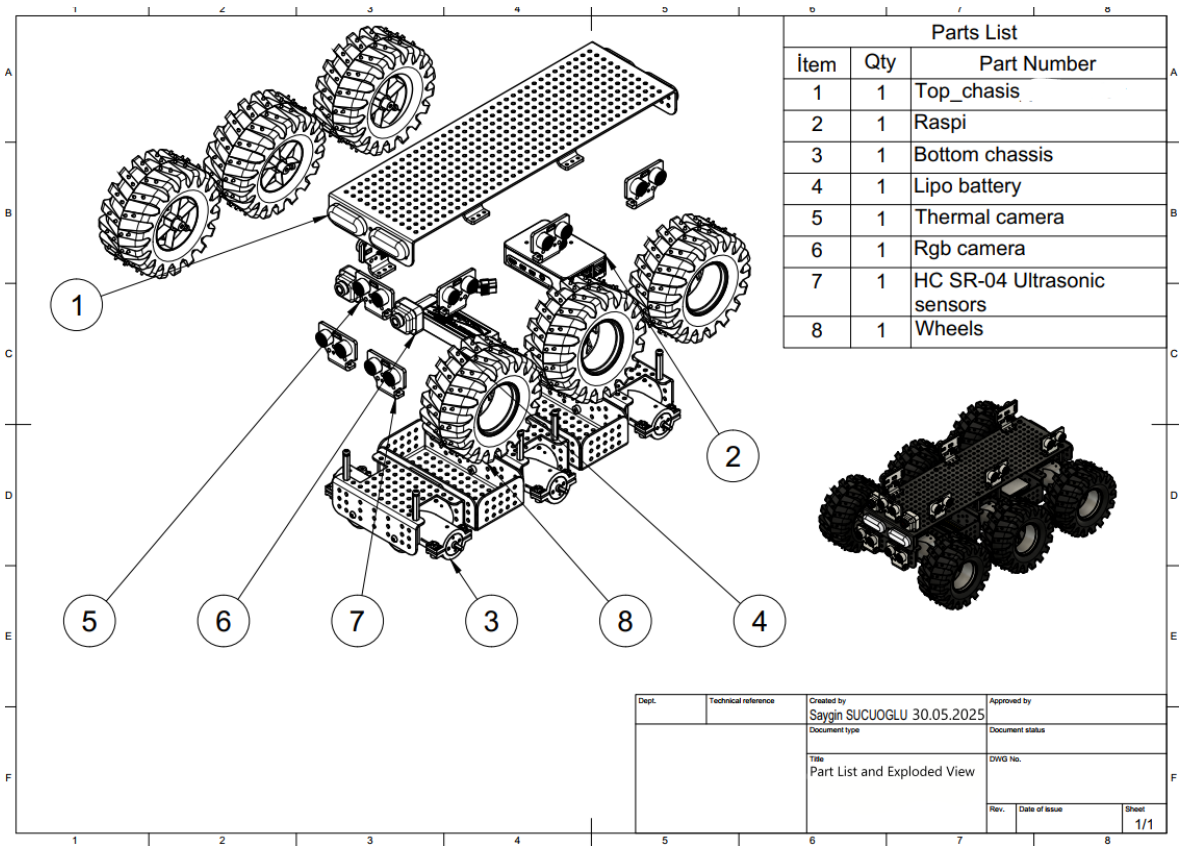

(a) Part list and exploded view

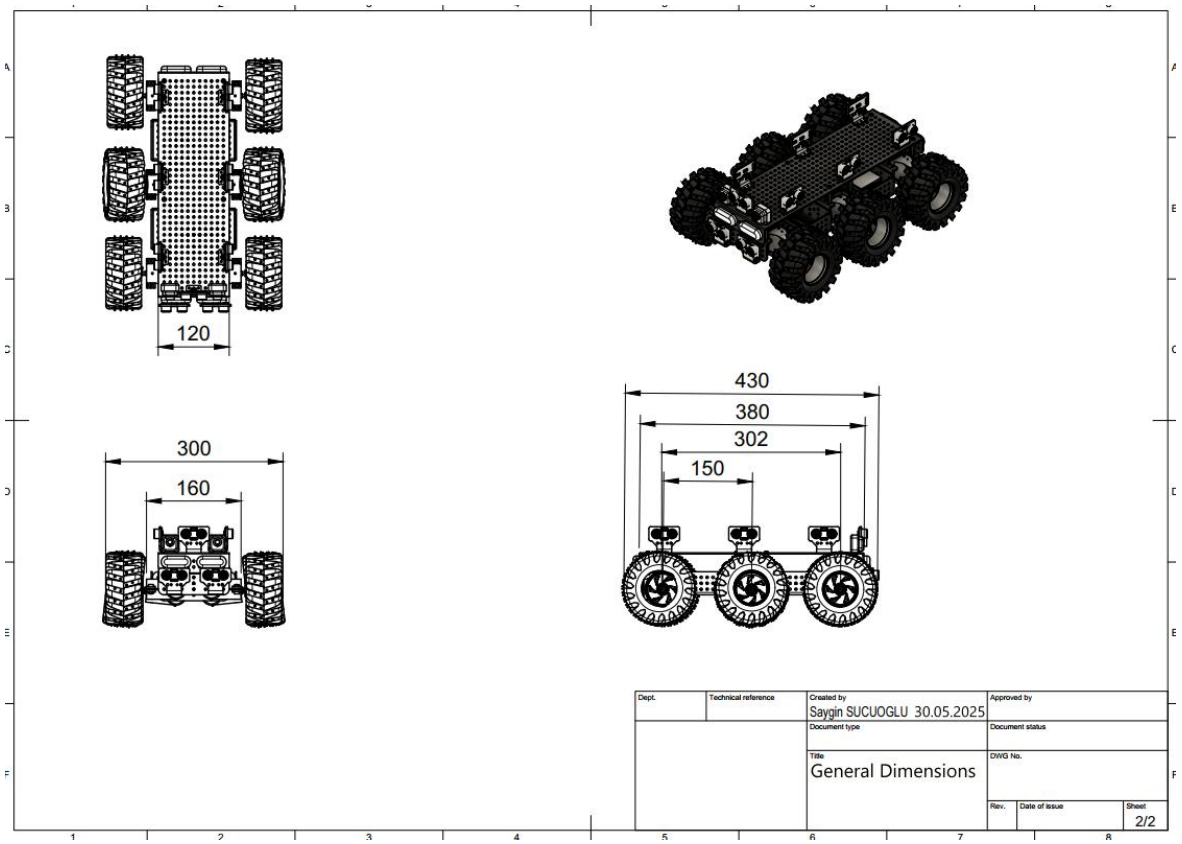

(b) Part list and exploded view (Engineering drawings)

Figure 4. Part list and exploded view and engineering drawings of the mobile robotic system, showing the dimensions, subcomponents, hardware integration and assembly layout.

2.2 Engineering Analyses of Non-Optimized Structure

Engineering analyses using finite element analysis (FEA) were performed to assess the structural strength and stability of mechanical design. A key objective was also to evaluate the suitability of the structure for topology optimization. For these analyses, the chassis material was defined as Aluminum 6061, and relevant loads were applied to determine the resulting stress values and factor of safety.

The simulations were conducted in the Static Structural environment of ANSYS Workbench 2024. Separate analyses were performed for the top and bottom frames. The applied loads for each component are illustrated in Figure 5. Forces of 300 N and 400 N were applied to the top and bottom frames, respectively. Additionally, torques of 1.1 Nm and 2.1 Nm—generated by the driver motors—were applied to the front and rear surfaces of the frames.

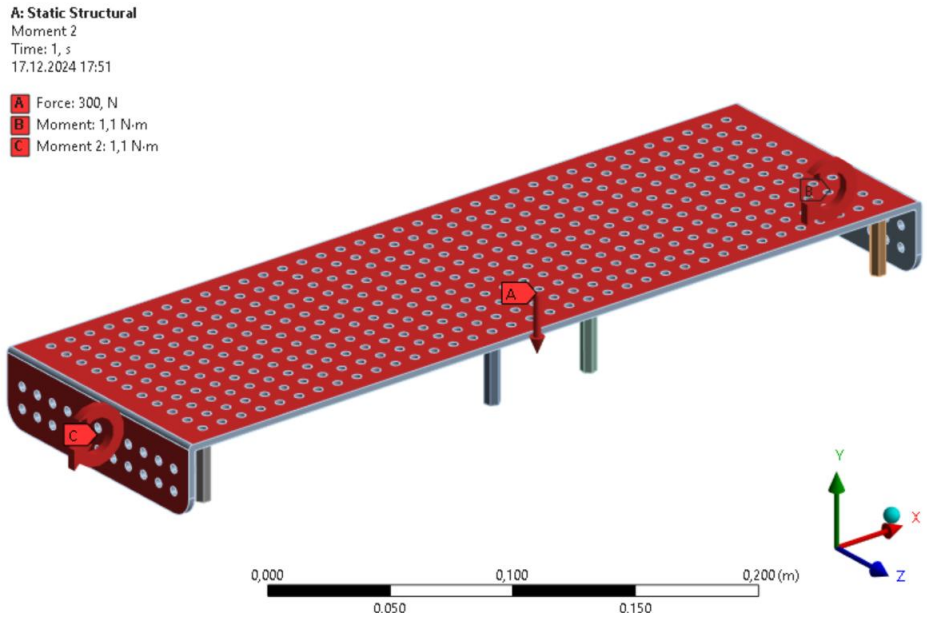

(a) Top frame

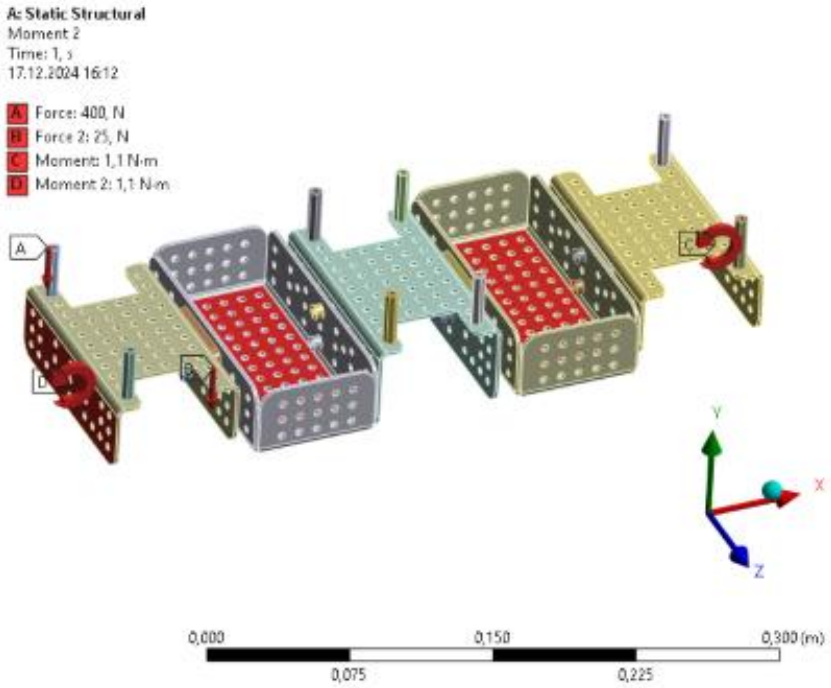

(b) Bottom frame

Figure 5. Topology-optimized configurations of the top and bottom frames generated through density-based analysis, showing reduced weight while preserving structural integrity.

2.3 Topology Optimization Process

Topology optimization was carried out using the ANSYS Structural Optimization tool. The same loading conditions applied in the previous engineering analyses were used for consistency. The optimization type was set to topology density, with a threshold value of 50%. Connection regions of the frames were designated as preserved areas to ensure structural integrity and were excluded from the optimization process. After multiple iterations, optimized structural configurations were generated. Based on the resulting data and exported design files, new top and bottom frames were created. These optimized structures are illustrated in Figure 6.

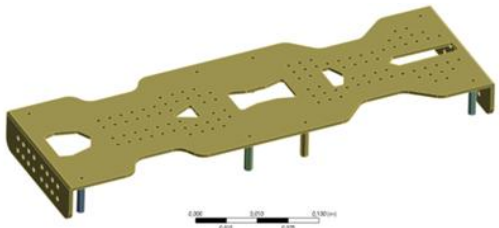

(a) Top frame

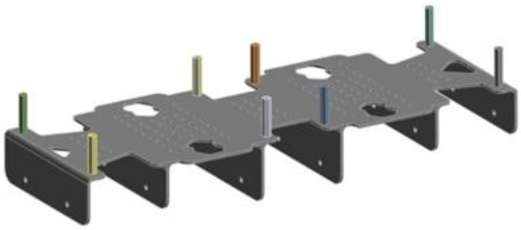

(b) Bottom frame

Figure 6. Optimized structures.

The weights of the top and bottom frames were reduced to 0.3 kg and 0.35 kg, respectively. These reductions are considered promising in terms of lowering the overall energy consumption of the system. To verify the structural integrity of the optimized frames, finite element analyses were performed using the same load conditions as those applied to the non-optimized structures. The results confirmed that the optimized designs maintained sufficient strength and stability.

2.4 Power Analysis Tool

A custom software tool was developed to enable energy consumption and weight analysis for robotic systems, employing Python's tkinter library to construct a user-friendly graphical user interface (GUI). This application was utilized to perform comparative power analysis between two robotic designs by processing part lists that include components such as motors, batteries, sensors, and chassis materials (Figure 7).

The interface allows users to input detailed specifications for each component, including voltage, current, quantity, and weight—directly reflecting the part list data. These entries are systematically aggregated, enabling iterative analysis and comprehensive evaluation. The tool performs real-time calculations of total power consumption and overall system weight, thereby supporting informed design optimization decisions.

An additional feature of the tool is its integrated image visualization function, which permits users to upload and display images of individual components within the GUI. This functionality enhances component identification and facilitates a more intuitive correlation between visual data and quantitative metrics, contributing to a more holistic approach to system design and evaluation.

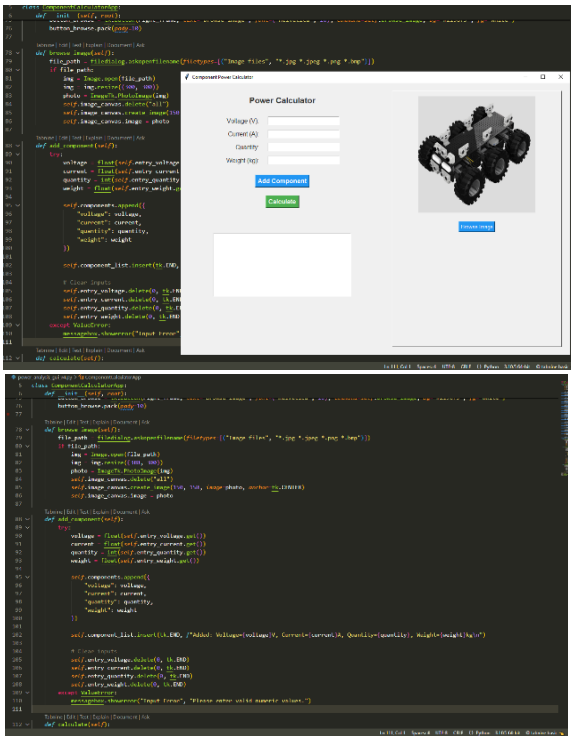

Figure 7. Power analysis tool.

In the comparative analysis of the two robotic designs, the developed tool facilitated the calculation of total energy requirements and weight distribution based on the detailed part lists. This capability enabled the identification of design efficiencies, including reduced power consumption and optimized chassis configurations with lower weight. By integrating component visualization with critical computational functions, the tool supports a streamlined and iterative design workflow while enhancing the clarity and completeness of engineering documentation.

This tool proves particularly valuable during early-stage design, prototyping, and comparative evaluation of mechanical and electronic systems, where rapid and accurate assessment of power and weight parameters is crucial for informed decision-making and overall performance optimization (Figure 8).

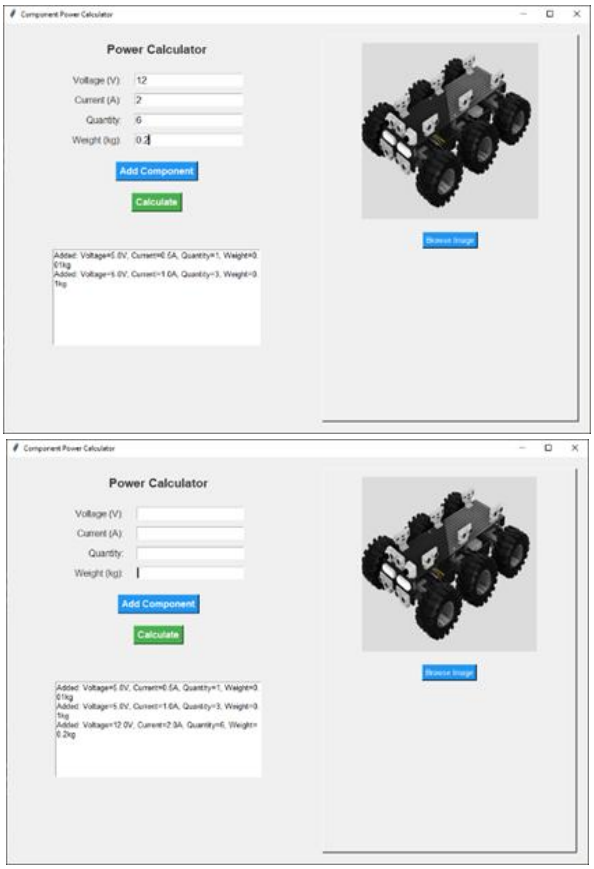

Figure 8. Calculations with power analysis tool.

2.5 New Optimized Assembly Model

In this phase of the study, a new assembly model was developed using the topology-optimized frames (Figure 9). Since the connection regions were preserved during the optimization process, they remained compatible for integration. The battery, controllers, and DC motors were successfully mounted onto the bottom frame, while all cameras and sensors were positioned on the top frame. The optimized structure was thus fully assembled and prepared for subsequent power analysis.

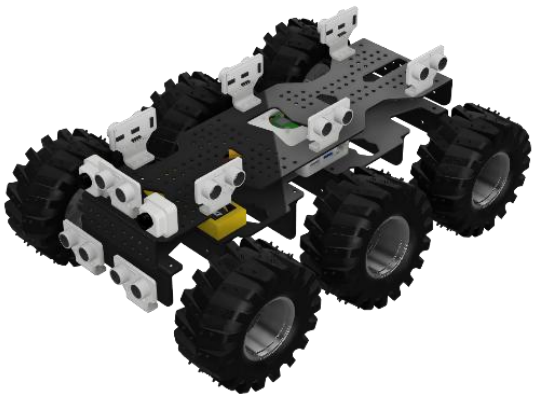

Figure 9. Assembly model of optimized structure.

3. Results and Discussion

3.1. Engineering Analyses Results of Non-Optimized and Optimized Structures

The analysis results strongly supported the implementation of topology optimization as a necessary design enhancement. In the initial non-optimized configuration, the top and bottom frames had approximate weights of 0.4 kg and 0.5 kg, respectively, with each part modeled using a uniform plate thickness of 3 mm. Under the applied loading conditions, the calculated factor of safety (FoS) was approximately 2.7, indicating a structurally conservative design with excess material usage. The corresponding von Mises stresses were recorded in the range of 40–45 MPa, well below the yield strength of the Aluminum 6061 material. These findings suggested that the structure possessed significant potential for mass reduction without compromising mechanical integrity, thereby validating the feasibility of topology optimization to improve overall energy efficiency.

Following the optimization process, the structural frames were redesigned based on the density distribution maps generated by the topology solver. Critical connection regions were preserved to ensure assembly compatibility and mechanical continuity. Finite element analyses of the optimized frames showed that the weight of the top and bottom frames was reduced to 0.3 kg and 0.35 kg, respectively representing a total reduction of approximately 25%. Despite the reduction in mass, the structural performance remained within acceptable limits. The factor of safety decreased to approximately 1.8, while the von Mises stress values remained consistent, around 45 MPa. Importantly, there were no significant increases in localized stress concentrations or indications of mechanical failure. All the data obtained from engineering analyses are shown in Figures 10 and 11, respectively.

These results confirm that the optimized frames retain adequate strength and stability while achieving meaningful reductions in material usage and energy consumption. By lowering the total system weight, the robotic platform benefits from improved energy efficiency, extended battery life, and enhanced mobility. Thus, the application of topology optimization not only satisfies mechanical performance requirements but also contributes to the development of a more sustainable and operationally efficient robotic system.

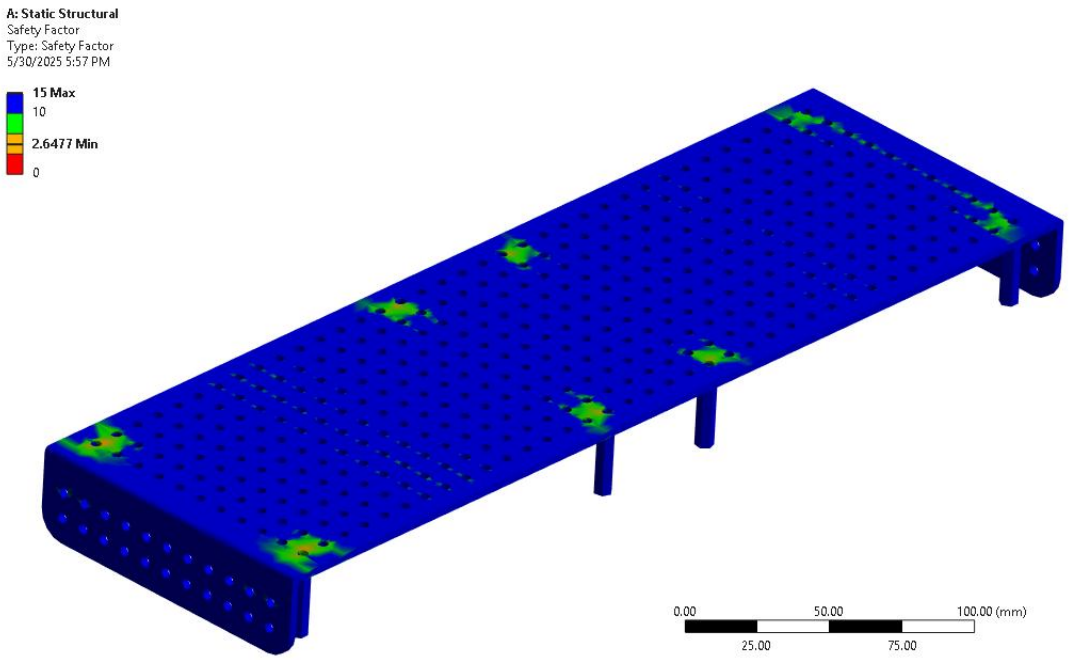

(a) FOS of non-optimized top frame

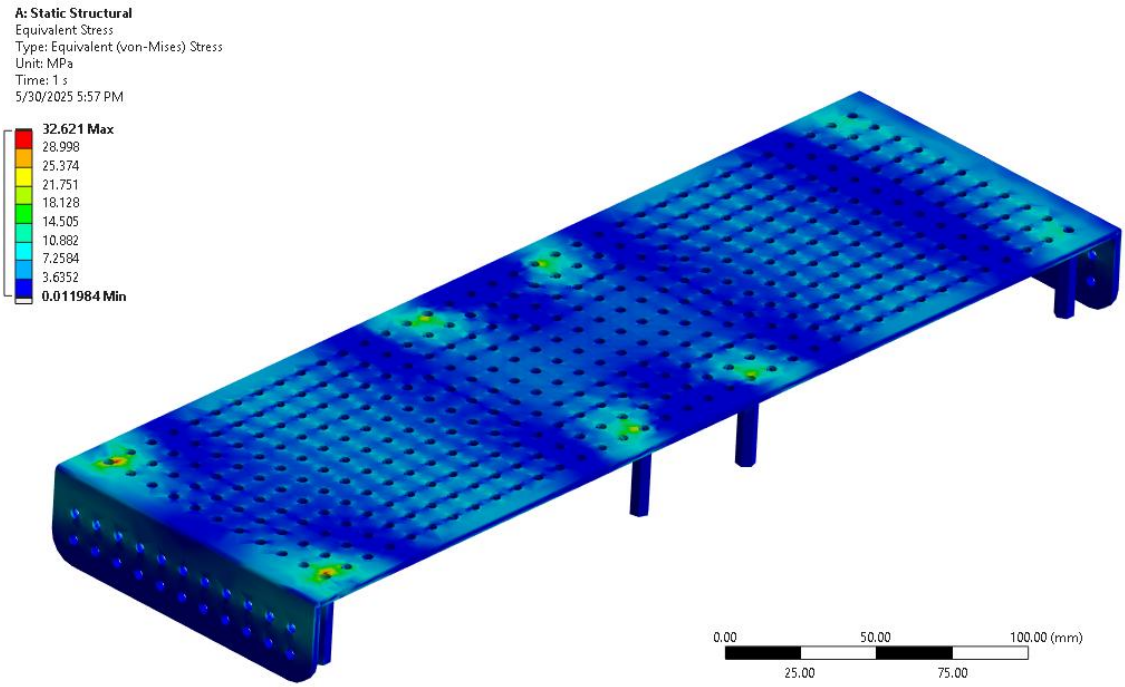

(b) Occurred stresses of non-optimized top frame

Figure 10. Finite element analysis results of the top frame before topology optimization, showing factor of safety and stress distribution.

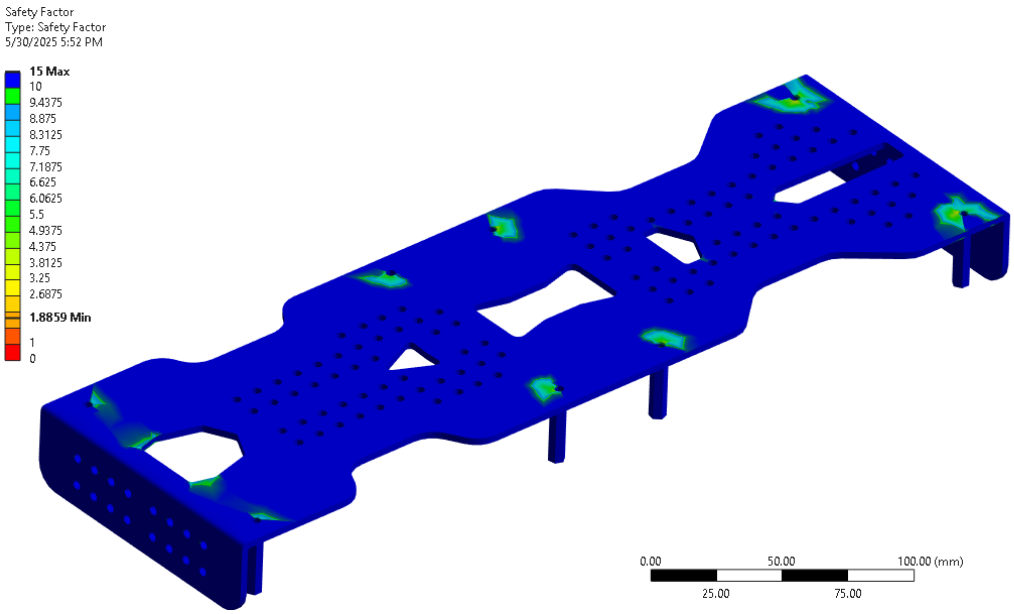

(a) FOS of optimized top frame

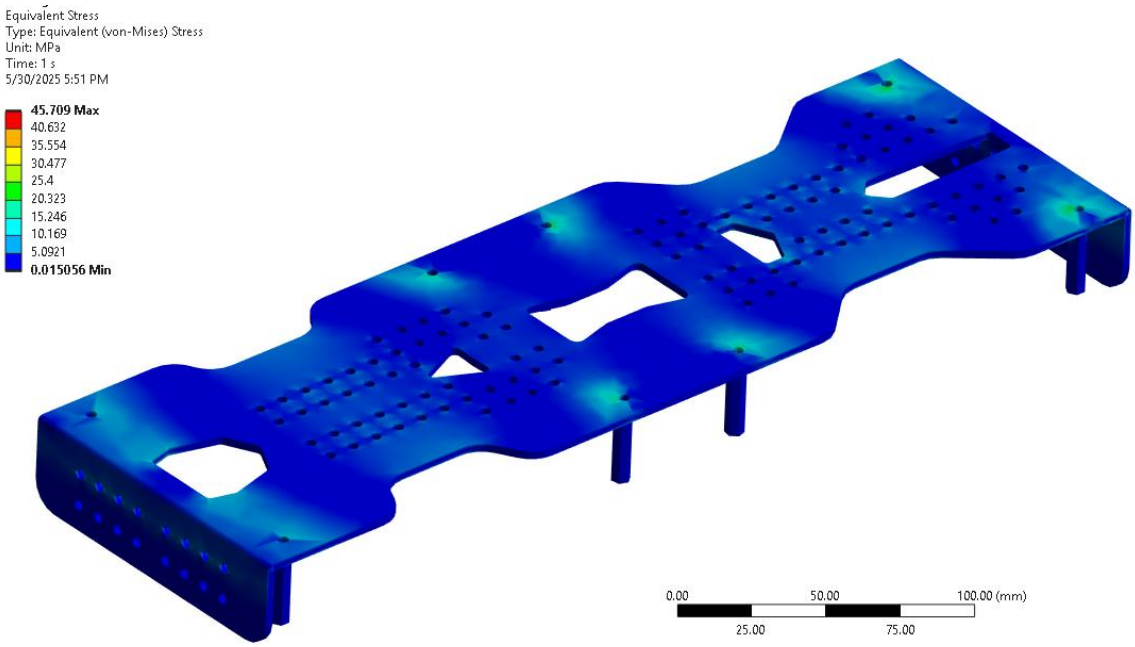

(b) Occurred stresses of optimized top frame

Figure 11. Finite element analysis results of the top frame after topology optimization, showing factor of safety and stress distribution.

3.2. Power Analysis Results

A comprehensive power analysis was conducted to evaluate the energy efficiency and operational performance of the optimized mobile early fire detection robot in comparison to its non-optimized counterpart. The primary objective was to quantify the benefits achieved through topology optimization, particularly in terms of reduced structural weight, power consumption, and overall energy requirements.

The analysis was based on conventional electrical and energy calculation principles, including the following formulas:

- Power (P) = Voltage (V) × Current (I)
- Total Energy (E) = Power (P) × Time (t)
- Total Power Consumption = Σ (Power usage of individual components)
- Weight Comparison = Σ (Weight of all components in each design)

Key assumptions incorporated into the analysis included:

- A standard Li-Po battery voltage of 11.1V (3S configuration)
- DC motors operating at 12V with a nominal current of 2A per motor
- Ultrasonic sensors drawing 30mA at 5V
- RGB and thermal cameras consuming 500mA at 5V

- Raspberry Pi and motor controllers requiring 1A at 5V

The comparative analysis between the non-optimized and optimized robotic platforms indicated notable gains in energy efficiency, with measurable reductions in both power consumption and system weight. These findings confirm the effectiveness of topology optimization in enhancing the energy performance of mobile robotic systems. The detailed data is presented in Table 1.

Table 1. Data summarization of power analysis

Component	Non-optimized	Optimized	Remarks
Chassis weight (gr)	900	650	Optimized design is lighter.
Total power requirement (W)	90	80	Optimized design consumes less power.
Energy consumption per Hour (Wh)	90	80	Lower energy demand for same duration.

Calculations assume six DC motors (12V, 2A), one Li-Po battery (11.1V), RGB + thermal cameras (5V, 500mA), ultrasonic sensors (5V, 30mA), Raspberry Pi + motor controllers (5V, 1A), with an operating duration of one hour.

The results demonstrate that the optimized design achieved a 25% reduction in chassis weight, contributing directly to decreased energy consumption and enhanced operational efficiency. The total power consumption of the optimized robot was 10 W lower than that of the non-optimized structure, confirming improved energy management.

The weight reduction, achieved through topology optimization, led to a decreased load on the drive motors, which in turn reduced the power requirements. This improvement enhances the robot's operational duration, making it more suitable for extended fire detection tasks in remote or hazardous environments.

Furthermore, the lower energy consumption of the optimized design enables the use of smaller or fewer battery modules without compromising operational endurance. This contributes to a lighter and more cost-effective system, emphasizing the importance of structural optimization in the development of energy-efficient robotic platforms.

The optimized structure significantly improved both structural and energy efficiency, highlighting the benefits of topology optimization in mobile robotics.

Overall, the power analysis results validate the effectiveness of topology optimization in improving the energy performance and functionality of mobile fire detection robots. The optimized system not only achieved 25% weight reduction but also demonstrated an 11% decrease in energy consumption, underscoring its potential for real-world applications in fire detection scenarios.

4. Conclusion

In this study, a comprehensive workflow encompassing design, development, topology optimization, and power analysis of a mobile early fire detection robotic system was successfully implemented. All subcomponents and complete assemblies were meticulously developed using advanced Computer-Aided Design (CAD) tools. Engineering analyses, including finite element analysis (FEA), were conducted to evaluate the structural strength of both the non-optimized and optimized configurations. These analyses validated the structural integrity and confirmed the necessity of applying topology optimization to enhance performance without compromising mechanical reliability.

Furthermore, a custom-built power analysis tool was developed to accurately assess and compare the energy consumption profiles of the non-optimized and optimized designs. The results demonstrated that the topology-optimized structure achieved a 25% reduction in chassis weight while maintaining acceptable safety margins and stress levels. This structural lightweighting process directly contributed to an 11% reduction in energy consumption, confirming the effectiveness of the optimization approach for mobile robotic applications operating in energy-sensitive scenarios such as early fire detection in remote environments.

The findings underscore the potential of topology optimization not only as a tool for mass reduction but also as a key enabler of energy-efficient design in robotic systems. The integration of structural optimization and tailored power assessment offers a holistic framework for designing high-performance, lightweight, and power-aware robotic platforms.

Future work will focus on several key areas:

- Experimental validation: A physical prototype will be developed to correlate simulation results with real-world operational behavior.
- Adaptive control algorithms: The current system will be expanded to incorporate adaptive control algorithms that dynamically adjust power distribution based on mission demands.
- Enhanced fire detection capability: The fire detection system will be improved through the integration of additional sensors and machine learning–based decision systems.
- Modular deployment: The system architecture will be adapted for modular deployment in larger coordinated robotic fleets to support scalable and cooperative fire monitoring applications in hazardous environments.

Author Contributions

The percentages of the author' contributions are presented below. The author reviewed and approved the final version of the manuscript.

	H.S.S
C	100
D	100
S	100
DCP	100
DAI	100
L	100
W	100
CR	100
SR	100
PM	100
FA	100

C=Concept, D= design, S= supervision, DCP= data collection and/or processing, DAI= data analysis and/or interpretation, L= literature search, W= writing, CR= critical review, SR= submission and revision, PM= project management, FA= funding acquisition.

Conflict of Interest

The author declared that there is no conflict of interest.

Ethical Consideration

Ethics committee approval was not required for this study because there was no study on animals or humans.

References

Abdusalomov A, Baratov N, Kutlimuratov A, Whangbo TK. 2021. An improvement of the fire detection and classification method using YOLOv3 for surveillance systems. Sensors, 21(19): 6519.

Ahn Y, Choi H, Kim BS. 2023. Development of early fire detection model for buildings using computer vision-based CCTV. J Build Eng, 65: 105647.

Barbieri L, Muzzupappa M. 2022. Performance-driven engineering design approaches based on generative design and topology optimization tools: a comparative study. Appl Sci, 12(4): 2106.

Biswas A, Ghosh SK, Ghosh A. 2023. Early fire detection and alert system using modified inception-v3 under deep learning framework. Procedia Comput Sci, 218: 2243–2252.

Cavazzuti M, Baldini A, Bertocchi E, Costi D, Torricelli E, Moruzzi P. 2020. High performance automotive chassis design: a topology optimization-based approach. Struct Multidiscip Optim, 62: 45–56.

Demir N, Sucuoglu HS, Bogrekci I, Demircioglu P. 2021a. Structural & dynamic analyses and simulation of mobile transportation robot. Int J 3D Print Technol Digit Ind, 5(3): 587–595.

Demir N, Sucuoglu HS, Bogrekci I, Demircioglu P. 2021b. Topology optimization of mobile transportation robot. Int J 3D Print Technol Digit Ind, 5(2): 210–219.

Di Biase V, Laneve G. 2018. Geostationary sensor based forest fire detection and monitoring: An improved version of the SFIDE algorithm. Remote Sens, 10(5): 741.

Dimitropoulos K, Barmpoutis P, Grammalidis N. 2014. Spatio-temporal flame modeling and dynamic texture analysis for automatic video-based fire detection. IEEE Trans Circuits Syst Video Technol, 25(2): 339–351.

Frizzi S, Kaabi R, Bouchouicha M, Ginoux JM, Moreau E, Fnaiech F. 2016. Convolutional neural network for video fire and smoke detection. IECON 2016 – 42nd Annu Conf IEEE Ind Electron Soc, October 23-26, Florence, Italy, pp: 877–882.

He X, Feng Y, Xu F, Chen FF, Yu Y. 2022. Smart fire alarm systems for rapid early fire warning: Advances and challenges. Chem Eng J, 450: 137927.

Khan F, Xu Z, Sun J, Khan FM, Ahmed A, Zhao Y. 2022. Recent advances in sensors for fire detection. Sensors, 22(9): 3310.

Li P, Zhao W. 2020. Image fire detection algorithms based on convolutional neural networks. Case Stud Therm Eng, 19: 100625.

Madsen D, Azeem HA, Sandahl M, van Hees P, Husted B. 2018. Levoglucosan as a tracer for smouldering fire. Fire Technol, 54(6): 1871–1885.

Meng L, Zhang W, Quan D, Shi G, Tang L, Hou Y, Gao T. 2020. From topology optimization design to additive manufacturing: Today's success and tomorrow's roadmap. Arch Comput Methods Eng, 27(3): 805-830.

Rahayu E, Isnomo YHP, Anshori MA. 2023. Automatic Early Warning System Design with Firefighter Synchronization Based on Internet of Things (IoT). J Telecommun Netw, 13(1): 103–108.

Saeed F, Paul A, Karthigaikumar P, Nayyar A. 2020. Convolutional neural network based early fire detection. Multimed Tools Appl, 79(13): 9083–9099.

Sucuoglu HS. 2015. The development of fire detection robot. Master's thesis, Adnan Menderes Univ, Fen Bilimleri Enstitusu, Aydın, Türkiye, pp:45-78.

Sucuoglu HS. 2020. Development of a robotic system with hybrid locomotion for both indoor and outdoor fire detection operations. PhD thesis, Adnan Menderes Univ, Fen Bilimleri Enstitusu, Aydın, Türkiye, pp:67-85.

Sucuoglu HS, Bogrekci I, Demircioglu P. 2018. Development of mobile robot with sensor fusion fire detection unit. IFAC-PapersOnLine, 51(30): 430–435.

Sucuoglu HS, Bogrekci I, Demircioglu P. 2019. Real time fire detection using faster R-CNN model. Int J 3D Print Technol Digit Ind, 3(3): 220–226.

Sucuoglu HS, Bogrekci I, Demircioglu P, Turhanlar O. 2020. Design & FEA and multi body system analysis of human rescue robot arm. In: Adv Mechatronics Solut, Springer, London, UK, 651–656.

Wei X, Wang Y, Dong Y. 2014. Design of fire detection system in buildings based on wireless multimedia sensor networks. Intell Control Autom, 2014: 3008–3012.

Yang M, Qian S, Wu X. 2024. Real-time fire and smoke detection with transfer learning based on cloud-edge collaborative architecture. IET Image Process, London, UK, pp:47-58.

Yurdem H, Degirmencioglu A, Cakir E, Gulsoylu E. 2019. Measurement of strains induced on a three-bottom moldboard plough under load and comparisons with finite element simulations. Measurement, 136: 594–602.

Zamal MFB, Sayed S, Bhuiyan T, Rahman M. 2017. An Efficient Multi-sensing and GSM Equipped Fire Monitoring System. In: MATEC Web Conf, 140: 01003.

Zhang RC, Du JH. 2010. Fuzzy clustering algorithm of early fire based on process characteristic. Key Eng Mater, 437: 339–343.

Zhao Y, Ban Y. 2022. Early Detection of Wildfires with GOES-R Time Series and Deep GRU-Network.

Zhong Z, Wang M, Shi Y, Gao W. 2018. A convolutional neural network-based flame detection method in video sequence. Signal Image Video Process, 12: 1619–1627.

Zhu JH, Zhang WH, Xia L. 2016. Topology optimization in aircraft and aerospace structures design. Arch Comput Methods Eng, 23: 595–622.

Black Sea Journal of Engineering and Science
doi: 10.34248/bsengineering.1739969

Open Access Journal
e-ISSN: 2619 – 8991

Araştırma Makalesi (Research Article)
Cilt 8 - Sayı 5: 1617-1627 / Eylül 2025
(Volume 8 - Issue 5: 1617-1627 / September 2025)

FARKLI ARAZİ KULLANIMLARINDA TOPRAK ORGANİK KARBON MİKTARININ BELİRLENMESİ: ALAÇAM İLÇESİ ÖRNEĞİ

Ali İMAMOĞLU[1]*

[1]*Sinop University, Faculty of Education, Department of Turkish and Social Sciences Education Sinop Türkiye*

Özet: Organik karbon deposu olan toprak, çeşitli sebeplerle tehdit altındadır. Arazi bozulumu ve erozyonla zarar gören toprakla birlikte, karbon depoları da azalmaktadır. Bu araştırma farklı arazi kullanımları altında organik karbon miktarının değişimini ortaya koymak amacıyla gerçekleştirilmiştir. Araştırma Samsun ili, Alaçam ilçesi sınırlarında gerçekleştirilmiştir. Arazi çalışmaları ile 32 adet toprak örneği alınmıştır. Örneklerin yarısı tarım alanlarından yarısı ise mera arazilerinden alınmıştır. Toplanan örnekler önişlemlerle analize hazır hale getirilmiş, toprak organik madde gibi fiziksel ve kimyasal bazı analizlere tabi tutulmuşlardır. Sonuçlar ArcGİS 10.2.2 programı ile jeoistatistik yapılarak uygun yöntemle haritalandırılmıştır. Tanımsal istatistikler ise SPSS 17.0 paket programı ile gerçekleştirilmiştir. Elde edilen sonuçlara göre istatistiksel olarak anlamlı fark bulunmamakla birlikte tarım alanlarında organik karbonun mera arazilerine göre daha düşük değerler gösterdiği tespit edilmiştir. İlçe arazilerinin yaklaşık %8'inde karbon değerlerinin 1.09-1.92 ton/ha gibi düşük değerler gösterdiği belirlenmiştir. Mera arazilerine ve orman alanlarının daha fazla bulunduğu güney kesimlerde ise karbon içeriği 3.70 ton/h kadar çıkmaktadır. Araştırma sonucuna göre, tarım alanlarında karbon miktarının düşük olması sahanın tarımsal arazi deseni ve arazi kullanımının toprak karbonunu azalttığını göstermektedir.

Anahtar kelimeler: Toprak, Karbon, Tarım, Mera

Determination of Soil Organic Carbon Content Under Different Land Use Types: A Case Study of Alaçam District

Abstract: As a reservoir of organic carbon, soil is under threat due to various factors. Along with soil degradation and erosion, carbon stocks are also decreasing. This study was conducted to reveal the changes in organic carbon content under different land use types. The research was carried out within the Alaçam district in Samsun province. 32 soil samples were collected during fieldwork, half obtained from agricultural lands and the other half from pasture areas. The collected samples were subjected to preliminary processing and then analyzed for specific physical and chemical properties such as texture and organic matter. The results were geostatistically analyzed and mapped using ArcGIS 10.2.2 software. Descriptive statistical analyses were performed using the SPSS 17.0 package. According to the results, although no statistically significant difference was found, organic carbon values in agricultural lands were lower than in pasture areas. It was determined that approximately 8% of the district's land area exhibited low carbon values ranging from 1.09 to 1.92 tons/ha. In the southern parts, where pastures and forested areas are more concentrated, carbon content reaches 3.70 tons/ha. The study results indicate that the low carbon content in agricultural lands suggests that the agricultural land-use pattern and practices reduce soil carbon stocks.

Keywords: Soil, Carbon, Agriculture, Pasture

***Sorumlu yazar (Corresponding author):** Sinop University, Faculty of Education, Department of Turkish and Social Sciences Education Sinop Türkiye
E mail: aliimamoglu@yandex.com (A. İMAMOĞLU)
Ali İMAMOĞLU https://orcid.org/0000-0001-9197-1029

Gönderi: 11 Temmuz 2025 **Received:** July 11, 2025
Kabul: 09 Eylül 2025 **Accepted:** September 09, 2025
Yayınlanma: 15 Eylül 2025 **Published:** September 15, 2025

Cite as: İmamoğlu A. 2025. Determination of soil organic carbon content under different land use types: a case study of alaçam district. BSJ Eng Sci, 8(5): 1617-1627.

1. Giriş

Toprak karasal organik karbonun en fazla bulunduğu temel yaşam kaynaklarımızın birisidir. Topraklarımız, çeşitli sebeplerle giderek daha fazla tehdit altında kalmaktadır. Bu süreç gıda ve tarım güvenliğine zarar vermektedir. Sonuçta toprak varlığı hızla tüketilmekte ve bozulmaktadır. Arazi bozulumu ve erozyonla toprakların azalması ya da toprakların verimsizleşmesi türlerin soyunun tükenmesi ve yaşam standartlarının düşmesine sebep olan önemli faktörlerdendir (Chappell vd., 2019; Herrick vd., 2019). Toprak bozulumu ya da erozyon ile toprağın kaybı gibi durumları doğru anlamanın kaynağı toprakları fiziksel, kimyasal ve biyolojik olarak tanımaktan geçmektedir. Ekberli ve Dengiz, (2017) yaptıkları araştırmada toprak fiziksel ve kimyasal verilerinin ortaya konulmasının, toprakta verimliliğin korunması tahmin edilmesi ve geliştirilmesine yönelik teknik oluşturmak için bir zorunluluk olduğunu belirtmişlerdir. Toprak organik karbonu temelde bitki ve hayvan artıkları ile mikroorganizmalar tarafından üretilir ve toprak şartlarına bağlı olarak belirli miktarda ayrışır (İmamoğlu ve Dengiz, 2017). Toprak organik karbonu; organik maddenin ana bileşenidir ve toprak strüktürü, suyun toprakta depolanması, infiltrasyonu gibi temel toprak özelliklerini desteklemesi sebebiyle toprağın verimliliği, sağlığı ve devamlılığı açısından oldukça

önemlidir (TÜBİTAK Bilgem YTE, 2018). Ayrıca toprak organik karbonu seviyelerindeki küçük değişikliklerin küresel iklim değişikliğinin hafifletilmesinde önemli rol üstlenebileceği öngörülmektedir (Berhane vd., 2020). Li vd. (2025), tuzlu-alkali topraklarda organik iyileştirme yoluyla toprak organik karbonunun (SOC) artırılmasının ürün verimini %36,5 oranında artırabileceğini belirtmiş, Liu vd. (2023) ise aynı topraklarda saman ekleyerek organik karbon içeriğini %58 oranında artırmayı başarmışlardır. Buna göre arazi kullanımı ile ilgili pratiklerin yeniden gözden geçirilmesi gerekmektedir.

Bu çalışmada, coğrafi faktörlere bağlı olarak değişiklik gösteren toprak organik karbon içeriğinin belirlenmesi ve sonuçların arazi kullanımı ile ilişkisinin belirlenmesi amaçlanmaktadır. Farklı arazi kullanımları altında toprak organik karbon içeriğinin nasıl değişiklik gösterdiği belirlenecek ve duruma uygun çözüm önerileri sunulacaktır.

2. Materyal ve Yöntem

2.1. Araştırma Alanı Yeri ve Sınırları

Alaçam ilçesi Samsun ili sahil kesiminde, yaklaşık 630 km2'lik yüz ölçümü ile küçük bir sahil yerleşmesidir (Şekil 1). Yükseltinin az olduğu düz düze yakın alanlarda tarım alanları ve yer yer meraların yoğunlaştığı ilçe arazileri güneye doğru ilerledikçe bitki örtüsü bakımından zenginleşir. Yer yer gelişmiş kayın ağaçlarının bulunduğu saf ormanlar ve çamlarla meşelerin birarada bulunduğu karışık ormanlar görülmektedir. İklim bakımından tipik Karadeniz ikliminin hakim olduğu ilçe topografik yapısı sebebiyle Samsun'un birçok ilçesi gibi yağışa duyarlıdır.

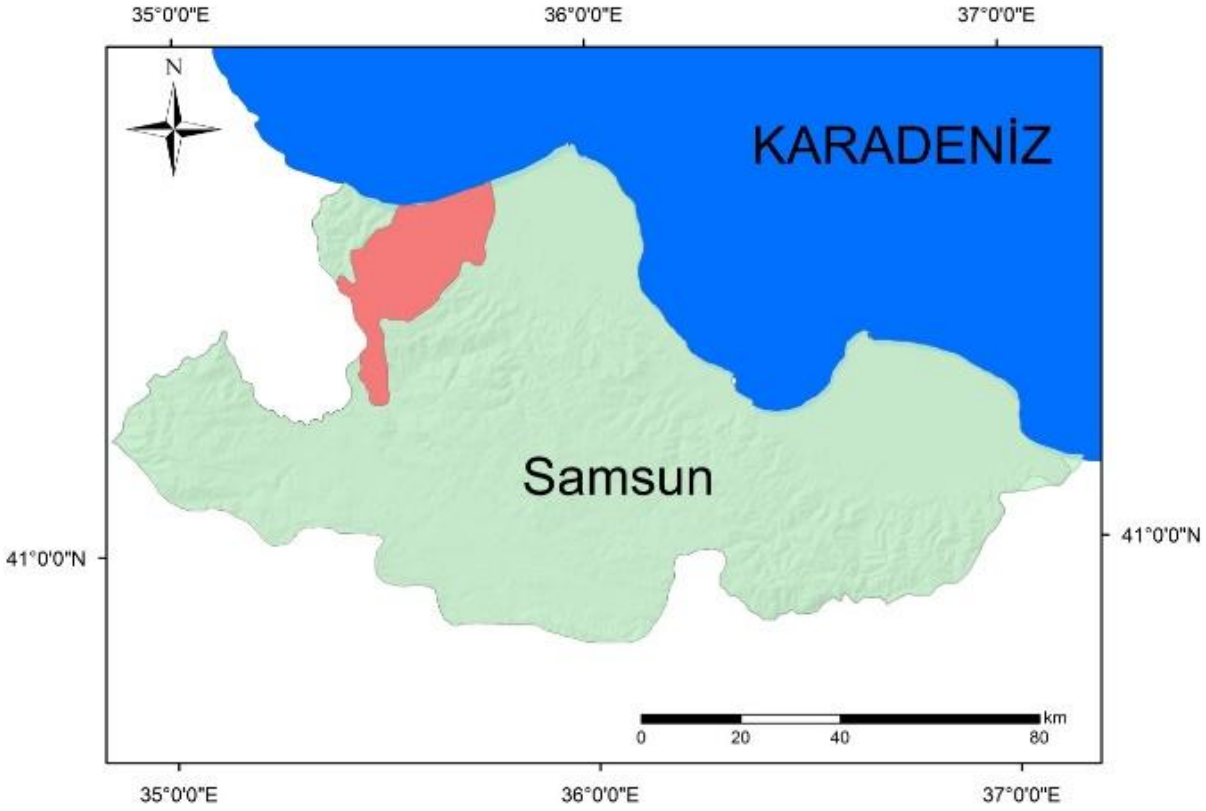

Şekil 1. Alaçam ilçe sınırları.

2.2. Yöntem

Alaçam ilçesi topraklarında farklı topografik yapılarda 32 farklı noktadan toprak örneği alınmıştır. Bu örneklerin yarısı tarım alanlarından diğer yarısı ise mera arazilerinden seçilmiştir (Şekil 2). Toplanan örnekler önişlemlerle analize hazır hale getirilmiş ve fiziksel ve kimyasal bazı analizlere tabi tutulmuşlardır.

Analiz sonuçları ArcGİS 10.2.2 programı ile jeoistatistik yapılarak uygun yöntemle dağılış haritaları oluşturulmuştur. Tanımsal istatistikler ise SPSS 17.0 paket programı ile gerçekleştirilmiştir.

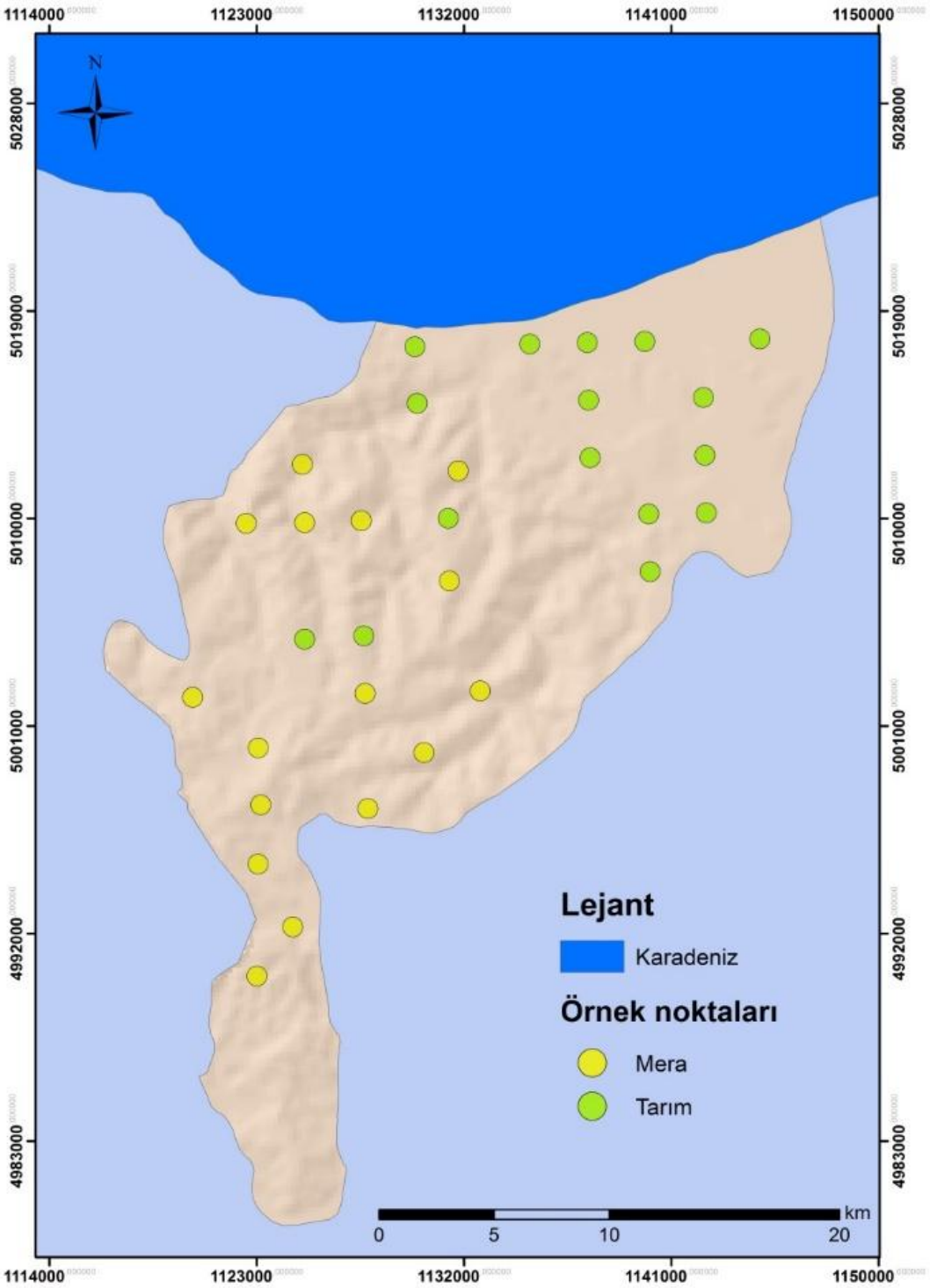

Şekil 2. Örnek alım noktaları.

Toprak örneklerinde yapılan analizlerde, kütle yoğunluğu (Blake ve Hartge, 1986) ve organik madde Walkley-Black yöntemi kullanılmıştır (Nelson ve Sommers, 1982).

$$TOK = \frac{1 - \delta i\% * pi * Ci * Ti}{100} \quad (1)$$

Eşitlik 1'de; % δi bölünmenin volümetrik oranının >2 mm temsil eder (kaya parçacıkları, ρi kütle yoğunluğudur (g.cm^{-3}), Ci TOK içeriğidir (ton.ha−1) ve Ti, i tabakasının kalınlığını temsil eder (cm).

Haritalandırma işlemi sırasında yaygın kullanılan jeoistatistik yöntemler IDW, RBF ve Kriging yöntemlerinden doğal (ordinary), evrensel (universal), basit (simple) kriging enterpolasyon hesaplamaları kullanılmıştır. Bu hesaplamada RMSE değeri yani hata payı en düşük olan yöntem belirlenmiş ve Inverse Distance Weighting (IDW) ile haritalama işlemi gerçekleştirilmiştir.

3. Bulgular

3.1. Tanımsal ve Jeoistatistiksel analizler

Araştırma alanından alınan örneklerde tanımsal istatistikler yapılmış ve toprakların normal dağılım özelliği gösterip göstermediği Kolmogorov-Smirnov (K-S) testi ve Shapiro-Wilk testi ile kontrol edilmiştir (Tablo 1). Çoklu karşılaştırma testi ile de arazi kullanımları arasında farklılık olup olmadığı belirlenmiştir. Tukey (Çoklu Karşılaştırma Testi) P=0,194, P>0,05 sonucu elde edilmiş ve tarım ve mera grupları arasında istatistiksel olarak anlamlı bir fark tespit edilememiştir.

Carbon miktarının dağılışının belirlenmesinde enterpolasyon yöntemleri denenmiş ve hata kareler ortalaması (RMSE) en düşük yöntem kullanılmıştır. Alanın Carbon değerlerine ait enterpolasyon değerleri Tablo 2'de verilmiştir.

Tablo 1. Toprak organik karbonu tanımsal istatistikleri

Grup	Min.	Maks.	Ort.	Std. Sapma	CV (%)	Çarpıklık	K-S (p)	Shapiro-Wilk (p)
Mera	1,18	3,36	2,38	0,51	21,57	-0,11	0,587	0,373
Tarım	1,09	3,74	2,09	0,68	32,69	0,87	0,905	0,290

Tablo 2. Toprak Organik Karbon enterpolasyonu için RMSE değerleri tablosu

Jeoistatistiksel Modeller			
Inverse Distance Weighting (IDW)		1	**0,612**
		2	0,645
		3	0,682
Radial Basis Functions (RBF)		Completely Regularized Spline	0,672
		Thin Plate Spline	0,856
Kriging	Ordinary Kriging	Spherical	0,944
		Exponential	0,951
		Gaussian	0,937
	Simple Kriging	Spherical	0,961
		Exponential	0,961
		Gaussian	0,959
	Universal Kriging	Spherical	0,973
		Exponential	0,978
		Gaussian	0,965

3.2. Topografik Özellikler

Alaçam ilçesi topografyasına baktığımızda kıyı kesiminin genellikle düz ve alçak rakımlı alanlar olduğu, güney ve iç kesimlere doğru yükseltinin kademeli olarak arttığı görülmektedir (Şekil 3). İlçe de yaklaşık 17 km sahil şeridi bulunmaktadır. Ortalama yükseltisi 15 metre olan ilçede ova düzlükleri ve düze yakın araziler özellikle tarım için elverişli bir zemin sunmaktadır.

İlçede kıyı kesiminde düşük eğim değerleri olan düzlük araziler tarımın yanında yerleşme amacıyla da kullanılmaktadır. Yükselti arttıkça eğim değerlerinin de %20'yi aşan oranlara ulaştığı ve vadiler boyunca derince yarılmış dik yamaçların oluştuğu gözlemlenmektedir (Şekil 4). Öte yandan Canik dağları genelinde görüldüğü gibi burada da farklı seviyelerde aşınım yüzeyleri göze çarpmaktadır.

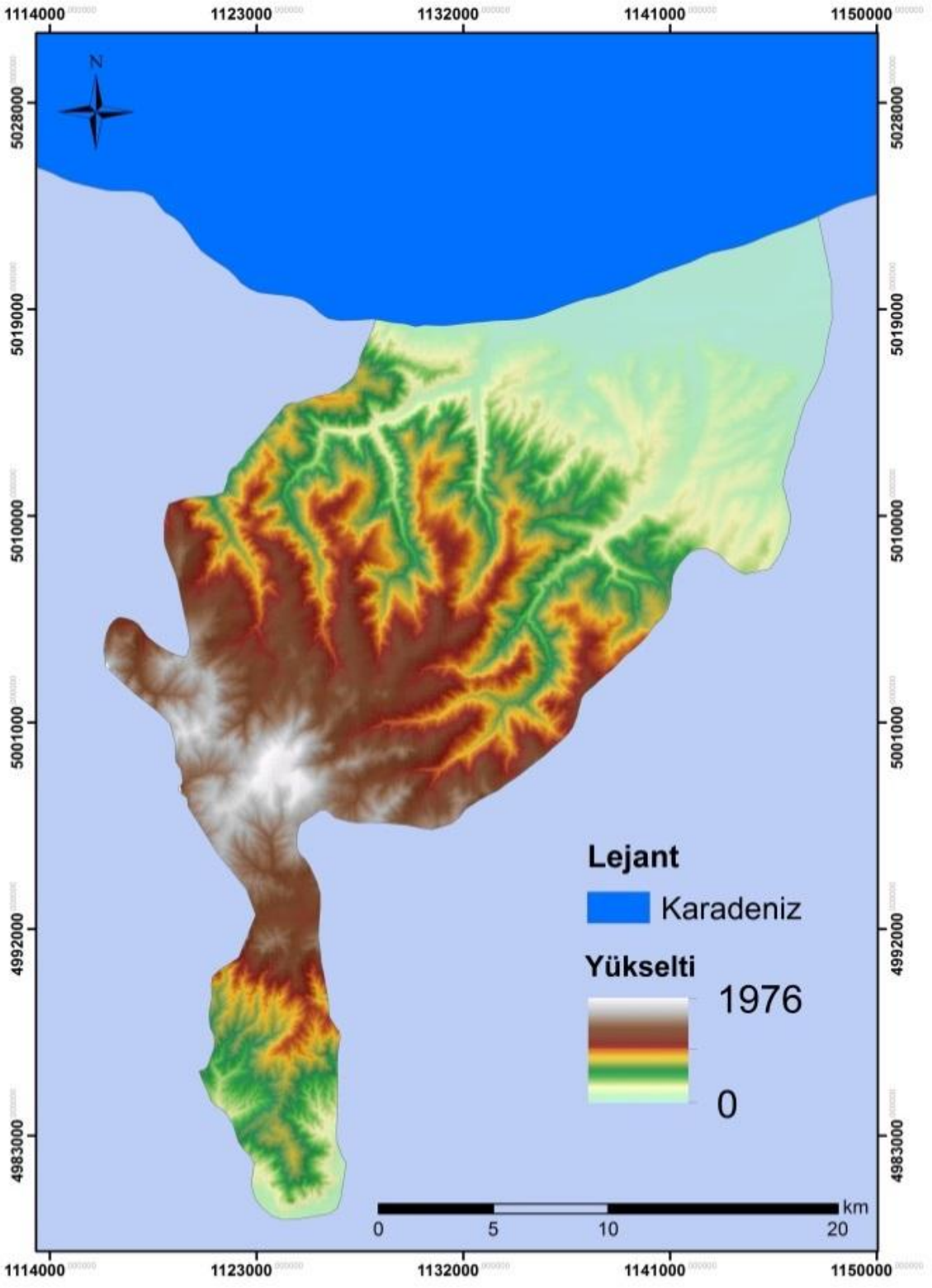

Şekil 3. Yükselti haritası.

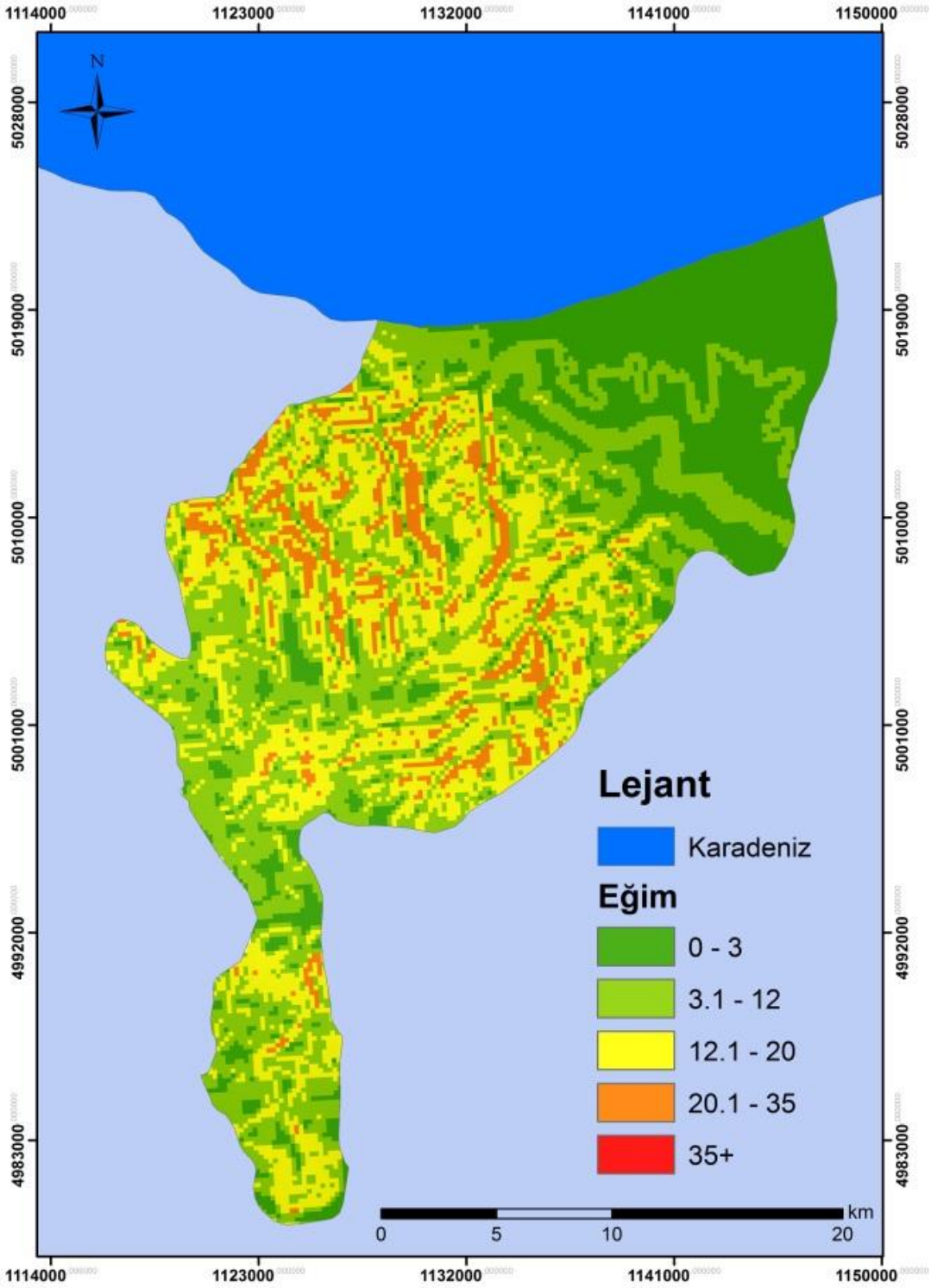

Şekil 4. Eğim haritası.

3.3. Arazi Kullanımı

Ova düzlüğünde yoğun olarak çeltik tarlaları, sulanabilen ve sulanamayan tarım alanları ve karışık tarım faaliyetlerinin bulunduğu alanlar bulunmaktadır. İlçe sınırlarının yaklaşık %60'ını kaplayan mera ve orman arazileri yükselti arttıkça baskın hale gelirken, bu meraların çoğunun orman sınırları içinde yer aldığı, hatta bazılarının verimliliğini kaybetmiş eski tarım alanları olduğu arazi çalışmalarında tespit edilmiştir (Şekil 5, Tablo 3). Bu durum, tarımsal baskının orman ve mera alanlarına kaydığını göstermektedir. Toprak bozulmasının güzel bir örneği olan bu olay toprağın kademeli bir bozulum süreci yaşadığının göstergesidir. Tarım alanlarında ise arazi çalışmalarında sürekli artan bir çeltik tarımı gözlemlenmiş sulanabilir araziler ve karışık tarım alanlarının önemli bir kısmı çeltik alanlarına dönüştürülmüştür.

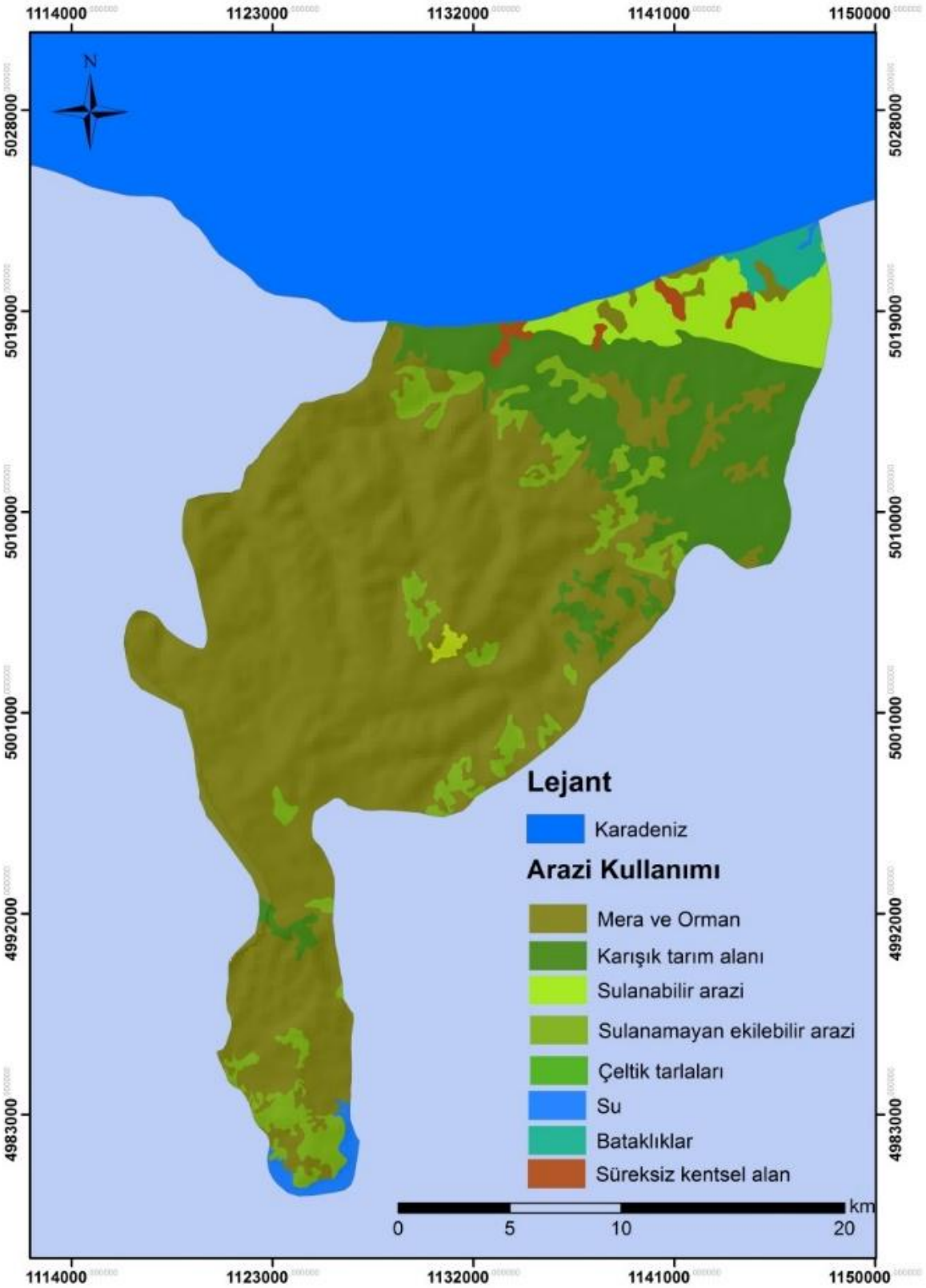

Şekil 5. Arazi kullanımı haritası.

Tablo 3. Arazi kullanımı

Arazi kullanımı Sınıfları	Alan (km2)	Alan (%)
Mera ve Orman	401,60	63,54
Karışık tarım alanı	127,80	20,22
Sulanamayan ekilebilir arazi	23,20	3,67
Sulanabilir arazi	37,30	5,90
Çeltik tarlaları	12,70	2,01
Su	7,5	1,19
Bataklıklar	14,00	2,22
Süreksiz kentsel alan	7,90	1,25
	632,00	100,00

3.4. Toprak Organik Karbonu

Toprak organik karbon miktarlarına bakıldığında mera arazileri ile tarım alanları arasında istatistiksel olarak anlamlı bir fark tespit edilememiştir olmasına rağmen karbon haritası incelendiğinde tarım alanlarında karbon miktarının daha düşük olduğu görülmektedir. Mera arazilerinden alınan örneklerde ise karbon miktarları küçükte olsa fark göstermekte ve bir miktar yüksek sonuçlar görülmektedir. Bu durum bitki örtüsünün karbon miktarına etkili olduğunu aynı zamanda tarım alanlarında tarımsal faaliyetler sebebiyle karbon miktarının daha düşük olduğunu düşündürmektedir. Arazi kullanım haritasında mera ve orman olarak görülen araziler, en yüksek karbon miktarının tespit edildiği alanlara karşılık gelmektedir (Şekil 6). Çeltik alanları ve karışık tarım alaları ise karbon değerlerinin 1.09-1.92 ton/ha gibi düşük değerlerin olduğu alanlara karşılık gelip bu sınıf araziler sahanın yaklaşık %8'inde görülmektedir (Şekil 6, Tablo 4).

Tablo 4. Toprak Organik Karbon miktarı

Carbon Sınıfları	Alan (km^2)	Alan (%)
1.09-1.92	51,03	8,1
1.93-2.12	184,6	29,2
2.13-2.35	188,2	29,8
2.36-2.60	165,8	26,2
2.61-3.70	42,37	6,7
Toplam	632	100,0

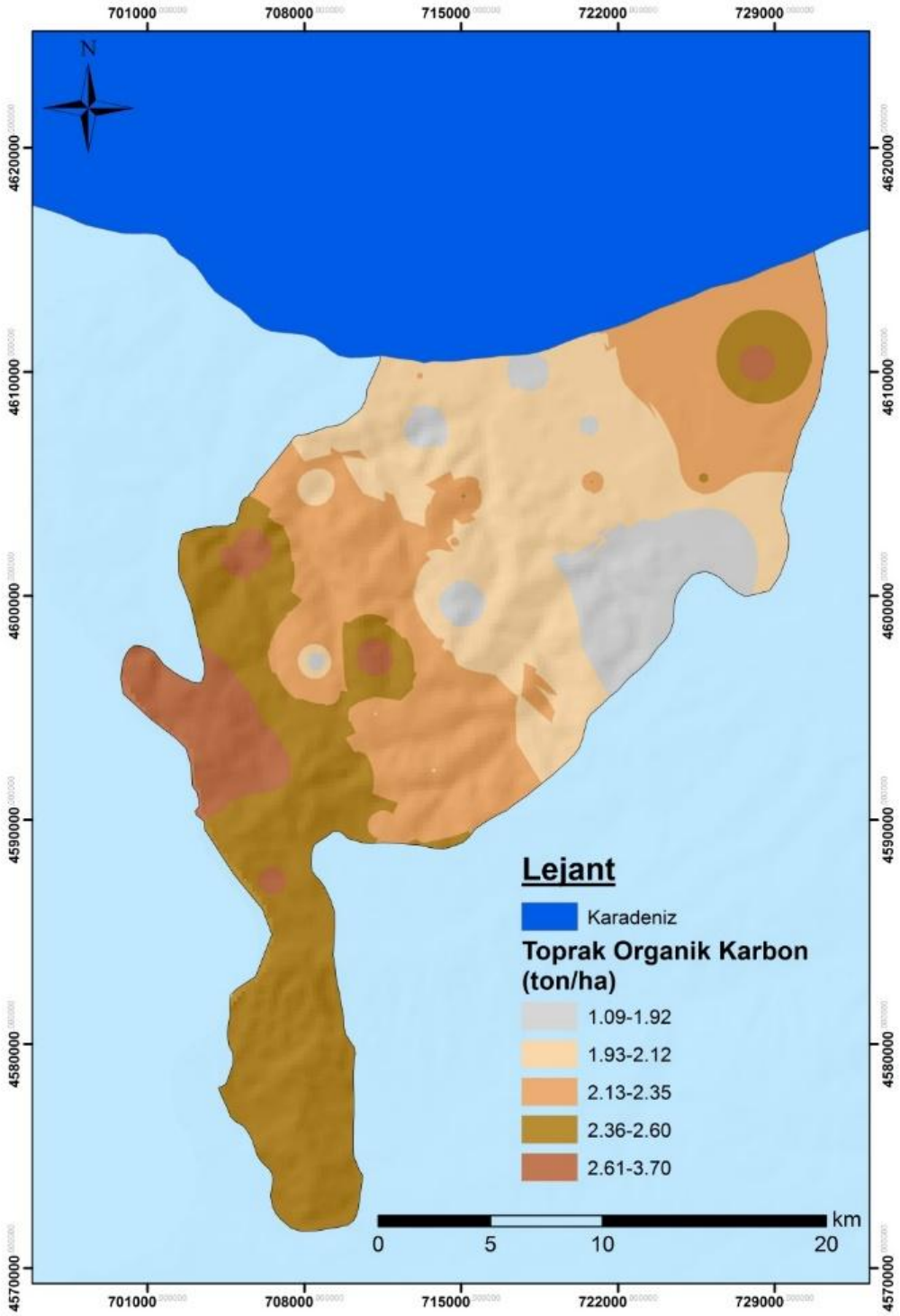

Şekil 6. Toprak organik karbon haritası.

4. Tartışma ve Sonuç

Araştırma sonucu tarım alanları ve meralar arasında istatistiksel olarak anlamlı bir fark tespit edilememiştir. Fakat karbon haritası ve arazi kullanım haritaları karşılaştırıldığında mera arazilerinin tarım alanlarına göre daha yüksek karbon içeriğine sahip oldukları görülmüştür. Elde edilen sonuç (TÜBİTAK Bilgem YTE, 2018) Sonuç raporunda Türkiye orman mera ve tarım alanlarındaki oranlarla uyum göstermektedir. Artan karbon değerleri yükselti ile de uyum göstermektedir. Bu durum alçak rakımlardaki sahalarda tarım alanlarının daha fazla alan kaplaması ile ilgili olabileceği düşünülmektedir. İmamoğlu ve Dengiz, (2019) yaptıkları çalışmada Akhisarda ova seviyesinde organik karbon miktarının daha düşük olduğunu orman alanlarına gittikçe ve yükselti arttıkça karbon miktarının arttığını tespit etmişlerdir. Yılmaz ve Dengİz, (2021) Vezirköprü ilçesinde gerçekleştirdikleri çalışmada da benzer şekilde en düşük karbon miktarlarının tarım arazilerinde olduğu

sonucuna ulaşmışlardır. Budak ve Günal, (2018) Dicle havzasında gerçekleştirdikleri karbon çalışmasında arazi kullanımlarının karbon miktarına etkisini incelemişler ve önemli istatistiksel anlamlılık tespit etmişlerdir.

Toprak organik maddesinin doğal alanlarda tarım alanlarına göre daha yüksek olduğu bilinmektedir (Özyazıcı vd., 2016). Bunun sebebi toprağa karışan organik karbondaki azalma ve tarımsal faaliyetler ile karbonun hızla ortamdan uzaklaşması, erozyonal süreçlerle ortaya çıkan kayıplar olduğu görülmektedir (Lal, 2002; Yılmaz ve Dengiz, 2021). Literatür bu araştırma sonuçları ile uyumlu olup tarım alanlarındaki karbon miktarının düşüklüğünü açıklamaktadır.

Alaçam ilçesinde ormanların mera arazilerine ya da tarım alanlarına dönüştürüldüğü, mera arazilerinin tarım alanlarına dönüştürüldüğü gözlemlenmiştir. TÜBİTAK Bilgem YTE, (2018) Raporuna göre; 1 milyon ha "Mera" alanının "Tarım" alanına dönüşmesi sonucu, TOK stoklarında yaklaşık 13,8 milyon ton karbon azalışı görülebilmektedir. Bu durumun tersine çevrilmesi karbon stoklarında artış sağlaması açısından önemli ve gereklidir.

Toprak organik karbon miktarının belirlenmesi, milli servet olan topraklarımızın organik madde miktarlarının arttırılması, toprak kalitesinin arttırılması ve sürdürülebilir toprak kullanımı açısından önem arz etmektedir. Düşük karbon miktarı olan alanların belirlenmesi buralarda yapılan arazi kullanımının kontrollü olarak yeniden düzenlenmesi konusunda bir önbilgi sunmaktadır. Bu bilgiler doğrultusunda, problemli alanlarda gerekirse farklı tarım desenleri uygulanması gerekmektedir. Özellikle ilçede artan çeltik tarımının toprakları nasıl etkilediği güncel çalışmalar ile ortaya konulmalı ve buna göre bir düzenleme yapılmalıdır. Ayrıca problemli alanlara yönelik erozyon çalışmaları gerçekleştirilmeli, kaybolan toprakla birlikte ortamdan uzaklaşan karbon da kurtarılmalıdır.

Katkı Oranı Beyanı

Yazarın katkı yüzdeleri aşağıda verilmiştir. Yazar makaleyi incelemiş ve onaylamıştır.

	A.İ.
K	100
T	100
Y	100
VTI	100
VAY	100
KT	100
YZ	100
KI	100
GR	100
PY	100
FA	100

K= kavram, T= tasarım, Y= yönetim, VTI= veri toplama ve/veya işleme, VAY= veri analizi ve/veya yorumlama, KT= kaynak tarama, YZ= Yazım, KI= kritik inceleme, GR= gönderim ve revizyon, PY= proje yönetimi, FA= fon alımı.

Çatışma Beyanı

Yazar bu çalışmada hiçbir çıkar ilişkisi olmadığını beyan etmektedir.

Etik Onay Beyanı

Bu araştırmada hayvanlar ve insanlar üzerinde herhangi bir çalışma yapılmadığı için etik kurul onayı alınmamıştır.

Kaynaklar

Berhane M, Xu M, Liang Z, Shi J, Wei G, Tian X. 2020. Effects of long-term straw return on soil organic carbon storage and sequestration rate in North China upland crops: A meta-analysis. Glob Change Biol, 26(4): 2686-2701.

Blake GR, Hartge KH. 1986. Bulk density. In: Klute A (ed) Part 1—Physical and Mineralogical Methods. Am Soc Agron—Soil Sci Soc Am, Madison, Wisconsin, US, pp: 65-87.

Budak M, Günal H. 2018. Yukarı Dicle Havzasında farklı arazi kullanımları altındaki toprakların karbon depolama potansiyelleri. Anadolu J For Res, 4(1): 61-74.

Chappell A, Webb NP, Leys JF, Waters CM, Orgill S, Eyres MJ. 2019. Minimising soil organic carbon erosion by wind is critical for land degradation neutrality. Environ Sci Policy, 93: 43-52.

Ekberli İ, Dengiz O. 2017. Bazalt Ana Materyali ve Farklı Topografik Pozisyonlar Üzerinde Oluşmuş Toprakların Bazı Topografik ve Fiziko-Kimyasal Özellikleri Arasındaki Doğrusal Regresyon Modellerinin Belirlenmesi. Toprak Su Derg, 15: 15.

Herrick JE, Neff J, Quandt A, Salley S, Maynard J, Ganguli A, Bestelmeyer B. 2019. Prioritizing land for investments based on short- and long-term land potential and degradation risk: A strategic approach. Environ Sci Policy, 96: 52-58.

İmamoğlu A, Dengiz O. 2017. Determination of soil erosion risk using RUSLE model and soil organic carbon loss in Alaca catchment (Central Black Sea region, Türkiye). Rend Lincei 28(1): 11-23.

İmamoğlu A, Dengiz O. 2019. Mikro havza ölçeğinde toprak organik karbon içeriği ile arazi kullanımı-arazi örtüsü

ilişkisinin belirlenmesi. II. Uluslararası Coğrafya Eğitimi Kongresi, 3-5 Ekim, Eskişehir, Türkiye, pp: 2195-2204.

Lal R. 2002. The potential of soils of the tropics to sequester carbon and mitigate the greenhouse effect. In: Advances in Agronomy, pp:1-30.

Li T, Wang S, Liu S, Zhang X, Dong H, Dai S, Ma X. 2025. Trade-offs of organic amendment input on soil quality and crop productivity in saline-alkali land globally: A meta-analysis. Eur J Agron, 164: 127471.

Liu D, Song C, Xin Z, Fang C, Liu Z, Xu Y. 2023. Agricultural management strategies for balancing yield increase, carbon sequestration, and emission reduction after straw return for three major grain crops in China: A meta-analysis. J Environ Manage, 340: 117965.

Nelson DW, Sommers LE. 1982. Total carbon, organic carbon and organic matter. In: Methods of Soil Analysis, Madison, Wisconsin, US, pp: 539-579.

Özyazıcı MA, Dengiz O, Aydoğan M, Bayraklı B, Kesim E, Urla Ö, Yıldız H, Ünal E. 2016. Orta ve Doğu Karadeniz Bölgesi tarım topraklarının temel verimlilik düzeyleri ve alansal dağılımları. Anadolu J Agric Sci, 31(1): 136.

TÜBİTAK Bilgem YTE. 2018. Toprak organik karbonu projesi. toprak organik karbonu miktarı tahminleme modeli raporu (No. 100311). TÜBİTAK, Ankara, Türkiye, ss: 28.

Yılmaz M, Dengiz O. 2021. Bazı toprak özellikleri ile ilişkili olarak arazi kullanımı ve arazi örtüsünün toprak organik karbon stokuna etkisi. Turk J Agric Res, 8(2): 154-167.

Black Sea Journal of Engineering and Science
doi: 10.34248/bsengineering.1760309

Open Access Journal
e-ISSN: 2619 – 8991

Araştırma Makalesi (Research Article)
Cilt 8 - Sayı 5: 1628-1633 / Eylül 2025
(Volume 8 - Issue 5: 1628-1633 / September 2025)

ALÜMİNYUM KLORÜR ($ALCL_3$) BAZLI KLOR-ALKALİ ELEKTROLİZİ İLE HİDROJEN ÜRETİMİNİN EKSERJİ TEMELLİ İNCELENMESİ

Serdal DAMARSEÇKİN[1]*

[1]*Sirnak University, Faculty of Engineering, Department of Renewable Energy Systems Engineering, 73000, Şırnak, Türkiye*

Özet: Bu çalışmada, klor-alkali proseslerinde geleneksel olarak tercih edilen sodyum klorür çözeltilerine alternatif oluşturabilecek nitelikte, alüminyum klorür ($AlCl_3$) esaslı bir elektroliz sistemi tasarlanmış ve sistemin farklı sıcaklık ve voltaj düzeylerinde sergilediği ekserji performansı deneysel olarak değerlendirilmiştir. Deneysel düzenek, sabit elektrolit debisi (0,3 g/s) koşulunda, 20 °C ve 45 °C sıcaklıklar ile 5,0 V, 7,5 V ve 10,0 V hücre gerilimleri altında test edilmiştir. Çalışmada kullanılan laboratuvar tipi hücrede anot ve katot bölmeleri, Al^{3+} iyonlarının seçici geçişine imkân tanıyan Nafion 212 membranıyla birbirinden ayrılmıştır. Her iki bölmede beşer adet grafit elektrot kullanılmıştır. Elektrolit akış hızının hidrojen ve klor üretimi üzerindeki etkisi deneysel olarak önemsiz bulunmuş ve bu nedenle sabit tutulmuştur. Deney süresince anot bölgesinde meydana gelen klor gazı üretimi, elektrot yüzeylerinde kimyasal aşınmaya neden olmuş; bu durum, klor gazı veriminin hidrojen gazına kıyasla daha düşük olmasına neden olmuştur. Elde edilen deneysel bulgulara göre, hidrojen üretim hızı 20 °C sıcaklık ve 5,0 V gerilim altında en düşük seviyede olup 0,94 mL/dk olarak kaydedilmiş, buna karşılık 45 °C ve 10,0 V koşullarında 3,577 mL/dk ile en yüksek üretim hızına ulaşılmıştır. Ekserji verimliliği, düşük sıcaklık ve gerilim koşullarında % 1,544 seviyesinde kalırken, en yüksek verim % 4,98 ile yüksek sıcaklık ve voltaj kombinasyonunda gözlemlenmiştir. Bu kapsamda, $AlCl_3$ çözeltisiyle çalışan elektroliz sisteminin literatürde ilk kez termodinamik verimlilik (ekserji) açısından deneysel olarak incelendiği vurgulanmakta olup, bu tür sistemlerin klor-alkali teknolojileri içerisinde alternatif ve yenilikçi bir yaklaşım sunduğu değerlendirilmiştir. Ayrıca, reaksiyon sonucunda hidrojenin yanı sıra, ekonomik değeri yüksek olan $Al(OH)_3$ bileşiğinin oluşması, sürecin çevresel sürdürülebilirliğini ve ekonomik cazibesini artıran önemli bir unsur olarak öne çıkmaktadır.

Anahtar kelimeler: Hidrojen üretimi, Klor-alkali reaktör, Enerji, Ekserji

Exergy-Based Investigation of Hydrogen Production via Aluminum Chloride ($AlCl_3$)-Based Chlor-Alkali Electrolysis

Abstract: In this study, an electrolysis system based on aluminum chloride ($AlCl_3$) was designed as a potential alternative to the conventionally used sodium chloride solutions in chlor-alkali processes. The exergy performance of the system was experimentally investigated under varying temperature and cell voltage conditions. The experimental setup was tested at a constant electrolyte flow rate of 0.3 g/s, with temperature levels of 20 °C and 45 °C, and cell voltages of 5.0 V, 7.5 V, and 10.0 V. In the laboratory-scale cell used in the study, the anode and cathode compartments were separated by a Nafion 212 membrane, which allows the selective passage of Al^{3+} ions. Five graphite electrodes were employed in each compartment. Since the effect of electrolyte flow rate on hydrogen and chlorine gas production was found to be negligible, it was kept constant throughout the experiments. During operation, the generation of reactive chlorine at the anode side led to chemical degradation of the electrode surfaces, resulting in lower chlorine output compared to hydrogen production. According to the experimental findings, the lowest hydrogen generation rate was measured as 0,94 mL/min under 20 °C and 5.0 V conditions, while the highest rate reached 3,577 mL/min at 45 °C and 10.0 V. Regarding exergy efficiency, the lowest value was calculated as 1,544 % at low temperature and voltage, and the highest efficiency was recorded as 4,98 % under the highest tested conditions. This study highlights that the $AlCl_3$-based system was experimentally evaluated for the first time in terms of thermodynamic (exergy) efficiency, offering a novel and alternative approach within chlor-alkali technologies. Moreover, in addition to hydrogen gas, the system facilitates the formation of aluminum hydroxide ($Al(OH)_3$), a value-added by-product, thereby enhancing both the environmental sustainability and economic feasibility of the process.

Keywords: Hydrogen production, Chlor-alkali reactor, Energy, Exergy

***Sorumlu yazar (Corresponding author):** Sirnak University, Faculty of Engineering, Department of Renewable Energy Systems Engineering, 73000, Şırnak, Türkiye
E mail: serdalseckin@hotmail.com (S. DAMARSEÇKİN)
Serdal DAMARSEÇKİN https://orcid.org/0000-0003-4427-6220

Gönderi: 07 Ağustos 2025 **Received:** August 07, 2025
Kabul: 09 Eylül 2025 **Accepted:** September 09, 2025
Yayınlanma: 15 Eylül 2025 **Published:** September 15, 2025
Cite: Damarseçkin S. 2025. Exergy-based analysis of hydrogen production by aluminum chloride ($AlCl_3$) based chlor-alkali electrolysis. BSJ Eng Sci, 8(5): 1628-1633.

1. Giriş

Küresel ölçekte enerji ve sanayi sektörlerinde çevresel sürdürülebilirliğin sağlanması, sera gazı salınımlarının azaltılmasını zorunlu kılmaktadır. Bu bağlamda, karbon içermeyen üretim süreçlerinin geliştirilmesi, emisyonların düşürülmesinde temel stratejilerden biri olarak öne çıkmaktadır. Hidrojen, özellikle yakıt hücreleri (Sabeeh vd. 2019; Singla vd., 2021) ve enerji dönüşüm

sistemleri (Shadidi vd., 2021) kapsamında, fosil kaynaklara çevreci bir alternatif sunması nedeniyle dikkat çekmekte ve geniş ölçekli uygulama potansiyeli taşımaktadır.

Hidrojen, günümüzde öncelikli olarak amonyak ve metanol gibi kimyasal bileşiklerin üretiminde kullanılmakta olup, son yıllarda enerji taşıyıcısı rolüyle stratejik bir konuma yükselmiştir. Bu gelişme, hidrojen üretim teknolojilerine yönelik bilimsel ve teknolojik ilginin artmasına neden olmuştur. Ancak mevcut üretim kapasitesinin büyük bir bölümü, doğal gazın buharla reformasyonu gibi fosil kaynaklara dayalı yöntemlerden sağlanmaktadır ve bu oran yaklaşık %96'dır (Hammer vd., 2004; Konieczny vd., 2008; Bičáková ve Straka, 2012). Alternatif olarak gösterilen ve çevresel açıdan daha sürdürülebilir olan suyun elektrolizi yöntemi ise küresel üretimde çok sınırlı bir paya (%4 civarında) sahiptir. Bunun temel nedeni, bu yöntemin yüksek enerji girdisi gerektirmesi ve bu nedenle ekonomik olarak dezavantajlı bir seçenek hâline gelmesidir (Sigurvinsson vd., 2006; Zhang vd., 2015).

Bu bağlamda, klor-alkali elektroliz sistemleri, yalnızca hidrojen değil, aynı zamanda değerli yan ürünlerin eş zamanlı olarak üretilebilmesi açısından alternatif bir yaklaşım sunmaktadır. Bu süreçte, genellikle NaCl çözeltisinin elektrolizi gerçekleştirilmekte ve bunun sonucunda klor (Cl_2), hidrojen (H_2) ve sodyum hidroksit (NaOH) elde edilmektedir. Hücre tasarımlarında kullanılan membran yapılar, iyonların kontrollü geçişini sağlayarak anot ve katot bölümleri arasında istenmeyen iyonik karışımı önlemektedir (Brinkmann, 2014). Literatürde, işlem parametrelerinin (örneğin hücre gerilimi, sıcaklık, tuz konsantrasyonu ve membran türü) hidrojen üretim verimliliği üzerindeki etkileri ayrıntılı biçimde analiz edilmiştir (Rabbani vd., 2014). Ayrıca, farklı klorür tuzlarının (NaCl, KCl, $CaCl_2$ gibi) bu sistemlerde oluşturduğu performans farkları karşılaştırmalı çalışmalarda ele alınmıştır (Erden ve Karakilcik, 2024).

Klor-alkali elektroliz süreçlerinde yaygın olarak kullanılan konvansiyonel tuz çözeltilerine alternatif bir yaklaşım olarak, bu çalışmada alüminyum klorür ($AlCl_3$) tabanlı yeni bir sistem önerilmektedir. $AlCl_3$'nin tercih edilmesi, yalnızca hidrojen gazı üretimi açısından değil, aynı zamanda elektrokimyasal reaksiyonlar sonucunda ortaya çıkan ve çeşitli sanayi dallarında (örneğin su arıtma, kozmetik ve kimya endüstrileri) yaygın olarak değerlendirilen alüminyum hidroksit ($Al(OH)_3$) gibi stratejik bir yan ürünün elde edilmesine de olanak sağlamaktadır (Damarseckin, 2024).

Bu bağlamda, çalışma kapsamında iyon seçici membran içeren bölmeli bir elektroliz hücresinde, farklı sıcaklık ve hücre gerilimi seviyelerinde hidrojen üretim kapasitesi ile birlikte sistemin ekserji bazlı termodinamik performansı deneysel olarak analiz edilmiştir.

$AlCl_3$ esaslı elektroliz sistemlerine dair mevcut bilimsel literatür incelendiğinde, bu tür sistemlerin hem enerji verimliliği hem de termodinamik etkinliği yönünden kapsamlı bir biçimde değerlendirilmediği görülmektedir. Bu çalışma, alüminyum klorür çözeltisinin elektrokimyasal hidrojen üretimi süreçlerinde kullanımına dair ilk detaylı ekserji analizi örneklerinden biri olma niteliğindedir. Ayrıca, deneysel düzenekte yer alan membranlı hücre yapısı içerisinde, anot bölgesinde gözlenen elektrot bozulmalarının gaz üretim performansı üzerindeki etkisi de araştırılmış ve bu etkileşimler sistem bütünlüğü bağlamında tartışılmıştır.

Elde edilen veriler, yalnızca hidrojen üretimine ilişkin değil; aynı zamanda reaktör tasarımında kullanılan malzeme ömrü, enerji dönüşüm verimliliği ve yan ürün geri kazanımı gibi çoklu parametreleri dikkate alan bütüncül bir değerlendirme sunmaktadır. Böylece, bu çalışma alternatif elektrolit kullanımıyla sürdürülebilir enerji sistemlerinin geliştirilmesine katkı sağlamayı hedeflemekte ve klor-alkali teknolojilerine yeni bir perspektif kazandırmaktadır.

2. Materyal ve Yöntem

Deneysel çalışmada, elektrolit olarak hazırlanan 1 molar alüminyum klorür ($AlCl_3$) çözeltisi ile saf su, iki ayrı peristaltik pompa yardımıyla sabit kütlesel debiyle (0,3 g/s) elektrokimyasal hücreye yönlendirilmiştir. Reaktörde oluşan hidrojen gazının hacmi, standart laboratuvar koşulları olan 25 °C sıcaklık ve 1 atm basınç altında dereceli silindir aracılığıyla belirlenmiştir. Elde edilen hacimsel değerlerin kütle cinsine dönüştürülmesi, ideal gaz kanunu esas alınarak gerçekleştirilmiş; örneğin, 25 °C ve 1 atm koşullarında 100 litre H_2 gazının yaklaşık 8,1 gramlık bir kütleye karşılık geldiği varsayılmıştır. Bu doğrultuda, ölçülen hacimsel miktarlar basit oranlama yöntemiyle kütlesel değerlere çevrilmiştir. Hem hidrojen hem de klor gazının üretimi, hacimsel yer değişimi prensibine dayanan ölçüm tekniğiyle, dereceli silindirler kullanılarak ayrı ayrı izlenmiştir.

Deney sürecinde reaktör üzerine sırasıyla 5,0 V, 7,5 V ve 10,0 V düzeylerinde sabit doğru akım gerilimleri uygulanmış ve sistemin davranışı gözlemlenmiştir. Elektrolit ve saf su, ayrı hatlar üzerinden anot ve katot bölümlerine yönlendirilmiş; deneyler ise iki farklı sıcaklık ortamında, 20 °C ve 45 °C'de gerçekleştirilmiştir. Bu sayede, sıcaklık ve gerilim parametrelerinin hidrojen üretim performansı üzerindeki etkileri sistematik biçimde karşılaştırılmıştır.

Şekil 1 ve Şekil 2'de sunulan diyagramlar, deneysel klor-alkali sisteminin temel yapılandırmasını gözler önüne sermektedir. Bu sistem; bir elektrokimyasal reaktör, iki adet elektrolit besleme haznesi (biri saf su, diğeri 1M $AlCl_3$ çözeltisi içeren), iki atık toplama kabı, çift yönlü peristaltik pompalar, bir doğru akım (DC) güç kaynağı ve gaz hacmini ölçmek için kullanılan iki adet dereceli silindirden oluşmaktadır.

Reaktör gövdesi, anot ve katot olmak üzere iki ayrı bölmeden meydana gelmekte olup, bu bölmeler CNC kontrollü işleme yöntemiyle yüksek kimyasal direnç özelliklerine sahip 'derlin' isimli polimer malzemeden imal edilmiştir. Bu malzeme, özellikle agresif kimyasal

ortamlarda gösterdiği dayanıklılık nedeniyle tercih edilmiştir.

Sistemin temel işlevini sürdürebilmesi açısından en kritik bileşenleri membran ve elektrotlar oluşturmaktadır. Elektrot sistemi, her iki bölmede beşer adet olmak üzere toplamda 10 adet karbon çubuktan meydana gelmektedir. Karbon esaslı bu çubuklar, hem klor gazına karşı gösterdikleri yüksek kimyasal direnç hem de hidrojen üretim sürecine uygunlukları sayesinde elektrot malzemesi olarak seçilmiştir. Ayrıca, maliyet açısından avantaj sağlamaları, bu tercihleri destekleyici bir unsur olmuştur.

Her bir karbon elektrot çubuğu 0,2 cm yarıçapında ve 4 cm uzunluğundadır. Elektrotlar, membrana her iki taraftan da 0,5 cm mesafede, karşılıklı olarak simetrik biçimde konumlandırılmış beşli setler halinde yerleştirilmiştir. Elektrot çubukları arasında 1 cm aralık bırakılarak sistemin elektriksel ve iyonik geçirgenliği optimize edilmiştir. Bu düzenleme, hem gaz üretim verimini artırmak hem de elektrokimyasal kararlılığı sağlamak amacıyla planlanmıştır.

Şekil 1. Klor-alkali reaktörde elektroliz sistemi.

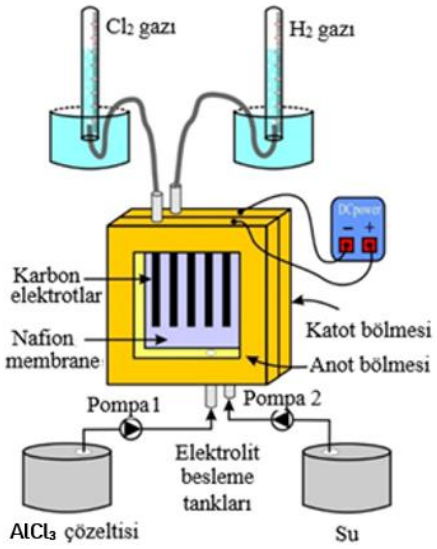

Şekil 2. Klor-alkali reaktörde elektroliz sisteminin şematik diyagramı.

Reaktörün anot ve katot bölmelerinde gerçekleşen elektrokimyasal süreçler aşağıda verilen yarı reaksiyonlarla tanımlanmaktadır. Katot bölmesinde, suyun indirgenmesi sonucu hidrojen gazı üretilirken; anot bölmesinde, alüminyum klorür çözeltisinden gelen klorür iyonları yükseltgenerek klor gazı açığa çıkmaktadır. Bu tepkimeler eşitlik 1 ve 2'de verilmektedir. Sistemin genel net reaksiyonu ise eşitlik 3'te verilmiştir.

Katot (indirgenme) reaksiyonu:

$$2H_2O + 2e^- \rightarrow H_2(g) + 2OH^-(s) \quad (1)$$

Anot (yükseltgenme) reaksiyonu:

$$2Cl^-(s) \rightarrow Cl_2(g) + 2e^- \quad (2)$$

Toplam hücre reaksiyonu:

$$2H_2O + 2Cl^-(s) \rightarrow 2OH^-(s) + H_2(g) + Cl_2(g) \quad (3)$$

$AlCl_3$ katı halde suya bırakıldığında, öncelikle tamamen iyonlaşarak çözünür (eşitlik 4):

$$AlCl_3(aq) \rightarrow Al^{3+}(aq) + 3Cl^-(aq) \quad (4)$$

Bunun ardından, Al^{3+} iyonları suda hidroksil iyonlarıyla reaksiyona girerek hidroksit kompleksleri oluşturmaktadır. Bu süreç hidroliz olarak adlandırılır (eşitlik 5):

$$Al^{3+} + 3H_2O \rightarrow Al(OH)_3 + 3H^+ \quad (5)$$

Reaksiyon sırasında, yan ürün olarak $Al(OH)_3$ bileşiği oluşmakta ve sistem içerisinde çökerek ayrışmaktadır. Diğer yandan, anot bölmesinde meydana gelen aktif klor türleri, oksijen (O_2), hipoklorit (ClO^-) ve klorat (ClO_3^-) gibi çeşitli bileşiklerin oluşumuna yol açan ikincil reaksiyonları da tetikleyebilmektedir (eşitlik 6-8).

$$2OH^- \rightarrow H_2O + \frac{1}{2}O_2(g) + 2e^- \quad (6)$$

$$Cl_2 + H_2O \leftrightarrow HClO + HCl \quad (7)$$

$$3HClO \rightarrow 2Cl^- + 3H^+ \quad (8)$$

Bu yan reaksiyonlar, klor gazının oluşum oranını azaltmakta ve anot bölgesindeki elektrotların kimyasal yıpranmasına yol açarak, sistemin genel gaz verimliliği üzerinde olumsuz bir etki yaratmaktadır.

Farklı sıcaklık ve gerilim koşullarında gerçekleştirilen deneyler sonucunda elde edilen hidrojen üretim miktarları, deneysel bulgularla ortaya konmuştur. Teorik olarak bu koşullarda hidrojenle molce eşdeğer miktarda klor gazı üretilmesi beklenmektedir. Ancak, anot bölgesindeki elektrotların yüzeyinde meydana gelen yıpranmalar ve klor iyonlarının çeşitli yan reaksiyonlara katılması nedeniyle, klor gazı üretimi hidrojen gazına kıyasla daha düşük seviyelerde gerçekleşmiştir.

Bir sistemin termodinamik analizinin yapılabilmesi için, ilgili kütle, enerji, entropi ve ekserji dengelerine dayalı denklemlerin oluşturulması gereklidir. Bu temel denklemler aracılığıyla, sistemin enerji verimliliği ve ekserjetik davranışı değerlendirilebilir (Çengel ve Boles, 2013). Termodinamik süreçlerde, kütle ve enerji korunumu sağlanırken, sistemde entropi üretimi gerçekleşir ve bu üretim, süreçteki tersinmezlikler nedeniyle ekserji kayıplarına yol açar. Ekserji, enerjinin kullanılabilirliğini ve kalitesini temsil eder; bu da belirli bir referans çevre koşuluna göre tanımlanır. Başka bir ifadeyle, ekserji analizi sistemden elde edilebilecek maksimum faydalı işi değerlendirme imkânı sunar (Dincer ve Rosen, 2012). Bu çerçevede, enerji analizinin yanı sıra ekserji analizi de uygulanmalı, böylece tersinmezliklerin neden olduğu verim kayıpları minimize edilmelidir (BoroumandJazi, 2013). Bu kapsamda, bir klor-alkali reaktöre ilişkin denge denklemleri, Şekil 3'te sunulan akış diyagramı temel alınarak oluşturulabilir.

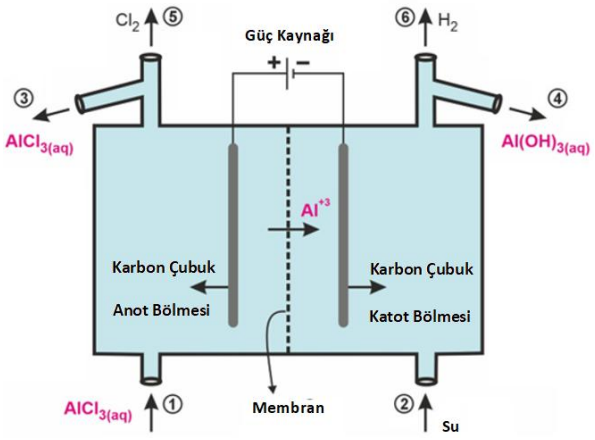

Şekil 3. Klor alkali reaktörünün akış şeması.

Reaktörün birim zamanda kütle dengesine ilişkin denklem şu formda yazılır (Damarseckin, 2024) (eşitlik 9):

$$\dot{m}_1 + \dot{m}_2 = \dot{m}_3 + \dot{m}_4 + \dot{m}_5 + \dot{m}_6 \quad (9)$$

Anot bölmesine verilen yoğunlaştırılmış tuzlu suyun kütle akış hızı $\dot{m}_1$, saf suyun kütle akış hızı ise $\dot{m}_2$ olarak gösterilmektedir. $\dot{m}_3$ ve $\dot{m}_4$ değerleri, sırasıyla anot bölmesinden akan seyreltilmiş tuzlu su ve katot bölmesinden akan konsantre bazın kütle akış hızlarını göstermektedir. Aynı zamanda, $\dot{m}_5$ ve $\dot{m}_6$ değerleri, anot ve katot bölmelerinden çıkan klor ve hidrojen gazlarının kütle akış hızlarını ifade eder.

Sistemde tüketilen elektrik enerjisi aşağıdaki formülle hesaplanır (eşitlik 10):

$$\dot{W}_{in} = Vit \quad (10)$$

Burada V, i ve t sırasıyla reaktöre uygulanan voltaj (volt cinsinden) ile reaktörden geçen akım (amper cinsinden) ve geçen süre (saniye cinsinden) değerleridir. Belirli bir zaman diliminde reaktör için ekserji denge denklemi şu formda yazılabilir (eşitlik 11):

$$\left(1 - \frac{T_0}{T}\right)\dot{Q}_{in} + \dot{W}_{in} + \dot{m}_1 ex_1 + \dot{m}_2 ex_2 = \dot{m}_6 ex_6 + \dot{m}_3 ex_3 + \dot{m}_4 ex_4 + \dot{m}_5 ex_5 + Ex_d \quad (11)$$

Burada, ex_{1-6}, reaktörün farklı bölmelerine kütle akış hızlarıyla birlikte giren ve çıkan özgül ekserji değerlerini göstermektedir. T_0 çevre sıcaklığını, T ise hücre sıcaklığını belirtmektedir. Isı girişi ve iş girişi hızları sırasıyla $\dot{Q}_{in}$ ve $\dot{W}_{in}$ ile ifade edilirken, Ex_d ise ekserji tahribat hızını temsil eder. Ekserji tahribatı, entropi üretimi ile doğru orantılı olduğundan, Ex_d aşağıdaki şekilde tanımlanabilir (eşitlik 12):

$$Ex_d = T_0 \dot{S}_{pro.} \quad (12)$$

Burada $\dot{S}_{pro.}$ üretilen entropi hızını ifade eder.

Ekserji verimliliğinin hesaplanması, sistemdeki tersinmezliklerin yol açtığı enerji kayıplarının analiz edilmesi ve performans artırıcı önlemlerin belirlenmesi bakımından büyük önem taşımaktadır. Bu bağlamda, mevcut klor-alkali reaktörün sadece hidrojen üretim sürecine ilişkin ekserji verimliliği, aşağıda verilen denklem çerçevesinde tanımlanmıştır:

$$\eta_{ex} = \frac{\dot{m}_6 ex_6}{\dot{W}_{in} + \dot{m}_1 ex_1 + \dot{m}_2 ex_2} \quad (13)$$

3. Bulgular ve Tartışma

Bu çalışmada, $AlCl_3$ çözeltisi kullanılarak yapılandırılan klor-alkali reaktör sisteminin farklı termodinamik koşullar altındaki (sıcaklık ve hücre voltajı) hidrojen üretim performansı ile ekserji temelli ikinci yasa verimliliği analiz edilmiştir. Şekil 4, 5 ve 6'da sunulan veriler doğrultusunda, sistemin ekserji verimliliğinde hem sıcaklık artışı hem de hücreye uygulanan potansiyel farkının yükseltilmesiyle birlikte belirgin bir artış gözlemlenmiştir.

Şekil 4, 0.3 g/s sabit elektrolit akış oranı ve 5 V sabit hücre gerilimi altında, $AlCl_3$ çözeltisinin 20 °C ve 45 °C çalışma sıcaklıklarındaki ekserji verimliliği değerlerini sunmaktadır. Benzer şekilde, Şekil 5'te 7.5 V sabit hücre

gerilimi koşulunda, aynı elektrolit akışı ve sıcaklık değerleri için elde edilen ekserji verimlilikleri karşılaştırılmaktadır. Şekil 6 ise sistem 10 V gerilimle çalıştırıldığında, yine 20 °C ve 45 °C sıcaklıklarındaki termodinamik performans değişimlerini göstermektedir.

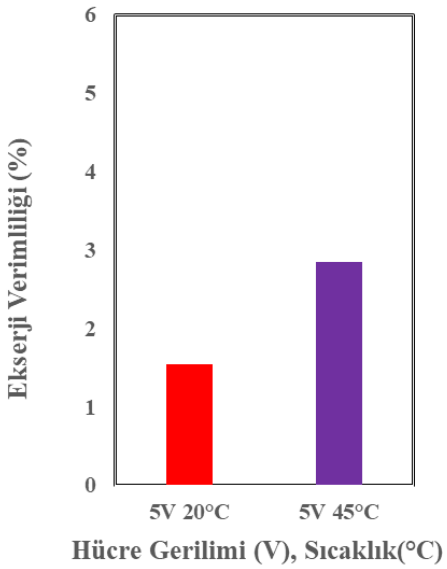

Şekil 4. Farklı sıcaklıklarda test edilen çözeltilerin ekserji verimlilikleri.

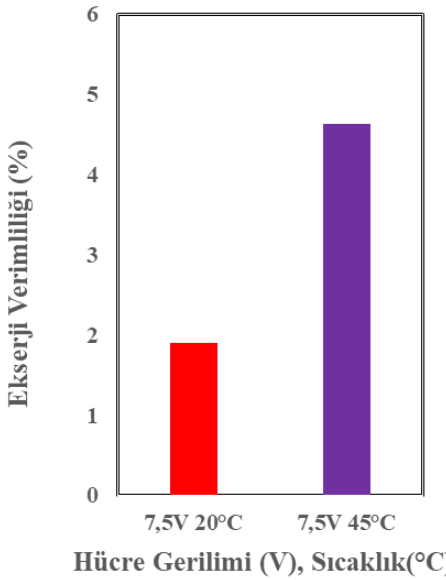

Şekil 5. Farklı sıcaklıklarda test edilen çözeltilerin ekserji verimlilikleri.

5 V hücre gerilimi altında $AlCl_3$ çözeltisiyle yürütülen deneysel çalışmalarda, 20 °C'de % 1,544 olan ekserji verimliliği, 45 °C'ye çıkarıldığında % 2,854'e ulaşmıştır; bu bulgular Şekil 4'te sunulmaktadır. 7,5 V gerilimle yapılan çalışmalarda ise verimlilik % 1,895'den % 4,63'e yükselmiş olup ilgili sonuçlar Şekil 5'te verilmiştir. 10 V'luk deneylerde ise ekserji verimliliği % 1,951'den % 4,98'e artmış ve bu eğilim Şekil 6'da gözlemlenmiştir. Bu artışın, sıcaklık yükseldikçe $AlCl_3$ çözeltisinde iyon taşınımının kolaylaşması ve elektrot yüzeyinde oluşabilecek pasif tabakaların çözünerek elektrokimyasal reaksiyon hızını artırmasıyla ilişkili olduğu değerlendirilmektedir. Roy vd. (2022) yaptıkları çalışmada belirttikleri gibi, bu tür çözeltilerde sıcaklık artışı reaksiyon kinetiği üzerinde olumlu etki yaratmaktadır.

Elde edilen bulgular, genel eğilim açısından Erden ve Karakılcık'ın (2024) farklı elektrolit tuzlarıyla gerçekleştirdiği çalışmalarla örtüşmektedir. Bulunan değerler Tablo 1'de gösterilmektedir. Bununla birlikte, bu çalışma, $AlCl_3$ çözeltisinin kullanıldığı sistemler özelinde ekserji analizi gerçekleştiren literatürdeki ilk örneklerden biri olma niteliği taşımaktadır. Öte yandan, deneysel süreçte gözlemlenen anot yüzeyi bozulmaları, $AlCl_3$ çözeltisinin aktif klor üretimi sırasında anot malzemesiyle kimyasal olarak etkileşime girerek yapısal aşınmalara yol açabileceğine işaret etmektedir. Bu durum, sistem tasarımında anot malzemesinin kimyasal dayanımının dikkate alınmasının gerekliliğini ortaya koymaktadır.

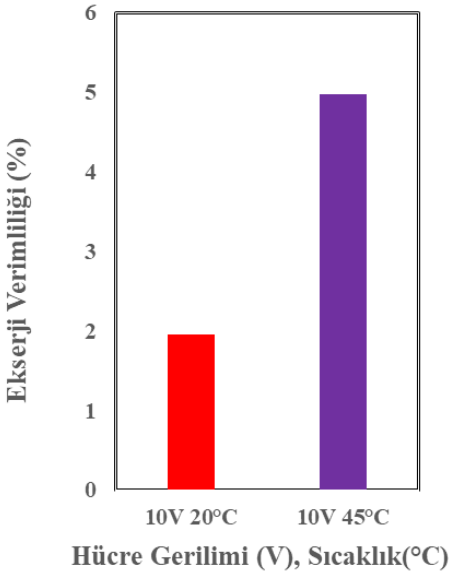

Şekil 6. Farklı sıcaklıklarda test edilen çözeltilerin ekserji verimlilikleri.

Tablo 1. Bazı tuz örneklerinin enerji ve ekserji verim değerleri (Erden ve Karakilcik, 2024)

Tuz	NaCl	KCl	$CaCl_2$	$AlCl_3$
Enerji 30 °C (%)	21,83	24,51	1196	-
Enerji 70 °C (%)	18,36	21,29	16,11	-
Ekserji 30 °C (%)	14,87	16,52	9,83	(20°C) 1,951
Ekserji 70 °C (%)	11,79	13,94	12,04	(45°C) 4,98

4. Sonuç

Elde edilen bulgular, ekserji verimliliği ve sistem davranışı açısından değerlendirildiğinde, $AlCl_3$ tabanlı klor-alkali sistemlerin sürdürülebilir hidrojen üretiminde potansiyel bir seçenek olarak dikkate alınabileceğini ortaya koymaktadır.

Katkı Oranı Beyanı

Yazarın katkı yüzdeleri aşağıda verilmiştir. Yazar makaleyi incelemiş ve onaylamıştır.

	S.D.
K	100
T	100
Y	100
VTI	100
VAY	100
KT	100
YZ	100
KI	100
GR	100
PY	100
FA	100

K= kavram, T= tasarım, Y= yönetim, VTI= veri toplama ve/veya işleme, VAY= veri analizi ve/veya yorumlama, KT= kaynak tarama, YZ= Yazım, KI= kritik inceleme, GR= gönderim ve revizyon, PY= proje yönetimi, FA= fon alımı.

Çatışma Beyanı

Yazar bu çalışmada hiçbir çıkar ilişkisi olmadığını beyan etmektedirler.

Etik Onay Beyanı

Bu araştırmada hayvanlar ve insanlar üzerinde herhangi bir çalışma yapılmadığı için etik kurul onayı alınmamıştır.

Kaynaklar

Bičáková O, Straka P. 2012. Production of hydrogen from renewable resources and its effectiveness. Int J Hydrogen Energy, 37: 16. https://doi.org/10.1016/j.ijhydene.2011.11.120

BoroumandJazi G, Rismanchi B, Saidur R. 2013. A review on exergy analysis of industrial sector. Renew Sustain Energy Rev, 27: 198–203. https://doi.org/10.1016/j.rser.2013.06.018

Brinkmann T, Santonja GG, Schorcht F, Roudier S, Sancho LD. 2014. Best available techniques (BAT) reference document for the production of chlor-alkali. European Commission, Joint Research Centre, Institute for Prospective Technological Studies.

Cengel YA, Boles MA. 2013. Termodinamik. 7. baskı. Palme Yayıncılık. Ankara, Türkiye, pp: 35-39.

Damarseckin S. 2024. Hydrogen production from $ZnCl_2$ salt: Application of chlor-alkali method. Int J Hydrogen Energy, 88: 888–897. https://doi.org/10.1016/j.ijhydene.2023.12.233

Dincer I, Rosen MA. 2012. Energy, environment, and sustainable development. Elsevier, Oxford, USA, pp: 56-96.

Erden M, Karakilcik M. 2024. Experimental investigation of hydrogen production performance of various salts with a chlor-alkali method. Int J Hydrogen Energy, 52: 546–560. https://doi.org/10.1016/j.ijhydene.2023.11.002

Hammer Th, Kappes Th, Baldauf M. 2004. Plasma catalytic hybrid processes: gas discharge initiation and plasma activation of catalytic processes. Catal Today, 89: 1–2. https://doi.org/10.1016/j.cattod.2004.03.059

Konieczny A, Mondal K, Wiltowski T, Dydo P. 2008. Catalyst development for thermocatalytic decomposition of methane to hydrogen. Int J Hydrogen Energy, 33: 1. https://doi.org/10.1016/j.ijhydene.2007.07.010

Rabbani M, Dincer I, Naterer GF. 2014. Experimental investigation of processing parameters and effects on chlor-alkali products in an electrolysis-based chlor-alkali reactor. Chem Eng Process, 82: 9–18. https://doi.org/10.1016/j.cep.2014.06.004

Roy H, Barua S, Ahmed T, Mehnaz F, Islam MdS, Mujtaba IM. 2022. A sustainable integration approach of chlor-alkali industries for the production of PVC and clean fuel hydrogen: prospects and Bangladesh perspectives. Processes, 10: 1638. https://doi.org/10.3390/pr10081638

Sabeeh G, Palanki S, Sylvester ND, El-Sharkh MY. 2019. Modeling and analysis of a hydrogen reformer for fuel cell applications. Heat Transf Eng, 40(13–14): 1153–1161. https://doi.org/10.1080/01457632.2018.1457262

Shadidi B, Najafi G, Yusaf T. 2021. A review of hydrogen as a fuel in internal combustion engines. Energies, 14(19): 6209. https://doi.org/10.3390/en14196209

Sigurvinsson J, Mansilla C, Arnason B, Bontemps A, Mareşal A, Sigfusson TI, Werkoff F. 2006. Heat transfer problems for the production of hydrogen from geothermal energy. Energy Convers Manag, 47: 20. https://doi.org/10.1016/j.enconman.2005.05.030

Singla MK, Nijhawan P, Oberoi AS. 2021. Hydrogen fuel and fuel cell technology for cleaner future: a review. Environ Sci Pollut Res Int, 28(13): 15607–15626. https://doi.org/10.1007/s11356-020-12231-8

Zhang X, O'Brien JE, Tao G, Zhou C, Housley GK. 2015. Experimental design, operation, and results of a 4 kW high temperature steam electrolysis experiment. J Power Sources, 297:90–97. https://doi.org/10.1016/j.jpowsour.2015.07.085

Black Sea Journal of Engineering and Science
doi: 10.34248/bsengineering.1749516

Open Access Journal
e-ISSN: 2619 – 8991

Research Article
Volume 8 - Issue 5: 1634-1644 / September 2025

MOLECULAR IDENTIFICATION, ENZYMATIC ACTIVITY AND ANTIBIOTIC RESISTANCE PROFILES OF BACTERIA ISOLATED FROM *Merlangius merlangus*

Huseyin Sezgin CAGLAR[1], Semra SAYGIN[1], Hayrettin SAYGIN[2]*

[1]*Ondokuz Mayis University, Faculty of Science, Department of Biology, 55139, Samsun, Türkiye*
[2]*Ondokuz Mayis University, Faculty of Science, Department of Molecular Biology and Genetics, 55139, Samsun, Türkiye*

Abstract: The present study intended to examine the cultivable bacterial microbiota of *Merlangius merlangus*, an ecologically valuable fish species from the Black Sea. Serial dilution and pre-enrichment steps were undertaken before isolation. Ten different isolates were isolated from muscle, gill, and intestinal tissues of fresh specimens. Molecular identification by 16S rRNA gene sequence showed all isolates to be members of *Enterobacteriaceae*, comprised of the genera *Morganella*, *Providencia*, *Proteus*, *Klebsiella*, and *Escherichia*. As one of the isolates (S09) was found to exhibit the highest similarity with a validly published species within the genus *Morganella*, with a relatively low value of 99.11%, it could be a new taxon. Extracellular enzyme tests showed variable presence of lipase and urease activities among isolates but no detectable amylase, caseinase, lecithinase, or DNase activities. Antimicrobial susceptibility testing was consistent with high rates of multidrug resistance, with eight isolates being resistant to three or more antibiotic groups. Resistance was greatest against amoxicillin/clavulanic acid, tetracycline, and sulfamethoxazole/trimethoprim, with all isolates showing susceptibility to imipenem. The observations point to the occurrence of metabolically active, environmentally adapted, and resilient bacterial forms in *M. merlangus*, with food safety implications and concern for antimicrobial resistance dissemination in aquatic ecosystems. Further, the uniqueness of the phylogenetic status of isolate S09 suggests an additional polyphasic taxonomic study. Future research involving metagenomes will be required to characterize host-associated bacterioplankton communities comprehensively, including their ecological functions.

Keywords: Fish microbiota, *Merlangius merlangus*, *Enterobacteriaceae*, Extracellular enzymatic activity, Antibiotic resistance, 16S rRNA gene phylogeny

***Corresponding author:** Ondokuz Mayis University, Faculty of Science, Department of Molecular Biology and Genetics, 55139, Samsun, Türkiye
E mail: hayrettin.saygin@omu.edu.tr (H. SAYGIN)
Huseyin Sezgin CAGLAR https://orcid.org/0009-0002-2713-3316
Semra SAYGIN https://orcid.org/0000-0002-3249-5074
Hayrettin SAYGIN https://orcid.org/0000-0002-8642-5872

Received: July 23, 2025
Accepted: September 09, 2025
Published: September 15, 2025

Cite as: Caglar HS, Saygin S, Saygin H. 2025. Molecular identification, enzymatic activity and antibiotic resistance profiles of bacteria isolated from *Merlangius merlangus*. BSJ Eng Sci, 8(5): 1634-1644.

1. Introduction

Merlangius merlangus (also referred to as whiting) is a demersal fish species (Asciutto et al., 2024) that is found widely in the northeastern Atlantic Ocean, as well as the Black and Mediterranean Seas (Muus and Nielsen, 1999; Yildiz et al., 2021; Calì et al., 2023; Froese and Pauly, 2024). It is ecologically significant due to its role as a mid-level predator in marine food webs (Nissar et al., 2023) and has significant economic value due to local commercial fishing (FAO, 2020; ICES, 2024). Since it is a species that is often consumed at many coasts, knowledge of microbes present on/in *M. merlangus* is relevant not just for fish health management but also for food safety issues and human health (Köker et al., 2021; Brauge et al., 2024).

Marine fish carry diverse microbial communities on their gills, skin, and in their gastrointestinal tracts (Chiarello et al., 2015; Pratte et al., 2018; Huang et al., 2020). These microorganisms perform vital functions in host metabolism, immune modulation, and inhibition of pathogen growth (Banerjee and Ray, 2017; de Bruijn et al., 2018). Fish can also be reservoirs or vectors for harmful or antibiotic-resistant bacteria (Cabello 2006; Hatosy and Martiny, 2015; Hossain et al., 2022) as well. Examining the fish microbiota from species like *M. merlangus* serves to advance knowledge of host-microbe interactions, marine disease ecology, and microbial transmission in food chains (Romero et al., 2014; Pękala-Safińska, 2018; Egerton et al., 2018).

Isolation of bacteria from fish species is an essential process in determining the microbial ecology of aquatic environments and assessing possible threats to fish health and human health (Sheng and Wang, 2021). Although traditional microbiological procedures are useful in providing early information on colony shape and general biochemical properties, these tend to fail to produce accurate species-level identification due to taxonomic overlap between taxa (Jackman, 2012). Molecular approaches, especially 16S rRNA gene

sequencing, represent a consistent and high-resolution option for determining bacterial taxonomy (Ntushelo, 2013). It enables accurate identification of both cultivable and non-cultivable bacteria, revealing an extended range of microbial diversity that could go unnoticed by traditional approaches (Justé et al., 2008).

Marine bacteria have been reported to possess the ability to produce diverse extracellular enzymes such as proteases, lipases, amylases, and cellulases (Hoppe et al., 2002; Birolli et al., 2019; Cheng et al., 2020). Besides playing a key role in the cycling of nutrients in marine environments, these enzymes also find immense industrial applications in biotechnology, pharmaceuticals, and food industries (Zhang and Kim, 2010; Trincone, 2017). After characterization of the enzymatic activity of isolates, it can identify promising strains for use on a commercial scale as well as understand their functional properties in fish microbiomes (Ray et al., 2012; Dhayalan et al., 2022).

The growth of antibiotic-resistant bacteria in aquatic ecosystems is an emerging concern worldwide, especially because of antibiotic overuse in aquatic farming and environmental pollution by human-related activities (Cabello, 2006; Hatosy and Martiny, 2015). Fish carry antibiotic-resistant bacteria that can be transferred to human beings by direct contact or ingestion (Gauthier, 2015). Antibiotic susceptibility patterns of fish-associated bacteria need to be monitored to identify the dissemination of resistance elements and design effective antimicrobial interventions in aquatic farming and fisheries management (Preena et al., 2020; Pepi and Focardi, 2021).

Despite the ecological and economic significance of *M. merlangus*, there are no systematic studies on their associated bacteria's molecular identity, enzymatic properties, and antibiotic resistance. Filling this knowledge void, in this study, we isolated bacteria from *M. merlangus*, carried out 16S rRNA gene identification, analyzed their extracellular enzymatic activities, and their resistance to antibiotics. This study offers important information on the microbiological status of *M. merlangus* and contributes to discussions on marine microbial ecology and public health.

2. Materials and Methods

2.1. Fish Sampling and Preparation

A total of ten *M. merlangus* (whiting) specimens during the commercial open season were obtained in 2024-February from local fishermen along the southern coast of the Black Sea, in the Samsun province of Türkiye. Immediately after capture, the fish were placed in sterile polyethylene bags, stored on ice (~4 °C), and transported to the laboratory within 3 hours of collection to minimize postmortem microbial shifts (Egerton et al., 2018). In the laboratory, each specimen was individually processed under aseptic conditions within a Class II biosafety cabinet to prevent external contamination. Fish were rinsed thoroughly with sterile seawater to remove external debris and transient microorganisms. Dissection was carried out using flame-sterilized instruments, and the gill arches, muscle tissues, and entire gastrointestinal tract were carefully excised. To standardize the bacterial isolation procedure and reduce individual variation, tissues from ten *M. merlangus* specimens were pooled by type, resulting in three composite samples: one each for gills, intestine, and muscle. Each composite tissue type was transferred into separate sterile containers containing 225 mL of alkaline peptone water (APW) supplemented with 1% NaCl to favor the enrichment of marine and halotolerant bacteria (Wanja et al., 2019). The APW medium was prepared by dissolving 6.75 g peptone, 6.75 g NaCl, and 1.0125 g potassium dihydrogen phosphate (KH_2PO_4) in 675 mL of distilled water. Tissue-enriched flasks were incubated at 37 °C for 24 hours to promote the proliferation of viable but potentially low-abundance bacterial populations prior to isolation.

2.2. Bacterial Isolation and Pure Culture Preparation

After enrichment, each of these tissue homogenates was diluted with sterile Ringer's solution to a dilution series up to 10^{-6} to decrease microbial content and allow for colony separation. 100 µL aliquots from each tissue homogenate (intestine, gills, muscle) from each dilution were aseptically streaked onto thiosulphate citrate bile salt sucrose (TCBS) agar (HiMedia Laboratories, India), and Nutrient agar (Merck, Germany) media with sterile glass spreaders, and then the dishes were left to incubate in an inverted direction at 37 °C for 24-48 hours for colony growth. TCBS agar was used in the current study to encourage selective isolation of halotolerant and potentially marine-derived bacteria. Whereas the use of TCBS is traditionally recommended to isolate *Vibrio* species, its composition of high salt and bile salts also favors the growth of some Gram-negative enterics that can survive in marine- and brackish-water environments (Alikunhi et al., 2017). While *M. merlangus* is a cold-seawater fish species, the use of an incubation temperature of 37°C was specifically intended to promote the growth of mesophilic bacteria of clinical and food safety interest. This method is routinely used in studies of human-associated and pathogenic bacteria in seafood since the mesophilic strains will be favored to grow in such conditions and may be harmful upon ingestion and handling (Santos et al., 2021; Kyule et al., 2022). Post-incubation, corresponding to each dilution step, bacterial colonies were analyzed for morphologically diverse colonies by differences in size, color, elevation, margin, and surface features. Bacterial colonies that were morphologically diverse were isolated to acquire a representative count of the culturable microbiota (Cantas et al., 2012). Ten such morphologically different colonies were selected in succession with subculture onto Nutrient agar plates for pure culture. Subculture plates were incubated at 37 °C for 24-48 hours. Long-term preservation of each of these pure cultures was carried out in a sterile 25% glycerol solution and stored in cryovials at -20 °C and -80 °C.

These isolates were maintained on Nutrient agar in addition to follow-up enzymatic as well as molecular work.

2.3. Genomic DNA Isolation and 16S rRNA Gene-Based Molecular Identification

Genomic DNA was isolated from fresh pure cultures of bacteria with PureLink Genomic DNA Mini Kit (Invitrogen, USA), according to the manufacturer's procedure with some optimizations. DNA concentration and purity were initially determined by a NanoDrop spectrophotometer (Thermo Scientific), and DNA integrity was checked by electrophoresis on a 1% agarose gel stained with ethidium bromide under UV illumination. Amplification of the 16S rRNA gene from bacteria was carried out with primer pair 27F (5′-AGAGTTTGATCMTGGCTCAG-3′) and 1525R (5′-AAGGAGGTGATCCAGCC-3′), which produces an amplicon of ~1500 bp. Amplification confirmation and fragment length were checked on a 1.5% agarose gel with a DNA ladder (100 bp with marker). Amplification products were cleaned up and sequenced with an ABI PRISM 3730 XL automated sequencer with universal primers 518F (5′-CCAGCAGCCGCGGTAATACG-3′) and 800R (5′-TACCAGGGTATCTAATCC-3′). Chromatogram files in ABI format were checked by Chromas version 1.45, and primers overlapped to get 16S rRNA gene nucleotide sequences in FASTA format for each isolate. 16S rRNA gene sequences resulting from each isolate were deposited in GenBank under accession PV407295 to PV407304. 16S rRNA gene sequences were uploaded to the EzBioCloud server (Yoon et al., 2017) and pairwise sequence similarity of closest phylogenetic neighbours was computed. Phylogenetic trees were reconstructed with MEGA X (Kumar et al., 2018) with the neighbour-joining method (Saitou and Nei, 1987). Topologies of resulting trees were checked by bootstrap resampling of 1000 replicates after Felsenstein (1985).

2.4. Enzymatic Activity Assays

The production of extracellular hydrolytic enzymes by the isolates was tested using substrate-supplemented agar media according to standard microbiological procedures. Six enzymes, namely lipase, amylase, caseinase, lecithinase, DNase, and urease, were screened with previously established methods. Basal medium comprised glucose (0.5 g/L), yeast extract (0.5 g/L), $MgSO_4.7H_2O$ (0.5 g/L), NaCl (0.5 g/L), K_2HPO_4 (1 g/L), and agar (15 g/L), with a final pH adjusted to 7.0-7.5 before autoclaving. Lipase production was tested on the basal medium containing tributyrin (Farooq et al., 2022), and amylase production was tested with starch-supplied agar plates by using an iodine staining method according to Albejo and Hamza (2017). Caseinase activity was determined using the protocol outlined by Stratev et al. (2015). Lecithinase activity was evaluated as described by Bunpa et al. (2016). DNase production was tested with commercial DNase test agar plates (Merck, Germany). Urease activity was tested with Christensen's urea agar (Cui et al., 2022). All media were prepared aseptically and inoculated with isolates by loop or spot seeding methods. Incubation was carried out at 37 °C for 24-48 h. Enzyme production was measured based on visual factors such as hydrolysis zones or changes in color.

2.5. Antibiotic Susceptibility Testing

The antimicrobial sensitivity of the bacterial isolates was tested according to the standard Kirby-Bauer disc diffusion method (Hudzicki, 2009). Overnight cultures on Nutrient agar were suspended in sterile saline to 0.5 McFarland turbidity standards. Each inoculum was distributed equally over plates of Mueller-Hinton Agar. Antibiotic discs impregnated with antibiotics were applied to inoculated plates. Amikacin (AK, 30 µg), gentamicin (CN, 10 µg), streptomycin (S, 10 µg), amoxicillin/clavulanic acid (AMC, 30 µg), ciprofloxacin (CIP, 5 µg), tetracycline (TE, 30 µg), sulfamethoxazole/trimethoprim (SXT, 25 µg), imipenem (IPM, 10 µg), linezolid (LZD, 30 µg), and amphotericin B (AMB, 20 µg) were tested. Antibiotics were selected based on their medical relevance and their reported use in human medicine and aquatic environments. Aerobically at 37 °C for 18-24 hours, plates were incubated. Zone diameters of inhibition around each disc were measured in millimeters, and susceptibility interpretations were determined according to CLSI's breakpoints (CLSI, 2023), with zone diameter breakpoints categorized as Susceptible (S), Intermediate (I), or Resistant (R).

3. Results

3.1. Isolation and Cultivation of Bacterial Strains

It was isolated a total of ten morphologically different bacterial isolates from the internal organs of specimens of *M. merlangus* (Figure 1). They were from three types of tissues: intestine (B01, B02, B03, B04), muscle (K06, K07), and gills (S08, S09, S11, S13). Of these, nine (except B03) were isolated on TCBS agar. All isolates had slightly different colony morphologies based on differences in pigmentation, edge, surface texture, and elevation.

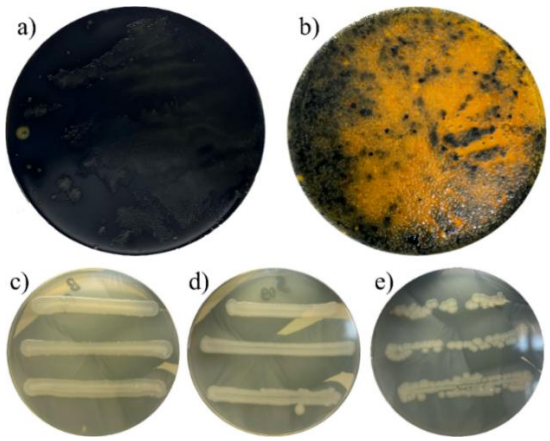

Figure 1. Representative images showing the isolation and pure culture of bacterial strains. (a, b) Growth on TCBS agar at different serial dilution levels, and (c, d, e) pure colonies of isolates B04, S09, and S13 on nutrient agar.

3.2. Molecular Identification via 16S rRNA Gene Sequencing

High-quality genomic DNA was successfully isolated from all of the isolates, and 16S rRNA gene amplification with universal primers produced ~1500 bp products from each one. Sanger sequencing with 518F and 800R internal primers produced clean, high-quality chromatograms amenable to downstream work. Sequence identity was established using the EzBioCloud database, with taxonomic identification based on ≥99% similarity with type strains. Sequences from all isolates demonstrated the highest sequence similarity with known members of the *Enterobacteriaceae*. *Morganella morganii* was most commonly encountered, present in isolates B01, K07, S08, and S09, each with ≥99.11% identity. Sequences also aligned with *Morganella psychrotolerans* at slightly lower similarity. Importantly, strain S09 had a comparatively poor 16S rRNA gene sequence similarity (99,11%) with its nearest validly described *Morganella* species and was positioned in a separate branch in phylogeny, indicating that it could be a putative new taxon of genus *Morganella*. Two isolates (B02 and B04) were found to be members of the genus *Providencia* with closest alignments with *Providencia alcalifaciens* and *Providencia rettgeri*, respectively. Isolate K06, which was obtained from muscle, showed a perfect alignment (100%) with *Proteus terrae*, while isolate S13 aligned best with *Proteus cibi* with 99.93% similarity. Importantly, isolate B03 was not isolated on TCBS agar but was identified as *Klebsiella aerogenes* (99.73%). The last isolate, S11, aligned with *Escherichia whittamii* (99.66%) and *Escherichia ruysiae* (99.52%) with some variation ratios in comparison. These identification findings, presented in Table 1, establish dominance by opportunistic enteric bacteria in *M. merlangus* microbiota. The taxa found are species with established clinical relevance, especially to nosocomial infections and foodborne infections. Further insight was achieved by representing phylogeny between isolates and their respective reference strains with a neighbor-joining tree (Figure 2), which confirmed species-level clusters and community affiliations at intra-genus levels. The distribution of bacterial genera varied according to the tissue type. *Morganella* was isolated from all tissue types, while *Providencia* was exclusively found in the intestine, and *Escherichia* was only detected in the gills. The genus-level distribution of isolates across different tissues is presented in Figure 3.

Table 1. Molecular identification of bacterial isolates based on 16S rRNA gene similarity

Isolate	Closest matching type strain	Similarity (%)	Variation ratio
	Morganella morganii subsp. *morganii* ATCC 25830^T	99.93	1/1463
B01	*Morganella morganii* subsp. *sibonii* DSM 14850^T	99.26	10/1355
	Morganella psychrotolerans U2/3^T	98.38	22/1356
	Providencia alcalifaciens DSM 30120^T	99.86	2/1463
B02	*Providencia rustigianii* DSM 4541^T	99.66	5/1463
	Providencia burhodogranariea DSM 19968^T	99.38	9/1463
	Klebsiella aerogenes KCTC 2190^T	99.73	4/1462
B03	*Raoultella ornithinolytica* JCM 6096^T	99.52	7/1457
	Raoultella terrigena ATCC 33257^T	99.24	11/1452
	Providencia rettgeri DSM 4542^T	99.73	4/1462
B04	*Providencia vermicola* OP1^T	99.59	6/1462
	Providencia huaxiensis WCHPr000369^T	99.59	6/1462
	Proteus terrae subsp. *terrae* N5/687^T	100.00	0/1443
K06	*Proteus terrae* subsp. *cibarius* JS9^T	99.73	4/1464
	Proteus cibi FJ2001126-3^T	99.37	9/1424
	Morganella morganii subsp. *morganii* ATCC 25830^T	99.66	5/1463
K07	*Morganella morganii* subsp. *sibonii* DSM 14850^T	98.97	14/1355
	Morganella psychrotolerans U2/3^T	98.23	24/1356
	Morganella morganii subsp. *morganii* ATCC 25830^T	99.73	4/1463
S08	*Morganella morganii* subsp. *sibonii* DSM 14850^T	99.04	13/1355
	Morganella psychrotolerans U2/3^T	98.16	25/1356
	Morganella morganii subsp. *morganii* ATCC 25830^T	99.11	13/1463
S09	*Morganella morganii* subsp. *sibonii* DSM 14850^T	99.04	13/1355
	Morganella psychrotolerans U2/3^T	98.08	26/1356
	Escherichia whittamii Sa2BVA5^T	99.66	5/1464
S11	*Escherichia ruysiae* OPT1704^T	99.52	7/1464
	Shigella flexneri ATCC 29903^T	99.32	10/1464
	Proteus cibi FJ2001126-3^T	99.93	1/1424
S13	*Proteus alimentorum* 08MAS0041^T	99.86	2/1380
	Proteus vulgaris ATCC 29905^T	99.80	3/1464

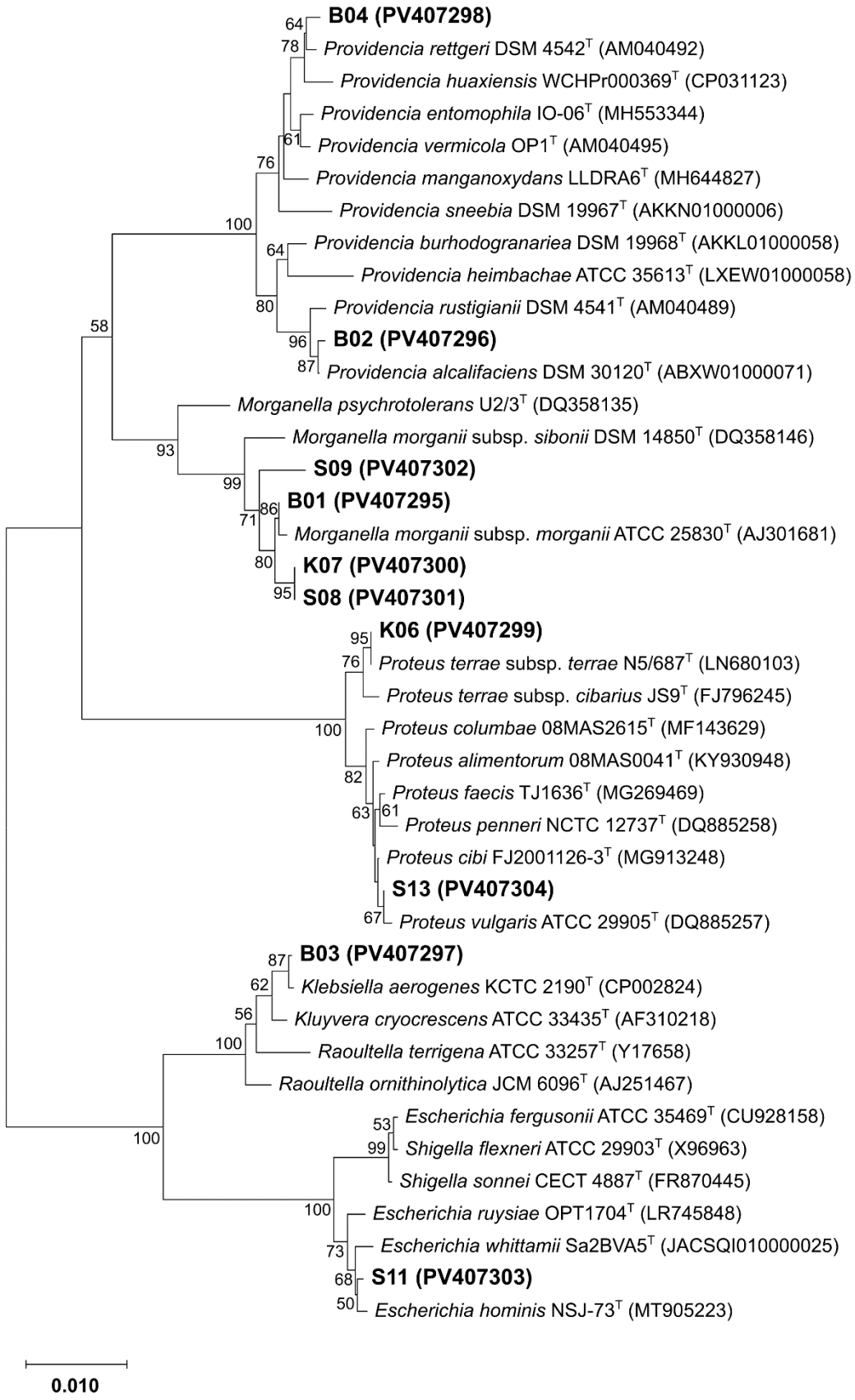

Figure 2. Phylogenetic relationships of bacterial isolates based on 16S rRNA gene sequences. The evolutionary history was inferred using the Neighbor-Joining method (Saitou and Nei, 1987). This analysis involved 41 nucleotide sequences. All positions containing gaps and missing data were eliminated (complete deletion option). There were a total of 1308 positions in the final dataset. Bootstrap values (>50%) based on 1,000 replicates are shown at the corresponding nodes.

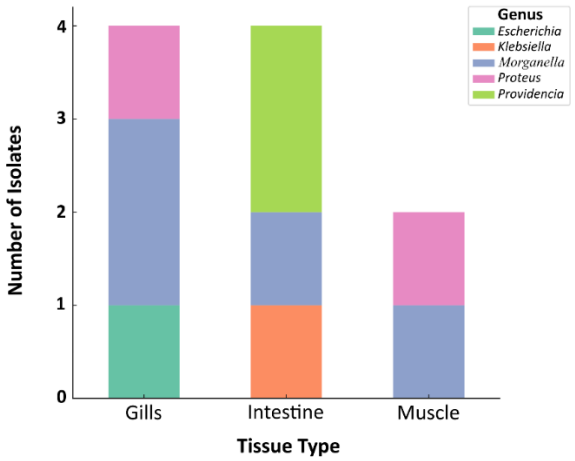

Figure 3. Bar chart showing the distribution of bacterial genera isolated from different tissues of *M. merlangus*. The number of isolates belonging to each genus is represented by colored segments within each tissue type (intestine, muscle, gills). This visual highlights genus-specific tissue localization patterns.

3.3. Extracellular Enzyme Activity Assays

Out of the ten isolates, screening for enzymic activity produced a selective profile based on the presence of lipase and urease activities. None was detected for amylase, caseinase, DNase, or lecithinase under experimental conditions. Lipase was confirmed in three isolates (B04, K06, and S13) by visibly evident hydrolysis zones on lipid-rich agar (Figure 4). Isolate K06 showed extremely high lipolytic activity, with a 30 mm in diameter clearing zone, which was the largest recorded of all. Urease was detected in seven isolates (B01, B04, K06, K07, S08, S09, and S13). Taken together, these findings illustrate that some isolates, especially *Proteus* and *Providencia* strains, possess enzymic functions applicable to lipid and nitrogen cycling with possible effects on tissue breakdown, spoilage, and host interaction (Table 2).

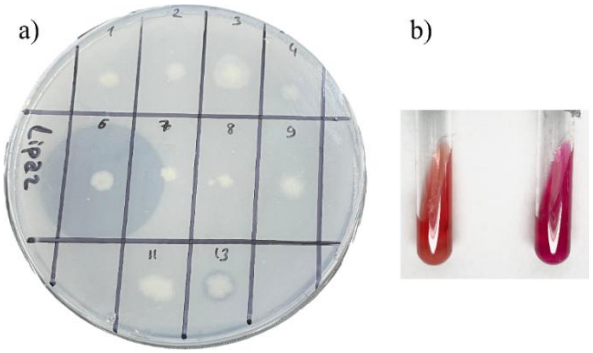

Figure 4. Representative results of lipase and urease activity assays in selected bacterial isolates. (a) Lipase-positive isolates B04, K06, and S13 showing clear zones, and (b) urease activity comparison between isolates B02 (negative, no color change) and K06 (positive, bright pink coloration).

Table 2. Extracellular enzyme activity profiles of isolates

Isolate	Lipase (mm)	Amylase	Caseinase	DNase	Lecithinase	Urease
B01	-	-	-	-	-	+
B02	-	-	-	-	-	-
B03	-	-	-	-	-	-
B04	6	-	-	-	-	+
K06	30	-	-	-	-	+
K07	-	-	-	-	-	+
S08	-	-	-	-	-	+
S09	-	-	-	-	-	+
S11	-	-	-	-	-	-
S13	8	-	-	-	-	+

Symbols: +, Positive activity; -, No activity observed. Zone diameters (in mm) are provided for positive reactions in lipase activity.

3.4. Antibiotic Susceptibility Testing

The antibiotic resistance profiles of the ten isolated bacteria presented varied resistance patterns against the tested agents (Figure 5). The profile presented in Table 3 caught most of the isolates with resistance to one antibiotic, and some with resistance to more than one class. Linezolid and amphotericin B did not show any inhibition zones in all isolates, indicating their minimal activity against Gram-negative bacteria. Resistance to amoxicillin/clavulanic acid was found to be the most prevalent, with eight isolates (B01, B02, B04, K06, K07, S08, S09, S13). Out of all aminoglycosides, amikacin was found with strong activity, with only resistance in B03. Gentamicin was less effective against B02, B03, S11, and S13 (Figure 6). The profile of ciprofloxacin was mostly effective, with some intermediate or resistance in K06 and S11, respectively. Imipenem showed full activity against all isolates, indicating no carbapenem resistance mechanisms. Streptomycin was found with intermediate or resistance profiles in some isolates, such as B04, K06, and S13. Resistance to tetracycline and sulfamethoxazole/trimethoprim was also prevalent. Six isolates showed reduced susceptibility to tetracycline, while three (K06, S11, S13) were resistant to sulfamethoxazole/trimethoprim.

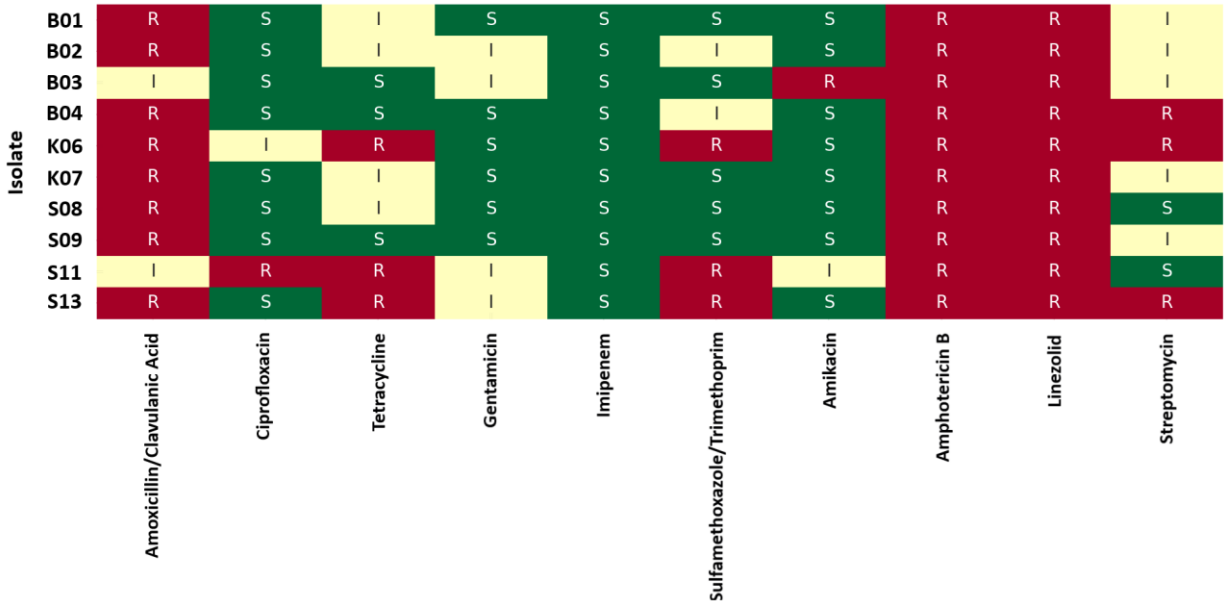

Figure 5. Heatmap representation of antibiotic susceptibility patterns of bacterial isolates. Each cell corresponds to the susceptibility result of an isolate (rows) against a specific antibiotic (columns). The resistance levels are color-coded as follows: green, susceptible (S); yellow, intermediate (I); red, resistant (R).

Table 3. Inhibition zone diameters (mm) of bacterial isolates against selected antibiotics*

Antibiotic	B01	B02	B03	B04	K06	K07	S08	S09	S11	S13
Amoxicillin/Clavulanic Acid	13 (R)	9 (R)	16 (I)	8 (R)	9 (R)	10 (R)	8 (R)	9 (R)	16 (I)	8 (R)
Ciprofloxacin	24 (S)	27 (S)	26 (S)	30 (S)	16 (I)	26 (S)	30 (S)	25 (S)	0 (R)	27 (S)
Tetracycline	14 (I)	14 (I)	26 (S)	18 (S)	0 (R)	12 (I)	13 (I)	9 (S)	10 (R)	0 (R)
Gentamicin	18 (S)	13 (I)	14 (I)	15 (S)	18 (S)	18 (S)	22 (S)	20 (S)	14 (I)	13 (I)
Imipenem	30 (S)	26 (S)	32 (S)	28 (S)	24 (S)	29 (S)	32 (S)	28 (S)	30 (S)	26 (S)
Sulfamethoxazole/Trimethoprim	25 (S)	11 (I)	22 (S)	15 (I)	0 (R)	22 (S)	16 (S)	18 (S)	0 (R)	0 (R)
Amikacin	22 (S)	19 (S)	14 (R)	24 (S)	25 (S)	20 (S)	24 (S)	19 (S)	16 (I)	23 (S)
Amphotericin B	0 (R)	0 (R)	0 (R)	0 (R)	0 (R)	0 (R)	0 (R)	0 (R)	0 (R)	0 (R)
Linezolid	0 (R)	0 (R)	0 (R)	0 (R)	0 (R)	0 (R)	0 (R)	0 (R)	0 (R)	0 (R)
Streptomycin	13 (I)	13 (I)	14 (I)	12 (R)	11 (R)	14 (I)	15 (S)	14 (I)	18 (S)	12 (R)

* Resistant values are evaluated according to CLSI (2023), S = Susceptible, I = Intermediate, R = Resistant.

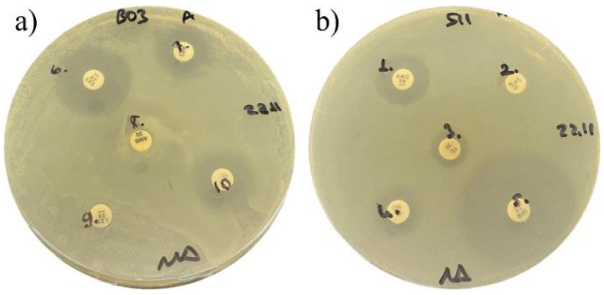

Figure 6. Representative antibiogram results of (a) isolate B03 and (b) isolate S11 for selected antibiotics on Mueller-Hinton agar.

4. Discussion

The present microbiological analysis of *M. merlangus* from the Black Sea presents a multi-faceted view of fish-associated bacteria colonizing a species of ecological and food-related interest. By uniting molecular identification, enzymatic characterization, and antibiotic susceptibility profiling, this study adds to an emerging interest in the overlap between environmental microbiology and human health. Repeated detection of members of *Enterobacteriaceae* in fish tissues highlights both microbial heterogeneity and the potential for opportunistic pathogenicity in marine hosts (Pitout and Laupland, 2008; Yang et al., 2020). Lipolytic and ureolytic capability, together with multidrug resistance, identify adaptive strategies that can facilitate survival under selective pressures whilst threatening at the same time risks associated with spoilage and antimicrobial resistance (AMR) dissemination (Ray et al., 2012; Yang, 2018; Algammal et al., 2022; Dewi et al., 2022). Global concern is understood, with AMR now considered a pressing public health issue. The World Health Organization (O'Neill, 2014) reports 700,000 drug-

resistant infection-related deaths annually, with a predicted rise to surpass cancer-related deaths by 2050 if effective intervention does not occur (WHO, 2019). Within these contexts, marine organisms like *M. merlangus* are potential sentinel species, reflecting not only ecological microbial dynamics but also the silent dissemination of determinants of resistance between interrelated aquatic and terrestrial environments.

In contrast to the selective nature of the TCBS agar that was used for isolation, which supports mainly *Vibrio* spp. preferentially (Uchiyama, 2000), the successful recovery of Gram-negative enteric bacteria reflects the ecological adaptability and salt resistance of some *Enterobacteriales* that enable them to survive in marine habitats (Paarup et al., 1999; Janda and Abbott, 2021). Importantly, that no Gram-positive bacteria or strict aerobes were isolated implies that the approach to isolation, effective for recovering dominant culturable taxa, may have precluded detecting smaller components of the community (Stefani et al., 2015). This is a limitation in all culture-based approaches and highlights the potential benefit of using molecular or metagenomic methods to overcome this in detecting a wider range of fish-associated microbiota (Yukgehnaish et al., 2020). Given the unique phylogenetic location (Figure 2) and low sequence similarity (Table 1) of isolate S09, a future polyphasic study, encompassing genomic, phenotypic, and chemotaxonomic characterization, will be required to clarify the taxonomic status and ascertain if it is a new *Morganella* species.

The enzymatic activities of the isolates exhibited two main extracellular activities: lipase and urease. Whereas these enzymatic activities are often considered to be associated with microbial virulence or spoilage ability (Stead, 1986; Rutherford, 2014), their presence could represent generalist metabolic adaptability or ecological adaptation in the host-associated microbiota (Ikeda-Ohtsubo et al., 2018). Lipase activity, which was detected in isolates B04, K06, and S13, may indicate the capacity to break down lipids in host tissues or in the local environment (Rameshwaram et al., 2018). Although such ability is largely attributed to fish spoilage mechanisms by releasing free fatty acids and volatile compounds, such an ability may also involve mutualistic or commensal functions, such as facilitating lipid digestion in the gastrointestinal tract of hosts (Ghaly et al., 2010). *Proteus* and *Providencia* members that showed this activity have been reported previously among constituents of normal gut microbiota of fish and aquatic animals (Ramkumar et al., 2014; Drzewiecka, 2016). Similarly, urease activity, which was detected in most isolates, may be involved in localized ammonia-mediated pH management and nitrogen cycling. In fish hosts, such an enzymatic capability may support urea metabolism, particularly in species that occupy nitrogenous or brackish habitats (Drzewiecka, 2016). Of interest, a lack of caseinase, amylase, lecithinase, and DNase activity under tested conditions further supports an indication that such isolates may lack strong extracellular virulence determinants. It is, however, possible that such enzymes are induced under certain environmental conditions.

Identification of multidrug-resistant (MDR) bacteria among isolates from *M. merlangus* highlights an emerging concern regarding the dissemination of antibiotic resistance in aquatic environments. Resistance to three or more antibiotic classes was exhibited by eight of every ten isolates, namely β-lactams, sulfonamides, tetracyclines, and aminoglycosides, meeting the definition for MDR status (Rabbani et al., 2017). These resistance patterns, especially widespread insensitivity to amoxicillin/clavulanic acid, tetracycline, and sulfamethoxazole/trimethoprim, reflect long-term environmental exposure to antibiotics (Song et al., 2017; Ng'eno et al., 2024). From a public health point of view, their presence in food fish like *M. merlangus* is alarming, especially with respect to seafood consumption and exposure via food chains. Cross-contamination by improper handling, undercooking, or during food processing can make these bacteria transmittable to humans.

5. Conclusion

This study provides a window into the microbial undercurrents that occupy *M. merlangus*, a species commonly prized for commercial value but seldom analyzed through the lens of resident microbiota. Bacterial genera to which these isolates belong are commonly known to contain opportunistic pathogens, which could pose issues with respect to fish health and food safety. *Enterobacteriaceae* dominance, coupled with selective enzymatic properties and ubiquitous antibiotic resistance, paints a picture of a microbiome influenced by marine ecology and anthropogenic activity. In an era increasingly characterized by interdependent ecosystems and shared microbial territories, such findings hold import outside taxonomic or tissue of origin. They address the silent movement of resistance genes, the effective permeability of boundaries between nature and human activity, and recognition that aquatic organisms are not only food resources but ecological indicators. As we move closer toward an integrated understanding of health between species and environments, such work highlights the need to explore host-associated microbiota from an ecological and health-based paradigm.

Author Contributions

The percentages of the authors' contributions are presented below. All authors reviewed and approved the final version of the manuscript.

	H.S.C.	S.S.	H.S.
C	20	40	40
D	20	40	40
S	-	50	50
DCP	50	25	25
DAI	20	40	40
L	40	30	30
W	10	45	45
CR	10	45	45
SR	10	45	45
PM	30	35	35
FA	50	50	-

C=Concept, D= design, S= supervision, DCP= data collection and/or processing, DAI= data analysis and/or interpretation, L= literature search, W= writing, CR= critical review, SR= submission and revision, PM= project management, FA= funding acquisition.

Conflict of Interest

The authors declared that there is no conflict of interest.

Ethical Consideration

In accordance with national and institutional guidelines, ethical approval was not required for this study, as the fish specimens (*Merlangius merlangus*) were obtained post-mortem from commercial fishers during routine fishing activities. No experimental procedures were performed on live animals. The collection and use of these samples did not involve any intervention, manipulation, or distress to living organisms, thereby exempting the study from formal ethical review.

Acknowledgements

This research was supported by The Scientific and Technological Research Council of Türkiye (TÜBİTAK), [grant number 1919B012309020].

References

Albejo AL, Hamza TA. 2017. Isolation and characterization of thermostable amylase producing bacteria from hot spring at Arba Minch Nech Sar National Park, Southern Ethiopia. Int J Novel Res Interdiscip Stud, 4: 9-16.

Algammal AM, Mabrok M, Ezzat M, Alfifi KJ, Esawy AM, Elmasry N, El-Tarabili RM. 2022. Prevalence, antimicrobial resistance (AMR) pattern, virulence determinant and AMR genes of emerging multi-drug resistant *Edwardsiella tarda* in Nile tilapia and African catfish. Aquaculture, 548: 737643. https://doi.org/10.1016/j.aquaculture.2021.737643

Alikunhi NM, Batang ZB, AlJahdali HA, Aziz MA, Al-Suwailem AM. 2017. Culture-dependent bacteria in commercial fishes: Qualitative assessment and molecular identification using 16S rRNA gene sequencing. Saudi J Biol Sci, 24: 1105-1116.

Asciutto E, Maioli F, Manfredi C, Anibaldi A, Cimini J, Isailović I, Marčeta B, Casini M. 2024. Spatio-temporal patterns of whiting (*Merlangius merlangus*) in the Adriatic Sea under environmental forcing. PLoS One, 19: e0289999. https://doi.org/10.1371/journal.pone.0289999

Banerjee G, Ray AK. 2017. Bacterial symbiosis in the fish gut and its role in health and metabolism. Symbiosis, 72: 1-11. https://doi.org/10.1007/s13199-016-0441-8

Birolli WG, Lima RN, Porto AL. 2019. Applications of marine-derived microorganisms and their enzymes in biocatalysis and biotransformation, the underexplored potentials. Front Microbiol, 10: 1453. https://doi.org/10.3389/fmicb.2019.01453

Brauge T, Bourdonnais E, Trigueros S, Cresson P, Debuiche S, Granier SA, Midelet G. 2024. Antimicrobial resistance and geographical distribution of *Staphylococcus* sp. isolated from whiting (*Merlangius merlangus*) and seawater in the English Channel and the North Sea. Environ Pollut, 345: 123434. https://doi.org/10.1016/j.envpol.2024.123434

Bunpa S, Sermwittayawong N, Vuddhakul V. 2016. Extracellular enzymes produced by *Vibrio alginolyticus* isolated from environments and diseased aquatic animals. Procedia Chem, 18: 12-17. https://doi.org/10.1016/j.proche.2016.01.002

Cabello FC. 2006. Heavy use of prophylactic antibiotics in aquaculture: a growing problem for human and animal health and for the environment. Environ Microbiol, 8: 1137-1144. https://doi.org/10.1111/j.1462-2920.2006.01054.x

Calì F, Stranci F, La Mesa M, Mazzoldi C, Arneri E, Santojanni A. 2023. Whiting (*Merlangius merlangus*) grows slower and smaller in the Adriatic Sea: New insights from a comparison of two populations with a time interval of 30 years. Fishes, 8: 341. https://doi.org/10.3390/fishes8070341

Cantas L, Sørby JRT, Aleström P, Sørum H. 2012. Culturable gut microbiota diversity in zebrafish. Zebrafish, 9: 26-37. https://doi.org/10.1089/zeb.2011.0712

Cheng TH, Ismail N, Kamaruding N, Saidin J, Danish-Daniel MJB. 2020. Industrial enzymes-producing marine bacteria from marine resources. Biotechnol Rep, 27: e00482.

Chiarello M, Villeger S, Bouvier C, Bettarel Y, Bouvier T. 2015. High diversity of skin-associated bacterial communities of marine fishes is promoted by their high variability among body parts, individuals and species. FEMS Microbiol Ecol, 91: fiv061. https://doi.org/10.1093/femsec/fiv061

Clinical and Laboratory Standards Institute. 2023. Performance standards for antimicrobial susceptibility testing. CLSI supplement M100, Clinical and Laboratory Standards Institute, Wayne, PA, USA, pp: 428.

Cui MJ, Teng A, Chu J, Cao B. 2022. A quantitative, high-throughput urease activity assay for comparison and rapid screening of ureolytic bacteria. Environ Res, 208: 112738. https://doi.org/10.1016/j.envres.2022.112738

de Bruijn I, Liu Y, Wiegertjes GF, Raaijmakers JM. 2018. Exploring fish microbial communities to mitigate emerging diseases in aquaculture. FEMS Microbiol Ecol, 94: fix161. https://doi.org/10.1093/femsec/fix161

Dewi RR, Hassan L, Daud HM, Matori MF, Zakaria Z, Ahmad NI, Aziz SA, Jajere SM. 2022. On-farm practices associated with multi-drug-resistant *Escherichia coli* and *Vibrio parahaemolyticus* derived from cultured fish. Microorganisms, 10: 1520.

Dhayalan A, Velramar B, Govindasamy B, Ramalingam KR, Dilipkumar A, Pachiappan P. 2022. Isolation of a bacterial strain from the gut of the fish, *Systomus sarana*, identification of the isolated strain, optimized production of its protease, the enzyme purification, and partial structural characterization. J Genet Eng Biotechnol, 20: 24.

https://doi.org/10.1186/s43141-022-00299-3

Drzewiecka D. 2016. Significance and roles of *Proteus* spp. bacteria in natural environments. Microb Ecol, 72: 741-758. https://doi.org/10.1007/s00248-015-0720-6

Egerton S, Culloty S, Whooley J, Stanton C, Ross RP. 2018. The gut microbiota of marine fish. Front Microbiol, 9: 873. https://doi.org/10.3389/fmicb.2018.00873

FAO. 2020. The State of Mediterranean and Black Sea Fisheries 2020. General Fisheries Commission for the Mediterranean, Rome, Italy. pp: 129. https://doi.org/10.4060/cb2429en

Farooq S, Ganai SA, Ganai BA, Mohan S, Uqab B, Nazir R. 2022. Molecular characterization of lipase from a psychrotrophic bacterium *Pseudomonas* sp. CRBC14. Curr Genet, 68: 243-251 https://doi.org/10.1007/s00294-021-01224-w

Felsenstein J. 1985. Confidence limits on phylogenies: An approach using the bootstrap. Evolution, 39: 783-791. https://doi.org/10.1111/j.1558-5646.1985.tb00420.x

Froese R, Pauly D. 2024. FishBase. URL: https://www.fishbase.se (accessed April 01, 2025).

Gauthier DT. 2015. Bacterial zoonoses of fishes: A review and appraisal of evidence for linkages between fish and human infections. Vet J, 203: 27-35.

Ghaly AE, Dave D, Budge S, Brooks MS. 2010. Fish spoilage mechanisms and preservation techniques: Review. Am J Appl Sci, 7: 859-877.

Hatosy SM, Martiny AC. 2015. The ocean as a global reservoir of antibiotic resistance genes. Appl Environ Microbiol, 81: 7593-7599. https://doi.org/10.1128/AEM.00736-15

Hoppe HG, Arnosti C, Herndl GJ. 2002. Ecological significance of bacterial enzymes in the marine environment. In: Burns RG, Dick RP, editors. Enzymes in the Environment: Activity, Ecology, and Applications. Marcel Dekker, New York, USA. pp: 73-107.

Hossain A, Habibullah-Al-Mamun M, Nagano I, Masunaga S, Kitazawa D, Matsuda H. 2022. Antibiotics, antibiotic-resistant bacteria, and resistance genes in aquaculture: risks, current concern, and future thinking. Environ Sci Pollut Res Int, 29: 11054-11075.

Huang Q, Sham RC, Deng Y, Mao Y, Wang C, Zhang T, Leung KM. 2020. Diversity of gut microbiomes in marine fishes is shaped by host-related factors. Mol Ecol, 29: 5019-5034. https://doi.org/10.1111/mec.15699

Hudzicki J. 2009. Kirby-Bauer disk diffusion susceptibility test protocol. Am Soc Microbiol, 15: 1-23.

ICES. 2024. Whiting (*Merlangius merlangus*) in divisions 7.b–c and 7.e–k (southern Celtic Seas and western English Channel). ICES Advice, 2024: whg.27.7b-ce-k. https://doi.org/10.17895/ices.advice.25019729

Ikeda-Ohtsubo W, Brugman S, Warden CH, Rebel JM, Folkerts G, Pieterse CM. 2018. How can we define "optimal microbiota?": A comparative review of structure and functions of microbiota of animals, fish, and plants in agriculture. Front Nutr, 5: 90. https://doi.org/10.3389/fnut.2018.00090

Jackman J. 2012. The microbe: the basics of structure, morphology, and physiology as they relate to microbial characterization and attribution. In: Cliff J, Kreuzer H, Ehrhardt C, Wunschel D, editors. Chemical and Physical Signatures for Microbial Forensics, pp: 13-34.

Janda JM, Abbott SL. 2021. The changing face of the family *Enterobacteriaceae* (Order: "*Enterobacterales*"): New members, taxonomic issues, geographic expansion, and new diseases and disease syndromes. Clin Microbiol Rev, 34: e00021-19. https://doi.org/10.1128/cmr.00174-20

Justé A, Thomma BPHJ, Lievens B. 2008. Recent advances in molecular techniques to study microbial communities in food-associated matrices and processes. Food Microbiol, 25: 745-761. https://doi.org/10.1016/j.fm.2008.04.009

Köker L, Aydın F, Gaygusuz Ö, Akçaalan R, Çamur D, İlter H, Ayoğlu FN, Altın A, Topbaş M, Albay M. 2021. Heavy metal concentrations in *Trachurus mediterraneus* and *Merlangius merlangus* captured from Marmara Sea, Turkey and associated health risks. Environ Manag, 67: 522-531. https://doi.org/10.1007/s00267-020-01352-y

Kumar S, Stecher G, Li M, Knyaz C, Tamura K. 2018. MEGA X: Molecular evolutionary genetics analysis across computing platforms. Mol Biol Evol, 35: 1547-1549. https://doi.org/10.1093/molbev/msy096

Kyule DN, Maingi JM, Njeru EM, Nyamache AK. 2022. Molecular characterization and diversity of bacteria isolated from fish and fish products retailed in Kenyan markets. Int J Food Sci, 2022: 2379323.

Muus BJ, Nielsen JG. 1999. Sea fish. Scandinavian Fishing Year Book, Hedehusene, Denmark, pp: 340.

Ng'eno E, Cobos ME, Kiplangat S, Mugoh R, Ouma A, Bigogo G, Ouma S, Peterson AT. 2024. Long-term antibiotic exposure landscapes and resistant *Escherichia coli* colonization in a densely populated setting. PLoS One, 19: e0302521. https://doi.org/10.1371/journal.pone.0302521

Nissar S, Bakhtiyar Y, Arafat MY, Andrabi SA, Bhat AA, Yousuf T. 2023. A review of the ecosystem services provided by the marine forage fish. Hydrobiologia, 850: 2871-2902. https://doi.org/10.1007/s10750-022-05033-1

Ntushelo K. 2013. Identifying bacteria and studying bacterial diversity using the 16S ribosomal RNA gene-based sequencing techniques: A review. Afr J Microbiol Res, 7: 5533-5540. https://doi.org/10.5897/AJMR2013.5966

O'Neill J. 2014. Antimicrobial resistance: Tackling a crisis for the health and wealth of nations. Rev Antimicrob Resist, 20: 1-16.

Paarup T, Nieto JC, Peláez C, Reguera JI. 1999. Microbiological and physico-chemical characterisation of deep spoilage in Spanish dry-cured hams and characterisation of isolated *Enterobacteriaceae* with regard to salt and temperature tolerance. Eur Food Res Technol, 209: 366-371. https://doi.org/10.1007/s002170050511

Pękala-Safińska A. 2018. Contemporary threats of bacterial infections in freshwater fish. J Vet Res, 62: 261-267. https://doi.org/10.2478/jvetres-2018-0037

Pepi M, Focardi S. 2021. Antibiotic-resistant bacteria in aquaculture and climate change: A challenge for health in the Mediterranean area. Int J Environ Res Public Health, 18: 5723. https://doi.org/10.3390/ijerph18115723

Pitout JD, Laupland KB. 2008. Extended-spectrum β-lactamase-producing *Enterobacteriaceae*: An emerging public-health concern. Lancet Infect Dis, 8: 159-166. https://doi.org/10.1016/S1473-3099(08)70041-0

Pratte ZA, Besson M, Hollman RD, Stewart FJ. 2018. The gills of reef fish support a distinct microbiome influenced by host-specific factors. Appl Environ Microbiol, 84: e00063-18. https://doi.org/10.1128/AEM.00063-18

Preena PG, Swaminathan TR, Kumar VJR, Singh ISB. 2020. Antimicrobial resistance in aquaculture: A crisis for concern. Biologia, 75: 1497-1517. https://doi.org/10.2478/s11756-020-00456-4

Rabbani MAG, Howlader MZH, Kabir Y. 2017. Detection of multidrug resistant (MDR) bacteria in untreated waste water disposals of hospitals in Dhaka City, Bangladesh. J Glob Antimicrob Resist, 10: 120-125. https://doi.org/10.1016/j.jgar.2017.04.009

Rameshwaram NR, Singh P, Ghosh S, Mukhopadhyay S. 2018.

Lipid metabolism and intracellular bacterial virulence: Key to next-generation therapeutics. Future Microbiol, 13: 1301-1328. https://doi.org/10.2217/fmb-2018-0013

Ramkumar R, Ravi M, Jayaseelan C, Rahuman AA, Anandhi M, Rajthilak C, Perumal P. 2014. Description of *Providencia vermicola* isolated from diseased Indian major carp, *Labeo rohita* (Hamilton, 1822). Aquaculture, 420: 193-197. https://doi.org/10.1016/j.aquaculture.2013.11.013

Ray AK, Ghosh K, Ringø E. 2012. Enzyme-producing bacteria isolated from fish gut: A review. Aquac Nutr, 18: 465-492. https://doi.org/10.1111/j.1365-2095.2012.00943.x

Romero J, Ringø E, Merrifield DL. 2014. The gut microbiota of fish. In: Merrifield D, Ringø E, editors. Aquaculture Nutrition: Gut Health, Probiotics and Prebiotics. Wiley-Blackwell, Oxford, USA, pp: 75-100.

Rutherford JC. 2014. The emerging role of urease as a general microbial virulence factor. PLoS Pathog, 10: e1004062. https://doi.org/10.1371/journal.ppat.1004062

Saitou N, Nei M. 1987. The neighbor-joining method: A new method for reconstructing phylogenetic trees. Mol Biol Evol, 4: 406-425.

Santos RA, Oliva-Teles A, Pousão-Ferreira P, Jerusik R, Saavedra MJ, Enes P, Serra CR. 2021. Isolation and characterization of fish-gut *Bacillus* spp. as source of natural antimicrobial compounds to fight aquaculture bacterial diseases. Mar Biotechnol, 23: 276-293.

Sheng L, Wang L. 2021. The microbial safety of fish and fish products: Recent advances in understanding its significance, contamination sources, and control strategies. Compr Rev Food Sci Food Saf, 20: 738-786. https://doi.org/10.1111/1541-4337.12671

Song J, Rensing C, Holm PE, Virta M, Brandt KK. 2017. Comparison of metals and tetracycline as selective agents for development of tetracycline resistant bacterial communities in agricultural soil. Environ Sci Technol, 51: 3040-3047. https://doi.org/10.1021/acs.est.6b05342

Stead D. 1986. Microbial lipases: Their characteristics, role in food spoilage and industrial uses. J Dairy Res, 53: 481-505.

Stefani FO, Bell TH, Marchand C, De La Providencia IE, El Yassimi A, St-Arnaud M, Hijri M. 2015. Culture-dependent and -independent methods capture different microbial community fractions in hydrocarbon-contaminated soils. PLoS One, 10: e0128272. https://doi.org/10.1371/journal.pone.0128272

Stratev D, Daskalov H, Vashin I. 2015. Characterisation and determination of antimicrobial resistance of β-haemolytic *Aeromonas* spp. isolated from common carp (*Cyprinus carpio* L.). Rev Med Vet (Toulouse), 166: 54-61.

Trincone A. 2017. Enzymatic processes in marine biotechnology. Mar Drugs, 15: 93. https://doi.org/10.3390/md15040093

Uchiyama H. 2000. Distribution of *Vibrio* species isolated from aquatic environments with TCBS agar. Environ Health Prev Med, 4: 199-204. https://doi.org/10.1007/BF02931258

Wanja DW, Mbuthia PG, Waruiru RM, Mwadime JM, Bebora LC, Nyaga PN, Ngowi HA. 2019. Bacterial pathogens isolated from farmed fish and source pond water in Kirinyaga County, Kenya. Int J Fish Aquat Stud, 7: 295-301.

World Health Organization. 2019. No time to wait: Securing the future from drug-resistant infections. Report to the Secretary-General of the United Nations. World Health Organization, Geneva, Switzerland, pp: 25.

Yang JH, Sheng WH, Hsueh PR. 2020. Antimicrobial susceptibility and distribution of extended-spectrum β-lactamases, AmpC β-lactamases and carbapenemases among *Proteus*, *Providencia* and *Morganella* isolated from global hospitalised patients with intra-abdominal and urinary tract infections: Results of the Study for Monitoring Antimicrobial Resistance Trends (SMART), 2008–2011. J Glob Antimicrob Resist, 22: 398-407. https://doi.org/10.1016/j.jgar.2020.04.011

Yang Y. 2018. Detection, activity measurement and phylogeny of ureolytic bacteria isolated from elasmobranch tissue. Masters Thesis, University of Southern Mississippi, USA, pp: 89.

Yildiz T, Uzer U, Yemişken E, Karakulak FS, Kahraman AE, Çanak Ö. 2021. Conserve immatures and rebound the potential: stock status and reproduction of whiting (*Merlangius merlangus* [Linnaeus, 1758]) in the Western Black Sea. Mar Biol Res, 17: 815-827. https://doi.org/10.1080/17451000.2021.2019787

Yoon SH, Ha SM, Kwon S, Lim J, Kim Y, Seo H, Chun J. 2017. Introducing EzBioCloud: A taxonomically united database of 16S rRNA gene sequences and whole-genome assemblies. Int J Syst Evol Microbiol, 67: 1613-1617. https://doi.org/10.1099/ijsem.0.001755

Yukgehnaish K, Kumar P, Sivachandran P, Marimuthu K, Arshad A, Paray BA, Arockiaraj J. 2020. Gut microbiota metagenomics in aquaculture: Factors influencing gut microbiome and its physiological role in fish. Rev Aquac, 12: 1903-1927. https://doi.org/10.1111/raq.12416

Zhang C, Kim SK. 2010. Research and application of marine microbial enzymes: Status and prospects. Mar Drugs, 8: 1920-1934. https://doi.org/10.3390/md8061920

Black Sea Journal of Engineering and Science
doi: 10.34248/bsengineering.1762537

Open Access Journal
e-ISSN:

Research Article
Volume 8 - Issue 5: 1645-1651 / September 2025

UTILIZATION OF CONCRETE WASTE AS A CEMENT REPLACEMENT: INFLUENCE OF CALCINATION ON REACTIVITY AND PERFORMANCE

Hüseyin ULUGÖL[1]*

[1]*Ankara University, Faculty of Engineering, Department of Civil Engineering, 06830, Ankara, Türkiye*

Abstract: Concrete waste is one of the major components of construction and demolition wastes, as well as a material that must be removed in an environmentally safe manner. With the inclusion of concrete waste as a minor additional constituent, the popularity of its utilization has gained importance. This study utilizes concrete waste with replacement ratios of 20%, 40%, and 60%, in both calcined and non-calcined forms. Two different calcination temperatures were applied to see the effect of calcination temperatures. Results show that as the replacement ratio of non-calcined concrete waste increases, mechanical performance decreases. However, calcination enhances the reactivity of concrete waste, and at an optimum replacement ratio of 20%, the compressive strength is higher than that of the reference specimen. After freeze-thaw cycles, specimens with 20% calcined concrete waste exhibit lower compressive strength losses compared to the reference specimen. Regarding the mass losses after freeze-thaw cycles, 20% concrete waste calcined at 950 °C have better performance than reference specimen. This study shows that with a 20% replacement ratio, calcined concrete waste can be used as a cement replacement material.

Keywords: Concrete waste, Calcination, Freeze-thaw, Strength loss, Electrical resistance

***Corresponding author:** Ankara University, Faculty of Engineering, Department of Civil Engineering, 06830, Ankara, Türkiye
E mail: hulugol@ankara.edu.tr (H. ULUGÖL)
Hüseyin ULUGÖL https://orcid.org/0000-0002-0186-3145

Received: August 12, 2025
Accepted: September 10, 2025
Published: September 15, 2025

Cite as: Ulugöl H. 2025. Utilization of concrete waste as a cement replacement: influence of calcination on reactivity and performance. BSJ Eng Sci, 8(5): 1645-1651

1. Introduction

Cement production plays a major role in environmental degradation, primarily due to its high consumption of natural resources and energy (Sari et al., 2020), as well as its contribution to nearly 7% of global CO_2 emissions (Neupane, 2022). To mitigate these negative impacts, the use of blended cements is encouraged under the TS EN 197-1 standard, incorporating materials such as fly ash (FA), blast furnace slag (BFS), natural pozzolans (NP), limestone, and silica fume (SF) to reduce clinker content. Although some of these are industrial byproducts and others are naturally occurring, they are well-known for their positive effects on mechanical and durability performance when used in cement blends.

More recently, even concrete waste (CW) has emerged as a viable component in blended cement formulations, in line with sustainability goals, as its generation rate continues to rise each year. The renovation of existing structures, as well as unfortunate events such as earthquakes and wars, are among the primary causes behind the accumulation of large volumes of CW. With the growing emphasis on sustainability and the circular economy, researchers have increasingly focused on the reuse of waste materials, including CW and other construction and demolition wastes (CDW). If not properly managed, the disposal of concrete waste can result in soil and groundwater contamination; furthermore, its bulky and inert nature contributes to land occupation and long-term environmental degradation (Maaze and Shrivastava, 2023). In this context, TS EN 197-6 permits the use of CW in cement blends at rates of up to 35%. However, despite this allowance, due to its highly crystalline structure—primarily composed of portlandite, calcite, and quartz—20% is generally recommended as the upper limit for replacement (Maaze and Shrivastava, 2023).

One of the most effective methods to compensate for the low reactivity caused by CW's crystalline structure is thermal activation. Studies report that CW becomes denser around 400 °C, while 800 °C is frequently cited as the optimum calcination temperature (Zhang et al., 2022). However, Xu et al. (2021) identified 750 °C as the optimal treatment temperature—among 550, 650, 750, 850, and 950 °C—based on maximum compressive strength results. In another study, 800 °C combined with a 10% replacement ratio was determined to be the most effective combination (Kim and Ubysz, 2024). According to Wu et al. (2021) CW treated between 600 and 800 °C exhibited the best performance at a 30% replacement level.

Although strength development with thermally activated CW has been reported, the durability performance of mortars incorporating CW remains less explored. Therefore, this study investigates not only the compressive strength development of mortars containing 20%, 40%, and 60% CW, but also evaluates their durability. In this context, mass and strength losses were measured after freeze–thaw cycling. Additionally, electrical resistance tests were conducted to assess the microstructural changes of the mortars.

2. Materials and Methods

This study evaluates both thermally treated and untreated concrete waste (CW) as a cement replacement material by assessing mechanical and durability performance.

2.1 Concrete Waste

Concrete waste obtained from a demolition site was first crushed in a jaw crusher with a 1 mm gap and then ground in a ball mill. The waste was obtained through selective demolition and consisted solely of concrete, without any impurities such as brick, gypsum, or other constituents. Previous studies revealed that the optimum grinding time is 60 minutes; otherwise, shorter grinding results in insufficient fineness, while longer grinding causes agglomeration (Zhao et al., 2020) and an increase in particle size. CW was thermally treated in a muffle furnace at temperatures of 750 °C and 950 °C for 2 hours.

2.2 Specimen Preparation and Method

Concrete waste replacement ratios were determined as 20%, 40% and 60%. The water-to-binder ratio was set to 0.6 due to the higher water demand of concrete waste. Although the water-to-binder ratio was kept constant at 0.6 in all mixtures, workability was still sufficient even at the 60% replacement level. This is attributed to the relatively high w/b ratio, which compensated for the increased water demand of CW. The specimens, whose mix proportions are shown in Table 1, were mixed in a laboratory mixer with a 5-liter capacity. The amounts of water and aggregate were 240 g and 1200 g, respectively, and were kept constant for all specimens. When ingredients were placed in the mixer, firstly dry ingredients were mixed for 60 s, then water was added and mixed for 60 s, after that the mortar inside the chamber was turned over manually using a mini shovel and finally, a further 60 seconds of mixing was performed. The produced specimens were cast in 40×40×160 mm prismatic molds and in cubic molds with an edge length of 50 mm, in two layers, each compacted using a 16 mm diameter rod. For each specimen group, six prismatic and three cubic specimens were produced (Figure 1) and placed in a curing environment with 95% relative humidity and a temperature of 23 °C. For each test type, three specimens were evaluated, and the reported values represent the mean results. Standard deviations were calculated and presented as error bars in the corresponding figures. In addition, the coefficient of variation was calculated for each group and found to be within an acceptable range (3–6%), confirming the reliability and reproducibility of the results.

Figure 1. Prismatic and cubic specimens.

Mechanical properties were evaluated on the 7th and 28th days. Flexural strength tests were performed on 40×40×160 mm prismatic specimens, and compressive strength was determined on the remaining halves after flexural testing. F–T resistance was assessed based on mass loss, strength loss, and changes in electrical resistance (ER) after the F–T cycles. The F–T procedure was conducted in accordance with TS EN 12390-9 "Testing hardened concrete – Part 9: Freeze–thaw resistance – Scaling". During testing, specimens were checked daily in the F–T cabinet. On the 10th day, when two specimens cracked and split at mid-span, the F–T process was terminated.

Table 1. Specimen constituents

ID	Concrete Waste		
	Cement (gr)	Amount (gr)	Treatment Temperature (°C)
Ref	400	-	-
C20	320	80	-
C40	240	160	-
C60	160	240	-
C20-750	320	80	750
C40-750	240	160	750
C60-750	160	240	750
C20-950	320	80	950
C40-950	240	160	950
C60-950	160	240	950

Electrical resistance measurements were carried out on 50 mm cubic mortar specimens using a two-electrode method. Before testing, all samples were saturated by immersing them in water for 24 hours, followed by gently wiping the surface with a damp cloth. Measurements were taken at room temperature after the

F–T cycles, both on reference specimens and those subjected to F–T. While mass and strength losses were evaluated using prismatic specimens, ER changes were determined on the cubic ones. The F–T-exposed samples were compared to specimens cured under identical conditions until the end of the F–T period. An image of the electrical resistance measurement setup is presented in Figure 2.

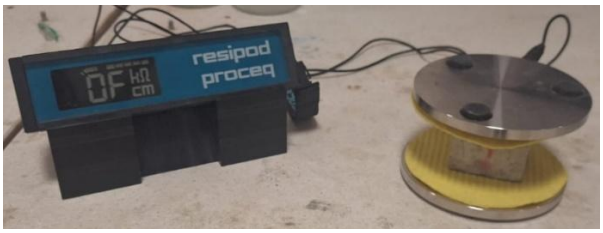

Figure 2. Image of the electrical resistance measurement setup.

3. Results and Discussion

3.1 Compressive and flexural strength

Flexural and compressive strength results at 7 and 28 days are presented in Figure 3. Since the C60 and C60-750 specimens failed easily without any measurable flexural strength on the bending device, their flexural strength values are reported as zero. Considering the flexural strength results, specimens with non-calcined concrete waste (C20, C40, and C60) exhibit lower flexural strengths compared to the reference specimen. However, when the concrete waste was calcined, an improvement in mechanical properties was observed. For instance, C20-750 exhibited flexural strengths of 4.6 and 7.1 MPa at 7 and 28 days, respectively, whereas C20 showed 4.3 and 6.3 MPa. C20-950 exhibited a similar performance in terms of flexural strength, with values of 4.9 and 5.2 MPa. At a 40% replacement ratio, a calcination temperature of 750 °C provided better performance than non-calcined CW, with C40-750 showing flexural strengths of 4.0 and 6.3 MPa at 7 and 28 days—higher than those of C40 (3.6 and 5.0 MPa). However, further increasing the calcination temperature resulted in a decrease in flexural strength for specimens containing 40% calcined CW.

Compressive strength results clearly reveal the effects of CW replacement level and calcination temperature. Non-calcined CW caused a reduction in compressive strength compared to the reference specimens. Moreover, as the replacement ratio increased, compressive strength further decreased. In contrast, calcined CW led to significant improvements. For example, C20-750 exhibited compressive strengths of 24.7 and 36.6 MPa at 7 and 28 days, respectively. When the calcination temperature increased to 950 °C, compressive strengths further increased to 32.2 and 41.9 MPa—the highest values among all specimens at the 20% replacement ratio.

Regardless of calcination, specimens with 60% CW replacement exhibited the lowest strength values. This is likely due to the high water absorption capacity of CW. As the replacement level increases, so does water demand. CW typically consists of aged aggregates surrounded by a residual cement matrix, which makes its water absorption higher than that of natural aggregates. Another contributing factor to the reduction in mechanical properties at 60% replacement is the dilution effect caused by the reduced cement content (Lothenbach et al., 2008).

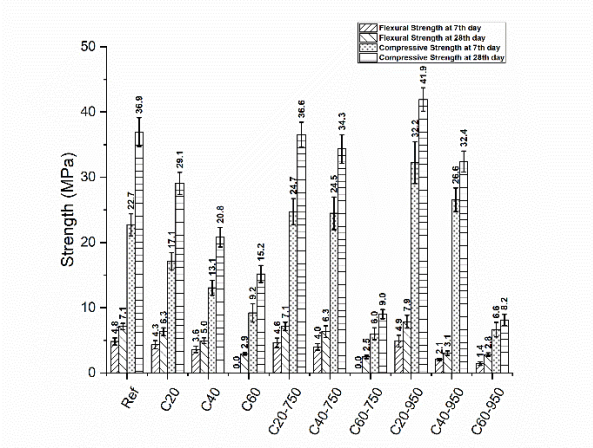

Figure 3. Flexural and compressive strength results at 7 and 28 days.

When considering specimens with 60% calcined CW, an additional factor is the quicklime content. Calcination temperatures above 600 °C lead to the formation of CaO (quicklime), and higher temperatures result in increased quicklime content. Although the water-to-binder ratio was set at 0.6, which is relatively high, hydration of quicklime requires additional water. Therefore, specimens with 60% calcined CW likely suffered from insufficient water for proper hydration of the cementitious matrix. Furthermore, an increased calcium-to-silica ratio may result in highly alkaline calcium silicates with lower strength (Mao and Ai, 2023).

Overall, the results indicate that calcination of CW significantly enhances both flexural and compressive strengths, particularly at lower replacement levels (20%). In contrast, higher replacement levels (60%) consistently lead to reduced mechanical performance, regardless of the calcination temperature. The improvement in mechanical properties with calcined CW can be attributed to the increased pozzolanic reactivity and improved particle packing after thermal treatment. However, excessive replacement ratios result in higher water demand and reduced binder content, leading to strength reductions.

3.2 Electrical resistance and mass changes

Electrical resistance results are presented in Figure 4. The results are expressed in kΩ·cm to normalize for specimen geometry and dimensions. Considering the electrical resistance (ER) results before the F–T procedure, the specimens generally exhibited lower resistance as their mechanical strength decreased. For example, while the Ref specimen showed 43.7 kΩ·cm, the

C20, C40, and C60 specimens exhibited 38.6, 37.2, and 35.2 kΩ·cm, respectively —consistent with the decreasing strength trend. This is attributed to the fact that lower strength is typically associated with higher pore volume (Cosoli et al., 2020). One of the main reasons for the parallel trend between strength and ER is that a porous structure negatively impacts both. The presence of interconnected pores facilitates water conductivity, thereby reducing both strength and electrical resistance. However, ER is not only influenced by the pore structure but also by factors such as mineral admixtures, water-to-cement ratio, moisture content, and aggregate type (Mathew and Vishnudas, 2025). Among the C20-750, C40-750, and C60-750 specimens, C60-750—despite its very low strength—exhibited the highest ER values. This is attributed to the filler effect of CW, which becomes dominant at such high replacement levels. Although 60% CW is unlikely to contribute significantly through pozzolanic activity, it may reduce total pore volume and clog the interconnected pore structure, thereby increasing ER (Cosoli et al., 2020). This finding indicates that electrical resistance is not solely governed by mechanical strength. In the case of C60-750, the relatively fine calcined CW particles likely acted as a filler, partially blocking interconnected pores and reducing ion mobility. As a result, even though the cementitious matrix was mechanically weak, the reduced pore connectivity contributed to higher electrical resistance values. A similar pattern is observed in the ER results of C20-950, C40-950, and C60-950, where C40-950 shows higher ER than C20-950, even though it has lower strength. In this case, the 40% CW likely acted as a filler material that blocked capillary pores and increased ER. However, C60-950 exhibited the lowest ER value among all calcined CW specimens. During mixing, CW calcined at 950 °C released a significant amount of heat, and C60-950 specimens experienced extensive cracking as a result. These cracks disrupted the matrix continuity and negated the filler effect, causing a drastic reduction in ER.

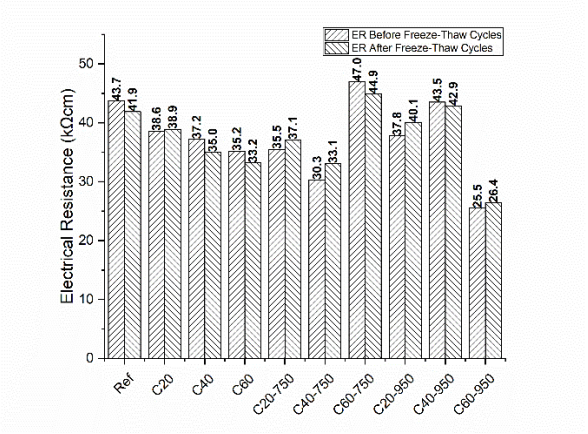

Figure 4. Electrical resistance results of specimens before and after freeze-thaw cycles.

In general, ER after F–T exposure showed a decreasing trend with decreasing compressive strength, in line with increased microcracking and enhanced pore connectivity. However, some exceptions were observed in the C20, C20-750, C40-750, C20-950, and C60-950 specimens. This behavior may be explained by the filler effect of calcined CW, which may have contributed to clogging interconnected pores or reducing effective ionic pathways. Additionally, partially saturated cracks formed during F–T cycling could have altered ER measurement results. Similar trends and anomalies have been reported in the literature (Chen et al., 2023), indicating that ER behavior post–F–T is not solely determined by mechanical deterioration, but also by changes in pore structure and moisture distribution. Furthermore, Dvoynikov et al. (2026) noted that temperature fluctuations can cause water evaporation, which may lead to inverse effects on electrical resistivity (ER), occasionally leading to increased ER values after F–T cycles.

Figure 5 presents the average mass changes of the specimens after F–T cycles. While the Ref specimen had a mass loss of 0.66%, both C20 and C40 showed nearly identical losses of 0.67%. However, when the replacement ratio increased to 60%, the C60 specimen exhibited a mass loss of 1.06%. Similarly, specimens incorporating calcined CW showed a comparable pattern: C60-750 and C60-950 had mass losses of 0.92% and 1.65%, respectively, representing the highest mass losses among the specimens treated at 750 °C and 950 °C, respectively. This can be attributed to the use of 60% CW, which results in a more permeable structure with a reduced volume of hydrated cement matrix, leading to lower durability under F–T conditions. In contrast, C20-950, which achieved the highest strength among all specimens, exhibited the lowest mass loss (0.57%). As expected, increased mechanical performance generally translates into enhanced F–T durability (Atasham ul Haq et al., 2025). Although C20-950 was the only specimen that outperformed the Ref specimen in terms of mass loss, other specimens such as C20, C40, C20-750, and C40-750 also exhibited values close to that of the Ref specimen (0.67%, 0.67%, 0.71%, and 0.69%, respectively). Whether calcined or not, a 20% CW replacement appears to offer favorable F–T durability in terms of mass loss.

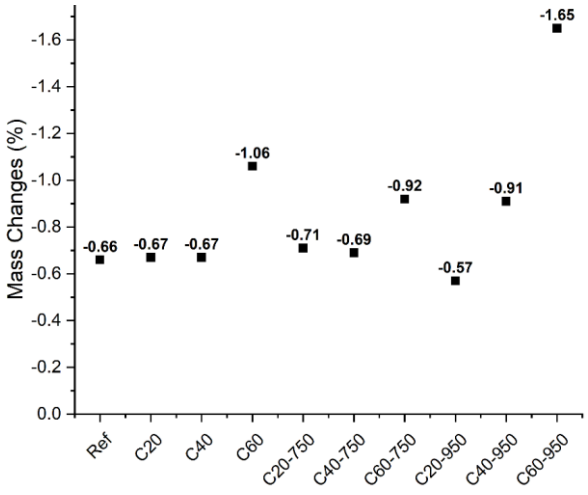

Figure 5. Mean mass changes of specimens after freeze-thaw cycles.

3.3 Flexural and compressive strength losses

After a 28-day curing period, the specimens were subjected to 10 freeze–thaw (F–T) cycles, and then tested to determine their flexural and compressive strengths, as well as to evaluate the corresponding strength losses. Flexural and compressive strength results, along with percentage losses, are presented in Figure 6. Damage caused by freeze–thaw exposure is primarily governed by two factors. First, the specimen must have sufficient tensile strength to resist the internal pressure from water freezing within capillary pores. Second, the pore structure plays a crucial role in determining F–T resistance. Generally, as a specimen's strength and compactness increase, so does its resistance to F–T damage. However, in some cases, specimens with a high volume of capillary pores—and consequently lower strength—may exhibit unexpectedly high F–T resistance due to the availability of pore volume that can accommodate freezing-induced expansion. This phenomenon is evident in the current study. For instance, while the Ref specimen experienced a 45.6% loss in flexural strength, the losses for C20, C40, and C60 were 38.7%, 37.8%, and 30.9%, respectively—demonstrating a decreasing trend in strength loss as initial flexural strength decreases.

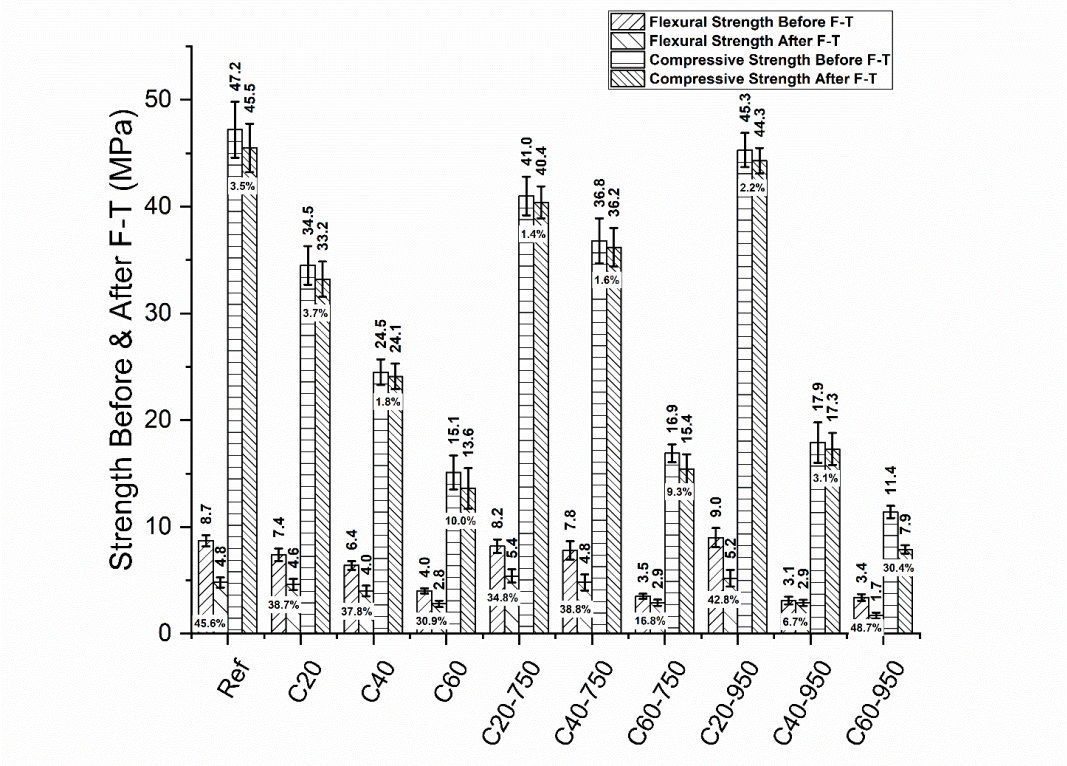

Figure 6. Flexural and compressive strength results and strength losses of specimens.

On the other hand, compressive strength was less affected by F–T cycles. The Ref specimen showed a compressive strength loss of only 3.5%, and C20 exhibited a similar loss of 3.7%. C40 had the lowest loss at 1.8%. However, when the replacement ratio increased to 60%, the compressive strength loss rose to 10.0% in C60. A similar increase in strength loss was observed in specimens with 60% calcined concrete waste (CW), especially at higher replacement levels. This trend is attributed to the more permeable structure of high-CW specimens, particularly when calcined. Calcined CW contains CaO (quicklime), which hydrates during mixing. This exothermic reaction consumes water and releases heat, accelerating water loss and leading to the formation of voids within the cement matrix. Moreover, the reduced cement content in these mixtures results in a dilution

effect, further weakening the matrix. Interestingly, the C60 specimen exhibited a lower flexural strength loss (30.9%) than the Ref specimen (45.6%), indicating better resistance to surface cracking under F–T conditions. However, its significantly higher compressive strength loss (10.0%) suggests internal structural degradation. This seemingly contradictory behavior can be explained by the different failure mechanisms associated with flexural and compressive strength. While flexural strength is more sensitive to surface-level microcracking—and may benefit from increased pore volume that buffers internal pressure—compressive strength is largely dependent on the integrity and compactness of the bulk matrix. Indeed, previous studies have shown that flexural strength tends to be more vulnerable to F–T degradation than compressive strength (Solatiyan et al., 2015). High replacement levels of cement with calcined CW result in fewer hydration products, reducing the internal load-bearing capacity. Additionally, the hydration of residual CaO creates localized voids due to rapid water consumption and heat generation, further contributing to compressive strength loss. Therefore, the improved flexural performance observed in high-CW specimens does not necessarily imply enhanced overall durability or structural performance under F–T exposure.

4. Conclusion

This study investigated the use of calcined and non-calcined concrete waste (CW) as a pozzolanic material in cementitious mortars. Based on the findings, the following conclusions can be drawn:

- A limited amount of CW can be effectively used as a cement replacement material, provided that the performance of the binder system is adequately controlled.
- Calcination significantly increases the reactivity of CW, leading to improved mechanical performance in mortars incorporating calcined CW.
- A 20% replacement level of calcined CW was identified as the optimum ratio, resulting in higher mechanical strength than both the reference and non-calcined CW specimens.
- Excessive use of calcined CW (e.g., 60%) led to substantial reductions in mechanical strength due to increased water demand, the dilution effect, and internal void formation caused by quicklime hydration.
- In terms of durability, incorporating 20% calcined CW enhanced freeze–thaw resistance, while 40% could still be considered acceptable with moderate mass loss and ER degradation.
- Electrical resistance results highlighted the filler effect of CW, especially at higher replacement levels, contributing to reduced pore connectivity and increased microstructural resistance in some cases.

In practical terms, the calcination of CW requires additional energy input. However, this demand can be significantly reduced by integrating the process with existing high-temperature industrial operations. For example, waste heat from cement kilns, steel plants, or other thermal processes could be utilized for CW calcination. Such strategies would minimize the environmental and economic costs while enhancing the industrial feasibility of using calcined CW as a sustainable cement replacement material.

Based on these results, it is recommended that future studies consider adjusting the water-to-cement (or water-to-binder) ratio to account for the presence of reactive CaO in calcined CW. Furthermore, optimizing curing regimes and investigating long-term durability under different environmental exposures would provide valuable insights for the broader application of CW in sustainable construction materials. These findings support the feasibility of incorporating thermally treated concrete waste into binder systems, offering a promising approach for both resource conservation and improved material performance.

In addition, extended durability tests such as sulfate resistance, chloride penetration, or carbonation should be considered in future studies to provide a more comprehensive understanding of the long-term performance of mortars incorporating calcined CW.

Author Contributions

The percentages of the author contributions are presented below. The author reviewed and approved the final version of the manuscript.

	H.U.
C	100
D	100
S	100
DCP	100
DAI	100
L	100
W	100
CR	100
SR	100
PM	100
FA	100

C=Concept, D= design, S= supervision, DCP= data collection and/or processing, DAI= data analysis and/or interpretation, L= literature search, W= writing, CR= critical review, SR= submission and revision, PM= project management, FA= funding acquisition.

Conflict of Interest

The author declared that there is no conflict of interest.

Ethical Consideration

Ethics committee approval was not required for this study because there was no study on animals or humans.

References

Atasham ul Haq M, Wang P, Wang Y, Cui H, Tahir M, Gong F, Li W. 2025. Optimization and utilization of air-entrained recycled brick aggregate concrete under freeze-thaw environment. Case Stud Constr Mater, 23: e04941.

Chen H, Xu N, Jiang P, Jiang L. 2023. Study on the effect of freeze–thaw action on the electrical conductivity and sensing properties of graphene-based cement composites. Materials (Basel), 16(2): 855.

Cosoli G, Mobili A, Tittarelli F, Revel G, Chiariotti P. 2020. Electrical resistivity and electrical impedance measurement in mortar and concrete elements: a systematic review. Appl Sci (Basel), 10(24): 1-43.

Dvoynikov MV, Kopteva AI, Romanova NA, Yurtaev SL, Gromov DA. 2026. Influence of thermal cycling on cement sheath integrity in permafrost conditions. Int J Eng, 39(1): 148-158.

Kim J, Ubysz A. 2024. Thermal activation of multi-recycled concrete powder as supplementary cementitious material for repeated and waste-free recycling. J Build Eng, 98: 111169.

Lothenbach B, Le Saout G, Gallucci E, Scrivener K. 2008. Influence of limestone on the hydration of Portland cements. Cem Concr Res, 38(6): 848-860.

Maaze MR, Shrivastava S. 2023. Development of framework in the selection and reuse of concrete waste and brick waste powder as pozzolanic material in cement concrete application using analytical hierarchy process technique. Constr Build Mater, 393: 132056.

Mao F, Ai H. 2023. A study on the hydrothermal synthesis of calcium silicate products by calcination of full-component waste concrete. Sustainability (Basel), 15(23): 16341.

Mathew J, Vishnudas S. 2025. Application of adaptive neuro fuzzy inference system for contemplating the factors affecting electrical resistivity of concrete. Innov Infrastruct Solut, 10(4): 141.

Neupane K. 2022. Evaluation of environmental sustainability of one-part geopolymer binder concrete. Clean Mater, 6(2): 100138.

Sari B, Geyik ŞY, Keskinkan O. 2020. Çimento üretim sektöründe ISO 14001 çevre yönetim sisteminin enerji kazanımı ve iklim değişikliği üzerine etkilerinin incelenmesi. Cukurova Univ J Fac Eng Archit, 35(4): 847-858.

Solatiyan E, Asadi M, Bozorgmehrasl M. 2015. Investigating the effect of freeze-thaw cycles on strength properties of concrete pavements in cold climates. Indian J Fundam Appl Life Sci, 5(S2): 2421-2428.

Wu H, Xu J, Yang D, Ma Z. 2021. Utilizing thermal activation treatment to improve the properties of waste cementitious powder and its newmade cementitious materials. J Clean Prod, 322: 129074.

Xu J, Kang A, Wu Z, Gong Y, Xiao P. 2021. The effect of mechanical-thermal synergistic activation on the mechanical properties and microstructure of recycled powder geopolymer. J Clean Prod, 327: 129477.

Zhang D, Zhang S, Huang B, Yang Q, Li J. 2022. Comparison of mechanical, chemical, and thermal activation methods on the utilisation of recycled concrete powder from construction and demolition waste. J Build Eng, 61: 105295.

Zhao Y, Gao J, Liu C, Chen X, Xu Z. 2020. The particle-size effect of waste clay brick powder on its pozzolanic activity and properties of blended cement. J Clean Prod, 242: 118521.

Black Sea Journal of Engineering and Science
doi: 10.34248/bsengineering.1744802

Open Access Journal
e-ISSN: 2619 – 8991

Research Article
Volume 8 - Issue 5: 1652-1658 / September 2025

IN SILICO ASSESSMENT OF AMINO ACID–PROTEIN INTERACTIONS IN CORONARY ARTERY DISEASE: MOLECULAR INSIGHTS FOR FUNCTIONAL BIOLOGY

Reşat DİKME[1]*, Adem NECİP[2]

[1]*Harran University, Vocational School of Health Services, Department of Dialysis, 63200, Şanlıurfa, Türkiye*
[2]*Harran University, Vocational School of Health Services, Department of Pharmacy Services, 63200, Şanlıurfa, Türkiye*

Abstract: This study aimed to evaluate the molecular-level interactions between six Coronary artery disease (CAD)-associated amino acids (L-arginine, L-cystine, L-asparagine, L-isoleucine, L-leucine, and trans-4-hydroxyproline) and four cardiovascular target proteins (Angiotensin-converting enzyme (ACE)–1O86, Endothelial nitric oxide synthase (eNOS)–3NOS, β_1-adrenergic receptor (β_1-AR)–2VT4, and Transient Receptor Potential Vanilloid 2 (TRPV2)–8FFM). Ligands were prepared using Schrödinger LigPrep, and proteins were optimized with the Protein Preparation Wizard. Molecular docking simulations were conducted using the Glide SP and XP algorithms. Binding affinities were calculated using GlideScore. Hydrogen bonds, ionic interactions, metal coordination, and π–alkyl contacts were analyzed via Maestro visualization software. L-cystine exhibited high binding affinity with all target proteins, showing particularly strong interactions with ACE (−10.663 kcal/mol) and eNOS (−6.735 kcal/mol). Trans-4-hydroxyproline also displayed favorable binding, supported by extensive hydrogen bonding and zinc coordination. In contrast, hydrophobic amino acids such as L-isoleucine and L-leucine showed weaker interactions. ACE presented the most favorable binding environment for the selected ligands. The strong binding affinities of L-cystine and trans-4-hydroxyproline, particularly to ACE and eNOS, suggest their potential as candidate inhibitors. These effects may be attributed to disulfide bridge formation and hydrogen bond capacity, respectively, which contribute to enhanced binding stability. L-cystine and trans-4-hydroxyproline emerge as promising inhibitor candidates for key cardiovascular proteins implicated in CAD. These findings underscore the potential of amino acid–based therapeutic modulation and provide valuable insight for rational drug design and biomarker development in cardiovascular disease.

Keywords: Amino acid–protein interaction, Molecular docking, Cardiovascular molecular targets, In silico analysis

***Corresponding author:** Harran University, Vocational School of Health Services, Department of Dialysis, 63200, Şanlıurfa, Türkiye
E mail: rdikme@harran.edu.tr (R. DİKME)
Reşat DİKME https://orcid.org/0000-0001-9157-7830
Adem NECİP https://orcid.org/0000-0002-2092-7829

Received: July 17, 2025
Accepted: September 11, 202
Published: September 15, 2025

Cite as: Dikme R, Necip A. 2025. In silico assessment of amino acid–protein interactions in coronary artery disease: Molecular insights for functional biology. BSJ Eng Sci, 8(5): 1652-1658.

1. Introduction

Coronary artery disease (CAD) is one of the leading causes of mortality worldwide and is characterized by endothelial dysfunction, oxidative stress, inflammation, and metabolic disturbances (Libby et al., 2019). In addition to traditional risk factors, there is increasing recognition that disruptions in systemic metabolism significantly contribute to the risk and progression of CAD (Ahn et al., 2022). In this context, growing evidence suggests that disturbances in amino acid metabolism may be closely associated with the molecular basis of the disease (Fan et al., 2016; Jauhiainen et al., 2021). Alterations in plasma amino acid levels not only hold potential as biomarkers for the diagnosis and monitoring of CAD but also provide molecular insights for identifying potential protein targets and underlying regulatory pathways contributing to its pathogenesis (Gammoh et al., 2024). Metabolomic analyses have reported significant changes in the levels of amino acids such as L-arginine, hydroxyproline, leucine, isoleucine, asparagine, and cystine in CAD patients (Yang et al., 2015; Melnychuk et al., 2023; Teav et al., 2024). The biological functions of these amino acids indicate that they play active roles in fundamental cardiovascular processes, including regulation of endothelial function, the renin–angiotensin system, myocardial contractility mechanisms, and redox homeostasis (Wu et al., 2018; Li et al., 2022). Therefore, a more detailed assessment of the protein targets with which these amino acids interact is critical for elucidating the molecular pathophysiology of CAD and developing novel therapeutic strategies. In this regard, the present study evaluates the molecular docking interactions between six amino acids (L-arginine, cystine, L-asparagine, L-isoleucine, L-leucine, and trans-4-hydroxyproline) and four cardiovascular proteins (Angiotensin-converting enzyme (ACE)–1O86, Endothelial nitric oxide synthase (eNOS)–3NOS, β_1-adrenergic receptor (β_1-AR)–2VT4, Transient Receptor Potential Vanilloid 2 (TRPV2)–8FFM). These proteins are

well-established biological targets that play central roles in the development and progression of CAD, each representing different pathophysiological mechanisms.

For example, ACE contributes to disease progression by promoting vasoconstriction and inflammation through the production of angiotensin II (Wang et al., 2020; Borghi and Levy, 2022). In contrast, eNOS exerts anti-inflammatory effects by inducing vasodilation through nitric oxide (NO) production. A reduction in NO bioavailability accelerates the atherosclerotic process (Ahmad et al., 2025; Kurhaluk et al., 2025). β_1-adrenergic receptors, which regulate cardiac function via the sympathetic nervous system, increase cardiac output but may predispose to heart failure under chronic activation (Alhayek et al., 2025). The TRPV2 ion channel, which is responsible for maintaining intracellular calcium balance, can lead to structural changes and remodeling in cardiomyocytes by regulating calcium flow (Miller et al., 2021). The amino acids included in this study are of particular interest due to their established biological relevance to these proteins. L-arginine serves as a substrate for the eNOS enzyme, thereby supporting vascular health (da Silva et al., 2023). Cystine has been identified as a more reliable biomarker for CAD compared to homocysteine (Lima et al., 2020). The branched-chain amino acids (BCAAs) isoleucine and leucine have been associated with endothelial dysfunction and metabolic disorders (McGarrah et al., 2023). Recent metabolomic studies have reported a possible association between L-asparagine and CAD. Trans-4-hydroxyproline has been identified as a key biomolecule involved in cardiac fibrosis processes (Barton et al., 2023). While numerous amino acids have been reported to be altered in CAD, this study focused on six that represent the most consistently reported changes and have direct mechanistic relevance to cardiovascular protein targets. This prioritization ensured that the analysis concentrated on metabolites with both strong empirical support and biological plausibility. In light of this information, our study not only aims to define the association between amino acids identified in metabolomic data and CAD but also to computationally model the interaction strengths of these amino acids with potential therapeutic target proteins. In this context, in silico evaluation of protein–ligand interactions may enhance our understanding of the underlying biological mechanisms of CAD and contribute to the development of novel therapeutic approaches.

2. Materials and Methods

2.1. Amino Acid Selection and Ligand Preparation

In this study, six amino acids (L-arginine, L-cystine, L-asparagine, L-isoleucine, L-leucine, and trans-4-hydroxyproline) known to be associated with CAD were selected based on literature reports (Lima et al., 2020; Barton et al., 2023; McGarrah et al., 2023). The selection was guided by findings from metabolomic studies reporting significantly altered plasma levels of these amino acids in CAD patients and their established biological roles in the cardiovascular system (da Silva et al., 2023; Kurhaluk et al., 2025). The ligand molecules were converted into three-dimensional structures using the Schrödinger LigPrep module. Protonation states and tautomeric forms were optimized at physiological pH (7.4) using the Epik tool (Kaya et al., 2025). Energy minimization was performed using the OPLS4 force field.

2.2. Protein Selection and Preparation

Four cardiovascular target proteins were included in the study: ACE (PDB ID: 1O86), eNOS (PDB ID: 3NOS), β_1-AR (PDB ID: 2VT4), and TRPV2 (PDB ID: 8FFM). These proteins are validated therapeutic targets that play central roles in the pathophysiology of CAD (11, 14–16). Crystal structures of the proteins were retrieved from the Protein Data Bank (PDB) and optimized using the Schrödinger Protein Preparation Wizard (Yildirim et al., 2025a). Water molecules outside the binding site were removed, missing atoms were added, and protonation states were adjusted to pH 7.4. Energy minimization was performed using the OPLS4 force field (Lu et al., 2021; Yildirim et al., 2025b).

2.3. Molecular Docking Analysis

Molecular interactions between ligands and target proteins were evaluated using the Schrödinger Suite 2023-1 (Schrödinger, LLC, New York, 2023). Docking simulations were conducted using the Glide module (Halgren et al., 2004; Demirbağ et al., 2025).

2.4. Docking Procedure

A grid box of approximately 20 × 20 × 20 Å was defined around the binding region of each target protein. Preliminary screening was conducted using the Glide Standard Precision (SP) protocol, followed by more detailed analysis with the Glide Extra Precision (XP) algorithm (Halgren et al., 2004; Yildirim et al., 2025b). Resulting ligand conformations were ranked by GlideScore, with more negative values indicating stronger binding affinities.

2.5. Interaction Analysis

Ligand-protein complexes with the highest binding scores were selected for detailed interaction analysis. Hydrogen bonds, π–π stacking, salt bridges, and hydrophobic contacts were visualized and interpreted using the Maestro interface (Demirbağ et al., 2025; Yildirim et al., 2025a).

3. Results

The Glide XP scores obtained in this study demonstrate the binding affinities of six selected amino acids (L-arginine, cystine, L-asparagine, L-isoleucine, L-leucine, and trans-4-hydroxyproline) toward four different cardiovascular target proteins (1O86, 3NOS, 8FFM, 2VT4) (Table 1). These scores reflect the thermodynamic favorability of the protein–ligand interactions, with more negative values indicating stronger and more stable binding.

Table 1. Docking score values (kcal/mol)

	1O86	3NOS	2VT4	8FFM
Arginine	-6.828	-4.652	-3.983	-3.771
Cystine	-10.663	-6.735	-5.706	-3.520
L-Asparagine	-8.467	-6.095	-5.334	-4.525
L-Isoleucine	-7.676	-5.889	-4.959	-3.489
L-Leucine	-7.785	-5.918	-4.481	-3.301
trans-*4-Hydroxyproline*	-9.372	-7.345	-5.581	-5.139

As presented in Table 1, the docking scores ranged from –3.301 to –10.663 kcal/mol. Among all ligands, cystine (–10.663 kcal/mol) and trans-4-hydroxyproline (–9.372 kcal/mol) exhibited the strongest binding affinities, particularly with 1O86 (ACE). This suggests that the 1O86 structure offers the most favorable binding environment for the selected ligands. The 3NOS (eNOS) structure also demonstrated significant interactions, especially with cystine (–6.735 kcal/mol) and L-asparagine (–6.095 kcal/mol). In contrast, 8FFM (TRPV2) and 2VT4 (β_1-AR) presented relatively weaker interaction profiles, as reflected by their lower binding scores compared to the other proteins.

From a ligand-centric perspective, cystine stood out due to its high binding affinities across all protein targets. This behavior may be attributed to its sulfur-containing side chains, which can form disulfide bridges and participate in hydrophobic interactions. Similarly, trans-4-hydroxyproline formed strong complexes with 1O86 and 3NOS proteins through hydrogen bonding facilitated by its hydroxyl group. While L-asparagine showed moderate binding scores, L-arginine, L-isoleucine, and L-leucine displayed weaker binding tendencies with comparatively lower affinities.

The 2D and 3D visualizations of the complexes formed between cystine and trans-4-hydroxyproline with all four target proteins are detailed in Figures 1 and 2, respectively. The strength of these interactions is likely related to the functional groups of the ligands and the electrostatic and steric complementarity of the protein binding pockets.

Overall, the 1O86 protein presented the most optimal binding environment, while cystine and trans-4-hydroxyproline emerged as amino acids capable of forming strong interactions with key cardiovascular protein targets. These findings underscore the potential of molecular docking analyses to contribute to drug design, protein engineering, and the identification of biomolecular recognition sites.

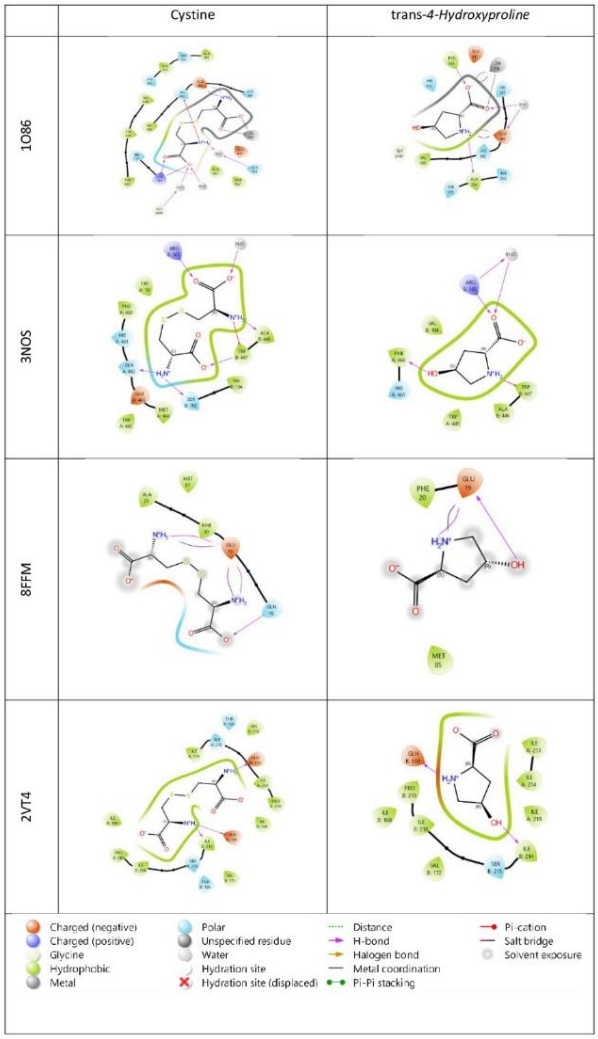

Figure 1. Protein-ligand interaction (2D). 1O86, 3NOS, 8FMM and 2VT4 were subjected to molecular docking studies with compound Cystine and trans-4-Hydroxyproline.

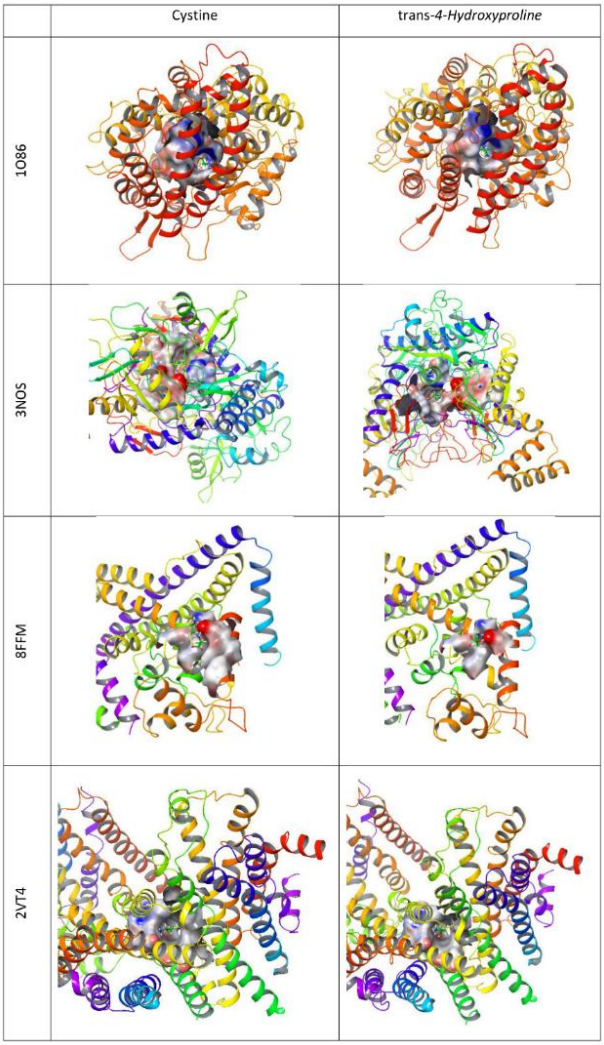

Figure 2. Protein-ligand interaction (3D). 1O86, 3NOS, 8FMM and 2VT4 were subjected to molecular docking studies with compound Cystine and trans-4-Hydroxyproline.

3.1. Protein–Ligand Interactions and Their Structural Basis

Interactions between proteins and ligands are critically important for molecular recognition and biological function. The analyses performed in this study revealed that the examined ligands engaged in diverse types of interactions with their target proteins.

3.2. Molecular-Level Evaluation of Protein–Ligand Interactions

The complexes formed by cystine and trans-4-hydroxyproline with four target proteins (1O86, 3NOS, 8FFM, and 2VT4) were evaluated in detail based on the types of interactions within their binding regions. It was observed that these ligands established hydrogen bonds, ionic interactions, metal coordination, van der Waals contacts, and π–alkyl interactions with the respective protein targets. These versatile interactions contribute significantly to the thermodynamic stability of the resulting complexes.

Hydrogen bonding facilitates specific and directional interactions between the ligand and the protein, enhancing the proper orientation and accommodation of the ligand within the active or binding pocket (Dikme et al., 2024). In addition, π–π and π–alkyl interactions with aromatic surfaces reduce the overall binding energy and increase the stability of the complex (Necip, 2024). Coordination with metal ions, particularly in metalloenzyme structures, stabilizes the binding process through strong and directed interactions.

In the case of 1O86 (ACE), both ligands formed metal coordination with the zinc ion (Zn701) and established hydrogen bonds and van der Waals interactions, resulting in highly stable complexes. Cystine interacted notably with Lys511, Gln281, and Glu384, while trans-4-hydroxyproline formed hydrogen bonds with residues such as Tyr523 and Ala354.

In the 3NOS (eNOS) structure, hydrogen bonds (e.g., ArgB365, TrpB447) and ionic interactions were predominant. Notably, π–alkyl contacts between cystine and PheA460, and trans-4-hydroxyproline and TrpA445, highlighted the aromatic nature of the binding region.

Although 8FFM (TRPV2) exhibited lower binding affinities, both ligands formed weak hydrogen bonds (Gln16, Glu19) and van der Waals contacts (Phe20, Met81) with the protein.

In the case of 2VT4 (β_1-AR), both cystine and trans-4-hydroxyproline engaged in hydrogen bonding and ionic interactions with GluA/B130 and IleB214. Hydrophobic residues such as ValA/B172 and ProA/B219 contributed to interactions reflecting the lipophilic character of the binding surface.

These findings demonstrate that ligands can establish multiple and distinct interaction types across different protein targets, and that binding stability is not solely determined by affinity values, but also by the diversity of interaction types. A summary of the interaction data is presented in Table 2.

Table 2. Protein-ligand interaction

		Hydrogen Bond	Ionic Interaction	Metal Coordination	Van der Waals	π-Alkyl
1O86	Cystine	Lys511, Gln281, Gly2000	Glu384	Zn701	Ala354, Ser355, Tyr520, Phe457	
	trans-4-Hydroxyproline	Tyr523, Glu384, Ala354		Zn701	Val380, Hie513	
3NOS	Cystine	TrpB447, ArgB365	ArgB365, GluA463		TrpA74, PheA460	TrpB447
	trans-4-Hydroxyproline	ArgB365, TrpB447, PheA460	ArgB365		TrpA445, ValB104	TrpB447
8FFM	Cystine	Gln 16	Glu 19		Phe20, Ala23, Met81	Phe20
	trans-4-Hydroxyproline	Glu 19			Phe 20	
2VT4	Cystine	GluA/B130, IleB214	GluA/B130		ProA/B219, ValA/B172, IleA/B218	
	trans-4-Hydroxyproline	GluB130, IleB214	GluB130		IleA/B213–218, ProB219, ValB172	

4. Discussion

This study demonstrated that protein–ligand interactions vary depending on the structural characteristics of the target proteins, and the binding stability of amino acids is significantly influenced by these structural differences. In particular, the consistently high binding affinity of cystine across all protein targets may be attributed to its capacity to form disulfide bridges and its high redox reactivity. Previous studies have also shown that cystine plays a critical role in oxidative stress pathways associated with cardiovascular diseases (Suzuki et al., 2018; Raad et al., 2020; Zhao et al., 2024). Furthermore, it has been reported that cystine contributes significantly to protein stability (Zhao et al., 2024).

Similarly, trans-4-hydroxyproline exhibited notably high binding affinity, particularly to the 1O86 protein, and its ability to form hydrogen bonds likely contributes to conformational stability. Prior studies have demonstrated that trans-4-hydroxyproline interacts with collagen structures in tissue remodeling processes (Rappu et al., 2019; Barton et al., 2023). In contrast, hydrophobic amino acids such as L-leucine and L-isoleucine showed weaker binding affinities, with higher (less negative) docking scores, indicating a lower compatibility with the selected protein binding pockets. This may be associated with the sensitivity of hydrophobic interactions to the microenvironment of the protein surface (Ye et al., 2022). Our findings indicate that multifaceted interactions—including hydrogen bonding, ionic interactions, and metal coordination—particularly with the 1O86 protein, enhance the binding stability. Cystine and trans-4-hydroxyproline emerged as strong candidate inhibitors. In particular, the metal coordination with Zn701 and the π–alkyl interactions observed within the 3NOS binding pocket appear to be critical mechanisms that enhance binding specificity. Zn^{2+} ions play a vital role in stabilizing binding cavities and regulating catalytic activity in metalloproteins. In zinc-containing proteins such as ACE, the formation of coordinate bonds with zinc by ligands increases binding selectivity (Borghi and Levy, 2022; Jeong et al., 2023).

These binding profiles are significant not only from a structural standpoint but also in terms of biological and therapeutic implications. For example, the high-affinity binding of cystine to ACE suggests that this amino acid could be considered as a molecular scaffold resembling ACE inhibitors. Similarly, the binding characteristics of trans-4-hydroxyproline to eNOS may provide a basis for developing therapeutic agents aimed at modulating vascular tone and endothelial function (Ahmad et al., 2018; da Silva et al., 2023).

Moreover, these results go beyond merely improving the understanding of protein–ligand recognition mechanisms; they also offer strategic guidance for ligand selection in future small-molecule inhibitor design. High-affinity ligands such as cystine and trans-4-hydroxyproline could be used as model compounds in such in silico studies, representing a valuable approach in rational drug design.

Structural analyses of protein–ligand interactions, such as those presented in this study, are of particular importance in in silico screening and early-phase drug discovery for cardiovascular targets (Stroik et al., 2018). Molecular docking analysis provides a cost-effective and high-throughput pre-screening strategy for identifying bioactive molecules (Halgren et al., 2004; Stroik et al., 2018; Demirbağ et al., 2025). In this context, our study not only modeled molecular interactions but also contributed to target validation, biomarker development, and functional compound selection.

Despite these promising insights, several methodological limitations of molecular docking must be acknowledged. Docking simulations rely on static crystal structures and therefore cannot fully capture protein flexibility or dynamic conformational changes that occur in vivo. Moreover, the simplified scoring functions may not entirely reflect the complex thermodynamics of biomolecular interactions. Consequently, while our results provide valuable preliminary molecular insights, experimental validation through in vitro assays and in

vivo studies remains essential to confirm the biological and clinical relevance of the predicted interactions.

4. Conclusion

Molecular docking analyses revealed that among the six amino acids investigated, Cystine and trans-4-Hydroxyproline exhibited the highest binding affinities across all target proteins, particularly ACE (1O86) and eNOS (3NOS). Their ability to form multiple interactions—such as hydrogen bonds, ionic interactions, metal coordination, and π–alkyl contacts—at the binding sites enhances their pharmacophore potential.

The findings suggest that these amino acids are not only associated with the pathophysiology of coronary artery disease (CAD), but may also serve as molecular scaffolds capable of modulating the function of key cardiovascular target proteins. In this context, Cystine may act as a lead structure for ACE inhibitors, while trans-4-Hydroxyproline emerges as a promising therapeutic candidate with potential to enhance vascular function via modulation of eNOS activity.

These results underscore the utility of molecular docking as a cost-effective, rapid, and reliable screening method in the early stages of drug discovery, especially for exploring the structural basis of protein–ligand interactions. However, limitations arising from the use of static models, exclusion of protein flexibility, and the lack of experimental validation highlight the need for more advanced analyses to assess the clinical relevance of the findings.

It is anticipated that future studies involving dynamic simulations and biological validation will reinforce the role of such computational approaches in the development of novel strategies targeting cardiovascular diseases.

Author Contributions

The percentages of the author's contributions are presented below. All authors reviewed and approved the final version of the manuscript.

	R.D.	A.N.
C	60	40
D	60	40
S	60	40
DCP	60	40
DAI	60	40
L	60	40
W	60	40
CR	60	40
SR	60	40

C=Concept, D= design, S= supervision, DCP= data collection and/or processing, DAI= data analysis and/or interpretation, L= literature search, W= writing, CR= critical review, SR= submission and revision,

Conflict of Interest

The authors declared that there is no conflict of interest.

Ethical Consideration

Ethics committee approval was not obtained as no studies on animals or humans were conducted in this study.

Financial Disclosures

The authors have no conflicts of interest to declare.

References

Ahmad A, Dempsey SK, Daneva Z, Azam M, Li N, Li PL, Ritter JK. 2018. Role of Nitric Oxide in the Cardiovascular and Renal Systems. Int J Mol Sci, 19(9): 2605.

Ahn HJ, Lee H, Park HE, Han D, Chang HJ, Chun EJ, Han HW, Sung J, Jung HO, Choi SY. 2022. Changes in metabolic syndrome burden and risk of coronary artery calcification progression in statin-naïve young adults. Atherosclerosis, 360: 27-33.

Alhayek S, Preuss CV. 2025. Beta 1 Receptors. In: StatPearls. Treasure Island (FL): StatPearls Publishing.

Barton AK, Tzolos E, Bing R, Singh T, Weber W, Schwaiger M, Varasteh Z, Slart RHJA, Newby DE, Dweck MR. 2023. Emerging molecular imaging targets and tools for myocardial fibrosis detection. Eur Heart J Cardiovasc Imaging, 24(3): 261-275.

Borghi C, Levy BI. 2022. Synergistic actions between angiotensin-converting enzyme inhibitors and statins in atherosclerosis. Nutr Metab Cardiovasc Dis, 32(4): 815-826.

da Silva DVT, Baião DDS, Almeida CC, Paschoalin VMF. 2023. A critical review on vasoactive nutrients for the management of endothelial dysfunction and arterial stiffness in individuals under cardiovascular risk. Nutrients, 15(11): 2618.

Demirbağ B, Yildirim M, Cimentepe M, Necip A, Unver H, Tiftik EN. 2025. Novel vanillin-derived Schiff Bases: Synthesis, characterization, antibacterial activity, enzyme inhibition, antioxidant activity, anti-inflammatory activity on LPS-induced RAW264.7 macrophage cell line, and In Silico studies. J Mol Struct, 1338: 142320.

Dikme TG, Necip A, Dikme R, Güneş S. 2024. Effect of phytosterols in apricot kernel on cholesterol: molecular docking. MEHES J, 2(3): 28-38.

Fan Y, Li Y, Chen Y, Zhao YJ, Liu LW, Li J, Wang SL, Alolga RN, Yin Y, Wang XM, Zhao DS, Shen JH, Meng FQ, Zhou X, Xu H, He GP, Lai MD, Li P, Zhu W, Qi LW. 2016. Comprehensive metabolomic characterization of coronary artery diseases. J Am Coll Cardiol, 68(12): 1281-1293.

Gammoh O, Aljabali AAA, Tambuwala MM. 2024. Plasma amino acids in major depressive disorder: between pathology to pharmacology. EXCLI J, 23:62-78.

Halgren TA, Murphy RB, Friesner RA, Beard HS, Frye LL, Pollard WT, Banks JL. 2004. Glide: a new approach for rapid, accurate docking and scoring. 2. Enrichment factors in database screening. J Med Chem, 47(7): 1750-1759.

Jauhiainen R, Vangipurapu J, Laakso A, Kuulasmaa T, Kuusisto J, Laakso M. 2021. The association of 9 amino acids with cardiovascular events in finnish men in a 12-year follow-up study. J Clin Endocrinol Metab, 106(12): 3448-3454.

Jeong WJ, Lee J, Eom H, Song WJ. 2023. A specific guide for metalloenzyme designers: introduction and evolution of metal-coordination spheres embedded in protein environments. Acc Chem Res, 56(18): 2416-2425.

Kaya B, Acar Çevik U, Necip A, Duran HE, Çiftçi B, Işık M, Soyer P, Bostancı HE, Kaplancıklı ZA, Beydemir Ş. 2025. Design, synthesis, biological evaluation, and molecular docking studies

of novel 1,3,4-thiadiazole derivatives targeting both aldose reductase and α-glucosidase for diabetes mellitus. ACS Omega, 10(18): 18812-18828.

Kurhaluk N, Tkaczenko H. 2025. L-Arginine and nitric oxide in vascular regulation-experimental findings in the context of blood donation. Nutrients, 17(4): 665.

Li M, Wu Y, Ye L. 2022. The role of amino acids in endothelial biology and function. Cells, 11(8): 1372.

Libby P, Buring JE, Badimon L, Hansson GK, Deanfield J, Bittencourt MS, Tokgözoğlu L, Lewis EF. 2019. Atherosclerosis. Nat Rev Dis Primers, 5(1): 56.

Lima A, Ferin R, Fontes A, Santos E, Martins D, Baptista J, Pavão ML. 2020. Cysteine is a better predictor of coronary artery disease than conventional homocysteine in high-risk subjects under preventive medication. Nutr Metab Cardiovasc Dis, 30(8): 1281-1288.

Lu C, Wu C, Ghoreishi D, Chen W, Wang L, Damm W, Ross GA, Dahlgren MK, Russell E, Von Bargen CD, Abel R, Friesner RA, Harder ED. 2021. OPLS4: Improving force field accuracy on challenging regimes of chemical space. J Chem Theory Comput, 17(7): 4291-4300.

McGarrah RW. 2023. Branched-chain amino acids in cardiovascular disease. Nat Rev Cardiol, 20(2): 77-89.

Melnychuk I, Sharayeva M, Kramarova V, Lyzogub V. 2023. Platelet amino acid spectrum and gut microbiota, their links in patients with coronary artery disease and atrial fibrillation. Gastroenterologia, 57(4): 227-233.

Miller M, Koch SE, Veteto A, Domeier T, Rubinstein J. 2021. Role of known transient receptor potential vanilloid channels in modulating cardiac mechanobiology. Front Physiol, 12: 734113.

Necip A. 2024. Kardiyovasküler hastalıklarda doğal ürünler: kurkumin ve quercetin moleküler docking. MEHES J, 2(1): 1-9.

Raad M, AlBadri A, Wei J, Mehta PK, Maughan J, Gadh A, Thomson L, Jones DP, Quyyumi AA, Pepine CJ, Bairey Merz CN. 2020. Oxidative stress is associated with diastolic dysfunction in women with ischemia with no obstructive coronary artery disease. J Am Heart Assoc, 9(10): e015602.

Rappu P, Salo AM, Myllyharju J, Heino J. 2019. Role of prolyl hydroxylation in the molecular interactions of collagens. Essays Biochem, 63(3): 325-335.

Stroik DR, Yuen SL, Janicek KA, Schaaf TM, Li J, Ceholski DK, Hajjar RJ, Cornea RL, Thomas DD. 2018. Targeting protein-protein interactions for therapeutic discovery via FRET-based high-throughput screening in living cells. Sci Rep, 8(1): 12560.

Suzuki S, Shino M, Fujikawa T, Itoh Y, Ueda E, Hashimoto T, Kuji T, Kobayashi N, Ohnishi T, Hirawa N, Tamura K, Toya Y. 2018. Plasma cystine levels and cardiovascular and all-cause mortality in hemodialysis patients. Ther Apher Dial, 22(5): 476-484.

Teav T, Königstein K, Wagner J, Knaier R, Infanger D, Streese L, Hinrichs T, Hanssen H, Ivanisevic J, Schmidt-Trucksäss A. 2024. Circulating amino acid signature features urea cycle alterations associated with coronary artery disease. Sci Rep, 14(1): 25848.

Wang K, Oudit G, Gheblawi M. 2020. Angiotensin converting enzyme 2: a double-edged sword. Circulation, 142(5): 426-428.

Wu CH, Mohammadmoradi S, Chen JZ, Sawada H, Daugherty A, Lu HS. 2018. Renin-Angiotensin system and cardiovascular functions. Arterioscler Thromb Vasc Biol, 38(7): e108-e116.

Yang RY, Wang SM, Sun L, Liu JM, Li HX, Sui XF, Wang M, Xiu HL, Wang S, He Q, Dong J, Chen WX. 2015. Association of branched-chain amino acids with coronary artery disease: A matched-pair case-control study. Nutr Metab Cardiovasc Dis, 25(10) :937-942.

Ye J, Zhang Y, Meng J. 2022. Protein–Ligand interactions for hydrophobic charge-induction chromatography: A QCM-D study. Appl Surf Sci, 572: 151420.

Yildirim M, Cimentepe M, Dogan K, Necip A, Amangeldinova M. 2025a. Next-generation antibacterial cryogels: Berberine-infused smart membranes with molecular docking-guided targeting of MRSA and MDR E. coli. Biophys Chem, 325: 107481.

Yildirim M, Dogan K, Necip A, Cimentepe M. 2025b. Naringenin-loaded pHEMA cryogel membrane: preparation, characterization, antibacterial activity and in silico studies. Chem Pap, 79(1): 211-220.

Zhao G, Zhang J. 2024. Molecular dynamics studies of disulfide bonds for enhancing the stability of serine protease PB92. New J Chem, 48(4): 1614-1622.

Black Sea Journal of Engineering and Science
doi: 10.34248/bsengineering.1760593

Open Access Journal
e-ISSN: 2619 – 8991

Review
Volume 8 - Issue 5: 1659-1673 / September 2025

MICROPLASTICS: AN OVERVIEW OF SOURCES, DISTRIBUTION, AND REMOVAL METHODS

Şule SANCAK[1], Arife ŞIMŞEK[2]*, Gülfem BAKAN[1]

[1]*Ondokuz Mayıs University, Faculty of Engineering, Department of Environmental Engineering, 55100, Samsun, Türkiye*
[2]*Ondokuz Mayıs University, Hemp Research Institute, 55100, Samsun, Türkiye*

Abstract: Microplastics (MPs), defined as plastic particles smaller than 5 mm, are persistent pollutants increasingly detected in both aquatic and terrestrial ecosystems due to widespread anthropogenic activity. Their small size and non-biodegradable nature allow them to accumulate and exert complex effects on biotic systems not only through physical presence but also by transporting harmful substances such as endocrine-disrupting chemicals and heavy metals. This review identifies primary and secondary sources of MPs, outlines their environmental distribution pathways, and evaluates their behavior in different ecosystems. Furthermore, it critically examines current microplastic removal technologies, highlighting limitations in spectroscopic and microscopic detection methods and comparing the effectiveness of traditional treatment systems with advanced approaches such as membrane filtration and nanomaterials. The study concludes with targeted recommendations for improving removal efficiency and monitoring strategies, emphasizing the need for interdisciplinary collaboration and policy support to address microplastic pollution sustainably.

Keywords: Aquatic and terrestrial ecosystems, Environmental distribution, Microplastics, Plastic pollution

***Corresponding author:** Ondokuz Mayıs University, Hemp Research Institute, 55100, Samsun, Türkiye
E mail: arife.simsek@omu.edu.tr (A. ŞİMŞEK)
Şule SANCAK https://orcid.org/0000-0003-3236-2316
Arife ŞİMŞEK https://orcid.org/0000-0002-7177-1764
Gülfem BAKAN https://orcid.org/0000-0002-2752-1303

Received: August 07, 2025
Accepted: September 09, 2025
Published: September 15, 2025

Cite as: Sancak Ş, Şimşek A, Bakan G. 2025. Microplastics: an overview of sources, distribution, and removal methods. BSJ Eng Sci, 8(5): 1659-1673.

1. Introduction

Although the rise in plastic production since the Industrial Revolution has often symbolized economic progress, the resulting unsustainable waste generation has become a major contributor to global environmental imbalances. Since the 19th century, plastics have been widely adopted due to their diverse functional characteristics, including mechanical strength, thermal resistance, and sound insulation (Kolluru and Raja; 2025). This lightweight and durable material is used in a wide range of products—including clothing fibers, medical equipment, and paints—to help preserve the freshness of food. Microplastics, particularly those that break down into microscopic particles, are concerning not only due to their small size but also because of their role as chemical carriers and their potential for biological accumulation (Razaviarani et al., 2024; Lin et al., 2025).

Global plastic production has now surpassed 359 million metric tons annually (Pilapitiya and Ratnayake, 2024). Nevertheless, inadequate plastic waste management and insufficient infrastructure for its reduction, reuse, or recycling have turned plastic pollution into a critical environmental issue worldwide (MacLeod et al., 2021). If current production trends continue, it is estimated that human-generated plastic waste will amount to nearly 26 billion metric tons by the year 2050 (Sharma et al., 2020). Insoluble plastic particles measuring between 1 µm and 1000 µm are categorized as microplastics, while those between 1 mm and 5 mm are typically identified as large microplastics (ISO, 2023; Lu et al., 2025). These particles appear in various physical forms—such as fragments, fibers, films, and spheres (Xu et al., 2020)—and are widespread across ecosystems, from oceanic currents to farmland soils. In terrestrial settings, microplastics have been shown to impact soil properties, including structure, porosity, water retention capacity, and nutrient cycling (Dissanayake et al., 2022; Wang et al., 2022). Additionally, they can serve as carriers for chemical additives, heavy metals, antibiotics, and microbial pathogens, thereby expanding the range of contamination and heightening ecological threats (Wang et al., 2020; Noornama et al., 2024).

In scientific references, the term "microplastic" was first coined by Thompson and is defined as synthetic particles, mostly <5 mm in size (Palansooriya et al., 2020). Microplastics are found everywhere in the environment (Bourzac, 2022). They are categorized based on their morphology, size, density, and different polymer properties. Based on their size, plastics are classified as macroplastics (>25 mm), mesoplastics (5-25 mm), and microplastics (1 µm-5 mm).

Microplastics are very persistent and have a slow degradation process (Andrady, 2011). The small size and larger surface area of microplastics increase their ability to adsorb heavy metals, metalloids, polycyclic aromatic

hydrocarbons, pharmaceuticals, and different dyes (Bourzac, 2022). The uncontrolled release of high concentrations of plastics continually pollutes the environment and causes adverse effects on human health, animal health, the natural environment, and ecosystems. Potential human impacts include obesity, asthma, respiratory irritation, cardiovascular disease, and cancer (Malankowska et al., 2021). Therefore, removing microplastics from natural environments is considered a priority for environmental and public health (Wang et al., 2019).

Microplastics enter both aquatic and terrestrial ecosystems through various pathways, including wastewater discharge, surface runoff, river runoff, and atmospheric transport (Hasan Anik et al., 2021; UNEP, 2021; Kalipci et al., 2024). They have been detected in nearly all environmental compartments, including shorelines, surface waters, the water column, sediments, soil, air, ice, and biota (Hasan Anik et al., 2021; UNEP, 2021;). The complexity and scale of microplastic pollution pose significant challenges to global management efforts due to gaps in understanding their distribution, behavior, and impacts in different environments. Furthermore, inconsistencies in classification and the lack of standard analysis methods create significant uncertainties in monitoring and risk assessment processes (UNEP, 2021).

Because there is no obligation to remove microplastics from receiving environments, it is not possible to achieve any limit values in national and international legislation. Therefore, wastewater treatment plants are not designed with microplastic removal in mind. However, findings in the literature indicate that most advanced treatment methods provide high efficiency in microplastic removal. Advanced treatment technologies such as membranes, rapid sand filtration, dissolved air flotation, and disk filters have been shown to yield successful microplastic removal results in wastewater treatment plants. It has also been reported that the effectiveness of microplastic removal can be increased in biological granular activated carbon filter treatment systems by adding electrocoagulation, biological active filters, powdered activated carbon ultrafiltration, and ultrafiltration to conventional treatment systems (Talvitie et al., 2017).

In the current scientific literature, studies on the formation mechanisms, environmental behavior, and biological impacts of microplastics are increasing; however, most of these studies are limited to local sampling and are insufficient to reach generally accepted conclusions. Furthermore, interactive modeling of the meteorological, geochemical, and biotic interactions that influence the environmental behavior of microplastics is still in its early stages. In this context, in developing strategies to prevent and control microplastic pollution, holistic models that include not only engineering-based approaches but also socio-political contexts are needed.

This study critically evaluates the sources, dispersal pathways, and removal strategies of microplastics, particularly the application limits and potential development areas of advanced treatment technologies. The aim is not only to describe the current situation but also to provide conceptual frameworks that will pave the way for new research areas.

2. Sources of Microplastics

To understand the spread of microplastics in the environment, it is necessary to thoroughly analyze the sources of their production and release. Microplastic sources are generally classified into two main groups: primary and secondary. This distinction is not only a matter of definitional convenience but also a critical parameter in determining control strategies.

Primary microplastics are microscopic plastic particles produced directly during industrial processes and widely used in areas such as cosmetics, cleaning products, paint, textiles, and pharmaceuticals. These microplastics are intentionally included in commercial products and are often transported directly into aquatic environments through sewage systems. This, combined with the inability of wastewater treatment systems to capture particles of this size, poses a serious environmental risk (Duis and Coors 2016; Ahmad et al., 2022; Shaji et al., 2025).

Secondary microplastics, on the other hand, are formed when large plastic materials transform into micro-sized materials over time as a result of physical, chemical, and biological decomposition processes. This process accelerates with the interaction of environmental factors such as UV radiation, temperature fluctuations, mechanical abrasion, and microbial degradation. This process promotes fragmentation by causing changes in the surface morphology of plastics, such as fracture, cracking, and bifurcation (Andrady, 2017; Hidayaturrahmab and Lee, 2019).

Figure 1 shows the classification of microplastics into primary and secondary categories based on their origin. When evaluated by polymer type, common plastic types such as polyethylene (PE), polypropylene (PP), polystyrene (PS), polyvinylchloride (PVC), and polyethylene terephthalate (PET) are seen as the dominant components in microplastic pollution (Enfrin et al., 2019). The specific gravity, surface hydrophobicity, additives, and chemical stability of these materials directly affect their behavior in environmental environments. For example, while low-density polymers can float on the water surface for a longer time, those with higher densities quickly pass into the sediment layer (Patidar et al., 2024; Kılıç et al., 2025).

Another important source is the textile industry. Recent research provides experimental evidence of the textile industry's role in microplastic pollution, showing that hundreds of thousands of microfibers can be released in a single wash cycle (Lin et al., 2025). In light of all these findings, the management of microplastic resources is not limited to waste reduction alone, but necessitates systemic interventions such as redesigning production processes, conducting product life cycle analyses, and tightening regulations.

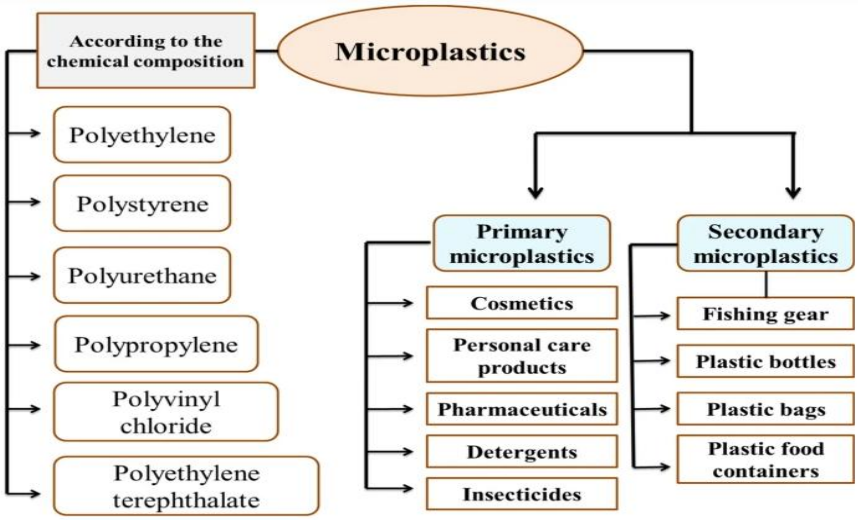

Figure 1. Classification of microplastics according to their sources and chemical components (Andrady, 2017).

3. Dispersion Mechanism of Microplastics

The behavior of microplastics in the environment is not limited to their physical mobility; it is determined by the interaction of chemical, biological, and atmospheric factors. In this context, understanding the dispersal mechanisms of microplastics is critical not only for the distribution of the pollutant but also for toxicological risk assessments, ecosystem modeling, and policy development.

3.1. Water and Sediment Environment

The interaction between water column dynamics and sediment matrices plays a pivotal role in the fate of microplastics. In natural systems, suspended sediments significantly enhance the downward transport and settlement of microplastics, with higher sediment loads increasing the scavenging of microplastic particles toward the bed (Mancini et al., 2023). Turbulent shear conditions further promote heterogeneous aggregation of microplastics with sediment particles, accelerating settlement compared to sediment-free environments; these aggregates may also be subject to resuspension under strong shear flows, potentially leading to secondary contamination events (Li et al., 2022) PubMed. In marine settings, sedimentary processes such as gravity-driven deposits reworked by persistent bottom currents form extensive drift deposits that act as long-term sinks for microplastics—particularly fibers—which can become entrained within these strata and preserved in the sedimentary record. Additionally, microplastics influence ecosystem engineers like tubificid worms, reducing their bioturbation activity and impairing nutrient fluxes at the sediment–water interface (Wazne et al., 2023)

The mobilization of microplastics in aquatic environments varies depending on current regimes, water density, temperature gradients, and particle specific gravity. The tendency of low-density polymers to remain suspended at the surface brings them into more frequent contact with planktonic organisms, while denser materials tend to settle in benthic zones. This sedimentation process is influenced by microenvironmental factors such as sediment structure, organic matter content, and the presence of microbial biofilms (Kopatz et al., 2023; Patidar et al., 2024).

Molecular interactions such as hydrogen bonds, Van der Waals interactions, and electrostatic attraction can facilitate the aggregation of microplastics with particulate matter and biopolymers in the environment. This increases the likelihood of microplastics undergoing chemical transformation processes, altering their reactive surface area and carrying capacity (Leiser et al, 2020; Zhang et al., 2022).

Furthermore, the potential for microplastics to be transported across trophic levels through biocondensation could have novel systemic effects on the structuring of food chains. Such transport has implications not only at the ecological but also at the socioeconomic level, potentially increasing public health risks, particularly in societies with high seafood consumption (Rao et al., 2020; Mutlu et al., 2025).

Aquatic plants and organisms are also important biological factors affecting the movement and distribution of microplastics in the environment. Aquatic plants can limit the free movement of microplastics by adsorbing them on their surfaces, which can contribute to maintaining water quality. Aquatic organisms such as fish, crustaceans, and plankton can ingest microplastics or absorb them through their skin, integrating them into the food chain (Hossain and Olden, 2022).

Furthermore, microorganisms attach to the surface of microplastics and form biofilms, affecting both the distribution of microplastics in the aquatic environment and their degradation processes. Aerobic microorganisms can alter the dispersal mechanism by breaking down microplastics into smaller particles (Ifeanyi et al., 2025).

3.2 Land Environment

As a balancing element between air and water, soil plays a crucial role in regulating the vital carbon, oxygen, and water cycles in the atmosphere and biosphere. Therefore,

it is necessary to evaluate the mechanisms of microplastic dispersion in soil and to thoroughly understand the effects of microplastics on soil. Microplastics that become incorporated into the soil in any way can be transported vertically and horizontally through the soil.

Agricultural activities such as harvesting and plowing, the porous structure and cracks on the soil surface, the extended plant roots, and the use of earthworms in their digestion processes all contribute to the transport of microplastics deep into the soil (Gabet et al., 2003).

Considering urban and rural living spaces and the activities in these areas, fragments from vehicle tires, waste from industrial activities, and the use of many products containing plastic can contaminate soil with microplastics (Fuller and Gautam, 2016).

Agricultural activities can undergo both horizontal and vertical transport due to earthworm movement, root development, and soil porosity. However, the mechanisms of this transport are still not fully understood (Gabet et al., 2003). The use of wastewater treatment sludge as fertilizer and plastic materials used in agriculture, such as greenhouse covers and water pipes, cause soil pollution (Gündoğdu et al., 2018).

Soil erosion is also a contributing factor in the transport of microplastics. Microplastics, particularly those transported from erosion-prone areas to aquatic ecosystems, are a significant source of pollution (Rehm et al., 2021). The mechanism of microplastic transport through runoff and soil erosion involves gaps. Microplastic transport is generally said to originate from canal beds and lake shores. However, the vast majority of studies have focused on large basins, and the sources are generally urban areas (Kiss et al., 2021; Rodrigues et al., 2018).

3.3. Atmospheric Dispersion

Microplastics can be resuspended from land surfaces into the atmosphere and travel long distances on wind. These particles can be directly inhaled by humans and other living organisms (Evangeliou et al., 2020).

The concentration, transport, and accumulation of microplastics in the atmosphere vary depending on meteorological conditions. Microplastic concentrations are higher in indoor areas, particularly due to lower air renewal rates (Chen et al., 2020; Dong et al., 2021).).

Microplastics can serve as nuclei in atmospheric cloud formation and contribute to climate change (Ganguly and Ariya, 2019). This suggests that microplastics in the atmosphere pose not only an environmental but also a climatic threat.

Sources of atmospheric microplastics are typically traffic emissions in urban areas, construction activities, open-air garbage burning, and textile abrasion. The respirable fractions of these particles (below PM2.5) are particularly important for human health (Shruti et al., 2022); Because they have the potential to reach alveoli directly through the respiratory tract, this poses a health risk that could have long-term effects on the cardiopulmonary system.

Meteorological factors (precipitation, drought, wind, sunlight) are decisive in the environmental spread of microplastics (Figure 2).

- Precipitation: Increases surface runoff, transporting terrestrial microplastics to aquatic environments.
- Drought: Increases particle concentration by reducing water volume (Haijiouni et al., 2022; Khalid et al., 2021).
- Wind: Can carry lightweight plastics long distances in the atmosphere.
- UV rays: Cause microplastics to break down into nanoplastics (Andrady et al., 2011).

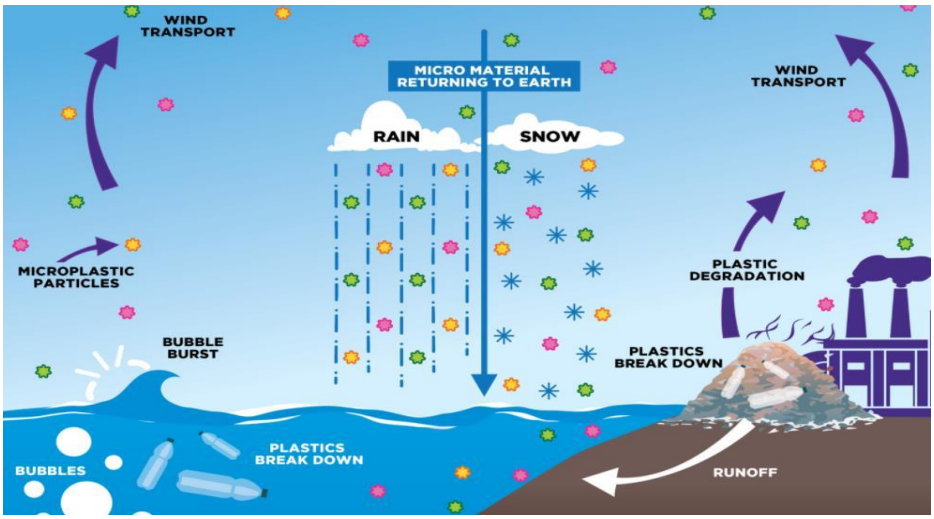

Figure 2. Dispersion of microplastics in the atmosphere (URL-1).

Rainfall facilitates the transport of microplastics from terrestrial to aquatic environments. Furthermore, microplastics suspended in the atmosphere reach water bodies with rainwater. The duration and intensity of rainfall directly affect the amount of microplastics in the aquatic environment. Hydrodynamic conditions influence the horizontal migration of microplastics, directing their deposition processes. For example, strong currents

reduce deposition, while calm waters can cause microplastics to be trapped in sediments. It has been reported that microplastic density is high at the beginning of a rainfall and decreases as the rainfall progresses (Rao et al., 2020).

Drought has the opposite effect of rainfall, leading to increased microplastic concentrations. A positive correlation has been reported between the length of dry periods and the concentration of microplastics in water. Exposure to sunlight is another factor affecting dispersal. Ultraviolet (UV) rays can alter the surface morphology and chemical structure of microplastics, causing them to decompose into smaller nanoplastics (Andrady et al., 2011).

Wind, especially during stormy conditions, can be effective in transporting microplastics to aquatic environments. When wind speeds decrease, microplastics are likely to settle into deeper layers. While low-density microplastics can be carried farther distances by wind, high-density microplastics tend to accumulate more locally (Liu et al., 2022).

4. Ecological and Health Impacts of Microplastics

The impacts of microplastics on ecosystem components are assessed not only at the level of physical obstruction or chemical contamination, but also through systemic dynamics that threaten ecological integrity. These impacts involve multilayered and interactive processes, from the organismal level to the biosphere.

4.1. Impacts on Ecological Systems

The effects of microplastics on environmental biota vary depending on trophic level-specific sensitivities and organismal life strategies. Laboratory and field-based studies in diverse taxonomic groups, such as zooplankton, benthic invertebrates, fish, and birds, indicate that microplastic ingestion can cause numerous physiological effects, such as digestive tract obstructions, reduced energy budgets, growth retardation, and behavioral disruptions (Wright et al., 2013).

At the ecosystem level, microplastics have the potential to alter habitat structure, reduce the permeability of benthic substrates, and disrupt trophic network relationships. This reduces ecological resilience and increases the system's vulnerability to external stressors. Furthermore, microplastics interact with other persistent organic pollutants (POPs) in the environment, acting as vectors, enabling the transport of contaminants to distant ecosystems (Mercogliano et al., 2020).

Due to their surface properties that promote biofilm formation, microplastics can restructure microbial diversity and lead to ecological niche occupation. This poses significant risks to public health, particularly in terms of the transmission and spread of pathogenic microorganisms in aquatic environments (Yan et al., 2024; Wu et al., 2024).

4.2. Effects on Human Health

4.2.1. Possible effects of microplastics on human health

While scientific data on the effects of microplastics on human health is still limited, recent studies have documented the entry of these particles into the human body through oral, dermal, and inhalation routes.

- Microplastics, which enter the human body through a variety of exposure routes, including drinking water, seafood, salt, air, and even breast milk, are thought to have the potential to migrate from the gastrointestinal tract to epithelial cells and enter the systemic circulation (Schwabl et al., 2019).
- Among the additives carried by these particles are chemicals with endocrine-disrupting and neurotoxic effects, such as phthalates, bisphenol A, brominated flame retardants, and heavy metals. Numerous in vitro and in vivo studies have shown that these substances cause oxidative stress by increasing reactive oxygen species at the cellular level, can lead to mitochondrial dysfunction, and can trigger genetic damage (Smith et al., 2018; Akbulut et al., 2025).
- Microplastics with a respirable fraction (PM2.5 and below) can trigger inflammatory processes in the pulmonary epithelium, increase fibrotic responses, and exacerbate chronic respiratory diseases such as asthma. Furthermore, microbial biofilms carried by microplastics are a mechanism that should be considered for pathogen transfer to the respiratory tract (Agull et al., 2021; Eberhard et al., 2024).

4.2.2. Some studies and findings

Figure 3 schematically illustrates the routes of human exposure to MPs and their potential harms. There are no clear results on whether microplastics inhaled by living organisms can enter the bloodstream, their effects on various lung diseases, or the tissue damage caused by microparticles (Amato-Lourenço et al., 2020).

In a study conducted on patients with malignant lung masses, 97% of the samples contained microfibers (Pauly et al., 1998). It is known that microplastics tend to accumulate in the alveoli and bronchi. The human body has defense mechanisms to prevent microplastic accumulation, including sneezing, phagocytosis, and the lymphatic system. However, these mechanisms cannot exclude conditions such as dust overload, cytotoxicity, and oxidative stress (Prata, 2017).

There are studies indicating that microplastics have been detected in the circulatory systems and tissues of some organisms, in addition to the digestive system. Studies on the placentas of women undergoing healthy pregnancies have shown the presence of microplastics (Ragusa et al.; 2021; Huang, 2022).

Microplastics, which are suggested to have suppressive effects on the human immune system, are assumed to have more serious effects, particularly in individuals with immunological compromise (e.g., children, the elderly, and chronically ill patients). However, supporting these hypotheses with robust epidemiological data should be a

priority for future science. Given this data, multidisciplinary research, long-term monitoring studies, and molecular biomarker-based analyses are needed to comprehensively assess the health impacts of microplastics.

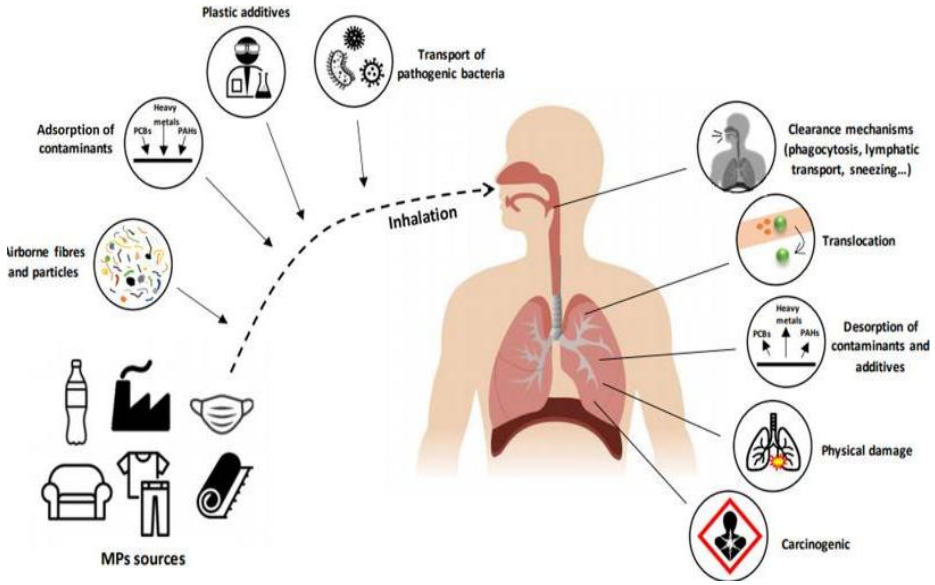

Figure 3. Human exposure pathways to microplastics and potential harms (Agullo et al., 2021).

5. Microplastic Removal Methods

Effectively removing microplastics from the environment is critical for reducing the negative impacts of these pollutants on the ecosystem and human health. Conventional and advanced treatment methods are used for this purpose. Removal efficiency varies depending on the type of method used, the size and density of the microplastics, and the characteristics of the environment.

5.1. Wastewater Treatment Technologies

Wastewater treatment plants (WWTPs) are one of the most significant sources of microplastics for aquatic and terrestrial environments (Alvim et al., 2020). Microplastics arriving at plants from primary and secondary sources accumulate in primary and secondary treatment sludge (Masia et al., 2020).

Figure 4 shows the MP sources entering WWTPs. Wastewater treatment plants consist of primary, secondary, and tertiary treatment processes, which are advanced treatment processes. Because these processes are not designed for microplastic removal, no specific microplastic removal process is implemented (Enfrin et al., 2019). Many factors, such as urban and industrial activities in the region, the economic status and lifestyle of the population, population density, facility type, and meteorological conditions, influence the amount of microplastics entering wastewater treatment plants (Okoffo et al., 2019).

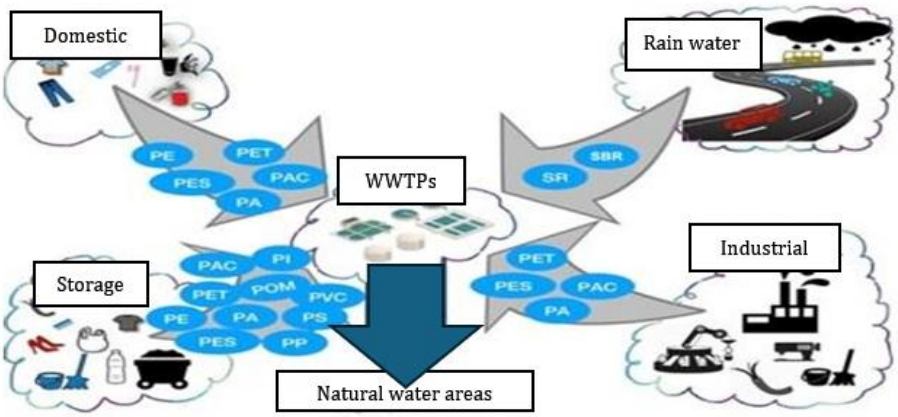

Figure 4. MP sources coming to WWTPs (Ngo et al., 2019).

It is known that microplastic removal in conventional systems, combined with primary and secondary treatment, yields efficient results (Carr et al., 2016; Talvitie et al., 2017). While conventional systems provide

good results in removing microplastics from treatment plants, it is considered possible that daily microplastic discharges are high because these plants operate at high flow rates (Mason et al., 2016; Lee and Kim, 2018; Liu et al., 2021).

Furthermore, it has been determined that a conventional membrane system can efficiently remove some microplastics from wastewater. Membrane technologies, one of the most widely used microplastic removal methods, demonstrate their suitability for microplastic treatment by enabling the removal of highly resistant pollutants found in a wide variety of complex industrial wastewaters (Gurung et al., 2016).

5.1.1. Physical methods

These methods are aimed at removing microplastics directly through physical processes.

- Filtration and Membrane Technologies:
  - Classical membrane systems can effectively remove some microplastics (Gurung et al., 2016).
  - Nanofiltration (NF) is a promising method for removing small particles between 1 nm and 1 µm in size. It can also separate microplastics and the contaminants adsorbed on them based on electrical charge differences (Enyoh et al., 2025).
  - NF also stands out with its low energy consumption and compact system advantages.
- Sedimentation:
  - It is possible to remove microplastics by sedimentation along with heavy metal salts (Lee et al., 2012; Shirasaki et al., 2016).
- Filtration-Sorption Combinations:
  - These systems provide high efficiency when used in conjunction with biological and chemical processes (Liu et al., 2021).

5.1.2. Chemical methods

Chemical methods allow microplastics to react with other substances to form larger structures or to settle.

- Coagulation and Agglomeration (Coagulation-Flocculation):
  - Fe and Al-based salts are used to convert small microplastics into larger, settleable particles.
  - This allows microplastics to be physically separated.
- Electrocoagulation:
  - This is an energy-efficient, low-sludge, and automation-friendly method applied in stirred-batch reactors. It is effective in removing microplastics such as polyethylene (Perren et al., 2018).

5.1.3. Biological methods

These are treatment systems that use microorganisms. Although microplastics are not directly biodegraded, they can be retained in biological processes.

- Activated Sludge Systems:
  - These systems, used in conventional treatment plants, can retain a significant portion of microplastics (Carr et al., 2016; Talvitie et al., 2017).
- Membrane Bioreactors (MBRs):
  - They combine activated sludge systems with membrane technology.
  - They offer higher efficiency in removing microplastics than traditional biological systems (Liu et al., 2021).

Table 1 summarizes the advantages and disadvantages of microplastic removal methods.

5.1.4. Integrated systems (Combinations)

These are systems that utilize physical, chemical, and biological methods together. They are preferred in advanced treatment facilities.

- Biological + Physical + Chemical Methods:
  - For example, MBR + electrocoagulation + coagulation systems can be used together to capture microplastics both mechanically and chemically.
  - Such integrated systems, combined with advanced physical-chemical processes, provide high microplastic removal throughout the entire process (Enfrin et al., 2019; Liu et al., 2021).

Because highly efficient microplastic removal cannot be achieved with a single method alone, interest in integrated systems has increased in recent years. Systems combining chemical flocculation and physical filtration, or hybrid approaches incorporating biological reactors supported by membrane modules, offer success rates exceeding 90% in particle removal (Liu et al., 2023).

However, to increase the field-scale applicability of these systems, pilot studies, cost-benefit analyses, and lifecycle assessments are needed.

Consequently, instead of single-pronged solutions in microplastic removal technologies, shifting to multi-parameter system approaches and modular, adaptive treatment designs will yield more meaningful results in terms of both technical efficiency and environmental sustainability.

5.2. Prevention Strategies

5.2.1. Personal restrictions

One of the most important factors in preventing microplastic pollution is individual awareness. Consumers can reduce microplastic formation by changing certain habits in their daily lives:

- Choosing microplastic-free cosmetic products and reducing the use of single-use plastics are basic measures that can be taken at the individual level.
- Proper separation and collection of household waste can reduce microplastic formation by preventing waste from dispersing into the environment.
- Clothing containing synthetic fibers releases microplastics during washing and drying. Therefore, it is recommended that clothes be washed only when necessary and dried in sunlight if possible.

Supporting organizations working on the environment and raising social awareness are also among the long-term effective methods (Saini and Sharma, 2022).

Table 1. Comparison of microplastic removal methods: advantages and disadvantages

Method Type	Method	Advantages	Disadvantages	References
Physical	Filtration/Membrane Technologies	Effective for small particle retention- Chemical free treatment- High removal efficiency- Compact systems (especially Nanofiltration)	High installation and energy costs- Membrane fouling- Frequent cleaning required	Gurung et al., 2016; Bayo et al., 2020; Enyoh et al., 2025
	Sedimentation	Cost-effective- Suitable for preliminary treatment- Effective for larger particles	Inefficient for small microplastics- Time-consuming- Incomplete removal	Shirasaki et al., 2016; Zhang et al., 2021
	Filtration-Sorption Combinations	High efficiency when combined with biological and chemical processes	Requires system integration	Liu et al., 2021
Chemical	Coagulation – Flocculation	High removal efficiency for small microplastics- Easy integration into existing systems	High chemical and energy consumption	Wulandari et al., 2024
	Electrocoagulation	Low chemical usage- Automation-friendly- Low sludge production	High energy cost- Requires specific reactors	Perren et al., 2018; Weisbart et al., 2020
Biological	Adsorption on Green Algae	Large surface area-to-volume ratio- Alginates secreted by algae retain microplastics	Limited efficiency- Not commercially widespread	Rios et al., 2007
	Bioremediation and Ingestion	Microbial biofilms facilitate retention- Utilizes natural processes	Mechanisms not fully understood- Slow process- Risk of microplastics entering food chains	Anand et al., 2023
	Activated Sludge Systems	Widely used in conventional treatment plants- Retains significant portion of microplastics	Limited efficiency for very small particles	Carr et al., 2016; Talvitie et al., 2017
	Membrane Bioreactors (MBRs)	Higher efficiency than conventional biological systems- Combines membrane filtration with biological treatment	High investment and operating costs- Risk of membrane fouling	Liu et al., 2021

5.2.2. National strategies

Many countries have implemented legal and policy measures to reduce microplastic pollution:

- The United States banned the use of microbeads in rinse-off cosmetic products with the Microbead-Free Water Act (MFWA) enacted in 2015 (MFWA, 2015; UNEP, 2018).
- The USEPA aimed to prevent micro- and nanoplastics from reaching the environment with the Draft National Strategy to Prevent Plastic Pollution published in 2023 (USEPA, 2023).
- Canada imposed restrictions on plastic use in 2020 and conducted public opinion surveys through the end of 2021 (CCME-ZPW, 2019).
- France, Belgium, Italy, Korea, New Zealand, Brazil, and India are other countries that have restricted the use of microbead-containing products (UNEP, 2018).

5.2.3. Global strategies

- Although the United Nations did not specifically address microplastics within the 2015 Sustainable Development Goals, UNEP has launched various prevention programs in this area (UNEP, 2022).
- UNEA (UN Environment Assembly) has been focusing on marine litter since 2014; by 2017, it had established expert teams to address microplastic pollution and, by 2022, had legally established this fight (UNEA, 2019; UNEP, 2022).
- The UN Sustainable Fashion Alliance is one of the key initiatives established to reduce microplastic pollution from textiles (UNEP, 2022).
- The European Commission prepared regulations on the impacts of microplastics as part of the Circular Economy Action Plan in 2020 (Ritchie and Roser, 2018).

5.3. Policies and Regulations

Increased awareness of plastic pollution has led to the development of prevention policies. However, increasing plastic production and consumption demonstrate that existing regulations are inadequate to address the microplastic problem. Therefore, new, more effective policies need to be developed (UN, 2022).

Country-Based Policies:

- Sweden: The recycling rate is over 95%. The country's goals include banning single-use plastics, innovating on biodegradable materials, and generating energy from waste.
- Germany: Plastic recycling is encouraged through the "Pfand" system, which uses returnable bottles.
- South Korea: Systems are enforced for waste separation and supported by sanctions.

- Japan: Stands out with its advanced waste separation systems and use of biodegradable plastics.
- The Netherlands: Constructs roads from recycled plastic; however, the microplastic impacts of this practice are not yet fully known.
- Canada: Aims to ban single-use plastic products by 2030.
- Costa Rica: Aims to become a plastic-free country by 2050 and promotes sustainability through ecotourism programs (URL-2).
- California: Banned microbeads in cosmetic products.
- Washington State: Mandatory plastic bottle refill stations with HB 1085.
- European Union (EU): Banned single-use plastics as of 2021 and developed programs to promote environmentally friendly products (Schultz, 2021).
- Türkiye: As part of the Zero Waste Program, plastic bags have been charged; according to reports by WWF- Türkiye and Boğaziçi University, Türkiye is among the countries that pollute the Mediterranean Sea the most. Therefore, it is expected to play a more active role in international prevention programs.

International Political Initiatives:

UN Plastics Treaty: This treaty, launched in 2022, aims to reduce plastic and microplastic pollution on a global scale (EPA, 2023).

6. Current Research and Future Perspectives

6.1. Current Findings on Microplastic Pollution

Microplastic pollution is a complex problem that threatens not only the environment but also human health. Therefore, continuous and multifaceted scientific research is crucial to identify the presence of microplastics in various environments and analyze their impacts.

Studies Conducted in Türkiye

- Salt Products: FTIR analysis was conducted on 36 samples of 9 different brands of rock, lake, and sea salt from across Türkiye, and 10 different types of microplastics were detected. These results are striking in demonstrating the potential risks microplastics pose to safe food (Özçifçi et al., 2023).
- Milk Samples: Samples taken from 588 dairy cows in the Marmara Region were analyzed using SEM-EDS and ATR-FTIR methods, and microplastics were detected in 89% of the samples (Zipak et al., 2024).
- Soft Drinks: There is evidence that microplastics were detected in all soft drink samples from 10 different brands in Türkiye (Altunışık, 2023).
- Milk-producing animals: The study was conducted on samples (n: 588) taken from various milk-producing animals in the Marmara Region, a major industrial and agricultural region in Türkiye. Microplastics were identified, classified, and quantified using microscopic analysis. Surface morphologies and chemical compositions were evaluated using advanced techniques such as Scanning Electron Microscope Energy Dispersive X-Ray Spectroscopy (SEM-EDS) and Attenuated Total Reflection-Fourier Transform Infrared Spectroscopy (ATR-FTIR). According to the results of the study, microplastics were detected in 89% of the milk samples (Zipak et al., 2024).

These findings indicate that microplastics are widespread in terrestrial and urban environments and should be considered for public health reasons.

International Findings

- Microplastics in Human Tissues: A study conducted at the University of New Mexico, USA, investigated the presence of microplastics in autopsy samples between 1997 and 2024, and found 30 times more microplastics in brain tissue than in liver and kidney tissue. Furthermore, the level of microplastics in samples from 2024 increased by 50% compared to 2016. The higher accumulation of microplastics in patients with dementia suggests that microplastics may be associated with neurological disorders by crossing the blood-brain barrier (Campen et al., 2025).
- Microplastic in breast milk storage bags: A study was conducted with six different brands of breast milk storage bags. The study evaluated the release of microplastics from milk bags to babies. The study identified irregularly shaped microplastics ranging in size from 1 to 300 μm in breast milk placed in these bags. Additionally, submicron-sized particles with irregular spherical or oval shapes ranging from 0.1 to 0.6 μm were also observed. Micro-Raman spectroscopy identified microplastic particles primarily as PE, followed by PET and nylon (Liu et al., 2023).

6.2. Advanced Technologies and Emerging Approaches

Laser technologies and nanofiltration systems have become prominent in recent years for the detection and removal of microplastics:

- Laser Techniques: Laser-based methods such as Raman spectroscopy, LDIR (Quantum Cascade Laser Imaging), LA-ICP-MS, and LIBS are frequently used for the analysis of microplastics (Farshidianfar et al., 2024; Yousaf and Bashir, 2024). These techniques enable the high-sensitivity identification of microplastics from environmental media (water, soil, air) (Sommer et al., 2021).
- Plasma-Assisted Removal: Polystyrene microplastics were degraded by non-thermal plasma-assisted catalytic oxidation at low temperatures, converting 98.4% of the CO_2 into CO_2. The reproducibility of the experiments and the increased CO_2 production demonstrate the stability of the method (Sima et al., 2024).
- Laser-Modified Membranes: Nanofiltration (NF) and ultrafiltration (UF) efficiencies are increased thanks to membranes that can be cleaned or modified using lasers. For example, superhydrophilic graphene oxide (LGO) membranes provide high filtration without

harmful additives (Sun et al., 2024; Pizzichetti et al., 2023).

- Laser-Induced Graphene (LIG): Magnetic Fe_3O_4-LIG particles grown using lasers effectively removed microplastics ranging in size from 2–50 μm from water within 300 minutes. This method is a high-throughput example of magnetic filtration integrated with laser technology (Jeong et al., 2023; Aragón et al., 2025).

6.3. Artificial Intelligence-Enabled Applications

Artificial intelligence (AI) offers revolutionary solutions for the detection, separation, and removal of microplastics from the environment. The use of AI is based on the analysis of microplastic detection, accumulation, separation, identification, and degradation using data processing systems, algorithms, and autonomous systems (Huang and Ullah, 2025). Figure 5 provides an example of an AI procedure used to identify microplastics. AI applications and details for microplastic detection and removal are provided below.

- Data Processing and Optimization: AI-powered algorithms make filtration processes more effective by optimizing pressure, flow rate, and membrane performance in filter systems (Cairone et al., 2024; Huang and Ullah, 2025).
- Machine Learning (ML): ML and neural network algorithms are used to identify plastic types by analyzing microscope and spectrometer data (Fang et al., 2023). AI systems integrated with LIBS technology can quickly identify plastic size and composition (Yang et al., 2023).
- Autonomous Robot Systems: AI-powered robots are used to detect, separate, and collect microplastics by analyzing environmental conditions. These systems can also learn the most appropriate strategy based on changing environmental conditions (Sarker et al., 2024).
- Waste Sorting Systems: Waste robots integrate with infrared sensing systems to ensure the accurate separation of plastics. These systems significantly increase separation accuracy (Martinez-Hernandez et al., 2024).
- Adsorbent Design: AI is also being used in the design of specialized magnetic nanoparticles and adsorbents to capture microplastics. This allows the development of specialized materials suitable for different pollution scenarios (Enyoh et al., 2022; Das et al., 2024).

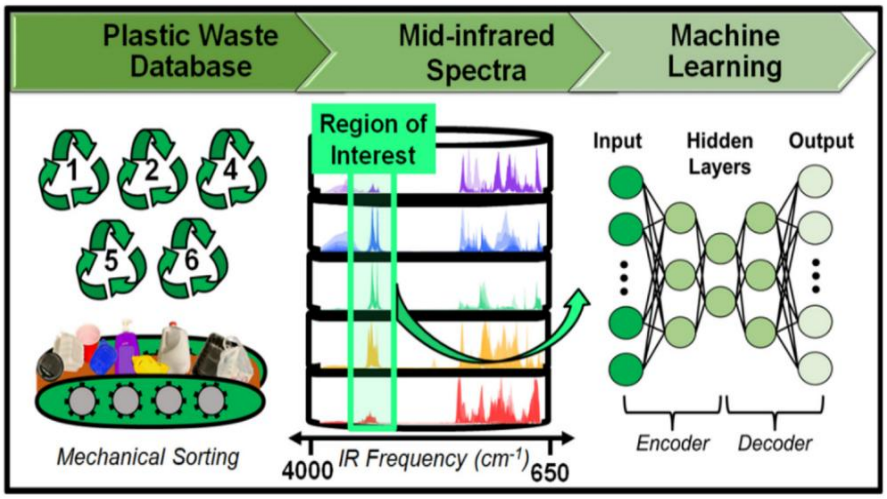

Figure 5. Diagram of the procedure applied in the detection of nano and microplastics with artificial intelligence (Lubongo et al., 2024).

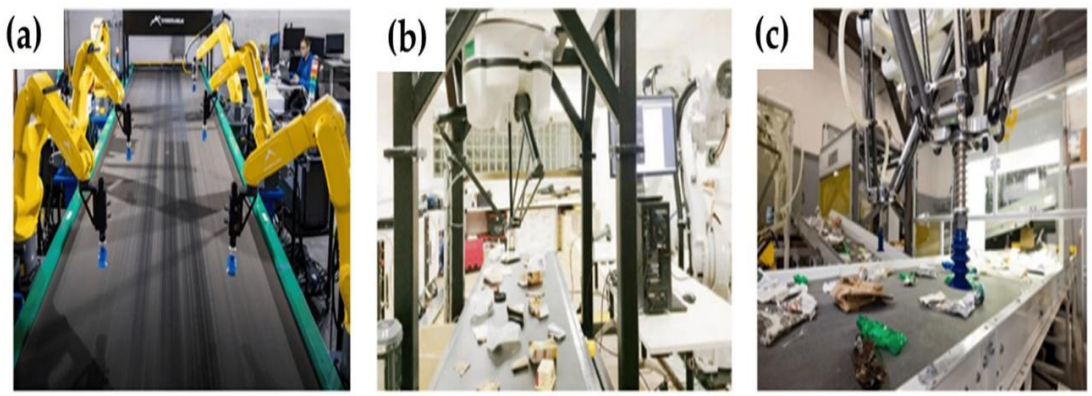

Figure 6. Artificial intelligence-supported separation robots for small plastics (b,c) and plastic waste (a) (Lubongo et al., 2024).

6.4. Emerging Imaging Systems

- Identification with FTIR: Machine learning-based software developed at Monash University that can analyze FTIR data was the first program capable of distinguishing microplastics by recognizing their "chemical signatures" (Frithjof et al., 2025).
- Satellites and Drones: ML systems integrated with image processing algorithms can detect microplastic concentrations on the sea surface and riverbeds, followed by physical cleaning with robotic systems.

Laser systems, nanofiltration technologies, and artificial intelligence applications developed in laboratory environments offer promising solutions for the detection and removal of microplastics. However, the scalability, cost-effectiveness, and environmental impacts of these technologies are still being investigated.

Low-cost alternatives such as biochar, activated carbon, and natural clays, supported by AI, may offer more applicable solutions in large-scale systems (Enyoh et al., 2022). These technologies may make it possible to combat microplastic pollution more effectively in the future.

7. Conclusion

Plastic waste breaks down under environmental conditions through physical and chemical processes, reaching micro-sized particles. When microplastics form as a result of this process, they can exhibit plankton-like behavior and easily enter the food chain. While their low density allows them to drift with plankton on the water surface, studies have shown that these particles also tend to accumulate in the water column and sediment layers.

With developing technologies, plastic products that are more durable and contain various additives pose a significant threat to both current environmental health and future ecosystems due to their potential to absorb toxic chemicals.

In recent years, many countries and international organizations have drawn attention to the impact of microplastics on the environment and living organisms and developed various policies on this issue. These policies include campaigns to raise consumer awareness, legal regulations, usage restrictions, and sanctions.

Microplastic pollution is not limited to aquatic systems but also poses a growing threat to terrestrial environments and the atmosphere. Increasing plastic production and consumption, in particular, increases the plastic load arriving at wastewater treatment plants; however, due to the small size and buoyancy of microplastics, existing treatment systems cannot completely remove these pollutants.

Although various methods have been developed to remove microplastics from environmental environments, most of these studies remain regional and laboratory-scale. To understand the impacts of microplastics on living organisms, greater focus is needed, particularly on exposure through drinking water and food.

Furthermore, one of the main problems noted in the literature is the lack of standard protocols for sampling, analysis, and reporting of microplastics. Studies conducted with different methods and criteria make it difficult to compare results and make generally accepted interpretations.

In this context, the microplastic removal performance of wastewater treatment systems, in particular, needs to be improved. Integrating advanced filtration techniques such as ultrafiltration (UF) and nanofiltration (NF) with conventional treatment systems can significantly increase removal efficiency. Therefore, diversifying research and developing scalable applications is crucial.

With the opportunities offered by today's technology, the use of artificial intelligence (AI)-supported systems in microplastic studies is rapidly becoming widespread. AI algorithms accelerate the detection, classification, distribution monitoring, and impact analysis of microplastics, while also increasing the reliability of the results. In this respect, AI applications are considered a promising tool in the fight against microplastics.

This study examines existing prevention strategies and policy approaches by holistically addressing the sources, environmental distribution, and biodiversity impacts of microplastics. Furthermore, focusing on innovative technologies for the removal of microplastics from the environment, it offers guiding and encouraging recommendations for future research.

Author Contributions

The percentages of the authors' contributions are presented below. All author reviewed and approved the final version of the manuscript.

	Ş.S.	A.Ş.	G.B.
C	40	30	30
D	40	40	20
S	10	20	70
DCP	40	40	20
DAI	40	30	30
L	50	30	20
W	40	40	20
CR	20	40	40
SR	20	60	20

C=Concept, D= design, S= supervision, DCP= data collection and/or processing, DAI= data analysis and/or interpretation, L= literature search, W= writing, CR= critical review, SR= submission and revision.

Conflict of Interest

The authors declared that there is no conflict of interest.

References

Agull AT, Karanasiou A, Moreno T, Lacorte S. 2021. Overview on the occurrence of microplastics in air and implications from the use of face masks during the COVID-19 pandemic. Sci Total Environ, 800: 149555. https://doi.org/10.1016/j.scitotenv.2021.149555

Ahmad S, Singh R, Arfin T, Neeti K. 2022. Fluoride contamination, consequences and removal techniques in water: a review. Environ Sci Adv, 1(5): 620–661.

Akbulut G, Kılıç E. 2025. Determination of Seasonal Microplastic Pollution Variation in Aquatic Environments: Case Study from Iskenderun Technical University Pond. Bull Environ Contam Toxicol, 114(3): 1-6. https://doi.org/10.1007/s00128-024-03979-7

Altunışık A. 2023. Prevalence of microplastics in commercially sold soft drinks and human risk assessment. J Environ Manage, 336: 117720. https://doi.org/10.1016/j.jenvman.2023.117720

Alvim CB, Mendoza-Roca JA, Bes-Pia A. 2020. Wastewater treatment plant as microplastics release source – Quantification and identification techniques. J Environ Manage, 255: 109739. https://doi.org/10.1016/j.jenvman.2019.109739

Amato-Lourenço LF, dos Santos Galvão L, de Weger LA, Hiemstra PS, Vijver MG, Mauad T. 2020. An emerging class of air pollutants: potential effects of microplastics to respiratory human health? Sci Total Environ, 749: 141676. https://doi.org/10.1016/j.scitotenv.2020.141676

Anand U, Dey S, Bontempi E, Ducoli S, Vethaak AD, Dey A, Federici S. 2023. Biotechnological methods to remove microplastics: a review. Environ Chem Lett, 21(3): 1787–1810. https://doi.org/10.1007/s10311-022-01552-4

Andrady AL. 2011. Microplastics in the marine environment. Mar Pollut Bull 62(8): 1596–1605.

Andrady AL. 2017. The plastic in microplastics: A review. Mar Pollut Bull, 119: 12–22.

Aragón D, García-Merino B, Barquín C, Bringas E, Rivero MJ, Ortiz I. 2025. Advanced green capture of microplastics from different water matrices by surface-modified magnetic nanoparticles. Sep Purif Technol, 354: 128813.

Bayo J, Olmos S, Lopez-Castellanos J. 2020. Microplastics in an urban wastewater treatment plant: The influence of physicochemical parameters and environmental factors. Chemosphere, 238: 124593. https://doi.org/10.1016/j.chemosphere.2019.124593

Bourzac K. 2022. Scientists race to study microplastic pollution in the atmosphere. Chem Eng News 100(7): 1-8.

Cairone S, Hasan SW, Choo KH, Li CW, Zarra T, Belgiorno V, Naddeo V. 2024. Integrating artificial intelligence modeling and membrane technologies for advanced wastewater treatment: Research progress and future perspectives. Sci Total Environ, 944: 173999.

Campen MJ, Nihart AJ, Garcia MA, El Hayek E, Liu R, Olewine M, Kingston JD, Castillo EF, Gullapalli RR, Howard T, Bleske B, Scott J, Gonzalez-Estrella J, Gross JM, Spilde M, Adolphi NL, Gallego DF, Jarrell HS, Dvorscak G, Zuluaga-Ruiz ME, West AB. 2025. Microplastics and Nanoplastics in Human Brain Tissues: Evidence of Accumulation and Potential Health Implications. Nat Med, 31: 1114–1119.

Carr SA, Liu J, Tesoro AG. 2016. Transport and fate of microplastic particles in wastewater treatment plants. Water Res 91: 174–182. https://doi.org/10.1016/j.watres.2016.01.002

CCME-ZPW. 2019. Recommended integrated management approach for plastic products to prevent waste and pollution. Environment and Climate Change, Quebec, Canada, pp: 174.

Chen XC, Chen XF, Zhao YH, Zhou H, Xiong X, Wu CX. 2020. Effects of microplastic biofilms on nutrient cycling in simulated freshwater systems. Sci Total Environ, 2020: 719.

Cristian EE, Devi A, Maduka TO, Tyagi L, Rana S, Akuwudike IS, Wang Q. 2025. A Review of Materials for the Removal of Micro- and Nanoplastics from Different Environments. Micro, 5(2): 17.

Das KP, Chauhan P, Staudinger U, Satapathy BK. 2024. Exploring sustainable adsorbents to mitigate micro-/nano-plastic contamination: Perspectives on electrospun fibrous constructs, biochar, and aerogels. Environ Sci Adv, 3: 1217–1243.

Dissanayake PD, Palansooriya KN, Sang MK, Oh DX, Park J, Hwang SY, Igalavithana AD, Gu C, Ok YS. 2022. Combined effect of biochar and soil moisture on soil chemical properties and microbial community composition in microplastic-contaminated agricultural soil. Soil Use Manage, 38(3): 1446–1458.

Dong H, Wang L, Wang X, Xu L, Chen Gong P, Wang C. 2021. Microplastics in a remote lake basin of the Tibetan Plateau: Impacts of atmospheric transport and glacial melting. Environ Sci Technol, 55: 12951–12960.

Duis K, Coors A. 2016. Microplastics in the aquatic and terrestrial environment: sources (with a specific focus on personal care products), fate and effects. Environ Sci Eur, 28(1): 1–25. https://doi.org/10.1186/s12302-015-0069-y

Eberhar DM, Simons GF, Fenning C. 2021. Ethnologue: Languages of the World, 24th Edition, pp: 143.

Enfrin M, Dumee LF, Lee J. 2019. Nano/microplastics in water and wastewater treatment processes Origin, impact and potential solutions. Water Res, 161: 621–638.

Enyoh CB, Devi A, Maduka TO, Tyagi L, Rana S, Akuwudike SA, Wang Q. 2025. A Review of Materials for the Removal of Micro- and Nanoplastics from Different Environments. Micro, 5(2): 17.

Enyoh CE, Fadare OO, Paredes M, Wang Q, Verla AW, Shafea L, Chowdhury T. 2022. An overview of physical, chemical and biological methods for removal of microplastics. In: Microplastics Pollution in Aquatic Media: Occurrence, Detection, and Removal; Springer: Berlin/Heidelberg, Germany, pp: 273–289.

EPA. 2023. Draft National Strategy to Prevent Plastic Pollution.

Evangeliou N, Tichý Q, Eckhardt S, Zwaaftink CG, Brahney J. 2020. Atmospheric transport is a major pathway of microplastics to remote regions. Nat Commun, 11. https://doi.org/10.1038/s41467-020-17201-9

Fang C, Luo Y, Naidu R. 2023. Microplastics and nanoplastics analysis: Options, imaging, advancements and challenges. Trends Anal Chem, 166: 117158.

Farshidianfar A, Nabavi SF, Farshidianfar MH. 2024. The Laser Manufacturing Process: Fundamentals of Process and Applications; CRC Press: Boca Raton, FL, USA, pp: 75-91.

Frithjof H, Boley M, Fong WK. 2025. Machine learning outperforms humans in microplastic characterization and reveals human labelling errors in FTIR data. J Hazard Mater, 487: 136989.

Fuller S, Gautam A. 2016. A procedure for measuring microplastics using pressurized fluid extraction. Environ Sci Technol, 50: 5774–5780. https://doi.org/10.1021/acs.est.6b00816

Gabet EJ, Reichman OJ, Seabloom EW. 2003. The effects of bioturbation on soil processes and sediment transport. Annu Rev Earth Planet Sci, 31: 249–273.

Ganguly M, Ariya PA. 2019. Ice Nucleation of Model Nanoplastics and Microplastics: A Novel Synthetic Protocol and the Influence of Particle Capping at Diverse Atmospheric Environments. ACS Earth Space Chem, 3: 1729–1739. https://doi.org/10.1021/acsearthspacechem.9b00132

Gündoğdu S. 2018. Contamination of table salts from Türkiye with microplastics. Food Addit Contam Part A, 35(5): 1006–1014.

Gurung K, Ncibi MC, Fontmorin JM, Särkkä H, Sillanpää M, 2016. Incorporating submerged MBR in conventional activated

sludge process for municipal wastewater treatment: a feasibility and performance assessment. J Membr Sci Technol, 6(3): 1-6.

Hasan Anik A, Hossain S, Alam M, Binte Sultan M, Hasnine MT, Rahman MM. 2021. Microplastics pollution: a comprehensive review on the sources, fates, effects, and potential remediation. Environ Nanotechnol Monit Manag, 16: 1-8. https://doi.org/10.1016/j.enmm.2021.100530

Hidayaturrahmab H, Lee TG. 2019. A study on characteristics of microplastic in wastewater of South Korea: Identification, quantification, and fate of microplastics during treatment process. Mar Pollut Bull, 146: 696–702.

Hossain MA, Olden JD. 2022. Global meta-analysis reveals diverse impacts of microplastics on freshwater and marine fish. Fish Fish, 23(6): 1439–1454.

Huang H, Ullah J. 2025. Application of artificial intelligence in the analysis of microplastics. In: Analysis of Microplastics and Nanoplastics; Elsevier: Amsterdam, The Netherlands, pp: 225–246.

Huang T. 2022. Maternal exposure to polystyrene nanoplastics during pregnancy and lactation causes liver and testicular toxicity in male mouse offspring. Food Chem Toxicol, 160: 112803. https://doi.org/10.1016/j.fct.2021.112803

Ifeanyi KE, Mustapha S, Khalid H, Paullett UO, Taiwo BA, Aanuoluwa TI, Abiola BO. 2025. Advancing environmental sustainability through emerging AI-based monitoring and mitigation strategies for microplastic pollution in aquatic ecosystems. World J Biol Pharm Health Sci, 22(2): 91–109.

ISO 24187. 2023. Principles for the analysis of microplastics present in the environment. ISO copyright Office, Vernier, Geneva, Switzerland, pp: 20.

Jeong SY, Sugita N, Shin BS. 2023. Fe3O4/Laser-Induced graphene as an adsorbent for microplastics emitted from household wastewater. Int J Precis Eng Manuf-Green Technol, 10: 807–818.

Kalipci E, Cuce H, Temel FA, Dereli MA, Turkmen A. 2024. Microplastic Pollution Profile in the Black Sea Region. Curr Innov Chem Mater Sci, 9: 53–76. https://doi.org/10.9734/bpi/cicms/v9/8473E

Khalid N, Aqeel M, Noman A. 2021. Linking effects of microplastics to ecological impacts in marine environments. Chemosphere, 264(2): 128541. https://doi.org/10.1016/j.chemosphere.2020.128541

Kılıç E, Uğurlu E, Yücel N. 2025. When it comes to microplastic pollution, is the aquaculture industry a victim or perpetrator? Ann Anim Sci, Inpress. https://doi.org/10.2478/aoas-2025-0033

Kiss T, Gönczy S, Nagy T, Mesaros M, Balla A. 2022. Deposition and Mobilization of Microplastics in a Low-Energy Fluvial Environment from a Geomorphological Perspective. Appl Sci, 12: 4367.

Kolluru SK, Raja VK. 2025. Ubiquitous microplastics, sources, impacts, and treatment: Importance of cost-effective ceramic membranes for MPs removal. Water Cycle, 6: 126–150.

Kopatz V, Wen K, Kovács T, Keimowitz AS, Pichler V, Widder J, Vethaak AD, Hollóczki O, Kenner L. 2023. Micro- and nanoplastics breach the blood–brain barrier (BBB): biomolecular corona's role revealed. Nanomaterials, 13: 814. https://doi.org/10.3390/nano13081404

Lee H, Kim Y. 2018. Treatment characteristics of microplastics at biological sewage treatment in Korea. Mar Pollut Bull, 2018: 09.050. https://doi.org/10.1016/j.marpolbul.2018.09.050

Leiser R, Wu GM, Neu TR, Wendt-Potthof K. 2020. Biofouling, metal sorption and aggregation are related to sinking of microplastics in a stratified reservoir. Water Res, 176: 115748.

Li W, Zu B, Hu L, Lan L, Zhang Y, Li J. 2022. Migration behaviors of microplastics in sediment-bearing turbulence: Aggregation, settlement, and resuspension. Mar Pollut Bull, 180: 113775. https://doi.org/10.1016/j.marpolbul.2022.113775

Lin W, Liao L, Ling L, Luo H, Jiang Y, Li X, Yao Y, Yang P. 2025. Combined effects of co-exposure to microcystin-LR and polystyrene microplastics on growth, brain pathology and thyroid hormone homeostasis in adult zebrafish. Ecotoxicol Environ Saf, 291: 117855.

Liu H, Lorenz C, Vianelo, Syberg K, Nielsen AH, Nielsen TG, Vollertsen J. 2023. Exploration of occurrence and sources of microplastics (>10 μm) in Danish marine waters. Sci Total Environ, 865: 161255.

Liu J, Dong C, Zhai Z, Tang L, Wang L. 2021. Glyphosate-induced lipid metabolism disorder contributes to hepatotoxicity in juvenile common carp. Environ Pollut, 269: 116186.

Liu Z, Zhuan Q, Zhang L, Meng L, Fu X, Hou Y. 2022. Polystyrene microplastics induced female reproductive toxicity in mice. J Hazard Mater, 424: 127629.

Lu G, Wang Z, Wang J, Zhang X. 2025. Transboundary impacts of microplastics within planetary boundaries: Regulation and responses of soil-plant systems under climate change. Environ Res, 282: 122080.

Lubongo C, Bin Daej MAA, Alexandridis P. 2024. Developments in technology for sorting plastic for recycling: the emergence of artificial intelligence and the rise of the robots. Recycling, 9: 59.

MacLeod M, Arp HPH, Tekman MB, Jahnke A. 2021. The global threat from plastic pollution. Science, 373(6550): 61–65.

Malankowska M, Echaide-Gorriz C, Coronas J. 2021. Microplastics in marine environment: a review on sources, classification, and potential remediation by membrane technology. Environ Sci Water Res Technol, 7(2): 243–258.

Mancini M, Serra T, Colomer J, Solari L. 2023. Suspended sediments mediate microplastic sedimentation in unidirectional flows. Sci Total Environ, 890: 164363. https://doi.org/10.1016/j.scitotenv.2023.164363

Martinez-Hernandez U, West G, Assaf T. 2024. Low-Cost recognition of plastic waste using deep learning and a multi-spectral near-infrared sensor. Sensors, 24(9): 2821.

Masia P, So D, Ardura A, Laca A, Borrell YJ, Dopico E, Laca A, Machado-Schiaffino G, Diaz M, Garcia-Vazquez E. 2020. Bioremediation as a promising strategy for microplastics removal in wastewater treatment plants. Mar Pollut Bull, 156: 111252. https://doi.org/10.1016/j.marpolbul.2020.111252

Mason SA, Garneau D, Sutton R, Chu Y, Ehmann K, Barnes J, Fink P, Papazissimos D, Rogers DL. 2016. Microplastic pollution is widely detected in US municipal wastewater treatment plant effluent. Environ Pollut, 218: 1045–1054. https://doi.org/10.1016/j.envpol.2016.08.056

Mercogliano R, Avio CG, Regoli F, Anastasio A, Colavita G, Santonicola S. 2020. Occurrence of microplastics in commercial seafood under the perspective of the human food chain: A review. J Agric Food Chem, 68: 5296–5301.

MFWA (U.S. Government Information Microbead-Free Waters Act). 2015. Public Law 114, 114th Congress, Washington DC, USA, pp: 102-121.

Mutlu T, Eryaşar AR, Karaoğlu K, Veske E, Gedik K. 2025. Microplastics pollution in Gulf of Bandırma, Sea of Marmara: Biota and sediment. Mar Pollut Bull 213: 117667. https://doi.org/10.1016/j.marpolbul.2025.117667

Ngo PL, Pramanik BK, Shah K, Roychand R. 2019. Pathway, classification and removal efficiency of microplastics in wastewater treatment plants. Environ Pollut, 255(Pt2): 113326. https://doi.org/10.1016/j.envpol.2019.113326

Nornama, Abidin MNZ, Abu Bakar, Hashim NA. 2024. Innovative

solutions for the removal of emerging microplastics from water by utilizing advanced techniques. Mar Pollut Bull, 206: 116752. https://doi.org/10.1016/j.marpolbul.2024.116752

Okoffo ED, O'Brien S, O'Brien JW, Tscharke BJ. 2019. Wastewater treatment plants as a source of plastics in the environment: a review of occurrence, methods for identification, quantification and fate. Environ Sci Water Res Technol, 11: 16–57.

Özçifçi Z, Başaran B, Akçay HK. 2023. Microplastic contamination and risk assessment in table salts: Türkiye. Food Chem Toxicol, 175: 113698. https://doi.org/10.1016/j.fct.2023.113698

Palansooriya KN, Wijesekara H, Bradney L, Kumarathilaka P, Bundschuh J, Bolan NS, Santos TR, Gu C, Ok YS. 2020. Characteristics of particulate plastics in terrestrial ecosystems. In: Particulate Plastics in Terrestrial and Aquatic Environments. CRC Press, London, UK, pp: 107–124.

Patidar K, Ambade B, Younis AM, Alluhayb AB. 2024. Characteristics, fate, and sources of microplastics contaminant in surface water and sediments of River water. Phys Chem Earth A/B/C, 134: 103596.

Pauly JL, Stegmeier SJ, Allaart HA, Cheney RT, Zhang PJ, Mayer AG, Streck RJ. 1998. Inhaled cellulosic and plastic fibers found in human lung tissue. Cancer Epidemiol Biomark Prev, 7(5): 419–428.

Perren W, Wojtasik A, Cai Q. 2018. Removal of microbeads from wastewater using electrocoagulation. ACS Omega, 3: 3357–3364.

Pilapitiya NT, Ratnayake AS. 2024. The world of plastic waste: A review. Cleaner Mater, 11: 100220.

Pizzichetti ARP, Pablos C, Álvarez-Fernández C, Reynolds K, Stanley S, Marugán J. 2023. Kinetic and mechanistic analysis of membrane fouling in microplastics removal from water by dead-end microfiltration. J Environ Chem Eng, 11: 109338.

Prata JC. 2017. Microplastics in the air: What are their effects on human health? Environ Pollut, 234: 115–126. https://doi.org/10.1016/j.envpol.2017.11.043

Ragusa A, Svelato A, Santacroce C, Catalano P, Notarstefano V, Carnevali O, Papa F, Rongioletti MCA, Baiocco F, Draghi S, D'Amore E, Rinaldo D, Matta M, Giorgini E. 2021. Plasticenta: first evidence of microplastics in human placenta. Environ Int, 146: 106274.

Rao Q, Deng X, Xia W, Chen J, Xie P. 202?. Rainfall is a significant environmental factor of microplastic pollution in inland waters. Sci Total Environ, 732: 139065.

Razaviarani V, Saudagar A, Gallage S, Shrinath S, Arab G. 2024. Comprehensive investigation on microplastics from source to sink. Clean Technol Environ Policy, 26(6): 1755–1782. https://doi.org/10.1007/s10098-024-02738-w

Rehm R, Zeyer T, Schmidt A, Fiener P. 2021. Soil erosion as transport pathway of microplastic from agriculture soils to aquatic ecosystems. Sci Total Environ, 795: 148774.

Rios LM, Moore C, Jones PR. 2007. Persistent organic pollutants carried by synthetic polymers in the ocean environment. Mar Pollut Bull, 54(8): 1230–1237. https://doi.org/10.1016/j.marpolbul.2007.03.022

Ritchie H, Roser M. 2018. Plastic pollution. Our World in Data, Oxford, UK, pp: 200-213.

Rodrigues MO, Gonçalves AMM, Gonçalves FJM, Nogueira HIS, Marques JC, Abrantes N. 2018. Effectiveness of a methodology of microplastics isolation for environmental monitoring in freshwater systems. Ecol Indic, 89: 488–495.

Saini A, Sharma JG. 2022. Emerging microplastic contamination in ecosystem: An urge for environmental sustainability. J Appl Biol Biotechnol, 10(5): 66–75.

Sarker MAB, Imtiaz MH, Holsen TM, Baki AB. 2024. Real-time detection of microplastics using an AI camera. Sensors, 24: 4394.

Schultz J. 2021. State Plastic Bag Legislation. National Environmental Legislators Group, London, UK, pp: 63.

Schwabl P, Köppel S, Königshofer P, Bucsics T, Trauner M, Reiberger T, Liebmann B. 2019. Detection of various microplastics in human stool: a prospective case series. Ann Intern Med, 171: 453–457.

Shaji A, Kamalesh R, Saravanan A, Yaashikaa PR, Vickram AS. 2025. A comprehensive review on bioremediation and biomonitoring of microplastics: Circular bioeconomy and future perspective. Groundw Sustain Dev, 30: 101479. https://doi.org/10.1016/j.gsd.2025.101479

Sharma MD, Elanjickal AI, Mankar JS, Krupadam RJ. 2020. Assessment of cancer risk of microplastics enriched with polycyclic aromatic hydrocarbons. J Hazard Mater, 398: 122994.

Shirasaki N, Matsushita T, Matsui Y, Marubayashi T. 2016. Etkisiinsan enterovirüsünün uzaklaştırılmasında alüminyum hidrolit türleriniPıhtılaşma sürecinde su. Chem Eng J, 284: 786–793.https://doi.org/10.1016/j.cej.2015.09.045.

Shruti VC, Pérez-Guevar F, Kutralam-Muniasam G. 2020. Metro station free drinking water fountain—A potential "microplastics hotspot" for human consumption. Environ Pollut, 261: 114227.

Sima J, Song J, Du X, Lou F, Zhu Y, Lei J, Huang Q. 2024. Complete degradation of polystyrene microplastics through non-thermal plasma-assisted catalytic oxidation. J Hazard Mater, 480: 136313.

Smith M, Love DC, Rochman CM, Neff RA. 2018. Microplastics in seafood and the implications for human health. Curr Environ Health Rep, 5(3): 375–386. https://doi.org/10.1007/s40572-018-0206-z

Sommer C, Schneider L, Nguyen J, Prume J, Lautze K, Koch M. 2021. Identifying microplastic litter with Laser Induced Breakdown Spectroscopy: A first approach. Mar Pollut Bull, 171: 112789.

Sun J, Xiong Y, Jia H, Han L, Yin K. 2024. Superb microplastics separation performance of graphene oxide tuned by laser bombardment. J Hazard Mater, 461: 132599.

Talvitie J, Mikola A, Koistinen A, Setealea O. 2017. Solutions to microplastic pollution – Removal of microplastics from wastewater effluent with advanced wastewater treatment technologies. Water Res, 401: 123.

Talvitie J, Mikola A, Koistinen A, Setealea O, 2017. Solutions to microplastic pollution; Removal of microplastics from wastewater effluent with advanced wastewater treatment technologies. Water Res, 401: 123.

UN. 2022. Nations Sign Up to End Global Scourge of Plastic Pollution. UN News: Global Perspective Human Stories. United Nations; Nairobi, Kenya. https://news.un.org/en/story/2022/03/1113142 (accessed date: July 13, 2024).

UNEA. 2019. Marine litter resolutions. United Nations Environment Assembly; Arendal, Norway, https://wedocs.unep.org/bitstream/handle/20.500.11822/36965/POLSOLSum.pdf (accessed date: July 13, 2024).

UNEP. 2018. Legal Restrictions on Single-Use Plastics and Microplastics. United Nations Environment Programme; Nairobi, Kenya. https://wedocs.unep.org/bitstream/handle/20.500.11822/36965/POLSOLSum.pdf (accessed date: July 13, 2024).

UNEP. 2021. From Pollution to Solution: A Global Assessment of Marine Litter and Plastic Pollution. https://wedocs.unep.org/bitstream/handle/20.500.11822/36965/POLSOLSum.pdf (accessed date: July 13, 2024).

UNEP. 2022. https://www.unep.org/resources/resolutions-treaties-and-decisions/UN-Environment-Assembly-5-2

URL-1. https://yesilgazete.org/gokten-plastik-yagiyor/ (accessed date: July 13, 2024).

URL-2. https://www.plastics-technology.com/articles/top-10-countries-leading-the-fight-against-plastic-pollution (access date: July 24, 2025)

USEPA. 2023. Draft National Strategy to Prevent Plastic Pollution: Part of the Building a Circular Economy for All Series: Executive Summary. United States Environmental Protection Agency; Washington, DC, USA, pp: 251-264.

Wang BL, Wang CF, Hu YW. 2022a. Sorption behavior of Pb (II) onto polyvinyl chloride microplastics affects the formation and ecological functions of microbial biofilms. Sci Total Environ, 832: 1-6.

Wang G, Lu J, Tong Y, Liu Z, Zhou H, Xiayihazi N. 2020. Occurrence and pollution characteristics of microplastics in surface water of the Manas River Basin, China. Sci Total Environ, 710: 136099. https://doi.org/10.1016/j.scitotenv.2020.136099

Wang L, Kaeppler A, Fischer D, Simmchen C. 2019. Photocatalytic TiO2 micromotors for removal of microplastics and suspended matter. ACS Appl Mater Interfaces, 11(36): 32937–32944.

Wang L, Li XG, Lv J, Fu T, Ma Q, Song W, Wang YP, Li FM. 2017. Continuous plastic-film mulching increases soil aggregation but decreases soil pH in semiarid areas. Soil Tillage Res, 167: 46-53.

Wazne M, Mermillod-Blondin F, Vallier M, Hervant F, Dumet A, Nel HA, Kukkola A, Krause S, Simon L. 2023. Microplastics in freshwater sediments impact the role of a main bioturbator in ecosystem functioning. Contam Aquat Terrestrial Environ, Environ Sci Technol, 57(8): 3042-3052. https://doi.org/10.1021/acs.est.2c05662

Weisbart C, Raghavan S, Muralidharan K, Potter BG. 2020. Feasibility of removal of graphene oxide particles from aqueous suspensions by DC/AC electrocoagulation. J Water Process Eng, 36: 101249.

Weston P. 2019. Scientists have found the name of the modern age: the Plastic Age. Sci Publish, London, UK, pp: 54.

Wright SL, Thompson RC, Galloway TS. 2013. The physical impacts of microplastics on marine organisms: a review. Environ Pollut, 178: 483–492. https://doi.org/10.1016/j.envpol.2013.02.031

Wu Y, Hu Q, Che Y, Niu Z. 2024. Opportunities and challenges for plastic depolymerization by biomimetic catalysis. Chem Sci, 15(17): 6200–6217. https://doi.org/10.1039/D4SC00070F

Wulandari M, Marpaung K, Prasaningtyas A, Yorika R, Harfadli MMA, Zulfikar A. 2024. Performance of rapid sand filter dual media for microplastic removal in the water: the effect of microplastic size and effective size of filter media. J Commun Based Environ Eng Manag, 8(1): 103–110.

Xu B, Liu F, Cryder Z, Huang D, Lu Z, He Y, Wang H, Lu Z, Brookes PC, Tang C, Gan J, Xu J. 2020. Microplastics in the soil environment: occurrence, risks, interactions and fate—a review. Crit Rev Environ Sci Technol, 50(21): 2175–2222. https://doi.org/10.1080/10643389.2020.1757107

Xu Y, Ou Q, Wang X, Hou F, Li P, van der Hoek JP, Liu G. 2023. Assessing the mass concentration of microplastics and nanoplastics in wastewater treatment plants by pyrolysis gas chromatography–mass spectrometry. Environ Sci Technol, 57: 3114.

Yan X, Chio C, Li H, Zhu Y, Chen X, Qin W. 2024. Colonization characteristics and surface effects of microplastic biofilms: Implications for environmental behavior of typical pollutants. Sci Total Environ, 937: 173141. https://doi.org/10.1016/j.scitotenv.2024.173141

Yang J, Xu YP, Chen P, Li JY, Liu D, Chu XL. 2023. Combining spectroscopy and machine learning for rapid identification of plastic waste: Recent developments and future prospects. J Clean Prod, 431: 139771. https://doi.org/10.1016/j.jclepro.2023.139771

Yousaf H, Bashir S. 2024. Laser-Induced Breakdown Spectroscopy for the Identification of Microplastics Collected from Arabian Sea of Pakistan. Water Air Soil Pollut, 235: 70. https://doi.org/10.1007/s11270-024-xxx

Zhang T, Jiang B, Xing B, Ya H, Lv M, Wang X. 2022. Current status of microplastic pollution in the aquatic environment, its interaction with other pollutants and its effects on aquatic organisms. Environ Sci Pollut Res, 1–30: 16830–16859. https://doi.org/10.1007/s11356-022-18504-8

Zhang Y, Jiang H, Bian K, Wang H, Wang C. 2021. A critical review of strategies for the control and removal of microplastics from aquatic environments. Environ Chem Eng, 9: 105463. https://doi.org/10.1016/j.jece.2021.105463

Zipak SR, Muratoglu K, Büyükünal SK. 2024. Microplastics in raw milk samples from the Marmara region in Türkiye. J Consum Prot Food Saf, 19: 175–186. https://doi.org/10.1007/s00003-023-01477-2